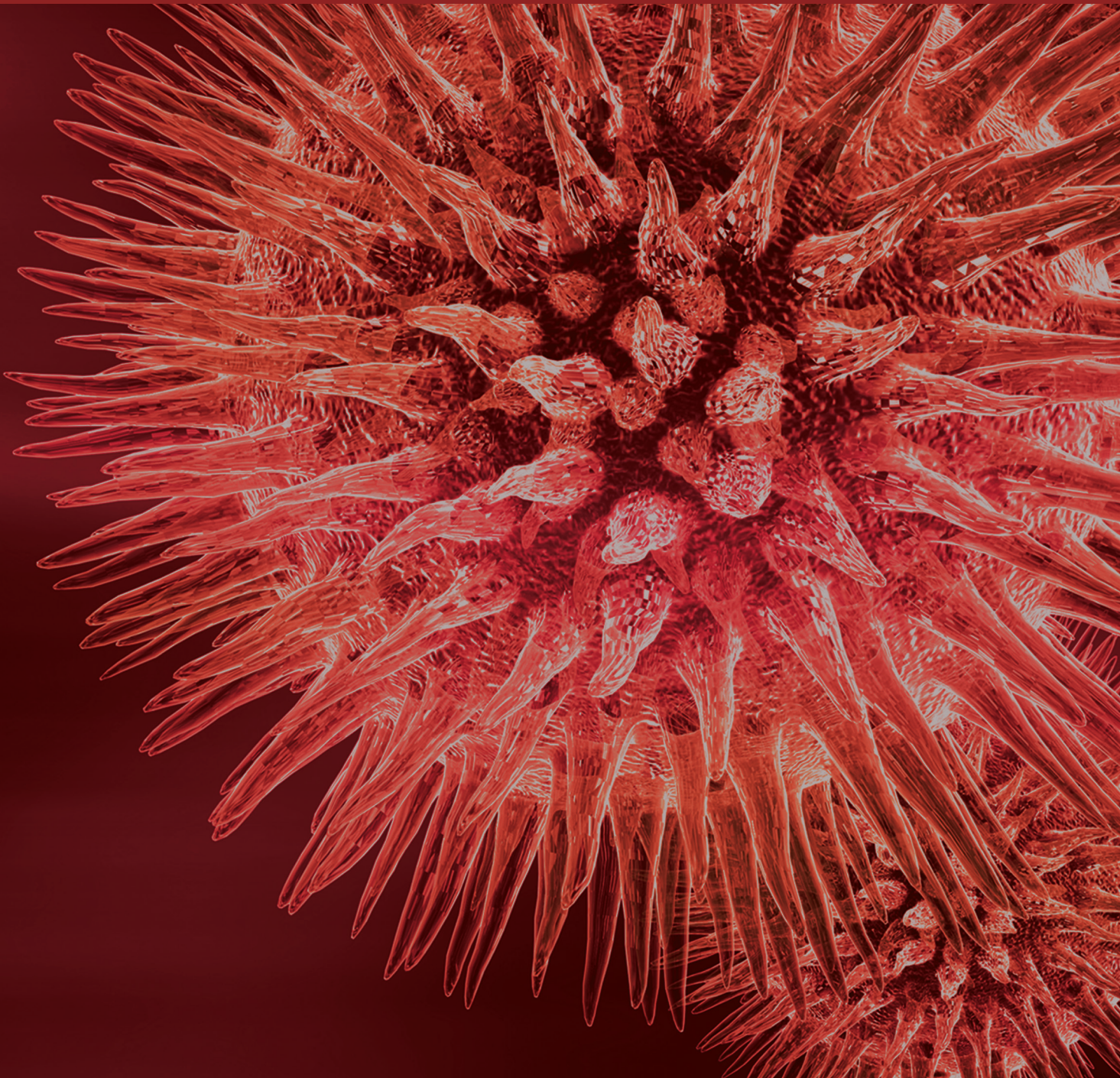


BioMed Research International

# Animal Models of Human Pathology 2014

Guest Editors: Monica Fedele, Oreste Gualillo, and Andrea Vecchione





---

# **Animal Models of Human Pathology 2014**

BioMed Research International

---

## **Animal Models of Human Pathology 2014**

Guest Editors: Monica Fedele, Oreste Gualillo,  
and Andrea Vecchione



---

Copyright © 2015 Hindawi Publishing Corporation. All rights reserved.

This is a special issue published in “BioMed Research International.” All articles are open access articles distributed under the Creative Commons Attribution License, which permits unrestricted use, distribution, and reproduction in any medium, provided the original work is properly cited.

# Contents

**Animal Models of Human Pathology 2014**, Monica Fedele, Oreste Gualillo, and Andrea Vecchione  
Volume 2015, Article ID 721348, 2 pages

**Animal Models and "Omics" Technologies for Identification of Novel Biomarkers and Drug Targets to Prevent Heart Failure**, Yunlong Hou, Juan M. Adrian-Segarra, Manfred Richter, Natalia Kubin, Jaeyoung Shin, Isabella Werner, Thomas Walther, Markus Schönburg, Jochen Pöling, Henning Warnecke, Thomas Braun, Sawa Kostin, and Thomas Kubin  
Volume 2015, Article ID 212910, 10 pages

**Animal Models of Peritoneal Dialysis: Thirty Years of Our Own Experience**, Krzysztof Pawlaczyk, Ewa Baum, Krzysztof Schwermer, Krzysztof Hoppe, Bengt Lindholm, and Andrzej Breborowicz  
Volume 2015, Article ID 261813, 9 pages

**Generation and Characterization of a Transgenic Mouse Carrying a Functional Human  $\beta$ -Globin Gene with the IVSI-6 Thalassemia Mutation**, Giulia Breveglieri, Irene Mancini, Nicoletta Bianchi, Ilaria Lampronti, Francesca Salvatori, Enrica Fabbri, Cristina Zuccato, Lucia C. Cosenza, Giulia Montagner, Monica Borgatti, Fiorella Altruda, Sharmila Fagoonee, Gianni Carandina, Michele Rubini, Vincenzo Aiello, Laura Breda, Stefano Rivella, Roberto Gambari, and Alessia Finotti  
Volume 2015, Article ID 687635, 20 pages

**Mineral and Skeletal Homeostasis Influence the Manner of Bone Loss in Metabolic Osteoporosis due to Calcium-Deprived Diet in Different Sites of Rat Vertebra and Femur**, Marzia Ferretti, Francesco Cavani, Alberto Smargiassi, Laura Roli, and Carla Palumbo  
Volume 2015, Article ID 304178, 12 pages

**Nonalcoholic Steatohepatitis: A Search for Factual Animal Models**, Sheila Cristina L. Sanches, Leandra Naira Z. Ramalho, Marlei Josiele Augusto, Deisy Mara da Silva, and Fernando Silva Ramalho  
Volume 2015, Article ID 574832, 13 pages

**Zebrafish as a Model for the Study of Human Myeloid Malignancies**, Jeng-Wei Lu, Meng-Shan Hsieh, Heng-An Liao, Yi-Ju Yang, Yi-Jung Ho, and Liang-In Lin  
Volume 2015, Article ID 641475, 9 pages

**T Helper 17/Regulatory T Cell Balance and Experimental Models of Peritoneal Dialysis-Induced Damage**, Georgios Liappas, Guadalupe Tirma González-Mateo, Pedro Majano, José Antonio Sánchez-Tomero, Marta Ruiz-Ortega, Raquel Rodrigues Díez, Pilar Martín, Raquel Sanchez-Díaz, Rafael Selgas, Manuel López-Cabrera, and Abelardo Aguilera Peralta  
Volume 2015, Article ID 416480, 9 pages

**Morphological and Biomechanical Differences in the Elastase and AngII *apoE*<sup>-/-</sup> Rodent Models of Abdominal Aortic Aneurysms**, Evan H. Phillips, Alexa A. Yrineo, Hilary D. Schroeder, Katherine E. Wilson, Ji-Xin Cheng, and Craig J. Goergen  
Volume 2015, Article ID 413189, 12 pages

**Manifestation of Hyperandrogenism in the Continuous Light Exposure-Induced PCOS Rat Model**, Xuezhi Kang, Lina Jia, and Xueyong Shen  
Volume 2015, Article ID 943694, 9 pages

**Animal Models of Depression and Drug Delivery with Food as an Effective Dosing Method: Evidences from Studies with Celecoxib and Dicholine Succinate**, João P. Costa-Nunes, Brandon H. Cline, Margarida Araújo-Correia, Andreia Valença, Natalyia Markova, Oleg Dolgov, Aslan Kubatiev, Naira Yeritsyan, Harry W. M. Steinbusch, and Tatyana Strekalova  
Volume 2015, Article ID 596126, 11 pages

***Mycobacterium*-Host Cell Relationships in Granulomatous Lesions in a Mouse Model of Latent Tuberculous Infection**, Elena Ufimtseva  
Volume 2015, Article ID 948131, 16 pages

**Novel Mechanisms of Spinal Cord Plasticity in a Mouse Model of Motoneuron Disease**, Rosario Gulino, Rosalba Parenti, and Massimo Gulisano  
Volume 2015, Article ID 654637, 10 pages

**Distention of the Immature Left Ventricle Triggers Development of Endocardial Fibroelastosis: An Animal Model of Endocardial Fibroelastosis Introducing Morphopathological Features of Evolving Fetal Hypoplastic Left Heart Syndrome**, Shogo Shimada, Christian Robles, Ben M. W. Illigens, Alejandra M. Casar Berazaluze, Pedro J. del Nido, and Ingeborg Friehs  
Volume 2015, Article ID 462469, 10 pages

**Layer 5 Pyramidal Neurons' Dendritic Remodeling and Increased Microglial Density in Primary Motor Cortex in a Murine Model of Facial Paralysis**, Diana Urrego, Julieta Troncoso, and Alejandro Múnera  
Volume 2015, Article ID 482023, 11 pages

**Osteoarticular Expression of Musashi-1 in an Experimental Model of Arthritis**, Francisco O'Valle, Magdalena Peregrina, Vicente Crespo-Lora, Pablo Galindo-Moreno, Maria Roman, Miguel Padial-Molina, Francisco Mesa, Jose Aneiros-Fernandez, David Aguilar, Elena Gonzalez-Rey, Mario Delgado, and Pedro Hernandez-Cortes  
Volume 2015, Article ID 681456, 9 pages

**Morphine Promotes Tumor Angiogenesis and Increases Breast Cancer Progression**, Sabrina Bimonte, Antonio Barbieri, Domenica Rea, Giuseppe Palma, Antonio Luciano, Arturo Cuomo, Claudio Arra, and Francesco Izzo  
Volume 2015, Article ID 161508, 8 pages

**Preclinical Murine Models for Lung Cancer: Clinical Trial Applications**, Amelia Kellar, Cay Egan, and Don Morris  
Volume 2015, Article ID 621324, 17 pages

**Experimentally Induced Mammalian Models of Glaucoma**, Makoto Ishikawa, Takeshi Yoshitomi, Charles F. Zorumski, and Yukitoshi Izumi  
Volume 2015, Article ID 281214, 11 pages

**Development of a Model of Chronic Kidney Disease in the C57BL/6 Mouse with Properties of Progressive Human CKD**, Zahraa Mohammed-Ali, Gaile L. Cruz, Chao Lu, Rachel E. Carlisle, Kaitlyn E. Werner, Kjetil Ask, and Jeffrey G. Dickhout  
Volume 2015, Article ID 172302, 10 pages

**Animal Models in Cardiovascular Research: Hypertension and Atherosclerosis**, Xin-Fang Leong, Chun-Yi Ng, and Kamsiah Jaarin  
Volume 2015, Article ID 528757, 11 pages

**Intratracheal Bleomycin Aerosolization: The Best Route of Administration for a Scalable and Homogeneous Pulmonary Fibrosis Rat Model?**, Alexandre Robbe, Alexandra Tassin, Justine Carpentier, Anne-Emilie Declèves, Zita Léa Mekinda Ngoni, Denis Nonclercq, and Alexandre Legrand  
Volume 2015, Article ID 198418, 10 pages

**Methylglyoxal Induced Basophilic Spindle Cells with Podoplanin at the Surface of Peritoneum in Rat Peritoneal Dialysis Model**, Ichiro Hirahara, Hideki Sato, Toshimi Imai, Akira Onishi, Yoshiyuki Morishita, Shigeaki Muto, Eiji Kusano, and Daisuke Nagata  
Volume 2015, Article ID 289751, 7 pages

**CD40 Ligand Deficient C57BL/6 Mouse Is a Potential Surrogate Model of Human X-Linked Hyper IgM (X-HIGM) Syndrome for Characterizing Immune Responses against Pathogens**, Catalina Lopez-Saucedo, Rodolfo Bernal-Reynaga, Jesus Zayas-Jahuey, Silvia Galindo-Gomez, Mineko Shibayama, Carlos Garcia-Galvez, Sergio Estrada-Parra, and Teresa Estrada-Garcia  
Volume 2015, Article ID 679850, 11 pages

**Biochemical and Functional Comparisons of *mdx* and *Sgcg*<sup>-/-</sup> Muscular Dystrophy Mouse Models**, Nathan W. Roberts, Jenan Holley-Cuthrell, Magdalis Gonzalez-Vega, Aaron J. Mull, and Ahlke Heydemann  
Volume 2015, Article ID 131436, 11 pages

**SERCA2 Haploinsufficiency in a Mouse Model of Darier Disease Causes a Selective Predisposition to Heart Failure**, Vikram Prasad, John N. Lorenz, Valerie M. Lasko, Michelle L. Nieman, Wei Huang, Yigang Wang, David W. Wiczorek, and Gary E. Shull  
Volume 2015, Article ID 251598, 21 pages

**The Ovariectomized Rat as a Model for Studying Alveolar Bone Loss in Postmenopausal Women**, Bryan D. Johnston and Wendy E. Ward  
Volume 2015, Article ID 635023, 12 pages

**Ciclamilast Ameliorates Adjuvant-Induced Arthritis in a Rat Model**, Zhi-cheng Zhang, Shui-juan Zhang, Bo Jin, Yujin Wu, Xin-fu Yang, Bing Yu, and Qiang-min Xie  
Volume 2015, Article ID 786104, 11 pages

**Inhibitory Effects of Eucalyptus and Banaba Leaf Extracts on Nonalcoholic Steatohepatitis Induced by a High-Fructose/High-Glucose Diet in Rats**, Yoshihisa Takahashi, Keiichiro Sugimoto, Yurie Soejima, Arisa Kumagai, Tatsuki Koeda, Aiko Shojo, Kazuya Nakagawa, Naoki Harada, Ryoichi Yamaji, Hiroshi Inui, Toshikazu Yamanouchi, and Toshio Fukusato  
Volume 2015, Article ID 296207, 9 pages

**Early-Onset Diabetic E1-DN Mice Develop Albuminuria and Glomerular Injury Typical of Diabetic Nephropathy**, Mervi E. Hyvönen, Vincent Dumont, Jukka Tienari, Eero Lehtonen, Jarkko Ustinov, Marika Havana, Hannu Jalanko, Timo Otonkoski, Päivi J. Miettinen, and Sanna Lehtonen  
Volume 2015, Article ID 102969, 11 pages

**Effect of Ovariectomy on Stimulating Intracortical Remodeling in Rats**, Chun Lei Li, Xi Ling Liu, Wei Xin Cai, Weijia William Lu, Roger A. Zwahlen, and Li Wu Zheng  
Volume 2014, Article ID 421431, 7 pages

## Editorial

# Animal Models of Human Pathology 2014

**Monica Fedele,<sup>1</sup> Oreste Gualillo,<sup>2</sup> and Andrea Vecchione<sup>3</sup>**

<sup>1</sup>*Istituto per l'Endocrinologia e l'Oncologia Sperimentale (IEOS), CNR, 80131 Naples, Italy*

<sup>2</sup>*Santiago University Clinical Hospital, Instituto de Investigación Sanitaria de Santiago (IDIS), 15706 Santiago de Compostela, Spain*

<sup>3</sup>*Department of Clinical and Molecular Medicine, Sapienza University of Rome, 00100 Rome, Italy*

Correspondence should be addressed to Monica Fedele; [mfedele@unina.it](mailto:mfedele@unina.it)

Received 30 March 2015; Accepted 30 March 2015

Copyright © 2015 Monica Fedele et al. This is an open access article distributed under the Creative Commons Attribution License, which permits unrestricted use, distribution, and reproduction in any medium, provided the original work is properly cited.

In this special issue we have assembled original research as well as review articles describing researches in which animal models, ranging from small vertebrates to larger animals, have been used for either understanding the molecular events underlying a disease or improving therapy in various fields of medicine. Despite the widespread use of *in vitro* systems that allow recapitulating almost all the processes involved in the development of a disease, only the use of animal models enable us to reproduce onset mechanisms of human disease, thereby providing the only system known today to test new drugs for therapeutic interventions. Last year has been an exciting year for animal models. Indeed one of the most extraordinary discoveries of the last years, which has been largely implemented in 2014 transforming and expanding our ability to model human diseases in animals, has been the CRISPR- (clustered regularly interspaced short palindromic repeat-) Cas9 (CRISPR-associated nuclease 9) system, an easy method to efficiently manipulate the genome of any organism [1, 2]. This gene editing approach is based on a RNA-guided nuclease (Cas9) that generates targeted double-stranded DNA breaks and coopts the endogenous cellular pathways to repair them while introducing precise changes into the genome. The specificity of the genomic locus where Cas9 is recruited is driven by a small guide RNA (gRNA) that is complementary to the target site. The CRISPR-Cas9 system is a revolutionary technology that is being applied in a wide variety of organisms, including mice, rats, zebrafish, monkeys, and butterflies [3–7]. One of the best explored human pathologies using this method has been cancer. Two sister studies published in December 2014 on Nature efficiently approached the CRISPR/Cas9 system to induce specific mutations in mice. The group of A. Ventura developed

a new mouse model of Eml4-Alk-driven lung cancer by inducing the specific chromosomal rearrangement that leads to the generation of the EML4-ALK oncogene. The resulting tumors display histopathological and molecular features typical of ALK(+) human non-small cell lung cancer (NSCLC) and respond to treatment with ALK inhibitors [8]; using a well-established mouse model of lung cancer, T. Jacks group functionally characterized a panel of candidate tumor suppressor genes by inducing specific knockout mutations by the CRISPR/Cas9 method [9].

On the side of preclinical studies for drug discovery, the 2014 year has been also characterized by a surge in the numbers of studies employing the zebrafish model to discover and test new anticancer drugs. Indeed, in an era of crisis like that one, we are going through chemical screens in zebrafish result much more rapid and less expensive than the current preclinical studies, which are often bulky and costly, thus limiting the number of new drugs that can efficiently proceed to be used as therapy [10]. The zebrafish is a powerful model system for studying human cancer because of the ease with which it can be genetically manipulated, and the opportunity to be directly observed in transparency. Therefore, several mutant and transgenic zebrafish have been generated to model human cancers and have been used for *in vivo* drug screenings. In particular, xenotransplantation of human cancer cells into zebrafish embryos enables a direct *in vivo* evaluation of patient-derived tumor material in a cost-effective and time-efficient manner.

We hope that this special issue will serve to all the readers as valuable source of scientific background and inspiration in this exciting field of research.

## Acknowledgment

We sincerely thank all the contributors, the reviewers, and the publishing team for their enthusiasm and hard work.

Monica Fedele  
Oreste Gualillo  
Andrea Vecchione

## References

- [1] L. Cong, F. A. Ran, D. Cox et al., “Multiplex genome engineering using CRISPR/Cas systems,” *Science*, vol. 339, no. 6121, pp. 819–823, 2013.
- [2] P. Mali, L. Yang, K. M. Esvelt et al., “RNA-guided human genome engineering via Cas9,” *Science*, vol. 339, no. 6121, pp. 823–826, 2013.
- [3] W. Y. Hwang, Y. Fu, D. Reyon et al., “Efficient genome editing in zebrafish using a CRISPR-Cas system,” *Nature Biotechnology*, vol. 31, no. 3, pp. 227–229, 2013.
- [4] D. Li, Z. Qiu, Y. Shao et al., “Heritable gene targeting in the mouse and rat using a CRISPR-Cas system,” *Nature Biotechnology*, vol. 31, no. 8, pp. 681–683, 2013.
- [5] H. Wang, H. Yang, C. S. Shivalila et al., “One-step generation of mice carrying mutations in multiple genes by CRISPR/Cas-mediated genome engineering,” *Cell*, vol. 153, no. 4, pp. 910–918, 2013.
- [6] Y. Wang, Z. Li, J. Xu et al., “The CRISPR/Cas System mediates efficient genome engineering in *Bombyx mori*,” *Cell Research*, vol. 23, no. 12, pp. 1414–1416, 2013.
- [7] Y. Niu, B. Shen, Y. Cui et al., “Generation of gene-modified cynomolgus monkey via Cas9/RNA-mediated gene targeting in one-cell embryos,” *Cell*, vol. 156, no. 4, pp. 836–843, 2014.
- [8] D. Maddalo, E. Manchado, C. P. Concepcion et al., “In vivo engineering of oncogenic chromosomal rearrangements with the CRISPR/Cas9 system,” *Nature*, vol. 516, no. 7531, pp. 423–427, 2014.
- [9] F. J. Sánchez-Rivera, T. Papagiannakopoulos, R. Romero et al., “Rapid modelling of cooperating genetic events in cancer through somatic genome editing,” *Nature*, vol. 516, no. 7531, pp. 428–431, 2014.
- [10] C. J. Veinotte, G. Dellaire, and J. N. Berman, “Hooking the big one: the potential of zebrafish xenotransplantation to reform cancer drug screening in the genomic era,” *Disease Models & Mechanisms*, vol. 7, no. 7, pp. 745–754, 2014.

## Review Article

# Animal Models and “Omics” Technologies for Identification of Novel Biomarkers and Drug Targets to Prevent Heart Failure

**Yunlong Hou,<sup>1</sup> Juan M. Adrian-Segarra,<sup>1</sup> Manfred Richter,<sup>2</sup> Natalia Kubin,<sup>1</sup> Jaeyoung Shin,<sup>1</sup> Isabella Werner,<sup>3</sup> Thomas Walther,<sup>2</sup> Markus Schönburg,<sup>2</sup> Jochen Pöling,<sup>1,4</sup> Henning Warnecke,<sup>4,5</sup> Thomas Braun,<sup>1</sup> Sawa Kostin,<sup>1</sup> and Thomas Kubin<sup>1</sup>**

<sup>1</sup>Department of Cardiac Development and Remodelling, Max Planck Institute for Heart and Lung Research, Ludwigstrasse 43, 61231 Bad Nauheim, Germany

<sup>2</sup>Department of Cardiac Surgery, Kerckhoff Clinic, Benekestrasse 2-8, 61231 Bad Nauheim, Germany

<sup>3</sup>Department of Thoracic and Cardiac Surgery, Goethe University Frankfurt am Main, 60323 Frankfurt am Main, Germany

<sup>4</sup>Department of Cardiac Surgery, Schüchtermann-Clinic, Ulmenallee 11, 49214 Bad Rothenfelde, Germany

<sup>5</sup>University of Witten/Herdecke, Alfred-Herrhausen-Straße 50, 58448 Witten, Germany

Correspondence should be addressed to Jochen Pöling; [jochen.poeling@mpi-bn.mpg.de](mailto:jochen.poeling@mpi-bn.mpg.de), Sawa Kostin; [sawa.kostin@mpi-bn.mpg.de](mailto:sawa.kostin@mpi-bn.mpg.de), and Thomas Kubin; [thomas.kubin@mpi-bn.mpg.de](mailto:thomas.kubin@mpi-bn.mpg.de)

Received 26 September 2014; Accepted 26 November 2014

Academic Editor: Oreste Gualillo

Copyright © 2015 Yunlong Hou et al. This is an open access article distributed under the Creative Commons Attribution License, which permits unrestricted use, distribution, and reproduction in any medium, provided the original work is properly cited.

It is now accepted that heart failure (HF) is a complex multifunctional disease rather than simply a hemodynamic dysfunction. Despite its complexity, stressed cardiomyocytes often follow conserved patterns of structural remodelling in order to adapt, survive, and regenerate. When cardiac adaptations cannot cope with mechanical, ischemic, and metabolic loads efficiently or become chronically activated, as, for example, after infection, then the ongoing structural remodelling and dedifferentiation often lead to compromised pump function and patient death. It is, therefore, of major importance to understand key events in the progression from a compensatory left ventricular (LV) systolic dysfunction to a decompensatory LV systolic dysfunction and HF. To achieve this, various animal models in combination with an “omics” toolbox can be used. These approaches will ultimately lead to the identification of an arsenal of biomarkers and therapeutic targets which have the potential to shape the medicine of the future.

## 1. Introduction

The need of the body for supply of nutrition and oxygen requires continuous cardiac contraction. Physiological workload such as endurance training and pregnancy increases ventricular mass in order to perpetuate the “status quo.” Ventricular architecture and the differentiation status of the myocardium are essentially maintained and are features of physiological hypertrophy [1–3]. When the heart is not able to respond physiologically, for example, due to coronary artery disease, arterial hypertension, or a cardiomyopathy, myocardial changes take place that affect the protein composition and protein localization on the cellular as well as on the extracellular level [4, 5]. This ventricular remodeling leads to the activation of an evolutionary conserved “fetal gene

program.” Reactivation of this program is a potential strategy when the heart is challenged by unfavorable mechanical and metabolic workloads in order to prevent transition from compensated hypertrophy to HF [3, 6, 7]. However, this initially “programmed cell survival” may also lead to pathophysiological alterations and compromised pump function when hypertrophic signals are chronically released [3, 6, 8, 9]. It is quite clear that the understanding of this transition is of clinical importance in order to halt and hopefully revert adverse cardiac remodeling. However, the classical view of HF as a simple hemodynamic disorder puts emphasis on a strategy to reduce unfavorable workload and does not address the complex interplay of structure and function [10].

It has been previously demonstrated that a structure-function relationship exists in human patients with end stage

HF [6, 8, 11–17]. The degree of myocardial dysfunction is inversely related to cardiomyocyte degeneration, fibrosis, and macrophage infiltration and suggests a mutual influence of cardiac structure and function. Importantly, the degree of postoperative recovery of patients with a poor *structure-function* relationship is less favourable [8, 9]. A consensus paper on cardiac remodeling stressed that the determination of the ejection fraction reliably initiates the treatment of HF but does not evoke consensus among physicians in the treatment regimen [18]. As a consequence, therapeutic interventions which only aim to improve cardiac output and blood flow do not necessarily target the altered ultrastructure of the heart and in addition do not necessarily prevent cardiac remodeling or attenuate HF. Therefore, this consensus paper concludes that “clinicians should understand the relationship between remodeling and HF progression” [18]. In addition, the list of genes and proteins known to be involved in HF is far from being complete and represents probably only the “tip of the iceberg” [15]. In order to achieve a more comprehensive understanding of the transition from compensated adaptation to HF the combination of state-of-the-art profiling techniques with adequate animal models should lead to the identification of disease relevant molecules [19, 20]. Here, we introduce animal models with critical features of human cardiac disease and relevant strategies to identify novel drug targets and biomarker utilizing proteome as well as transcriptome approaches.

## 2. Animal Models of Heart Failure Mimic the Human Cardiac Pathology

Under physiological workload all cardiac cavities are maintained in a “status quo” (Figure 1(a), Con). Increases in workload might be tolerated by a balanced enlargement of the heart until the workload exceeds the physiological cardiac capability to respond appropriately. Then cardiac remodeling is initiated and alterations of the cellular and extracellular protein composition turn into a major burden disturbing the structure-function relationship (Figures 4(a) and 4(b)). As a consequence alterations in the protein composition cause changes in hemodynamic load and vice versa. Patients with aortic stenosis show an increase in the thickness of the left ventricular wall, and the heart appears to be enlarged with an overall progression in mass of the ventricle and septum (Figure 1(a), HT). When the load is persistent the heart might undergo an irreversible decompensation and dilation [8, 21]. Myocardial structural changes observed in patients with aortic stenosis can be mimicked in a mouse model of transversal aortic constriction [20, 22]. Within the first three weeks the heart develops compensatory hypertrophy (Figure 1(b), HT), and if the heart is not released from hemodynamic overload, as seen in human patients, the chronic maladaptive response leads to cardiac dilation (Figure 1(a), HT) and potentially HF.

Another major cause of HF is myocardial infarction. Upon chronic underperfusion a complex remodeling process takes place, influencing chamber size, shape, and ventricular function. The ongoing global remodeling leads to an enlargement of the lumen diameter as well as a reduction

in the thickness of the left ventricular chamber and septum (Figure 1(a), MI). The human pathophysiology of an acute myocardial infarction can be mimicked in mice by ligation of the left anterior descending artery which interrupts blood flow and causes ischemia in the proximal area. Ventricular performance is lost in the ischemic area and cardiac remodeling leads to increased ventricular volume, chamber dilatation, and thinning of the walls (Figure 1(b), MI). When the infarct size and location are not too severe, the remaining cardiomyocytes might compensate the ventricular wall stress by eccentric hypertrophy.

A further chronic HF condition is termed dilated cardiomyopathy which is characterized by impaired contractility, thinning of ventricular walls, and increases in heart diameter and lumen size, resulting in the dilation of the ventricles (Figure 1(a), DCM). Despite this common phenotype of dilated cardiomyopathy the underlying cause is often linked to viral infections, inherited familial genes, autoimmune disease, or low-level chronic inflammation among others. In addition to cell death cardiomyocyte degeneration, involving the loss of the contractile machinery, has been documented in patients during the transition to HF and is an essential part of cardiac remodeling and dedifferentiation at different stages of DCM (Figure 1(c)) [6, 9, 13, 16, 23]. The increased presence of macrophages combined with elevated levels of various chemokines and cytokines such as MCP-1 (monocyte chemoattractant protein-1), TNF- $\alpha$ , and oncostatin M during the pathogenesis of dilated cardiomyopathy underscores the contribution of cardiac inflammation [6, 15, 24–26]. As a powerful chemoattractant MCP-1 directs monocytes/macrophages to the sites of injury thereby interfering with regeneration and remodeling of the myocardium [27, 28]. Adverse and harmful invasion of the heart by monocytes/macrophages is mimicked by the cardiomyocyte-restricted overexpression of MCP-1 in genetically modified mice. This strain develops inflammatory dilated cardiomyopathy (Figure 1(b), iDCM) and dies around 6 months due to massive infiltration of the heart and the release of inflammatory cytokines [15, 24]. Similar to human patients, the ventricular cavities of the inflamed heart are enlarged while the thickness of septal and ventricular wall appears to be reduced.

## 3. Identification of Novel Biomarkers and Therapeutic Targets on an “Omics” Platform

Presently the only biomarker in common clinical use for diagnosis and monitoring of HF is B-type natriuretic peptide (BNP), which is released from myocardium undergoing wall stress [29]. Although BNP has prognostic value and no significantly superior alternative HF marker is presently available [29], the usefulness of BNP as a HF marker is limited since it is also released into the circulation under various other disease conditions such as pulmonary embolism and ventricular hypertrophy. A recently described HF marker is fibroblast growth factor-23 (FGF23) [30, 31]. Increased levels of circulating FGF23 were observed in patients with systolic HF, and increased cardiac transcript and protein levels were

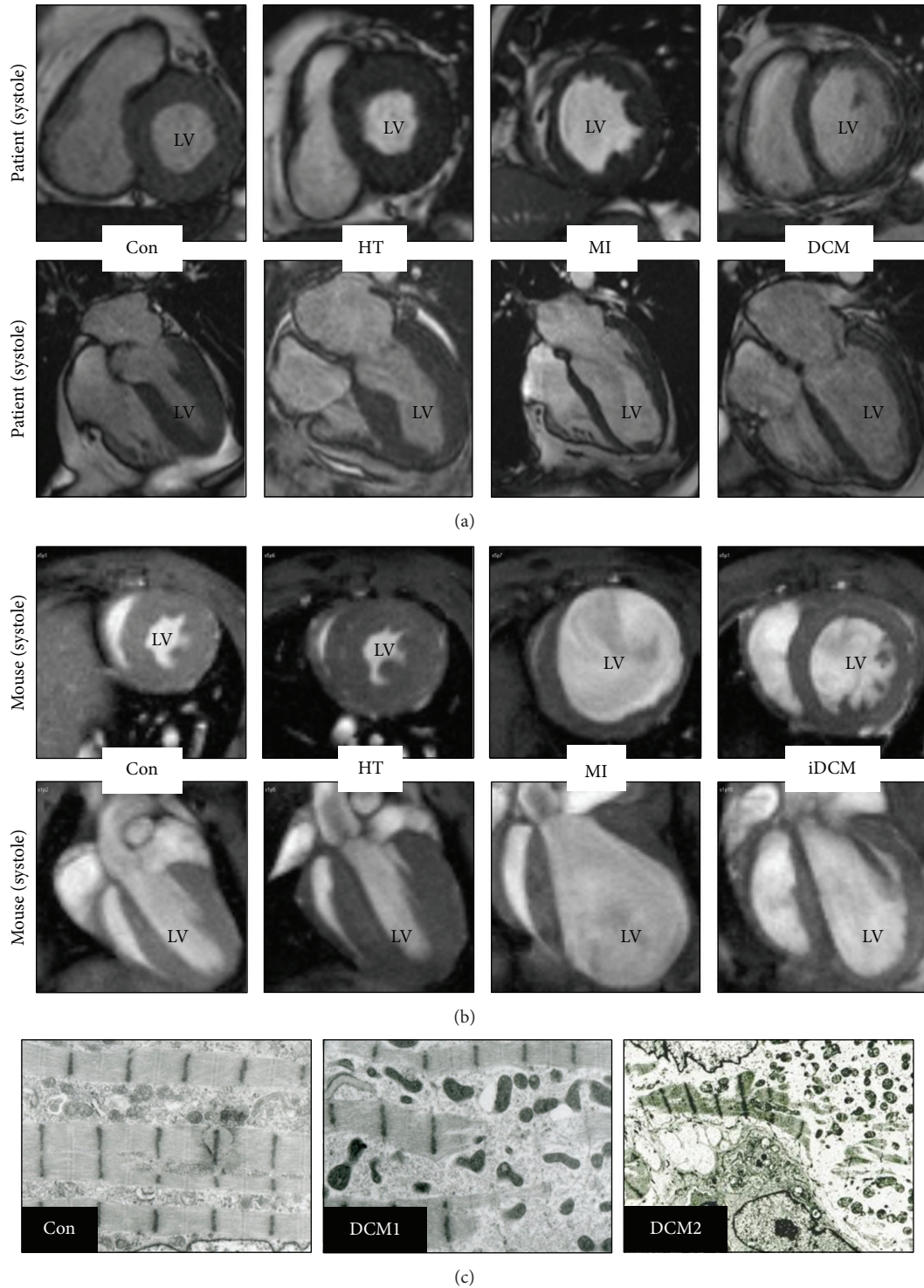


FIGURE 1: End-systolic midventricular short axis and long axis MRI frames of healthy and failing hearts from humans and mice. (a) MRI images from a healthy control (Con) and patients with aortic stenosis (HT), myocardial infarction (MI), and idiopathic dilated cardiomyopathy (DCM). (b) MRI images from mice 4 weeks after transaortic constriction (HT), 3 weeks after LAD ligation (LAD), and 6-month-old mice with a cardiac restricted overexpression of MCP-1 (iDCM). A healthy control animal is also shown (Con). Note the increase in size and ventricular mass of HT hearts while increases in heart size after MI and after development of (i) DCM are associated with ventricular thinning. Explanations are given in the text. (c) Electron microscopy pictures show different degrees of sarcomeric degeneration in patients with dilated cardiomyopathy (Con versus DCM1 and DCM2; EF < 30%). Human MRI images and electron micrographs were kindly provided by Professor Georg Bachmann and by Dr. Viktoria Polyakova, respectively. Mouse MRI images are adapted and modified from the “Venia legendi” work of J. Pöling.

detected in patients with myocarditis, ischemic cardiomyopathy, and dilated cardiomyopathy [30, 31]. Despite the potential of FGF23 to serve as a HF marker the increase of circulating FGF23 is often associated with faster progression of chronic kidney disease and a higher mortality of hemodialysis patients [32]. Probably the most widely applied biomarker tests are those related to myocardial infarction [29]. However, ischemic markers such as troponins, creatine kinase, and myoglobin are only detectable hours after the ischemic damage and make it impossible to rescue necrotic tissue. Despite their enormous value as diagnostic tools in everyday clinical practice, these assays might not necessarily be helpful, since their specificity and sensitivity are not guaranteed. Therefore, in addition to a comprehensive understanding of a structure-function relationship, there is a need to develop a complementary biomarker toolbox in order to better define the transition from compensatory adaptation to HF via stage-specific biomarker with the further goal of identifying novel drug targets. For this purpose a large-scale screen utilizing “omic” tool is necessary. Ideally, the suffix “omics” addresses the simultaneous analysis of the entire set of biological molecules in a certain field, which is defined by a prefix: proteomic and transcriptomic tools will be featured in this review. Generally there are two aims of “omic” studies: firstly, molecules which are causally involved in heart disease can be targeted by therapeutic intervention and, secondly, molecules which are altered in a predictable manner in response to the disease status can be used as stage-specific markers [29].

An ideal “omics” platform consists of complementary core facilities in order to obtain as much information as possible from fluids, cell cultures, and tissue samples (Figure 2(a)). Fluids are flush-frozen in liquid nitrogen after centrifugation and removal of insoluble material. Usually fluids do not need further processing and can be directly analysed by commercially available ELISA kits (single protein detection by specific antibodies in one sample) or kits using multiplex systems. Multiple cytokine and chemokine assays are multiplex bead-based assays able to simultaneously quantify up to 32 (or even more) targets in one sample. The main advantage of multiplex systems lies in the speed (data are obtained on the same day with little working effort) and sensitivity of determinations (down to picogram levels of proteins). Furthermore, a much lower amount of sample is needed compared to an ELISA due to simultaneous detection of multiple proteins. “Multiplexing” is especially powerful when using highly diluted samples, such as fluids, but might have limitations in the study of tissue biopsies that have to be homogenized in buffers containing detergents. Limitations are further seen in the number of commercially available kits containing panels of different antibodies recognizing predefined protein targets, and the specificity and accuracy of these multiplex systems might be sometimes a matter of concern.

Alternatively protein samples from either tissues or cell cultures can be processed by 2-dimensional gel electrophoresis. After homogenization in an appropriate buffer protein lysates are first separated due to their isoelectric point (isoelectric focusing), which is followed by a separation in the second dimension according to their size (gel electrophoresis).

Depending on the complexity of the sample this method is able to separate thousands of protein spots from a single sample in one gel (2DE, Figure 2(a)). Proteins are visualized by staining and gels are scanned and analysed with the corresponding software. Regulated proteins are excised and identified by mass spectrometry (MS). Complementary equipment such as HPLC to enrich certain proteins is often used. The main advantage of the 2DE-based mass spectrometry is the potential to analyse thousands of protein spots simultaneously and to discover newly regulated proteins, in contrast to multiplex detections and Western blot with predefined targets. This allows for large-scale screening of not yet defined biomarkers and drug targets in contrast to the antibody-based assays. Furthermore, the quality of present 2DE technology has improved to the point that once a protein spot has been identified in a gel set there is often no additional need for further MS identification. Limitations are seen in the exclusion of certain protein groups (due to hydrophobicity or size) and in the sensitivity (detection of a protein spot at the nanogram level) when no intermediate step such as HPLC enrichment is performed, and the work is often labour-intensive.

For these reasons, recent developments in proteomics have moved from traditional 2DE methods to gel-free systems [33]. Complex protein mixtures obtained from tissue, cell culture, or plasma samples are digested to peptides and separated by microcapillary reverse phase chromatography before introducing these peptides into the mass spectrometer. After detection of the eluted peptides with the mass spectrometer over a wide  $m/z$  (mass-to-charge ratio) range, individual peptides are then selected within the mass analyzer and further fragmented into a ladder of smaller molecules, which result in a second mass spectrum. By repeating this process in automatic routines thousands of MS/MS spectra are obtained, which lead to the identification of thousands of protein species by employing database search programs that match the measured peptides to their corresponding proteins. However, often the complexity of protein mixtures as well as the high abundance of some protein species, such as albumin in serum or actin in cell lysates, hampers the detection capacity of low-abundant proteins. In addition, quantification and comparison of protein expression levels in different samples are often difficult for MS-based gel-free systems.

Transcriptome analysis can also contribute valuable information to the discovery of new biomarkers, being capable of identifying changes in gene expression levels between different study groups, thus pinpointing candidate genes that may be up- or downregulated in a disease situation. DNA microarrays are particularly useful tools in this aspect: after collecting RNA samples from either tissue or cell cultures, cDNA is produced via a retrotranscriptase and hybridized with DNA probes attached to the surface of a manufactured chip. The degree of hybridization is then measured for every DNA probe and, since every gene is represented by multiple specific probes in the chip, an average expression level is calculated for each gene present in the DNA microarray [34].

Although undoubtedly useful, one of the main drawbacks of DNA microarray technology is its dependency on knowledge of the genomic sequence of the species to be studied. For the human genome as well as for some known

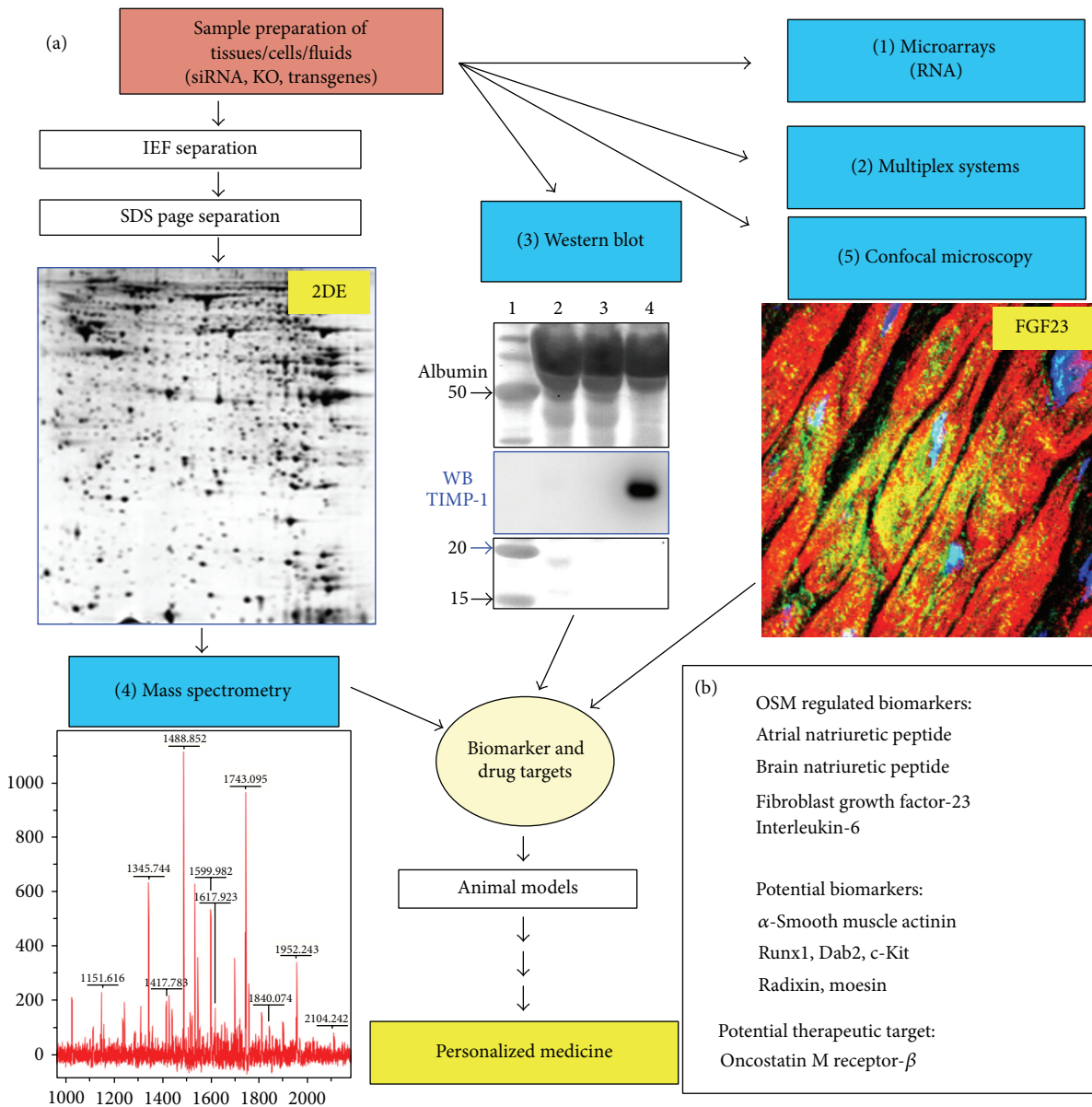


FIGURE 2: The design of an “omics” technology research platform consisting of complementary core facilities for the future of a personalized medicine (adapted and modified from the “Venia legendi” work of J. Pöling, 2013). (a) Multiplex systems, Western blot, and confocal microscopy are antibody based methods. The Western blot shows a stained membrane resolving 1  $\mu$ L of two serum samples (2&3) and 1  $\mu$ L of pericardial fluid (PCF) from a patient with HF and high myocardial level of oncostatin M (size marker was run parallel in 1). A strong signal of TIMP-1 was detected in PCF after antibody hybridization of the membrane and subsequent chemiluminescence detection (WB). When targets are not known the separation of proteins lysates by 2-dimensional gel electrophoresis (2DE) reveals thousands of not yet defined protein spots after silver staining (proteome analysis). Here, a cytoplasmic cardiac 2DE of a 3-day-old rat is shown. Then, gels are scanned and compared and a computer based software program identifies regulated spots. (4) The protein spot is excised and identified by mass spectrometry combined with database searches. (1) In addition RNA might be extracted from the same sample and expression levels of ten thousands of genes can be simultaneously analyzed on DNA microarrays (transcriptome analysis). (5) Confocal microscopy verifies observations and provides further information about the protein. A confocal image shows FGF23-positive cardiomyocytes in a patient with aortic stenosis and high myocardial level of oncostatin M. (b) ANP, BNP, interleukin-6, and FGF-23 were identified as oncostatin M-regulated biomarkers on this platform. Further potential biomarkers such as radixin and moesin are indicated.

animal genomes such as rat and mouse commercial DNA microarrays are available while for most animals arrays cannot be obtained. In this case sequence-based technologies that directly determine the nucleic acid sequence are a better

alternative, as technological advances have drastically lowered the cost of this type of analysis. RNA-seq consists of the extraction of RNA, its conversion to cDNA, and subsequent fragmentation before sequencing through next-generation

sequencing (NGS) technologies and bioinformatic analysis [35]. In any case, candidates identified through either DNA microarray or RNA-seq analysis should be confirmed, usually by first measuring the differential expression of the genes through reverse transcription quantitative real-time PCR (RT-qPCR) and then performing protein analysis.

A further cornerstone in the analysis of proteins is the continuing development of the Western blot technology. The enormous increase in the daily availability of new antibody products (as companies are responding to the challenge to develop antibodies against every single human protein), the increase in sensitivity of detection solutions as well as of imaging systems (Figure 2(a)) to visualize antibody targets (detection at low femtogram level), and the development of semiautomated systems in order to increase throughput provide excellent tools to perform proteome studies at midscale. The specificity and sensitivity of the Western blot approach often allow for a fast and selective analysis of molecular pathways within days, employing small equipment available in almost every laboratory without going through the whole proteome by MS. Once a signalling cascade (e.g. Erk1/2) has been identified this pathway can then be analysed in detail by a set of specific antibodies (Ras, Raf, MEK, etc.). A further significant advantage of Western blot over MS is the fact that the same antibodies can be utilized for confocal microscopy analysis, adding important information on the localization and expression pattern of the analytes in a certain tissue. However, the expense of individual antibodies and lack of a more advanced automation of Western blots significantly reduce the performance of this technique at large scale.

#### **4. Primary Cultures of Animal Cells as a Tool to Clarify Disease Mechanisms and Accelerate the Discovery of Novel Biomarkers and Drug Targets**

The complex proteome and transcriptome of the heart complicate the extraction of valuable information out of the huge amount of obtained data and simplification is needed. In our experience, the identification of disease-relevant proteins by an “omics” approach in a certain cardiac cell type might be hampered by the abundance of proteins of interest in other cell types. This was the case when we analyzed ezrin-radixin-moesin (ERM), a family of proteins crosslinking actin filaments with the plasma membrane, thus playing a role in cell motility and cell shape maintenance [36]. When ERM protein expression was assessed in samples from patients who have been diagnosed as suffering from dilated cardiomyopathy we found a reduction of moesin by a large-scale Western blot screen [6]. However, confocal microscopy revealed a reexpression and strong accumulation of moesin in cardiomyocytes of the same patients [14]. In order to explain this apparent contradiction we analyzed the expression pattern of moesin in heart tissue by confocal microscopy and found that smooth muscle and endothelial cells of vessels strongly expressed moesin but these vessels were reduced in number in the analyzed patients with DCM. We concluded that the reduced amount of moesin in the human diseased

myocardium was due to the depletion of vessels, which masked the reexpression of moesin in cardiomyocytes [14].

In order to accelerate the discovery of disease-relevant peptides animal culture models provide “simplified” systems for the analysis on an “omics” platform (Figure 3(a)). Primary cultures of cardiomyocytes are particularly suitable for “omics” studies, since adult cardiomyocytes are terminally differentiated and they transfer their epigenetic, genomic, and proteomic *in vivo* status into the culture dish, which might not be preserved in cell lines or passaged cells [37]. Primary cultures are, as defined by the Latin term “primus,” cells which are directly used for experiments after isolation from the animal and not further passaged. The strong correlation we demonstrated between differentially regulated proteins of remodeling cardiomyocytes *in vivo* and *in vitro* [6, 14, 15] has permitted us to find ERM proteins (Figures 3 and 4) and other potentially relevant candidates [6, 15, 31] in oncostatin M (Figure 2(b)) and IGF-1 (insulin-like growth factor-1) stimulated cultures of adult rat cardiomyocytes.

Despite their strength as “pumping units” adult cardiomyocytes are rather fragile and a good quality of cells can only be obtained when the heart is perfused on a Langendorff apparatus and collagenase disrupts the extracellular matrix, thus releasing rod-shaped cardiomyocytes [38]. The susceptibility of these cells to mechanical stress reflects the need of the cardiomyocyte to adapt to changes in cardiac architecture in order to avoid harmful mechanical distortion. In culture, remodeling of cardiomyocytes already starts within the first hours (Figures 3(a) and 3(b)) when ERM proteins accumulate at membrane areas different from the intercalated disc. When stimulated for one week with IGF-1, cardiomyocytes increase significantly in size and ezrin is mainly localized at the cellular extensions (Figure 3(c)) probably stabilizing tension during the growth process. In addition, cytoplasm and the nuclei were positive for ezrin. When the mechanical stress suffered during the isolation process becomes too severe freshly isolated cardiomyocytes lose their highly organized three-dimensional structure, round up, and die by blebbing (Figure 3(a) versus Figure 3(b)). Ezrin-positive blebs can be easily recognized as spherical protrusions of the membrane (Figure 3(b)). We made similar observations with moesin and radixin after stimulation with oncostatin M indicating that the translocation of ERM proteins belongs to a “rapid adaptive stress program” to compensate unfavorable mechanical distortion [14].

In order to understand whether our observations are also true in the remodeling myocardium we took advantage of the TAC hypertrophy model (Figure 4(a)). In the normal myocardium ezrin localizes to the intercalated disc. After 1 month of transaortic constriction—a time point when the heart is still able to recover if the constriction is removed—cardiomyocytes of some myocardial areas are increased in size and depict a diffuse pattern of ezrin in the intercalated disc. Some cardiomyocytes show an unusual localization of ezrin and the pattern resembles the extensions of IGF-1-treated cardiomyocyte cultures (white arrows). In other areas of the myocardium ezrin appears laterally in cardiomyocytes and the intercalated discs are hardly recognizable, indicating that most ezrin is translocated. We conclude that ezrin

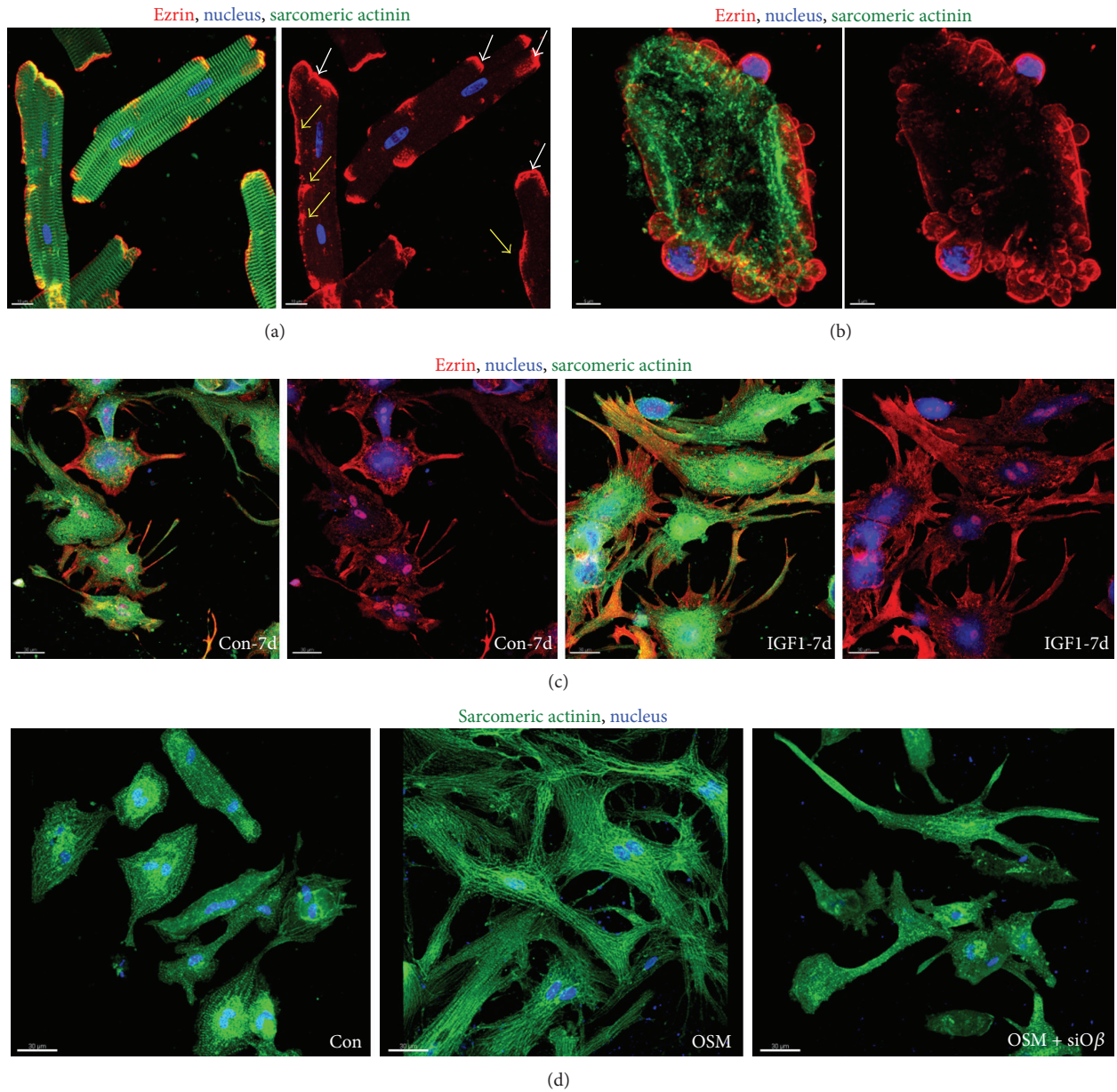


FIGURE 3: Cardiomyocytes respond to stress by membranous translocation of ERM proteins. (a) Fluorescence micrographs of freshly isolated adult rat cardiomyocytes (4 hours) show different degrees of ezrin translocation (yellow arrows). Ezrin is usually located at the intercalated disc (white arrows) but upon translocation it is detected laterally of the membrane. (b) Fluorescence micrographs demonstrate massive translocation of ezrin. Ezrin is part of the cell blebs which are, when occurring to this extent, characteristic for dying cells. (c) Fluorescence micrographs show increases and accumulation of ezrin in cell extensions of IGF-1 stimulated adult cardiomyocytes after seven days. Note that serum shows also some effects on ezrin localization in control cultures (Con). (d) Fluorescence images of oncostatin M receptor- $\beta$  siRNA treated adult rat cardiomyocytes (OSM + siO $\beta$ ) in culture demonstrate successful interruption of OSM induced remodeling after 7 days. Con indicates albumin treated control cultures.

translocation may serve as a mechanism to stabilize cardiomyocytes in the pressure-overloaded myocardium. In the human failing heart ERM proteins show an unusual localization and expression pattern. In contrast to the healthy heart, moesin is reexpressed in cardiomyocytes [14] and ezrin shows massive membranous and cytoplasmic accumulation. Taken together, these are signs that the cardiac damage led

to a structural remodelling of cardiomyocytes, although this adaptive attempt did not prevent HF.

A second advantage of animal cell culture systems resides in the possibility of selecting from the multitude of cardioactive substances individual cytokines and performing functional studies. By these means we have identified oncostatin M as a major modulator of cardiac remodeling, as well as a

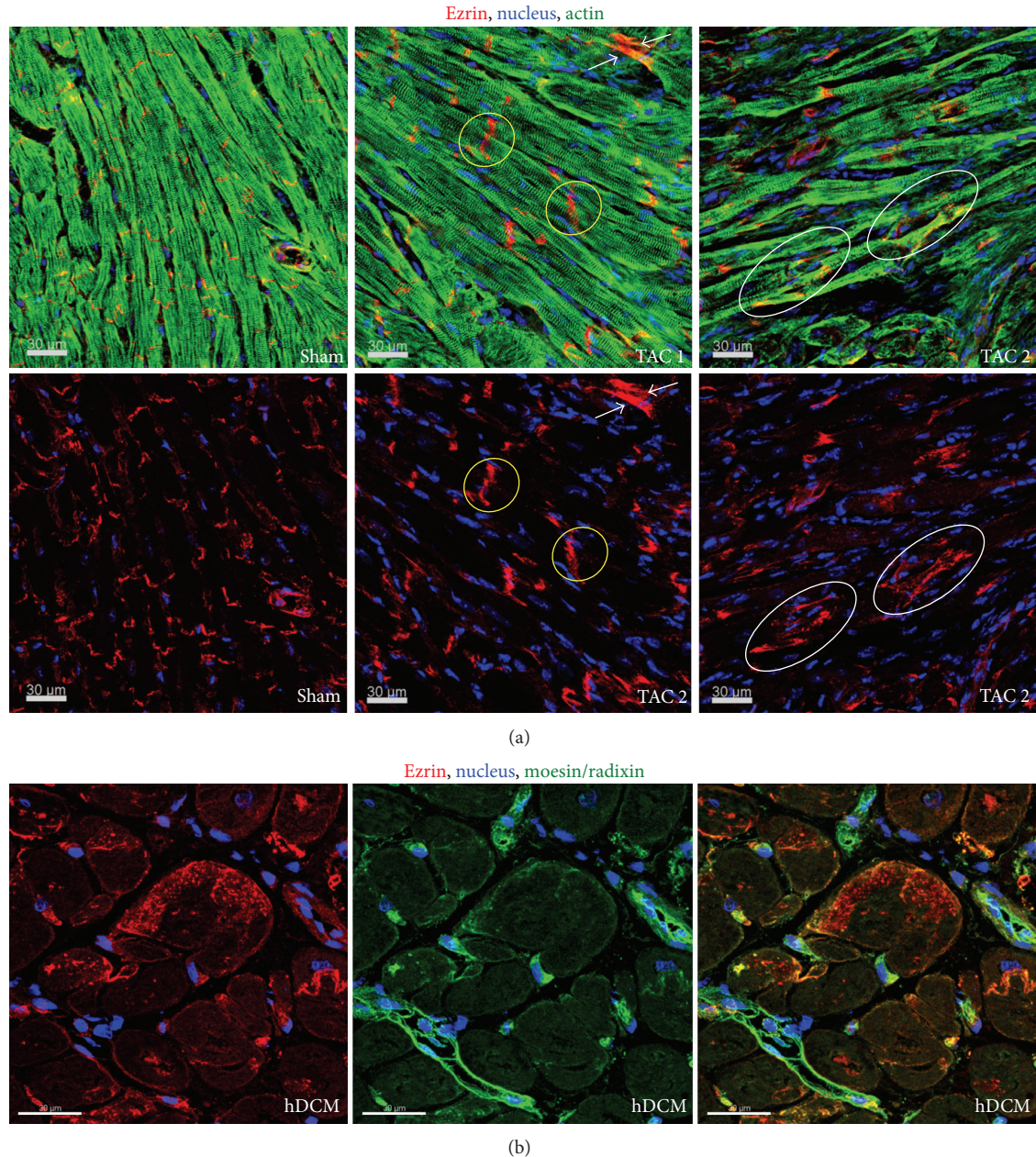


FIGURE 4: Spatial distribution of ezrin during adaptation and HF. (a) Longitudinal sections of the mouse myocardium 1 month after transaortic constriction (TAC). In sham operated animals ezrin shows a regular appearance at the intercalated disc, which is disturbed to a variable degree in mice after TAC (yellow circles). In the fluorescence micrographs cardiomyocytes show different degrees of ezrin translocation in cardiomyocytes (white arrows (TAC1) and oval circles (TAC2)). These animals recover after the release of constriction. (b) Fluorescence micrographs demonstrate massive lateral accumulation of ezrin in patients with end-stage HF. This pattern of moesin and radixin labeling corresponds with that previously described [14].

promising therapeutic target in dilated cardiomyopathy. We discovered that oncostatin M promotes *in vivo* functional deterioration and lethality when chronically activated [6, 15]. In addition pharmaceutical or genetic targeting of the oncostatin M receptor- $\beta$  ( $O\beta$ ) attenuated HF and reduced mortality in mice model with dilated cardiomyopathy [6, 15]. Furthermore, the relative ease in performing specific knock-downs of proteins by siRNA in adult cardiomyocytes can in

certain aspects be an alternative to the cumbersome construction of knock-out mice. As an example, Figure 3(d) shows how a simple knock-down of the oncostatin M receptor- $\beta$  ( $O\beta$ ) by siRNA blocks the remodeling effect of oncostatin M on adult cardiomyocytes. Taking advantage of this fact, we identified by an siRNA-based knock-down of various signaling cascades, combined with an extensive Western blot analysis, that remodeling of oncostatin M-stimulated adult

cardiomyocytes depends on Erk1/2 but not on p38 or SAP kinase pathways [6]. In the same study we observed markedly increased amounts of  $O\beta$  in patients with dilated cardiomyopathy. However, this cytokine is hardly detectable in the circulation and is, therefore, unsuitable to serve as a circulating biomarker. Since oncostatin M itself induces the expression of a variety of peptides in cultured cardiomyocytes, a transcriptome and proteome analysis of OSM-stimulated cardiomyocytes was performed for novel disease-relevant molecules. Among more than 500 strongly regulated proteins we identified radixin, moesin, ANP, BNP, and the upcoming HF marker FGF23 [6, 14, 15, 31] (Figure 2(b)). This observation was insofar surprising since it was assumed that the bone, but not the heart, is the main source of circulating FGF23 in heart diseases. The discovery of FGF23 on the transcript as well as protein level in the failing heart underlines the power of an “omics”-based initial analysis of primary animal cell cultures [31].

## 5. Conclusions

Despite the enormous efforts put worldwide into HF research, the number and specificity of cardiovascular biomarkers and targets are still regarded as dissatisfactory [3, 10, 29, 39]. However, the combination of well-established traditional methodologies with sophisticated “omics” toolboxes generates a highly promising platform and inspires great hope for the medicine of the future. High-throughput technologies are ideally suited to identify genes and proteins involved in heart diseases that may have gone undiscovered so far. Gene expression screens, such as DNA microarrays or RNA-seq, as well as large-scale protein expression profiling through 2DE or gel-free systems combined with mass spectrometry, generate an enormous amount of data from which novel therapeutic strategies and potential targets can be selected through careful bioinformatic analysis. Although undoubtedly powerful, large-scale screens still require the validation and further study of individual candidates through more traditional methods, such as Western blot and electron and confocal microscopy, in order to verify, localize, and characterize novel biomarkers and drug targets. Moreover, a mere “omics” approach of human tissue samples frequently leads into a “data jungle” hiding valuable disease-relevant clues. For these reasons, the selection of specific animal models such as transversal aortic constriction as a model for patients with aortic stenosis reduces the complexity of the human pathology and allows for a more focused analysis. The analytical capacity of these animal models might be expanded by genetically modified mice such as transgenes or knock-outs, which permit the understanding of disease-relevant processes. The greatest reductions in complexity offered by primary animal cell cultures might make them an ideal start-up on an “omics” platform before moving to *in vivo* models.

## Conflict of Interests

On behalf of all authors, the corresponding author states that there is no conflict of interests.

## Authors' Contribution

Yunlong Hou, Juan M. Adrian-Segarra, and Manfred Richter contributed equally to this paper.

## Acknowledgments

The authors are indebted to the excellent assistance of Brigitte Matzke, Jutta Wetzel and Kerstin Richter. IT support by Peter Hofmann is greatly acknowledged. This work was supported by the Stiftung William G. Kerckhoff Herz- und Rheumazentrum Bad Nauheim (Manfred Richter) supported by the German Heart Foundation/German Foundation of Heart Research. Juan M. Adrian-Segarra was supported by CardioNeT (Marie Curie ITN-2011-GA: 289600) and the Loewe-Zentrum Universities of Gießen and Marburg Lung Center (UGMLC).

## References

- [1] R. Fagard, “Athlete’s heart,” *Heart*, vol. 89, no. 12, pp. 1455–1461, 2003.
- [2] A. Mesa, C. Jessurun, A. Hernandez et al., “Left ventricular diastolic function in normal human pregnancy,” *Circulation*, vol. 99, no. 4, pp. 511–517, 1999.
- [3] M. Szibor, J. Pöling, H. Warnecke, T. Kubin, and T. Braun, “Remodeling and dedifferentiation of adult cardiomyocytes during disease and regeneration,” *Cellular and Molecular Life Sciences*, vol. 71, no. 10, pp. 1907–1916, 2014.
- [4] S. Hein and J. Schaper, “Pathogenesis of dilated cardiomyopathy and heart failure: insights from cell morphology and biology,” *Current Opinion in Cardiology*, vol. 11, no. 3, pp. 293–301, 1996.
- [5] S. Hein and J. Schaper, “The extracellular matrix in normal and diseased myocardium,” *Journal of Nuclear Cardiology*, vol. 8, no. 2, pp. 188–196, 2001.
- [6] T. Kubin, J. Poling, S. Kostin et al., “Oncostatin M is a major mediator of cardiomyocyte dedifferentiation and remodeling,” *Cell Stem Cell*, vol. 9, no. 5, pp. 420–432, 2011.
- [7] M. Rajabi, C. Kassiotis, P. Razeghi, and H. Taegtmeyer, “Return to the fetal gene program protects the stressed heart: a strong hypothesis,” *Heart Failure Reviews*, vol. 12, no. 3-4, pp. 331–343, 2007.
- [8] S. Hein, E. Arnon, S. Kostin et al., “Progression from compensated hypertrophy to failure in the pressure-overloaded human heart: structural deterioration and compensatory mechanisms,” *Circulation*, vol. 107, no. 7, pp. 984–991, 2003.
- [9] S. Hein, T. Block, R. Zimmermann et al., “Deposition of non-sarcomeric alpha-actinin in cardiomyocytes from patients with dilated cardiomyopathy or chronic pressure overload,” *Experimental & Clinical Cardiology*, vol. 14, no. 3, pp. e68–e75, 2009.
- [10] S. Heymans, E. Hirsch, S. D. Anker et al., “Inflammation as a therapeutic target in heart failure? A scientific statement from the Translational Research Committee of the Heart Failure Association of the European Society of Cardiology,” *European Journal of Heart Failure*, vol. 11, no. 2, pp. 119–129, 2009.
- [11] S. Hein, A. Elsässer, S. Kostin, R. Zimmermann, and J. Schaper, “Functional disturbances due to structural remodeling in the failing human heart,” *Archives des Maladies du Coeur et des Vaisseaux*, vol. 95, no. 9, pp. 815–820, 2002.
- [12] S. Hein, D. Scholz, N. Fujitani et al., “Altered expression of titin and contractile proteins in failing human myocardium,” *Journal*

- of Molecular and Cellular Cardiology*, vol. 26, no. 10, pp. 1291–1306, 1994.
- [13] A. Heling, R. Zimmermann, S. Kostin et al., “Increased expression of cytoskeletal, linkage, and extracellular proteins in failing human myocardium,” *Circulation Research*, vol. 86, no. 8, pp. 846–853, 2000.
- [14] J. Pöling, P. Gajawada, H. Lörchner et al., “The Janus face of OSM-mediated cardiomyocyte dedifferentiation during cardiac repair and disease,” *Cell Cycle*, vol. 11, no. 3, pp. 439–445, 2012.
- [15] J. Pöling, P. Gajawada, M. Richter et al., “Therapeutic targeting of the oncostatin M receptor- $\beta$  prevents inflammatory heart failure,” *Basic Research in Cardiology*, vol. 109, no. 1, article 396, 2014.
- [16] J. Schaper, R. Froede, S. Hein et al., “Impairment of the myocardial ultrastructure and changes of the cytoskeleton in dilated cardiomyopathy,” *Circulation*, vol. 83, no. 2, pp. 504–514, 1991.
- [17] J. Schaper, S. Kostin, S. Hein, A. Elsässer, E. Arnon, and R. Zimmermann, “Structural remodelling in heart failure,” *Experimental and Clinical Cardiology*, vol. 7, no. 2–3, pp. 64–68, 2002.
- [18] J. N. Cohn, R. Ferrari, and N. Sharpe, “Cardiac remodeling—concepts and clinical implications: a consensus paper from an International Forum on Cardiac Remodeling,” *Journal of the American College of Cardiology*, vol. 35, no. 3, pp. 569–582, 2000.
- [19] J. R. Goldsmith and C. Jobin, “Think small: zebrafish as a model system of human pathology,” *Journal of Biomedicine and Biotechnology*, vol. 2012, Article ID 817341, 12 pages, 2012.
- [20] C. Zaragoza, C. Gomez-Guerrero, J. L. Martin-Ventura et al., “Animal models of cardiovascular diseases,” *Journal of Biomedicine Biotechnology*, vol. 2011, Article ID 497841, 13 pages, 2011.
- [21] J. A. Hill and E. N. Olson, “Cardiac plasticity,” *The New England Journal of Medicine*, vol. 358, no. 13, pp. 1326–1380, 2008.
- [22] A. C. deAlmeida, R. J. van Oort, and X. H. Wehrens, “Transverse aortic constriction in mice,” *Journal of Visualized Experiments*, vol. 38, Article ID e1729, 2010.
- [23] J. Schaper, S. Hein, D. Scholz, and H. Mollnau, “Multifaceted morphological alterations are present in the failing human heart,” *Journal of Molecular and Cellular Cardiology*, vol. 27, no. 3, pp. 857–861, 1995.
- [24] P. E. Kolattukudy, T. Quach, S. Bergese et al., “Myocarditis induced by targeted expression of the MCP-1 gene in murine cardiac muscle,” *The American Journal of Pathology*, vol. 152, no. 1, pp. 101–111, 1998.
- [25] D. L. Mann, “Mechanisms and models in heart failure: a combinatorial approach,” *Circulation*, vol. 100, no. 9, pp. 999–1008, 1999.
- [26] Y. Seino, U. Ikeda, H. Sekiguchi et al., “Expression of leukocyte chemotactic cytokines in myocardial tissue,” *Cytokine*, vol. 7, no. 3, pp. 301–304, 1995.
- [27] S. Apostolakis, G. Y. H. Lip, and E. Shantsila, “Monocytes in heart failure: relationship to a deteriorating immune overreaction or a desperate attempt for tissue repair?” *Cardiovascular Research*, vol. 85, no. 4, pp. 649–660, 2010.
- [28] A. Martire, B. Fernandez, A. Buehler et al., “Cardiac overexpression of monocyte chemoattractant protein-1 in transgenic mice mimics ischemic preconditioning through SAPK/JNK1/2 activation,” *Cardiovascular Research*, vol. 57, no. 2, pp. 523–534, 2003.
- [29] A. V. Edwards, M. Y. White, and S. J. Cordwell, “The role of proteomics in clinical cardiovascular biomarker discovery,” *Molecular and Cellular Proteomics*, vol. 7, no. 10, pp. 1824–1837, 2008.
- [30] D. Gruson, T. Lepoutre, J.-M. Ketelslegers, J. Cumps, S. A. Ahn, and M. F. Rousseau, “C-terminal FGF23 is a strong predictor of survival in systolic heart failure,” *Peptides*, vol. 37, no. 2, pp. 258–262, 2012.
- [31] M. Richter, V. Polyakova, G. Gajawada et al., “Oncostatin M induces FGF23 expression in cardiomyocytes,” *Journal of Clinical & Experimental Cardiology*, 2012.
- [32] M. J. Damasiewicz, N. D. Toussaint, and K. R. Polkinghorne, “Fibroblast growth factor 23 in chronic kidney disease: new insights and clinical implications,” *Nephrology*, vol. 16, no. 3, pp. 261–268, 2011.
- [33] M. R. Roe and T. J. Griffin, “Gel-free mass spectrometry-based high throughput proteomics: tools for studying biological response of proteins and proteomes,” *Proteomics*, vol. 6, no. 17, pp. 4678–4687, 2006.
- [34] M. Wiltgen and G. P. Tilz, “DNA microarray analysis: principles and clinical impact,” *Hematology*, vol. 12, no. 4, pp. 271–287, 2007.
- [35] X. Qian, Y. Ba, Q. Zhuang, and G. Zhong, “RNA-seq technology and its application in fish transcriptomics,” *OMICS: A Journal of Integrative Biology*, vol. 18, no. 2, pp. 98–110, 2014.
- [36] S. Tsukita and S. Yonemura, “ERM proteins: head-to-tail regulation of actin-plasma membrane interaction,” *Trends in Biochemical Sciences*, vol. 22, no. 2, pp. 53–58, 1997.
- [37] H. Ando, T. Kubin, W. Schaper, and J. Schaper, “Cardiac microvascular endothelial cells express  $\alpha$ -smooth muscle actin and show low NOS III activity,” *The American Journal of Physiology—Heart and Circulatory Physiology*, vol. 276, no. 5, pp. H1755–H1768, 1999.
- [38] H. M. Piper, “Adult ventricular rat heart muscle cells,” in *Cell Culture Techniques in Heart and Vessel Research*, pp. 36–60, Springer, Berlin, Germany, 1990.
- [39] D. M. Kaye and H. Krum, “Drug discovery for heart failure: a new era or the end of the pipeline?” *Nature Reviews Drug Discovery*, vol. 6, no. 2, pp. 127–139, 2007.

## Review Article

# Animal Models of Peritoneal Dialysis: Thirty Years of Our Own Experience

Krzysztof Pawlaczyk,<sup>1,2</sup> Ewa Baum,<sup>3</sup> Krzysztof Schwermer,<sup>1</sup> Krzysztof Hoppe,<sup>1</sup>  
Bengt Lindholm,<sup>2</sup> and Andrzej Breborowicz<sup>3,4</sup>

<sup>1</sup>Department of Nephrology, Transplantology, and Internal Medicine, Poznan University of Medical Sciences, Poznan, Poland

<sup>2</sup>Divisions of Renal Medicine and Baxter Novum, Department of Clinical Science, Intervention, and Technology, Karolinska Institute, Stockholm, Sweden

<sup>3</sup>Department of Pathophysiology, Poznan University of Medical Sciences, Ulica Rokietnicka 8, 60-806 Poznan, Poland

<sup>4</sup>Higher Vocational State School, Kalisz, Poland

Correspondence should be addressed to Andrzej Breborowicz; [abreb@ump.edu.pl](mailto:abreb@ump.edu.pl)

Received 9 October 2014; Revised 23 December 2014; Accepted 10 January 2015

Academic Editor: Oreste Gualillo

Copyright © 2015 Krzysztof Pawlaczyk et al. This is an open access article distributed under the Creative Commons Attribution License, which permits unrestricted use, distribution, and reproduction in any medium, provided the original work is properly cited.

Experimental animal models improve our understanding of technical problems in peritoneal dialysis PD, and such studies contribute to solving crucial clinical problems. We established an acute and chronic PD model in nonuremic and uremic rats. We observed that kinetics of PD in rats change as the animals are aging, and this effect is due not only to an increasing peritoneal surface area, but also to changes in the permeability of the peritoneum. Changes of the peritoneal permeability seen during chronic PD in rats are comparable to results obtained in humans treated with PD. Effluent dialysate can be drained repeatedly to measure concentration of various bioactive molecules and to correlate the results with the peritoneal permeability. Additionally we can study *in vitro* conditions properties of the effluent dialysate on cultured peritoneal mesothelial cells or fibroblasts. We can evaluate acute and chronic effect of various additives to the dialysis fluid on function and permeability of the peritoneum. Results from such study are even more relevant to the clinical scenario when experiments are performed in uremic rats. Our experimental animal PD model not only helps to understand the pathophysiology of PD but also can be used for testing biocompatibility of new PD fluids.

## 1. Introduction

An important step in studying various aspects of peritoneal dialysis (PD) is to establish an animal model which can mimic a clinical situation and can be reproduced. Different animal models of peritoneal dialysis have been used in recent years [1–20]. Experimental animal models of peritoneal dialysis have been used both to study the physiology of peritoneal transport [21, 22] and for testing biocompatibility of dialysis solutions [23, 24]. Most of these studies were performed on nonuremic animals. The transgenic mouse and cellular models become available to target other relevant pathways and, with the application of multiplex assay and DNA/RNA array technologies in these models, it will become possible to assess the interactive relationships of various physiological and pathophysiological pathways in the peritoneum in relation to the systemic parameters [18].

In our lab we established an acute and chronic PD model in nonuremic rats and mouse [3, 19, 20, 23, 25–36]. This model has been modified to evaluate the different aspects of peritoneal dialysis [3, 19, 20, 37–48]. The main objective of our research was to evaluate the usefulness of the peritoneal dialysis animal model as a means to evaluate the changes taking place during the treatment with peritoneal dialysis and correlate these experimental results with those in a clinical setting. All the experiments were performed according to protocol approved by Animal Ethics Committee of the authors' institution.

## 2. Topography of the Peritoneal Cavity

When we compared the contribution of different parts of the peritoneum to the total peritoneal surface area in

humans, rabbits, and rats, significant differences were found [49]. The area of the diaphragm, which seems to play an important role in lymphatic drainage from the peritoneal cavity [50], is relatively larger in humans than in experimental animals [49]. Therefore, one may speculate that data from experimental studies evaluating the rate of the lymphatic drainage of dialysate performed in rats or rabbits may underestimate the significance of that process in humans [49]. The transperitoneal transport of water and solutes depends on the effective peritoneal surface area, which reflects the density of microvessels in the membrane, and is related to the anatomical area of the peritoneal membrane [34, 49]. Since the parietal peritoneum is larger in rats than in humans, one may speculate that results from the animal studies may overestimate the significance of that effect when compared to humans [34, 49]. We observed that kinetics of peritoneal dialysis in rats change as the animals age, and this effect is due not only to an increasing peritoneal surface area, but also to changes in the permeability of the peritoneum [34]. Thus, we should take into consideration these variations when comparing the results from *in vivo* experiments performed on rats of various ages and weights [34].

### 3. Animal Models of Acute Peritoneal Dialysis for Study of the Physiology of the Transperitoneal Transport of Solutes

During peritoneal dialysis there is a continuous exchange of fluids and solutes between the blood and dialysis fluid dwelling in the abdominal cavity. Due to hypertonicity of the dialysis solution, water is removed from the bloodstream into the peritoneal cavity and at the same time there is a bidirectional transport of solutes: glucose is absorbed into the blood and metabolites are diffusing from blood into the dialysate which results in cleaning of the body from the toxic compounds. Additionally, water removal during the process of peritoneal dialysis depends also on the amount of fluid which is drained from the peritoneal cavity by lymphatics [51].

In our lab we used an acute model of peritoneal dialysis which was initially performed in rabbits and afterwards in rats. In rats under short ether anesthesia, the abdominal cavity was punctured and dialysis solution was infused intraperitoneally. After a few minutes animals were awoken, with free access to food and water. At designated time periods, a group of animals was sacrificed by means of an anesthesia overdose. The abdominal cavity was opened and the residual dialysate was collected for measurements. Simultaneously blood samples were obtained from the heart. Using such a relatively simple model of dialysis, we were able to describe various mechanisms of water and solute transport during peritoneal dialysis. We found that alkalization of the dialysis fluid enhances lactate removal in animals with lactic acidosis due to hypoxia [52]. In another study, the enhancing effect of the local anesthetic procaine on peritoneal transport of solutes was reported and additionally, using our *in vitro* model of the isolated peritoneal membrane, we confirmed that procaine had a direct effect on mesothelial permeability [53]. In subsequent experiments combining *in vivo* acute model of peritoneal

dialysis in rabbits and *in vitro* study on the isolated peritoneal membrane, we also found that the effect of bupivacaine on the transperitoneal transport of solutes during dialysis was due to its direct action on the mesothelial cells [54, 55]. Using combined *in vivo* and *in vitro* experiments we documented that reduced peritoneal permeability to water and solutes in presence of chondroitin sulphate is due to its action on the peritoneal interstitium [36]. During acute experiments on rats we showed that inhibition of the intraperitoneal synthesis of nitric oxide resulted in an increased selectivity of the peritoneal permeability and an increased net ultrafiltration [32]. In another series of studies we investigated inflammatory states and changes in peritoneal transport of water and other molecules during acute peritoneal dialysis in rats after lipopolysaccharide (LPS) application [39]. The addition of LPS to a standard glucose-based dialysis solution induces a strong and acute intraperitoneal inflammatory reaction reflected by increased dialysate cell count, increased cytokine and VEGF levels, as well as increased solute transport, and decreased ultrafiltration, in a dose-dependent manner [39]. The changes in peritoneal transport in this *in vivo* rat model of acute LPS-induced peritoneal inflammation are similar to results obtained in continuous ambulatory PD patients in the early phases of the peritonitis [39]. Our finding that increased VEGF levels correspond to the intensity of inflammation supports the hypothesis that inflammation could be a key component of VEGF stimulation [39].

The last group of our experiments on the model of the acute peritoneal dialysis in rabbits focused on evaluation of factors affecting lymphatic drainage from the peritoneal cavity filled with the dialysis solution. We found that peritoneal lymphatic drainage is not steady during the intraperitoneal dialysate dwell and its value is modified by factors such as volume of the dialysate, its tonicity, and presence of protein or uremia [56].

In conclusion, we think that despite their technical simplicity, acute peritoneal dialysis experiments, especially when combined with *in vitro* studies on the isolated peritoneal membrane, provide vast information about function of the peritoneum as the dialysis membrane.

### 4. Biocompatibility of Peritoneal Dialysis

Peritoneal dialysis is not a biocompatible procedure. Intraperitoneal infusion of any solution results in initiation of an inflammatory reaction, causing progressive injury to the peritoneum. Additionally, dialysis fluid has nonphysiological composition (i.e., low pH, hypertonicity, and high-glucose concentration) which on one hand stimulates an inflammatory reaction and on the other hand may have a direct injuring effect to the peritoneum [57]. Some of the results found in experimental “short-term studies,” lasting several hours, may not be the same as those observed in patients maintained on PD for a long time [23, 37, 47, 48, 58, 59]. We developed an experimental chronic peritoneal dialysis model for repeated dwell study in rats. Application of the model of chronic peritoneal dialysis in rats where animals are exposed to the tested solutions for at least 4 weeks allows evaluation of their effects on structure and function of the peritoneum [48].

**4.1. Catheter Implantation: Surgical Procedure (Figures 1 and 2).** The catheters, patterned after a standard Tenckhoff catheter, were constructed from medical silicone tubing with two polyester cuffs (Figure 1). The peritoneal catheter was implanted in rats according to a described method [3, 23, 24, 35, 43]. Under anesthesia (Medetomidine and Midazolam, i.m. or ether inhalation), first a 3 cm long incision of skin on the abdomen was performed and the abdominal muscles (about 2 cm long incision) were cut (Figure 2). A vertical incision was made in the mid-line (in order to avoid bleeding) beneath the xiphoid process (Figure 2). Then the peritoneal cavity was opened and omentectomy was performed. The distal part of the sterile peritoneal catheter was inserted into the abdominal cavity. The cuff was attached to the superficial muscle layer by purse string sutures. The catheter was pulled up through a subcutaneous track up to the animal's neck and exteriorized between the ears [23, 37, 47, 48, 58, 59]. Then 10–15 mL of peritoneal dialysis fluid was infused into the peritoneal cavity via the catheter and immediately drained. After recovering from the surgical procedures, animals returned to their cages and were allowed full mobility over the period of the experiment. After implantation of the catheters, animals were randomly divided into experimental groups.

**4.2. Dialysis Procedure.** During the first week after catheter implantation, the instilled volume of standard glucose-based solution with antibiotics (Netilmicin 5 mg/L and Cefuroxime 60 mg/L) was gradually increased from 10 to 20 mL. Tested solutions were infused daily (1–4 times) into the peritoneal cavity via the catheter. The instilled fluid was allowed to absorb gradually from the abdominal cavity or drained after the completed dwell time. During the study, the animals were awake for infusion and drainage of fluids.

**4.3. PET (Peritoneal Equilibration Test).** PET was performed during a 2- or 4-hour exchange with hypertonic peritoneal dialysis solution according to the protocol used in our lab [27, 30, 37, 48]. Under ether anesthesia, a blood sample was drawn from the tail vein in each rat. Then, 30 mL of dialysis solution was infused into the peritoneal cavity of the animal. During the 4-hour exchange, the animals were awake, with free access to water and food. Dialysate samples were drawn at time 0 (instantly after infusion of the dialysate) at 30 minutes, 1 hour, 2 hours, and 4 hours of the dwell. After four hours, the residual dialysate in each rat was drained and its volume measured. Peritoneal permeability to glucose was assessed based on the decline of glucose concentration in the dialysate expressed by the ratio  $D/D_0$  ( $D$ , glucose concentration in the dialysate sample;  $D_0$ , glucose concentration in the dialysate at time 0). Peritoneal permeability to other solutes was measured by calculating the ratio of their concentration in the dialysate sample to their concentration in plasma.

Changes of peritoneal permeability seen during *in vivo* experimental models of chronic peritoneal dialysis in rats are comparable to results obtained in humans on CAPD [27, 60]. For the first time, we described an experimental chronic peritoneal dialysis model with repeated dwell studies with drainage in nonuremic rats and evaluated the effects of addition of heparin to glucose-based peritoneal dialysis

fluid on peritoneal fluid and solute transport [3]. Heparin may improve peritoneal fluid transport possibly as a result of better healing and reduced peritoneal inflammation, as was shown in this novel animal model of chronic peritoneal dialysis with repeated dwell studies [3]. We consider that repeated dwell studies with drainage might improve the understanding of changes in transperitoneal permeability during peritoneal dialysis [3, 27, 60]. The advantage of this model in relation to other peritoneal dialysis animal models is the ability to conduct peritoneal dialysis with fluid exchanges where the fluid drainage is conducive to effluent cell analysis and active substance concentration measurements [3, 27, 30, 37, 38, 40, 58]. It is of importance to evaluate, in a continuous fashion, transport across the membrane during the study and perform histopathological tissue assessment at the end of the experiment [38, 40, 42].

In studies using our experimental model of chronic peritoneal dialysis in rats we found that glucose has a more injurious effect on the peritoneum in comparison to mannitol [46]. At the same time hypertonic dialysis solutions containing glucose are less injurious than phosphate-buffered saline (PBS) fluid [26, 47]. In another study we found that dialysis fluids with neutral pH and low concentration of glucose degradation products cause a weaker intraperitoneal inflammatory reaction and fibrosis of the peritoneum, as opposed to the standard acidic solutions [25]. Using our model we were able to study not only the effects of chronic peritoneal dialysis on structure and function of the peritoneum, but also the function of the peritoneal cells responsible for the local host defense against infections. Hypertonicity of the dialysis solutions suppresses the function of the peritoneal cells, which may result in less injury to the peritoneum, yet at the same time increases predisposition to intraperitoneal infections [28]. On the other hand, new generations of the dialysis solutions with neutral pH and low concentration of GDPs suppress intraperitoneal inflammation while the function of the peritoneal leukocytes seems to improve, as reflected by a stronger response to endotoxin [30].

In another series of studies using our experimental model we looked at potential approaches which may result in better biocompatibility of the dialysis solutions. We did not find any advantage of the dipeptide glycylglycine as an alternative to glucose osmotic solute [33], but we did a whole series of studies which confirmed that N-acetylglucosamine (NAG) is safer and more biocompatible than glucose osmotic solute, suggesting that NAG can potentially be used in dialysis solutions [35]. We found also that NAG could be a better osmotic solute than glucose as it, in addition, does not cause systemic hyperinsulinemia [44]. Hypertonic solutions containing NAG have less suppressive effects than glucose on function of the peritoneal leukocytes [31] but at the same time suppress the intraperitoneal inflammation during acute peritonitis [41]. We found in *in vitro* experiments that NAG stimulates hyaluronan synthesis in peritoneal mesothelial cells and fibroblasts [61] which was confirmed in rats chronically exposed to the dialysis solution containing NAG as an osmotic solute [62]. In these animals there was an increased amount of hyaluronan in the peritoneal interstitium which resulted in reduced transperitoneal loss of

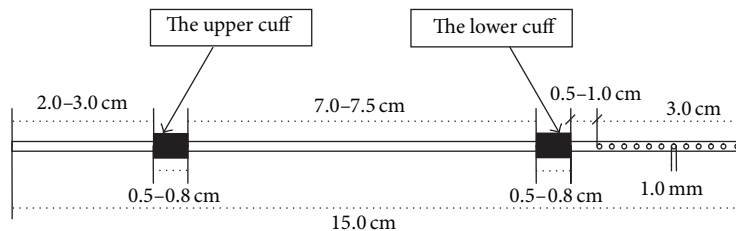


FIGURE 1: The structure of the catheter.

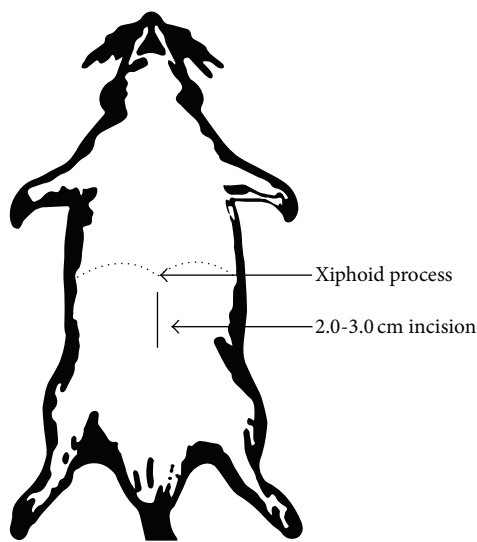


FIGURE 2: The site of incision.

proteins and increased net UF due to slower absorption of dialysate from the abdominal cavity. Our findings regarding NAG confirm our previous results from experiments with hyaluronan in the model of chronic dialysis in rats. In animals exposed to chronic peritoneal dialysis with the standard solution but supplemented with hyaluronan, less intraperitoneal inflammation and less peritoneal fibrosis were observed and, at the same time, transperitoneal protein loss was reduced whereas net UF increased [29].

This chronic peritoneal dialysis rat model allows us to examine also the influence of different substances exemplified by GDPs on changes in renal function and kidney structure in a case of reduced number of nephrons [38] and to achieve a background very similar to the clinical setting in patients treated with peritoneal dialysis.

## 5. Fibrosis in Chronic PD Model

Our model of chronic peritoneal dialysis in rats also served for evaluation of the potential approaches which can result in better preservation of the peritoneum during chronic dialysis. We discovered that not only glucose but also other components in the standard bioincompatible solutions such as high content of GDP, low pH, and low content of lactate could be responsible for peritoneal fibrosis [38]. The daily use of glucose-based peritoneal dialysis solutions in a chronic peritoneal dialysis rat model was associated with

morphological changes consistent with peritoneal fibrosis [38]. Whereas these changes in general were associated with the dialysate glucose concentration, the use of a more physiological bicarbonate/lactate-buffered peritoneal dialysis solution reduced but could not totally eliminate these effects [38]. We found that supplementation of the dialysis solution with precursors for glutathione synthesis in rats chronically exposed to peritoneal dialysis resulted in reduced fibrosis and neoangiogenesis within the peritoneum [63]. The protective effect of the glutathione supplemented solution in such conditions was additionally confirmed by *ex vivo* experiment studying the effects of dialysate effluents obtained from rats on the *in vitro* fate of cultured peritoneal mesothelial cells from the rats. We found that effluents from animals treated with glutathione caused weaker stimulation of the *in vitro* collagen synthesis compared to the control group [63]. Results from that study confirm that the *ex vivo* testing of the dialysate effluents on the *in vitro* cultured cells helps in understanding the *in vivo* pathomechanisms. In another study, we documented that supplementation of the dialysis fluid with an ACE inhibitor, enalapril, inhibits peritoneal fibrosis in chronically dialyzed rats which resulted in better net UF at the end of the 4-week study [43]. The TGF/Smad pathway appeared to play a role in this process, and we hypothesize that high-glucose peritoneal dialysis solutions, particularly bioincompatible peritoneal dialysis solutions, activate this pathway which may contribute to the observed changes in the peritoneum [38]. The addition of rosiglitazone to standard dialysis fluids can maintain the peritoneal morphology and increase ultrafiltration in a peritoneal dialysis rat model [40]. An intraperitoneal PPAR- $\gamma$  agonist may ameliorate morphological and functional changes of the peritoneum induced by standard peritoneal dialysis solutions in a chronic peritoneal dialysis rat model, while PPAR- $\gamma$  agonists in rats treated with newer biocompatible solutions showed less benefit [40]. Furthermore, adenovirus-mediated gene transfer of active transforming growth factor (TGF- $\beta$ ) into the peritoneum is also a useful technique in inducing peritoneal fibrosis similar to that observed in patients undergoing long-term peritoneal dialysis [7–17].

## 6. Spontaneous Peritonitis in Rats Undergoing Chronic PD

The use of bicarbonate/lactate mixture and/or bicarbonate results in improvements in various biocompatibility measurements as compared with acidic, lactate-buffered solutions [30, 64–69] although this was not clearly demonstrated in all

*in vivo* studies [70, 71]. In our next study, all peritoneal dialysis related procedures such as infusion and drainage were performed in a semisterile setting to induce spontaneous peritonitis [37]. Each day, dialysis fluid was infused in the morning (20 mL) and was drained after a 4-hour dwell [37]. Then the animals were reinfused with 20 mL of fresh solution. Samples for culture were collected once per week (4 hrs dialysate effluent) or when peritonitis was suspected (based on the peritoneal cells count (PCC) and/or effluent macroscopic evaluation) [37]. Upon the diagnosis of peritonitis, rats were treated by peritoneal dialysis for five or more days (if at all possible) and sacrificed by overdose of anesthesia [37]. We scored peritoneal adhesions in all animals at the end of the experimental study. Spontaneous peritonitis in rats on chronic PD, which could be diagnosed by PCC dialysate (PCC more than  $3,000/\text{mm}^3$  or a 3-fold increase of PCC), occurs as a linear function of time, allowing this model to be used for evaluating the susceptibility of infection (peritonitis) and the inflammatory response following intraperitoneal use of different solutions [37]. Bicarbonate/lactate-buffered solutions reduced the time to infection, improved (enhanced) the inflammatory response, and reduced the adhesion formation in the peritoneal cavity [37]. This indicates that, in addition to the high-glucose concentration, other toxic factor(s) in the standard glucose lactate-based peritoneal dialysis fluid, such as lower pH, higher GDP content, and lactate buffer, may contribute to more severe peritonitis and, subsequently, increased adhesion formation [37]. These data are in broad agreement both with our previous chronic *in vivo* studies, which showed that the use of antibiotics was associated with low incidence of intraperitoneal infection and a low rate of catheter obstruction and excellent technique survival [27, 30].

## 7. Effect of Peritoneal Dialysis on the Renal Function and Morphology

Preservation of the renal residual function is an important factor determining adequacy of dialysis. Survival of patients treated with chronic peritoneal dialysis is better in a group with preserved renal function [72]. We tested the effect of chronic peritoneal dialysis in rats after unilateral nephrectomy treated for 12 weeks with peritoneal dialysis on morphology and function of the remaining kidney [42]. Animals were infused twice daily with 20 mL of hypertonic dialysis fluid, allowing it to absorb gradually from the peritoneal cavity. Rats with a removed kidney but not treated with peritoneal dialysis were used as control. Although there was no difference in renal creatinine clearance between the studied groups, at the end of the experiment urinary albumin excretion was four times higher in rats treated with peritoneal dialysis and urinary excretion of N-acetyl- $\beta$ -D-glucosaminidase increased as well (+28%,  $P < 0.01$ ). Glomeruli in the remaining kidneys were equally hypertrophied in both groups. However, in rats treated with peritoneal dialysis, the amount of PAS-positive substances in the glomeruli and the amount of collagen in the peritubular area were higher than in the control group by 69%,  $P < 0.001$ , and 274%  $P < 0.001$ , respectively. Results of this study show that our animal model

of chronic peritoneal dialysis is suitable for studying the effect of such treatment on morphology and function of other organs. In another study, we found that chronic peritoneal dialysis in rats causes not only fibrosis of the peritoneal membrane, but also stimulates growth of the connective tissue within the liver [45]. In all animals, folding of the surface of the liver parenchyma was found to be due to penetration of the connective tissue elements between the hepatocytes. Due to such changes, groups of hepatocytes became detached and isolated from the remaining cells of the liver lobules.

## 8. Rat Model of Chronic Uremia on PD

Studying the effect of uremia on both peritoneal transport and biocompatibility of dialysis solutions is generally recommended; however, such experiments are laborious, difficult, and expensive, and only a few papers report on peritoneal dialysis in uremic animals. Gotloib et al. described a model of peritoneal dialysis in rabbits made uremic by partial nephrectomy (total nephrectomy on one side and 5/6 nephrectomy on the opposite side) [73]. However, in some of these models, the level of uremia was moderate [1, 6]. Furthermore, no detailed description of how uremia influences peritoneal permeability has been provided. In our study, we performed a bilateral total nephrectomy [58]. We evaluated the effect of uremia on peritoneal permeability in anephric rats [58]. Bilateral nephrectomy caused acute uremia in the studied animals. Removal of just one kidney induced no significant changes in blood urea or creatinine levels [58]. However, already at 36 hours after removal of the second kidney, blood creatinine increased from  $0.54 \pm 0.09$  mg/dL to  $9.47 \pm 1.06$  mg/dL ( $P < 0.001$ ) and blood urea increased from  $34.5 \pm 6.0$  mg/dL to  $465.6 \pm 50.8$  mg/dL ( $P < 0.001$ ) [58], similar to what is observed in patients without renal function and treated with CAPD. The animals required intensive dialysis, on some days with an increased number of exchanges (4–6 exchanges per day). To obtain adequate ultrafiltration, exchanges with hypertonic dialysis solution were necessary. However, the transperitoneal equilibration of creatinine was faster in uremic animals [58]. Common symptoms experienced by the uremic animals included diarrhea and decreased appetite and resulted in loss of body weight [58]. This has also been observed in other studies [1, 73]. We think that systemic changes induced by uremia—such as overhydration, hyperosmolality, change in blood pressure, and decreased hematocrit—can also influence peritoneal permeability [58]. Monitoring these parameters in an animal model is very difficult.

The experimental model of uremia in anephric rats described here may also be appropriate for evaluation of new biocompatible dialysis solution. Testing these parameters in the same animal, before induction of uremia and after development of uremia, may reduce variations in the results owing to interindividual changes [58].

## 9. Mouse Model of PD

The transgenic mouse and cellular models have already made a significant impact on defining basic mechanisms

that operate in the peritoneal membrane. The development of transgenic mice for describing pathways and molecules relevant to specific diseases together with the possibility of investigating minute biologic samples for numerous parameters simultaneously explains why the use of such models is set to transform research into practice [18]. To date, studies in null mice and cells derived from these animals provide direct mechanistic insights into the transport properties of the peritoneal membrane, the role of cytokines and chemokines in regulation of peritoneal inflammation, bacterial clearance and leukocyte recruitment, and pathways involved in structural and fibrogenic alterations that contribute to treatment failure [18]. Injection of IL-17 i.p. in experimental animals resulted in a time-dependent increase in the total number of cells in the peritoneal cavity [20]. Although IL-17A is generated by cells associated with adaptive immunity it appears to promote innate immune responses [19]. Our data indicate that the IL-17A-driven release of G-CSF from mesothelial cells may be an element of the peritoneal inflammatory response [19]. Mouse models also offer a vital preclinical resource in which the testing of various therapeutic strategies, arising from the mechanistic approaches, can be evaluated [18]. Barreto et al. found that pyrophosphate delivered via the intraperitoneal route using a PD solution does not appear to be deleterious to bone tissue in mice with chronic kidney disease [74]. This study indicates a potentially safe dose range which could be considered for future studies in the clinical setting [74]. Limitations of such models should be kept in mind, including the various growth and metabolic rates, the effect of the genetic background, and the possibility of adaptive mechanisms [18]. Despite these limitations, they nevertheless offer a tremendous resource that is poised to transform peritoneal research and lead to targeted interventions to prolong PD therapy [18].

## 10. Encapsulating Peritoneal Sclerosis (EPS)

EPS is a rare disease and the true incidence is unknown. It is not exclusive to PD but this review will focus on patients on PD or former PD patients [75]. For that reason, experimental models have been developed, which induced an EPS-like pattern by means of intraperitoneal application of several agents, for example, acidic glucose solution with pH inferior to 4 [76], chlorhexidine gluconate [77, 78], chlorhexidine acetate, povidone iodine, and also formaldehyde [79], as well as bleach plus whole blood [4]. Recently, mouse models have been established, which offer the possibility of investigating peritoneal transformations in the context of genetic alterations with specific regard to molecular mechanisms involved in that process [18]. Devuyt et al. investigated mice deficient in water channel aquaporin 1, which is involved in the transperitoneal transport or knock-in mice with mutants of gp130 involved in IL-6 signaling, which promotes the recruitment of T cells to the peritoneum [18]. Knowing that use of PD fluid containing GDPs generates advanced glycation end-products (AGE) [80], a comparison of wild-type mice with mice deficient in AGE receptor (RAGE) was performed. Peritoneal changes including inflammation,

neoangiogenesis, and fibrosis can be mediated in a RAGE-dependent fashion [81].

## 11. Conclusions

If put into practice, using animal models as described in this review may improve our understanding of underlying problems in peritoneal dialysis using interventions that cannot ethically be applied to inpatients, and such studies could therefore potentially contribute to solving crucial clinical problems, thereby lengthening peritoneal dialysis patients' lives, as well as permitting a longer and safer application of this type of dialysis modality in individual patients [3, 27, 30, 37, 58]. Recent advancements in virology have led to the development of a potent, safe, and nonpathogenic adeno-associated virus [82]. Similarly, innovations in nanotechnology have rendered numerous efficient and safe nanoparticles for gene therapy [82]. This study shows that both gold nanoparticles and adenoassociated virus mediated decorin gene therapies significantly decrease peritoneal fibrosis *in vivo* in a rodent model [82]. This approach has potential clinical translational in providing a therapeutic strategy to prevent peritoneal fibrosis in peritoneal dialysis patients [82]. Further studies conducted in animal models of peritoneal dialysis will allow the development and improvement of this important method of renal replacement therapy.

## Conflict of Interests

The authors declare that there is no conflict of interests regarding the publication of this paper.

## References

- [1] N. Lameire, W. van Biesen, M. van Landschoot et al., "Experimental models in peritoneal dialysis: a European experience," *Kidney International*, vol. 54, no. 6, pp. 2194–2206, 1998.
- [2] L. Gotloib, A. Shostak, V. Wajsbrot, and R. Kushnier, "High glucose induces a hypertrophic, senescent mesothelial cell phenotype after long in vivo exposure," *Nephron*, vol. 82, no. 2, pp. 164–173, 1999.
- [3] K. Pawlaczyk, M. Kuzlan-Pawlaczyk, B. Anderstam et al., "Effects of intraperitoneal heparin on peritoneal transport in a chronic animal model of peritoneal dialysis," *Nephrology Dialysis Transplantation*, vol. 16, no. 3, pp. 669–671, 2001.
- [4] S. Levine and A. Saltzman, "Abdominal cocoon: an animal model for a complication of peritoneal dialysis," *Peritoneal Dialysis International*, vol. 16, no. 6, pp. 613–616, 1996.
- [5] A. K. Oreopoulos, E. V. Balaskas, H. Rodela, G. H. Anderson, and D. G. Oreopoulos, "An animal model for the study of amino acid metabolism in uremia and during peritoneal dialysis," *Peritoneal Dialysis International*, vol. 13, no. 2, pp. S499–S507, 1993.
- [6] T. E. Miller, G. Findon, and L. Rowe, "Characterization of an animal model of continuous peritoneal dialysis in chronic renal impairment," *Clinical Nephrology*, vol. 37, no. 1, pp. 42–47, 1992.
- [7] M. Kolb, P. Bonniaud, T. Galt et al., "Differences in the fibrogenic response after transfer of active transforming growth factor-beta gene to lungs of 'fibrosis-prone' and 'fibrosis-resistant' mouse strains," *The American Journal of Respiratory Cell and Molecular Biology*, vol. 27, no. 2, pp. 141–150, 2002.

- [8] P. J. Margetts, M. Kolb, T. Galt, C. M. Hoff, T. R. Shockley, and J. Gaudie, "Gene transfer of transforming growth factor- $\beta$ 1 to the rat peritoneum: effects on membrane function," *Journal of the American Society of Nephrology*, vol. 12, no. 10, pp. 2029–2039, 2001.
- [9] Y. Motomura, H. Kanbayashi, W. I. Khan et al., "The gene transfer of soluble VEGF type I receptor (Flt-1) attenuates peritoneal fibrosis formation in mice but not soluble TGF- $\beta$  type II receptor gene transfer," *The American Journal of Physiology—Gastrointestinal and Liver Physiology*, vol. 288, no. 1, pp. G143–G150, 2005.
- [10] Y. Sekiguchi, C. Hamada, Y. Ro et al., "Differentiation of bone marrow-derived cells into regenerated mesothelial cells in peritoneal remodeling using a peritoneal fibrosis mouse model," *Journal of Artificial Organs*, vol. 15, no. 3, pp. 272–282, 2012.
- [11] P. J. Margetts, "Twist: a new player in the epithelial-mesenchymal transition of the peritoneal mesothelial cells," *Nephrology Dialysis Transplantation*, vol. 27, no. 11, pp. 3978–3981, 2012.
- [12] L. Liu, C.-X. Shi, A. Ghayur et al., "Prolonged peritoneal gene expression using a helper-dependent adenovirus," *Peritoneal Dialysis International*, vol. 29, no. 5, pp. 508–516, 2009.
- [13] J. Zhang, K.-H. Oh, H. Xu, and P. J. Margetts, "Vascular endothelial growth factor expression in peritoneal mesothelial cells undergoing transdifferentiation," *Peritoneal Dialysis International*, vol. 28, no. 5, pp. 497–504, 2008.
- [14] C. M. Hoff and P. J. Margetts, "Adenovirus-based transient expression systems for peritoneal membrane research," *Peritoneal Dialysis International*, vol. 26, no. 5, pp. 547–558, 2006.
- [15] P. J. Margetts, P. Bonniaud, L. Liu et al., "Transient overexpression of TGF- $\beta$ 1 induces epithelial mesenchymal transition in the rodent peritoneum," *Journal of the American Society of Nephrology*, vol. 16, no. 2, pp. 425–436, 2005.
- [16] P. J. Margetts, S. Gyorffy, M. Kolb et al., "Antiangiogenic and antifibrotic gene therapy in a chronic infusion model of peritoneal dialysis in rats," *Journal of the American Society of Nephrology*, vol. 13, no. 3, pp. 721–728, 2002.
- [17] P. J. Margetts, M. Kolb, L. Yu, C. M. Hoff, and J. Gaudie, "A chronic inflammatory infusion model of peritoneal dialysis in rats," *Peritoneal Dialysis International*, vol. 21, supplement 3, pp. S368–S372, 2001.
- [18] O. Devuyst, P. J. Margetts, and N. Topley, "The pathophysiology of the peritoneal membrane," *Journal of the American Society of Nephrology*, vol. 21, no. 7, pp. 1077–1085, 2010.
- [19] J. Witowski, K. Książek, C. Warnecke et al., "Role of mesothelial cell-derived granulocyte colony-stimulating factor in interleukin-17-induced neutrophil accumulation in the peritoneum," *Kidney International*, vol. 71, no. 6, pp. 514–525, 2007.
- [20] J. Witowski, K. Pawlaczyk, A. Breborowicz et al., "IL-17 stimulates intraperitoneal neutrophil infiltration through the release of GRO $\alpha$  chemokine from mesothelial cells," *The Journal of Immunology*, vol. 165, no. 10, pp. 5814–5821, 2000.
- [21] L. Tran, H. Rodela, N. J. Abernethy et al., "Lymphatic drainage of hypertonic solution from peritoneal cavity of anesthetized and conscious sheep," *Journal of Applied Physiology*, vol. 74, no. 2, pp. 859–867, 1993.
- [22] M. S. Park, O. Heimburger, J. Bergstrom, J. Waniewski, A. Werynski, and B. Lindholm, "Evaluation of an experimental rat model for peritoneal dialysis: fluid and solute transport characteristics," *Nephrology Dialysis Transplantation*, vol. 9, no. 4, pp. 404–412, 1994.
- [23] K. Wieczorowska-Tobis, K. Korybalska, A. Polubinska, M. Radkowski, A. Breborowicz, and D. G. Oreopoulos, "In vivo model to study the biocompatibility of peritoneal dialysis solutions," *The International Journal of Artificial Organs*, vol. 20, no. 12, pp. 673–677, 1997.
- [24] S.-E. Park, Z. J. Twardowski, H. L. Moore, R. Khanna, and K. D. Nolph, "Chronic administration of iron dextran into the peritoneal cavity of rats," *Peritoneal Dialysis International*, vol. 17, no. 2, pp. 179–185, 1997.
- [25] K. Wieczorowska-Tobis, A. Polubinska, T. P. Schaub et al., "Influence of neutral-pH dialysis solutions on the peritoneal membrane: a long-term investigation in rats," *Peritoneal Dialysis International*, vol. 21, supplement 3, pp. S108–S113, 2001.
- [26] K. Wieczorowska-Tobis, A. Polubinska, A. Breborowicz, and D. G. Oreopoulos, "A comparison of the biocompatibility of phosphate-buffered saline and dianeal 3.86% in the rat model of peritoneal dialysis," *Advances in Peritoneal Dialysis*, vol. 17, pp. 42–46, 2001.
- [27] K. Pawlaczyk, E. Garcia-Lopez, M. Kuzlan-Pawlaczyk et al., "The effect of icodextrin-based solutions on peritoneal transport in rats undergoing chronic peritoneal dialysis," *Peritoneal Dialysis International*, vol. 21, supplement 3, pp. S359–S361, 2001.
- [28] K. Wieczorowska-Tobis, A. Styszynski, A. Polubinska, M. Radkowski, A. Breborowicz, and D. G. Oreopoulos, "Hypertonicity of dialysis fluid suppresses intraperitoneal inflammation," *Advances in peritoneal dialysis. Conference on Peritoneal Dialysis*, vol. 16, pp. 262–266, 2000.
- [29] A. Polubinska, K. Pawlaczyk, M. Kuzlan-Pawlaczyk et al., "Dialysis solution containing hyaluronan: effect on peritoneal permeability and inflammation in rats," *Kidney International*, vol. 57, no. 3, pp. 1182–1189, 2000.
- [30] K. Pawlaczyk, M. Kuzlan-Pawlaczyk, K. Wieczorowska-Tobis et al., "Bicarbonate/lactate dialysis solution improves in vivo function of peritoneal host defense in rats," *Peritoneal Dialysis International*, vol. 19, supplement 2, pp. S370–S377, 1999.
- [31] M. Kuzlan-Pawlaczyk, K. Pawlaczyk, K. Wieczorowska-Tobis et al., "Effect of N-acetylglucosamine on function of peritoneal leukocytes," *Peritoneal Dialysis International*, vol. 19, supplement 2, pp. S365–S369, 1999.
- [32] A. Breborowicz, K. Wieczorowska-Tobis, K. Korybalska, A. Polubinska, M. Radkowski, and D. G. Oreopoulos, "The effect of a nitric oxide inhibitor (L-NAME) on peritoneal transport during dialysis in rats," *Peritoneal Dialysis International*, vol. 18, no. 2, pp. 188–192, 1998.
- [33] K. Wieczorowska-Tobis, K. Korybalska, A. Polubińska et al., "Long-term effects of glycylglycine peritoneal dialysis solution with neutral pH on peritoneum in rats," *Advances in Peritoneal Dialysis*, vol. 13, pp. 42–46, 1997.
- [34] M. Kuzlan, K. Pawlaczyk, K. Wieczorowska-Tobis, K. Korybalska, A. Breborowicz, and D. G. Oreopoulos, "Peritoneal surface area and its permeability in rats," *Peritoneal Dialysis International*, vol. 17, no. 3, pp. 295–300, 1997.
- [35] A. Breborowicz, K. Wieczorowska-Tobis, M. Kuzlan et al., "N-acetylglucosamine: a new osmotic solute in peritoneal dialysis solutions," *Peritoneal Dialysis International*, vol. 17, no. 2, pp. S80–S83, 1997.
- [36] A. Breborowicz, L. M. Radkowski, J. Knapowski, and D. G. Oreopoulos, "Effects of chondroitin sulphate on fluid and solute transport during peritoneal dialysis in rats," *Peritoneal Dialysis International*, vol. 11, no. 4, pp. 351–354, 1991.
- [37] K. Pawlaczyk, C. J. Holmes, S. Czekalski, A. Breborowicz, and B. Lindholm, "Effects of bicarbonate/lactate dialysis solution on

- the inflammatory response of spontaneous peritonitis in rats undergoing chronic peritoneal dialysis," *Blood Purification*, vol. 28, no. 3, pp. 200–208, 2009.
- [38] Q. Yao, K. Pawlaczyk, E. R. Ayala et al., "The role of the TGF/Smad signaling pathway in peritoneal fibrosis induced by peritoneal dialysis solutions," *Nephron Experimental Nephrology*, vol. 109, no. 2, pp. e71–e78, 2008.
- [39] K. Pawlaczyk, A. Polubinska, M. Numata et al., "Vascular endothelial growth factor in dialysate in relation to intensity of peritoneal inflammation," *International Journal of Artificial Organs*, vol. 31, no. 6, pp. 535–544, 2008.
- [40] Q. Yao, K. Pawlaczyk, E. R. Ayala et al., "Peroxisome proliferator-activated receptor- $\gamma$  agonists diminish peritoneal functional and morphological changes induced by bioincompatible peritoneal dialysis solution," *Blood Purification*, vol. 24, no. 5-6, pp. 575–582, 2006.
- [41] A. Bręborowicz, A. Potubinska, G. Wu, P. Tam, and D. G. Oreopoulos, "N-acetylglucosamine reduces inflammatory response during acute peritonitis in uremic rats," *Blood Purification*, vol. 24, no. 3, pp. 274–281, 2006.
- [42] A. Breborowicz, K. Pawlaczyk, A. Połubinska et al., "Effect of peritoneal dialysis on renal morphology and function," *Nephrology Dialysis Transplantation*, vol. 21, no. 12, pp. 3539–3544, 2006.
- [43] S. Duman, K. Wieczorowska-Tobis, A. Styszynski, B. Kwiatkowska, A. Breborowicz, and D. G. Oreopoulos, "Intraperitoneal enalapril ameliorates morphologic changes induced by hypertonic peritoneal dialysis solutions in rat peritoneum," *Advances in Peritoneal Dialysis. Conference on Peritoneal Dialysis*, vol. 20, pp. 31–36, 2004.
- [44] A. Breborowicz, A. Połubińska, M. Simon, P. Tam, and G. Wu, "N-acetylglucosamine—an osmotic solute for peritoneal dialysis without inducing hyperinsulinemia," *Blood Purification*, vol. 22, no. 2, pp. 183–187, 2004.
- [45] K. Wieczorowska-Tobis, R. Brelinska, A. Breborowicz, and D. G. Oreopoulos, "Morphologic changes in the liver of dialyzed rats—preliminary observations," *Advances in Peritoneal Dialysis Conference on Peritoneal Dialysis*, vol. 19, pp. 20–23, 2003.
- [46] A. Styszynski, B. Kwiatkowska, K. Wieczorowska-Tobis, A. Breborowicz, and D. G. Oreopoulos, "Glucose and mannitol have different effects on peritoneal morphology in chronically dialyzed rats," in *Advances in Peritoneal Dialysis Conference on Peritoneal Dialysis*, vol. 19, pp. 15–19, 2003.
- [47] K. Wieczorowska-Tobis, A. Styszynski, A. Breborowicz, and D. G. Oreopoulos, "Comparison of the biocompatibility of phosphate-buffered saline alone, phosphate-buffered saline supplemented with glucose, and dianeal 3.86%," *Peritoneal Dialysis International*, vol. 21, no. 3, pp. S362–S364, 2001.
- [48] K. Wieczorowska-Tobis, A. Polubinska, J. Wisniewska et al., "Multidirectional approach to study peritoneal dialysis fluid biocompatibility in a chronic peritoneal dialysis model in the rat," *Nephrology Dialysis Transplantation*, vol. 16, no. 3, pp. 655–656, 2001.
- [49] K. Pawlaczyk, M. Kuzlan, K. Wieczorowska-Tobis et al., "Species-dependent topography of the peritoneum," *Advances in Peritoneal Dialysis*, vol. 12, pp. 3–6, 1996.
- [50] R. A. Mactier, R. Khanna, Z. J. Twardowski, and K. D. Nolph, "Role of peritoneal cavity lymphatic absorption in peritoneal dialysis," *Kidney International*, vol. 32, no. 2, pp. 165–172, 1987.
- [51] R. Mactier, R. Khanna, Z. Twardowski, and K. D. Nolph, "Estimation of lymphatic absorption and intraperitoneal volume during hypertonic peritoneal dialysis," *ASAIO Transactions/American Society for Artificial Internal Organs*, vol. 34, no. 1, pp. 82–84, 1988.
- [52] A. Breborowicz and R. Szulc, "Removal of endogenous lactates via the peritoneum in experimental lactic acidosis," *Intensive Care Medicine*, vol. 7, no. 6, pp. 297–300, 1981.
- [53] A. Breborowicz and J. Knapowski, "Augmentation of peritoneal dialysis clearance with procaine," *Kidney International*, vol. 26, no. 4, pp. 392–396, 1984.
- [54] A. Breborowicz and J. Knapowski, "Local anesthetic—bupivacaine increases the peritoneal transport of solutes. Part I: in vivo study," *Peritoneal Dialysis Bulletin*, vol. 4, no. 4, pp. 221–223, 1984.
- [55] A. Breborowicz and J. Knapowski, "Local anesthetic—bupivacaine increases the transperitoneal transport of solutes. Part II: in vitro study," *Peritoneal Dialysis Bulletin*, vol. 4, no. 4, pp. 224–228, 1984.
- [56] A. Breborowicz, H. Rodela, and D. G. Oreopoulos, "Effect of various factors on peritoneal lymphatic flow in rabbits," *Peritoneal Dialysis International*, vol. 9, no. 2, pp. 85–90, 1989.
- [57] A. Breborowicz and D. G. Oreopoulos, "Evidence for the presence of chronic inflammation during peritoneal dialysis: therapeutic implications," *Peritoneal Dialysis International*, vol. 17, no. 2, pp. S37–S41, 1997.
- [58] K. Pawlaczyk, M. Kuzlan-Pawlaczyk, K. Wieczorowska-Tobis, A. Polubinska, A. Breborowicz, and D. G. Oreopoulos, "Evaluation of the effect of uremia on peritoneal permeability in an experimental model of continuous ambulatory peritoneal dialysis in anephric rats," *Advances in Peritoneal Dialysis Conference on Peritoneal Dialysis*, vol. 15, pp. 32–35, 1999.
- [59] K. Wieczorowska-Tobis, A. Polubinska, M. Kuzlan-Pawlaczyk, K. Pawlaczyk, A. Breborowicz, and D. G. Oreopoulos, "The characteristics of peritoneal healing after catheter insertion in a rat model of peritoneal dialysis," *Advances in Peritoneal Dialysis. Conference on Peritoneal Dialysis*, vol. 14, pp. 36–39, 1998.
- [60] E. García-López, K. Pawlaczyk, B. Anderstam et al., "Icodextrin metabolism and alpha-amylase activity in nonuremic rats undergoing chronic peritoneal dialysis," *Peritoneal Dialysis International*, vol. 27, no. 4, pp. 415–423, 2007.
- [61] A. Breborowicz, M. Kuzlan-Pawlaczyk, K. Wieczorowska-Tobis et al., "The effect of N-acetylglucosamine as a substrate for in vitro synthesis of glycosaminoglycans by human peritoneal mesothelial cells and fibroblasts," *Advances in Peritoneal Dialysis*, vol. 14, pp. 31–35, 1998.
- [62] G. Wu, K. Wieczorowska-Tobis, A. Polubinska et al., "N-acetylglucosamine changes permeability of peritoneum during chronic peritoneal dialysis in rats," *Peritoneal Dialysis International*, vol. 18, no. 2, pp. 217–224, 1998.
- [63] A. Styszynski, K. Wieczorowska-Tobis, R. Podkowka, A. Breborowicz, and D. G. Oreopoulos, "Effects of glutathione supplementation during peritoneal dialysis," *Advances in Peritoneal Dialysis. Conference on Peritoneal Dialysis.*, vol. 22, pp. 88–93, 2006.
- [64] R. K. Mackenzie, S. Jones, A. Moseley et al., "In vivo exposure to bicarbonate/lactate- and bicarbonate-buffered peritoneal dialysis fluids improves ex vivo peritoneal macrophage function," *American Journal of Kidney Diseases*, vol. 35, no. 1, pp. 112–121, 2000.
- [65] S. Jones, C. J. Holmes, R. T. Krediet et al., "Bicarbonate/lactate-based peritoneal dialysis solution increases cancer antigen 125

- and decreases hyaluronic acid levels," *Kidney International*, vol. 59, no. 4, pp. 1529–1538, 2001.
- [66] R. A. Mactier, T. S. Sprosen, R. Gokal et al., "Bicarbonate and bicarbonate/lactate peritoneal dialysis solutions for the treatment of infusion pain," *Kidney International*, vol. 53, no. 4, pp. 1061–1067, 1998.
- [67] R. K. Mackenzie, C. J. Holmes, A. Moseley et al., "Bicarbonate/lactate- and bicarbonate-buffered peritoneal dialysis fluids improve ex vivo peritoneal macrophage tnf $\alpha$  secretion," *Journal of the American Society of Nephrology*, vol. 9, no. 8, pp. 1499–1506, 1998.
- [68] S. Jones, C. J. Holmes, R. K. Mackenzie et al., "Continuous dialysis with bicarbonate/lactate-buffered peritoneal dialysis fluids results in a long-term improvement in ex vivo peritoneal macrophage function," *Journal of the American Society of Nephrology*, vol. 13, supplement 1, pp. S97–S103, 2002.
- [69] N. Topley, D. Kaur, M. M. Petersen et al., "In vitro effects of bicarbonate and bicarbonate-lactate buffered peritoneal dialysis solutions on mesothelial and neutrophil function," *Journal of the American Society of Nephrology*, vol. 7, no. 2, pp. 218–224, 1996.
- [70] H. T. Schambye, P. Flesner, R. B. Pedersen et al., "Bicarbonate-versus lactate-based CAPD fluids: a biocompatibility study in rabbits," *Peritoneal Dialysis International*, vol. 12, no. 3, pp. 281–286, 1992.
- [71] K. Suzuki, R. Khanna, K. D. Nolph, H. L. Moore, and Z. J. Twardowski, "Effects of bicarbonate dialysis solution on peritoneal transport in rats," *Advances in Peritoneal Dialysis*, vol. 12, pp. 24–26, 1996.
- [72] J. A. Diaz-Buxo, E. G. Lowrie, N. L. Lew, S. M. H. Zhang, X. Zhu, and J. M. Lazarus, "Associates of mortality among peritoneal dialysis patients with special reference to peritoneal transport rates and solute clearance," *American Journal of Kidney Diseases*, vol. 33, no. 3, pp. 523–534, 1999.
- [73] L. Gotloib, P. Crassweller, H. Rodella et al., "Experimental model for studies of continuous peritoneal dialysis in uremic rabbits," *Nephron*, vol. 31, no. 3, pp. 254–259, 1982.
- [74] F. C. Barreto, R. B. de Oliveira, J. Benchitrit et al., "Effects of pyrophosphate delivery in a peritoneal dialysis solution on bone tissue of apolipoprotein-E knockout mice with chronic kidney disease," *Journal of Bone and Mineral Metabolism*, vol. 32, no. 6, pp. 636–644, 2014.
- [75] N. Braun, M. D. Alscher, M. Kimmel, K. Amann, and M. Büttner, "Encapsulating peritoneal sclerosis—an overview," *Néphrologie & Thérapeutique*, vol. 7, no. 3, pp. 162–171, 2011.
- [76] H. Nakamoto, H. Imai, Y. Ishida et al., "New animal models for encapsulating peritoneal sclerosis—role of acidic solution," *Peritoneal Dialysis International*, vol. 21, supplement 3, pp. S349–S353, 2001.
- [77] S. H. Park, Y. L. Kim, and B. Lindholm, "Experimental encapsulating peritoneal sclerosis models: pathogenesis and treatment," *Peritoneal Dialysis International*, vol. 28, supplement 5, pp. S21–S28, 2008.
- [78] H. Suga, S. Teraoka, K. Ota et al., "Preventive effect of pirfenidone against experimental sclerosing peritonitis in rats," *Experimental and Toxicologic Pathology*, vol. 47, no. 4, pp. 287–291, 1995.
- [79] R. C. Mackow, J. F. Winchester, W. P. Argy et al., "Sclerosing encapsulating peritonitis in rats: an experimental study with intraperitoneal antiseptics," *Contributions to Nephrology*, vol. 57, pp. 213–218, 1987.
- [80] C. G. Schalkwijk, N. Posthuma, H. J. Ten Brink, P. M. Ter Wee, and T. Teerlink, "Induction of 1,2-dicarbonyl compounds, intermediates in the formation of advanced glycation end-products, during heat-sterilization of glucose-based peritoneal dialysis fluids," *Peritoneal Dialysis International*, vol. 19, no. 4, pp. 325–333, 1999.
- [81] V. Schwenger, "GDP and AGE receptors: mechanisms of peritoneal damage," *Contributions to Nephrology*, vol. 150, pp. 77–83, 2006.
- [82] K. Chaudhary, H. Moore, A. Tandon, S. Gupta, R. Khanna, and R. R. Mohan, "Nanotechnology and adeno-associated virus-based decorin gene therapy ameliorates peritoneal fibrosis," *American Journal of Physiology—Renal Physiology*, vol. 307, no. 7, pp. F777–F782, 2014.

## Research Article

# Generation and Characterization of a Transgenic Mouse Carrying a Functional Human $\beta$ -Globin Gene with the IVSI-6 Thalassemia Mutation

**Giulia Breveglieri,<sup>1,2</sup> Irene Mancini,<sup>1</sup> Nicoletta Bianchi,<sup>1</sup> Ilaria Lampronti,<sup>1</sup> Francesca Salvatori,<sup>1,2</sup> Enrica Fabbri,<sup>1</sup> Cristina Zuccato,<sup>1</sup> Lucia C. Cosenza,<sup>1,2</sup> Giulia Montagner,<sup>1</sup> Monica Borgatti,<sup>1</sup> Fiorella Altruda,<sup>3</sup> Sharmila Fagoonee,<sup>3</sup> Gianni Carandina,<sup>4</sup> Michele Rubini,<sup>5</sup> Vincenzo Aiello,<sup>5</sup> Laura Breda,<sup>6</sup> Stefano Rivella,<sup>6</sup> Roberto Gambari,<sup>1,2</sup> and Alessia Finotti<sup>1,2</sup>**

<sup>1</sup>Department of Life Sciences and Biotechnology, Biochemistry and Molecular Biology Section, Ferrara University, 44121 Ferrara, Italy

<sup>2</sup>Laboratory for the Development of Pharmacological and Pharmacogenomic Therapy of Thalassemia, Biotechnology Center, Ferrara University, 44121 Ferrara, Italy

<sup>3</sup>Department of Molecular Biotechnology and Health Sciences, Molecular Biotechnology Center, Turin University, 10126 Turin, Italy

<sup>4</sup>Laboratory for Chemical and Clinical Analysis and Microbiology, University Hospital, Cona, 44124 Ferrara, Italy

<sup>5</sup>Department of Biomedical and Specialty Surgical Sciences, Medical Genetic Unit, Ferrara University, 44121 Ferrara, Italy

<sup>6</sup>Division of Hematology-Oncology, Department of Pediatrics, Weill Cornell Medical College, New York, NY 10065, USA

Correspondence should be addressed to Roberto Gambari; [roberto.gambari@unife.it](mailto:roberto.gambari@unife.it) and Alessia Finotti; [alessia.finotti@unife.it](mailto:alessia.finotti@unife.it)

Received 8 September 2014; Revised 3 December 2014; Accepted 3 December 2014

Academic Editor: Oreste Gualillo

Copyright © 2015 Giulia Breveglieri et al. This is an open access article distributed under the Creative Commons Attribution License, which permits unrestricted use, distribution, and reproduction in any medium, provided the original work is properly cited.

Mouse models that carry mutations causing thalassemia represent a suitable tool to test *in vivo* new mutation-specific therapeutic approaches. Transgenic mice carrying the  $\beta$ -globin IVSI-6 mutation (the most frequent in Middle-Eastern regions and recurrent in Italy and Greece) are, at present, not available. We report the production and characterization of a transgenic mouse line (TG- $\beta$ -IVSI-6) carrying the IVSI-6 thalassemia point mutation within the human  $\beta$ -globin gene. In the TG- $\beta$ -IVSI-6 mouse (a) the transgenic integration region is located in mouse chromosome 7; (b) the expression of the transgene is tissue specific; (c) as expected, normally spliced human  $\beta$ -globin mRNA is produced, giving rise to  $\beta$ -globin production and formation of a human-mouse tetrameric chimeric hemoglobin  $^{\text{mu}}\alpha$ -globin<sub>2</sub>/ $^{\text{hu}}\beta$ -globin<sub>2</sub> and, more importantly, (d) the aberrant  $\beta$ -globin-IVSI-6 RNAs are present in blood cells. The TG- $\beta$ -IVSI-6 mouse reproduces the molecular features of IVSI-6  $\beta$ -thalassemia and might be used as an *in vivo* model to characterize the effects of antisense oligodeoxynucleotides targeting the cryptic sites responsible for the generation of aberrantly spliced  $\beta$ -globin RNA sequences, caused by the IVSI-6 mutation. These experiments are expected to be crucial for the development of a personalized therapy for  $\beta$ -thalassemia.

*This article is dedicated to the memory of Renzo Galanello and Antonio Cao.*

## 1. Introduction

In  $\beta$ -thalassemias, mutations of the  $\beta$ -globin gene or its regulatory regions cause absence ( $\beta^0$ ) or reduced synthesis ( $\beta^+$ ) of  $\beta$ -globin chains [1–4], associated with a corresponding

excess of the complementary  $\alpha$ -globins. The outcome of this unbalanced globin production is the destruction of erythroid precursors in bone marrow and at extramedullary sites (ineffective erythropoiesis) by apoptosis and short survival of red blood cells (RBCs) in the peripheral blood [5–9].

The disease is associated with morbidity and mortality due to severe chronic anemia or treatment-related complications.

More than 200 point mutations cause  $\beta$ -thalassemia [10] and can affect transcription, splicing of the primary transcript, translation, and stability of the  $\beta$ -globin mRNA. For instance,  $\beta^0$ 39-thalassemia is caused by a stop codon mutation that leads to premature termination of  $\beta$ -globin chain synthesis [11, 12]; the  $\beta^0$ IVSI-1 mutation suppresses the correct maturation of the  $\beta$ -globin RNA precursor [13], while the  $\beta^+$ IVSI-110 allele coexpresses an abnormally spliced  $\beta$ -globin mRNA and a normal one [14].

Recently, the effort of several research groups has focused on the development of possible therapeutic interventions designed for patients carrying specific  $\beta$ -thalassemia mutations (personalized therapy). For instance, Salvatori et al. reported the proof-of-principle that aminoglycosides are able to restore to some extent HbA production in erythroid cells from homozygous  $\beta^0$ 39-thalassemia patients [15]. Lonkar et al. described a PNA-based approach method for targeted correction of a thalassemia-associated  $\beta$ -globin mutation [16]. In addition, other groups approached a therapy based on the correction of aberrant pre-mRNA splicing [17, 18].

Mouse models for the different mutations causing thalassemia are, therefore, very important to test *in vivo* the activity of new potential approaches that target specific mutations [19]. The mouse  $\beta$ -globin locus contains four functional  $\beta$ -globin genes:  $\beta$ h1 and  $\epsilon^y$  (transcribed only during the embryonic phase of development and silenced in 14-15-day-old embryos) and the b1 ( $\beta^{\text{major}}$ ) and b2 ( $\beta^{\text{minor}}$ ) genes that are transcriptionally activated *in utero* around 11 days after conception [20]. Unlike in humans,  $\gamma$ -like globin genes are not present in mouse, and the embryonic to adult hemoglobin (Hb) switch occurs before birth (while in humans this switch occurs during the first 6 months after birth). Accordingly, mice homozygous for mutations that prevent expression of the  $\beta$ -globin genes die perinatally, due to the lack of expression of any Hb [19], although recently models mimicking  $\beta^0$ -thalassemia have been generated. These animals are viable at birth due to the prolonged expression of human fetal hemoglobin and then require chronic transfusions for survival [20, 21]. However, the most utilized adult murine models carry the complete deletion of one or both the mouse  $\beta$ -globin genes, showing phenotypic features similar to those observed in  $\beta$ -thalassemia intermedia patients [22, 23]. These animals do not carry any of the most common mutations observed in  $\beta$ -thalassemia in humans.

Therefore, murine models of  $\beta$ -thalassemia, which carry a mutated human  $\beta$ -globin gene in combination with the presence of deletions of the mouse  $\beta$ -like globin genes can be an invaluable tool to test new therapeutic strategies. For instance, Vadolas et al. generated a humanized mouse model carrying the common  $\beta^+$ IVSI-110 splicing mutation on a bacterial artificial chromosome including the human  $\beta$ -globin locus [24]. They examined heterozygous murine  $\beta$ -globin knock-out mice carrying either the IVSI-110 or the normal human  $\beta$ -globin locus. A 90% decrease in human  $\beta$ -globin chain synthesis in the IVSI-110 mouse model compared with the mouse model carrying the normal human  $\beta$ -globin locus

was observed. This notable difference is attributed to aberrant splicing. The humanized IVSI-110 mouse model accurately mimics the splicing defect found in  $\beta$ -thalassemia patients with this mutation. This mouse model therefore offers a platform to test strategies for the restoration of normal splicing. Other examples of “humanized” transgenic mice proposed as model systems for  $\beta$ -thalassemia have been reported [25–27].

The generation of new transgenic mice carrying other specific  $\beta$ -thalassemia mutations might help the characterization and development of drugs that selectively target specific mutations. The IVSI-6 mutation is the most frequent in the Middle-Eastern region and is also recurrent in Italy and Greece [28–30]. This mutation leads to the activation of three cryptic splicing sites, which generate three aberrantly spliced mRNAs. The production of a mouse that expresses such mutation could supply a model to test new compounds and therapies for this population of patients. Therefore, we developed a novel and the first transgenic line carrying the human IVSI-6  $\beta$ -globin gene.

## 2. Materials and Methods

**2.1. Vector Design and Construction.** For the production of transgenic mice, we designed a lentiviral vector containing the human  $\beta$ -globin gene under the control of its physiological promoter and a portion of the human locus control region (LCR), named pCCL. $\beta$ -globin.PGK.GFP.WPRE (T9W) [31]. The vector T9W-IVSI-6 was generated by *in vitro* mutagenesis, introducing the IVSI-6  $\beta$ -thalassemic point mutation inside the human  $\beta$ -globin gene. Mutagenesis has been performed by using the QuickChange II Site-Directed Mutagenesis Kit (Stratagene, La Jolla, CA, USA) [32]. A double stranded mutant oligonucleotide (5'-CCTGGGCAGGTTGGCATCAAGGTTACAAG-3') was used in order to introduce the IVSI-6 mutation into the  $\beta$ -globin gene. The mutagenesis reaction has been performed in a final volume of 25  $\mu$ L, containing 25 ng of plasmid template, 1x Reaction Buffer (20 mM Tris-HCl pH 8.8, 2 mM MgSO<sub>4</sub>, 10 mM KCl, 10 mM (NH<sub>4</sub>)<sub>2</sub>SO<sub>4</sub>, 0.1 mg/mL BSA, 0.1% Triton X-100), 0.5  $\mu$ L of dNTP Mix, 62.5 ng of mutagenesis primers, by using 1.25 U of PfuUltra HF DNA polymerase. The thermal reaction has been performed by using the GeneAmp PCR System 9600 (Perkin Elmer, Waltham, MA, USA): after a first denaturation at 94°C for 3 minutes, 22 cycles were performed, consisting of denaturation at 95°C for 30 seconds, annealing at 55°C for 1 minute and elongation at 68°C for 8 minutes. At the end of the mutagenesis reaction, the amplification product was digested with 5 U of the restriction endonuclease DpnI, at 37°C for 1 hour, so as to remove the parental not mutated DNA. 5  $\mu$ L of the digestion reaction was then used to transform 120  $\mu$ L of ultracompetent *E. coli* JM109 bacteria: DNA and bacteria were incubated on ice for 4 hours and, then, after a thermic shock at 42°C for 45 seconds and immediately on ice for 2 minutes, 1 mL of Luria Bertani Medium (LB Medium: 10 g/L bacto-tryptone, 5 g/L yeast extract, 10 g/L NaCl) was added and an incubation at 37°C for 1 hour under slow agitation was performed; finally bacteria have been plated on Petri plates containing semisolid medium (LB

TABLE 1: PCR primers employed for identification and characterization of transgenic mice.

Name	Sequence	Length (nt)	Melting temperature (°C)	Gene
<i>MuActF</i>	5' TGACGGGGTCAACCACACTGTGCCCATCTA 3'	30	81	Murine $\beta$ -actin
<i>MuActR</i>	5' CTAGAAGCATTTGCGGTGGACGATGGAGGG 3'	30	80	Murine $\beta$ -actin
<i>TransF</i>	5' TGCATTCATTTGTTGTTGTTTTTCT 3'	25	65	Transgene (LCR)
<i>TransF</i> [6FAM]	5' [6-FAM] TGCATTCATTTGTTGTTGTTTTTCT 3'	25	65	Transgene (LCR)
<i>TransR</i>	5' TGAATAAACTCCACCTCAAACGG 3'	24	67	Transgene (LCR)
<i>HuBetaF</i>	5' AGACCTCACCTGTGGAGCC 3'	20	68	Human $\beta$ -globin
<i>HuBetaR</i>	5' TCAGGAGTGGACAGATCCCC 3'	20	67	Human $\beta$ -globin
<i>MuActF1</i> [6FAM]	5' [6-FAM] TACTTTGGGAGTGGCAAGCC 3'	20	66	Murine $\beta$ -actin
<i>MuActR1</i>	5' TCTCCATGTCGTCACAGTTG 3'	20	66	Murine $\beta$ -actin

TABLE 2: Primers employed for RT-PCR analyses.

Name	Sequence	Length (nt)	Melting temperature (°C)	Transcript
<i>HuBetaF1</i>	5' GCATCTGACTCCTGAGGAGAAGTC 3'	24	67	Human $\beta$ -globin
<i>HuBetaF1</i> [6FAM]	5' [6-FAM] GCATCTGACTCCTGAGGAGAAGTC 3'	24	67	Human $\beta$ -globin
<i>HuBetaR</i>	5' TCAGGAGTGGACAGATCCCC 3'	20	67	Human $\beta$ -globin
<i>MuBetaF</i>	5' CCTGACTGATGCTGAGAAGGC 3'	21	66	Murine $\beta$ -globin
<i>MuBetaR</i>	5' GCAGAGGATAGGTCTCCAAAGCTATC 3'	26	67	Murine $\beta$ -globin
<i>MuAlphaF</i>	5' CTGAAGCCCTGAAAGGATGT 3'	21	66	Murine $\alpha$ -globin
<i>MuAlphaR</i>	5' ATTTGTCCAGAGAGGCATGCA 3'	21	67	Murine $\alpha$ -globin
<i>MuActF2</i>	5' TGTATTCCCCTCCATCGTGG 3'	20	67	Murine $\beta$ -actin
<i>MuActR2</i>	5' CACAGCTGGATGGCTACGTAC 3'	22	68	Murine $\beta$ -actin
<i>IVSI+13F</i>	5' GGGCAGGTTGGCATCAAG 3'	18	67	IVSI+13 altered spliced transcripts

Medium with 15 g/L bacto-agar) in the presence of 100  $\mu$ g/mL ampicillin and incubated at 37°C for one night. The bacterial clones obtained were screened for the incorporation of the recombinant plasmid construct, whose nucleotide sequence was finally confirmed by DNA sequencing.

**2.2. Production of Transgenic Mice by Microinjection.** The 6.1 Kb XcmI-ClaI fragment corresponding to the  $\beta^+$ IVSI-6 insert was purified with the QIAquick Gel Extraction Kit (QIAGEN, Hilden, Germany) according to manufacturer's instructions and sterile filtered with a 0.22  $\mu$ m Costar Spin-X column (Corning Incorporated, Corning, NY, USA). Five hundred DNA molecules/picoliter were microinjected in the pronucleus of fertilized eggs of 8-week-old FVB mice. The injected embryos were implanted into CBA/J X C57BL/6J pseudopregnant females and the offspring genotype was tested for the integration of the transgene as described below.

**2.3. Transgenic Mice.** Mouse strains were supplied by Molecular Biotechnology Center of Turin University. Maintaining and experimental procedures were done at Ferrara University with the approval of Ethics Committee.

**2.4. Purification of Murine Genomic DNA.** Murine genomic DNA was purified from mouse tails. Briefly, 1x DreamTaq Buffer (containing KCl,  $(\text{NH}_4)_2\text{SO}_4$ , 20 mM  $\text{MgCl}_2$ ) (Fermentas, Burlington, ON, Canada) and 0.2 mg/mL proteinase

K were added to a 0.2–0.5 cm tail snip in a final volume of 50  $\mu$ L, before incubating at 57°C in a water bath for 16–20 hours. The samples were briefly vortexed and incubated at 95°C for 10 minutes to inactivate proteinase K and, finally, after centrifuging at maximum speed for 5 minutes, the supernatant containing genomic DNA was collected. Purified genomic DNA was checked by 0.8% agarose gel electrophoresis and quantified by spectrophotometry.

**2.5. Synthetic Oligonucleotides.** The nucleotide sequences of PCR primers were designed using the Primer Express Oligonucleotide Selection Software, version 1.0 (Applied Biosystems, Life Technologies, Carlsbad, CA, USA) and are reported in Tables 1 and 2. HPLC-grade oligonucleotides were purchased from Sigma Genosys (Cambridge, UK).

**2.6. Polymerase Chain Reaction (PCR).** In each PCR reaction, 1  $\mu$ L of murine genomic DNA was amplified by DreamTaq DNA polymerase (Fermentas): PCR was performed in a final volume of 100  $\mu$ L, containing 1x DreamTaq Buffer (containing KCl,  $(\text{NH}_4)_2\text{SO}_4$ , 20 mM  $\text{MgCl}_2$ ), 33  $\mu$ M dNTPs, 150 ng of PCR primers, and 1.25 U of DreamTaq DNA polymerase. PCR primer pairs used (Table 1) were as follows: *MuActF* (forward) and *MuActR* (reverse), designed to amplify a 871 bp sequence located on the murine  $\beta$ -actin gene; *TransF* (forward) and *TransR* (reverse), which amplify a 154 bp sequence on the transgene; *HuBetaF* (forward) and *HuBetaR* (reverse),

designed to amplify a 449 bp sequence on the human  $\beta$ -globin gene. The amplification cycles used were as follows: denaturation, 30 sec, 95°C; annealing, 20 sec, temperature 1–2°C lower than primer melting temperatures; elongation, 72°C for a length of time depending on the PCR product size.

**2.7. Sequencing of PCR Products.** *HuBetaF-HuBetaR* PCR products, containing part of the human  $\beta$ -globin gene, were purified with MicroCLEAN (Microzone Limited, Haywards Heath, West Sussex, UK) and sequenced by using the ABI PRISM BigDye Terminator Cycle Sequencing Ready Reaction Kit, v1.0 (Applied Biosystems). Sequence reactions were performed in a final volume of 20  $\mu$ L, containing 40 ng of PCR template, 3.2 pmoles of primer *HuBetaR*, 1x Sequencing Buffer, and 8  $\mu$ L of Terminator Ready Reaction Mix. 45 amplification cycles were performed, as follows: denaturation, 96°C, 10 seconds; annealing, 65°C, 5 seconds; elongation, 65°C, 3 minutes. A denaturing 4% polyacrylamide gel electrophoresis was then carried out in an automated ABI PRISM 377 DNA Sequencer (Applied Biosystems), and final sequence data were analyzed by Sequencing Analysis 3.3 (Applied Biosystems) and Chromas Lite 2.01 (Copyright© 2003–2008 Technelysium Pty Ltd.) softwares.

**2.8. Quantification of Human  $\beta$ -Globin Genes in Transgenic Mice by Real-Time PCR.** Calibration curves were obtained using 50, 100, and 150 ng of genomic DNA from a hemizygous mouse and the  $\beta$ -actin gene as endogenous control. The relative  $\beta$ -globin/actin gene ratio in investigated mice was compared to the same ratio in the hemizygous control mouse. Quantitative real-time PCR assay was carried out using gene-specific double fluorescently labeled probes. The primers and probes used for real-time PCR analysis of human  $\beta$ -globin gene (Assay ID Hs00758889\_s1) and of mouse cytoplasmic  $\beta$ -actin (Assay ID Mm00607939\_s1) were purchased from Applied Biosystems. The hemizygous or homozygous status of transgenic mice was determined by relative real-time PCR, taking a hemizygous DNA as a reference, by using the comparative cycle threshold method [15, 33, 34].

**2.9. Quantitative Multiplex PCR of Short Fluorescent Fragments (QMPSF).** To determine transgene dosage comparing and discriminating homozygous from hemizygous samples, dosage quotients (DQ) were obtained by QMPSF assays as reported by Yau et al. [35] and Feriotta et al. [36]. A 2-fragment multiplex PCR assay was performed to amplify a 154 bp transgene sequence, using primers *TransF[6FAM]* and *TransR* (Table 1) and a 201 bp fragment belonging to the murine  $\beta$ -actin gene, used as a normalization control, by using primers *MuActF1[6FAM]* and *MuActR1* (Table 1). All forward primers in the assay were 5'-labeled with the fluorescent phosphoramidite 6-FAM (Sigma Genosys).

Amplifications were performed in 25  $\mu$ L volumes, containing 125 ng genomic DNA, 0.01–0.02  $\mu$ M forward primers (unlabeled reverse primers were used as 1.4-fold excess respect to the corresponding forward primers; relative ratios between transgene primers and  $\beta$ -actin primers were

0.3:0.6), 66  $\mu$ M dNTPs, and 0.7 U of DreamTaq DNA polymerase (Fermentas). After 6-minute initial denaturation at 96°C, a “hot start” amplification was initiated by adding DreamTaq DNA polymerase, followed by 19 cycles consisting of a 15 seconds denaturation step at 95°C, a 30 seconds annealing step at 64°C, and a 15 seconds extension step at 72°C, with a final extension for 45 minutes at 72°C. The PCR products were analyzed by electrophoresis and the fluorescent signals were identified by using the ABI GeneScan Analysis Software, version 3.1 (Applied Biosystems) to produce electropherograms in which areas under the peaks represent the amount of PCR products. The molecular weight marker used was the GeneScan 400HD [Rox] Dye Size Standard (Applied Biosystems), designed for sizing DNA fragments in the 50–400 nucleotides range. In order to determine transgene dosage and to compare and discriminate homozygous and hemizygous samples, dosage quotients (DQ) were obtained as elsewhere described [35, 36].

**2.10. Hematological Analysis.** Blood was collected from 16-week-old transgenic mice by retroorbital bleeding into tubes containing EDTA and analyzed by an automated Sysmex XE 2100 hematological analyzer (TOA Sysmex, Japan) at the Laboratory for Chemical and Clinical Analysis and Microbiology, University Hospital, Ferrara, Italy.

**2.11. Fluorescence In Situ Hybridization (FISH) Analysis.** Fibroblast cell cultures were established in DMEM medium (Gibco, Life Technologies, Carlsbad, CA, USA) with non-essential aminoacids (Sigma-Aldrich, St. Louis, MO, USA), penicillin/streptomycin and 10% fetal calf serum, from tail samples from transgenic mice. The cells were grown for 10–14 days and then harvested following colcemid inhibition of cell division for 3–6 h. Chromosome preparations were obtained by using standard techniques. A probe was prepared from the intact T9W-IVSI-6 vector, directly labeled by nick translation with the DIG-Nick Translation Mix (Roche Applied Science, Penzberg, Upper Bavaria, Germany) according to the manufacturer's protocol. The probe was hybridized and then detected with anti-digoxigenin-fluorescein Fab fragments (Roche Applied Science). The slides were mounted in Vectashield (Vector Laboratories, Burlingame, CA) containing 4',6-diamidino-2-phenylindole (DAPI) counterstain. FISH signals were examined with Olympus Provis epifluorescence microscope and images were captured using Leica Microsystems CytoVision imaging equipment and software (Applied Imaging, Leica-Microsystems, Wetzlar, Germany). The chromosomal site of transgene integration was determined by karyotypic analysis of banded chromosomes obtained using the DAPI image.

**2.12. RT-PCR.** Total RNA was obtained from 250  $\mu$ L of wild-type, hemizygous, and homozygous mouse whole blood using the Mouse RiboPure Blood RNA Isolation Kit (Ambion/Applied Biosystems, Austin, TX, USA). cDNA was synthesized from 250 ng of total RNA using Superscript VILO cDNA Synthesis kit (Invitrogen, Carlsbad, CA, USA). PCR was performed using a GeneAmp PCR 9700 System (Perkin

Elmer, Waltham, MA, USA), 1/20 of reverse transcription reaction mixture (cDNA), 125 ng of human genomic DNA or 20 ng of pCCL. $\beta$ -globin.PGK.GFP.WPRE (T9W) [31] vector DNA, 2 U of DyNAzyme DNA polymerase (Finnzymes, Oy, Espoo, FI), and 33  $\mu$ M deoxynucleoside triphosphates. The *HuBetaF1* forward and the *HuBetaR* reverse primers (Table 2) were designed to amplify a 153 bp fragment of the human  $\beta$ -globin transcript or a 283 bp product of the corresponding human genomic DNA. The *MuBetaF* forward and *MuBetaR* reverse primers (Table 2) were used to amplify a 147 bp product of the mouse  $\beta$ -globin transcript. The PCR conditions were as follows: 35 cycles of amplification, which included a 20-second denaturation step at 95°C, a 30-second annealing step at 66°C, and a 25-second elongation step at 72°C.

**2.13. Real-Time RT-PCR.** For RNA extraction, transgenic mouse tissues were homogenized using IKA T10 Basic Ultra-turrax (IKA Werke GmbH & Co. KG, Staufen, DE) directly in TRIzol Reagent (Invitrogen) and 1  $\mu$ g of the obtained total RNA was treated with RQ1 DNase (Promega, Madison, WI, USA) to remove genomic DNA contaminations. cDNAs were synthesized from 250 ng of total RNA using Superscript VILO cDNA Synthesis kit (Invitrogen). For quantitative real-time PCR reaction, 0.8/20  $\mu$ L of cDNA, 150 ng of each primer (Table 2), and 1x iQ SYBR Green Supermix (Bio-Rad, Hercules, CA, USA) were used for each reaction. *HuBetaF1* and *HuBetaR* primers were designed to amplify a 153 bp sequence present in transgenic human  $\beta$ -globin transcripts, *MuBetaF-MuBetaR* primers and *MuAlphaF-MuAlphaR* primers were designed to amplify a 147 bp sequence present in mouse  $\beta$ -globin transcript and a 306 bp sequence present in mouse  $\alpha$ -globin transcript, respectively, while *MuActF2* and *MuActR2* primers were designed to amplify a 331 bp sequence of mouse  $\beta$ -actin transcript (Table 2). Primer pairs and amplification conditions were validated by melting curve and electrophoretic analysis. Real-time PCR reactions were performed for a total of 40 cycles (95°C for 10 s, 66°C for 30 s, and 72°C for 25 s) using an iCycler IQ5 (Bio-Rad). The relative proportions of each template amplified were determined by using the IQ5 software (Bio-Rad), employing the  $\Delta\Delta C_t$  method [15, 33, 34] to compare gene expression data.

**2.14. Cell Lines and Culture Conditions.** Murine erythroleukemia (MEL) cells [37] were grown in modified Dulbecco's minimal essential medium (D-MEM, Lonza Group, Basel, CH) supplemented with 10% fetal bovine serum (BioWest, Nuaillé, France), penicillin (550 units/mL), and streptomycin (75 units/mL) (Lonza Group) at 37°C in 5% CO<sub>2</sub> humidified atmosphere. Cell growth was monitored daily using a Burkler chamber. Cell viability was measured by trypan blue staining (Burr, BDH Chemicals, Poole, England) [38].

**2.15. In Vitro Culture of Erythroid Progenitors from IVSI-6  $\beta$ -Thalassemia Patients.** Blood samples from healthy donors and homozygous IVSI-6 patients were collected after receiving informed consent. The two-phase liquid culture procedure was employed as previously described [39, 40]. Mononuclear cells were isolated from peripheral blood samples

of normal donors by Ficoll-Hypaque density gradient centrifugation and seeded in  $\alpha$ -minimal essential medium ( $\alpha$ -MEM, Sigma Genosys) supplemented with 10% FBS (Celbio, Milano, Italy), 1  $\mu$ g/mL cyclosporine A (Sandoz, Basel, Switzerland), and 10% conditioned medium from the 5637 bladder carcinoma cell line. The cultures were incubated at 37°C, under an atmosphere of 5% CO<sub>2</sub>. After 7 days in this phase I culture, the nonadherent cells were harvested, washed, and then cultured in phase II medium, composed of  $\alpha$ -MEM (Sigma Genosys), 30% FBS (Celbio), 1% deionized bovine serum albumin (BSA, Sigma Genosys), 10<sup>-5</sup> M  $\beta$ -mercaptoethanol (Sigma Genosys), 2 mM L-glutamine (Sigma Genosys), 10<sup>-6</sup> M dexamethasone (Sigma Genosys), and 1 U/mL human recombinant erythropoietin (EPO) (Tebu-bio, Magenta, Milano, Italy), and stem cell factor (SCF, BioSource International, Camarillo, CA, USA) at the final concentration of 10 ng/mL. Erythroid differentiation was assessed by benzidine staining, in a solution containing 0.2% benzidine HCl (Sigma Genosys) in 0.5 M glacial acetic acid, preactivated with 10% (v/v) of a solution 30% H<sub>2</sub>O<sub>2</sub> [36].

**2.16. Induction of Erythroid Differentiation and Transduction of MEL Cells.** MEL cells were stimulated to differentiation by dimethyl sulfoxide (DMSO) [37] (Sigma Genosys) and transduced with the lentiviral vectors T9W [31] or T9W-IVSI-6. The infection was performed by plating 2  $\times$  10<sup>6</sup> MEL cells in 3 mL of medium in a 6-well plate; then fresh 2% v/v DMSO was added and cells were incubated 18–20 hours at 37°C in a humidified incubator in an atmosphere of 5% CO<sub>2</sub>. Then, MEL cells were infected with T9W, a lentiviral vector carrying the human  $\beta$ -globin gene and large elements from the human locus control region (LCR), at an MOI (multiplicity of infection) of 0.5. We used polybrene at 8  $\mu$ g/mL final concentration to facilitate viral entry and then incubated the cells for 16 hours at 37°C in a humidified incubator in an atmosphere of 5% CO<sub>2</sub>. The infected cells were collected by centrifuging at 300 g for 5 minutes at room temperature, to remove the medium containing not integrated viral particles. The cells were then resuspended in 3 mL of fresh medium and replated in a 6-well plate. After 10 hours, MEL cells were collected and spun at 300 g for 5 minutes at room temperature. The treatment of MEL cells with T9W-IVSI-6 vector was performed as just described, after plating 5  $\times$  10<sup>5</sup> MEL cells in 1 mL of medium in a 24-well plate. Cells were counted in a Burkler chamber and the benzidine positive ones were determined as percentage as elsewhere reported [36].

**2.17. Western Blotting.** 10  $\mu$ L of 1:200 diluted mouse whole blood was analyzed and 4  $\mu$ g of human adult hemoglobin A<sub>0</sub> (H-0267, Sigma Genosys) was used as migration reference; proteins were denatured for 5 minutes at 98°C in SDS gel loading buffer 1x (50 mM Tris-HCl pH 6.8, 2% SDS, 100 mM Dithiothreitol (DTT), 0.1% bromophenol blue, 10% glycerol) and separated by SDS-PAGE, by using a 10 cm  $\times$  8 cm gel and Tris-glycine Buffer (25 mM Tris, 192 mM glycine, 0.1% SDS). The electrotransfer to 20 microns nitrocellulose membrane was performed for 3 hours at 400 mA and 4°C, in electrotransfer buffer (25 mM Tris, 192 mM glycine, 5% methanol).

The membrane was prestained in Ponceau S Solution (Sigma Genosys) to verify the transfer, washed with 25 mL Tris-buffered saline (TBS) (10 mM Tris-HCl pH 7.4, 150 mM NaCl) for 10 minutes at room temperature and incubated in 20 mL of blocking buffer (TBS, 0.1% Tween-20, 5% w/v nonfat dry milk) for 1 hour at room temperature. The membrane was then incubated with primary mouse monoclonal antibody (1:200) (sc-21757, Santa Cruz Biotechnology, Santa Cruz, CA, USA) targeting the human  $\beta$ -globin, in 10 mL of blocking buffer with gentle agitation overnight at 4°C. The day after, the membrane was washed three times for 5 minutes each with 20 mL of TBS/T (TBS, 0.1% Tween-20) and incubated with 25 ng/mL anti-mouse HRP-conjugated secondary antibody (1:2000) (Pierce Thermo Scientific, Rockford, IL, USA) in 10 mL TBS/T with gentle agitation for 1 hour at room temperature. After three washes, each with 15 mL of TBS/T for 5 minutes, finally the membrane was incubated with 5 mL of Western Lightning Chemiluminescence Reagent Plus (PerkinElmer Sciences, Waltham, MA, USA) with gentle agitation for 1 minute at room temperature and exposed to X-ray film (Amersham Hyperfilm ECL, GE Healthcare, Buckinghamshire, UK). For western blotting in nondenaturing conditions, 10  $\mu$ L of 1:200 diluted mouse whole blood, 30  $\mu$ g of MEL cells extracts, and 500 ng of human adult hemoglobin A<sub>0</sub> (H-0267, Sigma Genosys) were diluted in 1x native gel loading buffer (50 mM Tris-HCl pH 8.8, 0.1% bromophenol blue, 10% glycerol) and separated by a NATIVE-PAGE, by using a 10 cm  $\times$  8 cm gel and Tris-glycine buffer without SDS. The following steps and conditions were the same described above for denaturing western blotting.

**2.18. Capillary Electrophoresis (CE).** High voltage CE was performed by using the Minicap Flex Piercing capillary system (Sebia, Lisses, France). Manufacturer's guidelines were followed in performing the analysis. Sample processing required a 1:6 dilution of 50  $\mu$ L whole blood with hemolysing solution and vortexing for 5 seconds. After loading the primary sample tubes into the carousel, the instrument performed automated bar code reading, mixing of the samples by inversion, cap piercing, sampling, and dilution. Electrophoresis was performed at alkaline pH (9.4), high voltage (9500 V), and controlled temperature. The hemoglobin bands were detected by absorption photometry, and optical density measurements were converted to a migration image, displayed as a graph called "electropherogram." The migration position is measured in arbitrary units between 0 and 300 and can be quantified as a percentage. Results were acquired and examined by using the Sebia Phoresis REL 8.6.2 Software.

**2.19. RT-PCR for Alternatively Spliced Transcripts.** After RQ1 DNase (Promega) treatment, 250–500 ng of total RNA were used to synthesize cDNAs, using Superscript VILO cDNA Synthesis kit (Invitrogen), according to the manufacturer's instructions. PCR was performed using 2 out of 20  $\mu$ L of reverse transcription reaction mixture, 2 U of DyNAzyme DNA polymerase (Finnzymes) and 33  $\mu$ M deoxynucleoside triphosphates. Fluorescent PCR products were obtained using the *HuBetaF1[6-FAM]* forward and *HuBetaR* reverse

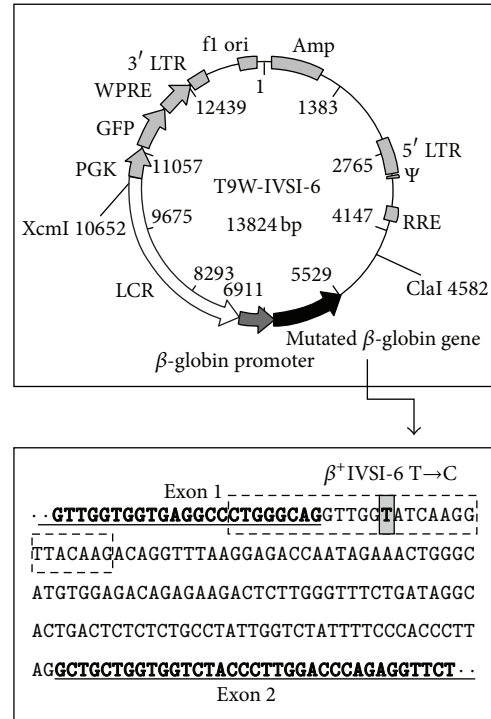


FIGURE 1: Map of the T9W-IVSI-6 vector showing the XcmI and ClaI restriction sites, used to cut the vector for microinjection. The human  $\beta$ -globin genomic region containing the  $\beta^+$ IVSI-6 thalassemic point mutation (grey box) is also reported. The final portion of the  $\beta$ -globin exon 1 and the first portion of the  $\beta$ -globin exon 2 are underlined and marked in bold characters. The position of mutagenesis primers is boxed with a dashed line.

primers (Table 2) and detected after electrophoresis in a denaturant polyacrylamide gel using the ABI GeneScan Analysis Software, version 3.1 (Applied Biosystems). For the specific amplification of the aberrant transcript caused by the activation of the cryptic splicing site at position IVSI+13, *IVSI+13F* forward and *HuBetaR* reverse primers (Table 2), designed to amplify, after retrotranscription, 84 bp of human  $\beta$ -globin alternatively spliced transcript or 202 bp of human pre-mRNA (containing all the first human  $\beta$ -globin intron), were employed. The PCR conditions were as follows: 40–50 cycles of amplification, with 10 seconds of denaturation at 95°C, 30 seconds of annealing at 66°C, and 15 seconds of elongation at 72°C. Negative controls (no template cDNA) were also run to assess specificity and to rule out contamination.

### 3. Results

**3.1. Vector Design and Construction.** For the generation of transgenic mice, we designed and produced a construct modifying the pCCL. $\beta$ -globin.PGK.GFP.WPRE (T9W) cassette previously described [31]. This cassette contains the human  $\beta$ -globin gene under the control of its physiological promoter and a portion of the human locus control region (LCR) (Figure 1). The construct, named T9W-IVSI-6, was generated by *in vitro* mutagenesis, by introducing the  $\beta^+$ IVSI-6 point

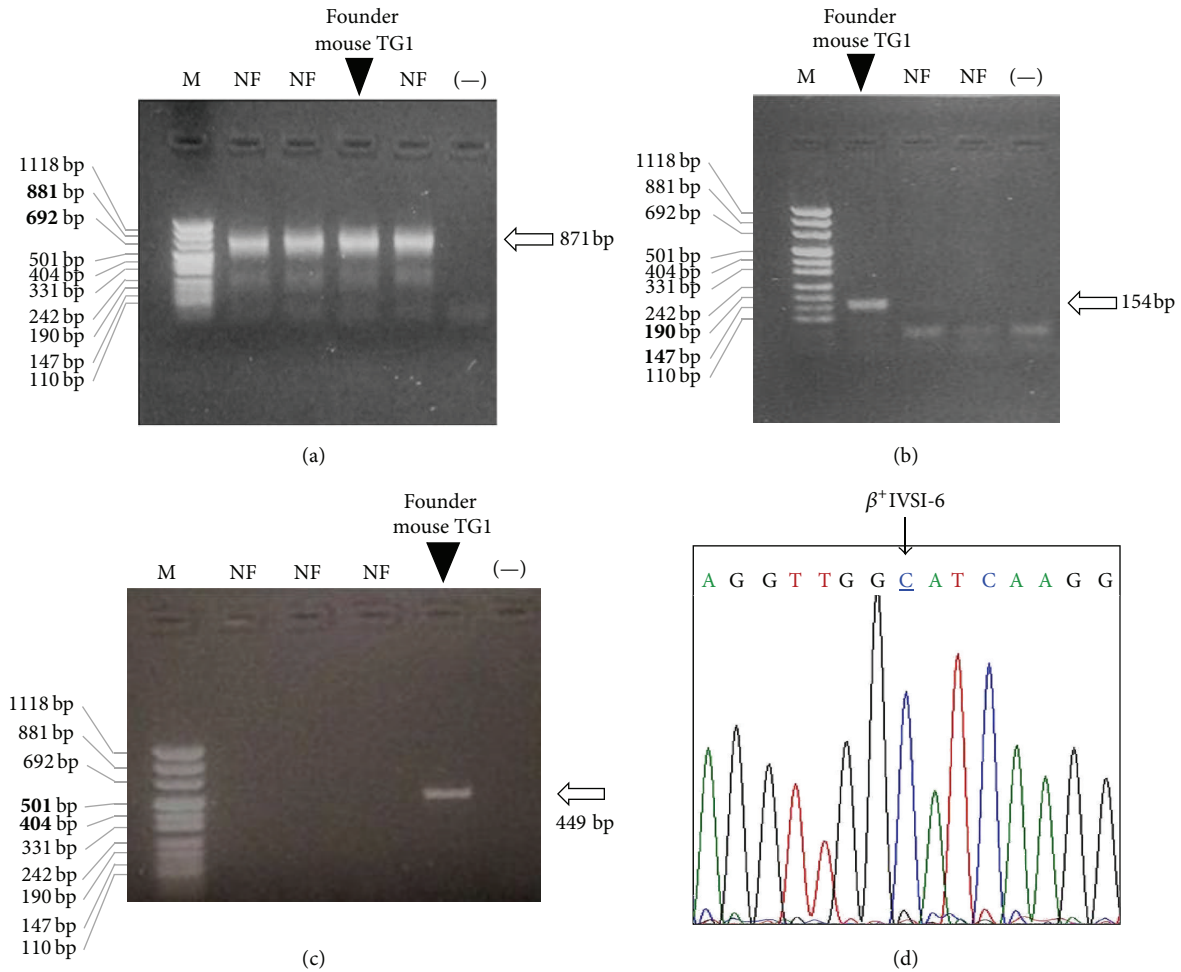


FIGURE 2: Identification of the founder mouse of the transgenic  $\beta^+$ IVSI-6 line. (a–c) Electrophoretic analyses of PCR products obtained by the amplification of murine genomic DNAs with primers *MuActF-MuActR* (a), *TransF-TransR* (b), and *HuBetaF-HuBetaR* (c), recognizing the murine  $\beta$ -actin gene, the transgene sequence, and the human  $\beta$ -globin gene, respectively. NF, negative founders; (-), negative control (water added to the amplification mixture); M, molecular weight ladder, pUC Mix Marker 8 (Fermentas). Arrows indicate the expected position of the specific amplification products; the lanes carrying the specific PCR products, relative to the founder mouse TG1, are also indicated. (d) Portion of electropherogram obtained by sequencing the *HuBetaF-HuBetaR* PCR product, obtained by the founder mouse TG1. The arrow indicates the peak corresponding to the  $\beta^+$ IVSI-6 thalassemic point mutation (underlined nucleotide).

mutation, one of the most common molecular defects present in the  $\beta$ -thalassemia populations of Italy and Greece, in the human  $\beta$ -globin gene.

**3.2. Production of the Transgenic Founder Mouse Carrying the Human  $\beta$ -Globin Gene with the  $\beta^+$ IVSI-6 Mutation (TG- $\beta$ -IVSI-6).** Potential TG- $\beta$ -IVSI-6 founder mice were produced by microinjection of the purified 6.1 Kb XcmI-ClaI fragment, corresponding to the  $\beta^+$ IVSI-6 insert, from the construct T9W-IVSI-6 (Figure 1).

For the screening and identification of the transgenic founders, murine genomic DNA was purified from the tails and analyzed by polymerase chain reaction (PCR). Figure 2(b) shows that only the genomic DNA of the TG- $\beta$ -IVSI-6 founder mouse (founder mouse TG1) was amplified by using *TransF* and *TransR* primers (Table 1), which anneal to the transgene sequence, while all the analyzed samples

were amplified by using PCR primers specific for the murine  $\beta$ -actin gene (Figure 2(a)). Accordingly, Figure 2(c) shows the electrophoretic analysis of PCR products obtained by the amplification of four samples of murine genomic DNA with primers *HuBetaF* and *HuBetaR* (Table 1), specific for the human  $\beta$ -globin gene: again, the expected 449 bp band was generated only by the amplification of genomic DNA belonging to the founder mouse TG1. The 449 bp PCR product shown in Figure 2(c) was sequenced to confirm that the  $\beta^+$ IVSI-6 thalassemic point mutation was present in the DNA of the TG- $\beta$ -IVSI-6 founder mouse (Figure 2(d)).

**3.3. Characterization of the TG- $\beta$ -IVSI-6 Homozygous Mice.** As a first step to produce homozygous  $\beta^+$ IVSI-6 transgenic lines, the founder mouse was back-crossed with wild-type mice. Figure 3(a) shows the electrophoretic migration of PCR products obtained by the amplification of genomic DNA

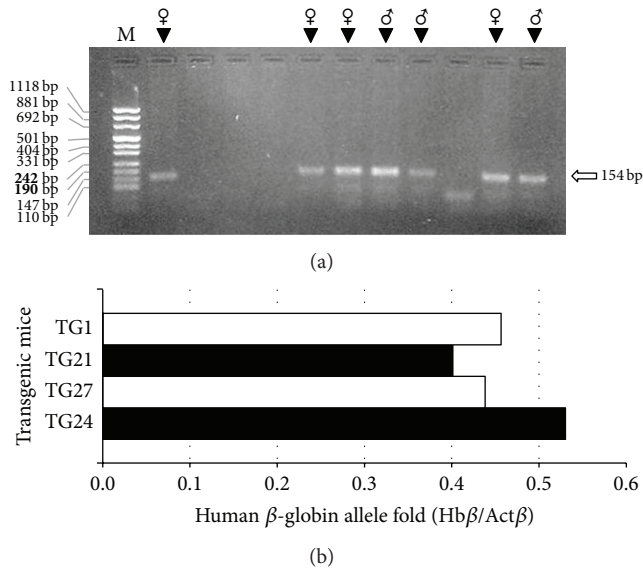


FIGURE 3: Identification of hemizygous mice among animals belonging to the F1 generation. (a) Agarose gel electrophoretic analysis of PCR products obtained by the amplification of genomic DNA purified from eleven mice with primers *TransF* and *TransR*, recognizing the transgene sequence. The arrow indicates the position of the expected 154 bp product; the sex of mice having generated a specific amplification band is also shown. M, molecular weight ladder, pUC Mix Marker 8 (Fermentas). (b) Human  $\beta$ -globin allele quantification by real-time PCR using primers and probes specific for human  $\beta$ -globin (*Hb $\beta$* ) gene and mouse cytoplasmic  $\beta$ -actin (*Act $\beta$* ) gene. Results of analysis of transgenic hemizygous mice TG21, TG24, and TG27, together with the founder mouse TG1, are reported as fold of human  $\beta$ -globin allele amount quantified with respect to the murine  $\beta$ -actin gene.

purified from eleven mice belonging to the F1 generation, with primers recognizing the transgene sequence. The arrow indicates the position of the 154 bp expected PCR product of the human  $\beta$ -globin transgene: we obtained three male and four female hemizygous mice. Homozygous animals were finally produced by crossing hemizygous F1 mice. In order to get preliminary information on the number of integration events occurring, quantitative real-time PCR assays were carried out by using gene-specific double fluorescently labeled probes. The analyses of three hemizygous mice (TG21, TG27 and TG24) are shown in Figure 3(b) and show a  $\beta$ -globin/ $\beta$ -actin ratio of about 0.5, compatible with a single copy integration of the transgene.

As a second step, in order to discriminate hemizygous and homozygous mice, real-time PCR analyses were performed. Figure 4(a) shows the real-time PCR analysis of six F2 transgenic mice, three of which are hemizygous (TG79, TG82, and TG84) and three homozygous (TG80, TG81, and TG83), according to the  $\beta$ -globin gene amplification compared to the F1 hemizygous TG24 mouse. These data were confirmed by quantitative multiplex PCR of short fluorescent fragments (QMPSF), as indicated by the representative example shown in Figure 4(b), performed on TG24 and TG81 mice. In the lower panel of Figure 4(b), the absolute value of human  $\beta$ -globin (transgene) and mouse  $\beta$ -actin (*Act $\beta$* ) peak areas are

indicated, together with their relative ratio in hemizygous and homozygous mice. These data indicate the establishment of the homozygous line.

**3.4. Chromosomal Localization of the Human  $\beta$ -IVSI-6 Transgene.** Figure 5 shows representative FISH analyses performed on wild-type, hemizygous, and homozygous  $\beta^+$ IVSI-6 transgenic mice, demonstrating that integration occurred at band F2 of the mouse chromosome 7. As clearly shown, no FISH signals were found in wild-type samples (Figures 5(h) and 5(i)). Only one chromosome 7 gave FISH signals in hemizygous samples (Figures 5(f) and 5(g)), while in homozygous samples both chromosomes gave FISH signals (Figures 5(a)–5(e)). These data support the concept that only one integration unit of the human  $\beta^+$ IVSI-6 transgene is present in the produced homozygous  $\beta^+$ IVSI-6 transgenic mice. These data have been reproduced several times obtaining identical results.

**3.5. Tissue Specific Expression of the Human  $\beta$ -IVSI-6 Transgene.** Figure 6(a) shows the RT-PCR analysis performed with total RNA isolated from wild-type (lanes e and h), transgenic hemizygous (lanes c and f) and transgenic homozygous (lanes d and g) TG- $\beta$ -IVSI-6 mice using *HuBetaF1* and *HuBetaR* primers (lanes c, d, e), which selectively amplify human  $\beta$ -globin transcript, and primers *MuBetaF* and *MuBetaR* (lanes f, g, h) specific for mouse  $\beta$ -globin transcript. All the samples, amplified using the murine specific primers, generated the expected 147 bp product, whereas the human  $\beta$ -globin PCR product (153 bp) was obtained only from transgenic animals, but not from wild-type mice. Genomic DNA and T9W vector DNA were also amplified with *HuBetaF1* and *HuBetaR* primer pair (lanes a and b), showing a 283 bp product containing the intronic sequence as well.

The analysis confirms the human  $\beta$ -IVSI-6 transgene expression and the quantitative RT-PCR analyses shown in Figure 6(b) support this evidence: amplification employing the *HuBetaF1* and *HuBetaR* primers (black bar) was indeed observed only in the blood of transgenic mice. No significant differences were found in the endogenous  $\alpha$  and  $\beta$ -globin expression between wild-type and transgenic mouse blood samples. The right panel of Figure 6(c) shows that high transgene expression is mainly observed in blood and to a much lower extent in the spleen. The transgene tissue specific expression was confirmed by comparing the amount of the human IVSI-6  $\beta$ -globin transgenic RNA to the endogenous murine  $\beta$ -globin mRNAs isolated from different tissues, including spleen, brain, liver, lung, stomach, and kidney (left panel of Figure 6(c)). The expression of human  $\beta$ -globin transcripts in transgenic mouse tissues (right panel, black bars) is comparable to the endogenous mouse  $\beta$ -globin transcripts (left panel, grey bars), and the highest transcription of both human and murine globin mRNAs was restricted to the splenic compartment, as expected; in addition, the results shown in Figure 6(c) demonstrate that the pattern of IVSI-6  $\beta$ -globin RNA expression is very similar to that of murine  $\beta$ -globin RNA, strongly suggesting that the tissue specific expression is maintained in the TG- $\beta$ -IVSI-6 line

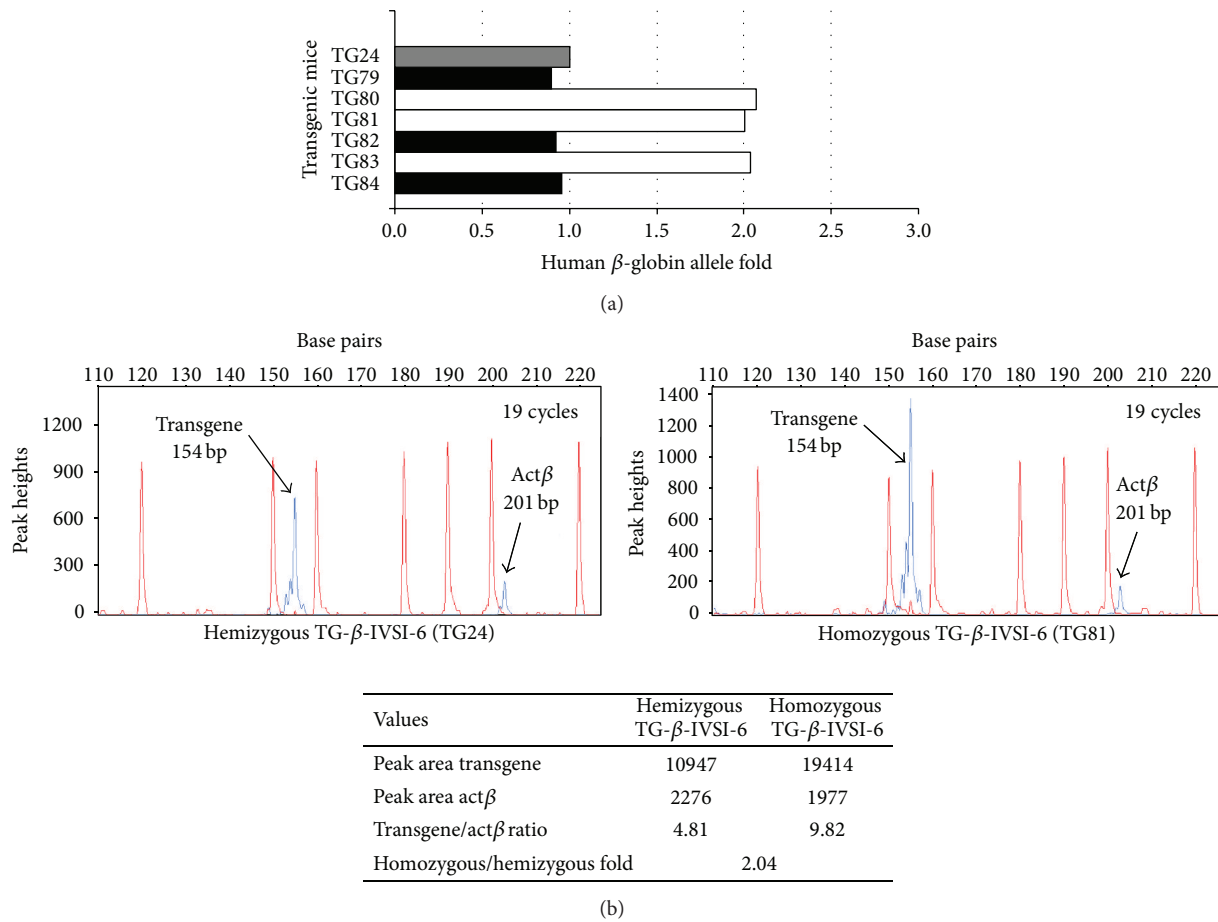


FIGURE 4: Discrimination between hemizygous and homozygous genotypes of transgenic mice by quantitative real-time PCR (a) or quantitative multiplex PCR of short fluorescent fragments (QMPSF) (b). (a) The amount of human  $\beta$ -globin allele was calculated using the comparative cycle threshold method [15, 33, 34] employing transgenic mouse TG24 as one copy control (hemizygous reference, grey). The black and white histograms represent hemizygous or homozygous transgenic (TG) mice, respectively. (b) Electropherograms obtained after denaturing polyacrylamide gel electrophoresis of amplification products of multiplex PCRs: primers employed (Table 1) were *TransF*[6FAM]-*TransR* and *MuActF1*[6FAM]-*MuActR1*, recognizing the transgene and the murine  $\beta$ -actin gene (*Act $\beta$* ), respectively; templates were genomic DNAs purified from a hemizygous (upper left panel) or a homozygous (upper right panel) mouse. Peaks generated by the molecular weight ladder (120, 150, 160, 180, 190, 200, 220 bp fragments) and by the amplification products (transgene and *Act $\beta$* , indicated by the arrows) are reported in red and blue, respectively. Values obtained, as peak areas, transgene/*Act $\beta$*  ratio and fold of ratios calculated from homozygous and hemizygous animals are shown in the lower part of panel (b).

analyzed. Moreover, the endogenous expression of murine  $\beta$ -like globin genes is not perturbed by the integration of the  $\beta$ -IVSI-6 transgene.

**3.6. Hematological Parameters of TG- $\beta$ -IVSI-6 Mice.** The hematological parameters of wild-type and transgenic TG- $\beta$ -IVSI-6 mice are reported in Table 3. In total, we analyzed 10 wild-type and 11 TG- $\beta$ -IVSI-6 mice, 16-week-old. No significant differences were observed in total hemoglobin content between males and females. Concerning the other parameters examined, no major differences were found, despite the fact that some hematological data support the possibility that TG- $\beta$ -IVSI-6 mice produce higher levels of RBC (red blood cells). In addition, it should be noted that RDW (red cell distribution width) is higher and that MCV

(mean corpuscular volume) and MCH (mean corpuscular hemoglobin) are lower in transgenic TG- $\beta$ -IVSI-6 mice in respect to wild-type mice.

**3.7. TG- $\beta$ -IVSI-6 Mice Produce Human  $\beta$ -Globin and Synthesize Mouse/Human  $^{\text{mu}}\alpha$ -Globin $_2$ / $^{\text{hu}}\beta$ -Globin $_2$  Hybrid Hemoglobin.** We performed a western blotting experiment to determine whether the accumulated human  $\beta$ -globin mRNA is translated into human  $\beta$ -globin protein (Figure 7(a)). A human specific primary antibody was used to label the human  $\beta$ -globin. No cross-reaction with any of the endogenous murine globins was observed. A  $\beta$ -globin specific band is detectable in samples from both hemizygous and homozygous TG- $\beta$ -IVSI-6 mice, demonstrating that the human  $\beta$ -globin mRNA produced by the transgene is translated into

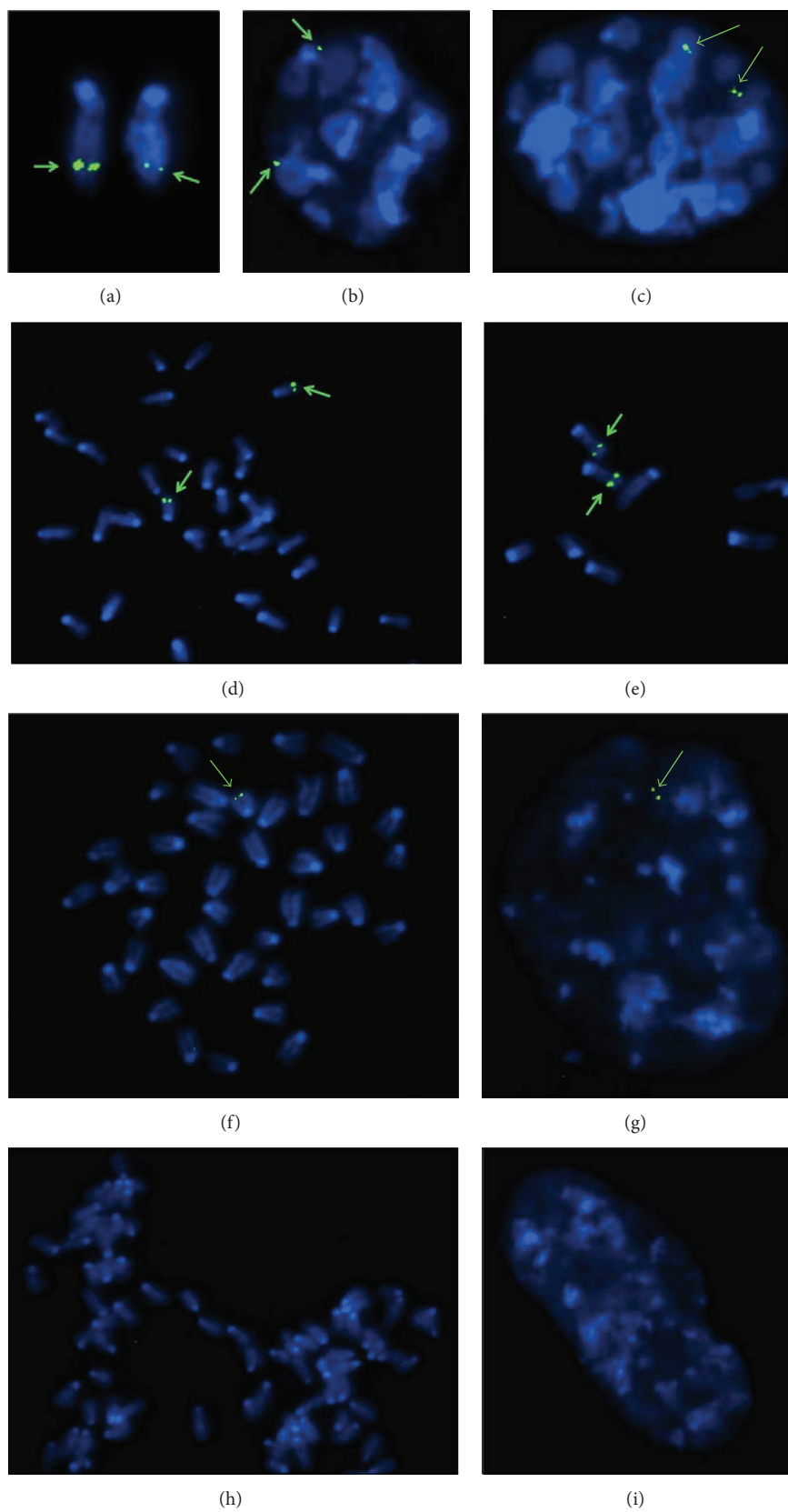


FIGURE 5: Fluorescence *in situ* hybridization results on metaphase (a, d, e, f, h) or G1 (b) and G2 (c, g, i) interphase nuclei of homozygous (a-e), hemizygous (f-g), and wild-type mice (h-i). The arrows indicate the integration site of the transgene, located in mouse chromosome 7.

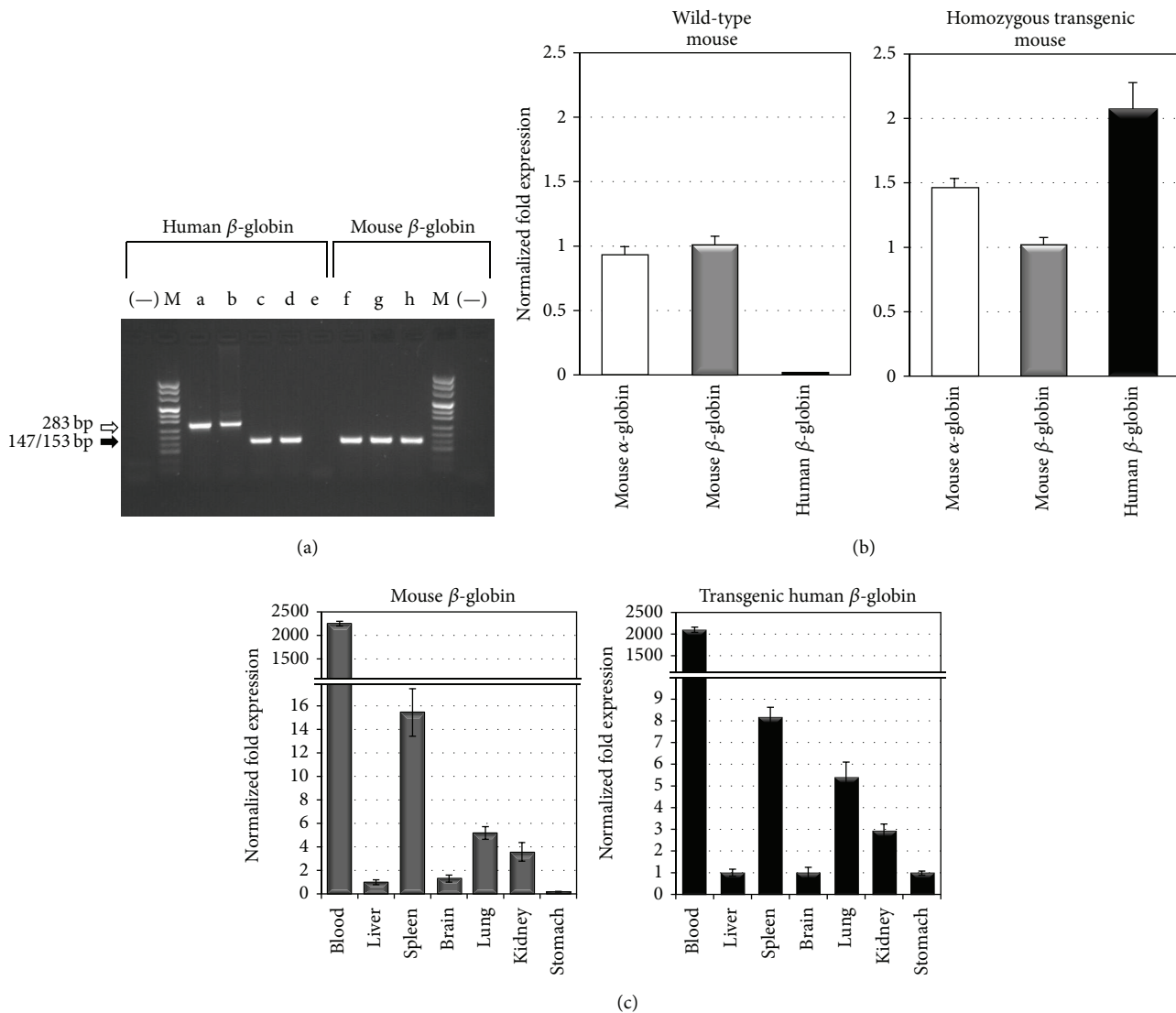


FIGURE 6: Expression of human  $\beta$ -globin transcripts in the transgenic TG- $\beta$ -IVSI-6 mouse model. (a) RT-PCR was performed with total RNA isolated from wild-type (lanes e and h), transgenic hemizygous (lanes c and f), and transgenic homozygous (lanes d and g) mice with primers *HuBetaF1* and *HuBetaR* (Table 2) designed to specifically amplify a 153 bp fragment of human  $\beta$ -globin transcripts (lanes a–e) and primers *MuBetaF* and *MuBetaR* (lanes f–h) designed to specifically amplify a 147 bp fragment of mouse  $\beta$ -globin transcripts (black arrow). Genomic DNA and pCCL- $\beta$ -globin.PGK.GFP.WPRE vector DNA were also used as control templates (lanes a and b, 283 bp, white arrow). M, molecular weight ladder, pUC Mix Marker 8 (Fermentas), (–), negative control for each primer pair. (b) SYBR Green real-time PCR was used to determine the relative expression of mouse  $\alpha$ -globin, mouse  $\beta$ -globin, and human  $\beta$ -globin transcripts in wild-type mouse blood (left side of the panel) and in homozygous transgenic mouse blood (right side of the panel). (c) Relative expression levels of mouse  $\beta$ -globin (grey bars) and human  $\beta$ -globin (black bars) transcripts in transgenic mouse tissues using real-time RT-PCR. Mean  $\pm$  SD values were determined for each fold difference; the relative proportions of  $\beta$ -globin/ $\beta$ -actin in each template were determined by using IQ5 software (Bio-Rad), employing the  $\Delta\Delta$ Ct method [15, 33, 34].

a normal  $\beta$ -globin. As expected, the amount of  $\beta$ -globin produced by homozygous mice is higher than that produced by hemizygous animals.

The native electrophoresis and western blotting analysis reported in Figure 7(b) suggest that a hybrid  $^{\text{mu}}\alpha$ -globin<sub>2</sub>/ $^{\text{hu}}\beta$ -globin<sub>2</sub> hemoglobin is present in both homozygous and hemizygous TG- $\beta$ -IVSI-6 mice. Control experiments were performed by using T9W-transduced MEL cells (see also Supplementary Figure S1 in the Supplementary Material

available online at <http://dx.doi.org/10.1155/2015/687635> for the analysis of the results obtained following transduction), confirming that a hybrid  $^{\text{mu}}\alpha$ -globin<sub>2</sub>/ $^{\text{hu}}\beta$ -globin<sub>2</sub> hemoglobin can be produced when the human  $\beta$ -globin gene is expressed under a murine cellular context (Figure 7(b), right side of the panel). The qualitative western blotting shown in Figure 7(b) does not provide conclusive information about the proportion of  $^{\text{mu}}\alpha$ -globin<sub>2</sub>/ $^{\text{hu}}\beta$ -globin<sub>2</sub> hemoglobin produced by the TG- $\beta$ -IVSI-6 mice. Therefore, in order to

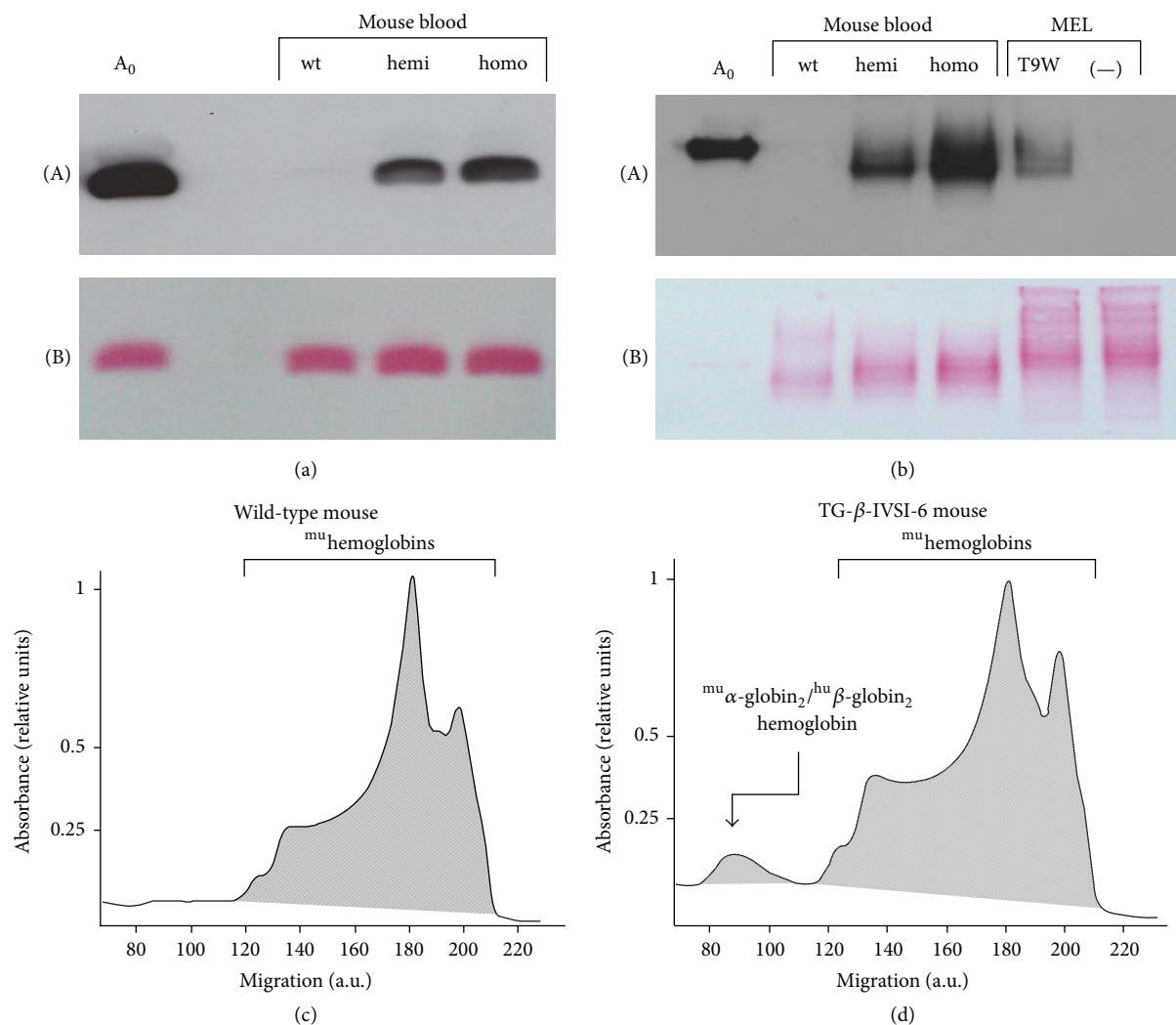


FIGURE 7: Analysis of transgenic protein synthesis in the TG-β-IVSI-6 mouse model. (a) Western blotting was employed to determine the presence of human β-globin in the blood of wild-type (wt), hemizygous (hemi), and homozygous (homo) mice by using a human β-globin specific primary antibody (A). Human adult A<sub>0</sub> hemoglobin was used as migration reference. (b) Native western blotting was performed by using a human β-globin specific primary antibody (A) and by employing, as a template, wild-type (wt), hemizygous (hemi), or homozygous (homo) mouse blood, and cell extracts obtained from MEL cells either infected with T9W lentiviral vector and treated with DMSO (T9W) or treated with DMSO only (-). Red Ponceau staining was used to verify that an equal amount of sample was loaded in each well and to verify the transfer to the membrane ((B) in panels (a) and (b)). (c, d) Capillary electrophoresis of whole blood from wild-type (c) and homozygous TG-β-IVSI-6 (d) mice. Peaks generated by murine hemoglobins and hybrid <sup>mu</sup>α-globin<sub>2</sub>/<sup>hu</sup>β-globin<sub>2</sub> hemoglobin are indicated; a.u., arbitrary units.

estimate the percentage of hybrid <sup>mu</sup>α-globin<sub>2</sub>/<sup>hu</sup>β-globin<sub>2</sub> hemoglobin with respect to the total murine hemoglobin production, high voltage capillary electrophoresis (CE) experiments were performed (Figures 7(c) and 7(d)). This system, unlike HPLC [41], allows a clear separation between the murine Hbmajor/Hbminor and the murine/human hybrid <sup>mu</sup>α-globin<sub>2</sub>/<sup>hu</sup>β-globin<sub>2</sub> hemoglobin. The results obtained indicate that the <sup>mu</sup>α-globin<sub>2</sub>/<sup>hu</sup>β-globin<sub>2</sub> hemoglobin is clearly detectable in transgenic animals (see the representative CE analysis shown in Figure 7(d)), representing  $3.9 \pm 0.4\%$  of the total hemoglobin produced in 6 TG-β-IVSI-6 mice analyzed.

**3.8. Presence of Aberrantly Spliced Molecules in TG-β-IVSI-6 Mice.** In Figure 8(a) a scheme of the mutation effects on human β-globin gene and mRNA is shown. The sequence containing the first and second β-globin gene exons is reported, and the site of the IVSI-6 mutation and the three cryptic splicing sites that may arise in IVSI-6 pre-mRNA are emphasized by coloured boxes (Figure 8(b)). A schematic representation and expected size of the normal and alternatively spliced β-globin transcripts in IVSI-6 thalassaemic cells are shown in Figure 9(a). As expected, the electropherogram of the β-globin RNA, amplified from erythroid progenitor cells (ErPCs) of a healthy donor, shows only a 153 bp peak

TABLE 3: Hematological data of transgenic mice carrying the human  $^{hu}\beta^{IVSI-6}$  globin locus.

Age (weeks)	Sex	Genotype	Hb (g/dL)	RBC ( $10^6/\mu\text{L}$ )	HCT (%)	MCV (fL)	MCH (pg)	MCHC (g/dL)	RDW (%)
16	♀	Wild-type ( $n = 5$ )	$13.7 \pm 0.4$	$8.2 \pm 0.4$	$42.9 \pm 1.8$	$52.5 \pm 2.7$	$16.8 \pm 0.8$	$31.9 \pm 0.3$	$16.1 \pm 0.9$
16	♀	Homozygous $^{hu}\beta^{IVSI-6}, ^{hu}\beta^{IVSI-6}$ ( $n = 5$ )	$13.8 \pm 0.2$	$8.8 \pm 0.1$	$43.6 \pm 1.0$	$49.3 \pm 0.7$	$15.6 \pm 0.2$	$31.7 \pm 0.5$	$17.2 \pm 0.2$
			NS	$P = 0.01$	NS	$P = 0.04$	$P = 0.02$	NS	$P = 0.03$
16	♂	Wild-type ( $n = 5$ )	$12.5 \pm 0.6$	$7.6 \pm 0.3$	$39.0 \pm 1.4$	$51.5 \pm 1.1$	$16.5 \pm 0.2$	$31.9 \pm 0.7$	$15.9 \pm 0.8$
16	♂	Homozygous $^{hu}\beta^{IVSI-6}, ^{hu}\beta^{IVSI-6}$ ( $n = 6$ )	$13.0 \pm 0.3$	$8.6 \pm 0.2$	$42.0 \pm 1.1$	$49.1 \pm 0.9$	$15.2 \pm 0.1$	$31.0 \pm 0.4$	$16.8 \pm 0.2$
			NS	$P = 0.0002$	$P = 0.003$	$P = 0.003$	$P < 0.0001$	$P = 0.03$	$P = 0.03$

Hematological values are expressed as means  $\pm$  SD. Hemoglobin concentration (Hb), red blood cell count (RBC), hematocrit (HCT), mean corpuscular volume (MCV), mean corpuscular hemoglobin (MCH), mean corpuscular Hb concentration (MCHC), red cell distribution width (RDW) are shown.  $n$  indicates the number of analyzed mice. The  $P$  values of Student's  $t$ -test, comparing each group of transgenic mice with wild-type mice controls, are also shown. NS corresponds to not statistically significant  $P > 0.05$ .

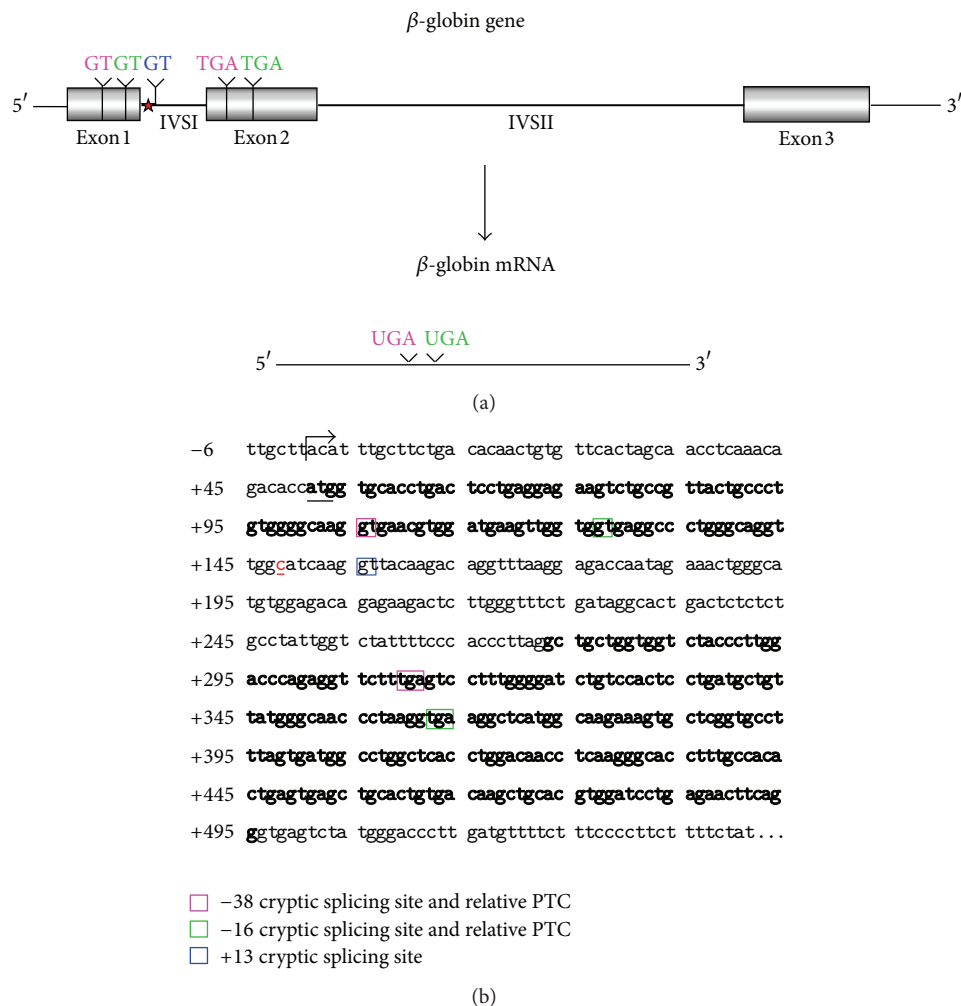


FIGURE 8: (a) Schematic representation of the human  $\beta$ -globin gene and mRNA. The three cryptic GT splicing sites activated by the IVSI-6 mutation and the two consequent stop codons are indicated with different colours. The IVSI-6 mutation (T  $\rightarrow$  C) is identified by a red star. (b) Genomic region containing the first and second exons of the human  $\beta$ -globin gene, in bold characters. The IVSI-6 mutation occurring at the sixth nucleotide of the first intron is shown in red. The coloured boxes indicate the three cryptic splicing sites activated by the mutation and the two consequent stop codons. The transcription and translation starting sites are also indicated.

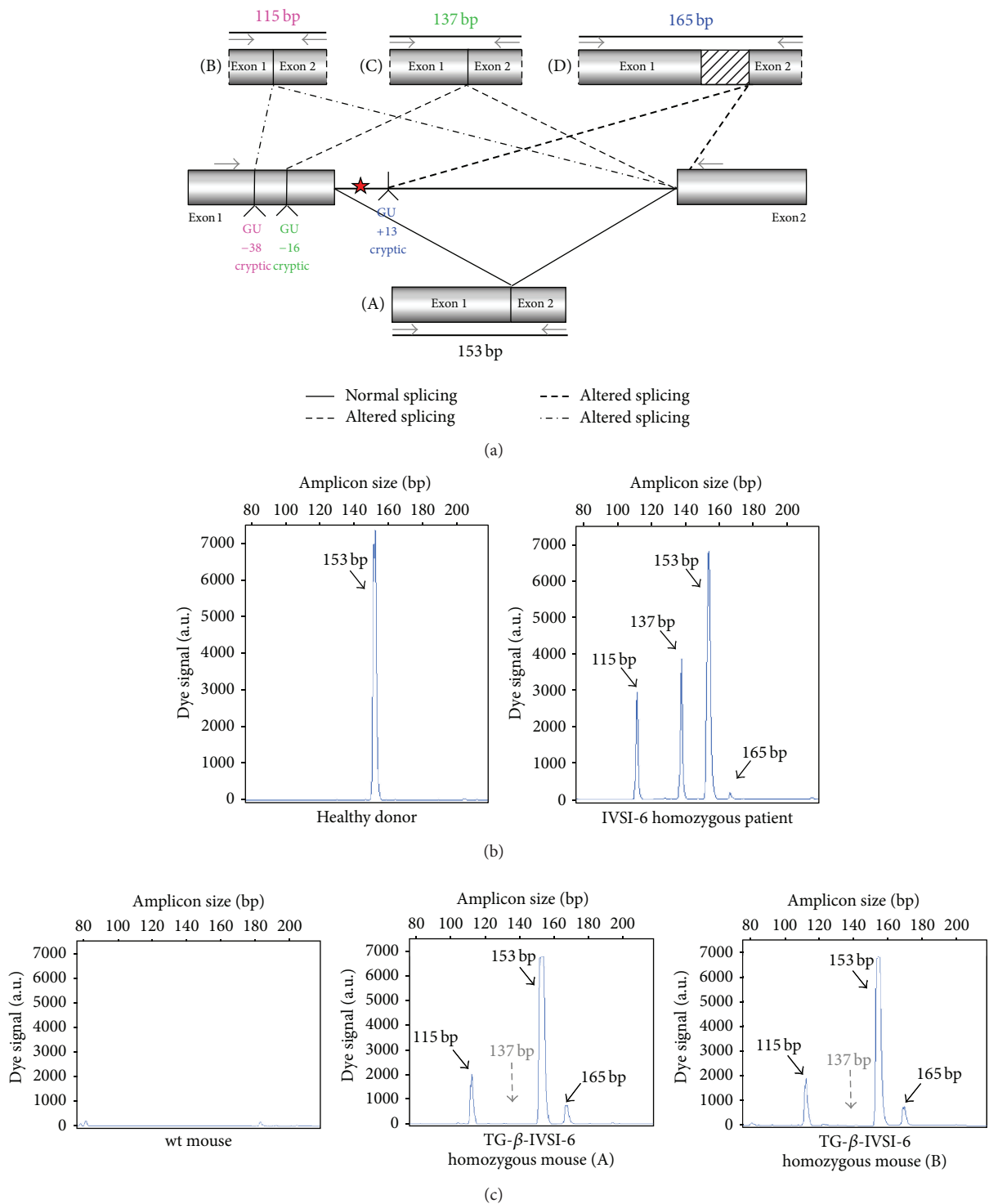


FIGURE 9: Normal and aberrant splicing in IVSI-6  $\beta$ -globin gene. (a) Schematic representation of the normal (A) and altered splicing (B, C, D) in IVSI-6 thalassemia. Grey arrows indicate the primers used to demonstrate the presence of the altered splicing. The positions of the cryptic splicing sites generated by the mutation and the respective lengths (in bp) of products obtained after PCR amplification of altered transcripts are indicated with different colours. A red star locates the IVSI-6 mutation. (b, c) Identification of aberrantly spliced transcripts in IVSI-6 patients and in the TG- $\beta$ -IVSI-6 mouse model. (b) Electropherograms generated by denaturing polyacrylamide gel electrophoresis of fluorescent RT-PCR products obtained from healthy donor blood (left panel) and IVSI-6 homozygous patient blood (right panel). (c) Electropherograms obtained from a wild-type and two TG- $\beta$ -IVSI-6 mice (A, B). Primers employed were *HuBetaF1*[6FAM]-*HuBetaR* (Table 2). Blue peaks indicate both alternatively spliced and canonic human transcripts.

TABLE 4: Relative contents of  $\beta$ -globin transcripts.

Sample	Experiment	Peaks (%)			
		115 bp -38 (cryptic)	137 bp -16 (cryptic)	153 bp +1 (normal)	165 bp +13 (cryptic)
Splicing site generating the transcript					
ErPCs from normal donors	1	0	0	100	0
	2	0	0	100	0
	3	0	0	100	0
ErPCs from homozygous $\beta$ -IVSI-6/ $\beta$ -IVSI-6 patients	1	19.9	13.6	65.8	0.7
	2	16.1	13.7	69.2	1.0
	3	14.4	18.7	66.2	0.7
TG- $\beta$ -IVSI-6 homozygous mouse #1	1	4.3	0.3	93.8	1.6
	2	7.6	0.1	88.6	3.7
TG- $\beta$ -IVSI-6 homozygous mouse #2	1	6.5	0.4	91.1	2.0
	2	5.6	0.2	92.0	2.2
K562( $\beta$ -IVSI-6) #1	1	21.6	2.2	74.6	1.6
	2	21.3	2.6	74.3	1.8
K562( $\beta$ -IVSI-6) #2	1	22.3	3.0	73.6	1.1
MEL(hu $\beta$ -globin gene)	1	0	0	100	0
MEL(hu $\beta$ -globin gene), DMSO treated	1	0	0	100	0
MEL(hu $\beta$ -IVSI-6 globin gene)	1	33.1	6.8	58.7	1.4
MEL(hu $\beta$ -IVSI-6 globin gene), DMSO treated	1	38.5	5.8	54.5	1.2

(Figure 9(b), left panel); conversely, the electropherogram of ErPCs from a homozygous IVSI-6 patient presents three additional peaks of 115, 137, and 165 bp (Figure 9(b), right panel), which represent the accumulation of the three abnormal transcripts generated by the -38, -16, and +13 cryptic GU donor splicing sites produced by the IVSI-6 point mutation, respectively. Notably, the 165 bp peak is present in lower amount, as was consistently observed in additional experiments using ErPCs from different patients (Table 4). As expected, no peak is generated by using RNA from wild-type mice (Figure 9(c), left panel), while when RNA from two TG- $\beta$ -IVSI-6 mice is employed, both normal and abnormal transcripts are observed (Figure 9(c), middle and right panels). It should be emphasized, however, that the 137 bp peak is not present in this representative experiment, or it is present in very low amounts, as seen in additional experiments (shown in Table 4). In order to understand this issue, we used K562 cell clones stably containing the T9W-IVSI-6 vector, named K562( $\beta$ -IVSI-6), and murine MEL cells transduced with the T9W or the T9W-IVSI-6 lentiviruses, named MEL (hu  $\beta$ -globin gene) and MEL (hu  $\beta$ -IVSI-6 globin gene), respectively. All the results obtained are shown in Table 4, demonstrating that, as expected, only the 153 bp peak is present in T9W-transduced MEL cells. Among the peaks generated by the activation of cryptic sites, the 115 bp peak is the most represented in the K562(IVSI-6) clones, as well as in MEL cells transfected with the T9W-IVSI-6 vector, while the 137 bp and 165 bp peaks are present in lower amounts. In any case the proportion of the 137 bp peak is higher than that

found in TG- $\beta$ -IVSI-6 homozygous mice. Similar patterns were observed in transduced DMSO-treated MEL cells. The different levels of transcripts (see Table 4) should be discussed by taking in consideration the hierarchy of splicing events associated with the differential extent of complementarity with U1 and U6 small nuclear RNAs (snRNAs), as suggested by Roca et al. (see also Figure 9 and Table 5) [42]. The low levels of the transcript corresponding to the 165 bp amplicon (Table 4) might be explained by the very low strength of its donor +13 cryptic splicing site, which do not generate PTCs (see Table 5). On the contrary, both the transcripts corresponding to the 115 bp and 137 bp amplicons generate PTCs, but the second one is highly unstable because of being more sensitive to nonsense mediated decay (NMD) [43, 44]. This might explain the low levels of this transcript found in TG- $\beta$ -IVSI-6 samples, as well as in MEL cells transduced with a human  $\beta$ -IVSI-6 globin gene vector (Table 4). In any case, we like to underline that aberrant transcripts were found to be present in all the IVSI-6 experimental systems analyzed.

The production of aberrant transcripts was also detected by a simple RT-PCR procedure as described in Figure 10. In this experiment, an RT-PCR reaction was performed by using RNA extracted from the ErPCs of either a healthy subject or an IVSI-6 homozygous patient and from transgenic mouse blood. For the PCR reaction the *IVSI+13F* forward primer and the *HuBetaR* reverse primer, designed to amplify a 84 bp fragment of the human  $\beta$ -globin alternatively spliced transcript or a 202 bp fragment of the human pre-mRNA (containing all the first human  $\beta$ -globin intron),

TABLE 5: Strengths of the normal and cryptic splicing sites generated by the  $\beta^+$ IVSI-6 thalassemic mutation.

Splicing site	Sequence	Base pairs	Strength			Amplicon size	Comments/Hypotheses
			(a)	(b)	(c)		
+1 (normal)	$3'-G\ U\ C\ C\ A\ \Psi\ \Psi\ C\ A-5'$ $5'-C\ A\ G\ \boxed{G\ U}\ U\ G\ G\ U-3'$ $3'-A\ G\ A\ C\ A-5'$	U1 7+	86.64	8.08	0.64	153 bp	
	U6 3+						
+1 (mutated IVSI-6)	$3'-G\ U\ C\ C\ A\ \Psi\ \Psi\ C\ A-5'$ $5'-C\ A\ G\ \boxed{G\ U}\ U\ G\ G\ C-3'$ $3'-A\ G\ A\ C\ A-5'$	U1 6+	84.46	5.52	0.14	153 bp	
	U6 2+						
-38 (cryptic)	$3'-G\ U\ C\ C\ A\ \Psi\ \Psi\ C\ A-5'$ $5'-A\ A\ G\ \boxed{G\ U}\ G\ A\ A\ C-3'$ $3'-A\ G\ A\ C\ A-5'$	U1 5+	83.50	5.54	0.21	115 bp	PTC. Unstable transcript, low sensitivity to NMD (in comparison with the -16 cryptic splicing site)
	U6 1						
-16 (cryptic)	$3'-G\ U\ C\ C\ A\ \Psi\ \Psi\ C\ A-5'$ $5'-G\ U\ G\ \boxed{G\ U}\ G\ A\ G\ G-3'$ $3'-A\ G\ A\ C\ A-5'$	U1 5+	90.40	6.13	0.54	137 bp	PTC. Unstable transcript, sensitive to NMD
	U6 2						
+13 (cryptic)	$3'-G\ U\ C\ C\ A\ \Psi\ \Psi\ C\ A-5'$ $5'-A\ A\ G\ \boxed{G\ U}\ U\ A\ C\ A-3'$ $3'-A\ G\ A\ C\ A-5'$	U1 5+	79.67	-0.83	0.46	165 bp	No PTC. GT located 7 nucleotides downstream the IVSI-6 mutation
	U6 1+						

Sequences of the normal and cryptic splicing sites generated by the  $\beta^+$ IVSI-6 thalassemic mutation. The cryptic donor GU (boxed) sites are numbered with respect to the +1 position of the normal one. Potential Watson-Crick base pairs to U1 (upper) and U6 (lower) are quantified: (+) indicates a G/U wobble base pair. Strengths of donor splicing sites are expressed as scores calculated with Human Splicing Finder Matrices from <http://www.umd.be/HSE/> (a) or MaxEntScan from <http://www.umd.be/HSE/> (b) or from [http://www.fruitfly.org/seq\\_tools/splice.html](http://www.fruitfly.org/seq_tools/splice.html) (c).

were employed. A scheme of the expected PCR products is reported in Figure 10(a). The results obtained demonstrated that  $\beta$ -globin RNA precursor sequences are present in all the samples, and aberrantly spliced  $\beta$ -globin RNA sequences are present only in samples from the IVSI-6 homozygous patient and TG- $\beta$ -IVSI-6 mouse (Figure 10(b)). Interestingly, the level of this aberrantly spliced transcript appears to be very high in the TG- $\beta$ -IVSI-6 sample, facilitating the possible *in vivo* validation of corrections of this genetic defect.

#### 4. Discussion

In this study we have reported the production and characterization of a transgenic mouse line carrying the human IVSI-6  $\beta$ -globin gene. The IVSI-6 mutation leads to anemia associated with a  $\beta$ -thalassemia intermedia phenotype. However, the association with a  $\beta^0$ -like mutation (such as

deletions,  $\beta^0$ 39, and  $\beta^0$ IVSI-1 mutations) and even  $\beta^+$  mutations renders the phenotype of the heterozygous compound more severe. Noticeably,  $\beta^+$ IVSI-6 thalassemia is the most common in the Middle-Eastern regions, including Egypt, Israel, Lebanon. For this reason, an *in vivo* system suitable to study possible therapeutic strategies that target the aberrantly spliced RNAs generated by this mutation is highly needed.

We generated a transgenic TG- $\beta$ -IVSI-6 mouse, which (a) displays a tissue specific expression of the transgene, fully overlapping with that of the endogenous murine  $\beta$ -globin gene; (b) as expected it produces normally spliced human  $\beta$ -globin mRNA, giving rise to  $\beta$ -globin production and formation of a human-mouse tetrameric chimeric hemoglobin  $\mu\alpha_2^{\text{hu}}\beta_2$  and, more importantly, (c) exhibits in blood cells aberrant IVSI-6  $\beta$ -globin RNAs. We conclude that, despite the fact that the human  $\beta$ -IVSI-6 transgene is located in the same mouse chromosome which carries the  $\beta$ -like globin

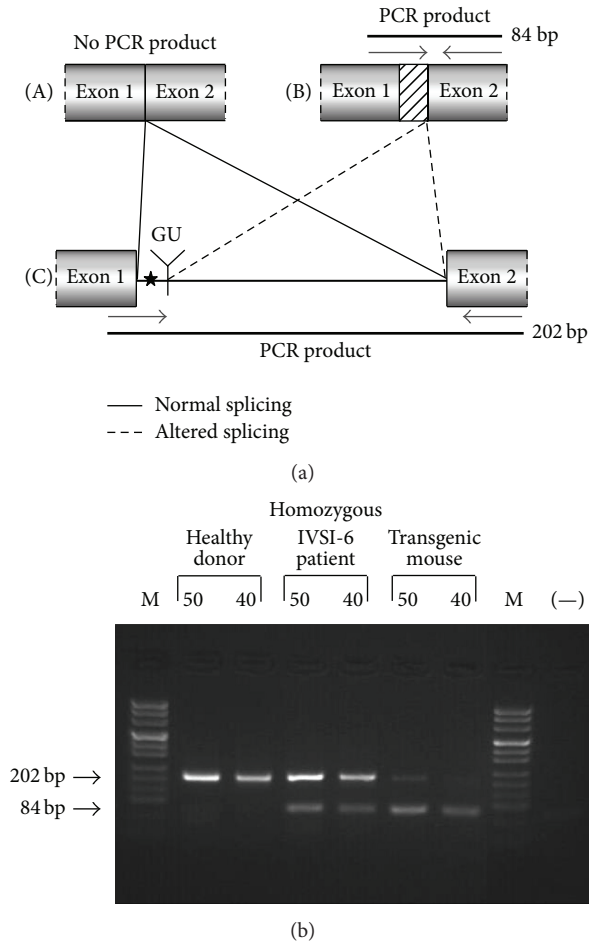


FIGURE 10: Identification of the aberrant transcripts generated by the activation of the cryptic splicing site at position IVSI+13, in the presence of IVSI-6 mutation. (a) Schematic representation of the human  $\beta$ -globin pre-mRNA spanning from the first to the second exon (C); the creation of a new aberrant donor splicing site (GU) in the first intron, the IVSI-6 mutation site (star), the location of primers used for PCR (arrows), and the PCR product lengths are indicated. Normal splicing (A) and predicted aberrant splicing (B) are also represented. (b) RT-PCR reaction was performed by using RNA from healthy subject blood, from IVSI-6 homozygous patient blood and from transgenic mouse blood. The *IVSI+13F* forward primer and the *HuBetaR* reverse primer (Table 2), designed to amplify a fragment of 84 bp from human  $\beta$ -globin altered spliced transcripts or a fragment of 202 bp from human pre-mRNA (containing all the first human  $\beta$ -globin intron), were used. The products obtained from each sample, at 40 and 50 cycles of PCR reaction, were loaded on a 3% agarose gel. M, molecular weight ladder, pUC Mix Marker 8 (Fermentas), (-), negative control.

cluster (mouse chromosome 7), both the  $\beta$ -IVSI-6 transgene and the  $\beta$ -like globin cluster are expressed as expected. It should be underlined that the hematological parameters of the homozygous TG- $\beta$ -IVSI-6 mice are very similar to those of the wild-type mice. The only significant difference we found in TG- $\beta$ -IVSI-6 mice is the low/absent production

of one aberrantly spliced transcript (the 137 bp amplicon, as shown in Figure 9). This might be explained by the fact that this particular spliced form is much more sensitive to NMD and so highly unstable (Table 5) [43, 44]. The issue of the different ratios of the transcripts corresponding to the 115, 137, 153, and 165 bp amplicons in the cellular systems considered (see Table 4) should be discussed by taking in consideration the hierarchy of splicing events associated with the differential extent of complementarity with U1 and U6 small nuclear RNAs (snRNAs), as suggested by Roca et al. (see Table 5) [42].

Despite the low stability of transcripts generated by the -16 cryptic splicing site, the presence of the other two aberrantly spliced forms (corresponding to the 115 bp and 165 bp peaks shown in Figure 9(c)) allows us to propose that the TG- $\beta$ -IVSI-6 mouse might be used as an *in vivo* model to characterize the effects of antisense oligodeoxynucleotides (ODNs) and ODN-mimics targeting the -38 and the +13 cryptic GU donor splicing sites responsible for the generation of aberrantly spliced human  $\beta$ -globin transcripts in IVSI-6  $\beta$ -thalassemia. The validation of the effects of molecules correcting the aberrant splicing caused by the IVSI-6 mutation can be performed *in vitro* using erythroid precursor cells isolated from these transgenic mice, as well as *in vivo* following administration of splicing correctors, as performed with different *in vitro* and *in vivo* experimental systems by several research groups [45-50].

In this respect, *ex vivo* experiments based on the correction of splicing defects causing  $\beta$ -thalassemia have been reported by several research groups using antisense phosphorothioate 2'-O-methyl-oligonucleotides [45, 46], morpholino-oligonucleotides [18, 47], 2'-O-(2-methoxy) ethyl-oligonucleotides [47], and peptide nucleic acids [48]. These antisense molecules have been used either free [45, 46] or delivered with peptides and lipid-based strategies [49]. For instance, El-Beshlawy et al. [18] reported the *ex vivo* correction of the aberrant splicing of IVSI-110  $\beta$ -globin pre-mRNA by antisense oligonucleotides (ASOs) against the 3' aberrant splicing site. In their study, ErPCs with the IVSI-110 mutation were treated with 20  $\mu$ mol/mL morpholino ASOs targeting the 3' aberrant splicing site. The results of this work suggested that ASOs can restore correct splicing of  $\beta$ -globin pre-mRNA, leading to correct gene product.

As far as *in vivo* experiments, few reports are available [17, 50] and none of them, to the best of our knowledge, are focused on the repair of the aberrant splicing caused by the  $\beta$ -IVSI-6 mutation. For instance, Svasti et al. [17] reported the repair of defective  $\beta$ -globin pre-mRNA in a mouse model of IVSII-654 thalassemia, by delivering a morpholino oligomer conjugated to an arginine-rich peptide as splice-switching oligonucleotide (SSO). Interestingly, the SSO blocked the aberrant splicing site in the targeted pre-mRNA and forced the splicing machinery to reselect existing correct splicing sites. These results suggest the applicability of ASOs for the treatment of thalassemia.

In this respect, it is worth noting that in most of third world countries, blood transfusion is of difficult application, due to the fact that availability of blood is low and blood is often contaminated. Therefore, novel pharmacological interventions are urgently needed [51, 52].

## 5. Conclusions

Molecules able to correct the effects of  $\beta$ -IVSI-6 thalassemia mutation will be of great therapeutic interest for the  $\beta$ -thalassemia patients of the Middle-Eastern region, in which this genotype is very common. To this aim the availability of experimental systems to validate the effects of molecules protecting the activated cryptic sites (in our case the -38, the -16, and the +13 cryptic GU donor splicing sites) in the case of  $\beta$ -IVSI-6 splicing site mutations are of great interest. Suitable *in vitro* experimental system might be erythroid precursor cells from homozygous  $\beta$ -IVSI-6 patients or K562 and MEL cells carrying a  $\beta$ -IVSI-6 gene. These experimental systems, while very informative on the effects *in vitro* of splicing-regulating molecules, do not help to reach conclusive experiments *in vivo*. Our transgenic  $\beta$ -IVSI-6 experimental system, even if partially reconstituting the splicing pattern caused by the  $\beta$ -IVSI-6 mutation, might be useful to verify the *in vivo* activity of oligonucleotide-based drugs targeting the -38 GU and the +13 GU cryptic splicing sites activated in IVSI-6  $\beta$ -thalassemia.

## Abbreviations

HPLC:	High performance liquid chromatography
FBS:	Fetal bovine serum
PBS:	Phosphate-buffered saline
RBC:	Red blood cell
bp:	Base pairs
Kb:	Kilobases
DMSO:	Dimethyl sulfoxide
PCR:	Polymerase chain reaction
TBS:	Tris-buffered saline
LCR:	Locus control region
QMPSF:	Quantitative multiplex PCR of short fluorescent fragments
ErPC:	Erythroid precursor cells
ODN:	Oligodeoxy nucleotides
Hb:	Hemoglobin
nt:	Nucleotides
FISH:	Fluorescence <i>in situ</i> hybridization.

## Conflict of Interests

All the authors reported no potential conflict of interests and approved the final version of the paper.

## Authors' Contribution

Giulia Breveglieri performed experiments and contributed to analyzing data and to writing the paper; Irene Mancini, Nicoletta Bianchi, Ilaria Lampronti, Francesca Salvatori, Enrica Fabbri, Cristina Zuccato, Lucia C. Cosenza, Giulia Montagner, and Monica Borgatti participated in performing the experiments; Fiorella Altruda and Sharmila Fagoonee contributed to microinjection procedure and critically reviewed the paper; Gianni Carandina participated in analyzing the mice hematological parameters; Michele Rubini and Vincenzo Aiello collaborated for FISH experiments; Laura Breda

and Stefano Rivella produced the T9W lentiviral vector and critically reviewed the paper; Roberto Gambari was the supervisor of the project, the principal coordinator of Grants funding the research, wrote the paper, and finally approved the version to be published; Alessia Finotti was the principal investigator, took primary responsibility for the paper, performed experiments, contributed to analyzing data and to writing the paper, and finally approved the version to be published.

## Acknowledgments

Roberto Gambari is supported by a grant by MIUR (Italian Ministry of University and Research), by Fondazione Cariparo (Cassa di Risparmio di Padova e Rovigo), by CIB, by UE FP7 THALAMOSS Project (THALAssaemia MOdular Stratification System for personalized therapy of beta-thalassemia, contract n° 306201-FP/-HEALTH-2012 INNOVATION-1), and by Telethon (contract n° GGPI0124). Stefano Rivella is supported by Cooley's Anemia Foundation (CAF) and by grants from the Carlo and Micol Schejola Foundation, the Children's Cancer and Blood Foundation, and NIH-R21DK065169. This research is also supported by Associazione Veneta per la Lotta alla Talassemia (AVLT), Rovigo. The authors would like to thank Dr. Eleonora Gallerani (Department of Life Sciences and Biotechnology, Ferrara University) for the technical support in mouse bleeding, Maddalena Iannicella (Department of Molecular Biotechnology and Health Sciences, Molecular Biotechnology Center, Turin University) for the technical expertise in the microinjection procedure and Dr. Claudia Melandri (Laboratory for Chemical and Clinical Analysis and Microbiology, University Hospital, Ferrara) for the analysis of the hematological parameters of the transgenic mice.

## References

- [1] M. H. Steinberg, B. G. Forget, D. R. Higgs, and R. L. Nagel, "Disorders of hemoglobin: genetics, pathophysiology and clinical management," *Journal of the Royal Society of Medicine*, vol. 94, no. 11, pp. 602–603, 2001.
- [2] S. L. Thein, "Genetic insights into the clinical diversity of beta thalassaemia," *British Journal of Haematology*, vol. 124, no. 3, pp. 264–274, 2004.
- [3] J. M. Old, "Screening and genetic diagnosis of haemoglobin disorders," *Blood Reviews*, vol. 17, no. 1, pp. 43–53, 2003.
- [4] A. Bank, "Regulation of human fetal hemoglobin: new players, new complexities," *Blood*, vol. 107, no. 2, pp. 435–443, 2006.
- [5] S. L. Thein, "Beta-thalassaemia prototype of a single gene disorder with multiple phenotypes," *International Journal of Hematology*, vol. 76, no. 2, supplement, pp. 96–104, 2002.
- [6] S. Fucharoen and P. Winichagoon, "Thalassemia and abnormal hemoglobin," *International Journal of Hematology*, vol. 76, supplement 2, pp. 83–89, 2002.
- [7] S. L. Schrier, "Pathophysiology of thalassemia," *Current Opinion in Hematology*, vol. 9, no. 2, pp. 123–126, 2002.
- [8] B. Wonke, "Clinical management of  $\beta$ -thalassemia major," *Seminars in Hematology*, vol. 38, no. 4, pp. 350–359, 2001.

- [9] D. Rund and E. Rachmilewitz, "Pathophysiology of  $\alpha$ - and  $\beta$ -thalassemia: therapeutic implications," *Seminars in Hematology*, vol. 38, no. 4, pp. 343–349, 2001.
- [10] S. Tuzmen and A. N. Schechter, "Genetic diseases of hemoglobin: diagnostic methods for elucidating  $\beta$ -thalassemia mutations," *Blood Reviews*, vol. 15, no. 1, pp. 19–29, 2001.
- [11] S. H. Orkin and S. C. Goff, "Nonsense and frameshift mutations in  $\beta$ 0-thalassemia detected in cloned  $\beta$ -globin genes," *The Journal of Biological Chemistry*, vol. 256, no. 19, pp. 9782–9784, 1981.
- [12] G. W. Hall and S. Thein, "Nonsense codon mutations in the terminal exon of the beta-globin gene are not associated with a reduction in beta-mRNA accumulation: a mechanism for the phenotype of dominant beta-thalassemia," *Blood*, vol. 83, no. 8, pp. 2031–2037, 1994.
- [13] R. P. Naja, H. Kaspar, H. Shbaklo, N. Chakar, N. J. Makhoul, and P. A. Zalloua, "Accurate and rapid prenatal diagnosis of the most frequent East Mediterranean beta-thalassemia mutations," *The American Journal of Hematology*, vol. 75, no. 4, pp. 220–224, 2004.
- [14] W. Piyamongkol, J. C. Harper, J. D. A. Delhanty, and D. Wells, "Preimplantation genetic diagnostic protocols for  $\alpha$ - and  $\beta$ -thalassaemias using multiplex fluorescent PCR," *Prenatal Diagnosis*, vol. 21, no. 9, pp. 753–759, 2001.
- [15] F. Salvatori, G. Breviglieri, C. Zuccato et al., "Production of beta-globin and adult hemoglobin following G418 treatment of erythroid precursor cells from homozygous beta(0)39 thalassemia patients," *The American Journal of Hematology*, vol. 84, no. 11, pp. 720–728, 2009.
- [16] P. Lonkar, K.-H. Kim, J. Y. Kuan et al., "Targeted correction of a thalassemia-associated  $\beta$ -globin mutation induced by pseudo-complementary peptide nucleic acids," *Nucleic Acids Research*, vol. 37, no. 11, pp. 3635–3644, 2009.
- [17] S. Svasti, T. Suwanmanee, S. Fucharoen et al., "RNA repair restores hemoglobin expression in IVS2-654 thalassaemic mice," *Proceedings of the National Academy of Sciences of the United States of America*, vol. 106, no. 4, pp. 1205–1210, 2009.
- [18] A. El-Beshlawy, A. Mostafa, I. Youssry et al., "Correction of aberrant pre-mRNA splicing by antisense oligonucleotides in beta-thalassemia Egyptian patients with IVSI-110 mutation," *Journal of Pediatric Hematology/Oncology*, vol. 30, no. 4, pp. 281–284, 2008.
- [19] L. Breda and S. Rivella, "Mouse models for the cure of  $\beta$ -thalassemia and sickle cell anemia," *Minerva Biotechnologica*, vol. 15, no. 2, pp. 107–121, 2003.
- [20] Y. Huo, S. C. McConnell, and T. M. Ryan, "Preclinical transfusion-dependent humanized mouse model of  $\beta$  thalassemia major," *Blood*, vol. 113, no. 19, pp. 4763–4770, 2009.
- [21] Y. Huo, S. C. McConnell, S. R. Liu et al., "Humanized mouse model of Cooley's anemia," *The Journal of Biological Chemistry*, vol. 284, no. 8, pp. 4889–4896, 2009.
- [22] D. J. Ciavatta, T. M. Ryan, S. C. Farmer, and T. M. Townes, "Mouse model of human  $\beta$ 0 thalassemia: targeted deletion of the mouse  $\beta$ <sup>maj</sup>- and  $\beta$ <sup>min</sup>-globin genes in embryonic stem cells," *Proceedings of the National Academy of Sciences of the United States of America*, vol. 92, no. 20, pp. 9259–9263, 1995.
- [23] B. Yang, S. Kirby, J. Lewis, P. J. Detloff, N. Maeda, and O. Smithies, "A mouse model for beta 0-thalassemia," *Proceedings of the National Academy of Sciences of the United States of America*, vol. 92, no. 25, pp. 11608–11612, 1995.
- [24] J. Vadolas, M. Nefedov, H. Wardan et al., "Humanized  $\beta$ -thalassemia mouse model containing the common IVSI-110 splicing mutation," *The Journal of Biological Chemistry*, vol. 281, no. 11, pp. 7399–7405, 2006.
- [25] D. Jamsai, F. Zaibak, J. Vadolas et al., "A humanized BAC transgenic/knockout mouse model for HbE/beta-thalassemia," *Genomics*, vol. 88, no. 3, pp. 309–315, 2006.
- [26] D. Jamsai, F. Zaibak, W. Khongnium et al., "A humanized mouse model for a common  $\beta$ 0-thalassemia mutation," *Genomics*, vol. 85, no. 4, pp. 453–461, 2005.
- [27] J. Lewis, B. Yang, R. Kim et al., "A common human  $\beta$  globin splicing mutation modeled in mice," *Blood*, vol. 91, no. 6, pp. 2152–2156, 1998.
- [28] S. El-Gawhary, S. El-Shafie, M. Niazi, M. Aziz, and A. El-Beshlawy, "Study of  $\beta$ -thalassemia mutations using the polymerase chain reaction-amplification refractory mutation system and direct DNA sequencing techniques in a group of Egyptian thalassemia patients," *Hemoglobin*, vol. 31, no. 1, pp. 63–69, 2007.
- [29] K. V. Kakavas, A. Noulas, C. Chalkias et al., "Identification of the four most common  $\beta$ -globin gene mutations in Greek  $\beta$ -thalassaemic patients and carriers by PCR-SSCP: advantages and limitations of the method," *Journal of Clinical Laboratory Analysis*, vol. 20, no. 1, pp. 1–7, 2006.
- [30] M. A. El-Latif, D. Filon, D. Rund, A. Oppenheim, and M. Kanaan, "The beta<sup>+</sup>-IVS-I-6 (T  $\rightarrow$  C) mutation accounts for half of the thalassemia chromosomes in the Palestinian populations of the mountain regions," *Hemoglobin*, vol. 26, no. 1, pp. 33–40, 2002.
- [31] L. Breda, D. A. Kleinert, C. Casu et al., "A preclinical approach for gene therapy of  $\beta$ -thalassemia," *Annals of the New York Academy of Sciences*, vol. 1202, pp. 134–140, 2010.
- [32] A. Finotti, S. Treves, F. Zorzato, R. Gambari, and G. Feriotto, "Upstream stimulatory factors are involved in the P1 promoter directed transcription of the AbetaH-J-J locus," *BMC Molecular Biology*, vol. 9, article 110, 2008.
- [33] S. A. Bustin and R. Mueller, "Real-time reverse transcription PCR (qRT-PCR) and its potential use in clinical diagnosis," *Clinical Science*, vol. 109, no. 4, pp. 365–379, 2005.
- [34] A. Finotti, M. Borgatti, V. Bezzeri et al., "Effects of decoy molecules targeting NF-kappaB transcription factors in Cystic fibrosis IB3-1 cells: recruitment of NF-kappaB to the IL-8 gene promoter and transcription of the IL-8 gene," *Artificial DNA, PNA & XNA*, vol. 3, no. 2, pp. 97–296, 2012.
- [35] S. G. Yau, M. Bobrow, C. G. Mathew, and S. J. Abbs, "Accurate diagnosis of carriers of deletions and duplications in Duchenne/Becker muscular dystrophy by fluorescent dosage analysis," *Journal of Medical Genetics*, vol. 33, no. 7, pp. 550–558, 1996.
- [36] G. Feriotto, F. Salvatori, A. Finotti et al., "A novel frameshift mutation (+A) at codon 18 of the  $\beta$ -globin gene associated with high persistence of fetal hemoglobin phenotype and  $\delta\beta$ -thalassemia," *Acta Haematologica*, vol. 119, no. 1, pp. 28–37, 2008.
- [37] R. Gambari, M. Terada, A. Bank, R. A. Rifkind, and P. A. Marks, "Synthesis of globin mRNA in relation to the cell cycle during induced murine erythroleukemia differentiation," *Proceedings of the National Academy of Sciences of the United States of America*, vol. 75, no. 8, pp. 3801–3804, 1978.
- [38] D. I. Tanyong, P. Winichagoon, D. Siripin, W. Seevakool, and S. Fucharoen, "Role of interleukin-3 and signaling pathways on  $\beta$ -thalassemia/HbE erythroid progenitor cell in culture," *Southeast Asian Journal of Tropical Medicine and Public Health*, vol. 38, no. 5, pp. 897–903, 2007.

- [39] E. Fibach, N. Bianchi, M. Borgatti, E. Prus, and R. Gambari, "Mithramycin induces fetal hemoglobin production in normal and thalassemic human erythroid precursor cells," *Blood*, vol. 102, no. 4, pp. 1276–1281, 2003.
- [40] I. Lampronti, N. Bianchi, M. Borgatti, E. Fibach, E. Prus, and R. Gambari, "Accumulation of  $\gamma$ -globin mRNA in human erythroid cells treated with angelicin," *European Journal of Haematology*, vol. 71, no. 3, pp. 189–195, 2003.
- [41] L. Breda, C. Casu, S. Gardenghi et al., "Therapeutic hemoglobin levels after gene transfer in  $\beta$ -thalassemia mice and in hematopoietic cells of  $\beta$ -thalassemia and sickle cells disease patients," *PLoS ONE*, vol. 7, no. 3, Article ID e32345, 2012.
- [42] X. Roca, R. Sachidanandam, and A. R. Krainer, "Determinants of the inherent strength of human 5' splice sites," *RNA*, vol. 11, no. 5, pp. 683–698, 2005.
- [43] X. Roca, R. Sachidanandam, and A. R. Krainer, "Intrinsic differences between authentic and cryptic 5' splice sites," *Nucleic Acids Research*, vol. 31, no. 21, pp. 6321–6333, 2003.
- [44] S. Danckwardt, G. Neu-Yilik, R. Thermann, U. Frede, M. W. Hentze, and A. E. Kulozik, "Abnormally spliced beta-globin mRNAs: a single point mutation generates transcripts sensitive and insensitive to nonsense-mediated mRNA decay," *Blood*, vol. 99, no. 5, pp. 1811–1816, 2002.
- [45] H. Sierakowska, M. J. Sambade, S. Agrawal, and R. Kole, "Repair of thalassemic human  $\beta$ -globin mRNA in mammalian cells by antisense oligonucleotides," *Proceedings of the National Academy of Sciences of the United States of America*, vol. 93, no. 23, pp. 12840–12844, 1996.
- [46] Z. Dominski and R. Kole, "Restoration of correct splicing in thalassemic pre-mRNA by antisense oligonucleotides," *Proceedings of the National Academy of Sciences of the United States of America*, vol. 90, no. 18, pp. 8673–8677, 1993.
- [47] T. Suwanmanee, H. Sierakowska, G. Lacerra et al., "Restoration of human  $\beta$ -globin gene expression in murine and human IVS2-654 thalassemic erythroid cells by free uptake of antisense oligonucleotides," *Molecular Pharmacology*, vol. 62, no. 3, pp. 545–553, 2002.
- [48] D. G. Wright, Y. Zhang, and J. R. Murphy, "Effective delivery of antisense peptide nucleic acid oligomers into cells by anthrax protective antigen," *Biochemical and Biophysical Research Communications*, vol. 376, no. 1, pp. 200–205, 2008.
- [49] A. R. Thierry, S. Abes, S. Resina et al., "Comparison of basic peptides- and lipid-based strategies for the delivery of splice correcting oligonucleotides," *Biochimica et Biophysica Acta—Biomembranes*, vol. 1758, no. 3, pp. 364–374, 2006.
- [50] S.-Y. Xie, W. Li, Z.-R. Ren, S.-Z. Huang, F. Zeng, and Y.-T. Zeng, "Correction of  $\beta$ 654-thalassaemia mice using direct intravenous injection of siRNA and antisense RNA vectors," *International Journal of Hematology*, vol. 93, no. 3, pp. 301–310, 2011.
- [51] R. Gambari, "Alternative options for DNA-based experimental therapy of  $\beta$ -thalassemia," *Expert Opinion on Biological Therapy*, vol. 12, no. 4, pp. 443–462, 2012.
- [52] A. Finotti and R. Gambari, "Recent trends for novel options in experimental biological therapy of  $\beta$ -thalassemia," *Expert Opinion on Biological Therapy*, vol. 14, no. 10, pp. 1443–1454, 2014.

## Research Article

# Mineral and Skeletal Homeostasis Influence the Manner of Bone Loss in Metabolic Osteoporosis due to Calcium-Deprived Diet in Different Sites of Rat Vertebra and Femur

Marzia Ferretti,<sup>1</sup> Francesco Cavani,<sup>1</sup> Alberto Smargiassi,<sup>1</sup> Laura Roli,<sup>2</sup> and Carla Palumbo<sup>1</sup>

<sup>1</sup>*Dipartimento di Scienze Biomediche, Metaboliche e Neuroscienze-Sezione di Morfologia Umana, Università di Modena e Reggio Emilia, Istituti Anatomici, 41124 Modena, Italy*

<sup>2</sup>*Laboratorio di Patologia Clinica Endocrinologia, Dipartimento Interaziendale ad Attività Integrata Medicina di Laboratorio ed Anatomia Patologica, AUSL Modena, 41126 Modena, Italy*

Correspondence should be addressed to Carla Palumbo; [carla.palumbo@unimore.it](mailto:carla.palumbo@unimore.it)

Received 23 September 2014; Accepted 16 December 2014

Academic Editor: Andrea Vecchione

Copyright © 2015 Marzia Ferretti et al. This is an open access article distributed under the Creative Commons Attribution License, which permits unrestricted use, distribution, and reproduction in any medium, provided the original work is properly cited.

Rats fed calcium-deprived diet develop osteoporosis due to enhanced bone resorption, secondary to parathyroid overactivity resulting from nutritional hypocalcemia. Therefore, rats provide a good experimental animal model for studying bone modelling alterations during biochemical osteoporosis. Three-month-old Sprague-Dawley male rats were divided into 4 groups: (1) baseline, (2) normal diet for 4 weeks, (3) calcium-deprived diet for 4 weeks, and (4) calcium-deprived diet for 4 weeks and concomitant administration of PTH (1-34) 40  $\mu\text{g}/\text{Kg}/\text{day}$ . Histomorphometrical analyses were made on cortical and trabecular bone of lumbar vertebral body as well as of mid-diaphysis and distal metaphysis of femur. In all rats fed calcium-deprived diet, despite the reduction of trabecular number (due to the maintenance of mineral homeostasis), an intense activity of bone deposition occurs on the surface of the few remaining trabeculae (in answering to mechanical stresses and, consequently, to maintain the skeletal homeostasis). Different responses were detected in different sites of cortical bone, depending on their main function in answering mineral or skeletal homeostasis. This study represents the starting point for work-in-progress researches, with the aim of defining in detail timing and manners of evolution and recovery of biochemical osteoporosis.

## 1. Introduction

Osteoporosis is a systemic skeletal disease that represents a significant public health problem in an increasingly aging society. It is characterized by net bone loss and microarchitectural deterioration of bone tissue, due to an imbalance between the resorption and formation phases in the bone remodelling cycle (increased bone resorption and reduced bone formation), with a consequent increase in bone fragility and susceptibility to fracture [1–10]. Osteoporosis can be mainly due to mechanical disuse or metabolic alterations. According to the latter, it is well known that both estrogen and calcium deficiencies are important risk factors in the pathogenesis of biochemical osteoporosis. Bone development requires adequate amounts of many nutrients and, among

these, calcium is the most important mineral element, since the skeleton represents the greatest calcium store in the body [11]. In fact, more than 95% of the body's calcium is present in bone tissue as hydroxyapatite, conferring rigidity, hardness, and structural integrity to the skeleton [12]. Low calcium intake (particularly common in many countries) and important decrease in calcium intestinal absorption are some of the most important causes involved in bone loss in aging population. Diet is a modifiable risk factor for osteoporosis and adequate amounts of calcium are essential lifelong to maintain healthy bone mass [13, 14]. Several investigations have underlined the role of serum calcium variations in etiopathogenesis of osteoporosis and fracture occurrence; low blood calcium level activates PTH which, in turn, stimulates the production in the kidney of vitamin

D that enhances the calcium uptake in the active sites of duodenum [15], while PTH decreases the urinary excretion of calcium and stimulates calcium resorption from bone [16].

It is well known that rats fed calcium-deprived diet develop osteoporosis, as a result of exaggerated bone resorption, induced by parathyroid overactivity, secondary to nutritional hypocalcemia [17–25]. Therefore, rats provide a good experimental animal model for studying bone remodelling alterations during biochemical osteoporosis. It has been reported by Shen and coworkers [26] that the bone mineral density in the rat femoral diaphysis was decreased by a calcium-deficient diet but not by ovariectomy. Other authors suggested that rat ovariectomy plus calcium deficiency results in a great decrease of bone volume and cross-sectional area compared to the calcium alone [27]. Similar results were also observed in an investigation of Donahue and coworkers [28] in which calcium-deficient ovariectomized rats showed decreased values of bone density, similar to those of estrogen-deficient osteoporotic women. Hara et al. [29] suggested that the interaction between ovariectomy and calcium-deficient diet implies different bone alterations in rats, depending on different skeletal segments and/or different skeletal regions with different metabolism. Moreover, dietary calcium deficiency, regardless of ovariectomy, induced bone loss and increased bone turnover in some skeletal segments, in particular in the hard palate, mandible, and proximal tibia. It is interesting to underline that when OVX rats were fed low calcium diet, the decrease in calcium absorption became more significant and resulting bone loss was particularly enhanced [30–32].

The aim of the present investigation was to study how the mineral and skeletal homeostasis influence the bone loss in metabolic osteoporosis due to calcium-deprived diet in different sites of the two bony architectures (trabecular versus cortical bone) in both axial and appendicular skeleton. This model seems to be a good starting point for successive studies on bone alterations during unbalanced calcium metabolism, frequently occurring in aging, with the final goal of defining timing and manners of bone mass recovery when calcium is restored in the diet and verifying the eventual differences of recovery between compact and spongy bones (i.e., the two bone architectures with different metabolism and target).

## 2. Materials and Methods

**2.1. Experimental Animals and Treatment.** Eighteen 3-month-old Sprague-Dawley male rats were purchased from Charles River Laboratories (Calco, Lecco, Italy). All rats were housed individually in single cages, to better check food intake of each rat, and maintained under laboratory controlled conditions ( $22 \pm 1^\circ\text{C}$ , 55–60% humidity, 12 h light:12 h dark). After 7 days of acclimation to housing conditions, the rats were randomized into four groups, indicated as follows:

Group 1 (baseline,  $n = 3$ ): sacrificed after 7 days of acclimation;

Group 2 (control,  $n = 5$ ): fed normal diet for 4 weeks;

Group 3 ( $n = 5$ ): fed calcium-deprived diet and distilled water *ad libitum* for 4 weeks;

Group 4 ( $n = 5$ ): fed calcium-deprived diet and distilled water *ad libitum*, plus concomitant administration of PTH (1-34)  $40 \mu\text{g}/\text{kg}/\text{day}$ , for 4 weeks.

Both normal and calcium-deprived diets were provided daily; at different times during the test period, the food container was briefly removed and weighed to determine quantity of food consumed.

The calcium-deprived diet is a casein based synthetic diet containing a very low amount of calcium (0.04% Ca). PTH (1-34) was supplied by Eli Lilly and Company (Indianapolis, USA), solubilised in saline ( $40 \mu\text{g}/\text{mL}$ ), and subcutaneously injected in a volume of  $100 \mu\text{L}/100 \text{ gr}$  body weight per rat.

Group 1 animals underwent a subcutaneous injection of calcein (Fluka, St. Louis, MO, USA)  $15 \text{ mg}/\text{kg}$ , two days before the sacrifice. Groups 2, 3, and 4 animals received a subcutaneous injection of calcein  $15 \text{ mg}/\text{kg}$  on the first day of the experimental period, a subcutaneous injection of oxytetracycline hydrochloride (Sigma, St. Louis, MO, USA)  $30 \text{ mg}/\text{kg}$  after 20 days, and a subcutaneous injection of Alizarin-Red S (Fluka, St. Louis, MO, USA)  $30 \text{ mg}/\text{kg}$  2 days before sacrifice, in order to evaluate newly formed bone during animal treatment.

The body weight of each animal was recorded at the time of arrival in the housing facility and before euthanasia. At the end of the treatment, all rats were anesthetized with ether and blood samples were collected by cardiac puncture; then, rats were euthanized by exsanguination under ether anesthesia.

All experiments were carried out according to the Bioethical Committee of the Italian National Institute of Health. Animal care, maintenance, and surgery were conducted in accordance with Italian law (D.L. number 116/1992) and European legislation (EEC number 86/609).

**2.2. Histology and Histomorphometry.** Soon after euthanasia, the fifth lumbar vertebra (L5) and the right femur of each animal were removed, deprived of soft tissues, fixed in sodium phosphate-buffered (PBS) 4% paraformaldehyde pH 7.4, dehydrated in graded ethanol, and embedded in methyl-methacrylate resin (Sigma Aldrich, Milan, Italy). The vertebrae and the femurs were transversally cut with a Leica SP 1600 diamond saw microtome cutting system (Leica SpA, Milan, Italy) to obtain serial  $200 \mu\text{m}$  thick sections. The sections, taken from the central level of the lumbar vertebral body and from the femur mid-diaphysis and distal metaphysis (for this last considering the more proximal section of the patellar groove), were glued to a glass slide and ground to a final thickness of about  $40 \mu\text{m}$ . These sections were superficially stained with Alizarin-Red and scanned with Epson 3200 perfection scanner at 3200 dpi resolution to perform histomorphometry by means of the software Image J (NIH, Bethesda, USA). The following *static histomorphometric parameters* were calculated: trabecular bone volume (BV/TV), trabecular thickness (Tb.Th), trabecular number (Tb.N), and trabecular separation (Tb.Sp) of the vertebral bodies and the femoral distal metaphyses; the cortical bone thickness (Ct.Th) of the anterolateral and posterior sides of

vertebral bodies; the total cross section area, the cortical bone area (Ct-B-Ar), and the medullary canal area of the femoral middiaphyses; the cortical bone area (Ct-B-Ar) of the femoral metaphyses.

The same sections were also further polished to remove the Alizarin-Red staining and used for evaluation of dynamic histomorphometry (by means of bone labelling technique), as a measure of newly formed bone during animal treatment, that is, to distinguish preexistent bone with respect to the bone formed during the period of administration of the calcium-deprived diet. The sections were photographed using a Nikon Eclipse 90i microscope (Tokyo, Japan) equipped with a DS-Fil Nikon digital camera and driven by the Nikon ACT-2U software; *dynamic histomorphometric parameters* were evaluated by means of the image analysis system software Image J (NIH, Bethesda, USA). The newly formed bone area (Nf B Ar) and the mineral apposition rate (MAR) were measured between the first two labels (calcein and oxytetracycline) on the anterior and posterior sides of the vertebral cortical bone as well as on the femoral mid-diaphysis. Moreover, the mineralizing surface (MS), marked with Alizarin, was measured on the femoral mid-diaphyses as well as on trabecular bone of vertebral bodies and femur metaphyses. MAR at the femur metaphyseal level was measured taking into consideration the second and third label (oxytetracycline and alizarin). All measurements were performed according to the ASBMR histomorphometry nomenclature [33].

In order to evaluate the presence of osteoid seams in trabecular bone of both femur metaphyses and vertebral bodies, one section (200  $\mu\text{m}$  thick) adjacent to those used for histomorphometry was glued to a metacrylate support, cut to obtain 5  $\mu\text{m}$  thick sections (Reichert-Jung 1150/Autocut), and stained with Gomori trichrome. The osteoid surface (OS/BS) was measured on trabecular bone.

**2.3. Serum Biochemical Analysis.** Blood samples were centrifuged to separate serum that was preserved in tubes, immediately separated by centrifugation (4°C) at 1,500 g for 15 min. Sera were then aliquoted into small volumes and stored at -20°C for successive analyses. The levels of total calcium (Ca) and inorganic phosphorus (P) in serum were determined using the high performance Beckman Coulter analyzer AU680 Chemistry System. The immune-metric assays for the determination of levels of osteoprotegerin (OPG), specific bone alkaline phosphatase (BALP), CTX (Beta CrossLaps), and bioactive-intact-PTH (1-84) in rat serum were provided by Pantec s.r.l. (Turin, Italy); all kits are intended for research use only. In particular, rat-OPG and rat-BALP are two ELISA kits produced by SunRed Hotecology Company (Shanghai, China); RatLaps is an EIA kit produced by Immunodiagnostic Systems Ltd. (Baldon, UK); rat bioactive-intact-PTH is an ELISA method produced by Immunotopics Inc. (San Clemente, CA). The small amounts of reagents supplied in the kits prevented the possibility to perform automated procedures on laboratory analytical platform. To minimize the variables influencing the test, all good laboratory practice principles were applied: immediate storage of samples after serum separation at -20°C; manual execution of tests in close agreement to the manufacturer's

TABLE 1: Body weights of rat at the time of arrival and sacrifice.

Group	Arrival weight	Sacrifice weight
1	406 $\pm$ 48	426 $\pm$ 48
2	405 $\pm$ 32	526 $\pm$ 47
3	405 $\pm$ 32	528 $\pm$ 70
4	397 $\pm$ 25	504 $\pm$ 40

All values are expressed as mean  $\pm$  sd, ANOVA followed by Bonferroni's test. Group 1: baseline; Group 2: control, normal diet; Group 3: calcium-deprived diet for 4 weeks; Group 4: calcium-deprived diet, plus concomitant administration of PTH (1-34) 40  $\mu\text{g}/\text{kg}/\text{day}$ , for 4 weeks.

instructions; execution of all tests over two consecutive days in order to avoid repeated freeze/thaw cycles of samples.

**2.4. Statistical Analysis.** One-way analysis of variance (ANOVA) with Bonferroni test between treatment groups and controls was performed using the Software STATA 11.0 (StataCorp, Texas, USA). Values of  $P < 0.05$  indicate significant differences between groups.

### 3. Results

**3.1. Body Weight.** Table 1 reports mean values of body weights of all groups recorded both at the time of arrival in the housing facility and at sacrifice; no significant differences were found among groups.

**3.2. Histology and Histomorphometry.** The observations reported in the present paper refer to morphological and histomorphometric evaluations performed on transverse sections of the 5th lumbar vertebra and right femur at middiaphyseal and distal metaphyseal levels of all rats.

**3.2.1. Vertebra (L5).** Concerning the vertebral sections, in rats fed calcium-deprived diet, as expected, bone trabeculae are less abundant and cortical bone appears less thick with respect to rats fed normal diet (Figure 1).

Table 2 shows the mean values of the trabecular bone volume (BV/TV), the trabecular thickness (Tb.Th), the trabecular number (Tb.N), and the trabecular separation (Tb.Sp). The results are in line with the morphological observations in showing a statistically significant decrement of trabecular bone of the vertebral body in rats fed calcium-deprived diet (Groups 3 and 4), with respect to rats fed normal diet (Groups 1 and 2). In fact, significant lower values of BV/TV and Tb.N are observed in both groups of rats fed calcium-deprived diet with respect to rats fed normal diet. Similar results were recorded for Tb.Sp, since significant higher distance among bony trabeculae was recorded in both groups of rats fed calcium-deprived diet with respect to rats fed normal diet. As far as trabecular thickness is concerned, instead, significant lower values of Tb.Th were recorded only in rats fed calcium-deprived diet plus PTH (1-34) administration (Group 4) with respect to baseline rats (Group 1).

The results of cortical bone thickness (Ct.Th) in anterolateral as well as in posterior sides of the vertebral body are shown in Table 3: in the anterolateral side, the mean values

TABLE 2: Static histomorphometric parameters of trabecular bone in L5 vertebral body sections.

Group	BV/TV (%)	Tb.Th ( $\mu\text{m}$ )	Tb.N ( $n/\text{mm}$ )	Tb.Sp ( $\mu\text{m}$ )
1	24.54 $\pm$ 2.28	59.56 $\pm$ 3.14	4.14 $\pm$ 0.54	185.12 $\pm$ 28.70
2	23.35 $\pm$ 2.31	53.29 $\pm$ 2.28	4.39 $\pm$ 0.52	180.33 $\pm$ 26.25
3	14.97 $\pm$ 3.55 <sup>*,##</sup>	50.75 $\pm$ 6.50	2.93 $\pm$ 0.41 <sup>*,##</sup>	298.79 $\pm$ 53.81 <sup>*,##</sup>
4	14.36 $\pm$ 0.73 <sup>*,##</sup>	47.07 $\pm$ 2.12 <sup>*</sup>	3.03 $\pm$ 0.06 <sup>*,##</sup>	285.34 $\pm$ 11.12 <sup>*,##</sup>

All values are expressed as mean  $\pm$  sd, ANOVA followed by Bonferroni's test: <sup>\*</sup> $P < 0.05$ , <sup>\*\*</sup> $P < 0.01$  versus Group 1; <sup>##</sup> $P < 0.001$  versus Group 2. Group 1: baseline; Group 2: control, normal diet; Group 3: calcium-deprived diet for 4 weeks; Group 4: calcium-deprived diet, plus concomitant administration of PTH (1-34) 40  $\mu\text{g}/\text{kg}/\text{day}$ , for 4 weeks.

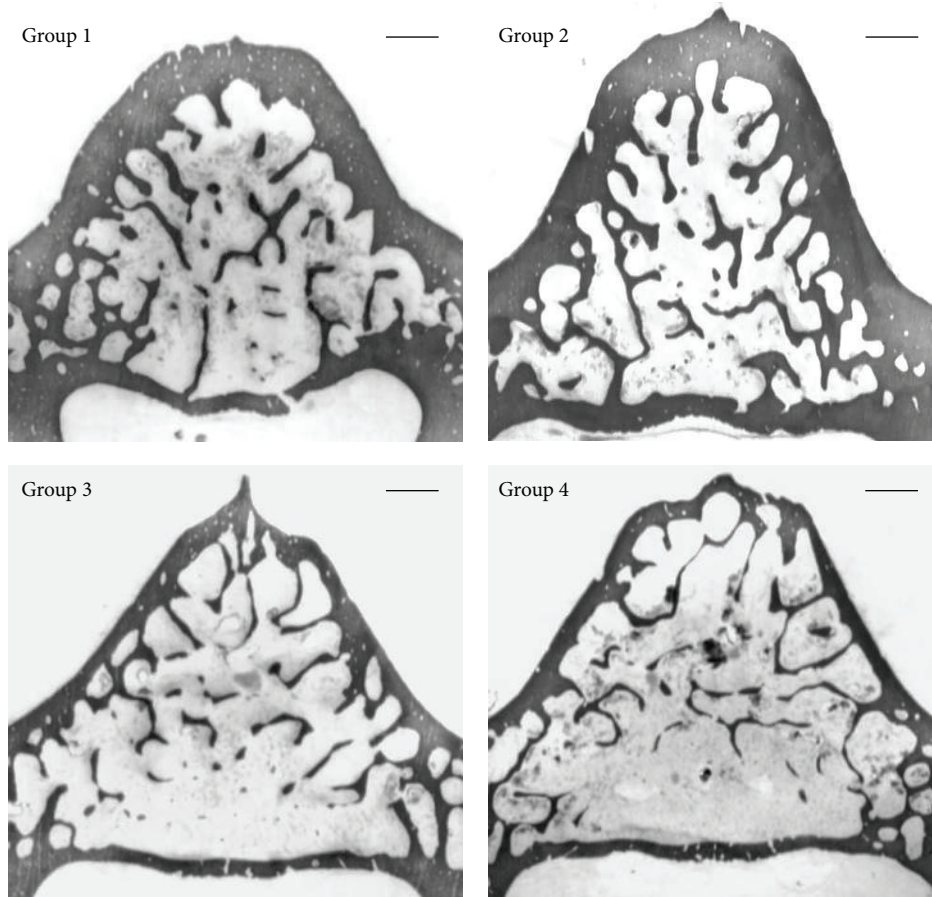


FIGURE 1: Scans showing bone histology of the transversal sections of the 5th lumbar vertebral body of all animal groups. Group 1: baseline; Group 2: control, normal diet; Group 3: calcium-deprived diet for 4 weeks; Group 4: calcium-deprived diet, plus concomitant administration of PTH (1-34) 40  $\mu\text{g}/\text{kg}/\text{day}$ , for 4 weeks. Scale bar: 500  $\mu\text{m}$ .

are significantly lower in both groups of rats fed a calcium-deprived diet than in the rats fed a normal diet; otherwise, in vertebral posterior side the mean values are similar in all groups.

Figure 2 shows histological transverse sections of the vertebral body from each animal group, under fluorescence microscope. The control group as well as the two groups fed calcium-free diet shows different locations of the labels of osteogenesis: concerning the anterior cortex the labels are observed at periosteal level, while in the posterior cortex the labels are located at the endosteal level. Moreover, in the two calcium-deprived diet groups, the endosteal surface of

the anterior cortex shows a thinner layer of bone between the calcein label (injected at the beginning of the experiment) and the bone marrow surface, with respect to control group.

The results of dynamic histomorphometry show that both in the anterior and posterior cortical bone the mean values of Nf B Ar and of MAR are always similar in all groups (Table 4). The trabecular bone shows intense red fluorescence (alizarin) mostly located on the surface of the few trabecular remnants of the groups fed calcium-deprived diet, being instead scarcely present in the animals fed normal diet (Figure 2: Groups 3-4 versus Group 2). Table 4 also shows the mean values of MS of trabecular bone; the results are

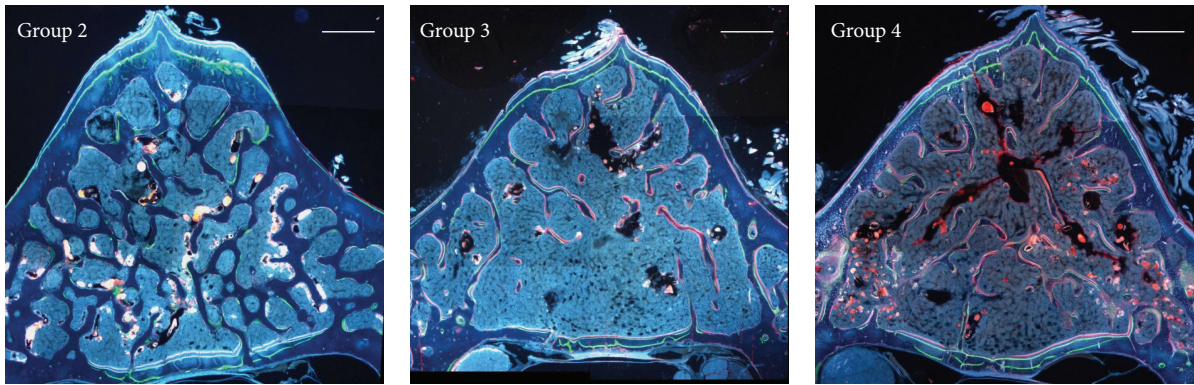


FIGURE 2: Fluorescence microscope micrographs showing transverse sections of the 5th lumbar vertebral body. Note the newly formed bone among three labels in the anterior and posterior cortical bone and the red fluorescence mostly on the surface of the few trabecular remnants of Groups 3 and 4. Group 2: control, normal diet; Group 3: calcium-deprived diet for 4 weeks; Group 4: calcium-deprived diet, plus concomitant administration of PTH (1-34) 40 µg/kg/day, for 4 weeks. Scale bar: 500 µm.

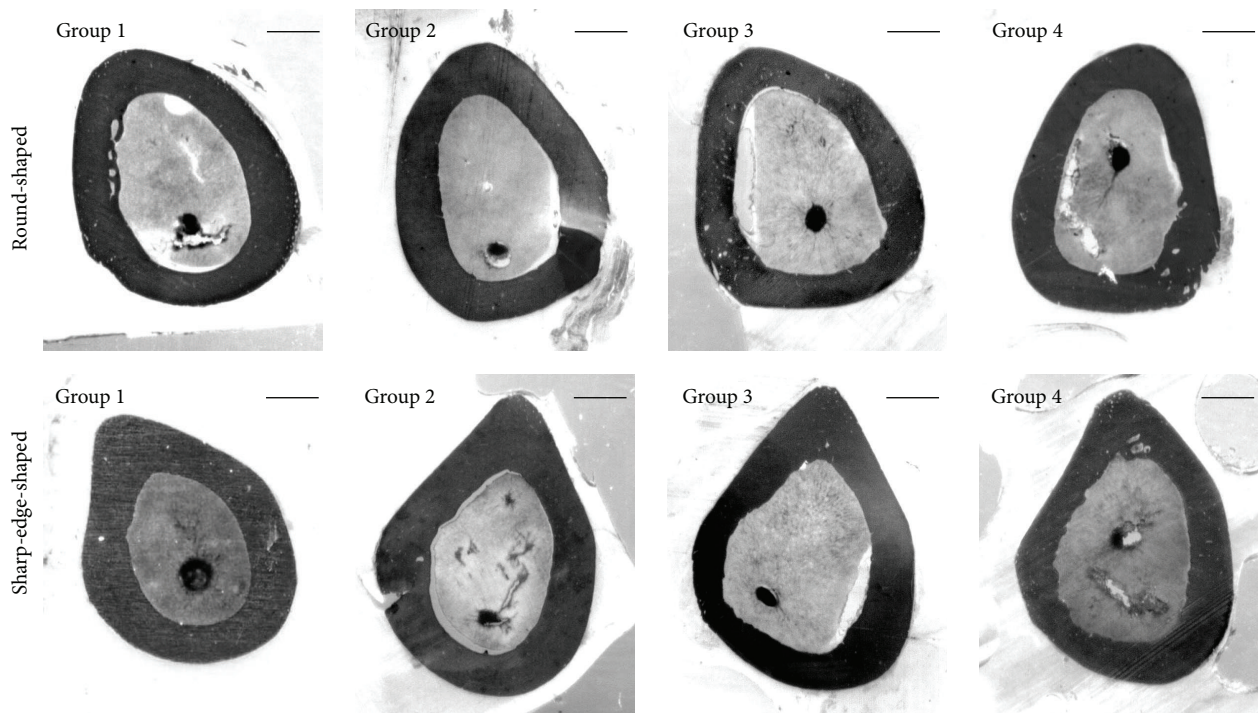


FIGURE 3: Scans showing bone histology of the transversal sections of the femoral mid-diaphysis of all animal groups. Group 1: baseline; Group 2: control, normal diet; Group 3: calcium-deprived diet for 4 weeks; Group 4: calcium-deprived diet, plus concomitant administration of PTH (1-34) 40 µg/kg/day, for 4 weeks. Scale bar: 750 µm.

in line with the morphological observations in showing a statistically significant increase of mineralization surface in the two groups fed calcium-deprived diet with respect to the control one.

Gomori trichrome stain performed on vertebral trabecular bone does not reveal the presence of osteoid seams (OS/BS) in all rats of the control group, while the value of OS/BS in all rat fed calcium-deprived diet ranges from 0 to 24%.

**3.2.2. Femoral Mid-Diaphysis.** Figure 3 shows the middiaphyseal femoral sections of all animals. In each group, among

all sections observed, two different morphologies were identified: (i) the more distal mid-diaphyseal sections show oval appearance; thus they were named “round-shaped” sections; (ii) the more proximal mid-diaphyseal sections show sharp-edge appearance (corresponding to the trochanter tertius); thus they were named “sharp-edge-shaped” sections.

Static histomorphometric parameters are reported in Table 5. Mean values of total cross section area and cortical bone area were similar in all groups both in *round-shaped* and in *sharp-edge-shaped* sections. The medullary canal areas are instead always larger in the rats fed calcium-deprived diets (Group 3) with respect to baseline and control ones in both

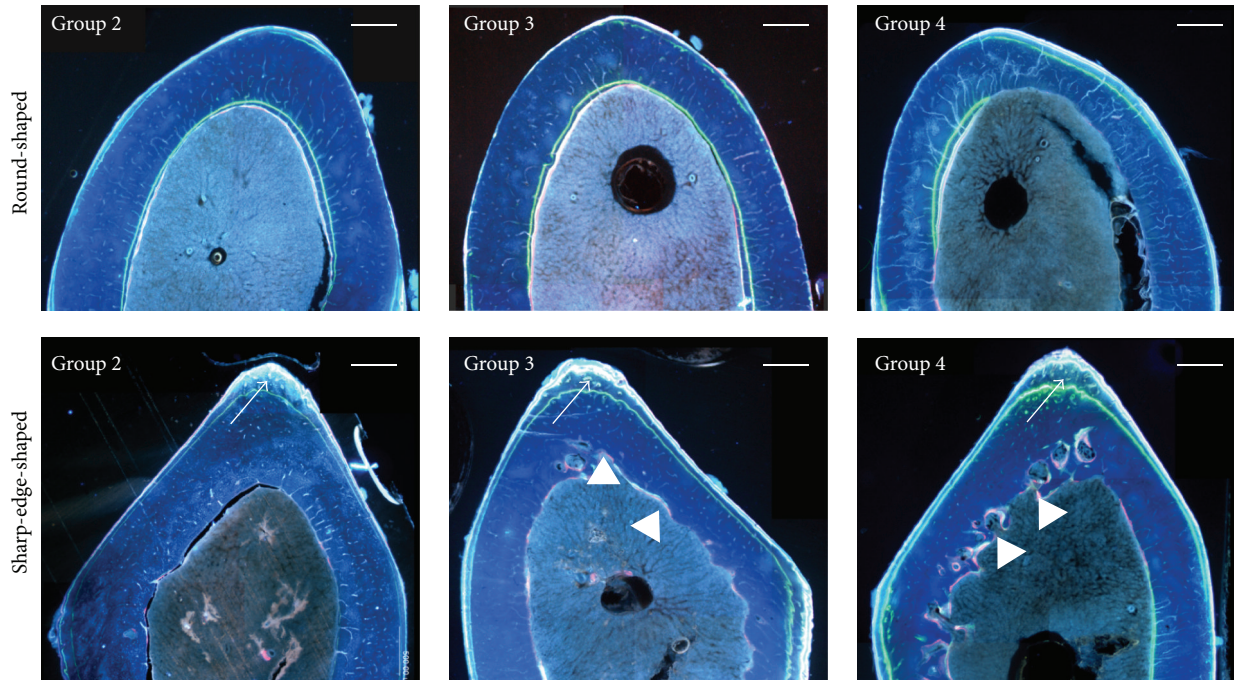


FIGURE 4: Fluorescence microscope micrographs showing a portion of transverse sections of the femoral mid-diaphysis. Note in *sharp-edge-shaped* sections the new bone deposition mostly located at the periosteal surface (arrows) and bone resorption at the endosteal surface (arrow heads). Group 2: control, normal diet; Group 3: calcium-deprived diet for 4 weeks; Group 4: calcium-deprived diet, plus concomitant administration of PTH (1-34) 40  $\mu\text{g}/\text{kg}/\text{day}$ , for 4 weeks. Scale bar: 500  $\mu\text{m}$ .

TABLE 3: Static histomorphometric parameters of cortical bone in L5 vertebral body sections.

Group	Anterolateral Ct.Th	Posterior Ct.Th
1	311.84 $\pm$ 71.47	176.15 $\pm$ 33.10
2	321.49 $\pm$ 35.97	168.85 $\pm$ 26.67
3	197.84 $\pm$ 9.54***,###	148.23 $\pm$ 35.69
4	162.67 $\pm$ 10.53***,###	130.37 $\pm$ 13.37

All values ( $\mu\text{m}$ ) are expressed as mean  $\pm$  sd, ANOVA followed by Bonferroni's test: \*\*\* $P < 0.001$  versus Group 1; ### $P < 0.001$  versus Group 2. Group 1: baseline; Group 2: control, normal diet; Group 3: calcium-deprived diet for 4 weeks; Group 4: calcium-deprived diet, plus concomitant administration of PTH (1-34) 40  $\mu\text{g}/\text{kg}/\text{day}$ , for 4 weeks.

*round-shaped* and *sharp-edge-shaped* sections; this difference is sometimes significant.

Figure 4 shows, for each animal group, details of histological transverse sections of the femur mid-diaphysis observed under fluorescence microscope. Bone labeling (index of bone osteogenesis) is present mainly at the periosteal surface, in particular in the *sharp-edge-shaped* sections in all groups; moreover, again in particular in *sharp-edge-shaped* sections, the endosteal surface shows an irregular outline (index of bone resorption) in all animals fed a calcium-deprived diet.

The results of dynamic histomorphometry concerning Nf B Ar, MAR, and MS are shown in Table 6: no significant differences were observed among all groups in both *round-shaped* and *sharp-edge-shaped* sections at the periosteal and endosteal level. It must be underlined that in four animals out of five in the two groups fed a calcium-deprived diet and in

two out of five animals in the control group we never observed new bone formation at the endosteal level in *sharp-edge-shaped* sections; this implies high values of standard deviation of Nf B Ar and MAR average.

3.2.3. *Femoral Metaphysis*. Figure 5 shows lower amount of trabecular bone in all animals fed a calcium-deprived diet with respect to basal and control ones.

Table 7 concerning static histomorphometry values shows (a) significant lower values of BV/TV and Tb.N in Groups 3 and 4 compared to Groups 1 and 2; (b) significantly increased Tb.Sp values in Groups 3 and 4 compared to Groups 1 and 2; (c) no differences among all groups for Tb.Th and Ct-B-Ar.

Figure 6 shows details of histological transverse sections of the femur metaphysis, observed under fluorescence microscope. New bone deposition is observed only at the endosteal level and around some trabeculae in all animal groups. Data reported in Table 8 confirm such histological observations; in particular, the only significant difference is recorded in MS that is higher in rats fed calcium-deprived diet plus PTH (1-34) with respect to control ones.

Gomori trichrome stain does not reveal the presence of osteoid seams (OS/BS) in all rats of the control group, while the value of OS/BS in all calcium-deprived diet animals ranges between 0 and 22%.

3.3. *Serum Biochemical Analysis*. In Table 9 are reported, for each rat, the values of parameters from sera collected at the end of experiment. The values of Ca, P, OPG, and

TABLE 4: Dynamic histomorphometric parameters in L5 vertebral body sections.

Group	Anterior Ct Nf B Ar (mm <sup>2</sup> )	Anterior Ct MAR (μm/day)	Posterior Ct Nf B Ar (mm <sup>2</sup> )	Posterior Ct MAR (μm/day)	Tb MS (%)
2	0.063 ± 0.08	4.10 ± 0.71	0.035 ± 0.01	3.47 ± 0.50	11.40 ± 2.30
3	0.075 ± 0.04	4.19 ± 1.40	0.033 ± 0.02	3.26 ± 0.66	53.03 ± 6.44 <sup>###</sup>
4	0.076 ± 0.01	4.22 ± 0.39	0.036 ± 0.07	3.42 ± 0.54	50.80 ± 9.52 <sup>###</sup>

All values are expressed as mean ± sd, ANOVA followed by Bonferroni's test: <sup>###</sup> *P* < 0.001 versus Group 2. Group 2: control, normal diet; Group 3: calcium-deprived diet for 4 weeks; Group 4: calcium-deprived diet, plus concomitant administration of PTH (1-34) 40 μg/kg/day, for 4 weeks.

TABLE 5: Static histomorphometric parameters in middiaphyseal femoral sections.

Group	Round-shaped sections			Sharp-edge-shaped sections		
	Total cross section area	Cortical bone area	Medullary canal area	Total cross section area	Cortical bone area	Medullary canal area
1	11.07 ± 0.61	6.61 ± 0.44	4.36 ± 0.57	10.94 ± 0.50	6.74 ± 0.48	4.19 ± 0.55
2	12.19 ± 1.38	7.35 ± 0.84	4.83 ± 0.54	12.43 ± 1.50	7.73 ± 0.88	4.70 ± 0.53
3	12.71 ± 0.75	6.90 ± 0.48	5.64 ± 0.38*	12.97 ± 0.87	7.25 ± 0.68	5.67 ± 0.32* <sup>#</sup>
4	11.71 ± 0.78	6.50 ± 0.35	5.17 ± 0.49	12.20 ± 0.89	6.67 ± 0.45	5.50 ± 0.46*

All values (mm<sup>2</sup>) are expressed as mean ± sd, ANOVA followed by Bonferroni's test: \* *P* < 0.05 versus Group 1; <sup>#</sup> *P* < 0.05 versus Group 2. Group 1: baseline; Group 2: control, normal diet; Group 3: calcium-deprived diet for 4 weeks; Group 4: calcium-deprived diet, plus concomitant administration of PTH (1-34) 40 μg/kg/day, for 4 weeks.

TABLE 6: Dynamic histomorphometric parameters (Nf B Ar-MAR-MS) in middiaphyseal femoral sections.

Group	Round-shaped sections		Sharp-edge-shaped sections	
	Periosteal Nf B Ar (mm <sup>2</sup> )	Endosteal Nf B Ar (mm <sup>2</sup> )	Periosteal Nf B Ar (mm <sup>2</sup> )	Endosteal Nf B Ar (mm <sup>2</sup> )
2	0.27 ± 0.10	0.18 ± 0.15	0.82 ± 0.23	0.05 ± 0.06
3	0.23 ± 0.09	0.14 ± 0.09	0.77 ± 0.34	0.001 ± 0.001
4	0.20 ± 0.10	0.06 ± 0.04	0.80 ± 0.34	0.005 ± 0.012
	Periosteal MAR (μm/day)	Endosteal MAR (μm/day)	Periosteal MAR (μm/day)	Endosteal MAR (μm/day)
2	2.38 ± 0.49	1.68 ± 0.92	3.67 ± 0.70	1.09 ± 0.99
3	2.82 ± 1.26	2.25 ± 0.55	3.65 ± 1.13	0.14 ± 0.32
4	2.56 ± 0.59	2.03 ± 1.09	3.84 ± 1.27	0.17 ± 0.37
	Periosteal MS (%)	Endosteal MS (%)	Periosteal MS (%)	Endosteal MS (%)
2	52.40 ± 12.91	41.78 ± 18.95	67.39 ± 18.58	29.25 ± 19.06
3	54.89 ± 12.62	42.77 ± 21.83	84.45 ± 10.06	49.94 ± 16.52
4	62.81 ± 14.60	41.81 ± 5.19	72.26 ± 20.26	41.77 ± 7.07

All values are expressed as mean ± sd, ANOVA followed by Bonferroni's test. Group 1: baseline; Group 2: control, normal diet; Group 3: calcium-deprived diet for 4 weeks; Group 4: calcium-deprived diet, plus concomitant administration of PTH (1-34) 40 μg/kg/day, for 4 weeks.

BALP do not show individual variability among the animals inside each group; moreover, the mean values do not show statistically significant differences among the various groups. Concerning, instead, the values of CrossLaps and PTH (1-84) the wide individual variability among the animals inside each group is to be noticed; also for these parameters, no differences were recorded in the mean values among all groups.

#### 4. Discussion

The present investigation analyses how the mineral and skeletal homeostasis influence the bone loss in metabolic osteoporosis due to calcium-deprived diet in different sites of the two bony architectures (trabecular versus cortical bone) in both axial and appendicular skeleton.

The first point to discuss concerns the different amount of bone mass recorded between the control group and the two groups of rats fed calcium-deprived diet; in fact, trabecular bone of vertebral bodies and femoral metaphyses (Tables 2 and 7) as well as cortical bone of the vertebral anterolateral part only (Table 3) are significantly reduced in rats fed calcium-deprived diet. Such bone reduction indicates that calcium-deprived diet induces marked bone resorption on those specific bone areas, mainly devoted in answering metabolic demands, according to the well-known mineral homeostasis, as also reported by other authors [26, 29, 30, 34, 35]. In all rats fed calcium-deprived diet, despite the significant reduction of trabecular bone volume and number, the remaining few trabeculae show active sites of bone deposition, demonstrated by the intense red fluorescence on their surfaces as well as by high MS values (Tables 4 and 8);

TABLE 7: Static histomorphometric parameters in distal metaphyseal femoral sections.

Group	BV/TV (%)	Tb.Th ( $\mu\text{m}$ )	Tb.N ( $n/\text{mm}$ )	Tb.Sp ( $\mu\text{m}$ )	Ct-B-Ar ( $\text{mm}^2$ )
1	18.26 $\pm$ 7.36	51.63 $\pm$ 10.19	3.16 $\pm$ 0.67	255.36 $\pm$ 104.87	6.01 $\pm$ 0.41
2	17.76 $\pm$ 4.78	50.36 $\pm$ 7.92	3.49 $\pm$ 0.51	241.08 $\pm$ 49.04	5.93 $\pm$ 0.70
3	6.94 $\pm$ 1.47 <sup>**#</sup>	42.88 $\pm$ 5.01	1.62 $\pm$ 0.40 <sup>****#</sup>	601.63 $\pm$ 165.23 <sup>***#</sup>	5.71 $\pm$ 0.19
4	7.50 $\pm$ 2.05 <sup>**#</sup>	43.89 $\pm$ 8.01	1.65 $\pm$ 0.19 <sup>****#</sup>	564.60 $\pm$ 84.57 <sup>**#</sup>	5.91 $\pm$ 0.60

All values are expressed as mean  $\pm$  sd, ANOVA followed by Bonferroni's test: \* $P < 0.05$ , \*\* $P < 0.01$  versus Group 1; # $P < 0.05$ , ## $P < 0.01$ , and ### $P < 0.001$  versus Group 2. Group 1: baseline; Group 2: control, normal diet; Group 3: calcium-deprived diet for 4 weeks; Group 4: calcium-deprived diet, plus concomitant administration of PTH (1-34) 40  $\mu\text{g}/\text{kg}/\text{day}$ , for 4 weeks.

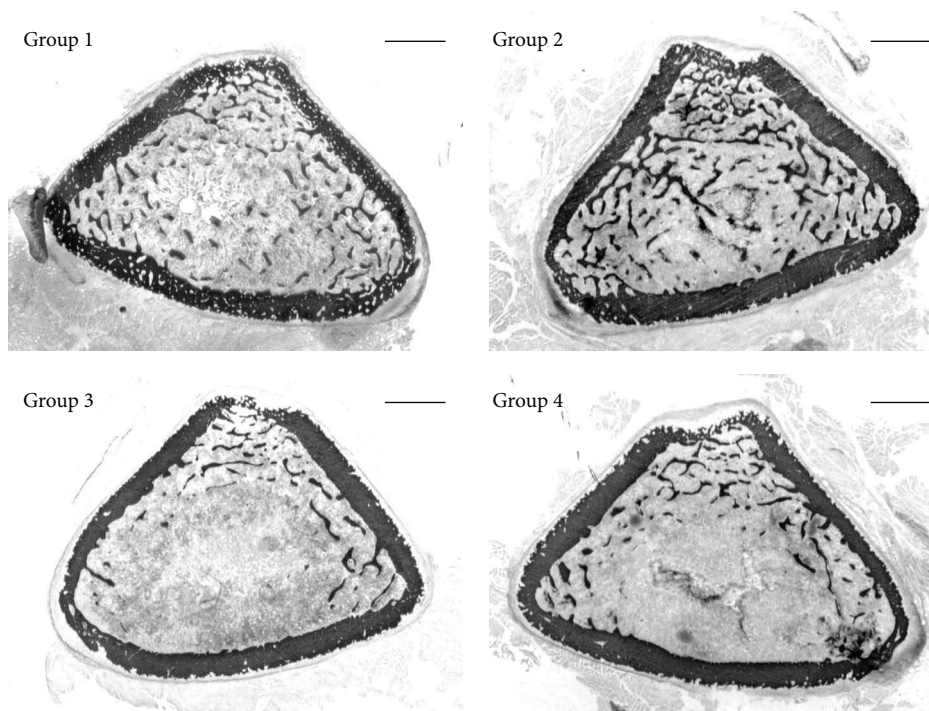


FIGURE 5: Scans showing bone histology in the transversal sections of the femoral distal metaphysis of all animal groups. Group 1: baseline; Group 2: control, normal diet; Group 3: calcium-deprived diet for 4 weeks; Group 4: calcium-deprived diet, plus concomitant administration of PTH (1-34) 40  $\mu\text{g}/\text{kg}/\text{day}$ , for 4 weeks. Scale bar: 1 mm.

this evidence does not occur in control group. Similar results were observed in OS/BS values, showing that new osteoid is deposited around the few trabecular remnants in calcium-deprived diet rats only. These findings might explain the fact that trabecular thickness is similar in all groups. Altogether these observations agree in suggesting that in all rats fed calcium-deprived diet bone deposition around the remaining few bony trabeculae occurs in answering mechanical demands, according to skeletal homeostasis. On the other hand, in control rats, since no metabolic alterations are observed and no bone mass loss occurs, skeletal homeostasis is not altered, the MS value is very low, and the osteoid secretion (inferable by OS/BS) is absent. Such consideration is particularly true for vertebral bodies trabeculae, whereas in femoral metaphyses the MS values show minor differences between the control group and the groups fed calcium-deprived diet (the difference reaches statistical significance only in the group treated with Teriparatide versus control group). Moreover, at both femoral and vertebral levels, it

is interesting to note that OS/BS values are at least half the values of MS in calcium-deprived rats; this finding is probably due to a high osteoid mineralization rate. Our results are in line with those of Shin and coworkers [36] that found in rats (4 weeks after ovariectomy) reduction of BV/TV and Tb N, as well as increase of Tb.Sp of both 4th lumbar vertebra and femur. They also report that, 8 weeks after ovariectomy, further increase of Tb.Sp mainly depends on trabecular thinning at vertebral level and on trabecular number decrease at femoral level. These last results matched with the findings of Thompson et al. [37] that observed after 8 weeks from ovariectomy that rat vertebrae lost bone by thinning trabeculae, whereas proximal tibiae lost bone by removing trabeculae.

The second point to discuss is that the anterolateral part of vertebral cortical bone shows intense modelling processes in all animal groups. In fact, independently of diet type, new bone deposition always occurs at the periosteal level, as shown by the presence of the 3 labels of osteogenesis in all

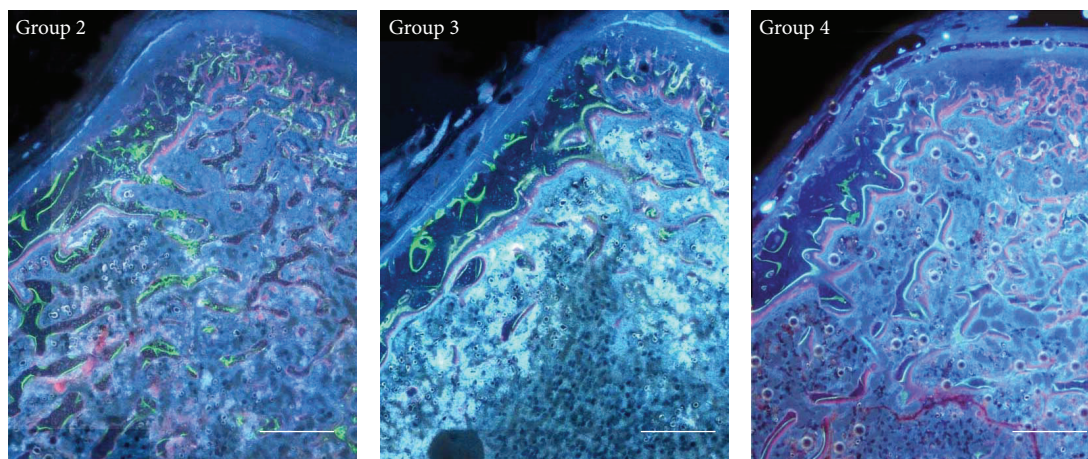


FIGURE 6: Fluorescence microscope micrographs showing portions of the transverse sections of the femoral distal metaphysis. New bone deposition is present only at the endosteal level and around some trabeculae. Group 2: control, normal diet; Group 3: calcium-deprived diet for 4 weeks; Group 4: calcium-deprived diet, plus concomitant administration of PTH (1-34) 40  $\mu\text{g}/\text{kg}/\text{day}$ , for 4 weeks. Scale bar: 500  $\mu\text{m}$ .

TABLE 8: Dynamic histomorphometric parameters in distal metaphyseal femoral sections.

Group	Endosteal MAR ( $\mu\text{m}/\text{day}$ )	Tb MS (%)
2	$2.91 \pm 0.45$	$34 \pm 7.88$
3	$2.87 \pm 0.11$	$48 \pm 4.55$
4	$2.81 \pm 0.38$	$50.5 \pm 7.23^{\#}$

All values are expressed as mean  $\pm$  sd, ANOVA followed by Bonferroni's test:  $^{\#}P < 0.05$  versus Group 2. Group 2: control, normal diet; Group 3: calcium-deprived diet for 4 weeks; Group 4: calcium-deprived diet, plus concomitant administration of PTH (1-34) 40  $\mu\text{g}/\text{kg}/\text{day}$ , for 4 weeks.

groups (Figure 2); thus, the lack of calcium in diet does not alter the amount of newly formed bone (Table 4). In all rats fed calcium-deprived diet only, intense resorption activity occurs at the endosteal level that leads to the thinning of cortical bone, as also shown by the small amount of bone observed between the calcein label (injected at the beginning of the experiment) and the bone marrow surface. These histological and histomorphometric data suggest that new bone deposition at the periosteal level likely depends on mechanical needs, whereas bone resorption at the endosteal level likely depends on metabolic demands. Moreover, in all groups the posterior part of vertebral cortical bone shows modeling processes due to new bone deposition at the endosteal level, in answering mechanical needs. These results suggest that cortical bone of the anterolateral side is mainly involved in mineral homeostasis with respect to the posterior one; in fact, the thickness of the anterolateral side of the cortex is significantly lower in rats fed calcium-deprived diet with respect to the control ones, while the thickness of the posterior side is similar in all groups.

As regards the femoral mid-diaphysis, the lack of calcium in the diet leads to an enlargement of the medullary canal due to resorption at the endosteal level, in particular in *sharp-edge-shaped* sections (Figure 3 and Table 5). The finding that only the medullary canal area shows differences

among groups, whereas the cortical bone area does not, likely depends on the amount of resorbed bone that is irrelevant when compared to the cortical bone area; this notwithstanding such difference is significant when compared to the medullary canal area. In *sharp-edge-shaped* sections (Figure 4) the medullary canal area increases in all animals fed calcium-deprived diet due to bone modelling that implies a marked periosteal bone deposition at the tertius trochanter (where mechanical loads are greater) and a significant endosteal bone erosion (where mechanical loads are lesser). Dynamic histomorphometric results show that (i) at the periosteal level the amount of newly formed bone is similar in all groups; (ii) at the endosteal level in *sharp-edge-shaped* sections newly formed bone deposition is virtually absent in animals fed calcium-deprived diet (Table 6) and the morphology of endosteal surface is irregular since bone resorption occurs. These observations are in line with data shown in literature [38] reporting that the pattern of cortical bone loss in osteoporosis begins from the endosteal surface of the cortex, where the enlargement of medullary canal occurs at the expense of the cortex inner side; bone loss usually does not occur at the periosteal surface.

In femoral cortex metaphysis, the values of Ct-B-Ar and endosteal MAR do not show differences among groups (Tables 7 and 8) and probably depend on different factors; Ct-B-Ar might be due to the high mechanical load acting on the skeletal region, whereas endosteal MAR likely depends on the bone modeling processes that lead to new bone deposition at the endosteal level and bone resorption at the periosteal one.

As far as serum parameters are concerned, it is not surprising to observe after one month of experiment that Ca and P levels are similar in all groups, as a consequence of the early bone response by means of mineral homeostasis. Also serum mean values of OPG and BALP are similar in all groups, because in all groups bone deposition due to skeletal growth is not altered by diet, in particular in cortical bone. Concerning CrossLaps and PTH (1-84), the excessive individual variability among the animals inside the same

TABLE 9: Values of serum levels at the end of the experiments: Ca, P, OPG, BALP, CrossLaps, and PTH (1-84).

Group	Ca mg/dL	P mg/dL	OPG ng/ml	BALP ng/ml	CrossLaps ng/mL	PTH (1-84) pg/ml
1	10.02	7.38	0.75	7.12	38.67	41.24
	10.42	5.87	0.67	7.22	59.76	40.65
	10.34	7.63	0.72	6.78	73.86	33.59
Mean value $\pm$ sd	10.26 $\pm$ 0.21	6.96 $\pm$ 0.95	0.71 $\pm$ 0.04	7.04 $\pm$ 0.23	57.40 $\pm$ 17.71	38.49 $\pm$ 4.25
2	9.89	6.67	0.75	6.53	36.62	45.35
	10.14	6.71	0.65	6.94	40.61	80.06
	9.46	8.13	0.76	6.51	45.31	84.18
	9.48	5.75	0.74	8.00	84.52	31.24
	9.75	6.00	0.68	6.55	52.53	31.82
Mean value $\pm$ sd	9.74 $\pm$ 0.28	6.65 $\pm$ 0.92	0.71 $\pm$ 0.04	6.90 $\pm$ 0.63	51.91 $\pm$ 19.16	54.52 $\pm$ 25.85
3	9.78	7.00	0.69	6.74	52.77	61.82
	10.10	6.55	0.60	6.33	86.80	79.47
	10.18	8.78	0.67	7.28	58.20	98.29
	9.90	6.86	0.57	6.59	83.06	39.47
	10.11	7.57	0.85	7.26	51.01	115.35
Mean value $\pm$ sd	10.01 $\pm$ 0.16	7.35 $\pm$ 0.87	0.67 $\pm$ 0.10	6.84 $\pm$ 0.41	66.36 $\pm$ 17.20	78.88 $\pm$ 29.79
4	10.36	6.97	0.70	6.82	120.33	80.06
	10.52	5.96	0.67	6.33	38.04	72.41
	9.86	7.35	0.76	7.00	85.78	41.24
	10.00	7.39	0.62	6.29	62.14	90.65
	10.11	7.46	0.71	6.90	47.00	45.35
Mean value $\pm$ sd	10.12 $\pm$ 0.28	7.04 $\pm$ 0.72	0.69 $\pm$ 0.05	6.63 $\pm$ 0.37	58.24 $\pm$ 20.88	62.41 $\pm$ 23.35

ANOVA followed by Bonferroni's test. Group 1: baseline; Group 2: control, normal diet; Group 3: calcium-deprived diet for 4 weeks; Group 4: calcium-deprived diet, plus concomitant administration of PTH (1-34) 40  $\mu$ g/kg/day, for 4 weeks.

group did not allow understanding and discussing the data obtained.

In conclusion, the relevance of this paper performed on the rat model lies in the detailed documentation of the fact that the lack of calcium in the diet does not lead to a unique bone answer. It is to be underlined in fact that the various answers recorded in the different sites of bony architectures pertaining to specific skeletal segments are due to the different main involvement of each skeletal region in maintaining mineral or skeletal homeostasis. As a consequence, the bone modeling processes are differently affected in answering induced biochemical osteoporosis. Regardless of the main topic of the present paper, data here reported on PTH (1-34) seems to indicate that Teriparatide, used with good results as therapeutic support in *recovering* bone fragility [39–42], does not display *preventive* effects, since no significant differences were found between the two groups of animals fed calcium-deprived diet with/without the drug administration.

The present investigation based on animal models represents a good starting point for successive studies on bone alterations during unbalanced calcium metabolism, as frequently occurring in aging, with the aim of studying in detail timing and manners of evolution and recovery in human biochemical osteoporosis with/without administration of PTH (1-34). In particular, the attention will be focused on the type of osteogenesis of the newly formed bone during bone mass recovering that, as previously demonstrated [43, 44],

can occur in two different manners (*static* and *dynamic* osteogenesis) and imply different bone quality by the mechanical viewpoint.

## Conflict of Interests

All authors who have taken part in this study have no conflict of interests with respect to the paper.

## Acknowledgments

The authors thank Dr. Paola Sena and Dr. Marta Benincasa for their valuable help in animal treatments and setting iconography, respectively. This study was supported by funds of Eli-Lilly, USA, that also provided PTH (1-34) and funds of "Fondazione di Vignola."

## References

- [1] M. Kleerekoper, A. R. Villanueva, J. Stanciu, D. S. Rao, and A. M. Parfitt, "The role of three-dimensional trabecular microstructure in the pathogenesis of vertebral compression fractures," *Calcified Tissue International*, vol. 37, no. 6, pp. 594–597, 1985.
- [2] S. L. Hui, C. W. Slemenda, and C. C. Johnston Jr., "The contribution of bone loss to postmenopausal osteoporosis," *Osteoporosis International*, vol. 1, no. 1, pp. 30–34, 1990.
- [3] D. B. Kimmel, R. R. Recker, J. C. Gallagher, A. S. Vaswani, and J. F. Aloia, "A comparison of iliac bone histomorphometric data in

- post-menopausal osteoporotic and normal subjects," *Bone and Mineral*, vol. 11, no. 2, pp. 217–235, 1990.
- [4] W. A. Peck, P. Burckhardt, C. Christiansen et al., "Consensus development conference: diagnosis, prophylaxis, and treatment of osteoporosis," *The American Journal of Medicine*, vol. 94, no. 6, pp. 646–650, 1993.
  - [5] R. P. Heaney, "Calcium, dairy products and osteoporosis," *Journal of the American College of Nutrition*, vol. 19, pp. 83S–99S, 2000.
  - [6] R. R. Recker and M. J. Barger-Lux, "The elusive concept of bone quality," *Current Osteoporosis Reports*, vol. 2, no. 3, pp. 97–100, 2004.
  - [7] C. Palumbo, M. Ferretti, L. Bertoni et al., "Influence of ferutinin on bone metabolism in ovariectomized rats. I: role in preventing osteoporosis," *Journal of Bone and Mineral Metabolism*, vol. 27, no. 5, pp. 538–545, 2009.
  - [8] M. Ferretti, L. Bertoni, F. Cavani et al., "Influence of ferutinin on bone metabolism in ovariectomized rats. II: role in recovering osteoporosis," *Journal of Anatomy*, vol. 217, no. 1, pp. 48–56, 2010.
  - [9] T.-H. Kim, J. W. Jung, B. G. Ha et al., "The effects of luteolin on osteoclast differentiation, function in vitro and ovariectomy-induced bone loss," *Journal of Nutritional Biochemistry*, vol. 22, no. 1, pp. 8–15, 2011.
  - [10] F. Cavani, M. Ferretti, G. Carnevale, L. Bertoni, M. Zavatti, and C. Palumbo, "Effects of different doses of ferutinin on bone formation/resorption in ovariectomized rats," *Journal of Bone and Mineral Metabolism*, vol. 30, no. 6, pp. 619–629, 2012.
  - [11] R. R. Recker, K. M. Davies, S. M. Henders, R. P. Heaney, M. R. Stegman, and D. B. Kimmel, "Bone gain in young adult women," *The Journal of the American Medical Association*, vol. 268, no. 17, pp. 2403–2408, 1992.
  - [12] A. E. Broadus, "Physiological functions of calcium, magnesium, and phosphorus and mineral balance," in *Primer on the Metabolic Bone Diseases and Disorders of Mineral Metabolism*, M. J. Favus, Ed., pp. 41–46, Raven Press, New York, NY, USA, 1993.
  - [13] A. Prentice, "Diet, nutrition and the prevention of osteoporosis," *Public Health Nutrition*, vol. 7, no. 1, pp. 227–243, 2004.
  - [14] J. W. Nieves, "Osteoporosis: the role of micronutrients," *The American Journal of Clinical Nutrition*, vol. 81, pp. 1232S–1239S, 2005.
  - [15] B. H. Arjmandi, D. A. Khalil, and B. W. Hollis, "Ipriflavone, a synthetic phytoestrogen, enhances intestinal calcium transport in vitro," *Calcified Tissue International*, vol. 67, no. 3, pp. 225–229, 2000.
  - [16] M. C. Linder, "Nutrition and metabolism of vitamins," in *Nutritional Biochemistry and Metabolism with Clinical Applications*, M. C. Linder, Ed., Elsevier, New York, NY, USA, 2nd edition, 1991.
  - [17] M. Harrison and R. Fraser, "Bone structure and metabolism in calcium-deficient rats," *Journal of Endocrinology*, vol. 21, pp. 197–205, 1960.
  - [18] J. Gershon-Cohen, J. F. McClendon, J. Jowsey, and W. C. Foster, "Osteoporosis produced and cured in rats by low and high calcium diets," *Radiology*, vol. 78, no. 2, pp. 251–252, 1962.
  - [19] C. D. Salomon, "Osteoporosis following calcium deficiency in rats," *Calcified Tissue Research*, vol. 8, no. 1, pp. 320–333, 1971.
  - [20] F. R. de Winter and R. Steendijk, "The effect of a low calcium diet in lactating rats; observations on the rapid development and repair of osteoporosis," *Calcified Tissue International*, vol. 17, no. 4, pp. 303–316, 1975.
  - [21] P. Rasmussen, "Calcium deficiency, pregnancy, and lactation in rats. Some effects on blood chemistry and the skeleton," *Calcified Tissue International*, vol. 23, no. 1, pp. 87–94, 1977.
  - [22] P. Rasmussen, "Calcium deficiency, pregnancy, and lactation in rats. Microscopic and microradiographic observations on bones," *Calcified Tissue International*, vol. 23, no. 1, pp. 95–102, 1977.
  - [23] H. A. Sissons, G. J. Kelman, and G. Marotti, "Mechanisms of bone resorption in calcium-deficient rats," *Calcified Tissue International*, vol. 36, no. 6, pp. 711–721, 1984.
  - [24] H. A. Sissons, G. J. Kelman, and G. Marotti, "Bone resorption in calcium-deficient rats," *Bone*, vol. 6, no. 5, pp. 345–347, 1985.
  - [25] U. Agata, J.-H. Park, S. Hattori et al., "The effect of different amounts of calcium intake on bone metabolism and arterial calcification in ovariectomized rats," *Journal of Nutritional Science and Vitaminology*, vol. 59, no. 1, pp. 29–36, 2013.
  - [26] V. Shen, R. Birchman, R. Xu, R. Lindsay, and D. W. Dempster, "Short-term changes in histomorphometric and biochemical turnover markers and bone mineral density in estrogen and/or dietary calcium-deficient rats," *Bone*, vol. 16, no. 1, pp. 149–156, 1995.
  - [27] R. S. Mazzeo, H. J. Donahue, and S. M. Horvath, "Endurance training and bone loss in calcium-deficient and ovariectomized rats," *Metabolism*, vol. 37, no. 8, pp. 741–744, 1988.
  - [28] H. J. Donahue, R. S. Mazzeo, and S. M. Horvath, "Endurance training and bone loss in calcium-deficient and ovariectomized rats," *Metabolism*, vol. 37, no. 8, pp. 741–744, 1988.
  - [29] T. Hara, T. Sato, M. Oka, S. Mori, and H. Shirai, "Effects of ovariectomy and/or dietary calcium deficiency on bone dynamics in the rat hard palate, mandible and proximal tibia," *Archives of Oral Biology*, vol. 46, no. 5, pp. 443–451, 2001.
  - [30] A. Hodgkinson, J. E. Aaron, A. Horsman, M. S. McLachlan, and B. E. Nrodin, "Effect of oophorectomy and calcium deprivation on bone mass in the rat," *Clinical Science and Molecular Medicine*, vol. 54, no. 4, pp. 439–446, 1978.
  - [31] B. E. C. Nordin, A. Horsman, D. H. Marshall, M. Simpson, and G. M. Waterhouse, "Calcium requirement and calcium therapy," *Clinical Orthopaedics and Related Research*, no. 140, pp. 216–239, 1979.
  - [32] D. N. Kalu, "The ovariectomized rat model of postmenopausal bone loss," *Bone and Mineral*, vol. 15, no. 3, pp. 175–191, 1991.
  - [33] A. M. Parfitt, M. K. Drezner, F. H. Glorieux et al., "Bone histomorphometry: standardization of nomenclature, symbols, and units," *Journal of Bone and Mineral Research*, vol. 2, no. 6, pp. 595–610, 1987.
  - [34] C. A. Peterson, J. A. C. Eurell, and J. W. Erdman Jr., "Alterations in calcium intake on peak bone mass in the female rat," *Journal of Bone and Mineral Research*, vol. 10, no. 1, pp. 81–95, 1995.
  - [35] N. Prabhakara Reddy and M. Lakshmana, "Prevention of bone loss in calcium deficient ovariectomized rats by OST-6, a herbal preparation," *Journal of Ethnopharmacology*, vol. 84, no. 2-3, pp. 259–264, 2003.
  - [36] Y.-H. Shin, D.-C. Cho, S.-H. Yu, K.-T. Kim, H.-J. Cho, and J.-K. Sung, "Histomorphometric analysis of the spine and femur in ovariectomized rats using micro-computed tomographic scan," *Journal of Korean Neurosurgical Society*, vol. 52, no. 1, pp. 1–6, 2012.
  - [37] D. D. Thompson, H. A. Simmons, C. M. Pirie, and H. Z. Ke, "FDA guidelines and animal models for osteoporosis," *Bone*, vol. 17, no. 4, pp. 125S–133S, 1995.

- [38] K. Higdon, A. Scott, M. Tucci et al., "The use of estrogen, DHEA, and diosgenin in a sustained delivery setting as a novel treatment approach for osteoporosis in the ovariectomized adult rat model," *Biomedical Sciences Instrumentation*, vol. 37, pp. 281–286, 2001.
- [39] R. Skripitz, T. T. Andreassen, and P. Aspenberg, "Strong effect of PTH (1–34) on regenerating bone: a time sequence study in rats," *Acta Orthopaedica Scandinavica*, vol. 71, no. 6, pp. 619–624, 2000.
- [40] R. Lindsay, H. Zhou, F. Cosman, J. Nieves, D. W. Dempster, and A. B. Hodsman, "Effects of a one-month treatment with PTH(1–34) on bone formation on cancellous, endocortical, and periosteal surfaces of the human ilium," *Journal of Bone and Mineral Research*, vol. 22, no. 4, pp. 495–502, 2007.
- [41] S. Tanaka, T. Kuroda, T. Sugimoto, T. Nakamura, and M. Shiraki, "Changes in bone mineral density, bone turnover markers, and vertebral fracture risk reduction with once weekly teriparatide," *Current Medical Research and Opinion*, vol. 30, no. 5, pp. 931–936, 2014.
- [42] E. S. Orwoll, W. H. Scheele, S. Paul et al., "The effect of teriparatide [human parathyroid hormone (1–34)] therapy on bone density in men with osteoporosis," *Journal of Bone and Mineral Research*, vol. 18, no. 1, pp. 9–17, 2003.
- [43] M. Ferretti, C. Palumbo, M. Contri, and G. Marotti, "Static and dynamic osteogenesis: two different types of bone formation," *Anatomy and Embryology*, vol. 206, no. 1–2, pp. 21–29, 2002.
- [44] M. Ferretti, C. Palumbo, L. Bertoni, F. Cavani, and G. Marotti, "Does static precede dynamic osteogenesis in endochondral ossification as occurs in intramembranous ossification?" *The Anatomical Record Part A: Discoveries in Molecular, Cellular, and Evolutionary Biology*, vol. 288A, no. 11, pp. 1158–1162, 2006.

## Review Article

# Nonalcoholic Steatohepatitis: A Search for Factual Animal Models

**Sheila Cristina L. Sanches, Leandra Naira Z. Ramalho, Marlei Josiele Augusto, Deisy Mara da Silva, and Fernando Silva Ramalho**

*Department of Pathology, School of Medicine of Ribeirão Preto, University of São Paulo, Avenida Bandeirantes 3900, Monte Alegre, 14049-900 Ribeirão Preto, SP, Brazil*

Correspondence should be addressed to Fernando Silva Ramalho; [framalho@fmrp.usp.br](mailto:framalho@fmrp.usp.br)

Received 26 September 2014; Revised 6 December 2014; Accepted 10 December 2014

Academic Editor: Monica Fedele

Copyright © 2015 Sheila Cristina L. Sanches et al. This is an open access article distributed under the Creative Commons Attribution License, which permits unrestricted use, distribution, and reproduction in any medium, provided the original work is properly cited.

Nonalcoholic fatty liver disease (NAFLD) is characterized by hepatic steatosis, which occurs in the absence of alcohol abuse. NAFLD can evolve into progressive liver injury and fibrosis in the form of nonalcoholic steatohepatitis (NASH). Several animal models have been developed to attempt to represent the morphological, biochemical, and clinical features of human NASH. The actual review presents a critical analysis of the most commonly used experimental models of NAFLD/NASH development. These models can be classified into genetic, nutritional, and a combination of genetic and nutritional factors. The main genetic models are *ob/ob* and *db/db* mutant mice and Zucker rats. The principal nutritional models employ methionine- and choline-deficient, high-fat, high-cholesterol and high-cholelate, cafeteria, and high-fructose diets. Currently, associations between high-fructose and various compositions of high-fat diets have been widely studied. Previous studies have encountered significant difficulties in developing animal models capable of reproducing human NASH. Some models produce consistent morphological findings, but the induction method differs significantly compared with the pathophysiology of human NASH. Other models precisely represent the clinical and etiological contexts of this disease but fail to provide accurate histopathological representations mainly in the progression from steatosis to liver fibrosis.

## 1. Introduction

Nonalcoholic fatty liver disease (NAFLD) is characterized by abnormal lipid accumulation in hepatocytes, which is known as steatosis and occurs in the absence of alcohol abuse. NAFLD is one of the most common forms of liver disease reported in current clinical practice. The prevalence of NAFLD is estimated to reach 30% of adults in developed countries, and greater than 10% of cases evolve into progressive liver injury in the form of nonalcoholic steatohepatitis (NASH) [1]. Because of the high prevalence of NAFLD in the obese population, NAFLD can be considered one of the manifestations of metabolic syndrome including central obesity, type II diabetes mellitus, hypertension, hyperglycemia, and hyperlipidemia [2]. Some factors also contribute directly to the development of NAFLD, such as a sedentary lifestyle and increased consumption of high-fat foods and beverages with high concentrations of fructose [3].

In addition, patients with steatosis, ballooning degeneration, Mallory's hyaline corpuscles, and fibrosis display a higher probability of developing cirrhosis compared with patients exhibiting steatosis alone. Thus, NAFLD includes a wide spectrum of liver abnormalities that may vary from simple steatosis to NASH (Figure 1). In this context, NASH can be identified by the presence of significant fibrosis and necroinflammatory activity in which collagen deposition is manifested as a peculiar perivenular and/or pericellular pattern [4]. Although the majority of patients can be effectively diagnosed with NAFLD using noninvasive tests, liver biopsy remains the gold standard for the accurate assessment of the graduation of steatosis, necroinflammatory changes, and fibrosis and allows NASH and steatosis to be distinguished [5, 6].

A recently developed grading to NASH incorporates the severity of hepatic steatosis, portal and lobular inflammation, and collagen deposition. Like this, the grading of the severity

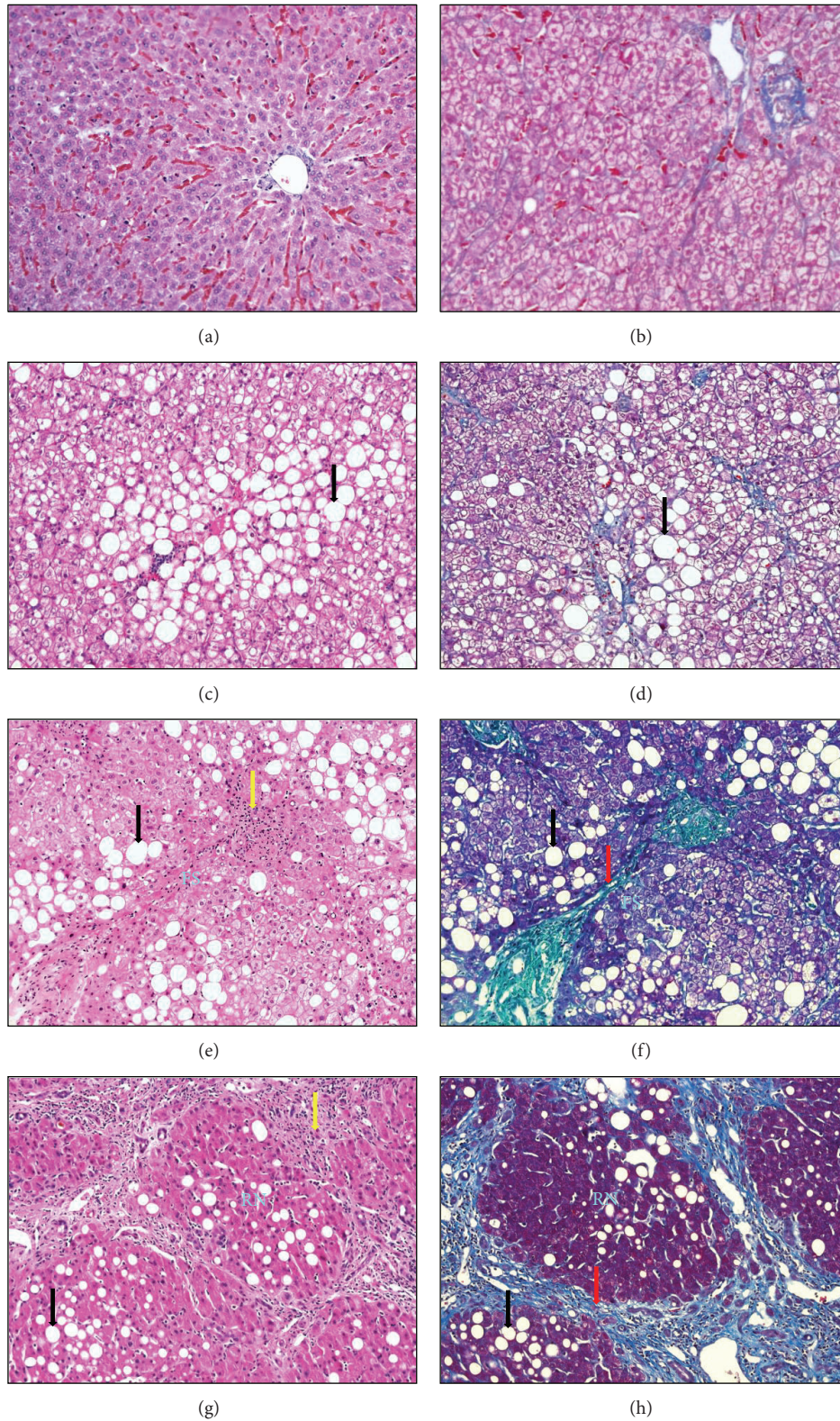


FIGURE 1: The representative photomicrographs present the progression of the histopathological alterations found in the spectrum of nonalcoholic fatty liver disease (NAFLD): (a)/(b) normal liver: no evidence of steatosis, inflammation, or fibrosis; (c)/(d) liver steatosis: moderate steatosis (34–66%), no evidence of inflammation or fibrosis; (d)/(e) nonalcoholic steatohepatitis (NASH): moderate steatosis (34–66%), mild inflammation, and moderate fibrosis with a fibrous septa (FS); (f)/(g) liver cirrhosis secondary to NASH: moderate steatosis (34–66%), moderate inflammation, and severe fibrosis with a regenerative nodule (RN) (Hematoxylin & Eosin and Masson Trichrome staining,  $\times 200$ ). The black, red, and yellow arrows show steatosis, fibrosis, and inflammation, respectively.

of hepatic steatosis varies as follows: grade 0, minimal or no evidence of steatosis (<5% of hepatocytes affected); grade 1, mild steatosis (5 to 32% of hepatocytes affected); grade 2, moderate to severe steatosis (33 to 66% of hepatocytes affected); grade 3, severe steatosis (>66% of hepatocytes affected). The portal and lobular inflammation is also scored as follows: grade 0, minimal or no evidence of inflammation; grade 1, mild inflammation; grade 2, moderate to severe inflammation; grade 3, severe inflammation. The collagen deposition varies as follows: grade 0, minimal or no evidence of fibrosis; grade 1, mild fibrosis; grade 2, moderate to severe fibrosis; grade 3, severe fibrosis [4]. Another similar method for NASH grading is the SAF system, which comprises a semiquantitative score of steatosis (S), inflammatory activity (A), and fibrosis (F) [7].

The mechanisms involving the pathogenesis of NASH are not completely clarified. One of the main hypotheses is “the theory of the two hits.” According to this theory, the “first hit” for NASH establishment is lipid accumulation in hepatocytes, mostly in the form of triglycerides, which results from an imbalance between the metabolic pathways that promote the hepatocyte uptake and synthesis of fatty acids and those that promote oxidation and export of fatty acids. Insulin resistance, found in obesity and type II diabetes, has been considered the most important factor in the development of hepatic steatosis (the “first hit”). Insulin resistance causes peripheral lipolysis and hyperinsulinemia. Lipolysis increases circulating free fatty acids (FFA) and hepatocyte uptake of fatty acids. Hyperinsulinemia intensifies the hepatic synthesis of fatty acids by inducing glycolysis and favors the accumulation of triglycerides within hepatocytes by decreasing the liver ability to reesterify and export triglycerides [8, 9].

In consequence of hepatic steatosis, hepatocytes develop vulnerability to oxidative stress, which may, in large part, be responsible for the progression of NAFLD from simple steatosis to steatosis associated with necroinflammatory activity and fibrosis. Therefore, oxidative stress has been reported as the “second hit.” Mitochondria play a central role in oxidation of fatty acids. Since mitochondrial fatty acid oxidation results in production of free radicals, mitochondria are the major cellular source of reactive oxygen species (ROS), mainly in the form of hydrogen peroxide. Oxidative stress has been described as a disturbance in the equilibrium status of ROS generation and the cellular antioxidant defense system. In hepatic steatosis, the imbalance between scarce endogenous antioxidant reserves and augmented mitochondrial production of free radicals results in oxidative damage to lipids, proteins, and DNA with subsequent cell death [9, 10]. Oxidative stress may trigger steatohepatitis by three main mechanisms: lipid peroxidation, cytokine induction, and induction of Fas ligand. In addition to directly inducing cellular destruction by massive membrane lipoperoxidation, ROS can act as second messengers in the regulation of genes encoding proinflammatory and profibrogenic cytokines such as tumor necrosis factor alpha (TNF- $\alpha$ ), transforming growth factor beta (TGF- $\beta$ ), and interleukin- (IL-) 8. ROS can also induce expression of the Fas ligand in hepatocytes, which normally express the membrane receptor Fas. The Fas ligand on one hepatocyte can interact with Fas on another

hepatocyte resulting in fractional liver cell killing (Figure 2) [8, 9].

Multiple intrinsic mechanisms have been suggested to trigger cell death and progression to NASH. However, diverse evidences show that hepatocellular apoptosis is increased both in animal models [11–13] and in human NASH [14–16]. Therefore, apoptosis has been considered the major mechanism of cell death in the NASH context, stimulating liver inflammation and fibrosis. The steatosis-induced oxidative stress promotes cell death through the activation of stress-related signaling pathways such as c-Jun N-terminal kinase (JNK) or p38 mitogen-activated protein (MAP) kinase. Both JNK and p38 MAP kinase are involved in mechanisms of apoptosis [17, 18]. Moreover, increase of the apoptosis frequency may be considered a profibrogenic event in progression of chronic liver diseases. Indeed, apoptosis fragments and ROS can stimulate Kupffer cells to release proinflammatory and profibrogenic cytokines, which induce activation of hepatic stellate cells. These cells are the major producers of extracellular matrix in the tissue repair reactions in response to chronic hepatic injury [19].

The mechanisms that involve apoptosis in NASH were investigated in rats using a high-fat diet for 12 weeks. The results showed that the index of hepatocellular apoptosis was significantly higher in rats fed with high-fat diet. The authors concluded that the hepatocellular apoptosis in this model was promoted by interacting between cyclooxygenase-2 and proinflammatory cytokines (TNF- $\alpha$  and IL-6) [20]. A recent study showed the contribution of caspase 3 on liver injury and fibrogenesis and supported a prominent role for the caspase 3 activation in the hepatocellular apoptosis and fibrogenesis in NASH secondary to the methionine- and choline-deficient (MCD) diet model [21]. In addition, it was suggested that the high-cholesterol and high-cholesterol (HChCh) diet can induce intense atherogenic stimulus and additionally promote apoptosis through the oxidized low density lipoprotein (oxLDL). The oxLDL presents a proinflammatory and proapoptotic potential and can induce liver fibrosis [22].

Additionally, a new theory known as “lipotoxicity” has been focus of interest. Current evidences suggest that lipotoxicity represents the major mechanism of hepatocyte dysfunction leading to disease progression in NASH. According to this theory, lipotoxic injury occurs in the setting of the excessive traffic of free fat acids, especially saturated fatty acids (SFA), rather than due to simple steatosis. Probably, lipid accumulation occurs in parallel with the generation of lipotoxic metabolites, which are primarily responsible for the progression of liver disease [19, 23]. According to this theory, a high-carbohydrate and high-SFA diet contributes to the excessive circulation of free fat acids and promotes the development of insulin resistance. Moreover, it has been shown that lipotoxicity leads to cell injury and death, via apoptosis or necrosis, and may constitute an important proinflammatory and profibrogenic stimulus in chronic liver disease [19, 24].

Although the pathophysiology and diagnosis of NASH have been thoroughly studied, many investigators are still searching for a specific treatment. Several animal archetypes are indispensable for reproducing reliable models displaying characteristics as similar as possible to human NASH.

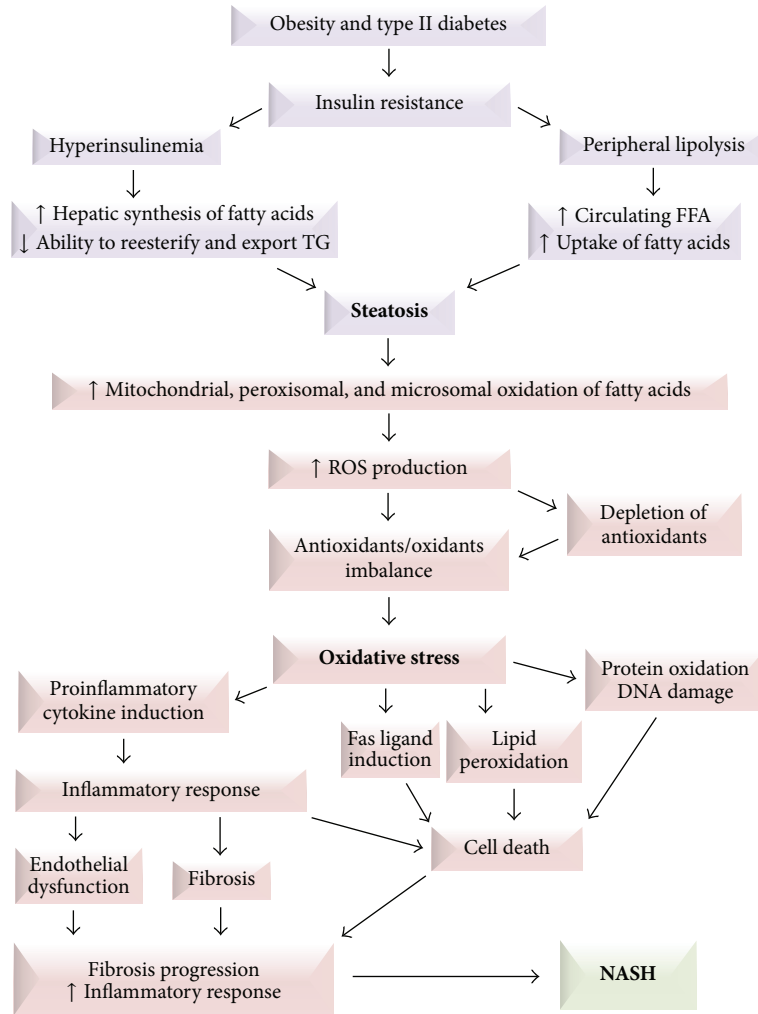


FIGURE 2: The main mechanisms involved in the pathophysiology of the nonalcoholic steatohepatitis (NASH). FFA: free fatty acids; ROS: reactive oxygen species; TG: triglycerides (adapted from Angulo, 2002 [8]).

## 2. An Approach of Actual Experimental Models of NASH

Several animal models have been developed to represent the pathophysiology, morphological findings, biochemical changes, and clinical features of human NASH. Accordingly, the employed animals should present metabolic abnormalities such as obesity, insulin resistance, fasting hyperglycemia, dyslipidemia, and altered adipokine profile. Furthermore, an animal NASH model should display steatosis, intralobular inflammation, hepatocellular ballooning, perisinusoidal fibrosis, and susceptibility to liver tumors. However, the extrapolation of diverse animal models of NAFLD/NASH to the human disease may be limited by the difficulty in reproducing both the clinical and morphological conditions. The current models can be classified into genetic, nutritional, and a combination of genetic and nutritional factors. The following models are the most commonly used animal models of NAFLD/NASH development.

## 3. Genetic Models

To better understand the role of the specific genes involved in fatty liver formation, several studies have attempted to identify the deletion or overexpression of some genes that may be involved in the development of NAFLD/NASH. The genetic alterations can act diversely in various pathways but all culminate with lipid hepatocellular deposits. The main known genetic variation results in increased ingestion of calories, higher hepatic influx of fatty acids, neolipogenesis, and decreased hepatic oxidation of FFA and triglycerides [25]. However, the genetic models almost exclusively induce the biochemical alterations of NAFLD, and the addition of modified diets is frequently required in these models to induce the morphological changes found in human NASH [26].

**3.1. SREBP-1c Transgenic Mice.** In mammals, intracellular levels of cholesterol and fatty acids are controlled through a

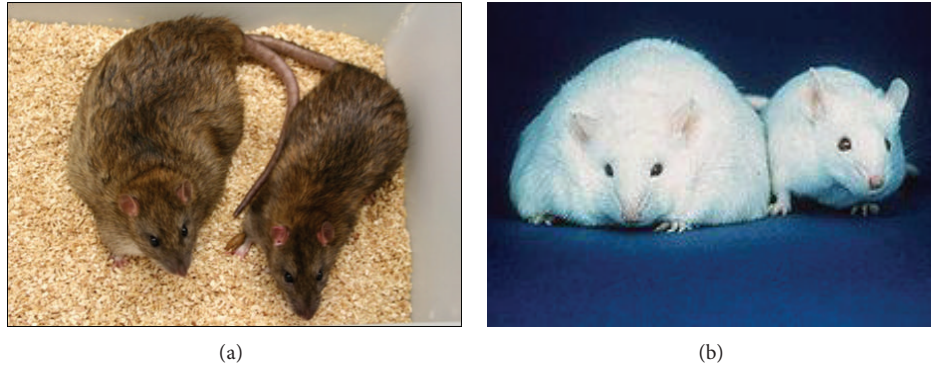


FIGURE 3: Genetic animal models used for the development of NAFLD/NASH: (a) Zucker rats—the recessive (*fa/fa*) genotype develops obesity and liver steatosis (at left side), while the dominant (*lean*) genotype is phenotypically normal (at right side of the picture); (b) *Ob/ob* mice—the mutant obese (*ob/ob*) mouse (at left side) may present threefold higher body weight relative to the wild type mouse (at right side of the picture) (The Jackson Laboratory).

feedback regulatory system mediated by a family of transcription factors called sterol regulatory element-binding proteins (SREBPs). SREBP-1c transgenic mice overexpress the transcription factor SREBP-1c. In this model, the dysregulation of adipocyte differentiation leads to insulin resistance and diabetes. Similar to some forms of congenital lipodystrophies, the amount of systemic fat tissue is decreased, but the animals present significant hepatic lipid accumulation [27]. When SREBP-1c transgenic mice are fed a high-fat diet, pronounced hepatic steatosis can be induced in a few days. A standard diet is sufficient to induce steatosis, lobular and perivenular inflammation, and pericellular fibrosis in these animals after a period of 8 weeks [28, 29]. Therefore, the morphological findings are similar to many of the morphological findings observed in NASH. However, human NAFLD/NASH is frequently associated with metabolic syndrome and increased visceral fat, while this animal model develops lipid deposits exclusively in the liver. Consequently, despite the satisfactory pathological features, this model may differ from the clinical context of human NASH [30].

**3.2. *Ob/ob* Mice.** *Ob/ob* mice exhibit a spontaneous mutation in the leptin gene (leptin deficient). Leptin (from the Greek *leptothos* = thin) is a peptide hormone produced by adipose tissue. When this substance is secreted by adipocytes, it reaches the hypothalamus in the central nervous system and participates in the regulation of feeding behavior and energy bursts. Leptin promotes reduced food intake and increases energy metabolism by affecting the hypothalamic-pituitary axis and regulating neuroendocrine mechanisms. Leptin is also involved in the modulation of fibrogenesis and cell death [31–33].

In the *ob/ob* mice, a mutation in the leptin gene causes leptin deficiency and decreased interaction between leptin and its receptor; therefore, the *ob/ob* mice are hyperphagic, extremely obese, and inactive [26] (Figure 3). In addition, these animals have an altered metabolic profile and exhibit hyperglycemia, insulin resistance, hyperinsulinemia, and spontaneous development of fatty liver [34]. However, the utility of the *ob/ob* mouse model is limited by concerns with

the development of liver fibrosis. In fact, the *ob/ob* mice are protected from fibrosis, and this phenomenon permitted the characterization of leptin as a key mediator of hepatic fibrogenesis. Because the progression to NASH does not occur spontaneously in this model, a secondary stimulus is necessary such as a MCD or high-fat diet or administration of lipopolysaccharide (endotoxin). Using these techniques, leptin-deficient mice can present reduced liver collagen deposits, which impairs the presence of important morphological characteristics of NASH such as fibrosis. Furthermore, mutations in the *ob* gene are not prevalent in obese subjects or patients with NASH, and leptin levels are not well correlated with the development of NAFLD/NASH [30, 35].

**3.3. *Db/db* Mice.** The *db/db* mouse model exhibits a spontaneous mutation in the leptin receptor gene (*Ob-Rb*). Although the *db/db* mice exhibit normal or elevated levels of leptin, they are resistant to the effects of leptin. Thus, the *db/db* animals are obese, present insulin resistance or diabetes, and develop macrovesicular hepatic steatosis. In addition, they may develop NASH after a second stimulus such as the intake of trans-fat or an MCD diet. When *db/db* mice are fed an MCD diet, they can develop significant liver fibrosis in contrast to *ob/ob* mice [36, 37]. The phenotype of the *db/db* mice better simulates the condition of human metabolic syndrome in many circumstances. However, these mice are limited because they do not spontaneously develop liver fibrosis or NASH without a second stimulus [30].

**3.4. Zucker Rats.** One of the most commonly used animal models of NAFLD, genetic obesity, and metabolic syndrome is the genetic model of obese Zucker rats (*fa/fa*). Zucker rats exhibit a spontaneous mutation in the leptin receptor (*fa* allele), which decreases the affinity of this receptor for leptin and changes the transduction signal. Zucker rats are homozygous for the *fa* allele, and heterozygous *fa* rats (*lean*) serve as the control. Zucker rats develop severe obesity and are hyperleptinemic, hyperphagic, inactive, obese, and insulin resistant (hyperinsulinemia, mild hyperglycemia, and hyperlipidemia) (Figure 3). Zucker rat hyperlipidemia is characterized by

increased very low density lipoprotein (VLDL) and high density lipoprotein (HDL) without significant changes in low density lipoprotein (LDL) and reduced expression of the hepatic LDL-receptor [38]. In addition to significantly increased body weight, the Zucker rats depend on the heterozygote controls to reproduce because the metabolic abnormalities are also associated with high infertility rates in these animals [39].

In Zucker model, macro/microvesicular steatosis is diffusely present, mainly in the periportal area. No other sign of progression to NASH is detected. The Zucker rats also display low hepatic GSH and vitamin E levels and decreased catalase activity. As a result of leptin resistance, increased expression of SREBP-1c and carbohydrate response element-binding protein (ChREBP) may also be observed. The increased expression of SREBP-1c mRNA was accompanied by augmented levels of lipogenic enzymes and triglyceride accumulation in the liver [26].

Similar to *ob/ob* and *db/db* mice, Zucker rats do not present spontaneous development of NASH and require a second stimulus to induce the progression from steatosis to NASH. Accordingly, Zucker rats fed with a diet rich in saturated fat (60% of energy supply derived from lard) for 8 weeks developed severe micro/macrovesicular steatosis and progression to steatohepatitis. Liver injury was accompanied by increased levels of alanine aminotransferase (ALT), TNF- $\alpha$  and TGF- $\beta$ , higher collagen deposition, and activation of hepatic stellate cells. Oxidative stress markers such as lipid peroxidation and protein carbonyl groups were increased, while the hepatic levels of reduced glutathione and antioxidant enzymes were diminished [40].

Although Zucker rats partially simulate human metabolic syndrome (obesity, insulin resistance, dyslipidemia, hyperinsulinemia, and liver), this animal model still has some disadvantages. Because leptin or leptin receptor mutations are rare in humans, Zucker rats may not reflect the clinical and pathological circumstances of the development of the NAFLD spectrum observed in humans. Furthermore, Zucker rats do not naturally develop steatohepatitis, are resistant to liver fibrosis, and require additional interventions to induce the progression of steatosis to NASH [26].

#### 4. Nutritional Models

Nutritional models intend to mimic the bad alimentary habits that culminate in obesity and NASH. Some diets may cause consistent liver damage, steatosis, lobular inflammation, ballooning degeneration, and perivenular fibrosis similar to the histopathological findings of human NASH. The metabolic profile may also be changed, resulting in type II diabetes and high levels of triglycerides and cholesterol similar to the clinical characteristics observed in human NAFLD/NASH [26].

The mouse strain C57/BL6 is capable of simulating some human metabolic diseases and lipid disorders when submitted to different experimental models [41]. Similar to humans, adult C57/BL6 mice have a strong genetic tendency to develop obesity, hyperinsulinemia, and glucose intolerance, independently of the offered diet. This phenomenon may be

further accentuated with the administration of a high-fat diet, which may result in obesity, insulin resistance, and steatosis similar to humans [32].

**4.1. Methionine- and Choline-Deficient Diet.** The MCD model is based on deficiency of methionine and choline, which are essential for liver  $\beta$ -oxidation and the production of VLDL. In addition to the methionine and choline deficiency, this diet contains a high quantity of sucrose (10% fat, 40% sucrose). The main results of the MCD diet are hepatocyte lipid accumulation and decreased synthesis of VLDL. Rats fed the MCD diet present weight loss (up to 40% at 10 weeks) and subsequent development of intense pericentral steatosis accompanied by necrosis and inflammation. The weight loss is based on reduction of corporal fat with a proportional decrease in liver size [32].

Mice fed the MCD diet also exhibit increased inflammatory responses through activation of liver macrophages due to the transcriptional factor nuclear factor kappa B (NF- $\kappa$ B), which is an important modulator of inflammatory and cell survival responses. In addition to NF- $\kappa$ B activation, concomitant augmentations in TNF- $\alpha$ , IL-6, and TGF- $\beta$  levels are also observed [42]. The MCD diet also promotes higher expression of the intercellular adhesion-1 molecule (ICAM-1), vascular cell adhesion molecule-1 (VCAM-1), and macrophage chemotactic protein-1 (MCP-1), which results in increased activity, migration, adhesion, and accumulation of neutrophils and macrophages in the liver [43]. Although these proinflammatory mechanisms are similar to human NASH, and the MCD diet promotes real liver damage, the triglyceride and cholesterol levels are also reduced in contrast with obese patients with NAFLD/NASH. Other discrepancies in the metabolic profile of the MCD diet are reduced levels of insulin, glucose, and leptin, which are opposite to the effects of human NASH [44, 45]. Because the MCD diet is deficient in nutrients, it is not an ideal representative model of human NASH because the intrinsic nutritional factors observed in the human diet are not represented in the MCD diet.

**4.2. High-Fat Diet.** Because of the strong links between NAFLD and metabolic syndrome, animals have also been submitted to the "Western-style diet" model, which aims to induce obesity, insulin resistance, and liver damage. In these models, the animals are fed a high-fat diet in which 45–75% of the caloric intake is derived from fat and/or variations containing trans-fat or cholesterol. In the majority of the high-fat diet models, the degree of liver injury is not severe compared with the MCD model. However, the high-fat diet can represent the detrimental eating habits of the Western diet and mimic the etiology of NAFLD/NASH [25, 46].

A classic example of a high-fat diet model proposed by Lieber et al. (2004) is based on a liquid diet containing fat (71%), carbohydrates (11%), and protein (18%). The animals fed this diet presented biochemical alterations similar to the profile of NASH in humans. The rats also developed increased insulin levels, insulin resistance, hepatocellular lipid accumulation, oxidative stress, and TNF- $\alpha$  levels. However, the hepatic histopathology results displayed discrete signs of

inflammation, mild steatosis, and the absence of the fibrosis progression in contrast with human NASH [47].

Other studies have intended to optimize the development of NASH through punctual modifications in the high-fat diet, such as enrichment with lard and cholesterol in a diet fed to Sprague-Dawley rats at 4, 8, 12, 24, 36, and 48 weeks. In this case, the liver weight increased at week 4, and hepatic steatosis was also observed. After week 8, the body weight started to increase. This finding was accompanied by augmented serum levels of FFA, cholesterol, and TNF- $\alpha$ . The serum ALT levels increased at week 12, and steatosis and inflammation occurred from weeks 12 through 48. Apparent hepatic perisinusoidal fibrosis did not occur until week 24, but collagen deposits were evident from weeks 36 to 48. This novel model may be potentially useful as a NASH model, although the main findings occurred only after week 24 [48].

Because of the presence of increased levels of ALT and triglycerides, liver neutrophil infiltration, and focal hepatocellular necrosis and apoptosis, high-fat diets are considered one of the best models to study the progression of steatosis to NASH. However, these models are limited because not all of the histopathological findings are consistent with those observed in human NASH, which is mainly due to the lack of progressive fibrosis. Furthermore, it takes a long time for the symptoms of the high-fat diet to significantly develop [25, 49].

Other techniques have been implemented to identify more severe histopathological alterations. In a study using C57/BL6 mice, an intragastric cannula was implanted to improve the intake of high-fat diets. In this model, an emulsion containing 37% of calories from fat (corn oil) and 39% of calories from dextrose was administered directly into the stomach. The treated mice developed hyperglycemia, hyperinsulinemia, hyperleptinemia, glucose intolerance, and insulin resistance. The mice also became obese with increased hepatic levels of fat. However, the histopathological analysis showed the development of mild hepatic steatosis [50]. In a study performed with Wistar rats using the same model of intragastric cannulation but with the administration of a trans-fat diet, the histopathological findings were more characteristic of the morphology found in human NASH [51].

Although this model can reproduce the histopathological pattern of NASH in humans, it failed to mimic the clinical and etiologic aspects because the administration of the diet to the animals was forced.

#### 4.3. Atherogenic (High-Cholesterol and High-Cholate) Diet.

Insulin resistance is a key event in the pathophysiological development of metabolic syndrome. Insulin resistance is associated with increased triglyceride and cholesterol levels and increased risk of cardiovascular disease. In some animal models, a relative insulin receptor insufficiency accompanied by increased plasma triglyceride concentrations during the development of obesity was observed, which is similar to the pathogenesis of insulin resistance in humans. Insulin resistant animals also exhibited an increased propensity to develop NAFLD/NASH [52, 53]. Based on these findings, other studies proposed new animal models fed an atherogenic diet with high levels of cholesterol and cholate, which could both lead to atherosclerosis and NASH. A mouse model

showed that a high-cholesterol and high-cholate (HChCh) diet can induce varied degrees of liver inflammation and augmented collagen gene expression. The HChCh diet also stimulates the liver to produce TNF- $\alpha$ , which increases the inflammatory response and causes the progression of NASH [54].

Mice fed the HChCh diet presented progressive formation of hepatic steatosis, inflammation, and fibrosis after 6–24 weeks. The addition of 60% fat from cocoa butter in the HChCh diet accelerated the development of these histopathological alterations within 12 weeks. Furthermore, the fat-enriched HChCh diet induced higher oxidative stress and consequent increases in the activation of hepatic stellate cells and the expression of  $\alpha$ -smooth muscle actin. These data suggest that the supplementation of HChCh diet with high-fat levels can cause hepatic morphological alterations of human NASH. However, metabolic status analysis of HChCh diet-fed animals showed an attenuation of the insulin resistance factors. In fact, during the course of the experiment, the animals lost 9% body weight, and the triglyceride levels were lower compared with the controls [25, 55].

Thus, although the HChCh diet enriched with fat can imitate the progression of human NASH, the metabolic profile showed important differences. Therefore, further studies are needed to assess whether changes in fat composition or addition of other dietary factors can improve the biochemical results of this model to increase its similarities to human NASH.

**4.4. Cafeteria Diet.** The incidence of metabolic syndrome, which is characterized by a combination of systemic dysfunctions including glucose intolerance, central obesity, dyslipidemia, and hypertension, has stimulated the development of new diet models mimicking the eating habits of the so-called modern Western diet. The aim of the cafeteria diet, also known as the Western diet, consists of industrially processed palatable foods containing high levels of fat, sugar, and salt. Therefore, this diet provides a robust model of human metabolic syndrome compared with the traditional high-fat diets and causes a phenotype of exaggerated obesity with glucose intolerance and inflammation [56]. However, this model presents some controversial results.

Young rats that received the cafeteria diet for 8 weeks developed metabolic syndrome along with obesity, higher hepatic weight, increased plasma levels of glucose, insulin and triglycerides, and insulin resistance [57]. In another study, hamsters fed the cafeteria diet for 15 weeks displayed significantly increased body weight and higher levels of plasma triglycerides, LDL-cholesterol, and glucose. Administration of the cafeteria diet resulted in a 35% decrease in adiponectinemia and insulinemia, augmented leptinemia, and increased homeostatic model assessment-insulin resistance (HOMA-IR). Although this diet induced insulin resistance and increased liver oxidative stress, proinflammatory mediators such as TNF- $\alpha$ , IL-6, and NF- $\kappa$ B were not enhanced [58]. In accordance with these studies, the cafeteria diet is primarily a model of human metabolic syndrome.

Another study developed a variation of the cafeteria diet containing 65% fat (mostly saturated fat) administered to

Wistar rats for 1 month. The animals presented consistent features of metabolic syndrome such as overweight, arterial hypertension, hypertriglyceridemia, hyperglycemia, insulin resistance, and liver steatosis but did not present significant liver inflammation or fibrosis [59]. In addition, Wistar rats fed standard chow with concurrently offered cafeteria food (cookies, cereals, cheese, processed meats, crackers, etc.) *ad libitum* for 15 weeks developed hyperphagia, resulting in severe obesity and prediabetes (glucose intolerance and hyperinsulinemia). This diet induced panlobular microvesicular steatosis, steatohepatitis, and chronic inflammation in white and brown adipose tissues [56]. Thus, according to these authors, this model closely reflects the etiopathogenesis of human NAFLD, although no study has demonstrated the presence of liver fibrosis.

**4.5. Fructose.** In humans, increased levels of fructose consumption, primarily in the form of corn syrup for soft drinks, are associated with increased severity of hepatic steatosis and fibrosis [60, 61]. Fructose, a monosaccharide primarily metabolized in the liver, controls the activity of glucokinase, which is the principle enzyme involved in hepatic glucose metabolism. Fructose is a potent and acute regulator of liver glucose uptake and glycogen synthesis. By interfering with glucose metabolism, the excessive fructose intake leads to postprandial hypertriglyceridemia, which increases visceral adipose deposition. Visceral adiposity contributes to hepatic triglyceride accumulation and insulin resistance by increasing the portal delivery of FFA to the liver [62–64].

Some animal and human studies show increased levels of triglycerides after ingestion of diets with fructose compared with diets containing complex carbohydrates or other sugars. This effect occurs due to increased lipogenesis in the detriment of gluconeogenesis, which results in increased hepatic synthesis of fatty acids and glycerol. The higher activity of lipogenic enzymes in the liver results in augmented levels of plasma total lipids and VLDL [63].

Mice submitted to an addition of 30% fructose in drinking water presented a fourfold increase in triglyceride levels and a marked increase in body weight along with steatosis after 8 weeks of ingestion [65]. No published data on animals demonstrated that administration of fructose alone can alter the metabolic parameters associated with NASH, but fructose has been reported to alter potent biochemical properties involved in promoting insulin resistance [66].

**4.6. Association of Fructose with Other Nutritional Models.** Dietary intervention using atherogenic or high-fat diets in addition to fructose represents a promising animal model for the induction of NASH with important similarities to the human disease.

Recently, a model diet was developed based on nutritional simulation of commonly consumed fast foods. In addition, the animals were maintained in conditions designed to promote sedentary behavior. These experimental circumstances are similar to those found in the majority of obesity patients in the Western culture. This archetype was termed the American lifestyle-induced obesity syndrome (ALIOS) model. The C57BL/6 mice were fed a high-fat diet containing

trans-fats (partially hydrogenated vegetable oil) and significant amounts of fructose in corn syrup for 1 to 16 weeks. These animals presented obesity, hyperinsulinemia, and insulin resistance. The addition of high amounts of fructose in the diet increased the food intake and contributed to impaired insulin sensitivity. Moreover, the use of trans-fats induced hepatic lipid deposition and contributed substantially to hepatocellular injury. Although the ALIOS model led to severe steatosis, liver fibrosis was scarce [67].

Another study with mice showed that the administration of high-fat foods and high-fructose/sucrose liquids leads to a synergistic effect that may induce liver inflammation and fibrogenesis. Furthermore, the ingestion of sucrose along with fructose most likely accelerated the occurrence of hepatic macrovesicular steatosis and NASH [63].

Another type of combination diet is a high-fat, high-carbohydrate diet using medium-chain trans-fatty acids as high-fat component, and fructose and sucrose (55% and 45%, resp.) as high-carbohydrate nutrients. This diet caused a significant increase in hepatic triglyceride content, plasma ALT, and liver weight in mice after 16 weeks. Hepatic fibrosis, oxidative stress, hepatic collagen1 mRNA, and plasma cholesterol levels were also significantly increased. Mice fed a high-fat, high-carbohydrate diet can develop obesity and hepatic fibrosis. Moreover, these animals displayed a NASH-like phenotype and an important increase in hepatic ROS similar to human NASH [68].

In addition, the offering of a high-fat diet accompanied with fructose syrup for male and female mice resulted in some alterations of NAFLD/NASH after 16 weeks. These animals presented augmented ALT, triglycerides, IL-1 $\beta$  and TNF- $\alpha$  levels and insulin resistance and the histological alterations of NASH such as collagen deposition, macro/microvesicular steatosis, and liver fibrosis. Although these findings are consistent with NASH, in the female mice, hepatic inflammation and fibrosis were insipient [69].

The metabolic and histological effects of a diet based in the “fast food” composition were also evaluated. Mice were fed for 25 weeks with a “fast food” diet composed by 40% energy as fat (12% SFA, 2% cholesterol) or a high-fat diet composed by 60% energy as fat (1% SFA). Both diets were supplemented with high amounts of fructose. The high-fat diet resulted in obesity, insulin resistance, and steatosis, but inflammation was minimal, and there was not liver fibrosis. However, in mice fed the “fast food” diet, obesity and insulin resistance were also observed, but the liver histology showed steatohepatitis with pronounced hepatocellular ballooning and progressive fibrosis. The “fast food” diet also induced a gene expression associated with increased fibrosis, inflammation, endoplasmic reticulum stress, and lipoapoptosis. Thus, a “fast food”-based diet, composed by high saturated fat, high-cholesterol, and high-fructose, may simulate with elevated fidelity the features of the human metabolic syndrome and NASH [70].

## 5. Rabbit Models

Rabbits have also been utilized to the development of NASH. Rats have a very short prepubertal stage and they come into

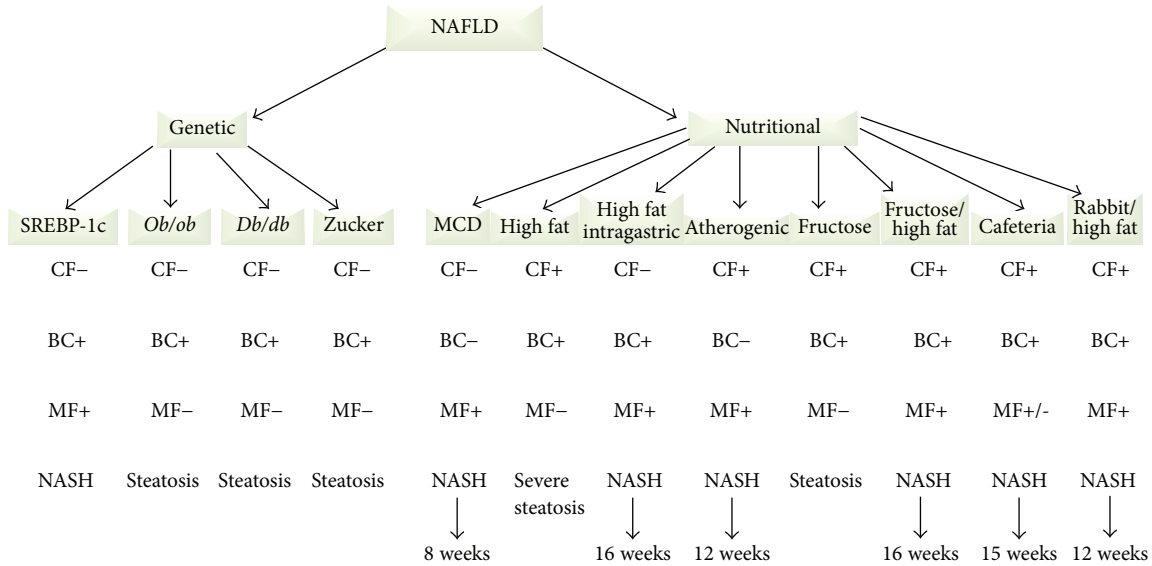


FIGURE 4: Comparison between the genetic (SREBP-1c, *Ob/ob*, *Db/db*, and Zucker) and nutritional (MCD, high-fat, high-fat intragastric, atherogenic, fructose, fructose/others, cafeteria, and rabbit high-fat diets) animal models concerning to the main clinical features (CF), biochemical changes (BC), morphological findings (MF), and the occurrence of liver steatosis or NASH.

the adulthood in only one month. Therefore, rats are not the ideal animals to reflect the physiopathological state of the majority of children diseases. On the other hand, rabbits present around of 8 months of prepubertal stage and seem to be the factual animals for mimicking pediatric NASH. In this manner, it was created as a model to simulate pediatric NASH wherein young rabbits (4–6 weeks old) were fed with a high-fat diet (standard diet + 10% lard + 2% cholesterol) for 12 weeks. In this study occurred a generation of typical hepatic alterations of NASH, as liver steatosis, hepatocellular ballooning, severe portal inflammation (a major characteristic of pediatric NASH), perisinusoidal fibrosis, besides weight gain, augmented liver weight and higher levels of proinflammatory cytokines (TNF- $\alpha$  and IL-6), thereby producing the key features of pediatric NASH [71].

Another rabbit model was employed to simulate the human NASH. In this study, the animals were fed during 9 months with a diet supplemented with 0.75% cholesterol and 12% corn oil. After this long experimental period, the rabbits displayed increased serum and hepatic levels of total cholesterol. The livers presented a whitish and nodular aspect. In addition, hepatic gene expression for proinflammatory cytokines (TNF- $\alpha$ , IL-1 $\beta$ , IL-10, and IL-18) was significantly augmented. It was also observed significant increase of mRNA levels for TGF- $\beta$  and collagen as well as advanced septal fibrosis. Moreover, the analysis of hepatic proteins and gene expression revealed an imbalance between antioxidant protection system and oxidative stress. Thus, this study showed a NASH model that features advanced fibrosis and may be useful for analyzing the molecular mechanisms of human NASH [72].

In another study, rabbits were fed with a high-fat diet supplemented with 20% corn oil and 1.25% (w/w) cholesterol for 8 weeks. In this model, the liver iron deposition derived from

the augmented erythrocyte phagocytosis induced insulin resistance, hepatic lipid accumulation, Kupffer cell activation, mild fibrosis, and increased oxidative stress. These results revealed molecular mechanisms similar to those involved in the pathogenesis of human NASH [73].

## 6. NAFLD/NASH Models: A Schematic Summary

Figure 4 intends to schematically present an analysis of the main morphological findings (MF), biochemical changes (BC), and clinical features (CF) found in the different animal models of NAFLD/NASH.

The SREBP-1c mutant mice fed a standard diet exhibited steatosis, liver inflammation, and fibrosis, which includes many of the morphological findings observed in NASH (MF+). Similar to humans, these animals develop insulin resistance and diabetes (BC+). Human NASH is frequently associated with increased visceral fat, and these animals present an exclusive lipid deposit in the liver. Because this mouse models included a genetic modification, the clinical features differ from the human conditions (CF-). Therefore, this model is incomplete if the full context of human NASH needs to be considered.

The *ob/ob* and *db/db* mutant mice are also genetic models. Although these mice were extremely obese and inactive, their clinical features are incompatible with the features of human disease because the etiology of NAFLD/NASH is not genetic in the vast majority of the cases (CF-). These animals have an altered metabolic profile, exhibiting hyperglycemia, insulin resistance, and hyperinsulinemia (BC+). Although these animals spontaneously develop steatosis, progression to NASH does not occur without additional secondary stimuli mainly using special diets (MF-).

Zucker rats are a genetic model of obesity and metabolic syndrome. Because leptin or leptin receptor mutations are rare in humans, Zucker rats do not reflect the clinical conditions of NASH observed in humans (CF<sup>-</sup>). These rats partially simulate human metabolic syndrome (obesity, insulin resistance, dyslipidemia, and hyperinsulinemia) (BC<sup>+</sup>). Zucker rats have been one of the most commonly used models of NAFLD and present diffuse steatosis mainly in the periportal area. However, a second stimulus is required to induce the progression of steatosis to NASH (MF<sup>-</sup>).

The MCD diet model results in many histological abnormalities that are similar to human NASH (MF<sup>+</sup>), but this model is not associated with insulin resistance or other biochemical alterations (BC<sup>-</sup>). MCD diet-treated rodents typically present decreased body weight. Furthermore, this model does not reflect human dietary habits (CF<sup>-</sup>).

The high-fat diet represents a realistic example of the modern Western lifestyle, and rodents treated with this diet frequently become obese (CF<sup>+</sup>). Although these animals show insulin resistance and increased triglycerides and VLDL levels resembling the profile of human NASH (BC<sup>+</sup>), the histopathological findings display steatosis without liver fibrosis (MF<sup>-</sup>). Thus, this model fails to simulate the progression to NASH.

The high-fat diet with intragastric cannula model leads to hyperglycemia, hyperinsulinemia, hyperleptinemia, and insulin resistance (BC<sup>+</sup>). The histological alterations show severe steatosis with progression to fibrosis (MF<sup>+</sup>) similar to human NASH. However, this model does not mimic the clinical and etiologic factors of NAFLD/NASH because the diet is forcibly administered (CF<sup>-</sup>).

The atherogenic diet, which includes high levels of cholesterol and cholate, accurately simulates the etiologic and clinical factors observed in human NASH (CF<sup>+</sup>). The rodents fed this diet present progressive hepatic steatosis, inflammation, and fibrosis after 12–24 weeks of induction, which replicate the histopathological findings of human NASH (MF<sup>+</sup>). However, the metabolic status is not consistent with human NASH because of the presence of insulin resistance attenuation, decreased body weight, and lower triglyceride levels (BC<sup>-</sup>).

The cafeteria diet exhibits high similarity with human dietary habits, and rodents fed this diet exhibit obesity, higher visceral adiposity, and augmented liver weight (CF<sup>+</sup>). In addition, insulin resistance and increased plasma levels of glucose, insulin, and triglycerides resemble human NASH (BC<sup>+</sup>). However, the histopathological findings may display steatosis with or without inflammation, but there is no liver fibrosis. As a consequence, this model simulates partially the progression to NASH (MF<sup>+/-</sup>).

In the fructose diet models, clinical features can simulate the etiology of human NASH (CF<sup>+</sup>). Some studies show increased triglyceride levels, with potential induction of insulin resistance (BC<sup>+</sup>). However, no published animal data demonstrated that administration of fructose alone can alter the morphological findings and progression to NASH (MF<sup>-</sup>).

Nutritional models using combinations of high-fructose and other high-fat diets cause clinical and etiology characteristics similar to human NASH (CF<sup>+</sup>). Biochemical parameters such as insulin resistance and augmented triglycerides

levels were also observed (BC<sup>+</sup>). The histopathological findings, such as severe steatosis, inflammation, and progression of hepatic fibrosis, were also observed after 16 weeks of diet administration (MF<sup>+</sup>).

Nutritional models applied in rabbits are associated with the etiologic characteristics that are similar to human NASH (CF<sup>+</sup>), once the animals had been fed with a high-fat diet. Biochemical parameters such as increased serum levels of total cholesterol and triglyceride were also observed (BC<sup>+</sup>). The histopathological findings as severe steatosis, inflammatory infiltration, hepatocellular ballooning, severe portal inflammation, and septal fibrosis were also found after 16 weeks of diet administration (MF<sup>+</sup>).

## 7. Conclusion

The presentation of the genetic and nutritional models and combinations of these models confirms the difficulties in identifying an accurate model of human NASH in rodents. Some models produce consistent morphological findings, but their induction differs significantly from the pathophysiology of human NASH. Other models accurately represent the clinical and etiologic contexts of this disease but do not simulate the histopathological observations involving the progression from simple steatosis to liver fibrosis. Few rodent models produce effects that simulate human NASH, but these effects may occur after a long time. Rabbit models can produce consistent morphological findings, with characteristics very similar to the pathophysiology of human NASH, including advanced fibrosis.

## Conflict of Interests

The authors declare that there is no conflict of interests regarding the publication of this paper.

## Acknowledgments

This research was supported by CNPq (fellowship to Sheila C. Sanches no. 160028/2012-4), CAPES-PROAP, and FAEPA.

## References

- [1] M. Basaranoglu, S. Kayacetin, N. Yilmaz, E. Kayacetin, O. Tarcin, and A. Sonsuz, "Understanding mechanisms of the pathogenesis of nonalcoholic fatty liver disease," *World Journal of Gastroenterology*, vol. 16, no. 18, pp. 2223–2226, 2010.
- [2] E. Bugianesi, "Review article: steatosis, the metabolic syndrome and cancer," *Alimentary Pharmacology and Therapeutics, Supplement*, vol. 22, no. 2, pp. 40–43, 2005.
- [3] V. L. Misra, M. Khashab, and N. Chalasani, "Nonalcoholic fatty liver disease and cardiovascular risk," *Current Gastroenterology Reports*, vol. 11, no. 1, pp. 50–55, 2009.
- [4] E. M. Brunt, D. E. Kleiner, C. Behling et al., "Misuse of scoring systems," *Hepatology*, vol. 54, no. 1, pp. 369–370, 2011.
- [5] A. Wieckowska and A. E. Feldstein, "Diagnosis of nonalcoholic fatty liver disease: Invasive versus noninvasive," *Seminars in Liver Disease*, vol. 28, no. 4, pp. 386–395, 2008.

- [6] J. K. Dyson, Q. M. Anstee, and S. McPherson, "Non-alcoholic fatty liver disease: a practical approach to diagnosis and staging," *Frontline Gastroenterology*, vol. 5, no. 3, pp. 211–218, 2014.
- [7] P. Bedossa, C. Poitou, N. Veyrie et al., "Histopathological algorithm and scoring system for evaluation of liver lesions in morbidly obese patients," *Hepatology*, vol. 56, no. 5, pp. 1751–1759, 2012.
- [8] P. Angulo, "Nonalcoholic fatty liver disease," *The New England Journal of Medicine*, vol. 346, no. 16, pp. 1221–1231, 2002.
- [9] K. Mehta, D. H. van Thiel, N. Shah, and S. Mobarhan, "Nonalcoholic fatty liver disease: pathogenesis and the role of antioxidants," *Nutrition Reviews*, vol. 60, no. 9, pp. 289–293, 2002.
- [10] A. P. Rolo, J. S. Teodoro, and C. M. Palmeira, "Role of oxidative stress in the pathogenesis of nonalcoholic steatohepatitis," *Free Radical Biology & Medicine*, vol. 52, no. 1, pp. 59–69, 2012.
- [11] A. Rashid, T.-C. Wu, C.-C. Huang et al., "Mitochondrial proteins that regulate apoptosis and necrosis are induced in mouse fatty liver," *Hepatology*, vol. 29, no. 4, pp. 1131–1138, 1999.
- [12] R. P. Witek, W. C. Stone, F. G. Karaca et al., "Pan-caspase inhibitor VX-166 reduces fibrosis in an animal model of nonalcoholic steatohepatitis," *Hepatology*, vol. 50, no. 5, pp. 1421–1430, 2009.
- [13] G. C. Farrell, C. Z. Larter, J. Y. Hou et al., "Apoptosis in experimental NASH is associated with p53 activation and TRAIL receptor expression," *Journal of Gastroenterology and Hepatology*, vol. 24, no. 3, pp. 443–452, 2009.
- [14] A. E. Feldstein, A. Canbay, P. Angulo et al., "Hepatocyte apoptosis and Fas expression are prominent features of human nonalcoholic steatohepatitis," *Gastroenterology*, vol. 125, no. 2, pp. 437–443, 2003.
- [15] P. S. Ribeiro, H. Cortez-Pinto, S. Solá et al., "Hepatocyte apoptosis, expression of death receptors, and activation of NF- $\kappa$ B in the liver of nonalcoholic and alcoholic steatohepatitis patients," *American Journal of Gastroenterology*, vol. 99, no. 9, pp. 1708–1717, 2004.
- [16] R. M. Ramalho, H. Cortez-Pinto, R. E. Castro et al., "Apoptosis and Bcl-2 expression in the livers of patients with steatohepatitis," *European Journal of Gastroenterology and Hepatology*, vol. 18, no. 1, pp. 21–29, 2006.
- [17] M. V. MacHado and H. Cortez-Pinto, "Cell death and nonalcoholic steatohepatitis: where is ballooning relevant?" *Expert Review of Gastroenterology and Hepatology*, vol. 5, no. 2, pp. 213–222, 2011.
- [18] T. Luedde, N. Kaplowitz, and R. F. Schwabe, "Cell death and cell death responses in liver disease: mechanisms and clinical relevance," *Gastroenterology*, vol. 147, no. 4, pp. 765–783, 2014.
- [19] W. Peverill, L. W. Powell, and R. Skoien, "Evolving concepts in the pathogenesis of NASH: beyond steatosis and inflammation," *International Journal of Molecular Sciences*, vol. 15, no. 5, pp. 8591–8638, 2014.
- [20] Q. Cheng, N. Li, M. Chen et al., "Cyclooxygenase-2 promotes hepatocellular apoptosis by interacting with TNF- $\alpha$  and IL-6 in the pathogenesis of nonalcoholic steatohepatitis in rats," *Digestive Diseases and Sciences*, vol. 58, no. 10, pp. 2895–2902, 2013.
- [21] S. Thapaliya, A. Wree, D. Povero et al., "Caspase 3 inactivation protects against hepatic cell death and ameliorates fibrogenesis in a diet-induced NASH model," *Digestive Diseases and Sciences*, vol. 59, no. 6, pp. 1197–1206, 2014.
- [22] M. Rizzo, G. Montalto, and M. Vinciguerra, "Exploring lipid-related treatment options for the treatment of NASH," *Current Vascular Pharmacology*, vol. 12, no. 5, pp. 741–744, 2014.
- [23] B. A. Neuschwander-Tetri, "Hepatic lipotoxicity and the pathogenesis of nonalcoholic steatohepatitis: the central role of nontriglyceride fatty acid metabolites," *Hepatology*, vol. 52, no. 2, pp. 774–788, 2010.
- [24] N. Anderson and J. Borlak, "Molecular mechanisms and therapeutic targets in steatosis and steatohepatitis," *Pharmacological Reviews*, vol. 60, no. 3, pp. 311–357, 2008.
- [25] L. Hebbard and J. George, "Animal models of nonalcoholic fatty liver disease," *Nature Reviews Gastroenterology and Hepatology*, vol. 8, no. 1, pp. 34–44, 2011.
- [26] O. Kucera and Z. Cervinkova, "Experimental models of non-alcoholic fatty liver disease in rats," *World Journal of Gastroenterology*, vol. 20, no. 26, pp. 8364–8376, 2014.
- [27] I. Shimomura, R. E. Hammer, J. A. Richardson et al., "Insulin resistance and diabetes mellitus in transgenic mice expressing nuclear SREBP-1c in adipose tissue: model for congenital generalized lipodystrophy," *Genes & Development*, vol. 12, no. 20, pp. 3182–3194, 1998.
- [28] M. S. Strable and J. M. Ntambi, "Genetic control of de novo lipogenesis: role in diet-induced obesity," *Critical Reviews in Biochemistry and Molecular Biology*, vol. 45, no. 3, pp. 199–214, 2010.
- [29] H. Nakayama, S. Otabe, T. Ueno et al., "Transgenic mice expressing nuclear sterol regulatory element-binding protein 1c in adipose tissue exhibit liver histology similar to nonalcoholic steatohepatitis," *Metabolism: Clinical and Experimental*, vol. 56, no. 4, pp. 470–475, 2007.
- [30] Y. Takahashi, Y. Soejima, and T. Fukusato, "Animal models of nonalcoholic fatty liver disease/nonalcoholic steatohepatitis," *World Journal of Gastroenterology*, vol. 18, no. 19, pp. 2300–2308, 2012.
- [31] R. S. Ahima and J. S. Flier, "Leptin," *Annual Review of Physiology*, vol. 62, pp. 413–437, 2000.
- [32] Q. M. Anstee and R. D. Goldin, "Mouse models in non-alcoholic fatty liver disease and steatohepatitis research," *International Journal of Experimental Pathology*, vol. 87, no. 1, pp. 1–16, 2006.
- [33] A. Qamar, S. Z. Sheikh, A. Masud et al., "In vitro and in vivo protection of stellate cells from apoptosis by leptin," *Digestive Diseases and Sciences*, vol. 51, no. 10, pp. 1697–1705, 2006.
- [34] A. M. Diehl, "Lessons from animal models of NASH," *Hepatology Research*, vol. 33, no. 2, pp. 138–144, 2005.
- [35] A. E. Brix, A. Elgavish, T. R. Nagy, B. A. Gower, W. J. Rhead, and P. A. Wood, "Evaluation of liver fatty acid oxidation in the leptin-deficient obese mouse," *Molecular Genetics and Metabolism*, vol. 75, no. 3, pp. 219–226, 2002.
- [36] M. Wortham, L. He, M. Gyamfi, B. L. Copple, and Y.-J. Y. Wan, "The transition from fatty liver to NASH associates with SAMe depletion in db/db mice fed a methionine choline-deficient diet," *Digestive Diseases and Sciences*, vol. 53, no. 10, pp. 2761–2774, 2008.
- [37] A. Sahai, P. Malladi, X. Pan et al., "Obese and diabetic db/db mice develop marked liver fibrosis in a model of nonalcoholic steatohepatitis: role of short-form leptin receptors and osteopontin," *The American Journal of Physiology—Gastrointestinal and Liver Physiology*, vol. 287, no. 5, pp. G1035–G1043, 2004.
- [38] L. Fellmann, A. R. Nascimento, E. Tibiriça, and P. Bousquet, "Murine models for pharmacological studies of the metabolic syndrome," *Pharmacology & Therapeutics*, vol. 137, no. 3, pp. 331–340, 2013.

- [39] V. Vendramini, A. P. Cedenho, S. M. Miraglia, and D. M. Spaine, "Reproductive function of the male obese Zucker rats: alteration in sperm production and sperm DNA damage," *Reproductive Sciences*, vol. 21, no. 2, pp. 221–229, 2014.
- [40] M. Carmiel-Haggai, A. I. Cederbaum, and N. Nieto, "A high-fat diet leads to the progression of non-alcoholic fatty liver disease in obese rats," *The FASEB Journal*, vol. 19, no. 1, pp. 136–138, 2005.
- [41] S. C. Grubb, G. A. Churchill, and M. A. Bogue, "A collaborative database of inbred mouse strain characteristics," *Bioinformatics*, vol. 20, no. 16, pp. 2857–2859, 2004.
- [42] J. Yu, E. Ip, A. Dela Peña et al., "COX-2 induction in mice with experimental nutritional steatohepatitis: role as pro-inflammatory mediator," *Hepatology*, vol. 43, no. 4, pp. 826–836, 2006.
- [43] R. S. McCuskey, Y. Ito, G. R. Robertson, M. K. McCuskey, M. Perry, and G. C. Farrell, "Hepatic microvascular dysfunction during evolution of dietary steatohepatitis in mice," *Hepatology*, vol. 40, no. 2, pp. 386–393, 2004.
- [44] J. George, N. Pera, N. Phung, I. Leclercq, J. Y. Hou, and G. Farrell, "Lipid peroxidation, stellate cell activation and hepatic fibrogenesis in a rat model of chronic steatohepatitis," *Journal of Hepatology*, vol. 39, no. 5, pp. 756–764, 2003.
- [45] C. Z. Larter, M. M. Yeh, J. Williams, K. S. Bell-Anderson, and G. C. Farrell, "MCD-induced steatohepatitis is associated with hepatic adiponectin resistance and adipogenic transformation of hepatocytes," *Journal of Hepatology*, vol. 49, no. 3, pp. 407–416, 2008.
- [46] A. Ferramosca and V. Zara, "Modulation of hepatic steatosis by dietary fatty acids," *World Journal of Gastroenterology*, vol. 20, no. 7, pp. 1746–1755, 2014.
- [47] C. S. Lieber, M. A. Leo, K. M. Mak et al., "Model of nonalcoholic steatohepatitis," *The American Journal of Clinical Nutrition*, vol. 79, no. 3, pp. 502–509, 2004.
- [48] Z.-J. Xu, J.-G. Fan, X.-D. Ding, L. Qiao, and G.-L. Wang, "Characterization of high-fat, diet-induced, non-alcoholic steatohepatitis with fibrosis in rats," *Digestive Diseases and Sciences*, vol. 55, no. 4, pp. 931–940, 2010.
- [49] P. Starkel and I. A. Leclercq, "Animal models for the study of hepatic fibrosis," *Best Practice and Research: Clinical Gastroenterology*, vol. 25, no. 2, pp. 319–333, 2011.
- [50] Q.-G. Deng, H. She, J. H. Cheng et al., "Steatohepatitis induced by intragastric overfeeding in mice," *Hepatology*, vol. 42, no. 4, pp. 905–914, 2005.
- [51] Y. Zou, J. Li, C. Lu et al., "High-fat emulsion-induced rat model of nonalcoholic steatohepatitis," *Life Sciences*, vol. 79, no. 11, pp. 1100–1107, 2006.
- [52] F. R. Jornayvaz, V. T. Samuel, and G. I. Shulman, "The role of muscle insulin resistance in the pathogenesis of atherogenic dyslipidemia and nonalcoholic fatty liver disease associated with the metabolic syndrome," *Annual Review of Nutrition*, vol. 30, pp. 273–290, 2010.
- [53] J. K. Kim, M. D. Michael, S. F. Previs et al., "Redistribution of substrates to adipose tissue promotes obesity in mice with selective insulin resistance in muscle," *Journal of Clinical Investigation*, vol. 105, no. 12, pp. 1791–1797, 2000.
- [54] M. Mari, F. Caballero, A. Colell et al., "Mitochondrial free cholesterol loading sensitizes to TNF- and Fas-mediated steatohepatitis," *Cell Metabolism*, vol. 4, no. 3, pp. 185–198, 2006.
- [55] N. Matsuzawa, T. Takamura, S. Kurita et al., "Lipid-induced oxidative stress causes steatohepatitis in mice fed an atherogenic diet," *Hepatology*, vol. 46, no. 5, pp. 1392–1403, 2007.
- [56] B. P. Sampey, A. M. Vanhoose, H. M. Winfield et al., "Cafeteria diet is a robust model of human metabolic syndrome with liver and adipose inflammation: comparison to high-fat diet," *Obesity*, vol. 19, no. 6, pp. 1109–1117, 2011.
- [57] J. F. Lalanza, A. Caimari, J. M. Del Bas et al., "Effects of a post-weaning cafeteria diet in young rats: metabolic syndrome, reduced activity and low anxiety-like behaviour," *PLoS ONE*, vol. 9, no. 1, Article ID e85049, 2014.
- [58] J. Carillon, C. Romain, G. Bardy et al., "Cafeteria diet induces obesity and insulin resistance associated with oxidative stress but not with inflammation: improvement by dietary supplementation with a melon superoxide dismutase," *Free Radical Biology and Medicine*, vol. 65, pp. 254–261, 2013.
- [59] M. Pasarin, V. La Mura, J. Gracia-Sancho et al., "Sinusoidal endothelial dysfunction precedes inflammation and fibrosis in a model of NAFLD," *PLoS ONE*, vol. 7, no. 4, Article ID e32785, 2012.
- [60] X. Ouyang, P. Cirillo, Y. Sautin et al., "Fructose consumption as a risk factor for non-alcoholic fatty liver disease," *Journal of Hepatology*, vol. 48, no. 6, pp. 993–999, 2008.
- [61] M. F. Abdelmalek, A. Suzuki, C. Guy et al., "Increased fructose consumption is associated with fibrosis severity in patients with nonalcoholic fatty liver disease," *Hepatology*, vol. 51, no. 6, pp. 1961–1971, 2010.
- [62] F. R. Jornayvaz, M. J. Jurczak, H.-Y. Lee et al., "A high-fat, ketogenic diet causes hepatic insulin resistance in mice, despite increasing energy expenditure and preventing weight gain," *The American Journal of Physiology—Endocrinology and Metabolism*, vol. 299, no. 5, pp. E808–E815, 2010.
- [63] T. Ishimoto, M. A. Lanasa, C. J. Rivard et al., "High-fat and high-sucrose (western) diet induces steatohepatitis that is dependent on fructokinase," *Hepatology*, vol. 58, no. 5, pp. 1632–1643, 2013.
- [64] Z. Khitan and D. H. Kim, "Fructose: a key factor in the development of metabolic syndrome and hypertension," *Journal of Nutrition and Metabolism*, vol. 2013, Article ID 682673, 12 pages, 2013.
- [65] A. Spruss, G. Kanuri, S. Wagnerberger, S. Haub, S. C. Bischoff, and I. Bergheim, "Toll-like receptor 4 is involved in the development of fructose-induced hepatic steatosis in mice," *Hepatology*, vol. 50, no. 4, pp. 1094–1104, 2009.
- [66] J. S. Lim, M. Mietus-Snyder, A. Valente, J.-M. Schwarz, and R. H. Lustig, "The role of fructose in the pathogenesis of NAFLD and the metabolic syndrome," *Nature Reviews Gastroenterology and Hepatology*, vol. 7, no. 5, pp. 251–264, 2010.
- [67] L. H. Tetri, M. Basaranoglu, E. M. Brunt, L. M. Yerian, and B. A. Neuschwander-Tetri, "Severe NAFLD with hepatic necroinflammatory changes in mice fed trans fats and a high-fructose corn syrup equivalent," *The American Journal of Physiology—Gastrointestinal and Liver Physiology*, vol. 295, no. 5, pp. G987–G995, 2008.
- [68] R. Kohli, M. Kirby, S. A. Xanthakos et al., "High-fructose, medium chain trans fat diet induces liver fibrosis and elevates plasma coenzyme Q9 in a novel murine model of obesity and nonalcoholic steatohepatitis," *Hepatology*, vol. 52, no. 3, pp. 934–944, 2010.
- [69] M. Ganz, T. Csak, and G. Szabo, "High fat diet feeding results in gender specific steatohepatitis and inflammasome activation," *World Journal of Gastroenterology*, vol. 20, no. 26, pp. 8525–8534, 2014.

- [70] M. Charlton, A. Krishnan, K. Viker et al., "Fast food diet mouse: novel small animal model of NASH with ballooning, progressive fibrosis, and high physiological fidelity to the human condition," *The American Journal of Physiology—Gastrointestinal and Liver Physiology*, vol. 301, no. 5, pp. G825–G834, 2011.
- [71] J.-F. Fu, Y.-L. Fang, L. Liang, C.-L. Wang, F. Hong, and G.-P. Dong, "A rabbit model of pediatric nonalcoholic steatohepatitis: the role of adiponectin," *World Journal of Gastroenterology*, vol. 15, no. 8, pp. 912–918, 2009.
- [72] T. Ogawa, H. Fujii, K. Yoshizato, and N. Kawada, "A human-type nonalcoholic steatohepatitis model with advanced fibrosis in rabbits," *The American Journal of Pathology*, vol. 177, no. 1, pp. 153–165, 2010.
- [73] K. Otagawa, K. Kinoshita, H. Fujii et al., "Erythrophagocytosis by liver macrophages (Kupffer cells) promotes oxidative stress, inflammation, and fibrosis in a rabbit model of steatohepatitis: implications for the pathogenesis of human nonalcoholic steatohepatitis," *The American Journal of Pathology*, vol. 170, no. 3, pp. 967–980, 2007.

## Review Article

# Zebrafish as a Model for the Study of Human Myeloid Malignancies

Jeng-Wei Lu,<sup>1</sup> Meng-Shan Hsieh,<sup>1</sup> Heng-An Liao,<sup>1</sup> Yi-Ju Yang,<sup>1</sup>  
Yi-Jung Ho,<sup>2,3</sup> and Liang-In Lin<sup>1,4</sup>

<sup>1</sup>Department of Clinical Laboratory Sciences and Medical Biotechnology, College of Medicine, National Taiwan University, No. 1 Chang-Te Street, Taipei 100, Taiwan

<sup>2</sup>Institute of Preventive Medicine, National Defense Medical Center, No. 172 Dapu Road, New Taipei City 237, Taiwan

<sup>3</sup>Graduate Institute of Life Sciences, National Defense Medical Center, No. 161, Section 6, Minquan East Road, Taipei 114, Taiwan

<sup>4</sup>Department of Laboratory Medicine, National Taiwan University Hospital, No. 7 Chung-Shan Southern Road, Taipei 100, Taiwan

Correspondence should be addressed to Liang-In Lin; [lilin@ntu.edu.tw](mailto:lilin@ntu.edu.tw)

Received 26 September 2014; Revised 11 December 2014; Accepted 15 December 2014

Academic Editor: Monica Fedele

Copyright © 2015 Jeng-Wei Lu et al. This is an open access article distributed under the Creative Commons Attribution License, which permits unrestricted use, distribution, and reproduction in any medium, provided the original work is properly cited.

Myeloid malignancies are heterogeneous disorders characterized by uncontrolled proliferation or/and blockage of differentiation of myeloid progenitor cells. Although a substantial number of gene alterations have been identified, the mechanism by which these abnormalities interact has yet to be elucidated. Over the past decades, zebrafish have become an important model organism, especially in biomedical research. Several zebrafish models have been developed to recapitulate the characteristics of specific myeloid malignancies that provide novel insight into the pathogenesis of these diseases and allow the evaluation of novel small molecule drugs. This report will focus on illustrative examples of applications of zebrafish models, including transgenesis, zebrafish xenograft models, and cell transplantation approaches, to the study of human myeloid malignancies.

## 1. Introduction

Myeloid malignancies, including myeloproliferative neoplasms (MPNs), myelodysplastic syndrome (MDS), and acute myeloid leukemia (AML), are heterogeneous disorders characterized by uncontrolled proliferation or/and blockage of differentiation of abnormal myeloid progenitor cells [1]. MPNs are clonal hematopoietic stem cell disorders characterized by proliferation of one or more of the myeloid lineages. MDS is also a clonal hematopoietic disorder characterized by the simultaneous proliferation and apoptosis of hematopoietic cells, which leads to a normal state or hypercellularity of the bone marrow (BM) and pancytopenia in the peripheral blood (PB).

A substantial number of studies have revealed that MPN or MDS can evolve into AML in some patients [2]. AML is a heterogeneous disease that results from the clonal expansion of myeloblasts in the BM and PB and may involve only one or all myeloid cell lineages [3, 4]. Numerous recurrent

gene fusions (such as t(15;17)/*PML-RARA*, t(8;21)/*AML1-ETO*, inv(16)/*CBFB-MYH11*, and t(9;11)/*MLL-MLL2*) and point mutations (such as *NPM1*, *FLT3*, *KIT*, and *CEBPA*), associated with class I (proliferation advantage) and class II (differentiation blockage) mutations, have been identified over the past several decades. Recent comprehensive studies with whole-genome sequencing or whole-exome sequencing, RNA and microRNA sequencing, and DNA methylation analysis have successfully classified the related genes into nine categories based on the function of the mutated genes, including transcription factor gene fusions, *NPM1*, tumor suppressor genes, genes with chromosome modifiers, genes with DNA methylation, activated signaling genes, myeloid transcription factor genes, cohesion-complex genes, and spliceosome-complex genes [5]. However, the mechanisms which by these identified alterations interact to induce AML and distinguish driver from passenger mutations in leukemogenesis have yet to be elucidated.

The zebrafish is a popular research model in biomedical research fields, including embryonic development, human diseases, cancer studies, toxicity, and chemical screening [6]. From a genetic point of view, the current zebrafish genome has been fully sequenced, and many genes are conserved between the human and zebrafish genomes. The zebrafish genome is composed of 25 chromosomes and essentially contains the full vertebrate repertoire of genes. More importantly, approximately 84% of the human genes that cause diseases have a zebrafish ortholog [7]. Although zebrafish and mammalian hematopoietic organs belong to different sites, the genetic and cellular levels of hematopoiesis are conserved between these groups. Zebrafish carry their hematopoietic stem cells in the kidney marrow and have blood cell types similar to human beings [8, 9].

Compared to the mouse model, the zebrafish model is very suitable for large-scale genetic and high-throughput screening in many ways, and it allows more powerful induction of tumors by carcinogens [10]. The first zebrafish model of hematological malignancy was generated in 2003 using the mouse *Myc* gene driven by *recombinase activating gene 2* (*rag2*) promoters. This zebrafish model faithfully developed T-cell lymphoblastic leukaemia (T-ALL) that closely parallels the human disorder subtype [11]. Recently, the zebrafish system has been used to study genetic pathways and understand the pathogenesis involved in human cancers [12–14]. Thus, the zebrafish provides a unique model system to study disease mechanisms *in vivo*. This paper summarizes the benefits of using the zebrafish model to study myeloid leukaemogenesis, reviews current zebrafish models of specific myeloid malignancies, and gives future directions for zebrafish models in the study of human cancer. In addition, the bridge between basic science and translational research will be discussed.

## 2. Overview of Zebrafish Hematopoiesis

Hematopoiesis is a complex process that utilizes many transcription factors to form all of the blood cell lineages from common multipotent hematopoietic stem cells (HSCs). Various experimental tools and methods have been established to facilitate the understanding of hematopoiesis and blood-related disease mechanisms. The zebrafish is an ideal animal model to study hematopoietic development due to its experimental advantages. Although they possess some characteristics that are different from other vertebrates and mammals, such as the site of hematopoiesis, the lineages of blood cells as well as the transcriptional regulators associated with the fate of blood cells have been evolutionarily conserved [15, 16]. Similar to other vertebrates, two major waves of hematopoiesis, the primitive and definitive waves, sequentially occur in zebrafish hematopoiesis [17]. The first wave of definitive hematopoiesis produces a transient population of cells, termed erythroid myeloid progenitors (EMPs), in the posterior blood island (PBI). The population of primitive myeloid cells is predominantly different from that of hemangioblasts at the anterior lateral mesoderm (ALM) between 12 and 24 hours after fertilization (hpf) [18, 19]. However, the posterior lateral mesoderm (PLM) is the major

location of primitive erythroid progenitors and some myeloid cells [20–23]. Beginning at 24 hpf, these primitive blood cells enter the circulation and are distributed throughout the embryo. The definitive wave of hematopoiesis begins at approximately 26–30 hpf, and multipotent HSCs emerge from the hemogenic endothelium that resides in the ventral aspect of the dorsal aorta in the aorta-gonad-mesonephros (AGM) region [21, 24, 25]. They then migrate to the posterior region of the tail-caudal hematopoietic tissue (CHT), along with the circulation, after 36 hpf, and differentiate into cells during that period of time [26, 27]. Ultimately, HSCs from the AGM and CHT seed the kidney marrow approximately 4 days after fertilization (dpf) and give rise to all lineages of blood cells for the remainder of adult life. The CHT is analogous to the mammalian fetal liver or placenta, while the kidney marrow is functionally equivalent to mammalian bone marrow. In addition, some of HSCs also seed the thymus, where lymphopoiesis is initiated at approximately 3 dpf, and remain permanently after the maturation of lymphocytes.

Several zebrafish transcription factors that regulate hematopoiesis have been identified. The early stage markers *gata2*, *lmo2*, *flil*, and *scl* (*stem cell leukemia*) are master regulators that are coexpressed in both the ALM and PLM, where hemangioblast development occurs, from the 2nd to the 3rd somite stages [20, 21, 23]. These genes are expressed in the PLM and later in the intermediate cell mass (ICM) [28–31]. *lmo2*, *flil*, and *scl* may function as crucial factors necessary for normal erythroid and myeloid development [30–32]. In addition, *gata1* and *spil* (*pu.1*) are also involved in primitive hematopoiesis. *Gata1*, a transcription factor essential for erythropoiesis, is first detectable in cells of the PLM at 12 hpf and then in the anterior ICM [33, 34]. Conversely, expression of *spil*, an ETS transcription factor required for myeloid cell development, appears in the ALM and ICM between 16 and 30 hpf [35]. Later, these *spil* expressing progenitor cells differentiate into macrophages and granulocytes that express *l-plastin* (*lcp1*) and myeloperoxidase (mpo), respectively [18, 36]. *Runx1* has been shown to be required for definitive hematopoiesis based on knockdown experiments that resulted in reduced *c-myb* expression and lymphopoiesis, but it produces no apparent effect on the development of primitive hematopoiesis [24, 37–39].

## 3. Transgenic Technology for Studying Myeloid Malignancies Using Zebrafish

The available zebrafish transgenic technology has improved over the last two decades [40, 41]. Different systems have been used in transgenic zebrafish models, such as injection of linear DNA [40] or supercoiled plasmid DNA [41, 42] or injection of recombinant bacterial artificial chromosomes into embryos [42]. In recent years, a new transgenic technology related to *Tol2*-mediated transgenesis has been established. The *Tol2* element is a naturally occurring active transposable element found in vertebrate genomes. The *Tol2* transposon system is considered a useful gene transfer vector in organisms ranging from fish to mammals [43]. *Tol2*-mediated transgenesis is an excellent method for creating

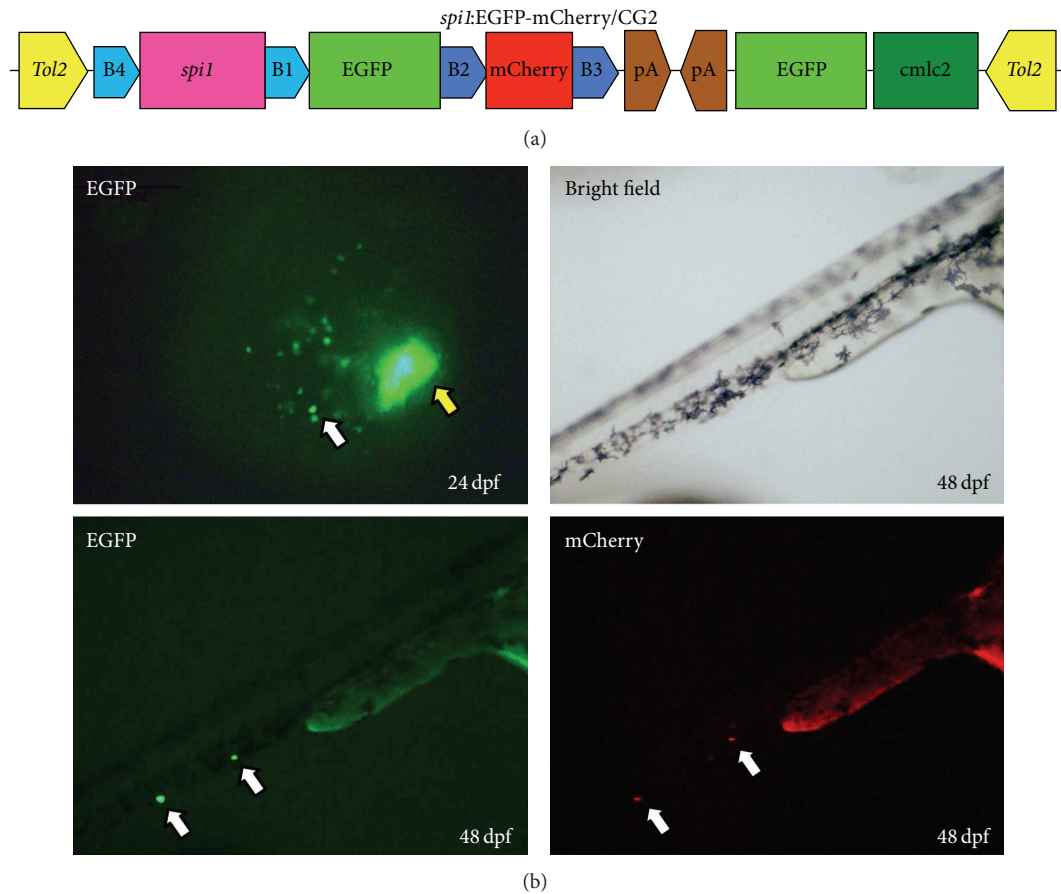


FIGURE 1: Expression of the *spi1*:EGFP-mCherry/CG2 transgenic fish. (a) Diagram of the *spi1*:EGFP-mCherry/CG2 construct that contains *Tol2* sequences and the *cmlc2*:GFP expression cassette. (b) Fluorescent images of TG (*spi1*:EGFP-mCherry/CG2) embryos at 24 or 48 hpf. The white arrowhead indicates *spi1* expressing myeloid cells and the yellow arrowhead fluorescence in heart.

transgenic zebrafish using coinjection of *Tol2* RNA, and the DNA fragment surrounded by the *Tol2* element transposon can be efficiently excised and integrated into the zebrafish genome [44, 45].

Constitutive expression systems have proven useful, but it is often observed that the expression of oncogenes may cause serious tumors and early lethality, preventing the complete characterization of their effects. Therefore, the use of an induction system can help to solve this problem. For example, Tet-On, Tet-Off, Mifepristone, Cre-loxP, Heat-shock, and GAL4-UAS inducible systems can be used. The duration and dosage of oncogene expression can be monitored with such a system, thus allowing the spatiotemporal control of gene expression [46].

A green fluorescent protein (GFP) reporter can be a useful marker for determining if mammalian promoters and ubiquitous or endogenous tissue-specific promoters can drive downstream transgene expressions in zebrafish [43]. It has been noted that *spi1* plays an important role in the development of myeloid (granulocytes and monocytes/macrophages) cells in zebrafish, and the *spi1* promoter can drive myeloid-specific expression in zebrafish. Ward et al. [47] and Hsu et al. [48] identified a 5.3 kb and a 9.0 kb promoter fragment

of zebrafish sequences upstream of the *spi1* coding sequence that is sufficient to drive the expression of downstream genes. Recently, a transgenic fish line with a *spi1*:EGFP-mCherry/CG2 construct was established for studying the cooperation of various genetic aberrations found in myeloid malignancies (Figure 1), and this model may become a useful zebrafish model for exploring leukemogenesis in myeloid cells.

#### 4. Myeloid Malignancies Animal Models in Zebrafish

RAS mutations associated with cancer frequently occur in patients with AML, suggesting a functional role for Ras in leukemogenesis. *AML1/ETO* rearrangements are detected frequently in AML, especially M2, and are associated with a relatively good prognosis [49]. *K-RASG12D* interacts with *AML1/ETO* to induce acute monoblastic leukemia in a mouse model [50]. The *NUP98-HOXA9* fusion oncogene is related to an inferior prognosis in de novo and treatment-related AML and induces AML in mouse models [51]. *NUP98-HOXA9* is associated with increased cell proliferation and survival as well as drug metabolism [52]. The *MOZ/TIF2*

fusion oncogene was described in a specific subgroup of AML that represents approximately 5% of M4/M5 AML [53]. The transforming properties of *MOZ/TIF2* have been demonstrated in mouse committed myeloid progenitors *in vitro* and *in vivo* [54, 55]. Constitutive activation of *Stat5* has been observed in hematological malignancies and is often triggered by leukemic oncoproteins, such as *Tel-Jak2* and *Bcr-Abl*, and *Stat5* has been shown to be involved in mediating the leukemic effects [56, 57]. Amplification of *MYCN* (*N-Myc*) is frequently found in AML patients and is considered a well-established poor prognostic marker in this disease. Overexpression of *MYCN* rapidly causes AML in mouse models [58, 59]. In AML patients, *FLT3* and *NPM* have important prognostic implications on the treatment outcome. Patients with mutated *NPM* have a favorable outcome, while patients with mutations in the *FLT3* gene generally have a poor prognosis. *NPM1* and *FLT3-ITD* mutations interact to induce AML in mouse models [60].

Several zebrafish models associated with myeloid malignancies have been reported. In a transgenic zebrafish model, *K-RASG12D* was expressed under the actin promoter and induced MPNs [61]. Induction of *NUP98-HOXA9* fusion genes in transgenic zebrafish under the *spil* promoter leads to MPNs at 19–23 months of age. However, in contrast to the mouse models, none of the *NUP98-HOXA9* transgenic fish developed AML [62–64]. Lewis et al. addressed the transient expression of constitutively active *Stat5* (*H298R/N714F*-mutant) in zebrafish, which leads to increased numbers of early and late myeloid cells, erythrocytes, and B cells [65]. Bolli et al. found that transient expression of the *NPM1* mutant in zebrafish increases the number of definitive hematopoietic cells, including erythromyeloid progenitors, in the posterior blood island and *c-myb/cd41+* cells in the ventral wall of the aorta [66].

In a transgenic zebrafish model, the *tel-jak2a* fusion oncogene was expressed in embryos under the control of the *spil* promoter, which resulted in disruption of embryonic hematopoiesis, including anemia and expansion of the myeloid compartment [67]. Transient expression of *AML1-ETO* under the control of a CMV promoter in zebrafish embryos caused disruption of normal hematopoiesis, aberrant circulation, internal hemorrhages, and cellular dysplasia [24]. Induction of *AML1-ETO* transgenic zebrafish with the *hsp70* promoter led to reprogramming of the multipotent hematopoietic progenitor cells from the erythroid cells to the myeloid cells in primitive hematopoiesis and disruption of definitive hematopoiesis in embryonic zebrafish [68].

Transient expression of *FLT3-ITD* in zebrafish embryos induced ectopic myeloid cell expansion and clustering, which were ameliorated by AC220 and associated with *stat5*, *erk1/2*, and *akt* phosphorylation. Overexpression of the *FLT3-ITD/TKD* (D835Y) double mutation in zebrafish embryos conferred resistance to AC220 treatment. This zebrafish model may be useful for assessing the pathogenic significance and therapeutic potential of novel gene mutations [69].

In a transgenic zebrafish model of AML, *MYCN*, under the control of a CMV minimal promoter and a *MOZ/TIF2* fusion gene generated by the *inv(8)(p11q13)* chromosomal abnormality expressed under the *spil* promoter, resulted in

altered hematopoiesis and was characterized by invasion of the kidney marrow by immature myeloid cells [58, 70]. Until now, only two published zebrafish AML models have developed overt leukemia (Table 1).

Recently, a transgenic zebrafish model that expresses *AML1-ETO* oncogenes has been reported as an excellent animal model for uncovering new therapeutic targets involved in oncogene-regulated hematopoietic differentiation [71]. According to these studies, the use of human genes produces greater fidelity and reliability in the translation of results associated with the interaction of molecular signaling pathways and disease therapy. In conclusion, the zebrafish is an excellent animal model for elucidating the mechanisms of leukemogenesis and provides an effective drug screening platform.

## 5. Drug Screening in Zebrafish Using Xenograft Model

One of the most extensively used *in vivo* animal models in the investigation of molecular mechanisms is xenotransplantation in immune-deficient animals. The zebrafish genome is nearly 100% homologous to the human genome in key domains [72]. The xenograft animal model has been utilized to investigate tumor biology, especially tumor cell proliferation, invasion, metastasis, and angiogenesis for decades, and the zebrafish model has been used as an alternative to mammalian models to assess the efficacy and toxicity of cancer drugs since 2005 [73].

Engrafting of human tumor cells into the yolk sac of zebrafish embryos at 48 hpf can be used as a xenograft model of zebrafish due to the lack of an adaptive immune response at this stage [74]. To achieve maximum embryo transparency, embryos were incubated in egg medium with 0.3% phenylthiourea (PTU) to prevent pigment formation. As in mouse systems, the *in vivo* spatial resolution of the adult mouse is limited due to the normal opacification of the skin and subdermal structures. However, the body of zebrafish embryos is transparent, which allows the observation of labeled tumor cells and evaluation of the effects of cancer drugs. Due to the size of zebrafish embryos, high-throughput drug screening can be conducted in a 96-well format [74]. Several reports have verified that the results from zebrafish xenograft models are similar to those from mouse models [75, 76]. Taken together, the findings suggest that the zebrafish model may be a rapid, simple, sensitive, and reproducible xenograft model compared to the mouse model (Table 2).

Leukemia cells labeled with CM-Dil, a lipophilic fluorescent tracking dye, were injected into 2-day-old zebrafish larvae and used to evaluate the efficacy of imatinib and all-trans retinoic acid (ATRA) on the proliferation of K562 cells and NB4 cells, respectively [6], and these cells have also been used in *ex vivo* cell proliferation assays [77]. A novel phenotype-based *in vivo* screening method that uses leukemia stem cells (LSCs) xenotransplanted into zebrafish has been demonstrated. Aldehyde dehydrogenase-positive (ALDH+) cells reflecting LSCs were implanted into young zebrafish at 48 hpf, and the efficacy of various therapeutic

TABLE 1: Zebrafish animal models of myeloid malignancies.

Gene name	Promoter and expression construct	Type	Refs
<i>MYCN</i>	MYCN-HSE-EGFP	AML	[58]
<i>MYST3/NCOA2</i>	spi-1-MYST3/NCOA2-EGFP	AML	[70]
<i>kRASG12D</i>	B-actin-LoxP-EGFP-LoxP-kRASG12D; hsp70-Cre	MPD	[61]
<i>NUP98-HOXA9</i>	spi-1-loxP-EGFP-loxP-NUP98-HOXA9; hsp70-Cre	MPN	[62]
<i>Stat5.1</i> mutants	Constitutively active mutants of Stat5.1	Tumor-like lesions; increased numbers of early and late myeloid cells, erythrocytes, and B cells	[65]
<i>NPM1</i> mutant	pCS2cmv-NPM1c-EGFP	No AML; increased numbers of definitive hematopoietic cells	[66]
<i>tel-jak2a</i>	pCS2cmv-Flag-tel-jak2a; spi-1-Flag-tel-jak2a	No AML; anemic; perturbed intermediate cell mass; accumulation of large cells near the heart	[67]
<i>AML1</i>	pCS2cmv-runx1	No AML; enlarged heart and ectopic blood	[24]
<i>AML1-ETO</i>	pCS2cmv-RUNX1-CBF2T1	No AML; defective development of blood and circulation and internal hemorrhaging	[24]
<i>AML1-ETO</i>	hsp-AML1-ETO	No AML; loss of gata1 hematopoietic cells in the posterior blood islands	[68]
<i>AML1-ETO</i> + Gro3 MO	hsp-AML1-ETO	No apparent AML; enhanced the accumulation of blast cells	[68]
<i>FLT3-ITD</i>	CMV-FLT3-ITD-T2a-EGFP	Ectopic myeloid cell expansion	[69]
	CMV-FLT3-TKD-T2a-EGFP	Ectopic myeloid cell expansion resistant to AC220	
	CMV-FLT3-ITD-TKD-T2a-EGFP	Conferred resistance to AC220 treatment	

AML: acute myeloid leukemia; MPD: myeloproliferative disorder; MPN: myeloproliferative neoplasm; MO: morpholino.

TABLE 2: The advantages and weaknesses in the xenograft model of zebrafish and mouse.

	Item	Zebrafish	Mouse
Strengths	Maintenance cost	Low	Available
	Maintenance space	Small	Large
	Offspring	Large number	Less number
	Immune system	Lack in early zebrafish embryos	Innate and adaption
	Observation	Visualization (transparency and transgenic lines)	Limitation
	Readout time	Hours to days	Days to months
	Cell numbers required for xenotransplantation per animal	Less	Large
	High-throughput drug screening	Available	Limitation
Weaknesses	Size of organs/vessels	Small	Large
	Body temperature	Low	High
	Lack of organs	Breast, lung, etc.	
	Zebrafish antibodies	Limitation	More
	Adult immune-permissive lines	Unavailable	Available

agents was evaluated by high-content imaging [78]. From the transplanted tumor clusters, the number of migrating tumors and their areas were measured within concentric rings at a defined distance from the main tumor by calculating the area, total luminance value, and average radius of the tumor [62]. For cell proliferation assays, positive embryos were divided into two groups; one group was maintained

at 35°C for 24 h, while the other group was incubated with or without drug for 72 h. At the end of each time period, the embryos were enzymatically dissociated into a single cell suspension, and the number of fluorescent cells in the suspension was counted. The number of fluorescent cells present at 72 h divided by the number of fluorescent cells present at 24 h represents the fold increase in the cell number

[78]. These studies established the efficacy of a zebrafish xenograft platform as a rapid assessment of the effect of novel compounds on leukemia cell proliferation *in vivo*. Taken together, these findings suggest that the zebrafish xenograft model can be used as a platform for drug screening, a tool to rapidly assess the efficacy of novel compounds on the proliferation of human leukemia cells *ex vivo* and for providing information for subsequent preclinical mouse studies and clinical trials.

## 6. Zebrafish Models for Hematopoietic Cell Transplantation Biology

Hematopoietic stem cells are the source of all the blood cells needed by an organism during its lifetime. The study of hematopoiesis has been markedly facilitated by hematopoietic stem cell transplantation (HSCT), which involves transplanting donor blood cell populations into recipient animals. It is known that immune-matching is not required in embryonic recipients less than 5 days after fertilization because thymic development does not occur until that time in zebrafish [79]. Therefore, HSCT could be applied in experiments related to the development of quantitative long-term repopulating assays and the generation of histocompatible zebrafish lines [80].

The first hematopoietic cell transplantation in zebrafish revealed that hematopoietic cell transplantation could rescue multilineage hematopoiesis in embryonic lethal *gata1*<sup>-/-</sup> mutants over six months of age [15]. The 2-day-old embryos were used as transplant recipients to partly circumvent graft rejection by performing short-term multilineage hematopoietic engraftment [15]. Subsequently, Traver et al. demonstrated an allogeneic HSCT into adult recipient zebrafish conditioned by a sublethal dose of gamma irradiation and established transplantation assays to evaluate the function of HSCs in zebrafish [81]. Self-renewal is a feature of cancer, and Smith et al. initially demonstrated high-throughput imaging methods to experimentally assess cell transplantation and evaluate the gene pathways involved in cancer self-renewal [82]. However, these approaches require donor cells from the same strain of syngeneic zebrafish or the recipient immune system to be transiently ablated by whole-body  $\gamma$ -irradiation before transplantation [15, 81, 82], making long-term engraftment studies difficult. In 2011, lethally irradiated animals could be rescued by transplantation of whole kidney marrow cells. The key zebrafish genes at the major histocompatibility complex locus on chromosome 19 were identified, and transplantation of hematopoietic stem cells was successfully performed based on immune-matching [80]. Recently, *rag2*<sup>E450fs</sup> mutant zebrafish, which have reduced numbers of functional T and B cells, were successfully created, and these animals could be used as universal recipients for allograft cell transplantation. This is the first established immunocompromised zebrafish model, and it may produce a new era of stem cell self-renewal and large-scale cell transplantation studies [83]. These advances provide unique opportunities to investigate the mechanisms of engraftment.

## 7. Concluding Remarks

AML is a heterogeneous disorder characterized by acquired genetic changes in hematopoietic progenitor cells. Numerous recurrent gene fusions and point mutations have been identified over the past several decades. However, the mechanism by which these identified alterations interact to induce AML and distinguish driver from passenger mutations in leukemogenesis remains unknown. Chemotherapy is currently used as the standard treatment for AML, except for AML-M3, which shows a good therapeutic response when treated with all-trans retinoic acid (ATRA) or arsenic trioxide, and the majority of AML patients relapse after complete remission or acquire drug resistance, indicating the need for efficacious therapeutic strategies. Several small molecule inhibitors have been developed that showed efficacy in preclinical studies; however, approval of these agents for clinical treatment is still challenging.

The zebrafish genome has been fully sequenced and has a substantial number of conserved genes compared to the human genome. The genetic and cellular levels of hematopoiesis are conserved between these organisms. Several zebrafish models associated with myeloid malignancies have been previously reported, including transgenic zebrafish that exhibit *K-RASG12D*, *NUP98-HOXA9*, *Stat5 (H298R)*, *Stat5 (N714F)*, *NPM1*, *tel-jak2a*, *AML1-ETO*, *FLT3-ITD*, *FLT3-TKD (D835Y)*, *MYCN*, or *MOZ/TIF2* expression. Several zebrafish transgenic technologies have also been introduced, including *Tol2*-mediated transgenesis and GFP-mCherry transgenic lines driven by a myeloid-specific *spil* promoter. In addition, xenograft zebrafish models used for high-throughput drug screening and leukemia xenotransplantation in zebrafish used for *in vivo* chemotherapy response assays have also been addressed.

## Conflict of Interests

The authors declare that they have no conflict of interests regarding the publication of this paper.

## Acknowledgment

This study was supported by a research grant from the National Science Council (NSC 100-2320-B-002-074-MY3 and NSC-102-2628-B-002-029-MY3), Taiwan.

## References

- [1] S. H. Swerdlow, N. C. Harris, E. S. Jaffe et al., *WHO Classification of Tumours of Haematopoietic and Lymphoid Tissues*, International Agency of Research on Cancer (IARC), Lyon, France.
- [2] Y. Koh, I. Kim, J.-Y. Bae et al., "Prognosis of secondary acute myeloid leukemia is affected by the type of the preceding hematologic disorders and the presence of trisomy 8," *Japanese Journal of Clinical Oncology*, vol. 40, no. 11, pp. 1037–1045, 2010.
- [3] F. Ferrara and C. A. Schiffer, "Acute myeloid leukaemia in adults," *The Lancet*, vol. 381, no. 9865, pp. 484–495, 2013.

- [4] M. R. O'Donnell, C. N. Abboud, J. Altman et al., "Acute myeloid leukemia," *Journal of the National Comprehensive Cancer Network*, vol. 10, no. 8, pp. 984–1021, 2012.
- [5] S.-J. Chen, Y. Shen, and Z. Chen, "A panoramic view of acute myeloid leukemia," *Nature Genetics*, vol. 45, no. 6, pp. 586–587, 2013.
- [6] B. Pruvot, A. Jacquelin, N. Droin et al., "Leukemic cell xenograft in zebrafish embryo for investigating drug efficacy," *Haematologica*, vol. 96, no. 4, pp. 612–616, 2011.
- [7] Q. Li and J. Uitto, "Zebrafish as a model system to study skin biology and pathology," *Journal of Investigative Dermatology*, vol. 134, no. 6, article e21, 2014.
- [8] S. A. Renshaw and N. S. Trede, "A model 450 million years in the making: zebrafish and vertebrate immunity," *Disease Models & Mechanisms*, vol. 5, no. 1, pp. 38–47, 2012.
- [9] G. J. Lieschke and N. S. Trede, "Fish immunology," *Current Biology*, vol. 19, no. 16, pp. R678–R682, 2009.
- [10] G. B. Pliss, M. A. Zabezhinski, A. S. Petrov, and V. V. Khudoley, "Peculiarities of N-nitramines carcinogenic action," *Archiv für Geschwulstforschung*, vol. 52, no. 8, pp. 629–634, 1982.
- [11] D. M. Langenau, D. Traver, A. A. Ferrando et al., "Myc-induced T cell leukemia in transgenic zebrafish," *Science*, vol. 299, no. 5608, pp. 887–890, 2003.
- [12] W. Zheng, Z. Li, A. T. Nguyen, C. Li, A. Emelyanov, and Z. Gong, "Xmrk, Kras and Myc transgenic zebrafish liver cancer models share molecular signatures with subsets of human hepatocellular carcinoma," *PLoS ONE*, vol. 9, no. 3, Article ID e91179, 2014.
- [13] M. Schiavone, E. Rampazzo, A. Casari et al., "Zebrafish reporter lines reveal *in vivo* signaling pathway activities involved in pancreatic cancer," *Disease Models & Mechanisms*, vol. 7, no. 7, pp. 883–894, 2014.
- [14] X. Le, E. K. Pugach, S. Hettmer et al., "A novel chemical screening strategy in zebrafish identifies common pathways in embryogenesis and rhabdomyosarcoma development," *Development*, vol. 140, no. 11, pp. 2354–2364, 2013.
- [15] D. Traver, B. H. Paw, K. D. Poss, W. T. Penberthy, S. Lin, and L. I. Zon, "Transplantation and *in vivo* imaging of multilineage engraftment in zebrafish bloodless mutants," *Nature Immunology*, vol. 4, no. 12, pp. 1238–1246, 2003.
- [16] A. J. Davidson and L. I. Zon, "The 'definitive' (and 'primitive') guide to zebrafish hematopoiesis," *Oncogene*, vol. 23, no. 43, pp. 7233–7246, 2004.
- [17] J. L. Galloway and L. I. Zon, "3 ontogeny of hematopoiesis: examining the emergence of hematopoietic cells in the vertebrate embryo," *Current Topics in Developmental Biology*, vol. 53, pp. 139–158, 2003.
- [18] P. Herbomel, B. Thisse, and C. Thisse, "Ontogeny and behaviour of early macrophages in the zebrafish embryo," *Development*, vol. 126, no. 17, pp. 3735–3745, 1999.
- [19] M. O. Crowhurst, J. E. Layton, and G. J. Lieschke, "Developmental biology of zebrafish myeloid cells," *The International Journal of Developmental Biology*, vol. 46, no. 4, pp. 483–492, 2002.
- [20] E. C. Liao, B. H. Paw, A. C. Oates, S. J. Pratt, J. H. Postlethwait, and L. I. Zon, "SCL/Tal-1 transcription factor acts downstream of cloche to specify hematopoietic and vascular progenitors in zebrafish," *Genes and Development*, vol. 12, no. 5, pp. 621–626, 1998.
- [21] M. A. Thompson, D. G. Ransom, S. J. Pratt et al., "The cloche and spadetail genes differentially affect hematopoiesis and vasculogenesis," *Developmental Biology*, vol. 197, no. 2, pp. 248–269, 1998.
- [22] S. Sumanas, T. Joraniak, and S. Lin, "Identification of novel vascular endothelial-specific genes by the microarray analysis of the zebrafish cloche mutants," *Blood*, vol. 106, no. 2, pp. 534–541, 2005.
- [23] V. N. Pham, N. D. Lawson, J. W. Mugford et al., "Combinatorial function of ETS transcription factors in the developing vasculature," *Developmental Biology*, vol. 303, no. 2, pp. 772–783, 2007.
- [24] M. L. Kalev-Zylinska, J. A. Horsfield, M. V. C. Flores et al., "Runx1 is required for zebrafish blood and vessel development and expression of a human RUNX1-CBF2T1 transgene advances a model for studies of leukemogenesis," *Development*, vol. 129, no. 8, pp. 2015–2030, 2002.
- [25] C. E. Burns, T. DeBlasio, Y. Zhou, J. Zhang, L. Zon, and S. D. Nimer, "Isolation and characterization of runxa and runxb, zebrafish members of the runt family of transcriptional regulators," *Experimental Hematology*, vol. 30, no. 12, pp. 1381–1389, 2002.
- [26] E. Murayama, K. Kissa, A. Zapata et al., "Tracing hematopoietic precursor migration to successive hematopoietic organs during zebrafish development," *Immunity*, vol. 25, no. 6, pp. 963–975, 2006.
- [27] H. Jin, J. Xu, and Z. Wen, "Migratory path of definitive hematopoietic stem/progenitor cells during zebrafish development," *Blood*, vol. 109, no. 12, pp. 5208–5214, 2007.
- [28] H. W. Detrich III, M. W. Kieran, F. Y. Chan et al., "Intraembryonic hematopoietic cell migration during vertebrate development," *Proceedings of the National Academy of Sciences of the United States of America*, vol. 92, no. 23, pp. 10713–10717, 1995.
- [29] L. J. Patterson, M. Gering, and R. Patient, "Scl is required for dorsal aorta as well as blood formation in zebrafish embryos," *Blood*, vol. 105, no. 9, pp. 3502–3511, 2005.
- [30] L. J. Patterson, M. Gering, C. E. Eckfeldt et al., "The transcription factors Scl and Lmo2 act together during development of the hemangioblast in zebrafish," *Blood*, vol. 109, no. 6, pp. 2389–2398, 2007.
- [31] H. Zhu, D. Traver, A. J. Davidson et al., "Regulation of the *lmo2* promoter during hematopoietic and vascular development in zebrafish," *Developmental Biology*, vol. 281, no. 2, pp. 256–269, 2005.
- [32] K. A. Dooley, A. J. Davidson, and L. I. Zon, "Zebrafish scl functions independently in hematopoietic and endothelial development," *Developmental Biology*, vol. 277, no. 2, pp. 522–536, 2005.
- [33] A. B. Cantor and S. H. Orkin, "Transcriptional regulation of erythropoiesis: an affair involving multiple partners," *Oncogene*, vol. 21, no. 21, pp. 3368–3376, 2002.
- [34] J. F. Amatrua and L. I. Zon, "Dissecting hematopoiesis and disease using the zebrafish," *Developmental Biology*, vol. 216, no. 1, pp. 1–15, 1999.
- [35] E. W. Scott, M. C. Simon, J. Anastasi, and H. Singh, "Requirement of transcription factor PU.1 in the development of multiple hematopoietic lineages," *Science*, vol. 265, no. 5178, pp. 1573–1577, 1994.
- [36] C. M. Bennett, J. P. Kanki, J. Rhodes et al., "Myelopoiesis in the zebrafish, *Danio rerio*," *Blood*, vol. 98, no. 3, pp. 643–651, 2001.
- [37] E. J. Paik and L. I. Zon, "Hematopoietic development in the zebrafish," *International Journal of Developmental Biology*, vol. 54, no. 6–7, pp. 1127–1137, 2010.
- [38] C. E. Burns, D. Traver, E. Mayhall, J. L. Shepard, and L. I. Zon, "Hematopoietic stem cell fate is established by the Notch-Runx pathway," *Genes & Development*, vol. 19, no. 19, pp. 2331–2342, 2005.

- [39] M. Gering and R. Patient, "Hedgehog signaling is required for adult blood stem cell formation in zebrafish embryos," *Developmental Cell*, vol. 8, no. 3, pp. 389–400, 2005.
- [40] G. W. Stuart, J. V. McMurray, and M. Westerfield, "Replication, integration and stable germ-line transmission of foreign sequences injected into early zebrafish embryos," *Development*, vol. 103, no. 2, pp. 403–412, 1988.
- [41] G. W. Stuart, J. R. Vielkind, J. V. McMurray, and M. Westerfield, "Stable lines of transgenic zebrafish exhibit reproducible patterns of transgene expression," *Development*, vol. 109, no. 3, pp. 577–584, 1990.
- [42] P. Culp, C. Nüsslein-Volhard, and N. Hopkins, "High-frequency germ-line transmission of plasmid DNA sequences injected into fertilized zebrafish eggs," *Proceedings of the National Academy of Sciences of the United States of America*, vol. 88, no. 18, pp. 7953–7957, 1991.
- [43] A. Deiters and J. A. Yoder, "Conditional transgene and gene targeting methodologies in zebrafish," *Zebrafish*, vol. 3, no. 4, pp. 415–429, 2006.
- [44] K. Kawakami, A. Shima, and N. Kawakami, "Identification of a functional transposase of the Tol2 element, an Ac-like element from the Japanese medaka fish, and its transposition in the zebrafish germ lineage," *Proceedings of the National Academy of Sciences of the United States of America*, vol. 97, no. 21, pp. 11403–11408, 2000.
- [45] A. Urasaki, G. Morvan, and K. Kawakami, "Functional dissection of the Tol2 transposable element identified the minimal cis-sequence and a highly repetitive sequence in the subterminal region essential for transposition," *Genetics*, vol. 174, no. 2, pp. 639–649, 2006.
- [46] X. Huang, A. T. Nguyen, Z. Li, A. Emelyanov, S. Parinov, and Z. Gong, "One step forward: the use of transgenic zebrafish tumor model in drug screens," *Birth Defects Research Part C: Embryo Today*, vol. 93, no. 2, pp. 173–181, 2011.
- [47] A. C. Ward, D. O. McPhee, M. M. Condrón et al., "The zebrafish spil promoter drives myeloid-specific expression in stable transgenic fish," *Blood*, vol. 102, no. 9, pp. 3238–3240, 2003.
- [48] K. Hsu, D. Traver, J. L. Kutok et al., "The pu.1 promoter drives myeloid gene expression in zebrafish," *Blood*, vol. 104, no. 5, pp. 1291–1297, 2004.
- [49] E. K. Cho, S. M. Bang, J. Y. Ahn et al., "Prognostic value of AML1/ETO fusion transcripts in patients with acute myelogenous leukemia," *The Korean Journal of Internal Medicine*, vol. 18, no. 1, pp. 13–20, 2003.
- [50] S. Zhao, Y. Zhang, K. Sha et al., "KRAS (G12D) cooperates with AML1/ETO to initiate a mouse model mimicking human acute myeloid Leukemia," *Cellular Physiology and Biochemistry*, vol. 33, no. 1, pp. 78–87, 2014.
- [51] F. J. Giles, A. Keating, A. H. Goldstone, I. Avivi, C. L. Willman, and H. M. Kantarjian, "Acute myeloid leukemia," *Hematology/the Education Program of the American Society of Hematology*, pp. 73–110, 2002.
- [52] G. Ghannam, A. Takeda, T. Camarata, M. A. Moore, A. Viale, and N. R. Yaseen, "The oncogene Nup98-HOXA9 induces gene transcription in myeloid cells," *Journal of Biological Chemistry*, vol. 279, no. 2, pp. 866–875, 2004.
- [53] M. Carapeti, R. C. T. Aguiar, J. M. Goldman, and N. C. P. Cross, "A novel fusion between MOZ and the nuclear receptor coactivator TIF2 in acute myeloid leukemia," *Blood*, vol. 91, no. 9, pp. 3127–3133, 1998.
- [54] B. J. P. Huntly, H. Shigematsu, K. Deguchi et al., "MOZ-TIF2, but not BCR-ABL, confers properties of leukemic stem cells to committed murine hematopoietic progenitors," *Cancer Cell*, vol. 6, no. 6, pp. 587–596, 2004.
- [55] K. Deguchi, P. M. Ayton, M. Carapeti et al., "MOZ-TIF2-induced acute myeloid leukemia requires the MOZ nucleosome binding motif and TIF2-mediated recruitment of CBP," *Cancer Cell*, vol. 3, no. 3, pp. 259–271, 2003.
- [56] S. Xi, Q. Zhang, W. E. Gooding, T. E. Smithgall, and J. R. Grandis, "Constitutive activation of Stat5b contributes to carcinogenesis in vivo," *Cancer Research*, vol. 63, no. 20, pp. 6763–6771, 2003.
- [57] T. S. Lin, S. Mahajan, and D. A. Frank, "STAT signaling in the pathogenesis and treatment of leukemias," *Oncogene*, vol. 19, no. 21, pp. 2496–2504, 2000.
- [58] L.-J. Shen, F.-Y. Chen, Y. Zhang et al., "MYCN transgenic zebrafish model with the characterization of acute myeloid leukemia and altered hematopoiesis," *PLoS ONE*, vol. 8, no. 3, Article ID e59070, 2013.
- [59] H. Kawagoe, A. Kandilci, T. A. Kranenburg, and G. C. Grosveld, "Overexpression of N-Myc rapidly causes acute myeloid leukemia in mice," *Cancer Research*, vol. 67, no. 22, pp. 10677–10685, 2007.
- [60] M. Mallardo, A. Caronno, G. Pruneri et al., "NPMc+ and FLT3-ITD mutations cooperate in inducing acute leukaemia in a novel mouse model," *Leukemia*, vol. 27, no. 11, pp. 2248–2251, 2013.
- [61] X. Le, D. M. Langenau, M. D. Keefe, J. L. Kutok, D. S. Neuberg, and L. I. Zon, "Heat shock-inducible Cre/Lox approaches to induce diverse types of tumors and hyperplasia in transgenic zebrafish," *Proceedings of the National Academy of Sciences of the United States of America*, vol. 104, no. 22, pp. 9410–9415, 2007.
- [62] A. M. Forrester, C. Grabher, E. R. McBride et al., "NUP98-HOXA9-transgenic zebrafish develop a myeloproliferative neoplasm and provide new insight into mechanisms of myeloid leukaemogenesis," *British Journal of Haematology*, vol. 155, no. 2, pp. 167–181, 2011.
- [63] E. Kroon, U. Thorsteinsdottir, N. Mayotte, T. Nakamura, and G. Sauvageau, "NUP98-HOXA9 expression in hemopoietic stem cells induces chronic and acute myeloid leukemias in mice," *The EMBO Journal*, vol. 20, no. 3, pp. 350–361, 2001.
- [64] M. Iwasaki, T. Kuwata, Y. Yamazaki et al., "Identification of cooperative genes for NUP98-HOXA9 in myeloid leukemogenesis using a mouse model," *Blood*, vol. 105, no. 2, pp. 784–793, 2005.
- [65] R. S. Lewis, S. E. M. Stephenson, and A. C. Ward, "Constitutive activation of zebrafish Stat5 expands hematopoietic cell populations in vivo," *Experimental Hematology*, vol. 34, no. 2, pp. 179–187, 2006.
- [66] N. Bolli, E. M. Payne, C. Grabher et al., "Expression of the cytoplasmic NPM1 mutant (NPMc+) causes the expansion of hematopoietic cells in zebrafish," *Blood*, vol. 115, no. 16, pp. 3329–3340, 2010.
- [67] S. M. N. Onnebo, M. M. Condrón, D. O. McPhee, G. J. Lieschke, and A. C. Ward, "Hematopoietic perturbation in zebrafish expressing a tel-jak2a fusion," *Experimental Hematology*, vol. 33, no. 2, pp. 182–188, 2005.
- [68] J. R. J. Yeh, K. M. Munson, Y. L. Chao, Q. P. Peterson, C. A. Macrae, and R. T. Peterson, "AML1-ETO reprograms hematopoietic cell fate by downregulating scl expression," *Development*, vol. 135, no. 2, pp. 401–410, 2008.

- [69] B.-L. He, X. Shi, C. H. Man et al., "Functions of flt3 in zebrafish hematopoiesis and its relevance to human acute myeloid leukemia," *Blood*, vol. 123, no. 16, pp. 2518–2529, 2014.
- [70] J. Zhuravleva, J. Paggetti, L. Martin et al., "MOZ/TIF2-induced acute myeloid leukaemia in transgenic fish," *British Journal of Haematology*, vol. 143, no. 3, pp. 378–382, 2008.
- [71] J. R. J. Yeh, K. M. Munson, K. E. Elagib, A. N. Goldfarb, D. A. Sweetser, and R. T. Peterson, "Discovering chemical modifiers of oncogene-regulated hematopoietic differentiation," *Nature Chemical Biology*, vol. 5, no. 4, pp. 236–243, 2009.
- [72] P. Goldsmith, "Zebrafish as a pharmacological tool: the how, why and when," *Current Opinion in Pharmacology*, vol. 4, no. 5, pp. 504–512, 2004.
- [73] L. M. J. Lee, E. A. Seftor, G. Bonde, R. A. Cornell, and M. J. C. Hendrix, "The fate of human malignant melanoma cells transplanted into zebrafish embryos: assessment of migration and cell division in the absence of tumor formation," *Developmental Dynamics*, vol. 233, no. 4, pp. 1560–1570, 2005.
- [74] M. Konantz, T. B. Balci, U. F. Hartwig et al., "Zebrafish xenografts as a tool for *in vivo* studies on human cancer," *Annals of the New York Academy of Sciences*, vol. 1266, no. 1, pp. 124–137, 2012.
- [75] Y. Zhang, J. Wang, J. Wheat et al., "AML1-ETO mediates hematopoietic self-renewal and leukemogenesis through a COX/ $\beta$ -catenin signaling pathway," *Blood*, vol. 121, no. 24, pp. 4906–4916, 2013.
- [76] J. W. Astin, S. M. F. Jamieson, T. C. Y. Eng et al., "An *in vivo* anti-lymphatic screen in zebrafish identifies novel inhibitors of mammalian lymphangiogenesis and lymphatic-mediated metastasis," *Molecular Cancer Therapeutics*, vol. 13, no. 10, pp. 2450–2462, 2014.
- [77] D. P. Corkery, G. Dellaire, and J. N. Berman, "Leukaemia xenotransplantation in zebrafish—chemotherapy response assay *in vivo*," *British Journal of Haematology*, vol. 153, no. 6, pp. 786–789, 2011.
- [78] B. Zhang, Y. Shimada, J. Kuroyanagi, N. Umemoto, Y. Nishimura, and T. Tanaka, "Quantitative phenotyping-based *in vivo* chemical screening in a zebrafish model of leukemia stem cell xenotransplantation," *PLoS ONE*, vol. 9, no. 1, Article ID e85439, 2014.
- [79] C. E. Willett, A. Cortes, A. Zuasti, and A. G. Zapata, "Early hematopoiesis and developing lymphoid organs in the zebrafish," *Developmental Dynamics*, vol. 214, no. 4, pp. 323–336, 2014.
- [80] J. L. O. de Jong, C. E. Burns, A. T. Chen et al., "Characterization of immune-matched hematopoietic transplantation in zebrafish," *Blood*, vol. 117, no. 16, pp. 4234–4242, 2011.
- [81] D. Traver, A. Winzeler, H. M. Stern et al., "Effects of lethal irradiation in zebrafish and rescue by hematopoietic cell transplantation," *Blood*, vol. 104, no. 5, pp. 1298–1305, 2004.
- [82] A. C. H. Smith, A. R. Raimondi, C. D. Salthouse et al., "High-throughput cell transplantation establishes that tumor-initiating cells are abundant in zebrafish T-cell acute lymphoblastic leukemia," *Blood*, vol. 115, no. 16, pp. 3296–3303, 2010.
- [83] Q. Tang, N. S. Abdelfattah, J. S. Blackburn et al., "Optimized cell transplantation using adult *rag2* mutant zebrafish," *Nature Methods*, vol. 11, no. 8, pp. 821–824, 2014.

## Review Article

# T Helper 17/Regulatory T Cell Balance and Experimental Models of Peritoneal Dialysis-Induced Damage

**Georgios Liappas,<sup>1,2</sup> Guadalupe Tirma González-Mateo,<sup>1,2</sup> Pedro Majano,<sup>3</sup> José Antonio Sánchez-Tomero,<sup>4</sup> Marta Ruiz-Ortega,<sup>5</sup> Raquel Rodrigues Díez,<sup>5</sup> Pilar Martín,<sup>6</sup> Raquel Sanchez-Díaz,<sup>6</sup> Rafael Selgas,<sup>2</sup> Manuel López-Cabrera,<sup>1</sup> and Abelardo Aguilera Peralta<sup>3</sup>**

<sup>1</sup>Department of Immunology, Centro de Biología Molecular Severo Ochoa (CBM), Consejo Superior de Investigaciones Científicas (CSIC), 28049 Madrid, Spain

<sup>2</sup>Department of Nephrology, Instituto de Investigación del Hospital Universitario La Paz (IdiPAZ), 28046 Madrid, Spain

<sup>3</sup>Department of Molecular Biology, Instituto de La Princesa (IP), 28006 Madrid, Spain

<sup>4</sup>Nephrology Service, Hospital Universitario de La Princesa (IP), 28006 Madrid, Spain

<sup>5</sup>Laboratory of Cellular Biology and Rare Diseases, Fundación Jiménez Díaz, Universidad Autónoma de Madrid (UAM), 28040 Madrid, Spain

<sup>6</sup>Department of Molecular and Vascular Inflammation, Centro Nacional de Investigaciones Cardiovasculares (CNIC), 28029 Madrid, Spain

Correspondence should be addressed to Guadalupe Tirma González-Mateo; [guadalupe.gonzalez@idipaz.es](mailto:guadalupe.gonzalez@idipaz.es) and Abelardo Aguilera Peralta; [abelardo.aguilera@salud.madrid.org](mailto:abelardo.aguilera@salud.madrid.org)

Received 18 September 2014; Accepted 29 December 2014

Academic Editor: Monica Fedele

Copyright © 2015 Georgios Liappas et al. This is an open access article distributed under the Creative Commons Attribution License, which permits unrestricted use, distribution, and reproduction in any medium, provided the original work is properly cited.

Fibrosis is a general complication in many diseases. It is the main complication during peritoneal dialysis (PD) treatment, a therapy for renal failure disease. Local inflammation and mesothelial to mesenchymal transition (MMT) are well known key phenomena in peritoneal damage during PD. New data suggest that, in the peritoneal cavity, inflammatory changes may be regulated at least in part by a delicate balance between T helper 17 and regulatory T cells. This paper briefly reviews the implication of the Th17/Treg axis in fibrotic diseases. Moreover, it compares current evidences described in PD animal experimental models, indicating a loss of Th17/Treg balance (Th17 predominance) leading to peritoneal damage during PD. In addition, considering the new clinical and animal experimental data, new therapeutic strategies to reduce the Th17 response and increase the regulatory T response are proposed. Thus, future goals should be to develop new clinical biomarkers to reverse this immune misbalance and reduce peritoneal fibrosis in PD.

## 1. Introduction

An effective inflammatory response is essential not only for the resolution of infections but also for wound healing after injury. The repair is mediated by the collaboration of various mechanisms launched by an acute inflammatory reaction. This process implicates the release of chemokines and cytokines and the migration of various cells of the immune system. If a sustained inflammatory reaction that is not resolved properly becomes chronic, it could lead

to fibrosis due to the accumulation of extracellular matrix (ECM) components [1].

Peritoneal dialysis (PD) is a form of renal replacement therapy alternative to haemodialysis that is widely used around the world for patients suffering from renal failure disease [2, 3]. The process uses the peritoneum as a semipermeable membrane across which PD fluids (PDFs) and dissolved substances (electrolytes, urea, glucose, and other small molecules) are exchanged from the blood [4]. The peritoneal membrane (PM) acts as a protective barrier against injury

and pathogens, where humoral and cellular responses are generated. The treatment consists of the instillation and periodical renovation of a hyperosmotic PDF in the peritoneal cavity through a permanent installed catheter. However, the mechanical damage due to PDF instillation and the exposure of peritoneal cells to glucose degradation products (GDPs) and advanced glycation end products (AGEs) (due to the nonphysiological nature of this PDF) generates inflammation. Along these lines, it has been demonstrated *in vitro* that GDPs and AGEs stimulate NF $\kappa$ B-mediated transcription and the secretion of cytokines and chemokines by human peritoneal mesothelial cells [5]. In addition, the presence of the catheter [6] and peritonitis episodes during treatment [7] appears to be responsible for various alterations of the PM structure and functionality. The final consequence is the generation of vascular alterations [8] and peritoneal fibrosis [3, 9], leading to an ultrafiltration failure [10, 11] that impedes the dialysis process (Figure 1). Although in recent decades great effort has been made to improve catheter design [6] and the biocompatible solutions used [12–14], complications are still common [15, 16]. It has also been demonstrated that inflammation is present in PD patients. Increased serum concentrations of IL-6, TNF- $\alpha$ , VEGF, and C-reactive proteins have been reported in patients, suggesting that PD leads to increased systemic inflammation [17]. Moreover, there is evidence in animal models of chronic peritoneal exposure to PDF showing that this procedure induces PM inflammation and fibrosis [18]. The use of an anti-inflammatory drug (a Cox-2 inhibitor) reduced this peritoneal inflammatory response and consequently the fibrosis. This result confirms the role of inflammation in peritoneal fibrosis [19].

Inflammation is driven by various cell populations including macrophages, neutrophils, and lymphocyte subsets. The differentiation of T cells is crucial for immune and inflammatory responses and its regulation may be a therapeutic target to control peritoneal damage. It has been found that there are different rates between CD4<sup>+</sup> and CD8<sup>+</sup> cells in the peritoneum during PD with respect to healthy individuals [20]. It has been postulated that the presence of AGEs is responsible for an increase in the population of CD8<sup>+</sup> (T cytotoxic) lymphocytes [21]. Regarding CD4<sup>+</sup> (T helper) subsets, in general terms Th1 cells produce high levels of IFN- $\gamma$ , while Th2 cells secrete predominantly IL-4 [22]. There is some controversy about the pattern of response that is generated in patients undergoing treatment with PDF. It is described that there is a deviation toward Th2 pattern of PD in stable patients [23]. However, during episodes of acute peritonitis, a Th1 immune response is developed [24, 25]. In addition to these two classical T helper cell subsets (Th1 and Th2), a third and fourth subpopulation, designated regulatory T (Treg) and T helper 17 (Th17) cells, have emerged as independent differentiation pathways [26, 27]. While the predominance of Th17 cells induces the secretion of a large number of proinflammatory cytokines, Treg cells restrict inflammatory responses and are associated with immune-tolerance [28]. Very little is known about the involvement of these subpopulations in the deterioration of the peritoneum during dialysis. The imbalance between these situations may

cause fibroproliferative diseases and could be an important cause of morbidity and mortality.

In this review we discuss the implication of Th17 and Treg cells in kidney function and fibrotic diseases in different animal experimentation models. More specifically we will focus on the origin of peritoneal damage and its relationship with the intraperitoneal presence of these particular subsets of T lymphocytes, as well as on its clinical implication in peritoneal damage in PD patients, which frequently results in an inability to continue with the treatment.

## 2. T Helper 17 and Regulatory T Cell Differentiation and Their Plasticity

Th17 cells represent a subset of T helper cells that secrete mainly interleukin- (IL-) 17 as well as other proinflammatory cytokines, and they have been related to many autoimmune and chronic inflammatory diseases [29]. There is a balance between Th17 and Treg cells that depends on the activation of the transcription factor ROR $\gamma$ t (factors retinoic acid receptor-related orphan receptor  $\gamma$ t) and Stat3 (signal transducer and activator of transcription 3), or FoxP3 (forkhead box P3) and Stat5, respectively, which regulate the immune response through the secretion of pro- and anti-inflammatory cytokines [30–33]. On the other hand, the importance of Treg cells to the maintenance of peripheral tolerance under noninflammatory conditions throughout life has also been confirmed. In fact, mice lacking Treg cells presented a fatal inflammatory response [34, 35].

The main cytokines involved in Th17/Treg balance are the TGF- $\beta$  (transforming growth factor beta) and IL-6 (interleukin-6) [27, 36, 37]. IL-6 is strongly induced in cells of the innate immune system upon stimulation of pattern recognition receptors such as toll like receptors (TLR) or C-type receptors. It has been shown that mice lacking IL-6 present a deficiency in the differentiation of effector T cells [38, 39]. TGF- $\beta$  in the absence of IL-6 induces Foxp3, thus pushing T-cell differentiation away from the Th17 transcriptional program and decidedly toward the Treg lineage [33]. Moreover, in the central nervous system, TGF- $\beta$  without the synergy of IL-6 will force T cells to differentiate through the T regulatory cell lineage [40]. In contrast, the proinflammatory cytokine IL-6 in the absence of TGF- $\beta$  activates Stat3 by phosphorylating it, which overcomes Foxp3 inhibition of ROR $\gamma$ t transcriptional activity. This process leads to the upregulation of the IL-23R, thus pushing T-cell differentiation toward a Th17 fate [33]. Therefore the cytokine environment is essential for the predominance of an inflammatory or an anti-inflammatory response (Figure 2).

## 3. Th17 and Tissue Fibrosis

Fibroproliferative diseases such as idiopathic pulmonary, liver, cardiovascular, and renal fibrosis are usually associated with chronic inflammation, as has been described previously [41–45]. When an inflammatory response becomes chronic, the accumulation of ECM is more extensive and the function of the organ is compromised. A number of studies have

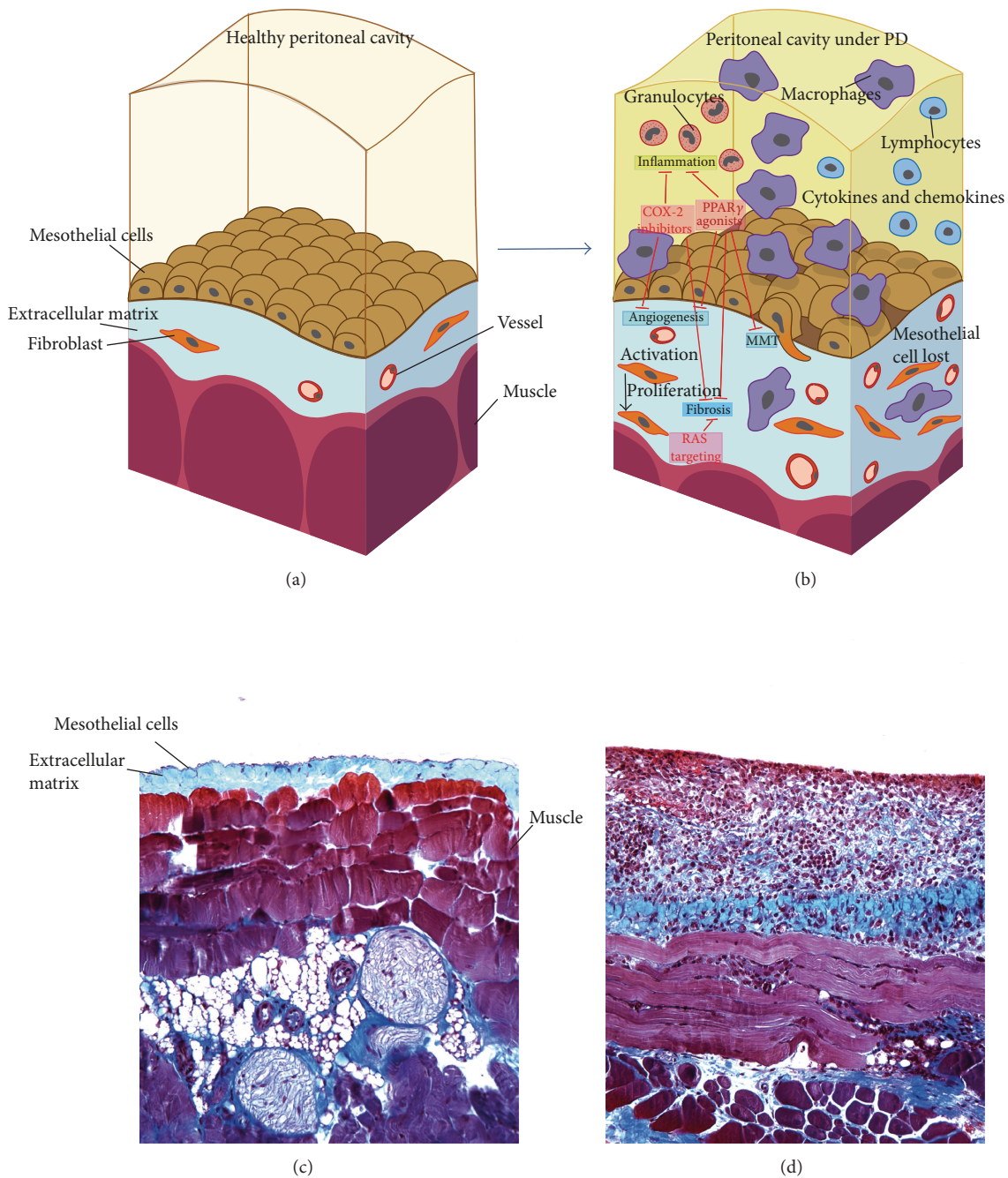


FIGURE 1: PM schemas and biopsies representing the normal peritoneal structure and its changes during PD. Possible therapeutic approaches. (a) and (b) are adapted with permission from Aguilera et al. (2013). Available from <http://www.intechopen.com/books/the-latest-in-peritoneal-dialysis/the-mesothelial-to-mesenchymal-transition-a-pathogenic-and-therapeutic-key-for-peritoneal-membrane-f> [80]. (a) Realistic representation of a healthy peritoneal cavity. A preservation of the mesothelial layer is clearly seen, only a few fibroblasts and vessels are visible, and only a small layer of extracellular matrix lies in the compact zone of the muscle layer. (b) After exposure to PD liquids, the structure of the PM starts to change dramatically with the appearance of more fibroblasts, macrophages, and inflammatory cytokines and finally with deposition of more extracellular matrix (ECM) cells. Inflammation and fibrosis will be the result of these changes. Some drugs like COX-2 inhibitors, PPAR $\gamma$  agonists, or RAS targeting are possible therapeutic strategies to protect from PD complications such as inflammation, angiogenesis, fibrosis, and/or MMT. (c) A peritoneal biopsy of a mouse peritoneal membrane that was treated with physiological saline is shown as control. The PM is well preserved and fibrotic response is absent. (d) Peritoneal biopsy of a mouse PM that was exposed to PDF for 40 days. A significant fibrotic response can be observed with a larger ECM and many inflammatory cells.

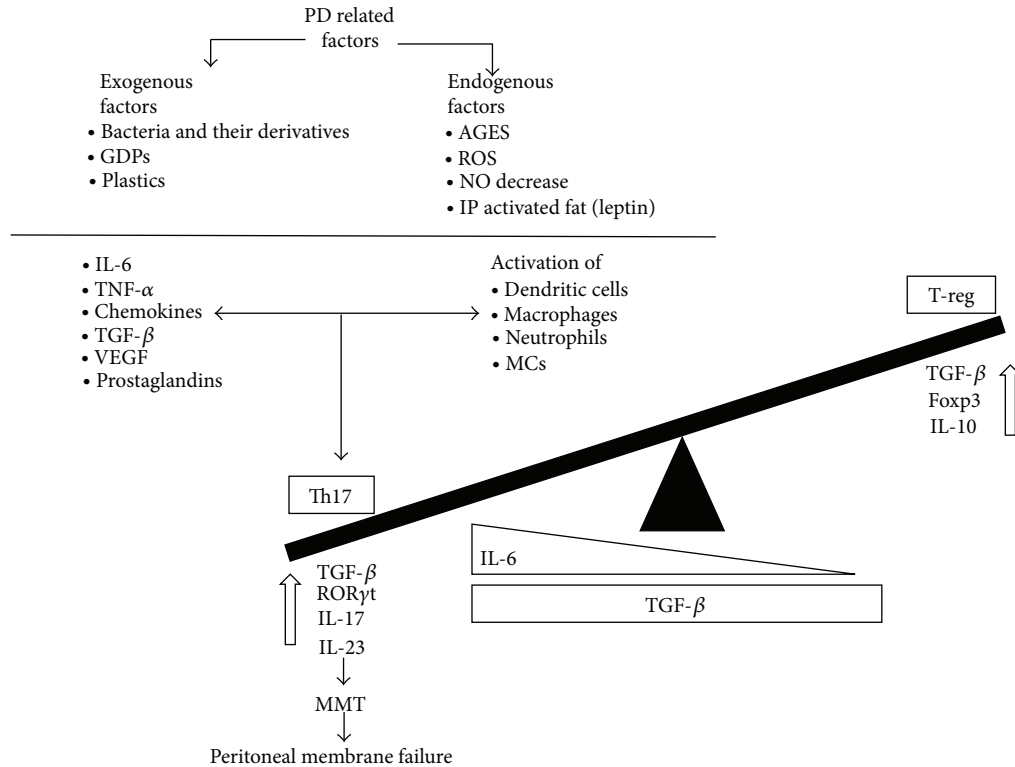


FIGURE 2: Mechanisms of Th17/Treg-balance in the peritoneal cavity in PD. Th17 predominance. In the peritoneal cavity local factors activate dendritic cells, macrophages, and neutrophils to produce proinflammatory molecules (IL-6, TNF $\alpha$ , TGF- $\beta$ , VEGF, chemokines, and prostaglandins). Immune cells and proinflammatory molecules are reciprocally activated; thus cells induce proinflammatory molecule release and vice versa. These molecules activate Th17 cells and IL-17 production, which may result in fibrosis and MMT. This occurs in the presence of continuously high TGF- $\beta$  levels. In contrast, in the presence of inactive immune cells together with low IL-6 levels, Treg cells are activated, releasing IL-10 and TGF- $\beta$  that may block MMT. Abbreviations: GDPs: glucose-derived products. IP: intraperitoneal. AGES: advanced glycation end products.

highlighted the roles of Th17/Treg/Th1/Th2 responses in the pathogenesis of tissue fibrosis [46, 47]. Among these responses, Th17 cells may mediate strong inflammation by producing a cocktail of cytokines such as IL-6, IL-17A, IL-17F, and IL-22, among which IL-17A has been characterized as the major effector cytokine in causing a sustained inflammatory response.

Recent studies have investigated the role of Th17 response in fibrosis. It has been reported that administration of IL-17A *in vitro* increased the synthesis and secretion of collagen in alveolar epithelial cells in a pulmonary fibrosis model. Moreover, all IL-17-associated signaling pathways were mainly activated in fibrotic lung biopsies, and a blockade of IL-17A attenuated tissue injury, inflammation, and fibrosis in acute and chronic injuries [48].

Furthermore, IL-17 has also been reported to be involved in the pathogenesis of chronic liver fibrosis [44, 49–51]. The same mechanism was proposed in another study on liver damage in chronic hepatitis B patients who presented an elevated Th17 cells population [52].

Th17 cells also play a crucial role in autoimmune myocarditis, as based on *in vitro* and *in vivo* experiments which confirm that IL-17 induced cardiac fibrosis by activating the protein kinase C- $\beta$ /Erk1/2/NF- $\kappa$ B pathway [53].

Moreover, the regulatory molecule CD69, through the regulation of Th17 effector responses, limits myocardial inflammation, fibrosis, and subsequent heart failure [54].

Recent studies have shown the importance of Th17 cells, and the hallmark cytokine IL-17A, in immune-mediated glomerulonephritis, including experimental antimyeloperoxidase glomerulonephritis, crescentic glomerulonephritis, and lupus nephritis [55, 56]. Th17 cells participate in renal damage, as demonstrated by an experimental study in mice showing that Th17 cell injection caused albuminuria and neutrophils infiltration in the kidney [57]. Recent studies also show the presence of Th17 cells and elevated renal production of IL-17A in nonimmune experimental renal diseases, including a model of unilateral ureteral obstruction [58]. In experimental ischaemia reperfusion, neutrophils, but not Th17 cells, were the main sources of IL-17A and contribute to renal injury by natural killer T activation and IL-12/IFN- $\gamma$  production [59]. In renal allograft rejection, positive staining for IL-17A has been detected in tubular cells [60], as we have observed in an experimental model of CCN2-mediated renal damage, suggesting that renal cells could produce this cytokine and contribute to extending the damage. With this model we recently demonstrated that a blockade of IL-17A diminished renal inflammation [58].

Based on all the above studies, IL-17 has been proposed as a drug target in many fibrotic diseases [61].

#### 4. Regulatory T Cells and Tissue Fibrosis

Although an induced Th17 response is connected to fibrogenesis, a relative decrease in the number of Treg cells may also be involved in the pathogenesis of inflammatory and fibrotic diseases. The evaluation of these cells in the context of experimentally induced fibrosis has been challenging, and Treg depletion in mice has been demonstrated to attenuate the development of lung fibrosis [62]. Moreover, in an experimental animal model of cardiac fibrosis, the depletion of Treg cells and/or adoptive transfer of isolated Tregs ameliorated cardiac fibrosis, indicating a protective role of regulatory T cell in tissue fibrosis [63]. Recently, it has been reported that Treg cells are essential for preventing from accumulation of fibrocytes and collagen deposition in a pulmonary disease animal model. In this study, it was shown that a blockade of Treg cells increased the accumulation of solid collagen and progression of the disease [64]. Finally, in another study (Keloid fibrotic disease) the potential role of Treg cells in attenuating collagen synthesis was investigated. This group found that the imbalance of Tregs may contribute to the development of this fibrotic disease and that the correction of this imbalance may be of therapeutic value [65].

#### 5. Th17 and Treg Lymphocyte Subsets in the Peritoneal Cavity on PD

PD-related factors locally stimulate Th17 cells and can be subdivided into two groups: exogenous and endogenous. The exogenous factors include bacteria and their derivatives, which enter into the peritoneal cavity through PD-catheter or via intestinal translocation and can provoke peritonitis episodes [66]. Peritoneal endogenous factors such as AGEs [67] could be involved in the induction of IL-17 levels by activating IL-6 and TGF- $\beta$  proinflammatory cytokines, respectively. Although there is little data regarding how advanced glycation end products (AGEs) are implicated in peritoneal dialysis damage, their implication in posttransplantation and diabetic kidneys showed an induction of IL-6 and TGF- $\beta$ , which are promoters of Th17 differentiation (Figure 2). Thus, it is plausible that the induced Th17 activity may have a poor fate in peritoneal damage during peritoneal dialysis. In nondiabetic PD patients, an elevation of IL-17 in peritoneal cavity effluents followed by a peritonitis episode was demonstrated [66], which is one of the main complications that lead to peritoneal fibrosis in PD patients [3].

Currently, it is accepted that mesothelial to mesenchymal transition (MMT) is a key process in PM survival in PD. Mesothelial cells lose their basolateral and basoapical polarity, acquiring a fibroblastoid phenotype with migration capacity. The cells invade the submesothelial compact zone where they synthesize ECM and VEGF, which are responsible for fibrosis and angiogenesis, respectively [68, 69]. IL-17 itself is capable of inducing epithelial to mesenchymal transition

in bronchial cells [70]. Although this effect has not been demonstrated in the peritoneum, it is very likely that IL-17 also contributes to PM deterioration via MMT induction.

The definitive evidence on IL-17 involvement in PM damage on PD was recently provided by Rodrigues-Díez et al. (2014). This study demonstrated in both mice and human samples that IL-17 is overexpressed in peritoneal biopsies. This was the first report to demonstrate that IL-17 participates in the typical fibrotic changes suffered in PM during long-term PD (induced fibronectin,  $\alpha$ -smooth muscle actin, and fibroblast specific protein-1 expression). Moreover, to better elucidate the effects of IL-17 on PM, intraperitoneal IL-17 was injected in mice, reproducing the changes that normally take place in PD patients. On the other hand, the use of a neutralizing IL-17A antibody injected intraperitoneally in mice exposed to PDF for 35 days blockaded the anatomical changes in the PM and reduced peritoneal fibrosis [71].

On the other hand, Treg cells are strongly connected with immune tolerance. Patients in end-stage renal disease with their suppressed immune response suffer impaired Treg cell responses [72]. Currently, there is not much evidence regarding the role of Treg cells in the peritoneal cavity during PD. To our knowledge, there is one study focusing on the function of Treg cells on peritoneal damage. This study concluded that rosiglitazone, a PPAR $\gamma$  agonist, augments the intraperitoneal IL-10 levels (Treg-associated cytokine), increases the recruitment of CD4<sup>+</sup> CD25<sup>+</sup> FoxP3<sup>+</sup> (regulatory T cells), and finally attenuates peritoneal fibrosis in an experimental mouse PD model [73].

Evidence suggests that Th17 cells share common progenitors with Treg cells and that the developmental pathways of these two subsets are reciprocally regulated [74]. In fact, it has been recently demonstrated that a reduction in IL-17 secretion due to Treg cell activation is associated with a diminished fibrotic response specifically in PD. The vitamin D pathway has been shown to regulate inflammatory responses. In regard to this, the effect of paricalcitol, a vitamin D receptor activator, was tested in a mouse model of PD to evaluate its effect on inflammatory cells and on the outcome of peritoneal fibrosis. It was found that the group that was treated with PDF presented increased levels of IL-17 cytokine in the peritoneal effluents compared with the group that was treated with paricalcitol diluted in the PDF. Moreover, the increased IL-17 concentration was perfectly correlated with the thickness of the peritoneum, meaning IL-17 is a profibrotic cytokine. This effect was related to an increased number of Tregs in the group that was treated with paricalcitol [75].

#### 6. Therapeutic Approaches to Prevent Peritoneal Damage Using the Th17/Treg-Axis: From Animal Models to PD Patients

Accepting the evidence above that Th17 and Treg subsets are involved in peritoneal damage in PD, we propose the following therapeutic strategies.

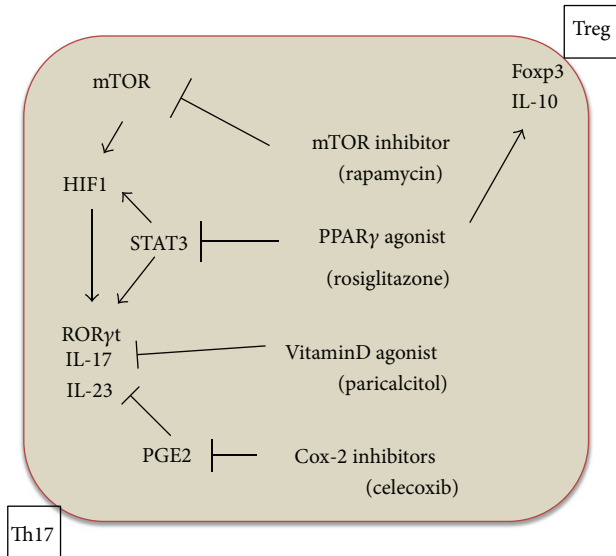


FIGURE 3: Therapeutic approaches to prevent peritoneal damage using the Th17/Treg-axis as a target. One of the most important modulators of Th17/Treg activity is the concentration of branch chain amino acids (BCAA). Although the data in relation to BCAA plasma levels in a uraemic state are contradictory, many articles indicate that these amino acids are decreased in uraemia due to systemic acidosis, inflammation, amino acid misbalances, and liquid overload. Normal or relative normal BCAA levels activate an mTOR (mammalian Target of Rapamycin) cascade including HIF1 and ROR $\gamma$ t and subsequently IL-17 and IL-23 production. Rapamycin, an mTOR inhibitor, would block this cascade, thus providing an anti-inflammatory/antifibrotic and possibly anti-MMT effect. Moreover, PPAR $\gamma$  agonists can also inhibit Th17 differentiation through a direct blockade of Stat3 transcription factor and HIF-1. Ultimately ROR $\gamma$ t is downregulated, and IL-17 and IL-23 production is decreased. However the PPAR $\gamma$  agonists are also able to act on the anti-inflammatory cascade. In the peritoneal cavity in PD, rosiglitazone augments IL-10 levels and Treg activity (upregulation of FoxP3<sup>+</sup>). This process could be one of the most important mechanisms by which PPAR $\gamma$  agonists protect the PM. In addition, paricalcitol, a specific vitamin D activator, has been recently shown to inhibit IL-17 production and PM fibrosis and possibly decrease MMT. Finally, celecoxib, a Cox2 inhibitor, decreases IL-17 production by blocking the E2 prostaglandin levels and thus attenuates the PM damage induced by PDF.

### 6.1. Use Drugs and Molecular Strategies

**6.1.1. mTOR Inhibitors.** The mTOR inhibition by Rapamycin may diminish IL-17 production. The mTOR activation induces hypoxia induced factor-1 (HIF-1) and ROR $\gamma$ t activation and subsequently IL-17 and IL-23 production [76]. Thus, these drugs may provide an anti-inflammatory/antifibrotic effect and possibly an anti-MMT action as was demonstrated by Aguilera et al. [77] (Figure 3).

**6.1.2. Peroxisome Proliferator-Activated Receptors- (PPAR-)  $\gamma$  Agonists.** The use of PPAR $\gamma$  agonists, for example, rosiglitazone, may be a therapeutic alternative to prevent peritoneal damage [78]. These receptors show a double protective effect.

First, they inhibit the Th17 differentiation via a Stat3 cascade blockade, which results in a downregulation of ROR $\gamma$ t and a decrease in IL-17 production [79]. Moreover, in an animal model study in which the effect of rosiglitazone in the preservation of the peritoneal membrane was investigated, it was found that rosiglitazone augmented the intraperitoneal IL-10 levels (Treg-associated cytokine) and increased the recruitment of CD4<sup>+</sup> CD25<sup>+</sup> FoxP3<sup>+</sup> (regulatory T cells) [73] (Figure 3).

**6.1.3. Vitamin D Receptor Activators.** Another interesting drug that could ultimately have a beneficial effect on PM in PD is paricalcitol. Using a mice PD model, it was demonstrated that the PM thickening was reduced in mice treated with paricalcitol in comparison with the nontreated group. Moreover, in the effluents of mice treated with paricalcitol, an increased number of Treg cells and lower IL-17 levels were found in comparison with the nontreated group. In addition, the IL-17 levels measured in peritoneal effluent showed a positive linear correlation with the PM thickness [75]. These data suggest a direct involvement of IL-17 in peritoneal injury and paricalcitol may act on this target (Figure 3).

**6.1.4. COX-2 Inhibitors.** Celecoxib, a cyclooxygenase- (Cox-) 2 inhibitor agent, was shown to prevent the PM damage in PD when administrated orally to a group of mice in PD, acting directly on the inflammatory cascade in general. After 5 weeks of treatment, the celecoxib group showed a fibrotic response similar to healthy controls, while the untreated group exposed to PD only developed considerable fibrosis [19] (Figure 3).

## 7. Discussion

One of the most devastating complications of PD treatment is peritoneal fibrosis. The endogenous and exogenous factors mentioned above related to PDF generate a chronic inflammatory response in the peritoneal cavity. The balance between Th17 and Treg cells is guided by proinflammatory cytokines secreted from Th17 cells and anti-inflammatory cytokines produced from regulatory T cells. Any factor that may alter this balance can lead to peritoneal deterioration and finally to peritoneal damage. The high levels of various proinflammatory molecules such as IL-6 and TGF- $\beta$  cytokines during PD create an environment that induces a chronic inflammatory condition in the peritoneal cavity and generates peritoneal fibrosis. This emergent concept suggests that the immune imbalance is the fundamental key for PM deterioration in PD.

Moreover, Th17 signaling with high IL-17 levels has been implicated in the aetiology of several types of inflammatory and fibrotic diseases. Therefore, components of the IL-17 and Treg cells pathway are considered highly “druggable” and are important targets for the treatment of these inflammatory and fibrotic diseases. Current evidence indicates that IL-17 inhibition and Treg activation are logical therapeutic strategies for the treatment of animal peritoneal fibrosis [71, 73, 75].

In conclusion, the importance of developing new therapies to protect the peritoneal membrane blocking the IL-17 secretion or activating the Treg pathway has been demonstrated. Some novel therapeutic strategies tested in animal models and *in vitro* include the administration of m-Tor inhibitors, PPAR $\gamma$  agonists, vitamin D receptor activators, and Cox-2 inhibitors. Lessons learned from regulators of Th17/Treg-axis may aid in the future clinical implementation of these agents with the goal of reducing peritoneal fibrosis and improving patients' life undergoing PD.

## 8. Conclusion

PD-related factors are responsible for Th17 activation/Treg deactivation in the peritoneal cavity during peritoneal dialysis. The Th17/Treg-axis is important for maintaining the anatomical and functional integrity of the PM. Therefore, the Th17/Treg-axis may be considered a future therapeutic target.

## Conflict of Interests

The authors declare that there is no conflict of interests regarding the publication of this paper.

## Acknowledgments

This work was supported in part by grants from Ministerio de Economía y competitividad SAF2010-21249 to Manuel López-Cabrera, Comunidad Autónoma de Madrid 2010-BMD2321 (FIBROTEAM) to Manuel Lopez Cabrera, and Fondo de Investigaciones Sanitarias RETICS 06/0016 and PI 09/0064 to Rafael Selgas and FIS 12/01175 to Abelardo Aguilera Peralta. Georgios Liappas is fully supported from European Union, Seventh Framework Program "EuTRiPD," under Grant Agreement PITN-GA-2011-287813. The authors would like to thank Juliette Siegfried and her team at ServingMed.com for editing the language of the paper.

## References

- [1] J. D. Williams, K. J. Craig, N. Topley et al., "Morphologic changes in the peritoneal membrane of patients with renal disease," *Journal of the American Society of Nephrology*, vol. 13, no. 2, pp. 470–479, 2002.
- [2] C. Chaimovitz, "Peritoneal dialysis," *Kidney International*, vol. 45, no. 4, pp. 1226–1240, 1994.
- [3] R. T. Krediet, "The peritoneal membrane in chronic peritoneal dialysis," *Kidney International*, vol. 55, no. 1, pp. 341–356, 1999.
- [4] J. Waniewski, "Peritoneal fluid transport: mechanisms, pathways, methods of assessment," *Archives of Medical Research*, vol. 44, no. 8, pp. 576–583, 2013.
- [5] J. Nevado, C. Peiró, S. Vallejo et al., "Amadori adducts activate nuclear factor-kappaB-related proinflammatory genes in cultured human peritoneal mesothelial cells," *British Journal of Pharmacology*, vol. 146, no. 2, pp. 268–279, 2005.
- [6] G. R. Silberhumer, H. Pokorny, G. Györi, and F. Mühlbacher, "Surgical aspects of peritoneal dialysis," *Wiener Medizinische Wochenschrift*, vol. 163, no. 11-12, pp. 288–294, 2013.
- [7] L. F. Fried, J. Bernardini, J. R. Johnston, and B. Piraino, "Peritonitis influences mortality in peritoneal dialysis patients," *Journal of the American Society of Nephrology*, vol. 7, no. 10, pp. 2176–2182, 1996.
- [8] M. A. M. Mateijssen, A. C. van der Wal, P. M. E. M. Hendriks et al., "Vascular and interstitial changes in the peritoneum of CAPD patients with peritoneal sclerosis," *Peritoneal Dialysis International*, vol. 19, no. 6, pp. 517–525, 1999.
- [9] L. S. Aroeira, A. Aguilera, J. A. Sánchez-Tomero et al., "Epithelial to mesenchymal transition and peritoneal membrane failure in peritoneal dialysis patients: Pathologic significance and potential therapeutic interventions," *Journal of the American Society of Nephrology*, vol. 18, no. 7, pp. 2004–2013, 2007.
- [10] A. Lupo, C. Rugu, A. Lapolla et al., "The dialytic failure of the peritoneal membrane," *Contributions to Nephrology*, vol. 131, pp. 90–96, 2001.
- [11] J. Plum, S. Hermann, A. Fuschöller et al., "Peritoneal sclerosis in peritoneal dialysis patients related to dialysis settings and peritoneal transport properties," *Kidney International, Supplement*, vol. 59, no. 78, pp. S42–S47, 2001.
- [12] O. Devuyt, P. J. Margetts, and N. Topley, "The pathophysiology of the peritoneal membrane," *Journal of the American Society of Nephrology*, vol. 21, no. 7, pp. 1077–1085, 2010.
- [13] K. Wieczorowska-Tobis, A. Styszynski, A. Breborowicz, and D. G. Oreopoulos, "Comparison of the biocompatibility of phosphate-buffered saline alone, phosphate-buffered saline supplemented with glucose, and Dianeal 3.86%," *Peritoneal Dialysis International*, vol. 21, no. 3, pp. S362–S364, 2001.
- [14] C. J. Holmes, "Biocompatibility of peritoneal dialysis solutions," *Peritoneal Dialysis International*, vol. 13, no. 2, pp. 88–94, 1993.
- [15] A. J. Collins, W. Hao, H. Xia et al., "Mortality risks of peritoneal dialysis and hemodialysis," *The American Journal of Kidney Diseases*, vol. 34, no. 6, pp. 1065–1074, 1999.
- [16] R. Selgas, M.-J. Fernandez-Reyes, E. Bosque et al., "Functional longevity of the human peritoneum: how long is continuous peritoneal dialysis possible? Results of a prospective medium long-term study," *American Journal of Kidney Diseases*, vol. 23, no. 1, pp. 64–73, 1994.
- [17] R. Pecoits-Filho, P. Stenvinkel, A. Yee-Moon Wang, O. Heimbürger, and B. Lindholm, "Chronic inflammation in peritoneal dialysis: the search for the holy grail?" *Peritoneal Dialysis International*, vol. 24, no. 4, pp. 327–339, 2004.
- [18] G. T. González-Mateo, J. Loureiro, J. A. Jiménez-Hefferman et al., "Chronic exposure of mouse peritoneum to peritoneal dialysis fluid: structural and functional alterations of the peritoneal membrane," *Peritoneal Dialysis International*, vol. 29, no. 2, pp. 227–230, 2009.
- [19] L. S. Aroeira, E. Lara-Pezzi, J. Loureiro et al., "Cyclooxygenase-2 mediates dialysate-induced alterations of the peritoneal membrane," *Journal of the American Society of Nephrology*, vol. 20, no. 3, pp. 582–592, 2009.
- [20] I. Griveas, G. Visvardis, A. Fleva et al., "Lymphocytes subsets in the course of continuous ambulatory peritoneal dialysis (CAPD)," *Renal Failure*, vol. 26, no. 6, pp. 641–646, 2004.
- [21] A. Glik and A. Douvdevani, "T lymphocytes: the 'cellular' arm of acquired immunity in the peritoneum," *Peritoneal Dialysis International*, vol. 26, no. 4, pp. 438–448, 2006.
- [22] T. R. Mosmann and R. L. Coffman, "TH1 and TH2 cells: different patterns of lymphokine secretion lead to different functional properties," *Annual Review of Immunology*, vol. 7, pp. 145–173, 1989.
- [23] T. Yokoyama, K. Nitta, K. Futatsuyama et al., "Identification of T helper cell subsets in continuous ambulatory peritoneal dialysis patients," *Nephron*, vol. 89, no. 2, pp. 215–218, 2001.

- [24] A. Brauner, B. Hylander, and B. Wretling, "Tumor necrosis factor- $\alpha$ , interleukin- $1\beta$ , and interleukin-1 receptor antagonist in dialysate and serum from patients on continuous ambulatory peritoneal dialysis," *The American Journal of Kidney Diseases*, vol. 27, no. 3, pp. 402–408, 1996.
- [25] H.-H. Wang and C.-Y. Lin, "Interleukin-12 and -18 levels in peritoneal dialysate effluent correlate with the outcome of peritonitis in patients undergoing peritoneal dialysis: implications for the type I/type II T-cell immune response," *American Journal of Kidney Diseases*, vol. 46, no. 2, pp. 328–338, 2005.
- [26] P. Martín, M. Gómez, A. Lamana et al., "CD69 association with Jak3/Stat5 proteins regulates Th17 cell differentiation," *Molecular and Cellular Biology*, vol. 30, no. 20, pp. 4877–4889, 2010.
- [27] E. Bettelli, Y. Carrier, W. Gao et al., "Reciprocal developmental pathways for the generation of pathogenic effector TH17 and regulatory T cells," *Nature*, vol. 441, no. 7090, pp. 235–238, 2006.
- [28] D. R. Littman and A. Y. Rudensky, "Th17 and regulatory T cells in mediating and restraining inflammation," *Cell*, vol. 140, no. 6, pp. 845–858, 2010.
- [29] J. C. Waite and D. Skokos, "Th17 response and inflammatory autoimmune diseases," *International Journal of Inflammation*, vol. 2012, Article ID 819467, 10 pages, 2012.
- [30] I. I. Ivanov, B. S. McKenzie, L. Zhou et al., "The orphan nuclear receptor ROR $\gamma$ t directs the differentiation program of proinflammatory IL-17<sup>+</sup> T helper cells," *Cell*, vol. 126, no. 6, pp. 1121–1133, 2006.
- [31] T. J. Harris, J. F. Grosso, H.-R. Yen et al., "An in vivo requirement for STAT3 signaling in TH17 development and TH17-dependent autoimmunity," *Journal of Immunology*, vol. 179, no. 7, pp. 4313–4317, 2007.
- [32] X. O. Yang, A. D. Panopoulos, R. Nurieva et al., "STAT3 regulates cytokine-mediated generation of inflammatory helper T cells," *Journal of Biological Chemistry*, vol. 282, no. 13, pp. 9358–9363, 2007.
- [33] L. Zhou, J. E. Lopes, M. M. W. Chong et al., "TGF- $\beta$ -induced Foxp3 inhibits T<sub>H</sub>17 cell differentiation by antagonizing ROR $\gamma$ t function," *Nature*, vol. 453, no. 7192, pp. 236–240, 2008.
- [34] J. M. Kim, J. P. Rasmussen, and A. Y. Rudensky, "Regulatory T cells prevent catastrophic autoimmunity throughout the lifespan of mice," *Nature Immunology*, vol. 8, no. 2, pp. 191–197, 2007.
- [35] K. Lahl, C. Loddenkemper, C. Drouin et al., "Selective depletion of Foxp3<sup>+</sup> regulatory T cells induces a scurfy-like disease," *Journal of Experimental Medicine*, vol. 204, no. 1, pp. 57–63, 2007.
- [36] M. Veldhoen, R. J. Hocking, C. J. Atkins, R. M. Locksley, and B. Stockinger, "TGF $\beta$  in the context of an inflammatory cytokine milieu supports de novo differentiation of IL-17-producing T cells," *Immunity*, vol. 24, no. 2, pp. 179–189, 2006.
- [37] P. R. Mangan, L. E. Harrington, D. B. O'Quinn et al., "Transforming growth factor- $\beta$  induces development of the T<sub>H</sub>17 lineage," *Nature*, vol. 441, no. 7090, pp. 231–234, 2006.
- [38] H. P. Eugster, K. Frei, M. Kopf, H. Lassmann, and A. Fontana, "IL-6-deficient mice resist myelin oligodendrocyte glycoprotein-induced autoimmune encephalomyelitis," *European Journal of Immunology*, vol. 28, no. 7, pp. 2178–2187, 1998.
- [39] E. B. Samoilova, J. L. Horton, B. Hilliard, T.-S. T. Liu, and Y. Chen, "IL-6-deficient mice are resistant to experimental autoimmune encephalomyelitis: roles of IL-6 in the activation and differentiation of autoreactive T cells," *Journal of Immunology*, vol. 161, no. 12, pp. 6480–6486, 1998.
- [40] T. Korn, A. C. Anderson, E. Bettelli, and M. Oukka, "The dynamics of effector T cells and Foxp3<sup>+</sup> regulatory T cells in the promotion and regulation of autoimmune encephalomyelitis," *Journal of Neuroimmunology*, vol. 191, no. 1–2, pp. 51–60, 2007.
- [41] S. Tamada, T. Asai, N. Kuwabara et al., "Molecular mechanisms and therapeutic strategies of chronic renal injury: the role of nuclear factor  $\kappa$ B activation in the development of renal fibrosis," *Journal of Pharmacological Sciences*, vol. 100, no. 1, pp. 17–21, 2006.
- [42] L. M. Blanco-Colio, J. L. Martín-Ventura, B. Muñoz-García et al., "TWEAK and Fn14. New players in the pathogenesis of atherosclerosis," *Frontiers in Bioscience*, vol. 12, no. 10, pp. 3648–3655, 2007.
- [43] T. A. Wynn, "Cellular and molecular mechanisms of fibrosis," *The Journal of Pathology*, vol. 214, no. 2, pp. 199–210, 2008.
- [44] Z. Tan, X. Qian, R. Jiang et al., "IL-17A plays a critical role in the pathogenesis of liver fibrosis through hepatic stellate cell activation," *Journal of Immunology*, vol. 191, no. 4, pp. 1835–1844, 2013.
- [45] S. A. Hasan, B. Eksteen, D. Reid et al., "Role of IL-17A and neutrophils in fibrosis in experimental hypersensitivity pneumonitis," *The Journal of Allergy and Clinical Immunology*, vol. 131, no. 6, pp. 1663.e5–1673.e5, 2013.
- [46] H.-Z. Yang, B. Cui, H.-Z. Liu et al., "Targeting TLR2 attenuates pulmonary inflammation and fibrosis by reversion of suppressive immune microenvironment," *The Journal of Immunology*, vol. 182, no. 1, pp. 692–702, 2009.
- [47] K. J. Aitken, C. Tolg, T. Panchal et al., "Mammalian target of rapamycin (mTOR) induces proliferation and de-differentiation responses to three coordinate pathophysiologic stimuli (mechanical strain, hypoxia, and extracellular matrix remodeling) in rat bladder smooth muscle," *The American Journal of Pathology*, vol. 176, no. 1, pp. 304–319, 2010.
- [48] S. Mi, Z. Li, H.-Z. Yang et al., "Blocking IL-17A promotes the resolution of pulmonary inflammation and fibrosis via TGF- $\beta$ -dependent and -independent mechanisms," *Journal of Immunology*, vol. 187, no. 6, pp. 3003–3014, 2011.
- [49] L. Wang, S. Chen, and K. Xu, "IL-17 expression is correlated with hepatitis B-related liver diseases and fibrosis," *International Journal of Molecular Medicine*, vol. 27, no. 3, pp. 385–392, 2011.
- [50] A. Lemmers, C. Moreno, T. Gustot et al., "The interleukin-17 pathway is involved in human alcoholic liver disease," *Hepatology*, vol. 49, no. 2, pp. 646–657, 2009.
- [51] D. Fenoglio, F. Bernuzzi, F. Battaglia et al., "Th17 and regulatory T lymphocytes in primary biliary cirrhosis and systemic sclerosis as models of autoimmune fibrotic diseases," *Autoimmunity Reviews*, vol. 12, no. 2, pp. 300–304, 2012.
- [52] J.-Y. Zhang, Z. Zhang, F. Lin et al., "Interleukin-17-producing CD4<sup>+</sup> T cells increase with severity of liver damage in patients with chronic hepatitis B," *Hepatology*, vol. 51, no. 1, pp. 81–91, 2010.
- [53] Y. Liu, H. Zhu, Z. Su et al., "IL-17 contributes to cardiac fibrosis following experimental autoimmune myocarditis by a PKC $\beta$ /Erk1/2/NF- $\kappa$ B-dependent signaling pathway," *International Immunology*, vol. 24, no. 10, pp. 605–612, 2012.
- [54] A. Cruz-Adalia, L. J. Jiménez-Borreguero, M. Ramírez-Huesca et al., "CD69 limits the severity of cardiomyopathy after autoimmune myocarditis," *Circulation*, vol. 122, no. 14, pp. 1396–1404, 2010.
- [55] A. R. Kitching and S. R. Holdsworth, "The emergence of Th17 cells as effectors of renal injury," *Journal of the American Society of Nephrology*, vol. 22, no. 2, pp. 235–238, 2011.

- [56] J.-E. Turner, H.-J. Paust, O. M. Steinmetz, and U. Panzer, "The Th17 immune response in renal inflammation," *Kidney International*, vol. 77, no. 12, pp. 1070–1075, 2010.
- [57] S. A. Summers, O. M. Steinmetz, M. Li et al., "Th1 and Th17 cells induce proliferative glomerulonephritis," *Journal of the American Society of Nephrology*, vol. 20, no. 12, pp. 2518–2524, 2009.
- [58] R. Rodrigues-Díez, R. R. Rodrigues-Díez, S. Rayego-Mateos et al., "The C-terminal module IV of connective tissue growth factor is a novel immune modulator of the Th17 response," *Laboratory Investigation*, vol. 93, no. 7, pp. 812–824, 2013.
- [59] L. Li, L. Huang, A. L. Vergis et al., "IL-17 produced by neutrophils regulates IFN- $\gamma$ -mediated neutrophil migration in mouse kidney ischemia-reperfusion injury," *The Journal of Clinical Investigation*, vol. 120, no. 1, pp. 331–342, 2010.
- [60] A. Loverre, T. Tataranni, G. Castellano et al., "IL-17 expression by tubular epithelial cells in renal transplant recipients with acute antibody-mediated rejection," *The American Journal of Transplantation*, vol. 11, no. 6, pp. 1248–1259, 2011.
- [61] S. Ivanov and A. Lindén, "Interleukin-17 as a drug target in human disease," *Trends in Pharmacological Sciences*, vol. 30, no. 2, pp. 95–103, 2009.
- [62] F. Liu, J. Liu, D. Weng et al., "CD4+CD25+Foxp3+ regulatory T cells depletion may attenuate the development of silica-induced lung fibrosis in mice," *PLoS ONE*, vol. 5, no. 11, Article ID e15404, 2010.
- [63] Y. Cao, W. Xu, and S. Xiong, "Adoptive transfer of regulatory T Cells protects against Coxsackievirus B3-induced cardiac fibrosis," *PLoS ONE*, vol. 8, no. 9, Article ID e74955, 2013.
- [64] X. Peng, M. W. Moore, H. Peng et al., "CD4+CD25+FoxP3+ regulatory tregs inhibit fibrocyte recruitment and fibrosis via suppression of FGF-9 production in the TGF- $\beta$ 1 exposed murine lung," *Frontiers in Pharmacology*, vol. 5, article 80, 2014.
- [65] N. Murao, K.-I. Seino, T. Hayashi et al., "Treg-enriched CD4+ T cells attenuate collagen synthesis in keloid fibroblasts," *Experimental Dermatology*, vol. 23, no. 4, pp. 266–271, 2014.
- [66] H.-H. Wang, T.-Y. Lee, and C.-Y. Lin, "Kinetics and involvement of interleukin-17 in the outcome of peritonitis in nondiabetic patients undergoing peritoneal dialysis," *Journal of the Chinese Medical Association*, vol. 74, no. 1, pp. 11–15, 2011.
- [67] D. Maksić, M. Colić, V. Stanković-Popović, M. Radojević, and D. Bokonjić, "Systemic and intraperitoneal proinflammatory cytokines profiles in patients on chronic peritoneal dialysis," *Medicinski Pregled*, vol. 60, supplement 2, pp. 53–57, 2007.
- [68] J. Loureiro, G. González-Mateo, J. Jimenez-Heffernan, R. Selgas, M. López-Cabrera, and A. Aguilera Peralta, "Are the mesothelial-to-mesenchymal transition, sclerotic peritonitis syndromes, and encapsulating peritoneal sclerosis part of the same process?" *International Journal of Nephrology*, vol. 2013, Article ID 263285, 7 pages, 2013.
- [69] M. Yáñez-Mó, E. Lara-Pezzi, R. Selgas et al., "Peritoneal dialysis and epithelial-to-mesenchymal transition of mesothelial cells," *The New England Journal of Medicine*, vol. 348, no. 5, pp. 403–413, 2003.
- [70] X. Ji, J. Li, L. Xu et al., "IL4 and IL-17A provide a Th2/Th17-polarized inflammatory milieu in favor of TGF- $\beta$ 1 to induce bronchial epithelial-mesenchymal transition (EMT)," *International Journal of Clinical and Experimental Pathology*, vol. 6, no. 8, pp. 1481–1492, 2013.
- [71] R. Rodrigues-Díez, L. S. Aroeira, M. Orejudo et al., "IL-17A is a novel player in dialysis-induced peritoneal damage," *Kidney International*, vol. 86, pp. 303–315, 2014.
- [72] T. K. Hendrikx, E. A. F. J. Van Gurp, W. M. Mol et al., "End-stage renal failure and regulatory activities of CD4+CD25bright+FoxP3+ T-cells," *Nephrology Dialysis Transplantation*, vol. 24, no. 6, pp. 1969–1978, 2009.
- [73] P. Sandoval, J. Loureiro, G. González-Mateo et al., "PPAR- $\gamma$  agonist rosiglitazone protects peritoneal membrane from dialysis fluid-induced damage," *Laboratory Investigation*, vol. 90, no. 10, pp. 1517–1532, 2010.
- [74] A. Ueda, L. Zhou, and P. L. Stein, "Fyn promotes Th17 differentiation by regulating the kinetics of ROR $\gamma$ t and Foxp3 expression," *Journal of Immunology*, vol. 188, no. 11, pp. 5247–5256, 2012.
- [75] G. T. González-Mateo, V. Fernández-Míllara, T. Bellón et al., "Paricalcitol reduces peritoneal fibrosis in mice through the activation of regulatory T cells and reduction in IL-17 production," *PLoS ONE*, vol. 9, no. 10, Article ID e108477, 2014.
- [76] A. Ikejiri, S. Nagai, N. Goda et al., "Dynamic regulation of Th17 differentiation by oxygen concentrations," *International Immunology*, vol. 24, no. 3, pp. 137–146, 2012.
- [77] A. Aguilera, L. S. Aroeira, M. Ramírez-Huesca et al., "Effects of rapamycin on the epithelial-to-mesenchymal transition of human peritoneal mesothelial cells," *International Journal of Artificial Organs*, vol. 28, no. 2, pp. 164–169, 2005.
- [78] S. G. Kim and W. H. Lee, "AMPK-dependent metabolic regulation by PPAR agonists," *PPAR Research*, vol. 2010, Article ID 549101, 10 pages, 2010.
- [79] L. Klotz, S. Burgdorf, I. Dani et al., "The nuclear receptor PPAR $\gamma$  selectively inhibits Th17 differentiation in a T cell-intrinsic fashion and suppresses CNS autoimmunity," *The Journal of Experimental Medicine*, vol. 206, no. 10, pp. 2079–2089, 2009.
- [80] A. Aguilera, J. Loureiro, G. González-Mateo, R. Selgas, and M. López-Cabrera, "The mesothelial to mesenchymal transition a pathogenic and therapeutic key for peritoneal membrane failure," in *The Latest in Peritoneal Dialysis*, chapter 2, InTech, 2013.

## Research Article

# Morphological and Biomechanical Differences in the Elastase and AngII *apoE*<sup>-/-</sup> Rodent Models of Abdominal Aortic Aneurysms

Evan H. Phillips,<sup>1</sup> Alexa A. Yrineo,<sup>1</sup> Hilary D. Schroeder,<sup>1</sup> Katherine E. Wilson,<sup>2</sup> Ji-Xin Cheng,<sup>1</sup> and Craig J. Goergen<sup>1</sup>

<sup>1</sup>Weldon School of Biomedical Engineering, Purdue University, 206 S. Martin Jischke Drive, West Lafayette, IN 47907, USA

<sup>2</sup>Department of Biomedical Engineering, John A. White, Jr. Engineering Hall, 790 W. Dickson Street, Suite 120, Fayetteville, AR 72701, USA

Correspondence should be addressed to Evan H. Phillips; [phill128@purdue.edu](mailto:phill128@purdue.edu)

Received 11 October 2014; Accepted 18 December 2014

Academic Editor: Oreste Gualillo

Copyright © 2015 Evan H. Phillips et al. This is an open access article distributed under the Creative Commons Attribution License, which permits unrestricted use, distribution, and reproduction in any medium, provided the original work is properly cited.

An abdominal aortic aneurysm (AAA) is a potentially fatal cardiovascular disease with multifactorial development and progression. Two preclinical models of the disease (elastase perfusion and angiotensin II infusion in apolipoprotein-E-deficient animals) have been developed to study the disease during its initiation and progression. To date, most studies have used *ex vivo* methods to examine disease characteristics such as expanded aortic diameter or analytic methods to look at circulating biomarkers. Herein, we provide evidence from *in vivo* ultrasound studies of the temporal changes occurring in biomechanical parameters and macromolecules of the aortic wall in each model. We present findings from 28-day studies in elastase-perfused rats and AngII *apoE*<sup>-/-</sup> mice. While each model develops AAAs specific to their induction method, they both share characteristics with human aneurysms, such as marked changes in vessel strain and blood flow velocity. Histology and nonlinear microscopy confirmed that both elastin and collagen, both important extracellular matrix molecules, are similarly affected in their levels and spatial distribution. Future studies could make use of the differences between these models in order to investigate mechanisms of disease progression or evaluate potential AAA treatments.

## 1. Introduction

Abdominal aortic aneurysms (AAAs) are a potentially life-threatening disease, generally defined as a focal dilation of the aorta to 50% above normal [1]. AAAs accounted for approximately 11,000 deaths in the United States in 2009 and had a prevalence rate of 12.5% for men 75 to 84 years of age in 2006 [2]. The maximum aortic diameter and rate of vessel expansion in patients are the most important clinical measures in monitoring AAA progression. However, the unpredictable nature of aortic aneurysm rupture has led to the active investigation of potential biomarkers and imaging strategies that can be used to better predict the risk of rupture or improve treatments [3].

Preclinical animal research is important to better understand aneurysm pathophysiology, identify biomarkers, and

develop treatment strategies that can be translated to the clinic. Researchers have used two common small animal models in order to investigate AAA disease progression [4, 5] or experimental treatment effects [6–8]. In one model, pressurized intra-aortic elastase perfusion in the infrarenal aorta of rats [9, 10] or mice [11] induces mechanical expansion of the vessel. The perfused region further expands as macrophages infiltrate the vessel wall and matrix proteins in the vessel wall remodel [9, 11]. With the second model, subcutaneous systemic infusion of angiotensin II (AngII) in genetically modified hyperlipidemic mice (*apoE*<sup>-/-</sup>) leads to aortic dissection and expansion of the suprarenal aorta [5, 12]. Due to these induction mechanisms, there are fundamental differences between each model, but they both mimic portions of the human disease [13]. Given the multifactorial

development of AAAs *in vivo*, studies that rigorously quantify and monitor progression in multiple disease models are of high value in contributing to our understanding of vessel dynamics and AAA heterogeneity.

Noninvasive imaging technologies used in the clinic, such as magnetic resonance imaging (MRI) and ultrasound (US), are now being used in preclinical AAA research [14]. Research groups have used MRI and US in longitudinal studies to monitor changes in aortic diameter [15–18] and vessel motion [19–21]. Without the aid of these noninvasive imaging techniques, studies are typically limited to a single experimental time point per animal. This increases the total number of animals needed and prevents studying further disease progression once the animal is sacrificed. Furthermore, dynamic *in vivo* measurements such as vessel motion and blood flow are not possible.

In this paper, we present the results of longitudinal ultrasound studies using the elastase and AngII *apoE*<sup>-/-</sup> animal models to compare the changes in four important anatomic and biomechanical parameters: aneurysm diameter, aneurysm volume, circumferential cyclic strain, and blood flow velocity. Additionally, we show results from semiquantitative AAA histological tissue analysis *ex vivo* to detect changes in elastin and collagen content for each model. Finally, we demonstrate the use of label-free nonlinear optical microscopy as a surrogate for histology. Our findings suggest that the biomechanical parameters measured here change drastically due to vessel wall remodeling as the aortic diameter and volume increase. By measuring these parameters in individual AAA rats and mice during disease progression, further *in vivo* studies investigating potential therapeutics can be performed.

## 2. Materials and Methods

**2.1. Animal Care and Maintenance.** Male Sprague Dawley rats (281–347 g; 10–11 weeks old) from Harlan Laboratories (Indianapolis, IN) and male and female apolipoprotein-E-deficient mice (20–36 g; 17 ± 7.8 weeks old; B6.129P2-*ApoE*<sup>*tm1Unc*</sup>/J strain) from The Jackson Laboratory (Bar Harbor, ME) were used for elastase perfusion and osmotic pump studies, respectively. All animals were allowed free access to standard rodent chow and water. We recorded animal weights prior to surgery, after surgery, and on subsequent study days. All studies lasted up to 29 days postsurgery at which point animals were euthanized (isoflurane and carbon dioxide asphyxiation). The Purdue Animal Care and Use Committee approved all experiments.

**2.2. Elastase Perfusion Surgery in Rats.** We induced AAAs in Sprague Dawley rats ( $n = 11$ ) using an intra-aortic elastase perfusion procedure described previously [9]. Briefly, the infrarenal aorta was surgically exposed in an anesthetized rat (2% isoflurane) and proximal and distal aortic sites were temporarily ligated with 6-0 silk sutures. Type I porcine pancreatic elastase solution (E1250, Lot number SLBD0685V; Sigma Aldrich, St. Louis, MO) was pressure-perfused (100 mm Hg) for 30 minutes into the ligated aorta through an aortotomy proximal to the aortic bifurcation. We

tested both low (0.44–0.48 U/mL;  $n = 6$ ) and high (25 U/mL;  $n = 5$ ) elastase solutions.

**2.3. Implantations of Angiotensin II-Loaded Miniosmotic Pumps in Mice.** We used a second AAA model [12] in which continuous angiotensin II (AngII) infusion in apolipoprotein-E-deficient (*apoE*<sup>-/-</sup>) mice induces suprarenal AAA formation typically between 3 and 14 days after implantation of miniosmotic pumps (ALZET Model 2004; DURECT Corporation, Cupertino, CA). AngII powder (MW: 1046.19; Bachem, Torrance, CA) was solubilized in 0.9% sodium chloride and loaded into miniosmotic pumps for systemic hormone delivery (1000 ng/kg/min infusion rate and 28-day duration) following subcutaneous implantation in the dorsum of mice ( $n = 7$ ).

**2.4. Small Animal Ultrasound Imaging.** We performed *in vivo* ultrasonography of rats and mice kept unconscious under inhalant anesthesia (1–2.5% isoflurane). Prior to imaging, animals were positioned supine on an adjustable heated stage and sterile eye lubricant was applied to each eye. We noninvasively monitored heart and respiration rate through stage electrodes and body temperature using a rectal probe. Hair on the ventral abdomen was removed with a depilatory cream and warm transmission ultrasound gel was applied on the exposed skin surface.

For detection and longitudinal monitoring of aortic diameter, aortic volume, vessel wall motion, and blood flow dynamics, we used a high-resolution small animal ultrasound system (Vevo2100 Imaging System; VisualSonics, Toronto, ON, Canada). We acquired transaxial and longitudinal ultrasound data prior to surgeries (day 0) and at days 3, 7, 14, 21, and 28 postsurgery using VisualSonics linear array transducers MS550D (25–55 MHz, 40 MHz center frequency) and MS250D (13–24 MHz, 21 MHz center frequency) in mice and rats, respectively. The transducer was positioned perpendicular to the animal and held in contact with the gel during imaging. We adjusted the angle of the stage as necessary to allow optimal visualization of the aorta in the long and short axes. We used anatomical landmarks, such as the inferior vena cava, renal veins, and aortic bifurcation, for orientation and the presence of vessel wall motion for discriminating arterial from venous flow.

High-resolution, two-dimensional cine loops in brightness mode (B-mode; 300 frames), motion mode (M-mode; five-second acquisition), pulsed wave (PW), and color Doppler (five-second acquisitions) were acquired in aortic regions with and without vessel expansion. We adjusted the transducer beam angle and PW Doppler angle (30–60 degrees from the vertical) in order to accurately detect the magnitude and direction of blood flow in the selected aortic area. Additionally, we used respiration and cardiac gating for transaxial B-mode volumes (0.19 mm step size) of the infrarenal aorta of rats (3 cm scan distance) and the suprarenal aorta of mice (1.5 cm scan distance).

**2.5. Blood Pressure Measurements.** We measured blood pressures from the tails of conscious *apoE*<sup>-/-</sup> mice in the study

prior to pump implantation and on days 3, 14, and 28 after implantation. Prior to implantation, mice were acclimated to restraint holders and the tail cuffs used for taking blood pressure measurements (CODA 2 Channel Standard, Kent Scientific, Torrington, CT).

**2.6. Ultrasound Analysis.** We analyzed all ultrasound data (days 0, 3, 7, 14, 21, and 28) from rats and mice with Vevo2100 software (VisualSonics) to determine maximum aortic diameter, AAA true and false lumen volumes, circumferential cyclic strain, and mean blood flow velocity. All measurements on cine loops were made in quintuplicate and averaged.

B-mode volumes of the abdominal aorta were segmented in a semiautomated fashion by drawing serial contours (step size: 760  $\mu\text{m}$  and smaller). The length and location of maximum AAA diameter in relation to the right renal artery in mice or the aortic bifurcation in rats were used to guide volume measurements at earlier time points. In other words, earlier day volumes were segmented over the same anatomical length and started at the same anatomical position. In the AngII *apoE*<sup>-/-</sup> mice, volumes of both the AAA lumen and total AAA (including the vessel wall) were segmented individually. False lumen volumes were calculated as the difference between the total AAA and the true lumen.

We further calculated effective maximum diameter from these segmented volumes. We identified the slice showing maximal aortic cross-sectional area and calculated effective maximum diameter using the equation for area of a circle and the measured area. In three instances, aortic diameter measurements from long-axis B-mode were substituted for the displayed effective maximum diameter measurements, as the collected volumes were not clear enough to provide effective maximum diameter values.

Aortic diameters in areas of maximal vessel expansion as seen in long axis were also measured from high-temporal resolution B-mode cine loops (50 frames/sec for MS250D; 233 frames/sec for MS550D). We employed a straight-line distance measurement tool to calculate the length from the posterior to anterior vessel wall at peak systole and end diastole, corresponding to systolic ( $D_S$ ) and diastolic ( $D_D$ ) diameters. Mean aortic diameter ( $D_M$ ) for a given animal on a given day was calculated as follows:

$$D_M = \frac{1}{3} [D_S - D_D] + D_D. \quad (1)$$

We calculated circumferential cyclic strain values from M-mode diameter measurements in areas showing maximum vessel expansion seen in long axis. The distance between two lines of strong specular reflection seen in the anterior and posterior vessel walls was used to determine maximum and minimum vessel wall displacement. These respective values correspond to the timing of peak systole and end diastole. In order to calculate Green-Lagrange circumferential cyclic strain, the following formula was used [20, 22]:

$$\frac{1}{2} \left[ \left( \frac{D_S}{D_D} \right)^2 - 1 \right] \times 100\%. \quad (2)$$

Curvature in the suprarenal aorta, however, requires a geometric correction to be applied to the initial diameter

( $D_i$ ) measurements made for the AngII *apoE*<sup>-/-</sup> mice. The angle ( $\theta$ ) between vertical and a line segment perpendicular to anterior and posterior vessel walls in the AAA was determined. Prior to the circumferential cyclic strain calculation above, the following equation was used to calculate geometrically corrected diameter ( $D_c$ ) values:

$$D_c = D_i * \cos \theta. \quad (3)$$

Mean blood flow velocity values were calculated from velocity waveforms on PW Doppler images. A velocity waveform area analysis tool was used to calculate this value over individual cardiac cycles displayed on a velocity/time plot.

**2.7. Animal Perfusion and Dissection.** After euthanasia, animals underwent a series of pressure perfusions through the left ventricle (transcardial perfusion). We successively perfused 0.9% sodium chloride (to flush the systemic vasculature), 4% paraformaldehyde (to fix the aorta), and 1% molten agarose (to preserve vessel patency upon cooling) using a syringe pump connected to a feeding needle or polyethylene tube (0.64 mm outer diameter) inserted in the left ventricle. The heart, aorta, and kidneys were later dissected from the animal and fixed in 4% paraformaldehyde for 24 hours. Aortic tissue was kept in phosphate-buffered saline until gross vessel dissection (four 2-3 mm-long cross-sections) in proximal, aneurysmal, and distal areas and then held in 70% alcohol until processing.

**2.8. Aortic Tissue Histology and Staining.** Aortic segments were paraffin-embedded, thin-sectioned (5  $\mu\text{m}$ ), and adjacent sections stained with hematoxylin and eosin (H&E), Verhoeff Van-Gieson (VVG)/hematoxylin, and Masson's trichrome (MTC) as per standard protocols. The latter two stains were used to differentiate elastin bands (black) and collagen fibers (blue), respectively, from surrounding structures. Stained tissue sections were scanned at 40x magnification.

**2.9. Nonlinear Optical Microscopy.** H&E-stained aortic sections were imaged using two nonlinear optical (NLO) microscopy techniques, two-photon excitation fluorescence (TPEF), and second harmonic generation (SHG) for label-free imaging of endogenous macromolecules. A custom-built femtosecond laser system (140 fs pulse width; 80 MHz repetition rate) was used for simultaneous TPEF/SHG imaging at 800 nm excitation (Chameleon Ultra I; Coherent, Santa Clara, CA). A tightly focused beam (39 mW average power) was directed through a 20x air or 60x water immersion objective on an inverted microscope (IX70, Olympus, Melville, NY). FV300 software (Olympus, Melville, NY) was used for image capture and thresholding of forward-emitted SHG and back-reflected TPEF autofluorescence signals detected by separate photomultiplier tubes (PMTs). A dichroic mirror (550dcxr, Chroma Technologies, Rockingham, VT) separated the excitation beam from back-reflected TPEF signal. Band-pass filters were chosen according to a previous publication focused on label-free imaging of collagen and elastin in swine arteries [23].

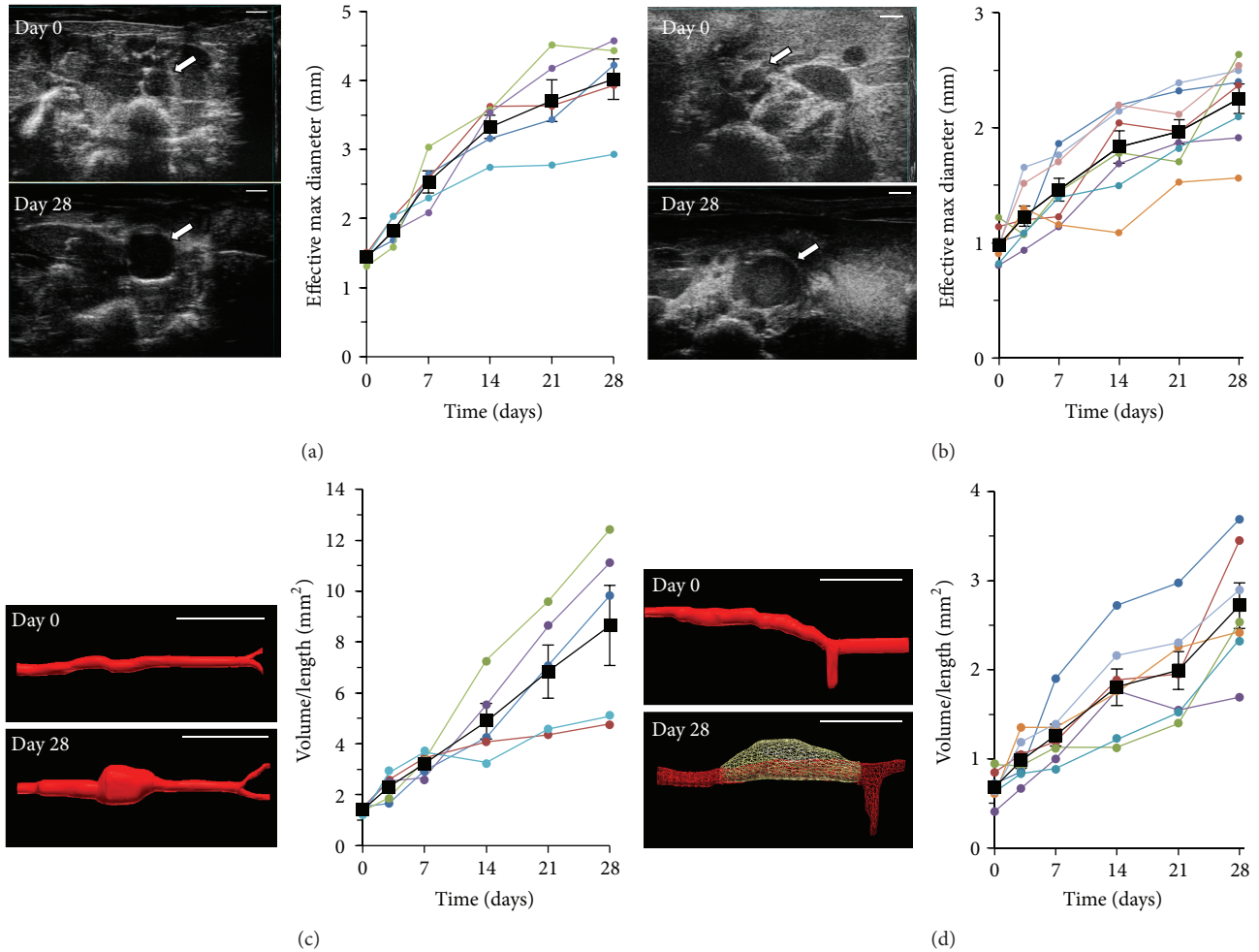


FIGURE 1: AAA diameter and volume increases over 28 days. Representative B-mode images (maximum aortic cross-section), aortic volumes (days 0 and 28), and longitudinal measurements of effective maximum diameter ((a), (b)) and volume/length ((c), (d)) in high-concentration-elastase rats ((a), (c)) and AngII *apoE*<sup>-/-</sup> mice ((b), (d)). Arrows point to abdominal aorta in cross-section. Volume segmentations: 30 mm in rats and 15 mm in mice (0.19 mm step size). Scale bars: 2 mm (a), 1 mm (b), 10 mm (c), and 5 mm (d).

**2.10. Image Processing and Semiquantitative Analysis.** VVG images of aneurysmal and control (i.e., proximal or distal) aortic sections from the suprarenal (AngII *apoE*<sup>-/-</sup> mice) or infrarenal (elastase rats) aortas were analyzed using a semiautomated thresholding technique described previously [20] to acquire semiquantitative measures of elastin area. The thresholding technique was further modified to generate binary images of collagen pixels from corresponding MTC images. Hand-selected regions of interest were placed in three locations on the aortic adventitia of each image to measure the density of pixels corresponding to collagen and averaged.

**2.11. Statistical Analysis.** We used paired *t*-tests and two-sample *t*-tests in order to assess statistical significance of a parameter between two time points or between AAA and a healthy region. Additionally, we used one-way analysis of variance to test for significant differences in mean systolic or diastolic blood pressure at multiple times postimplantation as compared to baseline (Dunnett's test). Significance at  $\alpha = 0.05$  was used for all tests.

### 3. Results

**3.1. Small Animal Ultrasonography of AAAs Enables Longitudinal Monitoring of Aortic Diameter Expansion and Volume Growth over Time.** Two-dimensional and three-dimensional B-mode scans enabled us to comprehensively image aortas in AngII *apoE*<sup>-/-</sup> mice and high-concentration-elastase rats in the short- (transaxial) and long-axis (sagittal) orientations. Figure 1 shows representative B-mode images of the planes of section where the maximal aortic cross-sectional area was found at days 0 and 28 for the high-concentration-elastase rat (Figure 1(a)) and AngII *apoE*<sup>-/-</sup> mouse (Figure 1(b)) studies. During the course of the studies, we clearly identified areas of local aortic expansion (arrows in Figures 1(a) and 1(b) for day 28) and tracked this increase in effective maximum diameter (Figures 1(a) and 1(b), graphs). Proximal and distal aortic areas with normal vessel morphology were imaged and showed no overall increase in diameter (data not shown).

Table 1 shows the average increases in effective maximum diameter by the end of the study. Over 28 days, AAAs in

TABLE 1: Summary of values measured at days 0 and 28 in low- and high-concentration-elastase rats and AngII *apoE*<sup>-/-</sup> mice.

	Elastase rats (0.44–0.48 U/mL) (mean ± SE (n = 6))		Elastase rats (25 U/mL) (mean ± SE (n = 5))		AngII <i>apoE</i> <sup>-/-</sup> mice (1000 ng·kg <sup>-1</sup> ·min <sup>-1</sup> ) (mean ± SE (n = 7))	
	Day 0	Day 28	Day 0	Day 28	Day 0	Day 28
	Effective maximum diameter (mm)	1.48 ± 0.04	1.55 ± 0.05	1.43 ± 0.03	4.02 ± 0.29*	1.01 ± 0.05
Aortic maximum diameter (mm)	1.15 ± 0.09	1.46 ± 0.14	1.05 ± 0.03	3.85 ± 0.49*	0.95 ± 0.05	2.06 ± 0.13*
Volume/length (mm <sup>2</sup> )	1.72 ± 0.06	2.06 ± 0.29	1.41 ± 0.06	8.65 ± 1.57*	0.70 ± 0.08	2.76 ± 0.26*
Length (mm)	6.92 ± 0.40		7.88 ± 0.83		7.07 ± 0.65	
False lumen volume (mm <sup>3</sup> )	NA	NA	NA	NA	0	11.1 ± 1.57*
Circumferential cyclic strain (%)	17.28 ± 1.34	6.18 ± 0.72*	12.67 ± 1.39	2.14 ± 0.27*	12.6 ± 1.4	2.5 ± 0.61*
Mean BFV (perfused region/AAA) (mm/s)	NA	230 ± 28.4	NA	85.3 ± 29.6°	NA	189 ± 99.9 <sup>^</sup>
Mean BFV (healthy region) (mm/s)	318 ± 11.3		370 ± 55.4	322 ± 41.9*	374 ± 44.7	401 ± 57.3

Statistical significance shown for  $\alpha = 0.05$ : \* versus the vessel measurement at day 0; <sup>^</sup> versus healthy region measurement at day 28; ° versus healthy region measurement at day 0.

Data are given as mean ± SE. BFV: blood flow velocity; NA: not applicable.

high-concentration-elastase rats grew  $181 \pm 13.8\%$  relative to baseline (Figure 1(a)), and those in AngII *apoE*<sup>-/-</sup> mice grew by  $126 \pm 10.5\%$  (Figure 1(b)). High-concentration-elastase rats exhibited obvious formation of AAAs postsurgery and a progressive increase ( $94 \mu\text{m}/\text{day}$  on average) in effective maximum diameter (Figure 1(a)) thereafter (1.78–3.39 mm larger at day 28 than at baseline, 95% CI;  $P < 0.05$ ). Low-concentration-elastase rats, however, did not show significant vessel expansion by ultrasound or a significant change in effective maximum diameter over 28 days (Table 1). Given the spontaneous development of initial aortic expansion in the AngII *apoE*<sup>-/-</sup> model (between days 3–14), maximum aortic diameter was  $86.7 \pm 8.36\%$  larger at day 14 imaging on average (Figure 1(b)) with a growth rate of  $198 \mu\text{m}/\text{day}$  thereafter until day 28.

We further measured AAA volumes from segmented three-dimensional B-mode scans (Table 1). In high-concentration-elastase rats, there was a noticeable volume expansion in the perfused region as compared to low-concentration-elastase rats. Volume/length values for the high-concentration-elastase rats increased by  $516 \pm 96.0\%$  after 28 days (Figure 1(c)). In AngII *apoE*<sup>-/-</sup> mice, we observed saccular AAAs with volume/length values increasing by  $297 \pm 42.5\%$  for AAA total volumes (Figure 1(d)). False lumens were identified at day 3 ( $n = 2$ ), day 7 ( $n = 2$ ), and day 14 ( $n = 3$ ) imaging. Between days 3 and 28, these volumes increased in size by  $774 \pm 512\%$  overall. As well, we found that there was a significant change in the percentage of AAA volume attributable to the false lumen ( $20.8 \pm 11.8\%$  versus  $57.1 \pm 10.2\%$ , resp.;  $P < 0.001$ ).

### 3.2. Circumferential Cyclic Strain Rapidly Decreases in AAAs.

We observed abrupt changes in vessel wall displacement and Green-Lagrange circumferential cyclic strain values in high-concentration-elastase rats (Figure 2(a), graph) and AngII *apoE*<sup>-/-</sup> mice (Figure 2(b), graph) at day 3 relative to baseline ( $-69.9 \pm 26.2\%$ ,  $P = 0.0048$ ;  $-49.7 \pm 11.9\%$ ,  $P = 0.026$ , resp.). These values decreased in the suprarenal aortas of some mice where vessel motion had diminished, but initial

aortic expansion had not yet occurred. Between days 3 and 28, we measured continued reductions in these values ( $-43.9 \pm 28.3\%$ ,  $P = 0.0048$ ;  $-60.7 \pm 19.6\%$ ,  $P = 0.054$ , resp.) and visualized stiffer vessel walls in AAAs (see Supplementary Videos 1 and 2 of the Supplementary Material available online at <http://dx.doi.org/10.1155/2015/413189>). In low-concentration-elastase rats, we also found that the Green-Lagrange circumferential cyclic strain values significantly decreased over 28 days (Table 1) likely due to mechanical damage from the pressurized infusion during surgery independent of AAA formation. Circumferential cyclic strain values remained stable in proximal and distal aortic areas of all rats and mice over 28 days (data not shown). Blood pressure data acquired in live AngII *apoE*<sup>-/-</sup> mice showed that on average they became hypertensive as early as day 3 after implantation, although this increase was not statistically significant ( $P < 0.1$ ). The tail cuff technique is inherently noisy, meaning that the increase in blood pressure did not reach significance of  $P < 0.05$ . However, longitudinal measurements (Figure 2(b) inset) provided evidence of continued hypertension in the animals over the course of the study.

### 3.3. Mean Blood Flow Velocity Decreases in Both AAA Models and Recirculates in Suprarenal AAAs.

With progression of disease in the high-concentration-elastase rats, we found that mean blood flow velocity progressively decreased over time (Figure 3(a), graph). Overall decreases in this value at areas adjacent to an AAA were visually evident (Supplementary Videos 3 and 4) and measurable (Figure 3(a), velocity waveform plots). We found comparable reductions in AAA mean blood flow velocity (Table 1) at day 28 relative to day 0 ( $76.9 \pm 29.1\%$ ;  $P < 0.05$ ) and to adjacent healthy regions at day 28 ( $73.5 \pm 27.3\%$ ;  $P < 0.001$ ). In low-concentration-elastase rats, we found that the mean blood flow velocity in the perfused region had slightly decreased after 28 days ( $P = 0.0532$ ) (Table 1).

PW Doppler scans on AngII *apoE*<sup>-/-</sup> mice did not provide a complete dataset. However, we clearly observed a shift to complex aortic flow patterns by days 21 and 28 imaging

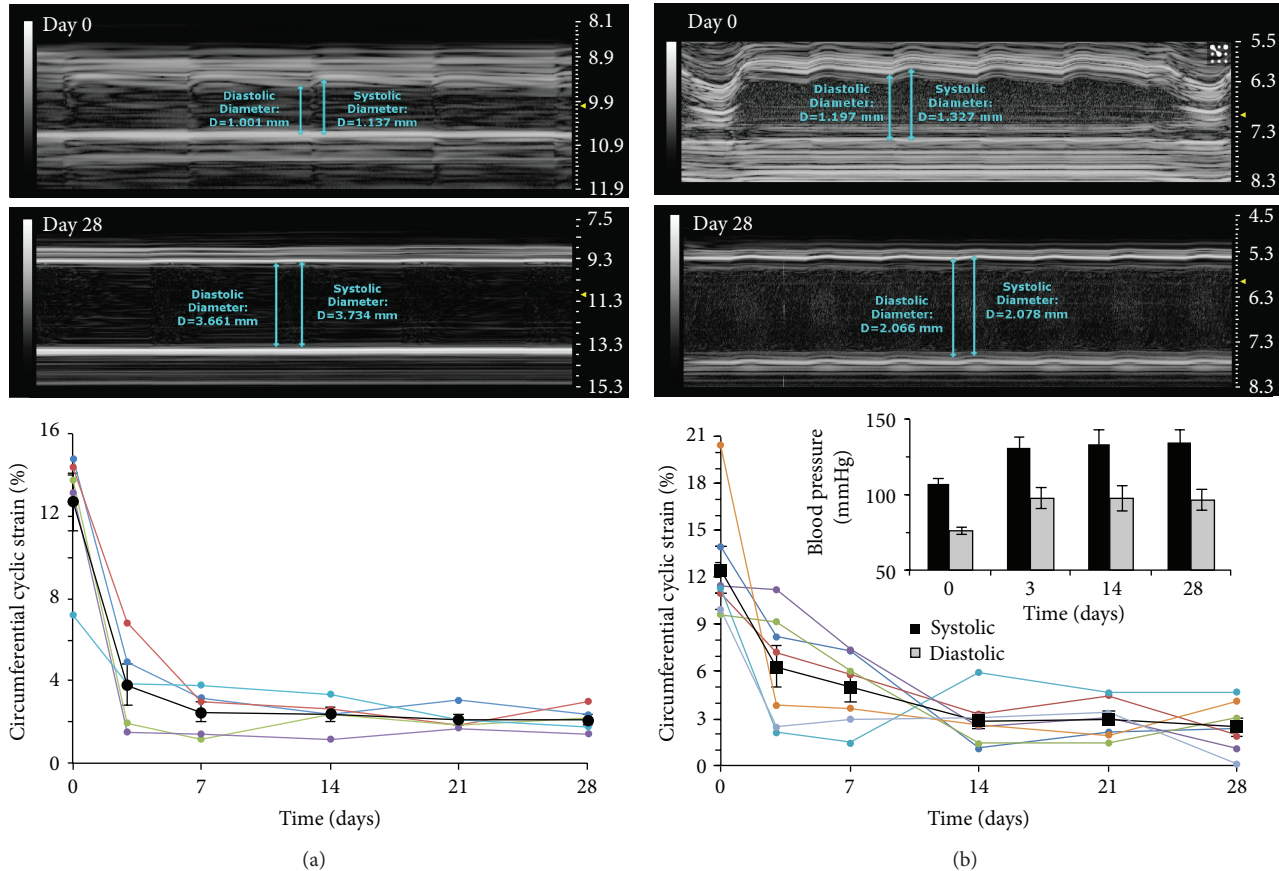


FIGURE 2: Circumferential cyclic strain decreases over 28 days. Representative long-axis M-mode tracings (days 0 and 28) and longitudinal measurements of circumferential cyclic strain at site of AAA for high-concentration-elastase rats (a) and AngII *apoE*<sup>-/-</sup> mice (b). Inset in (b): longitudinal measurements of systolic and diastolic blood pressure in AngII *apoE*<sup>-/-</sup> mice.

(Supplementary Video 5). Smaller areas of reduced or recirculating flow were seen adjacent to focal dissection points (Supplementary Video 6). As a result, we measured marked reductions in mean blood flow velocity and a change in flow direction at day 28 relative to day 0 in mice (Figure 3(b), velocity waveforms). We found comparable reductions in AAA mean blood flow velocity at day 28 relative to day 0 ( $49.6 \pm 26.9\%$ ;  $P = 0.192$ ) and to adjacent healthy regions at day 28 ( $52.9 \pm 28.9\%$ ;  $P < 0.05$ ) (Table 1).

**3.4. AAAs Exhibit Elastin Degradation and Collagen Deposition by Histological Staining.** Dissections of rats and mice showed the anticipated shape of AAAs *in situ* as was seen by ultrasound prior to sacrifice (Figures 4(a) and 4(b)). The short-axis B-mode images in Figures 4(c) and 4(d) reveal the inner vessel walls and maximum cross-sectional diameters and areas in each AAA model prior to dissection. MTC staining for collagen (Figures 5(a) and 5(b)) and VVG staining for elastin (Figures 5(c) and 5(d)) revealed changes in the distribution and overall content of these proteins in the AAA wall. The most noticeable changes are the degradation and loss of elastin bands in high-concentration-elastase rats and significant collagen deposition in the AngII *apoE*<sup>-/-</sup> mice. Collagen accumulates as disorganized collagen fibers, as is seen with fibrosis, and fails to support

the aortic wall architecture [24]. We found that reductions in elastin content were statistically significant using high elastase concentration ( $90 \pm 3.9\%$ ;  $P = 0.002$ ) relative to healthy regions (Figure 5(e)). Low-concentration-elastase rats exhibited a smaller amount of elastin degradation ( $49 \pm 3.1\%$ ;  $P = 0.122$ ) in some of the aortas (images not shown). Additionally, the morphology of collagen changed in both low- and high-concentration-elastase rats, appearing stringier and more detached than healthy collagen fibers. In these areas, we found a statistically significant decrease in the amount of collagen in high-concentration-elastase rats ( $63 \pm 10\%$  reduction;  $P = 0.04$ ). Collagen in low-concentration-elastase rats also decreased ( $54 \pm 11\%$ ), albeit not significantly ( $P = 0.13$ ).

AngII *apoE*<sup>-/-</sup> mice consistently showed collagen deposition in and around transmural hematomas resulting from false lumen formation. We found an  $82 \pm 27\%$  increase ( $P = 0.0611$ ) in collagen content in these areas relative to healthy regions (Figure 5(f)). Conversely, our measurements of elastin content in proximity to the hematomas showed similar levels to those for healthy regions ( $P = 0.73$ ), as a focal dissection point where elastin had been degraded was not always seen in our sections.

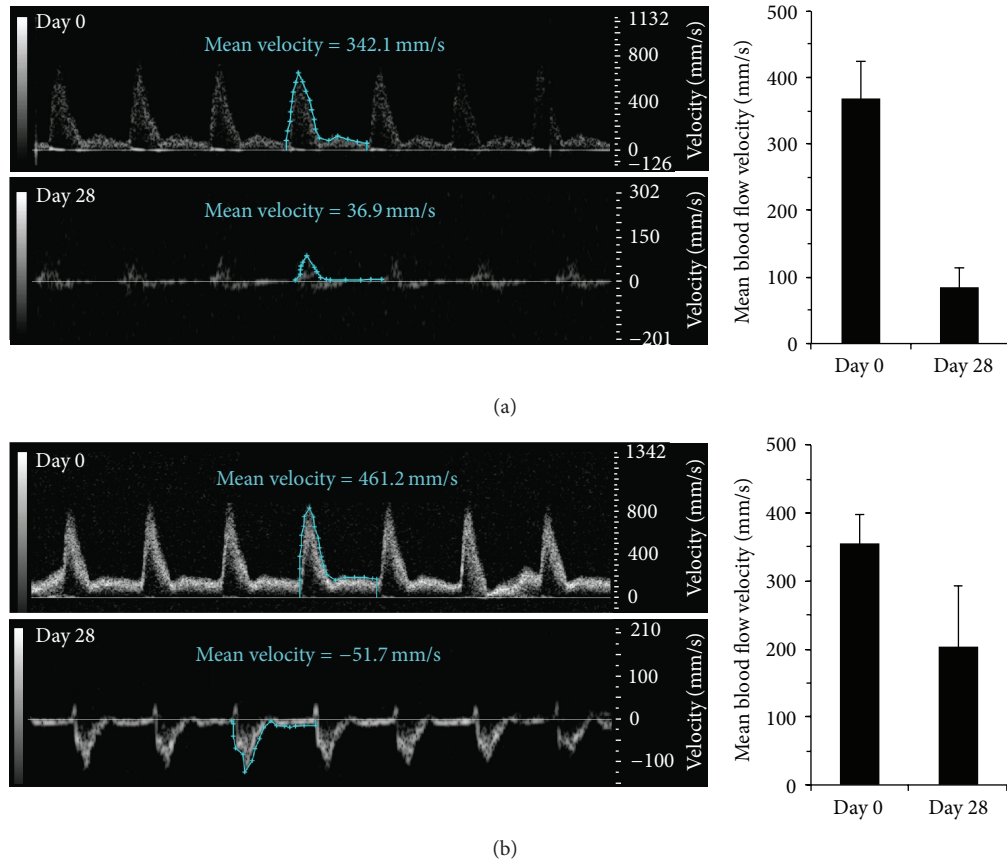


FIGURE 3: Mean aortic blood flow velocity decreases after 28 days. Representative velocity waveforms on long-axis PW Doppler acquisitions (days 0 and 28) and corresponding measurements of mean blood flow velocities at site of AAA in high-concentration-elastase rats (a) and AngII *apoE*<sup>-/-</sup> mice (b).

**3.5. Nonlinear Optical Microscopy Enables Label-Free Imaging of Elastin and Collagen in Ex Vivo AAA Tissue.** We also tested the use of NLO microscopy to detect elastin and collagen in AAA tissues. We found that AAAs from elastase rats showed changes in TPEF signal according to elastase concentration. Elastin fibers were clearly absent or degraded in elastase perfused aortic tissue (white arrows in Figure 6(a)), similar to the findings seen with VVG staining. In contrast, healthy regions demonstrated strong autofluorescence signal due to the presence of elastin. The emission filter used also detected autofluorescence signal from agarose gel in the aortic lumen (asterisks in Figure 6) and adventitial proteins, likely collagen and fibrin. Adventitial collagen, as detected by SHG signal, was observed in both types of AAAs (black arrows in Figure 6). This signal was visually apparent in and around transmural hematomas in the AngII *apoE*<sup>-/-</sup> model where collagen deposition is pronounced. In the adventitia of elastase-perfused aortas, a change in overall SHG signal intensity and spatial distribution may also be occurring.

#### 4. Discussion

This work demonstrates that we can sensitively detect and monitor biomechanical changes occurring during progression of AAAs in both the elastase and AngII *apoE*<sup>-/-</sup>

models. We showed reductions in both circumferential cyclic strain and mean blood flow velocity within AAAs relative to adjacent healthy regions. We also found substantial elastin fragmentation and collagen deposition with label-free microscopy. Taken together, these results suggest that differences in AAA growth, strain, and blood flow velocity are useful parameters that reveal time-dependent changes in each model.

While aortic diameter measurements are standard for determining maximum aortic expansion in both human [25–27] and small animal [15–18, 28, 29] AAAs, the data from this study suggest that aortic volumes may be a more useful metric for characterizing aneurysm expansion. Indeed, simple diameter measurements from B-mode images depend on the acquisition location and measurement technique. Aortic volumes, on the other hand, should be less dependent on location and technique as the entire aorta can be acquired in one three-dimensional volume. This technique can also account for changes in the length of a growing AAA not exhibiting accompanying increases in diameter. Similar to the volumetric ultrasound images others have collected [30, 31], we observed an increase in the length of AngII *apoE*<sup>-/-</sup> AAAs. The average AAA volume-to-length ratios in our AngII *apoE*<sup>-/-</sup> mice (mean  $\pm$  SE;  $2.8 \pm 0.3$  mm<sup>2</sup> at

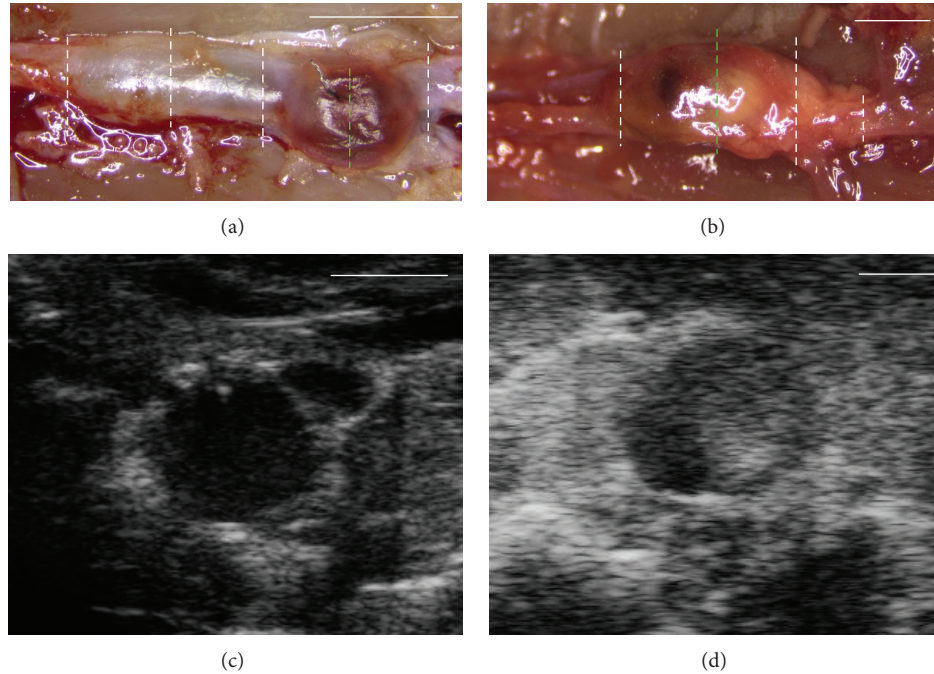


FIGURE 4: Gross dissection of AAAAs shows shape of AAAAs detected by B-mode images. End-of-study dissection images of AAAAs *in situ* and short-axis B-mode images at day 28 from a high-concentration-elastase rat ((a), (c)) and an AngII *apoE*<sup>-/-</sup> mouse ((b), (d)). B-mode images taken at the approximate anatomical locations marked by green dashed lines ((a) and (b)). White dashed lines indicate locations selected for histology. Scale bars: 5 mm (a); 2 mm (b); 2 mm (c); and 1 mm (d).

day 28) compare well with a previous report using MRI (mean  $\pm$  SD;  $2.5 \pm 0.6 \text{ mm}^2$  at day 28 [21]). Likewise, these values for the high concentration elastase rats ( $8.7 \pm 1.6 \text{ mm}^2$  at day 28) compare well to elastase-perfused mice ( $1.1 \pm 0.2 \text{ mm}^2$  at day 28 [21]) when accounting for animal weight (rats are roughly 10 times bigger than mice). We also observed several mice and rats in this study where the diameter measurements plateaued, but the volume/length ratio continued to increase (Figure 1). These results suggest that in some cases the aneurysms were lengthening without significant diameter expansion. A recent article also used three-dimensional ultrasound but for *ex vivo* measurements of AAAAs from AngII *apoE*<sup>-/-</sup> mice [32]. These volumes, however, were segmented over a short 2 mm length in all cases, making a direct comparison to our measurements with variable lengths difficult. Future studies to compare volumes of the same AAAAs *in vivo* and *ex vivo* by ultrasound may be warranted, as the changes in the overall size and shape of AAAAs following transcatheter perfusion are not fully known.

With both AAA models, we noted that circumferential cyclic strain sometimes decreased independently of vessel expansion. In AngII *apoE*<sup>-/-</sup> mice, four animals had reductions in circumferential cyclic strain (>33%) but normal effective maximum diameters (<150% baseline) at day 3. Three animals showed abrupt aortic expansion in parallel with large reductions in circumferential cyclic strain (>75%). Consistent with this finding is blood pressure data, which shows sustained hypertension starting at day 3. This is expected with AngII infusion, leading to a shift in the loading

response up the stress-strain curve. At these early time points we would not expect there to be substantial vessel remodeling. Further studies with greater numbers of mice are needed to improve our understanding of the relationship between vessel expansion and circumferential cyclic strain reductions in AngII-induced AAAAs. For rats infused with low-concentration elastase, we observed reductions in circumferential cyclic strain despite negligible increases in aortic diameter or volume over 28 days (Table 1). This may be due to pressure-induced vessel damage, ligation of branching vessels, or other effects of the surgical procedure. Two groups have previously carried out studies to track changes in circumferential strain values in the aortas of AngII *apoE*<sup>-/-</sup> mice [19, 21]. Favreau et al. [19] calculated linear or Cauchy strain values using ultrasound and found a roughly 40% reduction in cyclic strain in the supraceliac aorta at day 3 (similar to the circumferential cyclic strain reduction of  $-49.7 \pm 11.9\%$  we observed). Ideally, the nonlinear strain components accounted for by circumferential cyclic strain should not be neglected since strain values up to 25% cannot be considered small [22]. Goergen et al. [21] calculated circumferential cyclic strain values from magnetic resonance angiography (MRA) images of elastase ( $19.4 \pm 2.5\%$ ) and AngII *apoE*<sup>-/-</sup> ( $20.8 \pm 4.2\%$ ) mice at baseline in relative agreement with our values ( $15.2 \pm 1.2\%$  in high- and low-concentration-elastase rats and  $12.6 \pm 1.4\%$  in AngII *apoE*<sup>-/-</sup> mice). However, we observed comparatively larger reductions by day 28. High-concentration-elastase rats in our study showed an  $83.1 \pm 31.1\%$  reduction, while their elastase mice had a  $44.8 \pm 0.1\%$

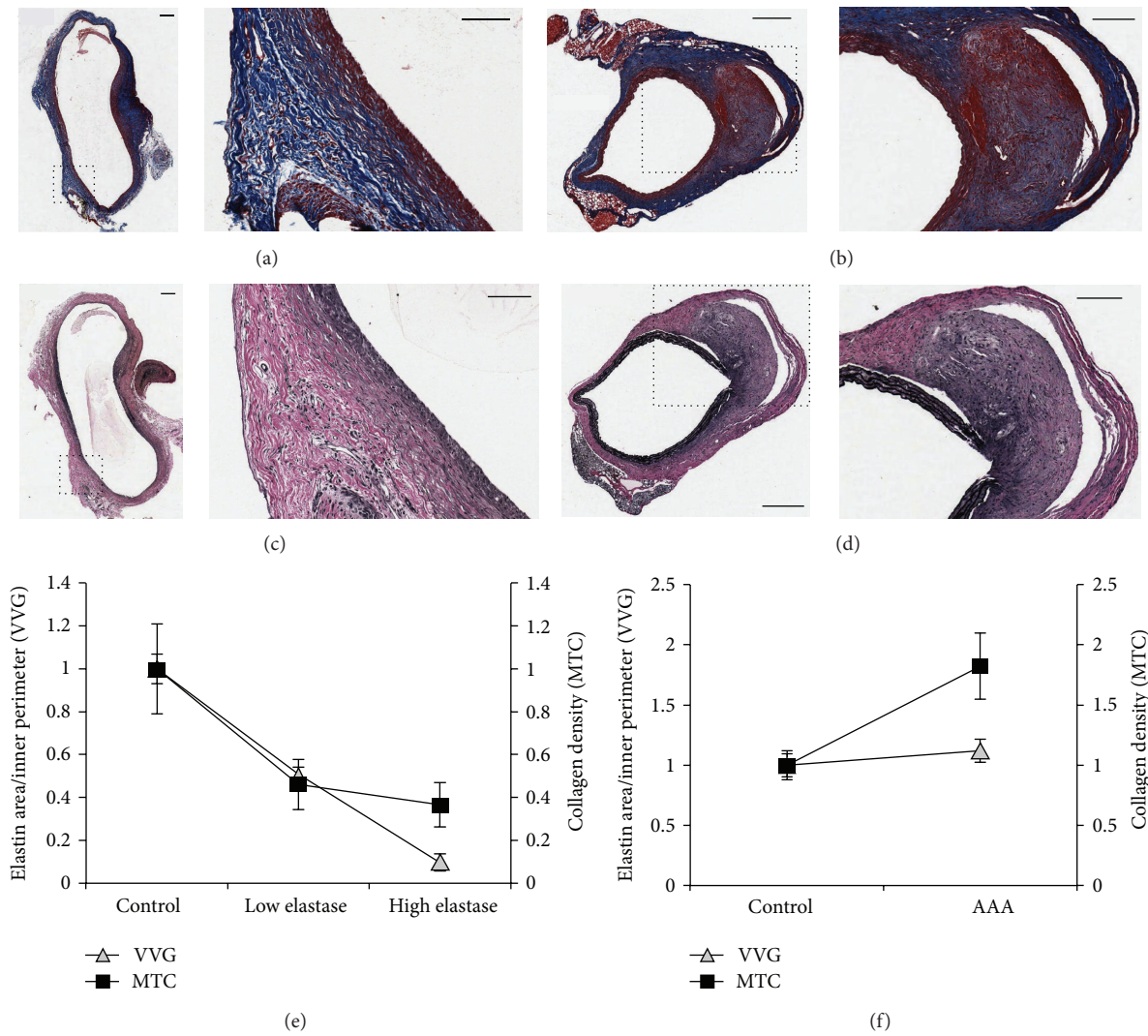


FIGURE 5: Histological staining reveals qualitative and semiquantitative differences in elastin and collagen content of AAAs. Representative MTC ((a), (b)) and VVG ((c), (d)) images of AAA tissue from a high concentration elastase rat ((a), (c)) and an AngII *apoE*<sup>-/-</sup> mouse ((b), (d)). Normalized measurements of mean elastin and collagen content ((e), (f)) in high- (*n* = 5) and low- (*n* = 4) concentration-elastase rats (e) and AngII *apoE*<sup>-/-</sup> mice (*n* = 6) (f). Controls (*n* = 3 in each group) are sections with healthy regions. Scale bars: 200  $\mu$ m at low and 100  $\mu$ m at high magnification. Level of magnification: 8x ((a), (c)) and 2x ((b), (d)) relative to low magnification.

decrease. AngII *apoE*<sup>-/-</sup> mice in this study showed an  $80.2 \pm 21.6\%$  reduction, while the other paper showed a  $52 \pm 16.3\%$  decrease in this same model. This difference may be due to the higher spatial resolution and fundamental contrast differences between the Vevo2100 ultrasound system and MRA using a 4.7 T magnet. As MRA highlights unsaturated spins or nuclei from flowing blood, its disadvantage lies in accurately visualizing solid aneurysm regions where blood flow is not present. For the AngII *apoE*<sup>-/-</sup> mice, MRA showed maximal reductions in circumferential cyclic strain and increases in aortic diameter coincided in the days 7 to 14 interval [21]. This delay compared to our findings of earlier reductions in strain may be attributable to the fact that we primed the pumps in physiological saline solution for at least 12 hours prior to implantation.

Many previous efforts have used qualitative assessments of VVG- and MTC-stained vessels to confirm elastin breakage and collagen deposition [33, 34]. We focused on a quantitative approach that would provide a more robust comparison between suprarenal AAAs and infrarenal AAAs from high- and low-concentration-elastase rats. Goergen et al. previously quantified differences in elastin content of VVG-stained aortas [21] and found that the anterior wall in elastase-perfused mice showed significantly greater elastin loss than the posterior wall in the same region. We implemented a similar code with the addition of vessel wall collagen analysis in order to determine the magnitude of change in AAA areas relative to adjacent healthy areas.

The use of NLO microscopy (SHG and TPEF) was included in these studies as it is a powerful label-free

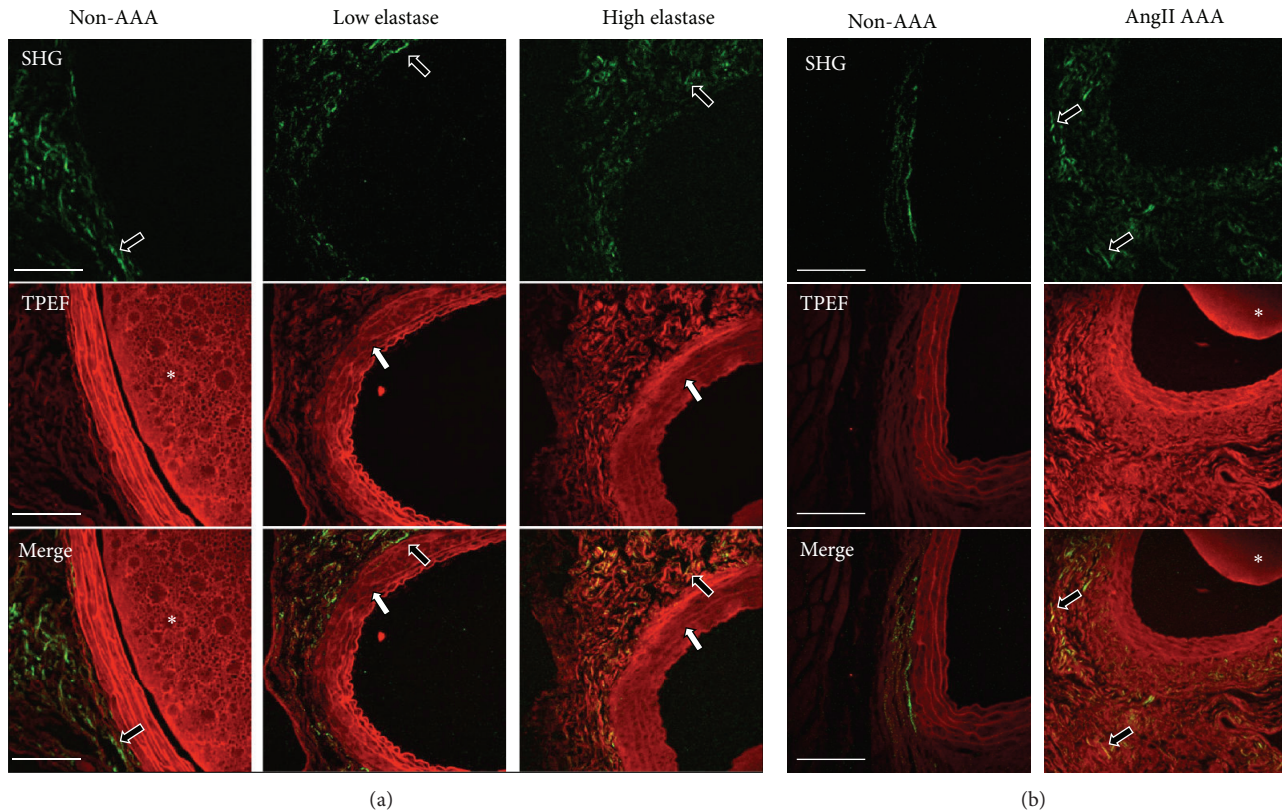


FIGURE 6: Nonlinear optical microscopy provides a label-free approach for examination of AAA tissue morphology and protein content. SHG (green), TPEF (red), and merged SHG/TPEF nonlinear optical images of representative aortic tissue sections from healthy and AAA regions in low- and high-concentration-elastase rats (a), and AngII *apoE*<sup>-/-</sup> mice (b). Scale bars: 100  $\mu$ m. Black arrows point to adventitial collagen; white arrows point to degraded elastin bands; and asterisks indicate agarose gel in lumen.

technique that can be used to study vascular diseases. Changes in the content and morphology of elastin and collagen are clearly tied with inflammatory and proteolytic effects occurring in AAA progression. Future studies could benefit from three-dimensional mapping and quantification of elastin and collagen fibers. Cui et al. demonstrated the use of multiphoton microscopy for volumetric analysis of these macromolecules in the aorta and skin of a murine Marfan model [35], while Haskett et al. determined vessel fiber alignment after mechanical testing of AAAs [36]. Le et al. originally measured the emission spectra of collagen and elastin in atherosclerotic Ossabaw pig arteries using a similar microscopy set-up [23]. Taken together, these previous studies and our work suggest that a label-free imaging approach has several advantages over standard histological staining and microscopy. Primarily, it obviates the need for tissue processing and chemical staining. The tissue can be imaged in a near-native state and variability in tissue stain application is no longer an issue. It also permits analysis of thicker tissue sections than is feasible with confocal microscopy. Similar to how volumetric ultrasound measurements of AAAs provide more information than simple two-dimensional measures, the use of volumetric quantification from thicker tissue specimens could also be useful when imaging *ex vivo* sections.

There are several limitations in the present study. First, the presence of abdominal gas in animals can disrupt ultrasound

imaging. If not resolved within a few minutes, we changed the orientation of the transducer relative to the body to minimize this interference. However, this reorientation sometimes limited our ability to visualize all regions of the aorta and to detect accurate blood flow patterns. Additionally, the Doppler measurements in the study had large variations. This was likely due to variations in the Doppler angle when acquiring PW images. Thus, tilting and rotating the animals could be done in order to optimize the Doppler angle for long-axis PW and color Doppler measurements in the aorta where the vessel often runs parallel to the transducer.

## 5. Conclusions

We carried out longitudinal studies *in vivo* in order to image and measure several parameters relevant to AAA development. Elastase-perfused rats and AngII *apoE*<sup>-/-</sup> mice exhibited large reductions in circumferential cyclic strain and mean blood flow velocity over 28 days. These parameters had temporal differences in each model that were not necessarily correlated with increases in effective maximum diameter or AAA volume. The results suggest that vessel strain and blood flow are important metrics and may be indicative of underlying disease processes in AAAs.

We used small animal ultrasound for this study, as it offered us rapid imaging speed and versatility in imaging

acquisitions and was relatively inexpensive compared to other tomographic imaging. Furthermore, semiquantitative histology and nonlinear optical microscopy allowed us to further characterize our findings *ex vivo*. We feel that quantifying macromolecular changes in elastin and collagen is helpful for sensitively characterizing AAAs from both the elastase and AngII *apoE*<sup>-/-</sup> models. Future studies could use these methods to investigate mechanisms in pathogenesis and treatment effects relevant to AAAs and other cardiovascular diseases.

## Conflict of Interests

The authors declare that there is no conflict of interests regarding the publication of this paper.

## Authors' Contribution

Evan H. Phillips and Alexa A. Yrineo contributed equally to this paper.

## Acknowledgments

The authors gratefully acknowledge the help of several lab members: Amelia Adelsperger and Shadman Jubaer for performing ultrasound analysis, Amy Bogucki and Shelby Abrams for small animal ultrasound imaging and blood pressure measurements, Frederick Damen and Arvin Soepriatna for their MATLAB analysis code of MTC-stained tissues, and Delong Zhang, Chien-Sheng Liao, Bin Liu, and Jesse Zhang for assistance with the NLO microscopy set-up. Funding for this study was provided by an American Heart Association Scientist Development Grant (CJG, 14SDG18220010) and Purdue University.

## References

- [1] A. T. Hirsch, Z. J. Haskal, N. R. Hertz et al., "ACC/AHA 2005 Practice Guidelines for the management of patients with peripheral arterial disease (lower extremity, renal, mesenteric, and abdominal aortic): a collaborative report from the American Association for Vascular Surgery/Society for Vascular Surgery, Society for Cardiovascular Angiography and Interventions, Society for Vascular Medicine and Biology, Society of Interventional Radiology, and the ACC/AHA Task Force on Practice Guidelines (Writing Committee to Develop Guidelines for the Management of Patients With Peripheral Arterial Disease): endorsed by the American Association of Cardiovascular and Pulmonary Rehabilitation; National Heart, Lung, and Blood Institute; Society for Vascular Nursing; TransAtlantic Inter-Society Consensus; and Vascular Disease Foundation," *Circulation*, vol. 113, no. 11, pp. e463–e654, 2006.
- [2] A. S. Go, D. Mozaffarian, V. L. Roger et al., "Heart disease and stroke statistics-2013 update: a Report from the American Heart Association," *Circulation*, vol. 127, no. 1, pp. e6–e245, 2013.
- [3] F. A. M. V. I. Hellenthal, W. A. Buurman, W. K. W. H. Wodzig, and G. W. H. Schurink, "Biomarkers of abdominal aortic aneurysm progression. Part 2: inflammation," *Nature Reviews Cardiology*, vol. 6, no. 8, pp. 543–552, 2009.
- [4] G. M. Longo, W. Xiong, T. C. Greiner, Y. Zhao, N. Fiotti, and B. T. Baxter, "Matrix metalloproteinases 2 and 9 work in concert to produce aortic aneurysms," *The Journal of Clinical Investigation*, vol. 110, no. 5, pp. 625–632, 2002.
- [5] K. Saraff, F. Babamusta, L. A. Cassis, and A. Daugherty, "Aortic dissection precedes formation of aneurysms and atherosclerosis in angiotensin II-infused, apolipoprotein E-deficient mice," *Arteriosclerosis, Thrombosis, and Vascular Biology*, vol. 23, no. 9, pp. 1621–1626, 2003.
- [6] D. Petrincic, S. Liao, D. R. Holmes, J. M. Reilly, W. C. Parks, and R. W. Thompson, "Doxycycline inhibition of aneurysmal degeneration in an elastase-induced rat model of abdominal aortic aneurysm: preservation of aortic elastin associated with suppressed production of 92 kD gelatinase," *Journal of Vascular Surgery*, vol. 23, no. 2, pp. 336–346, 1996.
- [7] N. Miyama, M. M. Dua, J. J. Yeung et al., "Hyperglycemia limits experimental aortic aneurysm progression," *Journal of Vascular Surgery*, vol. 52, no. 4, pp. 975–983, 2010.
- [8] L. Maegdefessel, J. Azuma, R. Toh et al., "Inhibition of microRNA-29b reduces murine abdominal aortic aneurysm development," *The Journal of Clinical Investigation*, vol. 122, no. 2, pp. 497–506, 2012.
- [9] S. Anidjar, J.-L. Salzmann, D. Gentric, P. Lagneau, J.-P. Camilleri, and J.-B. Michel, "Elastase-induced experimental aneurysms in rats," *Circulation*, vol. 82, no. 3, pp. 973–981, 1990.
- [10] A. Tanaka, T. Hasegawa, Z. Chen, Y. Okita, and K. Okada, "A novel rat model of abdominal aortic aneurysm using a combination of intraluminal elastase infusion and extraluminal calcium chloride exposure," *Journal of Vascular Surgery*, vol. 50, no. 6, pp. 1423–1432, 2009.
- [11] R. Pyo, J. K. Lee, J. M. Shipley et al., "Targeted gene disruption of matrix metalloproteinase-9 (gelatinase B) suppresses development of experimental abdominal aortic aneurysms," *The Journal of Clinical Investigation*, vol. 105, no. 11, pp. 1641–1649, 2000.
- [12] A. Daugherty, M. W. Manning, and L. A. Cassis, "Angiotensin II promotes atherosclerotic lesions and aneurysms in apolipoprotein E-deficient mice," *The Journal of Clinical Investigation*, vol. 105, no. 11, pp. 1605–1612, 2000.
- [13] A. Daugherty and L. A. Cassis, "Mouse models of abdominal aortic aneurysms," *Arteriosclerosis, Thrombosis, and Vascular Biology*, vol. 24, no. 3, pp. 429–434, 2004.
- [14] D. B. Buxton, "Molecular imaging of aortic aneurysms," *Circulation: Cardiovascular Imaging*, vol. 5, no. 3, pp. 392–399, 2012.
- [15] B. Martin-McNulty, J. Vincelette, R. Vergona, M. E. Sullivan, and Y.-X. Wang, "Noninvasive measurement of abdominal aortic aneurysms in intact mice by a high-frequency ultrasound imaging system," *Ultrasound in Medicine and Biology*, vol. 31, no. 6, pp. 745–749, 2005.
- [16] C. Barisione, R. Charnigo, D. A. Howatt, J. J. Moorleghen, D. L. Rateri, and A. Daugherty, "Rapid dilation of the abdominal aorta during infusion of angiotensin II detected by noninvasive high-frequency ultrasonography," *Journal of Vascular Surgery*, vol. 44, no. 2, pp. 372–376, 2006.
- [17] G. H. Turner, A. R. Olzinski, R. E. Bernard et al., "In vivo serial assessment of aortic aneurysm formation in apolipoprotein E-deficient mice via MRI," *Circulation: Cardiovascular Imaging*, vol. 1, pp. 220–226, 2008.
- [18] J. Azuma, L. Maegdefessel, T. Kitagawa, R. L. Dalman, M. V. McConnell, and P. S. Tsao, "Assessment of elastase-induced murine abdominal aortic aneurysms: comparison of ultrasound imaging with *in situ* video microscopy," *Journal of Biomedicine and Biotechnology*, vol. 2011, Article ID 252141, 10 pages, 2011.

- [19] J. T. Favreau, B. T. Nguyen, I. Gao et al., "Murine ultrasound imaging for circumferential strain analyses in the angiotensin II abdominal aortic aneurysm model," *Journal of Vascular Surgery*, vol. 56, no. 2, pp. 462–469, 2012.
- [20] C. J. Goergen, K. N. Barr, D. T. Huynh et al., "In vivo quantification of murine aortic cyclic strain, motion, and curvature: implications for abdominal aortic aneurysm growth," *Journal of Magnetic Resonance Imaging*, vol. 32, no. 4, pp. 847–858, 2010.
- [21] C. J. Goergen, J. Azuma, K. N. Barr et al., "Influences of aortic motion and curvature on vessel expansion in murine experimental aneurysms," *Arteriosclerosis, Thrombosis, and Vascular Biology*, vol. 31, no. 2, pp. 270–279, 2011.
- [22] J. D. Humphrey and S. L. Delange, *An Introduction to Biomechanics*, Springer, New York, NY, USA, 2004.
- [23] T. T. Le, I. M. Langohr, M. J. Locker, M. Sturek, and J.-X. Cheng, "Label-free molecular imaging of atherosclerotic lesions using multimodal nonlinear optical microscopy," *Journal of Biomedical Optics*, vol. 12, no. 5, Article ID 054007, 10 pages, 2007.
- [24] J. H. N. Lindeman, B. A. Ashcroft, J.-W. M. Beenakker et al., "Distinct defects in collagen microarchitecture underlie vessel-wall failure in advanced abdominal aneurysms and aneurysms in Marfan syndrome," *Proceedings of the National Academy of Sciences of the United States of America*, vol. 107, no. 2, pp. 862–865, 2010.
- [25] F. A. Lederle, G. R. Johnson, S. E. Wilson et al., "Prevalence and associations of abdominal aortic aneurysm detected through screening," *Annals of Internal Medicine*, vol. 126, no. 6, pp. 441–449, 1997.
- [26] J. A. van Herwaarden, B. E. Muhs, K. L. Vincken et al., "Aortic compliance following EVAR and the influence of different endografts: determination using dynamic MRA," *Journal of Endovascular Therapy*, vol. 13, no. 3, pp. 406–414, 2006.
- [27] L. A. Pape, T. T. Tsai, E. M. Isselbacher et al., "Aortic diameter  $\geq 5.5$  cm is not a good predictor of type A aortic dissection: observations from the International Registry of Acute Aortic Dissection (IRAD)," *Circulation*, vol. 116, no. 10, pp. 1120–1127, 2007.
- [28] B. S. Knipp, G. Ailawadi, V. V. Sullivan et al., "Ultrasound measurement of aortic diameters in rodent models of aneurysm disease," *Journal of Surgical Research*, vol. 112, no. 1, pp. 97–101, 2003.
- [29] M. A. Bartoli, F. Kober, P. Cozzone, R. W. Thompson, M. C. Alessi, and M. Bernard, "In vivo assessment of murine elastase-induced abdominal aortic aneurysm with high resolution magnetic resonance imaging," *European Journal of Vascular and Endovascular Surgery*, vol. 44, no. 5, pp. 475–481, 2012.
- [30] R. Y. Cao, T. Amand, M. D. Ford, U. Piomelli, and C. D. Funk, "The murine angiotensin II-induced abdominal aortic aneurysm model: rupture risk and inflammatory progression patterns," *Frontiers in Pharmacology*, vol. 1, p. 9, 2010.
- [31] M. D. Ford, A. T. Black, R. Y. Cao, C. D. Funk, and U. Piomelli, "Hemodynamics of the mouse abdominal aortic aneurysm," *Journal of Biomechanical Engineering*, vol. 133, no. 12, Article ID 121008, 2011.
- [32] X. Zhang, S. Thatcher, C. Wu, A. Daugherty, and L. A. Cassis, "Castration of male mice prevents the progression of established angiotensin II-induced abdominal aortic aneurysms," *Journal of Vascular Surgery*, 2014.
- [33] Y.-X. Wang, B. Martin-McNulty, A. D. Freay et al., "Angiotensin II increases urokinase-type plasminogen activator expression and induces aneurysm in the abdominal aorta of apolipoprotein E-deficient mice," *The American Journal of Pathology*, vol. 159, no. 4, pp. 1455–1464, 2001.
- [34] T. Takayanagi, K. J. Crawford, T. Kobayashi et al., "Caveolin 1 is critical for abdominal aortic aneurysm formation induced by angiotensin II and inhibition of lysyl oxidase," *Clinical Science*, vol. 126, no. 11, pp. 785–794, 2014.
- [35] J. Z. Cui, A. Y. Tehrani, K. A. Jett, P. Bernatchez, C. van Breemen, and M. Esfandiari, "Quantification of aortic and cutaneous elastin and collagen morphology in Marfan syndrome by multiphoton microscopy," *Journal of Structural Biology*, vol. 187, no. 3, pp. 242–253, 2014.
- [36] D. Haskett, M. Azhar, U. Utzinger, and J. P. Vande Geest, "Progressive alterations in microstructural organization and biomechanical response in the ApoE mouse model of aneurysm," *Biomatter*, vol. 3, no. 3, Article ID e24648, 2013.

## Research Article

# Manifestation of Hyperandrogenism in the Continuous Light Exposure-Induced PCOS Rat Model

Xuezhi Kang,<sup>1,2</sup> Lina Jia,<sup>3</sup> and Xueyong Shen<sup>1,2</sup>

<sup>1</sup>College of Acupuncture and Moxibustion, Shanghai University of Traditional Chinese Medicine, Shanghai 201203, China

<sup>2</sup>Shanghai Research Center for Acupuncture and Meridians, Shanghai 201203, China

<sup>3</sup>Department of Traditional Chinese Medicine, Huadong Hospital, Fudan University, Shanghai 200040, China

Correspondence should be addressed to Lina Jia; [jia\\_ln@163.com](mailto:jia_ln@163.com) and Xueyong Shen; [snowysh@hotmail.com](mailto:snowysh@hotmail.com)

Received 18 September 2014; Accepted 25 November 2014

Academic Editor: Oreste Gualillo

Copyright © 2015 Xuezhi Kang et al. This is an open access article distributed under the Creative Commons Attribution License, which permits unrestricted use, distribution, and reproduction in any medium, provided the original work is properly cited.

Polycystic ovary syndrome (PCOS) is a complex endocrine and metabolic disorder, and its pathogenesis has yet to be completely clarified. A fully convincing animal model has not been established for PCOS. In earlier studies, researchers have shown that the exposure of rats to continuous light can induce PCOS; nevertheless, hyperandrogenism, a key characteristic observed in human PCOS, has not been reported previously. In the present study, we found that (1) body weights decreased in female rats in a continuous light environment with both ovarian and uterine augmentation; (2) the estrous cycle in rats under continuous light environment was disordered, and polycystic ovary-like changes occurred, accompanied with fur loss and lethargy; and (3) serum testosterone levels in rats in a continuous light environment significantly increased. Our data suggest that continuous light can lead to the occurrence of PCOS in female rats without the need for drugs; this is a reasonable PCOS animal model that is more consistent with the natural disease state in humans; and poor sleep habits or negligence of sleep hygiene may be an important lifestyle factor in pathogenesis of PCOS.

## 1. Introduction

Polycystic ovary syndrome (PCOS) is a complex endocrine and metabolic disorder associated with ovulatory dysfunction, abdominal obesity, and infertility, and it affects 5%–10% of women of reproducing age [1]. In 1935, Stein and Leventhal published a case series of seven women with amenorrhea and bilateral polycystic ovaries. At the National Institutes of Health (NIH) consensus conference held in 1990, PCOS was defined as chronic anovulation with clinical and/or biochemical hyperandrogenism, excessive androgen secretion or activity; clinical manifestations of acne and hirsutism are the primary characteristics of PCOS [2]. The pathogenesis of PCOS is uncertain, although lifestyle may be an important factor. In recent years, the understanding of the pathogenesis of this disease has significantly advanced; however, a fully convincing animal model for PCOS has not been established [3]. Depending on which PCOS-related disorder is investigated, the most suitable animal model should be utilized.

Voluntary sleep restriction has become widespread in modern society [4]. In humans, chronic partial sleep loss and behavioral and sleep disorders have been linked with obesity and metabolic syndrome [5]. Many women with PCOS have psychological problems and sleep disorders that significantly reduce sleep quality [6]. The risk for obstructive sleep apnea (OSA) is higher in obese women with PCOS [7]. In female mammals, ovulation is induced by luteinizing hormone (LH) secretion surge from the pituitary gland, an event which is itself stimulated by gonadotropin releasing hormone (GnRH) secretion from neurons in the hypothalamus [8]. In rodents, the LH surges that trigger ovulation are controlled by cyclic light-dark photoperiods [9]. A disturbance of these light-dark photoperiods within a 24-hour period can disrupt normal cycling in rats and inhibit ovulation [10]; exposure of female rats to a constant light environment was developed as an alternative approach for inducing PCOS [11, 12].

According to the literature, PCOS can be induced in rats in fewer than 75 days of continuous exposure to 600-lux light

[12]. Research on the constant light modeling method was published in the 1970s. Due to the limitations of the experimental conditions and the awareness of PCOS [13], hyperandrogenism, a key characteristic observed in human PCOS, was not reported in this model [14]. The purpose of this study was to determine the level of testosterone in the rat model and reevaluate the constant light exposure-induced PCOS rat model with a contemporary perspective to unequivocally provide a PCOS animal model for future research that is more consistent with the natural disease state.

## 2. Materials and Methods

**2.1. Animals.** All animal procedures were performed in accordance with the guidelines of the Animal Care and Use Committee of Huadong Hospital and Shanghai Research Center for Acupuncture and Meridians. Six-week-old female Sprague Dawley (SD) rats were purchased from the Shanghai Experimental Animal Center of Chinese Academy of Sciences and were housed at 22–25°C in a custom-designed experimental box. All rats were allowed to eat and drink freely.

**2.2. Equipment and Reagents.** The custom-designed light experiment box had a length, width, and height of 120 cm, 45 cm, and 180 cm, it was vertically divided into four equal and independent chambers (length, width, and height of 120 cm, 45 cm, and 45 cm for each chamber) with independent ventilation. A fluorescent lamp (color temperature: 6500 K, illumination: 600 lux) was installed in every chamber and had lights controlled by a microcomputer switch that allowed free adjustment of the illumination time. This study also utilized a microscope (Nikon, ECLIPSE Ti-S, Japan) and microplate reader (Thermo, Multiskan FC, China); all other chemicals and reagents were purchased from the China National Pharmaceutical Group Corporation.

**2.3. Continuous Light/Dark.** The female rats were randomly divided into control and experimental groups and placed in the light experiment box. The control group was under a circadian rhythm of 12:12 h light-dark cycle (L/D, lights on at 8 a.m. Beijing standard time). The rats in the experimental group were exposed to a continuous light environment (L/L, lights on 24 hours every day) for 16 weeks.

**2.4. Vaginal Smears.** Daily vaginal smears were performed on all rats, and their estrous cycles were observed. A sterile cotton swab was soaked in 0.9% saline before it was smeared around the first 1/3 of the vaginal wall. The cotton swab was removed and was smeared in the same direction on a glass slide. The cells were evaluated under light microscopy, and the samples were classified as 1 of the 4 stages of the estrous cycle. Diestrus vaginal smears were identified by the presence of high numbers of leukocytes, proestrus vaginal smears were identified by the presence of small-nucleated epithelial cells, estrus smears were identified by large numbers of cornfield epithelial cells, and metestrus smears were identified by the presence of leukocytes.

**2.5. ELISA Analysis.** At the end of 16 weeks, the rats were anesthetized, and blood samples were obtained from the inferior vena cava and placed into Vacutainer tubes with coagulant. Serum was separated and stored at –80°C for subsequent testosterone determination by enzyme-linked immunosorbent assay (ELISA) (Testosterone EIA Kit, Cayman Chemical, item number 582701, made in USA). ELISA was performed according to the instruction manual of the EIA kit.

**2.6. Histology.** Ovary tissue from all rats was harvested after euthanasia. After weighing with a precision balance (Sartorius, BT 125D, Germany), the ovaries were fixed with 4% formaldehyde buffer, embedded in paraffin, sectioned into 4 μm slides, and stained with hematoxylin-eosin (H&E). The sections were observed, and photographs were taken using a Nikon microscope (CLIPSE Ti-S, Japan).

**2.7. Statistical Analysis.** Data are presented as the means ± SE. Statistical significance was determined using either Student's *t*-test or Fisher's exact test. Statistical significance was defined as  $P < 0.05$ , and two-tailed tests were used. All data analysis and graphing were carried out using Origin 8.0 software (Origin Lab, USA) or SPSS 19.0 for Windows.

## 3. Results

**3.1. Continuous Light-Induced Changes in Body, Ovarian, and Uterus Weights.** Changes in body, ovarian, and uterine weight were monitored in all animals. Compared with the control group, body weight growth in L/L rats became slow after 5 weeks (body weights of L/L group versus control at the end of 5 weeks:  $256.56 \pm 4.85$  g versus  $265.67 \pm 3.61$  g,  $P > 0.05$ ). After 12 weeks, the difference of body weights in two groups was statistically significant (body weights of L/L group versus control at the end of 12 weeks:  $277.91 \pm 5.76$  g versus  $299.08 \pm 4.60$  g,  $P < 0.01$ ) and persisted for the remainder of the experiment (Figure 1).

We compare the weight of the bilateral ovaries: either the left ovary or the right ovary in the L/L group was heavier than that in the L/D group (left ovary,  $P < 0.05$ ; right ovary,  $P < 0.01$ ) (Figure 2). Similar to the weight of the ovaries, hypertrophied uteri were present in the L/L rats. Uterine weights in the L/L rats were higher than those in the L/D group (Figure 3) ( $P < 0.05$ ).

**3.2. Changes in the Estrous Cycle.** Using daily vaginal smears, estrous cyclicity was analyzed at the beginning, after 4 weeks and after 16 weeks of the experimental process. Figure 4 shows the following results: (1) before continuous light, vaginal smears on four consecutive days show a disciplinary transmutation with a sequence of diestrus, proestrus, estrus, and metestrus (Figure 4(a)) and (2) at the end of 4 weeks, 8 of the 12 rats (66.7%) (Table 1) in the continuous light group displayed an indiscriminate estrous cycle. We observed that, in the vaginal smears, the cyclicity stopped at a proestrous state on all four days (Figure 4(b)). Using Fisher's exact test, the difference was significant ( $P = 1.35E - 3$ ). (3) At the end

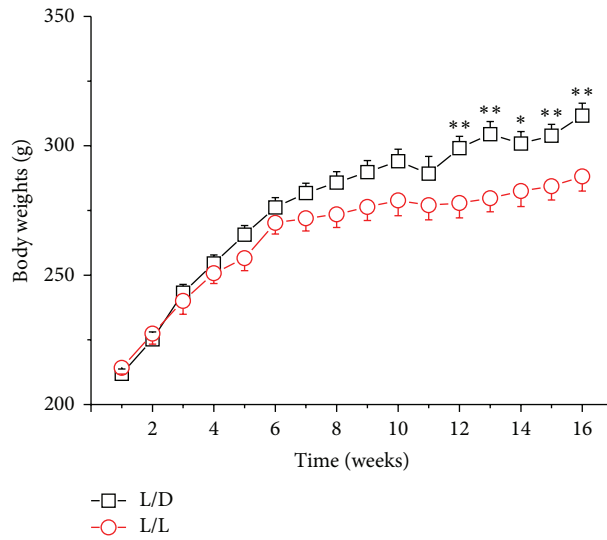


FIGURE 1: The changes of rats' body weights;  $n = 24$ , with 12 rats in each group. \*  $P < 0.05$ , \*\*  $P < 0.01$  L/L group versus control (L/D).

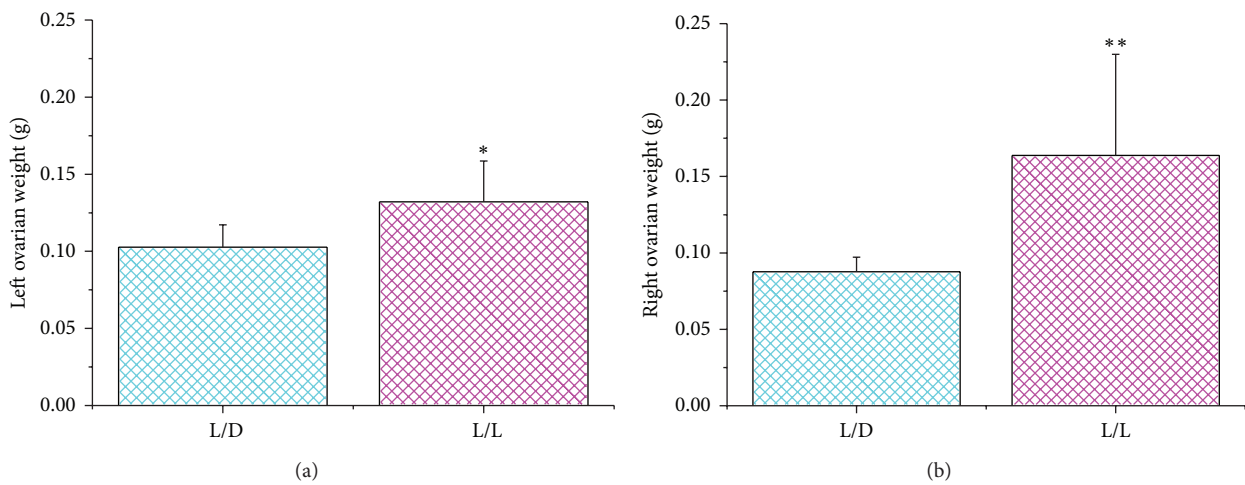


FIGURE 2: The left ovarian weights (a) and right ovarian weights (b) in the two groups. There was a statistically significant difference between them (\*  $P < 0.05$ , \*\*  $P < 0.01$  L/L group versus control).

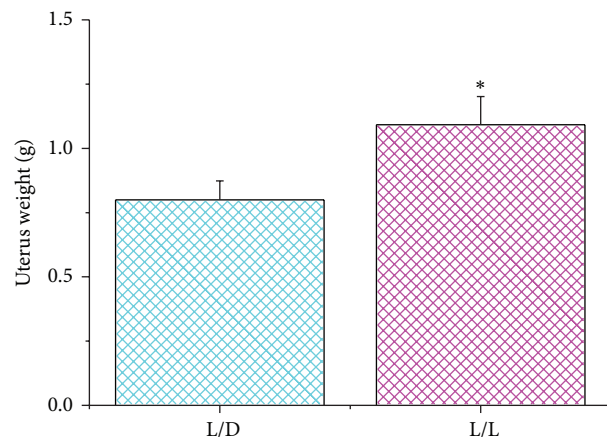


FIGURE 3: The average uterine weight in the two groups (\*  $P < 0.05$  L/L group versus control).

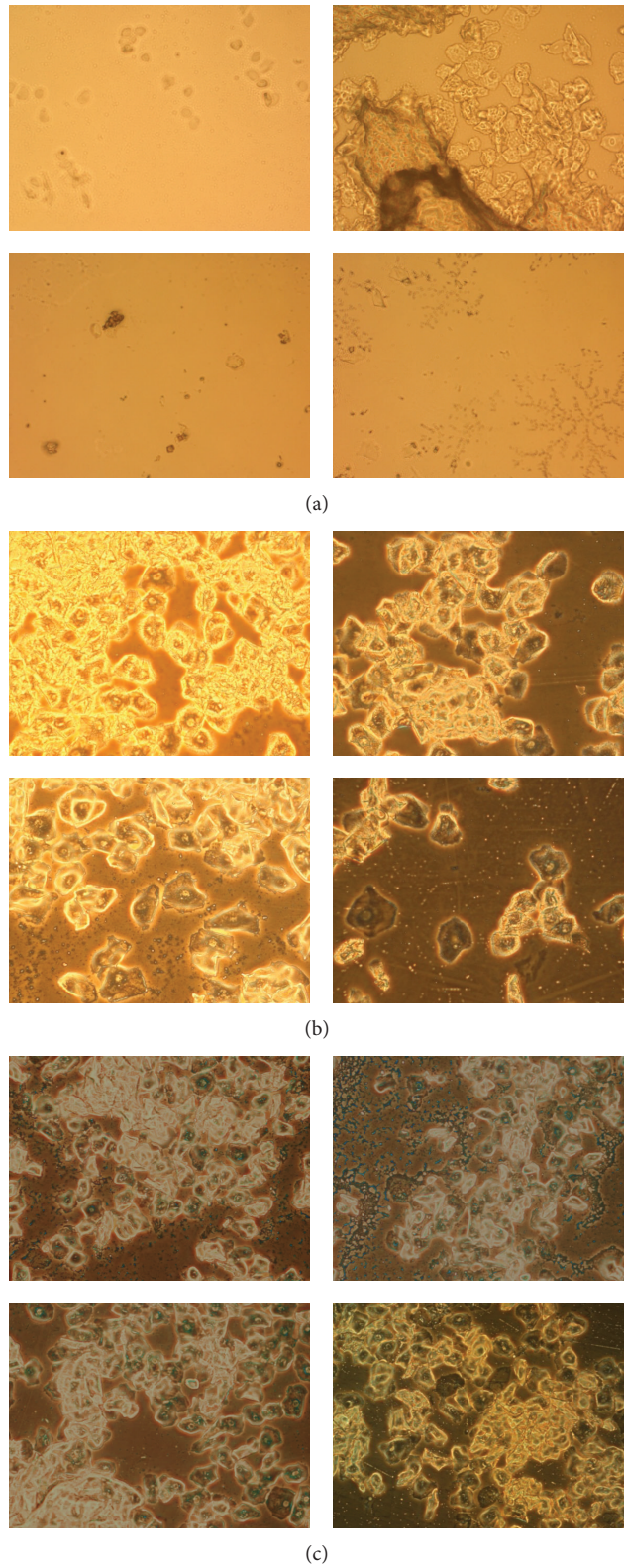


FIGURE 4: Typical vaginal smear for four consecutive days in different experimental periods and different groups. (a) Normal rat's vaginal smear; (b) L/L group in the 4 weeks; (c) L/L group in the 16 weeks. Magnification is 100x.

TABLE 1: Incidence of estrous cycle disorders at the end of 4 weeks of continuous light.

Groups	No. of rats with ECDs	No. of rats without ECDs	Total	Incidence	<i>P</i> value
L/D	0	12	12	0%	$1.346E - 3$
L/L	8	4	12	66.7%	
Total	8	16	24	—	

Abbreviation: ECDs: estrous cycle disorders.

TABLE 2: Incidence of estrous cycle disorders at the end of 16 weeks of continuous light.

Groups	No. of rats with ECDs	No. of rats without ECDs	Total	Incidence	<i>P</i> value
L/D	1	11	12	8.3%	$9.6148E - 6$
L/L	12	0	12	100%	
Total	13	11	24	—	

Abbreviation: ECDs: estrous cycle disorders.



FIGURE 5: Apparent states among rats in the continuous light group at the end of 16 weeks. (a) In the control group the rats were in good spirits and were agile, and their fur was clean and smooth. (b) In the continuous light group the rats showed a poor mental state, were lethargic, and had decreased activity, and their fur, especially on the lower back, was dirty and showed obvious loss.

of 16 weeks, all the L/L rats (12 of 12, 100%) showed an indiscriminate estrous cycle (Figure 4(c)), similar to that after 4 weeks; and 1 of 12 rats in control group also showed an indiscriminate estrous cycle (Table 2, L/D versus L/L  $P = 9.61E - 6$ ).

**3.3. Changes in Fur and Mental Status.** Similar to human PCOS, L/L rats demonstrated patches of diffuse fur loss, and their furs were unburnished grey compared to the shiny fur of the control group. Loss of fur from the dorsal and neck portions of the rats was clearly visible. The difference in fur loss in each group was evaluated by visual observation and was recorded by photographs (Figures 5(a) and 5(b)). All rats in the L/L group showed different degrees of depilation; some rats had serious loss on the back and neck, and some had loss on the hip. At the same time, in the continuous light group, all rats showed a poor mental state, exhibiting lethargy and decreased activity (Figure 5(b)).

**3.4. Ovarian Morphological Changes.** We observed enlarged ovaries in the L/L group, and transparent fluid was visible through the surface layer tissue (Figure 6(a)).

Histopathological examination of ovarian tissue samples showed polycystic ovarian tissue formation in the L/L

group, while the control group showed normal ovarian tissue histology. In the L/L group ovaries, thickening of the surface albuginea, under which there were many follicles in different phases, including atretic follicles and cystic dilating follicles, as well as fewer layers of granular cells and missing oocytes and corona radiating within the follicles, was present (Figure 6(c)). Ovaries in the control group showed multiple luteal, preantral, and antral follicles. The granular cells within the follicles showed multiple layers (Figure 6(b)). The incidences of this phenomenon were 0 of 12 in the L/D group and 10 of 12 (83.3%) in the L/L group (Table 3, L/D versus L/L,  $P = 6.73E - 5$ ).

**3.5. Elevated Testosterone Levels in Serum.** We compared the serum testosterone levels of the control and experimental groups and found that serum testosterone levels were significantly increased in the experimental group ( $30.11 \pm 5.98$  pg/mL versus  $89.91 \pm 16.72$  pg/mL,  $P = 0.00353$ ,  $n = 15$ ) (Figure 7).

## 4. Discussion

In the present study, we first observed that serum testosterone levels of female rats increased in a continuous light

TABLE 3: Incidence of polycystic ovary-like changes in histopathology at the end of 16 weeks of continuous light.

Groups	No. of rats with POLCs	No. of rats without POLCs	Total	Incidence	<i>P</i> value
L/D	0	12	12	0%	6.7304E - 5
L/L	10	2	12	83.3%	
Total	10	14	24	—	

Abbreviation: POLCs: polycystic ovary-like changes.

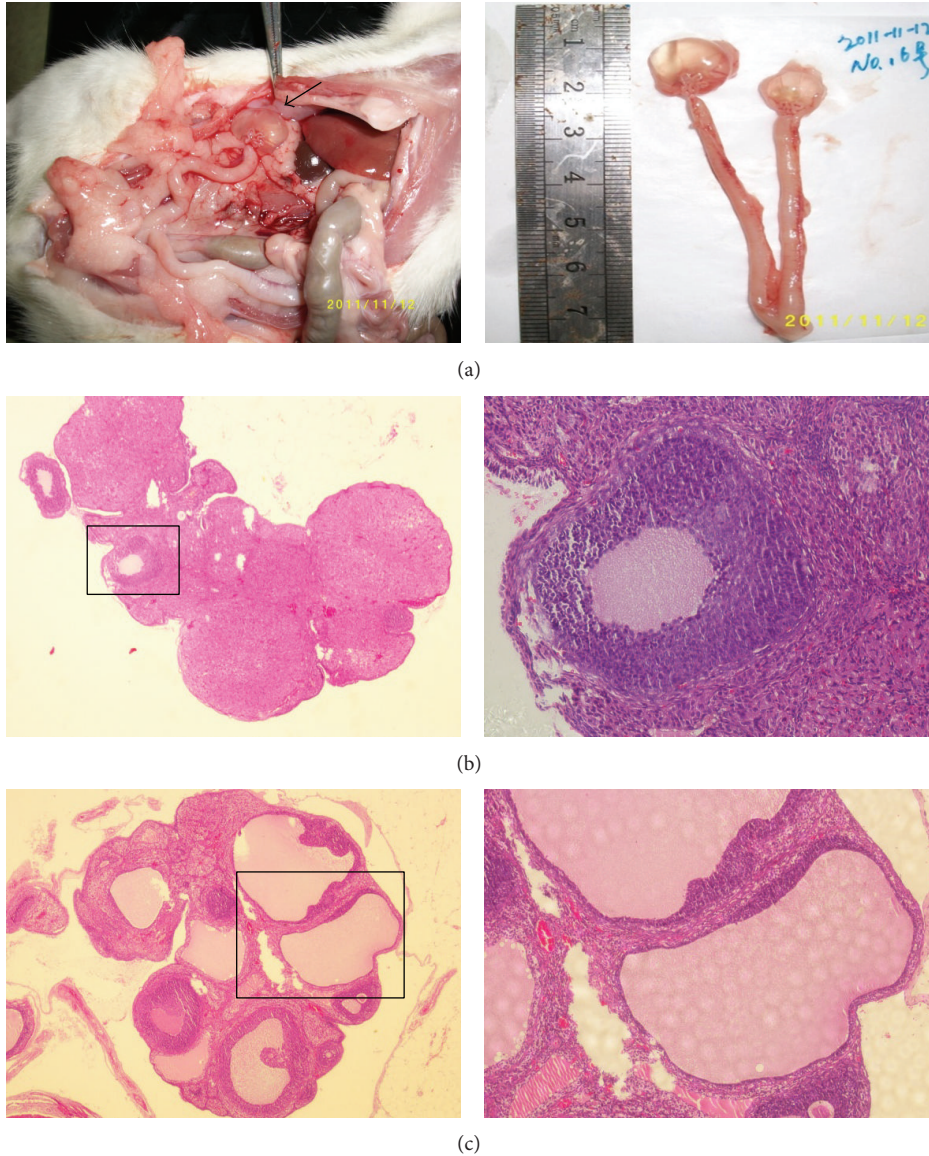


FIGURE 6: Macroscopic view and pathomorphological changes of rats' ovaries at the end of 16 weeks. (a) Left: macroscopic view of PCOS-induced ovaries (arrow) in rats. Right: the gross morphology of typical ovary and uterus. (b) Representative pathological section for L/D group; magnification is 40x (left) and 200x (right). (c) Representative pathological section for L/L group; magnification is 40x (left) and 100x (right).

environment; and also, our results show that body weights decreased in female rats in a continuous light environment with both ovarian and uterine augmentation; the estrous cycle in L/L rats was disordered, and polycystic ovary-like changes occurred, accompanied with fur loss and lethargy.

Steroid hormones play an important role in the effects of daylight changes. The hypothalamic suprachiasmatic nucleus (SCN) is the locus of a master clock that expresses androgen receptor (AR) in humans and regulates circadian rhythms in physiology and behavior. Research found that there is

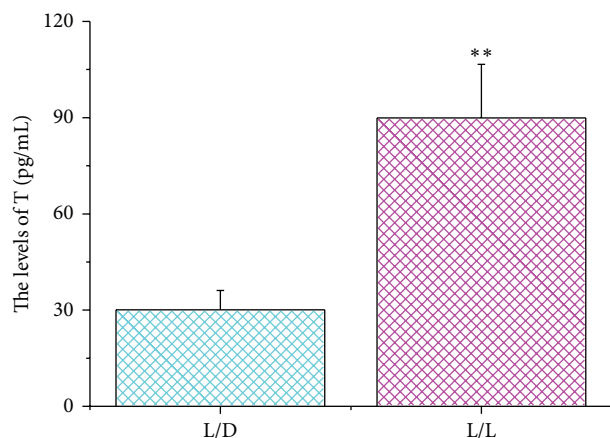


FIGURE 7: The levels of testosterone in rats' serum in different groups. The concentration of testosterone among rats in the continuous light group was greater than that in the control group (\*\* $P < 0.01$ , L/D group versus L/L group).

a correlation between plasma androgen levels and sleep onset in males, clock gene proteins expression in the SCN in response to the onset of environmental light [15, 16]. Testosterone concentration was positively correlated with SCN AR expression. Androgen can modulate SCN responsiveness to light and can modulate SCN timekeeping in a dose-dependent manner [17]. In mice, SCN restricts AR-containing cells and receives photic cues from the retina, and AR occurs in approximately half of the SCN neurons that respond directly to an acute light pulse by expressing FOS [18]. The SCN regulates the phasic release of hormones as well as the timing of the preovulatory LH surge necessary for ovulation in females [15]. In golden hamsters, the behavioral effects of androgen from seasonal changes in day length act are regulated via a pineal-dependent mechanism [19]. Meanwhile, males in the continuous dark condition (D/D) had higher serum androgen levels than in the L/L and L/D, while males in the L/L had higher serum prolactin levels [20]. Mice with a higher circulating testosterone concentration had more precise clocks and ran much faster, but for a shorter duration, than their counterparts with a low testosterone concentration. The LH surge is controlled by the anteroventral periventricular nucleus (AVPV) Kiss1 neurons, whose activity is gated by SCN signals in an estradiol- (E<sub>2</sub>-) dependent manner [21], and rats under L/L conditions induced a decrease in the serum estradiol level of rats in proestrus and an increase in rats in estrus [22]. Our study showed that serum testosterone levels of female rats increased obviously in a continuous light environment firstly, and it proves directly that the disorder of light conditions leads to the hormone level changes in female rats. This is a direct evidence which suggests the possibility that erratic lifestyle factor and bad sleep habits can lead to the onset of PCOS.

Earlier investigations have reported that the endometrium is thinner in women with PCOS and oligoamenorrhea [23], and, thus, the uteri are relatively small in humans with PCOS. Six of 8 hamsters exposed to L/L had ova in their oviducts at

autopsy, and they also had significantly larger uteri ( $P < 0.01$ ) than hamsters exposed to L/D [24, 25]. We found enlarged uteri filled with pus; these changes may be related to recurrent uterine infection. In rats, a lack of ovulation may cause a decrease in the ability of the reproductive system to self-clean due to long-term, repeated bacterial invasion because of the neuroendocrine system disorders and the consequent decline in immunity.

Rats exposed to constant light experience inhibition of the pineal gland function [26]; pinealocyte cell activity increases in rats exposed to constant darkness and decreases in rats exposed to constant light [27]. For rats exposed to constant dark or dim light, melatonin levels are completely suppressed [28]. In mammals, melatonin is synthesized by the pineal gland, and its synthesis is under direct control of the central circadian pacemaker that is located in the SCN of the hypothalamus [29]. Melatonin plays a role in the maintenance of proper follicular function and is thus important for ovulation and progesterone production [30]. Experiments in animals have confirmed beneficial effects of melatonin administration on oocyte maturation and embryo development [31]. Melatonin can reduce oxidative stress and contribute to oocyte maturation, embryo development, and the luteinization of granulosa cells. Melatonin can increase fertilization and pregnancy rates [32]. L/L induces constant estrous anovulatory (CEA) syndrome and blockage of pineal gland activity. Chronic treatment with melatonin is able to overcome the anovulatory state in approximately 70% of L/L-CEA rats, and the luteinizing effect of melatonin is significantly counteracted either by feeding the animals a tryptophan-poor diet or by injecting methiothepin (a blocker of central serotonergic receptors). Melatonin elicits luteinization in L/L-CEA rats through the brain serotonergic system [33]. Exposure to L/L regimens accelerates age-related switch-off of the estrous function in females [34].

Rats become stressed and anxious as a result of major changes in their environment. Constant light may lead to partial sleep deprivation; sleep deprivation is associated with physiological stress responses and an elevated cortisol response in the hypothalamic-pituitary-adrenal (HPA) axis [35]. Hair loss in this model indicates a neuro-endocrin-immune issue. In humans, autoimmune diseases are one of the most common reasons for alopecia areata, which can be considered a T-cell-mediated autoimmune disease [36]. In a rat model of alopecia areata, organ-specific autoimmune disease has been shown to have an important role in hair growth [37]. However, many hormones, and especially testosterone, influence hair growth. Androgenetic alopecia is the most common form of hair loss in men and women [38]. A testosterone-induced alopecia animal model has been used to research hair loss and treatments [39]. In hair follicles, the androgen binds to androgen receptors and exerts its effect directly [40]. Abnormal levels of androgen in our experiment may cause fur loss in rats. The experimental rats may also have disorders of the immune system that lead to fur loss.

## 5. Conclusions

In summary, the continuous light exposure-induced PCOS rat model simulates human sleep disorder. In this environment,

rats appeared to experience pathologically and physiologically high androgen levels. This model simulates PCOS in human beings and is more consistent with the natural disease state. The pathologic physiological phenomenon demonstrated in this model may elucidate new mechanisms of PCOS. Poor sleep habits or negligence of sleep hygiene may be an important lifestyle factor in pathogenesis of PCOS.

## Conflict of Interests

The authors declare that there is no conflict of interests regarding the publication of this paper.

## Acknowledgments

This work was supported by NSFC (81001569, 81102657, 81072874, and 81320108028), Shanghai Key Laboratory of Acupuncture Mechanism and Acupoint Function (14DZ2260500), NBRP (12CB518502, 2015CB54505), and CSA of TCM (ZYSNXD-CC-ZDXK-07).

## References

- [1] S. Franks, "Polycystic ovary syndrome," *The New England Journal of Medicine*, vol. 333, no. 13, pp. 853–861, 1995.
- [2] R. J. Norman, D. Dewailly, R. S. Legro, and T. E. Hickey, "Polycystic ovary syndrome," *The Lancet*, vol. 370, no. 9588, pp. 685–697, 2007.
- [3] D. Szukiewicz and J. T. J. Uilenbroek, "Polycystic ovary syndrome—searching for an animal model," *Journal of Medicine*, vol. 29, no. 5-6, pp. 259–275, 1998.
- [4] K. L. Knutson and E. van Cauter, "Associations between sleep loss and increased risk of obesity and diabetes," *Annals of the New York Academy of Sciences*, vol. 1129, pp. 287–304, 2008.
- [5] K. Spiegel, K. Knutson, R. Leproult, E. Tasali, and E. van Cauter, "Sleep loss: a novel risk factor for insulin resistance and type 2 diabetes," *Journal of Applied Physiology*, vol. 99, no. 5, pp. 2008–2019, 2005.
- [6] N. Shreeve, F. Cagampang, K. Sadek et al., "Poor sleep in PCOS; is melatonin the culprit?" *Human Reproduction*, vol. 28, no. 5, pp. 1348–1353, 2013.
- [7] B. Mokhlesi, B. Scoccia, T. Mazzone, and S. Sam, "Risk of obstructive sleep apnea in obese and nonobese women with polycystic ovary syndrome and healthy reproductively normal women," *Fertility and Sterility*, vol. 97, no. 3, pp. 786–791, 2012.
- [8] A. E. Herbison, R. Porteous, J.-R. Pape, J. M. Mora, and P. R. Hurst, "Gonadotropin-releasing hormone neuron requirements for puberty, ovulation, and fertility," *Endocrinology*, vol. 149, no. 2, pp. 597–604, 2008.
- [9] C. E. McCormack, "Acute effects of altered photoperiods on the onset of ovulation in gonadotropin treated immature rats," *Endocrinology*, vol. 93, no. 2, pp. 403–410, 1973.
- [10] A. L. Weber and N. T. Adler, "Delay of constant light-induced persistent vaginal estrus by 24-hour time cues in rats," *Science*, vol. 204, no. 4390, pp. 323–325, 1979.
- [11] K. B. Singh, "Induction of polycystic ovarian disease in rats by continuous light. II. Observations on mating, pregnancy, and the postpartum period," *The American Journal of Obstetrics and Gynecology*, vol. 104, no. 7, pp. 1004–1007, 1969.
- [12] S. F. Baldissera, L. D. Motta, M. C. Almeida, and J. Antunes-Rodrigues, "Proposal of an experimental model for the study of polycystic ovaries," *Brazilian Journal of Medical and Biological Research*, vol. 24, no. 7, pp. 747–751, 1991.
- [13] R. Rebar, H. L. Judd, S. S. C. Yen, J. Rakoff, G. Vandenberg, and F. Naftolin, "Characterization of the inappropriate gonadotropin secretion in polycystic ovary syndrome," *Journal of Clinical Investigation*, vol. 57, no. 5, pp. 1320–1329, 1976.
- [14] K. A. Walters, C. M. Allan, and D. J. Handelsman, "Rodent models for human polycystic ovary syndrome," *Biology of Reproduction*, vol. 86, no. 5, article 149, 2012.
- [15] A. Abizaid, G. Mezei, and T. L. Horvath, "Estradiol enhances light-induced expression of transcription factors in the SCN," *Brain Research*, vol. 1010, no. 1-2, pp. 35–44, 2004.
- [16] A. Fernandez-Guasti, F. P. Kruijver, M. Fodor, and D. F. Swaab, "Sex differences in the distribution of androgen receptors in the human hypothalamus," *Journal of Comparative Neurology*, vol. 425, no. 3, pp. 422–435, 2000.
- [17] M. P. Butler, I. N. Karatsoreos, J. L. Sauter, and R. Silver, "Dose-dependent effects of androgens on the circadian timing system and its response to light," *Endocrinology*, vol. 153, no. 5, pp. 2344–2352, 2012.
- [18] I. N. Karatsoreos, A. Wang, J. Sasanian, and R. Silver, "A role for androgens in regulating circadian behavior and the supra-chiasmatic nucleus," *Endocrinology*, vol. 148, no. 11, pp. 5487–5495, 2007.
- [19] E. L. Bittman, M. L. Tubbiola, G. Foltz, and C. M. Hegarty, "Effects of photoperiod and androgen on proopiomelanocortin gene expression in the arcuate nucleus of golden hamsters," *Endocrinology*, vol. 140, no. 1, pp. 197–206, 1999.
- [20] B. D. Fantie, R. E. Brown, and W. H. Moger, "Constant lighting conditions affect sexual behaviour and hormone levels in adult male rats," *Journal of Reproduction and Fertility*, vol. 72, no. 2, pp. 435–441, 1984.
- [21] J. L. Robertson, D. K. Clifton, H. O. de la Iglesia, R. A. Steiner, and A. S. Kauffman, "Circadian regulation of Kiss1 neurons: implications for timing the preovulatory gonadotropin-releasing hormone/luteinizing hormone surge," *Endocrinology*, vol. 150, no. 8, pp. 3664–3671, 2009.
- [22] D. V. Kliuchkov and V. A. Shul'ga, "The sex and corticosteroid hormones of rats selected for estrous-cycle reaction to constant illumination," *Zhurnal Evolutsionnoi Biokhimi i Fiziologii*, vol. 30, no. 5, pp. 676–682, 1994.
- [23] H. Leonhardt, B. Gull, K. Kishimoto et al., "Uterine morphology and peristalsis in women with polycystic ovary syndrome," *Acta Radiologica*, vol. 53, no. 10, pp. 1195–1201, 2012.
- [24] J. S. Ferraro and C. E. McCormack, "Gonadal regression despite light pulses coincident with locomotor activity in the syrian hamster," *Biology of Reproduction*, vol. 33, no. 1, pp. 93–102, 1985.
- [25] K. B. Singh, "Induction of polycystic ovarian disease in rats by continuous light. III. Mechanism of ovarian compensatory hypertrophy and ovulation after unilateral oophorectomy," *The American Journal of Obstetrics and Gynecology*, vol. 104, no. 7, pp. 1008–1011, 1969.
- [26] V. N. Anisimov, "Light pollution, reproductive function and cancer risk," *Neuroendocrinology Letters*, vol. 27, no. 1-2, pp. 35–52, 2006.
- [27] I. Kus, M. Sarsilmaz, O. A. Ozen et al., "Light and electron microscopic examination of pineal gland in rats exposed to constant light and constant darkness," *Neuroendocrinology Letters*, vol. 25, no. 1-2, pp. 102–108, 2004.

- [28] D. E. Blask, R. T. Dauchy, L. A. Sauer, J. A. Krause, and G. C. Brainard, "Light during darkness, melatonin suppression and cancer progression," *Neuroendocrinology Letters*, vol. 23, no. 2, pp. 52–56, 2002.
- [29] D. C. Klein, S. L. Coon, P. H. Roseboom et al., "The melatonin rhythm-generating enzyme: molecular regulation of serotonin N-acetyltransferase in the pineal gland," *Recent Progress in Hormone Research*, vol. 52, pp. 307–357, 1997.
- [30] C. C. Maganhin, L. F. Fuchs, R. S. Simoes et al., "Effects of melatonin on ovarian follicles," *European Journal of Obstetrics & Gynecology and Reproductive Biology*, vol. 166, no. 2, pp. 178–184, 2013.
- [31] H. Tamura, A. Takasaki, T. Taketani et al., "The role of melatonin as an antioxidant in the follicle," *Journal of Ovarian Research*, vol. 5, no. 1, article 5, 2012.
- [32] H. Tamura, A. Takasaki, T. Taketani et al., "Melatonin as a free radical scavenger in the ovarian follicle," *Endocrine Journal*, vol. 60, no. 1, pp. 1–13, 2013.
- [33] G. P. Trentini, B. Mess, C. F. de Gaetani, and C. Ruzsas, "Effect of melatonin on induction of ovulation in the light-induced constant estrous-anovulatory syndrome and possible role of the brain serotonergic system," *Journal of Endocrinological Investigation*, vol. 1, no. 4, pp. 305–310, 1978.
- [34] V. N. Anisimov, I. A. Vinogradova, A. V. Panchenko, I. G. Popovich, and M. A. Zabezhinski, "Light-at-night-induced circadian disruption, cancer and aging," *Current Aging Science*, vol. 5, no. 3, pp. 170–177, 2012.
- [35] J. Minkel, M. Moreta, J. Muto et al., "Sleep deprivation potentiates HPA axis stress reactivity in healthy adults," *Health Psychology*, vol. 33, no. 11, pp. 1430–1434, 2014.
- [36] A. Gilhar, A. Etzioni, and R. Paus, "Alopecia areata," *The New England Journal of Medicine*, vol. 366, no. 16, pp. 1515–1525, 2012.
- [37] K. J. McElwee, E. M. Spiers, and R. F. Oliver, "In vivo depletion of CD8+ T cells restores hair growth in the DEBR model for alopecia areata," *British Journal of Dermatology*, vol. 135, no. 2, pp. 211–217, 1996.
- [38] G. Cotsarelis and S. E. Millar, "Towards a molecular understanding of hair loss and its treatment," *Trends in Molecular Medicine*, vol. 7, no. 7, pp. 293–301, 2001.
- [39] M. Noubarani, H. Rostamkhani, M. Erfan et al., "Effect of *Adiantum capillus veneris* linn on an animal model of testosterone-induced hair loss," *Iranian Journal of Pharmaceutical Research*, vol. 13, supplement, pp. 113–118, 2014.
- [40] K. D. Kaufman, "Androgens and alopecia," *Molecular and Cellular Endocrinology*, vol. 198, no. 1-2, pp. 89–95, 2002.

## Research Article

# Animal Models of Depression and Drug Delivery with Food as an Effective Dosing Method: Evidences from Studies with Celecoxib and Dicholine Succinate

João P. Costa-Nunes,<sup>1,2,3</sup> Brandon H. Cline,<sup>4</sup> Margarida Araújo-Correia,<sup>2,5</sup> Andreia Valença,<sup>2,6</sup> Natalyia Markova,<sup>7,8</sup> Oleg Dolgov,<sup>9</sup> Aslan Kubatiev,<sup>7</sup> Naira Yeritsyan,<sup>10</sup> Harry W. M. Steinbusch,<sup>1</sup> and Tatyana Strekalova<sup>1,3,8</sup>

<sup>1</sup> Department of Neuroscience, School for Mental Health and Neuroscience, Maastricht University, Universiteitssingel 40, 6200 MD Maastricht, Netherlands

<sup>2</sup> CBA, Faculdade de Ciências, Universidade de Lisboa, Campo Grande, 1749-016 Lisboa, Portugal

<sup>3</sup> Instituto de Higiene e Medicina Tropical, Universidade Nova de Lisboa, Rua da Junqueira 100, 1349-008 Lisboa, Portugal

<sup>4</sup> INSERM U1119, Université de Strasbourg, Bâtiment 3 de la Faculté de Médecine, 11 rue Humann, 67000 Strasbourg, France

<sup>5</sup> Chronic Diseases Research Center, Faculdade de Ciências Médicas, Universidade Nova de Lisboa, Campo Mártires da Pátria 130, 1169-056 Lisboa, Portugal

<sup>6</sup> Faculdade de Medicina Veterinária, Universidade Técnica de Lisboa, Avenida da Universidade Técnica, 1300-477 Lisboa, Portugal

<sup>7</sup> Institute of General Pathology and Pathophysiology, Russian Academy of Medical Sciences, Baltiyskaya 8, Moscow 125315, Russia

<sup>8</sup> Institute of Physiologically Active Compounds, Russian Academy of Sciences, Severnii proesd 1, Chernogolovka, Moscow Region 142432, Russia

<sup>9</sup> Anokhin Institute of Normal Physiology, Russian Academy of Medical Sciences, Baltiyskaya 8, Moscow 125315, Russia

<sup>10</sup> Division of Cardiology, University Hospital Magdeburg, Leipziger Strasse 44, 39120 Magdeburg, Germany

Correspondence should be addressed to Tatyana Strekalova; [t.strekalova@maastrichtuniversity.nl](mailto:t.strekalova@maastrichtuniversity.nl)

Received 24 September 2014; Accepted 5 December 2014

Academic Editor: Andrea Vecchione

Copyright © 2015 João P. Costa-Nunes et al. This is an open access article distributed under the Creative Commons Attribution License, which permits unrestricted use, distribution, and reproduction in any medium, provided the original work is properly cited.

Multiple models of human neuropsychiatric pathologies have been generated during the last decades which frequently use chronic dosing. Unfortunately, some drug administration methods may result in undesirable effects creating analysis confounds hampering model validity and preclinical assay outcomes. Here, automated analysis of floating behaviour, a sign of a depressive-like state, revealed that mice, subjected to a three-week intraperitoneal injection regimen, had increased floating. In order to probe an alternative dosing design that would preclude this effect, we studied the efficacy of a low dose of the antidepressant imipramine (7 mg/kg/day) delivered via food pellets. Antidepressant action for this treatment was found while no other behavioural effects were observed. We further investigated the potential efficacy of chronic dosing via food pellets by testing the antidepressant activity of new drug candidates, celecoxib (30 mg/kg/day) and dicholine succinate (50 mg/kg/day), against standard antidepressants, imipramine (7 mg/kg/day) and citalopram (15 mg/kg/day), utilizing the forced swim and tail suspension tests. Antidepressant effects of these compounds were found in both assays. Thus, chronic dosing via food pellets is efficacious in small rodents, even with a low drug dose design, and can prevail against potential confounds in translational research within depression models applicable to adverse chronic invasive pharmacotherapies.

## 1. Introduction

The challenge to propose new powerful therapeutics for neuropsychiatric disorders, including antidepressants, has raised

important questions regarding the efficiency of preclinical approaches currently being used [1–3]. Numerous limitations of the models of human neuropsychiatric pathologies have been intensively discussed during the last years [4–6]. Apart

from a general problem of translational research, basic practical issues with animal models of neuropsychiatric conditions, however seemingly trivial, can essentially affect the validity of preclinical models, yet these can be addressed and resolved.

As with translational models in small rodents, these issues concern laboratory and procedural settings in animal studies. A number of experimental conditions have been shown to result in potential confounds for the practical application of animal models. The principals of these factors are commonly considered to include the circadian phase of manipulations [7, 8], cage enrichment [9–11], lighting conditions [12, 13], handling [14–16], vibration [17], the adverse taste of food or water [18, 19], and presence of and manipulations by an experimenter [20, 21]. They are sometimes believed to result in the remarkable variability in results that are extensively reported by the literature [18, 22–24]. The method and duration of dosing of experimental animals are one of the important sources of such confounds [25–27].

Various types of invasive treatments in rodents were shown to induce pain, inflammation, and distress, despite the proper use of standardized methods of application, especially when prolonged dosing is employed [28–30]. Obviously, this raises issues that concern not only the quality of studies, in which such dosing methods are used, but also animal welfare and ethical aspects. Nonetheless, in many cases, long and invasive drug administration to small rodents is problematic to avoid. This often applies, for instance, when non-water-soluble compounds have to be chronically administered, for example, during experimental conditions for which the induction of a desirable syndrome in an animal and/or the occurrence of the therapeutic drug's effect require a long time. The latter experimental situations are particularly typical for testing drugs in rodent models of depression where, for example, the induction of some key elements of depressive syndrome may take 2–12 weeks [24, 31, 32] and the occurrence of an antidepressant's effect, with most of the classical antidepressants, develops after 3–4 weeks of treatment [31, 33, 34].

In order to avoid the negative effects of chronic invasive dosing on overall animal welfare and experimental outcomes from standard models of depression, we evaluated the efficacy of drug delivery via food pellets in mice. First, we studied the effects of a three-week daily intraperitoneal vehicle injection in the mouse forced swim test, a common scheme of testing for the antidepressant-like effects of various treatments [32, 34, 35]. As this manipulation resulted in an increase of floating scores, a measure of “behavioural despair,” indicating a “prodepressant” effect of daily intraperitoneal injections for the experimental animals, we probed an alternative way of dosing using food pellets.

Though drug delivery with voluntarily consumed food is one of the common methods of dosing, its use in laboratory research is quite limited. Meanwhile, in many cases, this mode of pharmacological treatment is seen as advantageous because it enables the maintenance of a steady blood concentration for the drug, in contrast to bolus drug administration. However, it is sometimes viewed as insufficiently reliable due to its reliance on food intake and the variable bioavailability of some compounds depending on their delivery route [36, 37].

However, given that, in a reasonable proportion of the experimental situations, the consummatory behaviour of laboratory animals is not altered and the standard pharmacological agents, whose bioavailability and metabolism are well known not to be sensitive to the treatment method, are used, dosing with the voluntary intake of food pellets can probably be exploited much more frequently. Apart from the obvious benefits of animal wellbeing, the delivery of investigational drugs with food pellets can increase the validity of translational models as it simulates a human equivalent therapeutic dosing route.

In this study, we first used, via food pellets, a low dose of a classical antidepressant reference drug, imipramine (7 mg/kg/day), for which chronic administration via drinking water for 3 weeks was recently reported to evoke an antidepressant effect in a model of stress-induced anhedonia [38]. A low dose of antidepressant was selected because we sought to evaluate the usefulness of this dosing method at the lowest possible dosage limit which is used in other means of drug administration and because imipramine may exert side-effects when applied in higher concentrations [6]. The effects of imipramine delivered with self-made food pellets were tested in the forced swim test as well as, in order to exclude potential nonspecific effects of treatment, in a battery of behavioural tests including dark/light box, O-maze, novel cage, open field, and two-bottle sucrose test. Finally, to verify the applicability of this defined dosing method with food pellets, we tested the effects of new potential antidepressants: celecoxib, a non-water-soluble compound, at the dose of 30 mg/kg/day, which was selected based on previously published data [39, 40], and dicholine succinate whose dose was applied at 50 mg/kg/day based on previous results [42], in the forced swim and tail suspension tests. Imipramine, applied at 7 mg/kg/day [6, 36, 41, 42], and citalopram, 15 mg/kg/day [6, 33, 38], were used as pharmacological references.

## 2. Materials and Methods

**2.1. Animals and Housing.** Three-month-old C57BL/6N male mice were supplied by Instituto Gulbenkian de Ciência, Oeiras, Portugal, and housed individually in standard laboratory conditions under a reverse 12:12 h cycle (lights on at 21:00). Behavioural tests took place from the onset of the dark phase of the light cycle (9:00 h). The testing was carried out in a dark quiet room in morning hours. All procedures were in accordance with the European Union's Directive 2010/63/EU, Portuguese Law-Decrees DL129/92 (July 6th), DL197/96 (October 16th), and Ordinance Port. 131/97 (November 7th). This project was approved by the Ethical Committee of the New University of Lisbon.

**2.2. Study Flow with Chronic Intraperitoneal Injections.** This study used a broadly applied treatment, in small rodents, of chronic intraperitoneal injections [30]. We have chosen to expose mice to a three-week daily intraperitoneal injections of NaCl at volume 0.01 mL/g body weight (for scheme of study flow, see Figure 1(a)). Control mice were not treated but handled daily. Starting from the next day after this period,

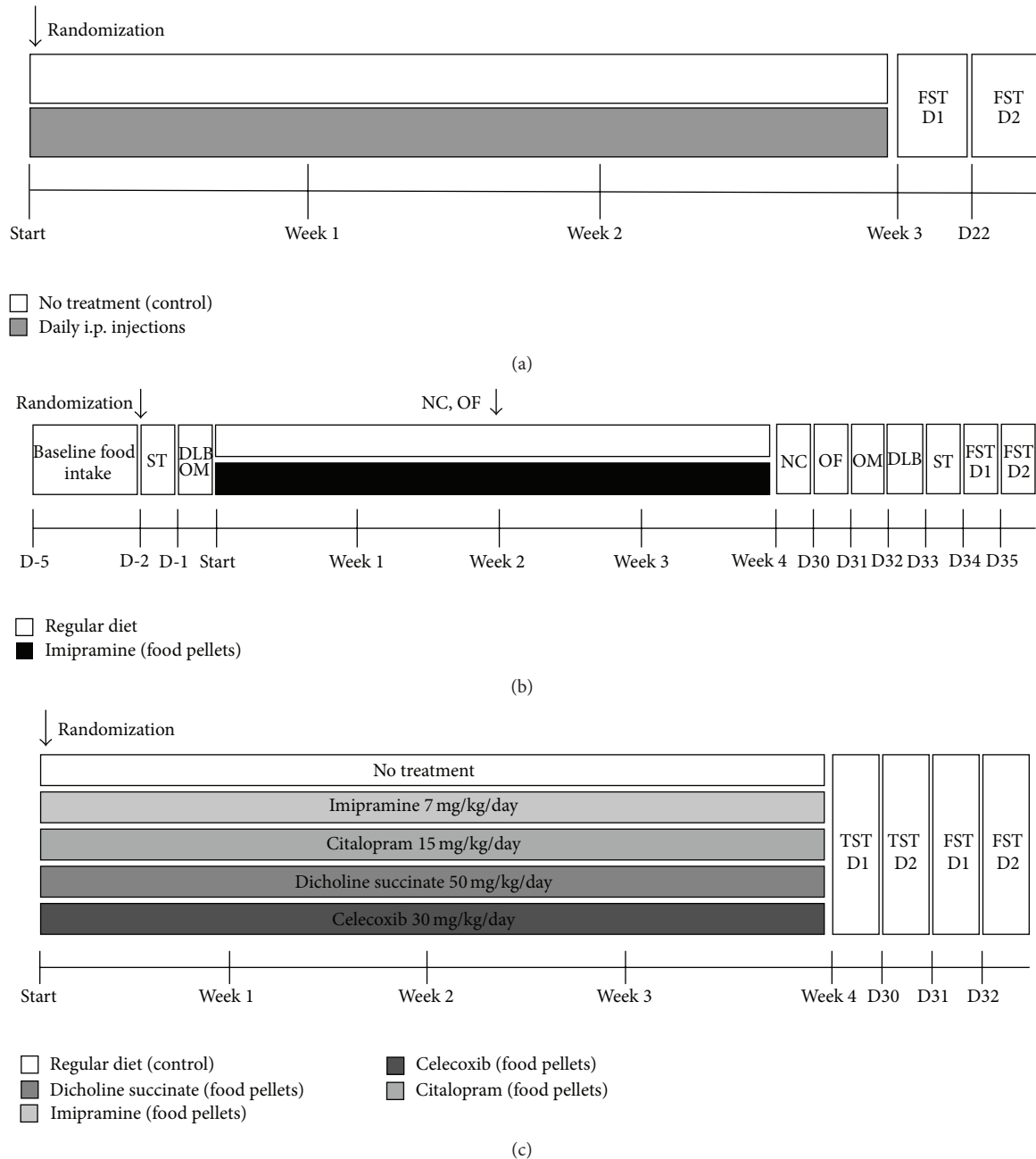


FIGURE 1: Experimental design. (a) Schematic timeline of studies with vehicle injections, chronic delivery with food pellets of (b) imipramine and (c) new drug candidates to antidepressants experiments. i.p.: intraperitoneal injection of a vehicle; FST: forced swim test; TST: tail suspension test; DLB: dark-light box; OM: O-maze; NCT: novel cage test; OF: open field; ST: sucrose test; d: days.

mice were tested in the two-day forced swim test as previously described [38, 41]. Behavioural data were scored using Noldus EthoVision XT 8.5 (Noldus Information Technology, Wageningen, Netherlands). Number of mice per group is indicated in figure legend.

2.3. Study Flow with Chronic Imipramine Delivery via Food Pellets. As a next step, we exposed mice to self-made food pellets that contained imipramine for four weeks. Prior to starting treatment, animals were balanced upon body weight.

The calculation of the used concentration of imipramine in food pellets was based on a daily food intake of experimental mice that constituted  $2.89 \pm 0.26$  g and a desirable dosage of 7 mg/kg/day. The selection of this dose was based on previously obtained data that showed the efficacy of the dose [38] and a lack of such with chronic imipramine delivery via drinking water at a dose of 2.5 mg/kg in mice. Control mice received a regular diet. Before the start and after four weeks of dosing, all mice were tested in the sucrose preference test, O-maze test, and the dark/light test, as described elsewhere

[43, 44]. After two and four weeks of dosing, locomotor activity of all mice was studied in the novel cage and open field tests, as described elsewhere [41, 42, 44]. At the end of behavioural testing, a two-day forced swim test with 6 min sessions was performed as previously described ([38, 41]; for scheme of study flow, see Figure 1(b)). Number of mice per group is indicated in figure legend.

**2.4. Study Flow with Chronic Delivery via Food Pellets of New Candidates to Antidepressants.** Next, we subjected mice to food pellets that contained imipramine, citalopram, celecoxib, or dicholine succinate for four weeks. Prior to starting treatment, animals were balanced upon body weight. The latter two drugs are regarded as compounds with potential antidepressant activity [39, 40, 42]. The calculation of drug concentrations was based on daily food intake of experimental mice, and desirable doses were 7 mg/kg/day, 15 mg/kg/day, 30 mg/kg, and 50 mg/kg, respectively. Control mice received regular diet. A two-day tail suspension test and a two-day forced swim test were carried out during four consecutive days after the termination of the dosing period, as described elsewhere [41, 43] (for scheme of study flow, see Figure 1(c)). Number of mice per group is indicated in figure legend.

**2.5. Preparation of Pellets.** Imipramine hydrochloride (Sigma-Aldrich, Munich, Germany), citalopram (Lundbeck, Copenhagen, Denmark), or celecoxib (Pfizer, Berlin, Germany) was added to commercial chow (Mucedola SRL, Milan, Italy) that was turned to powder by a blender. Small amounts of distilled water were added, and food pellets of a similar size to commercial pellets were formed and dried overnight (16 h) at 60°. New pellets were prepared twice a week in order to refresh the food supply of experimental groups. The content of drugs was adjusted to the dose indicated above and was based on the consumption of normal diet that was averaged over 3 days. Food pellets containing dicholine succinate (Buddha Biopharma Oy Ltd., Helsinki, Finland) were prepared in a similar way, using a 7% solution of the compound; the content of drug was adjusted to the abovementioned daily dose of this drug.

## 2.6. Behavioural Tests

**2.6.1. Forced Swim Test.** The Porsolt forced swim test has been used as described elsewhere [38, 41]. Mice were subjected to two 6 min swimming sessions spaced 24 h apart in a transparent cylinder (Ø 17 cm) filled with water (+23°C, water height 13 cm, height of cylinder 20 cm, and illumination intensity 25 Lux). Floating behaviour was defined by the absence of any directed movements of the animals' head and body and was scored with Noldus EthoVision XT 8.5 (Noldus Information Technology, Wageningen, Netherlands). Using this method, the latency of the first episode of floating and the duration of floating behaviour were recorded during the 6 min swimming session on Day 1 and Day 2 of the test. Latency to begin floating was scored as time between introduction of the animal into the pool and the first moment of complete immobility of the entire body for a duration of

>3 seconds. The total time spent floating, number of floating episodes, mean velocity, and distance moved were scored for the entire duration of the test using posttest video footage.

**2.6.2. Dark/Light Box.** The dark/light box (Technosmart, Rome, Italy) consisted of two plexiglass compartments, one black/dark (15 cm × 20 cm × 25 cm) and one lit (30 cm × 20 cm × 25 cm), connected by a tunnel. Anxiety-like behaviour was assessed by earlier validated measures [41, 43]. Mice were placed into the dark compartment, from where they could visit the lit box, illuminated by light of 25 Lux intensity. The latency of the first exit to the light compartment, the total duration of time spent in the lit box, and the number of visits to this anxiety-related compartment were scored by visual observation over 5 min.

**2.6.3. Elevated O-Maze.** The apparatus (Technosmart, Rome, Italy), which consisted of a circular path (runway width 5.5 cm, diameter 46 cm), was placed 50 cm above the floor. Two opposing arms were protected by walls (height 10 cm), and the illumination strength was 25 Lux. The apparatus was placed on a dark surface in order to reduce reflection and maintain control over lighting conditions during testing. Anxiety-like behaviour was assessed using previously validated parameters [38, 44]. Mice were placed in one of the closed-arm compartments of the apparatus. The latency of the first exit to the anxiety-related open compartments of the maze, the total duration of time spent therein, and the number of exits to the open arms were scored during a 5 min observation period.

**2.6.4. Novel Cage Test.** The novel cage test was performed to assess vertical activity, as described elsewhere [38]. Mice were introduced into a standard plastic cage the size of their home cage filled with small amounts of fresh sawdust. The number of exploratory rearings was counted under red light during a 5 min period.

**2.6.5. Open Field.** The open field apparatus consisted in four square arenas (50 cm × 50 cm × 50 cm), made of wood covered by white Resopal. Mice were put in the center and their behaviour was recorded on camera for 10 min. The open field was illuminated with white light (25 Lux). Distance moved and mean instant speed were analysed off-line using the Any-maze software (Stoelting Co., Wood Dale, IL, USA), as described elsewhere [45].

**2.6.6. Sucrose Test.** Animals were given 8 hours of free choice between two bottles of either 1% sucrose or normal drinking water, as described elsewhere [38]. At the beginning and end of the period, the bottles were weighed and consumption was calculated. The beginning of the test started with the onset of the dark (active) phase of animals' cycle. To prevent the possible effects of side-preference in drinking behaviour, the position of the bottles in the cage was switched at 4 hours, halfway through testing. No previous food or water deprivation was applied before the test. The 1% sucrose solution is used in tests performed across the experiment.

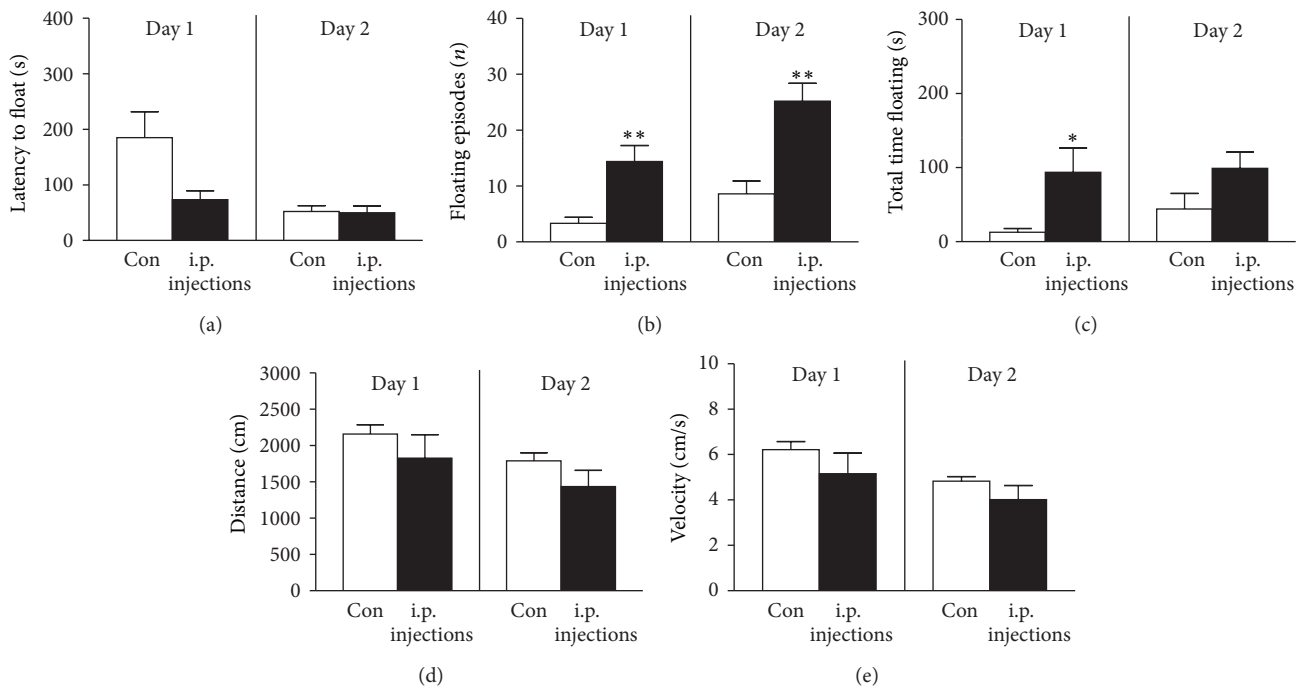


FIGURE 2: Chronic intraperitoneal injections increase depressive-like behaviour in the forced swim test. In comparison with control group, mice that received daily intraperitoneal saline injections over the course of three weeks had a nonsignificant reduction of the latency of floating (a) and significant increase of the total number of floating episodes (b) and total time spent floating (c). There were no significant differences in mean velocity (d) or distance swum (e) between control and injected groups. \*  $P < 0.05$ ; \*\*  $P < 0.01$  versus control (unpaired  $t$ -test). Con: control group ( $n = 7$ ); i.p. injection: a group of mice subjected to intraperitoneal injections with a vehicle ( $n = 5$ ). All data are means  $\pm$  SEM.

Percentage preference for sucrose is calculated using the following formula:

Sucrose Preference

$$= \left[ \frac{V(\text{Sucrose solution})}{V(\text{Sucrose solution}) + V(\text{Water})} \right] \times 100\%. \quad (1)$$

**2.6.7. Tail Suspension Test.** The protocol used in this study was adapted from a previously proposed procedure [41, 43]. Mice were subjected to the tail suspension by being hung by their tails with adhesive tape to a rod 50 cm above the floor for 6 min. Animals were tested in a dark room where only the area of the modified tail suspension construction was illuminated by a spotlight from the ceiling; the lighting intensity on the height of the mouse position was 25 Lux. The trials were recorded by a video camera positioned directly in front of the mice while the experimenter observed the session from a distance in a dark area of the experimental room. This procedure was carried out twice with a 24 h interval between tests. The latency of the first episode of immobility, the total duration of this behaviour, and mean velocity were scored using Noldus EthoVision XT 8.5 (Noldus Information Technology, Wageningen, Netherlands) according to the protocol that was previously validated [41]. In accordance with the commonly accepted criteria of immobility, the immobility behaviour was defined as the absence of any movements of

the animals' head and body. The latency of immobility was determined as the time between the onset of the test and the first bout of immobility.

**2.7. Statistical Analysis.** Data were analysed with GraphPad Prism version 5.00 for Windows (San Diego, CA, USA). Two-tailed unpaired  $t$ -tests were applied for two-group, two-tailed comparisons of independent data sets, as the distribution was normal. One-way ANOVA was used followed by a post hoc Dunnett for a comparison of more than two groups with a control; repeated measures ANOVA was used for analysis of repeated measures. The level of confidence was set at 95% ( $P < 0.05$ ) and data are shown as mean  $\pm$  SEM.

### 3. Results and Discussion

**3.1. Effects of 3-Week Intraperitoneal Vehicle Injections on Floating Behaviour.** Behaviour analysis revealed that animals subjected to injections displayed a nonsignificant decrease of latency to float as compared to control animals (Day 1:  $P = 0.11$ ,  $t = 1.73$ ; Day 2:  $P = 0.91$ ,  $t = 0.12$ , Figure 2(a), unpaired two-tailed  $t$ -test). The number of floating episodes and the duration of floating in the chronically injected group were significantly higher than in control animals (Day 1:  $P = 0.0037$ ,  $t = 3.89$  and  $P = 0.016$ ,  $t = 3.06$ ; Day 2:  $P = 0.0016$ ,  $t = 4.30$  and  $P = 0.11$ ,  $t = 1.77$ , resp.; Figures 2(b) and 2(c),

unpaired two-tailed  $t$ -test); mean velocity of swimming and distance moved were nonsignificantly decreased (Day 1:  $P = 0.25$ ,  $t = 1.25$  and  $P = 0.31$ ,  $t = 1.09$ ; Day 2:  $P = 0.18$ ,  $t = 1.43$  and  $P = 0.15$ ,  $t = 1.56$ , resp.; Figures 2(d) and 2(e), unpaired two-tailed  $t$ -test). This suggests increased “behavioural despair,” a sign of depressive-like state, in mice that received chronic manipulations with intraperitoneal injections.

Similar results were obtained in our previous experiments which demonstrated that three-and four-week daily injections in chronically stressed mice increased the number of individuals exhibiting signs of anhedonia, a reduced sensitivity to reward, in a sucrose preference test [18, 24]. Other studies showed that chronic intraperitoneal injections in rats evoke ultrasonic vocalizations at 22 kHz range, indicative of a negative emotional state that was reduced by preexposure of experimental animals to handling [16]. These “prodepressive” like changes found in this study could be potentially induced by well-recognized pathogenetic elements of depression, such as stress of manipulation [46] and pain experience [47, 48] and repeated situations of unescapable stress and helplessness [49], as well as inflammation [50].

**3.2. Effects of Chronic Imipramine Delivery via Food Pellets on Floating Behaviours and Other Variables.** In order to assess the efficacy of an alternative chronic dosing design that could preclude the adverse changes in behaviour described above, we evaluated the effects of four-week dosing of imipramine via food pellets in the forced swim test and supplementary behavioural paradigms. Animals subjected to imipramine treatment showed a significant increase in the latency to float and decreased immobility time, when compared to control animals (Day 1:  $P = 0.0002$ ,  $t = 5.19$  and  $P = 0.0008$ ,  $t = 4.42$ ; Day 2:  $P = 0.18$ ,  $t = 1.43$  and  $P = 0.0011$ ,  $t = 4.28$ , resp.; Figure 3(a), unpaired two-tailed  $t$ -test). Thus, an applied low dose of antidepressant treatment delivered with food pellets induced an antidepressant-like effect in the present study.

This result is in line with our previous findings that showed that a 3-week low dose administration of imipramine to C57BL6J mice via drinking water reduced such depressive symptoms as stress-induced decrease in sucrose intake and preference, hyperlocomotion, and elevated aggressive behaviour [38]. Similar behavioural results were obtained in the chronic stress depression model with CD1 mice [42] and in a model of elderly depression in 18-month-old C57BL6N mice [41]. The low dose imipramine antidepressant effects were accompanied by preservation of normal activity of brain peroxidation enzymes which were suppressed by chronic stress [38]. These effects are typical for antidepressant effect manifestations induced by tricyclics in rodents [35, 51].

Further, in order to rule out potential effects of imipramine administration on anxiety, locomotion, and liquid intake that were previously reported in mice treated with this drug at a dose of 15/mg/kg in C57BL6N mice, we performed supplementary tests in all mice. In both anxiety paradigms, dark-light box and O-maze, animals treated with imipramine showed no significant differences in their behaviour from the control group: in latency of the exit to the anxiety-related

areas, lit box and open arms ( $P = 0.94$ ,  $t = 0.08$  and  $P = 0.59$ ,  $t = 0.55$ , resp.; unpaired two-tailed  $t$ -test), time spent in the lit box and open arms ( $P = 0.80$ ,  $t = 0.26$  and  $P = 0.28$ ,  $t = 1.14$ , resp.; unpaired two-tailed  $t$ -test), and numbers of exits to these zones ( $P = 0.87$ ,  $t = 0.17$  and  $P = 0.13$ ,  $t = 1.63$ , resp.; unpaired two-tailed  $t$ -test, Figures 3(b) and 3(c)). In locomotory tests, in comparison with control mice, animals treated with imipramine exhibited normal vertical activity, as shown by the number of rearings in novel cage (Week 2:  $P = 0.33$ ,  $t = 1.01$ ; Week 4:  $P = 0.54$ ,  $t = 0.63$ , unpaired two-tailed  $t$ -test), as well as unchanged horizontal locomotion in the open field. In the latter test, no difference between groups was found in distance travelled (Week 2:  $P = 0.97$ ,  $t = 0.038$ ; Week 4:  $P = 0.31$ ,  $t = 1.05$ ) or mean instant velocity (Week 2:  $P = 0.98$ ,  $t = 0.026$ ; Week 4:  $P = 0.84$ ,  $t = 0.21$ ; Figure 3(d), unpaired two-tailed  $t$ -test). In a two-bottle sucrose preference test, there were no significant differences in water intake, sucrose solution intake, and sucrose preference between the groups ( $P = 0.47$ ,  $t = 0.75$ ;  $P = 0.32$ ,  $t = 1.04$ ;  $P = 0.20$ ,  $t = 1.35$ , resp.; unpaired two-tailed  $t$ -test, Figure 3(e)). Finally, body weight was not different between control and imipramine-treated groups ( $P = 0.20$ ,  $t = 1.37$ , data not shown, unpaired two-tailed  $t$ -test). There is no statistical significance using repeated measures ANOVA (data not shown).

Thus, the employed dosing with imipramine did not affect basic physiological variables, such as locomotion, liquid consumption, and body weight. Also, it did not affect the parameters of anxiety and sucrose ingestion, as reported in some studies that employ higher amounts of tricyclics [6, 31, 52, 53]. These results suggest that low dose imipramine treatment via voluntary food pellet intake can serve as an optimal pharmacological reference in animal models of depression that require prolonged antidepressant treatment of small rodents.

**3.3. Effects of Chronic Delivery via Food Pellets of New Candidates to Antidepressants in the Forced Swim and Tail Suspension Tests.** Next, we sought to investigate whether the defined method of antidepressant dosing with food pellets can be applicable with the testing of new drug candidates, one of which, celecoxib, is not soluble in water and, therefore, is problematic to deliver to the animals chronically. As such, we exposed a cohort of animals to food pellets containing new drug candidates: dicholine succinate or celecoxib. In addition, we used imipramine or citalopram as the antidepressant references.

In the forced swim test, one-way ANOVA revealed significant differences between the groups in the latency to float, total time spent floating, and velocity (Day 1:  $P = 0.0054$ ,  $F = 4.24$ ;  $P = 0.049$ ,  $F = 2.60$ ; and  $P = 0.22$ ,  $F = 3.18$ , resp., Figure 4(a)). Post hoc Dunnett test showed that, on Day 1, in comparison with the control group, the latency to swim was increased in animals treated with imipramine or dicholine succinate ( $P < 0.05$ ,  $q = 3.17$  and  $P < 0.01$ ,  $q = 3.20$ ), the duration of immobility was decreased in the imipramine-treated animals ( $P < 0.05$ ,  $q = 2.67$ ), and velocity was elevated in the dicholine succinate-treated group

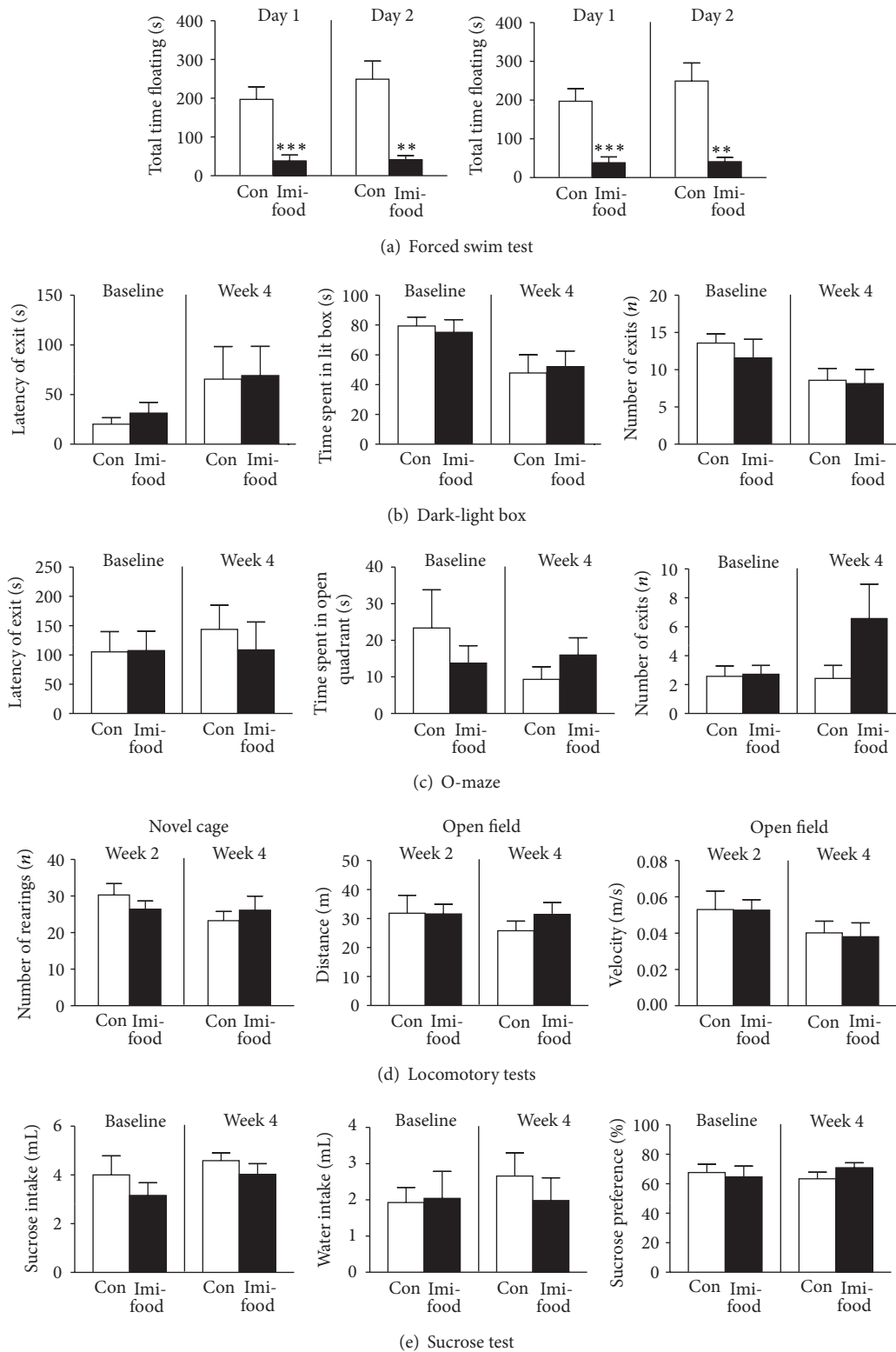


FIGURE 3: Effects of dosing with imipramine via food pellets on floating scores and other behaviours. (a) In comparison with control group, mice that received imipramine in food pellets over four weeks showed an increase of latency to float and total duration of floating in the forced swim test. No significant differences between the groups were found in parameters of anxiety (b) in the dark-light box and (c) O-maze tests. (d) Control and imipramine-treated mice showed similar numbers of rearings in the novel cage, distance travelled, and mean velocity in the open field test. (e) In the two-bottle sucrose preference test, water intake, sucrose solution intake, and sucrose preference were not different between imipramine-treated and control groups. \*\* $P < 0.01$ , \*\*\* $P < 0.001$  versus control (unpaired  $t$ -test). Con: control group ( $n = 7$ ); Imi-food: imipramine-treated group ( $n = 8$ ). All data are means  $\pm$  SEM.

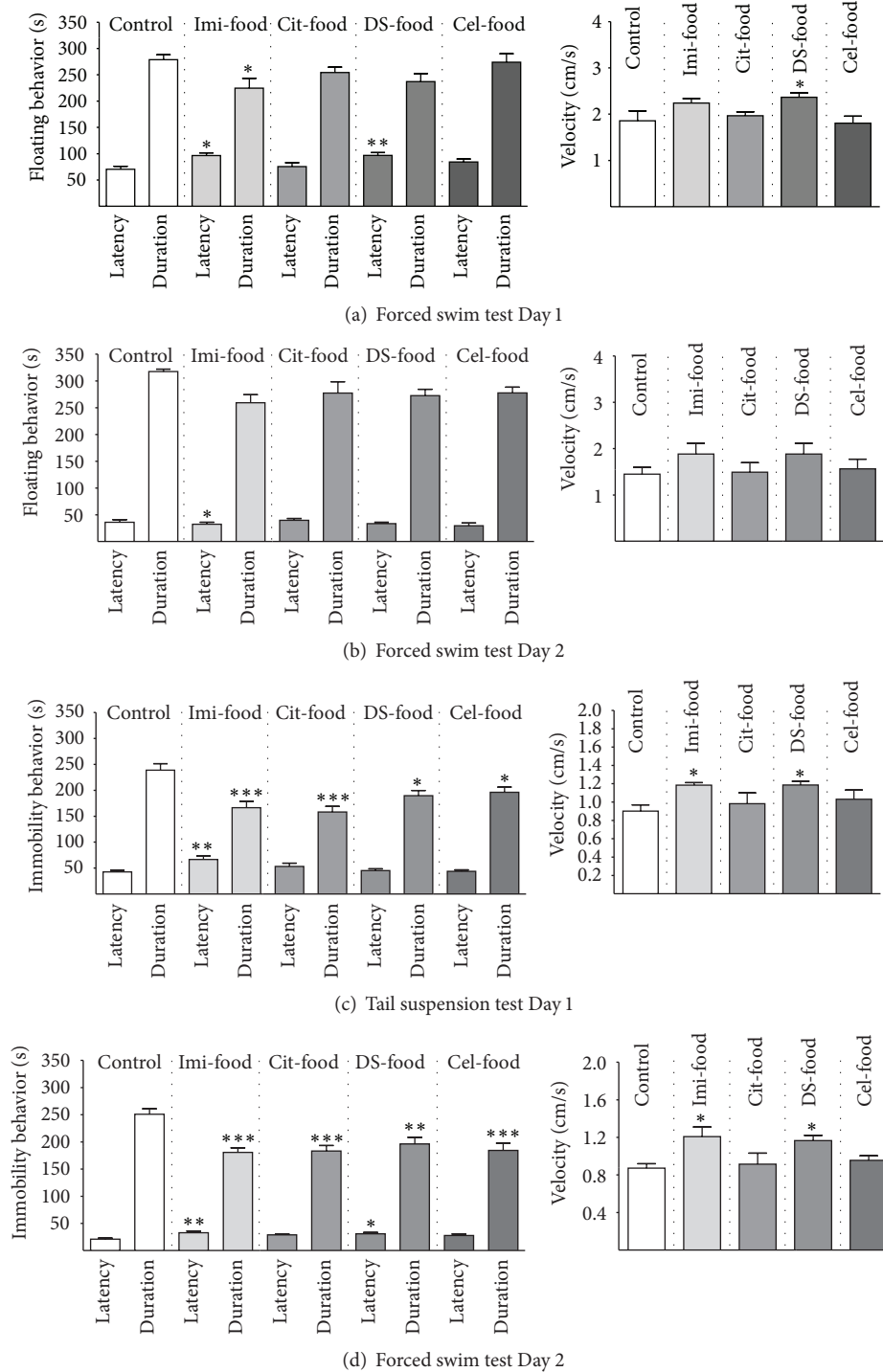


FIGURE 4: Effects of chronic delivery via food pellets of new candidates to antidepressants in the forced swim and tail suspension tests. (a) On Day 1 of the forced swim test, as compared with control, imipramine-treated animals elicited an increase in latency to float and reduced time spent floating, and dicholine succinate-treated groups displayed an increased swim velocity. (b) On Day 2 of the forced swim test, imipramine-treated group had higher latency to float in comparison to control mice; no other differences between treated and control groups were found. (c) On Day 1 of the tail suspension test, there was a significant increase of the latency of immobility and velocity in imipramine- and dicholine succinate-treated groups, as compared to controls. All treated groups showed a significant reduction of total time spent immobile, as compared to control animals. (d) On Day 2 of the tail suspension test, in comparison to control group, an increase of the latency of immobility was found in imipramine-treated group and an increase of velocity was observed in both imipramine- and dicholine succinate-treated mice. All animals that received a treatment demonstrated a significant reduction of total time spent immobile, in comparison to control group. \* $P < 0.05$ , \*\* $P < 0.01$ , and \*\*\* $P < 0.001$  versus control (one-way ANOVA with Dunnett *post hoc* tests). All groups were  $n = 10$ . Con: control group; Imi-food: imipramine-treated group; Cit-food: citalopram-treated group; DS-food: dicholine succinate-treated group; Cel-food: celecoxib-treated group. All data are means  $\pm$  SEM.

( $P < 0.05$ ,  $q = 2.62$ ). On Day 2 of the forced swim test, one-way ANOVA showed a trend to a statistically significant difference in the latency of floating and no differences in the duration of floating or velocity ( $P = 0.059$ ,  $F = 2.46$ ;  $P = 0.48$ ,  $F = 0.89$ ; and  $P = 0.40$ ,  $F = 1.04$ , resp., Figure 4(b)). Dunnett post hoc test revealed a significant increase in latency to float in the imipramine-treated group ( $P < 0.05$ ;  $q = 2.96$ ). As a reduction of the parameters of floating behaviour in the forced swim test is a well-established measure of antidepressant activity of various compounds [32, 35], these data suggest that the applied treatment with imipramine or dicholine succinate induces an antidepressant effect and that the employed dosing was effective.

With the tail suspension test, one-way ANOVA showed that, on Day 1, there were statistically significant differences between the groups in the latency and duration of immobility ( $P = 0.007$ ,  $F = 4.09$ ;  $P < 0.0001$ ,  $F = 3.43$ ; and  $P < 0.0001$ ,  $F = 3.43$ , resp., Figure 4(c)); a strong tendency to differences in velocity was found ( $P = 0.0505$ ,  $F = 2.57$ ). Post hoc Dunnett test revealed a significant difference in the latency of immobility from the control group in imipramine-treated animals ( $P < 0.01$ ,  $q = 3.380$ ) but not in other treatment groups. All groups that received pharmacological treatment had significantly reduced duration of immobility in comparison to control mice (imipramine-treated:  $P < 0.001$ ,  $q = 4.50$ ; citalopram-treated:  $P < 0.001$ ,  $q = 5.02$ ; dicholine succinate-treated:  $P < 0.05$ ,  $q = 3.07$ ; celecoxib-treated:  $P < 0.05$ ,  $q = 2.65$ ; Dunnett test). In comparison to control group, velocity was significantly increased in imipramine- and dicholine succinate-treated groups ( $P < 0.05$ ,  $q = 2.55$ ;  $P < 0.05$ ,  $q = 2.56$ , resp.; Dunnett test).

On Day 2 of the tail suspension test, statistically significant differences between the groups were found in the latency of immobility, the duration of immobility, and velocity ( $P = 0.0159$ ,  $F = 3.43$ ;  $P < 0.0002$ ,  $F = 6.90$ ; and  $P = 0.012$ ,  $F = 3.65$ , resp., one-way ANOVA; Figure 4(d)). Dunnett post hoc test showed a significant increase of the latency of immobility in imipramine- and dicholine succinate-treated animals, as compared with controls ( $P < 0.01$ ,  $q = 3.48$  and  $P < 0.05$ ,  $q = 2.75$ , resp.). All treated groups had significantly reduced duration of immobility, as compared with control mice (imipramine-treated:  $P < 0.001$ ,  $q = 4.46$ ; citalopram-treated:  $P < 0.001$ ,  $q = 4.31$ ; dicholine succinate-treated:  $P < 0.01$ ,  $q = 3.39$ ; celecoxib-treated:  $P < 0.001$ ,  $q = 4.24$ ; Dunnett test). Velocity was significantly increased in comparison with control mice in the imipramine- and dicholine succinate-treated groups ( $P < 0.05$ ,  $q = 2.97$ ;  $P < 0.05$ ,  $q = 2.59$ , resp.; Dunnett test). Since a decrease of immobility behaviour in the tail suspension test is generally considered as a manifestation of the antidepressant activity of various treatments [32, 54], these results evidence an antidepressant-like effect of the applied drugs and again the efficacy of the tested method of drug administration.

#### 4. Conclusions

Thus, as a desirable alternative to invasive dosing, such as chronic intraperitoneal injections, the administration of

various drugs via food pellets can be very efficient. The results from our study are in line with other successful attempts to avoid adverse drug delivery methodologies in translational research that showed, for example, the efficacy of treatment with analgesic therapy delivered via food in rats which were subjected to surgery [55]. The use of such methods could be particularly needed when repeated drug administration to stressed, operated, or immunodeficient laboratory animals is necessary and therefore could greatly improve not only animal welfare but also the validity of animal models.

#### Conflict of Interests

The authors declare that there is no conflict of interests regarding the publication of this paper.

#### Authors' Contribution

João P. Costa-Nunes and Brandon H. Cline equally contributed to this work.

#### Acknowledgments

The authors would like to thank Dr. Cláudia Oliveira from the CBA and Science Faculty of the University of Lisbon and Dr. Dinora Lopes from the Institute of Hygiene and Tropical Medicine for organizational support and Mrs. Margarida Rama for technical support. This work was supported by the Fundação para a Ciência e Tecnologia (FCT) and Internationale Stichting Alzheimer Onderzoek (ISAO), Netherlands, Grants N 09501 and RFBR to Tatyana Strekalova.

#### References

- [1] B. Munos, "Lessons from 60 years of pharmaceutical innovation," *Nature Reviews Drug Discovery*, vol. 8, no. 12, pp. 959–968, 2009.
- [2] H. E. Pigott, A. M. Leventhal, G. S. Alter, and J. J. Boren, "Efficacy and effectiveness of antidepressants: current status of research," *Psychotherapy and Psychosomatics*, vol. 79, no. 5, pp. 267–279, 2010.
- [3] N. Araragi and K.-P. Lesch, "Serotonin (5-HT) in the regulation of depression-related emotionality: insight from 5-HT transporter and tryptophan Hydroxylase-2 knockout mouse models," *Current Drug Targets*, vol. 14, no. 5, pp. 549–570, 2013.
- [4] T. R. Insel and B. J. Sahakian, "Drug research: a plan for mental illness," *Nature*, vol. 483, no. 7389, p. 269, 2012.
- [5] T. R. Insel, "From animal models to model animals," *Biological Psychiatry*, vol. 62, no. 12, pp. 1337–1339, 2007.
- [6] T. Strekalova, D. C. Anthony, O. Dolgov et al., "The differential effects of chronic imipramine or citalopram administration on physiological and behavioral outcomes in naïve mice," *Behavioural Brain Research*, vol. 245, pp. 101–106, 2013.
- [7] Y. Sato, N. Seo, and E. Kobahashi, "The dosing-time dependent effects of intravenous hypnotics in mice," *Anesthesia and Analgesia*, vol. 101, no. 6, pp. 1706–1708, 2005.
- [8] J. A. Beeler, B. Prendergast, and X. Zhuang, "Low amplitude entrainment of mice and the impact of circadian phase on

- behavior tests," *Physiology and Behavior*, vol. 87, no. 5, pp. 870–880, 2006.
- [9] K. M. Frick, N. A. Stearns, J.-Y. Pan, and J. Berger-Sweeney, "Effects of environmental enrichment on spatial memory and neurochemistry in middle-aged mice," *Learning and Memory*, vol. 10, no. 3, pp. 187–198, 2003.
- [10] D. P. Wolfer, O. Litvin, S. Morf, R. M. Nitsch, H.-P. Lipp, and H. Würbel, "Laboratory animal welfare: cage enrichment and mouse behaviour," *Nature*, vol. 432, no. 7019, pp. 821–822, 2004.
- [11] E. Munn, M. Bunning, S. Prada, M. Bohlen, J. C. Crabbe, and D. Wahlsten, "Reversed light-dark cycle and cage enrichment effects on ethanol-induced deficits in motor coordination assessed in inbred mouse strains with a compact battery of refined tests," *Behavioural Brain Research*, vol. 224, no. 2, pp. 259–271, 2011.
- [12] T. Strekalova, R. Spanagel, O. Dolgov, and D. Bartsch, "Stress-induced hyperlocomotion as a confounding factor in anxiety and depression models in mice," *Behavioural Pharmacology*, vol. 16, no. 3, pp. 171–180, 2005.
- [13] D. F. Fukushiro, L. F. Benetti, F. S. Josino et al., "Environmental novelty and illumination modify ethanol-induced open-field behavioral effects in mice," *Pharmacology Biochemistry and Behavior*, vol. 95, no. 1, pp. 13–22, 2010.
- [14] D. Wahlsten, P. Metten, and J. C. Crabbe, "A rating scale for wildness and ease of handling laboratory mice: results for 21 inbred strains tested in two laboratories," *Genes, Brain and Behavior*, vol. 2, no. 2, pp. 71–79, 2003.
- [15] F. Longordo, J. Fan, T. Steimer, C. Kopp, and A. Lüthi, "Do mice habituate to "gentle handling"? A comparison of resting behavior, corticosterone levels and synaptic function in handled and undisturbed C57BL/6J mice," *Sleep*, vol. 34, no. 5, pp. 679–681, 2011.
- [16] S. Cloutier, K. Wahl, C. Baker, and R. C. Newberry, "The social buffering effect of playful handling on responses to repeated intraperitoneal injections in laboratory rats," *Journal of the American Association for Laboratory Animal Science*, vol. 53, no. 2, pp. 168–173, 2014.
- [17] K. M. Ringgold, R. P. Barf, A. George, B. C. Sutton, and M. R. Opp, "Prolonged sleep fragmentation of mice exacerbates febrile responses to lipopolysaccharide," *Journal of Neuroscience Methods*, vol. 219, no. 1, pp. 104–112, 2013.
- [18] T. V. Strekalova, R. Cespuglio, and V. M. Koval'zon, "Depressive-like state and sleep in laboratory mice," *Zhurnal Vysheĭ Nervnoi Deiatelnosti Imeri I P Pavlova*, vol. 58, no. 6, pp. 728–737, 2008.
- [19] T. Strekalova and H. W. M. Steinbusch, "Measuring behavior in mice with chronic stress depression paradigm," *Progress in Neuro-Psychopharmacology and Biological Psychiatry*, vol. 34, no. 2, pp. 348–361, 2010.
- [20] R. E. Sorge, L. J. Martin, K. A. Isbester et al., "Olfactory exposure to males, including men, causes stress and related analgesia in rodents," *Nature Methods*, vol. 11, no. 6, pp. 629–632, 2014.
- [21] M. Bohlen, E. R. Hayes, B. Bohlen, J. D. Bailoo, J. C. Crabbe, and D. Wahlsten, "Experimenter effects on behavioral test scores of eight inbred mouse strains under the influence of ethanol," *Behavioural Brain Research*, vol. 272, pp. 46–54, 2014.
- [22] J. C. Crabbe, D. Wahlsten, and B. C. Dudek, "Genetics of mouse behavior: interactions with laboratory environment," *Science*, vol. 284, no. 5420, pp. 1670–1672, 1999.
- [23] S. Mandillo, V. Tucci, S. M. Hölter et al., "Reliability, robustness, and reproducibility in mouse behavioral phenotyping: a cross-laboratory study," *Physiological Genomics*, vol. 34, no. 3, pp. 243–255, 2008.
- [24] T. Strekalova, Y. Couch, N. Kholod et al., "Update in the methodology of the chronic stress paradigm: internal control matters," *Behavioral and Brain Functions*, vol. 7, article 9, 2011.
- [25] D. Wahlsten, N. R. Rustay, P. Metten, and J. C. Crabbe, "In search of a better mouse test," *Trends in Neurosciences*, vol. 26, no. 3, pp. 132–136, 2003.
- [26] N. Sousa, O. F. X. Almeida, and C. T. Wotjak, "A hitchhiker's guide to behavioral analysis in laboratory rodents," *Genes, Brain and Behavior*, vol. 5, no. 2, pp. 5–24, 2006.
- [27] T. Azar, J. Sharp, and D. Lawson, "Heart rates of male and female Sprague-Dawley and spontaneously hypertensive rats housed singly or in groups," *Journal of the American Association for Laboratory Animal Science*, vol. 50, no. 2, pp. 175–184, 2011.
- [28] S. Cloutier and R. C. Newberry, "Use of a conditioning technique to reduce stress associated with repeated intra-peritoneal injections in laboratory rats," *Applied Animal Behaviour Science*, vol. 112, no. 1-2, pp. 158–173, 2008.
- [29] T. E. Thiele and M. Navarro, "'Drinking in the dark' (DID) procedures: a model of binge-like ethanol drinking in non-dependent mice," *Alcohol*, vol. 48, no. 3, pp. 235–241, 2014.
- [30] K. Gärtner, D. Buttner, K. Dohler, R. Friedel, J. Lindena, and I. Trautschold, "Stress response of rats to handling and experimental procedures," *Laboratory Animals*, vol. 14, no. 3, pp. 267–274, 1980.
- [31] P. Willner, "Chronic mild stress (CMS) revisited: Consistency and behavioural-neurobiological concordance in the effects of CMS," *Neuropsychobiology*, vol. 52, no. 2, pp. 90–110, 2005.
- [32] J. Harro, "Animal models of depression vulnerability," *Current Topics in Behavioral Neurosciences*, vol. 14, pp. 29–54, 2013.
- [33] T. Strekalova, N. Gorenkova, E. Schunk, O. Dolgov, and D. Bartsch, "Selective effects of citalopram in a mouse model of stress-induced anhedonia with a control for chronic stress," *Behavioural Pharmacology*, vol. 17, no. 3, pp. 271–287, 2006.
- [34] D. H. Overstreet, "Modeling depression in animal models," *Methods in Molecular Biology*, vol. 829, pp. 125–144, 2012.
- [35] J. F. Cryan, R. J. Valentino, and I. Lucki, "Assessing substrates underlying the behavioral effects of antidepressants using the modified rat forced swimming test," *Neuroscience & Biobehavioral Reviews*, vol. 29, no. 4-5, pp. 547–569, 2005.
- [36] L. H. Pottenger, J. Y. Domoradzki, D. A. Markham, S. C. Hansen, S. Z. Cagen, and J. M. Waechter Jr., "The relative bioavailability and metabolism of bisphenol A in rats is dependent upon the route of administration," *Toxicological Sciences*, vol. 54, no. 1, pp. 3–18, 2000.
- [37] M.-L. Volvert, S. Seyen, M. Piette et al., "Benfotiamine, a synthetic S-acyl thiamine derivative, has different mechanisms of action and a different pharmacological profile than lipid-soluble thiamine disulfide derivatives," *BMC Pharmacology*, vol. 8, article 10, 2008.
- [38] B. H. Cline, D. C. Anthony, A. Lysko et al., "Lasting downregulation of the lipid peroxidation enzymes in the prefrontal cortex of mice susceptible to stress-induced anhedonia," *Behavioural Brain Research*, vol. 276, pp. 118–129, 2014.
- [39] A. M. Myint, H. W. M. Steinbusch, L. Goeghegan, D. Luchtman, Y. K. Kim, and B. E. Leonard, "Effect of the COX-2 inhibitor celecoxib on behavioural and immune changes in an olfactory bulbectomised rat model of depression," *NeuroImmunoModulation*, vol. 14, no. 2, pp. 65–71, 2007.
- [40] I. S. Maciel, R. B. M. Silva, F. B. Morrone, J. B. Calixto, and M. M. Campos, "Synergistic effects of celecoxib and bupropion in

- a model of chronic inflammation-related depression in mice,” *PLoS ONE*, vol. 8, no. 9, Article ID e77227, 2013.
- [41] E. Malatynska, H. W. M. Steinbusch, O. Redkozubova et al., “Anhedonic-like traits and lack of affective deficits in 18-month-old C57BL/6 mice: Implications for modeling elderly depression,” *Experimental Gerontology*, vol. 47, no. 8, pp. 552–564, 2012.
- [42] B. H. Cline, H. W. M. Steinbusch, D. Malin et al., “The neuronal insulin sensitizer dicholine succinate reduces stress-induced depressive traits and memory deficit: possible role of insulin-like growth factor 2,” *BMC Neuroscience*, vol. 13, no. 1, article 110, 2012.
- [43] N. Markova, A. Chernopiatko, C. A. Schroeter et al., “Hippocampal gene expression of deiodinases 2 and 3 and effects of 3,5-diiodo-L-thyronine T2 in mouse depression paradigms,” *BioMed Research International*, vol. 2013, Article ID 565218, 14 pages, 2013.
- [44] J. Costa-Nunes, O. Zubareva, M. Araújo-Correia et al., “Altered emotionality, hippocampus-dependent performance and expression of NMDA receptor subunit mRNAs in chronically stressed mice,” *Stress*, vol. 17, no. 1, pp. 108–116, 2014.
- [45] J. L. Pawluski, A. Valença, A. I. M. Santos, J. P. Costa-Nunes, H. W. M. Steinbusch, and T. Strekalova, “Pregnancy or stress decrease complexity of CA3 pyramidal neurons in the hippocampus of adult female rats,” *Neuroscience*, vol. 227, pp. 201–210, 2012.
- [46] M. N. Silverman and E. M. Sternberg, “Glucocorticoid regulation of inflammation and its functional correlates: from HPA axis to glucocorticoid receptor dysfunction,” *Annals of the New York Academy of Sciences*, vol. 1261, no. 1, pp. 55–63, 2012.
- [47] L. R. Miller and A. Cano, “Comorbid chronic pain and depression: who is at risk?” *Journal of Pain*, vol. 10, no. 6, pp. 619–627, 2009.
- [48] Y. Goffer, D. Xu, S. E. Eberle et al., “Calcium-permeable AMPA receptors in the nucleus accumbens regulate depression-like behaviors in the chronic neuropathic pain state,” *The Journal of Neuroscience*, vol. 33, no. 48, pp. 19034–19044, 2013.
- [49] C. R. Pryce, D. Azzinnari, S. Spinelli, E. Seifritz, M. Tegethoff, and G. Meinlschmidt, “Helplessness: a systematic translational review of theory and evidence for its relevance to understanding and treating depression,” *Pharmacology and Therapeutics*, vol. 132, no. 3, pp. 242–267, 2011.
- [50] R. Dantzer, J. C. O’Connor, M. A. Lawson, and K. W. Kelley, “Inflammation-associated depression: from serotonin to kynurenine,” *Psychoneuroendocrinology*, vol. 36, no. 3, pp. 426–436, 2011.
- [51] J. C. von Frijtag, R. van den Bos, and B. M. Spruijt, “Imipramine restores the long-term impairment of appetitive behavior in socially stressed rats,” *Psychopharmacology*, vol. 162, no. 3, pp. 232–238, 2002.
- [52] S. E. File and J. C. Tucker, “Behavioral consequences of antidepressant treatment in rodents,” *Neuroscience and Biobehavioral Reviews*, vol. 10, no. 2, pp. 123–134, 1986.
- [53] J. Mogensen, T. K. Pedersen, and S. Holm, “Effects of chronic imipramine on exploration, locomotion, and food/water intake in rats,” *Pharmacology Biochemistry and Behavior*, vol. 47, no. 3, pp. 427–435, 1994.
- [54] J. F. Cryan, C. Mombereau, and A. Vassout, “The tail suspension test as a model for assessing antidepressant activity: review of pharmacological and genetic studies in mice,” *Neuroscience and Biobehavioral Reviews*, vol. 29, no. 4-5, pp. 571–625, 2005.
- [55] L. Jessen, S. Christensen, and O. J. Bjerrum, “The antinociceptive efficacy of buprenorphine administered through the drinking water of rats,” *Laboratory Animals*, vol. 41, no. 2, pp. 185–196, 2007.

## Research Article

# ***Mycobacterium*-Host Cell Relationships in Granulomatous Lesions in a Mouse Model of Latent Tuberculous Infection**

**Elena Ufimtseva**

*The Institute of Biochemistry, Siberian Branch of the Russian Academy of Medical Sciences, 2 Timakova Street, Novosibirsk 630117, Russia*

Correspondence should be addressed to Elena Ufimtseva; ufiml@ngs.ru

Received 4 July 2014; Accepted 21 October 2014

Academic Editor: Monica Fedele

Copyright © 2015 Elena Ufimtseva. This is an open access article distributed under the Creative Commons Attribution License, which permits unrestricted use, distribution, and reproduction in any medium, provided the original work is properly cited.

Tuberculosis (TB) is a dangerous infectious disease characterized by a tight interplay between mycobacteria and host cells in granulomatous lesions (granulomas) during the latent, asymptomatic stage of infection. *Mycobacterium*-host cell relationships were analyzed in granulomas obtained from various organs of BALB/c mice with chronic TB infection caused by *in vivo* exposure to the Bacillus Calmette-Guérin (BCG) vaccine. Acid-fast BCG-mycobacteria were found to be morphologically and functionally heterogeneous (in size, shape, and replication rates in colonies) in granuloma macrophages, dendritic cells, and multinucleate Langhans giant cells. Cord formation by BCG-mycobacteria in granuloma cells has been observed. Granuloma macrophages retained their ability to ingest damaged lymphocytes and thrombocytes in the phagosomes; however, their ability to destroy BCG-mycobacteria contained in these cells was compromised. No colocalization of BCG-mycobacteria and the LysoTracker dye was observed in the mouse cells. Various relationships between granuloma cells and BCG-mycobacteria were observed in different mice belonging to the same line. Several mice totally eliminated mycobacterial infection. Granulomas in the other mice had mycobacteria actively replicating in cells of different types and forming cords, which is an indicator of mycobacterial virulence and, probably, a marker of the activation of tuberculous infection in animals.

## **1. Introduction**

*Mycobacterium tuberculosis* is an infectious agent that causes asymptomatic latent, chronic infection and can provoke active disease in man and animals. At the latent stage of tuberculous infection, mycobacteria can penetrate into organs and tissues and persist there for decades before a possible activation of the tuberculous process followed by the development of active disease [1–4]. Studies of the mechanisms of mycobacterial survival in the host organisms during latent TB infection and the mechanisms of their reactivation and replication are extremely important for the development of new vaccines, medicines, and methods for tuberculosis treatment. These works have since recently become especially important because of the emergence and spread of high-virulence strains of mycobacteria that possess multidrug and extensive drug resistance [5].

As is known, granulomas that form chronic inflammatory lesions and are composed of diverse immune cells,

mainly macrophages, are hallmarks of latent tuberculous infection in man and animals [6–9]. Failure, from the side of macrophages, to destroy the absorbed mycobacteria causes a risk of activation and the development of tuberculosis [4, 10, 11]. Although knowledge about the quantity and the functional state of mycobacteria during latent infection is important, this information about mycobacteria in granuloma cells remains insufficient. The bacteriological method, which is generally used for assessing the multiplicity of mycobacterial infection in animal organs and tissues, involves inoculation of their homogenates on special agar media and counting colony-forming units. However, this allows only generalized data on the number of mycobacteria during latent infection to be obtained [12–16]. Neither inspecting mycobacteria on the histological sections of animal tissues [17–20] nor *in vivo* studies of granulomas [21] in the livers of mice infected with BCG, an attenuated live strain of *Mycobacterium bovis*, allow the multiplicity of infection (MOI) in the granuloma cells to be inferred.

In the past decade, information on the state of mycobacteria (i.e., whether they are acid-fast or otherwise) and their metabolic status (i.e., whether they are replicating or otherwise) in cells has been obtained via infecting human and animal cells and cell cultures *in vitro* [22–25]. It has been demonstrated that populations of mycobacteria growing in macrophages and in extracellular environments are morphologically and functionally heterogeneous and contain bacteria with resistance to various drugs [26, 27]. Virulent and attenuated mycobacterial strains behaved differently in *in vitro* cell cultures. For example, the active replication of mycobacteria of only virulent strains was observed, using electron microscopy, both in phagosomes and in the cytoplasm of infected cells within a period of 2 to 7 days following infection *in vitro* [28, 29]. At the same time, BCG and attenuated strains of *M. tuberculosis* have been found only in vacuolar compartments of cells, which is where they were later destroyed before they could start to replicate. After invasion of mouse bone marrow macrophages by a virulent *M. tuberculosis* strain and BCG-mycobacteria *in vitro*, the respective parameters of the transcriptome and gene regulatory networks of mycobacterial genes were different [30].

The number of mycobacteria in granuloma macrophages in acute tuberculous infection after treatment with various antituberculosis drugs was assessed in zebrafish (*Danio rerio*) juveniles infected with *M. marinum* [26, 31]. Cord formation (the indicator of mycobacterial virulence) in zebrafish granulomas was observed exclusively outside cells [31, 32]. On the whole, these studies do not provide a complete picture of relationships between mycobacteria and granuloma cells that contain them. Therefore, knowledge about the exact mycobacterial counts in granuloma cells is essential for the study of tuberculous infection in animal and human organs and tissues both at the latent stage of tuberculosis and during its reactivation.

Infection of mice with *M. tuberculosis* is known to result in a fatal increase in bacterial burden, while the bacterial burden in chronically infected humans is low [33]. By contrast, the bacterial burden following infection of mice with the BCG vaccine is as low as it is observed in latent human infection with *M. tuberculosis*. That is why some researchers consider BCG infection in mice the model of choice for studying latent mycobacterial infection [21, 34, 35].

In this work, we have analyzed the relationships between intracellular mycobacteria and granuloma host cells in mice with latent TB infection. This analysis was performed using an *ex vivo* model of monolayer granuloma culture samples obtained from spleens, lungs, and bone marrow of mice infected with the BCG vaccine *in vivo* [9]. In a result, we assessed the functional state of the mycobacteria and their number in granuloma cells of various types from different organs of the mice. It was ascertained that these granuloma cells contained single BCG-mycobacteria and colonies resulting from replication, often in the same host cell. We have for the first time observed the formation of cords by replicating mycobacteria, presumably in the cytoplasm of granuloma macrophages and dendritic cells. Our study indicates that BCG-mycobacteria in granuloma cells obtained from various

organs of mice with chronic TB infection are functionally heterogeneous. The mice also differed in the number of BCG-containing cells in granulomas they had, which may indicate a difference in the mice's infection status during the latent period of disease.

## 2. Materials and Methods

**2.1. Animals.** Two-month-old BALB/c male mice were obtained from the Animal Breeding Facility of the Institute of Cytology and Genetics of the Siberian Branch of the Russian Academy of Sciences (Novosibirsk, Russia). Mice were bred and maintained under standard vivarium conditions, with water and food provided ad libitum. Animal experiments were conducted in accordance with “The Guidelines for Manipulations with Experimental Animals” issued by the Russian Ministry of Health (guideline 755). All experimental procedures were approved by the Local Ethical Committee of the Institute of Biochemistry, SB RAMS, Novosibirsk, Russia.

**2.2. Infection of Mice.** Mice were infected with a vaccine prepared from an attenuated live strain of *M. bovis* (the Bacillus Calmette-Guérin vaccine, BCG-1, Allergen, Stavropol, Russia) at a dose of 0.5 mg per mouse, which amounted to  $3 \times 10^6$  viable BCG-mycobacteria in 0.9% NaCl solution. Seventeen mice were each infected via tail vein injection with 100  $\mu\text{L}$  of the suspension and four mice were each infected intraperitoneally with 200  $\mu\text{L}$  of the suspension.

**2.3. Isolation and Ex Vivo Culture of Mouse Granulomas.** Mice were anesthetized and sacrificed by cervical dislocation. Isolation of granulomas from the spleens, lungs, and bone marrow of mice after 20 days, one month, and two months following infection was performed as previously described [9]. Bone marrow was flushed from femur bones with RPMI 1640 (BioloT, St. Petersburg, Russia). Granulomas in the RPMI 1640 growth medium containing 10% heat-inactivated fetal bovine serum, 2 mM glutamine, and 50  $\mu\text{g}/\text{mL}$  gentamicin (BioloT, St. Petersburg, Russia) were placed at low-medium density to 24-well tissue culture plates (Orange Scientific, Belgium) with glass coverslips at the bottom and cultured in 0.5 mL medium for several days at +37°C in an atmosphere containing 5% CO<sub>2</sub>. Granulomas were isolated from mice 1 and 2 on day 20 following intraperitoneal infection; mice 1 and 3 ÷ 5 after one month following intraperitoneal and intravenous infection, respectively; mice 4 ÷ 6, 8 ÷ 10, 12 ÷ 14, 16, and 21 ÷ 24 after two months following intravenous infection; and mouse 25 after two months following intraperitoneal infection. Peritoneal macrophages were isolated from mouse 2 after 20 days and mouse 25 after two months following intraperitoneal infection and cultured under the same conditions as the granuloma cells. After isolation of granulomas from the femur bones of mice 1 and 2 after 20 days following infection, the other bone marrow cells were cultured under the same conditions as the granuloma cells.

**2.4. Cell Staining.** After 2–5 days of *ex vivo* culture, granuloma cells and peritoneal and bone marrow macrophages

on coverslips were fixed with 4% formaldehyde solution in phosphate buffer saline (PBS, pH 7.4) for 10 minutes at room temperature. To visualize acid-fast bacteria, the preparations were washed with PBS and stained after Ziehl-Neelsen. The cells were further counterstained with 1% methylene blue. In the experiments using LysoTracker Red DND-99 (Invitrogen, USA, L7528), the cell preparations were incubated with 50 nM of the acidotropic dye for 5 minutes at +37°C in 5% CO<sub>2</sub> before fixation. The cell preparations were fixed as described above, washed with PBS, permeabilized within 2 minutes in 0.3% Triton-X100 solution, blocked in PBS containing 2% BSA, and finally incubated first with rabbit polyclonal primary antibodies to mycobacteria (Abcam, England, ab20832) diluted 1:200 and then with Alexa 488-conjugated goat anti-rabbit Ig secondary antibodies (Invitrogen, USA, A11034) diluted 1:400. Some of the fixed cell preparations were washed with PBS, blocked in PBS solution containing 2% BSA, and incubated with rat primary antibodies to mouse CD1d (BD Pharmingen, USA, 553843) or hamster antibodies to mouse CD80 labeled by PerCP-Cy 5.5 (BD Pharmingen, USA, 560526) diluted 1:50 and 1:100, respectively. Then, these preparations were washed with PBS, treated within 2 minutes in 0.3% Triton-X100 solution, and incubated with hamster primary antibodies to mouse IL-1 $\alpha$  (BD Pharmingen, USA, 550604) or rat primary antibodies to mouse IFN $\gamma$  (BD Pharmingen, USA, 559065) diluted 1:50 and 1:100, respectively. Fluorescent visualization of the proteins was enabled using goat polyclonal FITC-labeled antibodies against rat IgG (Abcam, England, ab6266) diluted 1:400. The other cell preparations were incubated with mouse monoclonal antibodies against hamster IgG (BD Pharmingen, USA, 550335) diluted 1:50 and then with Alexa 555-conjugated goat anti-mouse IgG secondary antibodies (Invitrogen, USA, A1422) diluted 1:400. The cell preparations were incubated with the appropriate antibodies for 60 minutes at room temperature. Fluorescent staining was analyzed using the VECTASHIELD Mounting Medium with DAPI (4',6-diamidino-2-phenylindole) (Vector Laboratories, USA, H-1200). The confocal images of the cells were recorded; the preparations were washed from VECTASHIELD Mounting Medium in PBS for 20 minutes and restained for acid-fast mycobacteria using the Ziehl-Neelsen stain.

**2.5. Microscopy.** The cytological preparations were examined at the Shared Center for Microscopic Analysis of Biological Objects of the Institute of Cytology and Genetics, SB RAS, using an Axioscop 2 *plus* microscope (Zeiss) and objectives with various magnifications (Zeiss), and photographed using an AxioCam HRC camera (Zeiss); the images were analyzed using the AxioVision 4.7 microscopy software (Zeiss). Cell preparations were stained with fluorescent dyes and examined under an LSM 780 laser scanning confocal microscope (Zeiss) using the LSM Image Browser and ZEN 2010 software (Zeiss).

**2.6. Statistical Analysis.** Statistical data processing was performed using MS Excel 2007 (Microsoft). Differences were tested for significance using Student's *t*-test.

### 3. Results

**3.1. BCG-Mycobacteria in Mouse Granuloma Cells.** Granulomas from spleens (S/) and bone marrow (BM/) were isolated on day 20 (20 d) following infection with BCG vaccine (this is how long it takes mice to develop adaptive immunity to BCG [21]), and granulomas from spleens and lungs (L/) were isolated after one month (1 m) and two months (2 m) following infection. All the granulomas were seeded into culture plates. The granulomas isolated after 20 days, one month, and two months following infection were denoted as Gran/20 d, Gran/1 m, and Gran/2 m, respectively. Because none of the mice had been observed to have acute tuberculous infection at the time of granuloma isolation, it was concluded that these granulomas were isolated at the latent, chronic stage of BCG infection. Monolayer cultures of cells that had migrated from each granuloma were obtained. The cellular composition of each granuloma isolated from mice after one month and two months following infection, the expression of leukocyte surface markers, and the production of proinflammatory cytokines and growth factors by granuloma cells had been characterized previously [9]. Any of the monolayer cultures of granuloma cells that may or may not retain cell clusters in the center of granulomatous lesions will be referred to as the "granuloma" throughout. Diffuse leukocyte infiltrates were obtained mainly from the spleen of mouse 6 S/2 m. Very few granulomas (or none at all) were isolated from each mouse lung. Only a few were obtained from bone marrow on day 20 following infection and many, from the spleens. All granulomas from mice 1/20 d and 2/20 d were solid and contained predominantly macrophages, dendritic cells (approximately 10% of the granuloma macrophage population), and a varying number of lymphocytes. Fibroblasts and neutrophils were occasionally observed in Gran/20 d granulomas; however, eosinophils, megakaryocytes, or multinucleate Langhans giant cells were not.

We determined, with the use of staining after Ziehl-Neelsen, the exact number and the functional state of acid-fast BCG-mycobacteria (which by definition have undamaged cell walls) in granuloma cells isolated from various organs of mice with latent TB infection. BCG-mycobacteria were mainly found in macrophages and rarely in dendritic cells (Figures 1(a)–1(i)). Langhans giant cells, too, contained BCG-mycobacteria (Figures 1(d) and 1(f)). No acid-fast BCG-mycobacteria were found in lymphocytes, fibroblasts, eosinophils, or megakaryocytes. After a thorough examination of 295 neutrophils in granulomas from mice and 288 neutrophils in the leukocyte infiltrates from mouse 6 S/2 m, BCG-mycobacteria were found only in two neutrophils, one from mouse 8 S/2 m and one from mouse 6 S/2 m. No acid-fast mycobacteria were found in the peritoneal macrophages of the mice that had not been exposed to BCG; however, such BCG-mycobacteria were found in 2.38% of a total of over 9000 peritoneal macrophages assayed from mouse 2/20 d and in 0.11% of a total of over 18,000 peritoneal macrophages assayed from mouse 25/2 m. Acid-fast mycobacteria were also found in 0.13% of a total of over 9000 bone marrow macrophages assayed from mouse 1/20 d and in 0.05% of

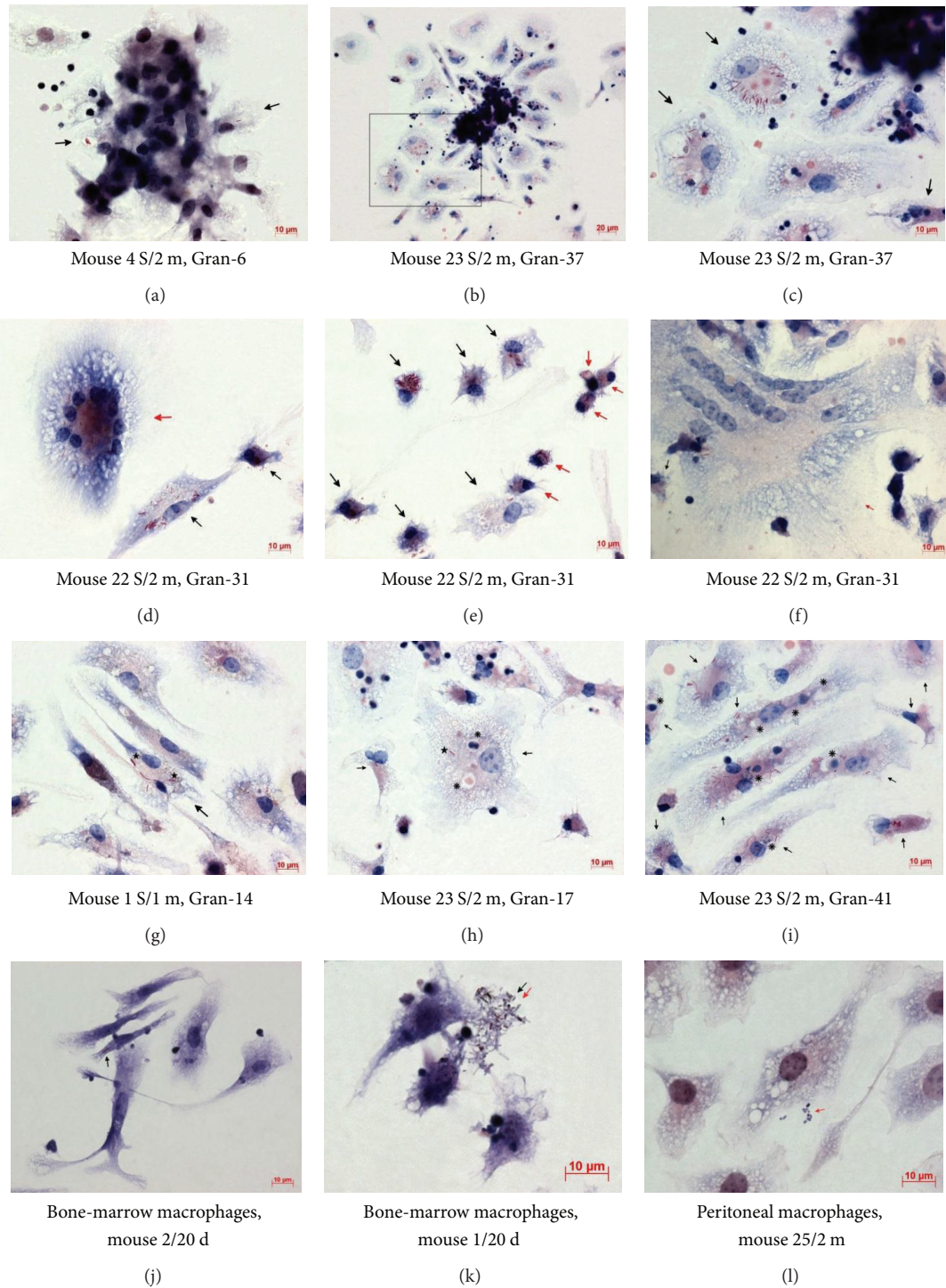


FIGURE 1: ((a)–(i)) BCG-mycobacteria in the cells of granulomas (Gran) obtained from spleens (S/) of mice after one month (/1 m) and two months (/2 m) following infection with BCG *in vivo* and after *ex vivo* culture for several days. ((a) and (c)–(j)) Infected macrophages (black arrows) and (e) infected dendritic cells (red arrows). ((a) and (b)) Granulomas with migrating cells. (c) A close-up of the granuloma fragment in the black frame in (b). ((d)–(i)) Fragments of granulomas. ((d) and (f)) Infected multinucleate Langhans giant cells (red arrows). ((g) and (h)) Replicating BCG-mycobacteria in macrophage vacuoles are indicated by black asterisks. ((h) and (i)) Vacuoles with debris of lymphocytes and thrombocytes in infected macrophages are indicated by black snowflakes. ((k) and (l)) Acid-fast (black arrows) and nonacid-fast (red arrows) mycobacteria outside bone marrow and peritoneal macrophages obtained from mice after 20 days (/20 d) and two months (/2 m) following infection with BCG *in vivo*. Acid-fast BCG-mycobacteria after Ziehl-Neelsen staining. Scale bars: 20  $\mu\text{m}$  (b) and 10  $\mu\text{m}$  ((a) and (c)–(l)).

a total of over 18,000 bone marrow macrophages assayed from mouse 2/20 d (Figure 1(j)). Each peritoneal and bone marrow macrophage had one *Mycobacterium* on most occasions. Dendritic cells in the cultures of peritoneal and bone marrow macrophage did not contain BCG-mycobacteria. Interestingly, some acid-fast and some nonacid-fast BCG-mycobacteria were found in extracellular locations in all tissue cultures of peritoneal and bone marrow macrophages isolated from mice on day 20 following infection (Figure 1(k)) and in the culture of peritoneal macrophages isolated from mouse 25 after two months following infection *in vivo* (Figure 1(l)).

BCG-mycobacteria observed in granuloma cells in the *ex vivo* culture were coccid- or rod-shaped and varied in size from 0.5 to 8  $\mu\text{m}$  (Figures 1(a)–1(i)). The smallest acid-fast mycobacteria were mainly found in macrophages of granulomas and the tissue cultures checked on day 20 following infection and in the peritoneal macrophages of mouse 25/2 m. The granulomas contained cells with a varying number of BCG-mycobacteria in them (Figures 1(a) and 1(c)–1(i)). Most granuloma macrophages each contained a single BCG-mycobacterium. At the same time, granulomas with macrophages each containing two or more BCG-mycobacteria were common. We observed BCG-mycobacteria paired in a V-shaped manner (Figures 1(d), 1(e), 1(g), and 1(h)). Mycobacteria are known to take on a V-shape during the late stages of cell division [36–38]. BCG-mycobacteria were detected near the nuclei and close to the cell membrane in different parts of the cells. Acid-fast mycobacteria were found both within visible membrane-bound vacuoles (the places where BCG-mycobacteria have sometimes been observed to grow) (Figures 1(a) and 1(g)–1(h)) and presumably in the cytoplasm of the macrophages, or so the lack of visible membrane structures around replicating microorganisms in large colonies suggests (Figures 1(c)–1(e) and 1(i)). However, a more detailed examination of granulomas' cellular compartments containing mycobacteria using antibodies against different endosomes and other cellular markers to characterize them at various stages of maturation, differentiation, and functional state appears to be necessary. BCG-mycobacteria were found either as single cells or as clusters of two or more replicating microorganisms (Figures 1(c)–1(j)) in the macrophages of all types and sizes (Figures 1(d) and 1(e)). Infected macrophages were found both at the periphery and in the center of granulomas in *ex vivo* culture. It is noteworthy that the number of BCG-mycobacteria in macrophages did not affect the ability of granuloma cells to migrate from solid granulomas in monolayer cell cultures *ex vivo*. The macrophages that had more than 30 BCG-mycobacteria in each and had active front edges of migrating cells were found at the periphery of the granulomas, and so were the macrophages that contained single or no BCG-mycobacteria (Figures 1(b) and 1(c)). It has been shown in zebrafish that, at the initial stage of infection with *M. marinum*, the more mycobacteria macrophages contain, the less mobile they are [39].

**3.2. The Number of Granulomas and Granuloma Cells with BCG-Mycobacteria in Mice.** For each of  $n$  granulomas

assayed (1 S/20 d,  $n = 32$ ; 2 S/20 d,  $n = 72$ ; 1 BM/20 d,  $n = 22$ ; 2 BM/20 d,  $n = 12$ ; 1 S/1 m,  $n = 36$ ; 3 S/1 m,  $n = 34$ ; 4 S/1 m,  $n = 44$ ; 5 S/1 m,  $n = 9$ ; 4 S/2 m,  $n = 96$ ; 5 S/2 m,  $n = 16$ ; 8 L/2 m,  $n = 2$ ; 8 S/2 m,  $n = 36$ ; 9 S/2 m,  $n = 60$ ; 10 S/2 m,  $n = 27$ ; 12 S/2 m,  $n = 29$ ; 13 S/2 m,  $n = 32$ ; 14 S/2 m,  $n = 9$ ; 16 S/2 m,  $n = 10$ ; 21 S/2 m,  $n = 9$ ; 22 S/2 m,  $n = 41$ ; 23 S/2 m,  $n = 52$ ; 24 S/2 m,  $n = 24$  and 25 S/2 m,  $n = 21$ ), we provide the number of infected cells, the number of BCG-mycobacteria in these cells, and the standard errors of the mean (SEM). Data reflecting the numbers of granulomas containing macrophages and dendritic cells with replicating and non-replicating BCG-mycobacteria as well as the numbers of such macrophages and dendritic cells in granulomas from mice are shown in Figures 2(a)–2(d). The mice differed in the number of splenic granulomas containing macrophages with BCG-mycobacteria they had and in the number of splenic granulomas containing macrophages with replicating BCG-mycobacteria they had (Figure 2(a)). The variance for the number of splenic granulomas containing macrophages with BCG-mycobacteria ranged from 14% (mouse 25 S/2 m) to 100% (mice 3 S/1 m, 10 S/2 m, 16 S/2 m, 21 S/2 m, and 23 S/2 m). Most granulomas had cells with replicating BCG-mycobacteria (Figure 2(a)). Splenic and bone marrow granulomas differed in the number of macrophages containing BCG-mycobacteria, single or replicating, they had (Figure 2(c)). Interestingly, granulomas containing small numbers of macrophages but large numbers of BCG-mycobacteria in them and granulomas containing large numbers of macrophages with a very few cells with acid-fast mycobacteria in them were observed in the same mice. The average number of macrophages with BCG-mycobacteria in granulomas varied from 1.5–5% (mice 1 BM/20 d, 2 BM/20 d, 1 S/1 m, 22 S/2 m, 24 S/2 m, and 25 S/2 m) to 25–30% (mice 3 S/1 m, 14 S/2 m, 21 S/2 m, and 23 S/2 m) of the total number of macrophages in the granulomas. Infected macrophages in splenic granulomas from most mice made up from 15% to 20% on most occasions. It is noteworthy that a large number of bone marrow granulomas from mice 1/20 d and 2/20 d had macrophages with acid-fast BCG-mycobacteria; however, the total number of infected macrophages was lower in them than in the splenic granulomas from the same mice. On the whole, granulomas, in which all macrophages had acid-fast BCG-mycobacteria, were not found.

Granulomas with infected dendritic cells in them were not identified in all BCG-infected mice. Additionally, such granulomas were fewer (6–15%) than those with infected macrophages in them (Figure 2(b)). A larger number of splenic granulomas (some 30%) with BCG-containing dendritic cells were found only in mouse 23 S/2 m. The number of infected dendritic cells varied substantially in granulomas from different mice, with the largest number being determined in the splenic granulomas from mice 4 S/2 m, 10 S/2 m, 13 S/2 m, and 22 S/2 m (Figure 2(d)). Most granuloma dendritic cells contained from one to three acid-fast mycobacteria. BCG-mycobacteria were observed either as single cells or as groups of replicating microorganisms presumably in the cytoplasm of dendritic cells (Figure 1(e)), because no visible vacuoles with mycobacteria were resolved in those cells. However, the intracellular compartments

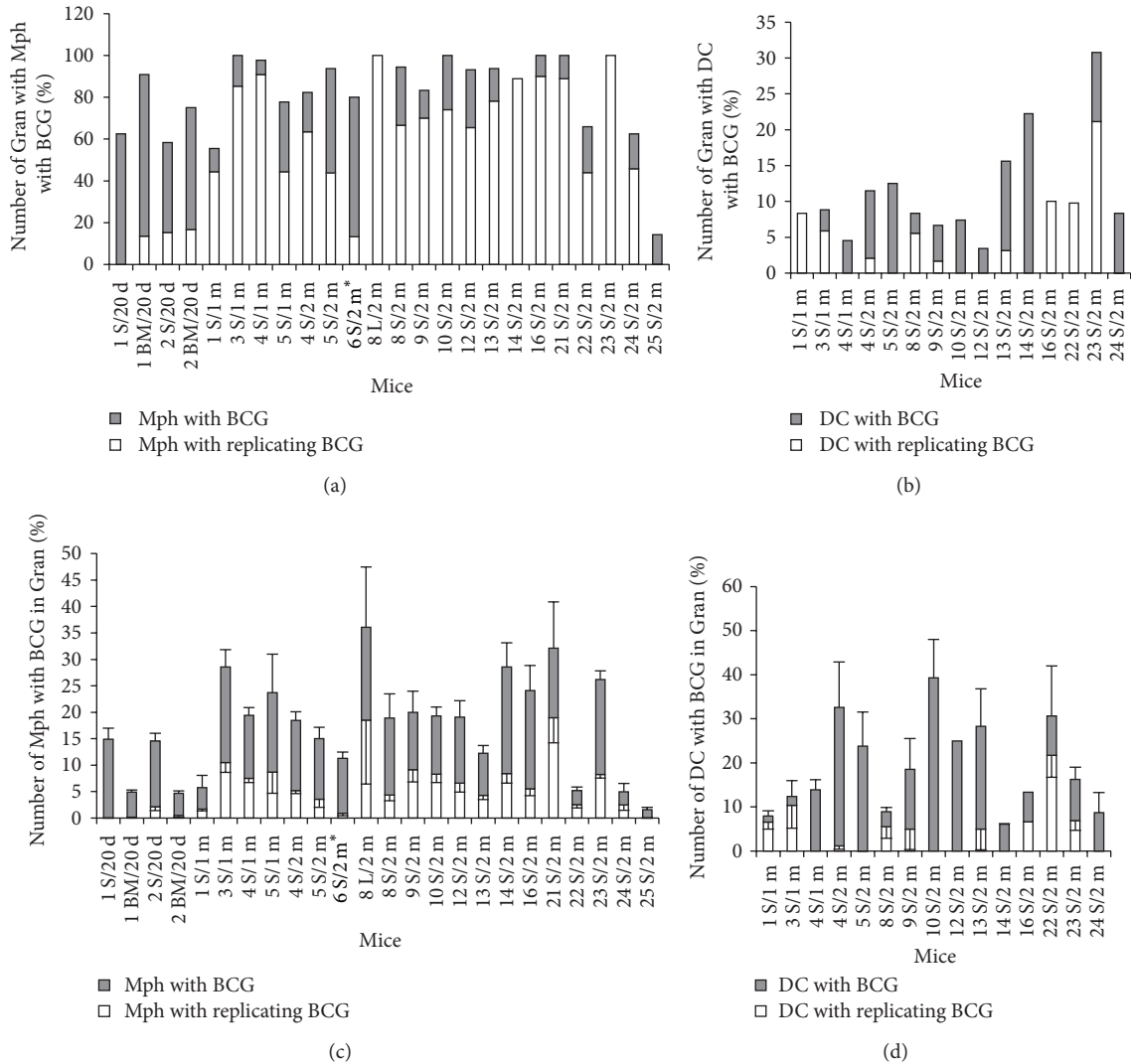


FIGURE 2: (a–d) Granulomas (Gran) obtained from the lungs (L/), spleens (S/), and bone marrow (BM/) of mice after 20 days (/20 d), one month (/1 m), and two months (/2 m) following infection with BCG *in vivo* and after *ex vivo* culture for several days, in which macrophages (Mph) or dendritic cells (DC) with acid-fast BCG-mycobacteria (BCG) in them were counted. ((a) and (b)) The figures represent the total number of granulomas with infected Mph and DC and the number of granulomas with Mph and DC with colonies of replicating BCG-mycobacteria expressed as a percentage of the total number of granulomas inspected. ((c) and (d)) The number of Mph (and DC) with any BCG (single or as colonies) and with colonies of replicating BCG, both expressed as a percentage of the total number of granuloma Mph (and DC). Data are expressed as the means  $\pm$  SEM. (\*) Leukocyte infiltrates from mouse 6 S/2 m.

where mycobacteria reside in mouse granuloma dendritic cells remain to be identified. It is noteworthy that Jiao and colleagues [40] found no evidence for BCG replication in dendritic cells isolated from spleens of mice after 12 days following infection with BCG *in vivo*. It is possible that the difference in the observations is due to the difference in the status of dendritic cells at the stages of acute and latent BCG infection in mice. However, no dendritic cells with BCG-mycobacteria in them were found in the leukocyte infiltrates of mouse 6 S/2 m, which was assayed presumably during acute TB infection, as they had an increased number of neutrophils [9]. No acid-fast mycobacteria were found in the dendritic cells of splenic granulomas isolated from mice

on day 20 following infection *in vivo*. A single mycobacterium was observed in a single dendritic cell within a single bone marrow granuloma from mouse 1/20 d.

Furthermore, we found BCG-mycobacteria in some multinucleate Langhans giant cells in splenic granulomas from different mice (Figures 1(d) and 1(f)). For example, in some granulomas from mouse 22 S/2 m, we observed Langhans giant cells with 7 nuclei, 10 nuclei (Figure 1(d)), and 42 nuclei (Figure 1(f)) containing one, 23, and 11 mycobacteria, respectively, both as single cells and as colonies of replicating mycobacteria. No acid-fast BCG-mycobacteria were found in Langhans giant cells with 6, 9, or 15 nuclei in other granulomas from the same mouse. It is very likely that BCG

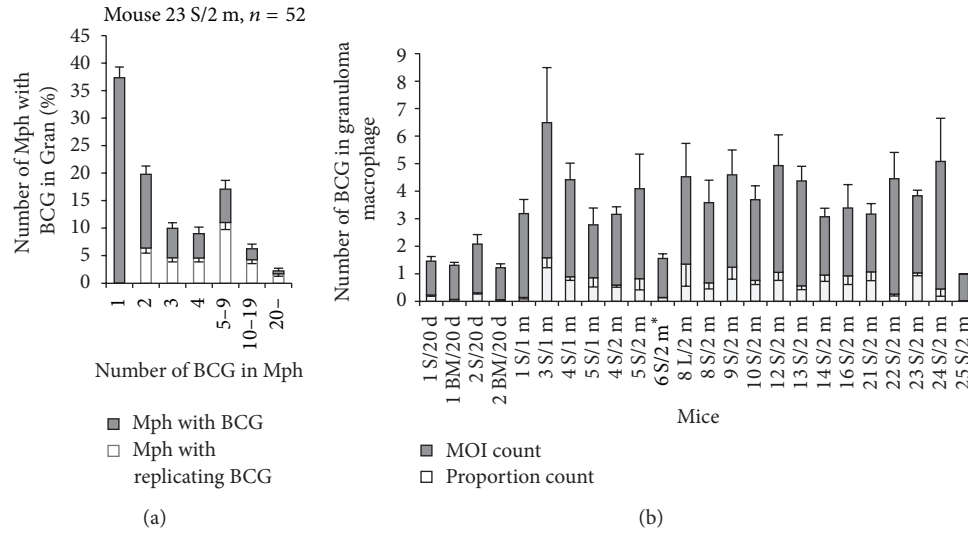


FIGURE 3: (a) Macrophages (Mph) with different numbers of BCG-mycobacteria (BCG) in the granulomas from mouse 23 S/2 m. Dark bars represent the number of Mph with different BCG numbers calculated as a percentage of the total number of infected Mph in the granulomas. White bars represent the number of Mph containing colonies of replicating BCG-mycobacteria calculated as a percentage of the total number of infected Mph in granulomas. (b) The number of BCG per macrophage in granulomas from different mice calculated as the number of BCG in macrophages relative the total number of infected macrophages (dark bars) or the total number of all granuloma macrophages (white bars) (see text for details). Data are expressed as the means  $\pm$  SEM. Abbreviations as in the legend to Figure 2. (\*) Leukocyte infiltrates from mouse 6 S/2 m.

occurred in the Langhans giant cells as a result of fusion of infected macrophages (Figure 1(f)); however, this assumption has yet to be verified.

**3.3. The Number of BCG-Mycobacteria in Mouse Granuloma Macrophages.** The number of BCG in macrophages varied within and between granulomas isolated from the same mouse. Furthermore, they varied between granulomas isolated from different mice. Macrophages with from one to up to 100 BCG-mycobacteria in each, either as single cells or as colonies of replicating mycobacteria (Figures 1(a) and 1(c)–1(i)), were observed, macrophages with two or more BCG-mycobacteria in each being less frequent than those with one mycobacterium in each (Figure 3(a)). Meanwhile, cells with a larger number of mycobacteria (30 or more) were observed in many splenic granulomas, but these cells were rare (Figure 3(a)). To determine the number of BCG-mycobacteria in the mouse granulomas, we used the following two BCG counts. One was calculated as follows: for each granuloma in a mouse, the total number of BCG-mycobacteria in all infected macrophages was determined and divided by the total number of these infected macrophages; the quotients were summed and their sum was divided by the total number of granulomas examined in that mouse. In fact, this count represents the MOI in the granuloma macrophages, and so it will be referred to as the “MOI count” throughout. The other was calculated as follows: for each granuloma in a mouse, the total number of BCG-mycobacteria in all infected macrophages was determined and divided by the total number of macrophages (both infected and not); the quotients were summed and their sum was divided by the total number of granulomas examined

in that mouse. This count reflects the proportion of infected granuloma cells, and so it will be referred to as the “proportion count” throughout (Figure 3(b)). These counts differed across the mice. For example, in mouse 3 S/1 m granulomas, both counts were elevated, which was indicative of a higher MOI in granuloma cells on the one hand and, on the other hand, of a high proportion of infected cells in granuloma macrophages. By contrast, in mice 22 S/2 m, the MOI count was elevated and the proportion count was considerably decreased, which implied that fewer granuloma macrophages were infected, while individual granuloma cells had a high bacterial load. It is noteworthy that macrophages in the granulomas from the lung and the spleen of mouse 8/2 m and from the bone marrow and the spleens of mice 1/20 d and 2/20 d had similar MOI counts and similar proportion counts (Figure 3(b)).

**3.4. Lack of Colocalization of BCG-Mycobacteria and Lyso-Tracker Dye in Mouse Granuloma Macrophages Producing the Proinflammatory Cytokines  $IFN\gamma$  and  $IL-1\alpha$ .** Macrophages in the splenic granulomas obtained from all mice had an enhanced ability for phagocytosis and destruction of damaged granuloma cells, mainly lymphocytes and thrombocytes and sometimes neutrophils, in the *ex vivo* culture. Phagosomes with engulfed lymphocytes and thrombocytes at various stages of degradation existed side by side with the vacuoles with acid-fast BCG-mycobacteria in granuloma macrophages (Figures 1(h) and 1(i)). It is noteworthy that no phagosomes with absorbed destroyed cells were observed in the dendritic cells.

We used the acidophilic fluorescent LysoTracker Red DND-99 probe to see if BCG-mycobacteria and acidic

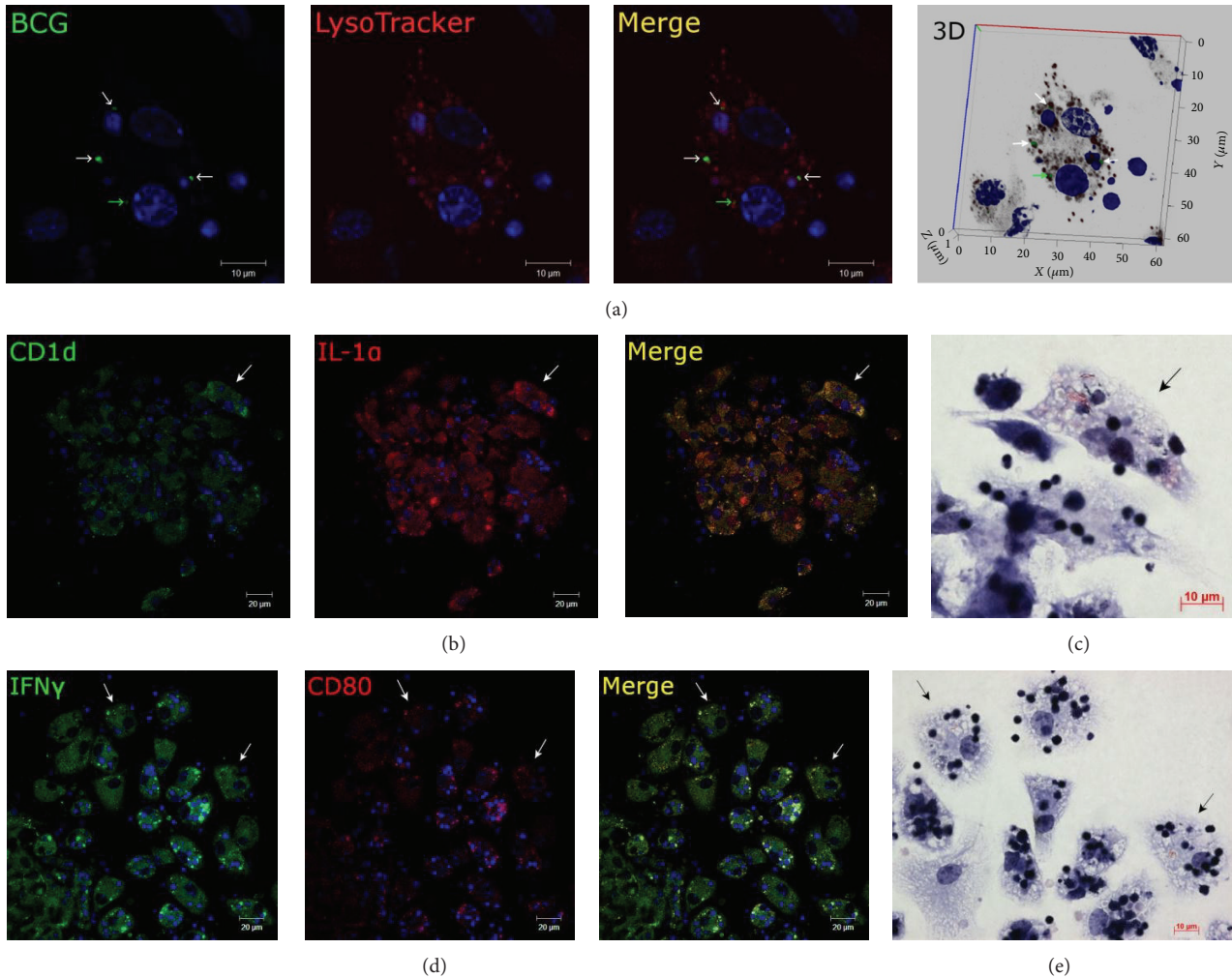


FIGURE 4: Representative confocal fluorescent images of granuloma macrophages stained for different markers. Fragments of splenic granulomas from mouse 2 after 20 days following BCG infection. Nuclei are stained by DAPI (blue signal). Scale bars: 10  $\mu\text{m}$  (a, c, e) and 20  $\mu\text{m}$  (b, d). (a) Mouse granuloma macrophages stained by the LysoTracker Red DND-99 dye (red signal) and mycobacterial LAM-specific antibodies (green signal) show lack of colocalization of BCG-mycobacteria and host cell lysosomes (lack of yellow signal). A single BCG-mycobacterium (green arrow) and replicating BCG-mycobacteria (white arrows). ((b) and (d)) Immunofluorescent localization of CD1d (green signal) and IL-1 $\alpha$  (red signal) and IFN $\gamma$  (green signal) and CD80 (red signal) in granuloma cells, respectively. Colocalization of the markers on the confocal images of cells (yellow signal). ((c) and (e)) The same granuloma fragments as in ((b) and (d)) remained for acid-fast BCG-mycobacteria by the Ziehl-Neelsen method. The same macrophages with replicating BCG-mycobacteria and producing proinflammatory cytokines and leukocyte surface markers are indicated by white arrows on the fluorescent ((b) and (d)) images and by black arrows on the Ziehl-Neelsen ((c) and (e)) images.

compartments of splenic and bone marrow granuloma cells as well as peritoneal and bone marrow macrophages from mice 1/20 d and 2/20 d show colocalization. The LysoTracker dye was used at a very low concentration in the cell-incubating medium only for 5 minutes before cell fixation in order to stain mainly lysosomes in the cells [41]. As a result, no colocalization of the acidophilic LysoTracker probe and BCG-mycobacteria detected by antibodies reacting with the major mycobacterial cell wall component glycolipid liparabinomannan (LAM) was observed (Figure 4(a)). Therefore, all LAM-labeled mycobacteria had avoided host killing in lysosomes and survived within the granuloma, peritoneal, and bone marrow macrophages of mice after 20 days following infection with BCG *in vivo*.

Our study of the proinflammatory cytokines IFN $\gamma$  and IL-1 $\alpha$ , bacterial lipids, the glycolipids-presenting molecule CD1d and the costimulatory molecule CD80 demonstrated a significant activation of granuloma cells, but not the peritoneal macrophages, from mice 1/20 d and 2/20 d through a higher expression of these markers regardless of mycobacterial load in the host cells (Figures 4(b) and 4(d)). It is noteworthy that the cytokine-producing granuloma macrophages with increased microbicidal potential too contained replicating acid-fast BCG-mycobacteria in Figures 4(b)–4(e). This result is similar to the previously observed significant increase in the production of proinflammatory cytokines IFN $\gamma$  and cell-associated IL-1 $\alpha$ , the growth factors GM-CSF and FGFb, the phagocytic receptors CD11b, CD11c, CD14,

and CD16/CD32, and the costimulatory molecules CD80, CD83, and CD86 in granuloma cells (with and without acid-fast BCG-mycobacteria) of mice after one and two months following infection with BCG vaccine *in vivo* [9].

Thus, we observed in the *ex vivo* culture of granuloma macrophages that, on the one hand, these macrophages retained their function to ingest engulfed granuloma cells (lymphocytes and thrombocytes) in the host's phagosomes and, on the other hand, that the host cells with increased production of the proinflammatory cytokines IFN $\gamma$  and IL-1 $\alpha$  had a reduced bactericidal capacity. This allowed BCG-mycobacteria to survive and actively replicate in mouse granuloma cells.

**3.5. The Cord Morphology of BCG Growth in Mouse Granuloma Cells.** Cording is a characteristic morphology of mycobacterial growth on solid and in liquid media, referring to the occurrence of colonies, in which the bacteria are arranged in the form of plaits, bundles, ropes, or cords, while drawing up in a line along their long axes and in close parallel arrangement. Previous studies [42, 43] provide evidence that the cord phenotype of mycobacterial growth correlates with the virulence of mycobacteria. It has been assumed that the cord morphology of mycobacteria is determined by the components of their cell walls and, first of all, by the glycolipids of trehalose-6,6'-dimycolate and its modifications [12, 44–46]. In zebrafish infected with *M. marinum*, cord formation by mycobacteria was for the first time observed in granulomas of juveniles *in vivo* and only in mycobacteria that were growing outside cells [31, 32]. It was for that reason proposed that cord formation is an attribute of the growth of only extracellular bacteria, no matter whether *in vivo* or *in vitro* [30, 31]. Our analysis of cells with acid-fast BCG-mycobacteria in splenic granulomas in *ex vivo* culture proved the presence of BCG cords in the cytoplasm of macrophages and dendritic cells (Figures 1(c)–1(e), 4(b) and 5(a)–5(f)). No visible membrane structures were resolved around the BCG cords in most granuloma cells (Figures 5(a)–5(b), 5(e)–5(f) and 5(h)); however, special studies are required for exploring the intracellular compartments available to the replicating mycobacteria in the mouse cells. Although BCG cords were found only in few granuloma macrophages (from 2% to 18% of infected macrophages in all granulomas), they were found in a large number of splenic granulomas of almost all of the mice, no matter what route of administration was used, and at all checkpoints following infection (Figures 4(b), 5(a)–5(i) and 6(a)–6(b)). By contrast, no extracellular growth of BCG-mycobacteria in granulomas was observed in *ex vivo* culture. Furthermore, no BCG-mycobacteria were observed outside granuloma cells. BCG-mycobacteria were occasionally found in apoptotic bodies and in fragments of the cell cytoplasm located in phagosomes of macrophages (Figure 5(l)) or outside cells (Figures 5(j) and 5(k)).

BCG cords were also observed in some dendritic cells (Figures 5(e) and 5(f)) in several granulomas from mice 9 S/2 m, 22 S/2 m, and 23 S/2 m. These mice had an increased number of granulomas containing macrophages with BCG cords. It is noteworthy that no cords were observed in

macrophages or dendritic cells of leukocyte infiltrates from the spleen of mouse 6 S/2 m.

The number of BCG-mycobacteria in the cords in mouse granuloma macrophages and dendritic cells varied from 5 to more than 30 and was from 10 to 20 on most occasions. It is noteworthy that BCG colonies with cords and acid-fast mycobacteria replicating in irregular clumps were often observed simultaneously in the same cell in different mouse granulomas (Figures 1(c)–1(i) and 5(a)–5(b), 5(d)–5(f), and 5(h)–5(i)).

**3.6. BCG-Mycobacteria in Mouse Spleen Granuloma Cells in Latent Tuberculosis.** It was found that the number of granulomas containing both macrophages with BCG-mycobacteria and macrophages with colonies of replicating mycobacteria in splenic granuloma cells had changed in the course of the latent TB infection (Figure 7(a)). Some increase in the number of granulomas containing macrophages with acid-fast mycobacteria was observed after 20 days, one month, and two months following infection; however, a considerable increase in the number of splenic granulomas with replicating microbes and BCG cords in macrophages was observed after one month and two months following infection ( $*P < 0.05$ , Figure 7(a)). The number of granuloma macrophages with replicating mycobacteria was increased considerably in Gran/1 m and Gran/2 m granulomas as compared with Gran/20 d granulomas ( $*P < 0.05$ , Figure 7(b)). No statistically significant change in the number of macrophages with cords was found between granulomas after 20 days, one month, or two months after infection (Figure 7(b)). However, there was a statistically significant difference in the number of cord-containing macrophages between granulomas from mice after one month and two months following infection ( $**P < 0.01$ , Figure 7(b)). No statistically significant difference was found in the number of granulomas with infected macrophages, the number of infected macrophages, or the number of colonies of replicating mycobacteria between granulomas from mice after one month and two months following infection *in vivo* (Figures 7(a) and 7(b)).

In Gran/1 m and Gran/2 m granulomas, the respective MOI counts were similar and so were the proportion counts; however, both counts were considerably higher in these granulomas than in Gran/20 d granulomas ( $*P < 0.05$ , Figure 7(c)). In the mice after one month and two months following infection, the respective numbers of granulomas with infected macrophages in them were similar (Figure 7(d)) and so were the respective numbers of infected macrophages (Figure 7(e)); however, both counts in these mice differed significantly from those in the mice after 20 days following infection. Thus, a considerable increase in the number of granulomas with macrophages containing two or more BCG-mycobacteria as well as in the number of macrophages with even more mycobacteria in them was observed at the end of the first month after BCG infection in the mice. Bacteriological determination of the number of mycobacteria in homogenates of various mouse organs and tissues [13, 45, 47] demonstrated that a logarithmic growth of mycobacterial populations during the first two weeks after infection generally reaches a plateau within the third and fourth weeks

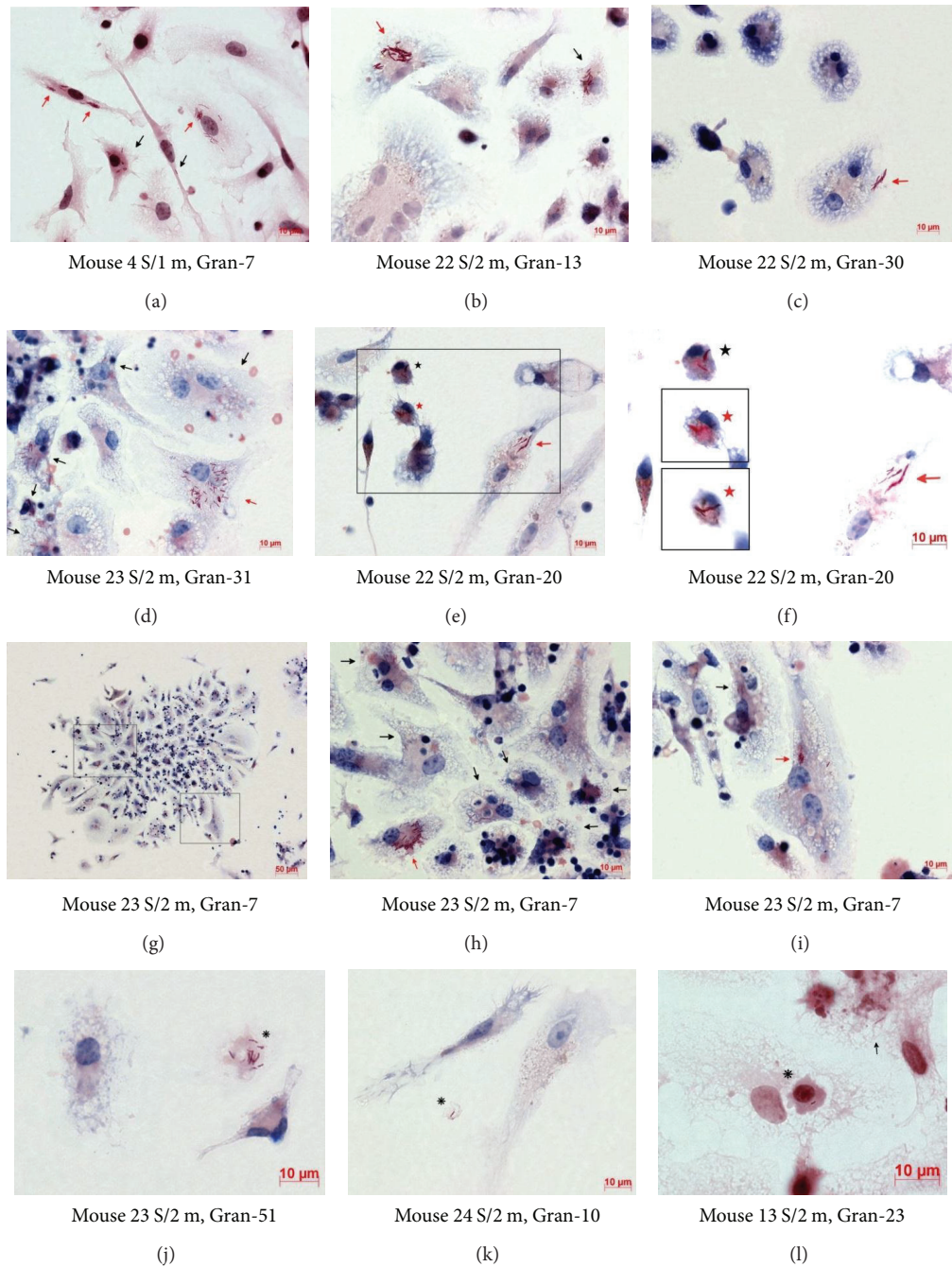


FIGURE 5: ((a)–(i)) BCG cords in the cells of granulomas (Gran) obtained from the spleens (S/) of mice after one month (/1 m) and two months (/2 m) following infection with the BCG vaccine *in vivo* and after *ex vivo* culture for several days. ((a)–(f) and (l)) Macrophages with BCG-mycobacteria (black arrows) and cords (red arrows). ((e) and (f)) Dendritic cells with BCG-mycobacteria (black asterisks) and BCG cords (red asterisks). (f) A high-contrast photo (e) of BCG-mycobacteria and BCG cords in the cytoplasm of dendritic cells. The same dendritic cell at different levels of sharpness is shown in the black frames. ((j) and (k)) BCG-mycobacteria outside granuloma cells (black snowflakes). (l) The only case when a granuloma macrophage had a vacuole (a black asterisk) with an apoptotic cell containing a mycobacterium. ((a)–(f) and (j)–(l)) Fragments of granulomas. ((h) and (i)) Close-ups of granuloma fragments in the black frames in (g). Acid-fast BCG-mycobacteria after Ziehl-Neelsen staining. Scale bars: 50  $\mu\text{m}$  (g) and 10  $\mu\text{m}$  ((a)–(f) and (h)–(l)).

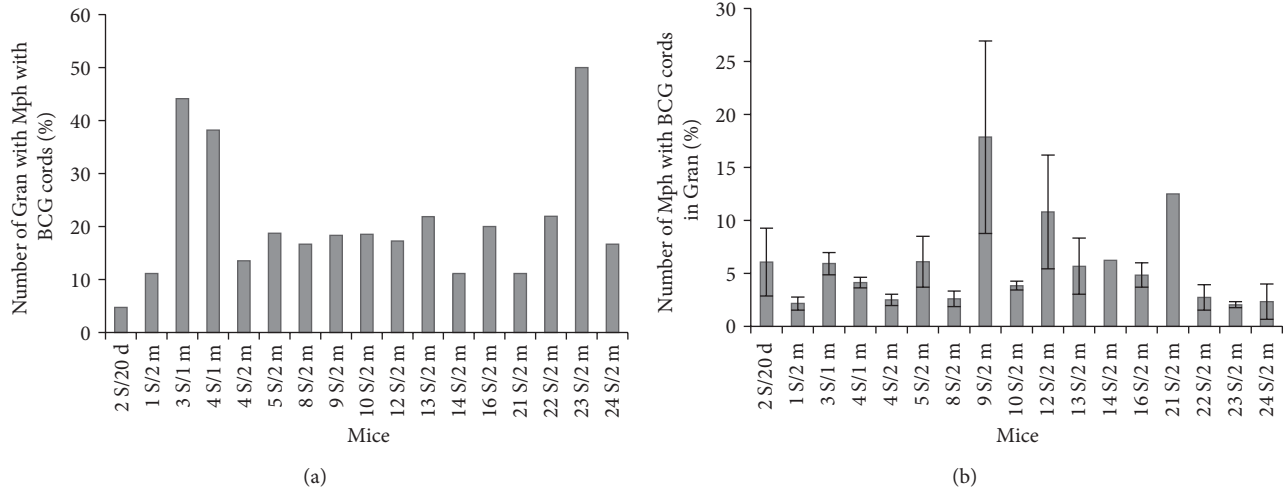


FIGURE 6: (a) The number of granulomas with Mph containing BCG cords expressed as a percentage of the total number of granulomas assayed. (b) The number of Mph with BCG cords in granulomas from different mice expressed as a percentage of the total number of macrophages in granulomas with Mph containing BCG cords. Data are expressed as the means  $\pm$  SEM. Abbreviations as in the legend to Figure 2.

and is there for months during latent TB infection. Therefore, our data on the BCG load in mouse granulomas in chronic tuberculosis are consistent with the results obtained by other researchers.

#### 4. Discussion

Studies of granulomas from mice with latent TB infection in *ex vivo* culture demonstrate that acid-fast BCG can be found in macrophages, dendritic cells, and multinucleate Langhans giant cells. The BCG-mycobacteria differed morphologically (in size and shape) and functionally (in replication rates) both in the same cell and in the granuloma cells of different types. A similar variability of *M. smegmatis* and *M. tuberculosis* cell growth and division during *in vitro* culture was demonstrated by Aldridge and colleagues [27] and that resulted in cell populations having different sensitivities to popular human antimycobacterial drugs.

In our study, BALB/c mice with latent TB infection differed both in the number of granulomas with infected cells they had and in the number of infected cells in granulomas they had. Furthermore, in the preparations obtained from each of the mice, granulomas had different sizes and contained different numbers of infected cells in them (from one to many more). No granulomas (not even the smallest) in which all the macrophages contained BCG were found. It is noteworthy that only acid-fast BCG-mycobacteria (which, again, have undamaged cell walls) were assayed in the host cells using the Ziehl-Neelsen method. These BCG-mycobacteria detected in the host cells of mouse granulomas probably remained in a metabolically active state, or so their capability of surviving and replicating in various cellular compartments suggests.

We have observed acid-fast BCG-mycobacteria in the visible vacuoles and apparently in the cytoplasm of mouse granuloma cells near the nuclei, which is where lysosomes

normally get together, and in other cell compartments. However, no colocalization of LAM-labeled mycobacteria and acidic compartments was observed in splenic or bone marrow granuloma cells nor was it in peritoneal or bone marrow macrophages on day 20 following infection *in vivo*. The lack of colocalization of some mycobacteria and LysoTracker dye in various types of cells infected by different mycobacterial strains in *in vitro* culture has been pointed out by many researchers [22, 48–50]; however, this is the first time that this phenomenon is observed in the macrophages of individual granulomas isolated from mice with latent TB infection *in vivo*. The arrest of the biogenesis of phagolysosomes with mycobacteria engulfed in them is thought to represent one of the key mechanisms by which mycobacteria avoid host killing and survive within cells [4, 8, 10]. Therefore, further research is required to elucidate the molecular mechanisms involved in the inhibition of phagosomal maturation in the cells of human and animal organisms during latent TB infection and after reactivation.

According to other studies [28, 29], various human and mouse cell lines infected *in vitro* rapidly eliminated attenuated mycobacteria (BCG) but did not eliminate virulent strains of *M. tuberculosis* or *M. bovis*. These studies demonstrated that some BCG-mycobacteria were killed by phagocytes in phagolysosomes and some died following apoptotic death of infected myeloid cells. However, in our study, we did not find macrophages or dendritic cells, with or without mycobacteria, that had a characteristic apoptotic morphology of cells in the *ex vivo* cultures of granulomas obtained from all BCG-infected mice. Furthermore, we have not found BCG-mycobacteria outside granuloma cells. It is possible that extracellular mycobacteria are absorbed by granuloma cells immediately, because, as was demonstrated previously [9], granuloma macrophages and dendritic cells in BCG-infected mice have an increased number of the phagocytic receptors CD11b, CD11c, CD14, and CD16/CD32,

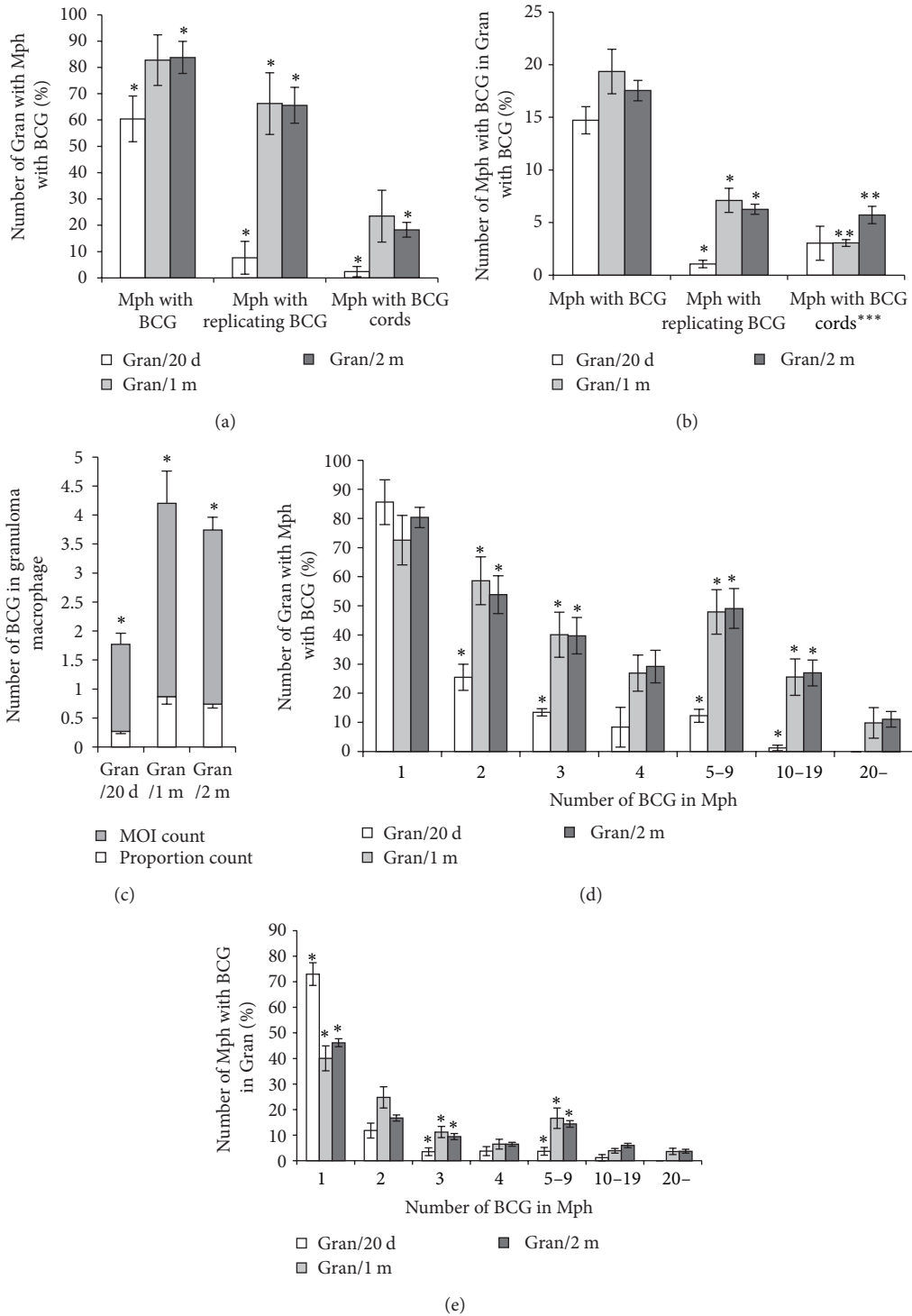


FIGURE 7: A comparison of the granulomas (Gran) isolated from mouse spleens after 20 days (Gran/20 d), one month (Gran/1 m), and two months (Gran/2 m) following infection with the BCG vaccine *in vivo* and several days in *ex vivo* culture. (a) The number of Gran containing macrophages (Mph) with acid-fast BCG-mycobacteria (BCG) is expressed as a percentage of the total number of Gran assayed. (b) The number of infected macrophages expressed as a percentage of the total number of macrophages in Gran with infected macrophages or (\*\*\* ) in Gran with Mph containing BCG cords. (c) The number of BCG per granuloma macrophage calculated as the number of BCG in the granuloma relative to the total number of infected granuloma macrophages (dark bars) or the total number of granuloma macrophages (white bars) (see text for details). (d) The number of Gran containing Mph with different BCG numbers expressed as a percentage of the total number of Gran with infected Mph. (e) The number of macrophages with different numbers of BCG in Gran expressed as a percentage of the total number of infected macrophages in granulomas. Data are expressed as the means  $\pm$  SEM. \* $P < 0.05$  (Gran/20 d versus Gran/1 m or Gran/20 d versus Gran/2 m), \*\* $P < 0.01$  (Gran/1 m versus Gran/2 m). Data relate to (a) Gran/20 d (2 mice,  $n = 104$ ), Gran/1 m (4 mice,  $n = 123$ ), Gran/2 m (14 mice,  $n = 462$ ), and ((b)-(e)) Gran/20 d (2 mice,  $n = 62$ ), Gran/1 m (4 mice,  $n = 104$ ), and Gran/2 m (14 mice,  $n = 386$ ).

which typically show colocalization in microdomains on the surface of granuloma cells. We have also observed the replication of a large number of BCG-mycobacteria in the visible small and large vacuoles of granuloma macrophages, which suggests that acid-fast mycobacteria are not being eliminated in these compartments. This observation disagrees with the inference made from *in vitro* culture that mycobacteria can survive only in macrophage compartments, where close apposition between the mycobacterial surface and the host's phagosome membrane was determined [51]. It is possible that the differences in the behavior of microbes in macrophages were accounted for by the differences in the culture systems (*in vitro* versus *ex vivo*) and the mycobacterial strains (*M. avium* versus BCG) used. However, our data obtained from *ex vivo* culture suggest that actively replicating acid-fast mycobacteria were also present in the visible vacuoles of peritoneal and bone marrow macrophages after BCG infection *in vitro* (unpublished data).

A comparison of the granulomas obtained from spleens after one month and two months following infection did not actually reveal any difference in the number of infected granuloma cells. However, a considerable amount of individual variability for this number was observed across the BALB/c mice. It is possible that some mice were more sensitive to BCG infection than the others, and so they had more bacilli in their granuloma cells. By contrast, the others were capable of having BCG infection controlled, and so they had fewer mycobacteria in the cells of their granulomas. It is therefore important to understand what intercellular and intracellular interactions and what factors in the host organism and in granulomas themselves account for the varying sensitivity of the mice to BCG infection.

In our study, BCG cords in the cytoplasm of mouse granuloma macrophages and dendritic cells were observed for the first time. Mycobacterial cords are supposed to be analogs of biofilms that are dramatically resistant to antimicrobial agents [52]. Cord formation by mycobacteria had previously been observed mainly in *in vitro* culture of different strains of *M. tuberculosis* on solid and in liquid media or in the process of extracellular growth of *M. marinum* in zebrafish granulomas *in vivo* [31, 42, 43]. Low rates of BCG replication *in vitro* are a well-known fact [29]. We observed cords formed by BCG-mycobacteria in the host cells that were the two-day-old *ex vivo* cultures of granulomas (mice 8/2 m, 9/2 m, and 10/2 m) and assumed that those cords must have been formed earlier, in the mouse granuloma cells *in vivo*. In some studies [29, 53–55], the attenuated phenotype of BCG-mycobacteria and their inability to replicate and/or leave phagosomal vacuoles in host cells in cell lines following *in vitro* infection were explained by the absence, in the BCG genome, of some genes that virulent strains of *M. bovis* and *M. tuberculosis* possess and, first of all, by the absence of the RD1 locus containing the genes coding for proteins of the secretion system ESX-1. However, cording was observed in some granulomas of zebrafish infected with *M. marinum* with the deletion of the RD1 locus, when replicating mycobacteria were outside granuloma cells [31]. It had previously been established [12, 45] that cord formation by mycobacteria (including BCG) growing on solid and in liquid media *in vitro* might be

controlled by the components of mycobacterial cell walls and, above all, by chemical modifications of mycolic acids. It was not known if the chemical modifications that account for cord formation were present in the cell walls of some BCG-mycobacteria in mouse granuloma cells. Probably, other mycobacteria did not have such chemical modifications of mycolic acids in the cell walls and represented groups of chaotically arranged replicating bacteria. These assumptions, however, require further studies.

Detection of granuloma macrophages with a large number of single BCG-mycobacteria, possibly in the cytoplasm of the host cells, raised the question as to how such host cells occur in mouse granulomas. It seemed possible that such cells could appear as a result of the replication of BCG-mycobacteria in the host cells and their subsequent migration from the colonies across the cells and/or between the cells. Another possible way of the occurrence of host cells with a large number of single BCG-mycobacteria in them is through phagocytosis of mycobacteria from the extracellular environment by granuloma macrophages followed by migration of mycobacteria from the phagosomes to the cytoplasm of the host cells, probably by lysis of vacuolar membranes. A similar mechanism of repeated infection of macrophages that engulf the necrotic cells containing mycobacteria has been revealed and studied in zebrafish granulomas at the initial stage of infection with *M. marinum* [39]. The migration of *M. marinum* from phagosomes to the cytoplasm of host cells and their traveling between granuloma macrophages with the help of actin and proteins bound to it have also been demonstrated [56–58]. In our experiments, we did not observe, in *ex vivo* culture, any granuloma macrophage or dendritic cell dead by necrosis, when BCG-mycobacteria could occur in extracellular locations after the host cells had been destroyed, or by apoptosis. According to some studies [28, 29], BCG-mycobacteria in human and mouse myeloid cell lines infected *in vitro* can only be found in phagosomes and phagolysosomes, which is where they are eliminated, while mycobacteria of virulent strains actively replicate in the vacuoles and/or the cytoplasm of the host cells. Some authors [29, 39, 55, 58–60] hypothesized that the processes of intracellular replication and intercellular dissemination of mycobacteria require the genetic locus known as RD1, which encodes the proteins ESAT-6 and GFP-10. These molecules are assumed to aid in phagosomal escape of virulent mycobacteria and their migration to the cytoplasm of host cells [29, 60]. However, our studies do not confirm this hypothesis: BCG-mycobacteria with the RD1 deletion [53] replicated actively in the visible vacuoles and presumably in the cytoplasm of granuloma host cells from mice with latent TB infection. It is possible that the mycobacteria behave differently in the host cells at the earliest stages of infection of macrophages *in vitro* and in granuloma cells obtained from mice after 20 days, one month, and two months following BCG infection *in vivo*. Further studies of the ways, factors, and mechanisms that influence the replication and dissemination of mycobacteria, including the vaccine strains, inside host cells, and between granuloma cells in mice with active and latent TB infection are required.

Importantly, the macrophages of the mouse granulomas being discussed retained their capacity of phagocytosis and ingestion of engulfed lymphocytes (with several features of apoptosis including nuclear fragmentation) and thrombocytes. At the same time, the mouse granuloma macrophages lacked bactericidal activity against BCG-mycobacteria that were located in the vacuoles and cytoplasm of the host cells with engulfed lymphocytes and thrombocytes. It has been noticed that the arrest of phagosome to phagolysosome maturation in granuloma macrophages was only confined to the compartments with BCG-mycobacteria inside. Our conclusions confirm the hypothesis proposed previously [10, 61] that those were the mycobacteria that are responsible for the ability to avoid degradation and survive in macrophage phagosomes. However, our study makes us disagree with the statement that mycobacterial infection of macrophages induces global modifications in the phagosomal functions of host cells that are observed in macrophages of various lines after infection *in vitro* [62]. It is noteworthy that vacuoles with BCG-mycobacteria in them do not seem to be static formations in granulomas from mice with latent TB infection. Rather, they are susceptible to change with the transition of mycobacteria from the vacuoles to the host cells' cytoplasm. The exact mechanisms of these processes are still not clear.

The macrophages of splenic and bone marrow granulomas obtained from mice after 20 days following BCG infection *in vivo* contained a lower number of acid-fast mycobacteria and the lowest number of replicating BCG-mycobacteria, as opposed to the granuloma cells of mice after one month and two months following BCG infection *in vivo*. At the same time, in our studies, the *in vitro* infection of mouse peritoneal and bone marrow macrophages with BCG resulted in a considerable growth of mycobacteria in the host cells after *in vitro* culture for 5 days (unpublished data). Therefore, the granuloma macrophages could control BCG infection in mice with latent tuberculosis *in vivo* and in the *ex vivo* culture. This could be true, because it has now and previously been demonstrated [9] that granuloma macrophages and dendritic cells of BCG-infected mice produce proinflammatory mediators, including the cytokines IFN $\gamma$ , IL-1 $\alpha$ , and GM-CSF. Moreover, most mycobacteria were efficiently eliminated in the hosts, as was shown by the mycobacterial counts in the peritoneal macrophages isolated from mice after 20 days following intraperitoneal infection with BCG *in vivo*. At this stage of latent tuberculosis, the dissemination of mycobacteria from the peritoneal cavity to other mouse organs, including the spleen, bone marrow, and lung, was already observed. Various numbers of solid granulomas were formed. Interestingly, acid-fast BCG-mycobacteria were found only in bone marrow macrophages, while it is only dendritic cells that are supposed to spread the microbes across the tissues of human and animal organisms so that miliary tuberculosis is eventually developed [8, 63, 64]. Thus, only a small number of BCG-mycobacteria survived in the granuloma cells and other host cells of mice after BCG infection *in vivo*. Identification of the differences in functional states that allow some of mycobacteria to reside and grow successfully in

the hosts with increased production of the proinflammatory cytokines IFN $\gamma$  and IL-1 $\alpha$  in granuloma cells, while the others will be killed and eliminated, is a matter of further research.

As is known, BCG-mycobacteria are attenuated for man and are widely used in vaccine prophylaxis of tuberculosis in children [55]. As far as BALB/c mice are concerned, we have discovered a large number of relationships between different types of granuloma cells and BCG-mycobacteria. Within the same mouse line, these relationships range from almost complete absence of mycobacteria in granuloma macrophages from mice, whose organisms have neutralized the BCG infection (mouse 25 S/2 m), to active replication of mycobacteria, with the formation of cords, which is an indicator of mycobacterial virulence in the host cells and, probably, a marker of the activation of TB infection in animals (mice 3 S/1 m and 23 S/2 m). Therefore, this experimental mouse model is interesting for a preliminary assessment of the effect of antituberculosis drugs on mycobacteria in granuloma cells in animals with different MOIs, because, as was pointed out in a review by Franzblau and colleagues [35], good concordance was found between the results on the sensitivity of *M. bovis* BCG and *M. tuberculosis* to diverse compounds.

## 5. Conclusions

Our findings of the persistence of BCG-mycobacteria in macrophages, dendritic cells, and multinucleate Langhans giant cells of mouse granulomas, which have been studied for the first time, represents an interesting example of long-lasting specific interactions between macro- and microorganisms in chronic TB infection in animals. It is our hope that using an *ex vivo* monolayer cultures of granuloma cells in a mouse model of latent TB infection, relatively safe for the researchers, will be useful as a tool for exploring TB-causing relationships between intracellular pathogens and the host organisms and studying of various molecular and cellular mechanisms by which pathogenic microorganisms survive in animals and avoid numerous host-protecting mechanisms of the innate and the adaptive immune system.

## Conflict of Interests

The author declares that she has no conflict of interests.

## Acknowledgments

The author is thankful to Dr. S. I. Baiborodin and T. E. Aleshina of the Shared Center for Microscopic Analysis of Biological Objects of the Institute of Cytology and Genetics, SB RAS, for technical support; Professor L. E. Panin of the Institute of Biochemistry, SB RAMS, for support to this work and helpful discussion; and Dr. A. V. Korepanova of Global Protein Sciences, GPRD, AbbVie, for carefully reading the paper and sharing valuable comments.

## References

- [1] N. M. Parrish, J. D. Dick, and W. R. Bishai, "Mechanisms of latency in *Mycobacterium tuberculosis*," *Trends in Microbiology*, vol. 6, no. 3, pp. 107–112, 1998.
- [2] G. R. Stewart, B. D. Robertson, and D. B. Young, "Tuberculosis: a problem with persistence," *Nature Reviews Microbiology*, vol. 1, no. 2, pp. 97–105, 2003.
- [3] R. J. North and Y.-J. Jung, "Immunity to tuberculosis," *Annual Review of Immunology*, vol. 22, pp. 599–623, 2004.
- [4] D. G. Russell, B. C. VanderVen, W. Lee et al., "*Mycobacterium tuberculosis* wears what it eats," *Cell Host and Microbe*, vol. 8, no. 1, pp. 68–76, 2010.
- [5] T. R. Frieden, T. R. Sterling, S. S. Munsiff, C. J. Watt, and C. Dye, "Tuberculosis," *The Lancet*, vol. 362, no. 9387, pp. 887–899, 2003.
- [6] J. Pieters, "*Mycobacterium tuberculosis* and the macrophage: maintaining a balance," *Cell Host and Microbe*, vol. 3, no. 6, pp. 399–407, 2008.
- [7] J. L. Flynn, J. Chan, and P. L. Lin, "Macrophages and control of granulomatous inflammation in tuberculosis," *Mucosal Immunology*, vol. 4, no. 3, pp. 271–278, 2011.
- [8] L. Jordao and O. V. Vieira, "Tuberculosis: new aspects of an old disease," *International Journal of Cell Biology*, vol. 2011, Article ID 403623, 13 pages, 2011.
- [9] E. Ufimtseva, "Investigation of functional activity of cells in granulomatous inflammatory lesions from mice with latent tuberculous infection in the new *ex vivo* model," *Clinical and Developmental Immunology*, vol. 2013, Article ID 371249, 14 pages, 2013.
- [10] A. L. K. Hestvik, Z. Hmama, and Y. Av-Gay, "Mycobacterial manipulation of the host cell," *FEMS Microbiology Reviews*, vol. 29, no. 5, pp. 1041–1050, 2005.
- [11] M. Behr, E. Schurr, and P. Gros, "TB: screening for responses to a vile visitor," *Cell*, vol. 140, no. 5, pp. 615–618, 2010.
- [12] M. S. Glickman, J. S. Cox, and W. R. Jacobs Jr., "A novel mycolic acid cyclopropane synthetase is required for cording, persistence, and virulence of *Mycobacterium tuberculosis*," *Molecular Cell*, vol. 5, no. 4, pp. 717–727, 2000.
- [13] H. M. S. Algood, P. L. Lin, D. Yankura, A. Jones, J. Chan, and J. L. Flynn, "TNF influences chemokine expression of macrophages *in vitro* and that of CD11b<sup>+</sup> cells *in vivo* during *Mycobacterium tuberculosis* infection," *The Journal of Immunology*, vol. 172, no. 11, pp. 6846–6857, 2004.
- [14] J. C. Leemans, T. Thepen, S. Weijer et al., "Macrophages play a dual role during pulmonary tuberculosis in mice," *The Journal of Infectious Diseases*, vol. 191, no. 1, pp. 65–74, 2005.
- [15] A. J. Wolf, B. Linas, G. J. Trevejo-Nuñez et al., "*Mycobacterium tuberculosis* infects dendritic cells with high frequency and impairs their function *in vivo*," *The Journal of Immunology*, vol. 179, no. 4, pp. 2509–2519, 2007.
- [16] C. L. Stallings, N. C. Stephanou, L. Chu, A. Hochschild, B. E. Nickels, and M. S. Glickman, "CarD is an essential regulator of rRNA transcription required for *Mycobacterium tuberculosis* persistence," *Cell*, vol. 138, no. 1, pp. 146–159, 2009.
- [17] L. H. Hogan, W. Markofski, A. Bock, B. Barger, J. D. Morrissey, and M. Sandor, "*Mycobacterium bovis* BCG-induced granuloma formation depends on gamma interferon and CD40 ligand but does not require CD28," *Infection and Immunity*, vol. 69, no. 4, pp. 2596–2603, 2001.
- [18] L. H. Hogan, K. Macvilay, B. Barger et al., "*Mycobacterium bovis* strain Bacillus Calmette-Guérin-induced liver granulomas contain a diverse TCR repertoire, but a monoclonal T cell population is sufficient for protective granuloma formation," *The Journal of Immunology*, vol. 166, no. 10, pp. 6367–6375, 2001.
- [19] T. Ulrichs, G. A. Kosmiadi, V. Trusov et al., "Human tuberculous granulomas induce peripheral lymphoid follicle-like structures to orchestrate local host defence in the lung," *The Journal of Pathology*, vol. 204, no. 2, pp. 217–228, 2004.
- [20] R. L. Hunter, M. Olsen, C. Jagannath, and J. K. Actor, "Trehalose 6,6'-dimycolate and lipid in the pathogenesis of caseating granulomas of tuberculosis in mice," *The American Journal of Pathology*, vol. 168, no. 4, pp. 1249–1261, 2006.
- [21] J. G. Egen, A. G. Rothfuchs, C. G. Feng, N. Winter, A. Sher, and R. N. Germain, "Macrophage and T cell dynamics during the development and disintegration of mycobacterial granulomas," *Immunity*, vol. 28, no. 2, pp. 271–284, 2008.
- [22] W. L. Beatty and D. G. Russell, "Identification of mycobacterial surface proteins released into subcellular compartments of infected macrophages," *Infection and Immunity*, vol. 68, no. 12, pp. 6997–7002, 2000.
- [23] D. Schnappinger, S. Ehrt, M. I. Voskuil et al., "Transcriptional adaptation of *Mycobacterium tuberculosis* within macrophages: insights into the phagosomal environment," *The Journal of Experimental Medicine*, vol. 198, no. 5, pp. 693–704, 2003.
- [24] R. Jayachandran, V. Sundaramurthy, B. Combaluzier et al., "Survival of mycobacteria in macrophages is mediated by coronin 1-dependent activation of calcineurin," *Cell*, vol. 130, no. 1, pp. 37–50, 2007.
- [25] D. Montoya, D. Cruz, R. M. B. Teles et al., "Divergence of macrophage phagocytic and antimicrobial programs in leprosy," *Cell Host and Microbe*, vol. 6, no. 4, pp. 343–353, 2009.
- [26] K. N. Adams, K. Takaki, L. E. Connolly et al., "Drug tolerance in replicating mycobacteria mediated by a macrophage-induced efflux mechanism," *Cell*, vol. 145, no. 1, pp. 39–53, 2011.
- [27] B. B. Aldridge, M. Fernandez-Suarez, D. Heller et al., "Asymmetry and aging of mycobacterial cells lead to variable growth and antibiotic susceptibility," *Science*, vol. 335, no. 6064, pp. 100–104, 2012.
- [28] M. G. Gutierrez, S. S. Master, S. B. Singh, G. A. Taylor, M. I. Colombo, and V. Deretic, "Autophagy is a defense mechanism inhibiting BCG and *Mycobacterium tuberculosis* survival in infected macrophages," *Cell*, vol. 119, no. 6, pp. 753–766, 2004.
- [29] N. van der Wel, D. Hava, D. Houben et al., "*M. tuberculosis* and *M. leprae* translocate from the phagolysosome to the cytosol in myeloid cells," *Cell*, vol. 129, no. 7, pp. 1287–1298, 2007.
- [30] K. H. Rohde, R. B. Abramovitch, and D. G. Russell, "*Mycobacterium tuberculosis* invasion of macrophages: linking bacterial gene expression to environmental cues," *Cell Host and Microbe*, vol. 2, no. 5, pp. 352–364, 2007.
- [31] H. Clay, H. E. Volkman, and L. Ramakrishnan, "Tumor necrosis factor signaling mediates resistance to *Mycobacteria* by inhibiting bacterial growth and macrophage death," *Immunity*, vol. 29, no. 2, pp. 283–294, 2008.
- [32] D. M. Tobin, J. C. Vary Jr., J. P. Ray et al., "The *lta4h* locus modulates susceptibility to mycobacterial infection in zebrafish and humans," *Cell*, vol. 140, no. 5, pp. 717–730, 2010.
- [33] J. L. Flynn, "Lessons from experimental *Mycobacterium tuberculosis* infections," *Microbes and Infection*, vol. 8, no. 4, pp. 1179–1188, 2006.
- [34] H. A. Schreiber, P. D. Hulseberg, J. Lee et al., "Dendritic cells in chronic mycobacterial granulomas restrict local anti-bacterial T cell response in a murine model," *PLoS ONE*, vol. 5, no. 7, Article ID e11453, 14 pages, 2010.

- [35] S. G. Franzblau, M. A. Degroote, S. H. Cho et al., "Comprehensive analysis of methods used for the evaluation of compounds against *Mycobacterium tuberculosis*," *Tuberculosis*, vol. 92, no. 6, pp. 453–488, 2012.
- [36] J. L. Dahl, "Electron microscopy analysis of *Mycobacterium tuberculosis* cell division," *FEMS Microbiology Letters*, vol. 240, no. 1, pp. 15–20, 2004.
- [37] N. R. Thanky, D. B. Young, and B. D. Robertson, "Unusual features of the cell cycle in mycobacteria: polar-restricted growth and the snapping-model of cell division," *Tuberculosis*, vol. 87, no. 3, pp. 231–236, 2007.
- [38] E. C. Hett and E. J. Rubin, "Bacterial growth and cell division: a mycobacterial perspective," *Microbiology and Molecular Biology Reviews*, vol. 72, no. 1, pp. 126–156, 2008.
- [39] J. M. Davis and L. Ramakrishnan, "The role of the granuloma in expansion and dissemination of early tuberculous infection," *Cell*, vol. 136, no. 1, pp. 37–49, 2009.
- [40] X. Jiao, R. Lo-Man, and P. Guernonprez, "Dendritic cells are host cells for *Mycobacteria* in vivo that trigger innate and acquired immunity," *The Journal of Immunology*, vol. 168, no. 3, pp. 1294–1301, 2002.
- [41] I. Johnson and M. T. Z. Spence, *The Molecular Probes Handbook: A Guide to Fluorescent Probes and Labeling Technologies*, Life Technologies Corporation, 2010.
- [42] G. Middlebrook, R. J. Dubos, and C. Pierce, "Virulence and morphological characteristics of mammalian tubercle bacilli," *The Journal of Experimental Medicine*, vol. 86, no. 2, pp. 175–184, 1947.
- [43] H. Bloch, "Studies on the virulence of tubercle bacilli; isolation and biological," *The Journal of Experimental Medicine*, vol. 91, no. 2, pp. 197–218, 1950.
- [44] A. Bekierkunst and E. Yarkoni, "Granulomatous hypersensitivity to trehalose-6,6'-dimycolate (cord factor) in mice infected with BCG," *Infection and Immunity*, vol. 7, no. 4, pp. 631–638, 1973.
- [45] A. Bhatt, N. Fujiwara, K. Bhatt et al., "Deletion of *kasB* in *Mycobacterium tuberculosis* causes loss of acid-fastness and subclinical latent tuberculosis in immunocompetent mice," *Proceedings of the National Academy of Sciences of the United States of America*, vol. 104, no. 12, pp. 5157–5162, 2007.
- [46] A. A. Elamin, M. Stehr, and M. Singh, "The cord factor: structure, biosynthesis and application in drug research—achilles heel of *Mycobacterium tuberculosis*?" in *Understanding Tuberculosis—New Approaches to Fighting Against Drug Resistance*, P.-J. Cardona, Ed., pp. 187–206, InTech, Vienna, Austria, 2012.
- [47] E. J. Muñoz-Eliás, J. Timm, T. Botha, W.-T. Chan, J. E. Gomez, and J. D. McKinney, "Replication dynamics of *Mycobacterium tuberculosis* in chronically infected mice," *Infection and Immunity*, vol. 73, no. 1, pp. 546–551, 2005.
- [48] L. E. Vla, R. A. Frattl, M. McFalone, E. Pagán-Ramos, D. Deretic, and V. Deretic, "Effects of cytokines on mycobacterial phagosome maturation," *The Journal of Cell Science*, vol. 111, no. 7, pp. 897–905, 1998.
- [49] L. Tailleux, O. Neyrolles, S. Honoré-Bouakline et al., "Constrained intracellular survival of *Mycobacterium tuberculosis* in human dendritic cells," *The Journal of Immunology*, vol. 170, no. 4, pp. 1939–1948, 2003.
- [50] S. S. Master, S. K. Rampini, A. S. Davis et al., "*Mycobacterium tuberculosis* prevents inflammasome activation," *Cell Host and Microbe*, vol. 3, no. 4, pp. 224–232, 2008.
- [51] C. de Chastellier, F. Forquet, A. Gordon, and L. Thilo, "Mycobacterium requires an all-around closely apposing phagosome membrane to maintain the maturation block and this apposition is re-established when it rescues itself from phagolysosomes," *Cellular Microbiology*, vol. 11, no. 8, pp. 1190–1207, 2009.
- [52] L. E. Connolly, P. H. Edelstein, and L. Ramakrishnan, "Why is long-term therapy required to cure tuberculosis?" *PLoS Medicine*, vol. 4, no. 3, article e120, pp. 435–442, 2007.
- [53] M. A. Behr, M. A. Wilson, W. P. Gill et al., "Comparative genomics of BCG vaccines by whole-genome DNA microarray," *Science*, vol. 284, no. 5419, pp. 1520–1523, 1999.
- [54] A. S. Pym, P. Brodin, R. Brosch, M. Huerre, and S. T. Cole, "Loss of RDI contributed to the attenuation of the live tuberculosis vaccines *Mycobacterium bovis* BCG and *Mycobacterium microti*," *Molecular Microbiology*, vol. 46, no. 3, pp. 709–717, 2002.
- [55] J. M. Pitt, S. Blankley, H. McShane, and A. O'Garra, "Vaccination against tuberculosis: how can we better BCG?" *Microbial Pathogenesis*, vol. 58, pp. 2–16, 2013.
- [56] L. M. Stamm, J. H. Morisaki, L.-Y. Gao et al., "*Mycobacterium marinum* escapes from phagosomes and is propelled by actin-based motility," *The Journal of Experimental Medicine*, vol. 198, no. 9, pp. 1361–1368, 2003.
- [57] L. M. Stamm, M. A. Pak, J. H. Morisaki et al., "Role of the WASP family proteins for *Mycobacterium marinum* actin tail formation," *Proceedings of the National Academy of Sciences of the United States of America*, vol. 102, no. 41, pp. 14837–14842, 2005.
- [58] D. M. Tobin and L. Ramakrishnan, "Comparative pathogenesis of *Mycobacterium marinum* and *Mycobacterium tuberculosis*," *Cellular Microbiology*, vol. 10, no. 5, pp. 1027–1039, 2008.
- [59] H. E. Volkman, T. C. Pozos, J. Zheng, J. M. Davis, J. F. Rawls, and L. Ramakrishnan, "Tuberculous granuloma induction via interaction of a bacterial secreted protein with host epithelium," *Science*, vol. 327, no. 5964, pp. 466–469, 2010.
- [60] D. Houben, C. Demangel, J. van Ingen et al., "ESX-1-mediated translocation to the cytosol controls virulence of mycobacteria," *Cellular Microbiology*, vol. 14, no. 8, pp. 1287–1298, 2012.
- [61] V. Deretic, I. Vergne, J. Chua et al., "Endosomal membrane traffic: convergence point targeted by *Mycobacterium tuberculosis* and HIV," *Cellular Microbiology*, vol. 6, no. 11, pp. 999–1009, 2004.
- [62] M. Podinovskaia, W. Lee, S. Caldwell, and D. G. Russell, "Infection of macrophages with *Mycobacterium tuberculosis* induces global modifications to phagosomal function," *Cellular Microbiology*, vol. 15, no. 6, pp. 843–859, 2013.
- [63] A. J. Wolf, B. Linas, G. J. Trevejo-Nuñez et al., "*Mycobacterium tuberculosis* infects dendritic cells with high frequency and impairs their function in vivo," *The Journal of Immunology*, vol. 179, no. 4, pp. 2509–2519, 2007.
- [64] A. Mortellaro, L. Robinson, and R.-C. Paola, "Spotlight on mycobacteria and dendritic cells: will novel targets to fight tuberculosis emerge?" *EMBO Molecular Medicine*, vol. 1, no. 1, pp. 19–29, 2009.

## Research Article

# Novel Mechanisms of Spinal Cord Plasticity in a Mouse Model of Motoneuron Disease

Rosario Gulino,<sup>1,2</sup> Rosalba Parenti,<sup>1</sup> and Massimo Gulisano<sup>1</sup>

<sup>1</sup>Department of Biomedical and Biotechnological Sciences, University of Catania, Via Santa Sofia 64, 95127 Catania, Italy

<sup>2</sup>IOM Ricerca s.r.l., Via Penninazzo 11, 95029 Viagrande, Italy

Correspondence should be addressed to Rosario Gulino; sarogulino@hotmail.com

Received 26 September 2014; Accepted 16 December 2014

Academic Editor: Andrea Vecchione

Copyright © 2015 Rosario Gulino et al. This is an open access article distributed under the Creative Commons Attribution License, which permits unrestricted use, distribution, and reproduction in any medium, provided the original work is properly cited.

A hopeful spinal cord repairing strategy involves the activation of neural precursor cells. Unfortunately, their ability to generate neurons after injury appears limited. Another process promoting functional recovery is synaptic plasticity. We have previously studied some mechanisms of spinal plasticity involving BDNF, Shh, Notch-1, Numb, and Noggin, by using a mouse model of motoneuron depletion induced by cholera toxin-B saporin. TDP-43 is a nuclear RNA/DNA binding protein involved in amyotrophic lateral sclerosis. Interestingly, TDP-43 could be localized at the synapse and affect synaptic strength. Here, we would like to deepen the investigation of this model of spinal plasticity. After lesion, we observed a glial reaction and an activity-dependent modification of Shh, Noggin, and Numb proteins. By using multivariate regression models, we found that Shh and Noggin could affect motor performance and that these proteins could be associated with both TDP-43 and Numb. Our data suggest that TDP-43 is likely an important regulator of synaptic plasticity, probably in collaboration with other proteins involved in both neurogenesis and synaptic plasticity. Moreover, given the rapidly increasing knowledge about spinal cord plasticity, we believe that further efforts to achieve spinal cord repair by stimulating the intrinsic potential of spinal cord will produce interesting results.

## 1. Introduction

A feasible strategy for central nervous system (CNS) repair after injury or neurodegenerative diseases involves the activation of endogenous neural precursor cells (NPCs). Multipotent NPCs have also been isolated from the spinal cord (SC) [1–3]. These cells could be mobilized after SC injury (SCI), but their ability to generate neurons appears limited [2–5].

Another process promoting a functional recovery after SCI consists in plastic changes involving synaptic plasticity [6]. We have previously studied some mechanisms of SC plasticity, by using a mouse model of motoneuron depletion induced by intramuscular injection of the retrogradely transported, ribosome-inactivating toxin, cholera toxin-B saporin (CTB-SAP) [7–10]. In particular, we have demonstrated that synaptic plasticity could be responsible, at least in part, for the spontaneous recovery of locomotion after injury [10–15] and that brain-derived neurotrophic factor (BDNF) could exert a fundamental role in this process [12, 16–18].

Intrinsic and extrinsic molecular factors regulating adult neurogenesis have been widely explored [19–21]. Sonic

hedgehog (Shh) is a secreted glycoprotein promoting proliferation of NPCs and their differentiation into neurons and oligodendrocytes, during both development and adulthood [22–25]. Notch-1 is a cell surface receptor working as a regulator of NPCs proliferation, cell fate, and dendritic and axonal morphology in embryonic as well as adult CNS [26–28], including SC [29, 30]. Numb is a signal transduction factor involved in stem cell maintenance and differentiation, as well as in neurogenesis, by antagonizing Notch-1 signalling [31–34]. Noggin is a secreted glycoprotein involved in the embryonic morphogenesis. In particular, this protein induces neural tissue by acting as an inhibitor of bone morphogenetic proteins [35–37]. So far, little is known about the possible role of Noggin in the adult SC. It has been found that Noggin stimulates NPCs proliferation and synaptic plasticity in the hippocampus [38–40].

Interestingly, in our neurotoxic SCI model, Shh, Notch-1, and Numb proteins were also involved in events of synaptic plasticity linked to the spontaneous recovery of locomotion [10, 13]. Moreover, in the same model, Noggin appeared

linked to the recovery of locomotion, but the mechanisms responsible for this effect remain unclear [13].

Transactive response DNA-binding protein of 43 kDa (TDP-43) is a nuclear DNA/RNA-binding protein involved in the regulation of transcription and RNA processing [41–43]. Recently, TDP-43 was identified into the cytoplasmic inclusions observed in amyotrophic lateral sclerosis (ALS), frontotemporal lobar degeneration, and Alzheimer disease [42, 44, 45], thus suggesting a putative toxic effect of TDP-43 aggregates. Recent findings suggest that some effects on motoneurons could be linked to the loss of function of the normal TDP-43 [42, 46–49]. Interestingly, it has been recently found that TDP-43 could be localized in the dendrites and may behave as a neuronal activity-responsive factor, probably affecting local RNA translation at the synapse [50–52]. Moreover, TDP-43 could have a role in motoneuron synaptic function [47, 53–56] and, in particular, it is probably involved in SC synaptic plasticity in our mouse CTB-SAP spinal lesion model [57].

In the present research, we would like to deepen the investigation of the role of the above-described factors in modulating the SC plasticity in a mouse model of neurotoxic motoneuron degeneration obtained by CTB-SAP lesion. For instance, the role of TDP-43 is particularly interesting, given its involvement in neurodegenerative diseases including ALS. Moreover, considering the described role of BDNF, Shh, Notch-1, Numb, and Noggin in the regulation of NPCs function and SC plasticity [10, 12, 13], we sought to characterize a functional model where these factors could collaborate in modulating the spontaneous SC plastic changes and the resulting functional recovery.

After histological and functional characterization of the model, compensatory changes within the SC, such as recovery of locomotion and cell proliferation, were evaluated in relation to the expression levels of TDP-43, BDNF, Shh, Notch-1, Numb, and Noggin.

## 2. Materials and Methods

Young adult male mice ( $n = 37$ ) (Charles River, Strain I29, 5 weeks of age) were used. Animal care and handling were carried out in accordance with the EU Directive 2010/63/EU. All experiments have been approved by our institutions as well as by the Italian Ministry of Health. All efforts were made to minimize the number of animals used and their suffering. Surgical procedures were performed under deep anaesthesia where necessary (isoflurane).

**2.1. Neurotoxic Lesion.** Motoneuron depletion was induced by injection of CTB-SAP (Advanced Targeting Systems, San Diego, CA, USA) into the medial and lateral gastrocnemius muscles at a dose of  $3.0 \mu\text{g}/2.0 \mu\text{L}$  PBS per muscle, as described previously [10]. After the bilateral injection of the toxin, mice were allowed to survive for either one week (LES-1 wk,  $n = 10$ ) or one month (LES-1 mo,  $n = 8$ ). Other animals received an equal volume of CTB-only vehicle, and they were then sacrificed at the same time points as lesioned ones (SHAM-1 wk,  $n = 3$ ; SHAM-1 mo,  $n = 3$ ). In order to perform histological and immunohistochemical evaluations

of the effects of neurotoxin lesion, six mice were injected unilaterally and then transcardially perfused at either one week ( $n = 3$ ) or one month ( $n = 3$ ) after the lesion. The efficiency of CTB-SAP in producing selective motoneuron depletion after injection in the target muscle has been proven [7–10], thus providing an effective model of primary neurodegeneration. Similar methods of selective neurotoxic lesion have been already used in our laboratory [58, 59]. Finally, a group of animals were left untreated and used as normal controls for western blot experiments (NC;  $n = 7$ ).

**2.2. Functional Test.** All bilaterally lesioned, as well as SHAM and NC, animals were subjected to grid walk test to evaluate the effects of lesion upon motor activity. Briefly, tests were performed blind to animal treatment, starting the day before lesion and then repeated at one week and at one month after toxin injection. Mice had to walk across a 50 cm long runway made of round metal bars placed at variable distance and moved at every trial to prevent habituation. The animals had to cross the runway three times per session. The number of footfalls relative to both hindlimbs at every crossing of the runway was counted and divided by the corresponding number of steps. Then, we calculated the average values between test repetitions.

**2.3. Histology, Immunohistochemistry, and Microscopy.** In order to evaluate the effects of the toxin on motoneuron depletion as well as on cell proliferation and glial reaction, the unilaterally CTB-SAP injected animals were perfused transcardially with phosphate-buffered 4% paraformaldehyde (pH 7.4). The lumbar SC was dissected out, postfixed for 1 hour, and then soaked overnight into a phosphate-buffered 20% sucrose solution at  $4^\circ\text{C}$ . Then,  $20 \mu\text{m}$  thick horizontal sections were cut on a freezing microtome and collected into three series subsequently used for immunofluorescence by using the following primary antibodies: mouse anti-ChAT (Immunological Sciences Cat. no. MAB10838; dilution 1:400) or mouse anti-glial-fibrillary-acidic-protein (GFAP) (Immunological Sciences, Rome, Italy; Cat. no. MAB16117; dilution 1:500). For double labelling, anti-Ki67 antibody (Abcam plc, Cambridge, UK; Cat. no. AB15580; dilution 1:200) was used together with anti-GFAP. In brief, sections were mounted on gelatin-coated slides, incubated for 1 hour in 5% normal donkey serum and 0.3% Triton X100 in PBS and then overnight at room temperature with the primary antibody solution containing 0.3% Triton X100 and 2% normal donkey serum. As negative control, the primary antibody has been omitted in some sections. After rinsing in PBS, sections were incubated for 1 h with the appropriate Alexa Fluor 488 or 568 donkey anti-mouse, anti-rabbit, or anti-goat secondary antibodies (Life Technologies, dilution 1:500), in PBS plus 2% normal donkey serum and 0.3% Triton X100. Then, sections were washed in PBS and counterstained for 5 minutes with DAPI (Life Technologies, dilution 1:20000) in PBS. Slides were coverslipped with PermaFluor (Thermo) and stored at  $4^\circ\text{C}$  until microscopy. The observation of immunostained sections was carried out by means of a laser confocal microscope (Leica Microsystems S.p.A., Milan, Italy).

**2.4. Western Blotting.** After the last test session, animals were sacrificed by decapitation. Lumbar SCs were dissected out and homogenized as previously described [10]. For western blot quantification, 20  $\mu\text{g}$  of protein was separated on a 4–20% polyacrylamide gel and transferred to a nitrocellulose membrane. Membranes were blocked for 1 hour with 5% BSA and incubated for 2 h with the following primary antibodies: mouse anti-ChAT (Immunological Sciences Cat. no. MAB10838; dilution 1:400), goat anti-BDNF (Santa Cruz Biotechnology Inc., Cat. no. sc-33905; dilution 1:200), goat anti-Shh (Santa Cruz Biotechnology Inc., Cat. no. sc-1194; dilution 1:300), rabbit anti-Notch-1 extracellular domain (Upstate Biotechnology, Millipore group; Cat. no. 07-218; dilution 1:700), goat anti-Numb (Santa Cruz Biotechnology Inc., Heidelberg, Germany; Cat. no. sc-15590; dilution 1:100), mouse anti-GFAP (Immunological Sciences, Rome, Italy; Cat. no. MAB16117; dilution 1:600), rabbit anti-Noggin (Millipore, Cat. no. AB5729; dilution 1:1000), and rabbit anti-TDP43 (Cell Signaling, Cat. no. 3449; dilution 1:1000). Then, membranes were washed and incubated for 1 h with the appropriate peroxidase-conjugate goat anti-rabbit (Thermo Scientific group; Cat. no. 1858415; dilution 1:6000), goat anti-mouse (Thermo Scientific group; Cat. no. 1858413; dilution 1:6000), or rabbit anti-goat (Millipore, Cat. no. AP106P; dilution 1:10000) secondary antibodies. Peroxidase activity was developed by enhanced chemiluminescent substrate (Pierce Biotechnology Inc., Thermo Scientific group; Cat. no. 34075) and visualized on a film (Kodak). Then, the protocol was repeated for quantification of actin, using a mouse anti-actin primary antibody (Millipore, Cat. no. MAB1501; dilution 1:700) followed by a goat anti-mouse secondary antibody (Pierce Biotechnology Inc., Cat. no. 1858413; dilution 1:5000). The films were digitally scanned and the relative 300 dpi grayscale images were used for optical density measurement by using Scion Image software. Density values were normalized to actin levels measured in the same membrane. All assays were performed in triplicate.

**2.5. Statistical Analysis.** Differences between lesioned and control groups in western blot and grid walk test data were evaluated by one-way ANOVA followed by Bonferroni's post hoc test.

In order to assess whether the motor performance could depend on the expression levels of the analysed proteins, we used the following multivariate regression model:

$$\begin{aligned} \text{MP} = & \beta_0 + \beta_1 [\text{ChAT}] + \beta_2 [\text{GFAP}] + \beta_3 [\text{BDNF}] \\ & + \beta_4 [\text{Shh}] + \beta_5 [\text{Notch-1}] + \beta_6 [\text{Numb}] \\ & + \beta_7 [\text{Noggin}] + \beta_8 [\text{TDP-43}] + \varepsilon, \end{aligned} \quad (1)$$

where MP is the predicted value of motor performance, the terms in square brackets are the mean optical densities values, as measured by western blot,  $\beta_0$ – $\beta_8$  represent the regression coefficients, and  $\varepsilon$  is the residual error. From this general model, we eliminated the nonsignificant terms by using backward stepwise regression. This procedure starts with the complete model and removes iteratively the least significant predictors until only significant variables remain. We used a

restrictive  $\alpha$  value ( $\alpha < 0.05$ ) for which a given variable was allowed into the model and selected only final models that explained at least 20% of the dataset variance ( $R^2 > 0.20$ ) with a  $P$  value of the regression ANOVA less than 0.01.

Where appropriate, we used the following multivariate regression model to find significant models explaining correlations between each protein and the others:

$$\begin{aligned} \text{Predicted [P]} = & \beta_0 + \beta_1 [\text{P1}] + \beta_2 [\text{P2}] + \beta_3 [\text{P3}] + \beta_4 [\text{P4}] \\ & + \beta_5 [\text{P5}] + \beta_6 [\text{P6}] + \beta_7 [\text{P7}] + \varepsilon, \end{aligned} \quad (2)$$

where [P1]–[P6] are the average optical density values of the analysed proteins, as measured by western blot; “Predicted[P]” is the predicted mean value of optical density relative to a given protein;  $\beta_0$ – $\beta_7$  represent the regression coefficients; and  $\varepsilon$  is the residual error. ChAT and GFAP protein expression levels have also been included in the model to account for any effect of motoneuron depletion and glial reaction. All analyses were performed by means of Systat 12 (Systat Software Inc.).

### 3. Results

All animals survived surgery except an animal belonging to the LES-1 mo group. Starting at two or three days after injection, all CTB-SAP injected mice showed a significant weakness of the hindlimb, although they were still able to walk and perform functional tests. SHAM lesioned and normal groups did not differ from each other in terms of motor performance and western blot data. Therefore, these groups were pooled together in a single control group (CTRL).

**3.1. Motoneuron Loss and Cell Proliferation in the Lesioned Lumbar SC.** The analysis of ChAT immunostained SC sections belonging to the unilaterally injected LES-1 wk group demonstrated evident motoneuron depletion within the lumbar SC ventral horn ipsilateral to the injected muscles, when compared to the contralateral side (Figure 1). This decrease (about 30%, as estimated by counting ChAT-positive motoneuron profiles in three horizontal sections per animal) was similar in animals sacrificed at one month after the lesion (not shown) and confirmed the results found in our previous studies [10, 12, 13]. Moreover, a population of Ki67-immunopositive profiles has been observed in the same area, ipsilaterally to the injected muscle (Figure 2(b)). Proliferating cells were conversely rare or absent in the contralateral side (Figure 2(a)). Confocal colocalization studies have shown that these cells are GFAP-positive astrocytes (Figures 2(c)–2(f)). Similar results have been found in animals killed one month after the lesion (not shown).

**3.2. Modifications of Protein Expression after CTB-SAP Lesion.** The analysis of western blot data revealed a significant (one-way ANOVA:  $F_{2,27} = 4.081$ ,  $P = 0.028$ ; Figures 3 and 4(a))  $25 \pm 7\%$  decrease of the average ChAT expression one week after the lesion (Bonferroni:  $P = 0.029$ ; Figures 3 and 4(a))

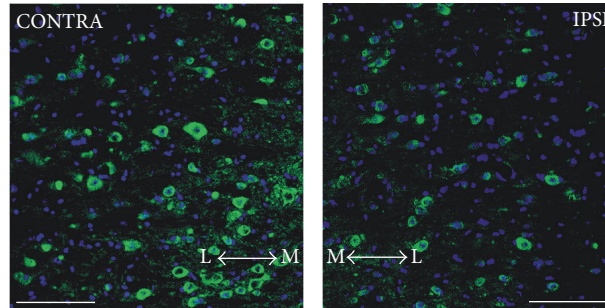


FIGURE 1: Fluorescence microscope images showing an example of lumbar SC section from a unilaterally lesioned animal, stained with anti-ChAT antibody plus 488 Alexa Fluor secondary antibody (green). Sections were counterstained with DAPI (blue) to visualize cell nuclei. The effect of neurotoxic lesion on the number of surviving motoneurons is evident in the right side of the cord, ipsilaterally to the injected muscle (IPSI), as compared to the contralateral side (CONTRA). Scale bar: 100  $\mu\text{m}$ . The arrows indicate the medial (M) to lateral (L) direction.

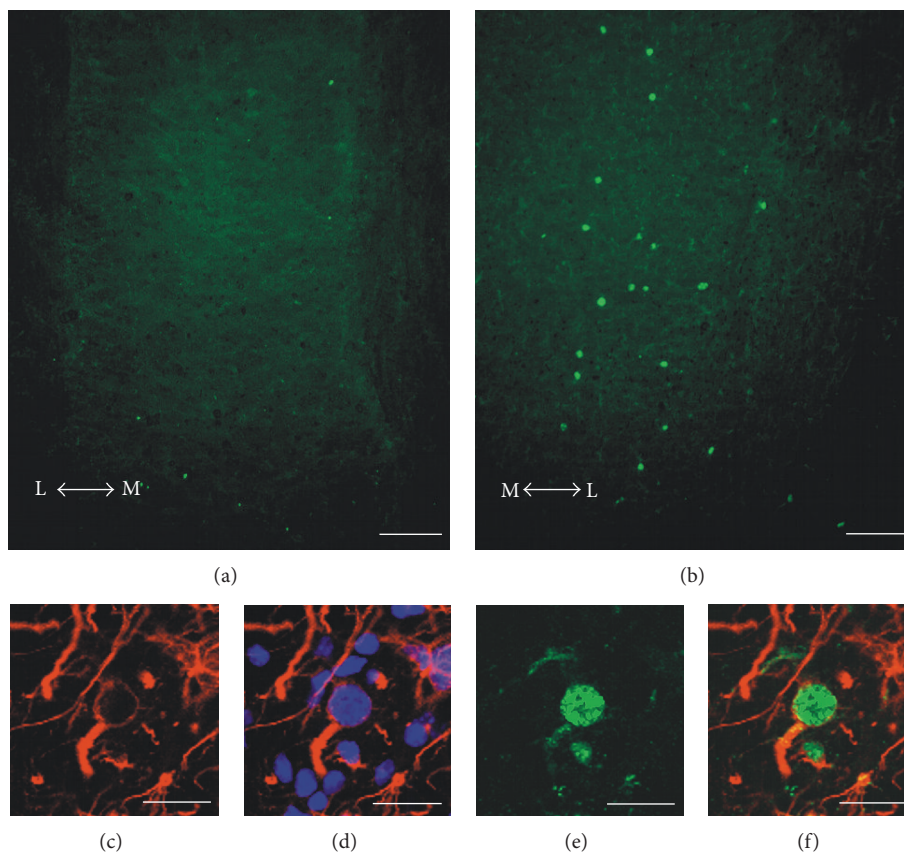


FIGURE 2: Panel of confocal images showing examples of immunostained lumbar SC sections collected from unilaterally lesioned mice. The panel shows the expression of Ki67 ((a), (b), green), in the right (lesioned) side (b), compared to the left (contralateral) side (a). The effect of CTB-SAP on cell proliferation is evident, although the number of proliferating cells is relatively low. Almost all the observed Ki67-positive cells ((b), (e), and (f), green) are also GFAP-positive ((c), (d), and (f), red). Sections were counterstained with DAPI to visualize cell nuclei (d). Scale bars: 100  $\mu\text{m}$  in (a), (b); 20  $\mu\text{m}$  in (c)–(f). The arrows indicate the medial (M) to lateral (L) direction.

and showed near-normal levels at one month (Bonferroni:  $P = 0.328$ ; Figures 3 and 4(a)). The average expression levels of Shh one week after the lesion showed a small decrease (one-way ANOVA:  $F_{2,27} = 4.669$ ,  $P = 0.018$ ; Bonferroni:  $P = 0.104$ ; Figures 3 and 4(d)) by  $8 \pm 3\%$  compared to control levels, which was restored at one month (Bonferroni:  $P = 0.022$ ; Figures 3 and 4(d)). Numb levels appeared significantly

(one-way ANOVA:  $F_{2,27} = 8.511$ ,  $P = 0.001$ ; Figures 3 and 4(f)) reduced by  $36 \pm 1\%$  at one week after lesion (Bonferroni:  $P = 0.001$ ; Figures 3 and 4(f)), and they were partially but significantly restored at one month, being not significantly different from control levels (Bonferroni:  $P = 0.103$ ; Figures 3 and 4(f)). The expression levels of Noggin were conversely significantly upregulated after lesion (one-way

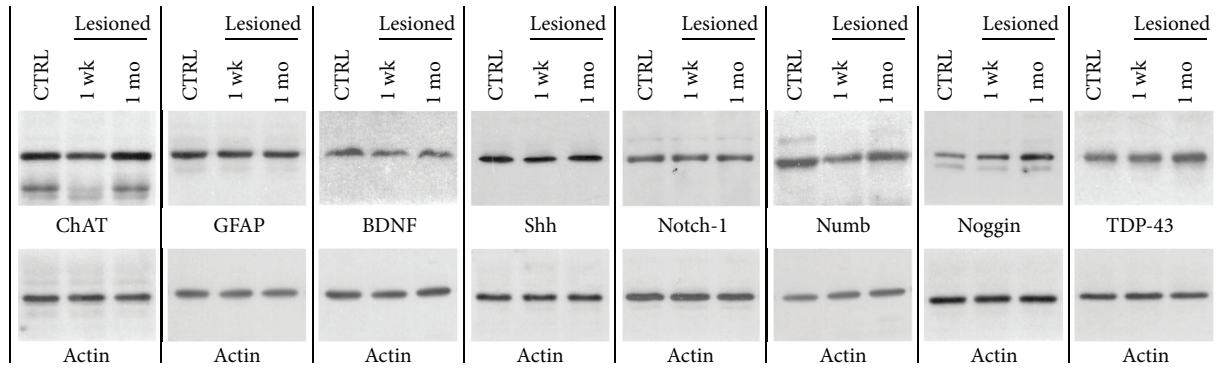


FIGURE 3: Western blots showing immunoreactive bands relative to ChAT, GFAP, BDNF, Shh, Notch-1, Numb, Noggin, and TDP-43, in relation to their corresponding actin signals in control and lesioned mice sacrificed at one week or one month after lesion.

ANOVA:  $F_{2,27} = 5.155$ ,  $P = 0.013$ ). In particular, we found an increase of Noggin expression by  $21 \pm 1\%$  at one week and by  $85 \pm 30\%$  at one month, respectively. These levels were not significantly higher than control levels at one week (Bonferroni:  $P = 0.995$ ; Figures 3 and 4(g)), but they became significantly higher at one month (Bonferroni:  $P = 0.011$ ; Figures 3 and 4(g)). No statistically significant variations were found for GFAP (one-way ANOVA:  $F_{2,27} = 3.277$ ,  $P = 0.053$ ; Figures 3 and 4(b)), BDNF (one-way ANOVA:  $F_{2,27} = 3.067$ ,  $P = 0.063$ ; Figures 3 and 4(c)), Notch-1 (one-way ANOVA:  $F_{2,27} = 0.364$ ,  $P = 0.698$ ; Figures 3 and 4(e)), and TDP-43 (one-way ANOVA:  $F_{2,27} = 2.360$ ,  $P = 0.114$ ; Figures 3 and 4(h)).

**3.3. Motor Deficits at the Grid Walk Test.** CTB-SAP lesion caused a significant effect on mice performance at the grid walk test (one-way ANOVA:  $F_{2,27} = 35.616$ ;  $P = 0.000$ ; Figure 5). One week after lesion, bilaterally lesioned mice showed a statistically significant fivefold increase of the number of footfalls/step compared with prelesion performance (Bonferroni:  $P = 0.000$ ; Figure 5). Interestingly, one month after the lesion, animals showed a significant 3.4-fold recovery in the number of footfalls (Bonferroni:  $P = 0.000$ ; Figure 5), reaching a grid walk performance significantly similar to prelesion levels (Bonferroni:  $P = 0.780$ ; Figure 5).

In order to address the possibility that the worsening of functional performance after injury and/or the following recovery could be linked to the protein expression levels, we used the multiple regression model in (1). LES-1wk and LES-1mo groups were pooled together and, after the application of backward stepwise regression, we obtained the model reported in Figure 6(a). The graph shows the highly significant correlation between the real values of grid walk performance and those predicted by the model ( $R_{16} = 0.718$ ,  $P = 0.004$ ; Figure 6(a)). It is evident that the expression levels of Noggin and Shh are good predictors of hindlimb performance and that they are inversely correlated with the number of footfalls. No association between variables was found within the control group (not shown).

Given the significant relationship between motor performance of lesioned animals and the expression levels of both Noggin and Shh, we again used a multivariate regression

model (2) to verify if these proteins could be associated with each other. The results have shown that the expression of Shh could be predicted by TDP-43 levels (Figure 6(b)). The results have also shown that TDP-43 levels are directly linked to Shh and Noggin expression and inversely correlated with Numb expression levels (Figures 6(c) and 6(e)). Conversely, the expression levels of Noggin are directly linked to those of both TDP-43 and Numb (Figure 6(d)). No association between variables was found within the control group (not shown).

#### 4. Discussion

In our previous studies [10, 12, 13], a neurotoxic SC lesion model was developed in order to study compensatory changes in the SC circuitry after selective motoneuron removal. The injection of CTB-SAP into the gastrocnemius muscle resulted in a partial depletion of lumbar motoneurons accompanied by the impairment of hindlimb function. The motoneuron loss was paralleled by a downregulation of ChAT within the lumbar SC at one week after the lesion. Given that the majority of acetylcholine release within the SC originates from motoneuronal activity, [60–62], it is likely that the observed downregulation of ChAT could be caused in large part by the motoneuron loss and in part by the consequent disruption of spinal circuitry. One month after the lesion, ChAT expression was partially restored, suggesting a partial recovery of the whole synaptic activity in the lumbar SC, which was accompanied by the restoration of motor performance, even though the motoneuron depletion is permanent. Therefore, an increased activity of the spared motoneurons could be responsible for both ChAT upregulation and functional recovery. On the other hand, the increased motoneuron activity could likely be supported by an upregulation of synaptic efficacy within the surrounding spinal circuitry. Similar to ChAT, Shh and Numb expression were downregulated at one week after the lesion and then restored at one month. Conversely, Noggin expression levels appeared gradually and significantly upregulated after the lesion. These results suggest that the expression of these proteins could be activity-dependent and probably linked to an increase of

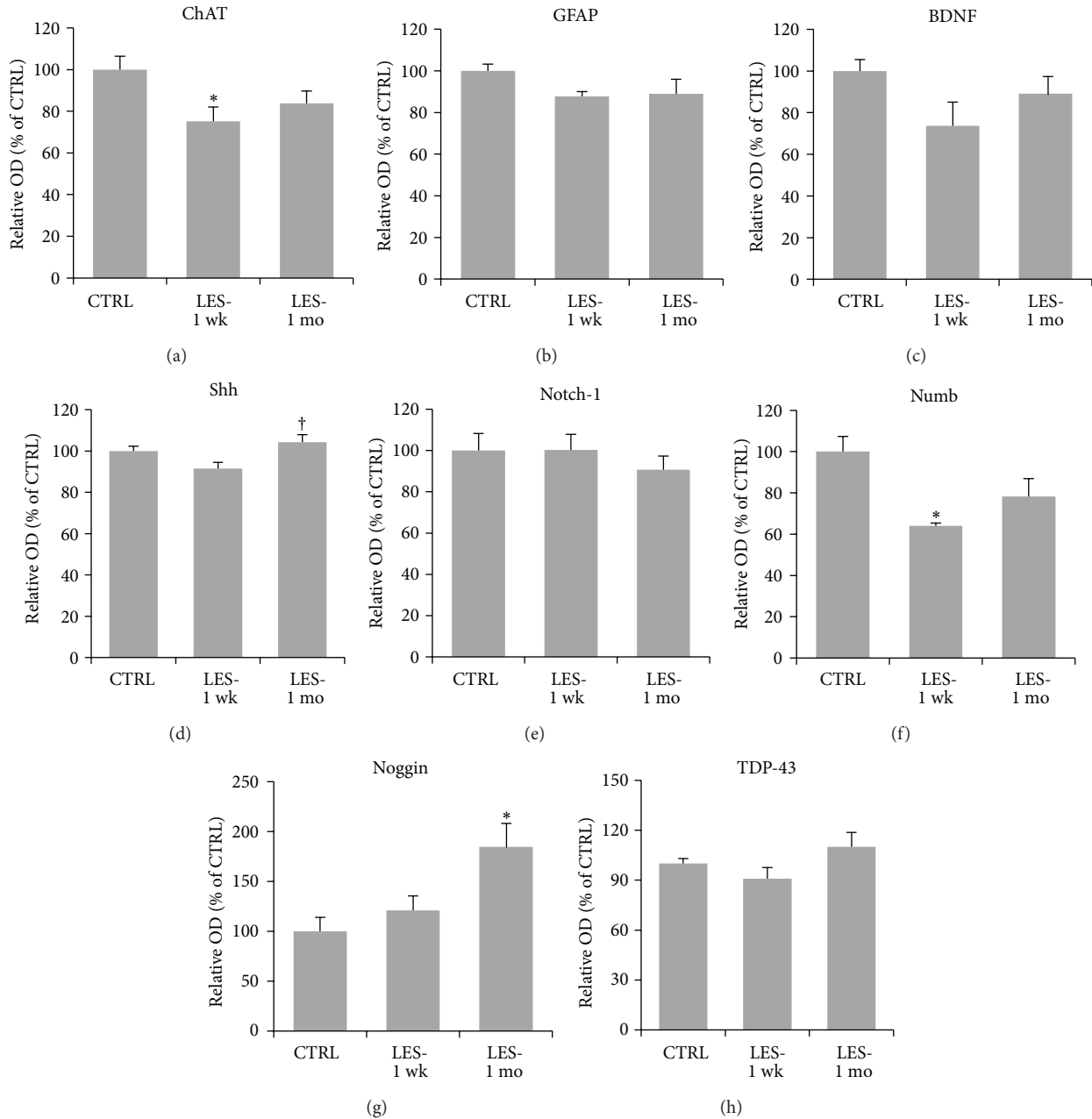


FIGURE 4: Graphs showing the average expression levels of proteins in SC homogenates from CTRL and lesioned animals analyzed at one week (LES-1 wk;  $n = 10$ ) and one month (LES-1 mo;  $n = 7$ ) after lesion, as measured by western blotting and normalized to actin levels. Values are mean  $\pm$  s.e.m. They are expressed as percent of CTRL levels. Asterisks (\*) indicate significant difference from CTRL levels, whereas the dagger (†) indicates significant difference from LES-1 wk levels, as calculated by Bonferroni's post hoc test.

SC neuronal activity that compensate for the cell death and disruption of circuitry caused by the neurotoxin.

As demonstrated by the multivariate regression analysis, the observed changes of Shh and Noggin protein expression are inversely correlated with the number of footfalls at the grid walk test, thus suggesting that an artificial increase of their expression would improve motor performance in lesioned animals. Since Shh and Noggin affect functional performance of lesioned animals, we used multivariate regression analysis to verify if their expression is linked with those

of the other proteins previously found to be involved in SC plasticity. The data have demonstrated that the expression levels of Shh are dependent on those of TDP-43. This finding is novel and interesting for a couple of reasons. In fact, it has been recently found that TDP-43 could regulate the local translation of mRNAs at the synapse, thus providing a complex modulation of synaptic strength [50–52]. Moreover, recent studies in our laboratory have demonstrated that TDP-43 could also modulate synaptic function by regulating the expression levels of both AMPA receptor subunits and

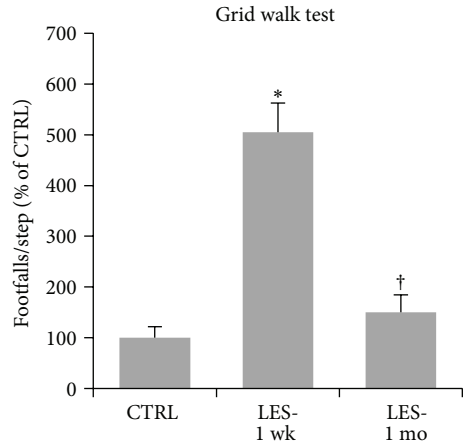
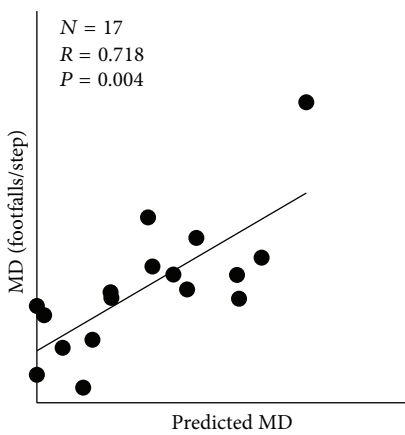
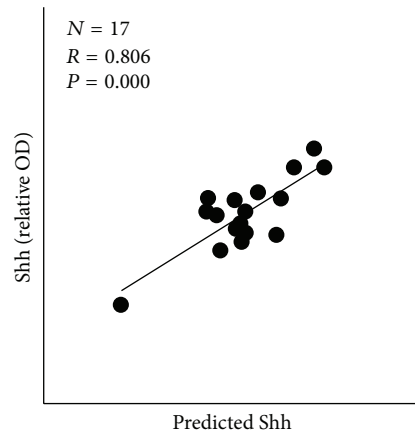


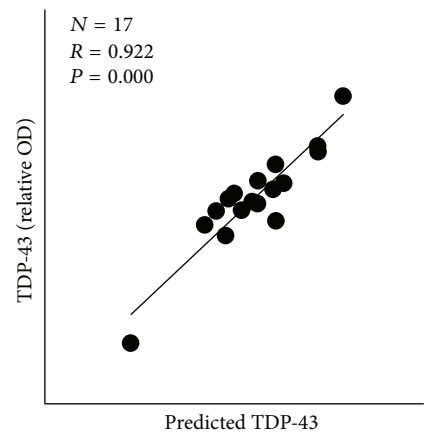
FIGURE 5: Motor performance scored at the grid walk test. Values are footfalls/step and are reported as mean ± s.e.m. They were normalized to control levels and expressed as percent of CTRL. Asterisk (\*) indicates significant difference from CTRL levels, whereas the dagger (†) indicates significant difference from LES-1 wk levels, as calculated by Bonferroni's post hoc test.



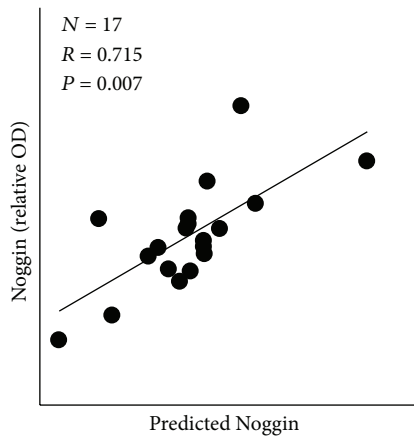
(a) Predicted MD = 0.549 - 0.361 [Shh] - 0.128 [Noggin]



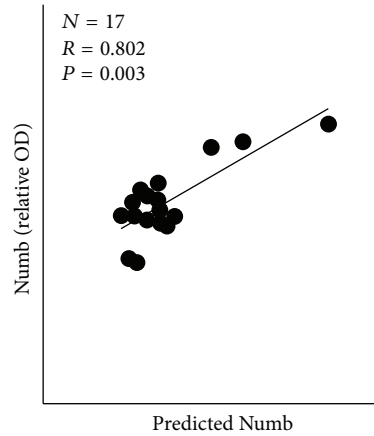
(b) Predicted Shh = 0.591 + 0.467 [TDP-43]



(c) Predicted TDP-43 = 1.174 [Shh] + 0.178 [Noggin] - 0.439 [Numb] - 0.099



(d) Predicted Noggin = 1.352 [TDP-43] + 1.430 [Numb] - 1.410



(e) Predicted Numb = 0.350 + 1.254 [Shh] + 0.322 [Noggin] - 1.197 [TDP-43]

FIGURE 6: Significant correlations between the actual values of functional performance (a) or protein expression levels ((b)–(e)) with those predicted by the multivariate regression models after the application of backward stepwise regression. The final regression models represented in the graphs are reported in the grey window.

synapsin-I [57]. Other recent findings have shown that the depletion of TDP-43 could cause synaptic effects and locomotor deficits in *Drosophila* [47, 53]. Interestingly, Shh seems to affect synaptic plasticity in a similar way [10, 12, 13, 63]. Therefore, the correlation between these proteins could be due to important functional association, which requires further investigation. Conversely, the mechanisms underlying the observed Noggin effect on motor activity are less clear. However, it is known that Noggin could stimulate functional recovery after SC injury by either enhancing axonal growth [64] or inducing neurogenesis [65]. Our results have shown that Noggin, whose expression levels increased after lesion, is strongly correlated with both TDP-43 (directly) and Numb expression (inversely). Moreover, Numb, whose expression levels were downregulated after lesion and then recovered in an activity-dependent manner, could also be modulated by either Shh (directly) or TDP-43 (inversely). The role of Numb in neurogenesis and synapse morphogenesis is well established [33, 34], whereas little is known about the possible role of Numb in mature neurons. However, it seems likely that this factor could participate in the axonal growth [31], as well as in the remodelling of dendritic spines and some aspects of synaptic function [66]. Here, we have shown that the Numb activity in the adult SC could take place in collaboration with other factors known to be involved in either neurogenesis and synaptic plasticity. The results collectively suggest differential roles of all these proteins in the SC, in either physiological or pathological conditions.

As demonstrated by Ki67 expression, a moderate cell proliferation occurs in the same SC area undergoing to motoneuron depletion. Colocalization studies have shown that almost all of these proliferating cells are GFAP-positive astrocytes. Glial reaction is a classical response to CNS injury that normally occurs as a result of tissue damage [67, 68]. Notably, our findings indicate that this process could also be caused by selective neurotoxic motoneuron degeneration, but its extent was limited, as demonstrated by the lack of GFAP increase after CTB-SAP lesion. This evidence is consistent with similar results obtained after neurotoxic lesion of cerebellar nuclei, which are also nonneurogenic CNS districts [69]. As previously introduced, Shh and Numb exert important roles in the regulation of adult neurogenesis [22, 24, 26–30, 33, 34]. Thus, it is reasonable to assume that the observed downregulation of Shh and Numb could be one of the factors involved in the glial reaction. Conversely, although the role of Noggin in stimulating neurogenesis in the adult brain is demonstrated [38, 39], its function in the lesioned SC is unclear. The observed Noggin increase after CTB-SAP injection could not likely be able to induce neurogenesis, but its effect in limiting glial reaction could not be excluded.

It is therefore likely that an experimental approach aimed at artificially modifying Shh, Numb, and Noggin signalling into the SC, during the first few weeks after the lesion, could enhance NPCs proliferation, reduce glial reaction, and remove some of the factors that inhibit neurogenesis. Moreover, the putative involvement of these factors in mechanisms of SC plasticity could anticipate a multiple positive effect of such treatments on the functional recovery.

Given the increasing interest in mouse models of TDP-43 gain or loss of function as models of neurodegenerative diseases, such as ALS animal models [70, 71], we believe that the elucidation of the physiological role of TDP-43 in the SC would provide an important contribution. Moreover, given the rapidly increasing knowledge about SC plasticity, we believe that further efforts to achieve SC repair by stimulating the intrinsic potential of SC will produce interesting results.

## Conflict of Interests

The authors declare that there is no conflict of interests regarding the publication of this paper.

## References

- [1] P. J. Horner, A. E. Power, G. Kempermann et al., "Proliferation and differentiation of progenitor cells throughout the intact adult rat spinal cord," *The Journal of Neuroscience*, vol. 20, no. 6, pp. 2218–2228, 2000.
- [2] C. B. Johansson, S. Momma, D. L. Clarke, M. Risling, U. Lendahl, and J. Frisén, "Identification of a neural stem cell in the adult mammalian central nervous system," *Cell*, vol. 96, no. 1, pp. 25–34, 1999.
- [3] S. Weiss, C. Dunne, J. Hewson et al., "Multipotent CNS stem cells are present in the adult mammalian spinal cord and ventricular neuroaxis," *Journal of Neuroscience*, vol. 16, no. 23, pp. 7599–7609, 1996.
- [4] A. J. Mothe and C. H. Tator, "Proliferation, migration, and differentiation of endogenous ependymal region stem/progenitor cells following minimal spinal cord injury in the adult rat," *Neuroscience*, vol. 131, no. 1, pp. 177–187, 2005.
- [5] H. Yang, P. Lu, H. M. McKay et al., "Endogenous neurogenesis replaces oligodendrocytes and astrocytes after primate spinal cord injury," *The Journal of Neuroscience*, vol. 26, no. 8, pp. 2157–2166, 2006.
- [6] V. R. Edgerton, N. J. K. Tillakaratne, A. J. Bigbee, R. D. de Leon, and R. R. Roy, "Plasticity of the spinal neural circuitry after injury," *Annual Review of Neuroscience*, vol. 27, pp. 145–167, 2004.
- [7] I. J. Llewellyn-Smith, C. L. Martin, L. F. Arnolda, and J. B. Minson, "Tracer-toxins: cholera toxin B-saporin as a model," *Journal of Neuroscience Methods*, vol. 103, no. 1, pp. 83–90, 2000.
- [8] R. G. Wiley and R. H. Kline IV, "Neuronal lesioning with axonally transported toxins," *Journal of Neuroscience Methods*, vol. 103, no. 1, pp. 73–82, 2000.
- [9] K. N. Fargo and D. R. Sengelaub, "Testosterone manipulation protects motoneurons from dendritic atrophy after contralateral motoneuron depletion," *The Journal of Comparative Neurology*, vol. 469, no. 1, pp. 96–106, 2004.
- [10] R. Gulino, V. Perciavalle, and M. Gulisano, "Expression of cell fate determinants and plastic changes after neurotoxic lesion of adult mice spinal cord by cholera toxin-B saporin," *The European Journal of Neuroscience*, vol. 31, no. 8, pp. 1423–1434, 2010.
- [11] R. Gulino, M. Dimartino, A. Casabona, S. A. Lombardo, and V. Perciavalle, "Synaptic plasticity modulates the spontaneous recovery of locomotion after spinal cord hemisection," *Neuroscience Research*, vol. 57, no. 1, pp. 148–156, 2007.

- [12] R. Gulino and M. Gulisano, "Involvement of brain-derived neurotrophic factor and sonic hedgehog in the spinal cord plasticity after neurotoxic partial removal of lumbar motoneurons," *Neuroscience Research*, vol. 73, no. 3, pp. 238–247, 2012.
- [13] R. Gulino and M. Gulisano, "Noggin and Sonic hedgehog are involved in compensatory changes within the motoneuron-depleted mouse spinal cord," *Journal of the Neurological Sciences*, vol. 332, no. 1-2, pp. 102–109, 2013.
- [14] O. Raineteau and M. E. Schwab, "Plasticity of motor systems after incomplete spinal cord injury," *Nature Reviews Neuroscience*, vol. 2, no. 4, pp. 263–273, 2001.
- [15] J. R. Wolpaw and A. M. Tennissen, "Activity-dependent spinal cord plasticity in health and disease," *Annual Review of Neuroscience*, vol. 24, pp. 807–843, 2001.
- [16] A. K. McAllister, L. C. Katz, and D. C. Lo, "Neurotrophins and synaptic plasticity," *Annual Review of Neuroscience*, vol. 22, pp. 295–318, 1999.
- [17] E. J. Huang and L. F. Reichardt, "Neurotrophins: roles in neuronal development and function," *Annual Review of Neuroscience*, vol. 24, pp. 677–736, 2001.
- [18] S. Vaynman, Z. Ying, and F. Gómez-Pinilla, "Interplay between brain-derived neurotrophic factor and signal transduction modulators in the regulation of the effects of exercise on synaptic-plasticity," *Neuroscience*, vol. 122, no. 3, pp. 647–657, 2003.
- [19] D. N. Abrous, M. Koehl, and M. Le Moal, "Adult neurogenesis: from precursors to network and physiology," *Physiological Reviews*, vol. 85, no. 2, pp. 523–569, 2005.
- [20] T. Hagg, "Molecular regulation of adult CNS neurogenesis: an integrated view," *Trends in Neurosciences*, vol. 28, no. 11, pp. 589–595, 2005.
- [21] P. M. Lledo, M. Alonso, and M. S. Grubb, "Adult neurogenesis and functional plasticity in neuronal circuits," *Nature Reviews Neuroscience*, vol. 7, no. 3, pp. 179–193, 2006.
- [22] M. Fuccillo, A. L. Joyner, and G. Fishell, "Morphogen to mitogen: the multiple roles of hedgehog signalling in vertebrate neural development," *Nature Reviews Neuroscience*, vol. 7, no. 10, pp. 772–783, 2006.
- [23] Y.-G. Han, N. Spassky, M. Romaguera-Ros et al., "Hedgehog signaling and primary cilia are required for the formation of adult neural stem cells," *Nature Neuroscience*, vol. 11, no. 3, pp. 277–284, 2008.
- [24] V. Palam, D. A. Lim, N. Dahmane et al., "Sonic hedgehog controls stem cells behavior in the postnatal and adult brain," *Development*, vol. 132, no. 2, pp. 335–344, 2005.
- [25] Y. Tanabe, H. Roelink, and T. M. Jessell, "Induction of motor neurons by Sonic hedgehog is independent of floor plate differentiation," *Current Biology*, vol. 5, no. 6, pp. 651–658, 1995.
- [26] A. Androutsellis-Theotokis, R. R. Leker, F. Soldner et al., "Notch signalling regulates stem cell numbers *in vitro* and *in vivo*," *Nature*, vol. 442, no. 7104, pp. 823–826, 2006.
- [27] J. J. Breunig, J. Silbereis, F. M. Vaccarino, N. Šestan, and P. Rakic, "Notch regulates cell fate and dendrite morphology of newborn neurons in the postnatal dentate gyrus," *Proceedings of the National Academy of Sciences of the United States of America*, vol. 104, no. 51, pp. 20558–20563, 2007.
- [28] E. C. Lai, "Notch signaling: control of cell communication and cell fate," *Development*, vol. 131, no. 5, pp. 965–973, 2004.
- [29] J. Akai, P. A. Halley, and K. G. Storey, "FGF-dependent Notch signaling maintains the spinal cord stem zone," *Genes and Development*, vol. 19, no. 23, pp. 2877–2887, 2005.
- [30] S. I. Yamamoto, M. Nagao, M. Sugimori et al., "Transcription factor expression and notch-dependent regulation of neural progenitors in the adult rat spinal cord," *The Journal of Neuroscience*, vol. 21, no. 24, pp. 9814–9823, 2001.
- [31] O. Berezhovska, P. McLean, R. Knowles et al., "Notch1 inhibits neurite outgrowth in postmitotic primary neurons," *Neuroscience*, vol. 93, no. 2, pp. 433–439, 1999.
- [32] M. A. McGill and C. J. McGlade, "Mammalian numb proteins promote Notch1 receptor ubiquitination and degradation of the Notch1 intracellular domain," *The Journal of Biological Chemistry*, vol. 278, no. 25, pp. 23196–23203, 2003.
- [33] P. H. Petersen, K. Zou, J. K. Hwang, Y. N. Jan, and W. Zhong, "Progenitor cell maintenance requires numb and numbl during mouse neurogenesis," *Nature*, vol. 419, no. 6910, pp. 929–934, 2002.
- [34] P. H. Petersen, K. Zou, S. Krauss, and W. Zhong, "Continuing role for mouse Numb and Numbl in maintaining progenitor cells during cortical neurogenesis," *Nature Neuroscience*, vol. 7, no. 8, pp. 803–811, 2004.
- [35] T. M. Lamb, A. K. Knecht, W. C. Smith et al., "Neural induction by the secreted polypeptide noggin," *Science*, vol. 262, no. 5134, pp. 713–718, 1993.
- [36] O. Wessely and E. M. de Robertis, "Neural plate patterning by secreted signals," *Neuron*, vol. 33, no. 4, pp. 489–491, 2002.
- [37] C. Krause, A. Guzman, and P. Knaus, "Noggin," *The International Journal of Biochemistry & Cell Biology*, vol. 43, no. 4, pp. 478–481, 2011.
- [38] M. A. Bonaguidi, C. Y. Peng, T. McGuire et al., "Noggin expands neural stem cells in the adult hippocampus," *The Journal of Neuroscience*, vol. 28, no. 37, pp. 9194–9204, 2008.
- [39] X.-T. Fan, W.-Q. Cai, Z. Yang, H.-W. Xu, and J.-H. Zhang, "Effect of antisense oligonucleotide of noggin on spatial learning and memory of rats," *Acta Pharmacologica Sinica*, vol. 24, no. 5, pp. 394–477, 2003.
- [40] M. Sun, M. J. Thomas, R. Herder, M. L. Bofenkamp, S. B. Selleck, and M. B. O'Connor, "Presynaptic contributions of chordin to hippocampal plasticity and spatial learning," *The Journal of Neuroscience*, vol. 27, no. 29, pp. 7740–7750, 2007.
- [41] E. Buratti and F. E. Baralle, "Multiple roles of TDP-43 in gene expression, splicing regulation, and human disease," *Frontiers in Bioscience*, vol. 13, no. 3, pp. 867–878, 2008.
- [42] T. J. Cohen, V. M. Y. Lee, and J. Q. Trojanowski, "TDP-43 functions and pathogenic mechanisms implicated in TDP-43 proteinopathies," *Trends in Molecular Medicine*, vol. 17, no. 11, pp. 659–667, 2011.
- [43] M. J. Strong, K. Volkening, R. Hammond et al., "TDP43 is a human low molecular weight neurofilament (hNFL) mRNA-binding protein," *Molecular and Cellular Neuroscience*, vol. 35, no. 2, pp. 320–327, 2007.
- [44] T. Arai, M. Hasegawa, H. Akiyama et al., "TDP-43 is a component of ubiquitin-positive tau-negative inclusions in frontotemporal lobar degeneration and amyotrophic lateral sclerosis," *Biochemical and Biophysical Research Communications*, vol. 351, no. 3, pp. 602–611, 2006.
- [45] E. H. Bigio, "TAR DNA-binding protein-43 in amyotrophic lateral sclerosis, frontotemporal lobar degeneration, and Alzheimer disease," *Acta Neuropathologica*, vol. 116, no. 2, pp. 135–140, 2008.
- [46] H. Aizawa, J. Sawada, T. Hideyama et al., "TDP-43 pathology in sporadic ALS occurs in motor neurons lacking the RNA editing enzyme ADAR2," *Acta Neuropathologica*, vol. 120, no. 1, pp. 75–84, 2010.

- [47] F. Feiguin, V. K. Godena, G. Romano, A. D'Ambrogio, R. Klima, and F. E. Baralle, "Depletion of TDP-43 affects *Drosophila* motoneurons terminal synapsis and locomotive behavior," *FEBS Letters*, vol. 583, no. 10, pp. 1586–1592, 2009.
- [48] T. Hideyama and S. Kwak, "When does ALS start? ADAR2-GluA2 hypothesis for the etiology of sporadic ALS," *Frontiers in Molecular Neuroscience*, vol. 4, article 33, 2011.
- [49] K.-J. Tsai, C.-H. Yang, Y.-H. Fang et al., "Elevated expression of TDP-43 in the forebrain of mice is sufficient to cause neurological and pathological phenotypes mimicking FTL-D-U," *The Journal of Experimental Medicine*, vol. 207, no. 8, pp. 1661–1673, 2010.
- [50] I.-F. Wang, L.-S. Wu, H.-Y. Chang, and C.-K. J. Shen, "TDP-43, the signature protein of FTL-D-U, is a neuronal activity-responsive factor," *Journal of Neurochemistry*, vol. 105, no. 3, pp. 797–806, 2008.
- [51] L. Liu-Yesucevitz, G. J. Bassell, A. D. Gitler et al., "Local RNA translation at the synapse and in disease," *The Journal of Neuroscience*, vol. 31, no. 45, pp. 16086–16093, 2011.
- [52] M. G. Thomas, M. L. Pascual, D. Maschi, L. Luchelli, and G. L. Boccaccio, "Synaptic control of local translation: the plot thickens with new characters," *Cellular and Molecular Life Sciences*, vol. 71, no. 12, pp. 2219–2239, 2014.
- [53] V. K. Godena, G. Romano, M. Romano et al., "TDP-43 regulates drosophila neuromuscular junctions growth by modulating futsch/MAP1B levels and synaptic microtubules organization," *PLoS ONE*, vol. 6, no. 3, Article ID e17808, 2011.
- [54] M.-J. Lin, C.-W. Cheng, and C.-K. J. Shen, "Neuronal function and dysfunction of drosophila dTDP," *PLoS ONE*, vol. 6, no. 6, Article ID e20371, 2011.
- [55] J.-W. Wang, J. R. Brent, A. Tomlinson, N. A. Shneider, and B. D. McCabe, "The ALS-associated proteins FUS and TDP-43 function together to affect *Drosophila* locomotion and life span," *The Journal of Clinical Investigation*, vol. 121, no. 10, pp. 4118–4126, 2011.
- [56] P. S. Estes, S. G. Daniel, A. P. Mccallum et al., "Motor neurons and glia exhibit specific individualized responses to TDP-43 expression in a *Drosophila* model of amyotrophic lateral sclerosis," *Disease Models and Mechanisms*, vol. 6, no. 3, pp. 721–733, 2013.
- [57] R. Gulino, S. Forte, R. Parenti, and M. Gulisano, "TDP-43 as a modulator of synaptic plasticity in a mouse model of spinal motoneuron degeneration," *CNS & Neurological Disorders—Drug Targets*. In press.
- [58] M. Coradazzi, R. Gulino, S. Garozzo, and G. Leanza, "Selective lesion of the developing central noradrenergic system: short- and long-term effects and reinnervation by noradrenergic-rich tissue grafts," *Journal of Neurochemistry*, vol. 114, no. 3, pp. 761–771, 2010.
- [59] R. Gulino, L. Litrico, and G. Leanza, "Long-term survival and development of fetal ventral spinal grafts into the motoneuron-depleted rat spinal cord: role of donor age," *Brain Research*, vol. 1323, pp. 41–47, 2010.
- [60] P. E. Phelps, R. P. Barber, C. R. Houser, G. D. Crawford, P. M. Salvaterra, and J. E. Vaughn, "Postnatal development of neurons containing choline acetyltransferase in rat spinal cord: an immunocytochemical study," *The Journal of Comparative Neurology*, vol. 229, no. 3, pp. 347–361, 1984.
- [61] L. F. Borges and S. D. Iversen, "Topography of choline acetyltransferase immunoreactive neurons and fibers in the rat spinal cord," *Brain Research*, vol. 362, no. 1, pp. 140–148, 1986.
- [62] R. Gulino, T. Cataudella, F. Casamenti, G. Pepeu, S. Stanzani, and G. Leanza, "Acetylcholine release from fetal tissue homotopically grafted to the motoneuron-depleted lumbar spinal cord. An *in vivo* microdialysis study in the awake rat," *Experimental Neurology*, vol. 204, no. 1, pp. 326–338, 2007.
- [63] N. Mitchell, R. S. Petralia, D. G. Currier et al., "Sonic hedgehog regulates presynaptic terminal size, ultrastructure and function in hippocampal neurons," *Journal of Cell Science*, vol. 125, no. 18, pp. 4207–4213, 2012.
- [64] I. Matsuura, J. Taniguchi, K. Hata, N. Saeki, and T. Yamashita, "BMP inhibition enhances axonal growth and functional recovery after spinal cord injury," *Journal of Neurochemistry*, vol. 105, no. 4, pp. 1471–1479, 2008.
- [65] T. Setoguchi, K. Nakashima, T. Takizawa et al., "Treatment of spinal cord injury by transplantation of fetal neural precursor cells engineered to express BMP inhibitor," *Experimental Neurology*, vol. 189, no. 1, pp. 33–44, 2004.
- [66] T. Nishimura, T. Yamaguchi, A. Tokunaga et al., "Role of Numb in dendritic spine development with a Cdc42 GEF intersector and EphB2," *Molecular Biology of the Cell*, vol. 17, no. 3, pp. 1273–1285, 2006.
- [67] J. W. Fawcett and R. A. Asher, "The glial scar and central nervous system repair," *Brain Research Bulletin*, vol. 49, no. 6, pp. 377–391, 1999.
- [68] G. Raivich, M. Bohatschek, C. U. A. Kloss, A. Werner, L. L. Jones, and G. W. Kreutzberg, "Neuroglial activation repertoire in the injured brain: graded response, molecular mechanisms and cues to physiological function," *Brain Research Reviews*, vol. 30, no. 1, pp. 77–105, 1999.
- [69] D. Cevolani, M. Bentivoglio, and P. Strocchi, "Glial reaction to volkensin-induced selective degeneration of central neurons," *Brain Research Bulletin*, vol. 54, no. 4, pp. 353–361, 2001.
- [70] P. McGoldrick, P. I. Joyce, E. M. C. Fisher, and L. Greensmith, "Rodent models of amyotrophic lateral sclerosis," *Biochimica et Biophysica Acta—Molecular Basis of Disease*, vol. 1832, no. 9, pp. 1421–1436, 2013.
- [71] W. Tsao, Y. H. Jeong, S. Lin et al., "Rodent models of TDP-43: recent advances," *Brain Research*, vol. 1462, pp. 26–39, 2012.

## Research Article

# Distention of the Immature Left Ventricle Triggers Development of Endocardial Fibroelastosis: An Animal Model of Endocardial Fibroelastosis Introducing Morphopathological Features of Evolving Fetal Hypoplastic Left Heart Syndrome

**Shogo Shimada, Christian Robles, Ben M. W. Illigens, Alejandra M. Casar Berazaluze, Pedro J. del Nido, and Ingeborg Friehs**

*Department of Cardiac Surgery, Boston Children's Hospital, Harvard Medical School, 300 Longwood Avenue, Boston, MA 02115, USA*

Correspondence should be addressed to Ingeborg Friehs; [ingeborg.friehs@childrens.harvard.edu](mailto:ingeborg.friehs@childrens.harvard.edu)

Received 26 September 2014; Accepted 22 November 2014

Academic Editor: Oreste Gualillo

Copyright © 2015 Shogo Shimada et al. This is an open access article distributed under the Creative Commons Attribution License, which permits unrestricted use, distribution, and reproduction in any medium, provided the original work is properly cited.

*Background.* Endocardial fibroelastosis (EFE), characterized by a diffuse endocardial thickening through collagen and elastin fibers, develops in the human fetal heart restricting growth of the left ventricle (LV). Recent advances in fetal imaging indicate that EFE development is directly associated with a distended, poorly contractile LV in evolving hypoplastic left heart syndrome (HLHS). In this study, we developed an animal model of EFE by introducing this human fetal LV morphopathology to an immature rat heart. *Methods and Results.* A neonatal donor heart, in which aortic regurgitation (AR) was created, was heterotopically transplanted into a recipient adult rat. AR successfully induced the LV morphology of evolving HLHS in the transplanted donor hearts, which resulted in the development of significant EFE covering the entire LV cavity within two weeks postoperatively. In contrast, posttransplants with a competent aortic valve displayed unloaded LVs with a trace of EFE. *Conclusions.* We could show that distention of the immature LV in combination with stagnant flow triggers EFE development in this animal model. This model would serve as a robust tool to develop therapeutic strategies to treat EFE while providing insight into its pathogenesis.

## 1. Introduction

Endocardial fibroelastosis (EFE), characterized by a diffuse endocardial thickening through collagen and elastin fibers, predominantly develops in immature left atrium (LA) and left ventricle (LV) [1, 2]. EFE has been described in association with a wide variety of diseases, such as viral myocarditis [3], lysosomal storage diseases [4], idiopathic or genetic dilated cardiomyopathies [5, 6], immunologic diseases [7, 8], and structural cardiac malformations [9, 10], such as hypoplastic left heart syndrome (HLHS). Although it has been speculated that an early hemodynamic insult on the immature LV plays a key role in the development of EFE, its precise pathogenesis has not been elucidated [11, 12].

Recent advances in fetal imaging have demonstrated that in a subset of HLHS patients progression of fetal aortic stenosis occurs relatively late in gestation [13]. Fetal aortic

balloon valvuloplasty (FAV) has been successfully performed to avert this progression in a selected patient population [14]. The development of EFE has been well described in the progression of this disease and has been shown to contribute to LV growth retardation and immediate, and more likely, long-term diastolic dysfunction [15, 16]. Disease progression is characterized by dramatic morphological changes of the affected LV. Initially, the LV appears normal in size with decreased contractility; then, it develops dilation with hyper-echogenic endocardium, indicative of EFE. Finally, later in gestation, it progresses into a hypocontractile state with LV hypoplasia that meets the diagnostic criteria for HLHS [17]. These clinical observations of the LV suggest that distention is a key factor in the development of EFE. In addition, it has been recognized that EFE is more likely to develop in a borderline developed LV rather than a diminutive LV, the latter being protected from distention since it has neither inlet

nor outlet [16, 18, 19]. Furthermore, most of LVs developing EFE from other etiologies are distended at the time of EFE manifestation [1, 2, 9, 20]. Collectively, these clinical observations implicate that distention of the immature LV may significantly add to the severity of EFE development, potentially on the basis of unknown intrinsic genetic or immunologic predispositions.

Based on our hypothesis that immaturity and stagnation of intracavitary flow would play a key role in the development of EFE, we reported our results on EFE development in a heterotopically transplanted neonatal rat heart model, where the LV had no intracavitary flow (i.e., preload) [21]. This animal model, however, showed variable degrees of EFE formation which we could only assess at postmortem analysis since echocardiographic evaluation was limited due to restricted view of the intra-abdominally located donor heart. In addition, postmortem analysis indicated a direct correlation between the degree of EFE and ventricular distention which was most likely a result of intraoperative technical difficulties resulting in the distortion of the aortic root. These combined observations of clinical and experimental data indicate that additional factors contribute to the pathophysiological mechanism of EFE formation. Thus, we refined our hypothesis, combining immaturity and stagnation of flow within the LV cavity with intentional LV distention and modification of the anatomical location of the heterotopically transplanted heart for echocardiographic monitoring. In order to test this hypothesis, we modified the previously described heterotopically transplanted immature heart model by introduction of acute LV distention through creation of severe aortic regurgitation without compromising coronary perfusion and femoral location of the donor graft.

## 2. Materials and Methods

All animal procedures in this study were conducted in accordance with the Principles of Laboratory Animal Care formulated by the National Society for Medical Research and the Guide for the Care and Use of Laboratory Animals prepared by the Institute of Laboratory Animal Resources and published by the National Institutes of Health (NIH Publication number 86-23, revised 1996). The animal protocols were reviewed and approved by the Institutional Animal Care and Use Committee at Boston Children's Hospital.

**2.1. Heterotopic Femoral Neonatal Rat Heart Transplantation.** Heterotopic femoral heart transplantations were performed between syngeneic Lewis rats (Charles River Laboratories International, Wilmington, MA) using the technique previously described with a few modifications [22]. The procedures were performed under a surgical microscope (Endure Medical, Georgia) with 6x to 40x magnification. Donors with AR creation served as a distended LV model ( $n = 10$ ) and those with an intact aortic valve served as unloaded LV model ( $n = 14$ ).

**2.1.1. Recipient Preparation.** Recipient rats (male, 150 to 200 g) were anesthetized via intraperitoneal injections of Ketamine (40 mg/kg) and Xylazine (10 mg/kg). Heparin

(300 IU/kg) was also administered intraperitoneally. Anesthesia was maintained by isoflurane inhalation (1 to 2%) through an endotracheal tube under mechanical ventilation (Inspira Advanced Safety Ventilator, Harvard Apparatus, Holliston, MA). A skin incision was made along the inguinal crease to expose the femoral artery and vein.

**2.1.2. Donor Preparation and Creation of Aortic Regurgitation.** Neonatal rats (postnatal day 2 to 4,  $10 \pm 2$  g) served as a donor. Anesthesia was induced in the same way as in the recipients. The chest was opened with a V-shaped incision to free the entire anterior rib cage for wide exposure. High potassium Krebs-Henseleit solution was administered via the inferior vena cava to obtain optimal cardiac preservation and eliminate blood. The distal ascending aorta and pulmonary trunk were cut and divided as proximally as possible to facilitate subsequent anastomoses. All other accessory vessels were ligated by 7-0 nylon sutures and cut off. The aortic valve was either damaged by inserting an ultrathin guide-wire (Roadrunner Extra-Support Wire Guide, diameter: 0.014 inch, COOK MEDICAL, Bloomington, IN) to create aortic regurgitation or left intact. The harvested heart was stored in cardioplegic solution at 4°C.

**2.1.3. End-to-End Anastomoses.** Microvascular clamps were placed on the recipient proximal femoral artery and vein separately. The distal femoral artery and vein were tied off before branching superficial caudal epigastric artery and vein. The harvested donor heart was then transferred into the recipient groin for transplantation. The donor's ascending aorta and pulmonary trunk were anastomosed to the recipient's femoral artery and vein, respectively, in an end-to-end manner. The arterial anastomosis was made by 8 to 10 interrupted stitches with 10-0 and 11-0 nylon sutures. The venous anastomosis was made by continuous running suture with an 11-0 nylon suture. After completion of the anastomoses, the microvascular clamps were removed. The transplanted hearts resumed beating within a minute and showed variable distention according to the degree of aortic regurgitation. The incision was closed following hemostasis. The recipient rat was then given analgesics (Buprenorphine: 0.1 mg/kg S.C., Meloxicam: 1 mg/kg S.C.) and extubated. The rat was allowed to recover and usually had no difficulty in ambulation. No limitation on feeding was imposed perioperatively and no antibiotics were given (Figures 1(a) and 1(b)).

**2.2. Heterotopic Abdominal Rat Heart Transplantation.** Conventional heterotopic abdominal heart transplantations using a 2-week-old donor with AR creation were performed as previously described ( $n = 3$ ) [23, 24]. Briefly, the donor heart harvest and AR creation was carried out in the same way as the femoral transplantation. The donor's great vessels were anastomosed to a recipient's infrarenal abdominal aorta and inferior vena cava, respectively, in an end-to-side manner. Postoperative care and time course of the experiments were the same as the femoral transplantation.

**2.3. Postoperative Trans-Femoral Echocardiography.** The transplanted hearts underwent echocardiographic evaluation for

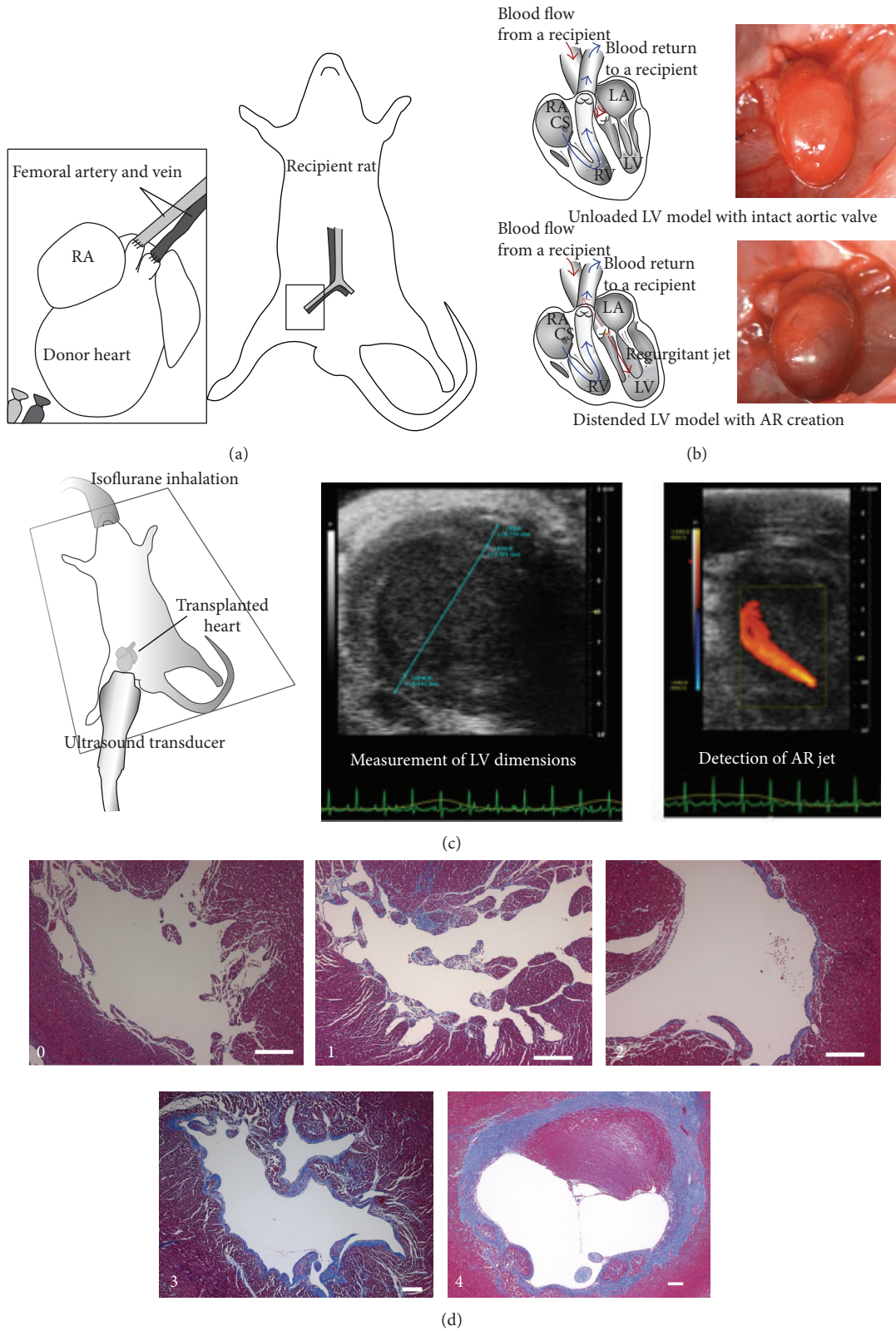


FIGURE 1: (a) Heterotopic femoral heart transplantation. (b) Schemes of blood circulation of transplanted hearts and representative photographs of the posttransplants. Reduced flow through the LV in the unloaded LV model with intact aortic valve (upper row) versus increased pressure and volume load in the distended LV model with AR creation (lower row). (c) Postoperative trans-femoral echocardiography. Representative images from a distended LV with AR. (d) A grading system for the amount of EFE. EFE scores (Grade 0, no EFE; Grade 1, islets of EFE; Grade 2, thin EFE tissue covering a half circumference of the endocardium; Grade 3, thin EFE tissue (less than  $100\ \mu\text{m}$ ) covering a full circumference of the endocardium; Grade 4, thick EFE tissue (more than  $100\ \mu\text{m}$ ) covering a full circumference of the endocardium). White scale bar,  $200\ \mu\text{m}$ .

LV dimensions, contractility, and aortic valvular function one week postoperatively. The recipient rat was anesthetized by isoflurane inhalation (1 to 2%) delivered via a nose cone and positioned supine on a heated platform for echocardiography (Vevo 2100, FUJIFILM VisualSonics, Toronto, Canada). A long axis view of the transplanted heart was visualized through an apical approach by a 40 MHz transducer (MS550D, FUJIFILM VisualSonics, Toronto, Canada). Data were acquired via this apical long axis view (Figure 1(c)).

**2.4. Histological Evaluation of the Transplanted Hearts.** The recipient rats were euthanized two weeks postoperatively. The transplanted hearts were explanted and fixed in 4% paraformaldehyde for 24 hours, embedded in paraffin, and sectioned to obtain either short or long axis view of the LV. Hematoxylin and Eosin staining, Masson's Trichrome staining, and Elastica van Gieson staining were performed on those sections using standard protocols to determine EFE. The degree of EFE was graded semiquantitatively on a scale from 0 to 4 (Grade 0, no EFE; Grade 1, islets of EFE; Grade 2, thin EFE tissue covering half of the circumference of the LV endocardium; Grade 3, thin EFE tissue (less than 100  $\mu\text{m}$ ) covering the full circumference of the LV endocardium; Grade 4, thick EFE tissue (more than 100  $\mu\text{m}$ ) covering the full circumference of the LV endocardium; Figure 1(d)). Images were acquired on a microscope (Axio Observer. Z1, Carl Zeiss Microscopy LLC, Peabody, MA).

**2.5. Statistical Analysis.** LV parameters of the posttransplants from echocardiographic measurements were assessed for group differences using an unpaired *t*-test. Comparisons of EFE scores between groups were made using nonparametric (Mann-Whitney) tests conducted with JMP (8.0.1, SAS Institute, Japan). Data are expressed as means  $\pm$  SEMs.  $P < 0.05$  was considered statistically significant.

### 3. Results

**3.1. AR Successfully Induced the LV Morphology of Evolving HLHS on the Transplanted Donor Hearts.** We conducted heterotopic femoral neonatal rat heart transplantations to test if AR creation could induce acute LV distention on the immature neonatal donor rat heart. The transplanted hearts with AR creation ( $n = 10$ ) were compared to those with an intact aortic valve ( $n = 14$ ) via postoperative transfemoral echocardiography. In the distended LV model, the LVs were markedly dilated by significant AR, whereas those in the unloaded LV model became contracted with reduced preload (LVDD (mm),  $3.33 \pm 0.47$  versus  $1.35 \pm 0.09$ ,  $P < 0.01$ ; LVDs (mm),  $2.84 \pm 0.50$  versus  $1.10 \pm 0.12$ ,  $P < 0.01$ ) (Figure 2(a)). Both groups showed decreased LV contractility without any significant difference (FS (%),  $18.45 \pm 3.73$  versus  $21.77 \pm 4.22$ , N.S.). These echo findings indicate that AR introduction could instantaneously alter the morphology of the transplanted hearts due to significant pressure and volume overload.

**3.2. EFE Developed in the Distended Immature LVs.** Histological evaluation was performed to determine if these

distended hearts developed significant EFE. In the distended LV model with AR, the explanted hearts were larger in size and all 10 cases developed significant EFE. In the most severe EFE cases (EFE score 4), EFE was macroscopically discernible as a thick white layer on the endocardial surface. Microscopic observations confirmed a collagen-rich fibrous tissue with elastin fibers covering the endocardial surface, which specified EFE (Figure 3(a)). In contrast, the unloaded LVs appeared contracted, and EFE developed only in 2 cases. Instead, a mural thrombus was organized in 3 out of 14 unloaded LVs and distinguished from EFE by the absence of elastin fibers (Figures 3(b) and 3(c)). EFE scores in the distended LV model were significantly higher than those in the unloaded LV model ( $2.90 \pm 0.26$  versus  $0.29 \pm 0.21$ ,  $P < 0.01$ ) (Figure 3(d)).

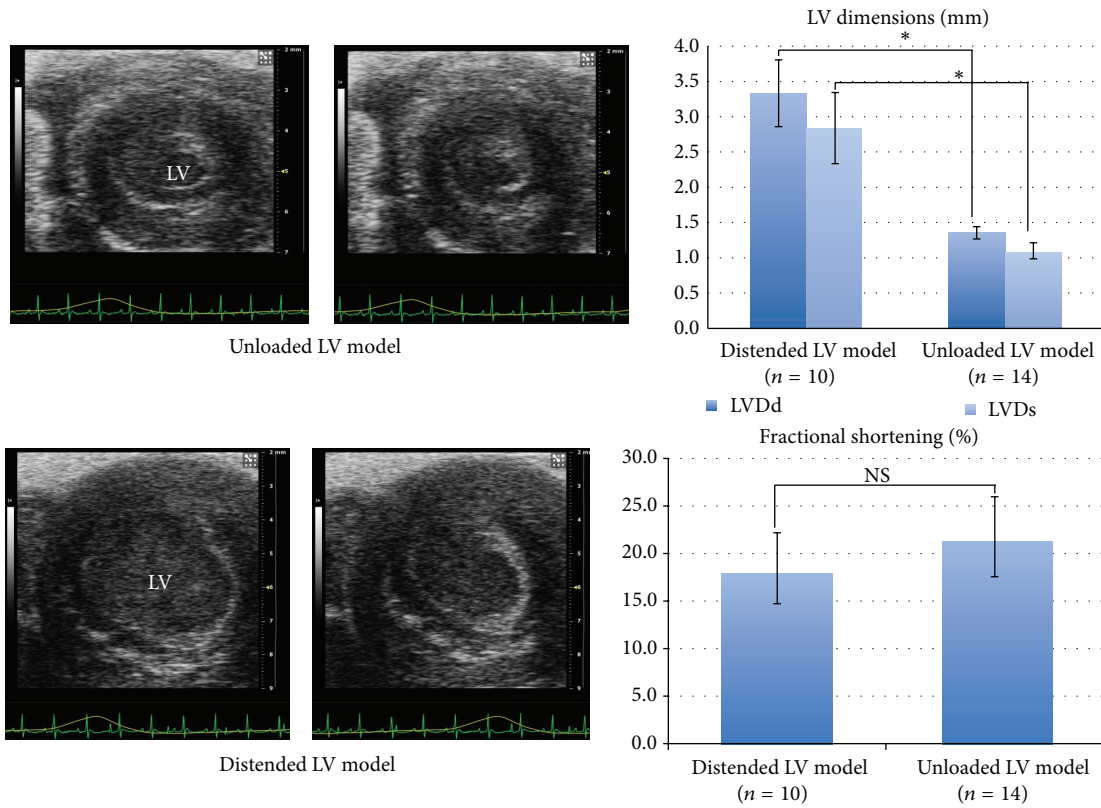
EFE develops almost exclusively in the early stage of life. We, therefore, performed the distended LV model using a relatively mature donor (2-week-old,  $n = 3$ ) (Figures 4(a) and 4(b)). In this model, none of the transplanted hearts developed EFE, and fibrosis was mainly distributed in the subendocardial layer instead of the endocardial surface (Figure 4(c)).

**3.3. EFE Increased in Proportion to the Severity of LV Distention.** Although all the distended LVs developed significant EFE, its degree varied. To further clarify the relationship between distention and EFE development, we compared echo data between the most severe EFE cases (Grade 4,  $n = 3$ ) and the others (Grade 2 and 3,  $n = 7$ ) from the distended LV model. Echo analyses revealed that the most severe degree of EFE (Grade 4) developed in the most dilated (LVDD (mm),  $5.24 \pm 0.54$  versus  $2.51 \pm 0.29$ ,  $P < 0.01$ ; LVDs (mm),  $2.84 \pm 0.50$  versus  $1.10 \pm 0.12$ ,  $P < 0.01$ ) and poorly contractile LVs (FS (%);  $3.15 \pm 1.28$  versus  $25.0 \pm 2.77$ ,  $P < 0.01$ ) (Figure 5). The severity of distention was directly associated with the amount of EFE.

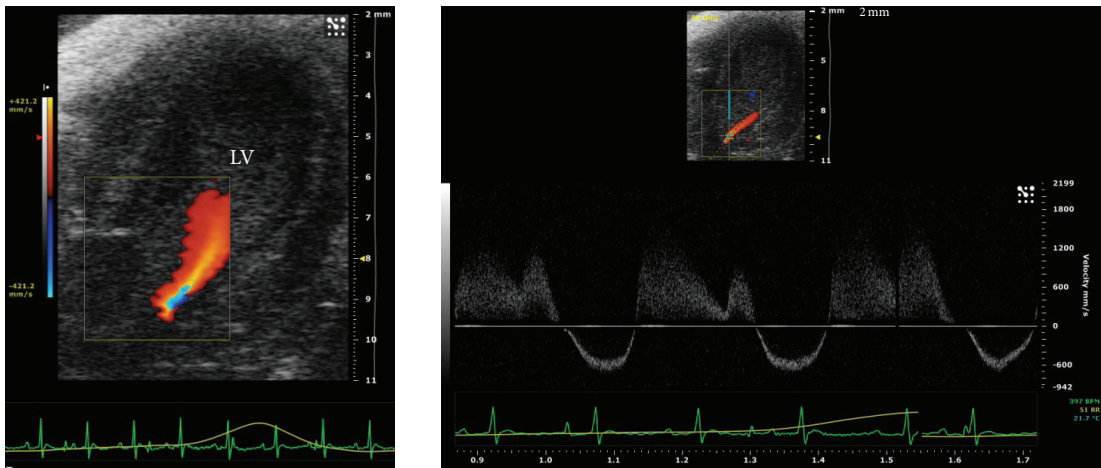
### 4. Discussion

In this study, we successfully created an animal model of EFE by introducing clinical features of evolving human fetal HLHS which included a combination of immaturity, stagnation of flow, and distention of the LV through volume/pressure overload. Our results indicate that the amount of EFE directly correlates with the severity of LV distention when added to immaturity and stagnation of intracavitary flow. These findings shed new light on the underlying mechanisms of EFE development, which are in line with clinical observations of fetal patients with aortic stenosis and impending HLHS development.

Although multiple animal models have produced LV hypertrophy by introducing left-sided obstruction, none have been successful in creating EFE [25, 26]. Major limitations using fetal experimental animals are difficulties in obtaining survival cases when applying major hemodynamic changes acutely. Creating aortic stenosis in an early gestational fetus gradually increases LV end-diastolic pressure but fails to create abrupt augmentation of LV pressure/volume load, which we observed in a subgroup of fetuses with aortic



(a)



AR detection in the distended LV model

(b)

FIGURE 2: Postoperative echocardiography. (a) Short axis views of LVs in diastole and systole. The distended LV model developed significantly larger LVs than those in the unloaded LV model (\*  $P < 0.01$ , NS: not significant). (b) Apical long axis view of a LV in the distended LV model. An AR jet was detected in a 2D echocardiography with color Doppler.

stenosis and evolving HLHS. Thus, as a consequence, no EFE developed in these animal models [25].

Fully vascularized cardiac transplantation in small animals has been established and reliably used to address a wide variety of issues. Multiple modifications have been attempted to facilitate construction of the anastomoses, which has been recognized as a technical challenge and requires a substantial

learning curve to achieve acceptable reproducibility [27]. Using a neonatal rat as a donor would be even more challenging given the small size and fragility. To overcome this potential vulnerability of the present model, postoperative monitoring was imperative. Therefore, we newly developed a heterotopic femoral heart transplantation model, in which a transplanted heart was vascularized by the recipient's

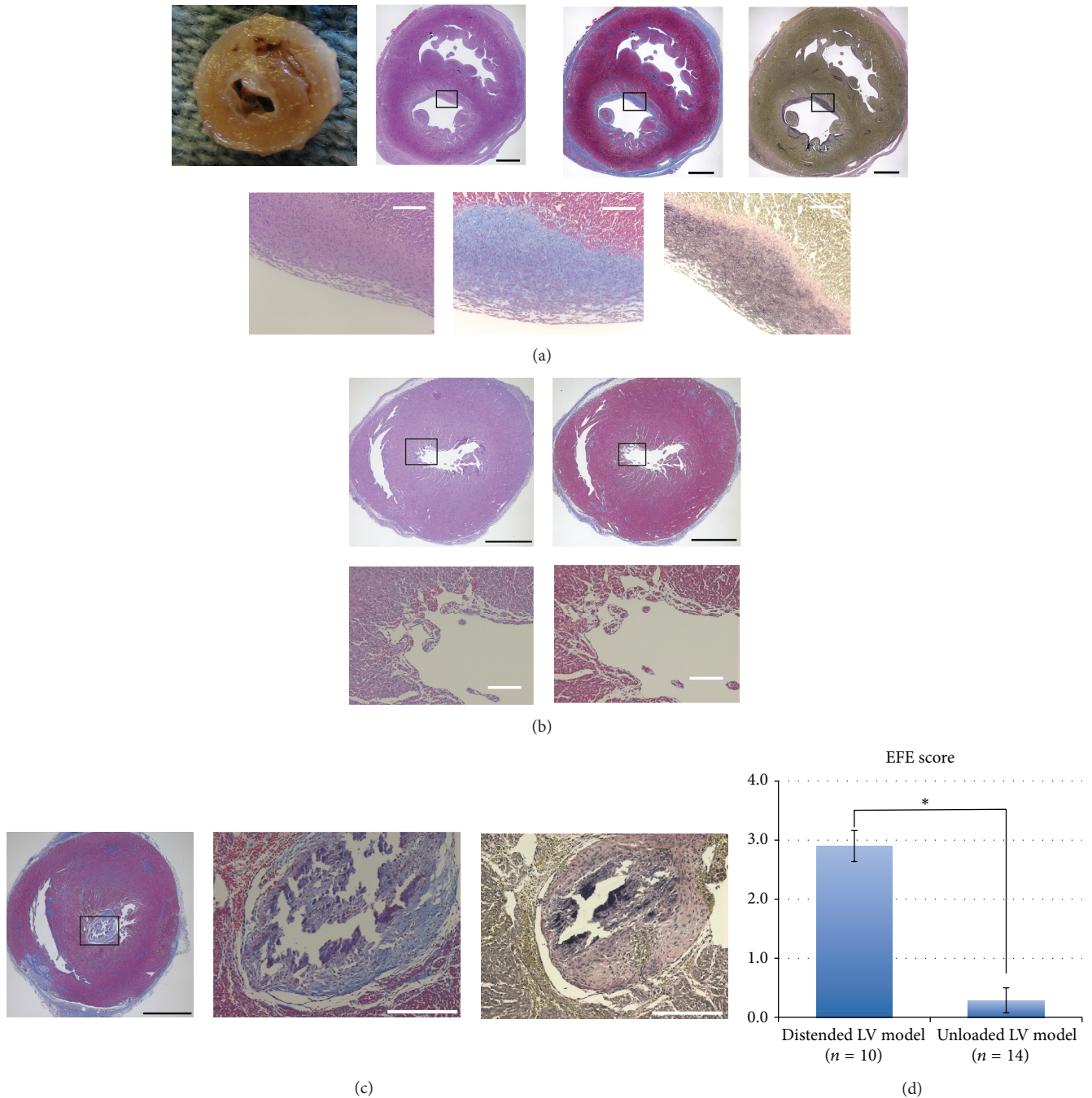


FIGURE 3: (a) A representative photograph and slides of the distended LV model. Each shows short axis views of the ventricles. The endocardium is covered by macroscopically discernible pearly white thick layers of fibroelastosis. Masson's Trichrome- and Elastica van Gieson-stained slides depict thick fibrous layers with an abundant collagen deposition (stained in blue) and stratified elastin fibers (black wavy lines) on the endocardial surface. (b) Representative Hematoxylin and Eosin- and Masson's Trichrome-stained slides in the unloaded LV model. The LV appears contracted with a thickened myocardial layer. No apparent fibrous tissue develops on the endocardium. (c) A case with a mural thrombus in the unloaded LV model. Masson's Trichrome-stained slides depict a large mural thrombus occupying the LV cavity. The mural thrombus has an abundant collagen deposition but no elastin fibers in an Elastica van Gieson-stained slide. Black scale bar, 1 mm; white scale bar, 200  $\mu$ m. (d) Comparison of EFE scores between the distended LV model and the unloaded LV model (\* $P < 0.01$ ).

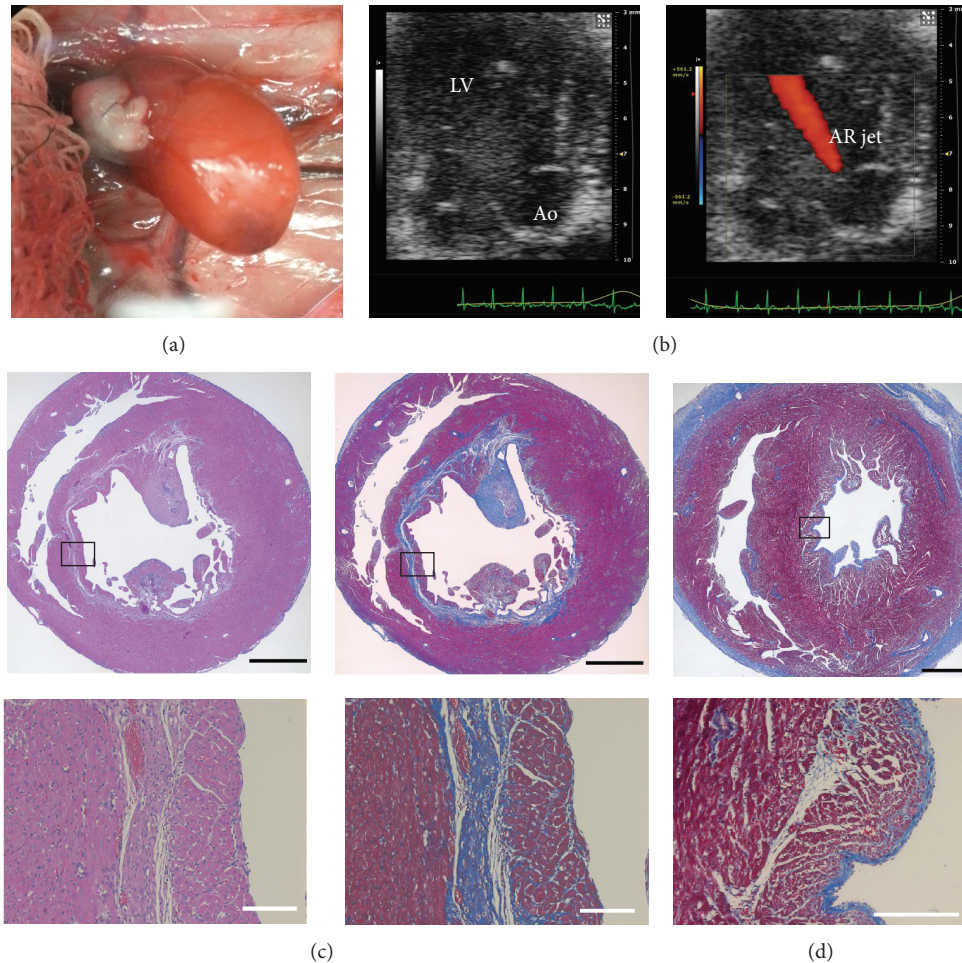


FIGURE 4: In comparison, the distended LV model using a 2-week-old donor. (a) A photograph of a transplanted donor heart in situ. (b) Representative echo images showing the apical long axis view of the LV. An AR jet was detected in a 2D echocardiography with color Doppler. (Ao: aorta). (c) Representative Hematoxylin and Eosin- and Masson's Trichrome-stained slides sectioned along the short axis. Collagen-rich fibrous layers (stained in blue) are seen in the subendocardial layer of a 2-week-old donor heart. (d) A Masson's Trichrome-stained slide from a neonatal donor heart for comparison. Fibrous layers are located on the endocardial surface of the LV. Black scale bar, 1 mm; white scale bar, 200  $\mu\text{m}$ .

femoral vessels and placed superficially in a groin pocket. Unlike the conventional abdominal transplantation model, this model made the posttransplant heart palpable and visible via postoperative trans-femoral echocardiography.

In the present study, the unloaded LV model did not produce significant EFE as indicated by our scoring data. The discrepancy toward our previously published results may be attributable to subtle technical differences, such as the way of placing a stitch, aligning the target vessels, positioning the posttransplant with possible distortion of the aortic root, and obtaining optimal hemostasis, given the nature of this technically demanding and thus fairly surgeon-dependent procedure. Technical differences resulted in altering degrees of compromised LV function, which potentially influenced EFE formation. We addressed this issue by refining our animal model through incorporation of LV distention, which provided reproducible degrees of LV dysfunction. Alternatively, it can be attributed to diagnostic challenges with EFE. A mural thrombus or other nonspecific endocardial fibrosis

could mimic EFE. In particular islet-type patchy fibrosis on the endocardium is difficult to determine due to the phenotypical ambiguity and indiscernible elastin fibers.

To fulfill distention of the LV, we introduced AR through direct damage of the aortic valve. AR mimics the clinical situation of a distended LV in some impending HLHS cases but does not occur as a prominent pathophysiologic feature in human fetuses. Thus, there is the potential that the direction and velocity of blood flow following AR through the LV or shear stress applied onto the endocardium could be completely different. The AR jet might, thereby, directly injure the endocardium and induce EFE formation regardless of LV distention. Since EFE in this study is distributed homogeneously over the full circumference of the endocardium, our results indicate that the AR jet does not directly injure the endocardium. Therefore, direct injury from an AR jet, which would have created spatially variable local lesions, is an unlikely contributor to EFE formation in this model. Direct localized endothelial injury could also have been caused by

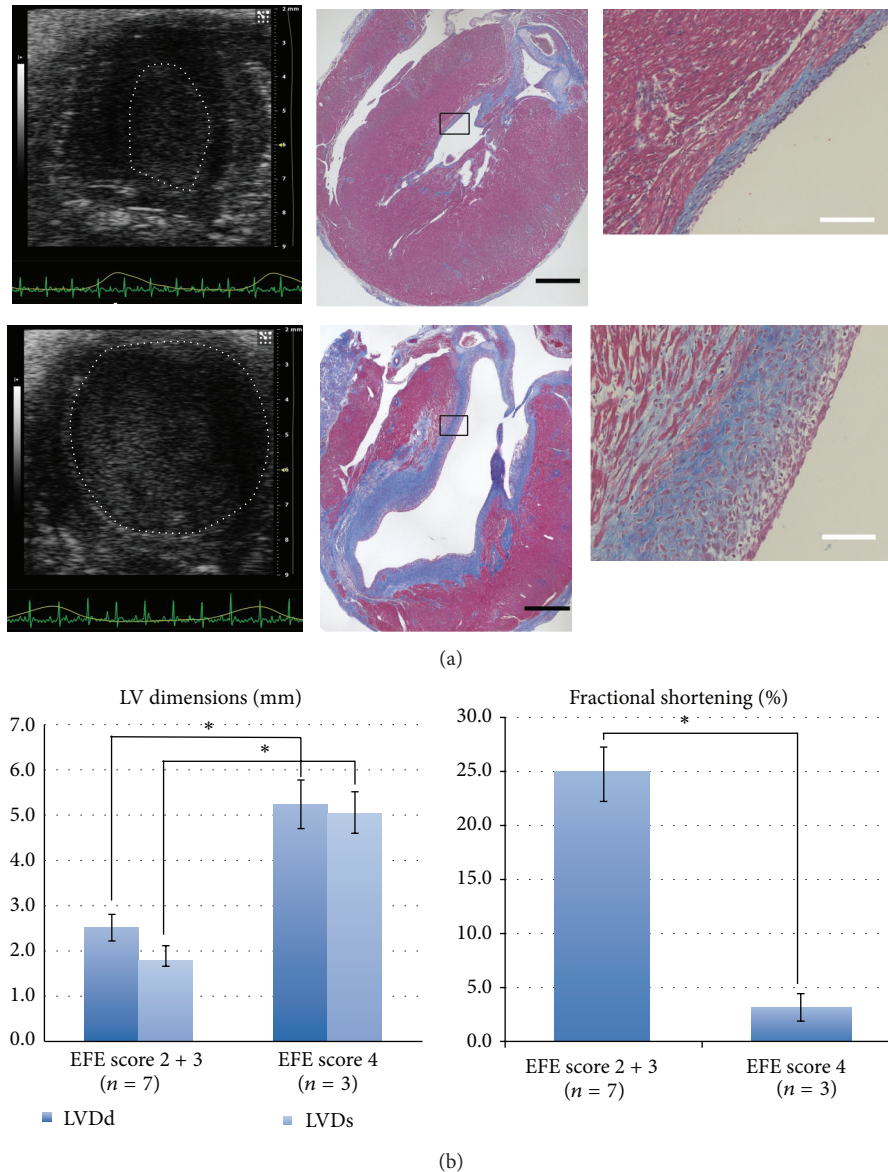


FIGURE 5: Relationship between LV distention and EFE amount. (a) Representative echo images and Masson's Trichrome-stained slides sectioned along the long axis. Mild LV distention created mild EFE (Grade 2) (upper row), whereas severe LV distention created severe EFE (Grade 4) (lower row). White dots in the echo images delineate the contour of the LV endocardium. Black scale bar, 1 mm; white scale bar, 200  $\mu\text{m}$ . (b) Comparison of the LV dimensions and fractional shortenings between Grade 2, 3 EFE cases and Grade 4 EFE cases ( $* P < 0.01$ ).

accidental trauma through the needle used for damaging the aortic valve leaflet. Initial attempts, in which we used a rigid thin needle to create AR, resulted in a localized fibrous scar lesion at the location of the injured endocardium (data not shown). This technical failure prompted us to use a flexible ultrathin guide-wire to create AR, which eliminated the risk of direct injury to the endocardium.

Difficulty in regulating the degree of AR generates different degrees of LV distention and results in variable amounts of EFE formation but at the same time provides a positive relationship between LV distention and the amount of EFE. Variable AR amounts also impose a challenge on a direct comparison between an immature donor group (P 2 to 4) and a relatively mature donor group (2-week-old) since

the severity of LV distention, which is represented by the size and function of the LV, is not directly comparable. In addition, susceptibility to distention may vary. However, the fact that the distended LV model with a 2-week-old donor created prominent subendocardial fibrosis but no EFE (Figure 4(c)) indicates that not only distention but also immaturity plays a key role in this pathological process. To the best of our knowledge, none of the animal models of AR using adult subjects have described EFE as a histological change [28, 29].

It is still controversial whether EFE is a distinct pathologic entity or a secondary phenomenon caused by stressors on the heart, such as mechanical overload. In order to explore benefits and limitations of therapeutic interventions on

the immature/fetal heart it is imperative to create a robust animal model of EFE to elucidate the underlying cause of EFE formation and to determine effective therapeutic agents targeting EFE. Intuitively, suppression of overgrowth of fibrotic layers on the endocardium, preferably combined with the mechanical relief of the distention such as FAV during the fetal stage, would provide a better chance to use the LV as systemic ventricle. Indeed, in experienced institutions, postnatal surgical resection of EFE has been performed in an attempt to restore and recruit the LV and improved outcome in selected cases has been reported [30, 31]. However, given the possibility that EFE is a protective response of the immature heart from mechanical overload, it might not be a useful therapeutic target during fetal development.

The current model shows that distention of the ventricle is one of the important mechanical factors which triggers the development of EFE in an age-dependent manner. These findings implicate that a relief of the underlying mechanical overload such as fetal aortic stenosis is of primary importance to mitigate EFE formation and exerts the greatest benefit if performed promptly when the mechanical overload appears. Since immediate relief of the mechanical overload to prevent EFE formation might not be feasible, alternative treatment strategies should potentially dissolve or reverse already present EFE.

## 5. Conclusions

We present an animal model where we could show that the distention of the immature LV triggers EFE formation by introducing morphopathological features of evolving human fetal HLHS. This model could serve as a robust tool to develop therapeutic strategies to treat EFE while providing insight into its pathogenesis.

## Conflict of Interests

The authors declare that there is no conflict of interests regarding the publication of this paper.

## Acknowledgment

The authors are grateful to the Animal Research Children's Hospital staff (Arthur Nedder, DVM, and veterinary technicians) for their overwhelming support and assistance in this project.

## References

- [1] F. J. Sellers, J. D. Keith, and J. A. Manning, "The diagnosis of primary endocardial fibroelastosis," *Circulation*, vol. 29, pp. 49–59, 1964.
- [2] J. H. Moller, R. V. Lucas Jr., P. Adams Jr., R. C. Anderson, J. Jorgens, and J. E. Edwards, "Endocardial fibroelastosis. A clinical and anatomic study of 47 patients with emphasis on its relationship to mitral insufficiency," *Circulation*, vol. 30, pp. 759–782, 1964.
- [3] J. Ni, N. E. Bowles, Y.-H. Kim et al., "Viral infection of the myocardium in endocardial fibroelastosis: molecular evidence for the role of mumps virus as an etiologic agent," *Circulation*, vol. 95, no. 1, pp. 133–139, 1997.
- [4] M. Y. Dincsoy, H. P. Dincsoy, A. D. Kessler, M. A. Jackson, and J. B. Sidbury Jr., "Generalized glycogenosis and associated endocardial fibroelastosis. Report of 3 cases with biochemical studies," *The Journal of Pediatrics*, vol. 67, no. 5, pp. 728–740, 1965.
- [5] A. N. Brady, B. M. Shehata, and P. M. Fernhoff, "X-linked fetal cardiomyopathy caused by a novel mutation in the TAZ gene," *Prenatal Diagnosis*, vol. 26, no. 5, pp. 462–465, 2006.
- [6] M. Kamisago, J. P. Schmitt, D. McNamara, C. Seidman, and J. G. Seidman, "Sarcomere protein gene mutations and inherited heart disease: a beta-cardiac myosin heavy chain mutation causing endocardial fibroelastosis and heart failure," *Novartis Foundation Symposium*, vol. 274, pp. 176–276, 2006.
- [7] L. E. Nield, E. D. Silverman, J. F. Smallhorn et al., "Endocardial fibroelastosis associated with maternal anti-Ro and anti-La antibodies in the absence of atrioventricular block," *Journal of the American College of Cardiology*, vol. 40, no. 4, pp. 796–802, 2002.
- [8] M. J. Newbould, G. R. Armstrong, and A. J. Barson, "Endocardial fibroelastosis in infants with hydrops fetalis," *Journal of Clinical Pathology*, vol. 44, no. 7, pp. 576–579, 1991.
- [9] D. H. Andersen and J. Kelly, "Endocardial fibro-elastosis. I. Endocardial fibro-elastosis associated with congenital malformations of the heart," *Pediatrics*, vol. 18, no. 4, pp. 513–538, 1956.
- [10] P. C. Ursell, C. A. Neill, R. H. Anderson, S. Y. Ho, A. E. Becker, and L. M. Gerlis, "Endocardial fibroelastosis and hypoplasia of the left ventricle in neonates without significant aortic stenosis," *British Heart Journal*, vol. 51, no. 5, pp. 492–497, 1984.
- [11] B. Black-Schaffer, "Infantile endocardial fibroelastosis; a suggested etiology," *A. M. A. Archives of Pathology*, vol. 63, pp. 281–306, 1957.
- [12] P. R. Lurie, "Changing concepts of endocardial fibroelastosis," *Cardiology in the Young*, vol. 20, no. 2, pp. 115–123, 2010.
- [13] L. K. Hornberger, S. P. Sanders, A. J. T. Rein, P. J. Spevak, I. A. Parness, and S. D. Colan, "Left heart obstructive lesions and left ventricular growth in the midtrimester fetus: a longitudinal study," *Circulation*, vol. 92, no. 6, pp. 1531–1538, 1995.
- [14] L. R. Freud, D. B. McElhinney, A. C. Marshall et al., "Fetal aortic valvuloplasty for evolving hypoplastic left heart syndrome: postnatal outcomes of the first 100 patients," *Circulation*, vol. 130, pp. 638–645, 2014.
- [15] D. B. McElhinney, M. Vogel, C. B. Benson et al., "Assessment of left ventricular endocardial fibroelastosis in fetuses with aortic stenosis and evolving hypoplastic left heart syndrome," *The American Journal of Cardiology*, vol. 106, no. 12, pp. 1792–1797, 2010.
- [16] K. G. Friedman, D. Schidlow, L. Freud, M. Escobar-Diaz, and W. Tworetzky, "Left ventricular diastolic function and characteristics in fetal aortic stenosis," *The American Journal of Cardiology*, vol. 114, pp. 122–127, 2014.
- [17] J. A. Feinstein, D. W. Benson, A. M. Dubin et al., "Hypoplastic left heart syndrome: current considerations and expectations," *Journal of the American College of Cardiology*, vol. 59, no. 1, pp. S1–S42, 2012.
- [18] H. Sugiyama, C. Yutani, K. Iida, Y. Arakaki, O. Yamada, and T. Kamiya, "The relation between right ventricular function and left ventricular morphology in hypoplastic left heart syndrome: angiographic and pathological studies," *Pediatric Cardiology*, vol. 20, no. 6, pp. 422–427, 1999.

- [19] J. M. Baffa, S.-L. Chen, M. E. Guttenberg, W. I. Norwood, and P. M. Weinberg, "Coronary artery abnormalities and right ventricular histology in hypoplastic left heart syndrome," *Journal of the American College of Cardiology*, vol. 20, no. 2, pp. 350–358, 1992.
- [20] G. K. Sharland, S. K. Chita, N. L. K. Fagg et al., "Left ventricular dysfunction in the fetus: relation to aortic valve anomalies and endocardial fibroelastosis," *British Heart Journal*, vol. 66, no. 6, pp. 419–424, 1991.
- [21] I. Friehs, B. Illigens, I. Melnychenko, T. Zhong-Hu, E. Zeisberg, and P. J. Del Nido, "An animal model of endocardial fibroelastosis," *Journal of Surgical Research*, vol. 182, no. 1, pp. 94–100, 2013.
- [22] C. R. Gordon, M. S. Matthews, D. R. Lefebvre et al., "A new modified technique for heterotopic femoral heart transplantation in rats," *Journal of Surgical Research*, vol. 139, no. 2, pp. 157–163, 2007.
- [23] K. Ono and E. S. Lindsey, "Improved technique of heart transplantation in rats," *The Journal of Thoracic and Cardiovascular Surgery*, vol. 57, no. 2, pp. 225–229, 1969.
- [24] C. P. Abbott, E. S. Lindsey, O. Creech Jr., and C. W. Dewitt, "A technique for heart transplantation in the rat," *Archives of Surgery*, vol. 89, pp. 645–652, 1964.
- [25] P. Eghtesady, E. Michelfelder, M. Altaye, E. Ballard, R. Hirsh, and R. H. Beekman III, "Revisiting animal models of aortic stenosis in the early gestation fetus," *Annals of Thoracic Surgery*, vol. 83, no. 2, pp. 631–639, 2007.
- [26] D. L. Levin, R. M. Perkin, M. Parkey, E. Mayhew, and R. Hartwig, "Experimental aortic stenosis in fetal lambs," *Circulation*, vol. 62, no. 6, pp. 1159–1164, 1980.
- [27] M. Niimi, "The technique for heterotopic cardiac transplantation in mice: experience of 3000 operations by one surgeon," *Journal of Heart and Lung Transplantation*, vol. 20, no. 10, pp. 1123–1128, 2001.
- [28] E. Plante, D. Lachance, S. Champetier et al., "Benefits of long-term  $\beta$ -blockade in experimental chronic aortic regurgitation," *American Journal of Physiology: Heart and Circulatory Physiology*, vol. 294, no. 4, pp. H1888–H1895, 2008.
- [29] D. Lachance, É. Plante, A.-A. Bouchard-Thomassin et al., "Moderate exercise training improves survival and ventricular remodeling in an animal model of left ventricular volume overload," *Circulation: Heart Failure*, vol. 2, no. 5, pp. 437–445, 2009.
- [30] S. M. Emani, D. B. McElhinney, W. Tworetzky et al., "Staged left ventricular recruitment after single-ventricle palliation in patients with borderline left heart hypoplasia," *Journal of the American College of Cardiology*, vol. 60, no. 19, pp. 1966–1974, 2012.
- [31] S. M. Emani, E. A. Bacha, D. B. McElhinney et al., "Primary left ventricular rehabilitation is effective in maintaining two-ventricle physiology in the borderline left heart," *Journal of Thoracic and Cardiovascular Surgery*, vol. 138, no. 6, pp. 1276–1282, 2009.

## Research Article

# Layer 5 Pyramidal Neurons' Dendritic Remodeling and Increased Microglial Density in Primary Motor Cortex in a Murine Model of Facial Paralysis

Diana Urrego,<sup>1,2</sup> Julieta Troncoso,<sup>1,3</sup> and Alejandro Múnera<sup>1,4</sup>

<sup>1</sup>Behavioral Neurophysiology Laboratory, Universidad Nacional de Colombia, 111321 Bogotá, Colombia

<sup>2</sup>Department of Molecular Biology of Neuronal Signals, Max-Planck Institute for Experimental Medicine, 37075 Goettingen, Germany

<sup>3</sup>Department of Biology, School of Sciences, Universidad Nacional de Colombia, 111321 Bogotá, Colombia

<sup>4</sup>Department of Physiological Sciences, School of Medicine, Universidad Nacional de Colombia, 111321 Bogotá, Colombia

Correspondence should be addressed to Alejandro Múnera; famunerag@unal.edu.co

Received 24 September 2014; Revised 22 December 2014; Accepted 13 January 2015

Academic Editor: Oreste Gualillo

Copyright © 2015 Diana Urrego et al. This is an open access article distributed under the Creative Commons Attribution License, which permits unrestricted use, distribution, and reproduction in any medium, provided the original work is properly cited.

This work was aimed at characterizing structural changes in primary motor cortex layer 5 pyramidal neurons and their relationship with microglial density induced by facial nerve lesion using a murine facial paralysis model. Adult transgenic mice, expressing green fluorescent protein in microglia and yellow fluorescent protein in projecting neurons, were submitted to either unilateral section of the facial nerve or sham surgery. Injured animals were sacrificed either 1 or 3 weeks after surgery. Two-photon excitation microscopy was then used for evaluating both layer 5 pyramidal neurons and microglia in vibrissal primary motor cortex (vM1). It was found that facial nerve lesion induced long-lasting changes in the dendritic morphology of vM1 layer 5 pyramidal neurons and in their surrounding microglia. Dendritic arborization of the pyramidal cells underwent overall shrinkage. Apical dendrites suffered transient shortening while basal dendrites displayed sustained shortening. Moreover, dendrites suffered transient spine pruning. Significantly higher microglial cell density was found surrounding vM1 layer 5 pyramidal neurons after facial nerve lesion with morphological bias towards the activated phenotype. These results suggest that facial nerve lesions elicit active dendrite remodeling due to pyramidal neuron and microglia interaction, which could be the pathophysiological underpinning of some neuropathic motor sequelae in humans.

## 1. Introduction

After peripheral nerve axotomy, injured motoneurons undergo both morphological and physiological modifications, including dendritic branches retraction [1, 2], enhanced brain-derived neurotrophic factor [3, 4], c-Fos, and c-Jun expression [5, 6], and changes regarding their active and passive electrophysiological properties [7–9]. Such modifications apparently facilitate motoneuronal survival and the regeneration of their axons. However, depending on whether it is central or peripheral, axotomy would induce motoneuronal death [10]. The mechanisms involved in axotomy induced motoneuronal death are not well understood; however, the loss of muscle fiber-derived trophic factors may

be partly responsible [11]. Peripheral nerve lesions have been used for evaluating injury-related neural plasticity not only in motoneurons but also in multiple brain structures. In fact, facial nerve axotomy in rodents has been widely used for studying vibrissal motor system plasticity at different levels [10].

It has been described that a layer 5 pyramidal neuron subpopulation in the vibrissal primary motor cortex (vM1) sends a monosynaptic projection to facial nucleus motoneurons [12]. Although, given such connectivity, it is plausible that facial motoneuron axotomy could transsynaptically induce modifications in vM1, such changes have scarcely been explored. In this vein, it has been described that peripheral facial nerve injury induces astroglial activation in vM1 and

other cortical areas as evidenced by transient enhancement of S-100 protein, glial fibrillary acidic protein, and connexin 43 expression [13]. Using c-Fos immunoreactivity as a marker for neuronal activation, it has been found that vM1 volume acutely responding to facial nerve axotomy in sighted rats is twofold smaller than in blind animals and that the degree of acute cortical activation is directly related to the degree of late motor recovery [14]. Significant retraction of layer 5 pyramidal neuron dendritic arborization in vM1 after contralateral facial nerve transection has been described using Golgi-Cox staining [15]. Persistent changes in the electrophysiological properties of layer 5 pyramidal neurons in the primary motor cortex (vM1) induced by facial nerve lesions have been described recently [16]. These changes included increased dendritic excitability of layer 5 pyramidal neurons that could be explained by membrane surface loss due to retraction of their dendritic arborization.

On the other hand, it has been shown that both axotomized [17] and denervated neurons undergo remodeling of their dendritic arborizations [18] following central nervous system (CNS) lesions. Additionally, it has been described that both axotomized and denervated neurons in the CNS display enhanced chemokine expression. Moreover, chemokines activate resident microglial cells and such activation is necessary for dendritic remodeling to occur [18]. It has also been shown that microglial accumulation around the perikarya of axotomized neurons in the CNS is closely related to axonal regeneration [19].

Taking into account the timing of facial nerve lesion induced changes in pyramidal neurons found in previous experiments of our group, the present study was aimed at evaluating the dendritic arborization of layer 5 pyramidal neurons and the density and morphology of the microglia surrounding them in vM1 at one and three weeks after contralateral facial nerve axotomy. To do so, TgH(CX3CR1-EGFP)xTgN(THY1.2-EYFP) transgenic mice were used as they express enhanced yellow fluorescent protein in pyramidal neurons and enhanced green fluorescent protein in microglial cells. Our results showed that peripheral facial nerve axotomy induced persistent shrinking of apical and basal dendrites of layer 5 pyramidal cells in vM1, accompanied by a significant increase of neighboring microglia density with a shift towards activated phenotype.

## 2. Experimental Procedures

**2.1. Subjects.** Twelve adult male TgH(CX3CR1-EGFP)xTgN(THY1.2-EYFP) mice, weighing  $23 \pm 1.5$  g (mean  $\pm$  standard error of the mean (SEM)), kindly supplied by the Glial Physiology and Imaging Group (Department of Neurogenetics, Max Planck Institute for Experimental Medicine, Göttingen, Germany) were used as subjects. The animals were housed in the Max Planck Institute for Experimental Medicine (Göttingen, Germany) mouse facility, having *ad libitum* access to food and water, and being kept in a sound-attenuated room with controlled humidity ( $40 \pm 5\%$ ) and temperature ( $20 \pm 1^\circ\text{C}$ ) using a 12 h light/dark cycle (lights on at 07:00 a.m.). All experimental procedures

were performed according to the Max-Planck-Society and European guidelines for the welfare of experimental animals and were approved by the local Ethics Committee. All efforts were made to minimize the number of animals used and avoid unnecessary suffering to the experimental subjects.

TgH(CX3CR1-EGFP)xTgN(THY1.2-EYFP) mice were obtained by crossbreeding homozygous CX3CR1-EGFP mice, in which enhanced green fluorescent protein (EGFP) expression in microglia is achieved by placing the EGFP reporter gene into the *Cx3cr1* locus encoding the chemokine receptor CX3CR1 [20], with transgenic THY1.2-EYFP mice expressing enhanced yellow fluorescent protein (EYFP) in projection neurons and their respective axons [21]. TgH(CX3CR1-EGFP) mice and TgN(THY1.2-EYFP) mice were of B6SJL background for more than 10 generations.

**2.2. Facial Nerve Lesion Surgery.** Eight randomly chosen mice underwent facial nerve transection surgery in aseptic conditions and under general anesthesia (100 mg/kg ketamine and 10 mg/kg xylazine, administered intraperitoneally). Briefly, the facial nerve's buccal branch and the upper division of the marginal mandibular branch were dissected and severed through a 0.5 cm horizontal incision made above the right mandibular angle; a 2 mm segment of the proximal stump was removed in each sectioned nerve branch to avoid nerve repair and the skin wound was sutured with discontinuous 5-0 silk stitches (Figure 1(a)). Nerve branch identity and lesion effectiveness were confirmed by electrical stimulation [22].

Four randomly chosen subjects underwent sham surgery (control). Briefly, the buccal branch and the upper division of the marginal mandibular branch of the facial nerve were dissected through a 0.5 cm horizontal incision above the right mandibular angle, but left intact; the skin wound was sutured with discontinuous 5-0 silk stitches.

**2.3. Histology.** Subjects undergoing facial nerve axotomy were allowed a recovery period of either 1 week ( $n = 4$ ) or 3 weeks ( $n = 4$ ) before being sacrificed for histological analysis. Sham-operated subjects ( $n = 4$ ) were allowed a one week recovery period before being killed for histological analysis (Figure 1(b)). After the recovery time had elapsed, the mice were deeply anesthetized with isoflurane (1.5–2.5%; mixed with 0.6 to 0.8 liters/min  $\text{O}_2$ ) and transcardially perfused with Hank's balanced salt solution (HBSS, Gibco) followed by 4% paraformaldehyde in 0.1 M phosphate buffered saline. The brains were dissected after the perfusion and postfixed overnight in 4% paraformaldehyde in 0.1 M phosphate buffered saline at  $4^\circ\text{C}$ . Serial 80  $\mu\text{m}$  thick coronal slices (1 to 2.5 mm rostral to bregma) containing the vM1 (i.e., medial agranular cortex, from midline to 1.5 mm lateral) were obtained using a vibratome (Leica VT 1000S, Leica Instruments, Germany).

**2.4. Microscopy.** Image stacks of the fixed brain sections were recorded using a two-photon laser scanhead (TriM-Scope, La Vision Biotec, Bielefeld, Germany) coupled to a fixed stage upright microscope (Axioscope 2 FS, Zeiss, Oberkochen,

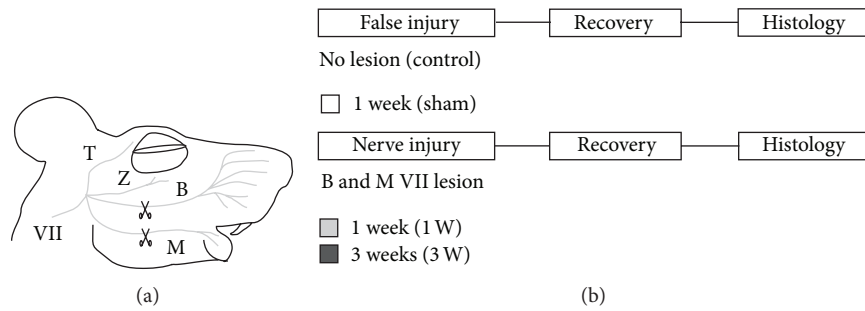


FIGURE 1: Experimental preparation and design. (a) Lateral view of a mouse's head, schematizing facial nerve branches innervating face muscles; the branches transected during irreversible nerve lesion surgery, as well as the approximate place where they were cut, are indicated by scissors. T, temporal; Z, zygomatic; B, buccal; and M, mandibular branches of VII facial nerve. (b) Schema of the experimental design showing its time line and indicating the color representing each group (white for sham, light gray for 1 week, and black for 3 weeks after facial nerve lesion).

Germany). Two-photon excitation at 910 nm achieved by a titanium-sapphire laser equipped with broadband optics (MaiTai BB, Spectra Physics) and emission fluorescence detection through a 530–600 nm band pass filter were used for detecting pyramidal neurons expressing EYFP. Excitation at 970 nm and fluorescence detection through a 500–530 nm band pass filter were used for detecting microglial cells expressing EGFP. Non-descanned detection (Hamamatsu, Japan) was used to record three-dimensional image stacks having 1,024 pixel  $\times$  1,024 pixel frame size (200  $\mu$ m  $\times$  200  $\mu$ m scan field) through a 40x, 1.3 numerical aperture oil objective (Zeiss).

**2.5. Data Processing and Analysis.** EYFP-expressing pyramidal neurons from layer 5 in vM1 were identified by their characteristic triangular soma shape, apical dendrites oriented towards the pial surface, and presence of dendritic spines. Image stacks containing the dendritic arborization of a given pyramidal neuron were then overlapped using ImageJ (<http://rsb.info.nih.gov/ij/>). Three layer 5 vM1 neurons whose dendritic trees were extensively represented in the overlapped stack were then selected for every subject for reconstruction using Neuromantic 1.6.3, an open source system for three-dimensional digital tracing of neurites [23].

The three-dimensionally reconstructed dendritic arborizations were then compressed to a single plane and skeletonized using ImageJ routines for Sholl analysis [24]. Briefly, concentric circles were traced, starting from the soma, increasing their radius by 4  $\mu$ m, and then the branches intersected by each circle were counted using an ImageJ routine. A plot illustrating how the number of branches varied as a function of distance from the soma was constructed and the area under the curve (AUC), the maximum, and the full width half maximum (FWHM) were calculated [25].

Dendritic spine density was estimated by counting the number of spines found in a randomly selected 10  $\mu$ m long segment of a dendritic branch. Dendritic branches were classified as either apical or basal and then as primary, secondary, or tertiary. An ImageJ routine was used for spine counting.

Microglial cells from layer 5 in vM1 were identified by their EGFP expression. Image stacks containing only layer 5 of vM1 (to do so, a region of interest encompassing 500 to 1000  $\mu$ m from pial surface in the medial agranular cortex was defined) were selected for analysis. Microglial cells per volume unit density and the area of each cell's soma were measured using automated ImageJ analyse particles routine (16-bit grayscale images' contrast was enhanced to discriminate individual cells, and then size and shape criteria were set to exclude noisy particles).

Differences among groups were statistically evaluated for every parameter using SigmaPlot 12.0 (Systat Software Inc., Chicago, USA) one-way analysis of variance (ANOVA) module; significance level was set at  $P < 0.05$ . Whenever ANOVA revealed a significant difference, Holm-Sidak *post hoc* multiple pairwise *t*-tests were performed to identify the source of such difference.

### 3. Results

**3.1. Vibrissal Paralysis.** Unilateral section of the buccal and mandibular facial nerve branches induced complete paralysis of the right mystacial vibrissae, which persisted for at least three weeks. The whiskers were oriented backwards during the first recovery week, forming a narrow bunch; from that time on, the whisker bunch progressively loosened but still remained immobile. Sham-operated mice whisking was not distinguishable from that of nonoperated mice (data not shown).

**3.2. Facial Nerve Lesion Induced Dendritic Remodeling of vM1 Pyramidal Neurons.** Facial nerve axotomy induced changes in the dendritic architecture of pyramidal neurons of the layer 5 in contralateral vM1 (Figure 2). The total length of the apical dendrites changed significantly after facial nerve injury ( $F_{(2, 33)} = 3.500$ ,  $P = 0.042$ ). One week after the injury (Figure 2(d)) apical dendrites became pruned and their total length became significantly shorter than that of sham-operated subjects ( $t = 2.560$ ,  $P = 0.045$ ). Apical dendrites had partially regrown three weeks after the lesion

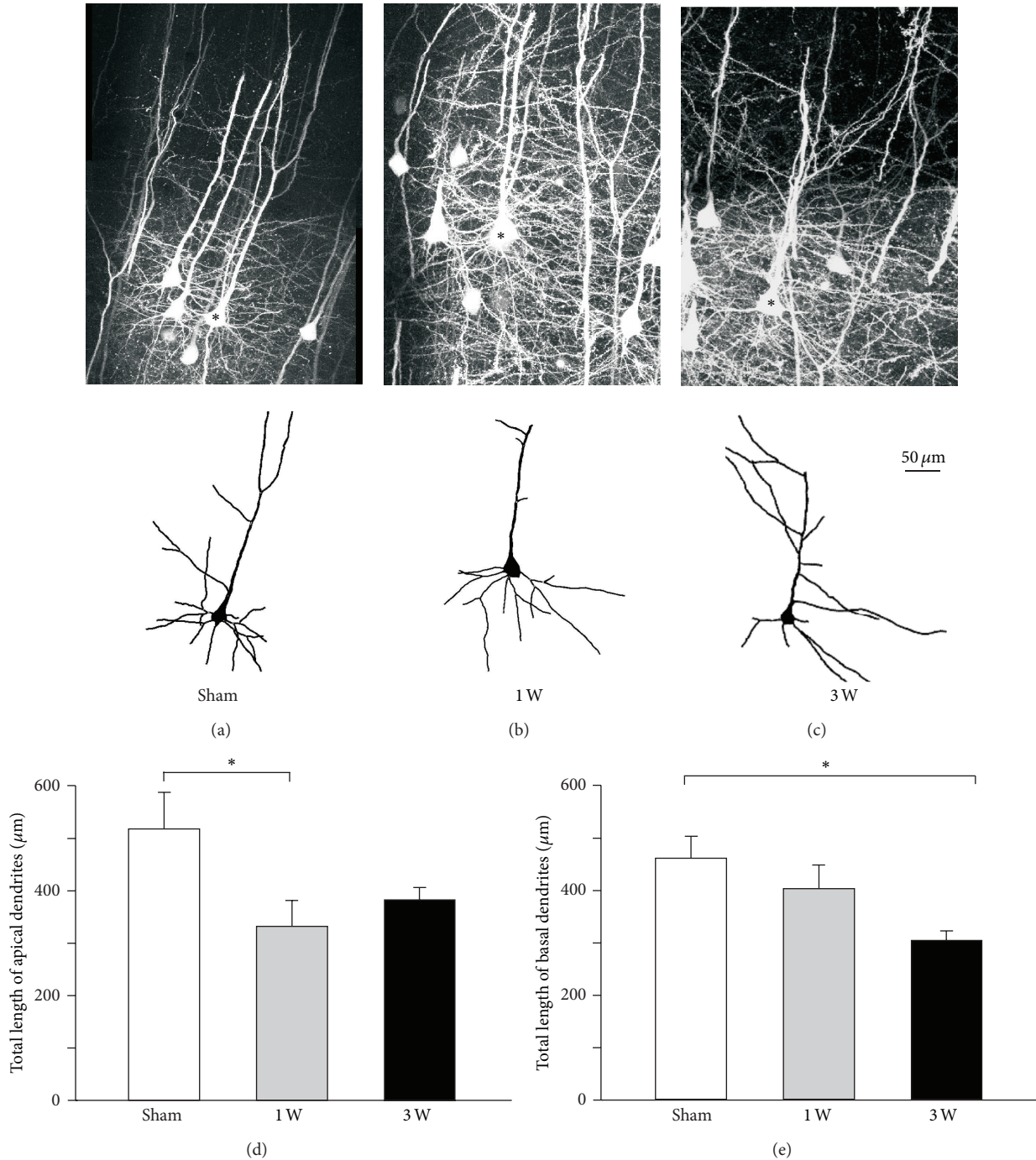


FIGURE 2: Differential apical and basal dendrite length modifications in vM1 layer 5 pyramidal neurons following facial nerve axotomy. (a, b, c) Top row, two-dimensional projection of stacks of two-photon confocal images of vibrissal motor cortex layer 5 pyramidal neurons expressing EYFP; bottom row, two-dimensional computer-assisted traces of layer 5 pyramidal neurons from sham and injured animals (reconstructed neurons are indicated by an asterisk in top row images). Micrographs and reconstructions obtained either from mice undergoing (a) sham surgery, (b) one week recovery after facial lesion, and (c) three-week recovery after facial lesion. (d) Total length of apical dendritic tree of layer 5 pyramidal neurons from each experimental group. (e) Total length of basal dendritic tree of layer 5 pyramidal neurons from each experimental group. Bars and error whiskers represent the mean + SEM. 1 W, 1 week after peripheral nerve lesion; 3 W, 3 weeks after peripheral nerve lesion; \* $P < 0.05$ .

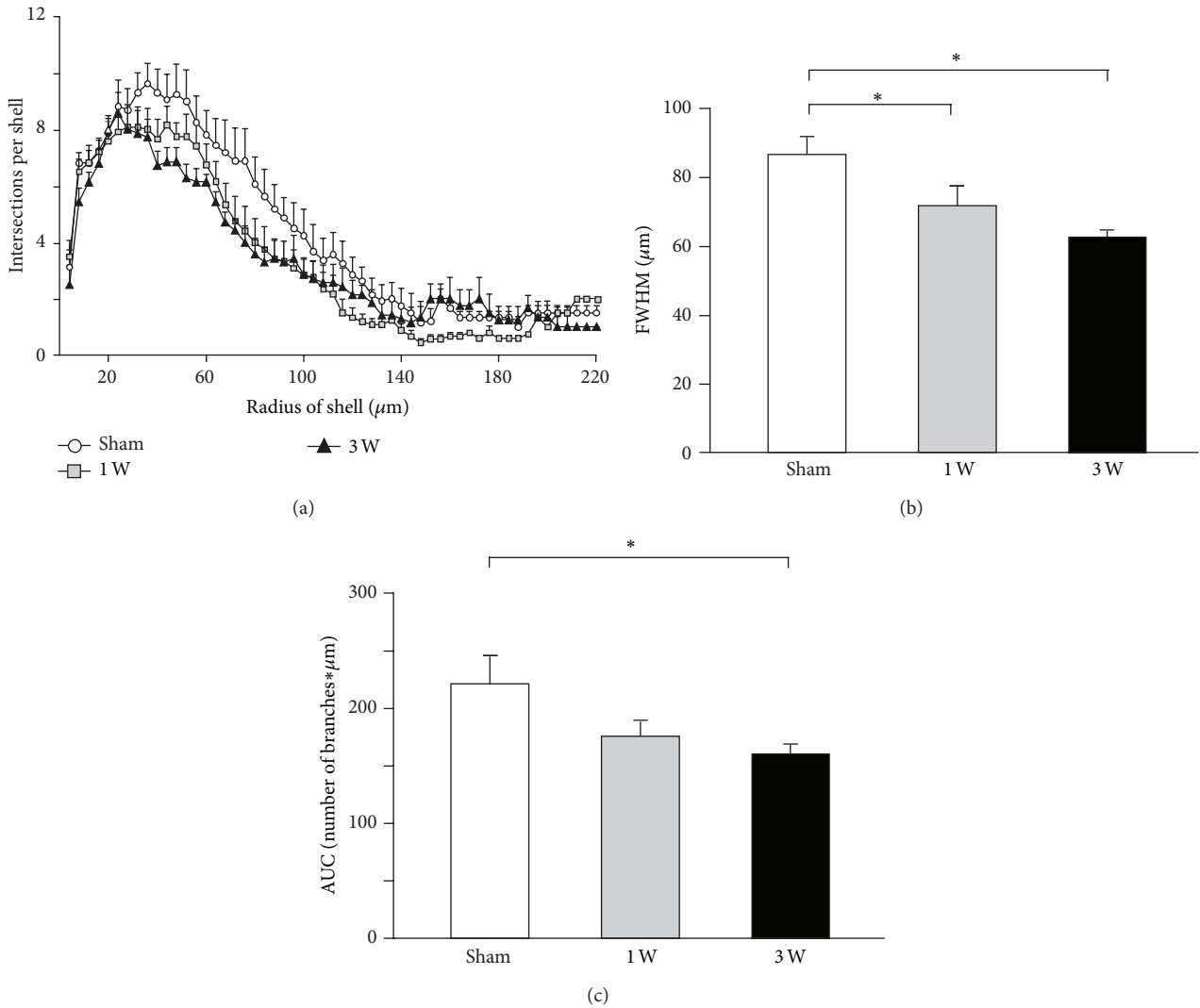


FIGURE 3: Overall dendritic tree shrinkage in vM1 layer 5 pyramidal neurons following contralateral facial nerve axotomy. (a) Sholl analysis indicating the number of dendrite branches crossing concentric circles around the cell body. Symbols and associated error bars correspond to the mean  $\pm$  SEM. (b) Full width half maximum (FWHM) of Sholl distribution from each experimental group. Bars and error whiskers represent the mean + SEM. (c) Sholl distribution area under the curve (AUC) from each experimental group. Bars and error whiskers represent the mean + SEM. 1 W, 1 week after peripheral nerve lesion; 3 W, 3 weeks after peripheral nerve lesion; \*  $P < 0.05$ .

(Figure 2(d)) and their total length was not significantly different from that of control subjects ( $t = 1.858, P = 0.139$ ).

Facial nerve axotomy also induced significant changes in the total length of basal dendrites of pyramidal neurons in contralateral vM1 ( $F_{(2, 33)} = 4.475, P = 0.019$ ). One week after the lesion (Figure 2(e)) basal dendrites' total length was not significantly different from that observed in sham-operated subjects ( $t = 1.093, P = 0.283$ ). However, three weeks after the injury (Figure 2(e)), the basal dendrites became pruned and their total length became significantly shorter than that of control subjects ( $t = 2.958, P = 0.017$ ).

Although the apical to basal total length ratio did not significantly change after facial nerve injury ( $F_{(2, 33)} = 2.161, P = 0.131$ ), the correlation between apical and basal dendrites' total length disappeared after facial nerve axotomy.

In fact, control subjects' total apical dendrite length was positively and significantly correlated to total basal dendrite length ( $r = 0.970, P = 0.001$ ). Due to the changes described above regarding apical and basal dendritic branches, such correlation became weaker and nonsignificant both one week ( $r = 0.312, P = 0.324$ ) and three weeks ( $r = -0.231, P = 0.659$ ) after facial nerve section.

The dendritic arborization of vM1 layer 5 pyramidal neurons shrank globally after contralateral facial nerve axotomy, as indicated by Sholl analysis of the distribution of the number of dendritic branches as a function of distance from the soma (Figure 3). The maximum for such distribution did not significantly change after facial nerve lesion (Figure 3(a);  $F_{(2, 33)} = 1.032, P = 0.368$ ). However, the FWHM became significantly smaller than control from the first week after

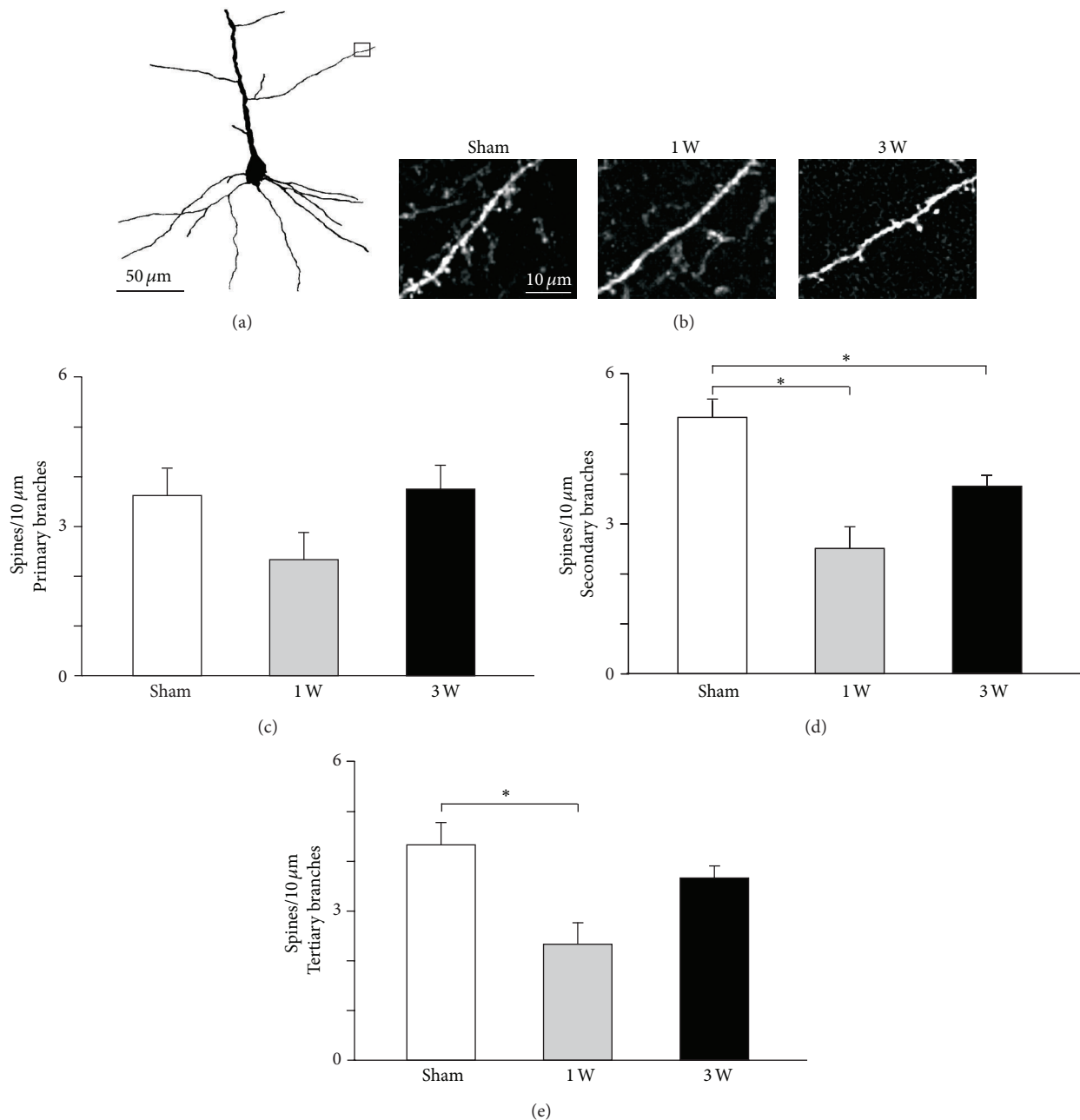


FIGURE 4: Apical dendritic spine density changes in vM1 layer 5 pyramidal neurons following facial nerve axotomy. (a) Two-dimensional computer-assisted trace of layer 5 pyramidal neuron from a representative mouse sacrificed 1 week after facial nerve lesion. The small rectangle indicates the area photographed in (b). (b) Representative microphotographs of second order dendritic spines from each experimental group. (c, d, e) Quantification of layer 5 pyramidal neurons spine density in 1st, 2nd, and 3rd order apical dendrites for each experimental group. Bars and error whiskers represent the mean + SEM. 1 W, 1 week after peripheral nerve lesion; 3 W, 3 weeks after peripheral nerve lesion; \* $P < 0.05$ .

facial nerve axotomy onwards and remained so for at least three weeks (Figure 3(b);  $F_{(2, 33)} = 7.468$ ,  $P = 0.002$ ; sham versus 1 week:  $t = 2.369$ ,  $P = 0.047$ ; sham versus 3 weeks:  $t = 3.829$ ,  $P = 0.002$ ). Meanwhile, the area under the curve for such distribution significantly changed after facial nerve section (Figure 3(c);  $F_{(2, 33)} = 3.844$ ,  $P = 0.032$ ), becoming significantly smaller than control after three weeks (sham versus 1 week:  $t = 1.986$ ,  $P = 0.108$ ; sham versus 3 weeks:  $t = 2.669$ ,  $P = 0.035$ ).

**3.3. Facial Nerve Axotomy Induced Dendritic Spine Pruning in vM1 Pyramidal Neurons.** The density of dendritic spines of vM1 layer 5 pyramidal neurons became significantly reduced after contralateral facial nerve injury (Figure 4). Spine pruning occurred in secondary and tertiary apical dendrite branches, but not in their primary branches (Figure 4(c);  $F_{(2, 33)} = 2.280$ ,  $P = 0.118$ ). Spine density in secondary apical dendrite branches became significantly reduced after facial nerve lesion and remained so for at least three weeks

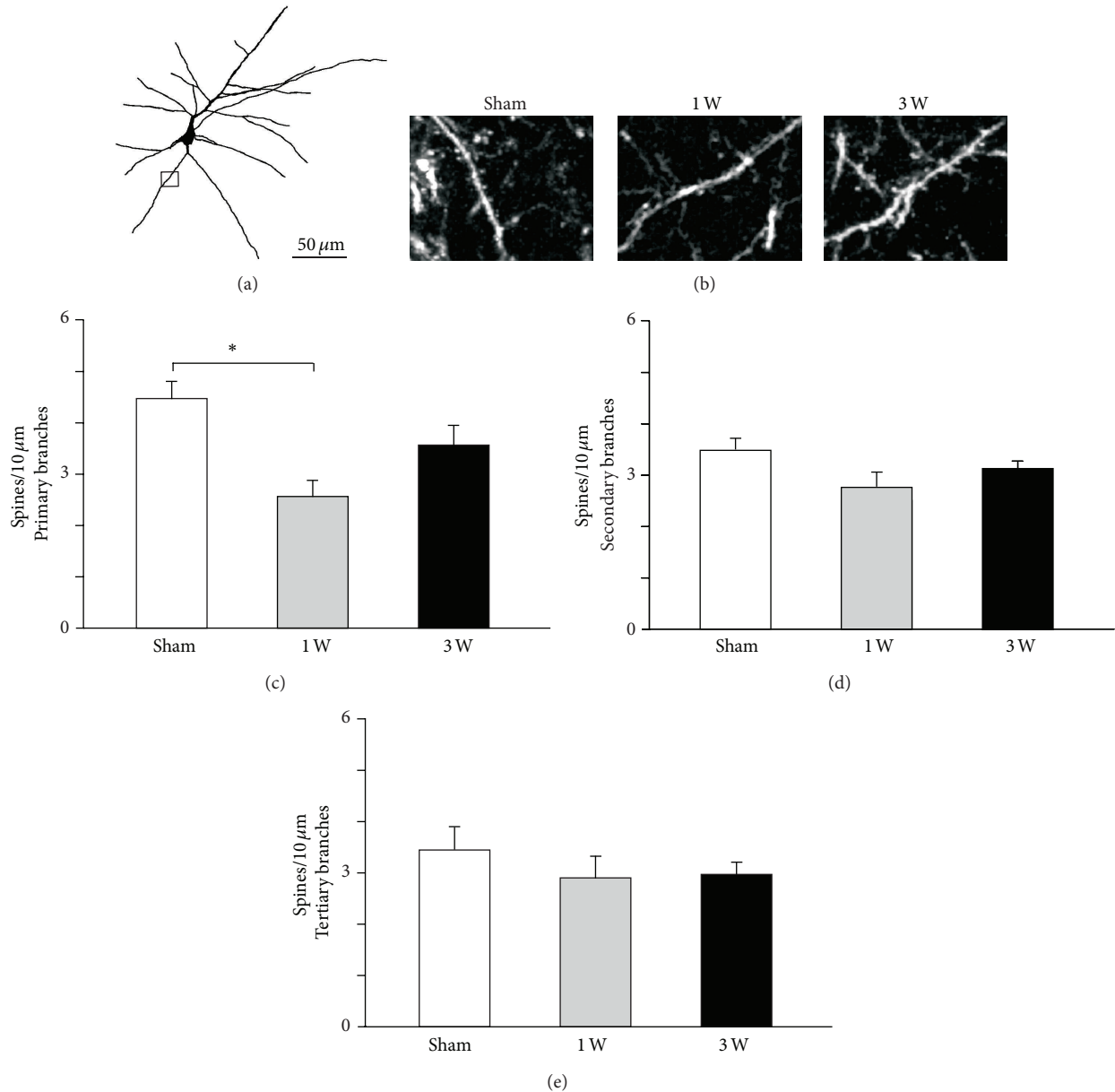


FIGURE 5: Basal dendritic spine density changes in vM1 layer 5 pyramidal neurons following facial nerve axotomy. (a) Two-dimensional computer-assisted trace of layer 5 pyramidal neuron from a representative mouse sacrificed 1 week after facial nerve lesion. The small rectangle indicates the area photographed in (b). (b) Representative microphotographs of first order dendritic spines for each experimental group. (c, d, e) Quantification of layer 5 pyramidal neurons spine density in 1st, 2nd, and 3rd order basal dendrites for each experimental group. Bars and error whiskers represent the mean + SEM. 1 W, 1 week after peripheral nerve lesion; 3 W, 3 weeks after peripheral nerve lesion; \* $P < 0.05$ .

(Figure 4(d);  $F_{(2,33)} = 14.345$ ,  $P < 0.001$ ; sham versus 1 week:  $t = 5.354$ ,  $P < 0.001$ ; sham versus 3 weeks:  $t = 2.805$ ,  $P = 0.017$ ). By contrast, dendritic spine pruning in the tertiary apical dendrite branches occurred only one week after facial nerve lesion but not three weeks later (Figure 4(e);  $F_{(2,33)} = 7.000$ ,  $P = 0.003$ ; sham versus 1 week:  $t = 3.674$ ,  $P = 0.003$ ; sham versus 3 weeks:  $t = 1.225$ ,  $P = 0.229$ ).

Contralateral facial nerve injury-induced spine pruning in the basal dendrites of vM1 layer 5 pyramidal neurons (Figure 5) was restricted to primary branches (Figure 5(c);  $F_{(2,33)} = 8.422$ ,  $P = 0.001$ ) and occurred transiently during

the first week after the lesion (sham versus 1 week:  $t = 4.099$ ,  $P < 0.001$ ; sham versus 3 weeks:  $t = 1.871$ ,  $P = 0.070$ ). There was a nonsignificant tendency in secondary basal dendrite branches towards decreased density of dendritic spines after contralateral facial nerve section (Figure 5(d);  $F_{(2,33)} = 3.256$ ,  $P = 0.051$ ). By contrast, spine density in tertiary basal dendrite branches did not significantly change after the injury (Figure 5(e);  $F_{(2,33)} = 2.035$ ,  $P = 0.217$ ).

3.4. Facial Nerve Section Induced Increased Microglial Density around vM1 Pyramidal Neurons. Evidence was found of

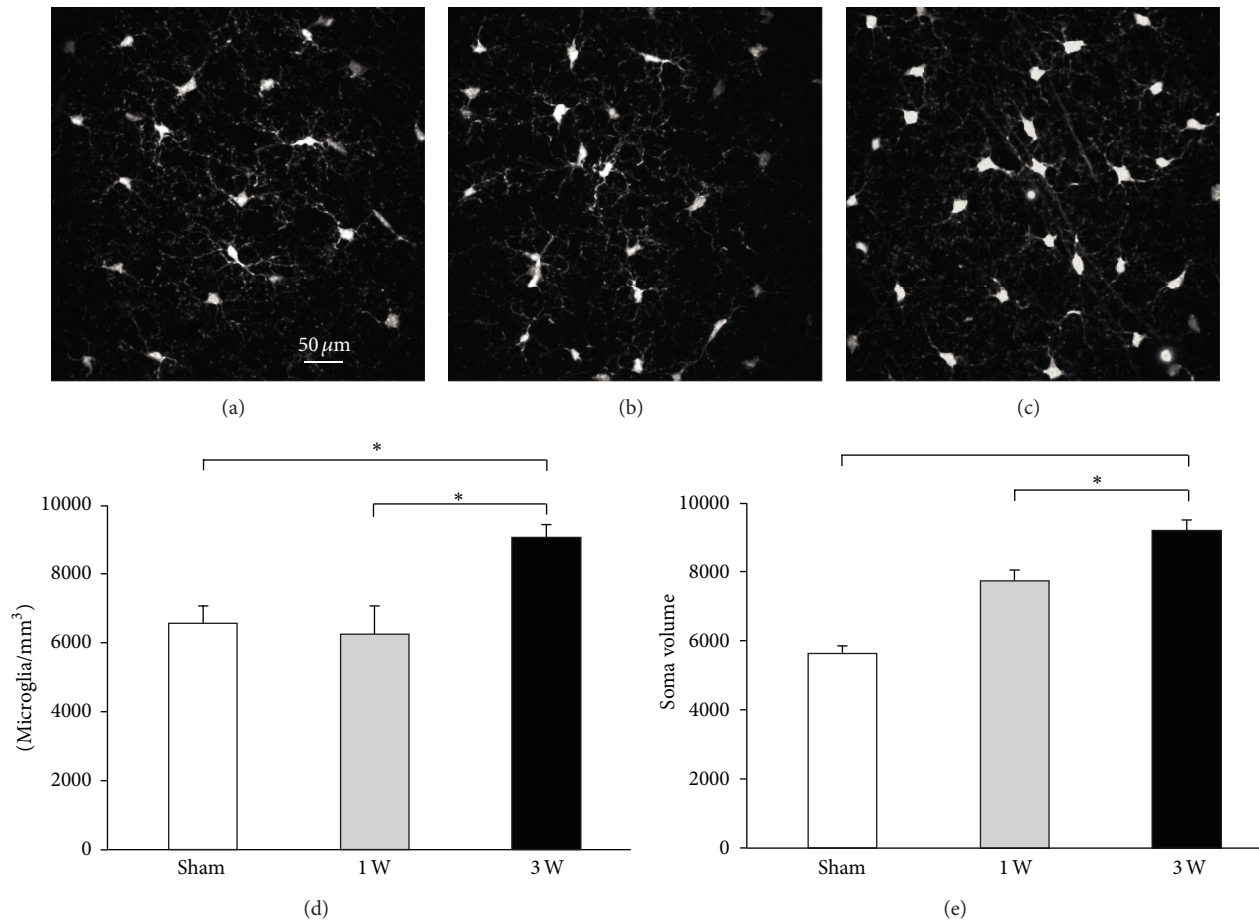


FIGURE 6: Increased microglial cell density and soma area surrounding vM1 layer 5 pyramidal neurons following facial nerve axotomy. (a, b, c) Microphotographs of microglia cells around vM1 layer 5 pyramidal neurons from representative sham (a), 1 week (b), and 3 weeks (c) mice. Quantification of cell density (d) and soma area (e) for microglial cells surrounding vM1 layer 5 pyramidal neurons from each experimental group. Bars and error whiskers represent the mean + SEM. 1 W, 1 week after peripheral nerve lesion; 3 W, 3 weeks after peripheral nerve lesion; \*  $P < 0.05$ .

microglial recruitment and bias towards activated phenotype surrounding vM1 layer 5 pyramidal neurons (Figure 6). The density of microglial cells surrounding vM1 layer 5 pyramidal neurons changed significantly after contralateral facial nerve lesion (Figure 6(d);  $F_{(2,33)} = 18.394$ ,  $P < 0.001$ ). One week (Figure 6(b)) after the axotomy there were no significant changes in microglial cell density (Figure 6(d); sham versus 1 week:  $t = 0.625$ ,  $P = 0.536$ ) with respect to that found in control subjects (Figure 6(a)). By contrast, three weeks after facial nerve injury (Figure 6(c)), heightened density was found for microglial cells surrounding vM1 layer 5 pyramidal neurons (Figure 6(d);  $t = 4.912$ ,  $P < 0.001$ ).

The morphology of the microglial cells surrounding vM1 layer 5 pyramidal neurons changed significantly after contralateral facial nerve axotomy (Figure 6(e);  $F_{(2,33)} = 5.161$ ,  $P = 0.011$ ). One week after the lesion (Figure 6(b)) there was a nonsignificant increase in the soma of microglial cells with respect to that found in control subjects (Figure 6(e);  $t = 1.890$ ,  $P = 0.131$ ). By contrast, three weeks after the axotomy (Figure 6(c)), microglial cell somata became significantly larger than control (Figure 6(e);  $t = 3.195$ ,  $P = 0.009$ ).

Also, three weeks after the injury, the processes of microglial cells became shorter and became oriented surrounding layer 5 pyramidal cells dendrites (Figure 6(c), arrows).

#### 4. Discussion

This research has shown that an irreversible lesion of the buccal and mandibular branches of the facial nerve induced not only complete and permanent vibrissal paralysis, but also progressive and long-lasting changes in the dendritic morphology of vM1 layer 5 pyramidal neurons as well as increased density and a shift towards activated phenotype in the surrounding microglia.

Our group has previously used the Golgi-Cox staining technique to show that irreversible peripheral facial nerve lesion in rats induces a significant retraction of the dendritic arborization of layer 5 pyramidal neurons in contralateral vM1 [15]. The present work has further characterized the dynamics of dendritic arborization remodeling, using two-photon confocal microscopy to scan EYFP-expressing pyramidal neurons of layer 5 in the vM1 of mice submitted to

irreversible facial nerve lesion. The dendritic arborization of the pyramidal cells underwent overall shrinkage, persisting for at least three weeks; however, such shrinkage was not homogeneous in space or time. In fact, apical dendrites underwent transient shortening one week after facial nerve lesion, which became almost completely reverted by the third week. By contrast, basal dendritic remodeling followed an inverse pattern after facial nerve section; although basal tree became progressively shorter, such change only became significant three weeks after axotomy. In addition, this work also led to finding that vM1 layer 5 pyramidal neurons underwent dendritic spine pruning after facial nerve injury occurring in distal apical and in proximal basal branches. vM1 layer 5 pyramidal neurons receive segregated sensory and motor input; somatosensory input, coming from primary somatosensory cortex and posteromedial thalamic nucleus, is primarily directed towards distal apical dendrite branches, while motor input, coming from M2, orbital cortex and motor thalamic nuclei, is primarily directed towards proximal basal dendrite branches and soma [26]. Horizontal projections from neighboring cortical columns are mainly distributed in layer 2/3, therefore impinging on apical dendrites of layer 5 pyramidal neurons [27]. Layer 5 pyramidal neurons' basal dendrites also receive recurrent excitatory input from axons of projecting neurons [28] and it has been suggested that such recurrent input synchronizes the firing of multiple corticofacial neurons during the generation of vibrissal motor commands [29]. Transient branch retraction and spine pruning in distal apical dendrites may therefore have been related to an initial retraction of regular somatosensory input succeeded by invasion by either horizontal projections from neighboring cortical columns or a different set of somatosensory input, which may have shifted commitment regarding somatosensory information. In addition, progressive retraction and spine pruning in proximal basal dendrites may be related to ongoing disengagement from motor input and synchronizing retrograde projections, which may render vM1 less efficient to generate motor commands.

A previous paper by our group described that vM1 layer 5 pyramidal neurons displayed increased dendritic excitability and decreased response to whisker-pad stimulation after contralateral facial nerve axotomy [16]. Both findings could be related to the structural modifications described herein; while a loss of dendritic membrane would cause increased excitability due to increased input resistance, a loss of synaptic input (as evidenced by dendritic spine pruning) would explain the decreased response to somatosensory stimulation. The aforementioned structural and functional modifications in vM1 layer 5 pyramidal neurons induced by contralateral facial nerve axotomy could have been caused by a loss of synaptic communication with target facial motoneurons and an imbalance in somatosensory information processing induced by vibrissal immobility.

On the one hand, facial motoneuron axotomy, apart from direct cellular damage, interrupts the trophic relationship between motoneurons and the muscle fiber they have used to innervate which, in turn, causes structural, metabolic, electrophysiological, and molecular alterations associated with a survival and regeneration programme, not only in

axotomized motoneurons, but also in their surrounding glial cells [10]. As a consequence of such response, vM1 layer 5 pyramidal neurons lose their synaptic targets within the facial nucleus due to progressive dendritic retraction and synaptic stripping of axotomized facial motoneurons, which implies that corticofacial neurons become deprived of the neurotrophic factors released by motoneurons. In fact, pyramidal tract lesion (which interrupts the trophic interaction between corticospinal neurons in the primary motor cortex and their targets) induces a reduction in somatic volume, increased excitability, and reduced inhibitory synaptic input in primary motor cortex layer 5 pyramidal neurons [30]. Moreover, it has been described that the premotor neuron phenotype changes after injury to the motoneurons over which they project [31].

On the other hand, vM1 reorganization after facial nerve lesion depends critically on the alteration of vibrissal somatosensory input. A section of the infraorbital nerve induces vibrissal representation shrinkage in neonatal rats [32] and a significant increase in the minimum intracortical vM1 stimulation intensity required to evoke vibrissal movements in adult rats [33]. Transiently restricting sensory and motor vibrissal functions, either by total whisker clipping [34] or botulinum toxin application in the whisker pad [35, 36], causes reversible shrinkage of the cortical representation of vibrissal musculature and its invasion by neighboring representations. Taken together, these antecedents suggest that vibrissal paralysis causes a remarkable imbalance in somatosensory input to vM1. Perturbation of whisker paralysis-induced vibrissal sensory function would then cause disruption of somatosensory afferents.

Irreversible facial nerve lesion induced increased density and a shift towards activated phenotype in the microglia surrounding vM1 layer 5 pyramidal neurons; such microglial changes occurred after a delay lasting longer than a week. To our knowledge, this is the first report ever of microglial recruitment and bias towards activated phenotype in vM1 following facial nerve section. The long delay of microglial response described here in vM1 is also noteworthy. In fact, microglial cells become activated by diverse injuries to CNS neurons; such activation occurs within tens of minutes after direct injury, as observed in the cortex after medial cerebral artery occlusion [37]. Microglial activation can follow a slower pace, within days, when lesion occurs far from the neuronal soma, as observed in facial motoneurons following facial nerve axotomy [38]. Microglial activation starts even later in structures secondarily affected by injury, like the thalamus after medial cerebral artery occlusion [37, 39].

It is plausible that the microglial response in vM1 reported here was due to biochemical changes in layer 5 corticofacial neurons induced by retrograde transsynaptic signaling from the axotomized facial motoneurons over which they project. Such retrograde signaling occurs after axotomy, since motor cortex astrocyte activation after peripheral facial nerve lesion has been reported to occur as soon as 1h after lesion and disappear 5-6 days later [13]. vM1 layer 5 pyramidal cells may thus have induced and controlled microglial activation through the secretion of diverse cytokines. In fact, neuronal secretion of C-X-C motif chemokine 10 elicits

microglial activation through interaction with microglial C-X-C chemokine receptor 3 and such activation is essential for dendritic remodeling after axotomy of corticospinal neurons [18]. Additionally, neuronal secretion of fractalkine prevents microglial neurotoxicity through interaction with microglial [40] and neuronal CX3CR1 receptor [41]. Moreover, it has been reported that marked microglial activation occurs around the cell bodies of intrinsic CNS neurons regenerating axons into a peripheral nerve graft, and such activation is closely correlated with axonal regeneration [39]. The observed microglial response in vM1 after facial nerve axotomy might therefore have been related to dendritic remodeling and spine pruning and axon growth towards a new synaptic target.

The facial nerve lesion induced structural changes in vM1 layer 5 pyramidal cells described here imply active reorganization of intrinsic cortical circuitry associated with controlled microglial response. Such reorganization seems to have been directly related to functional changes in vM1 layer 5 pyramidal neurons following facial axotomy, as described elsewhere [16]. Such structural and functional modifications may occur in people with facial palsy and may represent the pathophysiological underpinning of some of the functional sequelae found in them and in patients suffering other peripheral neuropathies. The facial nerve axotomy model is therefore helpful in understanding cortical plasticity related to peripheral nerve injury and the pathophysiology of neuropathic sequelae in human beings.

## 5. Conclusions

The facial nerve lesion induced facial paralysis and structural changes in vM1 layer 5 pyramidal cells that project to facial muscles. These central nervous system changes were long lasting and imply dendritic reorganization of pyramidal neurons and dendritic spine pruning of layer 5 pyramidal neurons. These changes were associated with surrounding microglial response and seem to have been directly related with functional changes in vM1 layer 5 pyramidal neurons. Such structural and functional modifications may occur in people with facial palsy and may represent the pathophysiological underpinning of some of the functional sequelae found in these patients.

## Abbreviations

1 W:	1 week
3 W:	3 weeks
ANOVA:	Analysis of variance
AUC:	Area under the curve
CNS:	Central nervous system
CX3CR1:	CX3 chemokine receptor 1
C-X-C:	Protein motif containing two cysteine residues separated by any amino acid
EGFP:	Enhanced green fluorescent protein
EYFP:	Enhanced yellow fluorescent protein
FWHM:	Full width half maximum
SEM:	Standard error of the mean

THY: Thymocyte differentiation antigen  
vM1: Vibrissal primary motor cortex.

## Conflict of Interests

The authors declare that there is no conflict of interests regarding the publication of this paper.

## Acknowledgments

This experiment was financed by grants from COLCIENCIAS (no. 1101-452-21092), DIB (no. 7480), and Fundación para la Promoción de la Investigación y la Tecnología (FPIT-911, no. 2425). The authors would like to thank Dr. Walter Stühmer for allowing Diana Urrego to perform the experiments at the Max Plank Institute for Experimental Medicine, Göttingen, Germany, Dr. Frank Kirchoff and the whole Max Plank Institute's Glial Physiology and Imaging Group for their kind donation of the transgenic mice used in this work, and Mr. Jason Garry for his help in editing the paper.

## References

- [1] T. Brännström and J.-O. Kellerth, "Recovery of synapses in axotomized adult cat spinal motoneurons after reinnervation into muscle," *Experimental Brain Research*, vol. 125, no. 1, pp. 19–27, 1999.
- [2] F. Peyghambari, M. R. Valojerdi, and T. Tiraihi, "A morphometric study on the early stages of dendrite changes in the axotomized motoneuron of the spinal cord in newborn rats," *Neurological Research*, vol. 27, no. 6, pp. 586–590, 2005.
- [3] Q. Yan, C. Matheson, O. T. Lopez, and J. A. Miller, "The biological responses of axotomized adult motoneurons to brain-derived neurotrophic factor," *The Journal of Neuroscience*, vol. 14, no. 9, pp. 5281–5291, 1994.
- [4] N. R. Kobayashi, A. M. Bedard, M. T. Hincke, and W. Tetzlaff, "Increased expression of BDNF and trkB mRNA in rat facial motoneurons after axotomy," *European Journal of Neuroscience*, vol. 8, no. 5, pp. 1018–1029, 1996.
- [5] C. A. Haas, C. Donath, and G. W. Kreutzberg, "Differential expression of immediate early genes after transection of the facial nerve," *Neuroscience*, vol. 53, no. 1, pp. 91–99, 1993.
- [6] A. B. Schmitt, S. Breuer, J. Liman et al., "Identification of regeneration-associated genes after central and peripheral nerve injury in the adult rat," *BMC Neuroscience*, vol. 4, article 8, 2003.
- [7] B. Gustafsson, "Changes in motoneurone electrical properties following axotomy," *Journal of Physiology*, vol. 293, pp. 197–215, 1979.
- [8] R. Laiwand, R. Werman, and Y. Yarom, "Electrophysiology of degenerating neurones in the vagal motor nucleus of the guinea-pig following axotomy," *Journal of Physiology*, vol. 404, pp. 749–766, 1988.
- [9] G. Z. Mentis, E. Díaz, L. B. Moran, and R. Navarrete, "Early alterations in the electrophysiological properties of rat spinal motoneurons following neonatal axotomy," *Journal of Physiology*, vol. 582, no. 3, pp. 1141–1161, 2007.
- [10] L. B. Moran and M. B. Graeber, "The facial nerve axotomy model," *Brain Research Reviews*, vol. 44, no. 2-3, pp. 154–178, 2004.

- [11] S. Wiese, M. Beck, C. Karch, and M. Sendtner, "Signalling mechanisms for survival of lesioned motoneurons," *Acta Neurochirurgica, Supplementum*, no. 89, pp. 21–35, 2004.
- [12] V. Grinevich, M. Brecht, and P. Osten, "Monosynaptic pathway from rat vibrissa motor cortex to facial motor neurons revealed by lentivirus-based axonal tracing," *The Journal of Neuroscience*, vol. 25, no. 36, pp. 8250–8258, 2005.
- [13] R. Laskawi, A. Rohlmann, M. Landgrebe, and J. R. Wolff, "Rapid astroglial reactions in the motor cortex of adult rats following peripheral facial nerve lesions," *European Archives of Oto-Rhino-Laryngology*, vol. 254, no. 2, pp. 81–85, 1997.
- [14] G. P. Peeva, S. K. Angelova, O. Guntinas-Lichius et al., "Improved outcome of facial nerve repair in rats is associated with enhanced regenerative response of motoneurons and augmented neocortical plasticity," *European Journal of Neuroscience*, vol. 24, no. 8, pp. 2152–2162, 2006.
- [15] D. Urrego, A. Múnera, and J. Troncoso, "Peripheral facial nerve lesion induced long-term dendritic retraction in pyramidal cortico-facial neurons," *Biomedica*, vol. 31, no. 4, pp. 560–569, 2011.
- [16] A. Múnera, D. M. Cuestas, and J. Troncoso, "Peripheral facial nerve lesions induce changes in the firing properties of primary motor cortex layer 5 pyramidal cells," *Neuroscience*, vol. 223, pp. 140–151, 2012.
- [17] A. L. A. Mascaro, P. Cesare, L. Sacconi et al., "In vivo single branch axotomy induces GAP-43-dependent sprouting and synaptic remodeling in cerebellar cortex," *Proceedings of the National Academy of Sciences of the United States of America*, vol. 110, no. 26, pp. 10824–10829, 2013.
- [18] A. Rappert, I. Bechmann, T. Pivneva et al., "CXCR3-dependent microglial recruitment is essential for dendrite loss after brain lesion," *The Journal of Neuroscience*, vol. 24, no. 39, pp. 8500–8509, 2004.
- [19] B. N. Shokouhi, B. Z. Y. Wong, S. Siddiqui et al., "Microglial responses around intrinsic CNS neurons are correlated with axonal regeneration," *BMC Neuroscience*, vol. 11, article 13, 2010.
- [20] S. Jung, J. Aliberti, P. Graemmel et al., "Analysis of fractalkine receptor CX<sub>3</sub>CR1 function by targeted deletion and green fluorescent protein reporter gene insertion," *Molecular and Cellular Biology*, vol. 20, no. 11, pp. 4106–4114, 2000.
- [21] P. G. Hirrlinger, A. Scheller, C. Braun et al., "Expression of reef coral fluorescent proteins in the central nervous system of transgenic mice," *Molecular and Cellular Neuroscience*, vol. 30, no. 3, pp. 291–303, 2005.
- [22] C. Moreno, O. Vivas, N. P. Lamprea, M. R. Lamprea, A. Múnera, and J. Troncoso, "Vibrissal paralysis unveils a preference for textural rather than positional novelty in the one-trial object recognition task in rats," *Behavioural Brain Research*, vol. 211, no. 2, pp. 229–235, 2010.
- [23] D. R. Myatt, T. Hadlington, G. A. Ascoli, and S. J. Nasuto, "Neuromantic—from semi-manual to semi-automatic reconstruction of neuron morphology," *Frontiers in Neuroinformatics*, vol. 6, article 4, 2012.
- [24] D. A. Sholl, "Dendritic organization in the neurons of the visual and motor cortices of the cat," *Journal of Anatomy*, vol. 87, no. 4, pp. 387–406, 1953.
- [25] D. Ristanović, N. T. Milošević, and V. Štulić, "Application of modified Sholl analysis to neuronal dendritic arborization of the cat spinal cord," *Journal of Neuroscience Methods*, vol. 158, no. 2, pp. 212–218, 2006.
- [26] B. M. Hooks, T. Mao, D. A. Gutnisky, N. Yamawaki, K. Svoboda, and G. M. G. Shepherd, "Organization of cortical and thalamic input to pyramidal neurons in mouse motor cortex," *The Journal of Neuroscience*, vol. 33, no. 2, pp. 748–760, 2013.
- [27] G. W. Huntley, "Correlation between patterns of horizontal connectivity and the extent of short-term representational plasticity in rat motor cortex," *Cerebral Cortex*, vol. 7, no. 2, pp. 143–156, 1997.
- [28] V. B. Mountcastle, "The columnar organization of the neocortex," *Brain*, vol. 120, no. 4, pp. 701–722, 1997.
- [29] J. Troncoso, A. Múnera, and J. M. Delgado-García, "Learning-dependent potentiation in the vibrissal motor cortex is closely related to the acquisition of conditioned whisker responses in behaving mice," *Learning and Memory*, vol. 14, no. 1, pp. 84–93, 2007.
- [30] G.-F. Tseng and D. A. Prince, "Structural and functional alterations in rat corticospinal neurons after axotomy," *Journal of Neurophysiology*, vol. 75, no. 1, pp. 248–267, 1996.
- [31] R. R. de la Cruz, A. M. Pastor, and J. M. Delgado-García, "Influence of the postsynaptic target on the functional properties of neurons in the adult mammalian central nervous system," *Reviews in the Neurosciences*, vol. 7, no. 2, pp. 115–149, 1996.
- [32] C. Veronesi, E. Maggiolini, and G. Franchi, "Postnatal development of vibrissae motor output following neonatal infraorbital nerve manipulation," *Experimental Neurology*, vol. 200, no. 2, pp. 332–342, 2006.
- [33] G. Franchi, "Persistence of vibrissal motor representation following vibrissal pad deafferentation in adult rats," *Experimental Brain Research*, vol. 137, no. 2, pp. 180–189, 2001.
- [34] A. Keller, N. D. Weintraub, and E. Miyashita, "Tactile experience determines the organization of movement representations in rat motor cortex," *NeuroReport*, vol. 7, no. 14, pp. 2373–2378, 1996.
- [35] G. Franchi, "Time course of motor cortex reorganization following botulinum toxin injection into the vibrissal pad of the adult rat," *European Journal of Neuroscience*, vol. 16, no. 7, pp. 1333–1348, 2002.
- [36] G. Franchi and C. Veronesi, "Time course for the reappearance of vibrissal motor representation following botulinum toxin injection into the vibrissal pad of the adult rat," *European Journal of Neuroscience*, vol. 20, no. 7, pp. 1873–1884, 2004.
- [37] K. Rupalla, P. R. Allegrini, D. Sauer, and C. Wiessner, "Time course of microglia activation and apoptosis in various brain regions after permanent focal cerebral ischemia in mice," *Acta Neuropathologica*, vol. 96, no. 2, pp. 172–178, 1998.
- [38] R.-S. Ruan, S.-K. Leong, and K.-H. Yeoh, "Glial reaction after facial nerve compression in the facial canal of the albino rat," *Acta Oto-Laryngologica*, vol. 114, no. 3, pp. 271–277, 1994.
- [39] A. McRae, E. Gilland, E. Bona, and H. Hagberg, "Microglia activation after neonatal hypoxic-ischemia," *Developmental Brain Research*, vol. 84, no. 2, pp. 245–252, 1995.
- [40] A. E. Cardona, E. P. Pioro, M. E. Sasse et al., "Control of microglial neurotoxicity by the fractalkine receptor," *Nature Neuroscience*, vol. 9, no. 7, pp. 917–924, 2006.
- [41] O. Meucci, A. Fatatis, A. A. Simen, and R. J. Miller, "Expression of CX<sub>3</sub>CR1 chemokine receptors on neurons and their role in neuronal survival," *Proceedings of the National Academy of Sciences of the United States of America*, vol. 97, no. 14, pp. 8075–8080, 2000.

## Research Article

# Osteoarticular Expression of Musashi-1 in an Experimental Model of Arthritis

**Francisco O'Valle,<sup>1</sup> Magdalena Peregrina,<sup>2</sup> Vicente Crespo-Lora,<sup>1</sup> Pablo Galindo-Moreno,<sup>3</sup> Maria Roman,<sup>4</sup> Miguel Padial-Molina,<sup>3</sup> Francisco Mesa,<sup>5</sup> Jose Aneiros-Fernandez,<sup>1</sup> David Aguilar,<sup>1</sup> Elena Gonzalez-Rey,<sup>6</sup> Mario Delgado,<sup>6</sup> and Pedro Hernandez-Cortes<sup>7</sup>**

<sup>1</sup>Department of Pathology and IBIMER, School of Medicine, University of Granada, 18012 Granada, Spain

<sup>2</sup>The Spanish Institute of Social Security (INSS), 18006 Granada, Spain

<sup>3</sup>Oral Surgery and Implant Dentistry Department, School of Dentistry, University of Granada, 18017 Granada, Spain

<sup>4</sup>Plastic Surgery Department, Virgen de las Nieves University Hospital, 18014 Granada, Spain

<sup>5</sup>Periodontics Department, School of Dentistry, University of Granada, 18017 Granada, Spain

<sup>6</sup>Parasitology and Biomedicine López-Neyra Institute, CSIC, 18016 Armilla, Granada, Spain

<sup>7</sup>Orthopedic Surgery Department, San Cecilio University Hospital of Granada, 18012 Granada, Spain

Correspondence should be addressed to Francisco O'Valle; [fovalle@ugr.es](mailto:fovalle@ugr.es)

Received 23 September 2014; Revised 11 January 2015; Accepted 20 January 2015

Academic Editor: Monica Fedele

Copyright © 2015 Francisco O'Valle et al. This is an open access article distributed under the Creative Commons Attribution License, which permits unrestricted use, distribution, and reproduction in any medium, provided the original work is properly cited.

**Background.** Collagen-induced arthritis (CIA), a murine experimental disease model induced by immunization with type II collagen (CII), is used to evaluate novel therapeutic strategies for rheumatoid arthritis. Adult stem cell marker Musashi-1 (Msi1) plays an important role in regulating the maintenance and differentiation of stem/precursor cells. The objectives of this investigation were to perform a morphological study of the experimental CIA model, evaluate the effect of TNF $\alpha$ -blocker (etanercept) treatment, and determine the immunohistochemical expression of Msi1 protein. **Methods.** CIA was induced in 50 male DBA1/J mice for analyses of tissue and serum cytokine; clinical and morphological lesions in limbs; and immunohistochemical expression of Msi1. **Results.** Clinically, TNF $\alpha$ -blocker treatment attenuated CIA on day 32 after immunization ( $P < 0.001$ ). Msi1 protein expression was significantly higher in joints damaged by CIA than in those with no lesions ( $P < 0.0001$ ) and was related to the severity of the lesions (Spearman's rho = 0.775,  $P = 0.0001$ ). **Conclusions.** Treatment with etanercept attenuates osteoarticular lesions in the murine CIA model. Osteoarticular expression of Msi1 protein is increased in joints with CIA-induced lesion and absent in nonlesioned joints, suggesting that this protein is expressed when the lesion is produced in order to favor tissue repair.

## 1. Introduction

Collagen-induced arthritis (CIA), a murine experimental disease model induced by immunization with type II collagen (CII), shares a number of clinical, histopathological, and immunological features with rheumatoid arthritis (RA) [1]. Although its etiology is unknown, the initial stages of RA and CIA involve multiple steps that can be divided into two main phases: the initiation and establishment of autoimmunity to collagen-rich joint components, and later events associated with progressively destructive inflammatory processes [1–4].

Progression of the autoimmune response involves the development of autoreactive Th1 and Th17 cells, their entry into the joint tissues, and the subsequent recruitment of inflammatory cells via multiple mediators [4]. The chronic nature of the inflammatory process in RA suggests a disturbance of immune regulation in the joint, probably caused by an excessive inflammatory response along with deficiency in the mechanisms controlling the immune response. Available therapies are based on immunosuppressive agents that inhibit the inflammatory component of RA and either reduce the relapse rate or delay disease onset. However, they have

multiple effects, some of which are undesirable, and in the long term they do not prevent progressive clinical disability [5].

Tumor necrosis factor alpha (TNF- $\alpha$ ) is a proinflammatory cytokine expressed in the pannus of the inflamed joint in RA [6–9]. TNF $\alpha$ -blocker drugs are among those currently used for the treatment of RA. The subcutaneous administration to RA patients of the TNF- $\alpha$  receptor antagonist etanercept (50 mg once a week) was found to induce clinical improvements not observed with the drugs previously used in this disease [10, 11]. In addition, the beneficial effects of TNF $\alpha$ -blocker therapy have been demonstrated by various research groups in a mouse model of CIA [12–17].

The adult stem cell marker Musashi-1 (Msi1) is an RNA-binding protein of 362 amino acids with two ribonucleoprotein motifs (RBD1 and RBD2) [18] of 39 kDa molecular weight. Msi1 is associated with the maintenance and asymmetric cell division of neural and epithelial progenitor cells [19]. It is expressed in various epithelial stem cells and plays an important role in regulating the maintenance and differentiation of stem/precursor cells [20, 21]. Msi1 is known to regulate progenitor cell function through the posttranscriptional regulation of its target RNA [20]. Msi1 also acts as an important positive regulator of cell proliferation and inhibitor of apoptosis by reducing Notch-1 expression [22].

Modulation of Msi1 immunohistochemical expression has been identified in a murine model of inflammatory colitis [23], and it has been speculated that Msi1 might promote cell proliferation by accelerating the cell cycle in neoplastic cells [24], suggesting a role for this protein in tissue repair in different processes and as a potential therapeutic target in regenerative medicine.

The objectives of this study were to morphologically analyze the experimental collagen-induced arthritis model, to evaluate the effect of treatment with a TNF $\alpha$ -blocker (etanercept), and to determine the immunohistochemical expression of Msi1 protein.

## 2. Material and Methods

**2.1. Induction and Treatment of Collagen-Induced Arthritis (CIA).** CIA was induced in 50 male DBA1/J mice (7 to 10 weeks old; Jackson Laboratories, Bar Harbor, ME) by subcutaneous injection into the tail base with 200  $\mu$ g bovine CII (Sigma, St. Louis, MO) at day 0 and with 100  $\mu$ g CII at day 21, both emulsified in complete Freund's adjuvant containing 200  $\mu$ g *Mycobacterium tuberculosis* H37 RA (Difco, Detroit, Michigan). Treatment consisted of the intraperitoneal injection of 2 mg of etanercept (Enbrel, Wyeth Europa Ltd., UK; E-group) or of phosphate-buffered saline (PBS; untreated control, C-group) once a week for four weeks (on days 25, 32, 39, and 46) starting at day 25 after immunization, when all mice showed established arthritis (clinical score >2). Mice were evaluated by two independent blinded examiners every other day and monitored for signs of arthritis onset according to the following clinical score: grade 0, no swelling; grade 1, slight swelling and erythema; grade 2, moderate swelling and edema; grade 3, extreme swelling and pronounced edema; or grade 4, joint rigidity. Each limb was graded, giving a

maximum possible score of 16 per animal. Paw swelling was assessed by measuring the thickness of the affected hind paws with 0 to 10 mm calipers (on days 25, 32, 39, 46, and 53). All experiments were performed in a European Union-certified laboratory following national guidelines for the ethical care of animals (RD 53/2013, EU Directive 63/2010).

**2.2. Cytokine Determination.** Protein extracts were isolated by homogenization of joints (50 mg tissue/mL) in 50 mM Tris-HCl, pH 7.4, with 0.5 mM DTT and proteinase inhibitor cocktail (10  $\mu$ g/mL, Sigma) for cytokine determination in joints, and serum samples were collected at the disease peak (day 40); serum and joint cytokine and chemokine levels were determined by specific sandwich ELISAs using capture/ biotinylated detection Abs from BD Pharmingen (San Diego, CA) according to the manufacturer's recommendations.

**2.3. Histopathological Study.** For the histopathological study, mice were anesthetized with ether and sacrificed by cervical dislocation at day 15 ( $n = 20$ ), 21 ( $n = 20$ ), or 28 ( $n = 10$ ) after commencement of treatment with etanercept or PBS (i.e., days 39, 46, and 53 after immunization). They were fixed in 10% buffered formalin for 24 hours, decalcified with Decalcifier I, containing formaldehyde (10% w/v), formic acid (8% w/v), and methanol (1% w/v) (Surgipath softener I Europe Ltd., Peterborough, UK) for 24 h in oven at 37°C. Next, the four limbs were sectioned longitudinally, dehydrated with alcohol, and embedded in paraffin in an automatic tissue processor Excelsior ES (Thermo Scientific, CA, USA); 4  $\mu$ m sections were stained with hematoxylin and eosin (H&E) or Masson trichrome stain. Histopathological changes were scored in a blinded manner based on cell infiltration, cartilage destruction, and bone erosion parameters as previously described [25]. Cell infiltration was scored on a scale of 0–3 according to the number of affected joints (0: none, 1: <2, 2: 3–5; 3: >5 joints), and the amount of inflammatory cells in the synovial cavity (exudate) and synovial tissue (infiltrate) was also recorded. Cartilage destruction was graded on a scale of 0–3, ranging from the appearance of dead chondrocyte (empty lacunae) to complete loss of articular cartilage. Bone erosions were graded on a scale of 0–3, ranging from normal bone appearance to fully eroded cortical bone structure in patella and femur condyle. Pannus and involvement of the bone marrow and/or soft tissue were treated as dichotomous variables (present or absent).

**2.4. Immunohistochemical Analysis.** Decalcified and paraffin-embedded sections were dewaxed, hydrated, and heat-treated in 1 mM EDTA pH 8 in an antigen retrieval PT module (Thermo Fisher Scientific Inc., Waltham, MA) at 95°C for 20 min. Sections were incubated for 16 h at 4°C with the prediluted polyclonal antibody against Musashi-1 (Sigma-Aldrich, Barcelona, Spain) at 1:100 dilution to identify cellular expression. An automatic immunostainer (Autostainer 480, Thermo Fisher Scientific Inc.) was used for the immunohistochemical study, applying the peroxidase conjugated micropolymer method and developing with diaminobenzidine (Ultravision Quanto, Master Diagnóstica, Granada, Spain). Expression was assessed semiquantitatively on a scale

TABLE 1: Comparative study of morphological variables in DBA1/J mice after 21 and 28 days of starting treatment.

Variables	Control group	Etanercept group*	P values <sup>†</sup>	Control group	Etanercept group*	P values <sup>†</sup>
	Day 46 after immunization			Day 53 after immunization		
Number of joints	2.1 ± 0.69	1.8 ± 0.88	0.412	2.45 ± 1.01	1.9 ± 0.56	0.006
Pannus	1 ± 0.21	0.9 ± 0.35	0.449	0.7 ± 0.31	1 ± 0	0.467
B & C injury	1.8 ± 0.71	1.3 ± 0.78	0.278	2 ± 0.94	1.55 ± 0.68	0.045
Inflammation	1.5 ± 1	1.3 ± 1	0.661	1.55 ± 0.83	1.1 ± 0.69	0.036
Bone marrow	0.6 ± 0.47	0.5 ± 0.39	0.613	0.55 ± 0.42	0.55 ± 0.43	0.930
Soft tissue	0.15 ± 0.15	0.2 ± 0.21	0.557	0.35 ± 0.31	0.15 ± 0.15	0.010
Mean score	6.85 ± 2.95	5.8 ± 3.37	0.469	8 ± 3.55	6 ± 2.12	0.011

Values are expressed as mean ± standard deviation; \* treatment: etanercept 2 mg/week; B & C: bone and cartilage; <sup>†</sup> Student's *t*-test. See Figure 3 for details.

of 0 to 3 (0: absence, 1: mild [ $<10\%$  positive cells], 2: moderate [10 to 25%], 3: intense [ $>25\%$ ] in bone tissue, hyaline cartilage, joint capsule, synovium, ligaments, striated muscle cells, endothelial cells, and adipocytes). The variables were subsequently categorized in two groups (presence/absence of osteoarticular lesion), calculating the total Msi1 expression score for each group.

2.5. *Statistical Analysis.* SPSS 20.0 (IBM Inc., Chicago, IL) was used for the statistical analysis. The normality of the distribution of variables was examined with the one-dimensional Kolmogorov-Smirnov test. Results were expressed as mean ± standard deviation for normally distributed continuous variables and frequencies for categorical variables. The bivariate tests and Spearman correlation coefficient used are reported in the table footnotes. A *P* value of 0.05 was accepted as the statistical significance threshold.

### 3. Results

The clinical score was significantly attenuated in mice with CIA after 1 week of systemic treatment with the TNF $\alpha$ -blocker etanercept ( $P < 0.001$ ) in comparison to untreated mice (Figure 1). This treatment also significantly reduced serum and joint tissue levels of Th1-mediated proinflammatory cytokines and increased levels of the anti-inflammatory cytokine IL10 (Figure 2).

The histopathological study demonstrated a CIA induction efficiency of 95% in DBA1/J mice, which showed pannus formation and chronic lymphocytic/monocytic inflammatory infiltrate with acute phenomena (neutrophil leukocytes) that involved the joint soft tissues (Figure 3). These mice also showed the presence of necrotic cells in the intra-articular space, secondary destruction of the joint cartilage, and increased destruction of bone tissue through osteoclastic activation, with sporadic involvement of the bone medulla and extension of inflammatory infiltrate into periarticular soft tissues (Figure 3). Injection of etanercept in CIA mice moderately decreased most of the histopathological signs of arthritis, especially after four weeks of treatment (day 53 after immunization, Table 1). No significant differences in morphologic variables were observed between untreated and etanercept-treated mice after three weeks of treatment (day 46 after immunization, Table 1); however, stratification

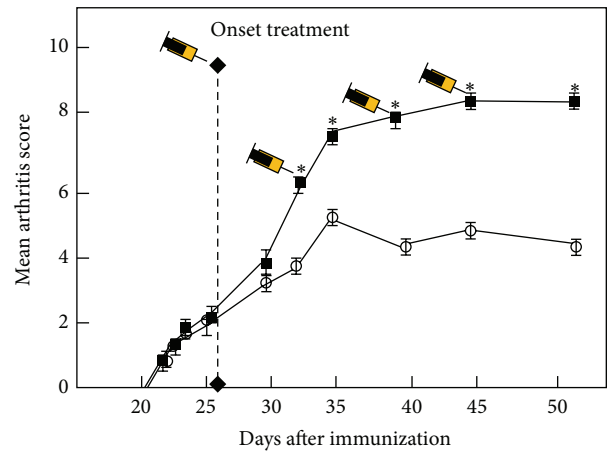


FIGURE 1: TNF $\alpha$ -blocker administration attenuates clinical CIA. Clinical scores in mice with CIA intraperitoneally treated from day 25 after immunization with PBS (control, C-group, closed squares) or TNF $\alpha$ -blocker (2 mg/week, E-group, open circles) once per week for four weeks. Values are the mean ± SD of 20 mice per group. Differences were significant at  $P < 0.001$  (asterisks) for E-group versus C-group at indicated time points.

of the histopathological results according to the absence or presence of lesions (0 = absence, 1 = presence) showed that the etanercept treatment attenuated the progression of clinical inflammation in the limbs (mean of 0.55 in the etanercept group versus 0.85 in control group after 21 days of treatment;  $P < 0.003$ , Student's *t*-test).

The immunohistochemical expression of Msi1 was then investigated in different tissue components in the joints of untreated and etanercept-treated CIA mice. Msi1-specific staining was mainly observed at nuclear level in chondrocytes and spindle-shaped mesenchymal cells of the articular capsule and ligaments (Figure 4). Scant expression was detected in osteocytes, synoviocytes, or inflammatory cells in articular or periarticular lesions or in medullary bone tissue (Figure 4). No Msi1 expression was observed in striated muscle cells or mature adipocytes (Figure 4).

Quantitative analysis of Msi1 expression in the different groups revealed significantly higher expression in joints with CIA-induced articular lesions than in joints without lesions ( $P < 0.0001$ , Student's *t*-test, Figure 4). Significant positive

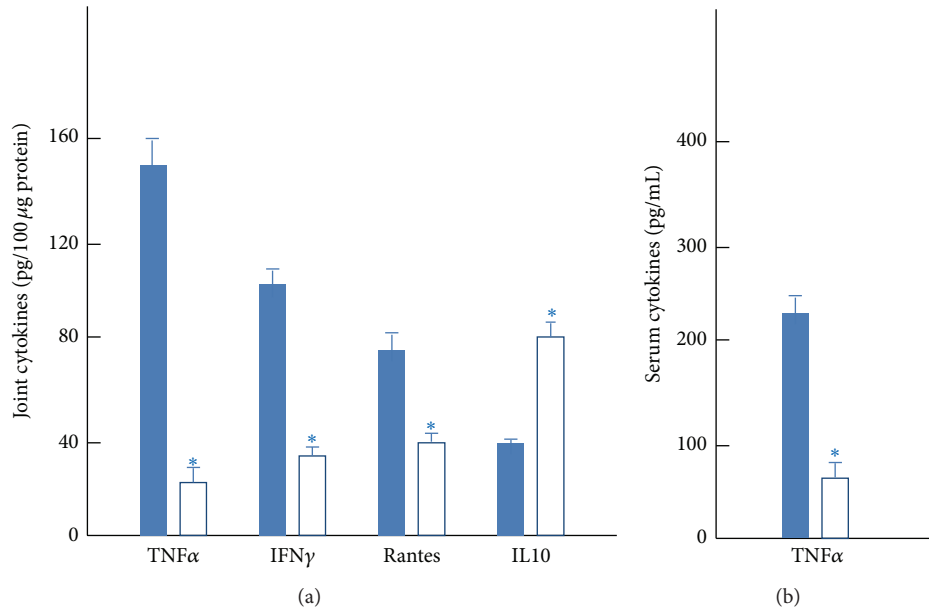


FIGURE 2: TNF $\alpha$ -blocker administration decreases inflammatory response in CIA. DBA1/J mice with established CIA (day 25 after immunization) were intraperitoneally injected with PBS (closed columns) or anti-TNF $\alpha$  (2 mg/week, open columns) once per week. Systemic and local expression of inflammatory mediators was assayed in protein extracts from joints of hind limbs (a) and sera (b) isolated at day 40 after immunization;  $n = 3$  to 4 mice/group. \* $P < 0.01$  versus controls.

TABLE 2: Spearman's correlation coefficient ( $\rho$ ) for Msi1 immunohistochemical expression between different articular components.

	Cartilage	Capsule	Ligament	Synovium
Cartilage	1	0.225*	0.308**	0.556**
Capsule		1	0.663**	0.389**
Ligament			1	0.260*
Synovium				1

\*Significant correlation at 0.05 (bilateral); \*\*significant correlation at 0.01 (bilateral).

correlations were also observed between the presence of osteoarticular lesion and Msi1 expression (Spearman's  $\rho$ : 0.775,  $P = 0.001$ ) and among Msi1 expression levels at the different sites (capsule, ligament, synovium, and cartilage) (Table 2). However, although a slight decrease in Msi1 expression was observed in affected joints in etanercept-treated CIA mice, no statistically significant differences in articular Msi1 expression were found between PBS-treated and etanercept-treated CIA mice after three ( $P = 0.449$ , Student's  $t$ -test) or four ( $P = 0.080$ , Student's  $t$ -test) weeks of treatment (Figure 5).

#### 4. Discussion

This study confirmed that TNF $\alpha$ -blocker treatment attenuates CIA-induced histopathological lesions in the joints of CIA-susceptible DBA1/J mice and revealed, for the first time, a more intense expression of Msi1 protein in cartilage, ligament, articular capsule, mesenchymal cells, and osteocytes in CIA-lesioned versus nonlesioned joints.

Although no animal model of RA completely replicates the human disease, the CIA model employed in this study has been widely used for the testing and development of RA therapies [26–29]. In fact, the CIA induction rate was very high (>95%) in the present study. Likewise, DBA1/J mice were selected rather than other animals (e.g., rats) [30] because better outcomes are obtained in genetically modified strains and the arthritis is more similar to human RA [31, 32]. Major insights into the molecular mechanisms of inflammatory arthritis recently emerged from the study of murine models of RA-like disease using genetically deficient or transgenic mice or a combined murine model (K/BxA<sup>g7</sup>) that spontaneously develops both RA-like disease and atherosclerosis [33]. However, these studies may be limited by the differences between human and murine immune systems. Current efforts to develop an animal model that utilizes human immune cells will allow study of their function in the initiation and propagation of inflammatory arthritis [34].

RA is a chronic debilitating disease in which the induction of autoimmunity to collagen-rich joint components underlies the onset of the disease and the subsequent destructive inflammatory process. Progression of the autoimmune response implies the development of autoreactive Th1 (producing IFN $\gamma$  and TNF $\alpha$ ) and Th17 (producing Th17) cells, their entry into articular tissue, and the release of proinflammatory cytokines and chemokines, which promote macrophage and neutrophil infiltration and activation [3, 35, 36]. Excessive production by infiltrating inflammatory cells of inflammatory cytokines, free radicals, and extracellular matrix-degrading enzymes plays a critical role in cartilage damage and bone erosion. A desirable therapeutic approach would be to prevent the activation of inflammatory and

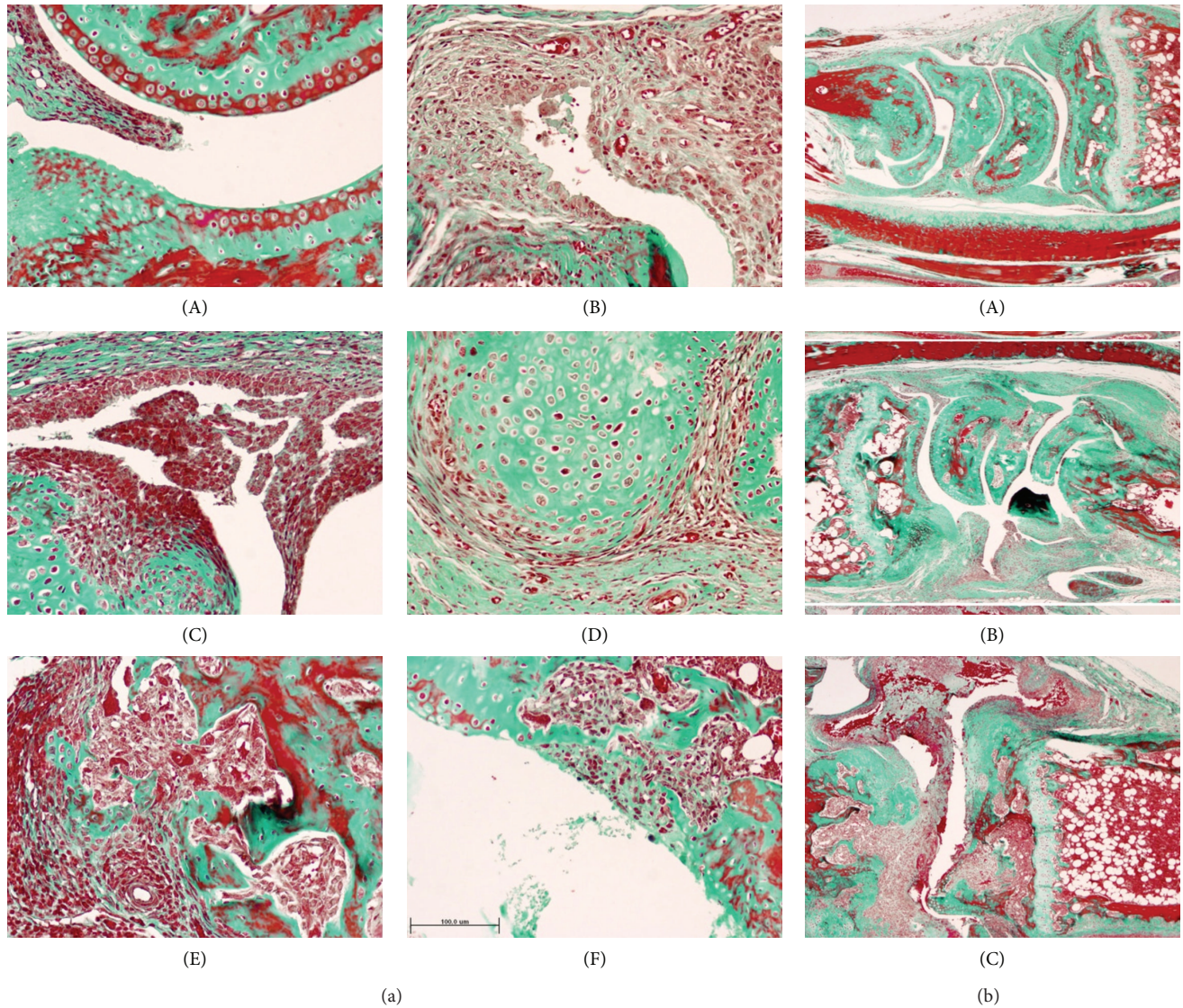


FIGURE 3: Morphological features of articular lesion in CIA model in DBA1/J mice. (a): (A) Unaffected joint. (B) Pannus. (C) Synovial hyperplasia with chronic inflammatory infiltrate. (D) Hyaline cartilage surrounded by spindle-shaped mesenchymal cells. (E) Bone destruction mediated by osteoclast activation. (F) Partial destruction of articular cartilage. Bar 100  $\mu\text{m}$  (Masson's trichrome, original magnification  $\times 20$ ). (b): (A) Limb without joint lesions. (B) Partial response to etanercept with persistence of pannus (E-group). (C) Intense joint lesion with pannus and chronic inflammatory infiltrate in articular cavity and partial destruction of bone tissue (C-group) (Masson's trichrome, original magnification  $\times 4$ ).

autoimmune components. Our group previously demonstrated that 5-aminoisoquinolinone, a poly(ADP-ribose) polymerase-1 inhibitor, significantly reduces the incidence and severity of established CIA, completely abrogating joint swelling and cartilage/bone destruction by downregulating inflammation and the Th1 response [37]. The administration of TNF $\alpha$ -blocker to arthritic mice decreases the CII-specific Th1-mediated cytokine response through direct action on the synovium [38–40]. The present results confirm that treatment of established CIA with etanercept reduces articular levels of Th1 cytokines (IFN $\gamma$  and TNF $\alpha$ ) and inflammatory chemokines. This effect may be directly related to a decrease in inflammatory infiltrates in the joints of etanercept-treated

mice. However, the fact that levels of the anti-inflammatory cytokine IL10 were increased by the injection of etanercept supports the proposition that this TNF $\alpha$ -blocker also promotes a bias towards a regulatory/anti-inflammatory response.

Etanercept and other blockers of TNF $\alpha$  action (infliximab, adalimumab, golimumab, and certolizumab pegol) offer specific anti-cytokine therapies but induce a general immunosuppressive action. Etanercept has become the drug of choice for late stage RA with reasonable safety, and the present study confirms that it attenuates the progression of histopathological lesions, as demonstrated in CIA murine models [12–17] and in the clinical setting [41, 42]. However,

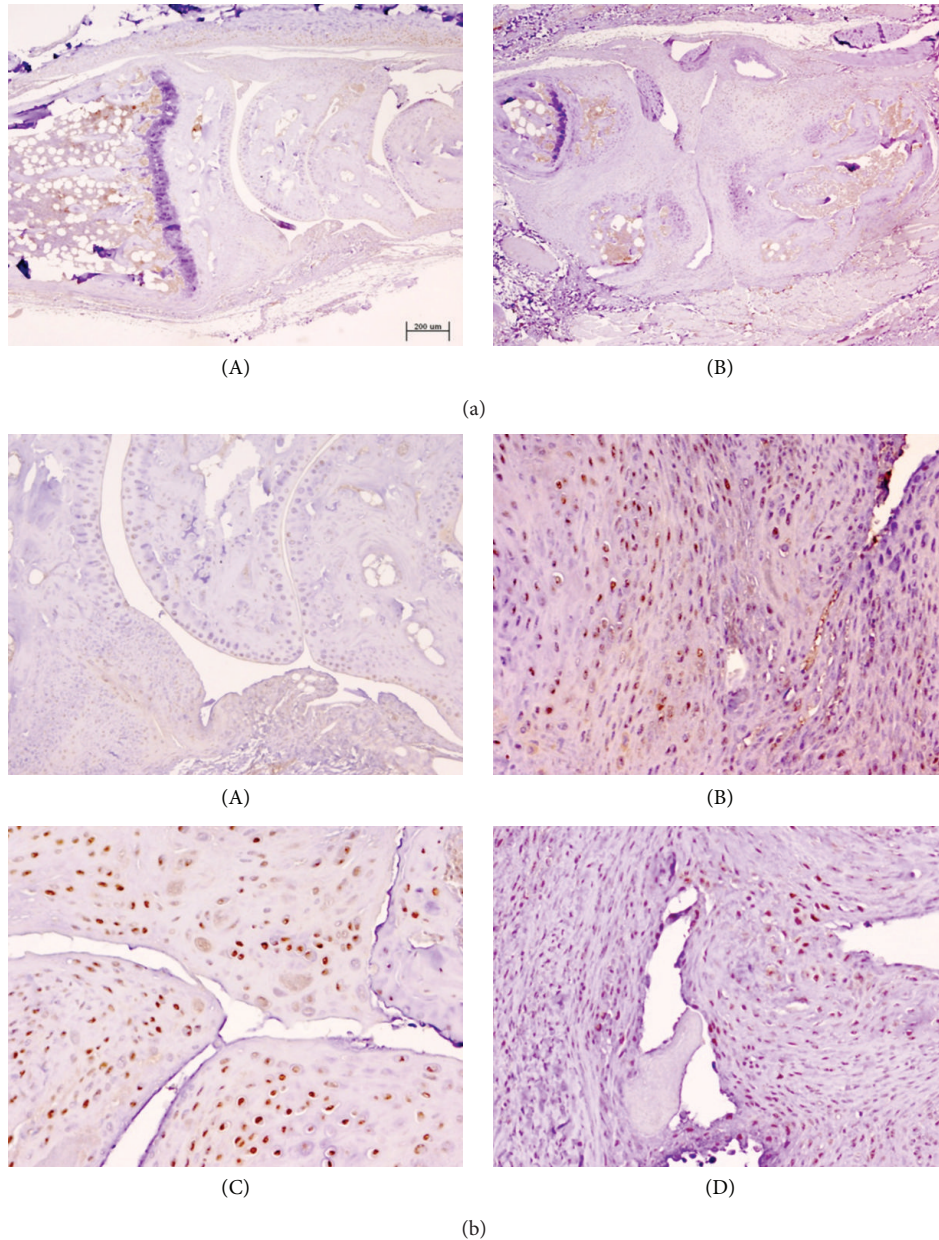


FIGURE 4: Immunohistochemical expression of Musashi-1 (Msi1) in CIA model in DBA1/J mice. (a): (A) Scant Msi1 expression was detected in chondrocytes, synoviocytes, and inflammatory cells in articular or periarticular lesions or in medullary bone tissue in joints with no morphological changes. (B) Nuclear expression of Msi1 in mesenchymal cells, articular capsule, and articular cartilage. Bar 200  $\mu\text{m}$  (micropolymer peroxidase-based method, original magnification  $\times 4$ ). (b): (A) Very scant nuclear Msi1 expression in joint with no morphological changes (E-group). (B), (C), and (D) Moderate Msi1 expression in mesenchymal cells, articular capsule, and articular cartilage in CIA-lesioned joints (C-group) (micropolymer peroxidase-based method, original magnification  $\times 20$ ).

etanercept must be taken frequently, it is expensive, and it increases the susceptibility of the patient to infections [43].

The present study provides the first report on the osteoarticular expression of Msi1. No direct evidence has been published to date linking Msi1 with osteoarticular regeneration. Msi1 is involved in the regulation of self-renewal of stem cells. In order to maintain their unlimited capacity to divide, stem cells require controlled temporal and spatial protein expression. The Musashi family of RNA-binding proteins exerts this essential translational control (via repression and

activation) in order to regulate multiple stem cell populations [44], and Msi1-dependent posttranscriptional enhancement of m-Numb is crucial in epithelial regeneration [45]. Nuclear expression of Msi1 was more intense in the presence of osteoarticular lesion and was not observed in nonlesioned joints, with or without anti-TNF $\alpha$  treatment. In previous studies on fractures in rats, we observed a marked increase in Msi1 expression in the reparative fibrocartilaginous tissue of the fracture callus (data not shown). Msi1 protein regulates the transcription and differentiation of mesenchymal stem

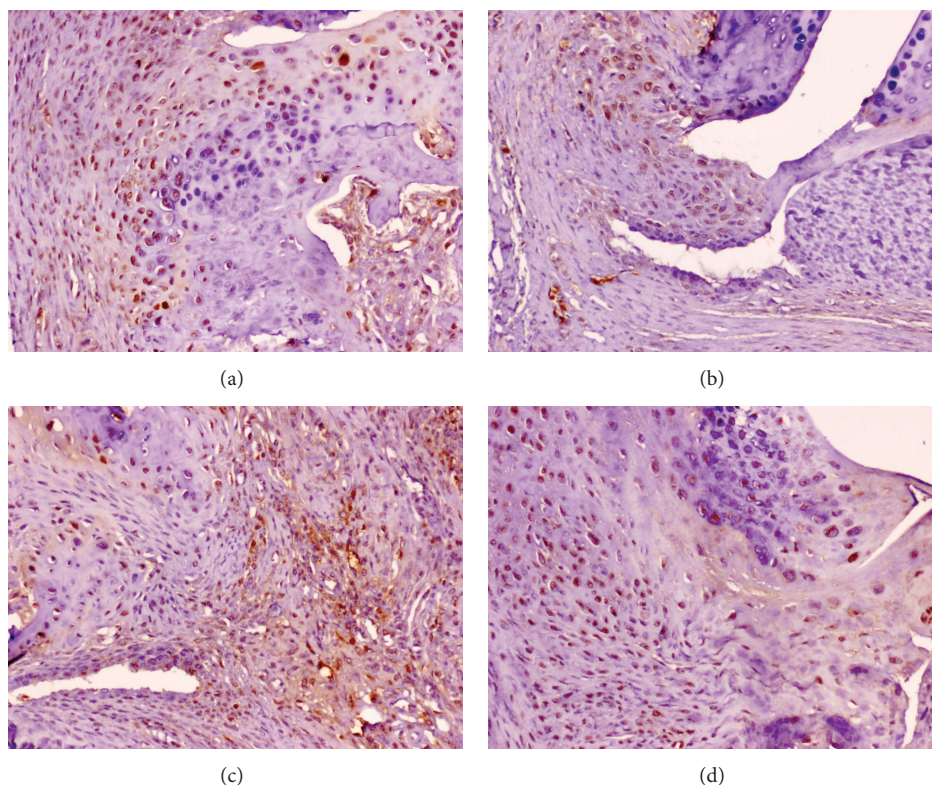


FIGURE 5: Representative immunohistochemical expression of Msi1 in E-group versus C-group in CIA model (DBA1/J mice). (a) Moderate Msi1 expression in mesenchymal cells, articular capsule, and articular cartilage in CIA-lesioned joints at 21 days after treatment (E-group); (b) moderate Msi1 expression in CIA-lesioned joints at 21 days after treatment (C-group); (c) joint Msi1 expression at 28 days after treatment (E-group); (d) joint Msi1 expression at 28 days after treatment (C-group) (micropolymer peroxidase-based method, original magnification  $\times 20$ ).

cells; therefore, its presence in these tissues suggests its involvement in tissue repair and regeneration processes.

Our novel findings on the expression of Msi1 in osteoarticular tissues may support the participation of this protein in tissue regeneration processes and suggest the involvement of adult mesenchymal stem cells in the repair of these tissues. These data may serve as a basis for future investigations on repair processes in cartilaginous and bone tissues.

## 5. Conclusions

Treatment with etanercept attenuates the osteoarticular lesions in the murine model of CIA. The osteoarticular expression of Msi1 protein is increased in joints with CIA-induced lesion and absent in nonlesioned joints, suggesting that this protein is expressed when the lesions are produced in order to favor tissue repair.

## Abbreviations

AIQ: 5-Aminoisoquinolinone  
 CIA: Collagen-induced arthritis  
 CII: Type II collagen  
 IFN $\gamma$ : Gamma interferon  
 Msi1: Musashi-1

RA: Rheumatoid arthritis  
 TNF $\alpha$ : Tumor necrosis factor alpha.

## Conflict of Interests

The authors do not have any financial interests, either directly or indirectly, in the products or information listed in the paper.

## Authors' Contribution

Francisco O'Valle, Pedro Hernandez-Cortes, Elena Gonzalez-Rey, and Mario Delgado conceived, designed, and performed the mouse model, coordinated in the study, and drafted the paper. Magdalena Peregrina, Pablo Galindo-Moreno, Maria Roman, Miguel Padial-Molina, and Francisco Mesa analyzed the clinical and biochemical data and drafted the paper. Vicente Crespo, Jose Aneiros Fernandez, and David Aguilar analyzed the morphology and immunohistochemical data. All authors read and approved the final version of this paper.

## Acknowledgments

The authors thank M.D. Rodríguez-Martínez, from the Pathology Department of the School of Medicine, University of

Granada, for her expert technical assistance and R. Davies, professional translator, for help with the English version of the paper. This investigation was partially supported by Research Group #CTS-138 (Junta de Andalucía, Spain).

## References

- [1] D. D. Anthony and T. M. Haqqi, "Collagen-induced arthritis in mice: an animal model to study the pathogenesis of rheumatoid arthritis," *Clinical and Experimental Rheumatology*, vol. 17, no. 2, pp. 240–244, 1999.
- [2] M. Feldmann, F. M. Brennan, and R. N. Maini, "Role of cytokines in rheumatoid arthritis," *Annual Review of Immunology*, vol. 14, pp. 397–440, 1996.
- [3] D. D. Brand, A. H. Kang, and E. F. Rosloniec, "Immunopathogenesis of collagen arthritis," *Springer Seminars in Immunopathology*, vol. 25, no. 1, pp. 3–18, 2003.
- [4] E. Gonzalez-Rey, A. Chorny, F. O'Valle, and M. Delgado, "Adrenomedullin protects from experimental arthritis by down-regulating inflammation and Th1 response and inducing regulatory T cells," *The American Journal of Pathology*, vol. 170, no. 1, pp. 263–271, 2007.
- [5] M. Feldmann and R. N. Maini, "Anti-TNF $\alpha$  therapy of rheumatoid arthritis: what have we learned?" *Annual Review of Immunology*, vol. 19, pp. 163–196, 2001.
- [6] J. C. Beckham, D. S. Caldwell, B. L. Peterson et al., "Disease severity in rheumatoid arthritis: relationships of plasma tumor necrosis factor- $\alpha$ , soluble interleukin 2-receptor, soluble CD4/CD8 ratio, neopterin, and fibrin D-dimer to traditional severity and functional measures," *Journal of Clinical Immunology*, vol. 12, no. 5, pp. 353–361, 1992.
- [7] F. M. Brennan, D. Chantry, A. Jackson, R. Maini, and M. Feldmann, "Inhibitory effect of TNF $\alpha$  antibodies on synovial cell interleukin-1 production in rheumatoid arthritis," *The Lancet*, vol. 2, no. 8657, pp. 244–247, 1989.
- [8] X. Sáez-Llorens, H. S. Jafari, K. D. Olsen, H. Nariuchi, E. J. Hansen, and G. H. McCracken Jr., "Induction of suppurative arthritis in rabbits by *Haemophilus* endotoxin, tumor necrosis factor- $\alpha$ , and interleukin-1 $\beta$ ," *Journal of Infectious Diseases*, vol. 163, no. 6, pp. 1267–1272, 1991.
- [9] D. Tracey, L. Klareskog, E. H. Sasso, J. G. Salfeld, and P. P. Tak, "Tumor necrosis factor antagonist mechanisms of action: a comprehensive review," *Pharmacology & Therapeutics*, vol. 117, no. 2, pp. 244–279, 2008.
- [10] S. Dhillon, K. A. Lyseng-Williamson, and L. J. Scott, "Etanercept: a review of its use in the management of rheumatoid arthritis," *Drugs*, vol. 67, no. 8, pp. 1211–1241, 2007.
- [11] B. Haraoui and V. Bykerk, "Etanercept in the treatment of rheumatoid arthritis," *Therapeutics and Clinical Risk Management*, vol. 3, no. 1, pp. 99–105, 2007.
- [12] G. J. Thorbecke, R. Shah, C. H. Leu, A. P. Kuruvilla, A. M. Hardison, and M. A. Palladino, "Involvement of endogenous tumor necrosis factor  $\alpha$  and transforming growth factor  $\beta$  during induction of collagen type II arthritis in mice," *Proceedings of the National Academy of Sciences of the United States of America*, vol. 89, no. 16, pp. 7375–7379, 1992.
- [13] R. O. Williams, M. Feldmann, and R. N. Maini, "Anti-tumor necrosis factor ameliorates joint disease in murine collagen-induced arthritis," *Proceedings of the National Academy of Sciences of the United States of America*, vol. 89, no. 20, pp. 9784–9788, 1992.
- [14] P. F. Piguet, G. E. Grau, C. Vesin, H. Loetscher, R. Gentz, and W. Lesslauer, "Evolution of collagen arthritis in mice is arrested by treatment with anti-tumor necrosis factor (TNF) antibody or a recombinant soluble TNF receptor," *Immunology*, vol. 77, no. 4, pp. 510–514, 1992.
- [15] P. H. Wooley, J. Dutcher, M. B. Widmer, and S. Gillis, "Influence of a recombinant human soluble tumor necrosis factor receptor FC fusion protein on type II collagen-induced arthritis in mice," *Journal of Immunology*, vol. 151, no. 11, pp. 6602–6607, 1993.
- [16] R. O. Williams, J. Ghrayeb, M. Feldmann, and R. N. Maini, "Successful therapy of collagen-induced arthritis with TNF receptor-IgG fusion protein and combination with anti-CD4," *Immunology*, vol. 84, no. 3, pp. 433–439, 1995.
- [17] Q. T. Wang, Y. J. Wu, B. Huang et al., "Etanercept attenuates collagen-induced arthritis by modulating the association between BAFRR expression and the production of splenic memory B cells," *Pharmacological Research*, vol. 68, no. 1, pp. 38–45, 2013.
- [18] T. Nagata, R. Kanno, Y. Kurihara et al., "Structure, backbone dynamics and interactions with RNA of the C-terminal RNA-binding domain of a mouse neural RNA-binding protein, Musashi1," *The Journal of Molecular Biology*, vol. 287, no. 2, pp. 315–330, 1999.
- [19] H. Okano, H. Kawahara, M. Toriya, K. Nakao, S. Shibata, and T. Imai, "Function of RNA-binding protein Musashi-1 in stem cells," *Experimental Cell Research*, vol. 306, no. 2, pp. 349–356, 2005.
- [20] H. Okano, T. Imai, and M. Okabe, "Musashi: a translational regulator of cell fate," *Journal of Cell Science*, vol. 115, no. 7, pp. 1355–1359, 2002.
- [21] Y. Kaneko, S. Sakakibara, T. Imai et al., "Musashi1: an evolutionally conserved marker for CNS progenitor cells including neural stem cells," *Developmental Neuroscience*, vol. 22, no. 1-2, pp. 139–153, 2000.
- [22] S. M. Sureban, R. May, R. J. George et al., "Knockdown of RNA binding protein musashi-1 leads to tumor regression in vivo," *Gastroenterology*, vol. 134, no. 5, pp. 1448–1458, 2008.
- [23] T. Fukui, H. Takeda, H.-J. Shu et al., "Investigation of Musashi-1 expressing cells in the murine model of dextran sodium sulfate-induced colitis," *Digestive Diseases and Sciences*, vol. 51, no. 7, pp. 1260–1268, 2006.
- [24] X. Liu, W. T. Yang, and P. S. Zheng, "Msi1 promotes tumor growth and cell proliferation by targeting cell cycle checkpoint proteins p21, p27 and p53 in cervical carcinomas," *Oncotarget*, vol. 5, no. 21, pp. 10870–10885, 2014.
- [25] M. Delgado, C. Abad, C. Martinez, J. Leceta, and R. P. Gomariz, "Vasoactive intestinal peptide prevents experimental arthritis by downregulating both autoimmune and inflammatory components of the disease," *Nature Medicine*, vol. 7, no. 5, pp. 563–568, 2001.
- [26] K. Kannan, R. A. Ortmann, and D. Kimpel, "Animal models of rheumatoid arthritis and their relevance to human disease," *Pathophysiology*, vol. 12, no. 3, pp. 167–181, 2005.
- [27] Y. G. Cho, M. L. Cho, S. Y. Min, and H. Y. Kim, "Type II collagen autoimmunity in a mouse model of human rheumatoid arthritis," *Autoimmunity Reviews*, vol. 7, no. 1, pp. 65–70, 2007.
- [28] R. Holmdahl, L. Jansson, E. Larsson, K. Rubin, and L. Klareskog, "Homologous type II collagen induces chronic and progressive arthritis in mice," *Arthritis & Rheumatism*, vol. 29, no. 1, pp. 106–113, 1986.

- [29] A. M. Malfait, R. O. Williams, A. S. Malik, R. N. Maimi, and M. Feldman, "Chronic relapsing homologous collagen-induced arthritis in DBA/1 mice as a model for testing disease-modifying and remission-inducing therapies," *Arthritis & Rheumatism*, vol. 44, no. 5, pp. 1215–1224, 2001.
- [30] J. M. Stuart, M. A. Cremer, A. S. Townes, and A. H. Kang, "Type II collagen-induced arthritis in rats. Passive transfer with serum and evidence that IgG anticollagen antibodies can cause arthritis," *Journal of Experimental Medicine*, vol. 155, no. 1, pp. 1–16, 1982.
- [31] R. Holmdahl, M. E. Andersson, T. J. Goldschmidt et al., "Collagen induced arthritis as an experimental model for rheumatoid arthritis. Immunogenetics, pathogenesis and autoimmunity," *APMIS*, vol. 97, no. 7, pp. 575–584, 1989.
- [32] R. O. Williams, "Rodent models of arthritis: relevance for human disease," *Clinical and Experimental Immunology*, vol. 114, no. 3, pp. 330–332, 1998.
- [33] S. Rose, M. Eren, S. Murphy et al., "A novel mouse model that develops spontaneous arthritis and is predisposed towards atherosclerosis," *Annals of the Rheumatic Diseases*, vol. 72, no. 1, pp. 89–95, 2013.
- [34] A. V. Misharin, G. K. Haines III, S. Rose, A. K. Gierut, R. S. Hotchkiss, and H. Perlman, "Development of a new humanized mouse model to study acute inflammatory arthritis," *Journal of Translational Medicine*, vol. 10, no. 1, article no. 190, 2012.
- [35] A. H. Tremouler and S. Albani, "Novel therapies for rheumatoid arthritis," *Expert Opinion on Investigational Drugs*, vol. 15, no. 11, pp. 1427–1441, 2006.
- [36] J. J. Goronzy and C. M. Weyand, "Rheumatoid arthritis," *Immunological Reviews*, vol. 204, no. 1, pp. 55–73, 2005.
- [37] E. Gonzalez-Rey, R. Martínez-Romero, F. O'Valle et al., "Therapeutic effect of a poly(ADP-ribose) polymerase-1 inhibitor on experimental arthritis by downregulating inflammation and Th1 response," *PLoS ONE*, vol. 2, no. 10, Article ID e1071, 2007.
- [38] R. O. Williams, "Collagen-induced arthritis in mice: a major role for tumor necrosis factor- $\alpha$ ," *Methods in Molecular Biology*, vol. 361, pp. 265–284, 2007.
- [39] J. Zwerina, S. Hayer, M. Tohidast-Akrad et al., "Single and combined inhibition of tumor necrosis factor, interleukin-1, and RANKL pathways in tumor necrosis factor-induced arthritis: effects on synovial inflammation, bone erosion, and cartilage destruction," *Arthritis and Rheumatism*, vol. 50, no. 1, pp. 277–290, 2004.
- [40] K. E. Donahue, G. Gartlehner, D. E. Jonas et al., "Systematic review: comparative effectiveness and harms of disease-modifying medications for rheumatoid arthritis," *Annals of Internal Medicine*, vol. 148, no. 2, pp. 124–134, 2008.
- [41] L. W. Moreland, S. W. Baumgartner, M. H. Schiff et al., "Treatment of rheumatoid arthritis with a recombinant human tumor necrosis factor receptor (p75)-Fc fusion protein," *The New England Journal of Medicine*, vol. 337, no. 3, pp. 141–147, 1997.
- [42] L. W. Moreland, M. H. Schiff, S. W. Baumgartner et al., "Phase III trial of DMARD failing rheumatoid arthritis patients with TNF receptor p75 Fc fusion protein (TNFR: Fc, ENBREL)," *Journal of Investigative Medicine*, vol. 46, p. 228A, 1998, Abstract.
- [43] É. Toussiot and D. Wendling, "The use of TNF- $\alpha$  blocking agents in rheumatoid arthritis: an overview," *Expert Opinion on Pharmacotherapy*, vol. 5, no. 3, pp. 581–594, 2004.
- [44] J. M. Sutherland, E. A. McLaughlin, G. R. Hime, and N. A. Siddall, "The Musashi family of RNA binding proteins: master regulators of multiple stem cell populations," *Advances in Experimental Medicine and Biology*, vol. 786, pp. 233–245, 2013.
- [45] T. Takahashi, H. Suzuki, T. Imai et al., "Musashi-1 post-transcriptionally enhances phosphotyrosine-binding domain-containing m-Numb protein expression in regenerating gastric mucosa," *PLoS ONE*, vol. 8, no. 1, Article ID e53540, 2013.

## Research Article

# Morphine Promotes Tumor Angiogenesis and Increases Breast Cancer Progression

**Sabrina Bimonte, Antonio Barbieri, Domenica Rea, Giuseppe Palma, Antonio Luciano, Arturo Cuomo, Claudio Arra, and Francesco Izzo**

*Istituto Nazionale per lo Studio e la Cura dei Tumori “Fondazione G. Pascale”, IRCCS, Via Mariano Semmola, 80131 Naples, Italy*

Correspondence should be addressed to Sabrina Bimonte; [s.bimonte@istitutotumori.na.it](mailto:s.bimonte@istitutotumori.na.it)

Received 31 July 2014; Accepted 14 October 2014

Academic Editor: Andrea Vecchione

Copyright © 2015 Sabrina Bimonte et al. This is an open access article distributed under the Creative Commons Attribution License, which permits unrestricted use, distribution, and reproduction in any medium, provided the original work is properly cited.

Morphine is considered a highly potent analgesic agent used to relieve suffering of patients with cancer. Several *in vitro* and *in vivo* studies showed that morphine also modulates angiogenesis and regulates tumour cell growth. Unfortunately, the results obtained by these studies are still contradictory. In order to better dissect the role of morphine in cancer cell growth and angiogenesis we performed *in vitro* studies on ER-negative human breast carcinoma cells, MDA.MB231 and *in vivo* studies on heterotopic mouse model of human triple negative breast cancer, TNBC. We demonstrated that morphine *in vitro* enhanced the proliferation and inhibited the apoptosis of MDA.MB231 cells. *In vivo* studies performed on xenograft mouse model of TNBC revealed that tumours of mice treated with morphine were larger than those observed in other groups. Moreover, morphine was able to enhance the neoangiogenesis. Our data showed that morphine at clinical relevant doses promotes angiogenesis and increases breast cancer progression.

## 1. Introduction

Morphine is an opiate-based drug largely used to relieve pains of patients with cancer in terminal phases, in order to improve their quality of life [1]. It was isolated for the first time in 1803 by Friedrich W. Sertürner [2]. It is noted that morphine explains its function by acting through opioid receptors localized in the brain named  $\mu$ ,  $\delta$ , and  $\kappa$  [3, 4]. Morphine relieves pain by acting directly on central nervous system (CNS), although its activity on peripheral tissue leads to many secondary complications, including immunosuppression, respiratory depression, addiction, and tolerance. Morphine is still considered the most effective analgesic clinically available used to relieve suffering of patients with cancer [5]. Several experimental studies performed on cancer cell lines and mouse models showed that morphine can also play a role in regulation of cancer cell growth. Unfortunately, at present the role of morphine in the regulation of tumor cell growth is not yet correctly established. The results obtained by these studies are still contradictory. Many reports showed that morphine was able to inhibit the growth of various

human cancer cell lines [6–12] or animal models [13–16]. On the contrary, other studies proved that morphine increased tumor cell growth in *in vivo* [17, 18] or *in vitro* [19] models. It has been demonstrated that morphine at clinically relevant doses stimulates angiogenesis *in vitro* [20], promotes tumour growth in breast cancer mouse model, and increases vascular permeability [21]. One explanation for these different results could be due to different concentration and/or time of administration of morphine applied. In fact, *in vitro* and *in vivo* studies showed that tumor suppression occurs after chronic high doses of morphine [11, 15, 16], while tumor-enhancing effects with morphine occur after administration of low daily doses or single dose of morphine [22]. Thus, there is a dilemma about the effects of morphine on cancer cell growth and angiogenesis [23]. Recently, it has been demonstrated that morphine stimulates cancer progression and mast cell activation and impairs survival in transgenic mice with breast cancer [24].

For these reasons, in order to elucidate the role of morphine in regulation of tumor growth and angiogenesis in triple negative breast cancer (TNBC), we performed *in vitro*

and *in vivo* studies on the ER-negative human breast carcinoma cells MDA.MB231. Our data showed that morphine at clinical relevant doses promotes tumor angiogenesis and increases breast cancer proliferation and migration.

## 2. Materials and Methods

**2.1. Materials.** Morphine sulphate used for *in vitro* and *in vivo* experiments was kindly gifted by Dr. Arturo Cuomo (IRCCS Fondazione Pascale) and was dissolved in distilled water to a concentration of 100 mM as a stock solution. Then the drug was added to MDA.MB231 cells in three different doses (1, 10, and 100  $\mu$ M). The antibody against PECAM-1 was obtained from Santa Cruz Biotechnology (Santa Cruz, CA). Anti-p53 antibody was kindly provided by Imgenex (San Diego, CA). The liquid DAB+ Substrate Chromogen System-HRP used for immunocytochemistry was obtained from DakoCytomation (Carpinteria, CA). Penicillin, streptomycin, Dulbecco's modified Eagle medium (DMEM), and fetal bovine serum (FBS) were obtained from Invitrogen (Grand Island, NY). Tris, glycine, NaCl, SDS, and bovine serum albumin (BSA) were obtained from Sigma Chemical (St. Louis, MO).

**2.2. Cell Lines.** ER-negative breast cancer cell line MDA.MB231 was obtained from American Type Culture Collection (Manassas, VA). Cells were cultured in RPMI-1640 supplemented with fetal bovine serum (FBS) 10%, antibiotics (penicillin 100 units/mL; streptomycin 100  $\mu$ g/mL), and l-glutamine (2 mM) at 37°C in an atmosphere of 5% of CO<sub>2</sub>.

**2.3. Proliferation Assay.** The effect of drug on cell proliferation was determined by using TACS 3-(4, 5-dimethylthiazol-2-yl)-2, 5-diphenyltetrazolium bromide (MTT) cell proliferation assay (Trevigen, Gaithersburg). The cells (2,000 per well) were incubated with or without morphine in triplicate in a 96-well plate and then incubated for 2, 4, and 6 days at 37°C. A MTT solution was added to each well and incubated for 2 h at 37°C. An extraction buffer (20% SDS and 50% dimethylformamide) was added, and the cells were incubated overnight at 37°C. The absorbance of the cell suspension was measured at 570 nm using a microplate reader (DAS Technologies, Chantilly, VA). This experiment was repeated twice, and the statistical analysis was performed to obtain the final values.

**2.4. Wound-Healing Assay.** MDA.MB231 cells were seeded at the density of  $40 \times 10^3$  cells per well into a 6-multiwell plate and cultured in DMEM medium supplemented with 1% FBS. At the time of confluence, cells were incubated in the absence or presence of morphine (1, 10, and 100  $\mu$ M) for 48 h after a slit made horizontally with a white tip at the center of each confluent well. Cell invasion on the slit of the confluent well was assessed at 0, 24, 48 hours, in each condition, by light microscopy.

**2.5. Mice.** Six eight-week-old female Foxn1<sup>nu/nu</sup> mice were purchased by Harlan, San Pietro al Natisone, Italy. Mice were housed five for cage in the standard mice plexiglass cages and

maintained on a 12 h light : 12 h dark cycle (lights on at 7.00 a.m.) in a temperature-controlled room ( $22 \pm 2^\circ\text{C}$ ) and with food and water ad libitum at all times. All the experiments performed on animal models were in compliance with the guidelines for the Care and Use of Laboratory Animals of the National Cancer Institute "Fondazione G. Pascale," IRCCS. Moreover, all experiments were performed by also following the European Directive 63/2010/UE and the Italian Law (DL 26/2014, authorized by Minister of Health, Italy). This study was carried out in accordance with the recommendations that cover all scientific procedures involving the use of live animals.

**2.6. Generation of Heterotopic Mouse Model of Breast Cancer and Experimental Protocol.** MDA.MB231 breast cancer cells were harvested from subconfluent cultures after a brief exposure to 0.25% trypsin. Trypsinization was stopped with medium containing 10% FBS. The cells were washed once in serum-free medium and suspended in PBS. Only suspensions consisting of single cells, with >90% viability, were used for the injections. A total of 16 female Foxn1<sup>nu/nu</sup> mice were used in this experiment and maintained in a barrier facility on HEPA-filtered racks. Animals were individually identified using numbered ear tags. All experiments were conducted in a biological laminar flow hood, and all surgical procedures were conducted with strict adherence to aseptic technique. The mice were anesthetized with Avertin solution injected intraperitoneally according to their weight. A suspension of  $2.5 \times 10^6$  MDA.MB231 cells in 25  $\mu$ L of PBS 1X/mouse was injected subcutaneously into the right-side flank area of mice. When tumors reached  $\sim 30\text{--}60 \text{ mm}^3$ , mice were randomized into the following treatment groups ( $n = 4$ ): (a) normal saline (control) and (b) morphine sulphate at 0.714 mg/kg mouse/day for first 15 days and then 1.43 mg/kg mouse/day (equivalent to 50 mg and 100 mg morphine per day, resp., for a 70 kg human). Tumor volumes were monitored once a week by using a digital caliper. Therapy was continued for 4 weeks and animals were sacrificed 2 weeks later. The tumor size was measured using digital caliper, and the tumor volume was estimated by the following formula: tumor volume ( $\text{mm}^3$ ) =  $(W \times L) \times 2 \times 1/2$ , where  $L$  is the length and  $W$  is the width of the tumor. Normally distributed data were represented as mean  $\pm$  S.E.M. Paired  $t$ -test one-tailed analysis was used to examine the significance of differences among groups (GraphPad Prism 5.0). A probability value with  $*P < 0.05$  and  $**P < 0.01$  was considered to be statistically significant. Fluorescein isothiocyanate- (FITC-) dextran (100  $\mu$ L) was injected into the tail vein of mice to visualize microvessels within 150  $\mu$ m (using single-photon microscopy) or  $\sim 600 \mu$ m (using multiphoton laser-scanning microscopy [MPLSM]) of a tumor/window interface. Half of the tumor tissue was formalin-fixed and paraffin-embedded for immunohistochemistry and routine H&E staining. The other half was snap-frozen in liquid nitrogen and stored at  $-80^\circ\text{C}$ .

**2.7. Preparation of Nuclear Extract from Tumor Samples.** Breast tumor tissues (75–100 mg/mouse) from control and

experimental mice were prepared according to standard protocols. The supernatant (nuclear extract) was collected and stored at  $-70^{\circ}\text{C}$  until use. Protein concentration was determined by the Bradford protein assay with BSA as the standard.

**2.8. Immunohistochemical Analysis for CD31 in Tumor Tissue.** Breast cancer tumor samples from controls and treated mice were embedded in paraffin and fixed with paraformaldehyde. After being washed in PBS, the slides were blocked with protein block solution (DakoCytomation) for 20 min and then incubated overnight with polyclonal anti-goat PECAM-1 (1:100). After the incubation, the slides were washed and then incubated with biotinylated link universal antiserum followed by horseradish peroxidase-streptavidin conjugate (LSAB+ kit). The slides were rinsed, and color was developed using 3, 3'-diaminobenzidine hydrochloride as a chromogen. Finally, sections were rinsed in distilled water, counterstained with haematoxylin, and mounted with DPX mounting medium for evaluation. Pictures were captured with a Photometrics CoolSNAP CF colour camera (Nikon, Lewisville, TX) and MetaMorph version 4.6.5 software (Universal Imaging, Downingtown, PA).

**2.9. Western Blot Analysis.** Breast tumor tissues (75–100 mg/mouse) from control and experimental mice were minced and incubated on ice for 1 h in 0.5 mL of ice-cold Lysis Buffer (10 mM Tris, pH 8.0, 130 mM NaCl, 1% Triton X-100, 10 mM NaF, 10 mM sodium phosphate, 10 mM sodium pyrophosphate, 2  $\mu\text{g}/\text{mL}$  aprotinin, 2  $\mu\text{g}/\text{mL}$  leupeptin, and 2  $\mu\text{g}/\text{mL}$  pepstatin). The minced tissue was homogenized using a Dounce homogenizer and centrifuged at  $16,000\times g$  at  $4^{\circ}\text{C}$  for 10 min. Western blotting analysis was performed according to standard protocols.  $\beta$ -Actin was used as loading control.

### 3. Results

**3.1. Morphine Enhances the Proliferation of Triple Negative Breast Cancer Cells, by Performing In Vitro Assays on MBA.** MB231 breast cancer cells. Wound-healing assay demonstrated that morphine enhances the migration of breast cancer cells at 48 h in dose dependent manner. These results were also confirmed by MTT assay and flow cytometry (Figure 1(e) and data not shown). In order to assess if morphine enhances the apoptosis in breast cancer cells, we performed western blotting analysis of p53 expression on cell lysate extracted from MBA.MB231 cells not treated and treated with morphine. (Figure 1(g)). Taken together, our data showed that morphine inhibits apoptosis and promotes proliferation in dose dependent manner. The same results were also obtained for MCF-7 cells (data not shown).

**3.2. Morphine Promotes Tumor Growth and Microvessel Formation in Heterotopic Mouse Model of Triple Negative Breast Cancer.** In order to study the role of morphine in the tumor growth *in vivo*, we generated a mouse model of breast

cancer by injection of MDA.MB231 cells subcutaneously into the right-side flank area of mice. When tumors reached  $\sim 30\text{--}60\text{ mm}^3$ , 2 weeks after cell injection, the mice were randomized into three groups: (a) normal saline (control) and (b) morphine sulphate at 0.714 mg/kg mouse/day for first 15 days and then 1.43 mg/kg mouse/day (equivalent to 50 mg and 100 mg morphine per day, resp., for a 70 kg human). Tumor volumes were monitored once a week by using a digital caliper. Therapy continued for 4 weeks and animals were sacrificed 2 weeks later. We also monitored the body weight of mice twice a week until the end of treatment. No difference was observed between the body weights of two groups of animals, indicating that treatments of mice with drug are not associated with toxicity effects. Mice were sacrificed at the end of treatment. The final tumor volumes on day 35 after the start of treatment showed a significant increase in the morphine group compared with control (Figure 2(a)). Interestingly, administration of morphine enhanced tumor volumes and resulted in rapid growth of tumors with respect to controls. In order to assess if morphine inhibits microvessel formation in breast tumors, fluorescein isothiocyanate- (FITC-) dextran was injected into the tail vein of mice. Our data demonstrate that morphine enhanced microvessel formation in mice tumors with respect to controls (Figures 2(b)-2(c)). In order to confirm these data, we performed an immunohistochemical staining with CD31 on tumor tissues from control and treated mice. Our data demonstrate that morphine promotes microvessel formation in breast tumors of mice treated with respect to controls (Figures 3(a)-3(b)).

### 4. Discussion

Several experimental studies performed *in vitro* and *in vivo* cancer cell lines and mouse models showed that morphine plays a role in regulation of cancer cell growth and metastasis. The results obtained by these studies are still controversial since many reports showed that morphine was able to inhibit the growth of various human cancer cell lines [6–12] or animal models [13–16]. On the contrary, other studies proved that morphine increased tumor cell growth in *in vivo* [17, 18] or *in vitro* [19] models. To study cancer cell growth promoting or inhibiting effects of morphine, several xenograft mouse models were generated. Tegeder et al. [13] generated a mouse model of breast cancer by subcutaneous injection of MCF-7 and MDA-MB231 cells in NMRI-nu/nu mice. In this paper, it has been demonstrated that morphine significantly reduced tumor growth through a p53-dependent mechanism. Additionally, in these mice, naloxone increased the growth-inhibitory effects of morphine. Similar results were obtained in rat model of colon cancer in which subcutaneous administration of morphine leads to significant decrease in the hepatic tumor burden. On the contrary, several experimental studies demonstrated that morphine increased tumor growth. Gupta et al. in orthotopic mouse model of breast cancer obtained by injection of MCF-7 cells into the mammary fat pad of nude mice demonstrated that morphine, in clinically relevant doses, increased tumor growth. This

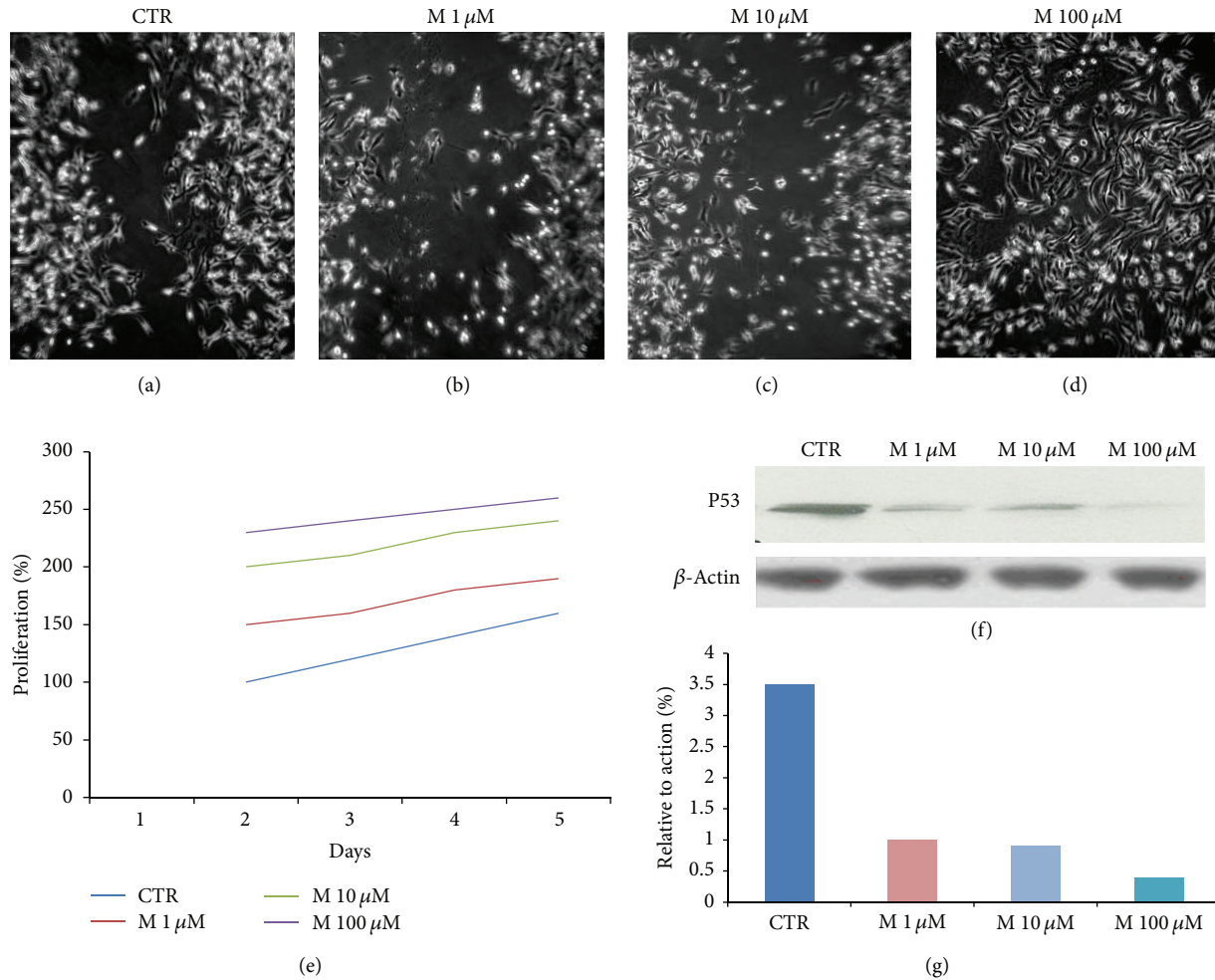


FIGURE 1: Morphine stimulates proliferation in MDA.MB231 cell lines. MDA.MB231 cells were incubated in medium containing (a) medium control, (b) 1  $\mu$ m morphine, (c) 10  $\mu$ m morphine, and (d) 100  $\mu$ m morphine. Cell migration rates were quantitatively assessed by counting the number of cells in the denuded area at 0, 24, and 48 h after wound induction. At 48 h after wound induction, there were clearly more cells in the denuded area of morphine treated cells than untreated cells. (e) MTT assay results show an enhancement of proliferation in breast cancer cells treated with morphine with respect to control cells. Data are representative of three independent experiments ( $P$  value < 0.05). (f-g) Western blot showing that morphine reduces the expression of p53 in MDA.MB231 cells treated with morphine (lanes 2, 3, and 4) with respect to controls (lane 1) in dose dependent manner.  $\beta$ -Actin was used as loading control.

was associated with increased angiogenesis and inhibition of apoptosis and promotion of cell cycle progression [20]. In this study, it was also reported that naloxone itself had no significant effect on angiogenesis. According to these results, in another study, it was demonstrated that morphine, subcutaneously administered in mice, increased the tumor growth in mouse model of leukaemia and sarcoma. In these mice, morphine had also a general immunosuppressive effect [25].

These contrasting results are probably associated with different concentration and/or time of administration of morphine. In fact, *in vitro* and *in vivo* studies demonstrated that tumor-enhancing effects with morphine occur after administration of low daily doses or single dose of morphine [22], while tumor suppression occurs after chronic high doses of morphine [11, 15, 16].

Thus, there is a dilemma about the effects of morphine on cancer cell growth and angiogenesis in various types of cancer [23]. The role of morphine in the regulation of tumor cell growth is not yet correctly established.

It has also been demonstrated that the  $\mu$ -opioid receptor, by which morphine exerts its action, directly regulates tumor growth and metastasis. On the basis of these results, different mechanisms of opioid receptor-mediated influence of morphine on tumor growth have been proposed. Morphine, as mentioned above, after binding to the  $\mu$ -opioid receptor, regulates cell cycle progression by stimulating mitogen-activated protein kinase (MAPK)/extracellular growth factor (Erk) pathways [20]. Alternatively, morphine can mediate apoptosis by activating phosphatidylinositol 3-kinase (PI3K)/protein kinase B (Akt) pathway [26]. Additionally, morphine by upregulation of urokinase plasminogen

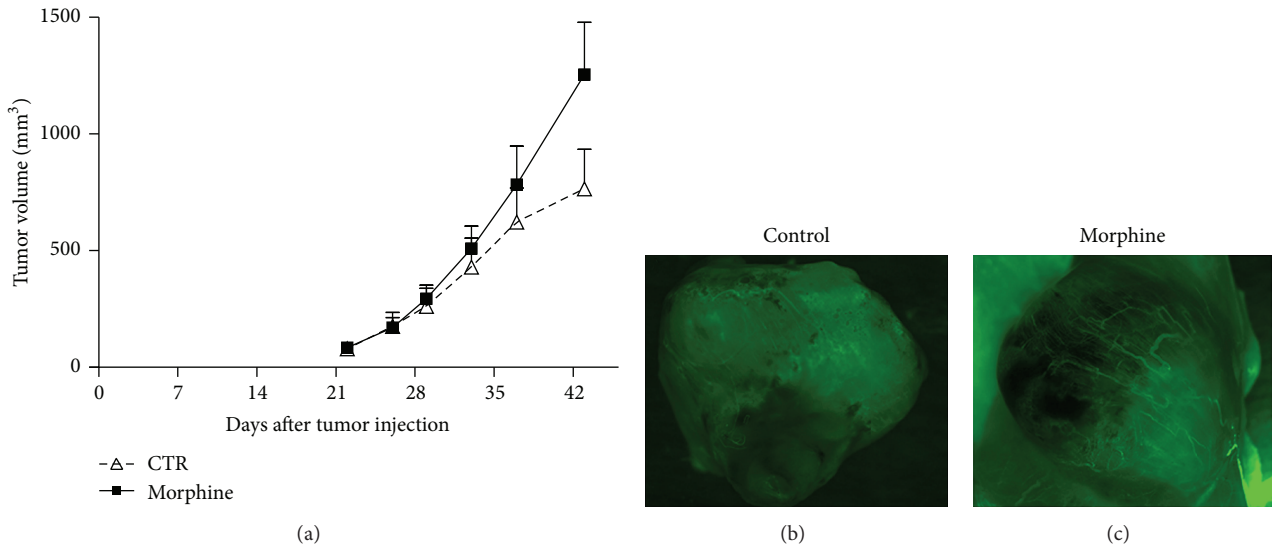


FIGURE 2: Morphine promotes the tumor growth in TBNC mouse model. (a) Morphine promotes tumor growth in breast tumor xenograft model. Breast tumor growth in mice treated with vehicle (•) and morphine (blacksquare). Tumor volumes increased after 28 days of morphine treatment until 35 days ( $P < 0.05$ ) as compared with control (vehicle-treated). Each point represents the mean of five separate experiments. (b-c) Measurements of fluorescence per second depicting microvessel tumor (FITC-DEXTRANE) using MacroFluo images showed that morphine enhances the angiogenesis in tumor of mice (b) with respect to controls (c).

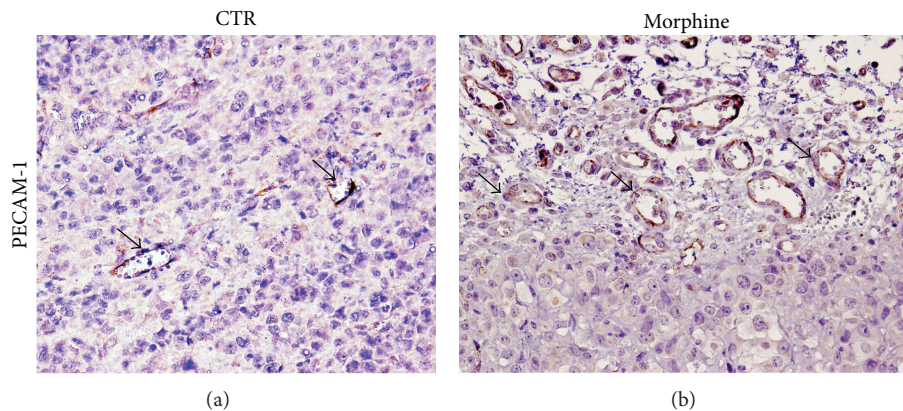


FIGURE 3: Morphine promotes angiogenesis formation in heterotopic mouse model of breast cancer. Immunohistochemical analysis for PECAM-1 showed the enhancement of PECAM-1 expression in morphine treated group (b), compared to controls (a). Arrows indicate positive staining of microvessel staining.

activator (uPA) expression induces metastasis formation [27], while by transactivation of VEGF receptor, it induces angiogenesis [28]. Finally, morphine affects also the function of T lymphocytes, leading to immunosuppression [29].

It has been proposed that morphine plays also a role in tumor apoptosis. Apoptosis is a form of cell death in which a programmed sequence of events leads to the elimination of cells without releasing harmful substances into the surrounding area. It is noted that apoptosis is regulated by two pathways: the mitochondrial-mediated pathway (intrinsic) [30] and death receptor-mediated pathway (extrinsic) [31]. It is noted that, in cancer cells, apoptosis is deregulated, and this leads to quick proliferation and tumor growth [32, 33]. Morphine was shown to induce apoptosis of macrophages, T

lymphocytes, and human endothelial cells [34, 35]. Experiments performed on human tumor cell lines demonstrated that morphine in high concentration induces apoptosis and inhibits cancer cell growth by activation of different signal pathways involving caspase 3/9 and cytochrome c, sigma-2 receptor. Additionally in SH-SY5Y cells, morphine has antiapoptotic effect by antagonizing doxorubicin [36]. These discrepancies, also in these cases, are associated with different cell line tumor type used and/or *in vivo* dose/time of morphine administrated.

Recent data demonstrated a role of morphine in angiogenesis. Angiogenesis is required for invasive tumor growth and metastasis and represents an important point in the control of cancer progression. Proangiogenic activity of

morphine was demonstrated in the MCF-7 breast cancer model. In these mice, morphine at clinically relevant concentrations enhanced tumor neovascularization [20]. In an animal model of hormone-dependent breast cancer, it has also been demonstrated that morphine promoted activation of vascular endothelial growth factor (VEGF) receptor and increased metastasis [21, 29]. It has been proposed that morphine explains its proangiogenic activity by stimulation of mitogen-activated protein kinase (MAPK) signalling pathway via G protein-coupled receptors and nitric oxide (NO). Alternatively, several *in vivo* studies provided evidence that morphine can induce tumor growth by upregulation of cyclooxygenase-2 (COX-2) [37–40] and or prostaglandin E2-mediated stimulation of angiogenesis [41–44]. On the contrary, several *in vivo* and *in vitro* studies demonstrated that morphine can inhibit angiogenesis by regulation of different pathways [8, 34, 45, 45–52]. These different results can be due to different experimental conditions (cell line tumor type used and/or dose/time of morphine). Morphine plays a role not only in tumor cell growth but also in metastasis formation, which is the main process related to most cancer deaths and failure in cancer treatment [53, 54].

For these reasons, in order to elucidate the role of morphine in regulation of tumor growth and angiogenesis in breast cancer we performed *in vitro* and *in vivo* studies on the MDA.MB231 breast cancer cells. These cells are triple negative (basal-like) breast cancer (TNBC) cells. It is noted that TNBC does not express the estrogen receptor (ER), progesterone receptor (PR), or human epidermal growth factor receptor type 2 (HER2). Due to lack of both hormone receptors and HER2 expression, patients with this type of breast cancer have no chance to benefit from the endocrine therapy and HER2 targeted therapy. In addition, we used immunodeficient mice that are able to mimic the compromised immune system of a patient with breast cancer. So in these experimental conditions, it has become interesting for us to study the role of morphine in the regulation of cancer cell growth and angiogenesis. Our data showed that morphine in TNBC at clinical relevant doses promotes tumor angiogenesis and increases breast cancer progression. For these reasons, it is very important for the management of severe pain associated with cancer to consider accurately the dose and route of administration of morphine in order to avoid severe effect of cancer progression. Further studies are ongoing in our laboratory in order to dissect the molecular mechanisms underlying the role of morphine in cancer development and metastasis formation in breast cancer. Specifically, we will generate orthotropic mouse models of breast cancer by using not only MDA.MB231 cells but also MCF-7 (human breast adenocarcinoma cell line) cells which represent estrogen receptor (ER) positive control cell lines. The results obtained from these data will shed light on the role of morphine in regulation of breast cancer progression.

### Conflict of Interests

The authors have no other relevant affiliations or financial interests with any organization or entity. No writing assistance was used in the production of paper.

### Acknowledgments

The authors would like to specially thank Massimiliano Spinelli, Data Manager of S.S.D. Sperimentazione animale, Istituto Nazionale per lo Studio e la Cura dei Tumori “Fondazione G. Pascale,” IRCCS, Italy, for kind help in providing informatics assistance and Dr. Di Napoli Daniele for supervising animal care. This work was supported by the 5x mille and current research programs of National Institute of Tumors, IRCCS “Foundation G. Pascale,” Naples (Italy).

### References

- [1] J. N. Lickiss, “Approaching cancer pain relief,” *European Journal of Pain*, vol. 5, pp. 5–14, 2001.
- [2] R. Schmitz, “Friedrich Wilhelm Sertürner and the discovery of morphine,” *Pharmacy in History*, vol. 27, no. 2, pp. 61–74, 1985.
- [3] G. W. Pasternak, “Pharmacological mechanisms of opioid analgesics,” *Clinical Neuropharmacology*, vol. 16, no. 1, pp. 1–18, 1993.
- [4] B. L. Kieffer and C. Gavériaux-Ruff, “Exploring the opioid system by gene knockout,” *Progress in Neurobiology*, vol. 66, no. 5, pp. 285–306, 2002.
- [5] P. W. Mantyh, “Cancer pain and its impact on diagnosis, survival and quality of life,” *Nature Reviews Neuroscience*, vol. 7, no. 10, pp. 797–809, 2006.
- [6] N. Sueoka, E. Sueoka, S. Okabe, and H. Fujiki, “Anti-cancer effects of morphine through inhibition of tumour necrosis factor- $\alpha$  release and mRNA expression,” *Carcinogenesis*, vol. 17, no. 11, pp. 2337–2341, 1996.
- [7] R. Maneckjee and J. D. Minna, “Opioids induce while nicotine suppresses apoptosis in human lung cancer cells,” *Cell Growth and Differentiation*, vol. 5, no. 10, pp. 1033–1040, 1994.
- [8] A. Pasi, B. Qu, R. Steiner, H.-J. Senn, W. Bar, and F. S. Messiha, “Angiogenesis: modulation with opioids,” *General Pharmacology*, vol. 22, no. 6, pp. 1077–1079, 1991.
- [9] A. Hatzoglou, E. Bakogeorgou, E. Papakonstanti, C. Stournaras, D. S. Emmanouel, and E. Castanas, “Identification and characterization of opioid and somatostatin binding sites in the opossum kidney (OK) cell line and their effect on growth,” *Journal of Cellular Biochemistry*, vol. 63, no. 4, pp. 410–421, 1996.
- [10] A. Hatzoglou, L. Ouafik, E. Bakogeorgou, K. Thermos, and E. Castanas, “Morphine cross-reacts with somatostatin receptor SSTR2 in the T47D human breast cancer cell line and decreases cell growth,” *Cancer Research*, vol. 55, no. 23, pp. 5632–5636, 1995.
- [11] R. Maneckjee, R. Biswas, and B. K. Vonderhaar, “Binding of opioids to human MCF-7 breast cancer cells and their effects on growth,” *Cancer Research*, vol. 50, no. 8, pp. 2234–2238, 1990.
- [12] M. Kampa, E. Bakogeorgou, A. Hatzoglou, A. Damianaki, P.-M. Martin, and E. Castanas, “Opioid alkaloids and casomorphin peptides decrease the proliferation of prostatic cancer cell lines (LNCaP, PC3 and DU145) through a partial interaction with opioid receptors,” *European Journal of Pharmacology*, vol. 335, no. 2-3, pp. 255–265, 1997.
- [13] I. Tegeder, S. Grösch, A. Schmidtke et al., “G protein-independent G1 cell cycle block and apoptosis with morphine in adenocarcinoma cells: involvement of p53 phosphorylation,” *Cancer Research*, vol. 63, no. 8, pp. 1846–1852, 2003.

- [14] M. P. Yeager and T. A. Colacchio, "Effect of morphine on growth of metastatic colon cancer *in vivo*," *Archives of Surgery*, vol. 126, no. 4, pp. 454–456, 1991.
- [15] T. Sasamura, S. Nakamura, Y. Iida et al., "Morphine analgesia suppresses tumor growth and metastasis in a mouse model of cancer pain produced by orthotopic tumor inoculation," *European Journal of Pharmacology*, vol. 441, no. 3, pp. 185–191, 2002.
- [16] Y. Harimaya, K. Koizumi, T. Andoh, H. Nojima, Y. Kuraishi, and I. Saiki, "Potential ability of morphine to inhibit the adhesion, invasion and metastasis of metastatic colon 26-L5 carcinoma cells," *Cancer Letters*, vol. 187, no. 1-2, pp. 121–127, 2002.
- [17] R. H. Simon and T. E. Arbo, "Morphine increases metastatic tumor growth," *Brain Research Bulletin*, vol. 16, no. 3, pp. 363–367, 1986.
- [18] J. W. Lewis, Y. Shavit, G. W. Terman, L. R. Nelson, R. P. Gale, and J. C. Liebeskind, "Apparent involvement of opioid peptides in stress-induced enhancement of tumor growth," *Peptides*, vol. 4, no. 5, pp. 635–638, 1983.
- [19] M. G. Sergeeva, Z. V. Grishina, and S. D. Varfolomeyev, "Morphine effect on proliferation of normal and tumor cells of immune origin," *Immunology Letters*, vol. 36, no. 2, pp. 215–218, 1993.
- [20] K. Gupta, S. Kshirsagar, L. Chang et al., "Morphine stimulates angiogenesis by activating proangiogenic and survival-promoting signaling and promotes breast tumor growth," *Cancer Research*, vol. 62, no. 15, pp. 4491–4498, 2002.
- [21] M. Farooqui, Y. Li, T. Rogers et al., "COX-2 inhibitor celecoxib prevents chronic morphine-induced promotion of angiogenesis, tumour growth, metastasis and mortality, without compromising analgesia," *British Journal of Cancer*, vol. 97, no. 11, pp. 1523–1531, 2007.
- [22] J. Zong and G. M. Pollack, "Morphine antinociception is enhanced in *mdr1a* gene-deficient mice," *Pharmaceutical Research*, vol. 17, no. 6, pp. 749–753, 2000.
- [23] S. Bimonte, A. Barbieri, G. Palma, and C. Arra, "The role of morphine in animal models of human cancer: does morphine promote or inhibit the tumor growth?" *BioMed Research International*, vol. 2013, Article ID 258141, 4 pages, 2013.
- [24] J. Nguyen, "Morphine stimulates cancer progression and mast cell activation and impairs survival in transgenic mice with breast cancer," *British Journal of Anaesthesia*, vol. 113, supplement 1, pp. i4–i13, 2014.
- [25] M. Ishikawa, K. Tanno, A. Kamo, Y. Takayanagi, and K.-I. Sasaki, "Enhancement of tumor growth by morphine and its possible mechanism in mice," *Biological and Pharmaceutical Bulletin*, vol. 16, no. 8, pp. 762–766, 1993.
- [26] M. Iglesias, M. F. Segura, J. X. Comella, and G. Olmos, " $\mu$ -opioid receptor activation prevents apoptosis following serum withdrawal in differentiated SH-SY5Y cells and cortical neurons via phosphatidylinositol 3-kinase," *Neuropharmacology*, vol. 44, no. 4, pp. 482–492, 2003.
- [27] K. Gach, J. Szemraj, J. Fichna, M. Piestrzeniewicz, D. S. Delbro, and A. Janecka, "The influence of opioids on urokinase plasminogen activator on protein and mRNA level in MCF-7 breast cancer cell line," *Chemical Biology and Drug Design*, vol. 74, no. 4, pp. 390–396, 2009.
- [28] P. A. Singleton and J. Moss, "Effect of perioperative opioids on cancer recurrence: a hypothesis," *Future Oncology*, vol. 6, no. 8, pp. 1237–1242, 2010.
- [29] C. Chen, M. Farooqui, and K. Gupta, "Morphine stimulates vascular endothelial growth factor-like signaling in mouse retinal endothelial cells," *Current Neurovascular Research*, vol. 3, no. 3, pp. 171–180, 2006.
- [30] D. R. Green and J. C. Reed, "Mitochondria and apoptosis," *Science*, vol. 281, no. 5381, pp. 1309–1312, 1998.
- [31] A. Ashkenazi and V. M. Dixit, "Apoptosis control by death and decoy receptors," *Current Opinion in Cell Biology*, vol. 11, no. 2, pp. 255–260, 1999.
- [32] D. Hanahan and R. A. Weinberg, "The hallmarks of cancer," *Cell*, vol. 100, no. 1, pp. 57–70, 2000.
- [33] M. O. Hengartner, "The biochemistry of apoptosis," *Nature*, vol. 407, no. 6805, pp. 770–776, 2000.
- [34] P.-N. Hsiao, M.-C. Chang, W.-F. Cheng et al., "Morphine induces apoptosis of human endothelial cells through nitric oxide and reactive oxygen species pathways," *Toxicology*, vol. 256, no. 1-2, pp. 83–91, 2009.
- [35] A. A. Kapasi, S. A. Coscia, M. P. Pandya, and P. C. Singhal, "Morphine modulates HIV-1 gp160-induced murine macrophage and human monocyte apoptosis by disparate ways," *Journal of Neuroimmunology*, vol. 148, no. 1-2, pp. 86–96, 2004.
- [36] X. Lin, Q. Li, Y.-J. Wang et al., "Morphine inhibits doxorubicin-induced reactive oxygen species generation and nuclear factor  $\kappa$ B transcriptional activation in neuroblastoma SH-SY5Y cells," *Biochemical Journal*, vol. 406, no. 2, pp. 215–221, 2007.
- [37] R. Arerangaiah, N. Chalasani, A. M. Udager et al., "Opioids induce renal abnormalities in tumor-bearing mice," *Nephron—Experimental Nephrology*, vol. 105, no. 3, pp. e80–e89, 2007.
- [38] D. Salvemini, T. P. Misko, J. L. Masferrer, K. Seibert, M. G. Currie, and P. Needleman, "Nitric oxide activates cyclooxygenase enzymes," *Proceedings of the National Academy of Sciences of the United States of America*, vol. 90, no. 15, pp. 7240–7244, 1993.
- [39] E. Nédélec, A. Abid, C. Cipolletta et al., "Stimulation of cyclooxygenase-2-activity by nitric oxide-derived species in rat chondrocyte: lack of contribution to loss of cartilage anabolism," *Biochemical Pharmacology*, vol. 61, no. 8, pp. 965–978, 2001.
- [40] M. Farooqui, Z. H. Geng, E. J. Stephenson, N. Zaveri, D. Yee, and K. Gupta, "Naloxone acts as an antagonist of estrogen receptor activity in MCF-7 cells," *Molecular Cancer Therapeutics*, vol. 5, no. 3, pp. 611–620, 2006.
- [41] D. Salvemini, K. Seibert, J. L. Masferrer, T. P. Misko, M. G. Currie, and P. Needleman, "Endogenous nitric oxide enhances prostaglandin production in a model of renal inflammation," *Journal of Clinical Investigation*, vol. 93, no. 5, pp. 1940–1947, 1994.
- [42] R. J. Griffin, B. W. Williams, R. Wild, J. M. Cherrington, H. Park, and C. W. Song, "Simultaneous inhibition of the receptor kinase activity of vascular endothelial, fibroblast, and platelet-derived growth factors suppresses tumor growth and enhances tumor radiation response," *Cancer Research*, vol. 62, no. 6, pp. 1702–1706, 2002.
- [43] K. M. Leahy, R. L. Ornberg, Y. Wang, B. S. Zweifel, A. T. Koki, and J. L. Masferrer, "Cyclooxygenase-2 inhibition by celecoxib reduces proliferation and induces apoptosis in angiogenic endothelial cells *in vivo*," *Cancer Research*, vol. 62, no. 3, pp. 625–631, 2002.
- [44] S. H. Chang, C. H. Liu, and R. Conway, "Role of prostaglandin E2-dependent angiogenic switch in cyclooxygenase 2-induced breast cancer progression," *Proceedings of the National Academy of Sciences of the United States of America*, vol. 101, no. 2, pp. 591–596, 2004.

- [45] C.-F. Lam, Y.-C. Liu, F.-L. Tseng et al., "High-dose morphine impairs vascular endothelial function by increased production of superoxide anions," *Anesthesiology*, vol. 106, no. 3, pp. 532–537, 2007.
- [46] J. Blebea, J. E. Mazo, T. K. Kihara et al., "Opioid growth factor modulates angiogenesis," *Journal of Vascular Surgery*, vol. 32, no. 2, pp. 364–373, 2000.
- [47] C.-F. Lam, P.-J. Chang, Y.-S. Huang et al., "Prolonged use of high-dose morphine impairs angiogenesis and mobilization of endothelial progenitor cells in mice," *Anesthesia and Analgesia*, vol. 107, no. 2, pp. 686–692, 2008.
- [48] J. L. Martin, R. Charboneau, R. A. Barke, and S. Roy, "Chronic morphine treatment inhibits LPS-induced angiogenesis: implications in wound healing," *Cellular Immunology*, vol. 265, no. 2, pp. 139–145, 2010.
- [49] S. Roy, S. Balasubramanian, J. Wang, Y. Chandrashekhar, R. Charboneau, and R. Barke, "Morphine inhibits VEGF expression in myocardial ischemia," *Surgery*, vol. 134, no. 2, pp. 336–344, 2003.
- [50] L. Koodie, S. Ramakrishnan, and S. Roy, "Morphine suppresses tumor angiogenesis through a HIF-1 $\alpha$ /p38MAPK pathway," *The American Journal of Pathology*, vol. 177, no. 2, pp. 984–997, 2010.
- [51] N. Faramarzi, A. Abbasi, S. M. Tavangar, M. Mazouchi, and A. R. Dehpour, "Opioid receptor antagonist promotes angiogenesis in bile duct ligated rats," *Journal of Gastroenterology and Hepatology*, vol. 24, no. 7, pp. 1226–1229, 2009.
- [52] R. L. Shapiro, J. G. Duquette, D. F. Roses et al., "Induction of primary cutaneous melanocytic neoplasms in urokinase-type plasminogen activator (uPA)-deficient and wild-type mice: cellular blue nevi invade but do not progress to malignant melanoma in uPA-deficient animals," *Cancer Research*, vol. 56, no. 15, pp. 3597–3604, 1996.
- [53] J. A. Engbring and H. K. Kleinman, "The basement membrane matrix in malignancy," *Journal of Pathology*, vol. 200, no. 4, pp. 465–470, 2003.
- [54] M. S. Widel, "Mechanisms of metastasis and molecular markers of malignant tumor progression. I. Colorectal cancer," *Postępy Higieny i Medycyny Doświadczalnej*, vol. 60, pp. 453–470, 2006.

## Review Article

# Preclinical Murine Models for Lung Cancer: Clinical Trial Applications

**Amelia Kellar, Cay Egan, and Don Morris**

*Departments of Oncology/Medicine, University of Calgary, 1331 29 Street NW, Calgary, AB, Canada T2N 4N2*

Correspondence should be addressed to Cay Egan; [egan@ucalgary.ca](mailto:egan@ucalgary.ca)

Received 9 October 2014; Accepted 24 November 2014

Academic Editor: Monica Fedele

Copyright © 2015 Amelia Kellar et al. This is an open access article distributed under the Creative Commons Attribution License, which permits unrestricted use, distribution, and reproduction in any medium, provided the original work is properly cited.

Murine models for the study of lung cancer have historically been the backbone of preliminary preclinical data to support early human clinical trials. However, the availability of multiple experimental systems leads to debate concerning which model, if any, is best suited for a particular therapeutic strategy. It is imperative that these models accurately predict clinical benefit of therapy. This review provides an overview of the current murine models used to study lung cancer and the advantages and limitations of each model, as well as a retrospective evaluation of the uses of each model with respect to accuracy in predicting clinical benefit of therapy. A better understanding of murine models and their uses, as well as their limitations may aid future research concerning the development and implementation of new targeted therapies and chemotherapeutic agents for lung cancer.

## 1. Introduction

Lung cancer is the leading cause of cancer mortality worldwide [1]. It is estimated that approximately 228,190 people were diagnosed with lung cancer in 2013, resulting in approximately 159,480 deaths in the United States [2]. Current chemotherapies prove to be only marginally effective in extending overall survival as five-year survival for anyone diagnosed with cancer of the lung or bronchus is about 16% [2]. The development and implementation of new, targeted agents may be aided by the availability of universally applicable experimental murine models for testing novel therapeutics. In order to generate and evaluate novel therapies for lung cancer, advanced preclinical models ideally should accurately mimic lung cancer progression, invasion, and metastasis as well as predicting clinical benefit of therapy for all types of lung cancer. A wide variety of murine model systems have been developed with the aim of not only evaluating novel therapeutics, but also examining the mechanisms underlying transformation, invasion and metastasis in human tumours with a view to better study prevention and screening as well as diagnostic and treatment strategies. This review will introduce the frequent mutations found in lung cancer patients and how these mutations have been incorporated into preclinical models to accurately evaluate novel therapies for lung

cancer. Characteristics of each model system as well as the advantages and disadvantages will be described. Relevant models will then be discussed with regard to how accurate each murine model is in successfully predicting outcome of therapy in clinical trials.

## 2. Mutations Associated with Lung Cancer Development

A better understanding of the most frequent driving mutations in lung cancer will aid in the progression towards more personalized therapy. Molecular markers have been identified that provide the basis for targeted therapies for lung cancer. Current prognostic molecular pathways for lung cancer include EGFR, K-Ras, p53, and EML4-ALK [3–9].

EGFR regulates a myriad of cell functions such as proliferation, angiogenesis, and apoptosis [6]. The most common EGFR activating mutations are in-frame deletions in exon 19 or point mutations in codon 858 in exon 21 [10]. Targeted therapies in the form of EGFR tyrosine kinase inhibitors, such as erlotinib and gefitinib as well as monoclonal antibodies against EGFR such as cetuximab, have been employed as treatments for the disease. EGFR-targeted therapies have proven to be effective in both first and second-line of treatment for patients with EGFR mutations [11].

Mutations in the K-Ras gene are present in approximately 30 percent of adenocarcinomas and are generally associated with a poor prognosis [12]. The K-Ras oncogene encodes a family of membrane-bound guanosine triphosphate- (GTP-) binding proteins that are involved in cell proliferation, migration, and apoptosis. The most common K-Ras mutations are in the form of point mutations on exons 12 and 13, typically resulting in constitutive activation of RAS [13]. Interestingly, cases of NSCLC exhibiting K-Ras mutations are predominantly resistant to the EGFR inhibitors, erlotinib, and gefitinib [14].

In addition to K-Ras, p53 is a well-established predictive and prognostic marker for NSCLC. Loss of the tumour suppressor gene, p53, leads to mitotic abnormalities during cellular development resulting in highly proliferative cells [15]. Transversions along the p53 gene are found in almost all human lung cancer tissues and have implicated p53 as a key molecular marker for lung cancer [16]. A comprehensive meta-analysis of the role of p53 as a prognostic factor for lung cancer survival revealed that mutated or inactive p53 was shown to be associated with a poor survival [17].

It has recently been reported that echinoderm microtubule-associated protein-like 4 (EML4) and anaplastic lymphoma kinase (ALK) gene fusions are present in approximately 3% of patients with NSCLC and that EML4 and ALK amplifications may play a role in NSCLC transformation [9]. NSCLC and SCLC have also been associated with mutations in the PI3K-Akt-mTOR pathway, LKB1, TITF1, beta-tubulin, ERCC1, and RRM1 [18–22].

### 3. Xenograft, *Ex Vivo*, and Orthotopic Models

For the purpose of this review, murine models can be divided into the following groups: xenograft, transgenic, syngeneic, and spontaneous model systems. Xenograft models require the injection of human cancer cells into immunocompromised mice, either subcutaneously, orthotopically, or systemically. Immunocompromised mice such as athymic nude and severe-compromised immunodeficient (SCID) mice are frequently utilized as implanted human cells are likely to be rejected by the host immune system in an immunocompetent system. Once implanted, cells require a growth period of one to eight weeks depending on cell type and the number of cells injected. Xenograft models are primarily used to examine tumour response to therapy *in vivo* prior to translation into clinical trials. Cell lines and current xenograft models for the study of lung cancer are summarized in Table 1.

Cancer cell lines vary in optimal cell number required for implantation, ranging from  $1 \times 10^6$ – $1 \times 10^7$  cells/injection site. Both the average number of tumours that engraft (tumour take) and the average time to palpable tumours are dependent on the number of cells implanted, growth characteristics of each cell-line such as doubling time, cell-size, density, morphology, and the use of growth factors such as matrigel. Cell lines commonly used to model adenocarcinoma are A549, H1975, HCC4006 and HCC827 [26, 28, 43], representing a spectrum of K-Ras and EGFR mutations. Current xenograft models for adenocarcinoma demonstrate an average tumour take of 50–100%, with the A549 cell-line as the most likely to

engraft [26, 28, 37, 38]. The tumour take as well as murine strain used for implantation are given in Table 1. Typically, these models require two to eight weeks following cell implantation in order to observe tumour growth substantial enough for evaluating drug efficacy.

Cell-lines that are commonly used to model carcinoma [27, 29, 32], large-cell carcinoma [31, 33–36], and squamous-cell carcinoma [36] in xenograft models include NCI-H1299, NCI-H460 and NCI-H226, respectively. The NCI-H460 cell-line has proven to be an advantageous model system as it requires small implantation cell numbers and limited growth time and has been shown to have a 100 percent tumour take when injected into the hind flank of CD-1 athymic nude mice [28, 36]. Both the NCI-H1299 and the NCI-H226 cell-lines are slightly more limited in their experimental uses as they have only a 45–100 percent tumour take and require at least four weeks to reach optimal tumour size in order to begin treatment [27, 29, 36, 65]. Models for SCLC are generally limited, however, the NCI-H69 and DMS-53 cell-lines are the most widely used for xenograft studies but can be problematic as they characteristically grow in suspension, resulting in difficulty in obtaining an accurate cell count prior to implantation [23–25]. These characteristics may contribute to a highly variable tumour take and growth rates of these models.

In addition to traditional xenograft models, *ex vivo* models can be used in which tumours are surgically removed from patients and tumour cells are grafted into the immunocompromised murine system either subcutaneously or orthotopically. These models are ideal for personalized therapy and provide relatively quick data concerning the most beneficial therapies for each patient [89–91]. In the study conducted by Dong et al. [91], thirty-two untreated samples of NSCLC were engrafted into the renal capsules of nonobese diabetic/SCID mice. Tumour growth was evaluated in response to cisplatin, docetaxel, and gemcitabine. *Ex vivo* tumour take was 90 percent and results were obtained over six to eight weeks. As a result, therapy regimens for each patient were tailored according to observed tumour response in the xenograft models. A good correlation was found between recurrence or metastasis in patients and the non-responsiveness of their tumour xenografts in mice.

There is ample evidence that growth properties of tumour cells are altered by specific genes whose expression is dependent on interactions within the tumour microenvironment. Therefore, it is vital that tumour microenvironment be accurately mirrored in murine models used to evaluate drug therapies. Orthotopic models provide a reliable representation of tumour environment as cells are implanted directly into the organ in which the disease originates. Current orthotopic models are reviewed in Table 1. The most practical orthotopic model involves endobronchial inoculation of the A549 or H460 cell-lines into athymic NCr-nu/nu mice [31]. The procedure results in a postsurgery mortality rate of less than 5 percent. The rate of tumour engraftment is 90 percent and tumour growth is monitored through high-resolution chest roentgenography or bioluminescence via transfection of luciferase containing constructs [92].

TABLE 1: Xenograft and orthotopic models for lung cancer.

Cell line	Description	Histology	Origin	Mutation	Adherence	Method of implantation	Animal model/s	Cell inoculation	Percentage tumor take	Palpable tumours	Metastatic potential	References
DMS-53	Small-cell carcinoma	SCLC	Male, age 54, smoking status unknown	Low Ras activity, p53 mutation	Adherent	Subcutaneous, hind flank injection	Female BALB/c nude mice Female nude athymic	10(6)–10(7) cells/mouse with PBS or matrigel	50–100%	4–8 weeks	Not previously described	[23, 24]
NCI-H69	Small-cell carcinoma	SCLC	Male, age 55, smoking status unknown	p53 deficient, wild type but low EGFR	Suspension, multicell aggregates	Subcutaneous, hind flank injection	Female athymic nu/nu/CR hind flank	5 × 10(6) cells/mouse with PBS or matrigel	80–100%	15 days–4 weeks	Not previously described	[25]
A549	Adenocarcinoma	NSCLC	Male, age 58, smoking status unknown	Ras mutation	Adherent	Subcutaneous, hind flank injection Endobronchial	BALB/cAnNCrIBR athymic (nu+/nu+) BALB/c or NMRI-nu/nu female mice	2 × 10 <sup>6</sup> –2 × 10(7) cells/mouse with matrigel 1 × 10(4)–1 × 10(6) cells/mouse	100%	2–5 weeks 9–61 days	Not previously described Yes. Left lung, liver and spleen	[26–30] [31]
H1299	Carcinoma	NSCLC	Male, age 43, smoking status unknown	N-Ras mutation, P53 negative High EGFR expression	Adherent	Subcutaneous, hind flank injection	Female athymic nude mice BALB/c nude mice	2 × 10 <sup>6</sup> –1 × 10 <sup>7</sup> cells/mouse with matrigel	45–100%	4–6 weeks	Not previously described	[27, 29, 32]
NCI-H460	Large cell carcinoma	NSCLC	Male, age and smoking status unknown	K-Ras mutation	Adherent	Subcutaneous, hind flank injection Endobronchial	Female athymic nude mice (Ncr nu/nu) Female athymic nude mice (Ncr nu/nu)	3 × 10(5)–1 × 10(7) cells/mouse with matrigel 1 × 10(4)–1 × 10(6) cells/mouse	100%	4–11 days 9–61 days	Not previously described Yes. Left lung, liver and spleen	[28, 31, 33–36] [31]
H1975	Adenocarcinoma	NSCLC	Female, non-smoker	EGFR mutation L858R and T790M	Adherent	Subcutaneous, hind flank injection	Female athymic (nu/nu) mice NMRI-nu/nu female mice	1 × 10(6)–1 × 10(7) cells/mouse with matrigel	50–100%	4–8 weeks	Not previously described	[28, 37]
NCI-H226	Squamous carcinoma	NSCLC	Male, age and smoking status unknown	P53 mutation	Adherent	Subcutaneous, hind flank injection	BALB/c nude mice Female SCID/SCID mice	8 × 10 <sup>6</sup> cells/mouse with PBS or matrigel	50–100%	4–8 weeks	Not previously described	[36]

TABLE 1: Continued.

Cell line	Description	Histology	Origin	Mutation	Adherence	Method of implantation	Animal model/s	Cell inoculation	Percentage tumor take	Palpable tumours	Metastatic potential	References
HCC827	Adenocarcinoma	NSCLC	Female, age 39, smoking status unknown	In-frame deletion (dE746-A750) in exon 19 of EGFR increased copy number	Adherent	Subcutaneous, hind flank injection	Female athymic (nu/nu) mice Female BALB/cA nude mice	2 × 10 <sup>7</sup> cells/mouse with matrigel	80–100%	4–5 weeks	Not previously described	[26, 28]
HCC4006	Adenocarcinoma	NSCLC	Male, age >50, smoking status unknown	In-frame deletion (dE746-A750) in exon 19 of EGFR	Adherent	Subcutaneous, hind flank injection	Female SCID/SCID mice	1–2 × 10 <sup>6</sup> cells/mouse with PBS or matrigel	50–100%	4–8 weeks	Not previously described	[38]
NCI-H358	Bronchioalviolar carcinoma	NSCLC	Male, age and smoking status unknown	Wild-type EGFR	Adherent	Subcutaneous, hind flank injection	Female athymic (nu/nu) mice	2 × 10 <sup>7</sup> cells/mouse with PBS or matrigel	100%	4–5 weeks	Not previously described	[26, 28, 39]
LLC	Lewis lung carcinoma	NSCLC	C57BL mouse	Not reported	Mixed, adherent and suspension	Subcutaneous, leg injection	Male C57BL mice	2 × 10 <sup>6</sup> cells/mouse	100%	7 days	Yes. Lung	[40]
NCI-H23	Adenocarcinoma	NSCLC	Male, 51 years	p53 mutation	Adherent	Subcutaneous	Female BALB-C nude mice	3 × 3 × 3 mm tumor fragment	100%	14 days	Not previously described	[36]
DMS-273	Small-cell carcinoma	SCLC	Female, 50 years	p53 mutation	Adherent	Subcutaneous	Female BALB-C nude mice	3 × 3 × 3 mm tumor fragment	100%	14 days	Not previously described	[36]
DMS-114	Small-cell carcinoma	SCLC	Male, 68 years	p53 mutation	Adherent	Subcutaneous	Female BALB-C nude mice	3 × 3 × 3 mm tumor fragment	100%	14 days	Not previously described	[36]
TL-1	Squamous carcinoma	NSCLC	Not reported	Not reported	Adherent	Subcutaneous	CB-17 scid/scid mice	2 × 10 <sup>6</sup> cells/mouse in saline	60–70%	3–4 weeks	Not previously described	[41]
NCI-H526	Carcinoma	SCLC	Male, 55 years	KIT positive	Suspension	Subcutaneous, hind flank injection	Female athymic nu/nu mice	5 × 10 <sup>6</sup> cells/mouse in saline	100%	20 days	Not previously described	[42]
NCI H82	Carcinoma	SCLC	Male, 40 years	KIT negative	Suspension	Subcutaneous, hind flank injection	Female athymic nu/nu mice	5 × 10 <sup>6</sup> cells/mouse in saline	100%	25 days	Not previously described	[42]
NCI-H358	Bronchioalviolar carcinoma	NSCLC	Male	Wt EGFR Mutated ras	Adherent	Subcutaneous, hind flank injection	Female athymic nu/nu mice	2 × 10 <sup>7</sup> cells/mouse with 1:1 PBS and matrigel	100%	Not reported	Not previously described	[28]

Xenograft models for lung cancer have advantages and disadvantages in comparison with classic transgenic and conditional murine models. Firstly, xenograft models utilize human tumour tissue, perhaps accurately representing the complexities of human tumours *in vivo*. Unlike their genetically engineered counterparts, xenograft models can be used to design individualized molecular therapy. In a study by John et al. [93], the ability of tumour fragments from patients undergoing curative surgery to engraft into primary tumour xenografts was found to be predictive of risk of disease recurrence. These findings, in conjunction with other *ex vivo* xenograft findings show that xenograft models are a useful evaluative tool for targeted molecular therapy and predicting patient outcome [91]. Xenograft models are also ideal for examining multitherapy approaches *in vivo*. Much chemotherapy is approved on the basis of a combination therapy regimen with other preexisting interventions, therefore, pre-clinical xenograft models are used to evaluate efficacy of these drug combinations prior to clinical trials [32, 76, 81, 94]. Orthotopic xenograft models provide the very valuable advantage of accurate representation of the tumour microenvironment in evaluating drug therapies. This allows for a reliable prediction of toxicity, and understanding of microenvironment-dependent responses to selected therapies.

Despite the advantages of using xenograft models in preclinical studies, there are also many limitations to these models that must be addressed. Immunocompromised mice must be used for xenograft models in order to combat the effects of the healthy immune system response against foreign cells. Syngeneic models, which will be discussed shortly, are alternative model systems used to combat this issue. Alternatively, orthotopic models combat the issue of inaccurate representation of tumour microenvironment as cells are implanted directly into the bronchi; however, once growth commences, it is more difficult to quantify than in the traditional xenograft model. Current orthotopic models used to study lung cancer are shown in Table 1. Despite the benefits of orthotopic systems, they can also be quite time consuming and challenging to replicate as cell inoculations are typically conducted endobronchially, requiring skillful precision and practice. These disadvantages may account for the lack of robust orthotopic models for lung cancer, lending to the preference towards the traditional hind flank xenograft model.

#### 4. Syngeneic Models

Syngeneic murine models entail the injection of immunologically compatible cancer cells into immunocompetent mice. The availability of syngeneic models to study lung cancer is very limited. The only reproducible syngeneic model for lung cancer to date is the Lewis lung carcinoma (LLC) model. LLC is a cell line established from the lung of a C57BL mouse bearing a tumour resulting from the implantation of primary Lewis lung carcinoma. The cell line is highly tumorigenic and is primarily used to model metastasis as well as evaluate the efficacy of chemotherapeutic agents *in vivo* [95]. For example, the LLC model was a successful preclinical model for Navelbine evaluation *in vivo*, prior to its implementation

in clinical trials [73, 74]. The LLC cell-line is typically injected orthotopically into the peritoneal cavity of C57B6 mice at  $1 \times 10^7$  cells per mouse and within two weeks of incubation, tumours reach  $2.2 \pm 0.4$  mm [40, 73]. Preclinical models for evaluation of chemotherapeutic agents are shown in Table 3.

The advantage of the LLC model is that implanted cells are immunologically compatible with the murine system, unlike the widely used xenograft models in which human cells are implanted into mouse tissue. As a result, LLC models can be created on an immunocompetent murine background, such as C57BL, and true immune and toxicity responses can be evaluated with respect to targeted therapies and tumour growth. In addition, because the LLC model can be both syngeneic and orthotopic, tumour microenvironment can be accurately depicted in the animal model. Despite its superiority as an animal model for lung cancer, the LLC model is associated with several limitations. As a syngeneic model, responses evaluated in a complete murine system may not be transferable to human conditions. As an orthotopic model, the LLC model can also result in difficulties in quantifying tumour growth without advanced imaging equipment and as such, it can be quite expensive, time-consuming, and difficult to reproduce.

#### 5. Transgenic and Conditional Transgenic Models

Genetically engineered models (GEM) are used to induce spontaneous neoplastic growth via transgenic, conditional, or drug-induced mechanisms. Transgenic mice are created by microinjection of DNA into the pronucleus of zygotes and injection of embryonic stem cells into blastocysts to produce the desired loss or gain of function mutations. Transgenic mouse models for lung cancer may be general, where tumours arise in lung and in organs other than the lung or specific, where the lung alone is the target of the transgene. The latter models are more useful, as the frequency of the development of lung cancer is often higher and the pathology of the disease is not complicated by tumours at other sites. The DNA construct for the transgene is created by linking a lung-specific promoter to the coding region of a target gene [96]. Transgenic mice are ideal for examining the role of genetic abnormalities in tumour initiation and progression. The current transgenic models that are used to study lung cancer are shown in Table 2.

One of the first viral oncogenes to be targeted to the lung was Simian virus T antigen (TAG). Tag binds to and inactivates p53 and pRB, both of which have been reported to be mutated or functionally altered in lung cancer [97]. Through the use of the lung specific promoters Clara cell secretory protein (CCSP), also known as uteroglobin promoter, and alveolar type II surfactant protein C (SP-C), these transgenes resulted in the development of adenocarcinoma in a murine model [53, 54]. The mice developed multifocal bronchioalveolar neoplasias very rapidly and often died before four months of age, making investigation of the early events in carcinogenesis difficult. An alternative model for pulmonary adenocarcinoma in distal lung epithelium has been developed in which transcription of TAG is driven by a lung

TABLE 2: Transgenic, conditional transgenic and carcinogen-inducible models for lung cancer (\* intratracheal instillation of Ad-Cre virus is required; TAG: simian virus T antigen; CCSP: clara cell secretory protein; SP-C: alveolar type II surfactant protein C; CaBP9K: rat calbindin-D9K; CCl10: clara cell 10 kDa secretory protein; CGRP: calcitonin gene-related peptide; rTA-reverse tetracycline transactivator protein; LSL: lox-stop-lox; hASHI: human achaete-scute homolog 1; EGFR: epidermal growth factor receptor; FGF: fibroblast growth factor).

Model type	Model	Background	Histology	Advantages	Disadvantages	References
<i>Conditional</i>						
Oncogenes	LSL K-Ras G12D* K-Ras4b G12D* K-Ras V12*	C57BL/6 C57BL/6 C57BL/6	Adenocarcinoma Adenocarcinoma Adenocarcinoma	(i) Limited number of cells can be targeted (ii) Ideal for studying early lung tumor development	(i) Limited metastasis (ii) (One mutation not sufficient to produce higher grade malignancy) (iii) Gene expression signature slightly different for human K-Ras	[44] [45] [46]
	Lkb1: LSL K-Ras <sup>G12D</sup>	C57BL/6	Adenocarcinoma/squamous cell carcinoma, large cell carcinoma in some cases	(i) Metastasis (ii) Limited number of cells can be targeted	(i) Very invasive, often early death of animal	[47]
Growth factor receptors	CCSP-rTA; Tet- $\sigma_7$ -EGFR <sup>L858R</sup> CCSP-rTA; Tet- $\sigma_7$ -EGFR <sup>DEL</sup>	FVB/N FVB/N	Bronchioalveolar carcinoma Bronchioalveolar carcinoma	(i) Turning on and off with tetracycline/doxycycline (ii) Can target expression to pulmonary epithelium (iii) Resemblance to human adenocarcinoma	(ii) Invasive metastasis within 4 weeks (iii) More difficult to study early cancer events	[48, 49]
Tumor suppressor genes	Trp53* Rb-Trp53*	C57/BL/6 or 129/Sv wild-type Athymic BALB/c nu/nu	Adenocarcinoma SCLC Neuroendocrine hyperplasia, SCLC	(i) Turning expression on and off (ii) Metastasis towards similar organs as human SCLC (iii) Share neuroendocrine features of SCLC	(i) Very invasive, often early death of animal (ii) More difficult to study early cancer events	[50]
Growth factors	CC10-rTA; Tet- $\sigma_7$ -CMV-FGF7	CBA/C57Bl6	Epithelial cell hyperplasia and adenomatous hyperplasia	(i) Hyperplasia disappears when doxycycline removed	(i) Limited metastasis (fails to accurately mimic human adenocarcinoma)	[51]
<i>Transgenic</i>						
Transcription factors	CC10-hASHI CC10-Tag; CC10-hASHI	FVB FVB	Hyperplasia and bronchioloalveolar metaplasia Adenocarcinoma with neuroendocrine differentiation	(i) Ideal for carcinogenesis and cancer prevention studies and the role of specific oncogene in growth, differentiation, transformation	(i) Measurable in late stage (ii) Metastasis not uniform (iii) Response to therapy is typically poor	[52]
Viral oncogenes	SP-C-TAG CCSP-TAG CaBP9K-TAG	FVB/N FVB/N FVB/N	Adenocarcinoma Adenocarcinoma Adenocarcinoma	(i) Typically 100% tumor take (ii) Ideal for carcinogenesis and cancer prevention studies	(i) Rapid onset and aggressive (ii) Difficult to examine early events in transformation (iii) Difficult to detect events independent of oncogene expression	[53] [54] [55]

TABLE 2: Continued.

Model type	Model	Background	Histology	Advantages	Disadvantages	References
	CGRP-H-Ras	FVB/N	Neuroendocrine hyperplasia and non-neuroendocrine adenocarcinoma	(i) Ideal for carcinogenesis and cancer prevention studies and the role of specific oncogene in growth, differentiation, and transformation (i) Aggressive presentation (ii) Ideal for carcinogenesis and cancer prevention studies	(i) Often early death of animal (ii) Relationship between Ras isoforms roles in transformation not fully understood	[56]
	SP-C-EML4-ALK	C57BL/6J	Adenocarcinoma	(i) Aggressive presentation (ii) Ideal for carcinogenesis and cancer prevention studies	(i) Often early death of animal (ii) No conditional expression	[57]
Oncogenes	SP-C-Myc CC10-Myc	CD2/F1 (DBA/2 × Balb/C) CD2/F1 (DBA/2 × Balb/C)	Adenocarcinoma Bronchioloalveolar hyperplasia	(i) Aggressive presentation (ii) Ideal for carcinogenesis and cancer prevention studies	(i) Do not often metastasize (ii) Metastasis not uniform (iii) Response to therapy is typically poor	[58]
	SP-C-c-Raf-1 SP-C-c-Raf-1-BxB	C57BL/6 × DBA-2 C57BL/6 × DBA-2	Adenoma Adenoma	(i) Aggressive presentation (ii) Ideal for carcinogenesis and cancer prevention studies	(i) Do not often metastasize (ii) Measurable in late stage (iii) Metastasis not uniform (iv) Response to therapy is typically poor	[59]
Growth factors	SP-C-RON	B6C3/F1 hybrid mice (C57BL/6 × C3H, Taconic)	Adenoma and adenocarcinoma	(i) Temporal-spatial expression (ii) Ideal for carcinogenesis and cancer prevention studies	(i) Metastasis not uniform (ii) Response to therapy is typically poor	[60]
Growth factor receptors	SP-C-IgEGF SP-C-cMyc; SpC-IgEGF	CD2/F1 (DBA/2 × Balb/C) CD2/F1 (DBA/2 × Balb/C)	Alveolar hyperplasia Bronchioloalveolar Adenocarcinoma	(i) Ideal for carcinogenesis and cancer prevention studies	(i) Metastasis not uniform (ii) Response to therapy is typically poor	[58]
Carcinogen inducible models	Inoculation Method	Background	Growth Properties	Advantages	Disadvantages	References
<i>Urethane</i>	Intraperitoneal	Inbred (A/J or SWR most widely used)	Adenoma			[61]
Benzo(a)pyrene	Intraperitoneal		Adenoma	(i) More likely to accurately predict clinical efficacy of chemotherapeutic agents	(i) Lethality	[62, 63]
N-Nitrosobis-(2-chloroethyl)ureas	Topical	Cr:NIH(S)	Adenosquamous carcinoma	(ii) Aggressive (iii) All tumor stages can be observed	(iii) Varying response to carcinogen (iv) Low rate of spontaneous development (v) Long incubation time	[64]
Dimethylhydrazine	Intraperitoneal		Adenoma			
Diethylnitrosamine	Intraperitoneal	A/J	Adenoma			
EthylNitrosourea	Intraperitoneal		Adenoma			
3-Methylcholanthrene	Intraperitoneal		Adenoma			[62]

specific 1011 base-pair DNA fragment of the rat Calbindin-D9K (CaBP9K) promoter [55]. In this model development of lung tumours was slower, with animals living to nearly a year, allowing analysis of early stages of tumour development.

In contrast to the TAG models which utilize lung promoter-viral oncogene fusion, human achaete-scute homolog-1 (hASH1) models have been developed that rely on the human transcription factor's fusion to the lung-specific clara cell 10 kDa secretory protein (CC10). Achaete-scute is a helix-loop-helix transcription factor involved in neural differentiation during fetal development. Neuroendocrine features are a hallmark of SCLC and some NSCLCs and the rationale behind development of this transgenic model was to investigate the effect of constitutive expression of achaete-scute in nonneuroendocrine airway epithelial cells that normally do not express it. Interestingly, expression resulted in the development of hyperplasia and bronchioalveolar metaplasia. hASH1-CC10 was also generated in combination with the TAG oncogene to promote the growth of adenocarcinoma with neuroendocrine differentiation and increased tumorigenesis [52, 98]. These models typically resulted in tumour growth in 100 percent of animals, but exhibited rapid and aggressive growth which prevented the analysis of early transformation events.

Transgenic mice have also been generated through the fusion of oncogenes with lung-cell-specific promoters such as calcitonin gene-related peptide (CGRP), SP-C or CC10. CGRP-Ha-Ras transgenic mice overexpress an activated form of the GTPase, v-Ha-Ras, that induces pulmonary neuroendocrine cell differentiation [99]. The CGRP promoter limits transgene expression to neuroendocrine and neural cells. These transgenic mice surprisingly developed primary lung tumours which were non-neuroendocrine in nature along with hyperplasia of pulmonary neuroendocrine cells and Clara cells. This suggested a common histogenesis of different pulmonary cell types [56]. The Raf kinase protooncogene transduces signals downstream of Ras. It has been shown that mutations at the amino terminus of Raf that mediate its interactions with Ras can constitutively activate the Raf kinase activity such that it can transform cells in culture [100, 101]. Overexpression of wild-type Raf in tissue culture cells sensitizes the cells to Ras transformation [102] and analysis of human lung cancer cell lines and lung biopsy material have revealed increased levels of Raf expression, suggesting this might be related to development of lung cancer [103]. To investigate this in a transgenic model, mice were engineered to express c-Raf under the control of the SP-C promoter. Approximately half of the transgenic mice developed lung adenomas with delayed tumour development, suggesting that secondary mutations needed to be acquired before tumours could develop [104].

The protooncogene c-myc, normally involved in controlling cell-cycle events, has been frequently found to be over-expressed in human pulmonary carcinoids and adenocarcinomas [105, 106]. SP-C-Myc transgenic mice overexpress an activated form of the Myc protein that acts as a transcription factor, resulting in the development of bronchioalveolar adenocarcinomas. Not all Myc transgenic mice develop lung cancer, again suggesting changes in addition

to overexpression of Myc need to occur before cancer can develop [58]. SP-C-EML4-ALK transgenic mice possess EML4-ALK gene fusion specifically within the lung epithelial cells, resulting in rapid development of adenocarcinomas [57].

Genes encoding growth factors and growth factor receptors are also feasible targets for the generation of transgenic mice. SP-C-RON transgenic mice present with constitutive activation of the receptor tyrosine RON (recepteur d'origine nantais), localized by the SP-C promoter to distal lung epithelial cells, resulting in the development of adenoma and adenocarcinomas [60]. SP-C-IgEGF and SP-C-IgEGF-Myc transgenic lines express a secretable form of the epidermal growth factor (IgEGF), a structural and functional homologue of transforming growth factor  $\alpha$  (TGF $\alpha$ ). In the case of SP-C-IgEGF-Myc, additional expression of the murine oncogene, c-Myc, under the control of the SP-C promoter is initiated [58]. These transgenic lines develop alveolar hyperplasia and bronchioalveolar adenocarcinoma, respectively. Both the SP-C-RON and SP-C-IgEGF/Myc lines facilitate spatial expression of the transgene, but result in nonuniform metastasis and a characteristically poor response to therapy, confirming that these transgenic lines are ideal for examining the role of specific oncogenes in tumour growth, differentiation, and transformation but not in drug evaluation studies [58].

In order to streamline preexisting murine models and generate a more precise method of recapitulating true gene expression patterns of lung cancer oncogenes *in vivo*, conditional transgenic models have been created. Conditional transgenic models are ligand-inducible transgenic systems that result in regulated expression of the gene of interest through the use of two transgene constructs, one which acts as a target and one as the regulator. The regulator transgene must first be activated by the addition of an exogenous compound in order to turn on transcription of the target transgene [48, 49, 107, 108]. Conditional transgenic models allow for temporal and spatial regulation of oncogenes, providing a more accurate representation of the events that induce lung cancer.

There are three primary conditional bitransgenic inducible systems in mice. The first is the reverse tetracycline transactivator (rtTA) inducible system, in which a tissue specific promoter such as CCSP drives the expression of rtTA in the tissue of interest. A second transgene is incorporated containing the target gene, fused to the tetracycline-responsive promoter (Tet-O<sub>7</sub>). Expression of the target gene is then regulated by the addition of tetracycline or doxycycline [48, 51, 107]. Conditional bitransgenic rtTA systems used to study lung cancer are shown in Table 2. The majority of the rtTA models, including those expressing transgenes for K-Ras, EGFR, and FGF7, are valuable models in that a small number of cells can be targeted and transgene expression can be regulated both temporally and spatially. Interestingly, when doxycycline is removed from the K-Ras models, lesions can no longer be detected, indicating the importance of the K-Ras oncogene in both initial tumour growth and maintenance [108]. Despite these advantages, models expressing either K-Ras and FGF7 transgenes exhibit limited metastasis, failing to

accurately mimic human adenocarcinoma *in vivo* [51, 108]. In contrast, models utilizing EGFR transgenes have been shown to metastasize early in development, resulting in early death of the animal and limited evaluation of early developmental events [48, 107].

An alternative to the rtTA system is the Cre/loxP recombination system, which facilitates the incorporation of somatic mutations in a select population of cells. The Cre/loxP system is ideal for examining both the conditional deletion of genes that cannot be examined in traditional knockout systems due to embryonic lethality, as well as the introduction of foreign genes in a tissue-specific manner. Cre is a 38 kDa recombinase protein that induces intramolecular and intermolecular recombination between loxP sites. A loxP site identifies the region for recombination, consisting of two 13 bp inverted repeats that are separated by an 8 bp asymmetric spacer region. Targeted mutations are “Floxed” (flagged by loxP sites) and through the addition of Cre recombinase, an endogenous gene or transgene is eliminated or activated by deletion of floxed sites [44–46, 50]. Current murine strains created using the Cre/loxP system are shown in Table 2. Cre transgenic strains can also be generated with Tet-inducible promoters [48]. The advantages of the Cre/loxP models are the ability to spatially regulate gene expression and evaluate events in lung cancer development [44–46].

Conditional transgenic strains resulting in conditional deletion of Trp53 alone and Trp53 in combination with pRb have proven to be one of the most valuable systems in modeling SCLC. Metastasis to select organs in these models has been shown to closely approximate metastatic events in humans as well as exhibit neuroendocrine features that are characteristic of human SCLC. Despite these advantages, these mice present with a very invasive phenotype, preventing examination of early transformation events [50].

Using the traditional Cre/loxP system, it is also possible to create a transcription block by floxing two sites in the region preceding an exon. The resulting null allele is dormant until Adeno-Cre is administered and the transcription stop is subsequently removed to allow for oncogenic mutation to occur. The lox-stop-lox (LSL) system is primarily used for K-RasG12D mutation in combination with other conditional knock-outs [47]. One of the most favored LSL models for lung cancer is the Lkb1:LSLK-RasG12D system which results in the development of adenocarcinoma and squamous cell carcinoma with metastasis that accurately reflects human metastatic events [47]. However, these strains often result in early death of the animal, and thus the system is not ideal for examining early transformation events.

## 6. Carcinogen-Inducible Models

In contrast to both transgenic and conditional transgenic systems, drug-induced models require the addition of a carcinogen to induce specific mutations leading to transformation events. The current carcinogen-inducible models for lung cancer are described in Table 2. Carcinogen-inducible models are typically generated in strains of inbred mice such as A/J or SWR which are most susceptible to spontaneous tumorigenesis [109]. Of these models,

the urethane-induced lung tumorigenesis model has several advantages. Intraperitoneal administration of urethane has been shown to be reliably reproducible and subsequent tumorigenesis develops in a time-dependent manner. Tumorigenesis progresses from hyperplasia to adenoma and eventual adenocarcinoma in response to sequential genetic changes that are characteristic of human lung cancer [61]. Of these genetic changes, K-Ras and p53 are the most prominent mutations associated with the urethane-induced model [61, 110]. The benzo(a)pyrene-induced system also models adenoma in mice, however, it has been shown to result in extremely variable growth patterns in independent experiments [63]. N-Nitrosobis-(2-chloroethyl) ureas such as N-nitroso-methyl-bischloroethylurea (NMBCU) and N-nitroso-trischloroethylurea (NTCU) have been shown to induce the growth of hyperplasia, dysplasia and metaplasia following topical administration in Cr:NIH(S) mice [64]. 3-Methylcholanthrene, diethylnitrosamine, ethylnitrosourea, and dimethylhydrazine have all been shown to induce reproducible growth of adenoma in A/J mice [62]. Although these models provide the distinct advantage of investigator control of tumorigenesis through carcinogen administration, there are also multiple disadvantages associated with these models such as variability in administration technique leading to discrepancies in results.

## 7. Future Directions

To date, Xenograft models have been most commonly used to analyze the behavior of human tumours and their response to therapeutics in a mouse model. The use of genetically modified mice is perhaps a more powerful tool for studying lung cancer development and treatment but establishment of these models can be very laborious, expensive and time-consuming. A number of initiatives, both publicly and privately funded, have now been developed to create repositories of gene-targeting vectors, genetically modified mouse strains and predeveloped embryonic stem cells carrying specific mutations. Several of these sources are reviewed in Dow and Lowe [111]. The availability of these resources should significantly reduce the time required to generate new mouse models of lung cancer.

It is now evident that RNA interference can be used in mice to reduce or shut down specific gene expression, offering an alternative to traditional knockout models, which generally only affect one copy of a gene. Short hairpin RNAs (shRNAs) expressed transgenically act without integration into genomic material and operate *in trans* to affect expression of both copies of a gene. Depending on how the transgenic model is created, the silencing effects of shRNAs can be reversible, allowing disruption of gene expression in a temporal manner for investigation of effects at specific times during development. A fast and scalable method for developing shRNA transgenic mice has been recently used to validate p19<sup>ARF</sup> as a therapeutic target for lung adenocarcinoma [112].

Embryonic stem cells (ESCs) have become another tool for rapid development of multiallelic mouse models. Multiple rounds of targeting disease-associated alleles in ESCs, followed by blastocysts injection and implantation, result in

chimeric animals where tumours develop from the engineered cells in the context of a normal microenvironment. Chimeric animals may be cross-bred, generating wholly ESC derived mice. This methodology has been used to develop two different models of lung adenocarcinoma to analyze activation of pathways downstream of specific mutations and to assess the potential of therapeutic targeting strategies [112, 113].

A major criticism of using mouse models to model human cancer is inherent in the biological differences between the two organisms. In some cases, drugs that look promising for cancer therapy in a mouse model fail in clinical trials due to differences in activity between the mouse gene product being targeted and its human counterpart [114–116]. The effect of the human gene in transgenic mouse models can in some cases be most effectively addressed using humanized mice, in which a copy of the human gene replaces the mouse gene. Transgenic expression of the human cytochrome P450 2A13 was achieved using a cloned bacterial artificial chromosome in a background null for the mouse homologue. The results of this study indicated that the human gene was more highly effective at activating a carcinogenic compound present in cigarette smoke than its mouse homologue and in contributing to lung tumourigenesis [117]. There is a great deal of interest in finding useful predictive and prognostic serum or blood biomarkers for lung cancer patients as these fluids are easier and less painful to obtain than lung biopsies. Recently, Taguchi et al. found they could identify thirteen proteins overexpressed specifically in the plasma of mice bearing EGFR or Ras mutations that developed lung adenocarcinomas [118]. A subset of these proteins was measured in the serum of NSCLC patients and a significant concordance with the mouse data was found. Mice bearing the EGFR mutation and treated with the EGFR inhibitor erlotinib showed reduced levels of the markers associated with EGFR expression, similar to the human patients. This shows promise for the use of mouse models as a tool to identify new biomarkers.

## 8. Discussion

Taking into consideration each of the distinct preclinical models to study lung cancer *in vivo*, it is reasonable to conclude that each model is well-suited for a specific mode of study. For example, xenograft models are well-suited for the timely evaluation of response to therapy *in vivo*. However, transgenic and conditional transgenic model systems that accurately mimic tumour histology, genetic abnormalities and tumour microenvironment of human lung cancer, such as the LSL K-Ras G12D model for adenocarcinoma, and the Trp53 AdenoCre model for SCLC, may provide more reliable results concerning response to therapy and toxicity. To date, the majority of preclinical models used to evaluate efficacy of targeted chemotherapeutics are xenografts models, presumably due in part to the four to eight week growth period required to obtain results. Conversely, the use of xenograft models in preclinical study can lead to disappointing results in clinical trials. Current chemotherapies and the preclinical models used to evaluate them are summarized in Table 3.

Of the seventeen therapies summarized in Table 3, only three therapies were evaluated in transgenic or conditional transgenic murine models prior to progressing to clinical trial. In addition, only two of the therapies listed in Table 3 were assessed in a syngeneic, orthotopic model system. Both EGFR inhibitors, erlotinib and BIBW2992, were tested preclinically using the CCSP-rtTA; Tet-O<sub>7</sub>-EGFR<sup>L858R</sup> model [26, 37, 49, 68, 70]. *In vivo*, both therapies resulted in dramatic tumour regression, however, phase I clinical trials for BIBW2992 resulted in no significant partial or complete responses in patients [70]. On the other hand, clinical trials for erlotinib were successful in extending median survival to 8.4 months compared to a maximum of 8.0 months with gefitinib. One-year survival was increased to 40% compared to 37% with doxorubicin [68], suggesting that the model system was successful in predicting clinical benefit in the case of erlotinib, but not BIBW2992. Interestingly, the EGFR inhibitor vandetinib was evaluated *in vivo* using a H1975 xenograft model as opposed to the CCSP-rtTA; Tet-O<sub>7</sub>-EGFR<sup>L858R</sup> model [119]. Vandetinib was found to significantly reduce tumour growth in the xenograft model, but resulted in limited response rates in clinical trials, which may be due in part to the fact that xenograft models cannot accurately recapitulate tumour microenvironment or predict immune response (Table 3). Thus, even the most complex murine models may predict clinical benefit of therapy in one case and not in another. Therefore, it is imperative that multiple models be used to evaluate efficacy of each therapy.

Syngeneic murine models prove to be reasonably successful in predicting clinical benefit of therapy in preclinical experiments (Table 3). The effects of navelbine and carboplatin were assessed in C57BL mice with LLC hind flank tumours. *In vivo*, IV navelbine administration resulted in 72.7 percent tumour regression [74]. Alternatively, IV carboplatin administration in combination with paclitaxel resulted in prolonged survival in 30–50 percent of the experimental population. Preclinical navelbine findings were shown to be translatable to clinical trials as median survival was extended to 34 weeks in patients [73]. Carboplatin-paclitaxel combination therapy was also shown to be effective in clinical trials as median survival was extended to 10.3 months in patients, further suggesting that the LLC model is a valuable tool for predicting clinical benefit of select therapies [81]. Interestingly, preclinical evaluation of monoclonal antibody therapy with bevacizumab and/or cetuximab has not been conducted in a syngeneic model system, but rather in xenograft systems [28, 85]. Both bevacizumab and cetuximab were shown to be effective in reducing tumour burden and extending survival both in preclinical and clinical trials [28, 84, 85, 88]. These studies raise several important questions concerning the translatability of preclinical study characteristics such as: clinically relevant dose, survival quantification and treatment regimen, to clinical trials.

It is important to note that preclinical and clinical dosages as well as treatment regimens vary widely between preclinical and clinical trials and even with the use of complex conditional transgenic models in preclinical studies, it is difficult to predict clinically relevant dose and appropriate treatment regimen for the patient population. There are

TABLE 3: Preclinical and clinical trial summaries for lung cancer therapies (CCSP: clara cell secretory protein; rtTA: reverse tetracycline transactivator protein; EGFR: epidermal growth factor receptor; RR: response rate; PFS: progression free survival).

Drug name	Route	Mechanism	Preclinical dosage	Preclinical frequency	FDA approval	Preclinical model	Preclinical results	Clinical Dosage	Clinical Frequency	Results of Clinical Trials	References
Geftinib	Oral	HER1/EGFR inhibitor	0.01 $\mu$ M 50–200 mg/kg	qd $\times$ 5 days $\times$ 2 weeks	2009	<b>Xenograft</b> -A549 cells in athymic nude	Tumor regression and increase in median survival	250 mg	qd	Positive	[66, 67]
Erlotinib	Oral	HER1/EGFR inhibition	0.5% (w/v) I.P. or 25 mg/kg/day	qd $\times$ 5 days $\times$ q4 weeks	2005	<b>Xenograft</b> -HCC827, A549, NCI358 cells in female BALB/cA nude mice <i>Transgenic</i> -CCSP-rtTA; Tet-0 <sub>7</sub> -EGFR <sup>L858R</sup>	Tumor regression observed in HCC827 xenografts	150 mg	qd	Positive	[26, 49, 68]
Vandetanib	Oral	VEGF/EGFR inhibitor	25 mg/kg	qd	Not approved	<b>Xenograft</b> -H1975 cells in female athymic nude mice <b>Xenograft</b> -H1975 cells in female athymic nude mice	Inhibition of tumor growth (not dramatic)	50–145 mg/m <sup>2</sup>	qd	Negative	[69]
BIBW2992	Oral	HER2/EGFR inhibitor	20 mg/kg	qd	October 2010 Phase III clinical trial	athymic NMRI-nu/nu mice <b>Transgenic</b> -CCSP-rtTA; Tet-0 <sub>7</sub> -EGFR <sup>L858R</sup>	Dramatic tumor regression T/C ratio 2%	20–70 mg	D1, 8, 15 q4 weeks	Positive	[37, 70]
Crizotinib	Oral	ALK inhibitor	10 mg/kg	qd	Phase III clinical trials	<b>Transgenic</b> -SP-C-EMI4-ALK in C57BL/6j mice <b>Immune</b> -C57Bl mice used for transplantation of LLC	Tumor regression and increase in median survival	250 mg	2 d $\times$ 6 months	Positive	[57, 71, 72]
Navelbine (Vinorelbine)	Oral, IV	Antimicrotubule chemotherapy	1.25–5 mg/kg	qd $\times$ 9 days	1994		72.7% inhibition of tumor growth	25–30 mg/m <sup>2</sup>	q weekly	Positive	[73, 74]
Paclitaxel	IV	Antimicrotubule chemotherapy	12–24 mg/kg	qd $\times$ 5 days	1992	<b>Xenograft</b> -A549, NCI-H23, NCI-H460, DMS-273, NCI-H226, and DMS-114 cells in nude mice	Significant tumor regression, more effective than cisplatin	135 mg/m <sup>2</sup>	q3 weeks	Positive	[36, 75]
Abraxane	IV	Antimicrotubule chemotherapy	250 mg/kg IP	qd $\times$ 3 weeks	Phase III clinical trials for lung cancer	<b>Xenograft</b> -H460 cells in female athymic nu/nu mice	Significant tumor regression	260 mg/m <sup>2</sup>	q3 weeks	Positive	[23, 34]
Gemcitabine	IV	Nucleoside analog chemotherapy	50–160 mg/kg	q3-4 days	2006	<b>Xenograft</b> -A549 and H1299 cells in female nude mice	Reduced mean tumor double time by 50% in 13 days	1000 mg/m <sup>2</sup>	D1, 8, 15 q28 days	Positive	[32, 76]
Pemetrexed	IV	Folate antimetabolite chemotherapy	30 mg/kg	q3-4 days	2004	<b>Xenograft</b> -H460 cells in female athymic nude	Tumor regression duration and dose dependent	500 mg/m <sup>2</sup>	q21 days	Positive	[35, 77]

TABLE 3: Continued.

Drug name	Route	Mechanism	Preclinical dosage	Preclinical frequency	FDA approval	Preclinical model	Preclinical results	Clinical Dosage	Clinical Frequency	Results of Clinical Trials	References
Doxorubicin	IV	Anthracycline antibiotic chemotherapy	3.0–12 mg/kg	qd	1950's	<b>Xenograft</b> -Nu/nu- Balb/c/ABom, normal Balb/c (13) CB-17 scid/scid with TL-1 s.c. 2 × 10(6) cells in 0.2mL saline (14)	Effective in arresting tumor growth	40–75 g/m <sup>2</sup>	q21–28 days	Positive	[41, 78]
Cisplatin	IV	Platinum-based chemotherapy	7 mg/kg I.P	qd × 2 weeks q4 weeks	1969	<b>Xenograft</b> -A549, HI299 nude mice <b>Transgenic</b> -LSLK- RasG12D on I29sv/ae background	Significantly reduced tumor burden, but left long-term resistance	60 to 100 mg/m <sup>2</sup>	q21 days	Positive	[32, 79, 80]
Carboplatin	IV	Platinum-based chemotherapy	50 mg/kg I.P.	qd	1989	<b>Xenograft</b> -A549 and HI299 cells in athymic nude mice <b>Immune</b> -C57B1 mice used for transplantation of LLC	Two-drug regimen response rates 30–50% prolonged median survival of >1 year	200– 360 mg/m <sup>2</sup>	q4 weeks	Positive	[32, 40, 81]
Etoposide	IV, oral	DNA topoisomerase II inhibitor	1–32 mg/kg	qd × 5 days	1960's	<b>Xenograft</b> -H460 cells in female athymic nude mice	Tumor growth regression	100 mg/m <sup>2</sup> IV 200 mg/m <sup>2</sup> PO	q3 weeks	Positive	[82, 83]
Bevacizumab	IV	Monoclonal antibody VEGF-A inhibitor	5 mg/kg	qd × 4 weeks	2004	<b>Xenograft</b> -HI299 cells in athymic BALB/c female nude mice	Reduced vascularity, reduced interstitial pressure and tumor growth	15 mg/kg	q3 weeks	Positive	[84, 85]
Sunitinib	oral	Multitargeted RTK inhibitor (VEGF, CKit, PDGF $\alpha$ , cRET)	40 mg/kg	qd × 6 weeks	Phase II clinical trials for lung cancer	<b>Xenograft</b> -NCl- H226, NCl-H526 or NCl-H82 in athymic female nu/nu mice	Significant tumor growth regression	37.5–50 mg	continuous qd or qd × 4 weeks q6 weeks	Negative	[42, 86]
Sorafenib	oral	Multi-targeted RTK inhibitor (VEGF, CKit, PDGF $\alpha$ , cRET)	40–80 mg/kg	qd × 9 days	Phase III clinical trials for lung cancer	<b>Xenograft</b> -H460, A549, NCl-H23 cells in female NCr-nu/nu mice	Significant tumor growth regression	400 mg	bid	Negative	[33, 87]
Cetuximab	IV	Monoclonal antibody EGFR inhibitor	20 $\mu$ L/g	q3 weeks	2008	<b>Xenograft</b> -A549, NCl-H358, HCC-827, HI975, H460 cells in female athymic nu/nu mice	Significant tumor growth inhibition	250– 400 mg/m <sup>2</sup>	400 mg/m <sup>2</sup> — 250 mg/m <sup>2</sup> q weekly	Negative	[28, 88]

several essential criteria for evaluating preclinical trial results prior to progression to clinical trials. Firstly, tumour growth inhibition of less than 50 percent in preclinical models does not typically translate into clinical benefit [69, 119]. Secondly, it is imperative that preclinical trial results show a survival benefit in response to therapy as this is one of the most telling criteria concerning drug efficacy *in vivo* [36, 79, 81]. Response to therapy cessation is also a valuable prognostic factor in preclinical studies. If therapy is discontinued and tumour growth resumes, relapse-free survival can be affected in patients and the likelihood of success in clinical trials may be limited [69, 119].

In summary, there are several valuable murine models available for the study of lung cancer; however, no one model can truthfully recapitulate all features of human lung cancer *in vivo*. Each model has both advantages and limitations and it is vital that these be taken into consideration prior to use in preclinical trials. Prior to choosing a model for experimentation, thought should be given to relevance of cell type, genetic abnormalities, temporal-spatial regulation of expression of target genes, tumour microenvironment, and the metastatic potential of each model. Despite recent advances, future research is needed, particularly with regards to developing models for SCLC and SCC as these are currently limited. Results obtained through the use of murine models as well as advancements in the development of new mouse models for lung cancer have provided much insight in the biology of lung cancer and lung cancer therapies. Ultimately, the use of these models in preclinical studies provides a vital framework from which to continue to evaluate therapies and identify predictive and prognostic markers *in vivo*.

## Conflict of Interests

The authors declare that there is no conflict of interests regarding the publication of this paper.

## References

- [1] J. R. Molina, P. Yang, S. D. Cassivi, S. E. Schild, and A. A. Adjei, "Non-small cell lung cancer: epidemiology, risk factors, treatment, and survivorship," *Mayo Clinic Proceedings*, vol. 83, no. 5, pp. 584–594, 2008.
- [2] R. Siegel, D. Naishadham, and A. Jemal, "Cancer statistics, 2013," *CA: A Cancer Journal for Clinicians*, vol. 63, no. 1, pp. 11–30, 2013.
- [3] L. Mao, J. S. Lee, J. M. Kurie et al., "Clonal genetic alterations in the lungs of current and former smokers," *Journal of the National Cancer Institute*, vol. 89, no. 12, pp. 857–862, 1997.
- [4] S. Todd, W. A. Franklin, M. Varella-Garcia et al., "Homozygous deletions of human chromosome 3p in lung tumors," *Cancer Research*, vol. 57, no. 7, pp. 1344–1352, 1997.
- [5] S. A. Belinsky, D. M. Klinge, C. A. Stidley et al., "Inhibition of DNA methylation and histone deacetylation prevents murine lung cancer," *Cancer Research*, vol. 63, no. 21, pp. 7089–7093, 2003.
- [6] S. Dacic, M. Flanagan, K. Ciepely et al., "Significance of EGFR protein expression and gene amplification in non-small cell lung carcinoma," *American Journal of Clinical Pathology*, vol. 125, no. 6, pp. 860–865, 2006.
- [7] R. S. Herbst, J. V. Heymach, and S. M. Lippman, "Molecular origins of cancer: lung cancer," *The New England Journal of Medicine*, vol. 359, no. 13, pp. 1367–1380, 2008.
- [8] J. L. Marks, S. Broderick, Q. Zhou et al., "Prognostic and therapeutic implications of EGFR and KRAS mutations in resected lung adenocarcinoma," *Journal of Thoracic Oncology*, vol. 3, no. 2, pp. 111–116, 2008.
- [9] S. Perner, P. L. Wagner, F. Demichelis et al., "EML4-ALK fusion lung cancer: a rare acquired event," *Neoplasia*, vol. 10, no. 3, pp. 298–302, 2008.
- [10] W. Pao, V. Miller, M. Zakowski et al., "EGF receptor gene mutations are common in lung cancers from "never smokers" and are associated with sensitivity of tumors to gefitinib and erlotinib," *Proceedings of the National Academy of Sciences of the United States of America*, vol. 101, no. 36, pp. 13306–13311, 2004.
- [11] R. Rosell, T. Moran, C. Queralt et al., "Screening for epidermal growth factor receptor mutations in lung cancer," *The New England Journal of Medicine*, vol. 361, no. 10, pp. 958–967, 2009.
- [12] G. J. Riely, M. G. Kris, D. Rosenbaum et al., "Frequency and distinctive spectrum of KRAS mutations in never smokers with lung adenocarcinoma," *Clinical Cancer Research*, vol. 14, no. 18, pp. 5731–5734, 2008.
- [13] W. Pao and N. Girard, "New driver mutations in non-small-cell lung cancer," *The Lancet Oncology*, vol. 12, no. 2, pp. 175–180, 2011.
- [14] E. Massarelli, M. Varella-Garcia, X. Tang et al., "KRAS mutation is an important predictor of resistance to therapy with epidermal growth factor receptor tyrosine kinase inhibitors in non-small cell lung cancer," *Clinical Cancer Research*, vol. 13, no. 10, pp. 2890–2896, 2007.
- [15] K. Fukasawa, T. Choi, R. Kuriyama, S. Rulong, and G. F. V. Woude, "Abnormal centrosome amplification in the absence of p53," *Science*, vol. 271, no. 5256, pp. 1744–1747, 1996.
- [16] S. N. Rodin and A. S. Rodin, "Human lung cancer and p53: the interplay between mutagenesis and selection," *Proceedings of the National Academy of Sciences of the United States of America*, vol. 97, no. 22, pp. 12244–12249, 2000.
- [17] E. Steels, M. Paesmans, T. Berghmans et al., "Role of p53 as a prognostic factor for survival in lung cancer: a systematic review of the literature with a meta-analysis," *European Respiratory Journal*, vol. 18, no. 4, pp. 705–719, 2001.
- [18] P. Sève, J. Mackey, S. Isaac et al., "Class III  $\beta$ -tubulin expression in tumor cells predicts response and outcome in patients with non-small cell lung cancer receiving paclitaxel," *Molecular Cancer Therapeutics*, vol. 4, no. 12, pp. 2001–2007, 2005.
- [19] Z. Zheng, T. Chen, X. Li, E. Haura, A. Sharma, and G. Bepler, "DNA synthesis and repair genes RRM1 and ERCC1 in lung cancer," *The New England Journal of Medicine*, vol. 356, no. 8, pp. 800–808, 2007.
- [20] K. A. Kwei, Y. H. Kim, L. Girard et al., "Genomic profiling identifies TITF1 as a lineage-specific oncogene amplified in lung cancer," *Oncogene*, vol. 27, no. 25, pp. 3635–3640, 2008.
- [21] S. M. Gadgeel and A. Wozniak, "Preclinical rationale for PI3K/Akt/mTOR pathway inhibitors as therapy for epidermal growth factor receptor inhibitor-resistant non-small-cell lung cancer," *Clinical Lung Cancer*, vol. 14, no. 4, pp. 322–332, 2013.
- [22] D. Han, S.-J. Li, Y.-T. Zhu, L. Liu, and M.-X. Li, "LKBI/AMPK/mTOR signaling pathway in non-small-cell lung cancer," *Asian Pacific Journal of Cancer Prevention*, vol. 14, no. 7, pp. 4033–4039, 2013.

- [23] O. S. Pettengill, G. D. Sorenson, D. H. Wurster-Hill et al., "Isolation and growth characteristics of continuous cell lines from small-cell carcinoma of the lung," *Cancer*, vol. 45, no. 5, pp. 906–918, 1980.
- [24] K. Rygaard, L. L. Vindelov, and M. Spang-Thomsen, "Expression of myc family oncoproteins in small-cell lung-cancer cell lines and xenografts," *International Journal of Cancer*, vol. 54, no. 1, pp. 144–152, 1993.
- [25] J. E. Taylor, A. E. Bogden, J.-P. Moreau, and D. H. Coy, "In vitro and in vivo inhibition of human small cell lung carcinoma (NCI-H69) growth by a somatostatin analogue," *Biochemical and Biophysical Research Communications*, vol. 153, no. 1, pp. 81–86, 1988.
- [26] A. A. Memon, S. Jakobsen, F. Dagnaes-Hansen, B. S. Sorensen, S. Keiding, and E. Nexø, "Positron emission tomography (PET) imaging with [<sup>11</sup>C]-labeled erlotinib: a micro-PET study on mice with lung tumor xenografts," *Cancer Research*, vol. 69, no. 3, pp. 873–878, 2009.
- [27] S. Akhtar, S. M. Meeran, N. Katiyar, and S. K. Katiyar, "Grape seed proanthocyanidins inhibit the growth of human non-small cell lung cancer xenografts by targeting insulin-like growth factor binding protein-3, tumor cell proliferation, and angiogenic factors," *Clinical Cancer Research*, vol. 15, no. 3, pp. 821–831, 2009.
- [28] P. Steiner, C. Joynes, R. Bassi et al., "Tumor growth inhibition with cetuximab and chemotherapy in non-small cell lung cancer xenografts expressing wild-type and mutated epidermal growth factor receptor," *Clinical Cancer Research*, vol. 13, no. 5, pp. 1540–1551, 2007.
- [29] M.-F. Chen, W.-C. Chen, C.-T. Wu et al., "p53 status is a major determinant of effects of decreasing peroxiredoxin I expression on tumor growth and response of lung cancer cells to treatment," *International Journal of Radiation Oncology, Biology, Physics*, vol. 66, no. 5, pp. 1461–1472, 2006.
- [30] D. Raben, C. Bianco, V. Damiano et al., "Antitumor activity of ZD6126, a novel vascular-targeting agent, is enhanced when combined with ZD1839, an epidermal growth factor receptor tyrosine kinase inhibitor, and potentiates the effects of radiation in a human non-small cell lung cancer xenograft model," *Molecular Cancer Therapeutics*, vol. 3, no. 8, pp. 977–983, 2004.
- [31] T. L. McLemore, M. C. Liu, P. C. Blacker et al., "Novel intrapulmonary model for orthotopic propagation of human lung cancers in athymic nude mice," *Cancer Research*, vol. 47, no. 19, pp. 5132–5140, 1987.
- [32] H. Wang, M. Li, J. J. Rinehart, and R. Zhang, "Pretreatment with dexamethasone increases antitumor activity of carboplatin and gemcitabine in mice bearing human cancer xenografts: in vivo activity, pharmacokinetics, and clinical implications for cancer chemotherapy," *Clinical Cancer Research*, vol. 10, no. 5, pp. 1633–1644, 2004.
- [33] C. A. Carter, C. Chen, C. Brink et al., "Sorafenib is efficacious and tolerated in combination with cytotoxic or cytostatic agents in preclinical models of human non-small cell lung carcinoma," *Cancer Chemotherapy and Pharmacology*, vol. 59, no. 2, pp. 183–195, 2007.
- [34] Z. Feng, G. Zhao, L. Yu, D. Gough, and S. B. Howell, "Preclinical efficacy studies of a novel nanoparticle-based formulation of paclitaxel that out-performs Abraxane," *Cancer Chemotherapy and Pharmacology*, vol. 65, no. 5, pp. 923–930, 2010.
- [35] B. A. Teicher, V. Chen, C. Shih et al., "Treatment regimens including the multitargeted antifolate LY231514 in human tumor xenografts," *Clinical Cancer Research*, vol. 6, no. 3, pp. 1016–1023, 2000.
- [36] T. Yamori, S. Sato, H. Chikazawa, and T. Kadota, "Anti-tumor efficacy of paclitaxel against human lung cancer xenografts," *Japanese Journal of Cancer Research*, vol. 88, no. 12, pp. 1205–1210, 1997.
- [37] D. Li, L. Ambrogio, T. Shimamura et al., "BIBW2992, an irreversible EGFR/HER2 inhibitor highly effective in preclinical lung cancer models," *Oncogene*, vol. 27, no. 34, pp. 4702–4711, 2008.
- [38] H. Su, C. Bodenstern, R. A. Dumont et al., "Monitoring tumor glucose utilization by positron emission tomography for the prediction of treatment response to epidermal growth factor receptor kinase inhibitors," *Clinical Cancer Research*, vol. 12, no. 19, pp. 5659–5667, 2006.
- [39] R. Sordella, D. W. Bell, D. A. Haber, and J. Settleman, "Gefitinib-sensitizing EGFR mutations in lung cancer activate anti-apoptotic pathways," *Science*, vol. 305, no. 5687, pp. 1163–1167, 2004.
- [40] R. S. Herbst, H. Takeuchi, and B. A. Teicher, "Paclitaxel/carboplatin administration along with antiangiogenic therapy in non-small-cell lung and breast carcinoma models," *Cancer Chemotherapy and Pharmacology*, vol. 41, no. 6, pp. 497–504, 1998.
- [41] S. S. Williams, T. R. Alosco, E. Mayhew, D. D. Lasic, F. J. Martin, and R. B. Bankert, "Arrest of human lung tumor xenograft growth in severe combined immunodeficient mice using doxorubicin encapsulated in sterically stabilized liposomes," *Cancer Research*, vol. 53, no. 17, pp. 3964–3967, 1993.
- [42] T. J. Abrams, L. B. Lee, L. J. Murray, N. K. Pryer, and J. M. Cherrington, "SU11248 inhibits KIT and platelet-derived growth factor receptor  $\beta$  in preclinical models of human small cell lung cancer," *Molecular Cancer Therapeutics*, vol. 2, no. 5, pp. 471–478, 2003.
- [43] Y. Sakuma, S. Matsukuma, Y. Nakamura et al., "Enhanced autophagy is required for survival in EGFR-independent EGFR-mutant lung adenocarcinoma cells," *Laboratory Investigation*, vol. 93, no. 10, pp. 1137–1146, 2013.
- [44] E. L. Jackson, N. Willis, K. Mercer et al., "Analysis of lung tumor initiation and progression using conditional expression of oncogenic K-ras," *Genes and Development*, vol. 15, no. 24, pp. 3243–3248, 2001.
- [45] D. A. Tuveson, A. T. Shaw, N. A. Willis et al., "Endogenous oncogenic K-ras(G12D) stimulates proliferation and widespread neoplastic and developmental defects," *Cancer Cell*, vol. 5, pp. 375–387, 2004.
- [46] R. Meuwissen, S. C. Linn, M. van der Valk, W. J. Mooi, and A. Berns, "Mouse model for lung tumorigenesis through Cre/lox controlled sporadic activation of the K-Ras oncogene," *Oncogene*, vol. 20, no. 45, pp. 6551–6558, 2001.
- [47] H. Ji, M. R. Ramsey, D. N. Hayes et al., "LKB1 modulates lung cancer differentiation and metastasis," *Nature*, vol. 448, no. 7155, pp. 807–810, 2007.
- [48] A.-K. T. Perl, J. W. Tichelaar, and J. A. Whitsett, "Conditional gene expression in the respiratory epithelium of the mouse," *Transgenic Research*, vol. 11, no. 1, pp. 21–29, 2002.
- [49] K. Politi, P.-D. Fan, R. Shen, M. Zakowski, and H. Varmus, "Erlotinib resistance in mouse models of epidermal growth factor receptor-induced lung adenocarcinoma," *Disease Models & Mechanisms*, vol. 3, no. 1-2, pp. 111–119, 2010.

- [50] R. Meuwissen, S. C. Linn, R. I. Linnoila, J. Zevenhoven, W. J. Mooi, and A. Berns, "Induction of small cell lung cancer by somatic inactivation of both Trp53 and Rb1 in a conditional mouse model," *Cancer Cell*, vol. 4, no. 3, pp. 181–189, 2003.
- [51] J. W. Tichelaar, W. Lu, and J. A. Whitsett, "Conditional expression of fibroblast growth factor-7 in the developing and mature lung," *The Journal of Biological Chemistry*, vol. 275, no. 16, pp. 11858–11864, 2000.
- [52] R. I. Linnoila, A. Sahu, M. Miki, D. W. Ball, and F. J. DeMayo, "Morphometric analysis of CC10-hASH1 transgenic mouse lung: a model for bronchiolization of alveoli and neuroendocrine carcinoma," *Experimental Lung Research*, vol. 26, no. 8, pp. 595–615, 2000.
- [53] F. J. DeMayo, M. J. Finegold, T. N. Hansen, L. A. Stanley, B. Smith, and D. W. Bullock, "Expression of SV40 T antigen under control of rabbit uteroglobin promoter in transgenic mice," *American Journal of Physiology—Lung Cellular and Molecular Physiology*, vol. 261, no. 2, part 1, pp. L70–L76, 1991.
- [54] K. A. Wikenheiser, J. C. Clark, R. I. Linnoila, M. T. Stahlman, and J. A. Whitsett, "Simian virus 40 large T antigen directed by transcriptional elements of the human surfactant protein C gene produces pulmonary adenocarcinomas in transgenic mice," *Cancer Research*, vol. 52, no. 19, pp. 5342–5352, 1992.
- [55] B. Chailley-Heu, C. Rambaud, A.-M. Barlier-Mur et al., "A model of pulmonary adenocarcinoma in transgenic mice expressing the simian virus 40 T antigen driven by the rat Calbindin-D9K (CaBP9K) promoter," *The Journal of Pathology*, vol. 195, no. 4, pp. 482–489, 2001.
- [56] M. E. Sunday, K. J. Haley, K. Sikorski et al., "Calcitonin driven v-Ha-ras induces multilineage pulmonary epithelial hyperplasias and neoplasms," *Oncogene*, vol. 18, no. 30, pp. 4336–4347, 1999.
- [57] M. Soda, S. Takada, K. Takeuchi et al., "A mouse model for EML4-ALK-positive lung cancer," *Proceedings of the National Academy of Sciences of the United States of America*, vol. 105, no. 50, pp. 19893–19897, 2008.
- [58] A. Ehrhardt, T. Bartels, A. Geick, R. Klocke, D. Paul, and R. Halter, "Development of pulmonary bronchiolo-alveolar adenocarcinomas in transgenic mice overexpressing murine c-myc and epidermal growth factor in alveolar type II pneumocytes," *British Journal of Cancer*, vol. 84, no. 6, pp. 813–818, 2001.
- [59] H. Rütters, P. Züribig, R. Halter, and J. Borlak, "Towards a lung adenocarcinoma proteome map: studies with SP-C/c-raf transgenic mice," *Proteomics*, vol. 6, no. 10, pp. 3127–3137, 2006.
- [60] Y.-Q. Chen, Y.-Q. Zhou, L.-H. Fu, D. Wang, and M.-H. Wang, "Multiple pulmonary adenomas in the lung of transgenic mice overexpressing the RON receptor tyrosine kinase," *Carcinogenesis*, vol. 23, no. 11, pp. 1811–1819, 2002.
- [61] J. Ohno, Y. Horio, Y. Sekido et al., "Telomerase activation and p53 mutations in urethane-induced A/J mouse lung tumor development," *Carcinogenesis*, vol. 22, no. 5, pp. 751–756, 2001.
- [62] G. D. Stoner, E. A. Greisiger, H. A. J. Schut et al., "A comparison of the lung adenoma response in strain A/J mice after intraperitoneal and oral administration of carcinogens," *Toxicology and Applied Pharmacology*, vol. 72, no. 2, pp. 313–323, 1984.
- [63] W. T. Gunning, P. M. Kramer, R. A. Lubet et al., "Chemoprevention of benzo(a)pyrene-induced lung tumors in mice by the farnesyltransferase inhibitor R115777," *Clinical Cancer Research*, vol. 9, no. 5, pp. 1927–1930, 2003.
- [64] S. Rehm, W. Lijinsky, G. Singh, and S. L. Katyal, "Mouse bronchiolar cell carcinogenesis. Histologic characterization and expression of Clara cell antigen in lesions induced by N-nitrosobis-(2-chloroethyl) ureas," *The American Journal of Pathology*, vol. 139, no. 2, pp. 413–422, 1991.
- [65] M. Qin, S. Chen, T. Yu, B. Escudero, S. Sharma, and R. K. Batra, "Coxsackievirus adenovirus receptor expression predicts the efficiency of adenoviral gene transfer into non-small cell lung cancer xenografts," *Clinical Cancer Research*, vol. 9, no. 13, pp. 4992–4999, 2003.
- [66] M. H. Cohen, G. A. Williams, R. Sridhara et al., "United States Food and Drug Administration drug approval summary: gefitinib (ZD1839; Iressa) tablets," *Clinical Cancer Research*, vol. 10, no. 4, pp. 1212–1218, 2004.
- [67] N. Thatcher, A. Chang, P. Parikh et al., "Gefitinib plus best supportive care in previously treated patients with refractory advanced non-small-cell lung cancer: results from a randomised, placebo-controlled, multicentre study (Iressa Survival Evaluation in Lung Cancer)," *The Lancet*, vol. 366, no. 9496, pp. 1527–1537, 2005.
- [68] R. Perez-Soler, "The role of erlotinib (Tarceva, OSI 774) in the treatment of non-small cell lung cancer," *Clinical Cancer Research*, vol. 10, part 2, pp. 4238s–4240s, 2004.
- [69] E. Ichihara, K. Ohashi, N. Takigawa et al., "Effects of vandetanib on lung adenocarcinoma cells harboring epidermal growth factor receptor T790M mutation *in vivo*," *Cancer Research*, vol. 69, no. 12, pp. 5091–5098, 2009.
- [70] F. A. L. M. Eskens, C. H. Mom, A. S. T. Planting et al., "A phase I dose escalation study of BIBW 2992, an irreversible dual inhibitor of epidermal growth factor receptor 1 (EGFR) and 2 (HER2) tyrosine kinase in a 2-week on, 2-week off schedule in patients with advanced solid tumours," *British Journal of Cancer*, vol. 98, no. 1, pp. 80–85, 2008.
- [71] D. E. Gerber and J. D. Minna, "ALK inhibition for non-small cell lung cancer: from discovery to therapy in record time," *Cancer Cell*, vol. 18, no. 6, pp. 548–551, 2010.
- [72] B. Hallberg and R. H. Palmer, "Crizotinib—latest champion in the cancer wars?" *The New England Journal of Medicine*, vol. 363, no. 18, pp. 1760–1762, 2010.
- [73] A. Papageorgiou, P. Stravoravdi, D. Sahnazidou, K. Natsis, E. Chrysogelou, and T. Toliou, "Effect of Navelbine on inhibition of tumor growth, cellular differentiation and estrogen receptor status on Lewis lung carcinoma," *Chemotherapy*, vol. 46, no. 3, pp. 188–194, 2000.
- [74] M. Marty, P. Fumoleau, A. Adenis et al., "Oral vinorelbine pharmacokinetics and absolute bioavailability study in patients with solid tumors," *Annals of Oncology*, vol. 12, no. 11, pp. 1643–1649, 2001.
- [75] M. E. Wall and M. C. Wani, "Camptothecin and taxol: discovery to clinic—thirteenth Bruce F. Cain Memorial Award Lecture," *Cancer Research*, vol. 55, no. 4, pp. 753–760, 1995.
- [76] C. J. A. Van Moorsel, H. M. Pinedo, G. Veerman, J. B. Vermorken, P. E. Postmus, and G. J. Peters, "Scheduling of gemcitabine and cisplatin in Lewis Lung tumour bearing mice," *European Journal of Cancer*, vol. 35, no. 5, pp. 808–814, 1999.
- [77] E. F. Smit, K. Mattson, J. von Pawel, C. Manegold, S. Clarke, and P. E. Postmus, "ALIMTA (pemetrexed disodium) as second-line treatment of non-small-cell lung cancer: a phase II study," *Annals of Oncology*, vol. 14, no. 3, pp. 455–460, 2003.

- [78] P. B. Johansen, "Doxorubicin pharmacokinetics after intravenous and intraperitoneal administration in the nude mouse," *Cancer Chemotherapy and Pharmacology*, vol. 5, no. 4, pp. 267–270, 1981.
- [79] A. J. Wozniak, J. J. Crowley, S. P. Balcerzak et al., "Randomized trial comparing cisplatin with cisplatin plus vinorelbine in the treatment of advanced non-small-cell lung cancer: a Southwest Oncology Group study," *Journal of Clinical Oncology*, vol. 16, no. 7, pp. 2459–2465, 1998.
- [80] T. G. Oliver, K. L. Mercer, L. C. Sayles et al., "Chronic cisplatin treatment promotes enhanced damage repair and tumor progression in a mouse model of lung cancer," *Genes & Development*, vol. 24, no. 8, pp. 837–852, 2010.
- [81] A. Sandler, R. Gray, M. C. Perry et al., "Paclitaxel-carboplatin alone or with bevacizumab for non-small-cell lung cancer," *The New England Journal of Medicine*, vol. 355, no. 24, pp. 2542–2550, 2006.
- [82] P. B. Jensen, H. Roed, T. Skovsgaard et al., "Antitumor activity of the two epipodophyllotoxin derivatives VP-16 and VM-26 in preclinical systems: a comparison of *in vitro* and *in vivo* drug evaluation," *Cancer Chemotherapy and Pharmacology*, vol. 27, no. 3, pp. 194–198, 1990.
- [83] J. C. Ruckdeschel, "Etoposide in the management of non-small cell lung cancer," *Cancer*, vol. 67, supplement 1, pp. 250–253, 1991.
- [84] D. H. Johnson, L. Fehrenbacher, W. F. Novotny et al., "Randomized phase II trial comparing bevacizumab plus carboplatin and paclitaxel with carboplatin and paclitaxel alone in previously untreated locally advanced or metastatic non-small-cell lung cancer," *Journal of Clinical Oncology*, vol. 22, no. 11, pp. 2184–2191, 2004.
- [85] S. Inoue, A. Hartman, C. D. Branch et al., "mda-7 in combination with bevacizumab treatment produces a synergistic and complete inhibitory effect on lung tumor xenograft," *Molecular Therapy*, vol. 15, no. 2, pp. 287–294, 2007.
- [86] M. A. Socinski, F. A. Scappaticci, M. Samant, M. M. Kolb, and M. F. Kozloff, "Safety and efficacy of combining sunitinib with bevacizumab + paclitaxel/carboplatin in non-small cell lung cancer," *Journal of Thoracic Oncology*, vol. 5, no. 3, pp. 354–360, 2010.
- [87] G. R. Blumenschein Jr., U. Gatzemeier, F. Fossella et al., "Phase II, multicenter, uncontrolled trial of single-agent sorafenib in patients with relapsed or refractory, advanced non-small-cell lung cancer," *Journal of Clinical Oncology*, vol. 27, no. 26, pp. 4274–4280, 2009.
- [88] N. Hanna, R. Lilenbaum, R. Ansari et al., "Phase II trial of cetuximab in patients with previously treated non-small-cell lung cancer," *Journal of Clinical Oncology*, vol. 24, no. 33, pp. 5253–5258, 2006.
- [89] I. Fichtner, J. Rolff, R. Soong et al., "Establishment of patient-derived non-small cell lung cancer xenografts as models for the identification of predictive biomarkers," *Clinical Cancer Research*, vol. 14, no. 20, pp. 6456–6468, 2008.
- [90] J. Merk, J. Rolff, M. Becker, G. Leschber, and I. Fichtner, "Patient-derived xenografts of non-small-cell lung cancer: a pre-clinical model to evaluate adjuvant chemotherapy?" *European Journal of Cardio-thoracic Surgery*, vol. 36, no. 3, pp. 454–459, 2009.
- [91] X. Dong, J. Guan, J. C. English et al., "Patient-derived first generation xenografts of non-small cell lung cancers: promising tools for predicting drug responses for personalized chemotherapy," *Clinical Cancer Research*, vol. 16, no. 5, pp. 1442–1451, 2010.
- [92] M. Nogawa, T. Yuasa, S. Kimura et al., "Monitoring luciferase-labeled cancer cell growth and metastasis in different *in vivo* models," *Cancer Letters*, vol. 217, no. 2, pp. 243–253, 2005.
- [93] T. John, D. Kohler, M. Pintilie et al., "The ability to form primary tumor xenografts is predictive of increased risk of disease recurrence in early-stage non-small cell lung cancer," *Clinical Cancer Research*, vol. 17, no. 1, pp. 134–141, 2011.
- [94] D. H. Johnson, D. M. Paul, K. R. Hande, and R. DeVore, "Paclitaxel plus carboplatin in the treatment of patients with advanced lung cancer: a Vanderbilt University Cancer Center phase II trial (LUN-46)," *Seminars in Oncology*, vol. 23, no. 6, pp. 42–46, 1996.
- [95] Y. Sakai, T. Sasahira, H. Ohmori, K. Yoshida, and H. Kuniyasu, "Conjugated linoleic acid reduced metastasized LL2 tumors in mouse peritoneum," *Virchows Archiv*, vol. 449, no. 3, pp. 341–347, 2006.
- [96] B. Zhao, S. Magdaleno, S. Chua et al., "Transgenic mouse models for lung cancer," *Experimental Lung Research*, vol. 26, no. 8, pp. 567–579, 2000.
- [97] A. K. Virmani and A. F. Gazdar, "Tumor suppressor genes in lung cancer," *Methods in Molecular Biology*, vol. 222, pp. 97–115, 2003.
- [98] R. I. Linnoila, B. Zhao, J. L. DeMayo et al., "Constitutive achaete-scute homologue-1 promotes airway dysplasia and lung neuroendocrine tumors in transgenic mice," *Cancer Research*, vol. 60, no. 15, pp. 4005–4009, 2000.
- [99] M. Mabry, T. Nakagawa, S. Baylin, O. Pettengill, G. Sorenson, and B. Nelkin, "Insertion of the v-Ha-ras oncogene induces differentiation of calcitonin-producing human small cell lung cancer," *The Journal of Clinical Investigation*, vol. 84, no. 1, pp. 194–199, 1989.
- [100] V. P. Stanton Jr., D. W. Nichols, A. P. Laudano, and G. M. Cooper, "Definition of the human raf amino-terminal regulatory region by deletion mutagenesis," *Molecular and Cellular Biology*, vol. 9, no. 2, pp. 639–647, 1989.
- [101] G. Heidecker, M. Huleihel, J. L. Cleveland et al., "Mutational activation of c-raf-1 and definition of the minimal transforming sequence," *Molecular and Cellular Biology*, vol. 10, no. 6, pp. 2503–2512, 1990.
- [102] A. Cuadrado, J. T. Bruder, M. A. Heidarani, H. App, U. R. Rapp, and S. A. Aaronson, "H-ras and raf-1 cooperate in transformation of NIH3T3 fibroblasts," *Oncogene*, vol. 8, no. 9, pp. 2442–2448, 1993.
- [103] U. R. Rapp, M. Huleihel, T. Pawson et al., "Role of raf oncogenes in lung carcinogenesis," *Lung Cancer*, vol. 4, no. 3–4, pp. 162–167, 1988.
- [104] E. Kerkhoff, L. M. Fedorov, R. Siefken, A. O. Walter, T. Papadopoulos, and U. R. Rapp, "Lung-targeted expression of the c-Raf-1 kinase in transgenic mice exposes a novel oncogenic character of the wild-type protein," *Cell Growth and Differentiation*, vol. 11, no. 4, pp. 185–190, 2000.
- [105] J. L. Broers, J. Viallet, S. M. Jensen et al., "Expression of c-myc in progenitor cells of the bronchopulmonary epithelium and in a large number of non-small cell lung cancers," *The American Journal of Respiratory Cell and Molecular Biology*, vol. 9, no. 1, pp. 33–43, 1993.
- [106] J. Lorenz, T. Friedberg, R. Paulus, F. Oesch, and R. Ferlinz, "Oncogene overexpression in non-small-cell lung cancer tissue: prevalence and clinicopathological significance," *Clinical Investigator*, vol. 72, no. 2, pp. 156–163, 1994.

- [107] K. Politi, M. F. Zakowski, P.-D. Fan, E. A. Schonfeld, W. Pao, and H. E. Varmus, "Lung adenocarcinomas induced in mice by mutant EGF receptors found in human lung cancers respond to a tyrosine kinase inhibitor or to down-regulation of the receptors," *Genes and Development*, vol. 20, no. 11, pp. 1496–1510, 2006.
- [108] G. H. Fisher, S. L. Wellen, D. Klimstra et al., "Induction and apoptotic regression of lung adenocarcinomas by regulation of a K-Ras transgene in the presence and absence of tumor suppressor genes," *Genes and Development*, vol. 15, no. 24, pp. 3249–3262, 2001.
- [109] S. de Seranno and R. Meuwissen, "Progress and applications of mouse models for human lung cancer," *European Respiratory Journal*, vol. 35, no. 2, pp. 426–443, 2010.
- [110] Y. Horio, A. Chen, P. Rice, J. A. Roth, A. M. Malkinson, and D. S. Schrupp, "Ki-ras and p53 mutations are early and late events, respectively, in urethane-induced pulmonary carcinogenesis in A/J mice," *Molecular Carcinogenesis*, vol. 17, no. 4, pp. 217–223, 1996.
- [111] L. E. Dow and S. W. Lowe, "Life in the fast lane: mammalian disease models in the genomics era," *Cell*, vol. 148, no. 6, pp. 1099–1109, 2012.
- [112] P. K. Premririt, L. E. Dow, S. Y. Kim et al., "A rapid and scalable system for studying gene function in mice using conditional RNA interference," *Cell*, vol. 145, no. 1, pp. 145–158, 2011.
- [113] Y. Zhou, W. M. Rideout, T. Zi et al., "Chimeric mouse tumor models reveal differences in pathway activation between ERBB family- and KRAS-dependent lung adenocarcinomas," *Nature Biotechnology*, vol. 28, no. 1, pp. 71–78, 2010.
- [114] N. E. Kohl, C. A. Omer, M. W. Conner et al., "Inhibition of farnesyltransferase induces regression of mammary and salivary carcinomas in ras transgenic mice," *Nature Medicine*, vol. 1, no. 8, pp. 792–797, 1995.
- [115] J. L. Bos, "Ras oncogenes in human cancer: a review," *Cancer Research*, vol. 49, no. 17, pp. 4682–4689, 1989.
- [116] E. C. Lernert, Y. Qian, A. D. Hamilton, and S. M. Sebt, "Disruption of oncogenic K-Ras4B processing and signaling by a potent geranylgeranyltransferase I inhibitor," *Journal of Biological Chemistry*, vol. 270, no. 45, pp. 26770–26773, 1995.
- [117] V. Megaraj, X. Zhou, F. Xie, Z. Liu, W. Yang, and X. Ding, "Role of CYP2A13 in the bioactivation and lung tumorigenicity of the tobacco-specific lung procarcinogen 4-(methylnitrosamino)-1-(3-pyridyl)-1-butanone: in vivo studies using a CYP2A13-humanized mouse model," *Carcinogenesis*, vol. 35, no. 1, pp. 131–137, 2014.
- [118] A. Taguchi, K. Politi, S. J. Pitteri et al., "Lung cancer signatures in plasma based on proteome profiling of mouse tumor models," *Cancer Cell*, vol. 20, no. 3, pp. 289–299, 2011.
- [119] R. B. Natale, D. Bodkin, R. Govindan et al., "Vandetanib versus gefitinib in patients with advanced non-small-cell lung cancer: results from a two-part, double-blind, randomized phase II study," *Journal of Clinical Oncology*, vol. 27, no. 15, pp. 2523–2529, 2009.

## Review Article

# Experimentally Induced Mammalian Models of Glaucoma

Makoto Ishikawa,<sup>1</sup> Takeshi Yoshitomi,<sup>1</sup> Charles F. Zorumski,<sup>2,3</sup> and Yukitoshi Izumi<sup>2,3</sup>

<sup>1</sup>Department of Ophthalmology, Akita Graduate University School of Medicine, 1-1-1 Hondo, Akita 010-8543, Japan

<sup>2</sup>Department of Psychiatry, Washington University School of Medicine, St. Louis, MO 63110, USA

<sup>3</sup>The Taylor Family Institute for Innovative Psychiatric Research, Washington University School of Medicine, St. Louis, MO, USA

Correspondence should be addressed to Makoto Ishikawa; mako@med.akita-u.ac.jp

Received 25 September 2014; Accepted 1 December 2014

Academic Editor: Oreste Gualillo

Copyright © 2015 Makoto Ishikawa et al. This is an open access article distributed under the Creative Commons Attribution License, which permits unrestricted use, distribution, and reproduction in any medium, provided the original work is properly cited.

A wide variety of animal models have been used to study glaucoma. Although these models provide valuable information about the disease, there is still no ideal model for studying glaucoma due to its complex pathogenesis. Animal models for glaucoma are pivotal for clarifying glaucoma etiology and for developing novel therapeutic strategies to halt disease progression. In this review paper, we summarize some of the major findings obtained in various glaucoma models and examine the strengths and limitations of these models.

## 1. Introduction

Glaucoma is characterized by progressive and accelerated loss of retinal ganglion cells (RGCs) and their axons [1]. Although the pathogenesis of glaucoma is not fully understood, it is believed that increased intraocular pressure (IOP) is a major contributor even in normal tension glaucoma [2]. In this context, a wide variety of animal models have been developed to study the effect of elevated IOP on the optic nerve and the RGC degeneration.

In general, animal glaucoma models are classified into two categories: natural-occurring models and induced models. A variety of natural-occurring glaucoma models have been described in different animal species including dog (beagle) [3], albino New Zealand rabbit [4], and DBA/2J mice [5–7]. It has been considered that the disturbance or obstruction of aqueous outflow could be the cause of IOP elevation, which induces a loss of RGCs and excavation of the optic nerve in these models [8]. Because naturally occurring glaucoma models are poor in controlling onset and pathological course of the disease, induced glaucoma models have been developed with the aim to create proper conditions for controlled experiments. The earliest models of induced glaucoma were developed in monkeys [9], and IOP elevation was induced by intraocular  $\alpha$ -chymotrypsin injections [10]. Thereafter, multiple *in vivo* glaucoma models have been

developed using laser photocoagulation of the perilimbal region [11], autologous fixed red blood cell (RBC) injection [12] or microbead injection into the anterior chamber [9], cauterization of episcleral veins [13], or hypertonic saline injection into the episcleral veins [14, 15]. Recently, *in vitro* [16] and *ex vivo* glaucoma models [17] have been developed to improve the accuracy and repeatability of experimental conditions and to examine pathological mechanisms especially in the acute phase of the IOP elevation. Hydrostatic pressure is applied to cells cultured on a rigid substrate or to isolated retinal tissues *in vitro* and *ex vivo*. More recently, transgenic mouse glaucoma models, which were genetically modified by the introduction of a foreign DNA sequence into a mouse egg, have emerged [18].

In this paper, we present a summary of experimentally induced mammalian glaucoma models that have been developed and used for the recent study of the different types of glaucoma and discuss limitations and potential use of each model.

## 2. *In Vivo* Glaucoma Models

**2.1. Laser Photocoagulation of the Perilimbal Region.** Multiple studies have used laser photocoagulation which induced sustained IOP elevation in monkeys [11], mice [19, 20], rats [21], and rabbits [22–24]. These models were primarily

developed to study retinal IOP-related posterior segment damage. The IOP elevations in eyes treated with laser photocoagulation are thought to result from increased resistance of outflow pathways such as angle closure, trabecular scarring, and obliteration of Schlemm's canal [11]. Gaasterland and Kupfer (1974) [11] applied repeated, circumferential argon laser photocoagulation to the trabecular meshwork in both eyes of each of the five Rhesus monkeys and induced a sustained IOP elevation in seven out of ten eyes by a marked reduction in outflow. The IOP range was between 24 and 50 mm Hg after the 4th treatment and remained elevated by 30 days. The main outcome analyzed to determine whether this experimental ocular hypertension can induce a glaucoma was indicated by the observed development of cupping of the optic disc and by the selective loss of retinal ganglion cells in histopathologic specimens. This model became the standard for laser-induced glaucoma in monkeys [25–29].

The advantage of the primate model is that the monkeys have eyes with similar anatomical characteristics to humans. Although monkeys are excellent animal models for studying human disease, there are several limitations to use monkeys, including ethical and economic factors [30, 31]. Laser photocoagulation requires expensive ophthalmic equipment and highly specialized techniques. Laser photocoagulation sometimes induces the inflammation of the anterior chamber and irreversible mydriasis [28].

In contrast to primate models, there are several advantages of using rodents (mice, rats, and rabbits) in glaucoma research. Rodents are inexpensive and easy to house and handle, their eyes are easy to obtain, and the sample number for studies can be large [32]. Aihara et al. (2003) [19] applied argon laser photocoagulation to the corneal limbus in Black Swiss mice after flattening the anterior chamber by aspiration of aqueous humor and successfully induced persistent elevation of IOP for at least 6 weeks in mouse eyes. The flattening of the anterior chamber appears to bring the trabecular meshwork into closer proximity to limbal areas targeted with the laser and may be useful in enhancing the effect of photocoagulation to obstruct the anterior chamber angle [19]. Significant increases in mean IOP during 4 to 12 weeks were detected in treated eyes [19]. Average IOPs in laser-treated eyes (IOPtx) versus contralateral control eyes (IOPc) during the first 4 weeks and during the entire 12-week study period were  $23.4 \pm 5.1$  mm Hg versus  $16.3 \pm 2.3$  mm Hg and  $20.1 \pm 3.5$  mm Hg versus  $16.2 \pm 2.4$  mm Hg, respectively [19]. Average IOPtx was significantly higher than the average IOPc during both periods ( $P < 0.001$ ) [19]. A treatment response was considered to be a success if either the mean of IOP measurements collected during the first 4 weeks was increased by 30% or more or the mean of all measurements collected during the 12-week study period was increased by 30% or more [19]. During the first 4 weeks, 14 (64%) of 22 eyes had an IOP increase of more than 30% [19]. During the entire 12-week study, 7 (37%) of 19 eyes maintained an IOP increase of greater than 30% [19]. The success rate of IOP elevation after a single procedure is relatively high compared with other glaucoma models. Histologic analysis at the end of the 12-week study showed that the angle was completely closed by the laser photocoagulation treatment

[20]. Disadvantages of this method include ocular inflammation induced by laser treatment, flattening of the anterior chamber, and variability of IOP magnitude and duration [19]. In addition, the IOP elevation was not sustained in the treated eyes, slowly declining to baseline by 8 weeks after treatment [19]. In optic nerve cross sections examined by electron microscopy 300  $\mu$ m posterior to the globe [20], mean axon density and total number of axons in the laser treated eyes were significantly decreased compared with the control eyes.

Other studies applying argon laser photocoagulation to the episcleral and limbal veins in C57BL/6 mice [33, 34] induced IOP elevations lasting for weeks after treatment, with decline to baseline levels approximately 8 weeks after treatment [34]. After laser treatment, mean IOP was increased in the treated eyes from the control mean of  $13 \pm 1.8$  mm Hg to  $20.0 \pm 2.8$  mm Hg at 4 weeks in C57BL/6 mice [33]. Peak IOP was  $32 \pm 2.5$  mm Hg in the experimental group. RGC loss was  $16.9\% \pm 7.8\%$  at 2 weeks ( $P < 0.05$ ) and  $22.4\% \pm 7.5\%$  at 4 weeks ( $P < 0.05$ ) after laser photocoagulation [33]. TUNEL staining showed that there were marked increases in the number of apoptotic nuclei in the ganglion cell layer in the treated eyes [33]. Laser photocoagulation of limbal and episcleral veins also induces transient ocular hypertension in albino CD-1 mice [35]. In albino CD-1 mice, the IOPs measured in operative eyes ( $27.6 \pm 2.6$  mm Hg) were significantly elevated above those measured in control eyes ( $12.3 \pm 1.0$  mm Hg) 4 hours after laser treatment and remained elevated at the second postoperative day (operative  $27.1 \pm 1.8$  mm Hg versus control  $13.4 \pm 0.3$  mm Hg) [35]. IOPs measured in laser-treated eyes declined to baseline and were similar to IOPs in control eyes by 1 week (operative  $15.4 \pm 1.3$  mm Hg versus  $12.4 \pm 0.6$  mm Hg). Overall, the elevation of IOP is transient in these laser models, and the level of cell loss is modest.

Similar to mice, rats are easy to maintain in the laboratory, and they can be used in large numbers [21, 36–40]. Laser photocoagulation has been applied to the trabecular meshwork alone [41] or the trabecular meshwork and episcleral veins [42] in rats, and the induced IOP elevation results in subsequent glaucomatous damage, including RGC loss [41, 42]. Levkovitch-Verbin et al. [42] induced experimental glaucoma unilaterally in Wistar rats, using a diode laser with wavelength of 532 nm aimed only at the trabecular meshwork (trabecular group) or at episcleral veins (combination treatment group) through the external limbus. IOP was increased in all eyes to higher than the normal mean IOP of  $19.4 \pm 2.1$  mm Hg after the laser treatment [42]. Peak IOP was  $34.0 \pm 5.7$  mm Hg in the trabecular group and  $49.0 \pm 6.1$  mm Hg in the combination group [42]. Mean IOP after 6 weeks was  $22.0 \pm 1.8$  mm Hg in glaucomatous eyes in the trabecular group compared with  $25.5 \pm 2.9$  mm Hg in the combination group [42]. IOP in the glaucomatous eyes was typically higher than in the control eyes for at least 3 weeks [42]. In the combination group, RGC loss was  $16.1\% \pm 14.4\%$  at 1 week ( $P < 0.01$ ),  $59.7\% \pm 25.7\%$  at 6 weeks ( $P < 0.001$ ), and  $70.9\% \pm 23.6\%$  at 9 weeks ( $P < 0.001$ ) [42]. The trabecular group had mean axonal loss of  $19.1\% \pm 14.0\%$  at 3 weeks ( $P < 0.004$ ) and  $24.3\% \pm 20.2\%$  at 6 weeks ( $P < 0.001$ ) [42]. Laser treatment led to closure of intertrabecular spaces and

the major outflow channel [42]. The retina and choroid were normal by ophthalmoscopy at all times after treatment. Light microscopic examination showed only loss of RGCs and their nerve fibers [42]. Although continuous IOP elevation over longer periods is ideal, 3 weeks of elevated IOP induces substantial RGC loss and axonal damage of the optic nerve, making the model attractive for most investigations [42].

There are several limitations to using laser-induced ocular hypertension in rats. First, differences in pigmentation of the trabecular meshwork markedly change the effects of laser photocoagulation to increase IOP. Second, repeated laser treatments induce ocular inflammation and corneal opacity [43].

**2.2. Red Blood Cell or Microbead Injections into the Anterior Chamber.** To circumvent the limitations and disadvantages of laser techniques, microbeads were injected into the anterior chamber to induce ocular hypertension in primates [9], pigs [30], mice [44], rats [45], and rabbits [46]. An alternative to microbead injection uses injection of autologous fixed red blood cells (RBCs) into the anterior chamber [12, 47]. Elevations in IOP observed in autologous RBCs- or microbead-injected eyes are thought to result from inhibition of aqueous outflow.

Experimental primate models of chronic IOP elevation were developed by Quigley and Addicks (1980) using autologous fixed RBCs (ghost cells) [12, 47]. Direct obstruction of the trabecular meshwork by ghost cells as well as swelling of trabecular cells following phagocytosis of cellular debris was observed by electron microscopy. The model has the advantages of producing IOP elevation easily (mean IOP, 24 mm Hg to 73 mm Hg) and without associated intraocular inflammation [12]. However, IOP elevations lasted from 2 to 42 days, and the extensive filling of the anterior chamber with ghost cells resulted in poor visibility of the optic disk [12]. Ghost cells are degenerating red blood cells without hemoglobin content. Subsequently, Weber and Zelenak (2001) [48] reported that multiple injections of sterile latex microspheres ( $2-4 \times 10^5$  sterile beads per injection) into the primate anterior chamber are simple and cost effective for inducing chronic IOP elevation [48]. In the treated eyes with multiple injections of latex microspheres, mean IOP was 17.8 mm Hg to 36.7 mm Hg, and peak IOP was 23 mm Hg to 65 mm Hg [48]. Different levels and durations of elevated IOP can be obtained by altering the frequency and number of microspheres injected [47]. This approach has the advantages of producing IOP elevations while preserving visibility of the optic disc, which is necessary for assessment of glaucoma development [48]. Fluorescent polystyrene microbead injection into the anterior chamber of C57BL/6 mice results in chronic IOP elevation ( $4.6 \pm 0.6$  mm Hg above control IOP) lasting for at least 3 weeks following a single injection [49]. Cone et al. (2012) [50] maintained the IOP elevation by a combination of polystyrene bead injection followed by viscoelastic solution injection into the mouse anterior chamber. The disadvantages of the mouse model include the relatively small size of the globe, which makes it hard to manipulate.

IOP elevations induced by microbeads have also been described in rat models [40]. In Wistar rats injected with microbeads, IOP elevation persists for two weeks and results in reduced density of the optic nerves [40, 51]. Wistar rats receiving weekly injections of hyaluronic acid show IOP elevation that persists for at least 10 weeks [51].

Taken together, microbead injection models offer a relatively easy technique without special equipment, and the IOP elevation can be modulated with subsequent injections of microbeads or viscous materials. The principal disadvantage is that microbeads can be difficult to retain in the anterior chamber angle after injection. To address these issues, Samsel et al. (2011) [52] developed a technique for induction of ocular hypertension using paramagnetic microbeads. Magnet is used to direct microbead to the anterior chamber angle. These beads have the advantage that they can be directed to the anterior chamber angle in the rodent eye to optimize occlusion of the trabecular meshwork. In this case, the paramagnetic microbeads could be directed to the iridocorneal angle using a handheld magnet [52].

**2.3. Episcleral Vein Obstruction.** Shareef et al. (1995) [15] developed an episcleral vein cauterization model of glaucoma in rat. This method is less invasive than laser photocoagulation and induces no complications in the anterior chamber [53]. Because of its efficacy and accessibility, the majority of the structural and functional studies in experimental glaucoma have used this method [13]. IOP elevations in this model are thought to involve increased outflow resistance [54].

Mouse glaucoma models induced by episcleral vein cauterization exhibit significantly elevated IOP ( $28 \pm 1.5$  mm Hg) for up to 4 weeks and loss of RGCs [54]. Photocoagulation of episcleral and limbal veins induces a doubling of IOP lasting for 4 hours in albino CD1 mice [55, 56]. Complications of episcleral vein cautery in mice include thermal damage to sclera, intraocular inflammation, and ocular surface damage.

To compare the effects of IOP elevation on ganglion cell size and death, Vecino and Sharma (2013) [57] used three experimental glaucoma models in rats: (i) injections of latex microspheres into the anterior chamber, (ii) injections of microspheres and hydroxypropylmethylcellulose into the anterior chamber, and (iii) cauterization of three episcleral veins. IOP elevation induced by episcleral vein coagulation was more stable and constant for at least 24 weeks as compared with the other two experimental glaucoma methods. Similar results were observed when the three methods were compared in rats [58] and pigs [44].

Morrison et al. [14] have suggested, however, that pathophysiology in the episcleral vein cautery model differs from the other two ocular hypertension models, and the pattern of RGC death might be different in this model. While axonal degeneration of RGCs is the predominant finding in the other IOP elevation models, episcleral vein cautery appears to produce general RGC loss, indicating the possibility that factors other than IOP elevation might contribute to RGC death in episcleral vein cautery models.

TABLE 1: Experimentally induced *in vivo* mammalian glaucoma models.

<i>In vivo</i> glaucoma models	Species	Main papers	Main outcomes measured	Cost	Limitation
Laser photocoagulation of the perilimbal region	Monkey	Gaasterland and Kupfer (1974) [11]	IOP, cupping, HR, HI, OF	Expensive (laser equipment)	Ocular inflammation Irreversible mydriasis Technical difficulties
	Mouse	Aihara et al. (2003) [19] Mabuchi et al. (2003) [20]	IOP IOP, HR		Ocular inflammation Variability of IOP Technical difficulties
	Rat	Levkovitch-Verbin et al. (2002) [42]	IOP, HR, HI		Hyphema, corneal opacity Ocular inflammation
RBC injections into the anterior chamber	Monkey	Quigley and Addicks (1980) [12, 47]	IOP, HR, HI, OF	Not expensive	Low visibility of optic discs by accumulation of RBC or microbeads
Microbead injections into the anterior chamber	Rat	Weber and Zelenak (2001) [48]	IOP, HR, HI		
	Mouse	Pang et al. (2005) [40] Sappington et al. (2010) [49]	IOP IOP, HR, HI		
Hyaluronic acid injection into the anterior chamber	Rat	Moreno et al. (2005) [51]	IOP, HR, HI, ERG		
Episcleral vein obstruction	Rat	Shareef et al. (1995) [15]	IOP	Not expensive	Scleral thermal burns (RGC death patterns may be different from those of other glaucoma models)
	Mouse	Ruiz-Ederra and Verkman (2006) [54]	IOP, HR, OF		
Episcleral vein saline injection	Rat	Morrison et al. (1997) [14]	IOP, HR, HI	Not expensive	Technical difficulties
	Mouse	Kipfer-Kauer et al. (2010) [59]	IOP, HR		

IOP: IOP measurement, cupping: assessment of optic disc cupping, HR: histological assessment of retinal nerve fibers and optic discs, HI: histological assessment of the iridocorneal angles, OF: outflow facility, ERG: electroretinography.

**2.4. Episcleral Vein Saline Injection.** Kipfer-Kauer et al. (2010) [59] have succeeded in inducing chronic IOP elevation in C57BL/6 mice by injection of 1.5 M hypertonic saline into a limbal vein. The hypertonic saline injection group revealed a mean IOP of  $9.99 \pm 3.3$  mm Hg versus  $7.42 \pm 2.2$  mm Hg in the contralateral control eye. Peak IOP in the hypertonic saline injection group was 15.6 mm Hg versus 11.6 mm Hg in the control group. Episcleral vein saline injection causes an increase in the resistance of aqueous outflow channels. To develop chronically elevated IOP in rats, episcleral veins were injected with hypertonic saline in Brown Norway rats, and IOP elevations (7 to 28 mm Hg above control pressure) were sustained after 4 weeks [14]. The anterior chamber angles showed the formation of the peripheral anterior synechia. Electron micrographs of eyes from this model showed glaucomatous damage of RGC axons [14].

The disadvantage of these latter models is the relative difficulty of the induction technique. Insertion of a microneedle into the rat episcleral vein requires considerable training and experience. An additional disadvantage is that the duration of IOP elevation is relatively short and sequential hypertonic saline injections are needed to produce longer lasting IOP changes [60].

Taken together, a wide variety of *in vivo* animal models have been developed to study the effect of elevated IOP on the optic nerve and RGC degeneration. However, the duration of IOP elevation in these models is transient without sequential

treatments. In addition, precise control over IOP elevation is difficult, and the timing of induction and progression of glaucoma are usually unpredictable. Table 1 is the summarization of characteristics of the experimentally induced *in vivo* mammalian glaucoma models.

### 3. *In Vitro* Glaucoma Models

While *in vivo* animal models are necessary to show that a phenomenon occurs in living organisms, experiments in live animals typically involve undefined and uncontrollable factors [43]. Therefore, *in vitro* experimental systems are useful for producing highly controlled experimental conditions to manipulate specific variables contributing to degenerative changes [43]. Recently, *in vitro* glaucoma models that use cells cultured on a rigid substrate have been described [16, 61–72]. These models have used RGCs, optic nerve head astrocytes, or other types of retinal cells and sometimes have been equipped with pressure loading systems.

The application of hydrostatic pressure induces remarkable changes including enhancement of RGC apoptosis [64, 66], alterations in astrocyte structure [57], cell migration [63], elastin synthesis [68], and production of neural cell adhesion molecules [69]. Obazawa et al. (2004) [73] developed a cell culture system for manipulating hydrostatic pressure to examine the expression of optineurin and myocilin genes in trabecular meshwork cells under normal and hyperbaric

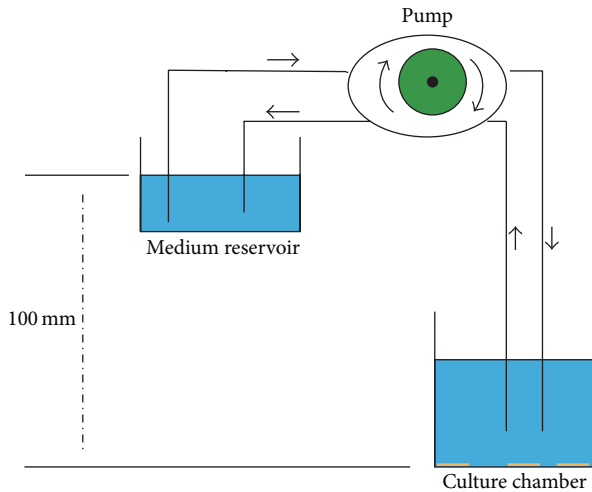


FIGURE 1: System used for hydrostatic pressure experiments. The culture chamber was filled with medium. The height of the medium reservoir was adjusted to maintain the pressure in the culture. For gas exchange, the medium was circulated by a peristaltic pump, and the pressure was monitored with the pressure gauge. This figure is the modification of Figure 1 of Lei et al. [61] and Figure 1 of Obazawa et al. [73].

conditions (Figure 1). Kashiwagi et al. (2004) [74] examined the survival and morphology of isolated RGCs subjected to centrifugal force loading using the unique device (Figure 2). The device includes a rotating vessel installed within a large incubator (model CPO2-1800; Hirasawa, Tokyo, Japan), a power supply unit, a control unit, and a cooling motor for removing heat generated by the motor installed outside the device. The rotor spins at 1 to 30 rotations per minute (rpm), with a rotation accuracy of 0.01 rpm. The equation for calculating centrifugal force ( $F$ ) is  $F$  (mm Hg)  $\cong 1.12r \times (\text{rpm}/1000) \times 750$ , where  $r$  is radial distance (in millimeters).

Recently, Yu et al. (2011) [75] developed a more convenient and simple pressure system using T75 culture flasks. An air mixture of 95% air and 5%  $\text{CO}_2$  is pumped into the flasks to obtain the desired pressure.

*In vitro* models are also useful for investigating the role of apoptotic mechanism in RGCs. RGC death induced by IOP elevation involves caspase activation as demonstrated using experimental rat models of glaucoma [76]. *In vitro* studies provide strong evidence that apoptosis of retinal neurons induced by different stimuli shares a common caspase cascade [66, 77], which can be inhibited using specific caspase inhibitors [78]. Additionally, Tezel and Yang (2004) [79] applied  $\text{TNF-}\alpha$  or hypoxia to primary cultures of rat RGCs for up to 48 hours and found that inhibition of caspases cannot block RGC death if the mitochondrial membrane potential is lost and cell death mediators (cytochrome c and apoptosis-inducing factor) are released.

Identification of precise cellular mechanisms in glaucoma requires isolation and primary culture of the RGCs. It has been known that *in vitro* experiments using primary cultures of RGCs are difficult to perform, mainly because of the limited yield and the typically postmitotic features of these

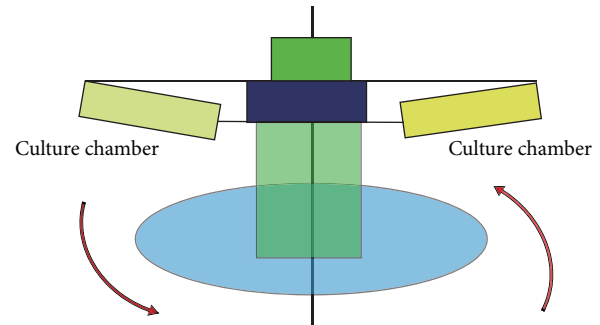


FIGURE 2: Schema of the centrifugal force loading device. The device is composed of two culture chambers and a motor unit for providing centrifugal force and rotor vessels. The isolated cells are situated at the bottom of the culture dish to become perpendicular to the direction of the centrifugal force and gravity vectors corresponding to a rotation speed. This figure is the modification of Figure 1 of Kashiwagi et al. [74].

neurons [80]. Therefore, early postnatal tissues are used in an attempt to optimize cell number and survival in culture. However, there are differences in cell responses between postnatal and adult cells that can limit interpretation of experimental results. In addition, it is difficult to examine interactions between RGCs and other types of cells such as retinal glia in specific mechanisms.

#### 4. *Ex Vivo* Glaucoma Models

We recently developed a new *ex vivo* experimental model for acute glaucoma that involves incubating rat retinal segments under hydrostatic pressure at the bottom of a deep cylinder [17] (Figure 3). Acute high pressures can induce retinal ischemia clinically and in *in vivo* glaucoma models [81, 82]. The *ex vivo* hydrostatic pressure model excludes the influence of ischemia and can thus allow examination of the direct effects of hydrostatic pressure on the otherwise intact retina, including changes in gene and protein expression [83, 84].

While the *ex vivo* system produces reliable results, we note several limitations. Survival factors for retinal neurons supplied from the blood stream or axonal transport are eliminated in *ex vivo* preparations, and the incubation period is limited by the duration in which the tissue can be kept alive. The advantages of this model include a higher degree of control over experimental variables and better preservation of neuron-neuron and neuron-glial interactions that are possible in dissociated cell preparations.

Of interest in this *ex vivo* model is the finding that axonal swelling in RGCs is induced in a pressure-dependent manner. In the central nervous system, activation of neuronal glutamate receptors induces swelling of cell bodies and dendrites [85–88] and also produces  $\text{Na}^+$ -dependent blebs in acutely isolated hippocampal neurons [89]. This swelling is caused by the influx of  $\text{Na}^+$  and  $\text{Ca}^{2+}$  and the passive redistribution of chloride and water across neuronal membranes [88–90]. Similar events occurring in axons could contribute to the findings observed in the *ex vivo* glaucoma model. Because

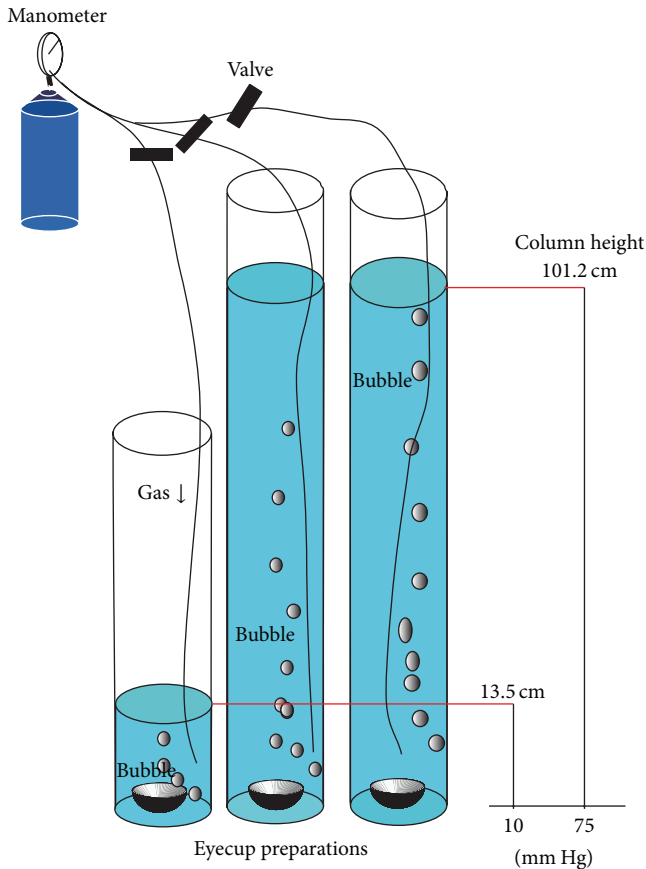


FIGURE 3: Outline of the experiment using *ex vivo* glaucoma model. Eyecups preparations were sunken to the bottom of a glass cylinder with different heights. Each cylinder was filled with incubation buffer at 30°C for 24 hours. The buffer was bubbled with 95% O<sub>2</sub>-5% CO<sub>2</sub>. Hydrostatic pressure at the bottom of the cylinder was calculated to be 10 mm Hg and 75 mm Hg when a CSF was added to a height of 13.5 cm and 101.2 cm, respectively. This figure is the modification of Figure 1 of Ishikawa et al. [17].

administration of glutamate receptor antagonists attenuated the axonal swelling, we hypothesize that glutamate-mediated changes contribute to axonal swelling under hyperbaric conditions.

To determine whether increased pressure triggers release of ATP, Reigada et al. (2008) [91] loaded air or nitrogen pressure to *ex vivo* bovine eyecups [91]. One milliliter of buffer solution was added to the bottom of each eyecup and the lid was sealed. Air or nitrogen was injected from a syringe until the pressure reading by digital manometry reached the desired level. When appropriate precautions were taken, pressure levels remained constant throughout the experiment. ATP released from retinal cells diffuses into the vitreous humor. Vitreous humor from each eyecup was collected, and ATP concentrations were determined. Elevated pressure led to an increase in extracellular ATP. This excess extracellular ATP may serve as a link between increased pressure and RGC death in acute glaucoma, suggesting a

possible role for ATP in neuronal damage accompanying increased intracranial pressure.

Table 2 is the summarization of characteristics of the experimentally induced *in vitro* and *ex vivo* mammalian glaucoma models.

## 5. Genetically Modified Mouse Glaucoma Models

There are numerous mouse models in which glaucoma-like pathology occurs as a result of genetic mutations [43, 92]. A main advantage of these glaucoma models is higher reproducibility of responses following IOP elevations compared to surgically induced models [42]. Because there is significant conservation in mouse and human genomes, the generation of mice with specific mutations identified in human glaucoma can be useful for understanding pathogenesis [43]. We briefly review studies that have utilized genetically modified mouse models to examine the roles of different genes in the glaucoma pathogenesis.

**5.1. GLAST and EAAC-1.** Normal tension glaucoma (NTG) is a condition in which clinical features are largely identical to those seen in primary open angle glaucoma (POAG) except for the relatively low IOP (<22 mm Hg). The pathophysiology of RGC degeneration and optic nerve damage in NTG remains unclear. To explore possible pathways of RGC degeneration, genetically modified mice with normal IOP have been used as models of NTG. Harada et al. [18] showed that mice with deficient expression of the glutamate transporters, GLAST or EAAC-1, demonstrate spontaneous RGC death and optic nerve degeneration without elevated IOP. In GLAST-deficient mice, administration of a glutamate receptor antagonist prevented RGC loss, indicating that GLAST helps to prevent excitotoxic retinal damage. Additionally, GLAST helps to maintain levels of the antioxidant glutathione in Müller cells by transporting glutamate, the substrate for glutathione synthesis, into the cells. Taken together, it appears that GLAST deficiency leads to RGC degeneration by both excitotoxic and oxidative stress mechanisms.

GLAST deficient mice were also used to investigate ASK1 deficiency on RGC death [93]. Apoptosis signal-regulating kinase 1 (ASK1) is a mitogen-activated protein kinase (MAPK) that plays an important role in stress-induced RGC apoptosis. Loss of ASK1 had no effects on the production of glutathione or malondialdehyde in the retina or on IOP. Tumor-necrosis-factor (TNF) induced activation of p38 MAPK and production of inducible nitric oxide synthase were also suppressed in ASK1-deficient Müller glial cells and RGCs, suggesting that ASK1 activation is involved in NTG.

**5.2. CYP1B1.** *CYP1B1* is a gene implicated in congenital glaucoma and codes the enzyme, cytochrome P450, family 1, subfamily b, polypeptide 1 [94, 95]. The role that *CYP1B1* plays in the pathophysiology of glaucoma and the development of anterior chamber anomalies is not known. Nonetheless, *CYP1B1*-deficient mice exhibit abnormalities in their aqueous drainage system that are similar to those reported in

TABLE 2: Experimentally induced *in vitro* and *ex vivo* mammalian glaucoma models.

	Species	Main papers	Pressure (mm Hg)	Duration (hours)	Main outcomes measured
<i>In vitro</i> glaucoma models					
Hydro pressure model	Porcine	Obazawa et al. (2004) [73]	3, 33	12, 24, 48, 72	Optineurin and myocilin expression in trabecular meshwork cells
Centrifugation model	Rat	Kashiwagi et al. (2004) [74]	16, 28, 33	24, 48	Expressional changes in mRNA in RGC and retinal glia
<i>Ex vivo</i> glaucoma models					
Hydro pressure model	Rat	Ishikawa et al. (2010) [17]	10, 25, 50, 75	24	Histology of the retinal nerve fiber, Glutamine synthetase activity
Gas pressure model	Bovine	Reigada et al. (2008) [91]	20–100	0.5	Retinal ATP release

human angle-closure glaucoma patients [96]. In contrast, other studies using *CYP1B1*-null mice revealed no evidence of IOP elevation [97]. Although *CYP1B1* knockout mice do not develop elevated IOP, they have abnormalities in their aqueous drainage system, small or absent Schlemm's canal, defects in trabecular meshwork, and peripheral anterior synechia of the iris [97]. A mouse model with mutations in both *CYP1B1* and *Tyr* was also developed and revealed that *Tyr* mutation modifies the phenotype associated with inheritance of mutant orthologs of *CYP1B1* and *Foxc1*, both of which have been shown to be involved in human angle-closure glaucoma [96, 97].

**5.3. Alpha-1 Subunit of Collagen Type 1.** More recently, a transgenic mouse model of POAG has emerged. This mouse model has a targeted mutation in the gene for the alpha-1 subunit of collagen type 1 and demonstrates progressive loss of RGC axons induced by IOP elevation [98]. Organization of the drainage structures seems normal in this model.

**5.4. Myocilin.** The myocilin gene (*Myoc*) encodes a secreted glycoprotein. Tyr437His mutation in *Myoc* leads to severe glaucoma in humans [99], and the mouse Tyr423His mutation corresponds to this human mutation [100]. Tyr423His *Myoc* mice demonstrate progressive degenerative changes in the peripheral RGC layer and optic nerve, with normal organization of aqueous drainage structures [101]. It has been suggested that mice expressing mutated mouse or human *Myoc* in the trabecular meshwork have characteristics of POAG [101, 102]. By contrast, expression of the mutated *Myoc* allele (Tyr423His) specifically in the iridocorneal angle does not lead to IOP elevation and does not produce degenerative changes in the retina [103]. These differences might be explained by differences in the levels of mutated *Myoc* expression as well as by differences in genetic background [103].

## 6. Conclusions

This paper describes animal models used in glaucoma research. These animal models are essential to elucidate the natural course of the disease and to develop novel therapeutic approaches. However, glaucoma is a disorder with

complicated pathogenesis that is far from being completely understood. Since the mechanisms of glaucoma differ among animal models, the selection of an animal model should be based on experimental needs and the hypothesis being tested. Experimentally, induced *in vivo* models have the advantage of studying certain changes in glaucoma in a living animal. However, the duration of IOP elevation in these models is transient without sequential treatments. In addition, precise control over IOP is difficult, and the timing of induction and progression of glaucoma are often unpredictable. While *in vivo* animal models are necessary to demonstrate that a phenomenon occurs in living organisms, *in vivo* animal experiments usually include undefined and uncontrollable factors. For this reason, *in vitro* systems have been useful for conducting highly controlled experiments in specific contexts. *In vitro* experiments using primary cultures of RGCs are not easy to perform, however, mainly because of the limited cellular yield in adult animals and the typically postmitotic feature of RGCs. Thus, early postnatal tissues are used in order to optimize cell number and survival in culture. It is important to note, however, that there are major differences in cell responses to external stimulation between postnatal and adult cells. In addition, it is difficult to examine the interaction between RGCs and other types of cells such as retinal glia under these conditions. Recently developed *ex vivo* models for acute glaucoma involve incubating rat retinal segments under hydrostatic pressure at the bottom of a deep cylinder. The *ex vivo* hydrostatic pressure model excludes the effects of ischemia and allows studying of the direct effects of pressure on the retina. Additionally, this model includes higher degrees of control over experimental variables and better preservation of neuron-neuron and neuron-glia interactions that are possible in dissociated cell preparations. *Ex vivo* models are limited by the absence of survival factors supplied by blood or axonal transport, and the incubation period is time limited. Going forward, it is likely that genetic models developed to test specific hypotheses will provide valuable information on pathophysiology and potentially lead to the discovery of new therapeutic targets. By using these animal models, we hope to continue to improve glaucoma prevention and treatment.

## Conflict of Interests

Charles F. Zorumski is a member of the Scientific Advisory Board of Sage Therapeutics. There are no other competing financial interests.

## Acknowledgments

The authors thank Sanae Takaseki and Yoko Hayami for technical support. This work was supported in part by JSPS KAKENHI Grant no. 24592666 to Makoto Ishikawa and by NIH Grants MH077791, MH101874, and AA017413 to Charles F. Zorumski and the Bantly Foundation.

## References

- [1] H. A. Quigley, R. W. Nickells, L. A. Kerrigan, M. E. Pease, D. J. Thibault, and D. J. Zack, "Retinal ganglion cell death in experimental glaucoma and after axotomy occurs by apoptosis," *Investigative Ophthalmology and Visual Science*, vol. 36, no. 5, pp. 774–786, 1995.
- [2] Y. Suzuki, A. Iwase, M. Araie et al., "Risk factors for open-angle glaucoma in a Japanese population: the Tajimi study," *Ophthalmology*, vol. 113, no. 9, pp. 1613–1617, 2006.
- [3] K. N. Gelatt, R. L. Peiffer Jr., R. M. Gwin, G. G. Gum, and L. W. Williams, "Clinical manifestations of inherited glaucoma in the beagle," *Investigative Ophthalmology & Visual Science*, vol. 16, no. 12, pp. 1135–1142, 1977.
- [4] A. E. Kolker, R. A. Moses, M. A. Constant, and B. Becker, "The development of glaucoma in rabbits," *Investigative Ophthalmology*, vol. 2, no. 4, pp. 316–321, 1963.
- [5] S. W. John, R. S. Smith, and O. V. Savinov, "Essential iris atrophy, pigment dispersion, and glaucoma in DBA/2J mice," *Investigative Ophthalmology & Visual Science*, vol. 39, no. 6, pp. 951–962, 1998.
- [6] M. G. Anderson, R. S. Smith, N. L. Hawes et al., "Mutations in genes encoding melanosomal proteins cause pigmentary glaucoma in DBA/2J mice," *Nature Genetics*, vol. 30, no. 1, pp. 81–85, 2002.
- [7] M. G. Anderson, K. S. Nair, L. A. Amonoo et al., "*Gpnmb*<sup>R150X</sup> allele must be present in bone marrow derived cells to mediate DBA/2J glaucoma," *BMC Genetics*, vol. 9, article 30, 2008.
- [8] E. Vecino and S. C. Sharma, "Glaucoma animal models," in *Glaucoma—Basic and Clinical Aspects*, S. Rumelt, Ed., pp. 319–334, InTech Europe Publisher, Rijeka, Croatia, 2013.
- [9] N. H. Kalvin, D. I. Hamasaki, and J. D. Gass, "Experimental glaucoma in monkeys. I. Relationship between intraocular pressure and cupping of the optic disc and cavernous atrophy of the optic nerve," *Archives of Ophthalmology*, vol. 76, no. 1, pp. 82–93, 1966.
- [10] S. Lessell and T. Kuwabara, "Experimental alpha-chymotrypsin glaucoma," *Archives of Ophthalmology*, vol. 81, no. 6, pp. 853–864, 1969.
- [11] D. Gaasterland and C. Kupfer, "Experimental glaucoma in the rhesus monkey," *Investigative Ophthalmology*, vol. 13, no. 6, pp. 455–457, 1974.
- [12] H. A. Quigley and E. M. Addicks, "Chronic experimental glaucoma in primates. I. Production of elevated intraocular pressure by anterior chamber injection of autologous ghost red blood cells," *Investigative Ophthalmology and Visual Science*, vol. 19, no. 2, pp. 126–136, 1980.
- [13] M. V. Fedorchak, I. P. Conner, C. A. Medina, J. B. Wingard, J. S. Schuman, and S. R. Little, "28-day intraocular pressure reduction with a single dose of brimonidine tartrate-loaded microspheres," *Experimental Eye Research*, vol. 125, pp. 210–216, 2014.
- [14] J. C. Morrison, C. G. Moore, L. M. H. Deppmeier, B. G. Gold, C. K. Meshul, and E. C. Johnson, "A rat model of chronic pressure-induced optic nerve damage," *Experimental Eye Research*, vol. 64, no. 1, pp. 85–96, 1997.
- [15] S. R. Shareef, E. Garcia-Valenzuela, A. Salierno, J. Walsh, and S. C. Sharma, "Chronic ocular hypertension following episcleral venous occlusion in rats," *Experimental Eye Research*, vol. 61, no. 3, pp. 379–382, 1995.
- [16] M. B. Wax, G. Tezel, S. Kobayashi, and M. R. Hernandez, "Responses of different cell lines from ocular tissues to elevated hydrostatic pressure," *British Journal of Ophthalmology*, vol. 84, no. 4, pp. 423–428, 2000.
- [17] M. Ishikawa, T. Yoshitomi, C. F. Zorumski, and Y. Izumi, "Effects of acutely elevated hydrostatic pressure in a rat ex vivo retinal preparation," *Investigative Ophthalmology and Visual Science*, vol. 51, no. 12, pp. 6414–6423, 2010.
- [18] T. Harada, C. Harada, K. Nakamura et al., "The potential role of glutamate transporters in the pathogenesis of normal tension glaucoma," *The Journal of Clinical Investigation*, vol. 117, no. 7, pp. 1763–1770, 2007.
- [19] M. Aihara, J. D. Lindsey, and R. N. Weinreb, "Experimental mouse ocular hypertension: establishment of the model," *Investigative Ophthalmology and Visual Science*, vol. 44, no. 10, pp. 4314–4320, 2003.
- [20] F. Mabuchi, M. Aihara, M. R. Mackey, J. D. Lindsey, and R. N. Weinreb, "Optic nerve damage in experimental mouse ocular hypertension," *Investigative Ophthalmology and Visual Science*, vol. 44, no. 10, pp. 4321–4330, 2003.
- [21] E. van der Zypen, "Experimental morphological study on structure and function of the filtration angle of the rat eye," *Ophthalmologica*, vol. 174, no. 5, pp. 285–298, 1977.
- [22] T. Gherezghiher, W. F. March, R. E. Nordquist, and M. C. Koss, "Laser-induced glaucoma in rabbits," *Experimental Eye Research*, vol. 43, no. 6, pp. 885–894, 1986.
- [23] B. Johnson, P. House, W. Morgan, X. Sun, and D.-Y. Yu, "Developing laser-induced glaucoma in rabbits," *Australian and New Zealand Journal of Ophthalmology*, vol. 27, no. 3-4, pp. 180–183, 1999.
- [24] R. J. Seidehamel and K. W. Dungan, "Characteristics and pharmacologic utility of an intraocular pressure (IOP) model in unanesthetized rabbits," *Investigative Ophthalmology*, vol. 13, no. 4, pp. 319–322, 1974.
- [25] H. A. Quigley, R. M. Sanchez, G. R. Dunkelberger, N. L. L'Hernault, and T. A. Baginski, "Chronic glaucoma selectively damages large optic nerve fibers," *Investigative Ophthalmology and Visual Science*, vol. 28, no. 6, pp. 913–920, 1987.
- [26] Y. Glovinsky, H. A. Quigley, and G. R. Dunkelberger, "Retinal ganglion cell loss is size dependent in experimental glaucoma," *Investigative Ophthalmology & Visual Science*, vol. 32, no. 3, pp. 484–491, 1991.
- [27] Y. Glovinsky, H. A. Quigley, and M. E. Pease, "Foveal ganglion cell loss is size dependent in experimental glaucoma," *Investigative Ophthalmology & Visual Science*, vol. 34, no. 2, pp. 395–400, 1993.
- [28] H. A. Quigley and R. M. Hahman, "Laser energy levels for trabecular meshwork damage in the primate eye," *Investigative*

- Ophthalmology and Visual Science*, vol. 24, no. 9, pp. 1305–1307, 1983.
- [29] C. B. Toris, G.-L. Zhan, Y.-L. Wang et al., “Aqueous humor dynamics in monkeys with laser-induced glaucoma,” *Journal of Ocular Pharmacology and Therapeutics*, vol. 16, no. 1, pp. 19–27, 2000.
- [30] J. Ruiz-Ederra, M. García, F. Martín et al., “Comparison of three methods of inducing chronic elevation of intraocular pressure in the pig experimental glaucoma,” *Archivos de la Sociedad Española de Oftalmología*, vol. 80, no. 10, pp. 571–579, 2005.
- [31] J. Ruiz-Ederra, M. García, M. Hernández et al., “The pig eye as a novel model of glaucoma,” *Experimental Eye Research*, vol. 81, no. 5, pp. 561–569, 2005.
- [32] R. A. Bouhenni, J. Dunmire, A. Sewell, and D. P. Edward, “Animal models of glaucoma,” *Journal of Biomedicine and Biotechnology*, vol. 2012, Article ID 692609, 11 pages, 2012.
- [33] R. L. Gross, J. Ji, P. Chang et al., “A mouse model of elevated intraocular pressure: retina and optic nerve findings,” *Transactions of the American Ophthalmological Society*, vol. 101, pp. 163–171, 2003.
- [34] J. Ji, P. Chang, M. E. Pennesi et al., “Effects of elevated intraocular pressure on mouse retinal ganglion cells,” *Vision Research*, vol. 45, no. 2, pp. 169–179, 2005.
- [35] C. T. Fu and D. Sretavan, “Laser-induced ocular hypertension in albino CD-1 mice,” *Investigative Ophthalmology & Visual Science*, vol. 51, no. 2, pp. 980–990, 2010.
- [36] J. Kipnis, E. Yoles, H. Schori, E. Hauben, I. Shaked, and M. Schwartz, “Neuronal survival after CNS insult is determined by a genetically encoded autoimmune response,” *The Journal of Neuroscience*, vol. 21, no. 13, pp. 4564–4571, 2001.
- [37] T. Daimon, M. Kazama, Y. Miyajima, and M. Nakano, “Immunocytochemical localization of thrombomodulin in the aqueous humor passage of the rat eye,” *Histochemistry and Cell Biology*, vol. 108, no. 2, pp. 121–131, 1997.
- [38] C. Remé, B. Aeberhard, and U. Urner, “The development of the chamber angle in the rat eye. Morphological characteristics of developmental stages,” *Graefes Archive for Clinical and Experimental Ophthalmology*, vol. 220, no. 3, pp. 139–153, 1983.
- [39] P. Nucci, G. Tredici, M. P. Manitto, G. Pizzini, and R. Brancato, “Neuron-specific enolase and embryology of the trabecular meshwork of the rat eye: an immunohistochemical study,” *International Journal of Biological Markers*, vol. 7, no. 4, pp. 253–255, 1992.
- [40] I.-H. Pang, W.-H. Wang, and A. F. Clark, “Acute effects of glaucoma medications on rat intraocular pressure,” *Experimental Eye Research*, vol. 80, no. 2, pp. 207–214, 2005.
- [41] J. Ueda, S. Sawaguchi, T. Hanyu et al., “Experimental glaucoma model in the rat induced by laser trabecular photocoagulation after an intracameral injection of india ink,” *Japanese Journal of Ophthalmology*, vol. 42, no. 5, pp. 337–344, 1998.
- [42] H. Levkovitch-Verbin, H. A. Quigley, K. R. G. Martin, D. Valenta, L. A. Baumrind, and M. E. Pease, “Translimbal laser photocoagulation to the trabecular meshwork as a model of glaucoma in rats,” *Investigative Ophthalmology and Visual Science*, vol. 43, no. 2, pp. 402–410, 2002.
- [43] T. V. Johnson and S. I. Tomarev, “Rodent models of glaucoma,” *Brain Research Bulletin*, vol. 81, no. 2–3, pp. 349–358, 2010.
- [44] M. R. Steinhart, F. E. Cone, C. Nguyen et al., “Mice with an induced mutation in collagen 8A2 develop larger eyes and are resistant to retinal ganglion cell damage in an experimental glaucoma model,” *Molecular Vision*, vol. 18, pp. 1093–1106, 2012.
- [45] Y. You, V. K. Gupta, J. C. Li, N. Al-Adawy, A. Klistorner, and S. L. Graham, “FTY720 protects retinal ganglion cells in experimental glaucoma,” *Investigative Ophthalmology and Visual Science*, vol. 55, no. 5, pp. 3060–3066, 2014.
- [46] Q. C. Ngumah, S. D. Buchthal, and R. F. Dacheux, “Longitudinal non-invasive proton NMR spectroscopy measurement of vitreous lactate in a rabbit model of ocular hypertension,” *Experimental Eye Research*, vol. 83, no. 2, pp. 390–400, 2006.
- [47] H. A. Quigley and E. M. Addicks, “Chronic experimental glaucoma in primates. II. Effect of extended intraocular pressure elevation on optic nerve head and axonal transport,” *Investigative Ophthalmology and Visual Science*, vol. 19, no. 2, pp. 137–152, 1980.
- [48] A. J. Weber and D. Zelenak, “Experimental glaucoma in the primate induced by latex microspheres,” *Journal of Neuroscience Methods*, vol. 111, no. 1, pp. 39–48, 2001.
- [49] R. M. Sappington, B. J. Carlson, S. D. Crish, and D. J. Calkins, “The microbead occlusion model: a paradigm for induced ocular hypertension in rats and mice,” *Investigative Ophthalmology & Visual Science*, vol. 51, no. 1, pp. 207–216, 2010.
- [50] F. E. Cone, M. R. Steinhart, E. N. Oglesby, G. Kalesnykas, M. E. Pease, and H. A. Quigley, “The effects of anesthesia, mouse strain and age on intraocular pressure and an improved murine model of experimental glaucoma,” *Experimental Eye Research*, vol. 99, no. 1, pp. 27–35, 2012.
- [51] M. C. Moreno, H. J. A. Marcos, J. O. Croxatto et al., “A new experimental model of glaucoma in rats through intracameral injections of hyaluronic acid,” *Experimental Eye Research*, vol. 81, no. 1, pp. 71–80, 2005.
- [52] P. A. Samsel, L. Kisiswa, J. T. Erichsen, S. D. Cross, and J. E. Morgan, “A novel method for the induction of experimental glaucoma using magnetic microspheres,” *Investigative Ophthalmology and Visual Science*, vol. 52, no. 3, pp. 1671–1675, 2011.
- [53] S. Yu, T. Tanabe, and N. Yoshimura, “A rat model of glaucoma induced by episcleral vein ligation,” *Experimental Eye Research*, vol. 83, no. 4, pp. 758–770, 2006.
- [54] J. Ruiz-Ederra and A. S. Verkman, “Mouse model of sustained elevation in intraocular pressure produced by episcleral vein occlusion,” *Experimental Eye Research*, vol. 82, no. 5, pp. 879–884, 2006.
- [55] C. T. Fu and D. Sretavan, “Laser-induced ocular hypertension in albino CD-1 mice,” *Investigative Ophthalmology and Visual Science*, vol. 51, no. 2, pp. 980–990, 2010.
- [56] R. L. Gross, J. Ji, P. Chang et al., “A mouse model of elevated intraocular pressure: retina and optic nerve findings,” *Transactions of the American Ophthalmological Society*, vol. 101, pp. 163–171, 2003.
- [57] E. Vecino and S. C. Sharma, “Glaucoma animal models,” in *Glaucoma—Basic and Clinical Aspects*, S. Rumelt, Ed., pp. 319–334, InTech Europe, Rijeka, Croatia, 2013.
- [58] J. H. Urcola, M. Hernández, and E. Vecino, “Three experimental glaucoma models in rats: comparison of the effects of intraocular pressure elevation on retinal ganglion cell size and death,” *Experimental Eye Research*, vol. 83, no. 2, pp. 429–437, 2006.
- [59] A. Kipfer-Kauer, S. J. McKinnon, B. E. Frueh, and D. Goldblum, “Distribution of amyloid precursor protein and amyloid- $\beta$  in ocular hypertensive C57BL/6 mouse eyes,” *Current Eye Research*, vol. 35, no. 9, pp. 828–834, 2010.
- [60] M. Rudzinski and H. U. Saragovi, “Glaucoma: validated and facile in vivo experimental models of a chronic neurodegenerative disease for drug development,” *Current Medicinal*

- Chemistry—Central Nervous System Agents*, vol. 5, no. 1, pp. 43–49, 2005.
- [61] Y. Lei, S. Rajabi, R. M. Pedrigi, D. R. Overby, A. Thomas Read, and C. Ross Ethier, "In vitro models for glaucoma research: effects of hydrostatic pressure," *Investigative Ophthalmology and Visual Science*, vol. 52, no. 9, pp. 6329–6339, 2011.
- [62] A. Agar, S. Li, N. Agarwal, M. T. Coroneo, and M. A. Hill, "Retinal ganglion cell line apoptosis induced by hydrostatic pressure," *Brain Research*, vol. 1086, no. 1, pp. 191–200, 2006.
- [63] M. Salvador-Silva, S. Aoi, A. Parker, P. Yang, P. Pecun, and M. R. Hernandez, "Responses and signaling pathways in human optic nerve head astrocytes exposed to hydrostatic pressure *in vitro*," *Glia*, vol. 45, no. 4, pp. 364–377, 2004.
- [64] A. Agar, S. S. Yip, M. A. Hill, and M. T. Coroneo, "Pressure related apoptosis in neuronal cell lines," *Journal of Neuroscience Research*, vol. 60, no. 4, pp. 495–503, 2000.
- [65] Q. Liu, W.-K. Ju, J. G. Crowston et al., "Oxidative stress is an early event in hydrostatic pressure-induced retinal ganglion cell damage," *Investigative Ophthalmology & Visual Science*, vol. 48, no. 10, pp. 4580–4589, 2007.
- [66] G. Tezel and M. B. Wax, "Increased production of tumor necrosis factor- $\alpha$  by glial cells exposed to simulated ischemia or elevated hydrostatic pressure induces apoptosis in cocultured retinal ganglion cells," *The Journal of Neuroscience*, vol. 20, no. 23, pp. 8693–8700, 2000.
- [67] W.-K. Ju, Q. Liu, K.-Y. Kim et al., "Elevated hydrostatic pressure triggers mitochondrial fission and decreases cellular ATP in differentiated RGC-5 cells," *Investigative Ophthalmology & Visual Science*, vol. 48, no. 5, pp. 2145–2151, 2007.
- [68] M. R. Hernandez, J. D. Pena, J. A. Selvidge, M. Salvador-Silva, and P. Yang, "Hydrostatic pressure stimulates synthesis of elastin in cultured optic nerve head astrocytes," *Glia*, vol. 32, no. 2, p. 122, 2000.
- [69] C. S. Ricard, S. Kobayashi, J. D. O. Pena, M. Salvador-Silva, O. Agapova, and M. R. Hernandez, "Selective expression of neural cell adhesion molecule (NCAM)-180 in optic nerve head astrocytes exposed to elevated hydrostatic pressure *in vitro*," *Molecular Brain Research*, vol. 81, no. 1-2, pp. 62–79, 2000.
- [70] B. Liu and A. H. Neufeld, "Nitric oxide synthase-2 in human optic nerve head astrocytes induced by elevated pressure *in vitro*," *Archives of Ophthalmology*, vol. 119, no. 2, pp. 240–245, 2001.
- [71] J. L. Yang, A. H. Neufeld, M. B. Zorn, and M. R. Hernandez, "Collagen type I mRNA levels in cultured human lamina cribrosa cells: effects of elevated hydrostatic pressure," *Experimental Eye Research*, vol. 56, no. 5, pp. 567–574, 1993.
- [72] P. Yang, O. Agapova, A. Parker et al., "DNA microarray analysis of gene expression in human optic nerve head astrocytes in response to hydrostatic pressure," *Physiological Genomics*, vol. 17, no. 2, pp. 157–169, 2004.
- [73] M. Obazawa, Y. Mashima, N. Sanuki et al., "Analysis of porcine optineurin and myocilin expression in trabecular meshwork cells and astrocytes from optic nerve head," *Investigative Ophthalmology and Visual Science*, vol. 45, no. 8, pp. 2652–2659, 2004.
- [74] K. Kashiwagi, Y. Iizuka, Y. Tanaka, M. Araie, Y. Suzuki, and S. Tsukahara, "Molecular and cellular reactions of retinal ganglion cells and retinal glial cells under centrifugal force loading," *Investigative Ophthalmology and Visual Science*, vol. 45, no. 10, pp. 3778–3786, 2004.
- [75] J. Yu, Y. Zhong, Y. Cheng, X. Shen, J. Wang, and Y. Wei, "Effect of high hydrostatic pressure on the expression of glutamine synthetase in rat retinal Müller cells cultured *in vitro*," *Experimental and Therapeutic Medicine*, vol. 2, no. 3, pp. 513–516, 2011.
- [76] S. J. McKinnon, D. M. Lehman, L. A. Kerrigan-Baumrind et al., "Caspase activation and amyloid precursor protein cleavage in rat ocular hypertension," *Investigative Ophthalmology & Visual Science*, vol. 43, no. 4, pp. 1077–1087, 2002.
- [77] G. Tezel and M. B. Wax, "The mechanisms of hsp27 antibody-mediated apoptosis in retinal neuronal cells," *Journal of Neuroscience*, vol. 20, no. 10, pp. 3552–3562, 2000.
- [78] G. Tezel and M. B. Wax, "Inhibition of caspase activity in retinal cell apoptosis induced by various stimuli *in vitro*," *Investigative Ophthalmology & Visual Science*, vol. 40, no. 11, pp. 2660–2667, 1999.
- [79] G. Tezel and X. Yang, "Caspase-independent component of retinal ganglion cell death, *in vitro*," *Investigative Ophthalmology and Visual Science*, vol. 45, no. 11, pp. 4049–4059, 2004.
- [80] T. V. Johnson and S. I. Tomarev, "Rodent models of glaucoma," *Brain Research Bulletin*, vol. 81, no. 2-3, pp. 349–358, 2010.
- [81] S. W. Park, K.-Y. Kim, J. D. Lindsey et al., "A selective inhibitor of Drp1, Mdivi-1, increases retinal ganglion cell survival in acute ischemic mouse retina," *Investigative Ophthalmology & Visual Science*, vol. 52, no. 5, pp. 2837–2843, 2011.
- [82] S. Yoneda, E. Tanaka, W. Goto, T. Ota, and H. Hara, "Topiramate reduces excitotoxic and ischemic injury in the rat retina," *Brain Research*, vol. 967, no. 1-2, pp. 257–266, 2003.
- [83] M. Ishikawa, T. Yoshitomi, C. F. Zorumski, and Y. Izumi, "Downregulation of glutamine synthetase via GLAST suppression induces retinal axonal swelling in a rat *ex vivo* hydrostatic pressure model," *Investigative Ophthalmology & Visual Science*, vol. 52, no. 9, pp. 6604–6616, 2011.
- [84] Y. Izumi, A. M. Benz, C. O. Kirby et al., "An *ex vivo* rat retinal preparation for excitotoxicity studies," *Journal of Neuroscience Methods*, vol. 60, no. 1-2, pp. 219–225, 1995.
- [85] J. W. Olney, T. Fuller, and T. de Gubareff, "Acute dendrotoxic changes in the hippocampus of kainate treated rats," *Brain Research*, vol. 176, no. 1, pp. 91–100, 1979.
- [86] R. S. Sloviter and D. W. Dempster, "'Epileptic' brain damage is replicated qualitatively in the rat hippocampus by central injection of glutamate or aspartate but not by GABA or acetylcholine," *Brain Research Bulletin*, vol. 15, no. 1, pp. 39–60, 1985.
- [87] F. Dessi, C. Charriaud-Marlangue, and Y. Ben-Ari, "Glutamate-induced neuronal death in cerebellar culture is mediated by two distinct components: a sodium-chloride component and a calcium component," *Brain Research*, vol. 650, no. 1, pp. 49–55, 1994.
- [88] C. Peterson, J. H. Neal, and C. W. Cotman, "Development of *N*-methyl-*D*-aspartate excitotoxicity in cultured hippocampal neurons," *Developmental Brain Research*, vol. 48, no. 2, pp. 187–195, 1989.
- [89] J. E. Friedman and G. G. Haddad, "Major differences in  $Ca_i^{2+}$  response to anoxia between neonatal and adult rat CA1 neurons: role of  $Ca_o^{2+}$  and  $Na_o^+$ ," *The Journal of Neuroscience*, vol. 13, no. 1, pp. 63–72, 1993.
- [90] S. M. Rothman, "The neurotoxicity of excitatory amino acids is produced by passive chloride influx," *Journal of Neuroscience*, vol. 5, no. 6, pp. 1483–1489, 1985.
- [91] D. Reigada, W. Lu, M. Zhang, and C. H. Mitchell, "Elevated pressure triggers a physiological release of ATP from the retina:

- possible role for pannexin hemichannels,” *Neuroscience*, vol. 157, no. 2, pp. 396–404, 2008.
- [92] S. J. McKinnon, C. L. Schlamp, and R. W. Nickells, “Mouse models of retinal ganglion cell death and glaucoma,” *Experimental Eye Research*, vol. 88, no. 4, pp. 816–824, 2009.
- [93] C. Harada, K. Namekata, X. Guo et al., “ASK1 deficiency attenuates neural cell death in GLAST-deficient mice, a model of normal tension glaucoma,” *Cell Death & Differentiation*, vol. 17, no. 11, pp. 1751–1759, 2010.
- [94] B. A. Bejjani, R. A. Lewis, K. F. Tomey et al., “Mutations in CYP1B1, the gene for cytochrome P4501B1, are the predominant cause of primary congenital glaucoma in Saudi Arabia,” *American Journal of Human Genetics*, vol. 62, no. 2, pp. 325–333, 1998.
- [95] M. Sarfarazi and I. Stoilov, “Molecular genetics of primary congenital glaucoma,” *Eye*, vol. 14, no. 3, pp. 422–428, 2000.
- [96] J. T. M. Buters, S. Sakai, T. Richter et al., “Cytochrome p450 CYP1B1 determines susceptibility to 7,12-dimethylbenz[*a*]anthracene-induced lymphomas,” *Proceedings of the National Academy of Sciences of the United States of America*, vol. 96, no. 5, pp. 1977–1982, 1999.
- [97] R. T. Libby, R. S. Smith, O. V. Savinova et al., “Modification of ocular defects in mouse developmental glaucoma models by tyrosinase,” *Science*, vol. 299, no. 5612, pp. 1578–1581, 2003.
- [98] F. Mabuchi, J. D. Lindsey, M. Aihara, M. R. Mackey, and R. N. Weinreb, “Optic nerve damage in mice with a targeted type I collagen mutation,” *Investigative Ophthalmology and Visual Science*, vol. 45, no. 6, pp. 1841–1845, 2004.
- [99] W. L. M. Alward, J. H. Fingert, M. A. Coote et al., “Clinical features associated with mutations in the chromosome 1 open-angle glaucoma gene (*GLC1A*),” *The New England Journal of Medicine*, vol. 338, no. 15, pp. 1022–1027, 1998.
- [100] I. Malyukova, H.-S. Lee, R. N. Fariss, and S. I. Tomarev, “Mutated mouse and human myocilins have similar properties and do not block general secretory pathway,” *Investigative Ophthalmology and Visual Science*, vol. 47, no. 1, pp. 206–212, 2006.
- [101] Y. Zhou, O. Grinchuk, and S. I. Tomarev, “Transgenic mice expressing the Tyr437His mutant of human myocilin protein develop glaucoma,” *Investigative Ophthalmology and Visual Science*, vol. 49, no. 5, pp. 1932–1939, 2008.
- [102] V. Senatorov, I. Malyukova, R. Fariss et al., “Expression of mutated mouse myocilin induces open-angle glaucoma in transgenic mice,” *The Journal of Neuroscience*, vol. 26, no. 46, pp. 11903–11914, 2006.
- [103] D. B. Gould, M. Reedy, L. A. Wilson, R. S. Smith, R. L. Johnson, and S. W. M. John, “Mutant myocilin nonsecretion in vivo is not sufficient to cause glaucoma,” *Molecular and Cellular Biology*, vol. 26, no. 22, pp. 8427–8436, 2006.

## Research Article

# Development of a Model of Chronic Kidney Disease in the C57BL/6 Mouse with Properties of Progressive Human CKD

Zahraa Mohammed-Ali,<sup>1</sup> Gaile L. Cruz,<sup>1</sup> Chao Lu,<sup>1</sup> Rachel E. Carlisle,<sup>1</sup> Kaitlyn E. Werner,<sup>1</sup> Kjetil Ask,<sup>2</sup> and Jeffrey G. Dickhout<sup>1</sup>

<sup>1</sup>Department of Medicine, Division of Nephrology, McMaster University and St. Joseph's Healthcare Hamilton, Hamilton, ON, Canada L8N 4A6

<sup>2</sup>Department of Medicine, Division of Respiratory, McMaster University and St. Joseph's Healthcare Hamilton, Hamilton, ON, Canada L8N 4A6

Correspondence should be addressed to Jeffrey G. Dickhout; [jdickhou@stjosham.on.ca](mailto:jdickhou@stjosham.on.ca)

Received 26 September 2014; Revised 16 December 2014; Accepted 29 December 2014

Academic Editor: Andrea Vecchione

Copyright © 2015 Zahraa Mohammed-Ali et al. This is an open access article distributed under the Creative Commons Attribution License, which permits unrestricted use, distribution, and reproduction in any medium, provided the original work is properly cited.

Chronic kidney disease (CKD) is a major healthcare problem with increasing prevalence in the population. CKD leads to end stage renal disease and increases the risk of cardiovascular disease. As such, it is important to study the mechanisms underlying CKD progression. To this end, an animal model was developed to allow the testing of new treatment strategies or molecular targets for CKD prevention. Many underlying risk factors result in CKD but the disease itself has common features, including renal interstitial fibrosis, tubular epithelial cell loss through apoptosis, glomerular damage, and renal inflammation. Further, CKD shows differences in prevalence between the genders with premenopausal women being relatively resistant to CKD. We sought to develop and characterize an animal model with these common features of human CKD in the C57BL/6 mouse. Mice of this genetic background have been used to produce transgenic strains that are commercially available. Thus, a CKD model in this strain would allow the testing of the effects of numerous genes on the severity or progression of CKD with minimal cost. This paper describes such a mouse model of CKD utilizing angiotensin II and deoxycorticosterone acetate as inducers.

## 1. Introduction

Although various models of chronic kidney disease (CKD) have been established in the rat [1], the ability to transgenically manipulate the rat is not nearly as well established as in the mouse. Further, many genetic knockout mouse strains, including tissue specific and conditionally inducible knockouts, are available on the C57BL/6 background [2]. However, this mouse has proven to be resistant to the development of CKD. C57BL/6 mice have shown resistance to the induction of CKD by standard techniques such as streptozotocin-induced diabetes [3], bovine serum albumin overload proteinuria [4], and reduced renal mass [5]. Thus, developing a mouse model of CKD on the C57BL/6 background, that shares salient pathological features of human CKD, allows the use of preexisting knockout strains. Experiments on these knockout strains would determine the effect of these genes on

the development of renal interstitial fibrosis, proteinuria and the chronic inflammatory response in CKD.

A model has been developed in the C57BL/6 that shows features of progressive human CKD, including proteinuria and inflammation [6]. In this model, mice are uninephrectomized, given Angiotensin (Ang) II infusion and deoxycorticosterone acetate (DOCA) with 1% salt in the drinking water. This model can be referred to as the Ang II/DOCA salt mouse. The use of Ang II and DOCA with a high salt diet in this model results in sodium retention and volume expansion and therefore hypertension [7]. As well, the reduction in renal mass promotes hyperfiltration, which contributes to proteinuria [8]. The dysregulation of the Renin-Angiotensin-Aldosterone system that is stimulated in this model plays a central role in cardiorenal syndrome [9]. This fact is well supported by the success of angiotensin converting enzyme (ACE) inhibitors and angiotensin receptor blockers (ARBs)

as first line therapies in the treatment of hypertension and kidney disease patients [9, 10]. As previously demonstrated by Kirchoff et al. (2008), this mouse model of CKD induces proteinuria and renal injury and increased systolic blood pressure [6]. In this paper, we will further characterize this model by quantifying the apoptotic responses in renal tubular epithelium, as well as renal interstitial fibrosis and the inflammatory response. Further, we sought to determine whether gender alters the severity of the development of these features of CKD in this model.

## 2. Methods and Materials

**2.1. Model of CKD in C57BL/6 Mice.** Ten-week-old mice (gender-balanced groups) underwent uninephrectomy (Unx) or a sham uninephrectomy under isoflurane/oxygen anaesthesia 2 weeks before the start of the experiment and were allowed to recover (Figure 1). The Unx mice were then given 1% sodium chloride in the drinking water and received DOCA pellet implants and Ang II infusion using osmotic minipumps. Model 1004 ALZET osmotic infusion pumps (Durect) containing Ang II in sterile water were subcutaneously implanted in the back of the necks of mice under isoflurane/oxygen anaesthesia to deliver a dose of 1.5 ng Ang II (Sigma) per minute per gram body weight. At this time, a 50 mg 21-day release DOCA pellet (Innovative Research of America, M-121) was also implanted subcutaneously. Mice that underwent the sham Unx were also treated with a sham procedure for subcutaneous implantation. All mice were sacrificed on day 21 after implantation. This animal utilization and the described procedures were approved by the McMaster University Research Ethics Board.

**2.2. Blood Pressure Measurements.** Blood pressure measurements were obtained with tail cuff plethysmography using a CODA (Kent Scientific) blood pressure analyzer before Ang II/DOCA implantation and also before sacrifice (Figure 1). Briefly, animals were placed in restraint and positioned on a heating pad with a tail cuff attached to the machine. The cuff then measured systolic blood pressure, diastolic blood pressure and heart rate.

**2.3. Urinalysis, Metabolic Cages, and Microalbumin ELISA.** Before the surgical procedure and after 3 weeks on treatment with AngII/DOCA salt, mice were placed in metabolic cages for 24 h urine collection (Figure 1). Urine samples were sent to our in-house laboratory to evaluate total protein concentrations and an ELISA was used to measure mouse urine albumin concentration (BETHYL Laboratories) to determine hypertension-induced proteinuria.

**2.4. Tissue Preparation for Histological Assessment and Immunohistochemical Analysis of Protein Cast Formation, Renal Interstitial Fibrosis, Apoptosis, and Glomerular Sclerosis.** Renal tissue was prepared for histological analysis. The tissue was fixed in 4% paraformaldehyde upon sacrificing the animal. The tissue was then embedded in paraffin blocks and sectioned (4  $\mu$ m) using a microtome. To assess protein cast

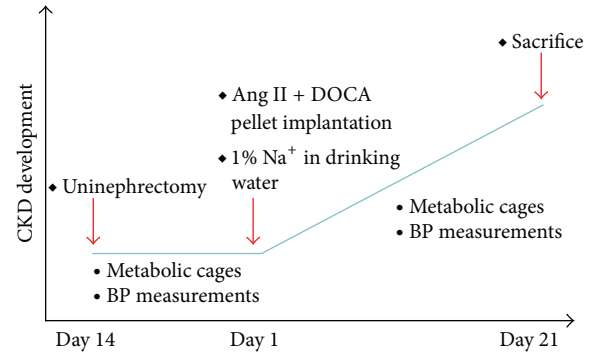


FIGURE 1: Ang II/DOCA salt model of chronic kidney disease in the C57BL/6 mouse. Graph describing the time course of CKD development.

formation and glomerular injury score, these tissues were stained with Periodic Acid Schiff (PAS) stain and imaged using a light microscope (Olympus).

Collagen deposition indicating extracellular matrix accumulation and renal interstitial fibrosis was evaluated using Masson's trichrome stain (Sigma-Aldrich).

To assess apoptosis, kidney sections were stained using the protocol and reagents provided by the TACS 2 TdT-Fluor *In Situ* Apoptosis Detection Kit (Trevigen, Cat # 4812-30-K). This method is based on specific binding of TdT to 3'-OH ends of DNA and the incorporation of biotinylated deoxyuridine at sites of DNA breaks. This signal is then amplified by avidin-peroxidase, allowing apoptotic cells where DNA fragmentation has occurred, to be visualized with light microscopy [11].

The sections were analyzed using an Olympus BX41 microscope. Immunohistochemistry sections were imaged with 20x and 40x objective lens. For the quantification of protein cast formation, apoptosis, and F4/80 staining, ten microscopic fields were randomly sampled in each of the cortex and the medulla. To score glomeruli, ten microscopic fields were randomly sampled from the cortex allowing the scoring of approximately 50 glomeruli per animal. Images were analyzed for protein cast formation using the MetaMorph program to select and quantify PAS-stained areas as a percentage of the total area of each image. The average of protein cast area density was then calculated for each animal. TUNEL-stained sections were processed using the cell count tool in Image J software. Glomerular sclerosis was assessed based on the scale and method used in a previous study [12].

Lungs from AngII/DOCA salt and sham mice were extracted without performing a bronchoalveolar lavage procedure and fixed in 4% paraformaldehyde for 24 hours. After standard paraffin embedding, 4  $\mu$ m thick specimens were sectioned and stained with H&E stain to visualize lung damage. Mouse hearts were weighed upon sacrifice and this parameter was normalized to body weight in grams to provide a measure of increase in cardiac mass. The hearts were then fixed in 4% paraformaldehyde for 24 hours, embedded in paraffin, sectioned, and stained with PAS to evaluate areas of hypertrophy.

**2.5. Statistical Analysis.** Statistical analysis was performed using GraphPad Prism software. *t*-tests were used to compare data between groups and significance is denoted by  $P < 0.05$ . Bar graphs show group averages and standard error of the mean as error bars.

### 3. Results

**3.1. Development of Hypertensive Proteinuria in Ang II/DOCA Salt Model.** Blood pressure measurements were taken using tail cuff measurements before the subcutaneous implantation of the osmotic pump containing Ang II and the DOCA pellet as well as at the end of the model before sacrificing the mice. Ang II/DOCA salt mice experienced a significant increase in systolic (Figure 2(a);  $P < 0.001$ ,  $N = 14$ ) and diastolic blood pressure (Figure 2(b);  $P < 0.001$ ,  $N = 14$ ) 21 days after implantation. Ang II/DOCA salt mice also had significantly higher systolic ( $P < 0.001$ ,  $N = 14$ ) and diastolic ( $P < 0.001$ ,  $N = 14$ ) blood pressure compared to sham operated controls 21 days after implantation. This hypertensive response was accompanied by an increase in total protein (Figure 2(c)) and albumin (Figure 2(d)) excreted in the urine over 24 h. Ang II/DOCA salt mice experienced significantly higher total protein ( $P = 0.009$ ,  $N = 14$ ) and total albumin ( $P < 0.001$ ,  $N = 14$ ) in 24 h urine compared to measurements obtained before implantation. Total 24 h urine protein ( $P = 0.006$ ,  $N = 14$ ) and albumin ( $P < 0.001$ ,  $N = 14$ ) were also significantly higher with Ang II/DOCA salt treatment compared to sham controls. In order to assess CKD progression in this model, the time course of the evolution of proteinuria was followed at days 0, 7, 14, 18, and 21 after Ang II/DOCA salt treatment. Proteinuria was significantly elevated at days 18 and 21 (Figure 2(e)).

**3.2. Characteristics of Renal Tissue Damage in Response to Ang II/DOCA Salt Treatment.** The proteinuria data was consistent with the immunohistological analysis of PAS-stained kidney sections showing the percentage of protein cast formation as compared to sham controls (Figure 3(a)). Kidneys from Ang II/DOCA salt mice showed a significantly higher percentage of protein cast formation as compared to sham controls. PAS staining images show increased protein cast formation in renal tubules of the cortex ( $P = 0.003$ ,  $N = 14$ ) and medulla ( $P = 0.01$ ,  $N = 14$ ) in Ang II/DOCA salt mice compared to sham controls (Figure 3(b)). Higher magnification images of PAS staining showed increased glomerular sclerosis in the cortex of Ang II/DOCA salt mice compared to sham mice as indicated by the arrows (Figure 3(c)). Quantification of glomerular sclerosis by two independent assessors utilizing the method of Rajj et al. [12] indicated that the Ang II/DOCA salt mice displayed significantly elevated glomerular sclerosis scores ( $P < 0.001$ ,  $N = 10$ ) compared to age-matched sham operated controls (Figure 3(d)).

In order to assess renal cell loss, we performed TUNEL staining. TUNEL staining images demonstrated increased apoptosis (Figure 3(e), arrows) in kidney micrographs of Ang II/DOCA salt mice compared to sham animals (Figure 3(f);  $P < 0.001$ ,  $N = 10$ ). Immunohistochemical staining for F4/80, a highly specific macrophage cell surface marker

[13], demonstrated a significant increase in macrophage infiltration density (Figure 3(g)) in response to Ang II/DOCA salt treatment compared to sham controls (Figure 3(h);  $P = 0.02$ ,  $N = 5$ ). To examine renal interstitial fibrosis, we stained kidney sections with Masson's trichrome stain. Indeed, in our Ang II/DOCA salt model, we saw increased collagen deposition as indicated by blue-stained fibres in the renal interstitium of areas showing kidney damage in the Ang II/DOCA salt mice compared to sham controls (Figure 3(i)).

**3.3. Impact of CKD on Cardiac and Lung Function and Morphology.** Microscope images of heart cross-section portrayed right and left ventricle hypertrophy in response to Ang II/DOCA salt treatment (Figure 4(a)). Cardiac muscle hypertrophy is an adaptation to fluid retention and hypervolemia resulting from the model. This phenomenon is confirmed by the increase in heart weights (mg/g of body weight) ( $P < 0.001$ ,  $N = 14$ ) observed in mice treated with Ang II/DOCA salt compared to sham controls (Figure 4(b)). Lung sections derived from Ang II/DOCA salt mice showed features of pulmonary edema, inflammatory infiltrates, and thickening of the alveoli. Signs of increased vessel thickness and capillaries congested with red blood cells are also observed (Figure 4(c)). Although further characterization is required, it is likely that the observed pulmonary changes are driven by sodium retention and the severe hypervolemic changes observed in this model.

**3.4. Impact of Gender on Renal Tissue Damage Induced by Ang II/DOCA Salt Model.** Both male ( $P = 0.02$ ,  $N = 7$ ) and female ( $P = 0.04$ ,  $N = 7$ ) Ang II/DOCA salt mice developed proteinuria compared to their respective sham controls as a result of the CKD model. However, male Ang II/DOCA salt mice showed significantly higher total protein in 24 h urine ( $P = 0.04$ ,  $N = 7$ ) compared to female Ang II/DOCA salt mice (Figure 5(a)). Total 24 h urine albumin measurements showed a similar trend where male Ang II/DOCA salt mice ( $P < 0.001$ ,  $N = 6$ ) experience a higher level of albumin in the urine compared to their sham controls and compared to female Ang II/DOCA salt mice ( $P = 0.03$ ,  $N = 6$ ). Although female Ang II/DOCA salt mice had a higher albumin level in 24 h urine ( $P = 0.11$ ,  $N = 6$ ) than their sham controls, this increase was not significant (Figure 5(b)). Protein cast formation was significantly higher in the cortex ( $P = 0.02$ ,  $N = 7$ ) and medulla ( $P = 0.04$ ,  $N = 7$ ) of Ang II/DOCA salt male mice and in the cortex ( $P = 0.004$ ,  $N = 7$ ) and medulla ( $P = 0.01$ ,  $N = 7$ ) of Ang II/DOCA salt female mice compared to their respective sham controls. The percentage of PAS-stained area was higher in the cortex ( $P = 0.048$ ,  $N = 7$ ) and medulla ( $P = 0.145$ ,  $N = 7$ ) of male mice treated with Ang II/DOCA salt compared to female mice treated with Ang II/DOCA salt (Figure 5(c)). TUNEL staining was used to assess the influence of gender on kidney cell death and, ultimately, nephron loss. Although female Ang II/DOCA salt mice experienced an increase in apoptosis ( $P = 0.03$ ,  $N = 5$ ) compared to female sham controls, the apoptosis observed in male mice treated with Ang II/DOCA salt was significantly higher ( $P = 0.002$ ,  $N = 5$ ) compared to Ang II/DOCA salt treated females (Figure 5(d)). In addition, Masson's trichrome

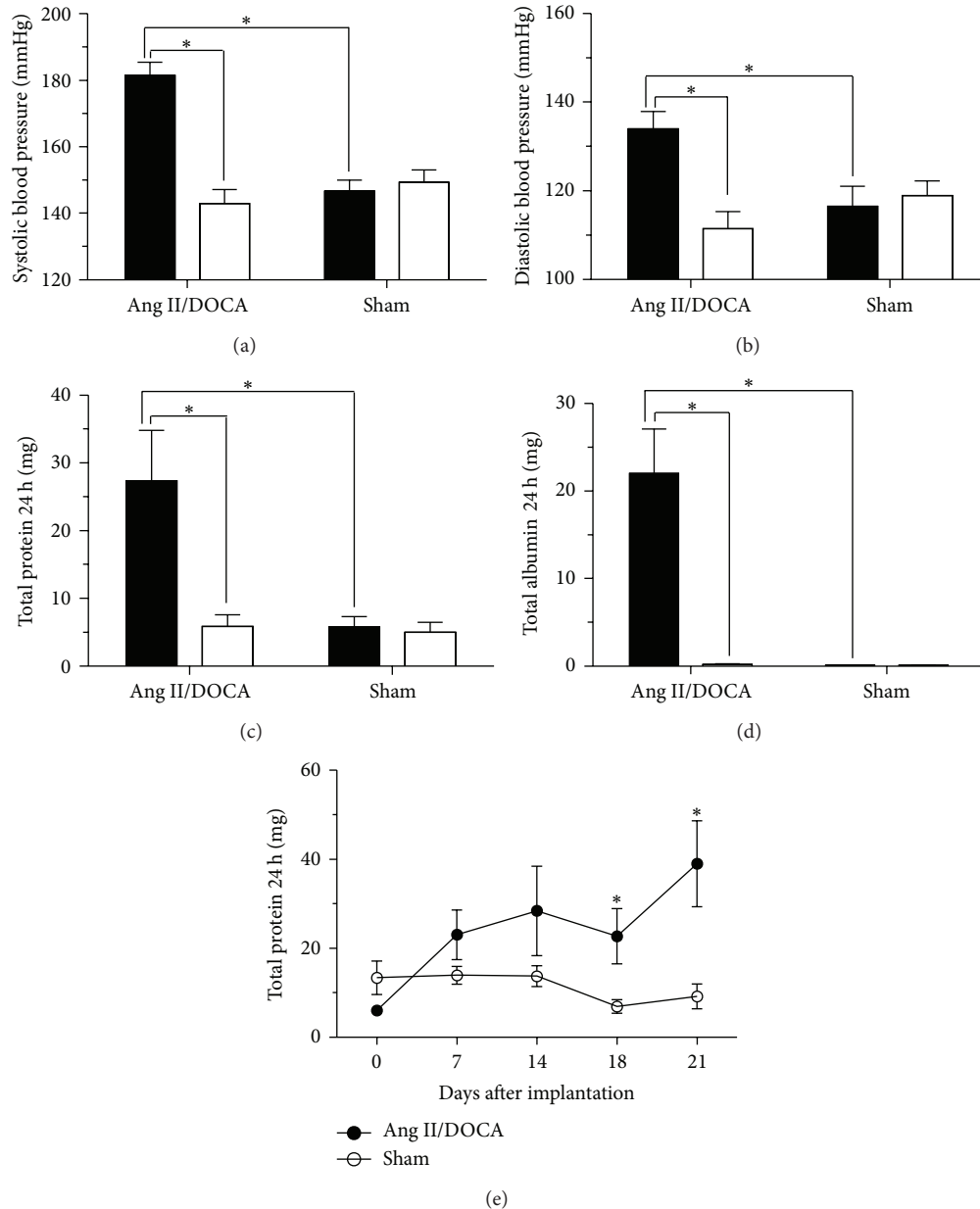


FIGURE 2: Development of hypertensive proteinuria in Ang II/DOCA salt model of CKD in the C57BL/6 mouse. For all graphs, \* indicates a significant difference between two groups where  $P < 0.05$ . For (a)–(d), □ signifies pretreatment, whereas ■ signifies 21-day posttreatment with Ang II/DOCA. (a), (b) Changes in systolic and diastolic blood pressure in response to Ang II/DOCA. (c), (d) Total 24 h urinary protein and albumin excretion with Ang II/DOCA treatment. (e) Time-course development of proteinuria, expressed as total 24-hour protein excretion at days 7, 14, 18, and 21 posttreatment with Ang II/DOCA.

staining showed a higher level of collagen deposition and renal interstitial fibrosis (indicated by blue staining) in male Ang II/DOCA salt mice compared to female Ang II/DOCA salt mice (Figure 5(e)).

#### 4. Discussion

CKD is characterized by reduction in glomerular filtration rate (GFR), albuminuria, and structural or functional abnormalities of the kidney [14]. CKD is increasing in prevalence globally and its comorbidities include cardiovascular disease,

increased all-cause and cardiovascular mortality, kidney disease progression to end stage renal disease (ESRD), and acute kidney injury [15, 16]. The financial impact of CKD places a large burden on health care systems with high costs associated with renal replacement therapy, dialysis, and cardiovascular complications [15]. The C57BL/6 mouse has been the most preferred strain for the generation of transgenic and knockout animal models and will be utilized to develop a genome-wide panel of knockout animals to characterize gene function [2]. The Ang II/DOCA salt model described here shows a robust CKD response that closely

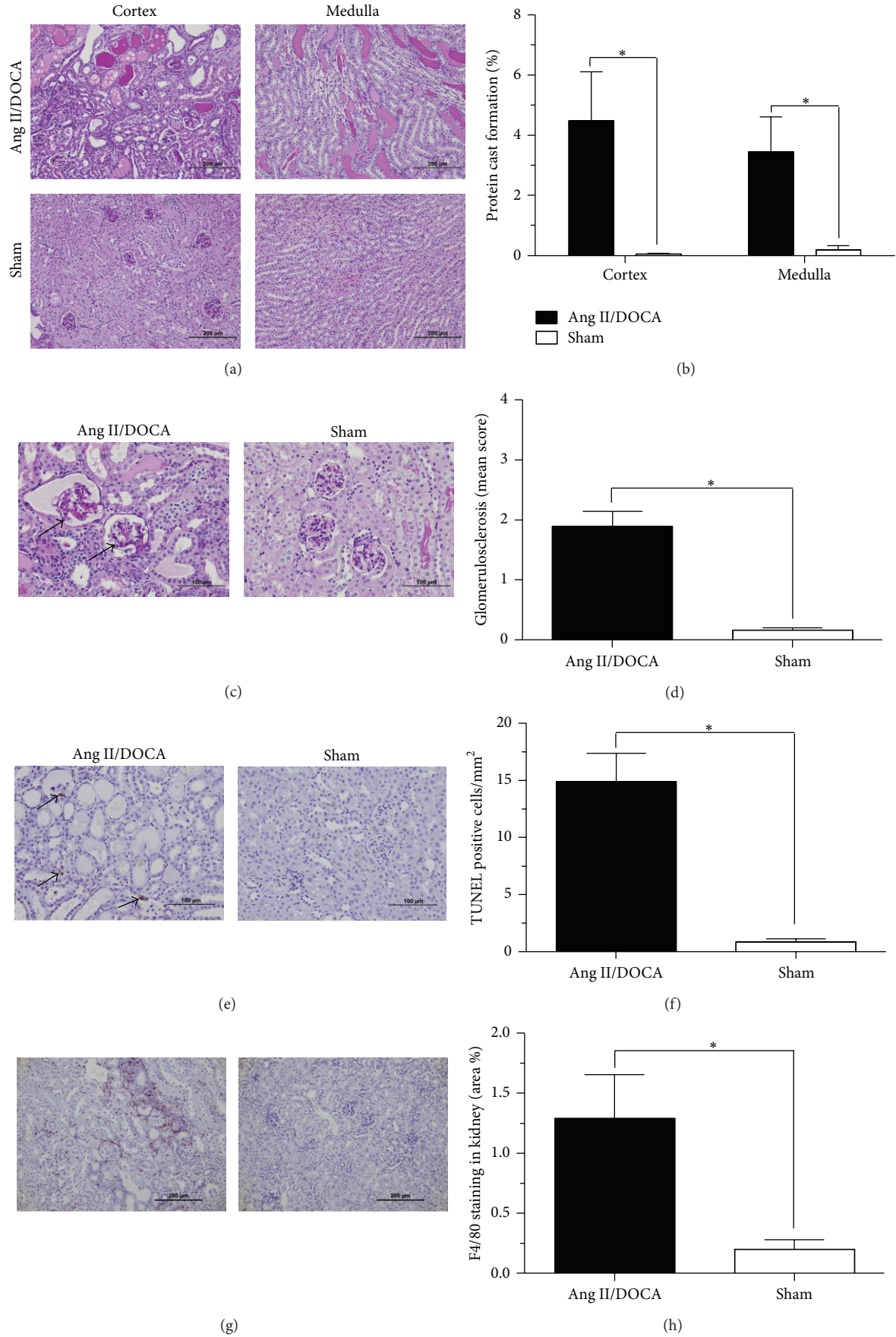
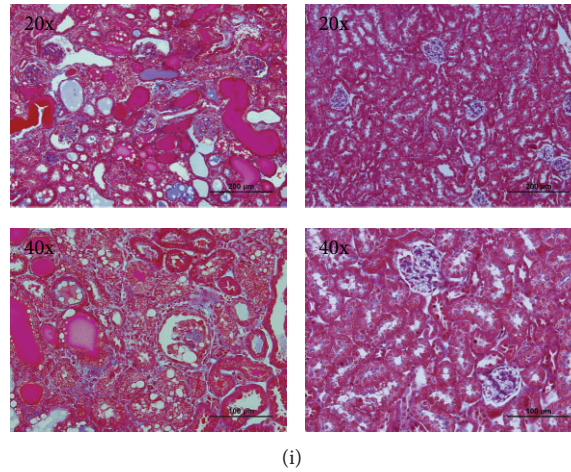
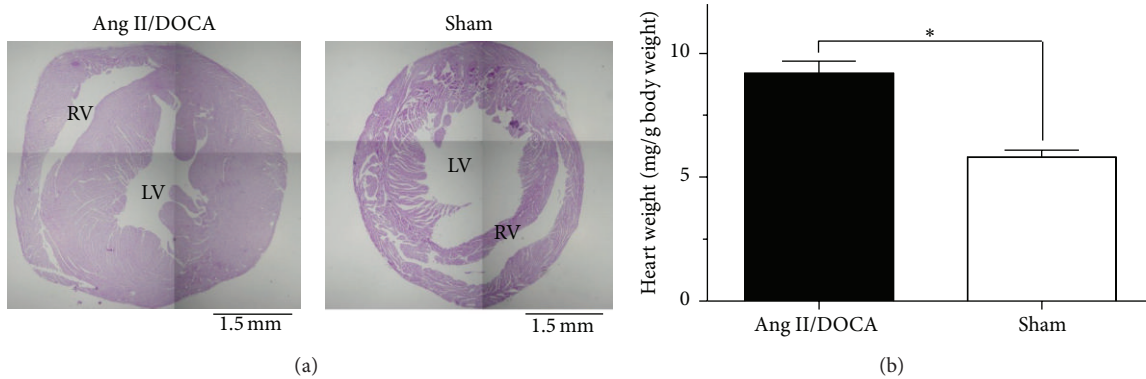


FIGURE 3: Continued.



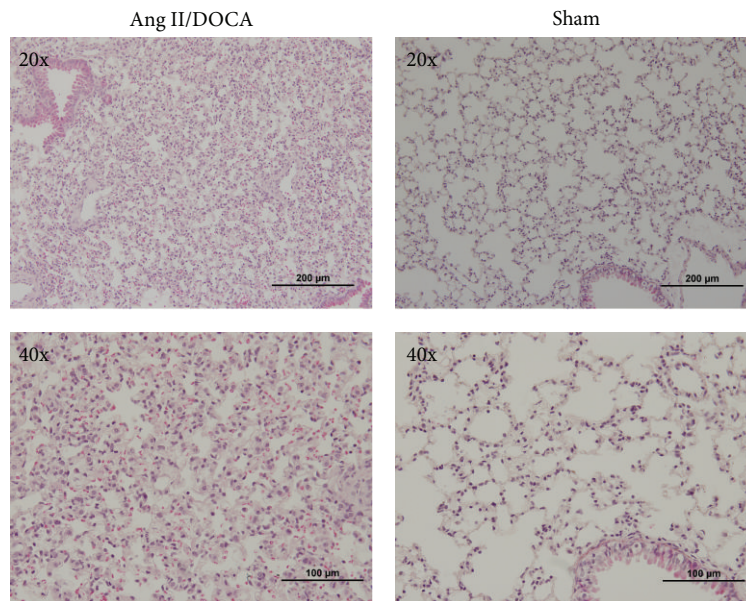
(i)

FIGURE 3: Renal tissue damage in response to Ang II/DOCA salt CKD mouse model. For all graphs, \* indicates a significant difference between two groups where  $P < 0.05$ . Effect of Ang II/DOCA salt model on (a), (b) protein cast formation in the cortex and medulla, (c), (d) glomerulosclerosis, (e), (f) apoptosis, (g), (h) macrophage (F4/80+ cells) infiltration, and (i) interstitial fibrosis (Masson's trichrome staining).



(a)

(b)



(c)

FIGURE 4: Effect of Ang II/DOCA salt model on cardiac and lung tissue. (a) Images of heart cross-section cardiac hypertrophy in Ang II/DOCA salt model. (b) Graph showing increase in heart weights (mg/g of body weight) in response to Ang II/DOCA where \* indicates a significant difference between two groups ( $P < 0.05$ ). (c) Lung damage (20x, 40x) in response to Ang II/DOCA compared to SHAM controls.

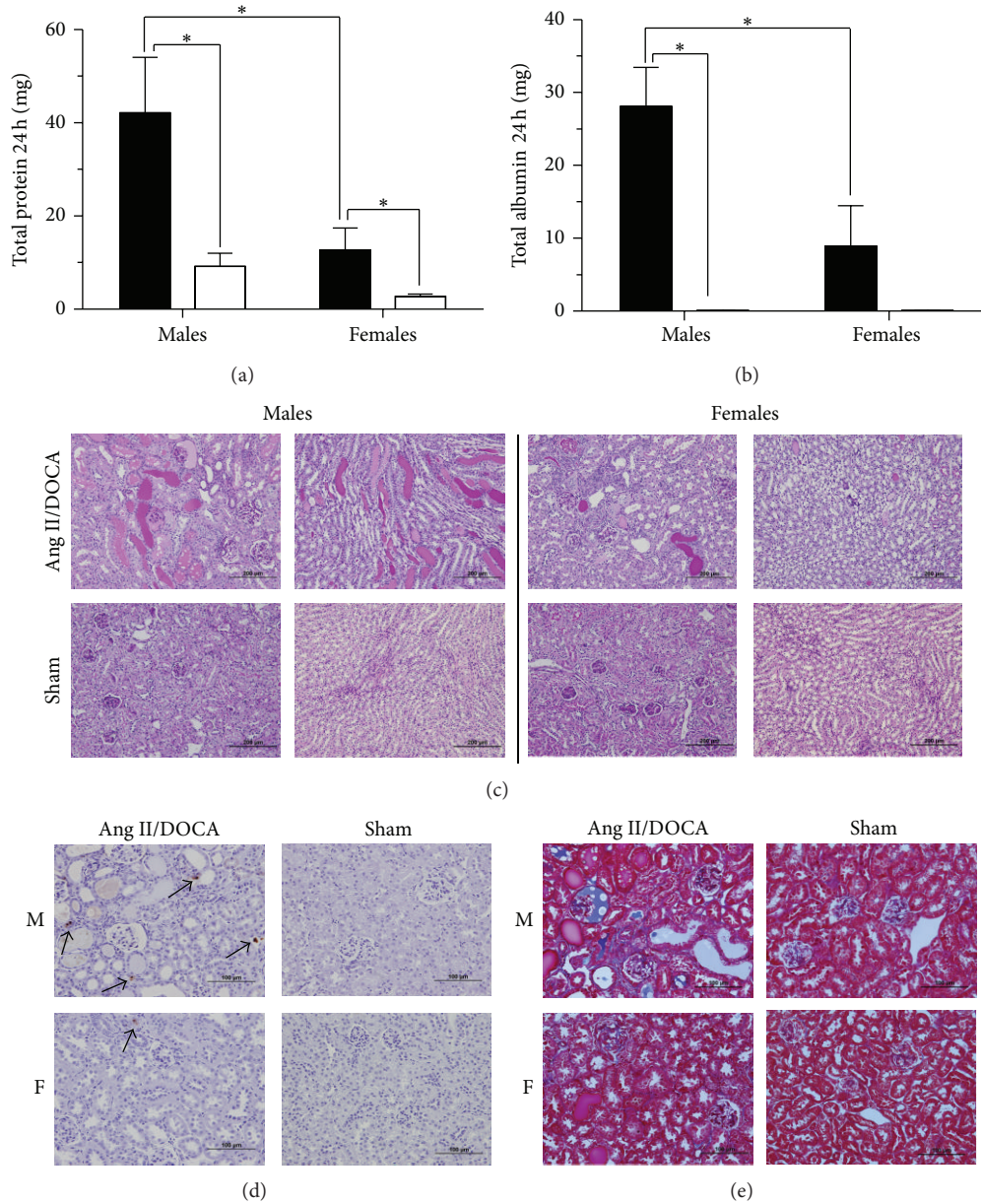


FIGURE 5: Impact of gender on CKD induced by Ang II/DOCA salt model. For all graphs, \* indicates a significant difference between two groups where  $P < 0.05$ . Ang II/DOCA salt is denoted by ■, whereas □ denotes SHAM operated controls. "M" and "F" indicate sections from male and female mouse kidneys, respectively. Influence of gender on the development of (a) proteinuria, (b) albuminuria, (c) protein cast formation, (d) apoptosis, and (e) interstitial fibrosis.

mimics human CKD. Developing this model allows the use of genetically modified mice in order to identify gene targets that play a role in CKD development and progression.

Similar to the description of the model provided by Kirchoff et al. [6], we found systolic blood pressure to be elevated; additionally, we determined that diastolic blood pressure was also elevated. We present data for the total 24-hour excretion of both protein and albumin in the urine, demonstrating that the Ang II/DOCA salt model induced significant proteinuria and albuminuria. This finding is similar to the increase in albuminuria/creatinine ratio described by Kirchoff et al. [6]. Further, we show the evolution of proteinuria in the

model at days 0, 7, 14, 18, and 21 where we observe a statistically significant increase in proteinuria at day 18 and day 21. We also demonstrated that protein cast formation and glomerular sclerosis were significantly increased in the model, similar to findings by Kirchoff et al. [6]. We further investigated renal injury by examining apoptosis through TUNEL staining and found it to be significantly elevated. Additionally, the kidneys were found to have a significant infiltration of macrophages and showed renal interstitial fibrosis through trichrome staining. Similar to Kirchoff et al. [6], we found end-organ damage in the heart characterized by cardiac hypertrophy. We extended these findings to examine

the lung, where we noted an edematous effusion in airspaces. Further, we characterized the model for gender differences and found that the female gender imparted protection from proteinuria, albuminuria, protein cast formation, apoptosis and renal interstitial fibrosis.

Hypertensive proteinuria is a common feature of CKD. Therefore, animal models that display this feature have been used to investigate disease-specific mechanisms, molecular pathogenesis and potential therapies [1]. The increased glomerular permeability during hypertensive CKD allows protein hyperfiltration into the proximal tubules causing renal tissue damage. Filtered albumin and other proteins that accumulate within intracellular compartments of proximal tubular cells perturb cell function by several mechanisms [17]. Hypertension is an important contributor to ESRD [18]. Proteinuria is associated with glomerular damage and podocyte depletion [19] and can be used in the classification of different stages of CKD clinically [20]. The Ang II/DOCA salt model displays hypertensive proteinuria that mirrors human CKD, as demonstrated by a significant increase in systolic and diastolic blood pressure, as well as proteinuria and albuminuria. Overt proteinuria evolved later in this model at days 18 and 21, indicating disease progression in response to glomerular injury. The glomerulosclerosis seen in our model involves inflammation and fibrosis around the area of the damaged glomeruli and could potentially result in tubular atrophy and degeneration [19]. Tubulointerstitial injury caused by proteinuria includes the formation of protein casts that may block the tubular lumen [19] and this phenomenon has been shown in our model.

As CKD progresses tubular cell atrophy results primarily due to apoptosis. An increase in apoptosis has been demonstrated using TUNEL staining on kidney sections from diabetic nephropathy patients [21] and from rats in the streptozotocin-induced diabetic nephropathy model [22]. In addition, apoptotic nuclei have been observed in polycystic human kidneys and kidney sections from mouse models of the disease [23]. The loss of renal tubular epithelial cells through apoptosis occurs in both acute and chronic kidney diseases [24]. Apoptotic cell loss from nephron segments leads to tubular atrophy and their loss eventually leads to a decline in GFR. Since the Ang II/DOCA salt model displays a robust apoptotic response, it could be used in identifying therapeutic targets against apoptosis that are able to halt CKD progression [24].

Macrophage infiltration has been studied as a universal feature of tubulointerstitial damage regardless of disease origin [25, 26] and is a key feature of experimental and human kidney disease models [26, 27]. Macrophages have been shown to release cytotoxic moieties such as proteolytic enzymes, reactive oxygen, and nitrogen species, as well as proinflammatory cytokines and chemokines [28]. By expressing cytokines such as TGF- $\beta$  and connective tissue growth factor, macrophages are able to induce myofibroblast differentiation and extra cellular matrix deposition, key processes in renal interstitial fibrosis [29, 30]. Increased macrophage infiltration is associated with glomerulosclerosis and tubulointerstitial fibrosis [27, 31, 32]. Both macrophage infiltration and renal interstitial fibrosis have been demonstrated in the

Ang II/DOCA salt model of CKD. Further studies would be focused on the time course of the development of these phenomena in order to establish pathways that lead to CKD progression.

CKD, through its effects on volume overload, plays an important pathophysiological role in multiple organ failure. The effect of volume overload on the heart is to develop cardiac hypertrophy through myocardial stretch. This effect is reflected in our model. As hypertrophy progresses from compensated to decompensated heart failure, volume overload affects the lungs and results in pulmonary edema [33]. This phenomenon is also reflected in our model.

The findings that Ang II/DOCA salt mice show a gender-based difference in severity of CKD are consistent with findings in the human population [34] and in agreement with previous clinical and experimental studies on the protective effect of female gender on the development of renal diseases [35–38]. Female mice, subjected to this model, show significantly lower levels of proteinuria. Ang II/DOCA salt female mice also experienced a trend for decreased protein cast formation and collagen deposition, thereby indicating a lower level of renal tissue damage compared to Ang II/DOCA salt male mice. A recent study identified gender difference as a modifier of susceptibility to ER stress-induced injury in tunicamycin-treated mice, a model of acute kidney injury, showing reduced renal pathology in female mice [39]. The reduced induction of apoptosis in female Ang II/DOCA salt mice in our CKD model is therefore in agreement with *in vivo* experiments of endoplasmic reticulum stress-induced acute kidney injury in the tunicamycin mouse models [39].

Clinical studies have demonstrated an association between male gender and a faster rate of CKD progression [36]. Interestingly, the impact of gender is restricted to premenopausal women and is, therefore, thought to be an estradiol-mediated protective effect [35]. This finding is supported by experimental studies. Aged male rats have been shown to develop decreased GFR, increased glomerular injury, and increased proteinuria earlier than female rats [37]. In addition, estradiol treatment caused a reduction in glomerulosclerosis, expression of adhesion, and extracellular matrix molecules and prevented tubular damage in animal models of unilateral nephrectomy and chronic renal allograft rejection [38, 40]. These studies indicate a renoprotective role for estradiol and although our experiments show that female gender imparts a protective effect on CKD development, the potential role of estradiol is still to be determined.

In conclusion, the Ang II/DOCA salt model produces a significant degree of CKD that mimics progressive human CKD in the C57BL/6 mouse. This pathology includes proteinuria, intertubular protein casts, renal interstitial fibrosis, and tubular epithelial cell apoptosis. As this model recapitulates many of the aspects of pathology found in human CKD [41], it will be of great utility to determine the specific effect of various candidate genes on CKD severity and progression. Further, a gender effect was observed where female mice showed lower proteinuria and apoptosis in the CKD model. Future work in this model may allow the precise molecular nature of the protective effect of the female gender to be determined.

## Conflict of Interests

The authors declare that there is no conflict of interests regarding publication of this paper.

## Acknowledgments

This work was supported by research grants to Jeffrey G. Dickhout from the Canadian Institutes of Health Research (OSO-115895 and MOP-133484). Financial support from St. Joseph's Healthcare Hamilton is also acknowledged. Jeffrey G. Dickhout also acknowledges salary support from St. Joseph's Healthcare Hamilton and holds a McMaster University, Department of Medicine Internal Career Research Award. Support from the Division of Nephrology at the Department of Medicine at McMaster University is also acknowledged. Dr. Jeffrey G. Dickhout also holds a Kidney Foundation of Canada, Krescent New Investigator Award.

## References

- [1] H.-C. Yang, Y. Zuo, and A. B. Fogo, "Models of chronic kidney disease," *Drug Discovery Today: Disease Models*, vol. 7, no. 1-2, pp. 13-19, 2010.
- [2] W. C. Skarnes, B. Rosen, A. P. West et al., "A conditional knockout resource for the genome-wide study of mouse gene function," *Nature*, vol. 474, no. 7351, pp. 337-344, 2011.
- [3] F. Zheng, G. E. Striker, C. Esposito, E. Lupia, and L. J. Striker, "Strain differences rather than hyperglycemia determine the severity of glomerulosclerosis in mice," *Kidney International*, vol. 54, no. 6, pp. 1999-2007, 1998.
- [4] N. Kato, Y. Watanabe, Y. Ohno et al., "Mapping quantitative trait loci for proteinuria-induced renal collagen deposition," *Kidney International*, vol. 73, no. 9, pp. 1017-1023, 2008.
- [5] A. El-Meanawy, J. R. Schelling, S. K. Iyengar et al., "Identification of nephropathy candidate genes by comparing sclerosis-prone and sclerosis-resistant mouse strain kidney transcriptomes," *BMC Nephrology*, vol. 13, no. 1, article 61, 2012.
- [6] F. Kirchhoff, C. Krebs, U. N. Abdulhag et al., "Rapid development of severe end-organ damage in C57BL/6 mice by combining DOCA salt and angiotensin II," *Kidney International*, vol. 73, no. 5, pp. 643-650, 2008.
- [7] D. L. Longo, D. L. Kasper, J. L. Jameson, A. S. Fauci, S. L. Hauser, and J. Loscalzo, "Clinical and laboratory manifestations of chronic kidney disease and uremia," in *Harrison's Principles of Internal Medicine*, p. 1410, McGraw-Hill, New York, NY, USA, 18th edition, 2012.
- [8] G. Remuzzi and T. Bertani, "Pathophysiology of progressive nephropathies," *The New England Journal of Medicine*, vol. 339, no. 20, pp. 1448-1456, 1998.
- [9] S. A. Atlas, "The renin-angiotensin aldosterone system: pathophysiological role and pharmacologic inhibition," *Journal of Managed Care Pharmacy*, vol. 13, no. 8, supplement B, pp. S9-S20, 2007.
- [10] A. H. Gradman, J. N. Basile, B. L. Carter et al., "Combination therapy in hypertension," *Journal of the American Society of Hypertension*, vol. 4, no. 2, pp. 90-98, 2010.
- [11] Y. Gavrieli, Y. Sherman, and S. A. Ben-Sasson, "Identification of programmed cell death in situ via specific labeling of nuclear DNA fragmentation," *Journal of Cell Biology*, vol. 119, no. 3, pp. 493-501, 1992.
- [12] L. Raij, S. Azar, and W. Keane, "Mesangial immune injury, hypertension, and progressive glomerular damage in Dahl rats," *Kidney International*, vol. 26, no. 2, pp. 137-143, 1984.
- [13] J. M. Austyn and S. Gordon, "F4/80, a monoclonal antibody directed specifically against the mouse macrophage," *European Journal of Immunology*, vol. 11, no. 10, pp. 805-815, 1981.
- [14] A. S. Levey, K.-U. Eckardt, Y. Tsukamoto et al., "Definition and classification of chronic kidney disease: a position statement from kidney disease: improving global outcomes (KDIGO)," *Kidney International*, vol. 67, no. 6, pp. 2089-2100, 2005.
- [15] M. Kerr, B. Bray, J. Medcalf, D. J. O'Donoghue, and B. Matthews, "Estimating the financial cost of chronic kidney disease to the NHS in England," *Nephrology Dialysis Transplantation*, vol. 27, supplement 3, pp. iii73-iii80, 2012.
- [16] V. Jha, G. Garcia-Garcia, K. Iseki et al., "Chronic kidney disease: global dimension and perspectives," *The Lancet*, vol. 382, no. 9888, pp. 260-272, 2013.
- [17] G. Remuzzi, N. Perico, M. Macia, and P. Ruggenenti, "The role of renin-angiotensin-aldosterone system in the progression of chronic kidney disease," *Kidney International*, no. 99, pp. S57-S65, 2005.
- [18] J. M. Turner, C. Bauer, M. K. Abramowitz, M. L. Melamed, and T. H. Hostetter, "Treatment of chronic kidney disease," *Kidney International*, vol. 81, no. 4, pp. 351-362, 2012.
- [19] K. S. Hodgkins and H. W. Schnaper, "Tubulointerstitial injury and the progression of chronic kidney disease," *Pediatric Nephrology*, vol. 27, no. 6, pp. 901-909, 2012.
- [20] A. S. Levey and J. Coresh, "Chronic kidney disease," *The Lancet*, vol. 379, no. 9811, pp. 165-180, 2012.
- [21] D. Kumar, S. Robertson, and K. D. Burns, "Evidence of apoptosis in human diabetic kidney," *Molecular and Cellular Biochemistry*, vol. 259, no. 1-2, pp. 67-70, 2004.
- [22] G. Liu, Y. Sun, Z. Li et al., "Apoptosis induced by endoplasmic reticulum stress involved in diabetic kidney disease," *Biochemical and Biophysical Research Communications*, vol. 370, no. 4, pp. 651-656, 2008.
- [23] D. Woo, "Apoptosis and loss of renal tissue in polycystic kidney diseases," *The New England Journal of Medicine*, vol. 333, no. 1, pp. 18-25, 1995.
- [24] A. B. Sanz, B. Santamaría, M. Ruiz-Ortega, J. Egido, and A. Ortiz, "Mechanisms of renal apoptosis in health and disease," *Journal of the American Society of Nephrology*, vol. 19, no. 9, pp. 1634-1642, 2008.
- [25] K. A. Nath, "The tubulointerstitium in progressive renal disease," *Kidney International*, vol. 54, no. 3, pp. 992-994, 1998.
- [26] K. S. Eardley and P. Cockwell, "Macrophages and progressive tubulointerstitial disease," *Kidney International*, vol. 68, no. 2, pp. 437-455, 2005.
- [27] Y. Wang and D. C. H. Harris, "Macrophages in renal disease," *Journal of the American Society of Nephrology*, vol. 22, no. 1, pp. 21-27, 2011.
- [28] B. Rodríguez-Iturbe, H. Pons, J. Herrera-Acosta, and R. J. Johnson, "Role of immunocompetent cells in nonimmune renal diseases," *Kidney International*, vol. 59, no. 5, pp. 1626-1640, 2001.
- [29] Y. Liu, "Renal fibrosis: new insights into the pathogenesis and therapeutics," *Kidney International*, vol. 69, no. 2, pp. 213-217, 2006.
- [30] F. M. Strutz, "EMT and proteinuria as progression factors," *Kidney International*, vol. 75, no. 5, pp. 475-481, 2009.

- [31] J. S. Duffield, "Macrophages and immunologic inflammation of the kidney," *Seminars in Nephrology*, vol. 30, no. 3, pp. 234–254, 2010.
- [32] A. B. Fogo, "Mechanisms of progression of chronic kidney disease," *Pediatric Nephrology*, vol. 22, no. 12, pp. 2011–2022, 2007.
- [33] N. Aspromonte, D. N. Cruz, C. Ronco, and R. Valle, "Role of bioimpedance vectorial analysis in cardio-renal syndromes," *Seminars in Nephrology*, vol. 32, no. 1, pp. 93–99, 2012.
- [34] W. L. Lee, M. H. Cheng, D. C. Tarng, W. C. Yang, F. K. Lee, and P. H. Wang, "The benefits of estrogen or selective estrogen receptor modulator on kidney and its related disease-chronic kidney disease-mineral and bone disorder: osteoporosis," *Journal of the Chinese Medical Association*, vol. 76, no. 7, pp. 365–371, 2013.
- [35] R. K. Dubey, S. Oparil, B. Imthurn, and E. K. Jackson, "Sex hormones and hypertension," *Cardiovascular Research*, vol. 53, no. 3, pp. 688–708, 2002.
- [36] S. R. Silbiger and J. Neugarten, "The impact of gender on the progression of chronic renal disease," *American Journal of Kidney Diseases*, vol. 25, no. 4, pp. 515–533, 1995.
- [37] C. Baylis, "Age-dependent glomerular damage in the rat. Dissociation between glomerular injury and both glomerular hypertension and hypertrophy. Male gender as a primary risk factor," *The Journal of Clinical Investigation*, vol. 94, no. 5, pp. 1823–1829, 1994.
- [38] S. E. Mulroney, C. Woda, M. Johnson, and C. Pesce, "Gender differences in renal growth and function after uninephrectomy in adult rats," *Kidney International*, vol. 56, no. 3, pp. 944–953, 1999.
- [39] R. Hodeify, J. Megyesi, A. Tarcsfalvi, H. I. Mustafa, N. S. Hti Lar Seng, and P. M. Price, "Gender differences control the susceptibility to ER stress-induced acute kidney injury," *The American Journal of Physiology—Renal Physiology*, vol. 304, no. 7, pp. F875–F882, 2013.
- [40] V. Müller, A. Szabó, O. Viklicky et al., "Sex hormones and gender-related differences: their influence on chronic renal allograft rejection," *Kidney International*, vol. 55, no. 5, pp. 2011–2020, 1999.
- [41] W. Metcalfe, "How does early chronic kidney disease progress? A background paper prepared for the UK consensus conference on early chronic kidney disease," *Nephrology Dialysis Transplantation*, vol. 22, supplement 9, pp. ix26–ix30, 2007.

## Review Article

# Animal Models in Cardiovascular Research: Hypertension and Atherosclerosis

Xin-Fang Leong,<sup>1,2</sup> Chun-Yi Ng,<sup>1</sup> and Kamsiah Jaarin<sup>1</sup>

<sup>1</sup>Department of Pharmacology, Universiti Kebangsaan Malaysia Medical Centre, Jalan Yaacob Latif, Bandar Tun Razak, Cheras, 56000 Kuala Lumpur, Malaysia

<sup>2</sup>Department of Clinical Oral Biology, Faculty of Dentistry, Universiti Kebangsaan Malaysia, Jalan Raja Muda Abdul Aziz, 50300 Kuala Lumpur, Malaysia

Correspondence should be addressed to Kamsiah Jaarin; [kamsiah@ukm.edu.my](mailto:kamsiah@ukm.edu.my)

Received 26 September 2014; Revised 17 December 2014; Accepted 14 January 2015

Academic Editor: Andrea Vecchione

Copyright © 2015 Xin-Fang Leong et al. This is an open access article distributed under the Creative Commons Attribution License, which permits unrestricted use, distribution, and reproduction in any medium, provided the original work is properly cited.

Hypertension and atherosclerosis are among the most common causes of mortality in both developed and developing countries. Experimental animal models of hypertension and atherosclerosis have become a valuable tool for providing information on etiology, pathophysiology, and complications of the disease and on the efficacy and mechanism of action of various drugs and compounds used in treatment. An animal model has been developed to study hypertension and atherosclerosis for several reasons. Compared to human models, an animal model is easily manageable, as compounding effects of dietary and environmental factors can be controlled. Blood vessels and cardiac tissue samples can be taken for detailed experimental and biomolecular examination. Choice of animal model is often determined by the research aim, as well as financial and technical factors. A thorough understanding of the animal models used and complete analysis must be validated so that the data can be extrapolated to humans. In conclusion, animal models for hypertension and atherosclerosis are invaluable in improving our understanding of cardiovascular disease and developing new pharmacological therapies.

## 1. Introduction

Research animals are valuable tools for understanding the pathophysiology and in developing therapeutic interventions for a disease. These animals are used in basic medical and veterinary research. Various animals have been reported as useful models in studying diseases afflicting humans and animals. Research animals include mice, rats, rabbits, guinea pigs, sheep, goats, cattle, pigs, primates, dogs, cats, birds, fish, and frogs [1]. Concerns have been raised concurrently with the rise of the use of animals over the years. This increase is mainly attributed to the use of genetically altered animals [1]. The similarities and differences between models must be taken into consideration for every project. Careful consideration should be given in choosing the most appropriate animal model to answer the specific research question of the study. With increasing awareness of animal welfare and research ethics, it is important to obtain accurate results using suitable models while reducing wastage of animals used for testing.

Animals are used in biomedical research for the following reasons.

(i) *Feasibility*. Animal models are relatively easy to manage, as compounding effects of dietary intake and environmental factors including temperature and lighting can be controlled. Therefore, there is relatively less environmental variation compared to human studies. Blood vessels and cardiac tissues can be isolated for detailed experimental and biomolecular investigations. Animals typically have a shorter life span than humans. Hence, they make good models, as they can be studied over their whole life cycle or even across several generations [2, 3].

(ii) *Similarities to Human*. Moreover, many animals are suitable due to their similarity in anatomical basis and physiological functions with humans. For example, chimpanzees and mice share about 99% and 98% of DNA with humans, respectively [4, 5]. As a result, animals have the tendency

to be affected by many health problems afflicting humans. Therefore, animals are good models for the study of human diseases.

(iii) *Drug Safety*. Preclinical toxicity testing, pharmacodynamics, and pharmacokinetics profile of drugs may be investigated on animals before the compounds or drugs are used in humans. This is vital, as prior to testing on humans, the effectiveness of a drug as potential treatment needs to be carried out on animals [6]. Interventions for diseases must be identified to eventually develop new medicines beneficial to humans and/or other animals. Drug safety profiles need to be determined in order to protect the animals, human, and environment. Harmful and detrimental effects of a drug need to be tested on a whole organism [6]. This can further ensure the dose to be employed in clinical trials, which do not cause fatality in the subsequent studies. The tested chemicals must also be safe for administration and avoid contaminating water, soil, and air. It is unethical to directly test drugs or chemicals on humans, thus warranting the need to use animals in the research, although this has been an issue debated by animal rights and welfare groups.

Before conducting research on animals, researchers must ensure that animals are essential for their experiments, with no viable alternatives. The use of 3Rs principle relating to animal research has been a practice since first introduced by Russell and Burch in 1959 [7]. The 3Rs refer to replacement, reduction, and refinement. Replacement means conducting experiments using nonanimal models, such as *in vitro* method with cell culture as well as with computer model simulation (*in silico*), whenever possible. Nevertheless, the information obtained from *in vitro* is typically limited when compared to *in vivo* studies. Reduction refers to the need to reduce the number of animals, either from previous studies or by using calculation of size sample with a good experimental design. Refinement refers to efforts to minimize pain and suffering of test animals, taking into consideration animal handling and surgical procedures, housing environment and living conditions, and improvements in animal husbandry. These 3Rs are aimed at providing humane and scientifically improved research involving or avoiding the use of animal models [8]. Guidelines for reporting animal study are available to ensure the justification of using animals, such as the Animals in Research: Reporting In Vivo Experiments (ARRIVE) guidelines [9] and the Gold Standard Publication Checklist (GSPC) [10].

Even though animal studies have contributed much to our understanding of mechanisms of diseases, their value in predicting the effectiveness of treatment strategies in clinical trials has remained controversial [11–13]. Clinical trials are essential, as animal studies do not predict with sufficient certainty what will happen in humans. Hence, the findings from animal studies may not be deemed suitable for extrapolation to humans. A report by Williams et al. [11] suggested that a recurrent failure of interventions to translate the results obtained in animal studies to the clinical settings may be due to the ability to control genetic background in animal studies. Controlling the genetic background produces more consistent results. Additionally, it is possible that some of the

genetic effects of the candidate loci are context-dependent. For example, the specific loci may play a significant role in sex (male versus female) or in age (young versus old) or in people of a specific body mass index or race [12, 13]. Since these characteristics are not usually investigated or analyzed in many of the studies, there is a possibility that the failure to replicate is due to interactions between genes and environmental factors as well as to gene-gene interactions. If there are interactions between environmental risk factors and genotypes, the validity of extrapolation may become complicated [14].

Moreover, this failure may be explained in part by the methodological flaws in animal studies, eventually leading to a systematic bias which might generate incorrect conclusions about efficacy of a drug or a compound [11]. Per Bracken [15], reasons for the failure of animal experiments which may be translated into human trials include poor experimental design, execution, and analysis [16]. Systematic reviews provide information on whether animal studies are being properly carried out and published. However, systematic reviews are not able to resolve all queries regarding the applicability and relevance of animal studies to humans [13]. Selection biases affect how literature is selected and subsequently included in the systematic review, due to the criteria set by the different authors. The objectives of animal experiments are typically to discover new knowledge or make advances in understanding the diseases, instead of predicting the outcomes of human trials. Therefore, data obtained from animal studies may be unsuitable or too diverse for meaningful comparison with and prediction of the results of human trials. Nevertheless, systemic reviews ensure that all animal studies are published regardless of outcome, in order to avoid unnecessary duplication of expensive animal experiments [17]. Furthermore, systematic reviews may improve the quality and translational value of animal research to human trial [18].

## 2. Animal Models for Hypertension

Hypertension is one of the major risk factors for cardiovascular diseases. It has become a major public health issue in most developed and developing countries [19–21]. According to the *Seventh Report of the Joint National Committee on Prevention, Detection, Evaluation and Treatment of High Blood Pressure*, high blood pressure (BP) is defined as systolic blood pressure (SBP) greater than 140 mmHg and/or diastolic blood pressure (DBP) greater than 90 mmHg [22]. Patients with SBP ranging between 120 mmHg and 139 mmHg, or DBP of 80 mmHg to 89 mmHg, are categorized as prehypertensive. They have a higher risk of developing hypertension and therefore require medical intervention [22].

Human essential hypertension is a complex multifactorial disease which is influenced by genetic and environmental factors. Various models of experimental hypertension have been primarily developed to mimic hypertensive responses observed in humans [23]. These models are beneficial in the pharmacological screening of potential antihypertensive drugs, in addition allowing researchers to have a better understanding of the etiology, development, and progression

of hypertension [24]. Since animal models of hypertension are a mimicry of human hypertension, many of these models have been developed using the etiological factors which have been hypothesized to have a contributory role in human hypertension, such as excessive salt intake, hyperactivity of renin-angiotensin-aldosterone system (RAAS), and genetic predisposition [24]. One animal model is insufficient for explaining the antihypertensive effects of a particular drug, because many pathways are involved in the development of BP dysregulation. In another word, several animal models are required to examine particular cardiovascular changes in an effective study [25]. Therefore, it is advisable that each of the studied models explains a unique pathway in the development of hypertension.

Several criteria need to be considered in order to develop an ideal animal model for hypertension. These factors include the feasibility and size of the animals, the reproducibility of the model, the ability to predict the potential antihypertensive properties of a drug, the similarity to human disease (mode of the disease: slow on-set versus acute), and economical, technical, and animal welfare considerations [23, 24]. In the past, dogs were mostly employed as a model to study hypertension. Currently, the preferred animal model is the rat. Along with rats, occasionally mice, monkeys, and pigs are also used as a model for experimental hypertension [26, 27]. These species have not been studied extensively for both practical and financial reasons. In 1963, Okamoto and Aoki introduced an experimental hypertension model without the involvement of physiological, pharmacological, or surgical intervention [28]. This model is known as the spontaneously hypertensive rat (SHR), which is the genetic strain of hypertensive rat. SHR has become the animal of choice for the screening of antihypertensive agents and the cornerstone of medical research in experimental hypertension [29].

Several forms of murine genetic models, including SHR, have become the focus of hypertensive research. The short life span, small size, and relatively low cost of the animals enable the researchers to study the natural history, genetic factors, and pathophysiological changes in hypertension [29]. Other strains have been developed, including the New Zealand strain [30], Milan strain [31], Dahl salt-sensitive strain [32], Sabra strain [33], and Lyon strain [34]. Essential hypertension is the most frequently encountered human type of hypertension. It is also known as primary hypertension, contributing to 95% of incidences. Essential hypertension is associated with genetic influences. Among the many strains of rat models SHR is generally used, even though it represents only a particular type of hypertension [35].

In addition to the genetic type of animal models, renovascular hypertension is a commonly employed model of hypertension. RAAS plays a pivotal role in this form of hypertension [36, 37]. In 1934, Goldblatt et al. developed a hypertension model through partial constriction of the renal artery in dog [38]. This has led to other renal-induced hypertension model using rats, rabbits, sheep, and cats [39]. When the renal artery is ligated or constricted, RAAS and the sympathetic nervous system are activated [40]. Renin is secreted by the kidneys when sympathetic activity is enhanced. Angiotensinogen is converted to angiotensin-I (Ang I) in the presence of renin.

Angiotensin-converting enzyme (ACE) plays a vital role in the regulation of BP via hydrolysis of the inactive form of Ang I to the active form, angiotensin II (Ang II). ACE is mainly located on the surface of the endothelium and epithelium involved in the constriction of blood vessels, subsequently leading to elevation of BP. Ang II is a potent vasoconstrictor and affects cardiovascular homeostasis. Apart from the role in vasoconstriction, Ang II also stimulates the release of aldosterone, further increasing blood volume and BP due to water and salt retention [41].

Nitric oxide (NO) has been demonstrated to be a potent vasodilator, and its release from the endothelium may be triggered by vasoactive substances such as acetylcholine (ACh) [42]. The endothelium preserves its integrity through endothelium-relaxing dependent factor, which is the best to be characterized as NO [43]. Therefore, NO plays an important role in the regulation of BP [44]. The production of NO is catalyzed by nitric oxide synthase (NOS). Deficiency of NOS has led to a reduction in NO synthesis [45, 46]. Impaired NO bioavailability will result in reduced endothelium-dependent vasorelaxation, eventually leading to hypertension. This NO-deficient model can be induced by oral administration of N<sup>ω</sup>-nitro-L-arginine methyl ester (L-NAME) up to eight weeks, resulting in a significant rise in both SBP and DBP, renal and hepatic markers, and inflammatory parameters in male Wistar rats [47]. Often, BP is elevated after four weeks of L-NAME treatment. Long-term administration of NOS inhibitors, such as L-NAME, provides a new form of hypertension with target organ damage. Studies have reported that L-NAME-induced hypertension has been associated with attenuated endothelium-dependent relaxations, cardiac and aortic tissue damage, renal vascular, and glomerular fibrosis [48–50]. Since the etiology of hypertension is different among the various animal models, it is imperative to make a rational choice for a specific model (Table 1). The choice will significantly affect the outcome of the study.

Soriguer et al. [51] conducted a study on cooking oils, reporting that repeatedly oxidized frying oil is an independent risk factor for hypertension. Hence, hypertension is related to the degradation of the dietary frying oil. Previously, adult male Sprague-Dawley rats aged 3 months were administered with 15% weight/weight (w/w) of repeatedly heated vegetable oils for 16 weeks [52] or 24 weeks [53–56]. Chronic consumption of heated oil diets causes an increase in BP. The BP-raising effect of the heated vegetable oils may be attributable to the diminished endothelium-dependent relaxation responses. Heated oil diet promotes oxidative stress, resulting in NO sequestration and inactivation. Furthermore, heated oil causes a significant increase in ACE activity and a reduction in heme oxygenase content. The thermal oxidation of vegetable oils promotes the generation of free radicals and may contribute to the pathogenesis of hypertension in rats. This heated oil-induced hypertension model employed male instead of female rats. Female hormones have been shown to have cardioprotective properties [57, 58]. BP was measured using the conventional heating tail-cuff method. Even though invasive methods such as carotid arterial cannulation may provide more accurate readings, these may cause injury in the animals and further complicated the experiment. In addition,

TABLE 1: Common animal models for hypertension with different etiology.

Experimental model	Description
Genetic hypertension (i) SHR (ii) Dahl salt-sensitive (iii) Transgenic	(i) SHR is developed by inbreeding Wistar rats (brother-to-sister) with the highest BP [28]. The BP increases at week 4 to week 6 and reach systolic BP of 180–200 mmHg [28]. SHR may develop cardiac hypertrophy, cardiac failure, renal dysfunction, and impaired endothelium-dependent relaxations [60–62]. (ii) Dahl salt-sensitive rats derived from Sprague-Dawley rats on the basis of administering high NaCl diet. Salt-sensitive rats become hypertensive when given normal salt diets; however these rats develop severe and fatal hypertension with high salt diet (8% NaCl) [32]. These rats may develop cardiac hypertrophy, severe cardiac failure, hypertensive nephropathy, impaired endothelium-dependent relaxations [63–65]. (iii) Transgenic model can be generated by overexpression of a specific gene, for example, the mouse Ren-2 gene, and TGR(mREN2)27 [66]. Manifestations include marked cardiac hypertrophy, moderate proteinuria, and impaired endothelium-dependent relaxations [67, 68].
Endocrine hypertension	(i) Administration of DOCA in a combination with high salt diet and unilateral nephrectomy [69]. (ii) DOCA-induced hypertension induces a low renin model of hypertension [70]. (iii) Increased cardiac weight, proteinuria, glomerulosclerosis, and impaired endothelium-dependent relaxations [71, 72].
Environmental hypertension	(i) Stress-induced hypertension using flashing lights, loud noise, restraint cage, and cold or hot stimuli [73, 74]. (ii) Activation of sympathetic nervous system and RAAS may contribute to the initiation of stress-induced hypertension [75, 76].
Pharmacological hypertension	(i) Nitric oxide-deficient model by administering NOS inhibitors such as L-NAME [77]. (ii) Increase in BP was reported during long-term oral treatment with NOS inhibitors [78, 79]. (iii) Development of endothelial dysfunction is gradually with increased of BP [80].
Renal hypertension	(i) This includes two-kidney one-clip hypertension (2K1C; constriction of one renal artery while the contralateral kidney is left intact), one-kidney one-clip hypertension (1K1C; one renal artery is constricted and the contralateral kidney is removed), and two-kidney two-clip hypertension (2K2C; constriction of aorta or both renal arteries) [81, 82]. (ii) In the two-kidney model, circulating renin and aldosterone levels are increased [83], which are most notably in the early phase of hypertension [84].

SHR: spontaneously hypertensive rat; BP: blood pressure; NaCl: sodium chloride; TGR: transgenic rat; RAAS: renin-angiotensin-aldosterone system; DOCA: deoxycorticosterone acetate; NOS: nitric oxide synthase; L-NAME: N<sup>ω</sup>-nitro-L-arginine methyl ester.

these studies were performed to compare and monitor the effects of heated oil diets among the experimental groups up to 24 weeks using large number of rats. Thus, the noninvasive tail-cuff method is more suitable for measuring BP for long-term studies [59].

### 3. Animal Models for Atherosclerosis

Atherosclerosis, or “hardening of the arteries,” is a chronic inflammatory disease characterized by endothelial dysfunction and disorganization of intimal architecture owing to the accumulation of lipid deposits, inflammatory cells and cell debris in the intima of elastic, and medium to large muscular arteries. It underlies many of the common causes of cardiovascular deaths, including stroke and heart attack [85]. Several modifiable (including advanced age, gender, and heredity) and nonmodifiable risk factors (including dyslipidemia, hypertension, sedentary lifestyle, tobacco smoking, and diabetes mellitus) have been identified for the development of atherosclerosis [86]. Many clinical and experimental attempts have been performed to understand the pathophysiology of the disease. Amongst them, animals have been used for more than a century to study atherosclerosis. The first evidence that experimental atherosclerosis could be induced in animals came into view as early as 1908 by Ignatowski, who demonstrated atherogenesis in the aortic

wall of rabbits fed a diet enriched in animal proteins including meat, eggs, and milk [87]. Since then, numerous animal models have been used for understanding the mechanisms involved in both induction and regression of atherosclerotic lesions [88, 89]. Rats, rabbits, dogs, pigs, and monkeys are well-established animal models for atherosclerosis, and thrombosis. Nonhuman primates, hamster, mouse, cat, and guinea pig have also been used, but with lesser extent [90].

Several studies documented a significant relationship between elevated levels of serum cholesterol and development of atherosclerotic plaques in experimental animals. High-fat diets such as the 1% or 2% cholesterol diet have been found to elevate serum low-density lipoprotein (LDL), inducing atherogenesis in certain animals such as hamsters [91] and guinea pigs [92]. Therefore, the use of high-fat diets in promoting atherosclerosis in animal models has been a valuable tool for studying pathogenesis, as well as for testing potential therapies in reversing the atherosclerotic process.

Overall, an ideal animal model should be representative of the human atherosclerosis and should be feasible and affordable. Although animal models have played a significant role in our understanding of induction of atherosclerotic lesions, they have some limitations (Table 2). Not all experimental animals, such as rats and mice, respond similarly to a given high-fat diet, due to inherent genetic differences. Rats and mice are not good models for atherosclerosis, because

TABLE 2: Advantages and disadvantages of common animal models for atherosclerosis.

Animal	Advantages	Disadvantages
Rats and mice	(i) Low cost (ii) High availability (iii) Easy to handle and maintain (iv) Manageable breeding (v) Well-established genomic sequencing permit genetic manipulation	(i) Typically resistant to atherogenesis (ii) Absence of plasma CETP activity [93] (iii) Most cholesterol is transported through HDL particles [94] (iv) The small size of mice limits frequent blood sampling and dissection of small arteries
Rabbits	(i) Easy to handle and maintain (ii) Relatively inexpensive (iii) High availability (iv) Sensitive to dietary cholesterol induction of atherosclerosis (v) Large enough to permit physiological experiments	(i) Lesion location less compared with humans [95] (ii) Deficiency in hepatic lipase leads to hepatotoxicity following prolonged cholesterol feeding [96]
Pigs	(i) An anatomically and physiologically similar cardiovascular system compared to humans [97] (ii) Susceptible to spontaneous atherosclerosis [98] (iii) Comparable patterns of plaque distribution [99] (iv) High availability (for miniature pigs)	(i) Large size with resultant management difficulties (ii) High maintenance cost
Dogs	(i) Easy to work with (ii) Ideal size (iii) High availability	(i) Highly resistant to atherogenesis (ii) Status and anthropomorphic attitudes toward dogs (iii) Differences in important aspects of their cardiovascular system than humans [100]
Hamsters	(i) Low cost (ii) High availability (iii) Easy to handle and maintain (iv) Carry a significant portion of its plasma cholesterol in LDL particles and is therefore close to humans [101] (v) Sensitive to high-fat diets [102]	(i) Inconsistency of lesion development and absence of advanced lesions [103] (ii) Require highly abnormal diets and/or treatment with a cytotoxic chemical agent, such as streptozotocin [104]
Guinea pigs	(i) Develop diet-induced atherosclerosis (ii) Most of cholesterol is transported in LDL particles [105] (iii) Ovariectomized guinea pigs showed a similar plasma lipid profile as in postmenopausal women [106]	(i) Require constant supplementation with vitamin C, which potentially acts as an antioxidant to interfere with atherogenesis [107]
Nonhuman primates	(i) Genetically resemblance to humans (ii) Similar omnivorous diet (iii) Similar metabolism (iv) Develop metabolic syndrome as they age [108]	(i) Expensive (ii) Low availability (iii) Live long (thus requiring lengthy experimental periods) (iv) Potential carriers of dangerous viral zoonoses [104] (v) Significant ethical issues
Pigeon	(i) Low cost (ii) Easy handling (iii) Susceptible to atherosclerosis (iv) Sufficient size	(i) Nonmammalian (ii) Lipoprotein compositions and metabolism are different [109] (iii) Differences in arterial histology [110]
Chicken	(i) Low cost (ii) High availability (iii) Develop atherosclerosis naturally in aorta and coronary arteries, with cholesterol feeding accelerating the pathogenesis [111]	(i) Nonmammalian (ii) Viral infection is associated with atherosclerosis [112, 113]

CETP: cholesterol ester transfer protein; HDL: high-density lipoprotein; LDL: low-density lipoprotein.

they are typically resistant to atherogenesis, and even diets as high as 10% w/w cholesterol are not usually sufficient to produce vascular lesions [121]. The lipid metabolism of a normal rat and a mouse is primarily based on high-density lipoprotein (HDL) rather than on LDL as in humans, which might be attributable to resistance to atherogenesis [122]. The use of other interventions, such as vitamin D<sub>3</sub>, to establish atherosclerotic calcification or aortic medial calcification,

is often required [123]. Furthermore, a high-fat diet may represent a toxic proinflammatory stimulus rather than a low and chronic inflammatory state to animals [124]. Moreover, from a nutritional perspective, the dilution of a chow diet with lipids may increase the caloric density of the diet and reduce the ratio of essential nutrients to dietary energy, potentially leading to an imbalance in nutrient intake in animals consuming the atherogenic diet [125].

TABLE 3: Genetically modified animal models for atherosclerosis.

Experimental model	Description
Apolipoprotein E knockout (ApoE <sup>-/-</sup> ) mice	Apolipoprotein E (apoE), a constituent of lipoprotein responsible for packaging cholesterol and other fats and carrying them through the bloodstream, is inactivated by gene targeting. They exhibit a higher total plasma cholesterol concentration of 11 mM compared to 2 mM in their parent C57BL/6 mice [114].
LDL receptor knockout (LDLR <sup>-/-</sup> ) mice	LDL receptor (LDLR) is a cell surface receptor in liver cells that mediates the endocytosis of apoE to clear cholesterol-abundant LDL particles from the circulation. Total plasma cholesterol levels increase twofold compared to those of wild-type, owing to a seven- to ninefold increase in intermediate density lipoproteins (IDL) and LDL without a significant change in HDL [115].
Scavenger receptor class B member 1 knockout (SR-BI KO) mice	Scavenger receptor class B member 1 (SR-BI) functions in facilitating the uptake of cholesterol from HDL in the liver. It plays a key role in determining the levels of plasma cholesterol (primarily HDL). Heterozygous and homozygous mutants show 31% and 125% increase, respectively, in plasma cholesterol concentrations than wild-types [116].
<i>db/db</i> mice	OB-R is a high affinity receptor for leptin, an important circulating signal for the regulation of feeding, appetite, and body weight. Fatty acid oxidation rates are progressively higher in <i>db/db</i> mice in parallel with the earlier onset and greater duration of hyperglycemia [117].
<i>ob/ob</i> mice	A mutation results in a structurally defective leptin that does not bind to the OB-R. Mice that are <i>ob/ob</i> have no leptin action and exhibit obesity and endothelial dysfunction [118].
Fatty Zucker rats	A spontaneous mutant gene ( <i>fa</i> or fatty) that affects the action of the leptin. They have high levels of lipids and cholesterol in their bloodstream and become noticeably obese by 3 to 5 weeks of age and over 40% lipid of their body composition by 14 weeks of age [119].
Cholesterol ester transfer protein (CETP) transgenic rats	CETP inhibits HDL-mediated reverse cholesterol transport by transferring cholesterol from HDL to very low-density lipoprotein (VLDL) and LDL, promoting atherogenesis. The animals exhibit 82% increase in non-HDL cholesterol in addition to 80% reduction in HDL cholesterol when compared to wild-type rats [120].

HDL: high-density lipoprotein; LDL: low-density lipoprotein.

A small, genetically reproducible, murine model of atherosclerosis has been long desired due to projections of relatively easy handling and breeding procedures as well as its low cost. Researchers have used genetic technology to produce a number of genetically modified murine models to overcome the many deficiencies of larger animals, particularly to allow studies of potential therapies that require large numbers of subjects. An exciting scientific breakthrough occurred in 1992, when Zhang et al. found that ApoE-deficient mice generated by gene targeting had five times higher plasma cholesterol level and developed foam cell-rich depositions in their proximal aortas by the age of 3 months [114]. This model was the very first line of genetically modified murine model for atherosclerosis studies introduced to the research community. Since then, further research has led to other genetically modified models that mimic important aspects of atherosclerosis, such as fatty streaks, deposition of foam cells, vulnerable and stable plaques, and related complications such as arterial calcification, ulceration, hemorrhage, plaque rupture, thrombosis, and stenosis. Fatty Zucker rats, cholesterol ester transfer protein (CETP) transgenic rats, LDL receptor-knockout (KO) mice, and *db/db* mice are a few of the genetically modified models developed over recent years (Table 3). The development of techniques for direct genetic modification that have been previously restricted to murine species is promising to produce other new strains.

According to the oxidation hypothesis of atherosclerosis [126], oxidized LDL (oxLDL) plays a key role in the initiation of the atherosclerotic lesion as well as in almost every step of the atherogenic process, from the formation

of cholesterol-laden foam cells in plaques to the functioning as chemoattractants for macrophages and vascular smooth muscle cells [126, 127]. Since the etiology of atherosclerosis is multifactorial, the potential lipid-raising effect and lipid oxidation might contribute to atherogenesis together. The potential atherogenic effect of heated oils has been studied in experimental animals. Staprāns et al. [128] reported an increase of  $\beta$ -very low-density lipoprotein ( $\beta$ -VLDL) fraction and the formation of fatty streak lesions in aortas in male New Zealand White rabbits fed a low-cholesterol (0.25%) diet containing 5% thermal-oxidized corn oil. Atherosclerotic lesions have also been observed in genetically modified murine models, that is, LDLR<sup>-/-</sup> and apoE<sup>-/-</sup> mice after chronic consumption of an oxidized cholesterol diet [129].

However, there are still limitations in the experimental animals used in the aforementioned studies. For instance, cholesterol diets in rabbits may lead to hepatic toxicity [96]. Furthermore, genetically modified mice are rather costly and may impose a substantial financial constraint to a research as well as limit the number of samples. Therefore, a more feasible and affordable alternative has been developed to induce atherosclerosis in rats. Adult female Sprague-Dawley rats were ovariectomized prior to 16-week administration of 2% cholesterol diet fortified with 15% w/w of heated vegetable oil [130–132]. Ovariectomy was performed to simulate a postmenopausal condition characterized by the absence of cardioprotective estrogen [133].

Although there was a trend of increasing total cholesterol (TC) in all oil-fed groups, only heated oil-treated rats showed

significant increase in serum TC compared to the control [130, 131]. There were pronounced focal disruptions in the aortic intimal layer of the rats fed heated oil. Moreover, mononuclear cells were also observed in the intimal layer [132]. Based on the findings, it is possible to overwhelm rats' natural resistance to atherosclerosis by removing the ovaries. A further attempt was made to induce atherosclerosis in male Sprague-Dawley rats, as the use of the previous ovariectomized models is confined to menopause-induced atherosclerosis. Rats fed with standard rat chow fortified with 15% w/w of heated oil for 16 to 24 weeks. Histological study of the heart revealed cardiac toxicity with the presence of necrosis in cardiac tissue [52]. The intimal layer was observed to be noticeably thickened due to a massive lipid accumulation in the subendothelial space [134]. Lectin-like oxidized low-density lipoprotein receptor-1 (LOX-1), an endothelial receptor for endocytosis of oxLDL, was significantly increased in heated oil-fed rats compared to the control [135]. There were significant positive correlations between LOX-1 and the expressions of vascular cell adhesion molecule-1 (VCAM-1) and intercellular adhesion molecule-1 (ICAM-1) in heated oil-fed rats [135]. We suggest that heated oil diet can be used to induce atherosclerosis in rat models. However, the atherosclerosis-inducing effect seems to be more prominent in the ovariectomized rats than in male rats, as a longer period of intervention is required in male animals. Though the male rat model requires a longer duration of diet treatment to develop atherosclerosis, it is free from any surgical intervention in contrast to female rats undergoing ovariectomy. The use of other interventions such as vitamin D<sub>3</sub> [123] may be helpful in the escalation of atherosclerotic plaque formation.

#### 4. Conclusion

Progress in cardiovascular disease control requires understanding of the pathogenesis of the disease and testing of potential therapies, both experimentally and clinically. Experimental animal models, particularly murine species, have been a useful tool in this regard. The ideal animal model of cardiovascular disease should be representative to human conditions metabolically and pathophysiologically. The development of genetically modified animal models has enabled researchers to manipulate a specific target (either gene or protein), the role of which in pathogenesis may be subsequently established. This has led to the discovery of a vast spectrum of potential targets for ameliorative intervention. While the use of animal models has undeniably offered novel insights into different important aspects of a disease, still there are no species which are absolutely suitable for all studies, given the multifactorial nature of cardiovascular disease. Therefore, it is of utmost importance to choose an appropriate model to study different parts of cardiovascular disease. Otherwise, many exciting research findings may fail when translating into human studies. An agreement on appropriate experimental models for the study of different facades of cardiovascular disease would be a viable and effective strategy to further the advancement in this field.

#### Conflict of Interests

The authors declare no conflict of interests regarding publication of this paper.

#### References

- [1] <https://www.gov.uk/government/statistics/statistics-of-scientific-procedures-on-living-animals-great-britain-2013>.
- [2] T. B. Franklin, H. Russig, I. C. Weiss et al., "Epigenetic transmission of the impact of early stress across generations," *Biological Psychiatry*, vol. 68, no. 5, pp. 408–415, 2010.
- [3] Z. T. Erickson, E. A. Falkenberg, and G. A. S. Metz, "Lifespan psychomotor behaviour profiles of multigenerational prenatal stress and artificial food dye effects in rats," *PLoS ONE*, vol. 9, no. 6, Article ID e92132, 2014.
- [4] The Chimpanzee Sequencing and Analysis Consortium, "Initial sequence of the chimpanzee genome and comparison with the human genome," *Nature*, vol. 437, no. 7055, pp. 69–87, 2005.
- [5] R. J. Mural, M. D. Adams, E. W. Myers et al., "A comparison of whole-genome shotgun-derived mouse chromosome 16 and the human genome," *Science*, vol. 296, no. 5573, pp. 1661–1671, 2004.
- [6] B. G. Katzung, S. Masters, and A. Trevor, *Basic and Clinical Pharmacology*, Appleton & Lange, Norwalk, Conn, USA, 12th edition, 2012.
- [7] W. M. S. Russell and R. L. Burch, *The Principles of Humane Experimental Technique*, London, UK, Methuen, 1959, [http://altweb.jhsph.edu/pubs/books/humane\\_exp/het-toc#](http://altweb.jhsph.edu/pubs/books/humane_exp/het-toc#).
- [8] M. Emerson, "Refinement, reduction and replacement approaches to in vivo cardiovascular research," *British Journal of Pharmacology*, vol. 161, no. 4, pp. 749–754, 2010.
- [9] C. Kilkenny, W. Browne, I. C. Cuthill, M. Emerson, and D. G. Altman, "Animal research: reporting in vivo experiments: the ARRIVE guidelines," *British Journal of Pharmacology*, vol. 160, no. 7, pp. 1577–1579, 2010.
- [10] C. R. Hooijmans, M. Leenaars, and M. Ritskes-Hoitinga, "A gold standard publication checklist to improve the quality of animal studies, to fully integrate the three Rs, and to make systematic reviews more feasible," *Alternatives to Laboratory Animals*, vol. 38, no. 2, pp. 167–182, 2010.
- [11] S. M. Williams, J. L. Haines, and J. H. Moore, "The use of animal models in the study of complex disease: all else is never equal or why do so many human studies fail to replicate animal findings?" *BioEssays*, vol. 26, no. 2, pp. 170–179, 2004.
- [12] H. B. van der Worp, D. W. Howells, E. S. Sena et al., "Can animal models of disease reliably inform human studies?" *PLoS Medicine*, vol. 7, no. 3, Article ID e1000245, 2010.
- [13] R. Greek and A. Menache, "Systematic reviews of animal models: methodology versus epistemology," *International Journal of Medical Sciences*, vol. 10, no. 3, pp. 206–221, 2013.
- [14] J. Hau, "Animal models for human diseases," in *Sourcebook of Models for Biomedical Research*, P. M. Conn, Ed., pp. 3–8, Humana Press, Totowa, NJ, USA, 2008.
- [15] M. B. Bracken, "Why animal studies are often poor predictors of human reactions to exposure," *Journal of the Royal Society of Medicine*, vol. 102, no. 3, pp. 120–122, 2009.
- [16] L. E. Mignini and K. S. Khan, "Methodological quality of systematic reviews of animal studies: a survey of reviews of basic research," *BMC Medical Research Methodology*, vol. 6, article 10, 2006.

- [17] E. S. Sena, C. L. Briscoe, D. W. Howells, G. A. Donnan, P. A. G. Sandercock, and M. R. MacLeod, "Factors affecting the apparent efficacy and safety of tissue plasminogen activator in thrombotic occlusion models of stroke: systematic review and meta-analysis," *Journal of Cerebral Blood Flow & Metabolism*, vol. 30, no. 12, pp. 1905–1913, 2010.
- [18] C. R. Hooijmans and M. Ritskes-Hoitinga, "Progress in using systematic reviews of animal studies to improve translational research," *PLoS Medicine*, vol. 10, no. 7, Article ID e1001482, 2013.
- [19] S. Yadav, R. Boddula, G. Genitta et al., "Prevalence & risk factors of pre-hypertension & hypertension in an affluent north Indian population," *Indian Journal of Medical Research*, vol. 128, no. 6, pp. 712–720, 2008.
- [20] G. Danaei, E. L. Ding, D. Mozaffarian et al., "The preventable causes of death in the United States: comparative risk assessment of dietary, lifestyle, and metabolic risk factors," *PLoS Medicine*, vol. 6, no. 4, Article ID e1000058, 2009.
- [21] World Health Organization, *Global Health Risks: Mortality and Burden of Disease Attributable to Selected Major Risks*, World Health Organization, Geneva, Switzerland, 2009.
- [22] A. V. Chobanian, G. L. Bakris, H. R. Black et al., "The seventh report of the joint national committee on prevention, detection, evaluation, and treatment of high blood pressure: the JNC 7 report," *The Journal of the American Medical Association*, vol. 289, no. 19, pp. 2560–2572, 2003.
- [23] S. A. Doggrel and L. Brown, "Rat models of hypertension, cardiac hypertrophy and failure," *Cardiovascular Research*, vol. 39, no. 1, pp. 89–105, 1998.
- [24] D. K. Badyal, H. Lata, and A. P. Dadhich, "Animal models of hypertension and effect of drugs," *Indian Journal of Pharmacology*, vol. 35, no. 6, pp. 349–362, 2003.
- [25] W. C. Dornas and M. E. Silva, "Animal models for the study of arterial hypertension," *Journal of Biosciences*, vol. 36, no. 4, pp. 731–737, 2011.
- [26] W. Wang, R. Liu, G. Cao et al., "A reliable rabbit model for hyperkinetic pulmonary hypertension," *The Journal of Thoracic and Cardiovascular Surgery*, vol. 140, no. 2, pp. 395–399, 2010.
- [27] F. Gross, "Experimental models of hypertension and their use in the evaluation of antihypertensive drugs," in *Arterial Hypertension: The Gestation and Birth of a WHO Expert Committee Report*, F. Gross and J. I. S. Robertson, Eds., pp. 198–208, G.K. Hall Medical Publishers, Boston, Mass, USA, 1980.
- [28] K. Okamoto and K. Aoki, "Development of a strain of spontaneously hypertensive rats," *Japanese Circulation Journal*, vol. 27, no. 3, pp. 282–293, 1963.
- [29] N. C. Trippodo and E. D. Frohlich, "Similarities of genetic (spontaneous) hypertension: man and rat," *Circulation Research*, vol. 48, no. 3, pp. 309–319, 1981.
- [30] F. H. Smirk and W. H. Hall, "Inherited hypertension in rats," *Nature*, vol. 182, no. 4637, pp. 727–728, 1958.
- [31] G. Bianchi, U. Fox, and E. Imbasciati, "The development of a new strain of spontaneously hypertensive rats," *Life Sciences*, vol. 14, no. 2, pp. 339–347, 1974.
- [32] L. K. Dahl, M. Heine, and L. Tassinari, "Role of genetic factors in susceptibility to experimental hypertension due to chronic excess salt ingestion," *Nature*, vol. 194, no. 4827, pp. 480–482, 1962.
- [33] N. Zamir, Y. Gutman, and D. Ben-Ishay, "Hypertension and brain catecholamine distribution in the Hebrew University Sabra, H and N rats," *Clinical Science and Molecular Medicine*, vol. 5, Supplement 5, 1978.
- [34] M. Vincent, H. Bornet, F. Berthezene, J. Dupont, and J. Sassard, "Thyroid function and blood pressure in two new strains of spontaneously hypertensive and normotensive rats," *Clinical Science and Molecular Medicine*, vol. 54, no. 4, pp. 391–395, 1978.
- [35] Y. M. Pinto, M. Paul, and D. Ganten, "Lessons from rat models of hypertension: from Goldblatt to genetic engineering," *Cardiovascular Research*, vol. 39, no. 1, pp. 77–88, 1998.
- [36] Z.-J. Sun and Z.-E. Zhang, "Historic perspectives and recent advances in major animal models of hypertension," *Acta Pharmacologica Sinica*, vol. 26, no. 3, pp. 295–301, 2005.
- [37] C. Fanelli and R. Zatz, "Linking oxidative stress, the renin-angiotensin system, and hypertension," *Hypertension*, vol. 57, no. 3, pp. 373–374, 2011.
- [38] H. Goldblatt, J. Lynch, R. F. Hanzal, and W. W. Summerville, "The production of persistent elevation of systolic blood pressure by means of renal ischemia," *Journal of Experimental Medicine*, vol. 59, no. 3, pp. 347–379, 1934.
- [39] P. Zandberg, "Animal models in experimental hypertension: relevance to drug testing and discovery," in *Pharmacology of Antihypertensive Drugs*, P. A. van Zwieten, Ed., vol. 3 of *Handbook of Hypertension*, Elsevier Science, New York, NY, USA, 1984.
- [40] T. Sawamura and T. Nakada, "Role of dopamine in the striatum, renin-angiotensin system and renal sympathetic nerve on the development of two-kidney, one-clip goldblatt hypertension," *The Journal of Urology*, vol. 155, no. 3, pp. 1108–1111, 1996.
- [41] J. M. Flack, S. A. Atlas, J. L. Pool, and W. B. White, "Renin-angiotensin aldosterone system and hypertension: current approaches and future directions," *Journal of Managed Care Pharmacy*, vol. 13, no. 8, supplement, pp. S2–S32, 2007.
- [42] S. Moncada and A. Higgs, "The L-arginine-nitric oxide pathway," *The New England Journal of Medicine*, vol. 329, no. 27, pp. 2002–2012, 1993.
- [43] R. F. Furchgott and P. M. Vanhoutte, "Endothelium-derived relaxing and contracting factors," *The FASEB Journal*, vol. 3, no. 9, pp. 2007–2018, 1989.
- [44] M. Hermann, A. Flammer, and T. F. Lüscher, "Nitric oxide in hypertension," *Journal of Clinical Hypertension*, vol. 8, no. 12, supplement 4, pp. 17–29, 2006.
- [45] R. Rahimian, G. P. Dubé, W. Toma, N. Dos Santos, B. M. McManus, and C. van Breemen, "Raloxifene enhances nitric oxide release in rat aorta via increasing endothelial nitric oxide mRNA expression," *European Journal of Pharmacology*, vol. 434, no. 3, pp. 141–149, 2002.
- [46] J.-C. Zhong, X.-Y. Yu, Y. Huang, L.-M. Yung, C.-W. Lau, and S.-G. Lin, "Apelin modulates aortic vascular tone via endothelial nitric oxide synthase phosphorylation pathway in diabetic mice," *Cardiovascular Research*, vol. 74, no. 3, pp. 388–395, 2007.
- [47] V. Ramanathan and M. Thekkumalai, "Role of chrysin on hepatic and renal activities of N<sup>ω</sup>-nitro-L-arginine-methyl ester induced hypertensive rats," *International Journal of Nutrition, Pharmacology and Neurological Diseases*, vol. 4, no. 1, pp. 58–63, 2014.
- [48] C. F. Kung, P. Moreau, H. Takase, and T. F. Luscher, "L-NAME hypertension alters endothelial and smooth muscle function in rat aorta: Prevention by trandolapril and verapamil," *Hypertension*, vol. 26, no. 5, pp. 744–751, 1995.
- [49] H. François, S. Placier, M. Flamant et al., "Prevention of renal vascular and glomerular fibrosis by epidermal growth factor receptor inhibition," *The FASEB Journal*, vol. 18, no. 7, pp. 926–928, 2004.

- [50] P. Nyadjeu, E. P. Nguenefack-Mbuyo, A. D. Atsamo, T. B. Nguenefack, A. B. Dongmo, and A. Kamanyi, "Acute and chronic antihypertensive effects of *Cinnamomum zeylanicum* stem bark methanol extract in L-NAME-induced hypertensive rats," *BMC Complementary and Alternative Medicine*, vol. 13, article 27, 2013.
- [51] F. Soriguer, G. Rojo-Martínez, M. C. Dobarganes et al., "Hypertension is related to the degradation of dietary frying oils," *The American Journal of Clinical Nutrition*, vol. 78, no. 6, pp. 1092–1097, 2003.
- [52] X. F. Leong, A. Aishah, U. Nor Aini, S. Das, and K. Jaarin, "Heated palm oil causes rise in blood pressure and cardiac changes in heart muscle in experimental rats," *Archives of Medical Research*, vol. 39, no. 6, pp. 567–572, 2008.
- [53] X.-F. Leong, M. N. M. Najib, S. Das, M. R. Mustafa, and K. Jaarin, "Intake of repeatedly heated palm oil causes elevation in blood pressure with impaired vasorelaxation in rats," *The Tohoku Journal of Experimental Medicine*, vol. 219, no. 1, pp. 71–78, 2009.
- [54] X.-F. Leong, M. R. Mustafa, S. Das, and K. Jaarin, "Association of elevated blood pressure and impaired vasorelaxation in experimental Sprague-Dawley rats fed with heated vegetable oil," *Lipids in Health and Disease*, vol. 9, article 66, 2010.
- [55] K. Jaarin, M. R. Mustafa, and X.-F. Leong, "The effects of heated vegetable oils on blood pressure in rats," *Clinics*, vol. 66, no. 12, pp. 2125–2132, 2011.
- [56] X.-F. Leong, J. Salimon, M. R. Mustafa, and K. Jaarin, "Effect of repeatedly heated palm olein on blood pressure-regulating enzymes activity and lipid peroxidation in rats," *Malaysian Journal of Medical Sciences*, vol. 19, no. 1, pp. 20–29, 2012.
- [57] J. D. Gardner, G. L. Brower, T. G. Voloshenyuk, and J. S. Janicki, "Cardioprotection in female rats subjected to chronic volume overload: synergistic interaction of estrogen and phytoestrogens," *American Journal of Physiology: Heart and Circulatory Physiology*, vol. 294, no. 1, pp. H198–H204, 2008.
- [58] C. Campos, C. L. Sartorio, K. R. Casali et al., "Low-dose estrogen is as effective as high-dose treatment in rats with postmenopausal hypertension," *Journal of Cardiovascular Pharmacology*, vol. 63, no. 2, pp. 144–151, 2014.
- [59] J. H. Kregel, J. B. Hodgin, J. R. Hagaman, and O. Smithies, "A noninvasive computerized tail-cuff system for measuring blood pressure in mice," *Hypertension*, vol. 25, no. 5, pp. 1111–1115, 1995.
- [60] L. Yan, J. D. Zhang, B. Wang et al., "Quercetin inhibits left ventricular hypertrophy in spontaneously hypertensive rats and inhibits angiotensin II-induced H9C2 cells hypertrophy by enhancing PPAR- $\gamma$  expression and suppressing AP-1 activity," *PLoS ONE*, vol. 8, no. 9, Article ID e72548, 2013.
- [61] W. J. Welch, H. Baumgärtel, D. Lübbers, and C. S. Wilcox, "Renal oxygenation defects in the spontaneously hypertensive rat: role of AT1 receptors," *Kidney International*, vol. 63, no. 1, pp. 202–208, 2003.
- [62] C. S. Packer, "Changes in arterial smooth muscle contractility, contractile proteins, and arterial wall structure in spontaneous hypertension," *Proceedings of the Society for Experimental Biology and Medicine*, vol. 207, no. 2, pp. 148–174, 1994.
- [63] S. Klotz, I. Hay, G. Zhang, M. Maurer, J. Wang, and D. Burkhoff, "Development of heart failure in chronic hypertensive Dahl rats: focus on heart failure with preserved ejection fraction," *Hypertension*, vol. 47, no. 5, pp. 901–911, 2006.
- [64] N. Tian, R. A. Rose, S. Jordan, T. M. Dwyer, M. D. Hughson, and R. D. Manning Jr., "N-Acetylcysteine improves renal dysfunction, ameliorates kidney damage and decreases blood pressure in salt-sensitive hypertension," *Journal of Hypertension*, vol. 24, no. 11, pp. 2263–2270, 2006.
- [65] Y.-N. Cao, K. Kuwasako, J. Kato et al., "Beyond vasodilation: the antioxidant effect of adrenomedullin in Dahl salt-sensitive rat aorta," *Biochemical and Biophysical Research Communications*, vol. 332, no. 3, pp. 866–872, 2005.
- [66] J. J. Mullins, J. Peters, and D. Ganten, "Fulminant hypertension in transgenic rats harbouring the mouse *Ren-2* gene," *Nature*, vol. 344, no. 6266, pp. 541–544, 1990.
- [67] O. Chung, T. Schips, P. Rohmeiss, N. Gretz, M. Strauch, and T. Unger, "Protein excretion and renal adaptation of transgenic mRen2 rats to changing oral sodium loads," *Journal of Hypertension*, vol. 11, no. 5, pp. S188–S189, 1993.
- [68] Y. M. Pinto, H. Buikema, W. H. van Gilst et al., "Cardiovascular end-organ damage in Ren-2 transgenic rats compared to spontaneously hypertensive rats," *Journal of Molecular Medicine*, vol. 75, no. 5, pp. 371–377, 1997.
- [69] H. Selye, C. E. Hall, and E. M. Rowley, "Malignant hypertension produced by treatment with deoxycorticosterone acetate and sodium chloride," *Canadian Medical Association Journal*, vol. 49, no. 2, pp. 88–92, 1943.
- [70] V. Chamorro, R. Wangenstein, J. Sainz et al., "Protective effects of the angiotensin II type I (AT1) receptor blockade in low-renin deoxycorticosterone acetate (DOCA)-treated spontaneously hypertensive rats," *Clinical Science*, vol. 106, no. 3, pp. 251–259, 2004.
- [71] A. Iyer, V. Chan, and L. Brown, "The DOCA-salt hypertensive rat as a model of cardiovascular oxidative and inflammatory stress," *Current Cardiology Reviews*, vol. 6, no. 4, pp. 291–297, 2010.
- [72] B. Klanke, N. Cordasic, A. Hartner, R. E. Schmieder, R. Veelken, and K. F. Hilgers, "Blood pressure versus direct mineralocorticoid effects on kidney inflammation and fibrosis in DOCA-salt hypertension," *Nephrology Dialysis Transplantation*, vol. 23, no. 11, pp. 3456–3463, 2008.
- [73] J. P. Henry, Y.-Y. Liu, W. E. Nadra et al., "Psychosocial stress can induce chronic hypertension in normotensive strains of rats," *Hypertension*, vol. 21, no. 5, pp. 714–723, 1993.
- [74] A. G. Bechtold, G. Patel, G. Hochhaus, and D. A. Scheuer, "Chronic blockade of hindbrain glucocorticoid receptors reduces blood pressure responses to novel stress and attenuates adaptation to repeated stress," *The American Journal of Physiology—Regulatory Integrative and Comparative Physiology*, vol. 296, no. 5, pp. R1445–R1454, 2009.
- [75] P. A. Smith, L. N. Graham, A. F. Mackintosh, J. B. Stoker, and D. A. S. G. Mary, "Sympathetic neural mechanisms in white-coat hypertension," *Journal of the American College of Cardiology*, vol. 40, no. 1, pp. 126–132, 2002.
- [76] S. C. Coste, V. L. Brooks, D. A. McCarron, D. C. Hatton, and Y. Qi, "Captopril and stress-induced hypertension in the borderline hypertensive rat," *Journal of Hypertension*, vol. 13, no. 12, pp. 1391–1398, 1995.
- [77] Y. Nishijima, X. Zheng, H. Lund, M. Suzuki, D. L. Mattson, and D. X. Zhang, "Characterization of blood pressure and endothelial function in TRPV4-deficient mice with L-NAME- and angiotensin II-induced hypertension," *Physiological Reports*, vol. 2, Article ID e00199, 2014.
- [78] F. Xavier, A. M. F. Magalhães, and J. A. R. Gontijo, "Effect of inhibition of nitric oxide synthase on blood pressure and renal sodium handling in renal denervated rats," *Brazilian Journal of Medical and Biological Research*, vol. 33, no. 3, pp. 347–354, 2000.

- [79] H. Rauchová, O. Pecháňová, J. Kuneš, M. Vokurková, Z. Dobešová, and J. Zicha, "Chronic *N*-acetylcysteine administration prevents development of hypertension in *H<sup>w</sup>*-nitro-L-arginine methyl ester-treated rats: the role of reactive oxygen species," *Hypertension Research*, vol. 28, no. 5, pp. 475–482, 2005.
- [80] I. Bernatova, "Endothelial dysfunction in experimental models of arterial hypertension: cause or consequence?" *BioMed Research International*, vol. 2014, Article ID 598271, 14 pages, 2014.
- [81] P. Wiesel, L. Mazzolai, J. Nussberger, and T. Pedrazzini, "Two-kidney, one clip and one-kidney, one clip hypertension in mice," *Hypertension*, vol. 29, no. 4, pp. 1025–1030, 1997.
- [82] J. Zeng, Y. Zhang, J. Mo, Z. Su, and R. Huang, "Two-kidney, two clip renovascular hypertensive rats can be used as stroke-prone rats," *Stroke*, vol. 29, no. 8, pp. 1708–1714, 1998.
- [83] H. Kiyomoto, H. Kobori, and A. Nishiyama, "Renin-angiotensin system in the kidney and oxidative stress: local renin-angiotensin-aldosterone system and NADPH oxidase-dependent oxidative stress in the kidney," in *Studies on Renal Disorders, Oxidative Stress in Applied Basic Research and Clinical Practice*, T. Miyata, K.-U. Eckardt, and M. Nangaku, Eds., pp. 71–91, Springer Science, Boston, Mass, USA, 2011.
- [84] J. Y. Moon, "Recent update of renin-angiotensin-aldosterone system in the pathogenesis of hypertension," *Electrolytes & Blood Pressure*, vol. 11, no. 2, pp. 41–45, 2013.
- [85] World Health Organization, *Global Atlas on Cardiovascular Disease Prevention and Control*, World Health Organization, Geneva, Switzerland, 2011.
- [86] G. Douglas and K. M. Channon, "The pathogenesis of atherosclerosis," *Medicine*, vol. 38, no. 8, pp. 397–402, 2010.
- [87] A. C. Ignatowski, "Influence of animal food on the organism of rabbits," *Izvestia Imperatorskoi Voenno-Medicinskoi Akademii (St Petersburg)*, vol. 16, pp. 154–176, 1908.
- [88] H. Beaufrère, "Atherosclerosis: comparative pathogenesis, lipoprotein metabolism, and Avian and exotic companion mammal models," *Journal of Exotic Pet Medicine*, vol. 22, no. 4, pp. 320–335, 2013.
- [89] F. R. Kapourchali, G. Surendiran, L. Chen, E. Uitz, B. Bahadori, and M. H. Moghadasian, "Animal models of atherosclerosis," *World Journal of Clinical Cases*, vol. 2, no. 5, pp. 126–132, 2014.
- [90] P. F. Bodary and D. T. Eitzman, "Animal models of thrombosis," *Current Opinion in Hematology*, vol. 16, no. 5, pp. 342–346, 2009.
- [91] T.-F. Tzeng, H.-J. Lu, S.-S. Liou, C. J. Chang, and I.-M. Liu, "Lipid-lowering effects of zerumbone, a natural cyclic sesquiterpene of *Zingiber zerumbet* Smith, in high-fat diet-induced hyperlipidemic hamsters," *Food and Chemical Toxicology*, vol. 69, pp. 132–139, 2014.
- [92] M. C. Podszun, N. Grebenstein, A. Spruss et al., "Dietary  $\alpha$ -tocopherol and atorvastatin reduce high-fat-induced lipid accumulation and down-regulate CD36 protein in the liver of guinea pigs," *The Journal of Nutritional Biochemistry*, vol. 25, no. 5, pp. 573–579, 2014.
- [93] Y. C. Haa and P. J. Barter, "Differences in plasma cholesteryl ester transfer activity in sixteen vertebrate species," *Comparative Biochemistry and Physiology—Part B: Biochemistry & Molecular Biology*, vol. 71, no. 2, pp. 265–269, 1982.
- [94] S. H. Quarfordt, B. Landis, G. Cucchiari, Y. Yamaguchi, and B. Oswald, "Plasma cholesterol transport in anhepatic rats," *Journal of Clinical Investigation*, vol. 89, no. 5, pp. 1564–1570, 1992.
- [95] M. H. Moghadasian, J. J. Frohlich, and B. M. McManus, "Advances in experimental dyslipidemia and atherosclerosis," *Laboratory Investigation*, vol. 81, no. 9, pp. 1173–1183, 2001.
- [96] A. E. Yanni, "The laboratory rabbit: an animal model of atherosclerosis research," *Laboratory Animals*, vol. 38, no. 3, pp. 246–256, 2004.
- [97] T. Gardner and D. Johnson, "Cardiovascular system," in *Experimental Surgery and Physiology: Induced Animal Models of Human Disease*, M. M. Swindle and R. J. Adams, Eds., pp. 74–124, Lippincott Williams & Wilkins, Philadelphia, Pa, USA, 1988.
- [98] V. Fuster, J. T. Lie, L. Badimon, J. A. Rosemark, and E. J. Bowie, "Spontaneous and diet-induced coronary atherosclerosis in normal swine and swine with von Willebrand disease," *Arteriosclerosis*, vol. 5, no. 1, pp. 67–73, 1985.
- [99] F. C. White, S. M. Carroll, A. Magnet, and C. M. Bloor, "Coronary collateral development in swine after coronary artery occlusion," *Circulation Research*, vol. 71, no. 6, pp. 1490–1500, 1992.
- [100] G. Kemming, J. B. Messick, W. Mueller et al., "Can we continue research in splenectomized dogs? Mycoplasma haemocanis: old problem—new insight," *European Surgical Research*, vol. 36, no. 4, pp. 198–205, 2004.
- [101] A. L. Lock, C. A. M. Horne, D. E. Bauman, and A. M. Salter, "Butter naturally enriched in conjugated linoleic acid and vaccenic acid alters tissue fatty acids and improves the plasma lipoprotein profile in cholesterol-fed hamsters," *Journal of Nutrition*, vol. 135, no. 8, pp. 1934–1939, 2005.
- [102] S. E. Dorfman, S. Wang, S. Vega-López, M. Jauhiainen, and A. H. Lichtenstein, "Dietary fatty acids and cholesterol differentially modulate HDL cholesterol metabolism in Golden-Syrian hamsters," *Journal of Nutrition*, vol. 135, no. 3, pp. 492–498, 2005.
- [103] A. Dillard, N. R. Matthan, and A. H. Lichtenstein, "Use of hamster as a model to study diet-induced atherosclerosis," *Nutrition & Metabolism*, vol. 7, article 89, 2010.
- [104] J. C. Russell and S. D. Proctor, "Small animal models of cardiovascular disease: tools for the study of the roles of metabolic syndrome, dyslipidemia, and atherosclerosis," *Cardiovascular Pathology*, vol. 15, no. 6, pp. 318–330, 2006.
- [105] M. L. Fernandez and D. J. McNamar, "Dietary fat-mediated changes in hepatic apoprotein B/E receptor in the guinea pig: effect of polyunsaturated, monounsaturated, and saturated fat," *Metabolism*, vol. 38, no. 11, pp. 1094–1102, 1989.
- [106] T. L. Zern, K. L. West, and M. L. Fernandez, "Grape polyphenols decrease plasma triglycerides and cholesterol accumulation in the aorta of ovariectomized guinea pigs," *Journal of Nutrition*, vol. 133, no. 7, pp. 2268–2272, 2003.
- [107] M. L. Fernandez and J. S. Volek, "Guinea pigs: a suitable animal model to study lipoprotein metabolism, atherosclerosis and inflammation," *Nutrition and Metabolism*, vol. 3, article 17, 2006.
- [108] B. C. Hansen and N. L. Bodkin, "Primary prevention of diabetes mellitus by prevention of obesity in monkeys," *Diabetes*, vol. 42, no. 12, pp. 1809–1814, 1993.
- [109] H. A. Barakat and R. W. St. Clair, "Characterization of plasma lipoproteins of grain- and cholesterol-fed White Carneau and Show Racer pigeons," *The Journal of Lipid Research*, vol. 26, no. 10, pp. 1252–1268, 1985.
- [110] L. C. Stout and L. W. Thorpe, "Histology of normal aortas in birds with emphasis on intimal thickening," *Atherosclerosis*, vol. 36, no. 4, pp. 545–558, 1980.

- [111] D. V. V. Dauber and L. N. N. Katz, "Experimental atherosclerosis in the chick," *Archives of Pathology*, vol. 36, no. 5, pp. 473–492, 1943.
- [112] D. P. Hajjar, C. G. Fabricant, C. R. Minick, and J. Fabricant, "Virus-induced atherosclerosis. Herpesvirus infection alters aortic cholesterol metabolism and accumulation," *The American Journal of Pathology*, vol. 122, no. 1, pp. 62–70, 1986.
- [113] C. G. Fabricant and J. Fabricant, "Atherosclerosis induced by infection with Marek's disease herpesvirus in chickens," *The American Heart Journal*, vol. 138, no. 5, part, pp. S465–S468, 1999.
- [114] S. H. Zhang, R. L. Reddick, J. A. Piedrahita, and N. Maeda, "Spontaneous hypercholesterolemia and arterial lesions in mice lacking apolipoprotein E," *Science*, vol. 258, no. 5081, pp. 468–471, 1992.
- [115] S. Ishibashi, M. S. Brown, J. L. Goldstein, R. D. Gerard, R. E. Hammer, and J. Herz, "Hypercholesterolemia in low density lipoprotein receptor knockout mice and its reversal by adenovirus-mediated gene delivery," *The Journal of Clinical Investigation*, vol. 92, no. 2, pp. 883–893, 1993.
- [116] A. Rigotti, B. L. Trigatti, M. Penman, H. Rayburn, J. Herz, and M. Krieger, "A targeted mutation in the murine gene encoding the high density lipoprotein (HDL) receptor scavenger receptor class B type I reveals its key role in HDL metabolism," *Proceedings of the National Academy of Sciences of the United States of America*, vol. 94, no. 23, pp. 12610–12615, 1997.
- [117] J. Buchanan, P. K. Mazumder, P. Hu et al., "Reduced cardiac efficiency and altered substrate metabolism precedes the onset of hyperglycemia and contractile dysfunction in two mouse models of insulin resistance and obesity," *Endocrinology*, vol. 146, no. 12, pp. 5341–5349, 2005.
- [118] B. Winters, Z. Mo, E. Brooks-Asplund et al., "Reduction of obesity, as induced by leptin, reverses endothelial dysfunction in obese (*Lep<sup>ob</sup>*) mice," *Journal of Applied Physiology*, vol. 89, no. 6, pp. 2382–2390, 2000.
- [119] L. M. Zucker and H. N. Antoniades, "Insulin and obesity in the Zucker genetically obese rat "fatty"," *Endocrinology*, vol. 90, no. 5, pp. 1320–1330, 1972.
- [120] Z. Zak, T. Gautier, L. Dumont et al., "Effect of cholesteryl ester transfer protein (CETP) expression on diet-induced hyperlipidemias in transgenic rats," *Atherosclerosis*, vol. 178, no. 2, pp. 279–286, 2005.
- [121] P. J. Dolphin, "Serum and hepatic nascent lipoproteins in normal and hypercholesterolemic rats," *Journal of Lipid Research*, vol. 22, no. 6, pp. 971–989, 1981.
- [122] X. Li, Y. Liu, H. Zhang, L. Ren, Q. Li, and N. Li, "Animal models for the atherosclerosis research: a review," *Protein and Cell*, vol. 2, no. 3, pp. 189–201, 2011.
- [123] J. Pang, Q. Xu, X. Xu et al., "Hexarelin suppresses high lipid diet and vitamin D3-induced atherosclerosis in the rat," *Peptides*, vol. 31, no. 4, pp. 630–638, 2010.
- [124] Y. Okada, K. Yamaguchi, T. Nakajima et al., "Rosuvastatin ameliorates high-fat and high-cholesterol diet-induced nonalcoholic steatohepatitis in rats," *Liver International*, vol. 33, no. 2, pp. 301–311, 2013.
- [125] A. H. Lichtman, S. K. Clinton, K. Iiyama, P. W. Connelly, P. Libby, and M. I. Cybulsky, "Hyperlipidemia and atherosclerotic lesion development in LDL receptor-deficient mice fed defined semipurified diets with and without cholate," *Arteriosclerosis, Thrombosis, and Vascular Biology*, vol. 19, no. 8, pp. 1938–1944, 1999.
- [126] M. T. Quinn, S. Parthasarathy, L. G. Fong, and D. Steinberg, "Oxidatively modified low density lipoproteins: a potential role in recruitment and retention of monocyte/macrophages during atherogenesis," *Proceedings of the National Academy of Sciences of the United States of America*, vol. 84, no. 9, pp. 2995–2998, 1987.
- [127] S. R. J. Maxwell and G. Y. H. Lip, "Free radicals and antioxidants in cardiovascular disease," *British Journal of Clinical Pharmacology*, vol. 44, no. 4, pp. 307–317, 1997.
- [128] I. Staprāns, J. H. Rapp, X.-M. Pan, D. A. Hardman, and K. R. Feingold, "Oxidized lipids in the diet accelerate the development of fatty streaks in cholesterol-fed rabbits," *Arteriosclerosis, Thrombosis, and Vascular Biology*, vol. 16, no. 4, pp. 533–538, 1996.
- [129] I. Staprāns, X.-M. Pan, J. H. Rapp, C. Grunfeld, and K. R. Feingold, "Oxidized cholesterol in the diet accelerates the development of atherosclerosis in LDL receptor- and apolipoprotein E-deficient mice," *Arteriosclerosis, Thrombosis, and Vascular Biology*, vol. 20, no. 3, pp. 708–714, 2000.
- [130] S. K. Adam, S. Das, I. N. Soelaiman, N. A. Umar, and K. Jaarin, "Consumption of repeatedly heated soy oil increases the serum parameters related to atherosclerosis in Ovariectomized rats," *The Tohoku Journal of Experimental Medicine*, vol. 215, no. 3, pp. 219–226, 2008.
- [131] S. K. Adam, I. N. Soelaiman, N. A. Umar, N. Mokhtar, N. Mohamed, and K. Jaarin, "Effects of repeatedly heated palm oil on serum lipid profile, lipid peroxidation and homocysteine levels in a post-menopausal rat model," *McGill Journal of Medicine*, vol. 11, no. 2, pp. 145–151, 2008.
- [132] S. K. Adam, S. Das, and K. Jaarin, "A detailed microscopic study of the changes in the aorta of experimental model of postmenopausal rats fed with repeatedly heated palm oil," *International Journal of Experimental Pathology*, vol. 90, no. 3, pp. 321–327, 2009.
- [133] W. B. Kannel and P. W. F. Wilson, "Risk factors that attenuate the female coronary disease advantage," *Archives of Internal Medicine*, vol. 155, no. 1, pp. 57–61, 1995.
- [134] T. K. Xian, N. A. Omar, L. W. Ying et al., "Reheated palm oil consumption and risk of atherosclerosis: evidence at ultrastructural level," *Evidence-Based Complementary and Alternative Medicine*, vol. 2012, Article ID 828170, 6 pages, 2012.
- [135] C.-Y. Ng, Y. Kamisah, O. Faizah, and K. Jaarin, "The role of repeatedly heated soybean oil in the development of hypertension in rats: association with vascular inflammation," *International Journal of Experimental Pathology*, vol. 93, no. 5, pp. 377–387, 2012.

## Research Article

# Intratracheal Bleomycin Aerosolization: The Best Route of Administration for a Scalable and Homogeneous Pulmonary Fibrosis Rat Model?

Alexandre Robbe,<sup>1</sup> Alexandra Tassin,<sup>1</sup> Justine Carpentier,<sup>1</sup> Anne-Emilie Declèves,<sup>1</sup>  
Zita Léa Mekinda Ngoni,<sup>2</sup> Denis Nonclercq,<sup>3</sup> and Alexandre Legrand<sup>1</sup>

<sup>1</sup>Laboratory of Respiratory Physiology, Pathophysiology and Rehabilitation, Research Institute for Health Sciences and Technology, University of Mons, 7000 Mons, Belgium

<sup>2</sup>Department of Pneumology, Erasme Hospital, 1070 Brussels, Belgium

<sup>3</sup>Laboratory of Histology, Research Institute for Health Sciences and Technology, University of Mons, 7000 Mons, Belgium

Correspondence should be addressed to Alexandre Legrand; alexandre.legrand@umons.ac.be

Received 6 October 2014; Accepted 9 January 2015

Academic Editor: Oreste Gualillo

Copyright © 2015 Alexandre Robbe et al. This is an open access article distributed under the Creative Commons Attribution License, which permits unrestricted use, distribution, and reproduction in any medium, provided the original work is properly cited.

Idiopathic pulmonary fibrosis (IPF) is a chronic disease with a poor prognosis and is characterized by the accumulation of fibrotic tissue in lungs resulting from a dysfunction in the healing process. In humans, the pathological process is patchy and temporally heterogeneous and the exact mechanisms remain poorly understood. Different animal models were thus developed. Among these, intratracheal administration of bleomycin (BLM) is one of the most frequently used methods to induce lung fibrosis in rodents. In the present study, we first characterized histologically the time-course of lung alteration in rats submitted to BLM instillation. Heterogeneous damages were observed among lungs, consisting in an inflammatory phase at early time-points. It was followed by a transition to a fibrotic state characterized by an increased myofibroblast number and collagen accumulation. We then compared instillation and aerosolization routes of BLM administration. The fibrotic process was studied in each pulmonary lobe using a modified Ashcroft scale. The two quantification methods were confronted and the interobserver variability evaluated. Both methods induced fibrosis development as demonstrated by a similar progression of the highest modified Ashcroft score. However, we highlighted that aerosolization allows a more homogeneous distribution of lesions among lungs, with a persistence of higher grade damages upon time.

## 1. Introduction

Idiopathic pulmonary fibrosis (IPF) is a severe form of fibrosing interstitial lung disease with unknown etiology and characterized by a progressive loss of lung function associated with dyspnea and cough. This heterogeneous pathology carries an invariable poor prognosis [1], with a median survival of less than three years from diagnosis. Over the last decade, numerous treatment options have been evaluated for IPF in large clinical trials. However, a great majority of those studies demonstrated a lack of efficacy or deleterious effects [2]. Moreover, only a minority of patients can be actually accommodated within clinical

trials or with lung transplantation [3]. Therapeutic options remain thus limited, despite an increased and recent interest for new antifibrotic and anti-inflammatory agents such as pirfenidone or nintedanib, which have demonstrated efficacy in several clinical studies. Pirfenidone was further approved for medication in many countries [2].

IPF pathogenesis remains poorly understood but increased evidence suggests the involvement of complex interactions between genetic predisposition, epigenetics, environment, and comorbidities [4]. Histologically, IPF is characterized by inflammatory cell proliferation, alveolar epithelial injury, fibroblast and myofibroblast hyperplasia, and extracellular matrix deposition [1, 5, 6]. The subsequent distortion

of the alveolar architecture leads to gas exchange impairment and ultimately respiratory failure and death. IPF pathological process is patchy and temporally heterogeneous, suggesting sequential injuries [6]. The inflammation process was first considered to precede fibrosis but, on the basis of later observations in animal models and the lack of efficacy of immunosuppressive therapy in patients [1, 7], the paradigm about IPF pathogenesis shifted to the idea that fibrosis could result from alveolar epithelial cell (AEC) injury and deregulated repair [1, 4]. Myofibroblasts were suggested to play a central role in this pathogenesis through extracellular matrix deposition and structural remodeling [7]. The heterogeneity of their phenotype could reflect multiple progenitors such as bone marrow or epithelial cells. *In vitro* [8] and *in vivo* [8, 9] studies supported the hypothesis that AECs could serve as a source of fibroblasts through a transdifferentiation mechanism of “epithelial-mesenchymal transition” (EMT). This phenomenon was observed during pulmonary fibrosis [7] but the principal origin of these cells is still controversial [8].

Different animal models have been developed to study the mechanisms involved in lung fibrogenesis and to evaluate potential therapies (bleomycin or fluorescein isothiocyanate administration, radiation damage, silica or asbestos instillation, transgenic mice, or viral vectors). Among these, bleomycin (BLM) administration is a widely used model and the best characterized in a variety of animals and through different routes of delivery [6]. BLM induce lung injuries via its ability to cause DNA strand breakage [10] and oxidant injury [11]. Even if the BLM-induced pulmonary fibrosis does not represent a strictly equivalent of IPF, it constitutes a polyvalent model that produces morphological alterations of lung fibrosis with a robust reproducibility [12]. It has allowed elucidating many of the biological processes involved in the pathogenesis of pulmonary fibrosis, including the contribution of TGF $\beta$  activation [12–15]. Coupled to transgenesis, this model was useful to decipher the role of genetic factors in the development of the disease [4]. Contrary to what has been described in original studies [16], reported disadvantages of BLM intratracheal (IT) model reside in its strain-dependence in mice and its resolving nature, with a variable and self-limiting fibrosis at late time-points [6]. Repetitive intratracheal administrations of BLM were described to mimic more effectively the chronic aspects of pulmonary fibrosis [17]. However, a recent systematic study, including lung function assessment during up to 6 months after a single insult of BLM in mice, has shown persistent degree of fibrosis at late time-points, with similarities to human IPF features [18]. In addition, a recent evaluation of the activated genes after BLM administration has suggested similarities between molecular signatures obtained during the late fibrosis phase and rapidly progressing IPF [19].

IT instillation, which is the most commonly used route for BLM administration in rodent, has the advantage of its low cost and its ability to deliver a well-defined dose to the lungs. Aerosol inhalation, in contrast, could result in a deposition in the upper respiratory tract. But, the most consistent disparity between these two methods relates to the BLM intrapulmonary distribution. While aerosol inhalation

allows a relatively homogeneous distribution of particles throughout the lungs, IT instillation can result in focally high doses of material or, at opposite, to nontreated lung area [20, 21]. Improvement of this point is still a matter of concern. We hypothesize that IT delivery by spraying may have the advantage of delivering a precise dose directly into the lungs and assuring a homogeneous distribution of BLM. This homogeneity could suppress the need of lesion-oriented sampling of lung tissue, simplifying and improving the sample-taking for biomolecular analyses. In the present study, we compared the time-course of histological alterations developed either by IT instillation or IT aerosolization of BLM in rats. This study reveals that aerosolization route allows a better distribution of fibrosis among lungs, with the presence of higher grade damages at later time-points.

## 2. Material and Methods

**2.1. Animals and Treatments.** All procedures met the standards of the national Belgian requirements regarding animal care and were carried out in accordance with the Animal Ethics and Welfare Committee of the University of Mons. All experiments were performed on 8-week-old male Wistar rats (about 250 g body weight) bred in our animal facility (accreditation number LA1500022). Rats were housed in cages at a room temperature (RT) of 22°C, with an ad libitum access to water and food. All efforts were made to minimize stress and animals were sedated before surgical procedure with an intraperitoneal injection of ketamine (Ketalar, Pfizer, 87.5 mg/kg of b.w.) and xylazine (Sigma-Aldrich, 12.5 mg/kg b.w.). For the present study, 47 Wistar rats received 2 IU/kg b.w. of BLM (Sanofi Aventia) intratracheally either by instillation ( $n = 22$ ; BLM diluted in 200  $\mu$ L saline buffer) or by aerosolization ( $n = 25$ ; BLM diluted in 100  $\mu$ L saline buffer). Sham ( $n = 17$ ) received the vehicle only (saline buffer) and controls ( $n = 3$ ) had no intervention. Instillation was realized by transtracheal injection using a 30 G needle at a flow of 40  $\mu$ L/second. Concerning intratracheal aerosolization, the oropharynx was first anesthetized using a local administration of lidocaine. A microsyringer (Model IA-1C, Penn-Century, US) connected to a High Pressure Syringe (Model FMJ-250, Penn-Century, US) was then inserted transorally into the tracheal lumen. The BLM solution was then aerosolized according manufacturer’s instructions, at a rate of about 15  $\mu$ L/second (particle size: 16–22  $\mu$ m; operating pressure: 3000 psi). This procedure was realized under fiberoptic laryngoscope to visualize epiglottis and ensure a good positioning of the microsyringer. Immediately after surgery, to minimize the risk of infection, rats received an intramuscular injection of antibiotic (Sodium Cefuroxime, Zinacef, 40 mg/kg b.w., GSK). At the end of the procedure, BLM and sham animals were sacrificed by exsanguination after Sodium Pentobarbital anesthesia (intraperitoneal injection of Nembutal, 60 mg/kg b.w., CEVA, Belgium) at days 3, 7, 14, 21, or 56 after BLM/saline administration.

**2.2. Histological Analysis.** Immediately after exsanguination, a bronchoalveolar lavage (using 40 mL sterile saline buffer) was performed for further biochemical investigations. Lungs

were then fixed by a transtracheal injection of a solution of Duboscq-Brasil fixator (10 mL). After ligation of the trachea and the opening of the ribcage, lungs were removed, incubated 48 hours in the Duboscq-Brasil fixator, and dehydrated. Lobes were then identified and embedded separately in paraffin. Sequential 5- $\mu\text{m}$  sections were made for each lobe from right and left lungs, using a Reichert Autocut 2040 microtome. Sections were then placed on silane-coated glass slides and stained with Trichrome Blue for morphological analysis. The number of total cells was calculated in the most cellularized field of 0.0625 mm<sup>2</sup> (with exclusion of bronchovascular axis) using a light microscope.

**2.2.1. Myofibroblast Quantification.** Myofibroblast staining was performed on deparaffinized and rehydrated lung sections by immunohistochemistry. Sections were immunostained using the streptavidin-biotin immunoperoxidase method (ABC method) as described in [22]. Briefly, the protocol included the following steps realized at RT in humid chamber: (1) a 1-hour incubation with a rabbit polyclonal antibody directed against  $\alpha$ -SMA (smooth muscle alpha-actin; 1:50) (2) incubation with a biotinylated goat anti-rabbit IgG antibody (1:50, Abcam, UK) for 30 min, and (3) incubation with ABC complexes (Dako, Denmark) for 30 minutes. Washing steps were performed in PBS. Bound peroxidase activity was visualized by incubation with DAB (3,3'-diaminobenzidine) 0.05% in PBS-0.02% H<sub>2</sub>O<sub>2</sub>. The sections were counterstained with Hemalun and Luxol fast blue and were finally mounted in a permanent medium. Controls for the specificity of immunolabeling included the omission of the primary antibody. Stained cells were numbered on ten fields of 0.0625 mm<sup>2</sup> (excluding bronchovascular axis), by random sampling and using a single blind method.

### 2.2.2. Fibrosis Quantification

**Determination of Collagen Surface.** The sections were observed on a Leitz Orthoplan microscope (10x magnification) equipped with a Ploem system for epi-illumination. Pictures were obtained by a PC-driven digital camera (Leica DC 300F, Leica Microsystems AG, Heerbrugg, Switzerland). For each of the lung regions, 3 fields of 0.3816 mm<sup>2</sup> were visualized. The computer software (KS 400 imaging system, Carl Zeiss vision, Hallbergmoos, Germany) allowed the morphometric analysis of images. Percentage of surface occupied by collagen was determined by calculating the ratio between blue and nonblue pixels after exclusion of alveolar airspace.

**Modified Ashcroft Scale.** Fibrosis was quantified using a modified Ashcroft scale (grade 0 to 8) designed for a standardized fibrosis evaluation in small animals [23]. Stages 1 to 3 are characterized by the presence of alveoli partly enlarged and rarefied. Gradual fibrotic changes are observed but fibrotic masses appear from rank 4. Single fibrotic masses become confluent at stage 5. Ranks 5 and 6 are characterized by variable alveolar septa which are mostly inexistent at stage 6. Lung structure is thus severely damaged at stage 5 and mostly not preserved at stage 6. Alveoli become partly obliterated

with fibrotic masses at grade 7 and complete occlusions are observed at stage 8. This procedure of fibrosis evaluation was applied on each lobe and two different counting methods were confronted. Firstly, the most affected part of the section was selected (MA-method) and secondly a random sampling was applied (RS-method). In both cases, the mean of 4 fields was calculated for each section. Each lobe section was analyzed using this procedure by two blinded observers.

**2.3. Statistical Analysis.** Results are presented as mean  $\pm$  SEM. Data concerning change in body weight, total cells, collagen surface, and myofibroblasts in the BLM instillation model were submitted to an analysis of variance (ANOVA) and a post hoc Duncan's test (SigmaStat/Plot 1.0 software, Germany). Fibrosis evolution over time (modified Ashcroft score) in both BLM models was compared using an ANOVA on ranks followed by a Kruskal Wallis test. The level of fibrotic damages after BLM instillation and aerosolization in late time-points was compared by the same method. Distribution in both lungs was compared by computing absolute differences between left and right scores. Levels of significance were taken as  $P < 0.05$ . Interobserver agreement was evaluated with the kappa index.

## 3. Results and Discussion

**3.1. BLM Instillation Model Allowed a Gradual Fibrosis Preceded by an Inflammatory Phase.** As reviewed in [6, 24], histological and biochemical characteristics of fibrosis are usually detectable in the BLM IT model around day 14, with a maximal response around days 21–28. However, histological damages are reported to be more variable at later time-points. Indeed, while original studies demonstrated the persistence of fibrosis for a few months, others described a resolution of the process beyond 28 days. With regards to those discrepancies, it was therefore necessary to first characterize the time-course of histological lesions after BLM instillation in our experimental conditions to facilitate subsequent comparisons. To this aim, fibrosis was assessed at 3, 7, 14, 21, and 56 days after BLM IT instillation (3–56 d) by quantification of the total cell number, percentage of surface occupied by collagen, and a modified Ashcroft score (Figure 1). Data about animal body weight, water consumption, and urine volume, measured in metabolic cages, are presented in Supplementary Material available online at <http://dx.doi.org/10.1155/2015/198418> (Figure S1). Despite a slight decrease of body weight after BLM administration, no statistical difference between sham and BLM animals can be reported concerning those parameters. Macroscopic observation of lungs from BLM rats revealed the presence of atelectatic violaceous bands and white area of various sizes which alternated with apparently healthy lung tissue. Microscopic visualization confirmed the heterogeneity of histological lesions. Some lobes were totally devoid of damages and others exhibited inflammatory infiltrates centered on bronchovascular axes at day 3 and day 7. Inflammation decreased at day 14 giving rise to fibrotic lesions (Figure 1(a)). Total cell number (Figure 1(b)) was increased in BLM animals, with a maximum at days 14–21 ( $P < 0.05$ ;

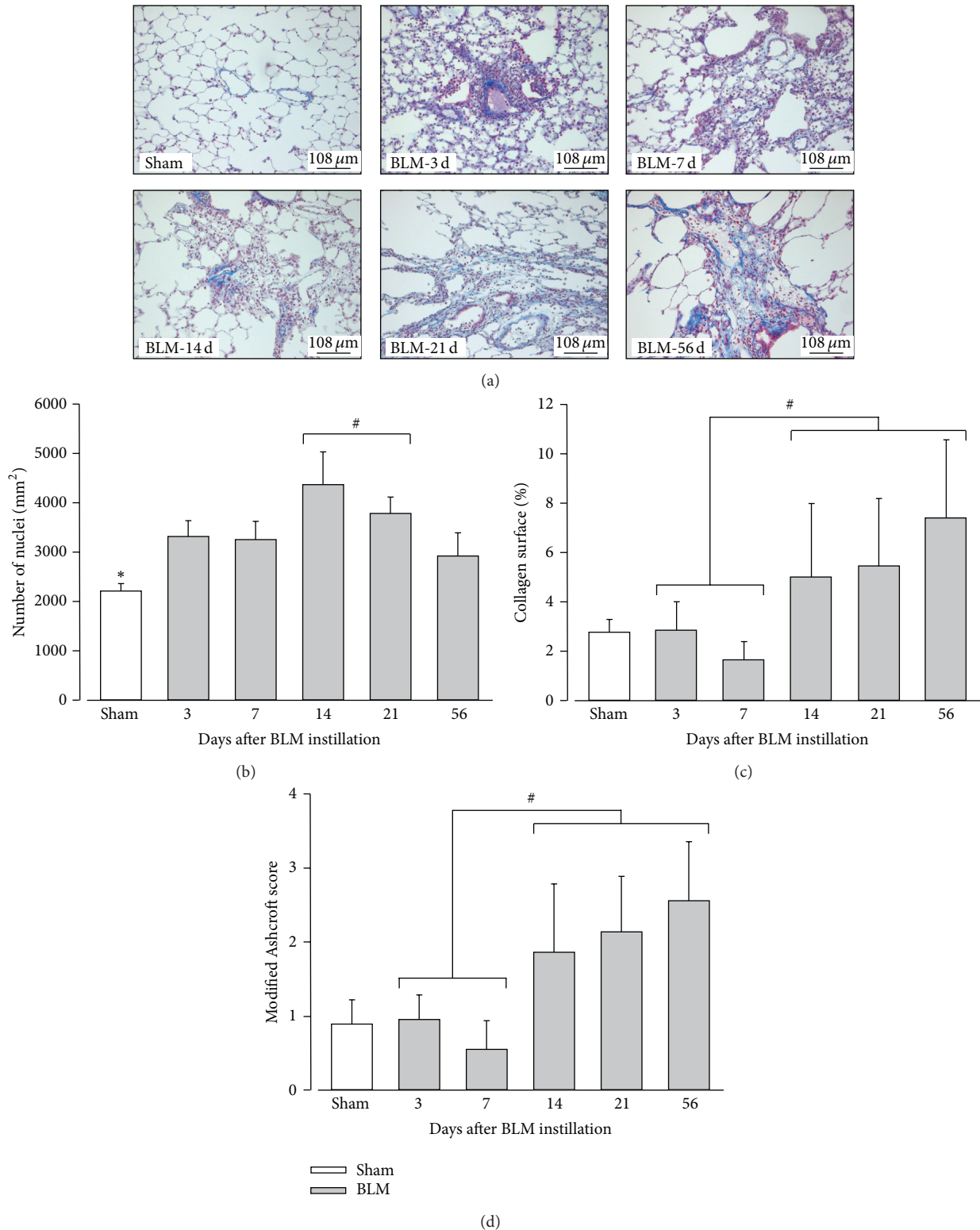
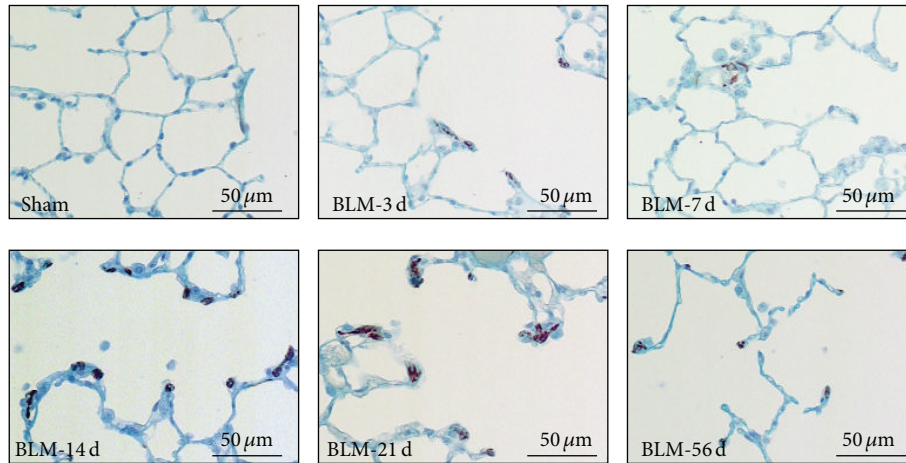
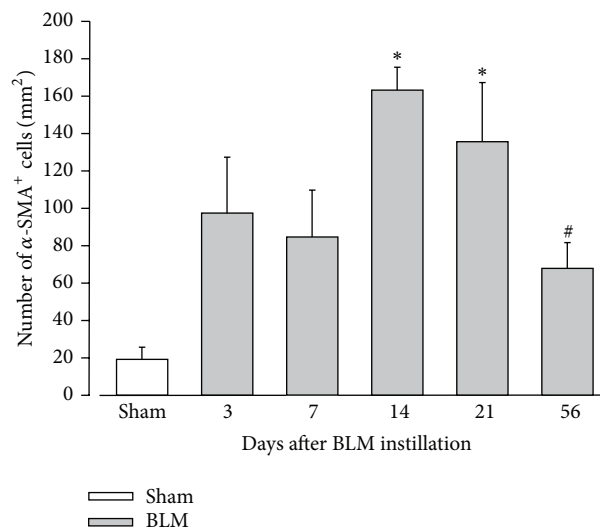


FIGURE 1: Evolution of histological alterations in rat lungs after BLM instillation. (a) Trichrome Blue staining in sham animals and in treated rats, 3, 7, 14, 21, and 56 days (3 d, 7 d, 14 d, 21 d, and 56 d) after bleomycin (BLM) instillation. Collagen is stained in blue and cells in red. Magnification: 100x. (b) Average number of cells per mm<sup>2</sup> lung surface in sham animals (in white) and 3, 7, 14, 21, and 56 days after BLM instillation (in grey). (c) Average percentage (%) of lung area occupied by collagen in sham animals (in white) and 3, 7, 14, 21, and 56 days after BLM instillation (in grey). (d) Quantification of lung fibrosis using a modified Ashcroft score in sham animals (in white) and 3, 7, 14, 21, and 56 days after BLM instillation (in grey; *n* = 3 per time-point). (b) \**P* < 0.05 Sham versus every other time-points; #*P* < 0.05 (14 + 21 d) versus (3, 7, and 56 d); ANOVA one way followed by Duncan's test. (c-d) #*P* < 0.05 early (3–7 d) versus later (14 to 56 d) time-points; ANOVA one way followed by a Duncan's test.



(a)



(b)

FIGURE 2: Evolution of myofibroblast number after BLM instillation. (a) Representative fields of lung sections from sham and BLM rats 3, 7, 14, 21, and 56 days after instillation. The immunohistochemistry was performed using an anti- $\alpha$ SMA (smooth muscle actin) antibody (bruin staining) and countercolored with Hemalun and Luxol blue (blue staining). (b) Average number of  $\alpha$ SMA-positive ( $\alpha$ -SMA<sup>+</sup>) cells in lung sections from sham (in white) and BLM (in grey;  $n = 3$  per time-point) rats at 3, 7, 14, 21, and 56 days after instillation. \* $P < 0.05$  versus Sham; ANOVA one way followed by Duncan's Test. # $P < 0.05$  versus 14 d; ANOVA one way followed by Duncan's Test.

14–21 d versus 3–7 d and versus 56 d). Because these cells appeared to exhibit different morphological characteristics upon time, the presence of myofibroblasts was assessed by  $\alpha$ -SMA immunostaining (Figure 2). Number of SMA-positive cells was significantly increased 14 and 21 days after BLM instillation synchronously with the beginning of fibrosis development. Then this number decreased significantly at day 56. So, the collagen-occupied surface (Figure 1(c)) and modified Ashcroft score (Figure 1(d)) were significantly different from days 14 to 56 when compared to early time-points (3–7 d). Collagen surface reached  $5.0 \pm 3.0$ ,  $5.4 \pm 2.7$ , and  $7.4 \pm 3.2\%$ , respectively, at 14, 21, and 56 days after BLM administration, whereas lungs from sham animals are characterized by a collagen surface of  $2.7 \pm 0.5\%$ . A modified Ashcroft score ranging between ranks 2 and 3 at

later time-points indicated the presence of fibrotic changes accompanied by partly enlarged and rarefied alveoli [23].

In accordance with the literature, BLM IT instillation leads firstly to an inflammatory phase that precedes a gradual development of fibrosis, with a transition occurring around day 14 after BLM delivery. Although the inflammatory process was not investigated specifically in our study by cell counting, total protein measurement in bronchoalveolar fluid, or lung TGF $\beta$  expression, inflammatory infiltrates were observed at early time-points. Total cell number mostly reflects alveolar inflammatory cells or active fibrosis, before and after day 14, respectively. This time-point is characterized by a significantly higher number of total cells, including in particular myofibroblasts, consistent with their previously reported role in collagen deposition [7, 25].

In our experimental conditions, fibrosis characteristics can be observed until 56 days after BLM instillation. The resolution of the process is therefore not observed at this time-point, even if its activity was decreasing based on the myofibroblast number. Further studies in later time-points are necessary to elucidate discrepancies about the resolving nature of this model. Via this route of administration, fibrotic lesions were, however, heterogeneously distributed, hampering interpretation of subsequent molecular analysis or evaluation of therapeutic strategies based on a random tissue-sampling.

**3.2. BLM IT Aerosolization Leads to a Progressive and More Homogeneously Distributed Fibrosis.** To improve distribution of fibrotic damages in the BLM model, we compare IT instillation to IT aerosolization of this drug. As a preliminary test, macroscopic analysis after Lissamine Green IT aerosolization has shown a homogeneous distribution of the dye among lungs. Histological alterations were then assessed after 3, 7, 14, 21, and 56 days after either BLM IT instillation or aerosolization. Data about animal body weight, water consumption, and urine volume in aerosolized animals are presented in Supplementary Material (Figure S2). As presented in Figure 3, we note that weight loss upon the two first days after BLM delivery was more pronounced in aerosolized rats as compared to instilled animals ( $P < 0.005$ ). Microphotographs of the most representative pulmonary lesions at each time-point are illustrated in Figure 4 as well as the total cell number and modified Ashcroft score in the aerosolized group. Comparison of fibrosis quantification using the modified Ashcroft score in both models is presented in Figure 5. As described after BLM instillation, inflammatory infiltrates were observed at early time-points after BLM aerosolization (Figure 4(a), 3–7 d), followed by a transition at day 14 to a fibrosis state. Total cell number reached a peak at this particular time-point (Figure 4(c)). In addition, perilesional emphysema (Figure 4, 14–56 d) and peribronchic lesions (Figure 4(b)) were present in both models at late time-points (14 to 56 d). A gradual increase of fibrotic changes was observed, reaching a significantly higher modified Ashcroft score at late time-points in both models, as compared to sham animals (Figure 5). Modified Ashcroft score differed between late and early time-points in both models when fields from the most affected part of each lobe were considered for quantification (MA-method, Figure 5(b)). Values obtained were on average  $1.3 \pm 0.1$  in shams and  $1.8 \pm 0.1$ ,  $1.9 \pm 0.4$ ,  $2.7 \pm 0.3$ ,  $2.8 \pm 0.5$ , and  $3.2 \pm 0.4$  in the instillation groups at days 3, 7, 14, 21, and 56, respectively. Corresponding values after aerosolization were  $1.4 \pm 0.1$ ,  $1.9 \pm 0.2$ ,  $3.8 \pm 0.1$ ,  $4.4 \pm 0.12$ , and  $4.6 \pm 0.3$  at the same time-points in BLM animals.

When randomly chosen fields were considered (RS-method, Figure 5(a)), the modified Ashcroft scores from late time-points were significantly higher compared to early time-points in aerosolized BLM animals but not in IT instilled rats. So, the mean value of the modified Ashcroft score for the aerosolized group reached  $2.3 \pm 0.2$  in the later time-point (day 56) but only  $0.9 \pm 0.1$  for the instilled group. These results could be explained by the presence of more focal lesions in lungs from instilled animal. Indeed, in average, lesions appeared more moderate when fields were randomly chosen,

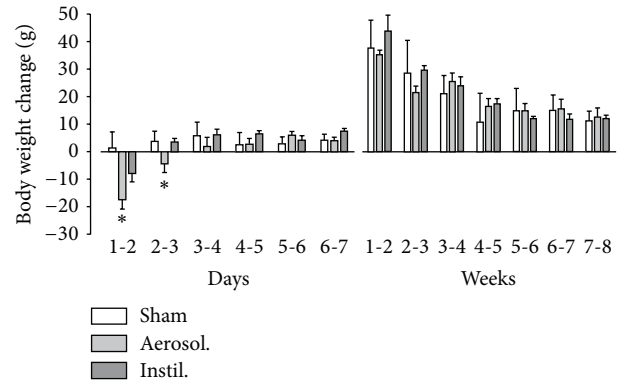


FIGURE 3: Time-course of body weight change after BLM administration. Data are represented as mean  $\pm$  SEM for the sham group ( $n = 17$ ) and after BLM aerosolization ( $n = 25$ ) or instillation ( $n = 22$ ). Observations were realized the first week daily and weekly then after up to day 56. \*  $P < 0.05$  Aerosol. versus Instil. and Sham; ANOVA one way followed by Duncan's Test.

likely due to the presence of lung area without any fibrotic lesion.

Data from both quantification methods therefore indicate a more homogeneous distribution of fibrotic lesions after IT aerosolization as compared to IT instillation. This was previously described in a rabbit model of fibrosis consisting in BLM intranasal nebulization [26]. This route was also shown to allow a more homogeneous distribution of material into the lungs in different species including mice [20, 21]. The oropharyngeal aspiration is another method often used in mice and consisting of pipetting BLM into the back of the oral cavity [27, 28]. Gravity and natural inhalation by the animal draw the liquid into the lung [29]. This method was shown to lead to a better distributed fibrotic area among lungs in mice and rats, compared to the intranasal method [30]. IT aerosolization using a sprayer has, however, the advantages of (i) providing a more direct access into the lungs and avoiding material loss in the upper respiratory tract and (ii) delivering solutions as microdroplets allowing a more peripheral and diffused material deposition as compared to liquids. In rats, procedures for intubation and aerosol delivery were described in [31, 32]. The usefulness of this noninvasive endotracheal route was demonstrated in mice by delivery of a suspension of fluorescent nanospheres [33]. IT aerosol delivery was therefore used to administer BLM in mice to model lung fibrosis [19, 34] and, in another context, to deliver siRNAs to modulate lung immunopathology in a murine model of tuberculosis [35, 36]. However, in mouse and especially in rats, IT instillation, rather than spraying, remains a frequently used route for BLM models [37–39].

In addition, our study reveals that interobserver agreement was better after aerosolization than instillation. So, in the aerosolized group, the agreement was moderate or substantial depending on the method used (MA or RS), whereas the kappa index disclosed only to a slight agreement for the instillation group whatever the field selection. The difference of fibrotic-lesion distribution between lungs

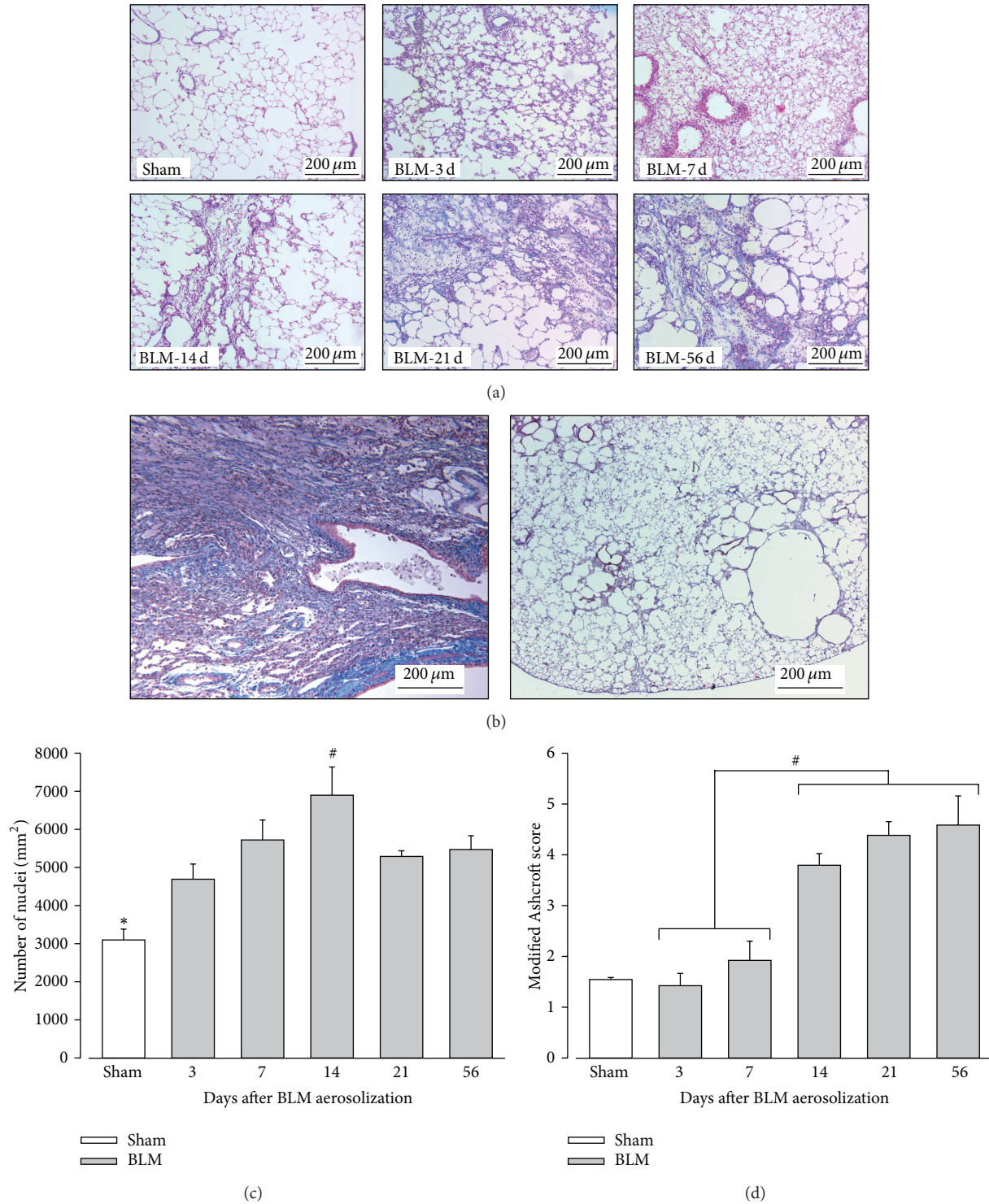


FIGURE 4: Evolution of pulmonary histopathological alterations after BLM aerosolization. (a) Trichrome Blue staining in sham animals and 3, 7, 14, 21, and 56 days (3 d, 7 d, 14 d, 21 d, and 56 d) after bleomycin (BLM) aerosolization. Collagen is stained in blue and cells in red. Magnification: 100x. (b) Left panel: peribronchial lesions are present at late time-points (days 14, 21, and 56) as after BLM instillation. Right panel: destructive lesions are observed at days 14 and 56. (c) Average number of cells per mm<sup>2</sup> lung surface in sham animals (in white) and 3, 7, 14, 21, and 56 days after BLM aerosolization (in grey). (d) Quantification of lung fibrosis using a modified Ashcroft score in sham animals (in white) and 3, 7, 14, 21, and 56 days after BLM aerosolization (in grey; n = 5 per time-point). (c) \*P < 0.05 Sham versus every other time-points; #P < 0.05: 14 d versus 3 d and 21 d; ANOVA one way followed by Duncan's test. (d) \*P < 0.05 early (3–7 d) versus late (14 to 56 d) time-points; ANOVA one way followed by a Duncan's test.

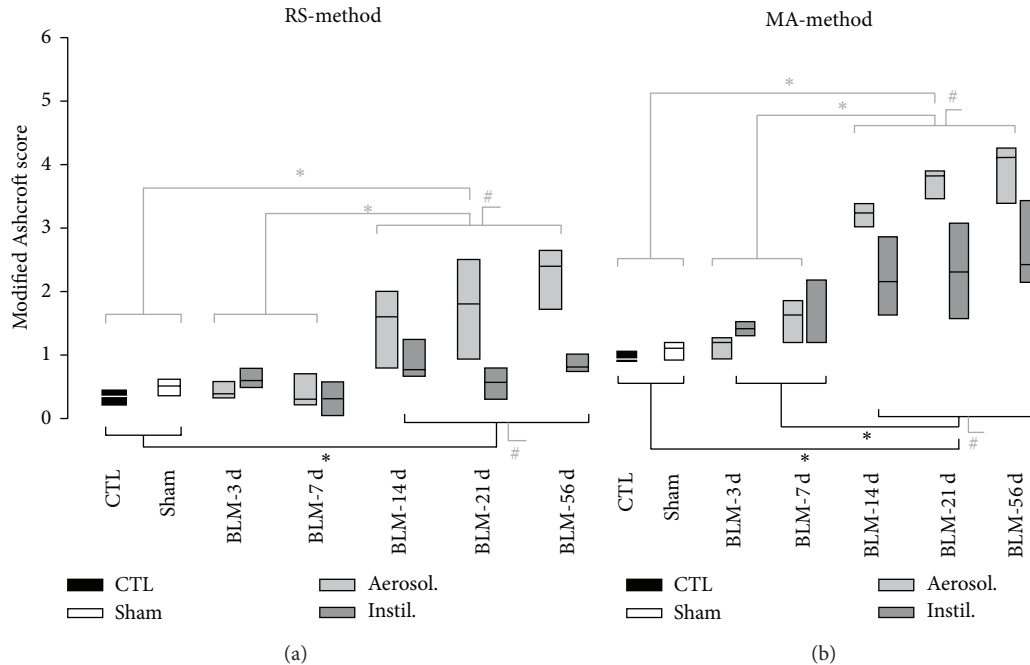


FIGURE 5: Comparison of fibrosis evolution after BLM instillation or aerosolization. Fibrosis was quantified in each lung lobe using a modified Ashcroft score, in control (CTL, in black), sham (in white), and BLM animals, at 3, 7, 14, 21, and 56 days after BLM instillation (Instil., in dark grey) or aerosolization (Aerosol., in grey). Two different methods were applied for quantification, as described in Section 2: RS- (random sampling-) method (a) and MA- (most affected field-) method (b). For statistical analysis, data from CTL and sham animals were grouped (CTL + sham) as well as results concerning BLM rats at early (3–7 d) and late (14 to 56 d) time-points. Grouped means are not different as compared by a Mann Whitney rank sum tests (CTL versus Sham) or using Kruskal Wallis one way analysis (3 versus 7 d; 14 versus 21 versus 56 d). Groups were compared as indicated, using a Kruskal Wallis one way (pairwise multiple comparison of means, Dunn's method). CTL:  $n = 3$ ; Sham:  $n = 17$ ; BLM Instil.:  $n = 22$ ; BLM Aerosol.:  $n = 25$ . \*  $P < 0.001$ : late versus early versus CTL + sham; #  $P < 0.001$ : Aerosol. versus Instil. versus CTL + sham at late time-points. Kappa index representing interobserver agreement was for the instillation model of 0.12 and 0.09 (RS-method and the MA-method, resp.) and for the aerosolization model 0.64 and 0.43.

(absolute difference between modified Ashcroft score in left and right lungs) is represented at Figure 6. Data outside the 90% confidence interval calculated from controls and sham values are 3 times more frequent in the instilled than in the aerosolized groups. Aerosolized animals exhibited a moderate difference between right and left lungs in terms of fibrosis, with only 16% of the values above the threshold (instead of 10% for controls and sham animals).

**3.3. BLM IT Aerosolization Allowed the Persistence of More Severe Fibrotic Lesions upon Time.** The increased loss of body weight induced by the aerosol method (Figure 3) suggests that pulmonary lesions have a higher systemic effect at least during the first few days after treatment. Moreover, as presented in Figure 5, the modified Ashcroft scores at late time-points (14–56 d) were significantly higher in the aerosolized groups independently of the quantification method used. When the RS-method is considered (Figure 5(a)), this difference could be explained by the presence of unaffected area in instilled lungs leading to a lowering of the mean Ashcroft score. However, on average, a higher score was also observed in the most affected lung area (MA-method) from aerosolized animals (Figure 5(b)) indicating the development of a more severe fibrosis (modified Ashcroft score between 4 and 5)

upon using this route of administration. In accordance with these data, we note that destructive lesions are only observed in the aerosolization group at days 14 and 56 (Figure 4(b)). We suggest that, with aerosolization, a better penetration of BLM into small airways and more scattered AECs alterations could lead to an amplified myofibroblastic stimulation and a subsequent increase in fibrotic tissue deposition. At the opposite, with instillation, the overwhelming of the alveoli could also decrease the oxygen pressure in the vicinity of BLM molecules and thereby reduce its toxicity. Further studies will be necessary to clarify the relationship between increased fibrotic damages at later time-points and more dispersed initial alterations.

## 4. Conclusion

Both intratracheal instillation and aerosolization of BLM induce the development of fibrosis following an initial inflammatory phase. However, the fibrotic process is more localized after BLM instillation and is restricted to overwhelmed area, which is a major drawback for the tissue sampling. In the present study, we demonstrate that the IT aerosolization route allows a more homogeneous distribution of fibrosis and is associated with more severe lesions upon time. As compared

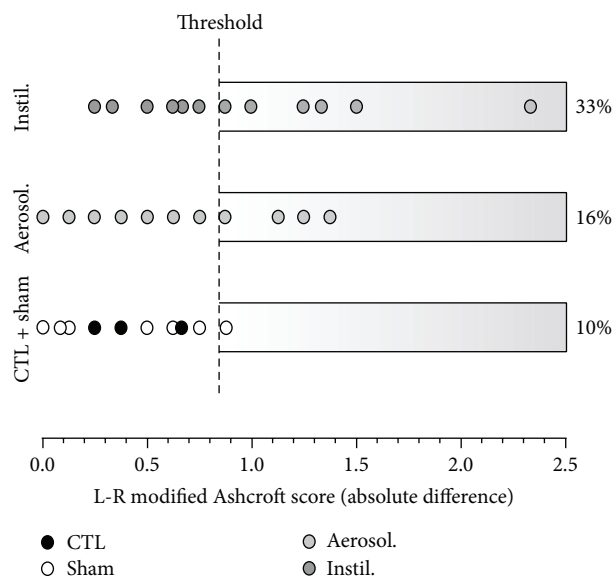


FIGURE 6: Difference between left and right lung fibrotic lesions after BLM aerosolization or instillation. This graph represents the modified Ashcroft score absolute difference between L and R lungs, for control and sham animals (CTL + sham; in white) and after BLM aerosolization (Aerosol., in grey) or instillation (Instil., in dark grey) at all time-points. Quantification was made using the MA-method by two observers. Each circle represents the mean between values obtained by both observers for each animal. The threshold was fixed to include 90% of the values of the CTL + sham group (confidence interval calculated as mean  $\pm$  1.66 SEM). 16% and 33% of the values are above this threshold for instilled and aerosolized animals, respectively. CTL + sham:  $n = 20$ ; BLM Instil.:  $n = 22$ ; BLM Aerosol.:  $n = 25$ .

to intranasal delivery, the IT spraying allows the delivery of a precise dose, avoiding drug loss in upper respiratory tracts.

Finally, it is necessary to consider whether BLM rodent models could be directly applicable to human IPF. In terms of histological alterations, both conditions result in the development of fibroblastic foci. In IPF, their location is heterogeneous and mostly basal and subpleural. In contrast, lesions are initially bronchocentric in several BLM IT models, although our conditions led to more peripheral damages. Moreover, BLM rodent models and IPF do not share a similar pattern of development and progression, and functional assessment has to be further realized to better understand similarities and differences between the two pathological states (reviewed in [24]).

In conclusion, despite the fact that BLM delivery in rodent does not perfectly reproduce IPF, it still constitutes a well-characterized model of pulmonary fibrosis which is still widely used today. IT aerosolization is a good alternative to the instillation method, allowing a homogeneous fibrosis thus limiting sample-dependent variability for subsequent biochemical analysis or testing of new therapeutic options.

## Conflict of Interests

The authors declare that there is no conflict of interests regarding the publication of this paper.

## Authors' Contribution

A. Robbe and A. Tassin contributed equally as first authors.

## Acknowledgments

The authors acknowledge V. Jenart for technical assistance during *in vivo* experiments as well as for her help for data analysis. The authors thank B. Blairon for his technical assistance and figure realization.

## References

- [1] H. V. Woodcock and T. M. Maher, "The treatment of idiopathic pulmonary fibrosis," *F1000Prime Reports*, vol. 6, article 16, 2014.
- [2] J. R. Covey and E. E. Mancl, "Recent evidence for pharmacological treatment of idiopathic pulmonary fibrosis," *Annals of Pharmacotherapy*, vol. 48, no. 12, pp. 1611–1619, 2014.
- [3] S. D. Nathan, O. A. Shlobin, N. Weir et al., "Long-term course and prognosis of idiopathic pulmonary fibrosis in the new millennium," *Chest*, vol. 140, no. 1, pp. 221–229, 2011.
- [4] I. V. Yang, "Epigenomics of idiopathic pulmonary fibrosis," *Epigenomics*, vol. 4, no. 2, pp. 195–203, 2012.
- [5] C. Kuhn III, J. Boldt, T. E. King Jr., E. Crouch, T. Vartio, and J. A. McDonald, "An immunohistochemical study of architectural remodeling and connective tissue synthesis in pulmonary fibrosis," *American Review of Respiratory Disease*, vol. 140, no. 6, pp. 1693–1703, 1989.
- [6] B. B. Moore and C. M. Hogaboam, "Murine models of pulmonary fibrosis," *American Journal of Physiology—Lung Cellular and Molecular Physiology*, vol. 294, no. 2, pp. L152–L160, 2008.
- [7] B. C. Willis, R. M. DuBois, and Z. Borok, "Epithelial origin of myofibroblasts during fibrosis in the lung," *Proceedings of the American Thoracic Society*, vol. 3, no. 4, pp. 377–382, 2006.
- [8] B. C. Willis, J. M. Liebler, K. Luby-Phelps et al., "Induction of epithelial-mesenchymal transition in alveolar epithelial cells by transforming growth factor- $\beta$ 1: potential role in idiopathic pulmonary fibrosis," *The American Journal of Pathology*, vol. 166, no. 5, pp. 1321–1332, 2005.
- [9] K. K. Kim, M. C. Kugler, P. J. Wolters et al., "Alveolar epithelial cell mesenchymal transition develops *in vivo* during pulmonary fibrosis and is regulated by the extracellular matrix," *Proceedings of the National Academy of Sciences of the United States of America*, vol. 103, no. 35, pp. 13180–13185, 2006.
- [10] J. W. Lown and S. K. Sim, "The mechanism of the bleomycin-induced cleavage of DNA," *Biochemical and Biophysical Research Communications*, vol. 77, no. 4, pp. 1150–1157, 1977.
- [11] E. A. Sausville, J. Peisach, and S. B. Horwitz, "A role for ferrous ion and oxygen in the degradation of DNA by bleomycin," *Biochemical and Biophysical Research Communications*, vol. 73, no. 3, pp. 814–822, 1976.
- [12] F. Chua, J. Gaudie, and G. J. Laurent, "Pulmonary fibrosis: searching for model answers," *The American Journal of Respiratory Cell and Molecular Biology*, vol. 33, no. 1, pp. 9–13, 2005.
- [13] M. Kolb, P. J. Margetts, T. Galt et al., "Transient transgene expression of decorin in the lung reduces the fibrotic response to bleomycin," *American Journal of Respiratory and Critical Care Medicine*, vol. 163, no. 3, pp. 770–777, 2001.

- [14] S. N. Giri, D. M. Hyde, and M. A. Hollinger, "Effect of antibody to transforming growth factor  $\beta$  on bleomycin induced accumulation of lung collagen in mice," *Thorax*, vol. 48, no. 10, pp. 959–966, 1993.
- [15] Q. Wang, Y. Wang, D. M. Hyde et al., "Reduction of bleomycin induced lung fibrosis by transforming growth factor  $\beta$  soluble receptor in hamsters," *Thorax*, vol. 54, no. 9, pp. 805–812, 1999.
- [16] R. S. Thrall, J. R. McCormick, R. M. Jack, R. A. McReynolds, and P. A. Ward, "Bleomycin-induced pulmonary fibrosis in the rat. Inhibition by indomethacin," *The American Journal of Pathology*, vol. 95, no. 1, pp. 117–130, 1979.
- [17] M. A. Mouratis and V. Aidinis, "Modeling pulmonary fibrosis with bleomycin," *Current Opinion in Pulmonary Medicine*, vol. 17, no. 5, pp. 355–361, 2011.
- [18] N. Limjunyawong, W. Mitzner, and M. R. Horton, "A mouse model of chronic idiopathic pulmonary fibrosis," *Physiological Reports*, vol. 2, no. 2, Article ID e00249, 2014.
- [19] R. Peng, S. Sridhar, G. Tyagi et al., "Bleomycin induces molecular changes directly relevant to idiopathic pulmonary fibrosis: a model for 'active' disease," *PLoS ONE*, vol. 8, no. 4, Article ID e59348, 2013.
- [20] K. E. Driscoll, D. L. Costa, G. Hatch et al., "Intratracheal instillation as an exposure technique for the evaluation of respiratory tract toxicity: uses and limitations," *Toxicological Sciences*, vol. 55, no. 1, pp. 24–35, 2000.
- [21] P. Vogel, V. R. Rivera, M. L. M. Pitt, and M. A. Poli, "Comparison of the pulmonary distribution and efficacy of antibodies given to mice by intratracheal instillation or aerosol inhalation," *Laboratory Animal Science*, vol. 46, no. 5, pp. 516–523, 1996.
- [22] D. Vanstherthem, A. Gossiaux, A.-E. Declèves et al., "Expression of nestin, vimentin, and NCAM by renal interstitial cells after ischemic tubular injury," *Journal of Biomedicine and Biotechnology*, vol. 2010, Article ID 193259, 10 pages, 2010.
- [23] R.-H. Hübner, W. Gitter, N. E. El Mokhtari et al., "Standardized quantification of pulmonary fibrosis in histological samples," *BioTechniques*, vol. 44, no. 4, pp. 507–517, 2008.
- [24] J. D. Williamson, L. R. Sadofsky, and S. P. Hart, "The pathogenesis of bleomycin-induced lung injury in animals and its applicability to human idiopathic pulmonary fibrosis," *Experimental Lung Research*, 2014.
- [25] S. H. Phan, "The myofibroblast in pulmonary fibrosis," *Chest*, vol. 122, pp. 286S–289S, 2002.
- [26] A. Günther, N. Lübke, M. Ermert et al., "Prevention of bleomycin-induced lung fibrosis by aerosolization of heparin or urokinase in rabbits," *The American Journal of Respiratory and Critical Care Medicine*, vol. 168, no. 11, pp. 1358–1365, 2003.
- [27] W. M. Foster, D. M. Walters, M. Longphre, K. Macri, and L. M. Miller, "Methodology for the measurement of mucociliary function in the mouse by scintigraphy," *Journal of Applied Physiology*, vol. 90, no. 3, pp. 1111–1117, 2001.
- [28] V. de Vooght, J. A. J. Vanoirbeek, S. Haenen, E. Verbeken, B. Nemery, and P. H. M. Hoet, "Oropharyngeal aspiration: an alternative route for challenging in a mouse model of chemical-induced asthma," *Toxicology*, vol. 259, no. 1-2, pp. 84–89, 2009.
- [29] D. M. Walters and S. R. Kleeberger, "Mouse models of bleomycin-induced pulmonary fibrosis," in *Current Protocols in Pharmacology*, chapter 5:unit 5.46, 2008.
- [30] C. Egger, C. Cagnet, C. Gérard et al., "Administration of bleomycin via the oropharyngeal aspiration route leads to sustained lung fibrosis in mice and rats as quantified by UTE-MRI and histology," *PLoS ONE*, vol. 8, no. 5, Article ID e63432, 2013.
- [31] R. Lizio, A. Westhof, C.-M. Lehr, and T. Klenner, "Oral endotracheal intubation of rats for intratracheal instillation and aerosol drug delivery," *Laboratory Animals*, vol. 35, no. 3, pp. 257–260, 2001.
- [32] R. Lizio, D. Marx, T. Nolte et al., "Development of a new aerosol delivery system for systemic pulmonary delivery in anaesthetized and orotracheal intubated rats," *Laboratory Animals*, vol. 35, no. 3, pp. 261–270, 2001.
- [33] M. Bivas-Benita, R. Zwier, H. E. Junginger, and G. Borchard, "Non-invasive pulmonary aerosol delivery in mice by the endotracheal route," *European Journal of Pharmaceutics and Biopharmaceutics*, vol. 61, no. 3, pp. 214–218, 2005.
- [34] J. E. Phillips, R. Peng, L. Burns et al., "Bleomycin induced lung fibrosis increases work of breathing in the mouse," *Pulmonary Pharmacology and Therapeutics*, vol. 25, no. 4, pp. 281–285, 2012.
- [35] A. G. Rosas-Taraco, D. M. Higgins, J. Sánchez-Campillo, E. J. Lee, I. M. Orme, and M. González-Juarrero, "Intrapulmonary delivery of XCL1-targeting small interfering RNA in mice chronically infected with *Mycobacterium tuberculosis*," *The American Journal of Respiratory Cell and Molecular Biology*, vol. 41, no. 2, pp. 136–145, 2009.
- [36] A. G. Rosas-Taraco, D. M. Higgins, J. Sánchez-Campillo, E. J. Lee, I. M. Orme, and M. González-Juarrero, "Local pulmonary immunotherapy with siRNA targeting TGF $\beta$ 1 enhances antimicrobial capacity in *Mycobacterium tuberculosis* infected mice," *Tuberculosis*, vol. 91, no. 1, pp. 98–106, 2011.
- [37] A. Gazdhar, I. Grad, L. Tamò, M. Gugger, A. Feki, and T. Geiser, "The secretome of induced pluripotent stem cells reduces lung fibrosis in part by hepatocyte growth factor," *Stem Cell Research & Therapy*, vol. 5, article 123, 2014.
- [38] Q. Ye, Y. Li, H. Jiang et al., "Prevention of pulmonary fibrosis via trichostatin A (TSA) in bleomycin induced rats," *Sarcoidosis, Vasculitis and Diffuse Lung Diseases*, vol. 31, pp. 219–226, 2014.
- [39] Z. I. Cleveland, R. S. Virgincar, Y. Qi, S. H. Robertson, S. Degan, and B. Driehuys, "3D MRI of impaired hyperpolarized  $^{129}\text{Xe}$  uptake in a rat model of pulmonary fibrosis," *NMR in Biomedicine*, vol. 27, no. 12, pp. 1502–1514, 2014.

## Research Article

# Methylglyoxal Induced Basophilic Spindle Cells with Podoplanin at the Surface of Peritoneum in Rat Peritoneal Dialysis Model

Ichiro Hirahara,<sup>1</sup> Hideki Sato,<sup>2</sup> Toshimi Imai,<sup>1</sup> Akira Onishi,<sup>1</sup> Yoshiyuki Morishita,<sup>1</sup> Shigeaki Muto,<sup>1</sup> Eiji Kusano,<sup>1</sup> and Daisuke Nagata<sup>1</sup>

<sup>1</sup>Department of Nephrology, Jichi Medical University, 3311-1 Yakushiji, Shimotsuke, Tochigi 329-0498, Japan

<sup>2</sup>Terumo Core Technology Center, 1500 Inokuchi, Nakai-machi, Ashigarakami-gun, Kanagawa 259-0151, Japan

Correspondence should be addressed to Ichiro Hirahara; hirahara@rpf.jp

Received 27 September 2014; Accepted 16 December 2014

Academic Editor: Andrea Vecchione

Copyright © 2015 Ichiro Hirahara et al. This is an open access article distributed under the Creative Commons Attribution License, which permits unrestricted use, distribution, and reproduction in any medium, provided the original work is properly cited.

Peritoneal dialysis (PD) is a common treatment for patients with reduced or absent renal function. Long-term PD leads to peritoneal injury with structural changes and functional decline. At worst, peritoneal injury leads to encapsulating peritoneal sclerosis (EPS), which is a serious complication of PD. In order to carry out PD safely, it is important to define the mechanism of progression of peritoneal injury and EPS. We prepared rat models of peritoneal injury by intraperitoneal administration of glucose degradation products, such as methylglyoxal (MGO) or formaldehyde (FA), chlorhexidine gluconate (CG), and talc. In rats treated with MGO, peritoneal fibrous thickening with the appearance of basophilic spindle cells with podoplanin, cytokeratin, and  $\alpha$ -smooth muscle actin at the surface of the peritoneum was observed. These cells may have been derived from mesothelial cells by epithelial-to-mesenchymal transition. In FA- or CG-treated rats, the peritoneum was thickened, and mesothelial cells were absent at the surface of the peritoneum. The CG- or MGO-treated rats presented with a so-called abdominal cocoon. In the talc-treated rats, extensive peritoneal adhesion and peritoneal thickening were observed. MGO-induced peritoneal injury model may reflect human histopathology and be suitable to analyze the mechanism of progression of peritoneal injury and EPS.

## 1. Introduction

Long-term peritoneal dialysis (PD) leads to peritoneal injury with functional decline, such as ultrafiltration loss. Peritoneal injury is often accompanied by histological changes, such as peritoneal fibrosis and sclerosis. At an early stage of peritoneal injury, epithelial-to-mesenchymal transition (EMT) of mesothelial cells is induced at the surface of the peritoneum, followed by evident diffuse fibrous thickening, neovascularization, and mononuclear cell infiltration [1, 2]. At worst, peritoneal injury leads to encapsulating peritoneal sclerosis (EPS), a serious complication of PD [3–7]. At advanced stages of EPS, the small intestine adheres and is encapsulated within a thick collagen-rich peritoneum to form a cocoon-like mass. EPS is associated with not only deterioration of peritoneal function but also clinical symptoms, such as ileus. EPS occurs in about 0.4%–3.3% of patients who undergo PD. However, EPS has a high mortality rate, and about half of the patients

with EPS die [4–7]. The causes of peritoneal injury and EPS have not been clarified, but they appear to develop through the interaction of multiple factors, such as infection with bacteria or fungi resulting in peritonitis; antiseptics; exogenous materials like particulates and plasticizers; and continuous exposure to nonphysiological PD solutions having high concentrations of glucose and glucose degradation products (GDPs), low pH, and high osmolarity [4, 7]. These factors may induce fibrosis, sclerosis, inflammation, angiogenesis, and vasculopathy in the peritoneum. The administration of corticosteroids, tamoxifen, and immunosuppressive agents and total parenteral nutrition are effective in an early stage of EPS development [4–6]. However, for an advanced stage of EPS, in which bowel adhesions have formed, the only effective therapeutic method is surgical dissection of the encapsulated peritoneum; this must be performed by skilled surgeons using specialized techniques [4–6]. Therefore, there is a compelling need for methods for the early diagnosis of

EPS. Animal models are often used to define the mechanism of progression of peritoneal injury and the evaluation of drugs or screening of predictive markers for EPS.

The aim of this study is to advance a peritoneal injury animal model reflecting human histopathology in order to elucidate the mechanism of progression of peritoneal injury. To perform PD safely, it is important to define the mechanism of pathogenesis and progression of peritoneal injury and EPS, and then it is necessary to prevent peritoneal injury from developing into EPS.

## 2. Materials and Methods

*2.1. Preparation of Animal Models of Peritoneal Injury.* We prepared four animal models that reflected the pathology of peritoneal injury. All of the groups were treated with intraperitoneal injections of various solutions. Animals used in this study were male Sprague-Dawley rats (5 to 6 weeks of age, weighing about 200 to 250 g; Charles River Japan, Kanagawa, Japan;  $n = 6/\text{group}$ ).

Rats in the groups treated with GDPs, such as methylglyoxal (MGO) or formaldehyde (FA), intraperitoneally received 100 mL/kg/day GDP containing PD fluids (PDFs) for 21 days. The PDFs used in the present study were prepared by adding 20 mM MGO or FA to PDF (2.5% glucose, 100 mM NaCl, 35 mM sodium lactate, 2 mM  $\text{CaCl}_2$ , and 0.7 mM  $\text{MgCl}_2$ ) and were then sterilized by filtration. The PDFs were prepared and adjusted to pH 5.0 just before injection every day. Rats in the chlorhexidine gluconate- (CG-) treated group intraperitoneally received 15 mL/kg/day 0.1% CG/15% ethanol/saline for 21 days. The solution was aseptically prepared. Rats in the talc-treated group intraperitoneally received 75 mL/kg/day talc suspension, which was prepared by dispersing 1 g of talc in 15 mL of saline followed by autoclave sterilization. The talc-treated group received one administration every 7 days for three weeks. The concentrations of MGO, FA, CG, and talc were decided based on previous reports [7–16]. As a control, a group treated with the PDF without adding MGO, FA, CG, or talc was also set. The control rats were given an intraperitoneal injection of 100 mL/kg/day PDF for 21 days. If solution remained in the peritoneal cavity, it was drained before the injection. When PDF had been injected for more than 3 weeks, it was difficult to inject it because of extensive peritoneal adhesion. Therefore, on the 22nd day after the start of the experiment, peritoneal equilibration test (PET) was performed. Subsequently, the parietal peritoneum was sampled for histological analysis from corresponding sites in each rat.

We performed our experiments in accordance with the NIH Guide for the Care and Use of Laboratory Animals. The animals were housed in an air-conditioned room at a constant temperature of  $23 \pm 2^\circ\text{C}$  and a relative humidity of  $50 \pm 10\%$  and kept under a 12-hour light/dark cycle with free access to sufficient pellet food and water. Adequate attention was paid to maintaining a hygienic environment and to preventing infectious peritonitis. Furthermore, a sterility test was performed using the dialysate drained for PET to check for the presence of aerobic bacteria, anaerobic bacteria, and

fungi in drained dialysate, and then all rats were confirmed to be uninfected.

*2.2. Peritoneal Equilibration Test (PET).* In order to analyze peritoneal function, the peritoneal permeability of glucose was estimated by PET. First, intra-abdominal fluid was drained out. After 50 mL/kg PDF containing 2.5% glucose had been intraperitoneally injected, drained dialysate was collected immediately at 0 minutes and at 90 minutes. The injection volume was set based on that used in a human clinical context. Glucose levels were determined by SRL Co., Ltd. (Tokyo, Japan). The ratio of the glucose level in drained dialysate obtained 90 minutes after the injection to that obtained immediately after the injection was defined as the  $D/D_0$  glucose level.

*2.3. Histological Analysis.* Left center parietal peritoneum was sampled from corresponding sites of each rat and was fixed with 10% FA/0.1 M phosphate buffer (pH 7.2). Peritoneal specimens were embedded in paraffin to prepare tissue sections of a thickness of 2–3  $\mu\text{m}$ . To determine the thickness of the peritoneum, the sections were sliced perpendicularly to the peritoneal surface. Each section was stained with hematoxylin-eosin (HE) to analyze cell type and with Azan to identify collagen fibers. The morphologic changes of the peritoneum were evaluated in a blind manner with photomicroscopy by a toxicological pathologist.

The thickness of the peritoneum was measured with image-analysis software (Win ROOF, Mitani Co., Fukui, Japan). The specimens of the peritoneum were obtained from two sites in each rat. The thickness was measured at 30 points per site (at 0.5 mm intervals within a range of 1.5 cm), and the average was calculated.

*2.4. Immunohistochemistry.* Peritoneal tissue samples embedded in paraffin were sectioned at a thickness of 2–3  $\mu\text{m}$ . These sections for analysis of cytokeratin or  $\alpha$ -smooth muscle actin ( $\alpha$ -SMA) were dewaxed with xylene. After endogenous peroxidase activity had been blocked with 3% hydrogen peroxide/methanol for 15 minutes, the sections were treated with 0.25% trypsin/1 mM EDTA for 2 hours at room temperature. These sections were treated for 2 hours at room temperature with a monoclonal antibody against  $\alpha$ -SMA (Sigma Chemical Co., St. Louis, MO, USA) at a dilution of 1:2000 to identify mesenchymal cells or for 2 hours at room temperature with prediluted monoclonal antibodies against pan-cytokeratin (Sigma Chemical Co.) at a dilution of 1:2 to identify mesothelial cells. For the analysis of podoplanin location, after dewaxing in xylene, the sections were autoclaved at  $121^\circ\text{C}$  for 10 min. After blocking with 3% hydrogen peroxide, the sections were treated overnight at  $4^\circ\text{C}$  with a rabbit polyclonal antibody against podoplanin (Bios Inc., Boston, MA, USA) at a dilution of 1:1000 to identify activated mesothelial cells. Sections were incubated with biotinylated anti-rabbit immunoglobulins for 30 min and then treated with streptavidin-horseradish peroxidase conjugate for 30 min followed by detection with DAB. These sections were also counterstained with Meyer's hematoxylin.

TABLE 1: Pathological findings of the peritoneum in peritoneal injury rats.

	MGO	FA	CG	Talc
Loss of monolayer of mesothelial cells	+++	+++	+++	-
Appearance of basophilic spindle cells	++	-	-	-
Phagocytosis in macrophages	-	-	+-	++
Foreign body inflammation	-	-	-	++
Edema	-	-	+	-
Mononuclear cell infiltration	++	+	++	++
Neovascularization	++	+	+	+
Fibrosis	+	+	+	+

MGO: methylglyoxal-treated rats, FA: formaldehyde-treated rats, CG: chlorhexidine gluconate-treated rats, and talc: talc-treated rats.  
 +: mild, ++: moderate, and +++: severe.

**2.5. Statistical Analysis.** Data are given as mean  $\pm$  SD. Statistical analysis was performed by Dunnett's multiple comparison test. A *P* value of less than 0.05 was accepted as significant.

### 3. Results

In the MGO-, FA-, and CG-treated rats, fist-like round liver edge and extensive adhesion of the bowel and stomach were observed. In the MGO- or CG-treated rats, the bowel adhesion, called an abdominal cocoon, was observed as a mass surrounded by thickened peritoneum (Figure 1). In the talc-treated rats, extensive adhesion of the peritoneum was observed, although the cocoon-like adhesion was not formed. By analysis of tissue sections of parietal peritoneum, peritoneal thickening occurred in the MGO-, FA-, CG-, and talc-treated rats. The thickness of the peritoneum in each group is shown in Figure 2(a). In the MGO-, FA-, CG-, and talc-treated groups, mononuclear cell infiltration, neovascularization, and fibrosis were observed in the peritoneum. In the MGO-treated rats, the peritoneal tissue consisted of dense collagen fibers. However, in the surface of the peritoneum, collagen was scarce, and basophilic spindle cells with podoplanin, cytokeratin, and  $\alpha$ -smooth muscle actin proliferated excessively (Figure 4). Deposition of fibrin was observed in parts of the peritoneal surface. In the FA-treated rats, mesothelial cells were deciliated and then cells were absent at the surface of the peritoneum. In the CG-treated rats, phagocytosis by macrophages, edema, and loss of mesothelial cells were also observed. The surface of the peritoneum was covered with a fibrin layer in some rats. In the talc-treated rats, foreign body inflammation was confirmed by multinucleated giant cell formation from macrophage by phagocytosis of talc particle. In control rats, there was a single layer of mesothelial cells at the surface of the thin peritoneum. The morphology of the peritoneum is shown in Figure 3 and pathological findings of the peritoneum in peritoneal injury rats are summarized in Table 1. There was no difference in morphology between saline- and PDF-treated rats (data not shown).

Peritoneal permeability was higher in the MGO-, FA-, CG-, and talc-treated rats than in the control rats (Figure 2(b)).

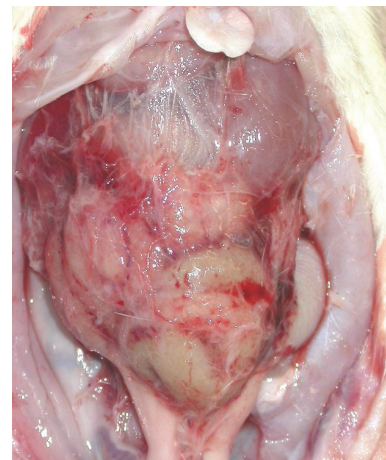


FIGURE 1: Appearance of organs in the peritoneal cavity in MGO-treated rat. The peritoneal injury models were prepared by repeated administration of MGO containing peritoneal dialysis fluids into the peritoneal cavity of rats for 21 days. Adhesion of bowel forming a cocoon-like mass was seen in the MGO-treated rats.

### 4. Discussion

In the peritoneum of EPS patients, the frequencies of fibrin deposition, fibroblast swelling, capillary angiogenesis, and mononuclear cell infiltration were significantly higher than those of non-EPS patients [17]. There are many candidate factors that could cause peritoneal injury and EPS in PD, but the mechanism of peritoneal deterioration has not been clarified [3–7]. In the present study, we prepared four animal models for a comparison of the pathology of peritoneal injury induced by different factors, namely, MGO, FA, CG, and talc [7–16]. In these animal models, enhanced peritoneal permeability (Figure 2(b)) was confirmed and extensive peritoneal adhesion was found, as in human EPS patients [1–5] (Figure 1). Thickening of the peritoneum, neovascularization, and mononuclear cell infiltration were observed in the peritoneum of these animal models (Figure 2(a)). These findings are similar to the pathological picture of the peritoneum in human EPS [3, 18]. However, these models do not necessarily reflect the human clinical pathology. It is important to recognize the characteristics of each model.

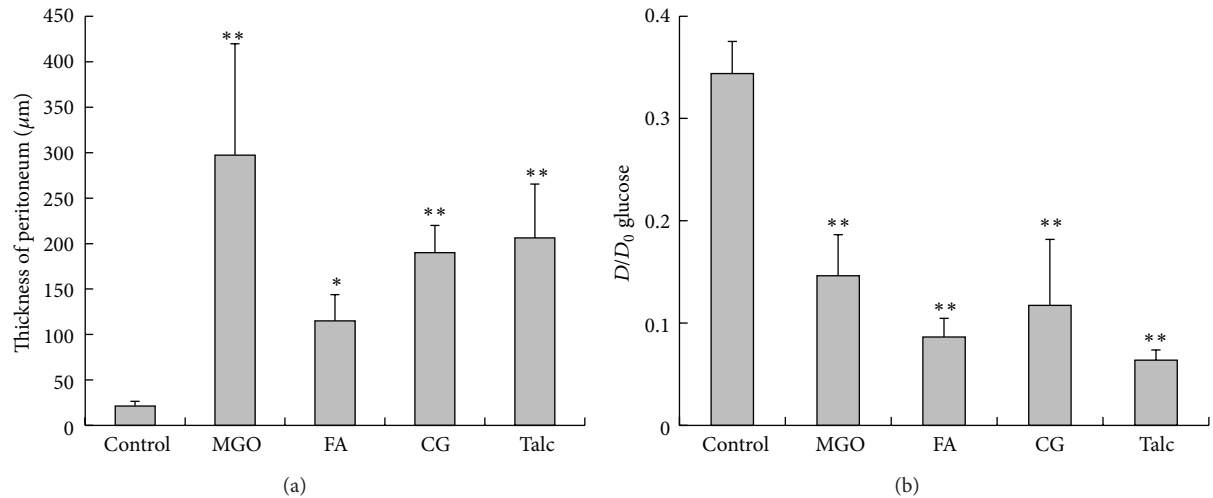


FIGURE 2: Peritoneal deterioration in the rat peritoneal injury models. (a) Thickness of parietal peritoneum. (b) The PET was performed in peritoneal injury animal models and  $D/D_0$  glucose level was obtained. Data are shown as mean  $\pm$  SD. Statistical analysis was performed by Dunnett's multiple comparison test against the control. \* $P < 0.05$  compared with the control. \*\* $P < 0.01$  compared with the control.

The first and second peritoneal injury animal models were made by intraperitoneally administering the PDFs supplemented with MGO or FA, respectively [7–10]. Conventional PDFs contain various GDPs, such as 5-hydroxymethylfurfural, furfuraldehyde, acetaldehyde, FA, glyoxal, MGO, 3-deoxyglucosone, and 3,4-dideoxyglucosone-3-ene [11]. These GDPs contribute greatly to the bioincompatibility of conventional PDFs and are risk factors for EPS. Glucose is safe and readily metabolized because it is the most important basic source of energy for metabolism. Therefore, glucose is widely used as an osmotic agent in commercial PDFs. However, glucose in PDFs is degraded to GDPs during heat sterilization and storage [12]. The resulting GDPs show strong oxidant activity and toxic effects on cell proliferation and cell function [10]. In particular, carbonyl compounds, such as MGO, FA, and 3,4-dideoxyglucosone-3-ene, are extremely cytotoxic [7, 10, 11]. These GDPs form advanced glycation end products (AGEs) that induce structural changes of the peritoneum or the loss of peritoneal function [8]. GDPs injure the peritoneum directly or via the accumulation of AGEs. The concentrations of MGO and FA, injected into the MGO and FA models, are reasonable given the results of permitted daily exposure (PDE) risk assessment [7]. GDP-induced peritoneal injury models may reflect human PD. In particular, in the MGO-induced model, basophilic spindle cells are observed in the surface of the peritoneum at an early stage and a cocoon-like bowel adhesion is also formed at a late stage [7, 8]. Basophilic spindle cells may be derived from mesothelial cells via EMT-like change induced by carbonyl stress of MGO or accumulation of AGE. These morphological changes of human peritoneum were often reported in a clinical context. The MGO-induced model may be suitable to analyze the mechanism of progression of peritoneal injury and EPS.

The third animal model was made by intraperitoneally administering an antiseptic, CG, as a chemical irritant to induce inflammation. Phagocytosis by macrophages induced

by aggregated grains of CG may be a trigger for this inflammation. This model is most often used to analyze peritoneal injury or EPS in animal studies [8, 9, 12–16]. However, it is thought that CG is not the main cause of peritoneal injury with thickening in PD patients because it is now scarcely used clinically as an antiseptic in this condition [9]. In addition, in this model, an extremely excessive dose of CG is administered compared with daily exposure in humans. Inflammation induced by CG caused the development of edema followed by fibrosis without EMT-like cells [8, 9, 12–16]. Therefore, the CG model is probably inadequate to analyze the mechanism of progression of peritoneal injury.

The fourth model was made by administering talc (hydrous magnesium silicate) as an exogenous material into the peritoneal cavity, since this agent has long been known to cause adhesion formation [14, 19]. In this peritoneal injury model, the volume of talc injected is extremely high and large particles such as talc are not observed in the human peritoneum. This model may thus not reflect the progression of human clinical peritoneal injury in PD.

In EMT, fully differentiated mesothelial cells undergo transition to a mesenchymal phenotype, a spindle-shaped morphology, concomitant with the acquisition of a mesenchymal marker,  $\alpha$ -SMA. Some studies showed that the EMT of mesothelial cells may be a triggering factor of peritoneal injury in PD patients [1, 2]. Transforming growth factor- $\beta$  (TGF- $\beta$ ) induces the EMT-like change of mesothelial cells via Snail, a zinc-finger transcription factor, and causes peritoneal fibrosis [1, 2, 8]. Podoplanin, which is a member of a type-1 transmembrane sialomucin-like glycoprotein family, serves as a marker of lymphatic endothelial cells but is also expressed by mesothelioma [19]. In the peritoneum of patients with EPS, podoplanin is expressed by activated mesothelial cells, lymphatic endothelial cells, and  $\alpha$ -SMA-positive myofibroblasts. Braun et al. reported the possibility that podoplanin-positive myofibroblasts are derived

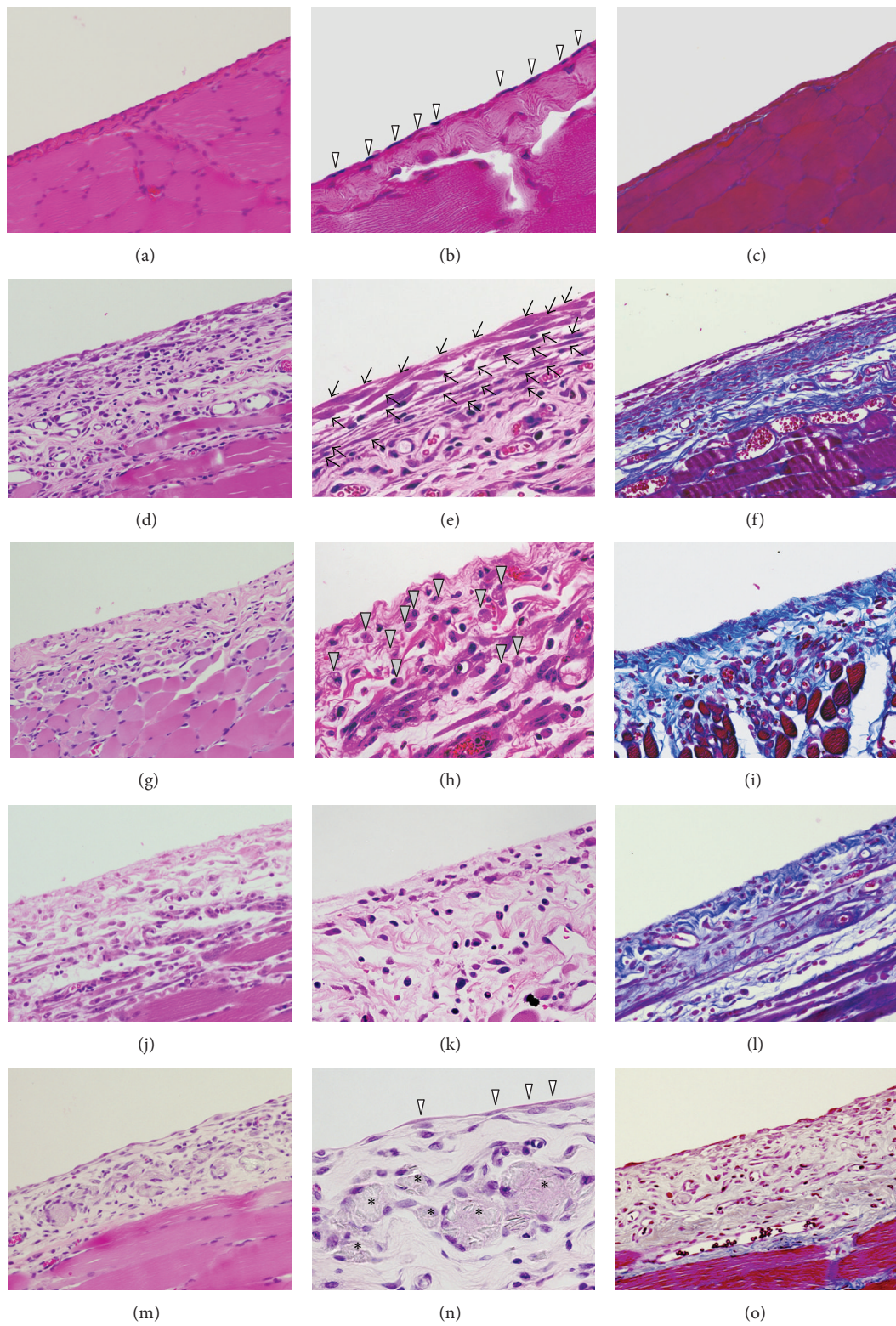


FIGURE 3: Histopathological findings of parietal peritoneum. The parietal peritoneum was analyzed histologically with HE stain (a, b, d, e, g, h, j, k, m, and n) or Azan stain (c, f, i, l, and o). Control rat: (a, b, and c). MGO-treated rat: (d, e, and f). FA-treated rat: (g, h, and i). CG-treated rat: (j, k, and l). Talc-treated rat: (m, n, and o). Mesothelial cells, spindle cells, phagocytosis by macrophages, and multinucleated giant cells are indicated by open arrow heads, arrows, closed arrow heads, and asterisks, respectively. (a, c, d, f, g, i, j, l, m, and o):  $\times 200$ , (b, e, h, k, and n):  $\times 400$ .

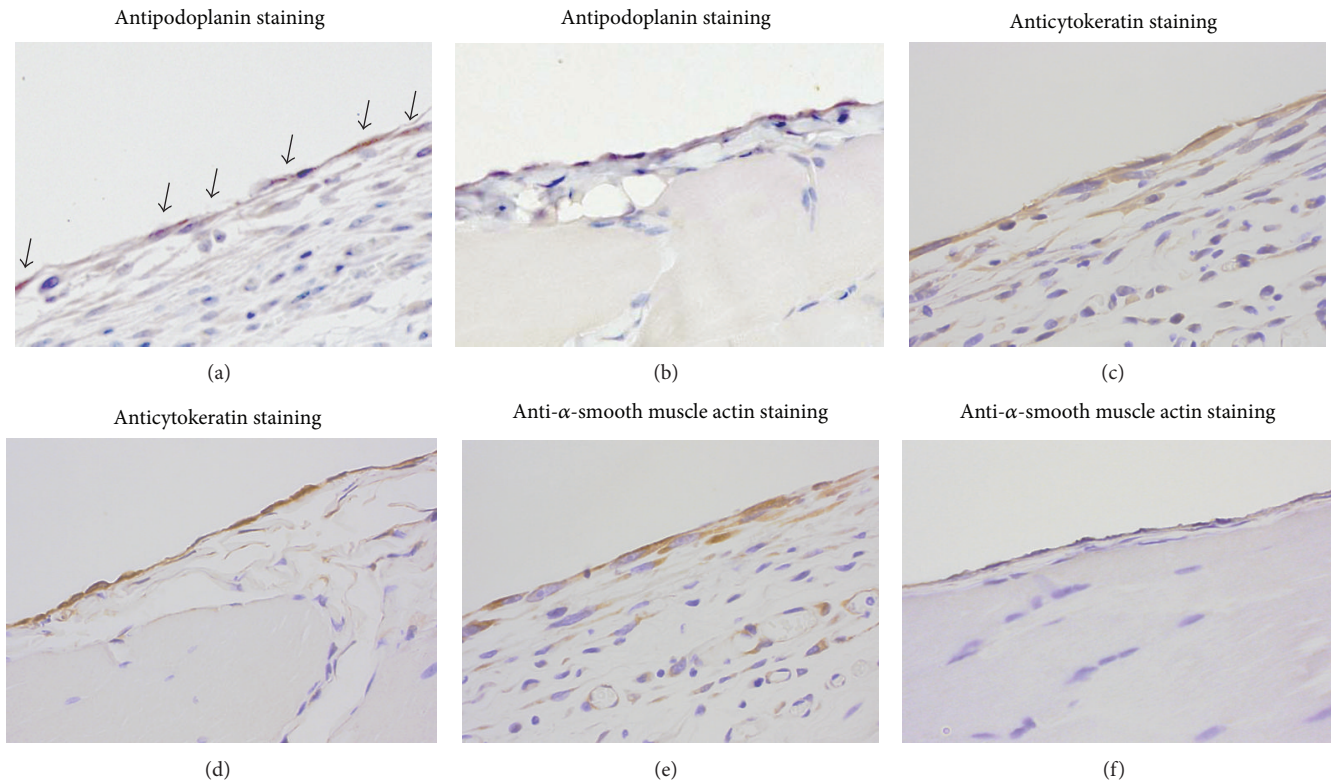


FIGURE 4: Characterization of cells at the surface of the peritoneum in the MGO-treated rats. In the parietal peritoneum, podoplanin-positive cells (a, b), cytokeratin-positive cells (c, d), and  $\alpha$ -smooth muscle actin-positive cells (e, f) were analyzed by immunostaining. Podoplanin-positive cells are indicated by arrows (a). MGO-treated rat: (a, c, and e). Control rat: (b, d, and f). Magnification:  $\times 400$ .

from mesothelial cells by EMT and these cells are a hallmark of EPS [20, 21]. In the present study, basophilic spindle-shaped cells with podoplanin, cytokeratin, and  $\alpha$ -SMA proliferated excessively in the MGO-treated rats. Podoplanin, cytokeratin, and  $\alpha$ -SMA are markers for activated mesothelium, mesothelial cells, and mesenchymal cells, respectively. The basophilic spindle-shaped cells may be derived from mesothelial cells by EMT-like change. On the other hand, Hou et al. reported that podoplanin was expressed on a subset of F4/80(+) macrophages, a subset which they have termed fibroblastic macrophages [22]. Miyamoto et al. reported that podoplanin was an inflammatory protein upregulated in Th17 cells [23]. In the present study, the podoplanin-positive basophilic spindle-shaped cells at the surface of peritoneum may be derived from fibroblastic macrophages or Th17 cells. Additional studies are needed to clarify the origin of the spindle-shaped cells.

There is little evidence about podoplanin-positive spindle-shaped cells, even though podoplanin might be a suitable morphological marker supporting the diagnosis and might be involved in the pathogenesis of EPS. To our knowledge, the present study is the first to report that podoplanin-positive spindle-shaped cells are induced in PD animal models. The MGO-induced peritoneal injury model may provide valid information about the mechanism of pathogenesis and progression of peritoneal injury developing into EPS.

## 5. Conclusion

MGO induced the podoplanin-positive basophilic spindle cells at the surface of the peritoneum in a peritoneal injury animal model. This animal model may reflect the progression of peritoneal injury of human PD patients, so additional studies using this animal model may contribute to clarifying the mechanism of peritoneal deterioration.

## Conflict of Interests

This study was supported by Terumo Core Technology Center. Ichiro Hirahara is also affiliated with this center. However, the authors have had no involvement that might raise the question of bias in the work reported or in the conclusions, implications, or opinions stated.

## Acknowledgment

The authors would like to thank Ms. Yuka Shouji (Terumo Core Technology Center) for help with the preparation of pathological tissue.

## References

- [1] A. Aguilera, M. Yáñez-Mo, R. Selgas, F. Sánchez-Madrid, and M. López-Cabrera, "Epithelial to mesenchymal transition as

- a triggering factor of peritoneal membrane fibrosis and angiogenesis in peritoneal dialysis patients," *Current Opinion in Investigational Drugs*, vol. 6, no. 3, pp. 262–268, 2005.
- [2] M. Yáñez-Mó, E. Lara-Pezzi, R. Selgas et al., "Peritoneal dialysis and epithelial-to-mesenchymal transition of mesothelial cells," *The New England Journal of Medicine*, vol. 348, no. 5, pp. 403–413, 2003.
- [3] V. C. Gandhi, H. M. Humayun, T. S. Ing et al., "Sclerotic thickening of the peritoneal membrane in maintenance peritoneal dialysis patients," *Archives of Internal Medicine*, vol. 140, no. 9, pp. 1201–1203, 1980.
- [4] Y. Kawaguchi, H. Kawanishi, S. Mujais, N. Topley, and D. G. Oreopoulos, "Encapsulating peritoneal sclerosis: definition, etiology, diagnosis, and treatment," *Peritoneal Dialysis International*, vol. 20, supplement 4, pp. S43–S55, 2000.
- [5] G. Balasubramaniam, E. A. Brown, A. Davenport et al., "The Pan-Thames EPS study: treatment and outcomes of encapsulating peritoneal sclerosis," *Nephrology Dialysis Transplantation*, vol. 24, no. 10, pp. 3209–3215, 2009.
- [6] M. C. Brown, K. Simpson, J. J. Kerseens, and R. A. Mactier, "Encapsulating peritoneal sclerosis in the new millennium: a national cohort study," *Clinical Journal of the American Society of Nephrology*, vol. 4, no. 7, pp. 1222–1229, 2009.
- [7] I. Hirahara, E. Kusano, S. Yanagiba et al., "Peritoneal injury by methylglyoxal in peritoneal dialysis," *Peritoneal Dialysis International*, vol. 26, no. 3, pp. 380–392, 2006.
- [8] I. Hirahara, Y. Ishibashi, S. Kaname, E. Kusano, and T. Fujita, "Methylglyoxal induces peritoneal thickening by mesenchymal-like mesothelial cells in rats," *Nephrology Dialysis Transplantation*, vol. 24, no. 2, pp. 437–447, 2009.
- [9] C. M. Hoff, "Experimental animal models of encapsulating peritoneal sclerosis," *Peritoneal Dialysis International*, vol. 25, supplement 4, pp. S57–S66, 2005.
- [10] M. Nakayama, A. Sakai, M. Numata, and T. Hosoya, "Hypervascular change and formation of advanced glycation endproducts in the peritoneum caused by methylglyoxal and the effect of an anti-oxidant, sodium sulfite," *American Journal of Nephrology*, vol. 23, no. 6, pp. 390–394, 2003.
- [11] M. Erixon, T. Lindén, P. Kjellstrand et al., "PD fluids contain high concentrations of cytotoxic GDPs directly after sterilization," *Peritoneal Dialysis International*, vol. 24, no. 4, pp. 392–398, 2004.
- [12] Y. Ishii, T. Sawada, A. Shimizu et al., "An experimental sclerosing encapsulating peritonitis model in mice," *Nephrology Dialysis Transplantation*, vol. 16, no. 6, pp. 1262–1266, 2001.
- [13] H. Io, C. Hamada, Y. Ro, Y. Ito, I. Hirahara, and Y. Tomino, "Morphologic changes of peritoneum and expression of VEGF in encapsulated peritoneal sclerosis rat models," *Kidney International*, vol. 65, no. 5, pp. 1927–1936, 2004.
- [14] I. Hirahara, Y. Ogawa, E. Kusano, and Y. Asano, "Activation of matrix metalloproteinase-2 causes peritoneal injury during peritoneal dialysis in rats," *Nephrology Dialysis Transplantation*, vol. 19, no. 7, pp. 1732–1741, 2004.
- [15] I. Hirahara, K. Umeyama, K. Urakami, E. Kusano, Y. Masunaga, and Y. Asano, "Serial analysis of matrix metalloproteinase-2 in dialysate of rat sclerosing peritonitis models," *Clinical and Experimental Nephrology*, vol. 5, no. 2, pp. 103–108, 2001.
- [16] I. Hirahara, K. Umeyama, K.-I. Shofuda et al., "Increase of matrix metalloproteinase-2 in dialysate of rat sclerosing encapsulating peritonitis model," *Nephrology*, vol. 7, no. 4, pp. 161–169, 2002.
- [17] D. W. Johnson, Y. Cho, B. E. R. Livingston et al., "Encapsulating peritoneal sclerosis: incidence, predictors, and outcomes," *Kidney International*, vol. 77, no. 10, pp. 904–912, 2010.
- [18] K. Honda and H. Oda, "Pathology of encapsulating peritoneal sclerosis," *Peritoneal Dialysis International*, vol. 25, supplement 4, pp. S19–S29, 2005.
- [19] N. Kimura and I. Kimura, "Podoplanin as a marker for mesothelioma," *Pathology International*, vol. 55, no. 2, pp. 83–86, 2005.
- [20] N. Braun, D. M. Alscher, P. Fritz et al., "Podoplanin-positive cells are a hallmark of encapsulating peritoneal sclerosis," *Nephrology Dialysis Transplantation*, vol. 26, no. 3, pp. 1033–1041, 2011.
- [21] N. Braun, P. Fritz, C. Ulmer et al., "Histological criteria for encapsulating peritoneal sclerosis—a standardized approach," *PLoS ONE*, vol. 7, no. 11, Article ID e48647, 2012.
- [22] T. Z. Hou, J. Bystrom, J. P. Sherlock et al., "A distinct subset of podoplanin (gp38) expressing F4/80+ macrophages mediate phagocytosis and are induced following zymosan peritonitis," *FEBS Letters*, vol. 584, no. 18, pp. 3955–3961, 2010.
- [23] Y. Miyamoto, H. Uga, S. Tanaka et al., "Podoplanin is an inflammatory protein upregulated in Th17 cells in SKG arthritic joints," *Molecular Immunology*, vol. 54, no. 2, pp. 199–207, 2013.

## Research Article

# CD40 Ligand Deficient C57BL/6 Mouse Is a Potential Surrogate Model of Human X-Linked Hyper IgM (X-HIGM) Syndrome for Characterizing Immune Responses against Pathogens

Catalina Lopez-Saucedo,<sup>1,2</sup> Rodolfo Bernal-Reynaga,<sup>1</sup>  
Jesus Zayas-Jahuey,<sup>1</sup> Silvia Galindo-Gomez,<sup>3</sup> Mineko Shibayama,<sup>3</sup> Carlos Garcia-Galvez,<sup>2</sup>  
Sergio Estrada-Parra,<sup>2</sup> and Teresa Estrada-Garcia<sup>1</sup>

<sup>1</sup>Department of Molecular Biomedicine, CINVESTAV-IPN, Avenue IPN 2508, Zacatenco, 07360 México, DF, Mexico

<sup>2</sup>Department of Immunology, Escuela Nacional de Ciencias Biológicas IPN, Prolongación de Carpio y Plan de Ayala, 11340 México, DF, Mexico

<sup>3</sup>Department of Infectomics and Molecular Pathogenesis, CINVESTAV-IPN, Avenue IPN 2508, Zacatenco, 07360 México, DF, Mexico

Correspondence should be addressed to Teresa Estrada-Garcia; [testrada@cinvestav.mx](mailto:testrada@cinvestav.mx)

Received 17 November 2014; Accepted 10 December 2014

Academic Editor: Monica Fedele

Copyright © 2015 Catalina Lopez-Saucedo et al. This is an open access article distributed under the Creative Commons Attribution License, which permits unrestricted use, distribution, and reproduction in any medium, provided the original work is properly cited.

Individuals with X-HIGM syndrome fail to express functional CD40 ligand; consequently they cannot mount effective protective antibody responses against pathogenic bacteria. We evaluated, compared, and characterized the humoral immune response of wild type (WT) and C57-CD40L deficient (C57-CD40L<sup>-/-</sup>) mice infected with *Citrobacter rodentium*. Basal serum isotype levels were similar for IgM and IgG3 among mice, while total IgG and IgG2b concentrations were significantly lower in C57-CD40L<sup>-/-</sup> mice compared with WT. Essentially IgG1 and IgG2c levels were detectable only in WT mice. C57-CD40L<sup>-/-</sup> animals, orally inoculated with  $2 \times 10^9$  CFU, presented several clinical manifestations since the second week of infection and eventually died. In contrast at this time point no clinical manifestations were observed among C57-CD40L<sup>-/-</sup> mice infected with  $1 \times 10^7$  CFU. Infection was subclinical in WT mice inoculated with either bacterial dose. The serum samples from infected mice ( $1 \times 10^7$  CFU), collected at day 14 after infection, had similar *C. rodentium*-specific IgM titres. Although C57-CD40L<sup>-/-</sup> animals had lower IgG and IgG2b titres than WT mice, C57-CD40L<sup>-/-</sup> mice sera displayed complement-mediated bactericidal activity against *C. rodentium*. *C. rodentium*-infected C57-CD40L<sup>-/-</sup> mice are capable of producing antibodies that are protective. C57-CD40L<sup>-/-</sup> mouse is a useful surrogate model of X-HIGM syndrome for studying immune responses elicited against pathogens.

## 1. Introduction

The hyper IgM syndromes (HIGM) are a group of primary immune deficiency disorders which are the result of a variety of genetic defects affecting the interaction between T-lymphocytes and B-lymphocytes, including class switch recombination and somatic hypermutation [1]. Among these HIGM syndromes the X-linked HIGM syndrome (X-HIGM) is the most frequently identified accounting for about 65 to 70% of all cases. X-HIGM syndrome results from mutations in the *cd40l* gene that encodes for the CD40 ligand (CD40L)

molecule [2]. CD40L is an inducible type II membrane glycoprotein, found on the surface of T cells after antigen stimulation that binds to the CD40 molecule on B cells. CD40-CD40L interaction plays a major role in isotype switching, induction of B and T cell proliferation, B cell affinity maturation, and germinal centre formation [3]. Cases of X-HIGM have been described in industrialized countries [4] and also in less developed areas of the world, as India and Latin America [5–7]. In a study conducted in six Latin American countries, including Mexico, of a total of 58 patients with HIGM clinical features, 37 had genetic defects;

of these 35 patients had CD40L deficiencies [6], revealing that X-HIGM is as well the most frequent HIGM syndrome in this region.

X-HIGM patients are characterized by low IgG and IgA serum concentrations and normal or elevated IgM concentrations [1]. In addition, X-HIGM patient's lymph nodes lack germinal centres and their antigen-specific responses may be decreased or are absent [1]. Patients develop clinical symptoms by age one year, and more than 90% are symptomatic by age four years [1, 8]. The range of clinical findings varies, even within the same family, and includes recurrent upper- and lower-respiratory tract bacterial infections, opportunistic infections, and recurrent or protracted diarrhoea [1]. Diarrhoea syndromes occur in over 50% of patients [2]. *Cryptosporidium parvum* has been the most common pathogen isolated from faeces of X-HIGM patients with diarrhoea from industrialized countries [1, 2], while it has been reported that *Giardia lamblia* was the most common pathogen identified in X-HIGM patients from Latin America [6]. However, in at least 50% of X-HIGM patients with recurrent or protracted diarrhoea no infectious agent can be detected [8]. This could be due to the fact that not all enteric pathogens are sought out. For instance, diarrheagenic *Escherichia coli* (DEC) are major pathogens associated with both acute and protracted bacterial diarrhoea worldwide, even so *E. coli* strains isolated from diarrhoeal stool samples are still considered commensal flora [9]. Hence, potentially DEC could be an important unknown cause of diarrhoea among X-HIGM patients.

In 1994, two C57BL/6 CD40L-deficient mice (C57-CD40L<sup>-/-</sup>) were developed by two independent groups [10, 11]. As in humans C57-CD40L<sup>-/-</sup> mice are characterized by low serum concentrations of IgG and IgA but normal, lower, or higher serum concentrations of IgM [10–12]. The C57-CD40L<sup>-/-</sup> mice have been successfully used to develop infection models of human intestinal pathogens including, for example, *C. parvum*, one of the most common pathogens identified among X-HIGM patients [13], and enterotoxigenic *E. coli*, a DEC pathotype [12]. *Citrobacter rodentium* is a natural noninvasive intestinal pathogen of mice that produces deathly diarrhoea in suckling mice and causes transmissible subclinical colonic hyperplasia in adult mice [14, 15]. Furthermore, *C. rodentium* mouse infection model has become the “gold standard” animal model for investigating the virulence mechanisms of pathogens producing the attaching-and-effacing (A/E) lesion [14, 16, 17]. A/E bacteria encompass the human enteric pathogens, enteropathogenic *E. coli* (EPEC) and enterohaemorrhagic *E. coli* (EHEC). *C. rodentium* studies have demonstrated that mice systemic pathogen-specific IgG and CD4<sup>+</sup> T cell responses are required for survival and resolution of bacteria colonizing the gut epithelium [18–20]. Furthermore, protective serum antibody responses in acute *C. rodentium* infection consisted of pathogen-specific IgM and IgG2b/IgG2c responses; these profiles are consistent with complement-fixing antibodies [20]. Therefore, the aims of this study were to evaluate and compare the oral infection *C. rodentium* in WT and C57-CD40L<sup>-/-</sup> mice and their systemic antibody response against this pathogen, as well as

to establish if C57-CD40L<sup>-/-</sup> mice are capable of producing complement-fixing antibodies against *C. rodentium*.

## 2. Materials and Methods

**2.1. Animals.** Five- to eight-week-old female and male wild type (WT) C57BL/6 mice and C57-CD40L<sup>-/-</sup> mice, derived from a C57BL/6 background, were used (Jackson Laboratory Bar Harbor, Maine, USA). Mice came from colonies that were specific-pathogen-free and sentinel animals were screened for common murine pathogens every 6 months or once a year. All animals were housed in autoclaved microisolator filtered cages, with sterile bedding and free access to sterilized food and water. During the experiments the cage beddings were changed daily. All experimental procedures were reviewed and approved by the CINVESTAV-IPN animal Ethical Committee.

**2.2. Bacterial Strain and Inoculum Preparation.** *Citrobacter rodentium* strain DBS 100 was used in all experiments, and this strain was kindly provided by Dr. Jose Luis Puente (Department of Molecular Microbiology, Institute of Biotechnology, UNAM, Mexico). *Citrobacter rodentium* was cultured on MacConkey agar for 18–24 h at 37°C. Briefly, one colony was grown overnight in 5 mL of Luria-Bertani (LB) broth at 37°C without shaking. Next day 1 mL of bacterial culture was resuspended in 50 mL of fresh LB broth, was incubated with shaking at 37°C for additional 4 h, and then was centrifuged at 13,000 rpm and the pellet was washed twice and resuspended in 1 mL of sterile physiological saline (SPS). Bacterial concentration was determined by measuring the optical density (OD) at 600 nm (Smart Spec 3000, Biorad), one OD = 5 × 10<sup>8</sup> CFU/mL. Finally, the bacterial suspension was adjusted to the concentration required for the experiments in a final volume of 50 µL.

**2.3. Mice Inoculation.** Mice were fasted for 6 h before oral inoculation, via a feeding needle, with *C. rodentium*. The inoculation dose was verified retrospectively by plating serial dilutions on trypticase soy agar plates and enumerating colonies. Sham controls were administered with an equal volume of SPS (50 µL).

**2.4. Monitoring of Faecal Shedding of *Citrobacter rodentium*.** To determine bacterial numbers in the stools, faecal pellets were collected from individual mice, weighed, and homogenised in 1 mL of SPS. Bacterial homogenates serial dilutions were plated on MacConkey agar and colony-forming units (CFU) were determined after overnight incubation at 37°C. *C. rodentium* colonies (pink-red centre with a transparent rim, slightly translucent) were selected and their identity was confirmed by a specific intimin-B protein gene (*eaeB*) PCR developed by us. We prepared bacterial lysates by resuspending single colonies in 1 mL of deionized water (Milli-Q System, Millipore, Bedford, MA), boiled for 1 min, and then freezing them until needed. Based on the *C. rodentium* intimin B gene sequence (GenBank accession number AF311901) the following primers

were designed: 5'-tgagcgcgccgcaaatggtt-3' (forward) and 5'-tgtgcgcttggcttcgct-3' (reverse). Briefly 1  $\mu$ L of bacterial lysate and primers in a final concentration of 0.2  $\mu$ M were added to a PCR tube that contained 24  $\mu$ L of reaction mix whose concentration has been previously described [21] and subjected to the following cycling conditions: 50°C (2 min, 1 cycle); 95°C (5 min, 1 cycle); 95°C, 50°C, and 72°C (45 s each temperature, 40 cycles) and a final extension step (10 min, 72°C) in a thermal cycler (iCycler System, Bio-Rad Laboratories, Inc., Hercules, CA). A 555-bp PCR product was visualized by agarose gel electrophoresis and ethidium bromide staining.

**2.5. Histological Analysis.** Mice were sacrificed by cardiac exsanguination under chloroform effect at day 14 after inoculation and the colons were removed. Segments (1 cm) of terminal colon from each mouse were collected, longitudinally cut, and pinned out flat with the mucosal side up. The tissues were fixed in 4% paraformaldehyde in PBS for 48 h at room temperature, dehydrated by gradient ethanol, cleared by xylene, and embedded in paraffin. Sections of 5  $\mu$ m were prepared and stained with haematoxylin and eosin. Sections were evaluated for changes in the mucosal architecture and the presence of an inflammatory infiltrate. Villus high was measured on ten villi in each slide, three slides per mice strain.

**2.6. *Citrobacter rodentium* Whole-Cell Sonicate Preparation.** The bacterium was grown as described above (see bacteria strain and inoculum preparation section). The bacteria culture was centrifuged at 13,000 rpm and the pellet was washed twice with phosphate-buffered saline pH 7.4 (PBS). Then the bacterial pellet was resuspended in 5 mL of PBS and subsequently sonicated five times by periods of 1 min, pulse each 10 s, and 40  $\mu$ m wave amplitude (ultrasonic processor). The bacterial sonicate was centrifuged at 13,000 rpm for 10 min and the supernatant was used for ELISA assays. Protein concentration was assessed by Bradford test (Bio-Rad 500-0006).

**2.7. Determination of Total Basal Immunoglobulin Concentrations.** Mice blood samples were collected from the mice tail vein and centrifuged, and serum aliquots were frozen at -70°C until tested. Total basal IgM, IgG, and IgG subclasses and IgA concentrations were determined in the serum by comparing the values of test sample dilution series in ELISA, with isotype-specific control standard curves (Cappel 50335, Jackson ImmunoResearch 015-000-003, and Cappel 50325 for the IgM and IgG-IgG subclasses and IgA, resp.). Briefly, individual wells of flat bottom ELISA plates (Corning Inc., Costar 3590) were coated with 60  $\mu$ L of capture antibody for IgM (Jackson ImmunoResearch 715 005-140), for IgG and IgG subclasses (ZYMED 61-6400) and IgA (Southern Biotech 1165-01), in a final concentration of 1.0  $\mu$ g/mL in carbonate-bicarbonate buffer pH 9.6 and incubated overnight at 4°C. Then plates were washed with 0.1% v/v Tween 20 in phosphate-buffered saline (PBS-T) and subsequently blocked with 1% BSA in PBS-T (blocking solution) for 1 h at 37°C.

TABLE 1: Serum dilutions to determine basal immunoglobulin concentrations.

Immunoglobulin	Serum dilutions	
	WT	C57-CD40L <sup>-/-</sup>
IgA	1:500 and 1:1000	1:250 and 1:500
IgM and total IgG	1:4000 and 1:8000	1:4000 and 1:8000
IgG1	1:1000 and 1:2000	1:250 and 1:500
IgG2c	1:250 and 1:500	1:250 and 1:500
IgG2b	1:2000 and 1:4000	1:1000 and 1:2000
IgG3	1:1500 and 1:3000	1:1500 and 1:3000

WT = wild type mice.

Then 60  $\mu$ L of serum samples diluted in blocking solution was added in duplicate into wells for 1 h at 37°C. Serum samples were diluted according to the Ig to be evaluated (see Table 1). Followed by washing and incubation with respective anti-mouse Ig-horseradish peroxidase conjugated secondary antibodies diluted 1:1000 in blocking solution for IgM (Pierce, 31440), IgG (Invitrogen, G21040), and IgA (Sigma A 4789) and 1:4000 for IgG subclasses (IgG1, IgG2b, IgG2c, and IgG3, SouthernBiotech, 1070-05, 1090-05, 1079-05, and 1100-05, resp.). All assays were developed using ABTS peroxidase substrate system (Sigma, A1888) and plates were read at 405 nm on an ELISA reader (Tecan, Sunrise). OD shown by the background controls was subtracted from the OD of each test sample.

**2.8. *C. rodentium*-Specific Antibody Titres.** At postinoculation selected times mice blood samples were collected from the mice tail vein and centrifuged and serum aliquots were frozen at -70°C until tested. Microtiter plates were coated overnight at 4°C with 60  $\mu$ L of carbonate-bicarbonate buffer pH 9.6 containing whole-cell sonicate lysate (10  $\mu$ g/mL). The plates were washed with PBS-T and blocked with blocking solution 1 h, 37°C. Then serially diluted serum in blocking solution was added in duplicate and incubated 1 h at 37°C. The next steps were developed as described above.

**2.9. Western Blot Analysis.** For immunoblots, *C. rodentium* whole-cell sonicate (35  $\mu$ g per well) boiled and unboiled was resolved in 10% SDS-PAGE gels (90 V, 400 mA for 110 min) and transferred to nitrocellulose membranes (90 V, 400 mA for 2 h). The membranes were blocked with PBS Tween 20 0.5%, plus BSA (10 mg/mL), dextrose 1M, and 10% (v/v) of glycerol (blocking solution) overnight at 4°C by slow shaking. Membranes were incubated with serum diluted 1:200 overnight at 4°C. After incubation, membranes were washed (10 min per wash) in PBS-T 0.1% three times and three times with PBS. Then membranes were incubated for 2 h at room temperature with anti-mouse Ig-horseradish peroxidase conjugated secondary antibodies for IgM (Pierce, 31440) and IgG (Invitrogen, G21040) diluted 1:1000 in blocking solution. After this period the membranes were washed once more as previously described. HRP-bound antibody was developed with Western Blotting Luminol Reagent (Santa Cruz) and visualized using a ChemiDoc™ MP system (Bio-Rad).

**2.10. Complement-Dependent Bactericidal Antibody Assays.** Mice serum to be tested was heat-inactivated by incubation at 56°C for 30 min and was diluted in Hanks' solution. WT mouse serum was first diluted in 1:100, followed by a 1:500 dilution and then twofold dilutions until 1:16000. C57-CD40L<sup>-/-</sup> mouse serum was first diluted 1:50, followed by twofold dilutions until 1:1600. Then 30 µL of each dilution was added to a tube containing 20 µL of a bacterial suspension (1000 ± 10) and incubated at 37°C for 30 min. After this period 50 µL of exogenous complement (guinea pig serum 10% in Hanks' solution) was added to each tube and incubated at 37°C for 30 min. Both incubations were done in a shaker at 25 rpm. To each tube 900 µL of Hanks' solution was added and then diluted 1:10, and 100 µL was taken and plated on trypticase soy agar plates, in duplicate, and incubated overnight at 37°C. Next day the number of CFU per plate was determined. The serum bactericidal antibody titre was defined as the reciprocal of the highest serum dilution that produced ≥50% killing in relation to the killing observed for the negative control (viable-bacteria count control). In order to validate the bactericidal activity four negative controls were included in all assays: (1) viable-bacteria count control (bacteria suspension without serum or guinea pig complement), (2) inactivated serum control (inactivated serum and bacteria suspension without guinea pig complement), (3) guinea pig complement control (guinea pig complement and bacteria suspension without serum), and (4) inactivated guinea pig complement control (inactivated guinea pig complement, inactivated serum, and bacteria suspension).

**2.11. Statistical Analysis.** Kolmogorov-Smirnov test was used to determine the data distribution. The paired Student's *t*-test was used to compare normally distributed values from groups of mice. The nonparametric Mann-Whitney test was used to compare nonnormally distributed values. Differences with a *P* value < 0.05 were considered significant. GraphPad Prism software (version 5.0) was used to generate graphs and to analyse the data.

### 3. Results

**3.1. *Citrobacter rodentium* Course of Infection in Wild Type and C57-CD40L<sup>-/-</sup> Mice.** In WT mice *C. rodentium* infection has been well characterized but has not been described in C57-CD40L<sup>-/-</sup> mice. Therefore, a set of mice of each strain was orally inoculated with a dose of 2 × 10<sup>9</sup> CFU of *C. rodentium* (a dose that already has been standardized for this model of infection). Mice were followed up until day 39; stools were collected daily for 18 days and every other day until day 39. CFU per gram of faeces (CFU/g) were similar in both mice strains during the first week of infection, though C57-CD40L<sup>-/-</sup> faeces were softer compared with WT faeces (Figures 1(a) and 1(b)). During the second week of infection once more both mice strains had similar CFU/g; even so, C57-CD40L<sup>-/-</sup> mice presented several clinical manifestations such as weight loss, dehydration, coat ruffling, hunched posture, and listlessness. As shown in Figure 1(b), all three C57-CD40L<sup>-/-</sup> mice died (the first one at day 17, the second

at day 29, and the last one at day 39). WT mice only produced soft faeces at week two but did not present any other clinical manifestation during the entire experiment.

**3.2. *Citrobacter rodentium* Infection in WT and C57-CD40L<sup>-/-</sup> Mice with a Dose of 5 × 10<sup>8</sup> and 1 × 10<sup>7</sup>.** In order to minimize the observed clinical manifestations induced by a dose 2 × 10<sup>9</sup> CFU in C57-CD40L<sup>-/-</sup> two lower *C. rodentium* infectious doses were tested. Both mice strains were orally inoculated with 5 × 10<sup>8</sup> CFU and followed up for 14 days. Stools were collected daily and both strains had similar numbers of CFU/g (Figure 2(a)). As with the dose of 2 × 10<sup>9</sup> CFU C57-CD40L<sup>-/-</sup> mice produced soft faeces during the first week and once more during the second week of infection several clinical manifestations were observed. Therefore, a dose of 1 × 10<sup>7</sup> CFU was tested, animal were followed up for 14 days, and it was observed that *C. rodentium* CFU/g among mice strains was not significantly different (Figure 2(b)). Even though, during the first week of infection, all C57-CD40L<sup>-/-</sup> mice had soft faeces, none presented any other clinical manifestations during the second week of infection. As with the dose of 2 × 10<sup>9</sup>, infection was subclinical in WT mice inoculated with either bacterial dose.

**3.3. Morphological and Histological Evaluation of Colons at 14 Days after Infection.** A hallmark feature of *C. rodentium* infection is colonic hyperplasia measured as an increase in crypt and villus high that is maximal after 10–14 days after infection [15, 22]. Other features of inflammation due to *C. rodentium* infection are decreased in colon length and increase in colon weight [23]. In order to establish if there were morphological and histological differences among mice strains after *C. rodentium* infection with 1 × 10<sup>7</sup> CFU, both mice strains were inoculated with a dose 1 × 10<sup>7</sup> CFU and control mice with sterile physiological saline (SPS). Then at day 14 after infection all mice were sacrificed and colons were removed. Colons from infected C57-CD40L<sup>-/-</sup> mice were shorter (*P* = 0.009) compared with colons of infected WT mice (Figure 3(a)). Difference in colon weight and villi high was pronounced between *C. rodentium*-infected mice (*P* < 0.001) and uninfected mice (Figures 3(b) and 3(c)). On the other hand, villi of infected WT were significantly higher (*P* = 0.0022) than in C57-CD40L<sup>-/-</sup> mice (Figure 3(c)). Histological analysis of colonic tissue of infected animals showed a mixed cellular infiltrate mostly in the submucosa but also some in the lamina propria. Surface epithelial erosion although present in both mice tissues was slightly more evident in C57-CD40L<sup>-/-</sup> mice (Figure 3(d)).

**3.4. Basal Total Concentrations of Serum Immunoglobulins.** Serum was collected from 17 WT and 19 C57-CD40L<sup>-/-</sup> adult mice (5- to 7-week-old), and isotype concentrations were determined by ELISA. IgM and IgG3 levels were essentially identical between mice strains (Figures 4(a) and 4(b)). Serum concentrations of IgA, total IgG, IgG1, IgG2b, and IgG2c were significantly lower (*P* < 0.0001) in CD40L deficient

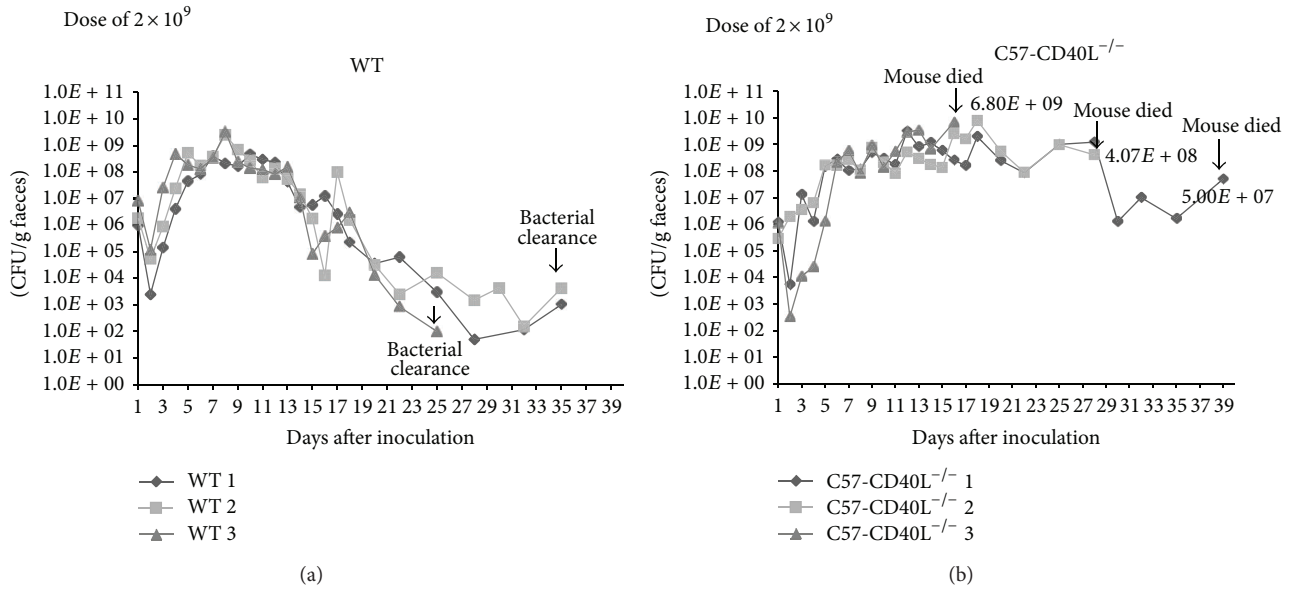


FIGURE 1: Course of *C. rodentium* infection in wild type (WT) and C57-CD40L<sup>-/-</sup> mice. (a) WT mice (black lines) and (b) C57-CD40L<sup>-/-</sup> mice (grey lines) were orally inoculated with  $2 \times 10^9$  CFU of *C. rodentium* and faecal bacterial numbers were determined. CFU/g of faeces per day and per mouse was plotted. While WT mice infected with  $2 \times 10^9$  CFU of *C. rodentium* cleared bacterial infection, C57-CD40L<sup>-/-</sup> mice died.

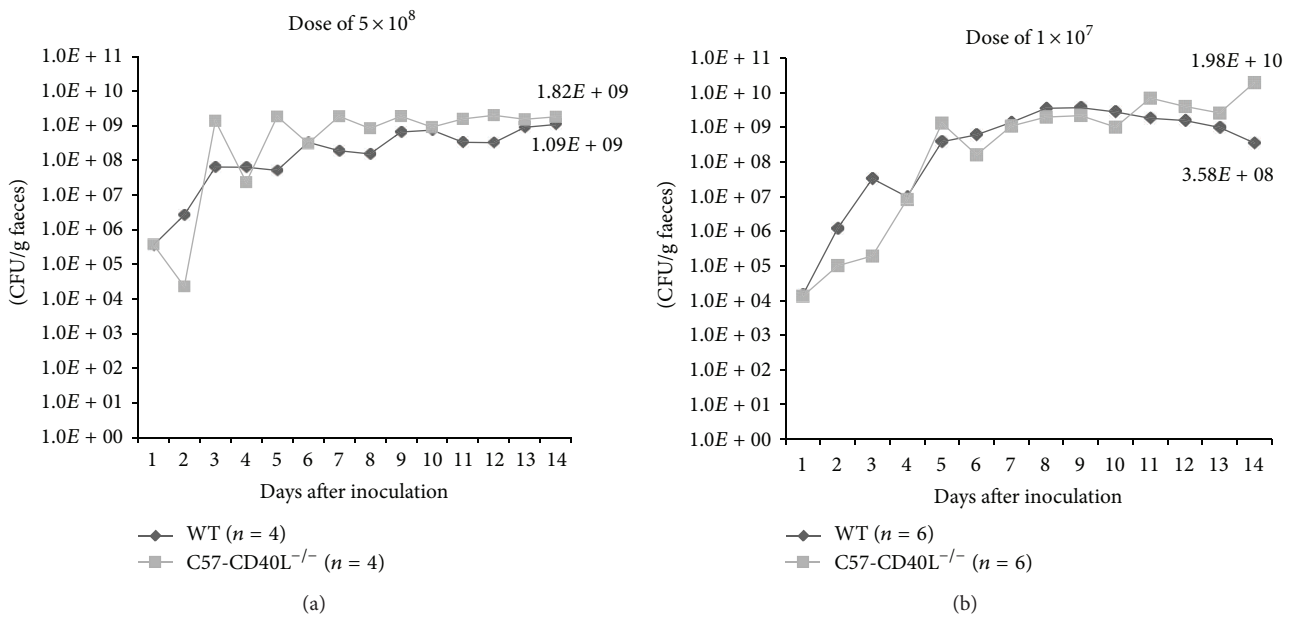


FIGURE 2: *C. rodentium* infection in WT and C57-CD40L<sup>-/-</sup> mice. WT (black lines) and C57-CD40L<sup>-/-</sup> mice (grey lines) were orally inoculated with  $5 \times 10^8$  (a) and  $1 \times 10^7$  (b) CFU of *C. rodentium*. Mean CFU/g of faeces per day and per mice strain was plotted. WT = wild type. No significant differences were observed between CFU per mice strain.

mice compared with isotype concentrations of WT (Figures 4(a) and 4(b)). The overall isotype concentration decrease between WT and C57-CD40L<sup>-/-</sup> mice was as follows: 51% for IgG2b, 65% for IgA, 69% for total IgG, 93% for IgG2c, and 96% for IgG1.

3.5. *C. rodentium*-Specific Serum Antibodies. *C. rodentium* infected WT mice characteristically develop strong pathogen-specific serum IgM responses that peak approximately 2 weeks after oral inoculation with this pathogen, while IgG responses rise above baseline and peak over

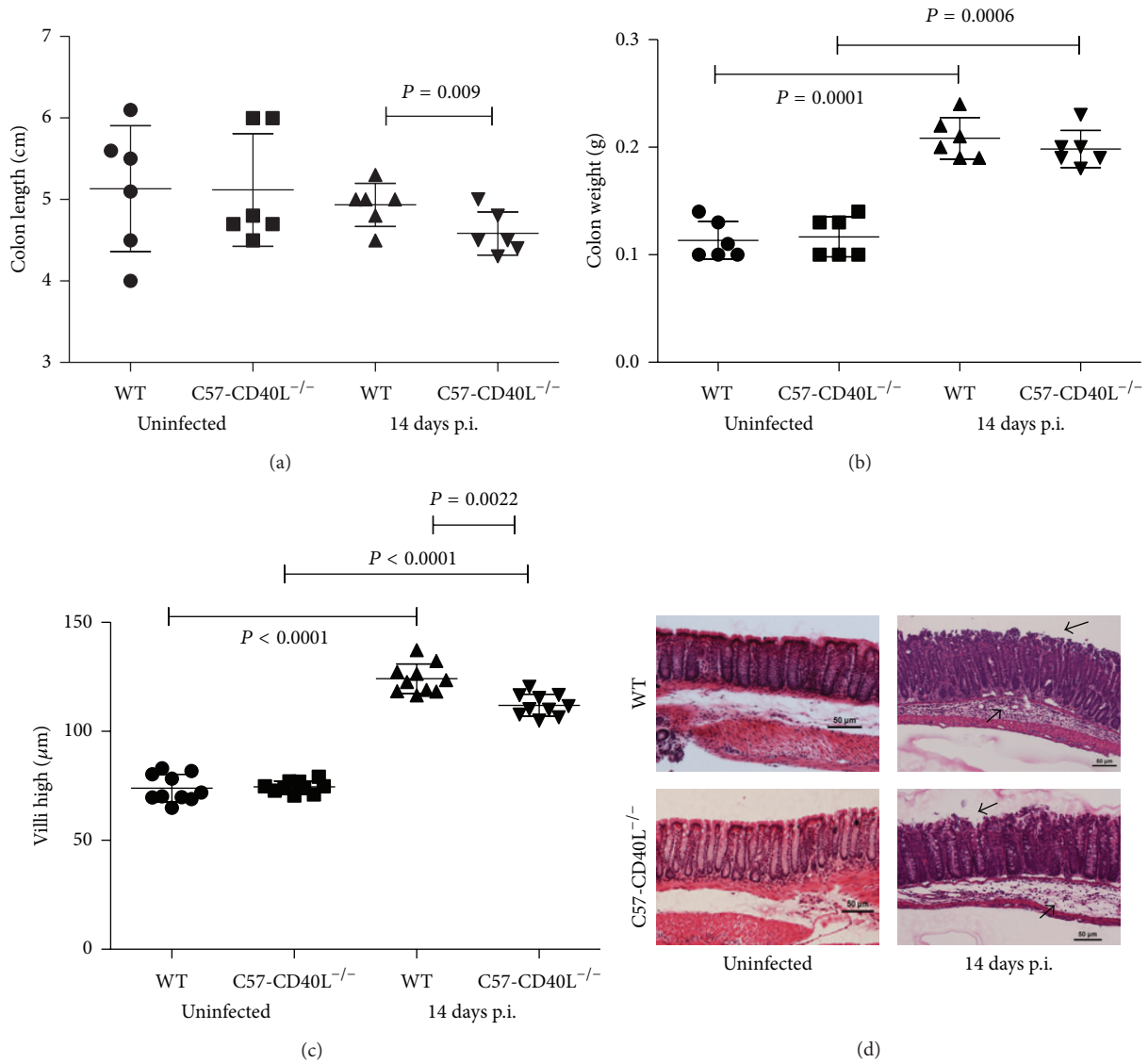


FIGURE 3: Morphological and histological analysis. Colons of wild type (WT) ( $n = 6$ ) and C57-CD40L<sup>-/-</sup> ( $n = 6$ ) mice uninfected and orally inoculated with  $1 \times 10^7$  CFU of *C. rodentium* were removed at day 14 after inoculation (p.i.). (a) Colon length. Infected C57-CD40L<sup>-/-</sup> mice colons lengths were significantly shorter than colons of infected WT mice. (b) Colon weight. Colons of infected-WT and -C57-CD40L<sup>-/-</sup> mice weighted more compared with colons of uninfected mice. (c) Villi high. Intestinal villi of both infected mice strains were significantly higher than villi of uninfected mice. Villi of infected WT mice were higher compared with villi of infected C57-CD40L<sup>-/-</sup> mice. Mean comparisons were done by paired Student's *t*-test. (d) Hematoxylin and eosin stained sections of distal colons. Arrows denote submucosal inflammatory cellular infiltrates and epithelial damage in the mucosa of infected mice.

subsequent weeks [24]. The serum samples of mice inoculated with  $1 \times 10^7$  CFU were collected at day 14 after inoculation and tested by ELISA using *C. rodentium* whole-cell sonicate as antigen. IgM-titre against *C. rodentium* was similar in both mice strains (Figure 5(a)). WT-infected mice produced significant higher concentrations of specific *C. rodentium* total IgG ( $P = 0.0045$ ) and IgG2b ( $P = 0.0345$ ) antibodies than CD40L deficient-infected mice (Figures 5(b) and 5(c)). At this time point, IgG2c *C. rodentium* specific antibodies were produced just above baseline by WT mice and were undetectable in C57-CD40L<sup>-/-</sup> mice (Figure 5(d)),

and IgG1 and IgG3 anti-*C. rodentium* antibodies were undetectable in both mice strains.

**3.6. Complement-Mediated Bactericidal Activity of Mice Serum against *C. rodentium*.** The protective serum antibody response in acute *C. rodentium* infection in WT mice consists of complement-fixing IgM and IgG2b/IgG2c antibodies [20]. Therefore, a serum bactericidal assay to measure antibody-dependent complement-mediated killing was implemented. Mice inoculated with a  $1 \times 10^7$  CFU were bled at day 14 after

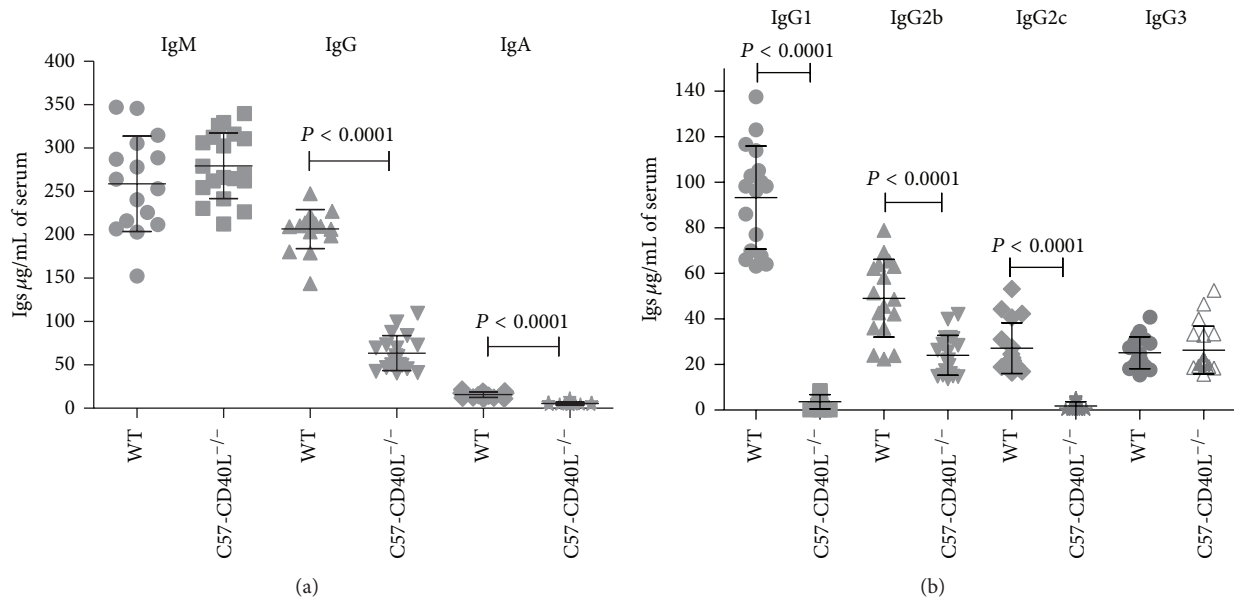


FIGURE 4: Basal Ig isotypes sera concentrations of WT ( $n = 17$ ) and C57-CD40L<sup>-/-</sup> ( $n = 19$ ) mice. (a) Basal IgM, IgG, and IgA concentrations. Ig concentrations were determined by extrapolation from a standard curve. The total mean IgM concentration was similar among mice strains. Total IgG and IgA serum concentrations of C57-CD40L<sup>-/-</sup> were significantly lower than concentrations of WT mice. (b) Basal IgG subclasses sera concentrations. IgG3 levels were essentially identical between the two groups and all other subclasses concentrations were significantly higher in WT than in CD40L deficient mice. Mean comparisons were done by Mann-Whitney  $U$ -test. WT = wild type.

inoculation. The sera of 11 immune C57-CD40L<sup>-/-</sup> mice and 12 WT mice were tested in the bactericidal assay. All tested serum samples had bactericidal activity with the exception of a serum from a CD40L deficient mouse. As shown in Figure 6, WT serum bactericidal titres were significantly higher ( $P < 0.0001$ ) compared with bactericidal titres of C57-CD40L<sup>-/-</sup> mice.

**3.7. Western Blots.** In order to identify specific antigens of *C. rodentium* whole-cell sonicate and serum from three individual mice per group were probed by Western blotting. Figure 7 shows a representative Western blot for each serum mice strain revealing that both C57-CD40L<sup>-/-</sup> and WT mouse reacted against various antigens. However, the genesis of certain isotypes against *C. rodentium* antigens was clearly CD40L dependent (Figure 7). For instance, when boiled sonicates were used as an antigen in immunoblot assays, IgM antibodies from infected WT mice recognized predominantly three bands (~50 kDa, ~42 kDa, and ~37 kDa) while only one band (~37 kDa band) of the three was recognized by the IgM antibodies of infected CD40L deficient mice. Moreover, it seems that CD40L-independent IgM and IgG antibodies are predominately directed towards the same antigens present in unboiled and boiled *C. rodentium* sonicates, compared with CD40L-dependent IgM and IgG antibodies (Figure 7).

#### 4. Discussion

Individuals with X-HIGM syndrome fail to express functional CD40L and as a consequence they cannot mount an

effective protective antibody response to opportunistic bacterial infections. During the nineties, two independent groups, developed C57-CD40L deficient mice and their humoral immune responses, were characterized [10, 11]. Over 50% of X-HIGM patients had recurrent or protracted diarrhoea. However, little is known of the systemic humoral immune response induced in X-HIGM patients against intestinal bacterial pathogens. In the present study we have characterized the humoral immune response of C57-CD40L<sup>-/-</sup> mice before and after *C. rodentium* infection. *C. rodentium* is a mouse noninvasive pathogen that produces diarrhoea and causes transmissible colonic hyperplasia in suckling and adult mice, respectively [15].

Infection of WT adult mice with a dose of  $2 \times 10^9$  *C. rodentium* CFU has been shown to be a subclinical self-limiting infection that produces sterilizing immunity. *C. rodentium* first colonizes the caecum, followed by a peak of bacteria load around days 7–10 after infection and complete clearance of the pathogen in the stools occurs 6 weeks after infection [22]. In this study when C57-CD40L<sup>-/-</sup> mice were orally inoculated with  $2 \times 10^9$  CFU, several clinical manifestations were observed (weight loss, dehydration, coat ruffling, hunched posture, and listlessness) since the second week of infection and eventually died. It has been shown that *C. rodentium*-specific IgG and CD4<sup>+</sup> T cell responses are required for WT mice survival and resolution of bacteria colonizing the gut epithelium [18–20]. Therefore, our results suggest that *C. rodentium*-infected C57-CD40L<sup>-/-</sup> mice do not produce pathogen-specific T cell-dependent antibodies. So far it has been shown that CD40L deficient mice do not

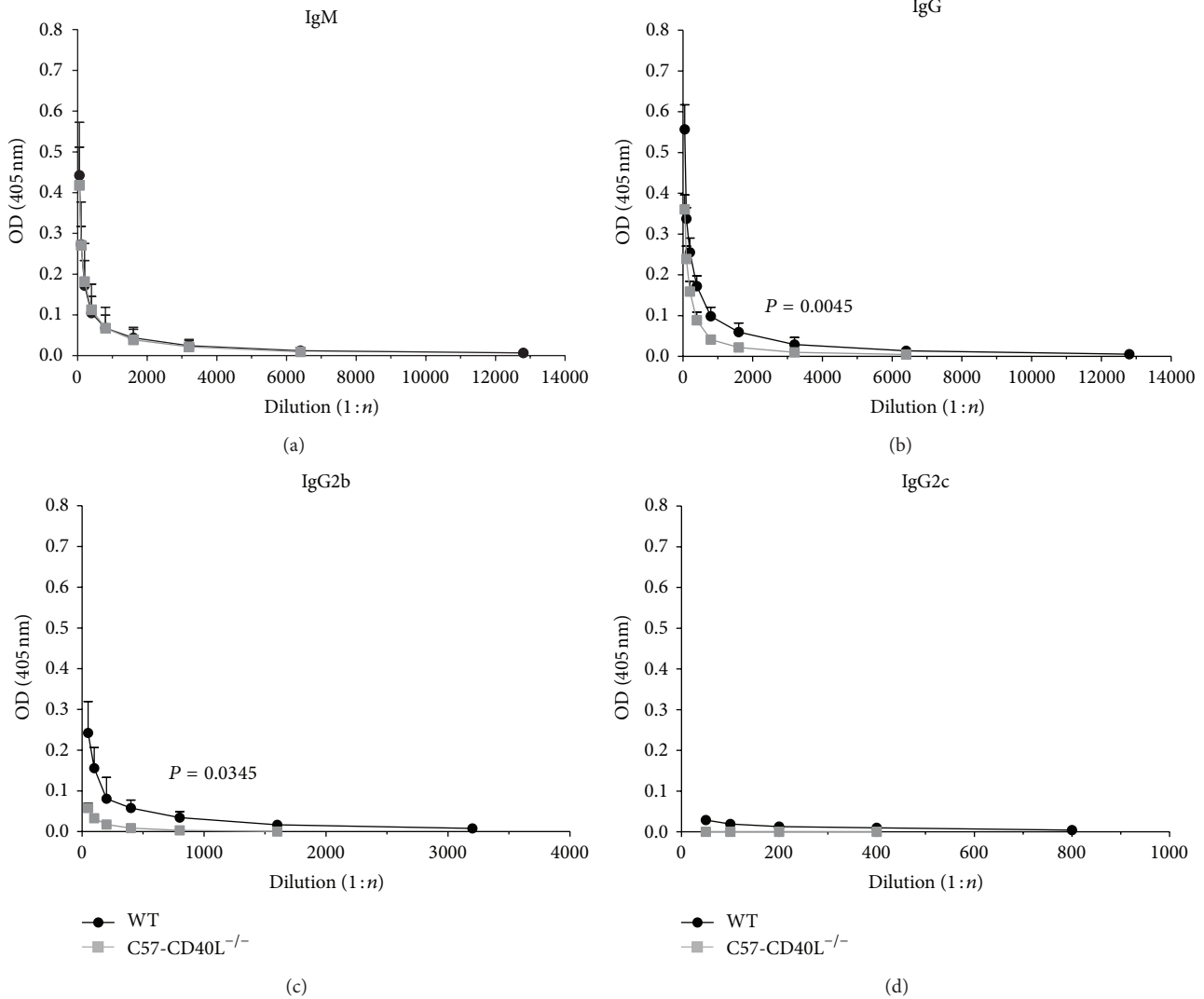


FIGURE 5: *C. rodentium*-specific sera antibodies of wild type (WT) ( $n = 6$ ) and C57-CD40L<sup>-/-</sup> ( $n = 6$ ) mice. Mice orally inoculated with  $1 \times 10^7$  CFU of *C. rodentium* were bled at day 14 after inoculation. Each point of these curves represents the mean  $\pm$  SD of the OD determinations. (a) The specific IgM titres were essentially identical between the two groups. (b) and (c)) The specific IgG and IgG2b titres were significantly lower for C57-CD40L<sup>-/-</sup> mice than WT mice. (d) IgG2c specific antibodies of both WT and C57-CD40L<sup>-/-</sup> mice were just above baseline and IgG1 and IgG3 isotypes were undetectable. Antibody titres are presented as means and data was analysed by Mann-Whitney *U*-test. OD = optical density, (1:n) = dilution factor.

produce specific IgG antibodies against TNP-KLH, a T cell-dependent antigen [10, 11]. In agreement, in this study, basal serum T-dependent IgG1 and IgG2c isotypes were almost undetectable in C57-CD40L<sup>-/-</sup> mice whereas T-independent Ig2b levels were only 49% less than that in WT mice. Overall these results are in accordance with previous reports of basal serum isotype levels in C57-CD40L<sup>-/-</sup> [10–12].

As expected immunoblots revealed that infected-WT mice serum recognized more antigens compared with infected-C57-CD40L<sup>-/-</sup> serum. Interestingly, immunoblot analysis revealed that CD40L-independent IgM and IgG antibodies are predominately directed towards the same antigens present in unboiled and boiled *C. rodentium* sonicates. Thus CD40L deficient mice are capable of generating *C. rodentium*

IgG specific antibodies independent of CD40-CD40L interactions and these antibodies are towards the same antigens recognized by IgM. In the present study a ~37 kDa protein was strongly recognized by *C. rodentium*-infected CD40 deficient mice sera (Figure 7). We speculate that maybe this ~37 kDa protein could be EspB, a 37 KDa protein secreted by pathogens producing A/E lesion as *C. rodentium*, EPEC, and EHEC [25, 26]. EspB has been shown to play an important role in adherence, pore formation, and effector translocation during infection [26]. EspB has also been reported to interact with EspA and EspD [26] simultaneously, and the complexes formed by these three proteins participate in the initial step of bacterial adherence [26]. Nevertheless, the chemical and exact identity of the major *C. rodentium* antigens that were

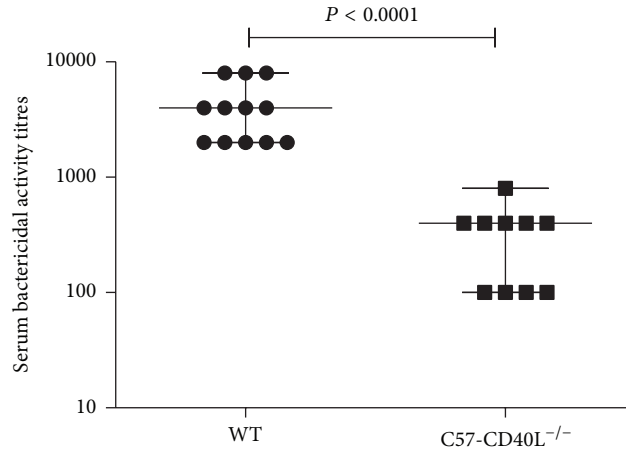


FIGURE 6: Complement-mediated bactericidal activity. Mice were orally inoculated with  $1 \times 10^7$  *C. rodentium* CFU and were bled at 14 days after inoculation. Both mice sera had bactericidal activity; C57-CD40L<sup>-/-</sup> mice ( $n = 11$ ) sera had significantly lower bactericidal activity compared with wild type (WT) ( $n = 12$ ) mice sera. Data for bactericidal activity are presented as medians and data was analysed by Mann-Whitney *U*-test.

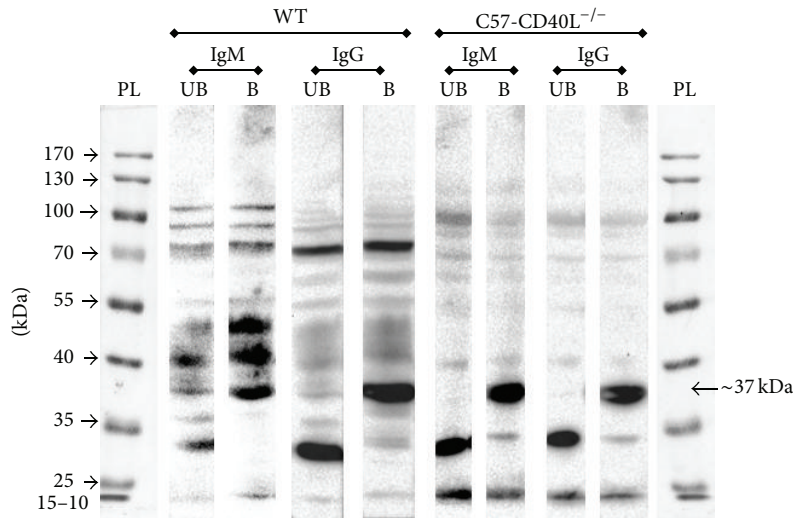


FIGURE 7: Western blot analysis of *C. rodentium* antiserum of wild type mice (WT) and C57-CD40L<sup>-/-</sup> mice. Mice were orally inoculated with  $1 \times 10^7$  *C. rodentium* CFU and were bled at 14 days after inoculation. Whole cell lysates were resolved in 10% gels by SDS-PAGE, and the serum was diluted 1 : 200. PL = protein ladder, UB = unboiled lysate, and B = boiled lysate.

differentially recognized by wild type and CD40L deficient mice sera remains to be determined.

Antibody-mediated immune responses play a critical role in the defence against extracellular pathogens. Hence, if specific antibodies against *C. rodentium* are produced, it is necessary to determine an infectious dose that minimizes the observed clinical manifestations induced by *C. rodentium* in C57-CD40L<sup>-/-</sup> mice. In the present study, no clinical manifestations were observed among C57-CD40L<sup>-/-</sup> mice, infected with  $1 \times 10^7$  CFU, at the second week after inoculation. It has been shown that *C. rodentium*-infected WT mice characteristically develop strong pathogen-specific serum IgM responses that peak approximately at two weeks after infection [24]. Accordingly at this time point we observed

that C57-CD40L<sup>-/-</sup> infected mice mounted a similar serum IgM specific response compared to infected WT mice. Likewise, at day 14 after inoculation CD40L deficient mice had similar *Borrelia burgdorferi*-specific serum IgM antibodies compared to control mice [27]. The importance of IgM in the resolution of spirochaetaemia has been substantiated; for example, mice that are incapable of secreting IgM failed to clear the infection and mechanism as IgM-dependent bacteria phagocytosis has been demonstrated [28]. On the other hand, mice incapable of secreting IgM infected with *C. rodentium* ( $5 \times 10^8$ ) successfully cleared *C. rodentium* infection [29]. We observed that the major serum IgG subclass produced by *C. rodentium*-infected CD40L deficient mice was the complement fixing IgG2b antibody, though

being in lower concentration than WT mice. Also IgG2b is the most prevalent isotype produced in serum and faeces of *C. rodentium*-infected WT mice at 15 days after infection [20]. Several studies have shown *C. rodentium*-specific IgG antibodies are required for WT mice survival and resolution of bacteria colonizing the gut epithelium [20, 29].

It is well known that protective antibody response against *C. rodentium* infection consists largely of complement-fixing antibodies [20]. Therefore, we tested the serum from *C. rodentium*-infected mice with a dose of  $1 \times 10^7$ , from the 14th day after infection, in a complement-mediated bactericidal assay. The serum from all animals (except from the serum of a CD40L deficient mouse) displayed a complement-mediated bactericidal activity against *C. rodentium*. Even so, C57-CD40L<sup>-/-</sup> mice serum bactericidal antibody titres were significantly lower than titres of WT. To the best of our knowledge, this is the first study that shows that serum from CD40L deficient mice has a complement-mediated bactericidal activity. It remains to be determined if this bactericidal activity provides a survival advantage to *C. rodentium* infected CD40L deficient mice. It has been shown that acute-phase serum transfer from infected C57-CD40L<sup>-/-</sup> mice with a high dose of *C. rodentium* ( $5 \times 10^8$  CFU) provided a survival advantage of some days to *C. rodentium*-infected CD4 deficient mice recipients but failed to provide complete protection [24]. On the other hand, transfer of serum from *B. burgdorferi*-infected C57-CD40L<sup>-/-</sup> mouse prevented *B. burgdorferi* infection in a severe combined immunodeficient mouse [27]. Overall, our results suggest that T cells defects due to the albescence of CD40L, which are important in controlling intracellular pathogens, do not play a major role in the clearance of *C. rodentium* and *B. burgdorferi* primary considered to be extracellular pathogens [28].

Likewise serum pathogen-specific IgM and IgG antibodies may have an important role in bacterial clearance in X-HIGM patients. Accordingly, a serum, containing high levels of IgM, from X-HIGM patient infected with *Helicobacter pylori* displayed a 100% killing activity, when tested in a complement-mediated bactericidal assay [30]. It has been documented that sera from X-HIGM patients in addition to normal or elevated concentrations of IgM also contain IgG and IgA in low concentrations, but IgG3 levels are almost normal [31]. IgG3 and IgM isotypes are the more efficient complement-fixing human antibodies [28]. Therefore, serum from XIGH patients may exhibit a complement-mediated bactericidal activity that could result in extracellular bacterial clearance and disease resolving.

## 5. Conclusions

This study demonstrated that C57-CD40L<sup>-/-</sup> mouse is a useful surrogate model of X-HIGM syndrome.

Since most infections in X-HIGM patients are chronic, C57-CD40L<sup>-/-</sup> mice will help to study the immune response elicited against human or surrogate human pathogens and to implement treatments that hopefully will help pathogen clearance in X-HIGM patients.

## Conflict of Interests

The authors declare that there is no conflict of interests regarding the publication of this paper.

## Acknowledgments

This work was supported by Grant nos. 34404-N, 46068, and 128779 of CONACYT, Mexico, to Teresa Estrada-Garcia, Rodolfo Bernal-Reynaga (219326) was supported by CONACYT scholarships, and Catalina Lopez-Saucedo (12BCD0047-I) was supported by COMECYT scholarships.

## References

- [1] J. Johnson, A. H. Filipovich, and K. Zhang, "X-linked hyper IgM syndrome," in *SourceGeneReviews*, R. A. Pagon, M. P. Adam, H. H. Ardinger et al., Eds., pp. 1993–2014, University of Washington, Seattle, Wash, USA, 2007.
- [2] A. Etzioni and H. D. Ochs, "The hyper IgM syndrome—an evolving story," *Pediatric Research*, vol. 56, no. 4, pp. 219–225, 2004.
- [3] U. Schönbeck and P. Libby, "The CD40/CD154 receptor/ligand dyad," *Cellular and Molecular Life Sciences*, vol. 58, no. 1, pp. 4–43, 2001.
- [4] B. Gathmann, B. Grimbacher, J. Beauté et al., "The European internet-based patient and research database for primary immunodeficiencies: results 2006–2008," *Clinical & Experimental Immunology*, vol. 157, supplement s1, pp. 3–11, 2009.
- [5] S. Gupta, M. Madkaikar, S. Singh, and S. Sehgal, "Primary immunodeficiencies in India: a perspective," *Annals of the New York Academy of Sciences*, vol. 1250, no. 1, pp. 73–79, 2012.
- [6] O. Cabral-Marques, S. Klaver, L. F. Schimke et al., "First report of Hyper-IgM syndrome registry of the latin american society for immunodeficiencies: novel mutation, unique infections, and outcomes," *Journal of Clinical Immunology*, vol. 34, pp. 146–156, 2014.
- [7] A. Vargas-Hernández, L. Berrón-Ruiz, T. Staines-Boone et al., "Clinical and genetic analysis of patients with X-linked hyper-IgM syndrome," *Clinical Genetics*, vol. 83, no. 6, pp. 585–587, 2013.
- [8] J. A. Winkelstein, M. C. Marino, H. Ochs et al., "The X-linked hyper-IgM syndrome: clinical and immunologic features of 79 patients," *Medicine*, vol. 82, no. 6, pp. 373–384, 2003.
- [9] M. A. Croxen, R. J. Law, R. Scholz, K. M. Keeney, M. Wlodarska, and B. B. Finlay, "Recent advances in understanding enteric pathogenic *Escherichia coli*," *Clinical Microbiology Reviews*, vol. 26, no. 4, pp. 822–880, 2013.
- [10] B. R. Renshaw, W. C. Fanslow III, R. J. Armitage et al., "Humoral immune responses in CD40 ligand-deficient mice," *The Journal of Experimental Medicine*, vol. 180, no. 5, pp. 1889–1900, 1994.
- [11] J. Xu, T. M. Foy, J. D. Laman et al., "Mice deficient for the CD40 ligand," *Immunity*, vol. 1, no. 5, pp. 423–431, 1994.
- [12] R. Bernal-Reynaga, R. Thompson-Bonilla, C. Lopez-Saucedo, M. Pech-Armenta, S. Estrada-Parra, and T. Estrada-Garcia, "C57-CD40 ligand deficient mice: a potential model for enterotoxigenic *Escherichia coli* (H10407) colonization," *Veterinary Immunology and Immunopathology*, vol. 152, no. 1-2, pp. 50–56, 2013.
- [13] M. Cosyns, S. Tsirkin, M. Jones, R. Flavell, H. Kikutani, and A. R. Hayward, "Requirement for CD40-CD40 ligand

- interaction for elimination of *Cryptosporidium parvum* from mice," *Infection and Immunity*, vol. 66, no. 2, pp. 603–607, 1998.
- [14] S. A. Luperchio and D. B. Schauer, "Molecular pathogenesis of *Citrobacter rodentium* and transmissible murine colonic hyperplasia," *Microbes and Infection*, vol. 3, no. 4, pp. 333–340, 2001.
- [15] S. W. Barthold, G. L. Coleman, R. O. Jacoby, E. M. Livestone, and A. M. Jonas, "Transmissible murine colonic hyperplasia," *Veterinary Pathology*, vol. 15, no. 2, pp. 223–236, 1978.
- [16] J. W. Collins, K. M. Keeney, V. F. Crepin et al., "Citrobacter rodentium: infection, inflammation and the microbiota," *Nature Reviews Microbiology*, vol. 12, no. 9, pp. 612–623, 2014.
- [17] E. Johnson and S. W. Barthold, "The ultrastructure of transmissible murine colonic hyperplasia," *The American Journal of Pathology*, vol. 97, no. 2, pp. 291–313, 1979.
- [18] C. P. Simmons, S. Clare, M. Ghaem-Maghani et al., "Central role for B lymphocytes and CD4<sup>+</sup> T cells in immunity to infection by the attaching and effacing pathogen *Citrobacter rodentium*," *Infection and Immunity*, vol. 71, no. 9, pp. 5077–5086, 2003.
- [19] L. Bry and M. B. Brenner, "Critical role of T cell-dependent serum antibody, but not the gut-associated lymphoid tissue, for surviving acute mucosal infection with *Citrobacter rodentium*, an attaching and effacing pathogen," *The Journal of Immunology*, vol. 172, no. 1, pp. 433–441, 2004.
- [20] C. Belzer, Q. Liu, M. C. Carroll, and L. Bry, "The role of specific IgG and complement in combating a primary mucosal infection of the gut epithelium," *European Journal of Microbiology and Immunology*, vol. 1, no. 4, pp. 311–318, 2011.
- [21] C. López-Saucedo, J. F. Cerna, N. Villegas-Sepulveda et al., "Single multiplex polymerase chain reaction to detect diverse loci associated with diarrheagenic *Escherichia coli*," *Emerging Infectious Diseases*, vol. 9, no. 1, pp. 127–131, 2003.
- [22] O. L. Wei, A. Hilliard, D. Kalman, and M. Sherman, "Mast cells limit systemic bacterial dissemination but not colitis in response to *Citrobacter rodentium*," *Infection and Immunity*, vol. 73, no. 4, pp. 1978–1985, 2005.
- [23] R. Mundy, T. T. MacDonald, G. Dougan, G. Frankel, and S. Wiles, "*Citrobacter rodentium* of mice and man," *Cellular Microbiology*, vol. 7, no. 12, pp. 1697–1706, 2005.
- [24] L. Bry, M. Brigl, and M. B. Brenner, "CD4<sup>+</sup> T-cell effector functions and costimulatory requirements essential for surviving mucosal infection with *Citrobacter rodentium*," *Infection and Immunity*, vol. 74, no. 1, pp. 673–681, 2006.
- [25] J. V. Newman, B. A. Zabel, S. S. Jha, and D. B. Schauer, "*Citrobacter rodentium* espB is necessary for signal transduction and for infection of laboratory mice," *Infection and Immunity*, vol. 67, no. 11, pp. 6019–6025, 1999.
- [26] H.-J. Chiu and W.-J. Syu, "Functional analysis of EspB from enterohaemorrhagic *Escherichia coli*," *Microbiology*, vol. 151, no. 10, pp. 3277–3286, 2005.
- [27] E. Fikrig, S. W. Barthold, M. Chen, I. S. Grewal, J. Craft, and R. A. Flavell, "Protective antibodies in murine Lyme disease arise independently of CD40 ligand," *The Journal of Immunology*, vol. 157, no. 1, pp. 1–3, 1996.
- [28] S. E. Connolly and J. L. Benach, "The versatile roles of antibodies in *Borrelia* infections," *Nature Reviews Microbiology*, vol. 3, no. 5, pp. 411–420, 2005.
- [29] C. Maaser, M. P. Housley, M. Iimura et al., "Clearance of *Citrobacter rodentium* requires B cells but not secretory immunoglobulin A (IgA) or IgM antibodies," *Infection and Immunity*, vol. 72, no. 6, pp. 3315–3324, 2004.
- [30] I. M. E. Desar, M. van Deuren, T. Sprong et al., "Serum bactericidal activity against *Helicobacter pylori* in patients with hypogammaglobulinaemia," *Clinical and Experimental Immunology*, vol. 156, no. 3, pp. 434–439, 2009.
- [31] G. R. McLean, K. K. Miller, J. W. Schrader, and A. K. Junker, "Biased immunoglobulin G (IgG) subclass production in a case of hyper-IgM syndrome," *Clinical and Diagnostic Laboratory Immunology*, vol. 11, no. 6, pp. 1192–1193, 2004.

## Research Article

# Biochemical and Functional Comparisons of *mdx* and *Sgcg*<sup>-/-</sup> Muscular Dystrophy Mouse Models

Nathan W. Roberts,<sup>1</sup> Jenan Holley-Cuthrell,<sup>1</sup> Magdalis Gonzalez-Vega,<sup>1</sup>  
Aaron J. Mull,<sup>1</sup> and Ahlke Heydemann<sup>1,2</sup>

<sup>1</sup>Department of Physiology and Biophysics, The University of Illinois at Chicago, Chicago, IL 60612, USA

<sup>2</sup>Center for Cardiovascular Research, The University of Illinois at Chicago, Chicago, IL 60612, USA

Correspondence should be addressed to Ahlke Heydemann; ahlkeh@uic.edu

Received 25 September 2014; Revised 13 January 2015; Accepted 13 January 2015

Academic Editor: Oreste Gualillo

Copyright © 2015 Nathan W. Roberts et al. This is an open access article distributed under the Creative Commons Attribution License, which permits unrestricted use, distribution, and reproduction in any medium, provided the original work is properly cited.

Mouse models have provided an essential platform to investigate facets of human diseases, from etiology, diagnosis, and prognosis, to potential treatments. Muscular dystrophy (MD) is the most common human genetic disease occurring in approximately 1 in 2500 births. The *mdx* mouse, which is dystrophin-deficient, has long been used to model this disease. However, this mouse strain displays a rather mild disease course compared to human patients. The *mdx* mice have been bred to additional genetically engineered mice to worsen the disease. Alternatively, other genes which cause human MD have been genetically disrupted in mice. We are now comparing disease progression from one of these alternative gene disruptions, the  $\gamma$ -sarcoglycan null mouse *Sgcg*<sup>-/-</sup> on the DBA2/J background, to the *mdx* mouse line. This paper aims to assess the time-course severity of the disease in the mouse models and determine which is best for MD research. The *Sgcg*<sup>-/-</sup> mice have a more severe phenotype than the *mdx* mice. Muscle function was assessed by plethysmography and echocardiography. Histologically the *Sgcg*<sup>-/-</sup> mice displayed increased fibrosis and variable fiber size. By quantitative Evan's blue dye uptake and hydroxyproline content two key disease determinants, membrane permeability and fibrosis respectively, were also proven worse in the *Sgcg*<sup>-/-</sup> mice.

## 1. Introduction

A satisfactory mouse model is required to fight the devastating effects of muscular dystrophy (MD). The mouse model must mimic the human disease in etiology, pathology, and potential therapy responses to be optimally useful. In the experiments presented in this paper we directly compared the progressive pathology of two MD mouse models side-by-side to identify the most severe and therefore the most human-similar and useful model. We produced comparative time-courses of disease progression of the *mdx* and  $\gamma$ -sarcoglycan null mice (official nomenclature, *Dmd*<sup>*mdx*</sup>, and *Sgcg*<sup>-/-</sup> D2) using quantitative membrane permeability and fibrosis assessments, plethysmography, and echocardiography.

Muscular dystrophy in humans is caused by mutations in a number of genes. The genes can be divided into 4 loosely aligned functional classes (1) dystrophin glycoprotein complex (DGC), which includes dystrophin and the sarcoglycans (Figure 1(a)), (2) extracellular matrix genes, (3) nuclear

membrane genes, and (4) signaling molecules. By far the most frequent mutations are found in the DGC component dystrophin, these mutations cause Duchenne (DMD) or Becker muscular dystrophies in humans and *mdx* in mice. Mutations in the  $\gamma$ -sarcoglycan gene of the DGC cause limb girdle muscular dystrophy type 2C (LGMD-2C) in humans and are designated *Sgcg*<sup>-/-</sup> in mice.

The pathology and treatments of human DMD and LGMD-2C are severe and similar [1]. After the initial disruption of the DGC, disease progression follows a very similar course (Figure 1(b)): (1) membrane permeability followed by mislocalized calcium, nitric oxide, and other signaling moieties, (2) repeated rounds of degeneration and regeneration, (3) inflammation, (4) necrosis, and (5) replacement with myofibroblasts and scar tissue leading to functional decline. These events do not occur in strict sequence and in a single muscle all of these events are occurring at the same time. The *mdx* and *Sgcg*<sup>-/-</sup> mice also display the same disease progression, but as we will demonstrate at different severity levels.

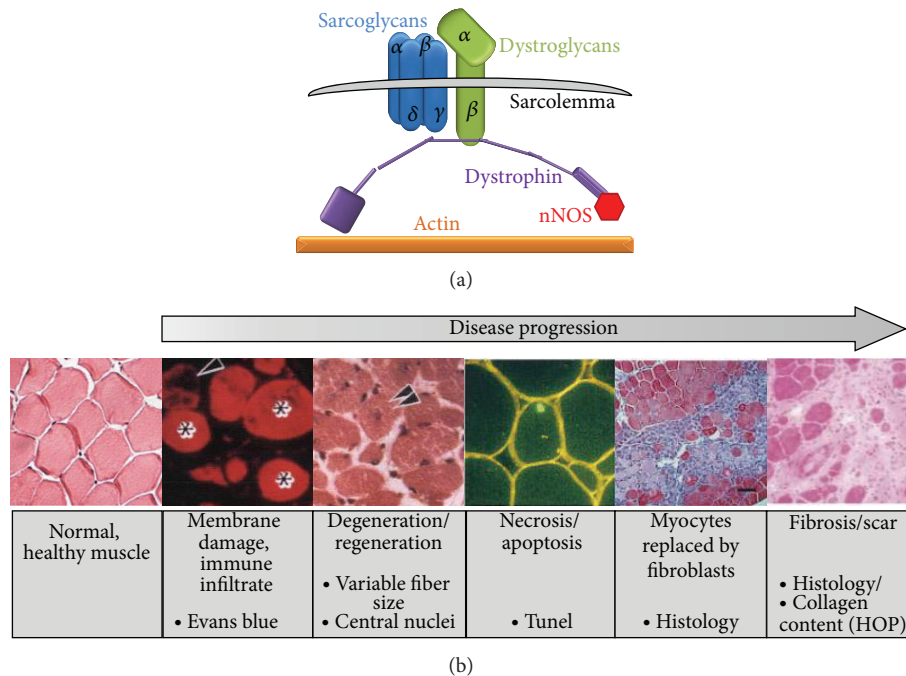


FIGURE 1: The dystrophin glycoprotein complex and muscular dystrophy pathology in mice. (a) Muscular dystrophy can occur from mutations in the genes that form the dystrophin glycoprotein complex. (b) Representative images demonstrating disease progression of muscular dystrophy in a mouse model.

As DMD is the most common form of human muscular dystrophy, the dystrophin deficient *mdx* mouse is the most commonly used animal model to represent this disease. The *mdx* mutation was spontaneously identified in a colony of C57BL/10 mice [2]. It was later identified to be in the dystrophin gene [3], which was also identified to be causative for DMD [4]. The originally mutated mouse was identifiable because the dystrophin gene is on the X-chromosome and the original male could be assessed in the hemizygous state.

However, the *mdx* mouse model is not an adequate representation of the human disease. The only muscle that is consistently affected is the diaphragm, which shows membrane permeability and fibrotic replacement [5]. In addition, the *mdx* mice have a peak of pathology at 4 weeks old and otherwise the mice have very little pathology (reviewed in [6]).

Additional genetic engineering and breeding have been conducted to worsen the disease. A double knockout was generated with both dystrophin and its homolog utrophin deleted [7]. These mice are severely affected and only half live beyond 8 weeks old (Deconinck and [7]). Recently another knock-out combination of both dystrophin and telomerase also caused a very severe phenotype [8]. These two mouse models do not reflect the etiology found in humans as they require a second genetic mutation to attain a severe phenotype. Dystrophin mutation in humans is sufficient to induce a severe phenotype and, untreated, death before the end of the third decade. While these models' phenotypes are severe, the causes of the severity are different than those found in humans. These additional factors must then be compensated for during investigations bringing into question whether the research could be translated to patients.

The mouse model we are assessing is the genetically engineered  $\gamma$ -sarcoglycan (*Sgcg*<sup>-/-</sup>) null mutation [9] on the DBA/2J (D2) background [10]. In the original publication, it was identified that the *Sgcg*<sup>-/-</sup> mice on the mixed C57BL/6J-129 background have a more severe cardiomyopathy than the *mdx* mice [9]. It was then demonstrated that the *Sgcg*<sup>-/-</sup> mutation is more severe when bred onto the D2 background [10]. The D2 mice carry a naturally occurring in-frame deletion within their Latent TGF $\beta$  Binding Protein 4 (LTBP4) gene; the deletion segregates at a high level with severe disease [11]. The deletion causes a further increase in the already MD-elevated levels of active TGF $\beta$ , which caused the excessive fibrosis observed in the *Sgcg*<sup>-/-</sup> D2 mice over three other comparison strains [11]. The D2 mouse strain also carries *Dyscalc*, a naturally occurring gene locus. This locus is linked to increased dystrophic cardiac calcinosis in numerous mouse lines including the D2, compared to mice lacking the *Dyscalc* gene locus [12]. Presence of the *Dyscalc* locus is sufficient to induce calcified lesions as a result of calcium deposits that accumulate after myofibers have necrosed, even in the wild type D2 mice. The causative gene is still under dispute, *Abcc6* [13] or *Emp3* [14]. While the products of these genes are known their exact functions are still under investigation. Additional breeding with the *mdx* mutation demonstrated that the *mdx* mutation presents more severely when bred onto the D2 background [15].

The ultimate usefulness of animal models is in the testing of potential patient therapies. Currently MD patients receive corticosteroids to diminish the skeletal deformities associated with MD and to keep the patients mobile as long as possible.

Corticosteroids have not been proven useful in the animal models [16]; they have limited usefulness in humans as well. They are associated with significant side-effects [17, 18] and are not tolerated well for the long periods required for this chronic disease [17, 18]. Recently, it is also advised to prophylactically prescribe angiotensin receptor blockers or angiotensin converting enzyme inhibitors (reviewed in [19]). Angiotensin receptor blockers have shown efficacy in both the *mdx* mouse model [20] and in humans [21]. Furthermore, two of the most promising future therapies for a subset of MD patients are exon-skipping and read-through technologies [22, 23]. Both of these therapies, now on the brink of phase 2 and 3 trials, have proven efficacious in restoring dystrophin expression in the *mdx* mouse model [24]. These two therapies are examples from many more promising therapies justifying the further production and use of MD mouse models.

## 2. Materials and Methods

**Animals.** Mice were housed following UIC, national and international animal welfare protocols. A 12-hour light/dark cycle is kept year round within the animal facility; food and water are ad libitum. The mice are watched by the veterinary staff of the Biological Research Laboratory at UIC. Animals were housed 5 to a cage after weaning. DBA2/J (D2) mice with the *Sgcg*<sup>+/-</sup> were graciously provided by Dr. Elizabeth McNally. The mice have since been bred using Het (*Sgcg*<sup>+/-</sup>) × Het breeding pairs and randomized selection of breeds to reduce user induced genetic drift. Het × Het and Het × KO (*Sgcg*<sup>-/-</sup>) breeding pairs were established to provide the necessary animals for this study. *Mdx* mice were acquired from Jackson Laboratories (Bar Harbor Maine); they were housed in the animal facility to ensure identical environments.

**Histology.** Following harvest the tissues designated for paraffin imbedding was placed into 1.5 mL tubes filled with 1 mL of neutral buffered formalin. The fixed tissues were taken to the UIC RRC Histology Core for paraffin imbedding, slicing, Masons Trichrome, Pico Sirius Red, and H&E staining. The resulting slides were imaged on an Aperio ScanScope CS (Leica Biosystems, Nussloch Germany) whole slide imager. Image Scope (Leica Biosystems) was used to visualize the slide images for analysis. ImageJ was used to quantify fiber size variability.

**Evans Blue Dye (EBD).** Two days before harvest each mouse is injected with EBD (Sigma Aldrich) at 5  $\mu$ L per gram of animal weight. EBD at 10 mg/mL in PBS was aliquoted and stored at -20C. Following sacrifice, tissue samples were minced and weighed in prelabelled 1.5 mL tubes. The tissues were frozen in liquid nitrogen and stored at -80C until processing. Tissues to be assayed were removed from the -80 freezer and 1 mL of Formamide (Sigma Aldrich) was added to each sample. The samples were then mixed by vortexing and incubating at 55°C for two hours. Following incubation the samples are mixed again by vortexing and spun down at 3 k rpm for 1 minute. 200  $\mu$ L of each sample and standards in triplicate (0  $\mu$ g, 0.625  $\mu$ g, 1.25  $\mu$ g, 2.5  $\mu$ g, 5  $\mu$ g, 10  $\mu$ g, and 20  $\mu$ g of EBD) were transferred to a corresponding well in

a 96-well plate and then assessed on a Bio-Tek Synergy HT plate reader at 620 nm. The standards are used to create a linear fit equation, which is then used to calculate the  $\mu$ g EBD concentration of each sample. The  $\mu$ g EBD concentration of each sample is then divided by the initial tissue weight giving a measure of  $\mu$ g EBD/mg tissue weight for each sample. All samples are normalized to the kidney average to mitigate possible injection errors and equalize the dose between mice.

**Hydroxyproline Assay (HOP).** The HOP protocol used follows a modified protocol from Flesch et al. [25]. Tissue samples were minced and weighed in prelabelled 1.5 mL tubes. 1 mL of 6 M hydrochloric acid (Sigma Aldrich, St. Louis, MO) was added to each tube. The tubes were heated at 105°C for 3 hours. After the heating period the samples were removed from the heat and left to cool to room temperature. 10  $\mu$ L of each sample was added to a clean, labelled, 1.5 mL tube with 150  $\mu$ L of isopropanol. After being mixed, 75  $\mu$ L of Solution A (1 part chloramine T (70 mg chloramine T (Sigma Aldrich) + 1 mL H<sub>2</sub>O) to 4 parts Acetate Citrate Buffer (57 g of Sodium Acetate (Sigma Aldrich), anhydrous, 435 mL of 1 M NaOH, 33.4 g of Citric Acid (Sigma Aldrich), 385 mL of Isopropanol, water to 1 liter)) is added. The samples are inverted twenty times and left to sit at room temperature for 10 minutes. Immediately following that, 1 mL of Solution B (3 parts Ehrlich's Reagent (3 g of p-dimethylaminobenzaldehyde (Sigma Aldrich), 10 mL of EtOH, 675  $\mu$ L of sulfuric acid (Thermo Fischer Scientific, Waltham MA) (mixed in drop by drop) to 13 parts isopropanol)) was added. The samples are again inverted twenty times to mix and then immediately placed into a 58°C water bath. Following a 30 minute incubation the samples are removed from the water bath, quickly mixed, and then buried in ice to quench the reaction. Cooled samples are then spun at 5 k for 1 minute, and 200  $\mu$ L of each sample is moved to a corresponding well in a 96-well plate. Along with standards in triplicate (0, 50, 100, 500, 1000, 500, 1000, and 2000 mM Hydroxyproline (Sigma Aldrich)) the samples are assessed by a Bio-Tek Synergy HT (Bio-Tek, Winooski VT) plate reader at 558 nm. The standards are used to create a linear fit equation, which is then used to calculate the mM hydroxyproline concentration of each sample. The mM hydroxyproline concentration is then divided by the initial tissue weight, giving a final mM hydroxyproline/tissue weight (mg) concentration for each sample.

**Plethysmography.** Three days before harvest respiratory function was assessed for each mouse. The Buxco Small Animal Plethysmography (Buxco/DSI, St. Paul MN) set-up, using FinePointe (Buxco/DSI), was used. In brief, the machine is calibrated before each day's assessments. Mice are loaded into chambers individually, given an adjustment period, and then assessed for 15 minutes each. Each animal is assessed in at least two chambers sequentially. Breath frequency (*f*) was used to cull extraneous data sets from any instances in which the animal may have held its breath or breathed very rapidly. This was done by finding the average *f* for each mouse per total session. Standard deviation was calculated by Microsoft Excel and any data sets falling outside of 1 standard deviation were removed from that individual mouse's data set. The new

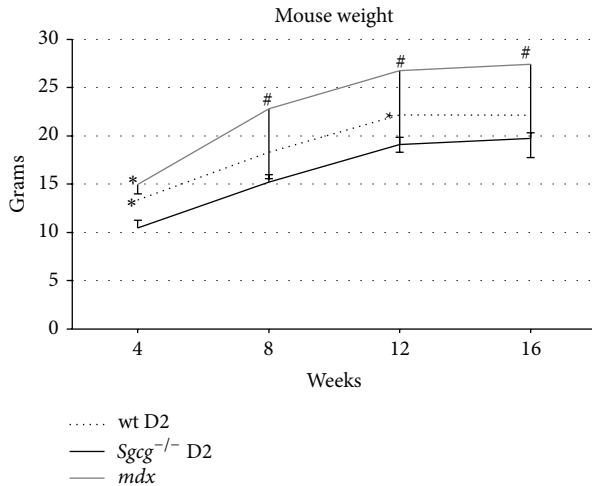


FIGURE 2: Consistent with severe pathology the *Sgcg*<sup>-/-</sup> D2 mice weighed less than their wild type D2 controls throughout the 16 weeks. Wild type D2 mice weighed significantly more than the *Sgcg*<sup>-/-</sup> D2 mice at 4 and 12 weeks. \**P* < 0.05 significance by Student's *t*-test versus *Sgcg*<sup>-/-</sup> D2 animals. *n* = 4–20.

average for each mouse was then calculated. Enhanced pause (Penh) is a mathematical comparison between early and late expirations a higher value represents increased pathology due to slower—more fibrotic—late expiration. It is calculated by FinePointe as  $Penh = (PEF/PIF) \times (Te/Rt - 1)$ , where PEF is peak expiratory height, PIF is peak inspiratory height, Te is expiratory time, and Rt is time to expire 65% of the volume.

**Echocardiography.** Cardiac function was assessed by Dr. Robert Gaffin of the UIC Center for Cardiovascular Research Physiology Core Labs using a Vevo 2100, with the manufacturer's supplied software.

**Statistics.** Statistical analysis was performed using Student *t*-tests on Microsoft Excel.

### 3. Results

Multiple murine MD mouse lines have been utilized by researchers to investigate the etiology, pathology, and possible treatments for various forms of this devastating disease. In addition, various comparisons have also been conducted ([10, 15, 26] as examples) to identify the proper model for each experiment. We now present data comparing two mutations which model the most common form of MD that of MD generated by mutations within the dystrophin-glycoprotein proteins. We have time course comparisons of biochemical, histological, and functional characterizations for the *mdx* and *Sgcg*<sup>-/-</sup> D2 mouse strains.

**3.1. Animal Weights.** Animal weights are an initial test of MD disease severity. It is well known that mild MD is associated with an increase in animal mass. Alternatively, a more severe MD is associated with decreased animal mass, likely as a result of muscle atrophy [10, 27]. Others have reported that

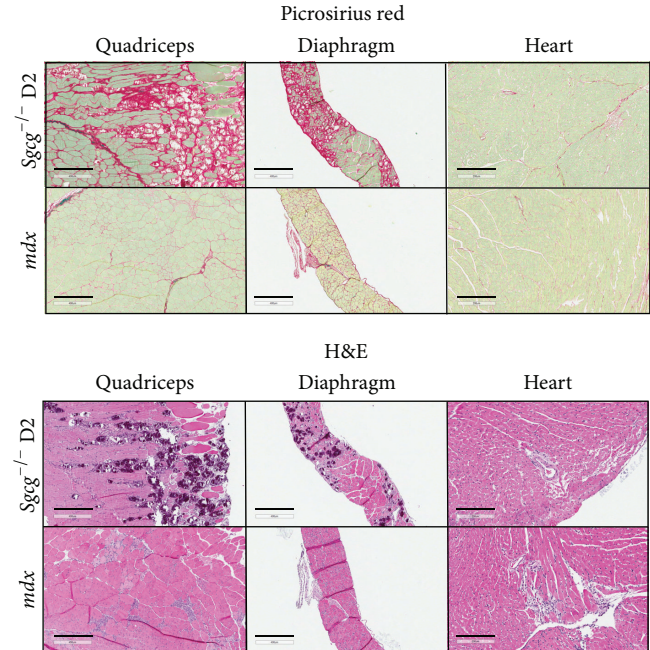


FIGURE 3: The *Sgcg*<sup>-/-</sup> D2 mice displayed the most severe pathology in histochemical assessments. By Pico Sirius Red staining the quadriceps and diaphragm of the *Sgcg*<sup>-/-</sup> D2 displayed far more red regions which correspond to fibrotic scarring than the *mdx* tissues. The hematoxylin and eosin pictures demonstrated the same fibrosis. The fibrosis in the cardiac left ventricles appeared quite similar between the two genotypes. Both mouse models demonstrated interstitial and perivascular fibrosis. Quadriceps and diaphragm legend bars represent 400  $\mu$ m. Heart legend bars represent 200  $\mu$ m.

the *mdx* mice gain weight with respect to their littermate controls [27] indicating a mild disease course and presumably due to hypertrophy. We now show that the *Sgcg*<sup>-/-</sup> D2 mice trend to lower weights than their WT controls at 4 and 12 weeks (Figure 2). We also show these animal weights to aid in the comparative analysis of the functional assessments below.

**3.2. Histologic Assessments.** The *Sgcg*<sup>-/-</sup> D2 quadriceps muscles have increased fibrosis, increased variation in fiber size, and increased central nuclei compared to age matched *mdx* mice (all 12 weeks old, Figure 3). In quadriceps the Pico Sirius Red staining indicates increased red, fibrotic areas in the *Sgcg*<sup>-/-</sup> D2 tissues (Figure 3). Similarly, the representative hematoxylin and eosin (H&E) images demonstrate larger blue/purple, fibrotic regions in the *Sgcg*<sup>-/-</sup> D2 mice in quadriceps. Quadriceps muscles from two *mdx* and two *Sgcg*<sup>-/-</sup> D2 mice were quantified for fiber size variability (FSV) with ImageJ software. As only two quadriceps muscles were compared, statistics were not performed. The *Sgcg*<sup>-/-</sup> D2 mice had a wider variation in fiber size (*Sgcg*<sup>-/-</sup> D2; 3453  $\pm$  2023  $\mu$ m and *mdx*; 2470  $\pm$  1830) indicating more ongoing regeneration and a more severe phenotype.

As expected the diaphragms from both mouse groups contained predominant interstitial fibrosis (central panels, Figure 3) and were several cell layers thicker than wild type

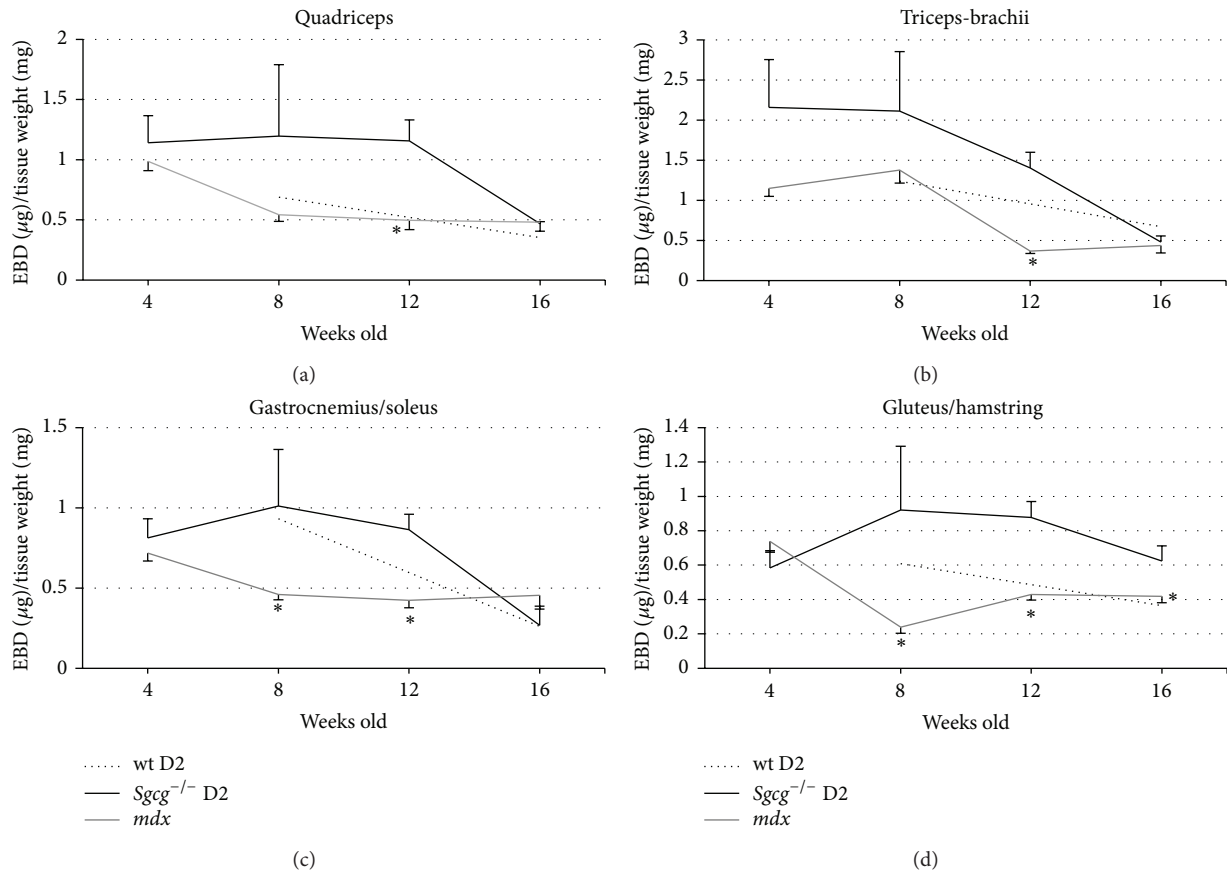


FIGURE 4: The *Sgcg*<sup>-/-</sup> D2 muscles demonstrated significantly increased membrane permeability at 12 weeks old. (a) *Sgcg*<sup>-/-</sup> D2 mice showed statistically higher EBD in their Quadriceps at 12 weeks compared to the *mdx* mice. (b) *Sgcg*<sup>-/-</sup> D2 mice showed statistically higher EBD in their Triceps-Brachii at 12 weeks compared to the *mdx* mice. (c) *Sgcg*<sup>-/-</sup> D2 showed statistically higher EBD in their Gastrocnemius and Soleus at 8 and 12 weeks compared to the *mdx* mice. (d) *Sgcg*<sup>-/-</sup> D2 Gluteus and Hamstrings showed higher EBD than the *mdx* mice at 8, 12, and 16 weeks. \*  $P < 0.05$  significance versus *Sgcg*<sup>-/-</sup> D2 animals. *Sgcg*<sup>+/+</sup> D2 at 4, 12 weeks  $n = 0$ , all others  $n = 3-15$ .

(wild type images in [9, 10]). The *Sgcg*<sup>-/-</sup> D2 diaphragms contained the most fibrotic areas by Pico Sirius Red staining and the largest accumulation of blue/purple regions in the H&E stained sections.

The cardiac ventricles appeared similarly affected by the muscular dystrophy pathology. Both images demonstrate interstitial and perivascular fibrosis. In addition the *mdx* heart contains some myofibroblast replacement of myofibers in the central portion of the H&E image.

**3.3. Membrane Permeability.** We assessed membrane permeability by quantitatively measuring the amount of Evans blue dye (EBD) that entered the damaged muscle fibers [10]. EBD binds albumin and only enters damaged muscle fibers [28]. The *Sgcg*<sup>-/-</sup> D2 skeletal muscle had significantly higher membrane permeability at 12 weeks across all four tissues assessed. Additionally the *Sgcg*<sup>-/-</sup> D2 mice had greater membrane permeability at 8 weeks in the Gastrocnemius/Soleus and at 8 and 16 weeks in the Gluteus/Hamstrings. Interestingly at 16 weeks an improvement in membrane permeability was identified in all *Sgcg*<sup>-/-</sup> D2 skeletal muscles assessed (Figure 4). The *mdx* disease was most severe at the 4-week

time point which was also followed by an improvement (Figure 4). This result is consistent with published reports that the *mdx* limb based skeletal muscles are severely affected at 4 weeks old and then improve [27, 29]. This indicates that the *Sgcg*<sup>-/-</sup> D2 mice succumb more severely to early disease pathology than the *mdx* mice and that both recover slightly due to as yet unknown reasons.

**3.4. Collagen Content.** To assess fibrosis we performed a quantitative hydroxyproline assay on the harvested muscles [10]. Hydroxyproline is a modified amino acid, which is only present in collagen and therefore is a quantitative marker for intramuscular fibrosis. The *Sgcg*<sup>-/-</sup> D2 muscles contained the largest amount of hydroxyproline in all limb-based muscles tested at almost all ages (Figure 5). This increase was significant in quadriceps at 12 and 16 weeks, in triceps-brachii at all times tested, Gastrocnemius/Soleus at 12 weeks, and Gluteus/Hamstring at 12 weeks. The only point when the *mdx* tissue contained more hydroxyproline was at 4 weeks in the gluteus/hamstring. Once again, the phenotype of the *Sgcg*<sup>-/-</sup> D2 mice progressively worsened until 12 weeks of age and then improved, while the *mdx* mouse phenotype improved after 4 weeks of age.

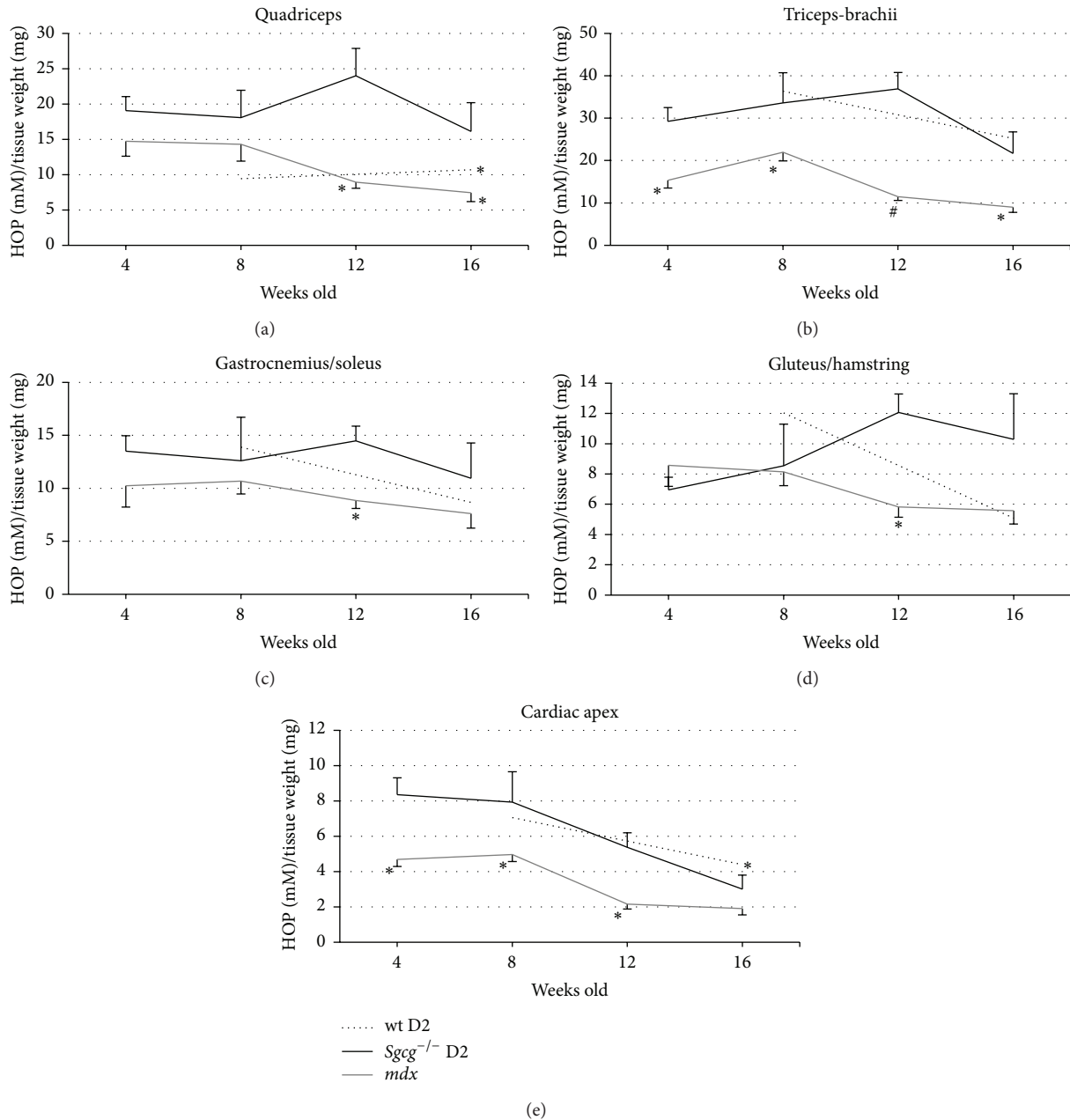


FIGURE 5: The *Sgcg*<sup>-/-</sup> D2 muscles were consistently more fibrotic than the age matched *mdx* mice by hydroxyproline assay. *Sgcg*<sup>-/-</sup> D2 mice showed significantly higher levels of Quadriceps fibrosis at 12 and 16 weeks versus the *mdx* mice and significantly more fibrosis than their *Sgcg*<sup>+/+</sup> D2 controls at 16 weeks. *Sgcg*<sup>-/-</sup> D2 mice had significantly higher fibrosis content in their Triceps-Brachii at all-time points compared to the *mdx* mice. At 12 weeks *Sgcg*<sup>-/-</sup> D2 mice have higher fibrosis content than the *mdx* mice in their Gastrocnemius/Soleus muscles. A similar pattern was seen in the Gluteus/Hamstring muscle group, and the *Sgcg*<sup>-/-</sup> mice had significantly higher fibrosis content at 12 weeks than the *mdx* mice. *Sgcg*<sup>-/-</sup> mice showed greater collagen content at 4, 8, and 12 weeks compared to the *mdx* mice. Additionally the *Sgcg*<sup>+/+</sup> mice had higher collagen content than the *Sgcg*<sup>-/-</sup> mice at 16 weeks. \**P* < 0.05, #*P* < 0.001 significance versus *Sgcg*<sup>-/-</sup> D2 animals. *Sgcg*<sup>+/+</sup> D2 at 4 and 12 weeks *n* = 0; *Sgcg*<sup>+/+</sup> D2 at 8 weeks *n* = 2; all others *n* = 3–16.

WT D2 mice displayed greater fibrosis at various time points and across all tissues compared to the *mdx* mouse. The D2 mouse line contains an in-frame deletion within the LTBP-4 gene. This mutation induces greater TGF- $\beta$ 1 activity leading to increased fibrosis in the D2 mouse line [11]. Fukada et al. 2009 do show that the *mdx* mutation bred into the

D2 line is more severe than the mutation in the C57BL/10 line; however the assessment ages are drastically different than those being used in the current study. Therefore, we cannot compare the observed decrease in fibrosis in our mice with the continued worsening phenotype observed by Fukada et al. [15].

The fibrosis content of the diaphragm was considered separately. The diaphragm develops differently than the limb-based skeletal muscles [30], is innervated differently [30], contains roughly the same quantity of Pax7 positive cells as the EDL and Biceps [31], and is the most severely affected muscle in the *mdx* [5] and *Sgcg*<sup>-/-</sup> D2 mice [10, Figure 3]. Many have conjectured as to why the diaphragm is the most severely affected muscle [5], but a well-accepted hypothesis has not been developed. Comparing the *mdx* and *Sgcg*<sup>-/-</sup> D2 diaphragm fibrosis revealed no significant differences.

The cardiac ventricle fibrosis also displayed a different pattern than the limb based skeletal muscles (Figure 5(e)). *Mdx* mice had less cardiac fibrosis than the *Sgcg*<sup>-/-</sup> D2 animals at all ages and this reached significance at 4, 8, and 12 weeks. Interestingly, by 16 weeks of age the HOP values showed no significant differences. Furthermore, hearts from both animal groups demonstrated reduced fibrosis after 8 weeks of age.

**3.5. Plethysmography.** We also analyzed the two different MD mouse models for respiratory function. Plethysmography is an often used and reliable assessment technique of diaphragm function [32, 33]. The diaphragm is normally very thin and very pliable. In muscular dystrophy the diaphragm becomes thick and rigid due to scar tissue [10]. Once rigid, the lungs require extended time for inspiration and expiration and a longer pause is apparent on the breath wave [32, 33]. These three metrics (times of inspiration (Ti), expiration (Te), and pause (PenH)) all measure the elasticity of the diaphragm and to a lesser extent the strength of the intercostal muscles.

*Sgcg*<sup>-/-</sup> D2 animals had significantly longer time inspiration (Ti) and time expiration (Te) than the *mdx* mice at 8, 12, and 16 and 12 and 16 weeks, respectively. Ti and Te are the measure of time that passes while the animal inhales or exhales, respectively. Additionally the *Sgcg*<sup>-/-</sup> D2 animals had significantly slower peak flows (fastest movement of air into the lungs) for inspiration and expiration (Figures 6(c) and 6(e)). Consistent with the longer inspiration and expiration parameters the *Sgcg*<sup>-/-</sup> D2 mice had significantly reduced breath frequency (breathes per minute, Figure 6(a)). The remainder of the plethysmography data can be accessed online in Supplemental Figure 1 in Supplementary Material available online at <http://dx.doi.org/10.1155/2015/131436>; when evaluating some of these parameters please be aware that the *mdx* mice are significantly larger than the D2 mice (Figure 1) and that this will affect many of the volume calculations. No difference was found in the Penh value between the *mdx* and *Sgcg*<sup>-/-</sup> D2 mice.

The D2 animals, regardless of genotype, were found to have reduced Ti, Te, Peak flow inspiration, and expiration at numerous time points compared to the *mdx* animals. Presently it can be hypothesized that the LTBP-4 mutations could be responsible for this impaired respiratory function due to increased fibrosis.

Our data is consistent with previously published plethysmography data. The following parameters, frequency, PIF, and PEF, were shown to be similar to the numbers presented in the current paper for 12-week old *mdx* mice [32]. These

parameters were all statistically different from the wild type C57BL/10 mice used as controls in that experiment. The *mdx* animals also had pathologically lower frequency of breaths and decreased peak flows than the C57BL/10 animals.

**3.6. Echocardiography.** To further assess the functional effects of MD on these two mouse strains an echocardiography time-course was conducted. Despite demonstrating increased ventricular fibrosis compared to the *mdx* mice (Figure 5(e)), the *Sgcg*<sup>-/-</sup> D2 animal's cardiac function was preserved at wild type levels (Figure 7). The *mdx* animals had significantly higher isovolumetric relaxation time (IVRT) and smaller fractional shortening and ejection fraction. The *mdx* animals had significantly higher isovolumetric relaxation time (IVRT), indicative of diastolic dysfunction, and smaller fractional shortening and ejection fraction, indicative of systolic dysfunction. Pulmonary artery acceleration time (PAAT) is a surrogate measure of pulmonary hypertension. A decrease in PAAT indicates increased pulmonary hypertension. PAAT was lower in the *Sgcg*<sup>-/-</sup> D2 animals than the *mdx* and significantly lower at 8 weeks of age, indicating that the *Sgcg*<sup>-/-</sup> D2 animals were more severely affected than the *mdx* mice. Please see supplemental Figure 2 for complete echocardiography data, and the authors would like to urge caution when comparing values that are dependent upon mouse size.

Despite increased fibrosis in the *Sgcg*<sup>-/-</sup> D2 hearts (Figures 3 and 5(e)) and previous publications [9], the *mdx* mice demonstrated significantly more severe cardiac pathology by echocardiography. Currently we do not have a full explanation for this, although it is obvious that fibrosis is only one of many pathologic occurrences in a muscular dystrophic heart. Conduction system defects have been identified in the *mdx* mouse heart [34]. In addition calcium is mislocalized in dystrophy [35] and therefore excitation and contraction will be detrimentally affected.

## 4. Conclusion

Animal models are an essential part of investigating disease etiology, progression, and preclinical trials. As muscular dystrophy (MD) is the most prevalent human genetic disease these mouse models are essential and a clear understanding of their pathology is required, including comparisons between those models already available. Multiple mouse MD model comparisons have been conducted. Fukada et al. previously bred the *mdx* mutation into the D2 mouse strain and compared the resulting strain to the historical *mdx* (C57BL/10) mouse [15]. The *mdx* mutation was identified to be more severe on the D2 background by muscle weights, fewer myofibers, increased fibrosis, and decreased strength. These authors identified that the D2 mouse strain has decreased satellite cell self-renewal and reasoned that this was the pertinent phenotypic causing difference [15]. An additional pair of manuscripts phenotypically described the *Sgcg*<sup>-/-</sup> mutation in four commonly used strains [10]. The D2 mice were found to have the most severe disease and using GWAS this was found to be largely due to a deletion within the Latent TGF $\beta$  Binding Protein 4 [11]. We now wished to directly

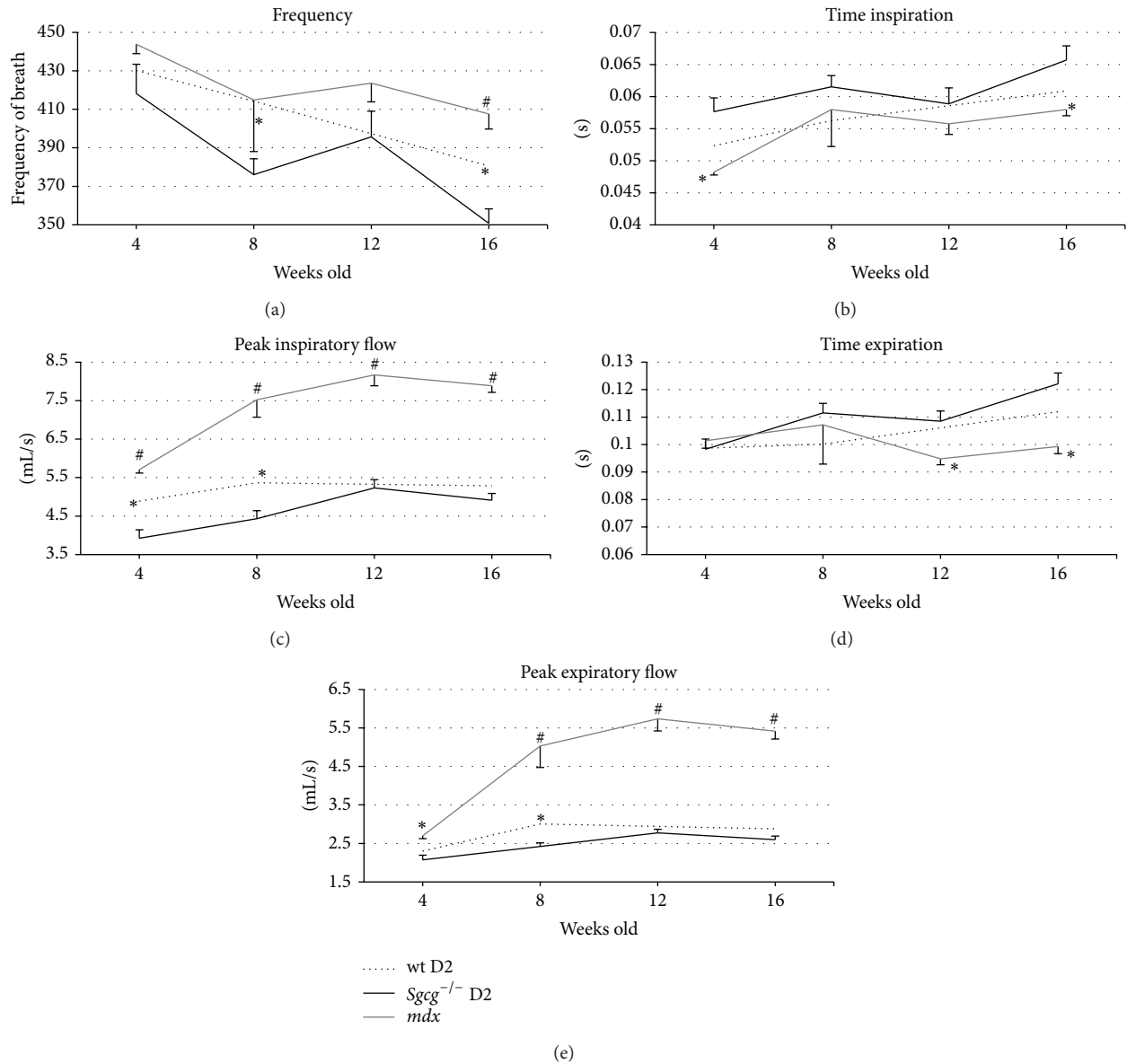


FIGURE 6: The *Sgcg*<sup>-/-</sup> D2 mice consistently had a more severe respiratory phenotype by plethysmography than the *mdx* animals. (a) At 8 and 16 weeks the *Sgcg*<sup>-/-</sup> D2 mice breathed significantly slower than the *Sgcg*<sup>+/+</sup> D2 mice. At 16 weeks the *Sgcg*<sup>-/-</sup> D2 mice also breathed significantly slower than the *mdx* mice. (b) *Sgcg*<sup>-/-</sup> D2 mice inhaled (*T<sub>i</sub>*) slower than the *mdx* mice at 4 and 16 weeks. (c) *Sgcg*<sup>-/-</sup> D2 mice had a lower peak inspiratory flow (PIFb) than the *mdx* mice at all-time points and lower than the *Sgcg*<sup>+/+</sup> D2 mice at 4 and 8 weeks. (d) *Sgcg*<sup>-/-</sup> D2 mice exhaled slower than the *mdx* mice at 12 and 16 weeks. (e) *Sgcg*<sup>-/-</sup> D2 mice had a lower peak expiratory flow (PEFb) than the *mdx* mice at all-time points and lower flow than the *Sgcg*<sup>+/+</sup> D2 at 8 weeks. \**P* < 0.05, #*P* < 0.001 significance versus *Sgcg*<sup>-/-</sup> D2 animals. *Sgcg*<sup>+/+</sup> D2 at 12 weeks *n* = 0, all others *n* = 4–10.

compare the severe *Sgcg*<sup>-/-</sup> D2 mouse to the highly used *mdx* mouse histologically, biochemically, and functionally.

The *Sgcg*<sup>-/-</sup> D2 mice were found to have increased membrane permeability and fibrosis in the limb based skeletal muscles analyzed. Many of the *Sgcg*<sup>-/-</sup> D2 muscles demonstrated statistically increased pathology for these two characteristics at most time points analyzed after the initial 4 week time point. The histology confirmed a more severe disease in the *Sgcg*<sup>-/-</sup> D2 mice at the 12-week time point.

Importantly the *Sgcg*<sup>-/-</sup> D2 mice demonstrated increased pulmonary hypertension by echocardiography compared to the *mdx* mice at all ages. Furthermore, by histology the *Sgcg*<sup>-/-</sup> D2 mouse also displayed more severe pathology in the quadriceps and diaphragm than the *mdx* model. In addition, as has often been noted, the diaphragms from both groups of mice are the most severely affected skeletal tissues. The reason behind the robust diaphragm pathology still eludes scientists.

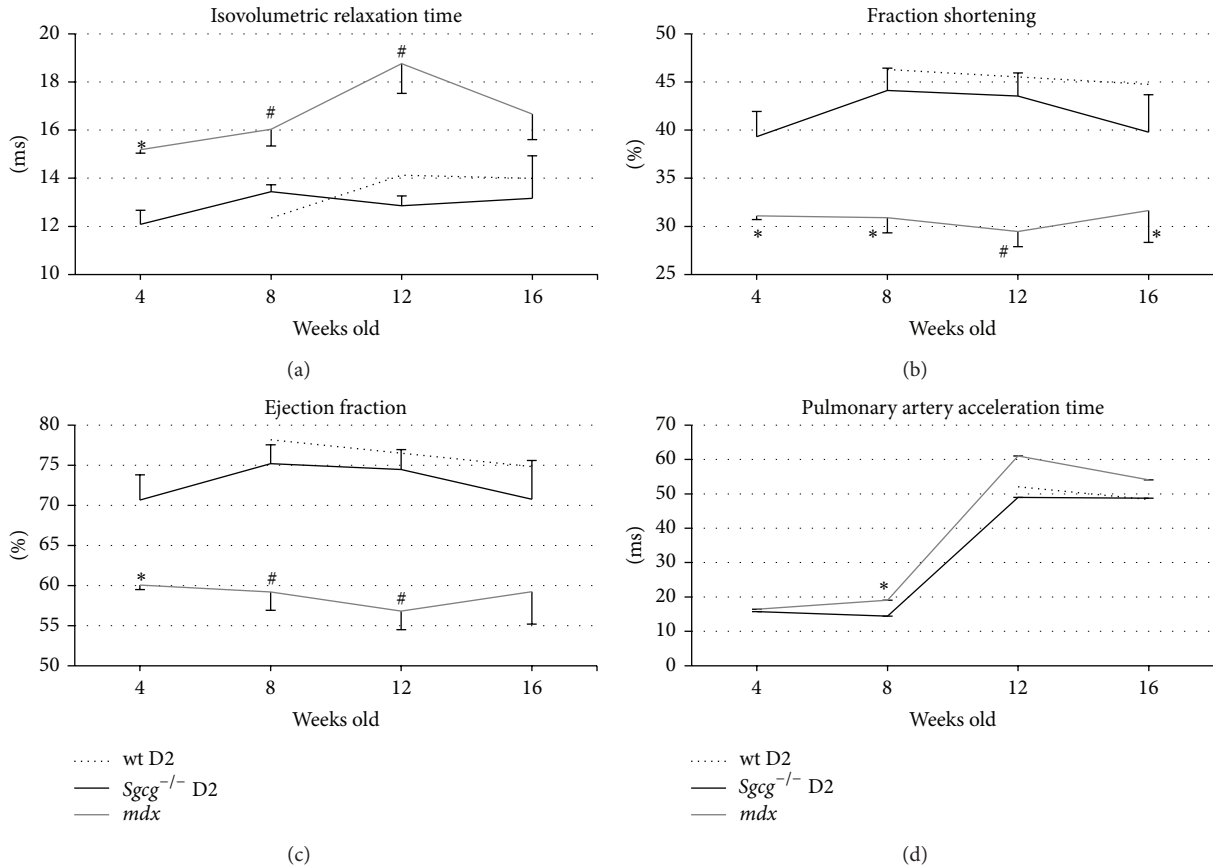


FIGURE 7: The *mdx* mice demonstrated a more severe cardiac functional pathology. (a) *Sgcg*<sup>-/-</sup> D2 mice had a shorter isovolumetric relaxation time (IVRT) than the *mdx* mice at all-time points. (b) The *Sgcg*<sup>-/-</sup> mice have a higher fractional shortening (FS%). (c) *Sgcg*<sup>-/-</sup> have a greater ejection fraction (EF%) than the *mdx* mice at 4, 8, and 12 weeks. (d) Pulmonary artery acceleration time (PA AT) was lower in the *Sgcg*<sup>-/-</sup> mice at 8 weeks compared to the *mdx* mice. \**P* < 0.05, #*P* < 0.001 significance versus *Sgcg*<sup>-/-</sup> D2 animals. *Sgcg*<sup>+/+</sup> D2 at 4 weeks *n* = 0, all others *n* = 4–23.

Many of the phenotypic differences are trending to significance. One limitation of these experiments is the limited number of animals used, due to the time-course nature of the data. Muscular dystrophy in mice and humans is notoriously variable even within the same organism (mice [10] and humans [36, 37]). Despite this caveat the trends are upheld for many tissues and across many time points indicating that the conclusions drawn are sound and the *Sgcg*<sup>-/-</sup> D2 mice present a better model of the human disease.

Both the *mdx* and *Sgcg*<sup>-/-</sup> D2 mouse phenotypes improve after an initial bout of pathology. Although this has been identified and discussed in the *mdx* mice for many years [5] we have not found an explanation for the reduction. In the current experiments the *mdx* mouse pathology is most severe at the 4 week time point, while the *Sgcg*<sup>-/-</sup> mice are most severely affected at 12 weeks. Possible mechanisms behind this phenotype recovery are; satellite cell recovery, immune response is dampened, beneficial scar tissue remodeling, reduced movement or, likely a combination of these and other mechanisms. Additional important questions remain. It would be of great interest to know why the different mouse

strains have their peak pathologies at different ages. And it would be ideal to understand if this recovery mechanism can be harnessed for human patients.

Even though we argue that the *Sgcg*<sup>-/-</sup> D2 mouse is a better model of human muscular dystrophy we must remember that it is still a model. There are many considerations when using mouse models to represent human disease (reviewed in [38]). There are the obvious differences: bipedal versus quadrupedal, free living with multiple stresses versus caged generally without physical activity, age, and size. The less obvious differences must also be considered. Slight differences in gene expression patterns, in signaling pathways, and in immune responses exist. As an example, important interspecies differences in the Notch signaling pathway have been identified [39].

To summarize, in this paper we provide data supporting that the *Sgcg*<sup>-/-</sup> D2 mouse is a more appropriate mouse model for muscular dystrophy research. While the mutations responsible for the development of muscular dystrophy within the strains are different, we set out to investigate which model develops a more severe—more human—phenotype.

Gathered data demonstrates that the *Sgcg*<sup>-/-</sup> D2 mouse develops a more severe phenotype in most assessed variables with the exception of cardiac function.

## Disclaimer

The funder had no role in study design, data collection and analysis, decision to publish, or preparation of the paper.

## Conflict of Interests

The authors have no conflict of interests, financial interests, or otherwise to declare.

## Acknowledgments

The authors thank Robert Gaffin of the UIC Center for Cardiovascular Research for the expert echocardiography. The authors also thank the UIC, Research Resources Core, Research Histology and Tissue Imaging Core. This research was funded by a grant from the National Institutes of Health (RO1 RHL102322A).

## References

- [1] S. Noguchi, E. M. McNally, K. Ben Othmane et al., "Mutations in the dystrophin-associated protein  $\gamma$ -sarcoglycan in chromosome 13 muscular dystrophy," *Science*, vol. 270, no. 5237, pp. 819–822, 1995.
- [2] G. Bulfield, W. G. Siller, P. A. L. Wight, and K. J. Moore, "X chromosome-linked muscular dystrophy (*mdx*) in the mouse," *Proceedings of the National Academy of Sciences of the United States of America*, vol. 81, no. 4, pp. 1189–1192, 1984.
- [3] A. S. Ryder-Cook, P. Sicinski, K. Thomas et al., "Localization of the *mdx* mutation within the mouse dystrophin gene," *The EMBO Journal*, vol. 7, no. 10, pp. 3017–3021, 1988.
- [4] E. P. Hoffman, R. H. Brown Jr., and L. M. Kunkel, "Dystrophin: the protein product of the Duchenne muscular dystrophy locus," *Cell*, vol. 51, no. 6, pp. 919–928, 1987.
- [5] H. H. Stedman, H. L. Sweeney, J. B. Shrager et al., "The *mdx* mouse diaphragm reproduces the degenerative changes of Duchenne muscular dystrophy," *Nature*, vol. 352, no. 6335, pp. 536–539, 1991.
- [6] G. B. Banks and J. S. Chamberlain, "The value of mammalian models for duchenne muscular dystrophy in developing therapeutic strategies," *Current Topics in Developmental Biology*, vol. 84, pp. 431–453, 2008.
- [7] R. M. Grady, H. Teng, M. C. Nichol, J. C. Cunningham, R. S. Wilkinson, and J. R. Sanest, "Skeletal and cardiac myopathies in mice lacking utrophin and dystrophin: a model for Duchenne muscular dystrophy," *Cell*, vol. 90, no. 4, pp. 729–738, 1997.
- [8] A. Sacco, F. Mourkioti, R. Tran et al., "Short telomeres and stem cell exhaustion model duchenne muscular dystrophy in *mdx*/mTR mice," *Cell*, vol. 143, no. 7, pp. 1059–1071, 2010.
- [9] A. A. Hack, C. T. Ly, F. Jiang et al., " $\gamma$ -sarcoglycan deficiency leads to muscle membrane defects and apoptosis independent of dystrophin," *Journal of Cell Biology*, vol. 142, no. 5, pp. 1279–1287, 1998.
- [10] A. Heydemann, J. M. Huber, A. Demonbreun, M. Hadhazy, and E. M. McNally, "Genetic background influences muscular dystrophy," *Neuromuscular Disorders*, vol. 15, no. 9-10, pp. 601–609, 2005.
- [11] A. Heydemann, E. Ceco, J. E. Lim et al., "Latent TGF- $\beta$ -binding protein 4 modifies muscular dystrophy in mice," *The Journal of Clinical Investigation*, vol. 119, no. 12, pp. 3703–3712, 2009.
- [12] B. T. Ivandic, J.-H. Qiao, D. Machleder, F. Liao, T. A. Drake, and A. J. Lusis, "A locus on chromosome 7 determines myocardial cell necrosis and calcification (dystrophic cardiac calcinosis) in mice," *Proceedings of the National Academy of Sciences of the United States of America*, vol. 93, no. 11, pp. 5483–5488, 1996.
- [13] H. Meng, I. Vera, N. Che et al., "Identification of *Abcc6* as the major causal gene for dystrophic cardiac calcification in mice through integrative genomics," *Proceedings of the National Academy of Sciences of the United States of America*, vol. 104, no. 11, pp. 4530–4535, 2007.
- [14] Z. Aherrahrou, L. C. Doehring, P. M. Kaczmarek et al., "Ultra-fine mapping of *Dyscalc1* to an 80-kb chromosomal segment on chromosome 7 in mice susceptible for dystrophic calcification," *Physiological Genomics*, vol. 28, no. 2, pp. 203–212, 2007.
- [15] S.-I. Fukada, D. Morikawa, Y. Yamamoto et al., "Genetic background affects properties of satellite cells and *mdx* phenotypes," *The American Journal of Pathology*, vol. 176, no. 5, pp. 2414–2424, 2010.
- [16] A. D. Guerron, R. Rawat, A. Sali et al., "Functional and molecular effects of arginine butyrate and prednisone on muscle and heart in the *mdx* mouse model of duchenne muscular dystrophy," *PLoS ONE*, vol. 5, no. 6, Article ID e11220, 2010.
- [17] M. L. Bianchi, A. Mazzanti, E. Galbiati et al., "Bone mineral density and bone metabolism in Duchenne muscular dystrophy," *Osteoporosis International*, vol. 14, no. 9, pp. 761–767, 2003.
- [18] J. G. Tidball and M. Wehling-Henricks, "Evolving therapeutic strategies for Duchenne muscular dystrophy: targeting downstream events," *Pediatric Research*, vol. 56, no. 6, pp. 831–841, 2004.
- [19] T. Matsumura, "Beta-blockers in children with Duchenne cardiomyopathy," *Reviews on Recent Clinical Trials*, vol. 9, no. 2, pp. 76–81, 2014.
- [20] C. F. Spurney, A. Sali, A. D. Guerron et al., "Losartan decreases cardiac muscle fibrosis and improves cardiac function in dystrophin-deficient *mdx* mice," *Journal of Cardiovascular Pharmacology and Therapeutics*, vol. 16, no. 1, pp. 87–95, 2011.
- [21] L. Viollet, P. T. Thrush, K. M. Flanagan, J. R. Mendell, and H. D. Allen, "Effects of angiotensin-converting enzyme inhibitors and/or beta blockers on the cardiomyopathy in Duchenne muscular dystrophy," *The American Journal of Cardiology*, vol. 110, no. 1, pp. 98–102, 2012.
- [22] C. Bertoni, C. Lau, and T. A. Rando, "Restoration of dystrophin expression in *mdx* muscle cells by chimeraplast-mediated exon skipping," *Human Molecular Genetics*, vol. 12, no. 10, pp. 1087–1099, 2003.
- [23] E. M. Welch, E. R. Barton, J. Zhuo et al., "PTC124 targets genetic disorders caused by nonsense mutations," *Nature*, vol. 447, no. 7140, pp. 87–91, 2007.
- [24] Y. Echigoya and T. Yokota, "Skipping multiple exons of dystrophin transcripts using cocktail antisense oligonucleotides," *Nucleic Acid Therapeutics*, vol. 24, no. 1, pp. 57–68, 2014.
- [25] M. Flesch, F. Schiffer, O. Zolk et al., "Contractile systolic and diastolic dysfunction in renin-induced hypertensive cardiomyopathy," *Hypertension*, vol. 30, no. 3, part 1, pp. 383–391, 1997.
- [26] S. Gibertini, S. Zanotti, P. Savadori et al., "Fibrosis and inflammation are greater in muscles of beta-sarcoglycan-null mouse

- than mdx mouse,” *Cell and Tissue Research*, vol. 356, no. 2, pp. 427–443, 2014.
- [27] A. M. Connolly, R. M. Keeling, S. Mehta, A. Pestronk, and J. R. Sanes, “Three mouse models of muscular dystrophy: the natural history of strength and fatigue in dystrophin-, dystrophin/utrophin-, and laminin alpha2-deficient mice,” *Neuromuscular Disorders*, vol. 11, no. 8, pp. 703–712, 2001.
- [28] R. Matsuda, A. Nishikawa, and H. Tanaka, “Visualization of dystrophic muscle fibers in Mdx mouse by vital staining with Evans blue: evidence of apoptosis in dystrophin-deficient muscle,” *The Journal of Biochemistry*, vol. 118, no. 3, pp. 959–964, 1995.
- [29] J. X. DiMario, A. Uzman, and R. C. Strohman, “Fiber regeneration is not persistent in dystrophic (MDX) mouse skeletal muscle,” *Developmental Biology*, vol. 148, no. 1, pp. 314–321, 1991.
- [30] A. J. Merrell and G. Kardon, “Development of the diaphragm—a skeletal muscle essential for mammalian respiration,” *FEBS Journal*, vol. 280, no. 17, pp. 4026–4035, 2013.
- [31] F. Calhabeu, S. Hayashi, J. E. Morgan, F. Relaix, and P. S. Zammit, “Alveolar rhabdomyosarcoma-associated proteins PAX3/FOXO1A and PAX7/FOXO1A suppress the transcriptional activity of MyoD-target genes in muscle stem cells,” *Oncogene*, vol. 32, no. 5, pp. 651–662, 2013.
- [32] P. Huang, G. Cheng, H. Lu, M. Aronica, R. M. Ransohoff, and L. Zhou, “Impaired respiratory function in *mdx* and *mdx/utrn*<sup>+/-</sup> mice,” *Muscle & Nerve*, vol. 43, no. 2, pp. 263–267, 2011.
- [33] C. A. Nelson, R. B. Hunter, L. A. Quigley et al., “Inhibiting TGF- $\beta$  activity improves respiratory function in mdx mice,” *The American Journal of Pathology*, vol. 178, no. 6, pp. 2611–2621, 2011.
- [34] D. M. Branco, C. M. Wolf, M. Sherwood, P. E. Hammer, P. B. Kang, and C. I. Berul, “Cardiac electrophysiological characteristics of the *mdx*<sup>5cv</sup> mouse model of Duchenne muscular dystrophy,” *Journal of Interventional Cardiac Electrophysiology*, vol. 20, no. 1-2, pp. 1–7, 2007.
- [35] J. F. Dunn and G. K. Radda, “Total ion content of skeletal and cardiac muscle in the mdx mouse dystrophy: Ca<sup>2+</sup> is elevated at all ages,” *Journal of the Neurological Sciences*, vol. 103, no. 2, pp. 226–231, 1991.
- [36] K. M. Flanigan, E. Ceco, K.-M. Lamar et al., “LTBP4 genotype predicts age of ambulatory loss in duchenne muscular dystrophy,” *Annals of Neurology*, vol. 73, no. 4, pp. 481–488, 2013.
- [37] V. Humbertclaude, D. Hamroun, K. Bezzou et al., “Motor and respiratory heterogeneity in Duchenne patients: implication for clinical trials,” *European Journal of Paediatric Neurology*, vol. 16, no. 2, pp. 149–160, 2012.
- [38] T. A. Partridge, “The mdx mouse model as a surrogate for Duchenne muscular dystrophy,” *FEBS Journal*, vol. 280, no. 17, pp. 4177–4186, 2013.
- [39] J. E. Church, J. Trieu, A. Chee et al., “Alterations in Notch signalling in skeletal muscles from *mdx* and *dko* dystrophic mice and patients with Duchenne muscular dystrophy,” *Experimental Physiology*, vol. 99, no. 4, pp. 675–687, 2014.

## Research Article

# SERCA2 Haploinsufficiency in a Mouse Model of Darier Disease Causes a Selective Predisposition to Heart Failure

Vikram Prasad,<sup>1</sup> John N. Lorenz,<sup>2</sup> Valerie M. Lasko,<sup>2</sup> Michelle L. Nieman,<sup>2</sup> Wei Huang,<sup>3</sup> Yigang Wang,<sup>3</sup> David W. Wiczorek,<sup>1</sup> and Gary E. Shull<sup>1</sup>

<sup>1</sup>Department of Molecular Genetics, Biochemistry and Microbiology, University of Cincinnati College of Medicine, Cincinnati, OH 45267, USA

<sup>2</sup>Department of Cellular and Molecular Physiology, University of Cincinnati College of Medicine, Cincinnati, OH 45267, USA

<sup>3</sup>Department of Pathology and Laboratory Medicine, University of Cincinnati College of Medicine, Cincinnati, OH 45267, USA

Correspondence should be addressed to Vikram Prasad; [prasad.vikram@gmail.com](mailto:prasad.vikram@gmail.com)

Received 26 September 2014; Revised 18 December 2014; Accepted 23 December 2014

Academic Editor: Monica Fedele

Copyright © 2015 Vikram Prasad et al. This is an open access article distributed under the Creative Commons Attribution License, which permits unrestricted use, distribution, and reproduction in any medium, provided the original work is properly cited.

Null mutations in one copy of *ATP2A2*, the gene encoding sarco/endoplasmic reticulum  $\text{Ca}^{2+}$ -ATPase isoform 2 (SERCA2), cause Darier disease in humans, a skin condition involving keratinocytes. Cardiac function appears to be unimpaired in Darier disease patients, with no evidence that SERCA2 haploinsufficiency itself causes heart disease. However, SERCA2 deficiency is widely considered a contributing factor in heart failure. We therefore analyzed *Atp2a2* heterozygous mice to determine whether SERCA2 haploinsufficiency can exacerbate specific heart disease conditions. Despite reduced SERCA2a levels in heart, *Atp2a2* heterozygous mice resembled humans in exhibiting normal cardiac physiology. When subjected to hypothyroidism or crossed with a transgenic model of reduced myofibrillar  $\text{Ca}^{2+}$ -sensitivity, SERCA2 deficiency caused no enhancement of the disease state. However, when combined with a transgenic model of increased myofibrillar  $\text{Ca}^{2+}$ -sensitivity, SERCA2 haploinsufficiency caused rapid onset of hypertrophy, decompensation, and death. These effects were associated with reduced expression of the antiapoptotic *Hax1*, increased levels of the proapoptotic genes *Chop* and *Casp12*, and evidence of perturbations in energy metabolism. These data reveal myofibrillar  $\text{Ca}^{2+}$ -sensitivity to be an important determinant of the cardiac effects of SERCA2 haploinsufficiency and raise the possibility that Darier disease patients are more susceptible to heart failure under certain conditions.

## 1. Introduction

In humans, loss of one copy of the *ATP2A2* gene causes Darier disease (DD), an acantholytic skin disease [1, 2]. *ATP2A2* encodes two alternatively spliced variants of sarco/endoplasmic reticulum  $\text{Ca}^{2+}$ -ATPase isoform 2 (SERCA2). These are SERCA2b, the ubiquitous endoplasmic reticulum (ER)  $\text{Ca}^{2+}$  pump, and SERCA2a, the cardiac and slow-twitch skeletal muscle sarcoplasmic reticulum (SR)  $\text{Ca}^{2+}$  pump [3]. In its capacity as the primary cardiac SR  $\text{Ca}^{2+}$  pump, SERCA2a facilitates muscle relaxation and replenishes SR  $\text{Ca}^{2+}$  stores needed for contraction [3]. Because reduced SERCA2 activity is often observed in heart disease [4] and DD mutations cause reductions in SERCA2 expression and activity [5], one might

expect these mutations to lead to heart disease in humans. However, two studies of DD patients with a mean age of ~47 years indicated that cardiac performance is normal and yielded no evidence of heart disease [6, 7]; these findings have been interpreted to suggest that a role for SERCA2 deficiency in heart disease, while relevant in rodent models, may be less important in humans [7]. However, while these results provide compelling evidence that *Atp2a2* heterozygosity does not impair cardiac function in middle-aged humans, they do not rule out the possibility that SERCA2 haploinsufficiency can increase susceptibility to disease progression and heart failure.

In earlier studies, ablation of one copy of the *Atp2a2* gene in mice of a mixed 129Svj and Black Swiss background caused

a reduction in cardiac SERCA2a protein expression to 65% of wild-type (WT) levels, with impaired contractility and relaxation [8]. However, true heart disease was not observed; in fact, the major phenotype of the *Atp2a2*<sup>+/-</sup> mice was the development of squamous cell tumors in keratinized epithelial tissues [9, 10]. Later studies on these mice revealed an increased susceptibility to pressure-overload cardiac hypertrophy [11] and a reduction of rate-dependent inotropy in isolated mutant hearts, relative to WT controls [12]. In the current study, we used *Atp2a2*<sup>+/-</sup> mice on an inbred FVB/N background; while these heterozygous (HET) mice continued to display effects of SERCA2 haploinsufficiency in keratinized epithelia, cardiac performance was apparently normal, more closely reflecting findings in DD patients [6, 7]. The HET model was well suited to determine if SERCA2 deficiency, while apparently benign under normal conditions, could exacerbate cardiac disease progression. Specifically, we investigated the interaction of SERCA2 haploinsufficiency with hypothyroidism, which is known to impair cardiac performance [13], and alterations in myofibrillar Ca<sup>2+</sup>-sensitivity, which causes pathological hypertrophy and heart failure [14, 15]. For the latter, double mutant mice were generated by crossing HET mice with transgenic lines expressing the Glu54Lys mutant  $\alpha$ -tropomyosin, which reduces myofibrillar Ca<sup>2+</sup>-sensitivity and leads to dilated cardiomyopathy [16, 17], and the Glu180Gly mutant  $\alpha$ -tropomyosin, which increases myofibrillar Ca<sup>2+</sup> sensitivity and causes hypertrophic cardiomyopathy [18, 19]. Our results reveal an unexpected selectivity in the effects of SERCA2 haploinsufficiency in heart, which should be taken into consideration in the management of Darier disease patients.

## 2. Materials and Methods

**2.1. Animal Models.** The original *Atp2a2*<sup>+/-</sup> line was backcrossed onto the inbred FVB/N background in excess of 15 generations to generate the HET mutant line utilized in this study. This *Atp2a2*<sup>+/-</sup> mouse line has been made available to researchers through the Jackson Labs repository. All other mice used in this study, including the WT, the transgenic mouse models carrying the Glu54Lys mutant  $\alpha$ -tropomyosin, which has dilated cardiomyopathy (DCM) [16], and the Glu180Gly mutant  $\alpha$ -tropomyosin, which has hypertrophic cardiomyopathy (HCM) [18], were also on the inbred FVB/N background. HET mice were bred with the DCM and HCM lines to generate double (DCM/HET and HCM/HET) and single mutant offspring. The hypothyroid model was prepared by treating WT and HET mice with 6-n-propyl thiouracil (PTU) exactly as previously described [20]. All procedures conformed to guidelines published by the NIH (*Guide for the Care and Use of Laboratory Animals*; publication number 86-23, revised 1996) and were approved by the Institutional Animal Care and Use Committee at the University of Cincinnati.

**2.2. Evaluation of Cardiac Function.** Anesthesia of mice with ketamine and inactin, analysis of cardiovascular function using pressure transducers inserted into the left ventricle

and right femoral vein, delivery of drugs *via* a cannula in the right femoral vein, and recording and analysis of data were performed exactly as described previously [13]. Analysis of cardiac function by M-mode echocardiography of mice, anesthetized using isoflurane inhalation, and analysis of data were performed exactly as described previously [21].

**2.3. Immunoblot Analyses.** Hearts were harvested from anesthetized mice and processed for immunoblot analysis as previously described [22]. Phosphorylation of phospholamban (PLN) in response to  $\beta$ -adrenergic stimulation was assessed in ventricles from mice that were anesthetized and surgically instrumented as described above and treated with dobutamine (16 ng/g body weight/min). Estimation of protein concentration in total homogenates, resolution of proteins by discontinuous, reducing SDS-PAGE, and immunoblot analyses were carried out as described [22]. All primary and secondary antibodies used have been previously described [22].

**2.4. Real-Time Polymerase Chain Reaction.** Hearts/ventricles were harvested from anesthetized mice and processed for real-time PCR (RT-PCR) analysis as previously described [22]. In addition to the primer pairs that have been previously described [22, 23], the following were used: *Hspa5* (GRP78/BiP), PrimerBank ID number 31981722a1; *Hsp90b1* (GRP94), PrimerBank ID number 6755863a1; *Casp12* (Caspase 12), PrimerBank ID number 31981868a1; *Ddit3* (CHOP), PrimerBank ID number 31982415a1; *Eif2ak3* (PERK), PrimerBank ID number 6857781a1; *Acox1*, PrimerBank ID number 26333821a1; *Fabp3*, PrimerBank ID number 6753810a1; *Orail*, PrimerBank ID number 93277106b1; *Stim1*, PrimerBank ID number 31981983a2; *Hax1*, PrimerBank ID number 6754160a1; *Rcan2*, PrimerBank ID number 46560586c1; and *Ppar $\gamma$* , PrimerBank ID number 187960104c1; primers for *Pln* (phospholamban) were adapted from PrimerBank ID number 213512815c1 (forward primer: 5' AAGTGCAATACCTCACTCG 3', reverse primer: 5' GATCAGCAGCAGACATATC 3'). mRNA levels for *Atp2b1* (QT01072106) and *Atp2b4* (QT01076271) were determined using QuantiTect Primer Assay Kits (Qiagen).

**2.5. Statistics.** Results are presented as means  $\pm$  standard error (SE). Individual comparisons were performed using a two-sided Student's *t*-test, and a *P* value of <0.05 was considered significant.

## 3. Results

**3.1. Cardiovascular Performance in WT and HET Mice.** Cardiovascular performance of adult FVB/N WT and HET mice was analyzed using a pressure transducer in the left ventricle under both basal conditions and upon  $\beta$ -adrenergic stimulation with dobutamine. No significant differences were observed in basal heart rate, mean arterial pressure, left ventricular end-diastolic pressure, or maximum rates of left ventricular pressure development or decay (Figure 1). Treatment with dobutamine led to similar changes in both genotypes, with no impairment of chronotropic, inotropic, or lusitropic responses. Rate of left ventricular pressure development was

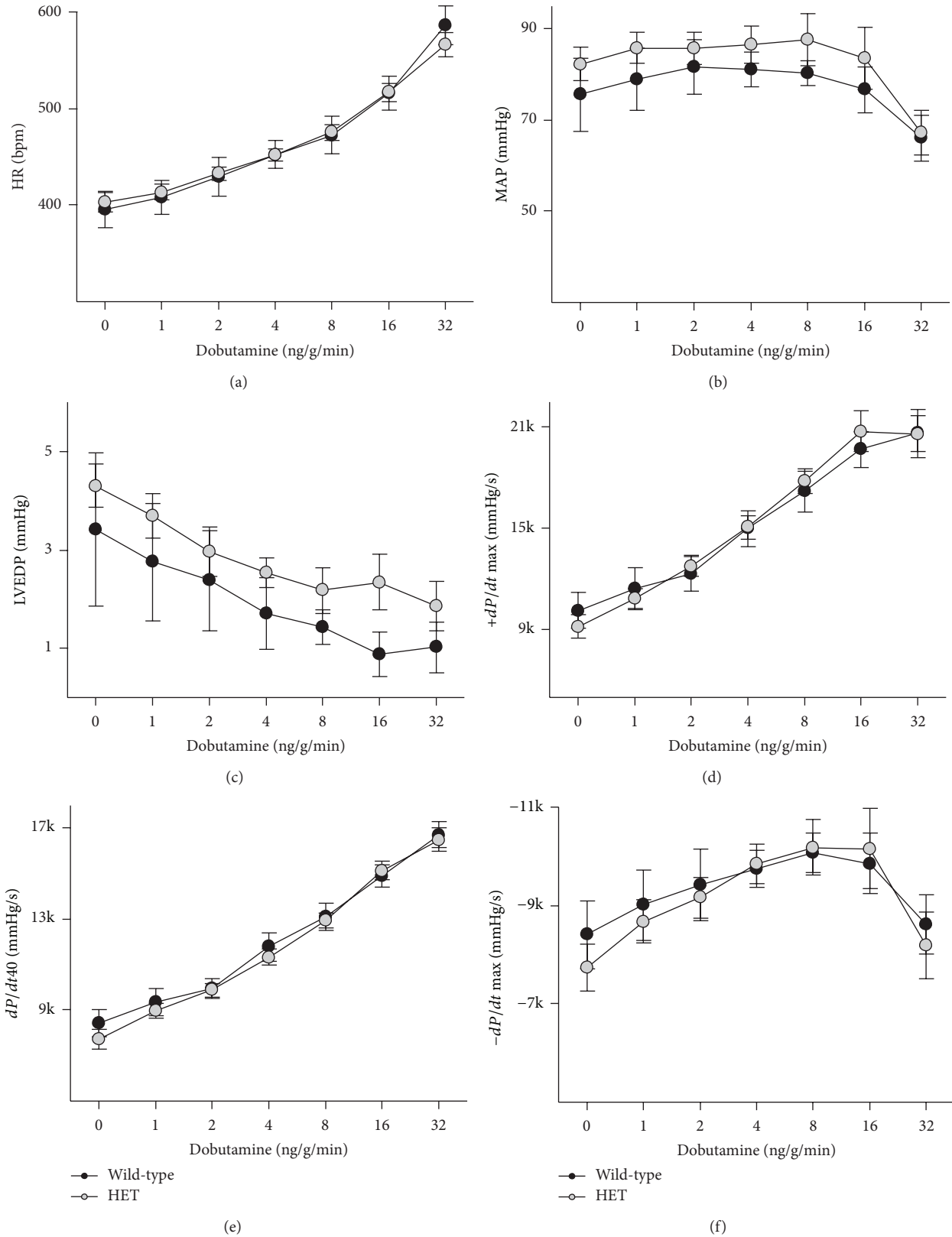


FIGURE 1: Cardiovascular function in *Atp2a2* heterozygous mice. Ventricular and arterial pressures were measured in anesthetized adult FVB/N wild-type and *Atp2a2*<sup>+/-</sup> mice under baseline conditions and upon  $\beta$ -adrenergic stimulation using dobutamine. (a) Heart rate (HR); (b) mean arterial pressure (MAP); (c) left ventricular end-diastolic pressure (LVEDP); (d) maximal rate of left ventricular pressure development (+dP/dt Max); (e) rate of left ventricular pressure development at 40 mmHg (dP/dt40); and (f) maximal rate of decay of left ventricular developed pressure (-dP/dt Max). Values are means  $\pm$  SE. *n* = at least 5 for each genotype.

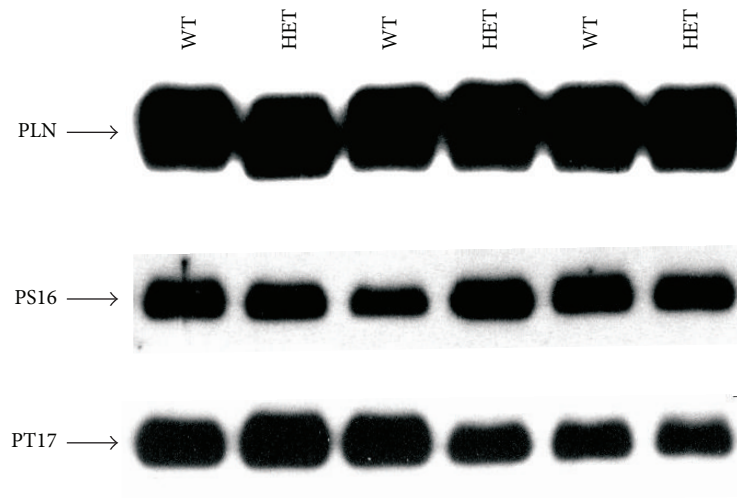
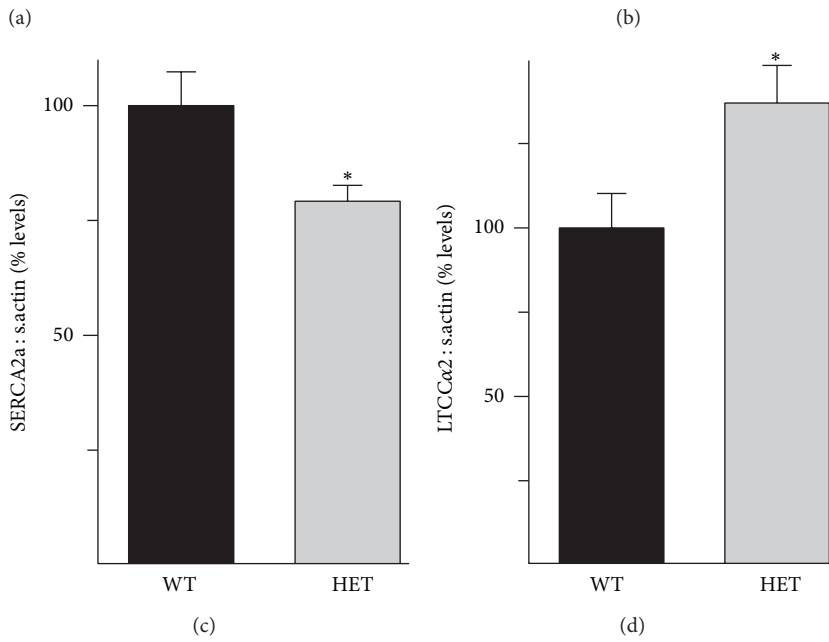
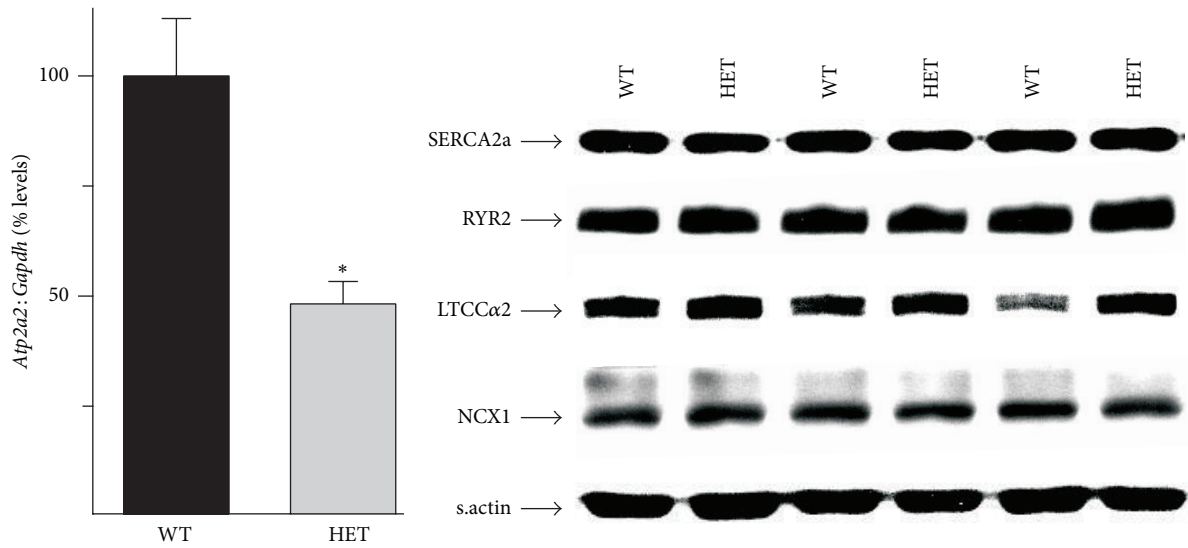


FIGURE 2: Continued.

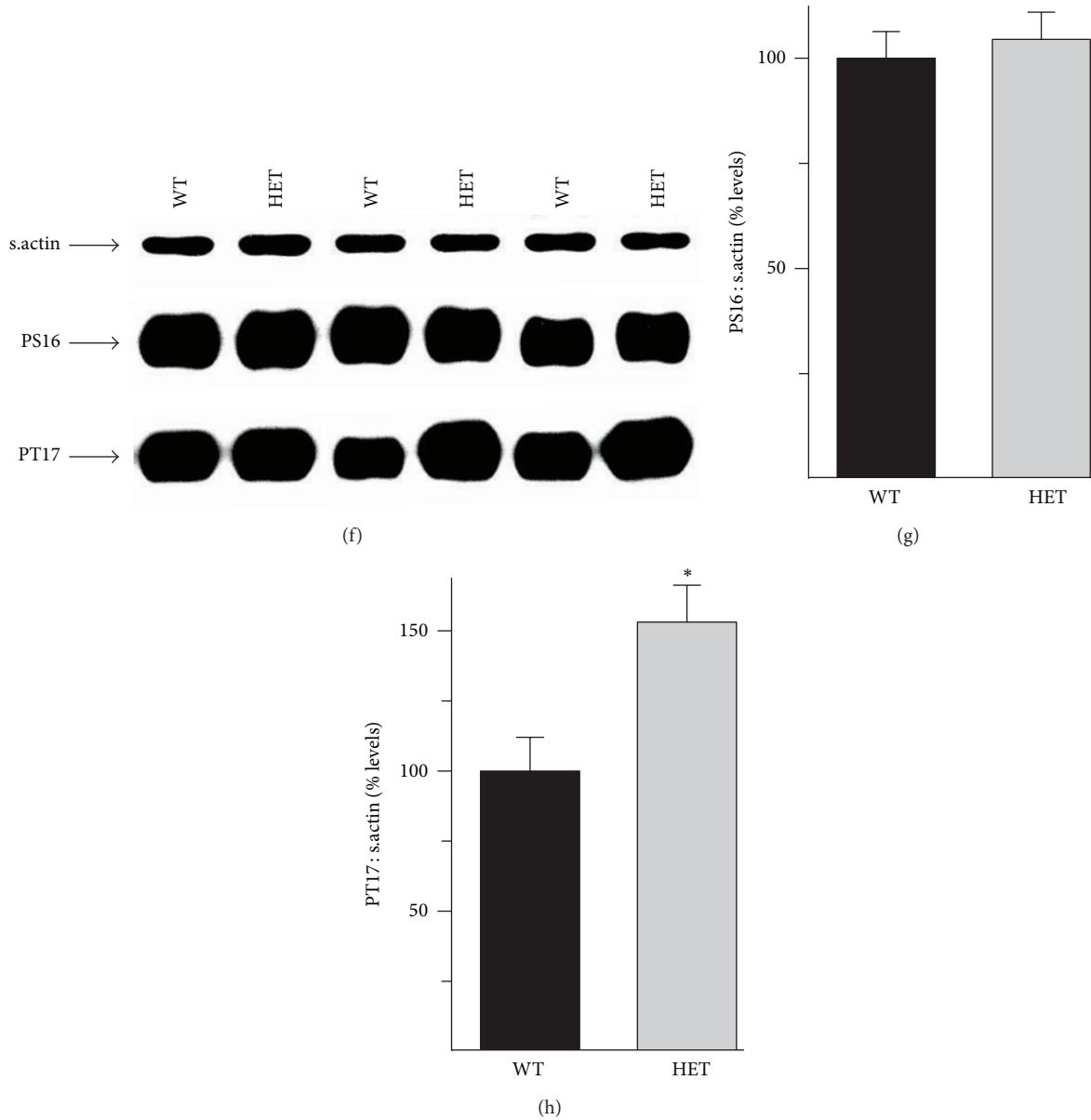


FIGURE 2: Effects of *Atp2a2* heterozygosity on expression of  $Ca^{2+}$  handling proteins in heart. Adult WT and *Atp2a2*<sup>+/-</sup> (HET) hearts were processed for analysis of mRNA and protein levels. (a) *Atp2a2* mRNA determined by RT-PCR; (b) immunoblot analysis of SERCA2a, ryanodine receptor isoform 2 (RYR2),  $\alpha 2$  subunit of L-type  $Ca^{2+}$  channel (LTCC $\alpha 2$ ), and  $Na^+/Ca^{2+}$  exchanger isoform 1 (NCX1). Quantitation of SERCA2a (c) and LTCC $\alpha 2$  (d) protein levels. Immunoblot analyses of phospholamban (PLN) and PLN phosphorylated on Ser16 (PS16) and Thr17 (PT17) were performed using heart samples from anesthetized surgically instrumented mice under both baseline conditions (e) and after  $\beta$ -adrenergic stimulation with dobutamine at 16 ng/g body weight/min (f, g, h). mRNA levels were normalized to *Gapdh* and protein levels were normalized to sarcomeric actin (s.actin). Values are means  $\pm$  SE. *n* = at least 4 for each genotype. \**P* < 0.05 versus WT controls.

also calculated at 40 mm Hg, to assess possible effects of the small but nonsignificant difference in mean arterial pressure (Figure 1(b)); however the two genotypes had virtually identical responses.

**3.2. Effects of *Atp2a2* Heterozygosity on Proteins Implicated in  $Ca^{2+}$ -Handling.** RT-PCR analysis of total RNA from WT and HET hearts revealed that mRNA levels of the *Atp2a2* gene, which codes for SERCA2, were reduced to  $48 \pm 5\%$  of WT

levels (Figure 2(a)). However, immunoblot analysis of total protein homogenates revealed a much smaller reduction in SERCA2a protein levels (to  $79 \pm 3\%$  of WT levels, Figures 2(b) and 2(c)) in HET hearts. This reduction was associated with an increase (to  $137 \pm 11\%$  of WT levels, Figures 2(b) and 2(d)) in expression of the  $\alpha 2$  subunit of the L-type  $Ca^{2+}$ -channel, which is the principal  $Ca^{2+}$ -uptake mechanism on a beat-to-beat basis. There were no changes in expression of either the ryanodine receptor isoform 2, which mediates  $Ca^{2+}$ -release

from the SR, or the  $\text{Na}^+/\text{Ca}^{2+}$  exchanger isoform 1 (NCX1, *Slc8a1*), which is the predominant  $\text{Ca}^{2+}$ -efflux mechanism in cardiac myocytes, in HET hearts (Figure 2(b)).

SERCA2 activity is negatively regulated by phospholamban (PLN), which binds to the  $\text{Ca}^{2+}$ -pump in a phosphorylation-dependent manner [24]. Reduced PLN expression and increased PLN phosphorylation on residues Ser16 (PS16) and Thr17 (PT17) can both enhance SERCA2a-mediated SR  $\text{Ca}^{2+}$ -sequestration [24]. However, immunoblot analysis revealed that PLN expression and baseline phosphorylation (Figure 2(e)) were unaltered in HET hearts. The inotropic and lusitropic effects of  $\beta$ -adrenergic stimulation are mediated, at least in part, via increased PLN phosphorylation, which facilitates more robust  $\text{Ca}^{2+}$ -cycling [24]. The normal increase in the cardiovascular performance of stimulated HET mice raised the possibility that  $\beta$ -adrenergic stimulated PLN phosphorylation was augmented to compensate for the reduction in SERCA2a levels. To test this hypothesis, PS16 and PT17 levels were determined in hearts from WT and HET mice stimulated with dobutamine. While PS16 levels were comparable between stimulated WT and HET hearts (Figures 2(f) and 2(g)), PT17 levels were elevated in stimulated HET hearts (by  $153 \pm 13\%$ ), when compared to similarly treated WT hearts (Figures 2(f) and 2(h)).

**3.3. *Atp2a2* Heterozygosity Does Not Exacerbate Cardiac Dysfunction Caused by Hypothyroidism.** Hypothyroidism is a well-recognized cardiovascular disease risk factor [25]. Studies in rabbits and mice have shown that it is associated with a reduction in cardiac SERCA2 expression [20, 26], raising the possibility that the impairment of cardiac function caused by hypothyroidism would be greater in *Atp2a2* heterozygous individuals. To test this hypothesis, hypothyroidism was induced in WT and HET mice and cardiac performance was assessed by *in vivo* catheterization. Cardiovascular function was similarly diminished in both WT and HET mice (Figures 3(a)–3(f)) under both baseline conditions and upon  $\beta$ -adrenergic stimulation.

**3.4. *Atp2a2* Heterozygosity Has No Appreciable Effect on the Cardiac Phenotype of Transgenic Mice with Dilated Cardiomyopathy.** Myofibrillar  $\text{Ca}^{2+}$ -sensitivity is a major determinant of cardiac function; in addition to altering force development, changes in  $\text{Ca}^{2+}$ -sensitivity can impact myofibrillar  $\text{Ca}^{2+}$ -buffering, diastolic  $\text{Ca}^{2+}$ -levels, and SERCA2-mediated cytosolic  $\text{Ca}^{2+}$ -clearance [14, 15, 27–29]. Transgenic expression of Glu154Lys mutant  $\alpha$ -tropomyosin in the DCM mouse heart lowers myofibrillar  $\text{Ca}^{2+}$  sensitivity, impairs contractility, and leads to dilated cardiomyopathy [16]. In order to determine the effects of SERCA2 haploinsufficiency, double mutant DCM/HET mice were analyzed. DCM/HET mice were viable and appeared normal. The increase in heart weight:body weight (HW:BW) and heart weight:tibial length ratios, determined in 8–10-week-old mice, was similar in both single mutant DCM and double mutant DCM/HET mice (Figure 4(a)). Echocardiographic analyses revealed that cardiac function was not compromised in DCM/HET mice when compared to DCM controls; in fact, fractional

shortening and ejection fraction trended slightly higher in DCM/HET hearts (Figure 4(b)). RT-PCR analysis showed that the increases in mRNA levels for *Nppa* (atrial natriuretic peptide), *Myh7* ( $\beta$ -myosin heavy chain), and *Acta1* (skeletal  $\alpha$ -actin), as markers of pathological hypertrophy, were not significantly different between DCM and DCM/HET hearts (Figure 4(c)). *Atp2a2* mRNA levels, which were reduced to  $69 \pm 4\%$  of WT levels in DCM hearts, were lower in DCM/HET hearts ( $42 \pm 4\%$  of WT levels; Figure 4(d)). However, the reduction in SERCA2a protein was more modest, with expression at  $86 \pm 2\%$  of DCM levels in DCM/HET hearts (Figure 4(e)).

**3.5. *Atp2a2* Heterozygosity Causes Rapid Progression of Hypertrophy and Decompensation in Transgenic HCM Mice.** Increased myofibrillar  $\text{Ca}^{2+}$ -sensitivity, which impairs relaxation, is associated with hypertrophic cardiomyopathy and has also been reported in end-stage heart failure [14, 15]. Cardiac expression of Glu180Gly mutant  $\alpha$ -tropomyosin in the HCM transgenic model increases myofibrillar  $\text{Ca}^{2+}$ -sensitivity, impairs relaxation, leads to development of fibrosis and hypertrophy, and causes death at 5–6 months of age [18]. To determine the effects of SERCA2 haploinsufficiency on the HCM phenotype, double mutant HCM/HET mice were generated as described above. SERCA2 haploinsufficiency caused a rapid onset of heart failure and death; 80% of HCM/HET mice were dead by 5 weeks of age and none survived beyond 6–7 weeks (Figure 5(a)). When compared to age-matched HCM controls, HCM/HET hearts displayed overt hypertrophy with pronounced left atrial remodeling as early as 4 weeks of age (Figure 5(b)). HW:BW ratios were higher in HCM/HET mice (Figure 5(c)), as were ratios of ventricular weight:body weight (Figure 5(d)), indicating that the increase in HW:BW was not simply a consequence of atrial remodeling. Consistent with these changes, mRNA levels for several markers of cardiac remodeling, which have been shown to be elevated in 4-week-old HCM hearts [23], were further increased in HCM/HET hearts; these included *Nppa* (Figure 5(e)), *Myh7* (Figure 5(f)), *Acta1* (Figure 5(g)), and *Ctgf*, encoding connective tissue growth factor (Figure 5(h)).

**3.6. Effect of *Atp2a2* Heterozygosity on Regulators of  $\text{Ca}^{2+}$ -Handling and Protein Phosphatases in HCM/HET Hearts.** RT-PCR analysis of 4-week-old WT, HCM, and HCM/HET hearts revealed that *Atp2a2* mRNA levels, which were reduced to  $72 \pm 5\%$  of WT levels in HCM hearts, were sharply reduced in HCM/HET hearts (to  $18 \pm 2\%$  of WT levels; Figure 6(a)). mRNA levels for PLN, which were maintained at WT levels in HCM hearts, were also reduced in HCM/HET hearts ( $53 \pm 3\%$  of WT levels; Figure 6(b)). However, expression of SERCA2a protein showed a smaller reduction of just  $23 \pm 5\%$  from HCM levels in HCM/HET hearts (Figures 6(c) and 6(d)), with no change seen in PLN protein levels (Figure 6(c)).

In addition to its role in contractility,  $\text{Ca}^{2+}$  is a regulator of key signaling cascades in heart; the  $\text{Ca}^{2+}$ -pools

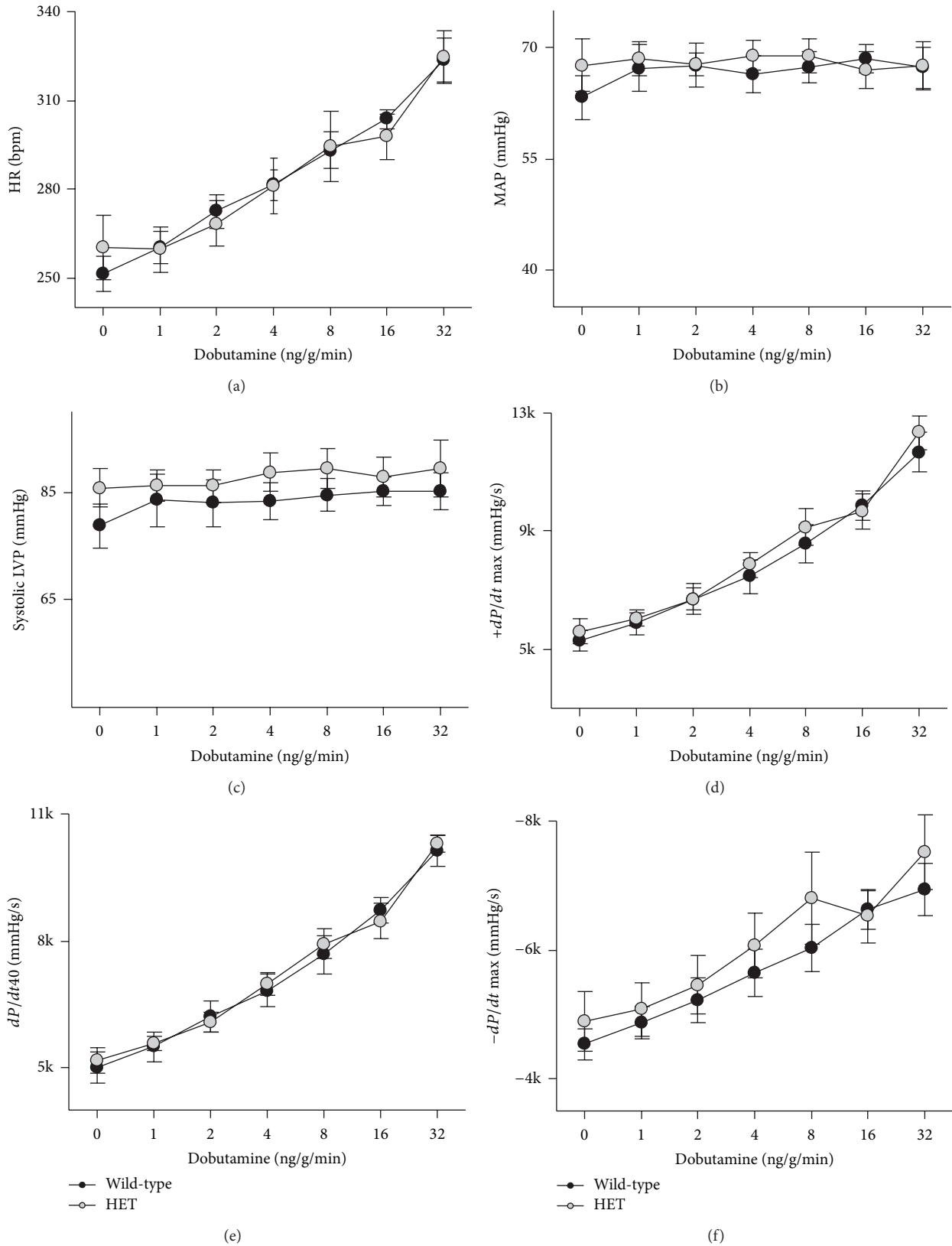


FIGURE 3: Effects of hypothyroidism on cardiovascular performance of *Atp2a2* heterozygous mice. Adult wild-type and *Atp2a2*<sup>+/-</sup> (HET) mice were rendered hypothyroid and cardiovascular performance was assessed under both baseline conditions and after  $\beta$ -adrenergic stimulation. (a) Heart rate (HR); (b) mean arterial pressure (MAP); (c) systolic left ventricular pressure (systolic LVP); (d) maximal rate of left ventricular pressure development (+dP/dt Max); (e) rate of left ventricular pressure development at 40 mmHg (dP/dt40); (f) maximal rate of decay of left ventricular developed pressure (-dP/dt Max). Values are means  $\pm$  SE. *n* = at least 4 for each genotype.

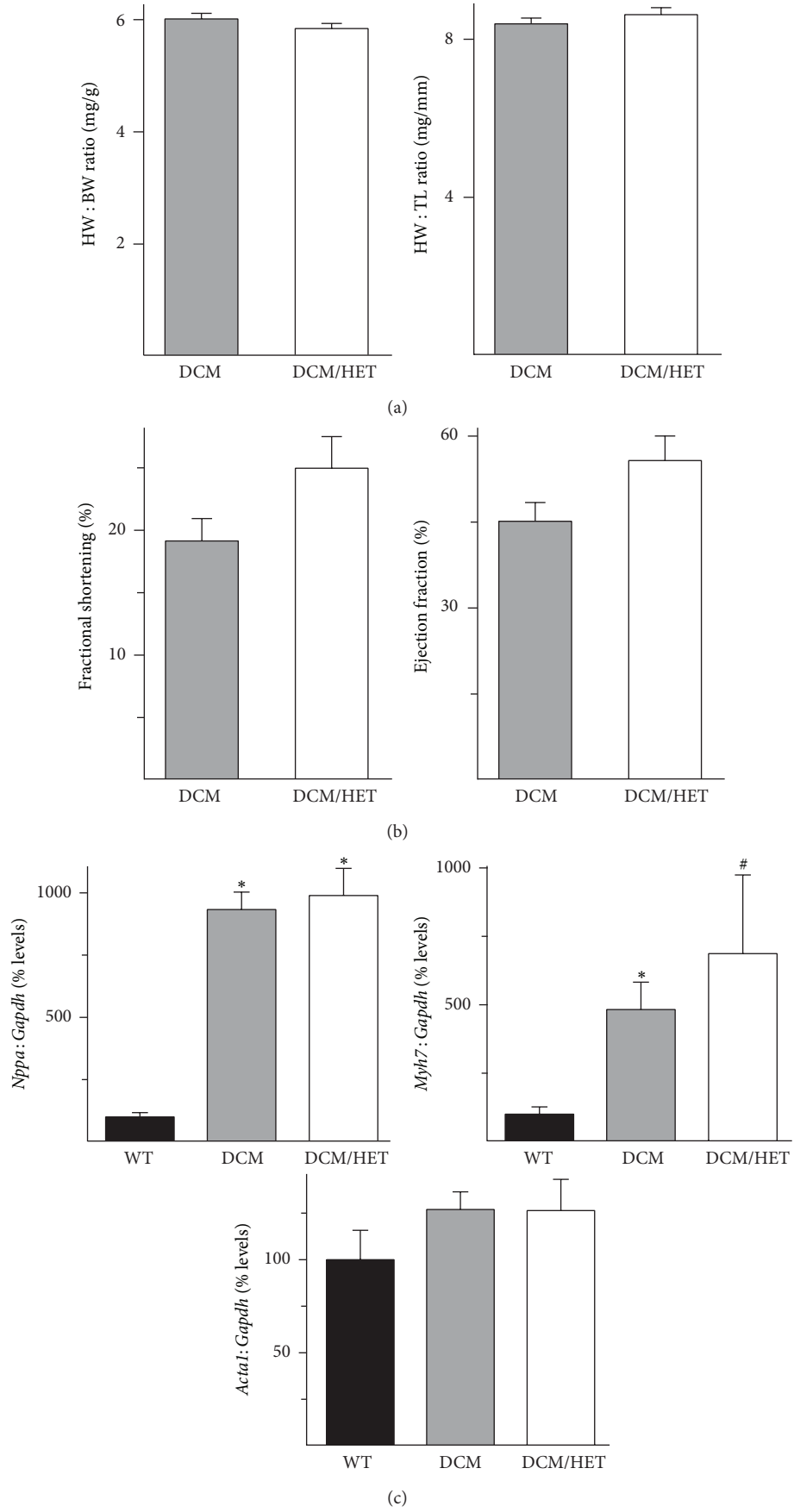


FIGURE 4: Continued.

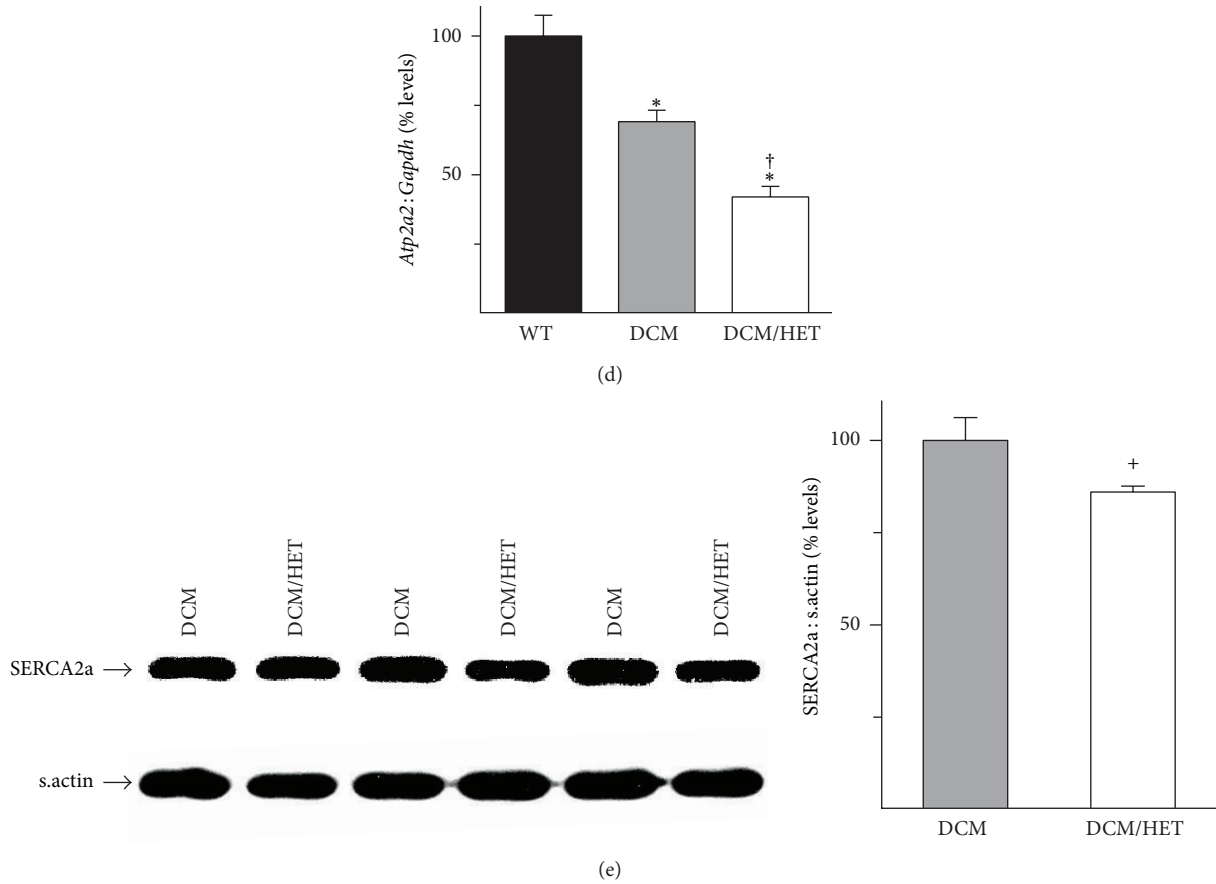


FIGURE 4: Effects of *Atp2a2* heterozygosity in a transgenic model of reduced myofibrillar  $Ca^{2+}$  sensitivity. WT mice, transgenic mice expressing the Glu154Lys mutant  $\alpha$ -tropomyosin, which causes dilated cardiomyopathy (DCM), and double mutant DCM/*Atp2a2*<sup>+/-</sup> (DCM/HET) mice were analyzed. Morphometric analyses revealed similar heart weight : body weight (HW : BW) and heart weight : tibial length (HW : TL) ratios in DCM and DCM/HET mice (a); echocardiographic analysis shows fractional shortening and ejection fraction in DCM and DCM/HET mice (b); RT-PCR analysis shows mRNA levels for (c) atrial natriuretic peptide (*Nppa*),  $\beta$ -myosin heavy chain (*Myh7*), and skeletal  $\alpha$ -actin (*Acta1*) and for *Atp2a2* (d). Immunoblot analysis of cardiac homogenates and quantitation show relative levels of SERCA2a (e) in DCM and DCM/HET hearts. mRNA levels were normalized to *Gapdh* and protein levels were normalized to sarcomeric actin (s.actin). Values are means  $\pm$  SE. *n* = at least 4 for each genotype. \* *P* < 0.05 versus WT controls; # *P* = 0.06 versus WT controls; + *P* = 0.05 versus DCM; † *P* < 0.05 versus DCM.

implicated in such regulatory functions are thought to exist in microdomains spatially distinct from bulk SR  $Ca^{2+}$ -stores [30], which are probably regulated by sarcolemmal  $Ca^{2+}$  pumps such as the plasma membrane  $Ca^{2+}$ -ATPases (PMCA). Impairments in cytosolic bulk  $Ca^{2+}$ -handling have the potential to perturb the spatial isolation of these  $Ca^{2+}$ -microdomains and can lead to a greater reliance on sarcolemmal  $Ca^{2+}$  pumps for  $Ca^{2+}$ -clearance. RT-PCR analysis revealed that mRNA levels for PMCA4 were increased in HCM hearts ( $141 \pm 4\%$  of WT levels) and remained similarly elevated in HCM/HET hearts (Figure 6(e)). In contrast, mRNA levels for PMCA1, which were not significantly altered in HCM hearts, were reduced in HCM/HET hearts (to  $80 \pm 6\%$  of WT levels, Figure 6(f)).

As described above, increased myofibrillar  $Ca^{2+}$ -buffering in HCM hearts has the potential to antagonize SR  $Ca^{2+}$ -sequestration, with effects on SR/ER  $Ca^{2+}$ -store levels. However, as we have previously demonstrated [22], the amplitude

of stimulated  $Ca^{2+}$ -transients is only modestly reduced in HCM myocytes, which raises the possibility that SR/ER  $Ca^{2+}$ -stores may be replenished by alternative mechanisms in these hearts. These can include mediators of store-operated  $Ca^{2+}$ -entry (SOCE); indeed, expression of mRNAs for both *Orail* (to  $155 \pm 19\%$  of WT levels) and *Stim1* (to  $178 \pm 9\%$  of WT levels), which encode proteins with well-characterized roles in stress-induced SOCE activity [31, 32], was increased in HCM hearts. Unexpectedly, this increase was reversed to WT levels in HCM/HET hearts (Figures 6(g) and 6(h)).

Increased expression or activity of the protein phosphatases calcineurin, protein phosphatase 1 (PP1), and protein phosphatase 2A (PP2A) is strongly associated with pathological hypertrophy and heart failure [33–36]. Protein levels of the catalytic subunits of calcineurin (CnA), PP1 (PP1-C), and PP2A (PP2A-C), which reflect expression of the respective holoenzymes, were assessed. While CnA and PP2A-C expression were comparable between HCM and

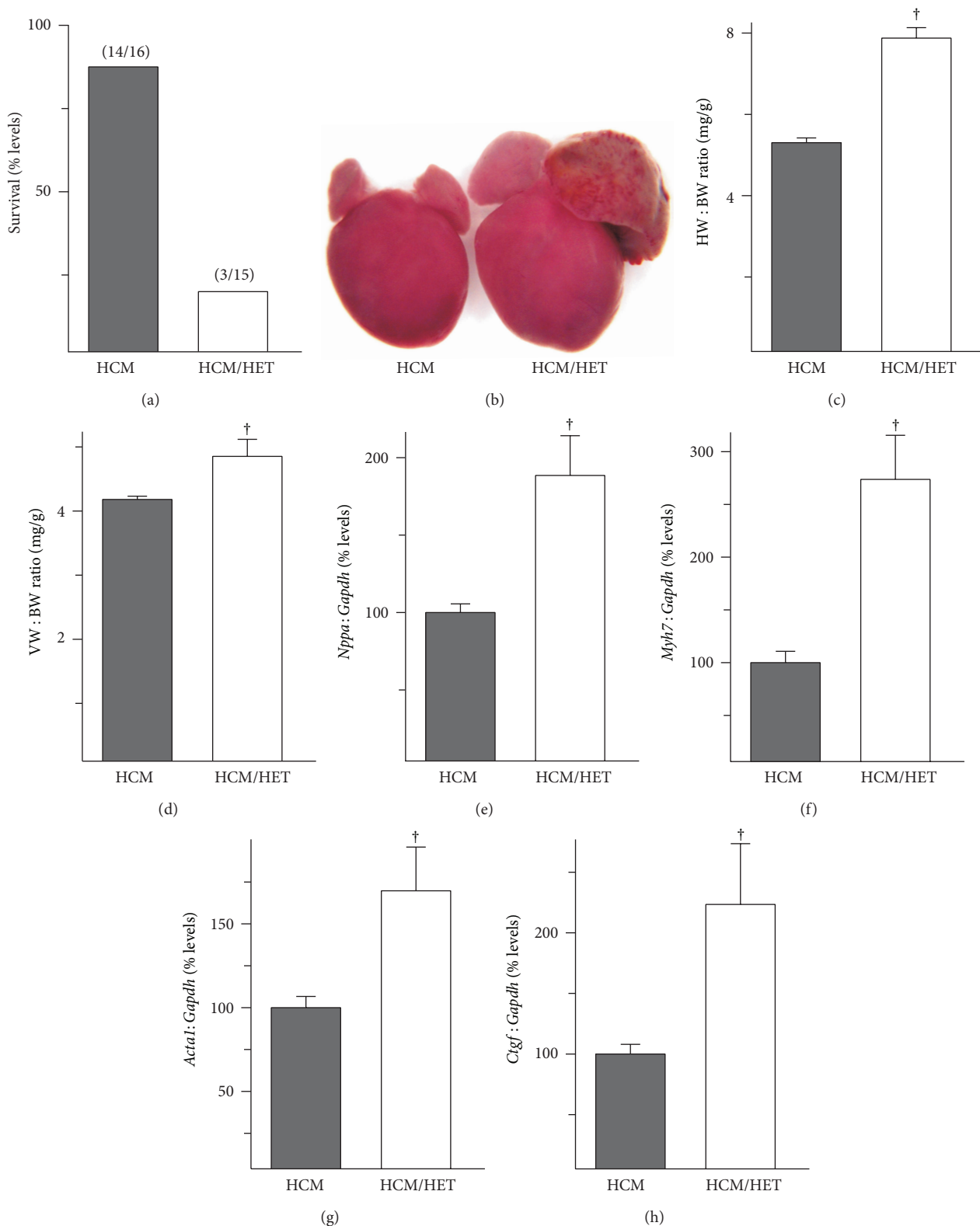


FIGURE 5: Effects of *Atp2a2* heterozygosity in a transgenic model of increased myofibrillar  $Ca^{2+}$  sensitivity. WT mice, mice expressing the Glu180Gly mutant  $\alpha$ -tropomyosin, which causes hypertrophic cardiomyopathy (HCM), and double mutant HCM/*Atp2a2*<sup>+/-</sup> (HCM/HET) mice were analyzed. Survival of HCM and HCM/HET mice was assessed at 5 weeks of age (a). Gross morphometry at 4 weeks of age showed (b) overt remodeling, (c) increased heart weight:body weight ratios (HW:BW), and (d) increased ventricular weight:body weight ratios (VW:BW) in HCM/HET mice. RT-PCR shows elevated mRNA levels in HCM/HET hearts for (e) atrial natriuretic peptide (*Nppa*), (f)  $\beta$ -myosin heavy chain (*Myh7*), (g) skeletal  $\alpha$ -actin (*Acta1*), and (h) connective tissue growth factor (*Ctgf*). mRNA levels were normalized to *Gapdh* expression. Values shown are means  $\pm$  SE.  $n =$  at least 4 for each genotype. † $P < 0.05$  versus HCM controls.

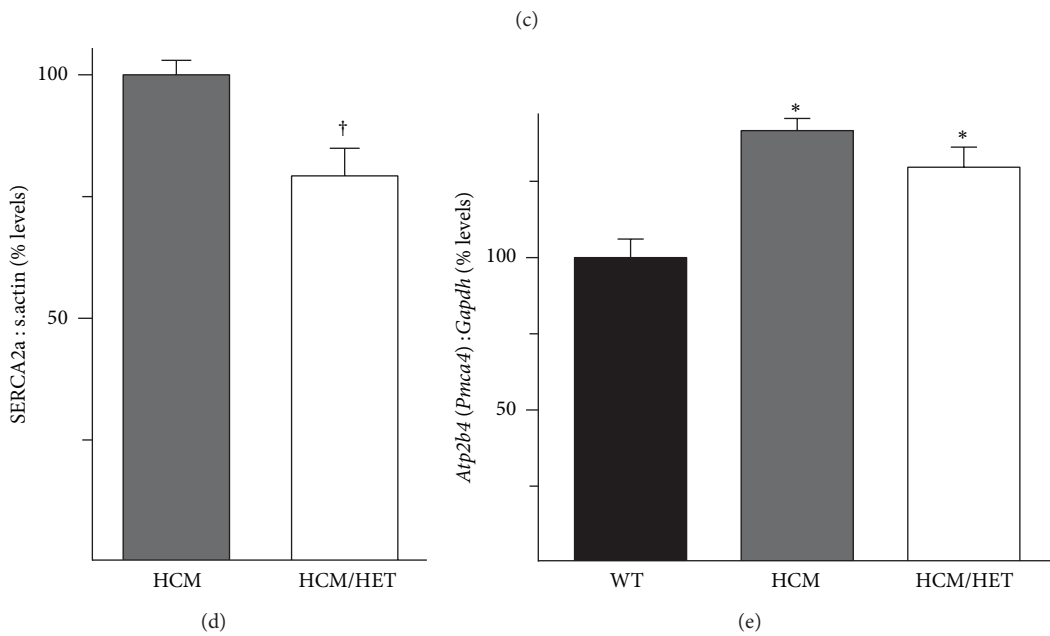
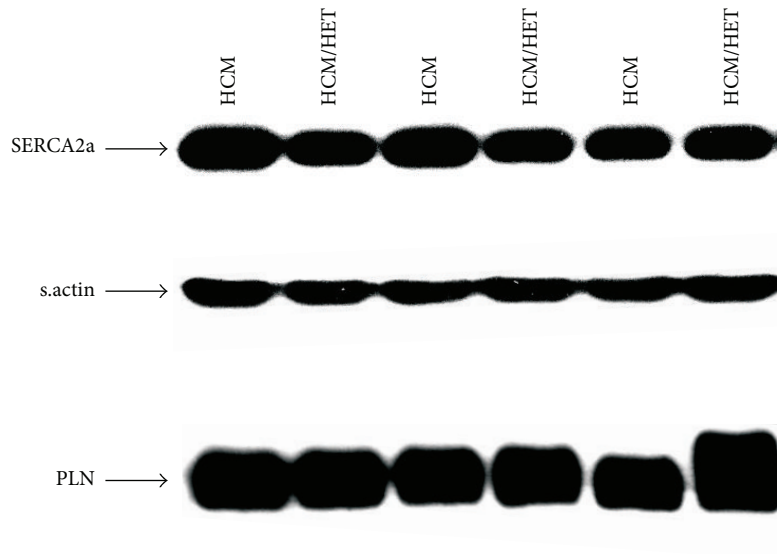
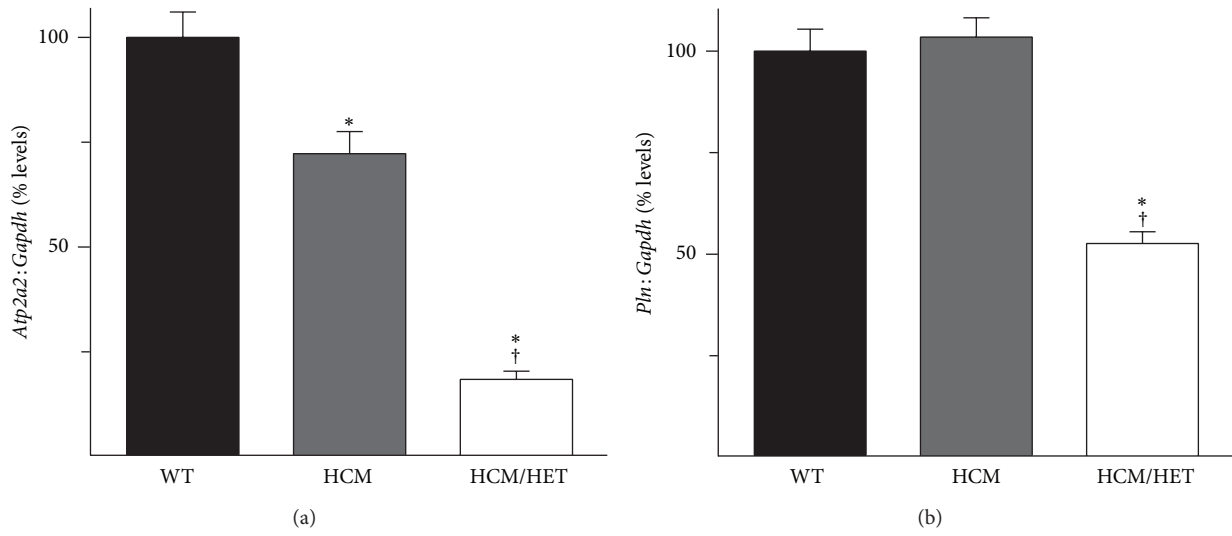


FIGURE 6: Continued.

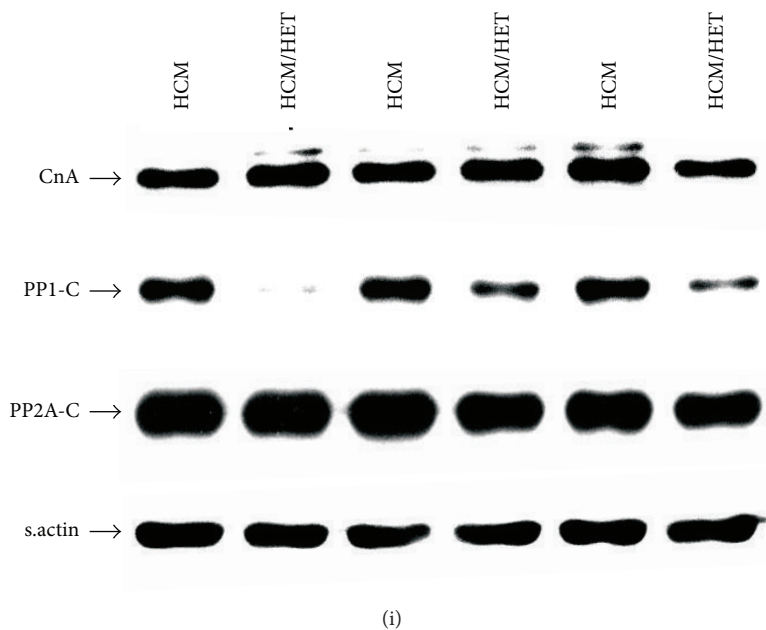
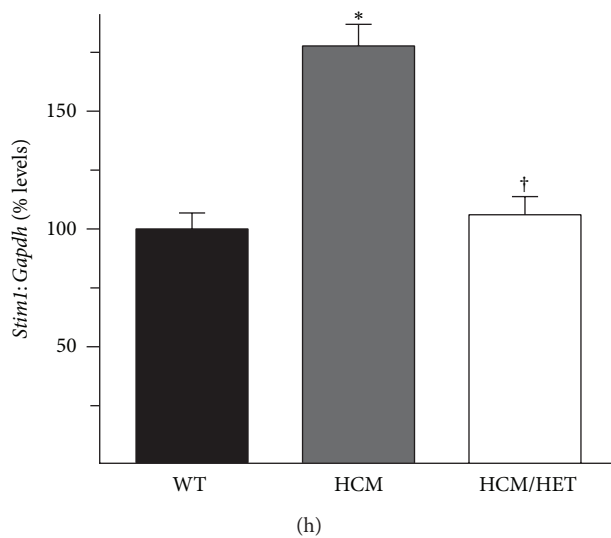
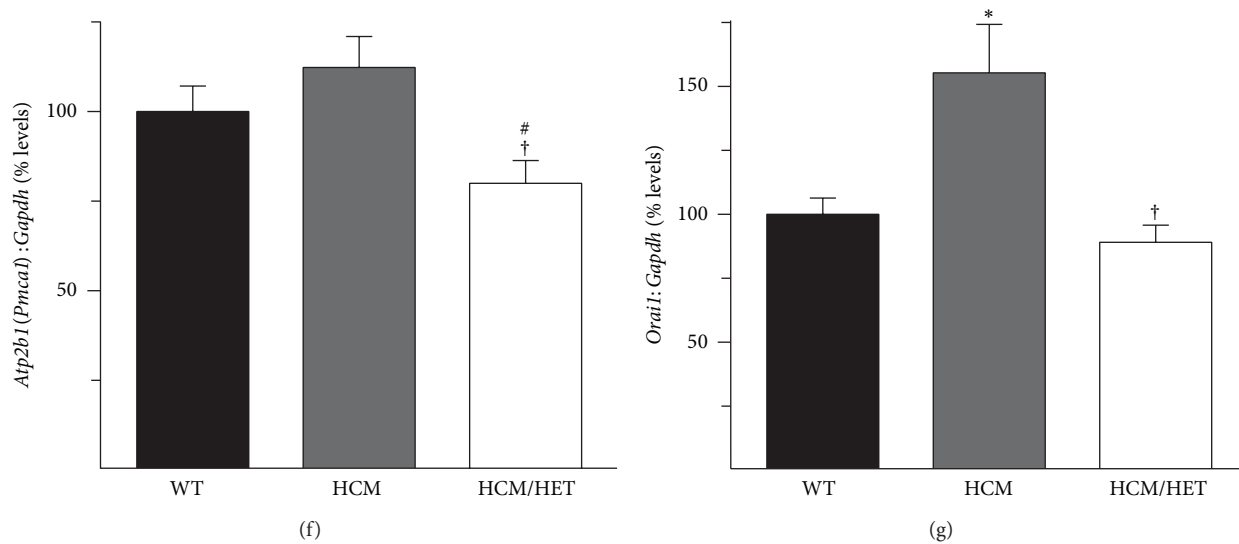


FIGURE 6: Continued.

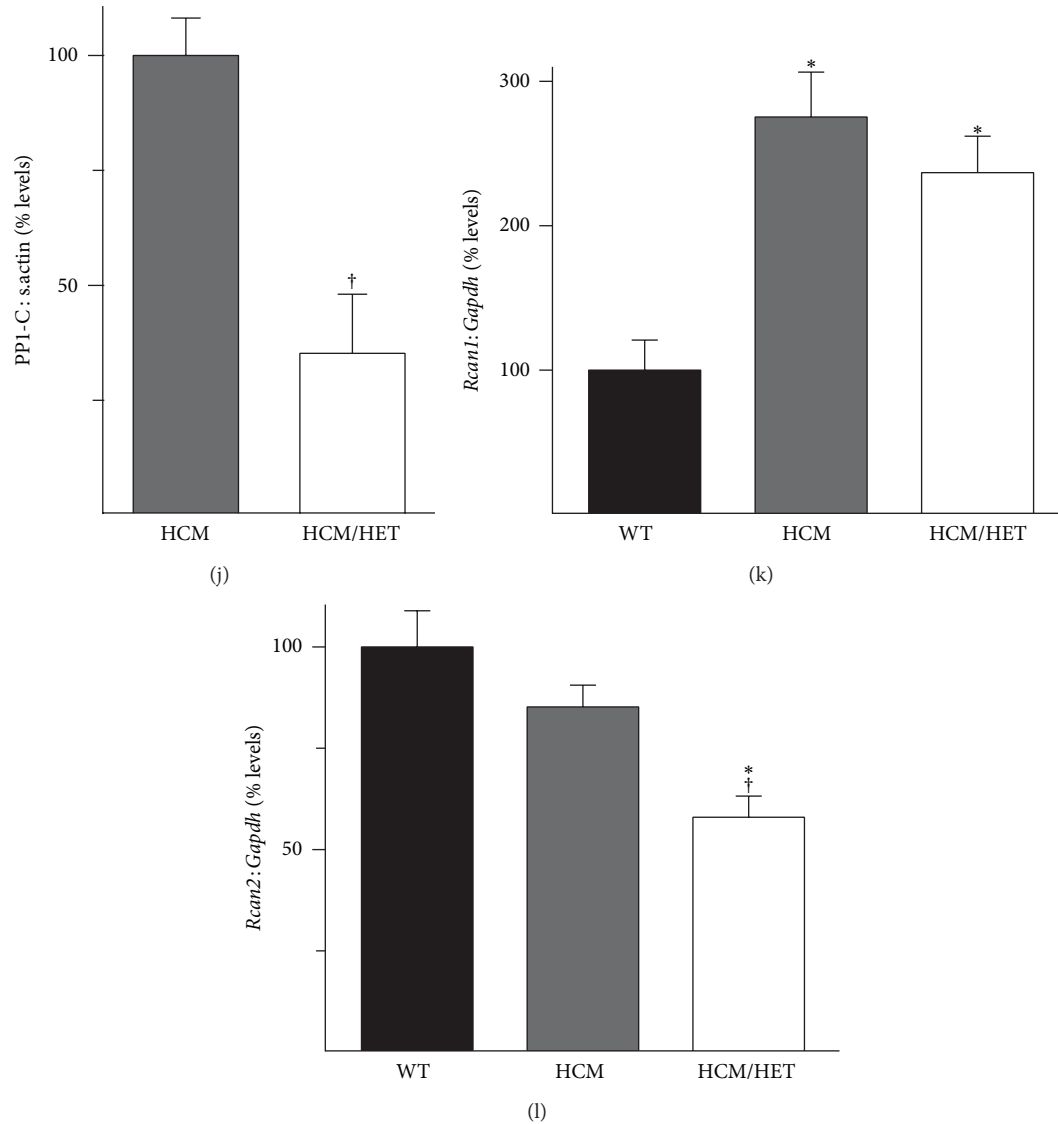


FIGURE 6: Effects of *Atp2a2* heterozygosity on regulators of  $\text{Ca}^{2+}$ -handling and phosphatases in HCM models. Hearts from WT mice, mice expressing the Glu180Gly mutant  $\alpha$ -tropomyosin (HCM), and HCM/*Atp2a2*<sup>+/-</sup> double mutant (HCM/HET) mice were processed for RT-PCR and immunoblots. RT-PCR analysis of mRNA for (a) SERCA2 (*Atp2a2*) and (b) phospholamban (*Pln*), (c) immunoblot analysis of SERCA2a and PLN, and (d) quantitation of SERCA2a protein. RT-PCR analyses of mRNA for (e) plasma membrane  $\text{Ca}^{2+}$ -ATPase isoform 4 (*Atp2b4*), (f) plasma membrane  $\text{Ca}^{2+}$ -ATPase isoform 1 (*Atp2b1*), (g) sarcolemmal calcium release-activated calcium modulator 1 (*Orail*), and (h) stromal interaction molecule 1 (*Stim1*) and (i) immunoblot analyses of the catalytic subunits of calcineurin (CnA), protein phosphatase 1, (PPI-C), and protein phosphatase 2A (PP2A-C) in HCM and HCM/HET hearts. (j) Quantitation of PPI-C protein levels. RT-PCR analyses of mRNA for (k) regulator of calcineurin 1 (*Rcan1*) and (l) regulator of calcineurin 2 (*Rcan2*). mRNA levels were normalized to *Gapdh* and protein levels were normalized to sarcomeric actin (s.actin). Values are means  $\pm$  SE.  $n =$  at least 4 for each genotype. \*  $P < 0.05$  versus WT controls; †  $P < 0.05$  versus HCM; #  $P = 0.08$  versus WT controls.

HCM/HET hearts (Figure 6(i)), PPI-C levels were reduced in HCM/HET hearts (Figures 6(i) and 6(j)). To address the possibility that calcineurin activity was augmented in HCM/HET hearts, mRNA levels for regulator of calcineurin 1 (calcipressin-1, *Rcan1*), a marker of calcineurin activity, were determined by RT-PCR analysis. While there was no difference in *Rcan1* levels between HCM and HCM/HET hearts (Figure 6(k)), mRNA levels of *Rcan2*, which codes for calcipressin-2, were significantly reduced

in HCM/HET hearts ( $58 \pm 5\%$  of WT levels; Figure 6(l)).

**3.7. Expression of ER Stress Markers and Regulators of Apoptosis in HCM/HET Hearts.** The reduction in SERCA2a protein levels, coupled with the downregulation of SOCE-related genes, raised the possibility that ER stress was elevated in HCM/HET hearts. We initially assessed expression of key ER stress markers in HCM hearts. RT-PCR analysis revealed

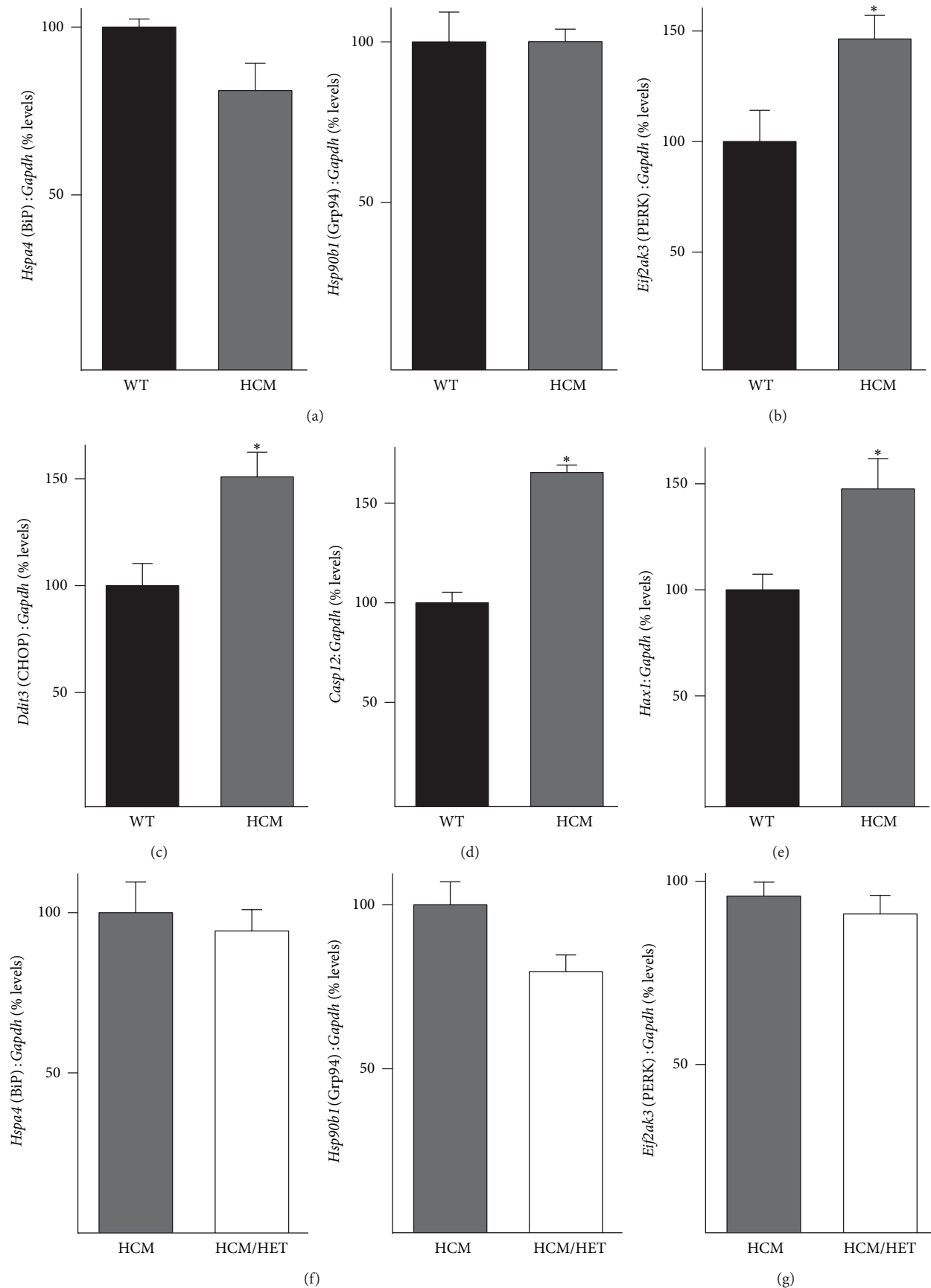


FIGURE 7: Continued.

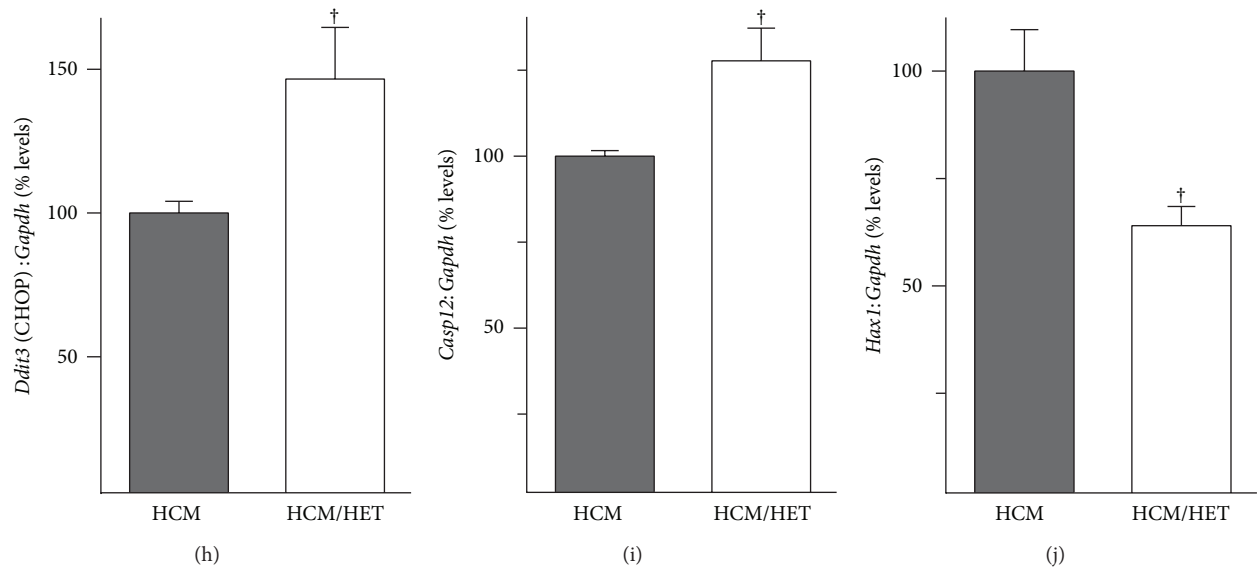


FIGURE 7: Effect of *Atp2a2* heterozygosity on markers of ER stress and apoptosis in HCM and HCM/HET hearts. Heart RNA from WT mice, mice expressing the Glu180Gly mutant  $\alpha$ -tropomyosin (HCM), and HCM/*Atp2a2*<sup>+/-</sup> double mutant (HCM/HET) mice was analyzed by RT-PCR. Panels (a)–(e) compare WT and HCM; panels (f)–(j) compare HCM and HCM/HET. mRNA levels are shown for (a, f) ER chaperones BiP/GRP78 (*Hspa4*) and GRP94 (*Hsp90b1*); (b, g) PERK (*Eif2ak3*); (c, h) CHOP (*Ddit3*); (d, i) caspase 12 (*Casp12*); and (e, j) HCLS1 associated protein X-1 (*Hax1*) in WT, HCM, and HCM/HET hearts. mRNA levels were normalized to *Gapdh*. Values shown are means  $\pm$  SE.  $n =$  at least 4 for each genotype. \* $P < 0.05$  versus WT controls; <sup>†</sup> $P < 0.05$  versus HCM.

no increase in mRNA for the ER chaperones BiP/GRP78 or GRP94 (Figure 7(a)). However, mRNA for PERK, a major kinase involved in ER stress responses, was increased in HCM hearts (to  $147 \pm 12\%$  of WT levels; Figure 7(b)). Furthermore, mRNAs for the ER stress related proapoptotic proteins CHOP ( $145 \pm 12\%$  of WT levels; Figure 7(c)) and CASP12 ( $164 \pm 5\%$  of WT levels; Figure 7(d)) were also increased in HCM hearts. These changes were associated with an increase (to  $148 \pm 14\%$  of WT levels; Figure 7(e)) in mRNA for the antiapoptotic protein HCLS1 associated protein X-1 (HAX1), which is localized to mitochondria and the SR [37].

There was no increase in mRNA levels for GRP78, GRP94, or PERK in HCM/HET hearts when compared to HCM controls (Figures 7(f) and 7(g)). However, mRNA levels for CHOP ( $143 \pm 16\%$  of HCM levels; Figure 7(h)) and CASP12 ( $128 \pm 9\%$  of HCM levels; Figure 7(i)) were further elevated in HCM/HET hearts. The increase seen in HAX1 mRNA in HCM hearts was reversed in HCM/HET hearts (to  $64 \pm 4\%$  of HCM levels; Figure 7(j)).

**3.8. Effect of *Atp2a2* Heterozygosity on Regulators of Energy Metabolism in HCM Hearts.** Impaired relaxation resulting from an increase in myofibrillar  $\text{Ca}^{2+}$ -sensitivity can energetically stress the heart [38]. The resultant dysregulation of energy metabolism has been suggested to contribute to the hypertrophic phenotype associated with sarcomeric mutations that increase myofibrillar  $\text{Ca}^{2+}$ -sensitivity [39, 40]. mRNA levels of *Ppar $\gamma$* , encoding peroxisome proliferator-activated receptor gamma, a regulator of lipid metabolism

that is implicated in the development of pathological hypertrophy [41], were normal in HCM hearts but reduced in HCM/HET hearts (to  $81 \pm 6\%$  of WT levels; Figure 8(a)). Hearts rely predominantly on lipids for their energy supply [42] and FABP3 is the cardiac/muscle-isoform of fatty acid binding proteins, which mediate the intracellular transport of long-chain fatty acids. Expression of the *Fabp3* gene was downregulated (to  $76 \pm 9\%$  of WT levels) in HCM hearts and further reduced in HCM/HET hearts (to  $49 \pm 5\%$  of WT levels; Figure 8(b)). Mitochondrial uptake of long-chain fatty acids is mediated by carnitine palmitoyltransferase 1b (CPT1b), the mRNA levels for which were reduced in HCM (to  $88 \pm 3\%$  of WT levels) and further reduced in HCM/HET (to  $61 \pm 2\%$  of WT levels) hearts (Figure 8(c)). CPT1b-mediated transfer of long-chain fatty acids can be inhibited by malonyl CoA, which is generated from acetyl-CoA by acetyl-CoA carboxylase beta (encoded by *Acacb*). While *Acacb* mRNA levels trended lower in HCM hearts, they were downregulated in HCM/HET hearts (to  $58 \pm 7\%$  of WT levels; Figure 8(d)). In addition, mRNA levels for acyl-CoA oxidase 1 (*Acox1*), which is the first enzyme of the  $\beta$ -oxidation pathway, were also reduced (to  $64 \pm 5\%$  of WT levels) in HCM/HET hearts (Figure 8(e)). Besides lipids, hearts also utilize glucose as an energy source [42]. Glucose uptake in heart is mediated by members of *Slc2a* glucose transporter family, of which GLUT4 (*Slc2a4*) is the predominant isoform in cardiac myocytes. mRNA levels for GLUT4 were reduced (to  $80 \pm 2\%$  of WT levels) in HCM hearts, with a more pronounced reduction (to  $47 \pm 2\%$  of WT levels) in HCM/HET hearts (Figure 8(f)).

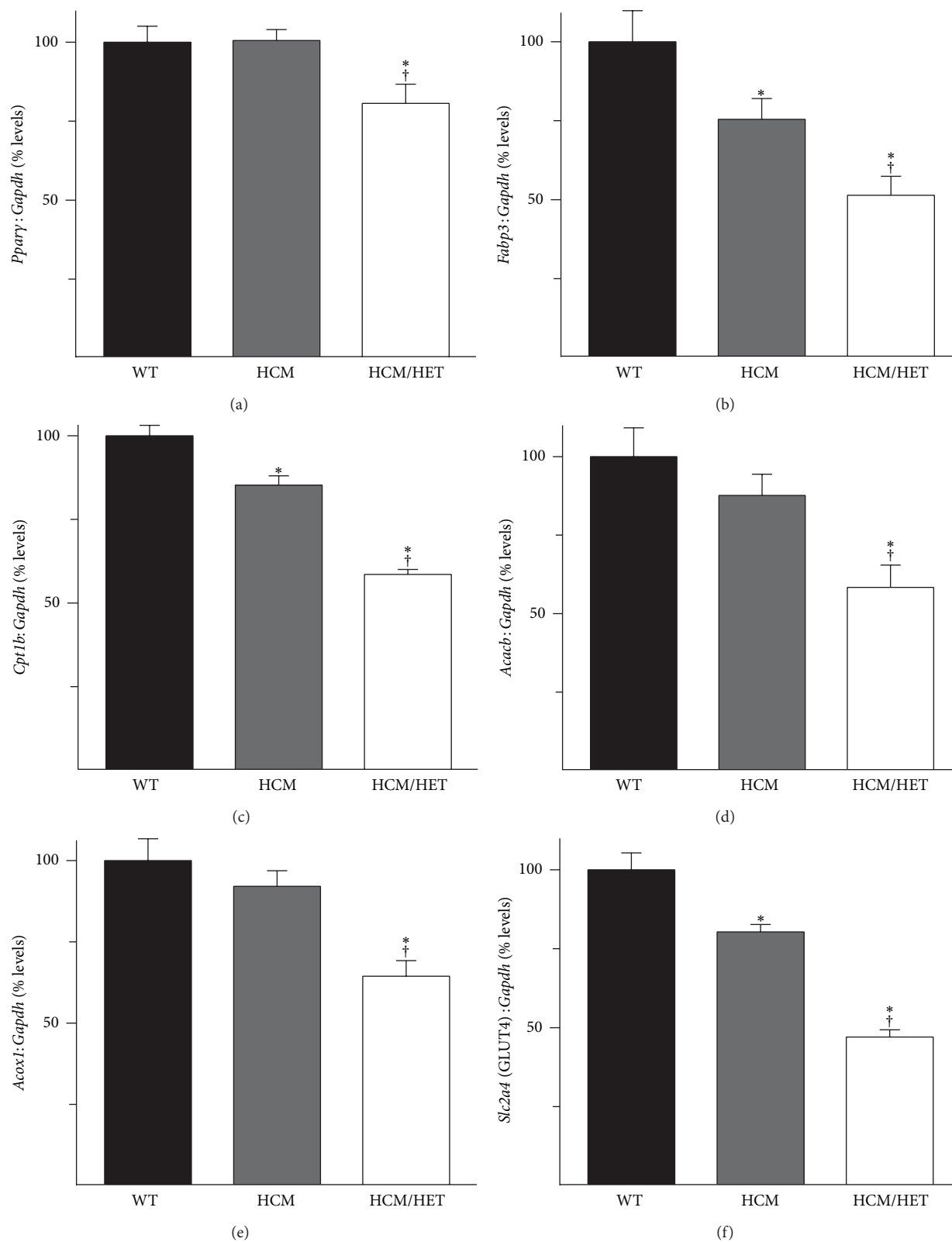


FIGURE 8: Effect of *Atp2a2* heterozygosity on regulators of energy metabolism in HCM and HCM/HET hearts. Heart RNA from WT mice, mice expressing the Glu180Gly mutant  $\alpha$ -tropomyosin (HCM), and HCM/*Atp2a2*<sup>+/-</sup> double mutant (HCM/HET) mice was analyzed by RT-PCR. mRNA levels are shown for (a) peroxisome proliferator-activated receptor gamma (*Pparγ*); (b) fatty acid binding protein 3 (*Fabp3*); (c) the muscle-isoform of carnitine palmitoyltransferase 1 (*Cpt1b*); (d) acetyl CoA-carboxylase beta (*Acacb*); (e) acyl-CoA oxidase 1 (*Acox1*); and (f) the GLUT4 glucose transporter (*Slc2a4*). mRNA levels were normalized to *Gapdh*. Values are means  $\pm$  SE.  $n =$  at least 4 for each genotype. \* $P < 0.05$  versus WT controls; † $P < 0.05$  versus HCM.

TABLE 1: Effect of *Atp2a2* heterozygosity on regulators of apoptosis and energy metabolism in DCM and DCM/HET hearts.

Gene	Relative mRNA levels (normalized to <i>Gapdh</i> )		
	WT <sup>‡</sup>	DCM	DCM/HET
CHOP ( <i>Ddit3</i> )	100 ± 10	103 ± 3	113 ± 10
Caspase 12 ( <i>Casp12</i> )	100 ± 7	122 ± 3*	120 ± 16
HCLS1 associated protein X-1 ( <i>Hax1</i> )	100 ± 5	91 ± 3	106 ± 12
Fatty acid binding protein 3 ( <i>Fabp3</i> )	100 ± 7	70 ± 4*	75 ± 7*
Carnitine palmitoyltransferase 1 ( <i>Cpt1b</i> )	100 ± 2	77 ± 3*	70 ± 8*
Glucose transporter 4 ( <i>Slc2a4</i> )	100 ± 12	88 ± 2	95 ± 8

<sup>‡</sup>Heart RNA from wild-type (WT) mice, transgenic mice expressing Glu154Lys mutant  $\alpha$ -tropomyosin (DCM), and DCM/*Atp2a2*<sup>+/-</sup> double mutant (DCM/HET) mice was analyzed by RT-PCR. Values are mean ± SE; *n* = at least 4 for each genotype; \* *P* < 0.05 versus WT controls.

**3.9. Biochemical Effects of *Atp2a2* Heterozygosity Seen in HCM/HET Hearts Are Lacking in DCM/HET Hearts.** As described above, *Atp2a2* heterozygosity did not exacerbate the cardiac disease phenotype of DCM mice. Given the dramatic effects of SERCA2 haploinsufficiency in HCM/HET hearts at the RNA/protein levels, we analyzed DCM/HET hearts to identify possible underlying similarities. Several mRNAs analyzed (*Casp12*, *Fabp3*, and *Cpt1b*) were altered in DCM hearts relative to WT hearts. However, RT-PCR analysis revealed that *Atp2a2* heterozygosity did not impact mRNA levels for *Ddit3* (CHOP), *Casp12*, *Hax1*, *Fabp3*, *Cpt1b*, or *Slc2a4* (GLUT4) in DCM/HET hearts when compared with DCM hearts (Table 1). Immunoblot analyses of total ventricular homogenates of DCM and DCM/HET mice showed no change in protein levels of CnA, PPI-C, or PP2A-C (data not shown).

#### 4. Discussion

While there is strong evidence that *ATP2A2* heterozygosity does not impair cardiovascular performance in humans either at rest or during exercise [6, 7], the opportunities to elucidate the molecular mechanisms that allow for cardiac function to be preserved in otherwise healthy DD patients are obviously limited. For example, it remains unknown if loss of one *ATP2A2* allele elicits the compensatory upregulation of the second functional allele or whether SERCA2a haploinsufficiency in human heart leads to a greater, and apparently effective, reliance on transsarcolemmal  $Ca^{2+}$ -flux. There have also been no studies to determine if DD patients are more susceptible to heart failure and decompensation in the context of secondary pathological insults. The *Atp2a2* heterozygous mouse model on the inbred FVB/N background offered a unique opportunity to address these questions, as it resembles human DD patients in displaying a skin/keratinized epithelial phenotype with no overt effects on cardiovascular function.

Expression of SERCA2a protein levels at ~80% of WT levels in HET hearts demonstrated a remarkable ability to upregulate expression of the single functional *Atp2a2* allele. This was unexpected given the evidence from transgenic lines that it is difficult to appreciably overexpress SERCA2 protein in mouse hearts [43, 44]. Given that *Atp2a2* mRNA levels were reduced by ~50% in HET hearts, it is reasonable

to assume that the increase in SERCA2a protein results principally from posttranscriptional adaptations; these could include augmented translation, extended SERCA2 protein half-life, and/or diminished SERCA2 protein degradation. The increase seen in LTCC $\alpha$ 2 protein levels is consistent with the idea that even modest reductions in SERCA2a expression might lead to a greater reliance on  $Ca^{2+}$ -handling across the sarcolemma. While such a shift would help preserve  $Ca^{2+}$ -homeostasis, it is likely to place a greater energetic burden on the heart. SERCA2 is unique in its stoichiometry of transporting 2  $Ca^{2+}$  ions/ATP hydrolyzed. In comparison, transsarcolemmal flux of  $Ca^{2+}$  via LTCC-influx, NCX1-efflux (with a stoichiometry of 3 $Na^+$ :1 $Ca^{2+}$ ), and  $Na^+$ / $K^+$ -ATPase-mediated  $Na^+$  removal effectively doubles the energy cost of  $Ca^{2+}$ -clearance.

Increased PLN phosphorylation can also serve to compensate for the reduction in SERCA2 levels [23], with evidence of a predominant role for phosphorylation at Ser16, but not Thr17, in  $\beta$ -adrenergic stimulation of inotropy and lusitropy in mouse hearts [45]. Therefore, it is difficult to ascribe any part of the normal  $\beta$ -adrenergic response seen in HET hearts to increased PLN phosphorylation, given that PS16 levels were unaltered and only PT17 levels were elevated in stimulated HET hearts. While phosphorylation at Thr17 is mediated by  $Ca^{2+}$ /calmodulin-dependent kinase CaMKII, dephosphorylation is mediated by PPI [46, 47]. Although immunoblot analysis showed no evidence of a reduction in PPI expression in HET hearts (data not shown), a clear reduction in PPI expression was observed in HCM/HET hearts relative to HCM controls, probably providing some compensation for the reduction in SERCA2 protein.

Reduction in SERCA2 expression/activity is closely associated with progression of heart disease and failure. While recent clinical trials provide strong evidence that enhancing SERCA2a expression can alleviate impairment of cardiac function [48–50], it remains unclear whether SERCA2a deficiency can itself precipitate decompensation and heart failure. This is highly relevant to DD patients, particularly in the context of aging or secondary pathological conditions affecting the heart. Hypothyroidism, which affects about 4.6% of the US population [51], is one such condition known to compromise cardiac function [13, 24] and reduce SERCA2

expression [20, 25]. The finding that *Atp2a2* heterozygosity does not exacerbate the effects of hypothyroidism in mice may result from the switch in myosin heavy chain (MHC) isoforms from  $\alpha$ -MHC to the slower  $\beta$ -MHC, which occurs in hypothyroidism, and is known to be energetically favorable [52]. Whether the effects of hypothyroidism are similarly unaffected by SERCA2 haploinsufficiency in human DD patients is an issue that remains to be clarified; it should be evaluated with no preconceptions, as the lack of an effect in the rodent model does not discount possible consequences in human DD patients.

A relative increase in  $\beta$ -MHC levels, which commonly occurs in diseased conditions, renders hearts more susceptible to chronic myocardial stress [53]. Although this outcome was not tested in the context of hypothyroidism in HET mice, we investigated the effects of *Atp2a2* heterozygosity in models of altered myofibrillar  $\text{Ca}^{2+}$ -sensitivity, which impose significant chronic contractile stress and are closely associated with the pathogenesis of cardiomyopathies and heart failure [54]. DCM mice, with reduced myofibrillar  $\text{Ca}^{2+}$ -sensitivity, have been reported to develop hypertrophy at 2 months of age, with significant dilation and myocyte disarray occurring by 5 months and mice starting to die at 4–6 months of age [16]. These effects were shown to be associated with down-regulation of SERCA2a, consistent with the possibility that *Atp2a2* heterozygosity would hasten disease pathogenesis. The absence of such an effect in DCM/HET mice however revealed that SERCA2 haploinsufficiency has limited effects in the context of reduced myofibrillar  $\text{Ca}^{2+}$ -sensitivity, which occurs during pathological conditions such as inflammation and sepsis [55].

The rapid onset of hypertrophy and decompensation in HCM/HET mice on the other hand strongly suggests that disease pathogenesis associated with increased myofibrillar  $\text{Ca}^{2+}$ -sensitivity may be exacerbated in DD patients. The catastrophic effects of SERCA2 haploinsufficiency in HCM/HET occurred despite SERCA2a protein levels being reduced by just 23% compared to levels in HCM hearts. This indicates that relatively modest reductions in SERCA2a expression can have profound effects in hearts with increased myofibrillar  $\text{Ca}^{2+}$ -sensitivity. This effect is likely due to the fact that, besides factors such as mechanical load and sarcolemmal  $\text{Ca}^{2+}$ -flux, dissociation of  $\text{Ca}^{2+}$  from myofibrils is facilitated by SERCA2-mediated  $\text{Ca}^{2+}$ -clearance [56]. The importance of this function is expected to be amplified in the context of elevated myofibrillar  $\text{Ca}^{2+}$ -sensitivity, making even small changes in SERCA2 expression/function highly consequential. Recent reports that elevating SERCA2 activity, either by increased expression of SERCA2a or ablation of phospholamban, attenuates disease progression in HCM mice [57, 58] are consistent with this hypothesis.

Perturbations in cytosolic  $\text{Ca}^{2+}$ -clearance are also associated with the generation of ventricular arrhythmias [56], which are strongly implicated in progression to heart failure and sudden death [59, 60]. Targeted SERCA2a gene therapy has been shown, in multiple models, to reduce ventricular arrhythmias in addition to improving cardiac function [4]. The highly advanced disease condition observed in

HCM/HET mice as young as 4 weeks of age precluded effective functional analyses of these mice. However, we examined left ventricular pressure measurements in HET mice and found no evidence of extrasystolic beats or other arrhythmias under either basal conditions or upon maximal  $\beta$ -adrenergic stimulation (data not shown).

The more rapid decompensation in HCM/HET hearts was associated with a reversal of the increase in *Orail* and *Stim1* levels seen in HCM hearts. The incidence of increased SOCE via ORAI1 and STIM1 in pathological hypertrophy has implicated these proteins in disease pathogenesis [31]. However, recent data from knockout models reveal a more nuanced role for these proteins in heart, with effects on  $\text{Ca}^{2+}$ -homeostasis and the development of compensatory hypertrophy [61, 62]. *Orail* deficiency was found to exacerbate loss of cardiac function and hasten progression to dilation and was associated with increased apoptosis [63]. Indeed, levels of proapoptotic *Chop* and *Casp12* were elevated in HCM/HET hearts and notably expression of antiapoptotic *Hax1*, which was elevated in HCM hearts, was reduced to WT levels in HCM/HET hearts. There is increasing evidence that the antiapoptotic function of the HAX1 protein is linked to its association with SR  $\text{Ca}^{2+}$ -handling [37, 64], where HAX1 has been shown to localize to the SR in a PLN-dependent manner [65]. HAX1 overexpression, which promotes cell survival, downregulates SERCA2 protein levels, whereas SERCA2 overexpression has been shown to antagonize its protective effects [66, 67]. Therefore, the reversion of HAX1 expression to WT levels may contribute to the preservation of SERCA2 levels in HCM/HET hearts, with potentially maladaptive effects on myocyte cell survival. Further detailed studies will be necessary to fully elucidate possible interactions between HAX1, which has been localized to mitochondria as well [37], and SERCA2 during HCM pathogenesis. Additional perturbations in myocardial energy metabolism, which are strongly implicated in hypertrophy and heart failure [38–41], are also likely to contribute to the rapid decompensation observed in HCM/HET hearts. Reductions in both CPT1b and GLUT4 have been shown to promote pathological hypertrophy and heart failure [68–70]. Conversely, we have recently demonstrated that protection against Tm180-related hypertrophy is associated with preservation of CPT1b and GLUT4 expression at WT levels [23].

In conclusion, our data show that the loss of one copy of the *Atp2a2* gene, which causes reduced expression of SERCA2a in heart, appears to be benign under normal conditions and even in some disease states. This finding is consistent with the results of studies in human DD patients, in which the loss of one *ATP2a2* allele caused no impairment of cardiac performance [6, 7]. However, our studies with the mouse model of DD also reveal that loss of a single copy of *Atp2a2* can lead to much more rapid decompensation, heart failure, and death in mice carrying an HCM mutation that increases myofibrillar  $\text{Ca}^{2+}$  sensitivity. These results suggest that DD patients may be less tolerant of the changes associated with increased myofibrillar  $\text{Ca}^{2+}$ -sensitivity in heart. In addition to being relevant to pathological conditions such as end-stage heart failure [15], the implications of this finding

could extend to the use of therapeutic agents that enhance myofibrillar  $\text{Ca}^{2+}$ -sensitivity in DD patients. For example, although long-term treatment with the  $\text{Ca}^{2+}$ -sensitizer levosimendan improves cardiac function in a model with cardiomyocyte-specific ablation of SERCA2, it also significantly increases fibrosis in SERCA2-deficient hearts [71]. While extrapolation of results from rodent models to human disease merits caution, our results suggest that progression of some types of heart disease is likely to be exacerbated by DD mutations. DD patients and their physicians should therefore be aware of the possibility of adverse interactions between SERCA2 haploinsufficiency and certain pathological conditions affecting cardiovascular health.

### Conflict of Interests

The authors declare that there is no conflict of interests regarding the publication of this paper.

### Acknowledgments

This work was supported by National Institutes of Health Grants HL061974 (GES) and HL107957 (YW), an American Heart Association Beginning Grant-in-Aid 11BGIA77220005 (VP), and a Near Horizons Pilot grant from the University of Cincinnati Heart, Lung and Vascular Institute (VP and JNL). The authors thank Maureen Bender for excellent animal husbandry.

### References

- [1] A. Sakuntabhai, V. Ruiz-Perez, S. Carter et al., "Mutations in ATP2A2, encoding a  $\text{Ca}^{2+}$  pump, cause Darier disease," *Nature Genetics*, vol. 21, no. 3, pp. 271–277, 1999.
- [2] A. Hovnanian, "Darier's disease: from dyskeratosis to endoplasmic reticulum calcium ATPase deficiency," *Biochemical and Biophysical Research Communications*, vol. 322, no. 4, pp. 1237–1344, 2004.
- [3] M. Periasamy, P. Bhupathy, and G. J. Babu, "Regulation of sarcoplasmic reticulum  $\text{Ca}^{2+}$  ATPase pump expression and its relevance to cardiac muscle physiology and pathology," *Cardiovascular Research*, vol. 77, no. 2, pp. 265–273, 2008.
- [4] M. B. Sikkil, C. Hayward, K. T. MacLeod, S. E. Harding, and A. R. Lyon, "SERCA2a gene therapy in heart failure: an anti-arrhythmic positive inotrope," *British Journal of Pharmacology*, vol. 171, no. 1, pp. 38–54, 2014.
- [5] Y. Miyauchi, T. Daiho, K. Yamasaki et al., "Comprehensive analysis of expression and function of 51 sarco(endo)plasmic reticulum  $\text{Ca}^{2+}$ -ATPase mutants associated with darier disease," *The Journal of Biological Chemistry*, vol. 281, no. 32, pp. 22882–22895, 2006.
- [6] S. Tavadia, R. C. Tait, T. A. McDonagh, and C. S. Munro, "Platelet and cardiac function in Darier's disease," *Clinical and Experimental Dermatology*, vol. 26, no. 8, pp. 696–699, 2001.
- [7] B. M. Mayosi, A. Kardos, C. H. Davies et al., "Heterozygous disruption of SERCA2a is not associated with impairment of cardiac performance in humans: implications for SERCA2a as a therapeutic target in heart failure," *Heart*, vol. 92, no. 1, pp. 105–109, 2006.
- [8] M. Periasamy, T. D. Reed, L. H. Liu et al., "Impaired cardiac performance in heterozygous mice with a null mutation in the sarco(endo)plasmic reticulum  $\text{Ca}^{2+}$ -ATPase isoform 2 (SERCA2) gene," *Journal of Biological Chemistry*, vol. 274, no. 4, pp. 2556–2562, 1999.
- [9] L. H. Liu, G. P. Boivin, V. Prasad, M. Periasamy, and G. E. Shull, "Squamous cell tumors in mice heterozygous for a null allele of *Atp2a2*, encoding the sarco(endo)plasmic reticulum  $\text{Ca}^{2+}$ -ATPase isoform 2  $\text{Ca}^{2+}$  pump," *Journal of Biological Chemistry*, vol. 276, no. 29, pp. 26737–26740, 2001.
- [10] V. Prasad, G. P. Boivin, M. L. Miller et al., "Haploinsufficiency of *Atp2a2*, encoding the sarco(endo)plasmic reticulum  $\text{Ca}^{2+}$ -ATPase isoform 2  $\text{Ca}^{2+}$  pump, predisposes mice to squamous cell tumors via a novel mode of cancer susceptibility," *Cancer Research*, vol. 65, no. 19, pp. 8655–8661, 2005.
- [11] J. E. J. Schultz, B. J. Glascock, S. A. Witt et al., "Accelerated onset of heart failure in mice during pressure overload with chronically decreased SERCA2 calcium pump activity," *The American Journal of Physiology—Heart and Circulatory Physiology*, vol. 286, no. 3, pp. H1146–H1153, 2004.
- [12] S. Huke, L. H. Liu, D. Biniakiewicz, W. T. Abraham, and M. Periasamy, "Altered force-frequency response in non-failing hearts with decreased SERCA pump-level," *Cardiovascular Research*, vol. 59, no. 3, pp. 668–677, 2003.
- [13] J. N. Lorenz and J. Robbins, "Measurement of intraventricular pressure and cardiac performance in the intact closed-chest anesthetized mouse," *The American Journal of Physiology—Heart and Circulatory Physiology*, vol. 272, no. 3, pp. H1137–H1146, 1997.
- [14] D. Fatkin and R. M. Graham, "Molecular mechanisms of inherited cardiomyopathies," *Physiological Reviews*, vol. 82, no. 4, pp. 945–980, 2002.
- [15] J. van der Velden, Z. Papp, R. Zaremba et al., "Increased  $\text{Ca}^{2+}$ -sensitivity of the contractile apparatus in end-stage human heart failure results from altered phosphorylation of contractile proteins," *Cardiovascular Research*, vol. 57, no. 1, pp. 37–47, 2003.
- [16] S. Rajan, R. P. H. Ahmed, G. Jagatheesan et al., "Dilated cardiomyopathy mutant tropomyosin mice develop cardiac dysfunction with significantly decreased fractional shortening and myofilament calcium sensitivity," *Circulation Research*, vol. 101, no. 2, pp. 205–214, 2007.
- [17] T. M. Olson, N. Y. Kishimoto, F. G. Whitby, and V. V. Michels, "Mutations that alter the surface charge of alpha-tropomyosin are associated with dilated cardiomyopathy," *Journal of Molecular and Cellular Cardiology*, vol. 33, no. 4, pp. 723–732, 2001.
- [18] R. Prabhakar, G. P. Boivin, I. L. Grupp et al., "A familial hypertrophic cardiomyopathy  $\alpha$ -tropomyosin mutation causes severe cardiac hypertrophy and death in mice," *Journal of Molecular and Cellular Cardiology*, vol. 33, no. 10, pp. 1815–1828, 2001.
- [19] L. Thierfelder, H. Watkins, C. MacRae et al., "Alpha-Tropomyosin and cardiac troponin T mutations cause familial hypertrophic cardiomyopathy: A disease of the sarcomere," *Cell*, vol. 77, no. 5, pp. 701–712, 1994.
- [20] T. D. Reed, G. J. Babu, Y. Ji et al., "The expression of SR calcium transport ATPase and the  $\text{Na}^+/\text{Ca}^{2+}$  exchanger are antithetically regulated during mouse cardiac development and in hypo/hyperthyroidism," *Journal of Molecular and Cellular Cardiology*, vol. 32, no. 3, pp. 453–464, 2000.
- [21] A. N. Wansapura, V. M. Lasko, J. B. Lingrel, and J. N. Lorenz, "Mice expressing ouabain-sensitive  $\alpha$ 1-Na,K-ATPase have increased susceptibility to pressure overload-induced cardiac

- hypertrophy," *The American Journal of Physiology—Heart and Circulatory Physiology*, vol. 300, no. 1, pp. H347–H355, 2011.
- [22] N. J. Al Moamen, V. Prasad, I. Bodi et al., "Loss of the AE3 anion exchanger in a hypertrophic cardiomyopathy model causes rapid decompensation and heart failure," *Journal of Molecular and Cellular Cardiology*, vol. 50, no. 1, pp. 137–146, 2011.
- [23] V. Prasad, J. N. Lorenz, V. M. Lasko et al., "Ablation of plasma membrane  $\text{Ca}^{2+}$ -ATPase isoform 4 prevents development of hypertrophy in a model of hypertrophic cardiomyopathy," *Journal of Molecular and Cellular Cardiology*, vol. 77, pp. 53–63, 2014.
- [24] D. H. MacLennan and E. G. Kranias, "Phospholamban: a crucial regulator of cardiac contractility," *Nature Reviews Molecular Cell Biology*, vol. 4, no. 7, pp. 566–577, 2003.
- [25] I. Klein and S. Danzi, "Thyroid disease and the heart," *Circulation*, vol. 116, no. 15, pp. 1725–1735, 2007.
- [26] M. Arai, K. Otsu, D. H. MacLennan, N. R. Alpert, and M. Periasamy, "Effect of thyroid hormone on the expression of mRNA encoding sarcoplasmic reticulum proteins," *Circulation Research*, vol. 69, no. 2, pp. 266–276, 1991.
- [27] H. Kögler and J. C. Rüegg, "Cardiac contractility: modulation of myofibrillar calcium sensitivity by  $\beta$ -adrenergic stimulation," *Israel Journal of Medical Sciences*, vol. 33, no. 1, pp. 1–7, 1997.
- [28] K. Brixius, P. Savvidou-Zaroti, U. Mehlhorn, W. Bloch, E. G. Kranias, and R. H. G. Schwinger, "Increased  $\text{Ca}^{2+}$ -sensitivity of myofibrillar tension in heart failure and its functional implication," *Basic Research in Cardiology*, vol. 97, supplement 1, pp. III11–III17, 2002.
- [29] M. Endoh, "Cardiac  $\text{Ca}^{2+}$  signaling and  $\text{Ca}^{2+}$  sensitizers," *Circulation Journal*, vol. 72, no. 12, pp. 1915–1925, 2008.
- [30] S. A. Goonasekera and J. D. Molkenin, "Unraveling the secrets of a double life: contractile versus signaling  $\text{Ca}^{2+}$  in a cardiac myocyte," *Journal of Molecular and Cellular Cardiology*, vol. 52, no. 2, pp. 317–322, 2012.
- [31] F. R. Giachini, V. V. Lima, J. L. Hannan, F. S. Carneiro, R. C. Webb, and R. C. Tostes, "STIM1/Orai1-mediated store-operated  $\text{Ca}^{2+}$  entry: the tip of the iceberg," *Brazilian Journal of Medical and Biological Research*, vol. 44, no. 11, pp. 1080–1087, 2011.
- [32] J. Soboloff, B. S. Rothberg, M. Madesh, and D. L. Gill, "STIM proteins: dynamic calcium signal transducers," *Nature Reviews Molecular Cell Biology*, vol. 13, no. 9, pp. 549–565, 2012.
- [33] J. D. Molkenin, J. R. Lu, C. L. Antos et al., "A calcineurin-dependent transcriptional pathway for cardiac hypertrophy," *Cell*, vol. 93, no. 2, pp. 215–228, 1998.
- [34] J. Neumann, T. Eschenhagen, L. R. Jones et al., "Increased expression of cardiac phosphatases in patients with end-stage heart failure," *Journal of Molecular and Cellular Cardiology*, vol. 29, no. 1, pp. 265–272, 1997.
- [35] M. Yamada, Y. Ikeda, M. Yano et al., "Inhibition of protein phosphatase 1 by inhibitor-2 gene delivery ameliorates heart failure progression in genetic cardiomyopathy," *The FASEB Journal*, vol. 20, no. 8, pp. 1197–1199, 2006.
- [36] U. Gergs, P. Boknik, I. Buchwalow et al., "Overexpression of the catalytic subunit of protein phosphatase 2A impairs cardiac function," *Journal of Biological Chemistry*, vol. 279, no. 39, pp. 40827–40834, 2004.
- [37] S. V. Yap, E. Vafiadaki, J. Strong, and A. Kontrogianni-Konstantopoulos, "HAX-1: a multifaceted antiapoptotic protein localizing in the mitochondria and the sarcoplasmic reticulum of striated muscle cells," *Journal of Molecular and Cellular Cardiology*, vol. 48, no. 6, pp. 1266–1279, 2010.
- [38] A. Kataoka, C. Hemmer, and P. B. Chase, "Computational simulation of hypertrophic cardiomyopathy mutations in Troponin I: influence of increased myofilament calcium sensitivity on isometric force, ATPase and  $[\text{Ca}^{2+}]_i$ ," *Journal of Biomechanics*, vol. 40, no. 9, pp. 2044–2052, 2007.
- [39] J. G. Crilley, E. A. Boehm, E. Blair et al., "Hypertrophic cardiomyopathy due to sarcomeric gene mutations is characterized by impaired energy metabolism irrespective of the degree of hypertrophy," *Journal of the American College of Cardiology*, vol. 41, no. 10, pp. 1776–1782, 2003.
- [40] C. Ferrantini, A. Belus, N. Piroddi, B. Scellini, C. Tesi, and C. Poggesi, "Mechanical and energetic consequences of HCM-causing mutations," *Journal of Cardiovascular Translational Research*, vol. 2, no. 4, pp. 441–451, 2009.
- [41] B. N. Finck, "The PPAR regulatory system in cardiac physiology and disease," *Cardiovascular Research*, vol. 73, no. 2, pp. 269–277, 2007.
- [42] G. D. Lopaschuk, J. R. Ussher, C. D. L. Folmes, J. S. Jaswal, and W. C. Stanley, "Myocardial fatty acid metabolism in health and disease," *Physiological Reviews*, vol. 90, no. 1, pp. 207–258, 2010.
- [43] H. He, F. J. Giordano, R. Hilal-Dandan et al., "Overexpression of the rat sarcoplasmic reticulum  $\text{Ca}^{2+}$  ATPase gene in the heart of transgenic mice accelerates calcium transients and cardiac relaxation," *The Journal of Clinical Investigation*, vol. 100, no. 2, pp. 380–389, 1997.
- [44] D. L. Baker, K. Hashimoto, I. L. Grupp et al., "Targeted overexpression of the sarcoplasmic reticulum  $\text{Ca}^{2+}$ -ATPase increases cardiac contractility in transgenic mouse hearts," *Circulation Research*, vol. 83, no. 12, pp. 1205–1214, 1998.
- [45] G. Chu, J. W. Lester, K. B. Young, W. Luo, J. Zhai, and E. G. Kranias, "A single site (Ser16) phosphorylation in phospholamban is sufficient in mediating its maximal cardiac responses to  $\beta$ -agonists," *Journal of Biological Chemistry*, vol. 275, no. 49, pp. 38938–38943, 2000.
- [46] C. Mundiña-Weilenmann, L. Vittone, M. Ortale, G. C. de Cingolani, and A. Mattiazzi, "Immunodetection of phosphorylation sites gives new insights into the mechanisms underlying phospholamban phosphorylation in the intact heart," *The Journal of Biological Chemistry*, vol. 271, no. 52, pp. 33561–33567, 1996.
- [47] A. Mattiazzi, C. Mundiña-Weilenmann, C. Guoxiang, L. Vittone, and E. Kranias, "Role of phospholamban phosphorylation on Thr17 in cardiac physiological and pathological conditions," *Cardiovascular Research*, vol. 68, no. 3, pp. 366–375, 2005.
- [48] A. Papolos and W. H. Frishman, "Sarcoendoplasmic reticulum calcium transport ATPase 2a: a potential gene therapy target in heart failure," *Cardiology in Review*, vol. 21, no. 3, pp. 151–154, 2013.
- [49] K. Zsebo, A. Yaroshinsky, J. J. Rudy et al., "Long-term effects of AAV1/SERCA2a gene transfer in patients with severe heart failure: analysis of recurrent cardiovascular events and mortality," *Circulation Research*, vol. 114, no. 1, pp. 101–108, 2014.
- [50] B. Greenberg, A. Yaroshinsky, K. M. Zsebo et al., "Design of a phase 2b trial of intracoronary administration of AAV1/SERCA2a in patients with advanced heart failure: the CUPID 2 trial (calcium up-regulation by percutaneous administration of gene therapy in cardiac disease phase 2b)," *Journal of the American College of Cardiology: Heart Failure*, vol. 2, no. 1, pp. 84–92, 2014.
- [51] S. H. Golden, K. A. Robinson, I. Saldanha, B. Anton, and P. W. Ladenson, "Prevalence and incidence of endocrine and metabolic disorders in the united states: a comprehensive

- review," *Journal of Clinical Endocrinology & Metabolism*, vol. 94, no. 6, pp. 1853–1878, 2009.
- [52] C. Holubarsch, R. P. Goulette, R. Z. Litten, B. J. Martin, L. A. Mulieri, and N. R. Alpert, "The economy of isometric force development, myosin isoenzyme pattern and myofibrillar ATPase activity in normal and hypothyroid rat myocardium," *Circulation Research*, vol. 56, no. 1, pp. 78–86, 1985.
- [53] M. Krenz and J. Robbins, "Impact of beta-myosin heavy chain expression on cardiac function during stress," *Journal of the American College of Cardiology*, vol. 44, no. 12, pp. 2390–2397, 2004.
- [54] K. A. Palmiter and R. J. Solaro, "Molecular mechanisms regulating the myofilament response to  $Ca^{2+}$ : implications of mutations causal for familial hypertrophic cardiomyopathy," *Basic Research in Cardiology, Supplement*, vol. 92, supplement 1, pp. 63–74, 1997.
- [55] L.-L. Wu, C. Tang, and M.-S. Liu, "Altered phosphorylation and calcium sensitivity of cardiac myofibrillar proteins during sepsis," *The American Journal of Physiology—Regulatory Integrative and Comparative Physiology*, vol. 281, no. 2, pp. R408–R416, 2001.
- [56] H. E. D. J. Ter Keurs and P. A. Boyden, "Calcium and arrhythmogenesis," *Physiological Reviews*, vol. 87, no. 2, pp. 457–506, 2007.
- [57] J. R. Peña, A. C. Szkudlarek, C. M. Warren et al., "Neonatal gene transfer of Serca2a delays onset of hypertrophic remodeling and improves function in familial hypertrophic cardiomyopathy," *Journal of Molecular and Cellular Cardiology*, vol. 49, no. 6, pp. 993–1002, 2010.
- [58] R. D. Gaffin, J. R. Peña, M. S. L. Alves et al., "Long-term rescue of a familial hypertrophic cardiomyopathy caused by a mutation in the thin filament protein, tropomyosin, via modulation of a calcium cycling protein," *Journal of Molecular and Cellular Cardiology*, vol. 51, no. 5, pp. 812–820, 2011.
- [59] J. M. McLenachan, E. Henderson, K. I. Morris, and H. J. Dargie, "Ventricular arrhythmias in patients with hypertensive left ventricular hypertrophy," *The New England Journal of Medicine*, vol. 317, no. 13, pp. 787–792, 1987.
- [60] A. Curcio, D. Torella, C. Iaconetti et al., "MicroRNA-1 down-regulation increases connexin 43 displacement and induces ventricular tachyarrhythmias in rodent hypertrophic hearts," *PLoS ONE*, vol. 8, no. 7, Article ID e70158, 2013.
- [61] H. E. Collins, X. Zhu-Mauldin, R. B. Marchase, and J. C. Chatham, "STIM1/Orai1-mediated SOCE: current perspectives and potential roles in cardiac function and pathology," *The American Journal of Physiology—Heart and Circulatory Physiology*, vol. 305, no. 4, pp. H446–H458, 2013.
- [62] H. E. Collins, L. He, L. Zou et al., "Stromal interaction molecule 1 is essential for normal cardiac homeostasis through modulation of ER and mitochondrial function," *The American Journal of Physiology—Heart and Circulatory Physiology*, vol. 306, no. 8, pp. H1231–H1239, 2014.
- [63] J. S. Horton, C. L. Buckley, E. M. Alvarez, A. Schorlemmer, and A. J. Stokes, "The calcium release-activated calcium channel Orai1 represents a crucial component in hypertrophic compensation and the development of dilated cardiomyopathy," *Channels*, vol. 8, no. 1, pp. 35–48, 2014.
- [64] E. Vafiadaki, D. A. Arvanitis, S. N. Pagakis et al., "The anti-apoptotic protein HAX-1 interacts with SERCA2 and regulates its protein levels to promote cell survival," *Molecular Biology of the Cell*, vol. 20, no. 1, pp. 306–318, 2009.
- [65] E. Vafiadaki, D. Sanoudou, D. A. Arvanitis, D. H. Catino, E. G. Kranias, and A. Kontrogianni-Konstantopoulos, "Phospholamban interacts with HAX-1, a mitochondrial protein with anti-apoptotic function," *Journal of Molecular Biology*, vol. 367, no. 1, pp. 65–79, 2007.
- [66] E. Vafiadaki, D. A. Arvanitis, S. N. Pagakis et al., "The anti-apoptotic protein HAX-1 interacts with SERCA2 and regulates its protein levels to promote cell survival," *Molecular Biology of the Cell*, vol. 20, no. 1, pp. 306–318, 2009.
- [67] W. Zhao, J. R. Waggoner, Z.-G. Zhang et al., "The anti-apoptotic protein HAX-1 is a regulator of cardiac function," *Proceedings of the National Academy of Sciences of the United States of America*, vol. 106, no. 49, pp. 20776–20781, 2009.
- [68] L. He, T. Kim, Q. Long et al., "Carnitine palmitoyltransferase-1b deficiency aggravates pressure overload-induced cardiac hypertrophy caused by lipotoxicity," *Circulation*, vol. 126, no. 14, pp. 1705–1716, 2012.
- [69] K. R. Haynie, B. Vandanmagsar, S. E. Wicks, J. Zhang, and R. L. Mynatt, "Inhibition of carnitine palmitoyltransferase1b induces cardiac hypertrophy and mortality in mice," *Diabetes, Obesity & Metabolism*, vol. 16, no. 8, pp. 757–760, 2014.
- [70] A. A. Domenighetti, V. R. Danes, C. L. Curl, J. M. Favaloro, J. Proietto, and L. M. D. Delbridge, "Targeted GLUT-4 deficiency in the heart induces cardiomyocyte hypertrophy and impaired contractility linked with  $Ca^{2+}$  and proton flux dysregulation," *Journal of Molecular and Cellular Cardiology*, vol. 48, no. 4, pp. 663–672, 2010.
- [71] V. Hillestad, F. Kramer, S. Golz, A. Knorr, K. B. Andersson, and G. Christensen, "Long-term levosimendan treatment improves systolic function and myocardial relaxation in mice with cardiomyocyte-specific disruption of the Serca2 gene," *Journal of Applied Physiology*, vol. 115, no. 10, pp. 1572–1580, 2013.

## Review Article

# The Ovariectomized Rat as a Model for Studying Alveolar Bone Loss in Postmenopausal Women

Bryan D. Johnston<sup>1</sup> and Wendy E. Ward<sup>1,2</sup>

<sup>1</sup>Faculty of Applied Health Sciences, Brock University, St. Catharines, ON, Canada L2S 3A1

<sup>2</sup>Centre for Bone and Muscle Health, Brock University, St. Catharines, ON, Canada L2S 3A1

Correspondence should be addressed to Wendy E. Ward; [wward@brocku.ca](mailto:wward@brocku.ca)

Received 7 October 2014; Accepted 2 March 2015

Academic Editor: Andrea Vecchione

Copyright © 2015 B. D. Johnston and W. E. Ward. This is an open access article distributed under the Creative Commons Attribution License, which permits unrestricted use, distribution, and reproduction in any medium, provided the original work is properly cited.

In postmenopausal women, reduced bone mineral density at the hip and spine is associated with an increased risk of tooth loss, possibly due to a loss of alveolar bone. In turn, having fewer natural teeth may lead to compromised food choices resulting in a poor diet that can contribute to chronic disease risk. The tight link between alveolar bone preservation, tooth retention, better nutritional status, and reduced risk of developing a chronic disease begins with the mitigation of postmenopausal bone loss. The ovariectomized rat, a widely used preclinical model for studying postmenopausal bone loss that mimics deterioration of bone tissue in the hip and spine, can also be used to study mineral and structural changes in alveolar bone to develop drug and/or dietary strategies aimed at tooth retention. This review discusses key findings from studies investigating mandible health and alveolar bone in the ovariectomized rat model. Considerations to maximize the benefits of this model are also included. These include the measurement techniques used, the age at ovariectomy, the duration that a rat is studied after ovariectomy and habitual diet consumed.

## 1. Introduction

A decline in ovarian production of estrogens at menopause often results in a rapid loss of trabecular microarchitecture, increased endocortical bone resorption, and increased cortical porosity; all culminating in the development of osteoporosis and the associated increased risk for fragility fracture (Figure 1) [1]. Specifically, the number of osteoclasts increases to a point where the rate of bone resorption exceeds the rate of bone formation [2].

Based on data from the WHO Global Burden of Disease project in 2000, an estimated 56 million people around the world experience disability caused by a fracture [3]. In 2010, there were 2.32 million new hip fractures in adults over 50 years of age worldwide, and approximately half of those hip fractures were due to osteoporosis in the femur neck (hip) [4]. Based on osteoporosis prevalence rates reported in the 2010 Census and NHANES (2005–2010), it is estimated that 10.2 million Americans over the age of 50 have osteoporosis while an additional 43.4 million have low bone mass that predisposes them to the development of osteoporosis [5]. It is

well documented that women are disproportionately affected by osteoporosis compared to men, primarily due to the more sudden decline in estrogen production experienced at menopause whereas sex steroid levels decline more gradually in men [3–6]. In the majority of postmenopausal women, the risk of experiencing a fragility fracture exceeds the risk of developing invasive breast cancer, stroke, and cardiovascular disease combined [7]. Moreover, there is substantive morbidity [8] associated with a fragility fracture and an increased risk of death, especially within the first year after fracture [9].

## 2. Osteoporosis, Estrogen, and Tooth Loss

Osteoporosis not only increases a woman's risk of fragility fracture at the hip, spine, and wrist, but it is also associated with the loss of teeth and tooth supporting alveolar bone [10–13]. For example, osteoporosis at the lumbar vertebrae, femoral neck, or total hip is a significant predictor of molar tooth loss [10]. A 5-year longitudinal study of 404 postmenopausal women confirmed that women in the highest tertile of annual BMD loss at the lumbar spine and

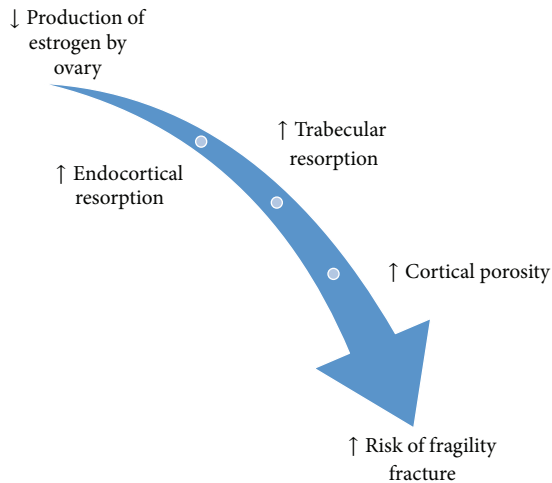


FIGURE 1: Overview of how osteoporosis develops after menopause. With the loss of endogenous estrogen production by the ovaries there is an increase in trabecular bone resorption, endocortical bone resorption, and cortical porosity that elevate a woman's risk of experiencing a fragility fracture.

femoral neck had an adjusted relative risk of 1.38 and 1.27 for tooth loss, respectively [11]. In a longitudinal study of even greater duration, 7 years, the relative risk of tooth loss in 180 postmenopausal women (serum estradiol (E2) < 25 pg/mL) was 4.38 with each 1% annual decrease in whole body BMD [12]. An increased loss of alveolar bone height and decreased alveolar crestal and subcrestal bone mineral density, all critical for providing support for teeth, were also reported in a 2-year longitudinal study of 38 women with osteopenia and osteoporosis at the lumbar spine. Between the first and second molars in particular, estrogen-deficient (mean serum E2 < 30 pg/mL) women lost more alveolar crestal bone density compared to estrogen-sufficient (mean serum E2 > 40 pg/mL) women [13]. Because tooth retention [14, 15] and functional dentition [16, 17] are key determinants of nutritional status the maintenance of alveolar bone is important for overall health. Risk of many chronic diseases such as obesity, type 2 diabetes, cardiovascular disease, and some cancers is elevated by poor diet. Thus, strategies that preserve the skeleton at key sites of fragility fracture—hip, spine, and wrist—as well as alveolar bone in the jaw are important for healthy aging.

While estrogen replacement therapy (ERT) has been consistently shown to reduce fragility fractures at the hip, spine, and wrist [18, 19] the effect on tooth retention and preserving alveolar bone has been less studied. However, a study of 42,171 postmenopausal women (aged ≤ 69 years) over a 2-year period as part of the Nurses' Health Study cohort reported that current use of hormone replacement therapy (HRT: estrogen alone, in combination with progestin, or progestin alone) was associated with a 24% decrease in the risk of tooth loss. In women using conjugated estrogen alone, at a dose of 0.3 mg per day, the risk of tooth loss was 31% lower compared to nonusers [20]. In a cohort of 3,921 older women, median age of 81 years, current ERT

(with or without progesterone) was associated with a 27% lower risk of tooth loss [21]. Another study showed that a group of postmenopausal women (72–95 years of age) who used ERT (reported as any use of estrogen) for greater than 8 years retained an average of 3.6 more teeth than women who never used ERT [22]. The duration of ERT (estrogen alone or in combination with progestogen) was also a significant predictor of total and posterior teeth remaining in a group of 330 postmenopausal Japanese women [23]. The mechanism behind tooth retention and ERT remains unclear, but one 3-year longitudinal study of 135 women aged 41–70 years concluded that women receiving 0.625 mg conjugated equine estrogen with or without 2.5 mg medroxyprogesterone acetate experienced a 0.9% increase in alveolar bone mass, as assessed by digitized radiographs, compared to nonusers [24]. HRT or ERT may therefore work to increase the stability of the tooth-supporting alveolar bone and thereby promote tooth retention and the opportunity to consume a wide variety of foods.

### 3. Tooth Loss and Nutritional Status

Retention of natural teeth is associated with healthier nutrient intakes that may have a role in prevention of chronic disease. For example, dietary calcium has been studied in relation to tooth loss because achieving recommended intakes of dietary calcium, in particular, is important for attenuating bone loss after menopause and during aging. As such, the recommended intake of calcium is 1200 mg per day in women aged 51–70 years and men over the age of 70 [25]. Among older men and women (≥65 years of age) with unknown smoking status, higher daily intake of calcium (884 versus 805 mg calcium) was associated with a greater number of teeth (≥21 versus 11–20 teeth) [14]. Another study reported lower tooth loss in a placebo-controlled 2-year study of nonsmoking women taking a calcium supplement of 500 mg per day; smoking women were excluded because smoking is a risk factor for tooth loss [12].

Fruit and vegetable intake in relation to tooth loss has also been studied. Data from NHANES III, a large cross-sectional study of Americans over the age of 50, showed a reduced number of posterior occlusal teeth associated with a lower daily intake of the recommended amount of fruit servings as reflected in a lower Healthy Eating Index (HEI) score and a higher BMI [16]. Additionally, having no posterior occlusal teeth was associated with a lower daily intake of the recommended amount of vegetable servings, also reflected in a lower HEI score [16]. Even when controlling for socioeconomic status, inadequate dentition (defined by <21 teeth remaining) was associated with reduced intakes of fruit (stone fruits and grapes/berries) and vegetable (stir-fried or mixed vegetables, sweetcorn/corn on the cob, mushrooms, lettuce, and soy beans/tofu) in a sample of 530 dentate Australian men and women over the age of 55 [17]. The link between tooth loss and reduced fruit and vegetable intake is important since a recent comprehensive review concluded that fruit and vegetable intake was associated with a reduced risk of chronic diseases such as hypertension,

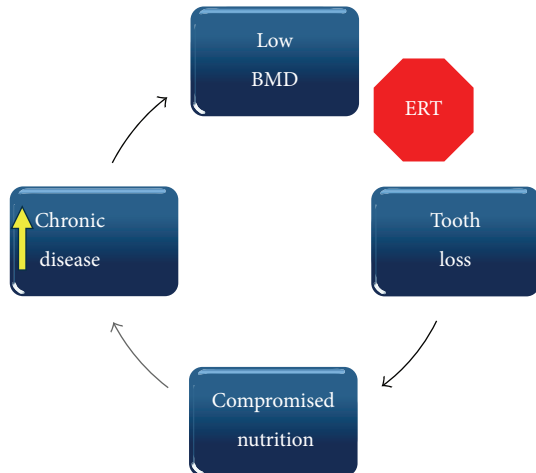


FIGURE 2: Cyclical relationship among low BMD, tooth loss, compromised nutrition, and risk for chronic disease. Estrogen or hormone replacement therapy (ERT, HRT) or other interventions that benefit other skeletal sites (hip, spine, and wrist) may prevent or slow the progression from low BMD to tooth loss. Retention of natural teeth allows individuals to eat a more healthful diet associated with a reduced risk of developing a chronic disease.

coronary heart disease, and stroke [26]. Interestingly the relationship between a reduced BMD in postmenopausal osteoporosis, higher rates of tooth loss, and reduced fruit and vegetable intake comes full circle given the study of 670 postmenopausal Chinese women that found higher fruit and vegetable intake was associated with higher whole body, lumbar spine, and hip BMD. Specifically, a daily increase of 100 g of fruits and vegetables was associated with a 6, 10, and 6 mg/cm<sup>2</sup> higher BMD at the whole body, lumbar spine, and hip, respectively. [27].

The relationship between osteoporosis, tooth loss, and compromised nutrition may prove to be cyclical (Figure 2) since compromised nutrition could exacerbate osteoporosis. As discussed in Section 2, HRT or ERT has been shown to promote tooth retention and may intervene in this self-perpetuating, negative cycle of tooth loss and the consequent higher risk of chronic disease development. Moreover, there are other pharmacological agents or diet interventions that may prove useful in stopping the cycle shown in Figure 2. The ovariectomized rat can be used to evaluate the effectiveness of an intervention for preserving alveolar bone. Findings from these studies provide an important step in developing interventions to promote and support bone health, including the retention of natural teeth, for postmenopausal women.

#### 4. The Ovariectomized Rat Model

The ovariectomized (OVX) rat model is the approved preclinical model by the Food and Drug Administration (FDA) [28] for studying how the decline in endogenous estrogen production by the ovaries at menopause leads to postmenopausal osteoporosis and how potential interventions can preserve bone metabolism in this state. Although the FDA guidelines do not specify which strain of rat to use, it is important to be

aware that there can be differences in bone mineral density, bone size, and biomechanical bone strength among inbred rat strains [29]. Interventions include pharmacological agents as well as lifestyle strategies such as diet. By 12 weeks of age, the female Sprague-Dawley rat, among the most common strains studied, has reached sexual maturity and has achieved peak bone mass for the whole body, femora, and tibiae [30]. Peak bone mass was defined as the point at which the rat skeleton had accrued its highest amount of areal BMD determined by dual-energy X-ray absorptiometry (DXA) in the whole body, femur, and tibia. However, longitudinal bone growth continues in the female rat until the epiphyseal growth plates close. At 12 weeks of age, the distal tibia growth plate has closed while the proximal tibia and lumbar vertebral growth plates remain open until 15 and 21 months, respectively [31]. Despite the continued skeletal growth, rats are commonly ovariectomized at 12 weeks of age since the rats are sexually mature and therefore capable of modeling bone loss due to estrogen deficiency [32]. By 9 months of age, longitudinal bone growth at the proximal tibia metaphysis has slowed to 3  $\mu\text{m}/\text{day}$ , while growth at the lumbar vertebral body has slowed to <1  $\mu\text{m}/\text{day}$  [33].

Two developmental stages have been used to describe the adult rat skeleton: “mature” from 3–6 months of age and “aged”  $\geq 6$  months of age. Skeletal growth is rapid from 1–3 months, reduced from 3–6 months, and negligible past 6 months of age [34]. In addition to continued longitudinal bone growth, the extent of ovariectomy-induced bone loss is dependent on both the skeletal site and the time since ovariectomy. For example, in the proximal tibia, a significant decrease in trabecular bone volume is observed 2 weeks after ovariectomy compared to sham control with a plateau by 14 weeks after ovariectomy [35]. At the femoral neck, a significant decrease in trabecular bone volume occurred at 4 weeks after ovariectomy with a plateau by 39 weeks after ovariectomy [36]. The lumbar vertebrae were much more resistant to ovariectomy-induced changes in trabecular bone volume than either the proximal tibia or femoral neck. It was not until 7 weeks after ovariectomy that a decrease in trabecular bone volume was significant and reached a plateau between 39 and 77 weeks after ovariectomy [37].

The effect of time since ovariectomy on the rat mandible is less clear so the studies discussed in this review are subsequently divided into those that are  $\leq 12$  weeks in duration and those that are  $\geq 12$  weeks in duration after ovariectomy. This time point was chosen since a 12-week period after ovariectomy has been shown to be sufficient to decrease trabecular bone volume at the proximal tibia [35], femoral neck [36], and lumbar vertebrae [37]. Additionally, only studies reporting changes to alveolar bone of the mandible, not maxilla, were included in this review. There is a broader body of literature to support changes to alveolar bone in the mandible of the OVX rat model and by limiting this review to the mandible, with detailed descriptions of the regions of interest (ROI) used in the studies, the changes to alveolar bone are standardized and more focused. Figure 3 is an image of a hemimandible from a Sprague-Dawley rat with key landmarks and directions highlighted and serves as a guide to the specific study ROI discussed in the next section.

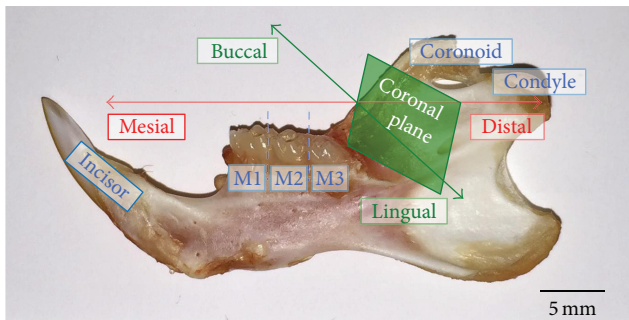


FIGURE 3: Hemimandible from a 6-month-old Sprague-Dawley rat. From left to right: incisor, 1st molar (M1), 2nd molar (M2), 3rd molar (M3), the coronoid process, and condyle. Mesial is the front, distal the back, buccal the lateral side, lingual the medial side, and the coronal plane divides the mandible into mesial and distal halves (photo by B. Johnston).



FIGURE 4:  $\mu$ -CT 2D sagittal slice through molar 1 (M1) of a 6-month-old Sprague-Dawley rat with interradicular septum. The interradicular septum is highlighted in red and extends from the furcation roof to the root apices. The occlusal surface of M1 is also highlighted in blue and the arrowhead denotes the approximate area of the central sulcus. The left side of the image is mesial and the right side is distal (image by B. Johnston).

Similarly, Figures 4 through 6 are included to assist the reader in identifying regions that have been analyzed in the studies that are discussed in this review. Figure 4 is a sagittal slice through the first molar (M1) with the interradicular septum containing alveolar bone highlighted. Figure 5 is a three-dimensional (3D) rendering of the 4 roots of M1 (mesial, lingual, buccal, and distal roots) and shows how these roots enclose the alveolar bone of the interradicular septum. Figure 6 is a 3D rendering of M1 in its bony socket and viewed as a cut-away to show landmarks used to define alveolar bone ROI.

*4.1. Short-Term Effects of Ovariectomy on Mandibular Health: Findings from Studies Less Than 12 Weeks after Ovariectomy.* Since robust ovariectomy-induced changes to bone structure

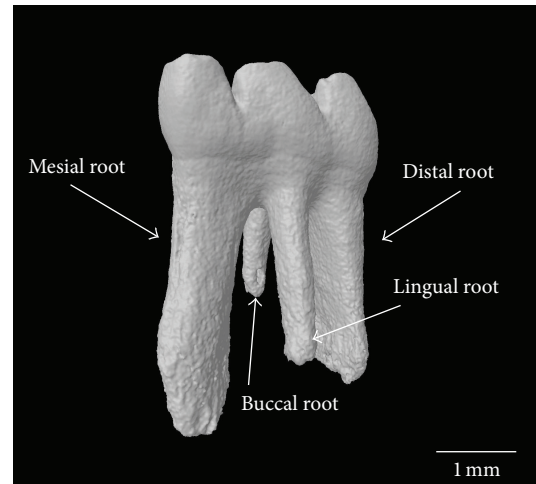


FIGURE 5:  $\mu$ -CT 3D reconstructed image of the four roots of molar 1 (M1). The mesial, distal, buccal, and lingual roots enclose the alveolar bone of the interradicular septum (image by B. Johnston).

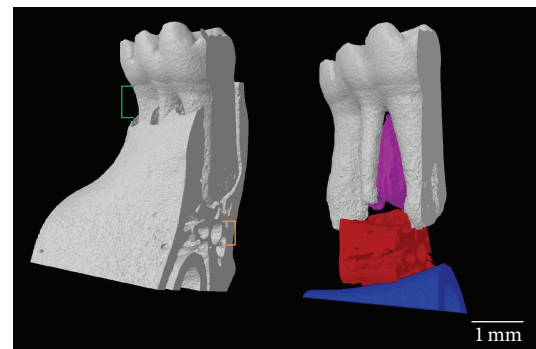


FIGURE 6: Landmarks to define ROI of alveolar bone at molar 1 (M1). M1 in its bony socket (left) with the distance between the cemento-enamel junction and bone crest (green) and the mandibular canal (orange). In a model of M1 with the bony socket removed (right) the alveolar bone of the interradicular septum (purple) is superior to the alveolar bone (red) between the incisor (blue) and the apices of the mesial and distal roots (image by B. Johnston).

at the proximal tibia, femur neck, and lumbar vertebrae are certainly manifest by 12 weeks and such changes only begin to be detectable earlier, 2–7 weeks after ovariectomy, it is likely difficult to detect changes in alveolar bone in rats prior to 12 weeks after ovariectomy. Thus, in only 3 of the 6 studies with an ovariectomy duration < 12 weeks, ovariectomy reduced either alveolar bone structure [38, 39] or density [40] (Table 1). In the studies that showed an effect from the ovariectomy, the time since ovariectomy was approximately 9 weeks. Of those studies, rats were ovariectomized at 17, 25, and 26 weeks of age [38–40]. The first study used histomorphometry to measure the M1 sagittal surface containing the central sulcus of the occlusal surface and both the mesial and distal root canals. The ROI was the entire interradicular septum of M1 extending from the furcation roof to the mesial and distal root apices (Figure 4). Relative to the sham group, there was lower bone volume

TABLE 1: Summary of studies investigating changes in mandibular health in rats less than 12 weeks after ovariectomy.

Rat strain	Sample size per group	Age at OVX (wks)	Time after OVX (wks)	Diet	Technology	Main findings for mandible, compared to sham control	Reference
Sprague-Dawley	$n = 5$	4	4	0.89% Ca	Radiographs	(i) No change in BMD (ii) No alveolar bone loss	[41]
Sprague-Dawley	$n = 8$	13	5	1.00% Ca	DXA, histomorphometry stereology	(i) No change in BMD, bone area fraction, or area moment of inertia	[42]
Fischer	$n = 8$	17	9	Unknown	Histomorphometry	(i) 25% decrease in BV/TV (ii) 17% decrease in Tb.N (iii) 32% increase in Tb.Sp (iv) No change in Tb.Th	[38]
Sprague-Dawley	$n = 10$	26	9	Unknown	$\mu$ -CT	(i) 7% increase in the tissue mineral density distribution grey values at the 5th percentile (ii) 25% increase in the tissue mineral density distribution coefficient of variation	[40]
Wistar	$n = 6$	17	9	Unknown	DXA	(i) No change in BMD	[43]
Wistar	$n = 6$	25	9	1.17% Ca, 0.91% P	$\mu$ -CT	(i) 15% decrease in BV/TV (ii) 14% decrease in Tb.Th (iii) 22% increase in Tb.Sp (iv) No change in Tb.N	[39]

BMD, bone mineral density; BV/TV, bone volume; Tb.N, trabecular number; Tb.Sp, trabecular separation; Tb.Th, trabecular thickness; DXA, dual-energy X-ray absorptiometry;  $\mu$ -CT, microcomputed tomography.

and trabecular number with higher trabecular separation but no difference in trabecular thickness between the sham and OVX groups.

Similar results were reported by a study that also investigated alveolar bone 9 weeks after ovariectomy, the only difference being an older age at ovariectomy, 25 versus 17 weeks [39]. The hemimandibles were scanned via micro-computed tomography ( $\mu$ -CT) between the mesial and distal roots of M1 at a resolution of 50  $\mu$ m. The ROI was delineated inferiorly by a plane connecting the apices of the buccal and lingual roots (Figure 5) and superiorly by a contour along the interradicular septum (Figure 4). Relative to the sham group, there was lower bone volume and trabecular thickness with higher trabecular separation. There was no difference between the trabecular number of the sham and OVX groups.

Changes in the alveolar bone density of Sprague-Dawley rats ovariectomized at 26 weeks of age and maintained for the same 9 weeks after ovariectomy were also reported [40]. To measure the tissue mineral density (TMD) distribution, hemimandibles were cut into 5 mm sections and scanned via  $\mu$ -CT at a resolution of 20  $\mu$ m. The ROI was a volume of alveolar bone extending 200  $\mu$ m from the surface of each tooth along the 5 mm section; if visualized in 3D the ROI would be a 200  $\mu$ m thick cast of the tooth surfaces in direct contact with the alveolar bone. This ROI included both the periodontal ligament (~150  $\mu$ m) and the alveolar bone in direct contact with the tooth surface (~50  $\mu$ m). There was a higher variability in the mineralization of alveolar bone in the OVX group than in the sham group. This higher variability implied more immature bone formation due to accelerated

bone remodeling. In summary, these studies have shown that by 9 weeks after ovariectomy there is a reduced alveolar bone volume and increased trabecular separation [38, 39] and the stability of the alveolar bone directly supporting the molars is also compromised [40].

Of the studies with an OVX duration < 12 weeks that did not report an effect on alveolar bone, two had times after ovariectomy of less than 9 weeks [41, 42] and one had a time after ovariectomy of exactly 9 weeks [43]. Methodological differences among the studies with an OVX duration of approximately 9 weeks may also explain why one study reported no effects [43] while 3 others reported effects [38–40]. The study with the shortest study period after ovariectomy measured mandibular BMD in Sprague-Dawley rats ovariectomized at 4 weeks of age and X-ray radiographs of hemimandibles were taken 4 weeks after ovariectomy [41]. The ROI began 1.5 cm mesial to M1 and extended until the end of the alveolar bone supporting the distal root of M3 (Figure 3). The ROI was delineated inferiorly by the crest of the incisor root and superiorly by the contours of the molar roots (Figure 6). This ROI included the alveolar bone supporting M1–M3 and the surrounding cortical bone. There was no difference between the BMD of the sham and OVX groups. Alveolar bone loss was also measured by calculating the difference in height between the cemento-enamel junction (CEJ) and the bone crest at the midpoint of the mesial root of each molar (Figure 6). There was no difference in alveolar bone loss between the sham and OVX groups.

At 5 weeks after ovariectomy, the mandibular BMD of Sprague-Dawley rats ovariectomized at 13 weeks was

TABLE 2: Summary of studies investigating mandibular health in rats for 12 weeks or more after ovariectomy.

Rat strain	Sample size per group	Age at OVX (wks)	OVX duration (wks)	Diet	Technology	Main findings for mandible, compared to sham control	Reference
Wistar	$n = 5$	6	12	1.15% Ca, 0.35% P	Histomorphometry	(i) 24% decrease in BV	[44]
Wistar	$n = 15$	35	13	0.01% Ca	pQCT	(i) 7% decrease in total BMD (ii) 11% decrease in Tb.BMD (iii) 1% decrease in Ct.BMD	[49]
Sprague-Dawley	$n = 6$	13	16	Unknown	DXA, pQCT	(i) No change in BMD (ii) 13% decrease in Tb.BMD (iii) No change in Ct.BMD	[51]
Lewis-Brown-Norway	$n = 12$	11	16	Unknown	$\mu$ -CT	(i) 18% decrease in BV/TV (ii) 28% decrease in Tb.Th (iii) 67% increase in Tb.Sp (iv) 22% increase in SMI	[45]
Wistar	$n = 12$	26	16	0.1% Ca	pQCT	(i) 3% decrease in total BMD	[50]
Sprague-Dawley	$n = 11$	28	17	1.1% Ca, 0.80% P	DXA, $\mu$ -CT	(i) No change in BMD (ii) 6% decrease in Tb.N (iii) 19% decrease in Conn.D (iv) No change in BV/TV (v) No change in Tb.Th	[46]
Sprague-Dawley	$n = 15$	26	29	1.0% Ca	DXA, histomorphometry	(i) No change in total or molar region BMD (ii) 8% decrease in bone area fraction (iii) No change in area moment of inertia	[47]
Lewis-Brown-Norway	$n = 6$	13	52	Unknown	Radiograph	(i) 16% decrease in Ct.Th	[52]
Fischer	$n = 6$	26	52	1.15% Ca, 0.88% P, 0.80 IU/g vit. D <sup>3</sup>	$\mu$ -CT	(i) 75% decrease in BV/TV (ii) 46% decrease in Tb.Th (iii) 58% decrease in Tb.N (iv) 354% increase in Tb.Sp	[48]

BMD, bone mineral density; Tb.BMD, trabecular BMD; Ct.BMD, cortical BMD; BV, bone volume (2D); BV/TV, bone volume (3D); Tb.N, trabecular number; Tb.Sp, trabecular separation; Tb.Th, trabecular thickness; Ct.Th, cortical thickness; SMI, structure model index; Conn.D, connective density; DXA, dual-energy X-ray absorptiometry;  $\mu$ -CT, microcomputed tomography.

measured using DXA [42]. The ROI of left hemimandibles was a rectangle extending from the angle mesial to M1 until the distal root of M3 (Figure 3). The following were included in the ROI: molars, alveolar bone, cortical bone, and the incisor root. There was no difference in BMD between the sham and OVX groups. Additionally, the mandibular bone area fraction and area moment of inertia were measured using coronal sections (Figure 3) of the distal most aspect of the M1 mesial root (Figure 5). An image of the newly exposed surface constituted the ROI and included the alveolar bone, cortical bone, and incisor root. There was no difference between bone area fraction or area moment of inertia between the sham and OVX groups.

Even 9 weeks after ovariectomy, Wistar rats ovariectomized at 17 weeks reported no difference between the mandibular BMD of the sham and OVX groups [43]. The mandibular BMD was measured by DXA equipped with small animal software. The ROI was a rectangle encompassing the alveolar, condylar, and coronoid processes; the molar crowns and incisor were removed (Figure 3). Since changes in alveolar bone structure [38, 39] and density [40] have been reported by ~9 weeks after ovariectomy, it is possible that

DXA may not be sensitive enough to detect the ovariectomy-induced changes in the rat mandible. Studies that follow for a longer time period after ovariectomy are likely needed to detect ovariectomy-induced loss of mandibular BMD by DXA. Future studies that use  $\mu$ -CT to measure changes in alveolar bone structure in response to ovariectomy are also needed. It is likely that  $\mu$ -CT would detect a more subtle change in alveolar bone after a shorter amount of time after ovariectomy than DXA due to its superior resolution, ability to quantify structural changes, and highly specific ROI in three-dimensions (3D). Also, in order to detect a robust change in alveolar bone after ovariectomy, that can be correlated with changes at other typical skeletal sites such as the long bones and lumbar vertebrae, a time after ovariectomy of greater than 12 weeks is likely needed.

*4.2. Longer-Term Effects of Ovariectomy on Mandibular Health: Findings from Studies That Are 12 Weeks or Longer after Ovariectomy.* All of the studies with an ovariectomy duration of longer than 12 weeks (Table 2) report a reduction in bone mineral and/or structural changes in alveolar bone. Of these 9 studies, 5 reported changes in alveolar bone

structure [44–48], 3 reported significant reductions in the BMD of alveolar bone [49–51], and a single study reported a decrease in the cortical thickness of alveolar bone [52].

Two studies used conventional histomorphometric methods to report changes in alveolar bone structure following ovariectomy [44, 47]. One study ovariectomized rats at 6 weeks of age and studied them until 12 weeks after ovariectomy [44]. To measure the mandibular histomorphometry, hemimandibles were sectioned coronally into 50  $\mu\text{m}$  thick slices (Figure 3). The ROI was a rectangle, with an area of 0.135  $\text{mm}^2$ , inferior to the apices of the buccal and lingual roots of M1 (Figure 5) and superior to the mandibular canal (Figure 6). There was a lower bone volume in the OVX group than in the sham group. Another study ovariectomized Sprague-Dawley rats at 26 weeks and maintained them for 29 weeks [47]. To measure the mandibular bone area fraction and the area moment of inertia, the left hemimandibles were sectioned coronally (Figure 3) between the mesial and buccal roots of M1 (Figure 5) and also between the roots of M2. The ROI for the bone area fraction was the entire surface of the M1 section with the molar crown/roots and incisor removed. The ROI for the area moment of inertia was the entire surface of the M2 section with the incisor removed. The bone area fraction of the OVX group was lower than the sham group. There was no difference between the moment of inertia between sham and OVX groups.

The remaining 3 studies to report changes in alveolar bone structure used  $\mu\text{-CT}$  [45, 46, 48]. To measure the mandibular morphometry of rats ovariectomized at 11 weeks and maintained for 16 weeks, left hemimandibles were scanned via  $\mu\text{-CT}$  beginning at the mesial plane of M1 and extending 25 slices toward the distal root (Figure 5); the scan was at a resolution of 15  $\mu\text{m}$  [45]. The ROI was delineated superiorly by the apex of the M1 mesial root (Figure 5) and inferiorly by the crest of the incisor socket (Figure 6). The buccal and lingual walls of cortical bone that flanked the ROI were removed. Relative to the sham group, there was a lower bone volume, lower trabecular thickness, higher trabecular separation, and a higher structure model index in the OVX group. A higher structure model index indicated a shift in trabeculae shape from plate-like to rod-like; rod-like trabeculae are thinner trabeculae and are thus indicative of structurally compromised alveolar bone.

Another study measured the mandibular morphometry of rats ovariectomized at 28 weeks and studied 17 weeks later by scanning the left hemimandibles using  $\mu\text{-CT}$ . This analysis was done between the mesial and distal borders of M1 (Figure 5) at a resolution of 16  $\mu\text{m}$  [46]. The ROI was an interpolated shape encompassing the alveolar bone from the apices of the buccal and lingual roots (Figure 5) to the crest of the incisor (Figure 6) and from the mesial to distal surfaces of the M1 interradicular septum (Figure 5). Relative to the sham group, there was a lower trabecular number and connectivity density in the OVX group but no differences in bone volume or trabecular thickness between the sham and OVX groups. A higher resolution  $\mu\text{-CT}$  scan and an ROI limited to the interradicular septum (Figure 4) are likely needed to observe changes in bone volume or trabecular thickness.

To investigate longer-term changes in mandibular morphometry, the right hemimandibles of rats ovariectomized at 26 weeks and studied 52 weeks later were scanned using  $\mu\text{-CT}$  at a resolution of 20  $\mu\text{m}$  [48]. The ROI was the interradicular septum of M1 delineated inferiorly by a straight line between the mesial and distal roots (Figure 4). Only a single sagittal slice exposing the interradicular septum of M1 was used for the ROI, not the entire volume of the interradicular septum. Relative to the sham group there was a lower bone volume, a lower trabecular thickness, a lower trabecular number, and a higher trabecular separation in the OVX group, indicating compromised structure of alveolar bone.

Of the studies to evaluate changes in mandibular BMD following ovariectomy using DXA, none reported any changes in BMD while each of the studies reported changes in mandibular density or structure by either pQCT [51],  $\mu\text{-CT}$  [46], or histomorphometry [47]. Of the 3 studies to evaluate changes in mandibular density by pQCT, all 3 reported a loss of BMD after ovariectomy [49–51]. These studies provide evidence that mandibular BMD measured by DXA cannot represent the changes in alveolar bone following ovariectomy in the rat and that higher resolution techniques such as pQCT or  $\mu\text{-CT}$  are needed.

In a study of rats ovariectomized at 35 weeks and studied at 13 weeks after ovariectomy, the BMD of hemimandibles was measured via pQCT between the mesial root of M1 and the distal root of M2 (Figure 3) at a voxel size of 100  $\mu\text{m}$  and a section thickness of 750  $\mu\text{m}$  [49]. The ROI was the entire surface of each coronal section with the molar crowns, roots, and the incisor root removed; this included both trabecular and cortical bone. Relative to the sham group, there was a lower total trabecular and cortical BMD in the OVX group.

Another study in younger ovariectomized rats (13 weeks old) that were studied 16 weeks after ovariectomy scanned hemimandibles using pQCT from the mesial border of M1 to the distal border of M3 (Figure 3) [51]. The ROI was the surface of each coronal pQCT section with the molar crowns/roots and the incisor root removed. The lowest trabecular BMD in the OVX group compared to the sham group was observed 3.5 mm from the mesial border of M1. There was no difference between the sham group and the OVX group cortical BMD. Additionally, the hemimandibles of rats ovariectomized at 26 weeks and maintained for 16 weeks after ovariectomy were scanned via pQCT at one 750  $\mu\text{m}$  thick coronal slice through the midpoint of M1 (Figure 3) at a resolution of 100  $\mu\text{m}$  [50]. The ROI was the entire surface of the coronal slice with the molar crown/roots and the incisor root removed. There was a lower total mandibular BMD in the OVX group compared to the sham group.

A long-term study of rats ovariectomized at 13 weeks and maintained for 52 weeks after ovariectomy measured changes in mandibular cortical bone thickness [52]. Left hemimandibles were exposed to a 70 kV, 7 mA X-ray source and images were digitally captured at a resolution of 12.5 line pairs/mm with a total image size of 640 by 480 pixels. The ROI was a computer-generated contoured shape encompassing the lower mandibular border; it began superiorly where the lower border met the incisor root and extended to the most inferior aspect of the lower border. There was a lower

TABLE 3: Summary of studies investigating estrogen replacement therapy and mandibular health in ovariectomized rats.

Rat strain	Sample size per group	Age at OVX (wks)	OVX duration (wks)	Estrogen dose; duration (wks)	Main findings for mandible, compared to OVX	Reference
Wistar	<i>n</i> = 4	Unknown	2	17 $\beta$ -estradiol 1.5 $\mu$ g/day continuous infusion; 2	(i) Less nuclei (osteoclasts)	[54]
Sprague-Dawley	<i>n</i> = 5	13	7	17 $\beta$ -estradiol 10 $\mu$ g/kg 5 days/wk; 7	(i) 36% less periodontal ligament space	[55]
Wistar	<i>n</i> = 14	11	11	17 $\beta$ -estradiol 20 $\mu$ g/kg daily; 11	(i) 41% greater bone density	[56]
Wistar	<i>n</i> = 15	26	16	Estriol 100 $\mu$ g/kg 5 days/wk; 12	(i) Improved trabecular BMD and BMC	[57]
Sprague-Dawley	<i>n</i> = 9	13	62	17 $\beta$ -estradiol 10 $\mu$ g/kg 4 days/wk; 10	(i) 38% less periosteal mineralizing surface (ii) 88% less endosteal double-labeled surface (iii) 51% less endosteal mineralizing surface (iv) 71% less endosteal mineral apposition rate	[58]

OVX, ovariectomized; BMD, bone mineral density; BMC, bone mineral content.

mandibular cortical thickness in the OVX group compared to the sham group.

In summary, the longer the time since ovariectomy, the greater the magnitude of the observed changes in alveolar bone structure. Likewise the age of the rat at ovariectomy determines its skeletal maturity, and thus changes in bone density and structure in a mature rat (>3 months of age) skeleton is more likely to mimic those in a mature adult human skeleton. An immature rat (<3 months of age) skeleton would experience competing skeletal growth after ovariectomy and that may skew any ovariectomy-induced changes. Robust changes to alveolar bone following ovariectomy have consistently been reported in studies that analyze mandible outcomes at or after 12 weeks after ovariectomy. The combination of studying a rat with a mature skeleton (at least 12 weeks of age (~3 months) and ideally closer to 6 months of age at ovariectomy to exclude skeletal growth) and a time after ovariectomy of at least 12 weeks would yield changes to alveolar bone structure and density that are optimal to represent postmenopausal bone loss. Future studies developing interventions to preserve alveolar bone should consider this time frame.

### 5. Effect of Dietary Calcium on Mandibular Health in Ovariectomized Rats

In addition to considering age at ovariectomy and time from ovariectomy, dietary calcium levels are also important to consider. Two studies [44, 48] that used the same level of calcium in the diet (1.15% Ca) but studied the rats for different periods of time after ovariectomy reported different percent changes in alveolar bone volume (24% versus 75%). Thus, the observed differences in alveolar bone volume are due to differences in the time after ovariectomy. In other

studies that were of similar length after ovariectomy (16 weeks [50] versus 13 weeks [49]), different dietary calcium levels affected mandibular outcomes. For example, a tenfold difference in dietary calcium, of which both levels were considered “low calcium” (0.1% calcium and 0.01% calcium), resulted in a 2.88% and 7.35% decrease in total mandibular BMD, respectively. Thus, mandibular health is dependent on the age at ovariectomy, time after ovariectomy, and the level of dietary calcium. To control for such variation, future studies could use semipurified diet such as the AIN93M that is specially formulated to meet the nutritional needs of the adult rat [53] and facilitates a standardization of the effects of diet on bone outcomes. Although not specifically studied in the ovariectomized rat model, other aspects of a diet including macronutrient or micronutrient content can also likely affect the outcomes of mandibular health if not tightly controlled among studies.

### 6. Estrogen Replacement Therapy Preserves Mandibular Health in Ovariectomized Rats

A single human trial has reported higher alveolar bone density with ERT [24], yet with the ovariectomized rat model it is clear that estrogen treatment can preserve both the periodontium [54, 55] and alveolar bone density [56, 57] and also reduce mandibular bone turnover [58] (Table 3). Rats that were ovariectomized at an unreported age and maintained for 2 weeks were divided into sham, OVX, and OVX + estrogen and were implanted with mini osmotic pumps to continuously deliver either vehicle (sham and OVX groups) or estrogen (OVX + estrogen group) [54]. The treatment that the OVX + estrogen group received was 1.5  $\mu$ g/day of 17  $\beta$ -estradiol; this dose was not standardized to body weight so it is difficult to place in the context of

the other studies. To measure mandibular osteoclastogenesis, right hemimandibles were sectioned into 5  $\mu\text{m}$  thick slices at the M1 mesial root (Figure 5) and stained for tartrate-resistant acid phosphatase (TRAP) activity. The ROI was the buccal periodontium surrounding the mesial root of M1. At 2 weeks after ovariectomy, there was less nuclei/osteoclast observed in the OVX + estrogen group compared to the OVX group. There was no difference in the number of nuclei/osteoclast between the sham and OVX + estrogen groups. Thus, estrogen treatment attenuated the ovariectomy-induced osteoclastogenesis observed in the rat buccal periodontium of M1.

Another study indicates that rats that were ovariectomized at 13 weeks of age were administered 17  $\beta$ -estradiol by injection at a dose of 10  $\mu\text{g}/\text{kg}$  for 5 days/week, for 7 weeks after ovariectomy [55]. To measure the periodontal ligament space, left hemimandibles were cut sagittally at the buccal/lingual midpoint (Figure 5) to expose M1–M3 and were scanned via scanning electron microscopy. The ROI was the distance between a molar root surface and the supporting alveolar bone at 3 randomly chosen sites per rat. There was a greater periodontal ligament space in the OVX group than in the sham group. Estrogen treatment inhibited the expansion of the periodontal ligament space and, by extension, alveolar bone resorption.

Rats ovariectomized at 11 weeks received a daily subcutaneous injection of 17  $\beta$ -estradiol at a dose of 20  $\mu\text{g}/\text{kg}$  for 11 weeks [56]. To measure the alveolar bone density, hemimandibles were sectioned into 6  $\mu\text{m}$  thick slices in the coronal plane (Figure 3) between the mesial and distal roots of M1 (Figure 5). The ROI was the volume of alveolar bone within 1000  $\mu\text{m}$  of the furcation roof on 5 equally spaced slices within the M1 interradicular septum. There was a lower alveolar bone density in the OVX group compared to the sham group. There was no difference in alveolar bone density between the sham and the OVX + estrogen groups.

A similar study also used Wistar rats ovariectomized at 11 weeks but treated the rats with an oral dose of estradiol at 100  $\mu\text{g}/\text{kg}$ , 5 days/week for 12 weeks after ovariectomy [57]. To measure changes in trabecular BMD and bone mineral content (BMC), the hemimandibles were scanned using pQCT at a resolution of 100  $\mu\text{m}$  at 11 slices beginning 0.5 mm from the mesial boarder of M1 to the distal border of M3 (Figure 3). The ROI extended from the superior edge of the incisor root (Figure 6) to the molar furcation roof and excluded the molar crown, roots, and surrounding cortical bone. The OVX + estrogen treated group had a higher trabecular BMD and BMC at multiple slices compared to the OVX group; the sites of greatest alveolar bone preservation were the slices directly beneath M1 and M2.

To measure longer-term changes in mandibular bone remodeling rats were ovariectomized at 13 weeks and left untreated for 52 weeks after ovariectomy [58]. After the 52-week period, one group received estrogen treatment for 10 weeks as a subcutaneous injection of 17  $\beta$ -estradiol for 4 days each week at a dose of 10  $\mu\text{g}/\text{kg}$ . Fluorochrome bone markers were also administered at 17 and 7 days prior to necropsy. To measure the mandibular histomorphometry, right hemimandibles were sectioned coronally at M2 (Figure 3) into

30  $\mu\text{m}$  thick slices and visualized with a fluorescence microscope to quantify bone turnover. There were two ROIs, the periosteal bone surface around the outside of the mandibular cortical bone and the endosteal bone surface around the trabeculae within the M2 supporting alveolar bone. On the periosteal surface, the mineralizing surface of the OVX group was higher than the OVX + estrogen group. On the endosteal surface, the double-labeled surfaces, mineralizing surfaces, and mineral apposition rates were all higher in the OVX group compared to the OVX + estrogen group. By reducing bone turnover in the rat mandible, estrogen treatment may work to preserve existing alveolar bone mass.

Estrogen treatment reduced osteoclastogenesis, stabilized bone turnover, and therefore preserved alveolar bone mass in the ovariectomized rat. However, the preservation of alveolar bone structure following estrogen treatment remains unclear. Future studies should correlate the preservation of alveolar bone structure following ERT with other key sites rich in trabecular bone that are known to respond to ERT in order to place the bone-sparing effects of ERT on alveolar bone in the context of systemic bone health.

## 7. Conclusions

Our review of the literature indicates that the ovariectomized rat experiences a deterioration of alveolar bone that resembles the loss that can be experienced by postmenopausal women. Moreover, the well-characterized loss of bone mineral and structure that occurs in the long bones and lumbar spine occurs concurrently with a loss of tooth-supporting alveolar bone in the mandible of the ovariectomized rat. This link between the traditional sites of bone loss (hip and lumbar spine) and alveolar bone emphasizes the ability of future intervention studies to have a bimodal effect on skeletal health, targeting both fracture prevention and tooth retention. Some considerations to maximize the benefits of this model include the measurement techniques used, the age at ovariectomy, and the duration for which a rat is studied after ovariectomy. Diet should also be controlled by adopting standardized diets such as AIN93M to ensure that differences among studies are not due to differences in specific nutrients such as calcium.

Ovariectomy-induced changes to alveolar bone in the preclinical rat model of postmenopausal osteoporosis are detected by traditional histomorphometry, pQCT, and  $\mu$ -CT, but not DXA. The rat should be at least 3 months of age when ovariectomized (ideally closer to 6 months of age) and the time after ovariectomy should also be at least 3 months. The alveolar bone region of interest should be limited to the interradicular septum of the first molar because it is the most well-characterized site and appears to respond positively to the established bone sparing effect of estrogens. The capacity of the alveolar bone to respond positively to estrogen replacement therapy highlights the possibility of additional interventions that target bone anabolism and reduce bone turnover. To date alveolar bone turnover in the ovariectomized rat has been reduced by bisphosphonate (alendronate [56] and risedronate [58]) treatment, and alveolar bone formation has been stimulated by calcitonin

[58] and intermittent parathyroid hormone treatment [59]. Such studies suggest that alveolar bone may be much more sensitive to strategies targeting systemic bone preservation in the preclinical model of postmenopausal bone loss than previously thought. Future studies investigating bone-preserving strategies for the typical sites of ovariectomy-induced bone loss such as the proximal tibia metaphysis, distal femur epiphysis, femoral neck, and lumbar vertebral bodies should include the alveolar bone of the M1 interradicular septum as a region of interest. Studies that show preservation of alveolar bone as well as skeletal sites that are well-established for bone loss after ovariectomy in this preclinical model will provide an important basis for interventions in postmenopausal women. The tight link between alveolar bone preservation, tooth retention, better nutritional status, and the reduced risk of developing chronic disease begins with the mitigation of postmenopausal bone loss. The ovariectomized rat model has the potential to be a preclinical model of postmenopausal alveolar bone loss and could facilitate future drug and nutritional strategies aimed at tooth retention and thus a reduced risk of developing chronic disease.

### Conflict of Interests

The authors declare that there is no conflict of interests regarding the publication of this paper.

### Acknowledgments

The authors thank Amanda Longo, Brock University, for her generous provision of the mandibles used in the figures and Dr. Phil Salmon, Bruker-microCT, for his expert guidance in the micro-CT analysis. Dr. Ward acknowledges the support provided through her NSERC Discovery Grants to study how diet and diet combined with pharmacological agents can modulate bone metabolism in the ovariectomized rat model as well as infrastructure support from the Canada Foundation for Innovation. Dr. Ward is a Canada Research Chair in Bone and Muscle Development.

### References

- [1] H. K. Väänänen and P. L. Härkönen, "Estrogen and bone metabolism," *Maturitas*, vol. 23, pp. S65–S69, 1996.
- [2] R. Pacifici, "Estrogen, cytokines, and pathogenesis of postmenopausal osteoporosis," *Journal of Bone and Mineral Research*, vol. 11, no. 8, pp. 1043–1051, 1996.
- [3] O. Johnell and J. A. Kanis, "An estimate of the worldwide prevalence and disability associated with osteoporotic fractures," *Osteoporosis International*, vol. 17, no. 12, pp. 1726–1733, 2006.
- [4] A. Odén, E. V. McCloskey, H. Johansson, and J. A. Kanis, "Assessing the impact of osteoporosis on the burden of hip fractures," *Calcified Tissue International*, vol. 92, no. 1, pp. 42–49, 2013.
- [5] N. C. Wright, A. C. Looker, K. G. Saag et al., "The recent prevalence of osteoporosis and low bone mass in the United States based on bone mineral density at the femoral neck or lumbar spine," *Journal of Bone and Mineral Research*, vol. 29, no. 11, pp. 2520–2526, 2014.
- [6] B. L. Riggs, S. Khosla, and L. J. Melton III, "A unitary model for involutional osteoporosis: estrogen deficiency causes both type I and type II osteoporosis in postmenopausal women and contributes to bone loss in aging men," *Journal of Bone and Mineral Research*, vol. 13, no. 5, pp. 763–773, 1998.
- [7] J. A. Cauley, N. S. Wampler, J. M. Barnhart et al., "Incidence of fractures compared to cardiovascular disease and breast cancer: the Women's Health Initiative Observational Study," *Osteoporosis International*, vol. 19, no. 12, pp. 1717–1723, 2008.
- [8] O. Johnell and J. Kanis, "Epidemiology of osteoporotic fractures," *Osteoporosis International*, vol. 16, no. 2, pp. S3–S7, 2005.
- [9] O. Johnell, J. A. Kanis, A. Odén et al., "Mortality after osteoporotic fractures," *Osteoporosis International*, vol. 15, no. 1, pp. 38–42, 2004.
- [10] J. Darcey, K. Horner, T. Walsh, H. Southern, E. J. Marjanovic, and H. Devlin, "Tooth loss and osteoporosis: to assess the association between osteoporosis status and tooth number," *British Dental Journal*, vol. 214, no. 4, pp. 1–10, 2013.
- [11] M. Iwasaki, K. Nakamura, A. Yoshihara, and H. Miyazaki, "Change in bone mineral density and tooth loss in Japanese community-dwelling postmenopausal women: a 5-year cohort study," *Journal of Bone and Mineral Metabolism*, vol. 30, no. 4, pp. 447–453, 2012.
- [12] E. A. Krall, R. I. Garcia, and B. Dawson-Hughes, "Increased risk of tooth loss is related to bone loss at the whole body, hip, and spine," *Calcified Tissue International*, vol. 59, no. 6, pp. 433–437, 1996.
- [13] J. B. Payne, R. A. Reinhardt, P. V. Nummikoski, and K. D. Patil, "Longitudinal alveolar bone loss in postmenopausal osteoporotic/osteopenic women," *Osteoporosis International*, vol. 10, no. 1, pp. 34–40, 1999.
- [14] A. Sheiham, J. G. Steele, W. Marcenes et al., "The relationship among dental status, nutrient intake, and nutritional status in older people," *Journal of Dental Research*, vol. 80, no. 2, pp. 408–413, 2001.
- [15] R. B. Ervin and B. A. Dye, "The effect of functional dentition on healthy eating index scores and nutrient intakes in a nationally representative sample of older adults," *Journal of Public Health Dentistry*, vol. 69, no. 4, pp. 207–216, 2009.
- [16] N. R. Sahyoun, C.-L. Lin, and E. Krall, "Nutritional status of the older adult is associated with dentition status," *Journal of the American Dietetic Association*, vol. 103, no. 1, pp. 61–66, 2003.
- [17] D. S. Brennan, K. A. Singh, P. Liu, and A. J. Spencer, "Fruit and vegetable consumption among older adults by tooth loss and socio-economic status," *Australian Dental Journal*, vol. 55, no. 2, pp. 143–149, 2010.
- [18] J. A. Cauley, J. Robbins, Z. Chen et al., "Effects of estrogen plus progestin on risk of fracture and bone mineral density: the Women's Health Initiative randomized trial," *Journal of the American Medical Association*, vol. 290, no. 13, pp. 1729–1738, 2003.
- [19] R. D. Jackson, J. Wactawski-Wende, A. Z. LaCroix et al., "Effects of conjugated equine estrogen on risk of fractures and BMD in postmenopausal women with hysterectomy: results from the women's health initiative randomized trial," *Journal of Bone and Mineral Research*, vol. 21, no. 6, pp. 817–828, 2006.
- [20] F. Grodstein, G. A. Colditz, and M. J. Stampfer, "Postmenopausal hormone use and tooth loss: a prospective study," *Journal of the American Dental Association*, vol. 127, no. 3, pp. 370–377, 1996.

- [21] A. Paganini-Hill, "The benefits of estrogen replacement therapy on oral health: the leisure world cohort," *Archives of Internal Medicine*, vol. 155, no. 21, pp. 2325–2329, 1995.
- [22] E. A. Krall, B. Dawson-Hughes, M. T. Hannan, P. W. F. Wilson, and D. P. Kiel, "Postmenopausal estrogen replacement and tooth retention," *The American Journal of Medicine*, vol. 102, no. 6, pp. 536–542, 1997.
- [23] A. Taguchi, M. Sanada, Y. Sueti et al., "Effect of estrogen use on tooth retention, oral bone height, and oral bone porosity in Japanese postmenopausal women," *Menopause*, vol. 11, no. 5, pp. 556–562, 2004.
- [24] R. Civitelli, T. K. Pilgram, M. Dotson et al., "Alveolar and postcranial bone density in postmenopausal women receiving hormone/estrogen replacement therapy: a randomized, double-blind, placebo-controlled trial," *Archives of Internal Medicine*, vol. 162, no. 12, pp. 1409–1415, 2002.
- [25] A. C. Ross, J. E. Manson, S. A. Abrams et al., "The 2011 report on dietary reference intakes for calcium and vitamin D from the Institute of Medicine: what clinicians need to know," *The Journal of Clinical Endocrinology and Metabolism*, vol. 96, no. 1, pp. 53–58, 2011.
- [26] H. Boeing, A. Bechthold, A. Bub et al., "Critical review: vegetables and fruit in the prevention of chronic diseases," *European Journal of Nutrition*, vol. 51, no. 6, pp. 637–663, 2012.
- [27] Y.-M. Chen, S. C. Ho, and J. L. F. Woo, "Greater fruit and vegetable intake is associated with increased bone mass among postmenopausal Chinese women," *British Journal of Nutrition*, vol. 96, no. 4, pp. 745–751, 2006.
- [28] D. D. Thompson, H. A. Simmons, C. M. Pirie, and H. Z. Ke, "FDA guidelines and animal models for osteoporosis," *Bone*, vol. 17, no. 4, supplement, pp. 125S–133S, 1995.
- [29] C. H. Turner, R. K. Roeder, A. Wiczorek, T. Foroud, G. Liu, and M. Peacock, "Variability in skeletal mass, structure, and biomechanical properties among inbred strains of rats," *Journal of Bone and Mineral Research*, vol. 16, no. 8, pp. 1532–1539, 2001.
- [30] S. Sengupta, M. Arshad, S. Sharma, M. Dubey, and M. M. Singh, "Attainment of peak bone mass and bone turnover rate in relation to estrous cycle, pregnancy and lactation in colony-bred Sprague-Dawley rats: suitability for studies on pathophysiology of bone and therapeutic measures for its management," *Journal of Steroid Biochemistry and Molecular Biology*, vol. 94, no. 5, pp. 421–429, 2005.
- [31] P. P. Lelovas, T. T. Xanthos, S. E. Thorma, G. P. Lyritis, and I. A. Dontas, "The laboratory rat as an animal model for osteoporosis research," *Comparative Medicine*, vol. 58, no. 5, pp. 424–430, 2008.
- [32] M. M. Leitner, A. E. Tami, P. M. Montavon, and K. Ito, "Longitudinal as well as age-matched assessments of bone changes in the mature ovariectomized rat model," *Laboratory Animals*, vol. 43, no. 3, pp. 266–271, 2009.
- [33] W. S. Jee and W. Yao, "Overview: animal models of osteopenia and osteoporosis," *Journal of Musculoskeletal & Neuronal Interactions*, vol. 1, no. 3, pp. 193–207, 2001.
- [34] D. N. Kalu, "The ovariectomized rat model of postmenopausal bone loss," *Bone and Mineral*, vol. 15, no. 3, pp. 175–191, 1991.
- [35] T. J. Wronski, M. Cintron, and L. M. Dann, "Temporal relationship between bone loss and increased bone turnover in ovariectomized rats," *Calcified Tissue International*, vol. 43, no. 3, pp. 179–183, 1988.
- [36] M. Li, Y. Shen, and T. J. Wronski, "Time course of femoral neck osteopenia in ovariectomized rats," *Bone*, vol. 20, no. 1, pp. 55–61, 1997.
- [37] T. J. Wronski, L. M. Dann, and S. L. Horner, "Time course of vertebral osteopenia in ovariectomized rats," *Bone*, vol. 10, no. 4, pp. 295–301, 1989.
- [38] M. Tanaka, S. Ejiri, E. Toyooka, S. Kohno, and H. Ozawa, "Effects of ovariectomy on trabecular structures of rat alveolar bone," *Journal of Periodontal Research*, vol. 37, no. 2, pp. 161–165, 2002.
- [39] K. Irie, Y. Sakakura, E. Tsuruga, Y. Hosokawa, and T. Yajima, "Three-dimensional changes of the mandible and alveolar bone in the ovariectomized rat examined by micro-focus computed tomography," *Journal of the Japanese Society of Periodontology*, vol. 46, no. 4, pp. 288–293, 2004.
- [40] M. S. Ames, S. Hong, H. R. Lee, H. W. Fields, W. M. Johnston, and D.-G. Kim, "Estrogen deficiency increases variability of tissue mineral density of alveolar bone surrounding teeth," *Archives of Oral Biology*, vol. 55, no. 8, pp. 599–605, 2010.
- [41] Y. Moriya, K. Ito, and S. Murai, "Effects of experimental osteoporosis on alveolar bone loss in rats," *Journal of oral Science*, vol. 40, no. 4, pp. 171–175, 1998.
- [42] R. P. Elovic, J. A. Hipp, and W. C. Hayes, "Maxillary molar extraction decreases stiffness of the mandible in ovariectomized rats," *Journal of Dental Research*, vol. 73, no. 11, pp. 1735–1741, 1994.
- [43] I. M. F. Patullo, L. Takayama, R. F. Patullo, V. Jorgetti, and R. M. R. Pereira, "Influence of ovariectomy and masticatory hypofunction on mandibular bone remodeling," *Oral Diseases*, vol. 15, no. 8, pp. 580–586, 2009.
- [44] T. Hara, T. Sato, M. Oka, S. Mori, and H. Shirai, "Effects of ovariectomy and/or dietary calcium deficiency on bone dynamics in the rat hard palate, mandible and proximal tibia," *Archives of Oral Biology*, vol. 46, no. 5, pp. 443–451, 2001.
- [45] J. Yang, S. M. Pham, and D. L. Crabbe, "Effects of oestrogen deficiency on rat mandibular and tibial microarchitecture," *Dentomaxillofacial Radiology*, vol. 32, no. 4, pp. 247–251, 2003.
- [46] A. Mavropoulos, R. Rizzoli, and P. Ammann, "Different responsiveness of alveolar and tibial bone to bone loss stimuli," *Journal of Bone and Mineral Research*, vol. 22, no. 3, pp. 403–410, 2007.
- [47] R. P. Elovic, J. A. Hipp, and W. C. Hayes, "Ovariectomy decreases the bone area fraction of the rat mandible," *Calcified Tissue International*, vol. 56, no. 4, pp. 305–310, 1995.
- [48] M. Tanaka, E. Toyooka, S. Kohno, H. Ozawa, and S. Ejiri, "Long-term changes in trabecular structure of aged rat alveolar bone after ovariectomy," *Oral Surgery, Oral Medicine, Oral Pathology, Oral Radiology, and Endodontics*, vol. 95, no. 4, pp. 495–502, 2003.
- [49] G. Jiang, H. Matsumoto, and A. Fujii, "Mandible bone loss in osteoporosis rats," *Journal of Bone and Mineral Metabolism*, vol. 21, no. 6, pp. 388–395, 2003.
- [50] G.-Z. Jiang, H. Matsumoto, M. Hori et al., "Correlation among geometric, densitometric, and mechanical properties in mandible and femur of osteoporotic rats," *Journal of Bone and Mineral Metabolism*, vol. 26, no. 2, pp. 130–137, 2008.
- [51] S. Kuroda, H. Mukohyama, H. Kondo et al., "Bone mineral density of the mandible in ovariectomized rats: analyses using dual energy X-ray absorptiometry and peripheral quantitative computed tomography," *Oral Diseases*, vol. 9, no. 1, pp. 24–28, 2003.
- [52] J. Yang, D. Farnell, H. Devlin, K. Horner, and J. Graham, "The effect of ovariectomy on mandibular cortical thickness in the rat," *Journal of Dentistry*, vol. 33, no. 2, pp. 123–129, 2005.

- [53] P. G. Reeves, F. H. Nielsen, and G. C. Fahey Jr., "AIN-93 purified diets for laboratory rodents: final report of the American Institute of Nutrition ad hoc writing committee on the reformulation of the AIN-76A rodent diet," *The Journal of Nutrition*, vol. 123, no. 11, pp. 1939–1951, 1993.
- [54] S. Kawamoto, S. Ejiri, E. Nagaoka, and H. Ozawa, "Effects of oestrogen deficiency on osteoclastogenesis in the rat periodontium," *Archives of Oral Biology*, vol. 47, no. 1, pp. 67–73, 2002.
- [55] S. Hidaka, Y. Okamoto, Y. Yamada et al., "Alterations in the periodontium after ovariectomy in rats: the effects of a Japanese herbal medicine, Chujo-to," *Phytotherapy Research*, vol. 14, no. 7, pp. 527–533, 2000.
- [56] P. M. Duarte, P. Gonçalves, M. Z. Casati, S. de Toledo, E. A. Sallum, and F. H. Nociti Jr., "Estrogen and alendronate therapies may prevent the influence of estrogen deficiency on the tooth-supporting alveolar bone: a histometric study in rats," *Journal of Periodontal Research*, vol. 41, no. 6, pp. 541–546, 2006.
- [57] G. Jiang, H. Matsumoto, J. Yamane, N. Kuboyama, Y. Akimoto, and A. Fujii, "Prevention of trabecular bone loss in the mandible of ovariectomized rats," *Journal of oral science*, vol. 46, no. 2, pp. 75–85, 2004.
- [58] J. Hunziker, T. J. Wronski, and S. C. Miller, "Mandibular bone formation rates in aged ovariectomized rats treated with anti-resorptive agents alone and in combination with intermittent parathyroid hormone," *Journal of Dental Research*, vol. 79, no. 6, pp. 1431–1438, 2000.
- [59] S. C. Miller, J. Hunziker, M. Mecham, and T. J. Wronski, "Intermittent parathyroid hormone administration stimulates bone formation in the mandibles of aged ovariectomized rats," *Journal of Dental Research*, vol. 76, no. 8, pp. 1471–1476, 1997.

## Research Article

# Ciclamilast Ameliorates Adjuvant-Induced Arthritis in a Rat Model

Zhi-cheng Zhang,<sup>1</sup> Shui-juan Zhang,<sup>1</sup> Bo Jin,<sup>2</sup> Yujin Wu,<sup>2</sup> Xin-fu Yang,<sup>2</sup> Bing Yu,<sup>1</sup> and Qiang-min Xie<sup>2,3</sup>

<sup>1</sup>College of Pharmaceutical Science, Zhejiang Chinese Medical University, No. 548 Binwen Road, Hangzhou 310053, China

<sup>2</sup>Department of Pharmacology, Zhejiang University School of Medicine, No. 866 Yuhangtang Road, Hangzhou 310058, China

<sup>3</sup>Laboratory Animal Center of Zhejiang University, Hangzhou 310058, China

Correspondence should be addressed to Bing Yu; yhz0796@sina.com and Qiang-min Xie; xieqm@zju.edu.cn

Received 26 July 2014; Revised 23 September 2014; Accepted 25 September 2014

Academic Editor: Monica Fedele

Copyright © 2015 Zhi-cheng Zhang et al. This is an open access article distributed under the Creative Commons Attribution License, which permits unrestricted use, distribution, and reproduction in any medium, provided the original work is properly cited.

We assessed the effect of a novel and selective phosphodiesterase 4 (PDE4) inhibitor, ciclamilast, on chronic inflammation in adjuvant-induced arthritis (AIA), a rat model of rheumatoid arthritis (RA), and acute inflammation in the rat and mouse model of carrageenan-induced paw edema and peritonitis. Our results showed that daily oral administration of ciclamilast at 1, 3, and 10 mg/kg dose-dependently inhibited the increase in hind paw volume of rats with AIA. The inhibition of paw edema was associated with inhibition of both the production of cytokines such as TNF- $\alpha$ , IL-1 $\beta$ , and IL-6 and cell infiltration assessed in subcutaneous paw tissue. Moreover, there was significantly less tissue destruction in the ciclamilast-treated rats compared to the vehicle-treated rats, as assessed by radiographic analysis and histopathological evaluation. In the two acute inflammation models, ciclamilast inhibited carrageenan-induced paw edema in rats and inflammatory cell migration into the peritoneal cavity in mice in a dose-dependent manner. These results not only suggest that ciclamilast, as a disease-modifying antirheumatic drug (DMARD), can attenuate RA but also provide proof of principle that a PDE4 inhibitor may be useful for the treatment of arthritis.

## 1. Introduction

Rheumatoid arthritis (RA) is a chronic inflammatory autoimmune disease characterized by synovial joints and subsequent progressive erosive destruction of articular cartilage, causing progressive damage to the musculoskeletal system, which contributes to loss of physical function and quality of life [1, 2]. RA prevalence rates in developed populations are approximately 0.5% to 1% of the adult population. The standardized mortality ratios vary from 1.28 to 2.98. Epidemiological studies have consistently demonstrated increased mortality in patients with RA compared with the expected rates in the general population [3]. At present, the drugs used to treat RA range from nonsteroidal anti-inflammatory drugs (NSAIDs) to disease-modifying antirheumatic drugs (DMARDs) such as methotrexate as the main treatment approach, while biological DMARDs such as antitumor necrosis factor (TNF), interleukin (IL)-1, and IL-6 are usually considered only when

patients fail to respond to conventional DMARDs. However, the lack of reliable treatment for early RA is a troublesome problem for doctors because most NSAID and DMARD treatments cause severe side effects including stomach ulcers and bleeding in the case of NSAIDs and high blood pressure, osteoporosis, weight gain, and infections in the case of DMARDs [4, 5].

There is therefore a need to develop effective anti-inflammatory drugs with fewer side effects. Phosphodiesterases (PDEs) are a superfamily of enzymes that catalyze the breakdown of cAMP and/or cyclic guanosine monophosphate (GMP) to their inactive forms. PDE4 is the main selective cAMP-metabolizing enzyme in inflammatory and immune cells. Because PDE4 is highly expressed in leukocytes and other inflammatory cells involved in the pathogenesis of inflammatory lung diseases, such as asthma and chronic obstructive pulmonary disease (COPD), inhibition of PDE4 has been predicted to have an anti-inflammatory

effect and thus therapeutic efficacy [6]. Targeting PDE4 has enormous clinical potential because it targets a central pathogenic process that bypasses complex antigen receptor-specific immunoregulatory mechanisms. Indeed, selective PDE4 inhibitors have generated substantial interest as treatment for several autoimmune conditions including rheumatoid arthritis, ankylosing spondylitis, Alzheimer's disease, psoriasis, psoriatic arthritis, sarcoidosis, systemic lupus erythematosus, inflammatory bowel disease, atopic dermatitis, and multiple sclerosis [7]. However, early PDE4 inhibitors such as rolipram and piclamilast (RP 73401) have limited and inconsistent efficacy and side effects that make their further development as treatments for these autoimmune diseases less desirable. Therefore, the search for novel structural classes of PDE 4 inhibitors such as apremilast [8, 9] and ciclamilast [10] that may not have the major side effects (nausea, vomiting, and headache) of the archetypal rolipram is ongoing. Ciclamilast is a structural analog of piclamilast. Our previous studies have confirmed that the inhibitory effect of orally administered ciclamilast on airway hyper-responsiveness is due to its inhibition of PDE4 expression, upregulation of cAMP-PDE activity, and downmodulation of PDE4 activity. We have also demonstrated anti-inflammation and antimucus hypersecretion effects in a murine model of asthma [10] and cigarette smoke-induced airway inflammation and injury in mice (unpublished data).

In this study, ciclamilast was carefully evaluated for its immunopharmacological efficacy against adjuvant-induced arthritis (AIA) in rats and its relevant effects on immune responses. We report that ciclamilast strongly inhibited AIA-induced inflammatory responses in rats. Furthermore, it significantly attenuated carrageenan-induced paw edema in rats and carrageenan-induced peritonitis in mice.

## 2. Materials and Methods

**2.1. Animals.** Inbred, female and male, specific pathogen-free ICR mice ( $22 \pm 3$  g, 8 weeks old) and Sprague-Dawley (SD) rats ( $220 \pm 20$  g, 9-10 weeks old) were purchased from the Shanghai Slac Laboratory Animal Co., Ltd. (China). The animals were housed in a room maintained at  $23 \pm 2^\circ\text{C}$  with  $50 \pm 10\%$  humidity and a 12-h light/12-h dark cycle (lights on from 8:00 a.m. to 8:00 p.m.). The animals were allowed free access to tap water and regular rodent chow. Rodent chow was withheld for 8 h before the final experiments. All of the animal care and handling procedures were approved by the Institutional Animal Care and Use Committee of Zhejiang University.

**2.2. Adjuvant-Induced Arthritis (AIA) in Rats.** Arthritis was induced by inoculation of the rats with Freund's complete adjuvant (CFA). Briefly, on day 0, rats were anesthetized with a mixture of ketamine and xylazine (80:10 mg/kg, intraperitoneally) and then injected with 0.1 mL CFA 1 mg/mL of heat-inactivated *Mycobacterium tuberculosis* in 85% paraffin oil and 15% mannide monooleate (Sigma Aldrich, St. Louis, MO, USA) intradermally at the base of the tail. Rats in the control groups were injected with an equal volume of saline

instead of CFA. Treatment and group designations are as follows: control (no adjuvant, no treatment); vehicle (2% sodium carboxymethylcellulose (CMC), Sigma Aldrich, St. Louis, MO, USA); 1, 3 and 10 mg/kg ciclamilast (cic, Beijing Joinn Drug Research Center, China); 0.1 mg/kg methotrexate (MTX, Sigma Aldrich, St. Louis, MO, USA), one of the most utilized disease-modifying antirheumatic drugs was used as a positive control and administered by oral gavage. Treatments were given daily from the first injection for a period of 27 days.

**2.3. Evaluation of Paw Edema in Arthritis.** Paw edema was determined by measurement of the paw volume using a water-replacement plethysmometer (YLS-7A; Jinan Yiyan Technology and Science Development Co., LTD, China). Measurements were obtained at baseline (1 day before CFA injection), and day 0 was the first CFA injection. Measurements were also obtained on days 2, 4, 6, 8, 10, 12, 14, 16, 18, 20, 22, 24, 26, and 28 following CFA injection.

**2.4. Radiographic Analysis and Organ Weights.** On day 28, hind limbs were subjected to radiographic analysis using an X-ray machine with a 0.5 mm focal spot, beryllium window, and X-OMAT TL film. The focal film distance was 61 cm, and exposures were 30 s at 45 kVp and 3 mA. Radiographs were analyzed by a board-certified radiologist who was blinded to the treatment groups. Semiquantitative scores were generated for radiographic changes in the joints in the following areas: soft-tissue volume, joint space, subchondral erosion, periostitis, osteolysis, subluxation, and degenerative joint changes. The values were based on increasing severity; day 26 was considered the highest possible score per paw [11]. The spleen and thymus were harvested from each rat, and the wet weight measured to determine spleen and thymic involution, which is the typical of AIA [11].

**2.5. Histopathology Evaluation.** Samples were obtained from the knee joint 28 days after adjuvant injection. The specimens were fixed in buffered 10% formalin and embedded in paraffin. They were serially sectioned onto microscope slides at a thickness of  $5 \mu\text{m}$  and then deparaffinized, stained with hematoxylin and eosin, and evaluated for morphological changes and cellular infiltration. Histopathological changes in the joints due to AIA were described and scored using semiquantitative grading with five scores (0: unremarkable, 1: minimal, 2: mild, 3: moderate, and 4: marked). AIA was scored as follows: 0: normal; 1: minimal synovitis without cartilage/bone erosion; 2: synovitis with some marginal erosion but with joint architecture maintained; 3: severe synovitis and erosion with loss of normal joint architecture.

**2.6. Determination of Tissue Cytokine Production.** To measure tissue cytokine levels, the animals were killed on day 28 by deep ether inhalation, and subcutaneous paw tissues were collected. Samples were placed in PBS containing 0.05% Tween-80, 0.1 mM phenylmethylsulfonyl fluoride, 0.1 mM benzethonium chloride, 10 mM EDTA, and 20 KI aprotinin A, homogenized, and centrifuged at 3000 g for 10 min.

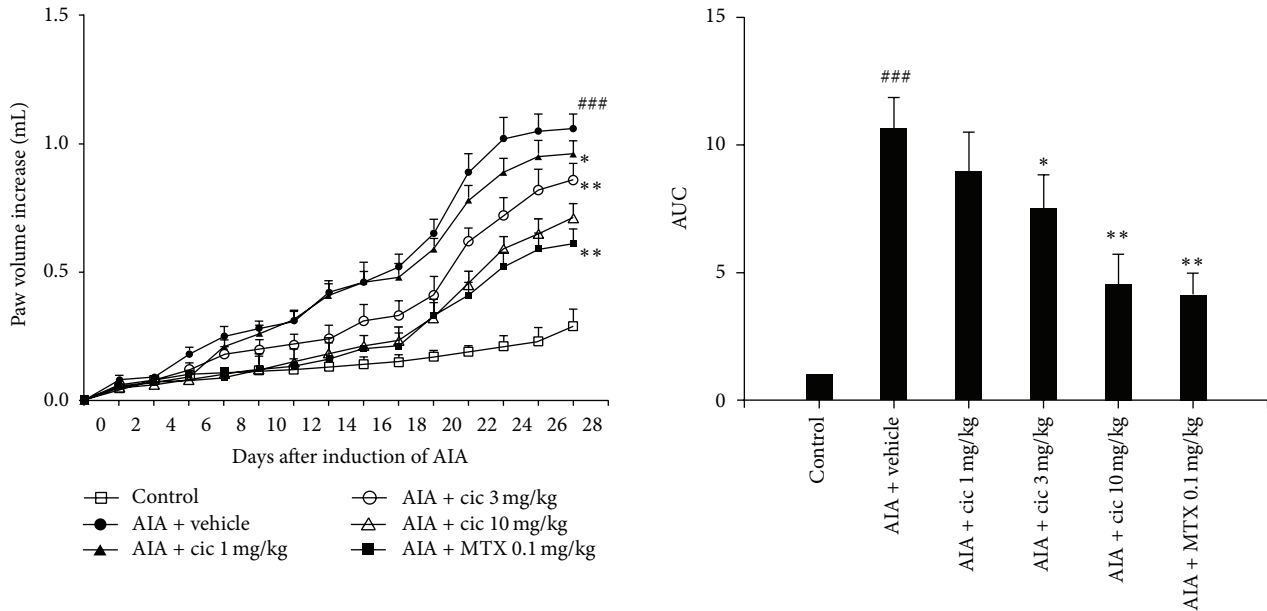


FIGURE 1: Anti-inflammatory effect of ciclamilast on AIA in rats. Time course of paw swelling on the contralateral paw and the area under curve (AUC) of paw swelling on the contralateral paw in rats with AIA on day 28. Control (no adjuvant, no treatment); vehicle, 1, 3, and 10 mg/kg ciclamilast (cic) and 0.1 mg/kg MTX were administered by oral gavage. Hind paw volume (mL) was measured before and after drug administration using a water-replacement plethysmometer. All drugs were administered by oral gavage. Statistical analysis was performed by one-way ANOVA (Dunnett's method) or Mann-Whitney *t*-test. ###*P* < 0.001 versus control; \**P* < 0.05, \*\**P* < 0.01 versus vehicle. Data represent the mean  $\pm$  S.E.M. (*n* = 9-10/group).

The supernatant was rapidly frozen and stored at  $-76^{\circ}\text{C}$  for later measurement of IL- $1\beta$ , IL-6, and TNF- $\alpha$  levels. Cytokine levels were evaluated using specific rat immunoassay ELISA kits according to the manufacturer's recommendations (eBioscience, San Diego, CA, USA).

**2.7. Carrageenan-Induced Paw Edema in Rats.** Male and female SD rats received a subplantar injection of 100  $\mu\text{L}$  of a 1% (w/v) suspension of  $\lambda$ -carrageenan (Sigma Aldrich, St. Louis, MO, USA) in the right hind paw [12]. Paw edema was determined by measurement of the paw volume using a water-replacement plethysmometer immediately before subplantar injection of carrageenan and then at 2, 4, 6, and 8 h afterwards. The data are presented as the variation in the paw volume (mL) and were compared to preinjection values. Ciclamilast at 1, 3, 10 mg/kg and 10 mg/kg indomethacin or vehicle (CMC 200  $\mu\text{L}$ ) was administered via oral gavage 30 min after intraplantar carrageenan injection.

**2.8. Carrageenan-Induced Peritonitis in Mice.** To study the effect of ciclamilast on carrageenan-induced peritonitis in mice, 1, 3, 10, and 20 mg/mg ciclamilast was administered by oral gavage. Male and female ICR mice received an intraperitoneal injection of 100  $\mu\text{L}$  of a 1% (w/v) suspension of carrageenan. The mice were killed by cervical dislocation under anesthesia 4 h later, and the peritoneal cavity was washed with 1.5 mL heparinized phosphate-buffered saline (PBS) to count peritoneal cells. Total cell counts were performed in a Neubauer chamber, and a differential cell (neutrophils) count of a total of 200 cells was performed using

Giemsa staining. The results are presented as the number of total leukocyte cells or neutrophils per milliliter of peritoneal exudate.

**2.9. Statistical Analysis.** Parametric data were evaluated using analysis of variance followed by the one-way ANOVA (Dunnett's method). Nonparametric data were assessed using the Mann-Whitney test. Differences were considered statistically significant at *P* < 0.05. The experiments were repeated at least two times. The SPSS statistical package 15.0 was used for statistical analysis.

### 3. Results

**3.1. Attenuation of Adjuvant-Induced Arthritis in Rats by Ciclamilast.** Paw volume significantly increased in the vehicle-treated rats compared with control rats (*P* < 0.001) from day 8 to day 28. Compared with the vehicle-treated rats, the 3 mg/kg or 10 mg/kg ciclamilast-treated rats and the 0.1 mg/kg MTX-treated rats showed an obvious decrease in paw edema (*P* < 0.05 or 0.01). Similarly, the area under the curve (AUC) of the 3 mg/kg or 10 mg/kg ciclamilast-treated and the 0.1 mg/kg MTX-treated groups also showed a trend toward less paw edema compared with the vehicle-treated rats (each *P* < 0.05 or 0.01) (Figure 1).

**3.2. Effect of Ciclamilast on Radiographic and Histopathological Changes.** As illustrated in the representative day 28 radiographs shown in Figure 2(a), the vehicle-treated rats displayed arthritic changes compared with the control rats.

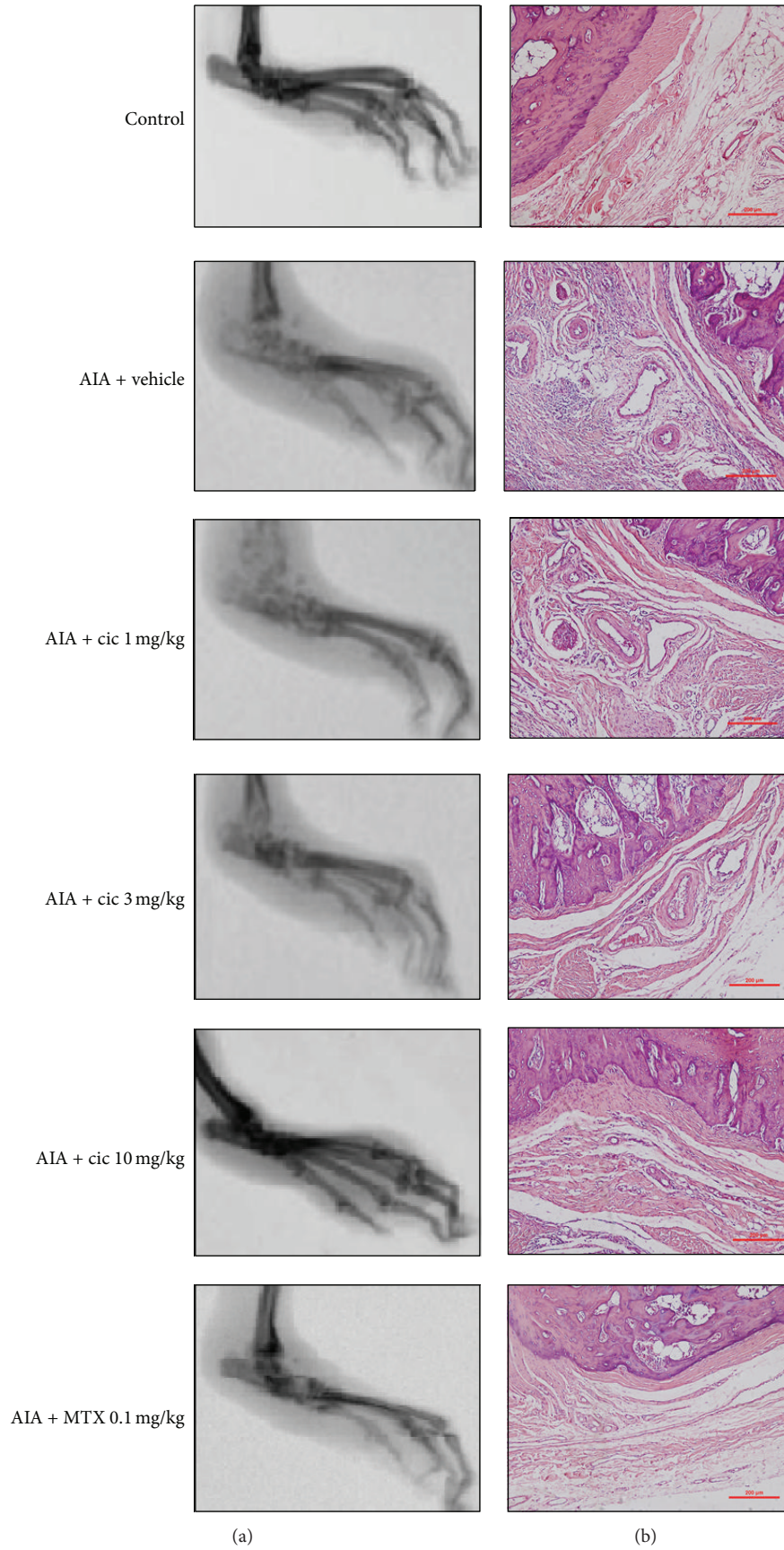


FIGURE 2: Continued.

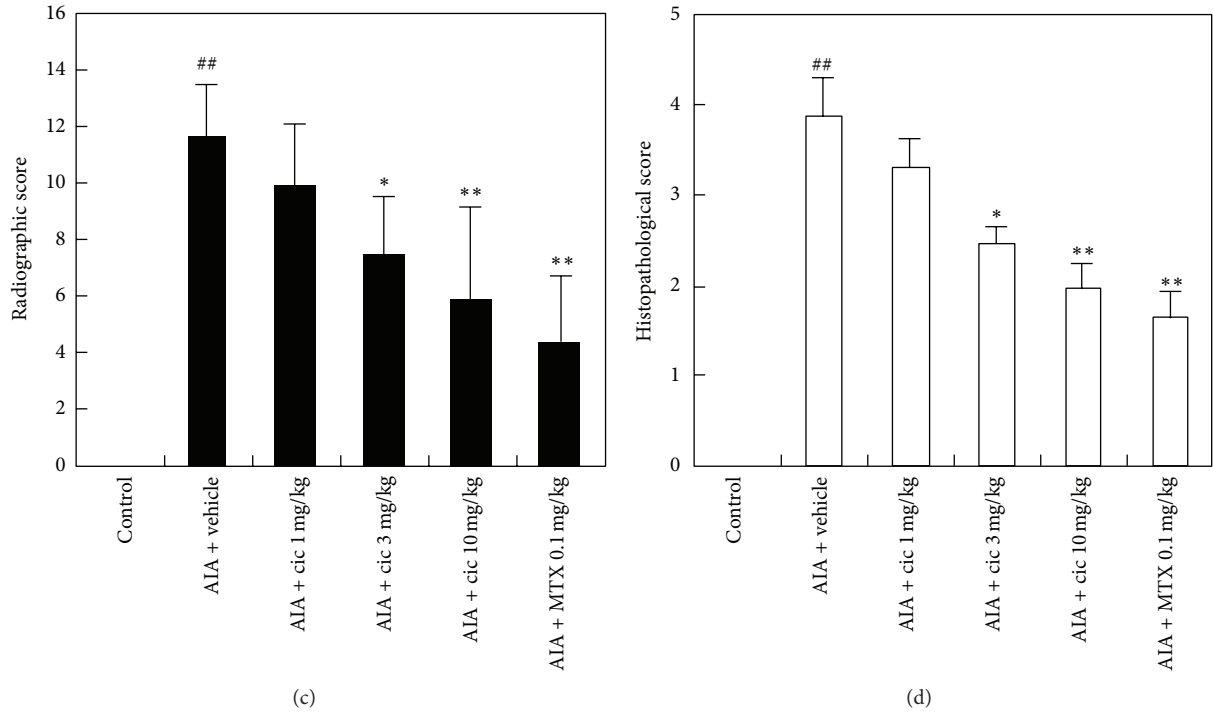


FIGURE 2: Radiographic (a) and histopathological images (b) of hind paws from representative rats on day 28. Note the evidence of swelling and tissue damage in the treatment rats compared with the control rats (a). Ciclamilast displayed potent and dose-dependent inhibitory effects on both swelling and bone changes and reduced the average radiographic (c) and histopathological scores (d).

These arthritic changes were characterized by tissue swelling and evidence of bone changes. For example, the vehicle-treated rats had an average radiographic score of  $11.6 \pm 1.9$ , whereas the control rats had a mean score of 0 (Figure 2(a)). When administered, ciclamilast displayed potent and dose-dependent inhibitory effects on both swelling and bone changes and showed a trend toward less paw swelling and bone injury when compared with the vehicle-treated rats (each  $P < 0.05$  or  $0.01$ ). The 0.1 mg/kg MTX-treated group also showed marked improvement compared with the vehicle-treated rats ( $P < 0.01$ ).

To further validate the antiarthritic effects of ciclamilast, the synovial lining and bone erosions were examined (Figure 2(b)). In the control rats, synovial cells formed a thin layer, and they were flat and quiescent. No leukocyte infiltration or bone erosions were observed. In AIA rats treated with vehicle, the synovial membrane cells became hyperplastic, and it formed a thick, multicelled layer, suggesting active proliferation. In addition, the synovial membrane showed infiltration by leukocytes and hyperemia with dilated blood microvessels (Figure 2(b)). In the synovial tissues of the ciclamilast- or MTX-treated rats (Figure 2(b)), cell hyperplasia and hypertrophy were significantly inhibited, fewer leukocytes were present, and fewer blood microvessels and bone erosions were seen. The vehicle-treated rats had an average histopathological score of  $3.85 \pm 0.43$ , whereas control rats had a mean score of 0 (Figure 2(d)). When administered, ciclamilast and MTX resulted in potent and dose-dependent inhibitory effects on both changes to the

synovial lining and bone injury when compared with the vehicle-treated rats (each  $P < 0.05$  or  $0.01$ ).

**3.3. Effect of Ciclamilast on Body and Immune Organ Weights.** Animals treated with vehicle or MTX weighed substantially less on day 28 compared with the control rats ( $P < 0.05$ ; Figure 3(a)). Treatment with MTX further reduced the rat body weight compared with the vehicle-treated rats ( $P < 0.05$ ). Ciclamilast at 1 mg/kg had no effect on body weight in comparison with the vehicle-treated rats. However, 3 and 10 mg/kg ciclamilast-treated rats exhibited a significant increase in body weight compared with the vehicle-treated rats ( $P < 0.05$ ). AIA rats treated with vehicle or ciclamilast displayed a marked increase in spleen wet weight compared with the control rats ( $P < 0.01$ ; Figure 3(b)). However, the MTX-treated rats had a marked decrease in spleen wet weight compared with the control rats and the vehicle-treated rats ( $P < 0.05$ ; Figure 3(b)). By day 28, the thymus weight in the vehicle-treated rats was markedly increased in comparison with the control rats ( $P < 0.05$ ; Figure 3(c)). Ciclamilast at 1, 3, and 10 mg/kg had no effect on the thymus wet weight compared with the vehicle-treated rats. However, the MTX-treated rats exhibited a marked decrease in thymus wet weight compared with the control rats and the vehicle-treated rats ( $P < 0.05$ ; Figure 3(c)).

**3.4. Effects of Ciclamilast on the Cytokine Levels of Subcutaneous Paw Tissues.** The IL-1, TNF- $\alpha$ , and IL-6 levels in

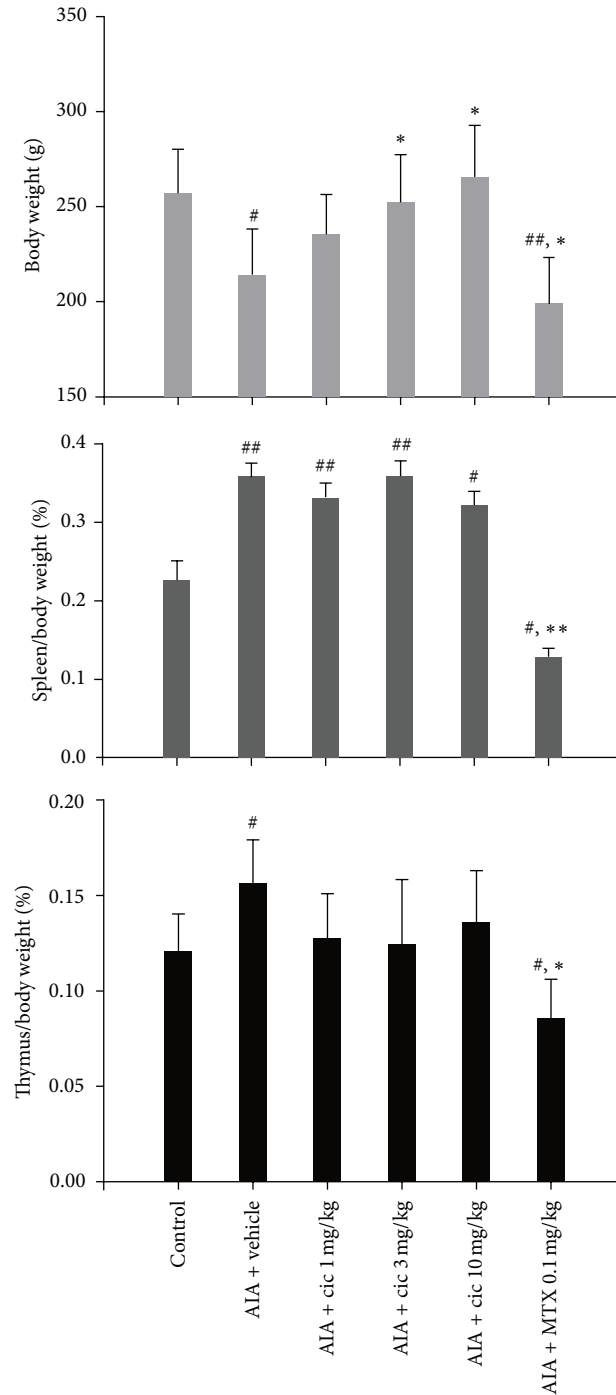


FIGURE 3: Effect of ciclamilast on body and immune organ weights. The wet weight of organs (spleen and thymus) harvested from rats with adjuvant-induced arthritis on day 28. Statistical analysis was performed by one-way ANOVA (Dunnett's method) or Mann-Whitney *t*-test. <sup>#</sup>*P* < 0.05, <sup>##</sup>*P* < 0.01 versus control; <sup>\*</sup>*P* < 0.05, <sup>\*\*</sup>*P* < 0.01 versus vehicle rats. Data represent the mean ± S.E.M. (*n* = 9-10/group).

paw tissues were significantly increased in vehicle-treated rats compared with control rats ( $P < 0.01$ ) at day 28. Compared with the vehicle-treated rats, the 1, 3, and 10 mg/kg ciclamilast and the 0.1 mg/kg MTX-treated rats showed an obvious dose-dependent decrease in proinflammatory factors (each  $P < 0.05$  or 0.01) (Figure 4).

**3.5. Attenuation of Carrageenan-Induced Edema in Rat Paws by Ciclamilast.** Paw volume was significantly increased in vehicle-treated rats compared with the control rats ( $P < 0.001$ ) from hour 2 to hour 8. Compared with the vehicle-treated rats, the 3 mg/kg and 10 mg/kg ciclamilast and the 10 mg/kg indomethacin groups showed an obvious decrease

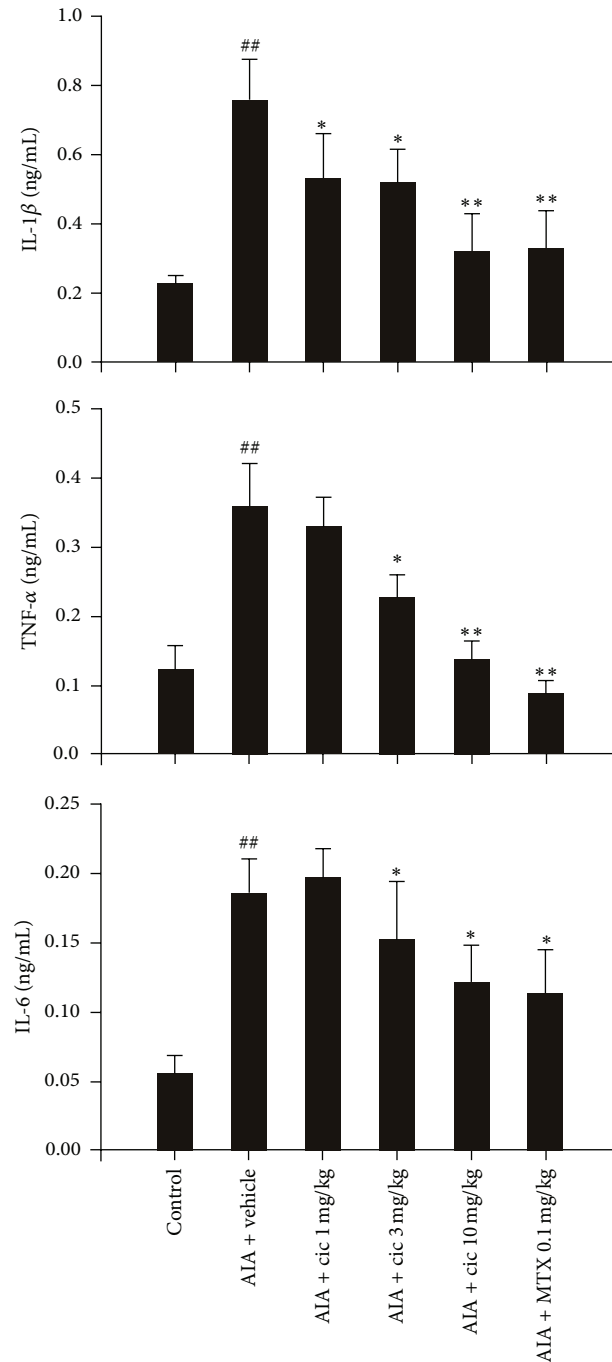


FIGURE 4: Effect of ciclamilast on the cytokine levels in paw tissue of rats with AIA. Rats with AIA were treated with vehicle or 1, 3, or 10 mg/kg ciclamilast or 0.1 mg/kg MTX via oral gavage from days 0 to 28 after adjuvant induction. Twenty-four hours after the last administration of ciclamilast, rats were killed. The subcutaneous tissue of the right hind paw and the surrounding tarsotibial joints were removed, homogenized, and used for assessment of cytokine levels by ELISA. Statistical analysis was performed by one-way ANOVA (Dunnett’s method) or Mann-Whitney *t*-test. <sup>#</sup>*P* < 0.05, <sup>##</sup>*P* < 0.01 versus control; <sup>\*</sup>*P* < 0.05, <sup>\*\*</sup>*P* < 0.01 versus vehicle rats. Data represent the mean ± S.E.M. (*n* = 9-10/group).

in paw edema (each *P* < 0.05, 0.01 or 0.001). Treatment with 1, 3, and 10 mg/kg ciclamilast inhibited paw edema by 21.4%, 39.9%, and 50.4%, respectively, 8 h after carrageenan administration (Figure 5). The inhibitory effect of 10 mg/kg indomethacin after the same time was 51.1%.

**3.6. Attenuation of Carrageenan-Induced Peritonitis in Mice by Ciclamilast.** Figure 6 shows that i.p. carrageenan increased the migration of inflammatory cells into the peritoneal cavity. However, ciclamilast significantly reduced the peritoneal total leukocyte count and neutrophil migration into

the peritoneal cavity in a dose-dependent manner. This result was consistent with the fact that neutrophils are the most abundant cells in primary inflammatory exudates.

#### 4. Discussion

In the present study, our results showed that daily oral administration of the PDE 4 inhibitor ciclamilast dose-dependently inhibited the increase in the hind paw volume of rats with AIA. The inhibition of paw edema was associated with inhibition of both the production of cytokines such as TNF- $\alpha$ , IL-1 $\beta$ , and IL-6 and cell infiltration as assessed in the subcutaneous paw tissues. Moreover, there was significantly less tissue destruction as assessed by radiographic analysis and histopathology evaluation in the ciclamilast-treated rats compared to the vehicle-treated rats. These results are in remarkably good agreement with previous studies demonstrating an inhibitory effect of rolipram in other models of arthritis in mice [13, 14]. In addition, Nyman and colleagues clearly demonstrated that the anti-inflammatory effects of rolipram were sustained for at least 7 days after the treatment had ceased [15]. Similarly, Francischi et al. [16] showed that rolipram stopped disease progression for several days in a collagen-induced arthritis model in rats. Overall, these results clearly demonstrate that inhibition of PDE 4 may be of clinical benefit in the treatment of arthritis in humans. In contrast, piclamilast (RP 73401) was not effective in an adjuvant-arthritis model and fluorescein-isothiocyanate- (FITC-) induced ear edema. Cho et al. [17] explained that its ineffectiveness may be due to the weak *in vitro* immunopharmacological properties of RP73401 on nitric oxide (NO) production, TNF- $\alpha$  release from differentiated U937, homotypic aggregation of U937 cells, and lymphocyte proliferation triggered by concanavalin A and IL-2. Moreover, it is likely that some pathological inducers such as phorbol 12-myristate 13-acetate (PMA) may alter the pharmacological sensitivity of RP73401 against rheumatoid arthritis-related immunopathological conditions. In the present study, we studied the antiarthritis effects of ciclamilast, a RP73401 structural analog with different side chain groups that was effective against inflammation in AIA compared with RP73401. In addition, ciclamilast also significantly attenuated carrageenan-induced paw edema in rats and carrageenan-induced leukocyte infiltration during peritonitis in mice. We suggest that the effectiveness of ciclamilast in these models may be due to the different side chain groups compared to the RP73401 structural formula. The chemical name of RP73401 is 3-cyclopentyloxy-N-(3,5-dichloro-4-pyridyl)-4-methoxybenzamide, and the molecular formula is C<sub>18</sub>H<sub>18</sub>C<sub>12</sub>N<sub>2</sub>O<sub>3</sub>. The chemical name of ciclamilast is 2-exonorbornyl-3-cyclopentyloxy-N-(3,5-dichloro-4-pyridyl)-4-methoxybenzamide, and its molecular formula is C<sub>20</sub>H<sub>20</sub>C<sub>12</sub>N<sub>2</sub>O<sub>3</sub>.

Our previous studies indicated that oral ciclamilast is effective in the treatment of experimentally induced airway inflammation accompanied by reduction of TNF- $\alpha$  levels in lung tissues [10]. However, whether ciclamilast can inhibit IL-1 $\beta$  and IL-6 and protect against arthritis remained unknown.

To confirm our hypothesis of the effects of ciclamilast, we used the AIA rat model. In this model, rats develop chronic swelling in multiple joints accompanied by an influx of inflammatory cells, erosion of joint cartilage, and destruction of joint bone integrity and loss of function. This model of chronic inflammation is due to a complex response involving different proinflammatory cytokines; therefore, there is a possibility of multiple interactions [18, 19]. The AIA model is a well-established experimental model used to study the pathophysiology of various types of human arthritis, particularly rheumatoid arthritis [20, 21]. It is also a good chronic inflammation model for the development of potential anti-inflammatory drugs useful for arthritis treatment [22, 23].

TNF- $\alpha$  is the major therapeutic target for rheumatoid arthritis. A key issue in the treatment of chronic arthritis is identifying the crucial molecules driving the transition from the acute phase to the chronic phase of the disease. However, IL-1 $\beta$  and IL-6, more than TNF- $\alpha$ , appear to be relevant in driving the transition, which suggests that these molecules should be targets for early intervention to stop the progression toward the chronic form of the disease [22]. In the present study, unfortunately, we did not analyze proinflammatory cytokines in the acute phase of the AIA model; we only analyzed the cytokines on day 28. However, we found a significant increase in IL-1 $\beta$  and IL-6 as well as TNF- $\alpha$  in subcutaneous paw tissues associated with cell infiltration and paw edema. We also found that ciclamilast reduced the TNF- $\alpha$  level in addition to the IL-1 $\beta$  and IL-6 levels (Figure 4). Our results suggested that ciclamilast may have effects on both the acute and chronic phases of arthritis. To demonstrate the effect of ciclamilast on the acute phase in arthritis, we added two acute inflammatory models, carrageenan-induced paw edema in rats and carrageenan-induced peritonitis in mice. In the two models, ciclamilast inhibited paw edema in rats (Figure 5) and inflammatory cell migration into the peritoneal cavity in mice (Figure 6) in a dose-dependent manner.

In the present study, we also examined joint pathology. The affected hind paws of each animal were removed at the end of the experiment and processed by radiographs and H&E staining. Representative images of radiographs and H&E-stained sections of the proximal interphalangeal joint of the vehicle-treated and ciclamilast-treated rats are shown in Figure 2. The radiographs showed significant bone loss, soft-tissue swelling, periosteal bone formation coupled to a narrowing of the joint spaces between the metatarsals, and decreased bone radiolucency in the vehicle-treated rats. The joint in the ciclamilast-treated rats showed a dose-dependent decrease in tissue swelling, lower periosteal bone formation, less narrowing of the joint spaces, and increased bone density compared with vehicle-treated rats. Radiographic analysis of the ankle joints confirmed destructive joint changes in all AIA groups and the alleviating effects of ciclamilast on joint pathology (Figure 2(a)). Ciclamilast treatment lowered radiographic scores compared with the vehicle-treated rats (Figure 2(c)). The images of H&E-stained sections showed clear flooding of inflammatory cell infiltrate and severe loss of architecture in the joints of the vehicle-treated rats. In contrast, the joint in the ciclamilast-treated rats showed

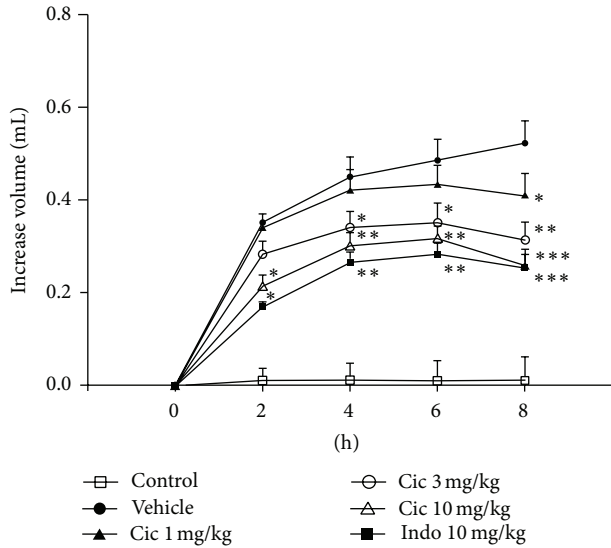


FIGURE 5: Inhibition of carrageenan-induced paw edema in rats by ciclamilast. Ciclamilast (Cic) or indomethacin (Indo) was administered p.o. 30 min after intraplantar injection of carrageenan (100  $\mu$ L of 1% carrageenan) into the left hind paw pad. At the specified times, paw volume was measured by a water-replacement plethysmometer. Statistical analysis was performed by one-way ANOVA (Dunnett's method) or Mann-Whitney *t*-test. \**P* < 0.05, \*\**P* < 0.01 and \*\*\**P* < 0.001 versus vehicle group. Data represent the mean  $\pm$  S.E.M. (*n* = 9-10/group).

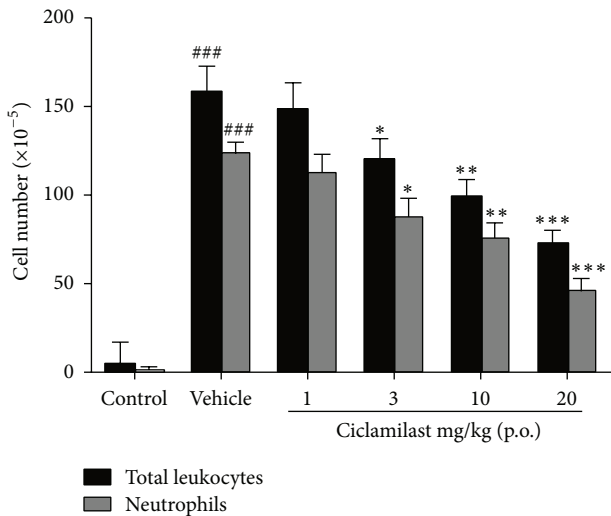


FIGURE 6: Anti-inflammatory effect of ciclamilast on carrageenan-induced peritonitis in mice. Mice received vehicle or ciclamilast, p.o., followed by injection of 1 mg carrageenan diluted in 100  $\mu$ L saline solution (i.p.) after 1h. Mice were killed 4h later, and the peritoneal cavity was washed with 1.5 mL of heparinized phosphate-buffered saline (PBS) to harvest the peritoneal cells. Statistical analysis was performed by one-way ANOVA (Dunnett's method) or Mann-Whitney *t*-test. \**P* < 0.05, \*\**P* < 0.01 and \*\*\**P* < 0.001 versus vehicle group. Data represent the mean  $\pm$  S.E.M. (*n* = 8/group).

a dose-dependent decrease in inflammatory cell infiltrate in the joint space and damage to the joint architecture with articular cartilage (Figure 2(b)). Ciclamilast treatment lowered the histopathological scores compared with the vehicle-treated rats (Figure 2(d)).

MTX is a folate inhibitor; the first reported application in RA was in 1962 [24]. Thereafter, MTX became the most important and most frequently prescribed RA treatment despite several new therapeutic options [25]. The effect of MTX is due to competitive inhibition of folate-dependent enzymes such as dihydrofolate reductase and thymidylate synthase, leading to inhibition of lymphocyte proliferation, and 5-aminoimidazole-4-carboxamide ribonucleotide-transformylase, causing high adenosine levels that in turn have in anti-inflammatory effects [26]. In the present study, we used MTX as the positive control because of this variety of pharmacological actions that are likely to account for its antiproliferative and immunosuppressive effects in rheumatoid arthritis and associated clinical effects [26]. Our results showed that MTX inhibited the increase in hind paw volume of rats with AIA. The inhibition of paw edema was associated with inhibition of both the production of cytokines such as TNF- $\alpha$ , IL-1 $\beta$ , and IL-6 and cell infiltration as assessed in the subcutaneous paw tissues. Moreover, there was significantly less tissue destruction as assessed by radiographic analysis and histopathology in the MTX-treated rats compared to the vehicle control. The anti-inflammatory effects of the PDE 4 inhibitor ciclamilast in arthritis may be attributed to action on multiple targets, to similar to MTX. However, unlike MTX, ciclamilast is not an immunosuppressive agent and cannot reduce immune organ weights such as the spleen and thymus in rats with AIA (Figure 3). These results are consistent with previous reports of MTX-mediated decreases in the weight of the spleen and thymus [27-29]. In addition, one of the most severe side effects of MTX treatment is the development of hepatic fibrosis [30, 31].

## 5. Conclusion

Using an *in vivo* model of AIA in rats, we demonstrated that treatment with ciclamilast resulted in a potent anti-inflammatory effect and protection against tissue destruction but no immunosuppressive action on immune organs. Mechanistically, ciclamilast inhibited an increase in the expression level of IL-1 $\beta$ , IL-6, and TNF- $\alpha$ , leading to potential effects on both the acute and chronic phases in the treatment of rheumatoid arthritis.

## Conflict of Interests

The authors declare that they have no competing interests.

## Authors' Contribution

Zhi-Cheng Zhang and Shui-Juan Zhang contributed equally to this work.

## Acknowledgments

This work was supported by grants from the National Science Foundation of China (Project no. 81373224). The authors also thank Elsevier language editing services for revising the English writing of this paper.

## References

- [1] U. Müller-Ladner, T. Pap, R. E. Gay, M. Neidhart, and S. Gay, "Mechanisms of disease: the molecular and cellular basis of joint destruction in rheumatoid arthritis," *Nature Clinical Practice: Rheumatology*, vol. 1, no. 2, pp. 102–110, 2005.
- [2] G. Plasqui, "The role of physical activity in rheumatoid arthritis," *Physiology & Behavior*, vol. 94, no. 2, pp. 270–275, 2008.
- [3] S. E. Gabriel and K. Michaud, "Epidemiological studies in incidence, prevalence, mortality, and comorbidity of the rheumatic diseases," *Arthritis Research and Therapy*, vol. 11, no. 3, article 229, 2009.
- [4] J. A. Singh, D. E. Furst, A. Bharat et al., "2012 update of the 2008 American College of Rheumatology recommendations for the use of disease-modifying antirheumatic drugs and biologic agents in the treatment of rheumatoid arthritis," *Arthritis Care & Research*, vol. 64, no. 5, pp. 625–639, 2012.
- [5] N. Vivar and R. F. van Vollenhoven, "Advances in the treatment of rheumatoid arthritis," *F1000Prime Reports*, vol. 6, article 31, 2014.
- [6] B. Beghè, K. F. Rabe, and L. M. Fabbri, "Phosphodiesterase-4 inhibitor therapy for lung diseases," *The American Journal of Respiratory and Critical Care Medicine*, vol. 188, no. 3, pp. 271–278, 2013.
- [7] N. Kumar, A. M. Goldminz, N. Kim, and A. B. Gottlieb, "Phosphodiesterase 4-targeted treatments for autoimmune diseases," *BMC Medicine*, vol. 11, no. 1, article 96, 2013.
- [8] F. E. McCann, A. C. Palfreeman, M. Andrews et al., "Apremilast, a novel PDE4 inhibitor, inhibits spontaneous production of tumour necrosis factor-alpha from human rheumatoid synovial cells and ameliorates experimental arthritis," *Arthritis Research and Therapy*, vol. 12, no. 3, article R107, 2010.
- [9] J. Cush and Research Institute, "The controlled trial of Apremilast for rheumatoid arthritis treatment," <http://clinicaltrials.gov/show/NCT01250548>.
- [10] Y.-M. Deng, Q.-M. Xie, H.-F. Tang et al., "Effects of ciclamilast, a new PDE 4 PDE4 inhibitor, on airway hyperresponsiveness, PDE4D expression and airway inflammation in a murine model of asthma," *European Journal of Pharmacology*, vol. 547, no. 1–3, pp. 125–135, 2006.
- [11] D. S. Fletcher, W. R. Widmer, S. Luell et al., "Therapeutic administration of a selective inhibitor of nitric oxide synthase does not ameliorate the chronic inflammation and tissue damage associated with adjuvant-induced arthritis in rats," *Journal of Pharmacology and Experimental Therapeutics*, vol. 284, no. 2, pp. 714–721, 1998.
- [12] C. J. Morris, "Carrageenan-induced paw edema in the rat and mouse," *Methods in Molecular Biology*, vol. 225, pp. 115–121, 2003.
- [13] S. E. Ross, R. O. Williams, L. J. Mason et al., "Suppression of TNF- $\alpha$  expression, inhibition of Th1 activity, and amelioration of collagen-induced arthritis by Rolipram," *Journal of Immunology*, vol. 159, no. 12, pp. 6253–6259, 1997.
- [14] L. Sekut, D. Yarnall, S. A. Stimpson et al., "Anti-inflammatory activity of phosphodiesterase (PDE)-IV inhibitors in acute and chronic models of inflammation," *Clinical & Experimental Immunology*, vol. 100, no. 1, pp. 126–133, 1995.
- [15] U. Nyman, Å. Müssener, E. Larsson, J. Lorentzen, and L. Klareskog, "Amelioration of collagen II-induced arthritis in rats by the type IV phosphodiesterase inhibitor Rolipram," *Clinical and Experimental Immunology*, vol. 108, no. 3, pp. 415–419, 1997.
- [16] J. N. Francischi, C. M. Yokoro, S. Poole, W. L. Tafuri, F. Q. Cunha, and M. M. Teixeira, "Anti-inflammatory and analgesic effects of the phosphodiesterase 4 inhibitor rolipram in a rat model of arthritis," *European Journal of Pharmacology*, vol. 399, no. 2-3, pp. 243–249, 2000.
- [17] J. Y. Cho, J. S. Park, K. U. Baik et al., "Differential effect of phosphodiesterase IV inhibitor RP73401 on various inflammatory and immune responses relevant to rheumatoid arthritis," *Pharmacological Research*, vol. 49, no. 5, pp. 423–431, 2004.
- [18] M. Hegen, J. C. Keith Jr., M. Collins, and C. L. Nickerson-Nutter, "Utility of animal models for identification of potential therapeutics for rheumatoid arthritis," *Annals of the Rheumatic Diseases*, vol. 67, no. 11, pp. 1505–1515, 2008.
- [19] A. Bendele, J. McComb, T. Gould et al., "Animal models of arthritis: relevance to human disease," *Toxicologic Pathology*, vol. 27, no. 1, pp. 134–142, 1999.
- [20] R. T. Owen, "Adjuvant induced polyarthritis—an overview," *Methods and Findings in Experimental and Clinical Pharmacology*, vol. 2, no. 4, pp. 199–204, 1980.
- [21] F. C. Colpaert, T. Meert, P. de Witte, and P. Schmitt, "Further evidence validating adjuvant arthritis as an experimental model of chronic pain in the rat," *Life Sciences*, vol. 31, no. 1, pp. 67–75, 1982.
- [22] G. Ferraccioli, L. Bracci-Laudiero, S. Alivernini, E. Gremese, B. Tolusso, and F. de Benedetti, "Interleukin-1 $\beta$  and interleukin-6 in arthritis animal models: roles in the early phase of transition from acute to chronic inflammation and relevance for human rheumatoid arthritis," *Molecular Medicine*, vol. 16, no. 11-12, pp. 552–557, 2010.
- [23] V. Kelly and M. Genovese, "Novel small molecule therapeutics in rheumatoid arthritis," *Rheumatology*, vol. 52, no. 7, pp. 1155–1162, 2013.
- [24] G. D. Kersley, "Amethopterin (methotrexate) in connective tissue disease-psoriasis and polyarthritis," *Annals of the Rheumatic Diseases*, vol. 27, no. 1, pp. 64–66, 1968.
- [25] M. E. Suarez-Almazor, E. Belseck, B. Shea, G. Wells, and P. Tugwell, "Methotrexate for rheumatoid arthritis," *Cochrane Database of Systematic Reviews*, no. 2, Article ID CD000957, 2000.
- [26] J. A. M. Wessels, T. W. J. Huizinga, and H.-J. Guchelaar, "Recent insights in the pharmacological actions of methotrexate in the treatment of rheumatoid arthritis," *Rheumatology*, vol. 47, no. 3, pp. 249–255, 2008.
- [27] M. L. Billingsley, N. Hall, and H. G. Mandel, "Trauma-induced glial proliferation: possible involvement of the immune system," *Immunopharmacology*, vol. 5, no. 2, pp. 95–101, 1982.
- [28] S. Watanabe, S. Sato, S. Nagase, K. Shimosato, and S. Ohkuma, "Effects of methotrexate and cyclophosphamide on polyamine levels in various tissues of rats," *Journal of Drug Targeting*, vol. 7, no. 3, pp. 197–205, 1999.
- [29] L. Feketeová, P. Jančová, P. Moravcová et al., "Effect of methotrexate on inflammatory cells redistribution in experimental adjuvant arthritis," *Rheumatology International*, vol. 32, no. 11, pp. 3517–3523, 2012.

- [30] S. Dogra and R. Mahajan, "Systemic methotrexate therapy for psoriasis: past, present and future," *Clinical and Experimental Dermatology*, vol. 38, no. 6, pp. 573–588, 2013.
- [31] C. M. Yeo, V. H. Chong, A. Earnest, and W. L. Yang, "Prevalence and risk factors of methotrexate hepatotoxicity in Asian patients with psoriasis," *World Journal of Hepatology*, vol. 5, no. 5, pp. 275–280, 2013.

## Research Article

# Inhibitory Effects of Eucalyptus and Banaba Leaf Extracts on Nonalcoholic Steatohepatitis Induced by a High-Fructose/High-Glucose Diet in Rats

Yoshihisa Takahashi,<sup>1</sup> Keiichiro Sugimoto,<sup>2,3</sup> Yurie Soejima,<sup>1</sup> Arisa Kumagai,<sup>1</sup> Tatsuki Koeda,<sup>4</sup> Aiko Shojo,<sup>3,5</sup> Kazuya Nakagawa,<sup>2</sup> Naoki Harada,<sup>4</sup> Ryoichi Yamaji,<sup>4</sup> Hiroshi Inui,<sup>3,6</sup> Toshikazu Yamanouchi,<sup>7</sup> and Toshio Fukusato<sup>1</sup>

<sup>1</sup>Department of Pathology, Teikyo University School of Medicine, Tokyo 173-8605, Japan

<sup>2</sup>Research and Development Center, Nagaoka Perfumery Co. Ltd., Ibaraki, Osaka 567-0005, Japan

<sup>3</sup>Center for Research and Development of Bioresources, Osaka Prefecture University, Sakai, Osaka 599-8531, Japan

<sup>4</sup>Division of Applied Life Sciences, Graduate School of Life and Environment Sciences, Osaka Prefecture University, Sakai, Osaka 599-8531, Japan

<sup>5</sup>Department of Nutrition and Health, Faculty of Human Development, Soai University, Suminoe-ku, Osaka 559-0033, Japan

<sup>6</sup>Department of Clinical Nutrition, College of Health and Human Sciences, Osaka Prefecture University, Habikino, Osaka 583-8555, Japan

<sup>7</sup>Department of Internal Medicine, Teikyo University School of Medicine, Tokyo 173-8605, Japan

Correspondence should be addressed to Yoshihisa Takahashi; [ytakaha-tky@umin.ac.jp](mailto:ytakaha-tky@umin.ac.jp)

Received 25 September 2014; Accepted 4 March 2015

Academic Editor: Andrea Vecchione

Copyright © 2015 Yoshihisa Takahashi et al. This is an open access article distributed under the Creative Commons Attribution License, which permits unrestricted use, distribution, and reproduction in any medium, provided the original work is properly cited.

Nonalcoholic steatohepatitis (NASH) is a liver disease associated with metabolic syndrome. The aim of this work was to examine whether eucalyptus (*Eucalyptus globulus*) leaf extract (ELE) and banaba (*Lagerstroemia speciosa* L.) leaf extract (BLE) inhibited NASH induced by excessive ingestion of fructose in rats. Wistar rats were divided into four groups according to four distinct diets: starch diet (ST), high-fructose/high-glucose diet (FG), FG diet supplemented with ELE, or FG diet supplemented with BLE. All rats were killed after 5 weeks of treatment. Serum alanine aminotransferase and total cholesterol levels were significantly lower in the BLE group than in the FG group. Liver histopathology, including steatosis, lipogranulomas, and perisinusoidal fibrosis, was significantly attenuated in the ELE and BLE groups compared with the FG group. Levels of 2-thiobarbituric acid reactive substances (TBARS), which reflect oxidative injury to the liver, were significantly suppressed by ELE and BLE. Western blotting analysis indicated that interleukin-6 expression levels were significantly lower in the ELE and BLE groups than in the FG group. These results suggest that ELE and BLE reduced lipogenesis, oxidative stress, and inflammatory cytokine expression and thus inhibited NASH induced by excessive ingestion of fructose in rats.

## 1. Introduction

Nonalcoholic fatty liver disease (NAFLD) is a condition in which excessive fat (primarily triacylglycerols (TAG)) accumulates in the liver of a patient without a history of alcohol abuse [1]. The histological spectrum of NAFLD pathology includes simple steatosis and nonalcoholic steatohepatitis

(NASH), which is characterized by lobular inflammation and hepatocellular injury, as well as hepatic steatosis. NASH is a progressive disease that can advance to liver cirrhosis and hepatocellular carcinoma [2, 3]. NAFLD/NASH is recognized as a hepatic manifestation of metabolic syndrome [4, 5]. Notably, the disorder is a growing clinical and public health concern, as the prevalence of NAFLD/NASH is rapidly

increasing worldwide due to the increased rate of obesity. As a result, it is currently the most common chronic liver disease [6, 7].

Excessive consumption of fructose, largely resulting from the rapid increase in the amount of high-fructose corn syrups (HFCSs) in the human diet, is considered to be one of the major factors contributing to the increasing rate of obesity and metabolic syndrome [8, 9]. Our group and others have shown that fructose-enriched diet causes metabolic syndrome and NAFLD/NASH in experimental animals [10–12]; therefore, fructose enrichment has become a common nutritional animal model of NAFLD/NASH. It has been reported that the amount of fructose consumption is higher in patients with NAFLD and that their hepatic ketohexokinase activity, which plays a crucial role in fructose metabolism in the liver, is elevated compared to healthy subjects [13].

Eucalyptus (*Eucalyptus globulus*) is an evergreen tree native to Australia, which is widely distributed around the world. The leaves of this plant are used as a traditional remedy for diabetes mellitus in South America and Africa, and its antihyperglycemic effect has been demonstrated in streptozotocin-induced diabetic mice [14]. We have previously shown that eucalyptus leaf extract (ELE) inhibits intestinal fructose absorption and suppresses the accumulation of hepatic TAG induced by the excessive ingestion of fructose in rats [15]. This inhibitory effect on intestinal fructose absorption has also been observed in human subjects [16]. Banaba (*Lagerstroemia speciosa* L.) is another folk medicine used to treat diabetes mellitus in various parts of the world, primarily Southeast Asia, and many clinical and experimental studies have confirmed its antihyperglycemic effect [17].

In the present study, we examined potential inhibitory effects of ELE and banaba leaf extract (BLE) on NASH induced by excessive ingestion of fructose in rats. We report that ELE and BLE inhibited the development and progression of hepatic lesions in our animal model of NAFLD/NASH. These effects were associated primarily with decreased lipogenesis, presumably due to the suppression of intestinal fructose absorption. In addition, assays for inflammation and oxidative stress suggested that the antioxidative and anti-inflammatory effects of ELE and BLE are important mediators of NASH inhibition.

## 2. Materials and Methods

**2.1. Ethics Statement.** This study was carried out in strict accordance with the recommendations of the Guide for the Care and Use of Laboratory Animals of the National Institutes of Health. The protocol was approved by the Animal Care and Use Committee of Osaka Prefecture University (permit number: 21-2). All the animals received humane care, and all efforts were taken to minimize suffering.

**2.2. Preparation of ELE and BLE.** Dried eucalyptus and banaba leaves were purchased from K. Kobayashi & Co., Ltd. (Kobe, Japan) and were extracted with boiling ethanol-water

TABLE 1: The composition of each experimental diet (g/1000 g diet).

	ST	FG	BLE	ELE
Cornstarch	700	0	0	0
Glucose	0	350	350	350
Fructose	0	350	350	350
Casein	170	170	170	170
Soybean oil	30	30	30	30
AIN-93G-MX mineral mix	35	35	35	35
Choline chloride	2	2	2	2
AIN-93VX vitamin mix	10	10	10	10
Methionine	3	3	3	3
Cellulose	50	50	40	40
BLE	0	0	10	0
ELE	0	0	0	10

BLE, banaba leaf extract; ELE, eucalyptus leaf extract.

(1:2, v/v) under reflux for 2 h. The extract was then filtered and evaporated to dryness *in vacuo*.

**2.3. Animals and Experimental Protocols.** Thirty 5-week-old male Wistar rats were purchased from Kiwa Laboratory Animals Co., Ltd. (Wakayama, Japan), and maintained on a starch diet for 1 week. Then, rats were divided into four groups according to diet: starch (ST) ( $n = 7$ ), high-fructose/high-glucose (FG) ( $n = 9$ ), FG diet supplemented with ELE ( $n = 7$ ), and FG diet supplemented with BLE ( $n = 7$ ). The latter two groups were termed ELE and BLE, respectively. The rats in the ST and FG group were fed a starch and FG diet *ad libitum*, respectively. The ELE and BLE groups were fed identically to the FG group, but their feed was supplemented with 1% (w/w) ELE or BLE. The composition of each diet is shown in Table 1. All rats were housed individually in a room with controlled temperature ( $23 \pm 2^\circ\text{C}$ ), humidity ( $60 \pm 10\%$ ), and light cycles (09:00–21:00). The diets were stored in a refrigerator at  $4^\circ\text{C}$ . The feed containers were refilled with fresh diet 3 times a week, and food consumption was recorded.

The rats were killed at 11 weeks of age, 5 weeks after commencing the diet. The rats were starved for 16 h, and their body weights were measured before killing them. Rats were starved overnight to avoid influences of food consumption on serum glucose and insulin levels. After the rats were anesthetized with isoflurane, blood samples from each rat were collected by cardiac puncture, and the serum was separated by centrifugation. The liver of each rat was excised and weighed, and samples were collected for histological analysis and snap freezing. The weight of epididymal adipose tissue (EAT) was also measured.

**2.4. Biochemical Analysis of Serum.** Serum aspartate aminotransferase (AST), alanine aminotransferase (ALT), alkaline phosphatase (ALP), cholinesterase (ChE), total cholesterol (T-Cho), high density lipoprotein (HDL-Cho), and glucose levels were determined by routine methods using the Hitachi 7700 Series (DDP) autoanalyzer (Hitachi High-Technologies Corporation, Tokyo, Japan). Arteriosclerotic index (AI) was

calculated as (T-Cho – HDL-Cho)/HDL-Cho. Serum insulin and adiponectin levels were measured by enzyme-linked immunosorbent assay (ELISA) using the rat insulin ELISA kit (RTU) (Shibayagi Co., Ltd., Shibukawa, Japan) and mouse/rat adiponectin ELISA kit (Otsuka Pharmaceutical Co., Ltd., Tokyo, Japan), respectively.

**2.5. Histological Analysis.** The central part of the largest liver lobe was fixed in 10% formaldehyde solution and processed for light microscopy by standard methods. The largest whole section was histologically evaluated. Azan-Mallory staining was performed in addition to hematoxylin and eosin staining to assess hepatic fibrosis. Histopathological features of steatohepatitis were evaluated semiquantitatively according to the validated histological scoring system of Kleiner et al. [18]. The degree of macro- and microvesicular steatosis was evaluated by the percentage of hepatocytes containing macro- and microvesicular fat, respectively, and graded as follows: grade 0 (<5%), grade 1 (5–33%), grade 2 (>33–66%), and grade 3 (>66%). Lobular inflammation was classified as follows: 0 (no foci), 1 (<2 foci per 200x field), 2 (2–4 foci per 200x field), or 3 (>4 foci per 200x field). Lipogranulomas were evaluated as follows: 0 (no foci), 1 (<1 foci per 200x field), 2 (1–2 foci per 200x field), or 3 (>2 foci per 200x field). Portal inflammation was graded as follows: 0 (none: no lymphocytes observed), 1 (mild: sparse lymphocytes present in some or all portal tracts), 2 (moderate: denser lymphocytic infiltration in most portal tracts), or 3 (severe: dense lymphocytic infiltration in most or all portal tracts). Portal fibrosis was evaluated as follows: 0 (none), 1 (mild: portal expansion), 2 (moderate: portal fibrosis with septa), 3 (severe: portal-portal or portal-central bridging septa without regenerative nodules), or 4 (cirrhosis). Intralobular perisinusoidal fibrosis was observed mainly in the periportal area and noted as follows: 0 (none), 1 (mild), or 2 (moderate). Fibrosis staging was classified as follows: 0 (none), 1 (perisinusoidal or portal), 2 (perisinusoidal and portal), 3 (bridging fibrosis), or 4 (cirrhosis).

**2.6. Determination of TAG Content in the Liver.** We measured TAG content in the liver to confirm the extent of hepatic steatosis in each experimental group. TAG in the liver was extracted according to the method described by Folch et al. [19] and quantified using a commercially available kit (L-type TG-H) (Wako Pure Chemical Industries, Ltd., Osaka, Japan) according to the manufacturer's instructions.

**2.7. 2-Thiobarbituric Acid Reactive Substances (TBARS) Levels in the Liver.** To assess oxidative injury in the liver, we measured the hepatic TBARS levels. The liver was homogenized with a polytron homogenizer in 1.15% KCl at 4°C. TBARS levels in the homogenate were determined using the OXItc TBARS assay kit (ZeptoMetrix, NY, USA) according to manufacturer instructions.

**2.8. Determination of Glucose-6-Phosphate Dehydrogenase (G6PDH).** The liver was homogenized with a polytron homogenizer in 25 mmol/L HEPES-KOH buffer of pH 7.4,

containing 0.15 mol/L KCl at 4°C. After centrifugation at 10,000 g for 20 min, we obtained supernatant for use as a crude solution containing active liver enzymes. G6PDH activity was measured as described previously [20]. Protein concentration was determined by the Bradford method [21], and activity of G6PDH was normalized to the protein concentration.

**2.9. Western Blotting.** We examined protein expression levels of inflammatory cytokines and cytokine receptor genes in the liver by Western blotting to elucidate molecular mechanisms of the effects of ELE and BLE. Liver samples were homogenized and centrifuged at 10,000 g at 4°C for 15 min, and the protein concentration in each was determined using a NanoDrop 2000 spectrophotometer (Thermo Fisher Scientific, Waltham, MA, USA). Aliquots of 50 µg protein were resolved by electrophoresis on 12.5% SDS-PAGE gels and transferred onto polyvinylidene fluoride membranes. These membranes were incubated in blocking buffer (5% nonfat milk powder in phosphate buffered saline (PBS)) for 1h followed by incubation with primary antibodies in 5% bovine serum albumin (BSA) in PBS overnight at 4°C, with gentle agitation. The primary antibodies used for Western blotting were as follows: Tumor Necrosis Factor- (TNF-) α (1:250 dilution, R&D Systems, Minneapolis, MN, USA), TNF Receptor 1 (TNFR1) (1:50 dilution, MBL, Nagoya, Japan), interleukin- (IL-) 6 (1:200 dilution, Santa Cruz Biotechnology, Dallas, TX, USA), and Monocyte Chemotactic Protein- (MCP-) 1 (1:500 dilution, Abcam, Cambridge, UK). As a loading control, blots were incubated with antibodies against β-actin (1:1000 dilution, Santa Cruz Biotechnology). The membranes were subsequently washed with 0.1% Tween-20 in PBS and incubated with anti-rabbit or anti-goat secondary antibodies (each 1:2000 in 0.1% Tween-20 in PBS) for 1h at room temperature. The blots were again washed with 0.1% Tween-20 in PBS, and the expression of antibody-linked protein was determined using ECL Western Blotting Detection Reagents (Amersham Pharmacia Biotech Inc., NJ, USA). The optical density of the bands was quantified by ImageQuant software (GE Healthcare Life Sciences, Little Chalfont, UK) and reported in arbitrary units. The protein expression level of each gene was normalized by the expression level of β-actin.

**2.10. Statistics.** For continuous variables, data are presented as mean ± standard deviation, and a one-way analysis of variance (ANOVA) followed by Dunnett's post hoc test was performed to assess the significance of the differences. For semiquantitative data obtained by histological assessment, data are presented as the median (min. to max.), and a Kruskal-Wallis test followed by Steel's post hoc test was performed to determine statistical significance.  $P < 0.05$  was considered statistically significant.

### 3. Results

**3.1. General Observations.** No rats died during the experiment. Table 2 shows data detailing food consumption levels,

TABLE 2: Food consumption, calorie intake, and body, liver, and EAT weight of rats.

	ST	FG	BLE	ELE
Food consumption (g)	750.2 ± 32.2	705.6 ± 41.4	678.3 ± 72.6 <sup>a</sup>	678.0 ± 44.9 <sup>a</sup>
Calorie intake (kcal)	2598.7 ± 111.4	2511.1 ± 147.3	2414.2 ± 258.3	2413.1 ± 159.6
Body weight (g)	358.2 ± 14.4	330.1 ± 10.5 <sup>a</sup>	310.5 ± 29.8 <sup>a</sup>	316.4 ± 24.4 <sup>a</sup>
Liver weight (g)	10.05 ± 1.46	10.43 ± 0.38	8.97 ± 1.18 <sup>b</sup>	9.92 ± 1.34
Liver/body weight ratio (%)	2.86 ± 0.23	3.16 ± 0.12 <sup>a</sup>	2.88 ± 0.19 <sup>b</sup>	3.13 ± 0.31
EAT weight (g)	4.95 ± 0.80	5.37 ± 1.11	4.18 ± 1.21 <sup>b</sup>	4.13 ± 1.01 <sup>b</sup>
EAT/body weight ratio (%)	1.41 ± 0.17	1.63 ± 0.35	1.33 ± 0.28	1.30 ± 0.27 <sup>b</sup>

Data are presented as mean ± standard deviation.

<sup>a</sup>Significantly different from the ST group ( $P < 0.05$ ). <sup>b</sup>Significantly different from the FG group ( $P < 0.05$ ).

EAT, epididymal adipose tissue.

TABLE 3: Serum data corresponding to each experimental group.

	ST	FG	BLE	ELE
AST (IU/L)	90.9 ± 14.6	91.1 ± 8.3	85.8 ± 7.8	87.1 ± 11.1
ALT (IU/L)	22.6 ± 6.7	28.7 ± 6.1 <sup>a</sup>	20.0 ± 1.4 <sup>b</sup>	23.7 ± 2.8
ALP (IU/L)	537.4 ± 153.6	552.4 ± 134.9	560.8 ± 128.5	518.6 ± 164.0
ChE (IU/L)	2.71 ± 0.95	2.89 ± 0.78	2.00 ± 0.89	2.43 ± 1.27
T-Cho (mg/dL)	92.8 ± 5.4	103.9 ± 15.7	84.1 ± 10.0 <sup>b</sup>	97.1 ± 18.2
HDL-Cho (mg/dL)	28.0 ± 2.1	30.8 ± 3.0	28.0 ± 2.9	30.1 ± 3.8
AI	2.28 ± 0.08	2.37 ± 0.20	2.00 ± 0.20 <sup>b</sup>	2.21 ± 0.33
Glucose (mg/dL)	114.3 ± 26.9	117.2 ± 22.3	117.0 ± 10.3	105.0 ± 4.8
Insulin (ng/mL)	1.56 ± 0.68	1.53 ± 0.99	1.21 ± 0.50	1.16 ± 0.14
Adiponectin (μg/mL)	4.97 ± 1.30	4.78 ± 0.97	4.43 ± 0.98	4.79 ± 0.39

Data are presented as mean ± standard deviation.

<sup>a</sup>Significantly different from the ST group ( $P < 0.05$ ). <sup>b</sup>Significantly different from the FG group ( $P < 0.05$ ).

AI, arteriosclerotic index; ALP, alkaline phosphatase; ALT, alanine aminotransferase; AST, aspartate aminotransferase; ChE, cholinesterase; HDL-Cho, high density lipoprotein; T-Cho, total cholesterol.

calorie intake, and body, liver, and EAT weights of rats in each group. Food consumption levels were lower in the FG, ELE, and BLE groups than in the ST group, and this difference was statistically significant for the ELE and BLE groups. Calorie intake also tended to be lower in the FG, ELE, and BLE groups than in the ST group. Body weight was found to be significantly lower in the FG, ELE, and BLE groups than in the ST group. Liver weight was higher in the FG group than in the ST group. In contrast, liver weight was lower in the ELE and BLE groups than in the FG group, and this difference was statistically significant for the BLE group. Liver/body weight ratio was significantly higher in the FG group than in the ST group, while it was significantly lower in the BLE group than in the FG group. EAT weight was higher in the FG group than in the ST group, and it was significantly lower in the ELE and BLE groups than in the FG group. EAT/body weight ratio was also higher in the FG group than in the ST group. EAT/body weight ratio was lower in the ELE and BLE groups than in the FG group, and the difference was statistically significant for the ELE group.

**3.2. Biochemical Data for Serum.** Table 3 shows the data obtained through biochemical analysis of serum obtained from each group. ALT levels were significantly higher in the FG group than in the ST group, while they were lower in

the ELE and BLE groups than in the FG group. This difference was statistically significant for the BLE group. T-Cho levels were higher in the FG group than in the ST group. They were lower in the ELE and BLE groups than in the FG group, and the difference was statistically significant for the BLE group. Similarly, AI was higher in the FG group than in the ST group; it was lower in the ELE and BLE groups than in the FG group and the difference was statistically significant for the BLE group. Assays for AST, ALP, ChE, HDL-Cho, glucose, insulin, and adiponectin levels revealed no significant differences among the experimental groups.

**3.3. Histological Findings.** Differences in the histological appearance among liver lobules were not conspicuous in any of the rats. Although rats in the ST group showed only mild steatosis and inflammation, rats in the FG group showed liver histopathology consistent with NASH (Figures 1(a) and 1(b)). Steatosis and perisinusoidal fibrosis in the FG group was mainly distributed in zone 1. Table 4 summarizes the histological findings of each group. The grade of macrovesicular steatosis was significantly higher in the FG group than in the ST group. In keeping with ELE and BLE preventing NASH-related pathologies, macro- and microvesicular steatosis were significantly lower in the ELE and BLE groups than in the FG group (Figures 1(c) and 1(d)). The grade of microvesicular

TABLE 4: Histological findings for each experimental group.

	ST	FG	BLE	ELE
Macrovesicular steatosis	0 (0-1)	2 (1-3) <sup>a</sup>	0 (0-1) <sup>b</sup>	0 (0-1) <sup>b</sup>
Microvesicular steatosis	2 (1-3)	2 (1-3)	1 (0-1) <sup>a,b</sup>	1 (1-2) <sup>b</sup>
Lobular inflammation	2 (0-2)	2 (1-2)	1 (0-2)	2 (1-2)
Portal inflammation	1 (1-1)	1 (1-1)	1 (0-1)	1 (1-1)
Lipogranulomas	0 (0-0)	2 (1-3) <sup>a</sup>	0 (0-1) <sup>b</sup>	0 (0-0) <sup>b</sup>
Portal fibrosis	0 (0-0)	1 (0-1) <sup>a</sup>	0 (0-1)	0 (0-1)
Perisinusoidal fibrosis	0 (0-0)	1 (1-1) <sup>a</sup>	0 (0-1) <sup>b</sup>	0 (0-1) <sup>b</sup>
Fibrosis stage	0 (0-0)	2 (1-2) <sup>a</sup>	0 (0-2)	1 (0-2) <sup>a</sup>

Data are presented as the median (min.–max.).

<sup>a</sup>Significantly different from the ST group ( $P < 0.05$ ). <sup>b</sup>Significantly different from the FG group ( $P < 0.05$ ).

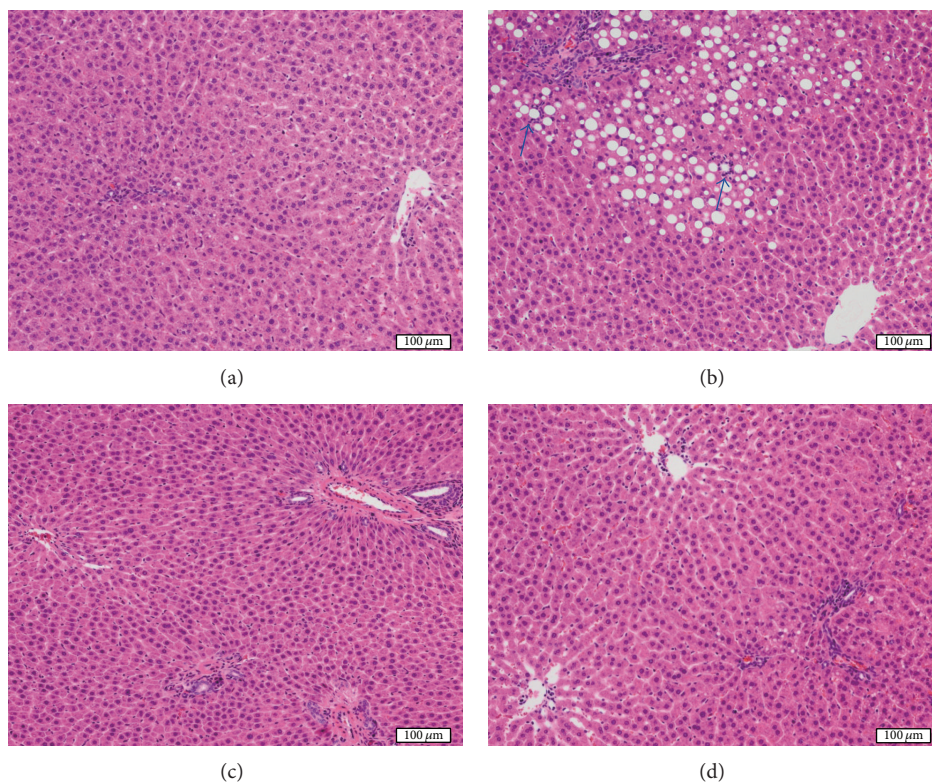


FIGURE 1: Histological appearance of the liver. Although rats in the ST group show only mild steatosis and inflammation (a), rats in the FG group show marked steatosis and scattered foci of lobular inflammation (arrows) (b). Steatosis is markedly alleviated in rats of the BLE (c) and ELE (d) groups.

steatosis in the BLE group was also found to be significantly lower than that of the ST group.

Lobular inflammation tended to be milder in the BLE group than in the FG group, but statistically significant differences were not observed among any experimental groups. With regard to portal inflammation, there were no significant differences among the experimental groups. The number of lipogranulomas was significantly higher in the FG group than in the ST group, and the granuloma number was lowered by ELE and BLE administration compared to the FG group.

We further tested the effects of ELE or BLE treatment on the development of various forms of fibrosis in response to an FG diet. The degree of portal fibrosis was significantly more

severe in the FG group than in the ST group and it was lower in the ELE and BLE groups than in the FG group, but the differences were not statistically significant. While the degree of perisinusoidal fibrosis was significantly more severe in the FG group than in the ST group, it was significantly milder in the ELE and BLE groups than in the FG group. Fibrosis stage was significantly higher in the FG and ELE groups than in the ST group. Fibrosis stage also tended to be lower in the ELE and BLE groups than in the FG group, but the differences were not statistically significant.

3.4. TAG Content, TBARS Levels, and G6PDH Activity in the Liver. TAG content, TBARS levels, and G6PDH activity in

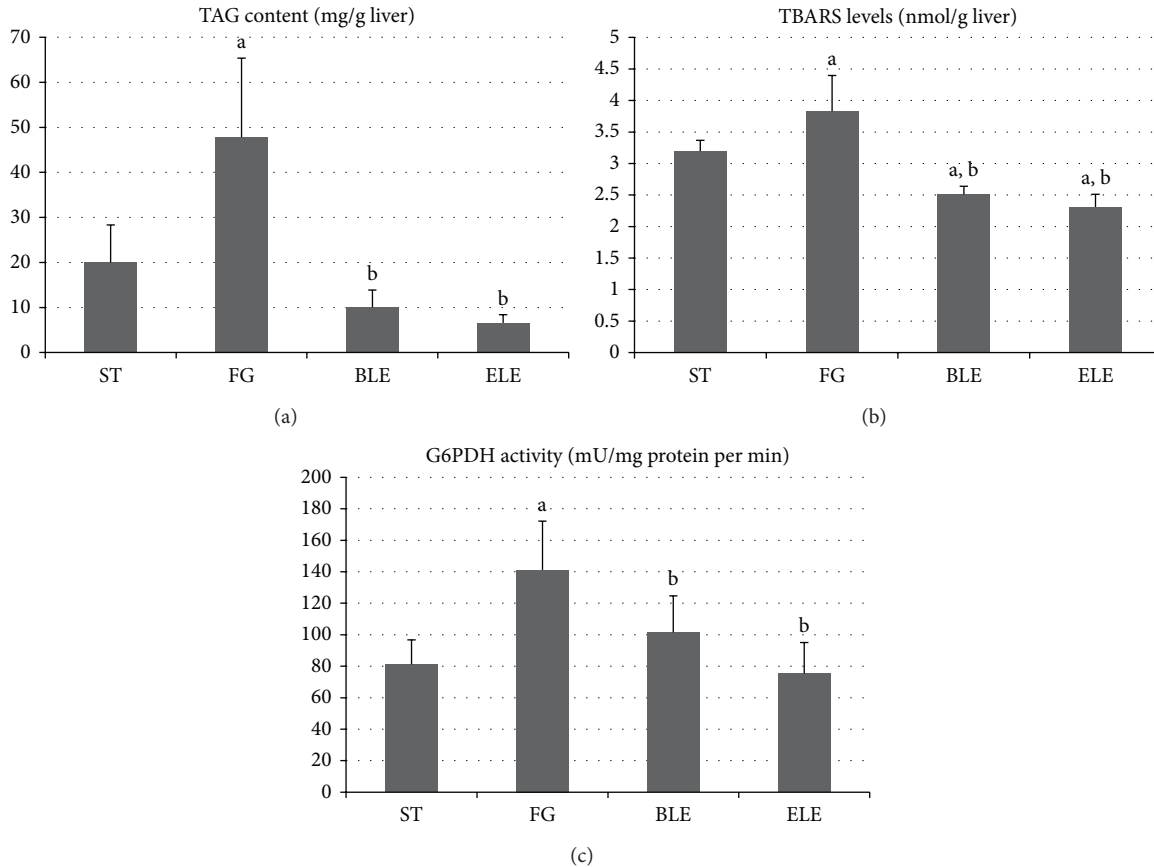


FIGURE 2: TAG content, TBARS levels, and G6PDH activity in the liver. TAG content (a), TBARS levels (b), and G6PDH activity (c) in the liver are significantly higher in the FG group than in the ST group, and they are significantly lower in the ELE and BLE groups than in the FG group. TBARS levels in the ELE and BLE groups are also significantly lower than those in the ST group. <sup>a</sup>Significantly different from the ST group ( $P < 0.05$ ). <sup>b</sup>Significantly different from the FG group ( $P < 0.05$ ).

the liver were significantly higher in the FG group than in the ST group, and they were significantly lower in the ELE and BLE groups than in the FG group (Figure 2). TBARS levels in the ELE and BLE groups were also found to be significantly lower than those in the ST group.

**3.5. Protein Expression Levels of Inflammatory Cytokine and Receptor Genes.** Figure 3 shows Western blotting results revealing the protein expression levels of the inflammatory cytokines or receptors: TNF- $\alpha$ , TNFR1, IL-6, and MCP-1. IL-6 expression levels were significantly higher in the FG group than in the ST group, and they were significantly lower in the ELE and BLE groups than in the FG group. With regard to TNF- $\alpha$ , TNFR1, and MCP-1 expression levels, there were no significant differences among the experimental groups, with the exception of significantly higher TNF- $\alpha$  expression in the BLE group than in the ST group.

#### 4. Discussion

In the present study, we have shown that ELE and BLE attenuate NASH induced by a fructose-enriched diet in rats.

To the best of our knowledge, this is the first study to examine the preventative effects and potential therapeutic benefits of ELE and BLE on NAFLD/NASH in detail.

There are a variety of established nutritional animal models of NAFLD/NASH [22]. We focused on NAFLD/NASH induced by excessive intake of fructose. Although the high-fructose diet model of NASH is well established [10–12, 22], in this study, we used a high-fructose/high-glucose diet to render the experimental diet more similar to the human diet. HFCSs, which are used as sweeteners and thought to substantially contribute to the increasing prevalence of obesity and metabolic syndrome [23, 24], contain glucose as well as fructose. Indeed, the levels of fructose and glucose contents in most foodstuffs are practically identical. As evidence that our method is an appropriate animal model of NASH, liver histopathology similar to NASH and increased serum ALT level were induced in rats as a result of a high-fructose/high-glucose diet. Steatosis and perisinusoidal fibrosis in our model was predominant in zone 1, in contrast to typical forms of NAFLD/NASH in adult humans. We obtained similar findings in a previous study using a pure high-fructose diet [12]. Thus, this pattern may be the characteristic of NAFLD/NASH caused by excessive consumption of fructose. Unexpectedly,

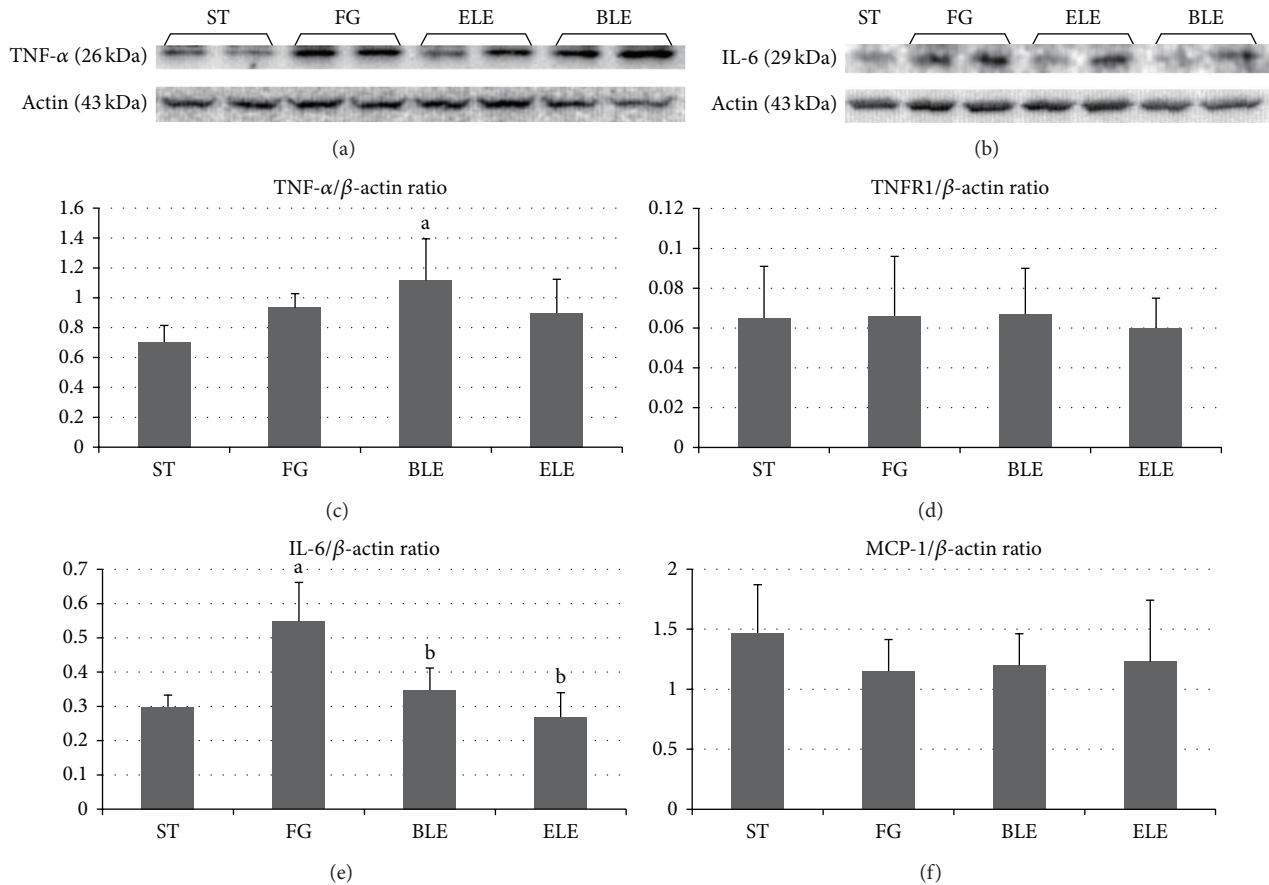


FIGURE 3: Protein expression levels of inflammatory cytokine and receptor genes determined by Western blotting. IL-6 expression levels are significantly higher in the FG group than in the ST group, and they are significantly lower in the ELE and BLE groups than in the FG group ((b), (e)). TNF-α ((a), (c)), TNFR1 (d), and MCP-1 (f) expression levels did not show significant differences among the experimental groups, with the exception of significantly higher TNF-α expression in the BLE group than in the ST group. <sup>a</sup>Significantly different from the ST group ( $P < 0.05$ ). <sup>b</sup>Significantly different from the FG group ( $P < 0.05$ ).

body weight in the FG group was significantly lower than that of the ST group. This phenomenon is most probably explained by our observation that food consumption and calorie intake in the FG group tended to be lower than those in the ST group. This was probably due to the taste of the FG diet, which was less preferred compared to the ST diet. We designed the ST diet to be tasty; however, the FG diet contained large amount of fructose and glucose, which might have made it too sweet. Furthermore, in our previous study, the energy intake in the high-fructose diet group was found to be significantly lower than that in the starch diet group [12]. Food consumption tended to be lower in the ELE and BLE groups than in the FG group, although the differences were not statistically significant. Possibly, the addition of ELE and BLE resulted in a further taste loss of the diet. However, EAT weight in the FG group was higher than that in the ST group; this result was consistent with abdominal obesity typically associated with metabolic syndrome.

Liver weight and liver/body weight ratios were significantly lower in the BLE group than in the FG group, consistent with amelioration of NASH. We determined that

the decrease in liver weight was not due to hepatotoxicity, as liver injury was not observed upon histological assessment. Serum levels of ALT, T-Cho, and AI were significantly lower in the BLE group than in the FG group. This suggests that BLE administration significantly improved hypercholesterolemia and hepatocellular injury. Although the differences were not statistically significant, these serological data tended to be lower in the ELE group than in the FG group as well, suggesting there may be a similar, if perhaps not as robust, effect of ELE. Statistically significant differences in the serum levels of AST and ALP were not observed among the experimental groups. However, these serological markers are less specific to liver cell injury than ALT.

Evaluation of liver histopathology revealed that macro- and microvesicular steatosis, lipogranulomas, and perisinusoidal fibrosis were significantly milder in both ELE and BLE groups than in the FG group. These data indicate that ELE and BLE attenuated pathological findings of NASH. Because the largest whole section of the largest liver lobe was examined and heterogeneity among liver lobules was not remarkable, the observed histological findings likely reflected the whole

aspect of the liver. A significant inhibitory effect of ELE and BLE on liver steatosis was further confirmed by quantification of TAG content in the liver.

Fructose absorbed in the small intestine is transported mainly to the liver and metabolized to triose phosphates by the action of ketohexokinase, aldolase B, and triokinase without the participation of 6-phosphofructokinase, which is the main rate-controlling step in glycolysis [25]. Therefore, fructose can serve as a relatively unregulated acetyl-CoA and is more lipogenic than glucose. Lipogenic enzymes such as G6PDH and fatty acid synthase are activated and hepatic TAG concentration is significantly elevated after excessive consumption of sucrose or fructose [26, 27].

We previously reported that ELE inhibits intestinal fructose absorption [15]. A decrease in fructose absorption would result in the reduction of lipogenesis in the liver. Indeed, hepatic G6PDH activity was significantly lower in the ELE group than in the FG group, and only very small amounts of TAG accumulated in the liver of the ELE group, in contrast to the FG group. When considering these and our previous study, we speculated that ELE prevents NASH induced by the excessive ingestion of fructose mainly by decreasing its intestinal absorption. BLE also reduced lipogenesis and prevented NASH in rats fed with the high-fructose/high-glucose diet, suggesting that BLE as well as ELE inhibits the intestinal absorption of fructose. In fact, when rats were orally given BLE 10 min before the administration of fructose, the intestinal fructose absorption, as determined by measuring the elevated concentration of fructose in the portal vein, was significantly suppressed (unpublished data), in accordance with previous observations for ELE [15].

TBARS is a marker of lipid peroxidation. A “two-hit” hypothesis has been proposed for the pathogenesis of NASH [28], and oxidative stress is considered to be an important cause of the “second hit.” Markers of oxidative stress, including TBARS, are markedly elevated after fructose administration in rodents [11, 29]. In the present study, TBARS levels were significantly higher in the FG group than in the ST group, while they were significantly lower in the ELE and BLE groups than in the FG group. These results suggest that NASH induced by the high-fructose/high-glucose diet was associated with increased oxidative stress, an effect that was inhibited by ELE and BLE.

We observed by Western blot analysis that IL-6 expression levels were significantly higher in the FG group than in the ST group, while they were significantly lower in the ELE and BLE groups than in the FG group. IL-6 is hypothesized to sensitize the liver to injury, stimulate hepatocyte apoptosis, induce insulin resistance, and participate in NASH development [30]. Our results thus suggest that NASH brought on by a high-fructose/high-glucose diet is associated with increased IL-6 expression and that inhibition of NASH by ELE and BLE may be explained in part by decreased IL-6 expression.

It is well established that ELE and BLE contain a wide spectrum of polyphenols with strong antioxidative effects, such as hydrolysable tannins [17, 31]. Hydrolysable tannins and aglycones ameliorated lipopolysaccharide-induced liver injury by inhibition of inducible nitric oxide synthase (iNOS) expression in mice [32]. It has been reported that fructose-fed

iNOS knockout mice did not exhibit increased levels of lipid peroxidation, phospho-I $\kappa$ B and nuclear factor  $\kappa$ B activity, and TNF- $\alpha$  expression in the liver of rats [33]. We thus speculate that these physiological functions have a composite effect on the suppression of inflammation in the liver.

## 5. Conclusions

We show that ELE and BLE inhibit NASH induced by high-fructose/high-glucose diet in rats. This preventative effect is primarily associated with reduced lipogenesis, possibly due to the suppression of the intestinal fructose absorption. In addition, decreased oxidative stress and inflammatory cytokine expression might also provide a mechanism by which NASH is inhibited by ELE and BLE.

## Conflict of Interests

Keiichiro Sugimoto and Kazuya Nakagawa are employed by Nagaoka Perfumery Co., Ltd. Hiroshi Inui received funding from Nagaoka Perfumery Co., Ltd.

## Acknowledgments

This work was supported by JSPS KAKENHI Grants nos. 20193568 and 23580181. The authors thank the Teikyo Academic Research Center for giving advice on statistical analysis.

## References

- [1] A. J. McCullough, “The clinical features, diagnosis and natural history of nonalcoholic fatty liver disease,” *Clinics in Liver Disease*, vol. 8, no. 3, pp. 521–533, 2004.
- [2] G. C. Farrell and C. Z. Larter, “Nonalcoholic fatty liver disease: from steatosis to cirrhosis,” *Hepatology*, vol. 43, no. 2, pp. S99–S112, 2006.
- [3] J. C. Cohen, J. D. Horton, and H. H. Hobbs, “Human fatty liver disease: old questions and new insights,” *Science*, vol. 332, no. 6037, pp. 1519–1523, 2011.
- [4] G. Marchesini, M. Brizi, G. Bianchi et al., “Nonalcoholic fatty liver disease: a feature of the metabolic syndrome,” *Diabetes*, vol. 50, no. 8, pp. 1844–1850, 2001.
- [5] G. Marchesini, E. Bugianesi, G. Forlani et al., “Nonalcoholic fatty liver, steatohepatitis, and the metabolic syndrome,” *Hepatology*, vol. 37, no. 4, pp. 917–923, 2003.
- [6] A. J. McCullough, “Update on nonalcoholic fatty liver disease,” *Journal of Clinical Gastroenterology*, vol. 34, no. 3, pp. 255–262, 2002.
- [7] J. M. Clark, F. L. Brancati, and A. M. Diehl, “The prevalence and etiology of elevated aminotransferase levels in the United States,” *The American Journal of Gastroenterology*, vol. 98, no. 5, pp. 960–967, 2003.
- [8] P. J. Havel, “Dietary fructose: implications for dysregulation of energy homeostasis and lipid/carbohydrate metabolism,” *Nutrition Reviews*, vol. 63, no. 5, pp. 133–157, 2005.
- [9] R. J. Johnson, M. S. Segal, Y. Sautin et al., “Potential role of sugar (fructose) in the epidemic of hypertension, obesity and

- the metabolic syndrome, diabetes, kidney disease, and cardiovascular disease," *The American Journal of Clinical Nutrition*, vol. 86, no. 4, pp. 899–906, 2007.
- [10] Z. Ackerman, M. Oron-Herman, M. Grozovski et al., "Fructose-induced fatty liver disease: Hepatic effects of blood pressure and plasma triglyceride reduction," *Hypertension*, vol. 45, no. 5, pp. 1012–1018, 2005.
- [11] F. Armutcu, Ö. Coskun, A. Gürel et al., "Thymosin alpha 1 attenuates lipid peroxidation and improves fructose-induced steatohepatitis in rats," *Clinical Biochemistry*, vol. 38, no. 6, pp. 540–547, 2005.
- [12] T. Kawasaki, K. Igarashi, T. Koeda et al., "Rats fed fructose-enriched diets have characteristics of nonalcoholic hepatic steatosis," *Journal of Nutrition*, vol. 139, no. 11, pp. 2067–2071, 2009.
- [13] X. Ouyang, P. Cirillo, Y. Sautin et al., "Fructose consumption as a risk factor for non-alcoholic fatty liver disease," *Journal of Hepatology*, vol. 48, no. 6, pp. 993–999, 2008.
- [14] S. K. Swanston-Flatt, C. Day, C. J. Bailey, and P. R. Flatt, "Traditional plant treatments for diabetes. Studies in normal and streptozotocin diabetic mice," *Diabetologia*, vol. 33, no. 8, pp. 462–464, 1990.
- [15] K. Sugimoto, J. Suzuki, K. Nakagawa et al., "Eucalyptus leaf extract inhibits intestinal fructose absorption, and suppresses adiposity due to dietary sucrose in rats," *British Journal of Nutrition*, vol. 93, no. 6, pp. 957–963, 2005.
- [16] K. Sugimoto, T. Kawasaki, M. Tomoda et al., "Lowering of postprandial hyperfructosemia in humans by eucalyptus leaf extract: a randomized, double-blind, placebo-controlled crossover study," *Food Science and Technology Research*, vol. 16, no. 5, pp. 509–512, 2010.
- [17] S. J. Stohs, H. Miller, and G. R. Kaats, "A review of the efficacy and safety of banaba (*Lagerstroemia speciosa* L.) and corosolic acid," *Phytotherapy Research*, vol. 26, no. 3, pp. 317–324, 2012.
- [18] D. E. Kleiner, E. M. Brunt, M. Van Natta et al., "Design and validation of a histological scoring system for nonalcoholic fatty liver disease," *Hepatology*, vol. 41, no. 6, pp. 1313–1321, 2005.
- [19] J. Folch, M. Lees, and G. H. Sloane Stanley, "A simple method for the isolation and purification of total lipides from animal tissues," *The Journal of biological chemistry*, vol. 226, no. 1, pp. 497–509, 1957.
- [20] G. E. Glock and P. McLean, "Further studies on the properties and assay of glucose 6-phosphate dehydrogenase and 6-phosphogluconate dehydrogenase of rat liver," *The Biochemical Journal*, vol. 55, no. 3, pp. 400–408, 1953.
- [21] M. M. Bradford, "A rapid and sensitive method for the quantitation of microgram quantities of protein utilizing the principle of protein-dye binding," *Analytical Biochemistry*, vol. 72, no. 1-2, pp. 248–254, 1976.
- [22] Y. Takahashi, Y. Soejima, and T. Fukusato, "Animal models of nonalcoholic fatty liver disease/nonalcoholic steatohepatitis," *World Journal of Gastroenterology*, vol. 18, no. 19, pp. 2300–2308, 2012.
- [23] R. H. Lustig, L. A. Schmidt, and C. D. Brindis, "Public health: the toxic truth about sugar," *Nature*, vol. 482, no. 7383, pp. 27–29, 2012.
- [24] M. B. Vos and J. E. Lavine, "Dietary fructose in nonalcoholic fatty liver disease," *Hepatology*, vol. 57, no. 6, pp. 2525–2531, 2013.
- [25] P. A. Mayes, "Intermediary metabolism of fructose," *The American Journal of Clinical Nutrition*, vol. 58, no. 5, supplement, pp. 754S–765S, 1993.
- [26] H. Fukuda, N. Iritani, and T. Tanaka, "Effects of high-fructose diet on lipogenic enzymes and their substrate and effector levels in diabetic rats," *Journal of Nutritional Science and Vitaminology*, vol. 29, no. 6, pp. 691–699, 1983.
- [27] S. Osaki, T. Kimura, T. Sugimoto, S. Hizukuri, and N. Iritani, "L-arabinose feeding prevents increases due to dietary sucrose in lipogenic enzymes and triacylglycerol levels in rats," *Journal of Nutrition*, vol. 131, no. 3, pp. 796–799, 2001.
- [28] C. P. Day and O. F. W. James, "Steatohepatitis: a tale of two 'hits'?" *Gastroenterology*, vol. 114, no. 4, pp. 842–845, 1998.
- [29] J. D. Botezelli, L. T. Cambri, A. C. Ghezzi, R. A. Dalia, F. A. Voltarelli, and M. A. R. De Mello, "Fructose-rich diet leads to reduced aerobic capacity and to liver injury in rats," *Lipids in Health and Disease*, vol. 11, article 78, 2012.
- [30] V. Braunersreuther, G. L. Viviani, F. Mach, and F. Montecucco, "Role of cytokines and chemokines in non-alcoholic fatty liver disease," *World Journal of Gastroenterology*, vol. 18, no. 8, pp. 727–735, 2012.
- [31] K. Sugimoto, K. Nakagawa, S. Hayashi et al., "Hydrolyzable tannins as antioxidants in the leaf extract of eucalyptus globulus possessing tyrosinase and hyaluronidase inhibitory activities," *Food Science and Technology Research*, vol. 15, no. 3, pp. 331–336, 2009.
- [32] K. Sugimoto, S. Sakamoto, K. Nakagawa et al., "Suppression of inducible nitric oxide synthase expression and amelioration of lipopolysaccharide-induced liver injury by polyphenolic compounds in *Eucalyptus globulus* leaf extract," *Food Chemistry*, vol. 125, no. 2, pp. 442–446, 2011.
- [33] A. Spruss, G. Kanuri, K. Uebel, S. C. Bischoff, and I. Bergheim, "Role of the inducible nitric oxide synthase in the onset of fructose-induced steatosis in mice," *Antioxidants and Redox Signaling*, vol. 14, no. 11, pp. 2121–2135, 2011.

## Research Article

# Early-Onset Diabetic E1-DN Mice Develop Albuminuria and Glomerular Injury Typical of Diabetic Nephropathy

**Mervi E. Hyvönen,<sup>1,2</sup> Vincent Dumont,<sup>1</sup> Jukka Tienari,<sup>1,3,4</sup>  
Eero Lehtonen,<sup>1,5</sup> Jarkko Ustinov,<sup>6</sup> Marika Havana,<sup>1</sup> Hannu Jalanko,<sup>2</sup>  
Timo Otonkoski,<sup>2,6</sup> Päivi J. Miettinen,<sup>2,6</sup> and Sanna Lehtonen<sup>1</sup>**

<sup>1</sup> Department of Pathology, Haartman Institute, University of Helsinki, Haartmaninkatu 3, 00290 Helsinki, Finland

<sup>2</sup> Children's Hospital, University of Helsinki, 00290 Helsinki, Finland

<sup>3</sup> Department of Pathology, HUSLAB, Helsinki University Central Hospital, 05850 Hyvinkää, Finland

<sup>4</sup> Department of Pathology, HUSLAB, Helsinki University Central Hospital, 00290 Helsinki, Finland

<sup>5</sup> Laboratory Animal Centre, University of Helsinki, 00790 Helsinki, Finland

<sup>6</sup> Biomedicum Stem Cell Center, University of Helsinki, 00290 Helsinki, Finland

Correspondence should be addressed to Sanna Lehtonen; [sanna.h.lehtonen@helsinki.fi](mailto:sanna.h.lehtonen@helsinki.fi)

Received 8 August 2014; Revised 26 September 2014; Accepted 29 September 2014

Academic Editor: Monica Fedele

Copyright © 2015 Mervi E. Hyvönen et al. This is an open access article distributed under the Creative Commons Attribution License, which permits unrestricted use, distribution, and reproduction in any medium, provided the original work is properly cited.

The transgenic E1-DN mice express a kinase-negative epidermal growth factor receptor in their pancreatic islets and are diabetic from two weeks of age due to impaired postnatal growth of  $\beta$ -cell mass. Here, we characterize the development of hyperglycaemia-induced renal injury in the E1-DN mice. Homozygous mice showed increased albumin excretion rate (AER) at the age of 10 weeks; the albuminuria increased over time and correlated with blood glucose. Morphometric analysis of PAS-stained histological sections and electron microscopy images revealed mesangial expansion in homozygous E1-DN mice, and glomerular sclerosis was observed in the most hyperglycaemic mice. The albuminuric homozygous mice developed also other structural changes in the glomeruli, including thickening of the glomerular basement membrane and widening of podocyte foot processes that are typical for diabetic nephropathy. Increased apoptosis of podocytes was identified as one mechanism contributing to glomerular injury. In addition, nephrin expression was reduced in the podocytes of albuminuric homozygous E1-DN mice. Tubular changes included altered epithelial cell morphology and increased proliferation. In conclusion, hyperglycaemic E1-DN mice develop albuminuria and glomerular and tubular injury typical of human diabetic nephropathy and can serve as a new model to study the mechanisms leading to the development of diabetic nephropathy.

## 1. Introduction

Diabetic nephropathy affects every third patient with type 1 diabetes [1]. Advances in the management of diabetes may reduce or postpone the risk of renal complication [2], and, indeed, the incidence of nephropathy in type 1 diabetes has been reported to be declining [3]. Still, diabetic nephropathy is an important cause of morbidity in patients with diabetes and associates also with cardiovascular disease [4] and all-cause mortality [5]. The number of patients needing renal replacement therapy is rapidly increasing, mainly due to the global increase in the prevalence of type 2 diabetes [6, 7].

The first clinical sign of diabetic nephropathy is microalbuminuria [8], indicating an injury in the glomerular filtration barrier. The disease often progresses to macroalbuminuria (defined as urinary albumin excretion  $>300$  mg/24 h) [9], and even nephrotic-range proteinuria is observed [10]. Subsequent decline in the glomerular filtration rate can lead to end-stage renal disease [11].

Pathological characteristics of diabetic nephropathy constitute predominantly of glomerular lesions [12]. Thickening of the glomerular basement membrane (GBM) is observed early in type 1 diabetes [13]. The most important pathologic feature is mesangial expansion, which is correlated to clinical

findings of nephropathy [14] and to progression in albumin excretion [15]. The accumulation of mesangial matrix may eventually lead to nodular glomerular sclerosis, described first by Kimmelstiel and Wilson [16]. In advanced nephropathy, also tubular atrophy and interstitial fibrosis are observed [17].

Glomerular epithelial cells, podocytes, form the glomerular filtration barrier together with endothelial cells and the GBM. Both the structure and number of podocytes are affected in diabetes. Widening of podocyte foot processes, surrounding the glomerular capillaries, has been observed in renal biopsies of diabetic patients with increased albumin excretion [18, 19]. Reduced number of podocytes, reported in both type 1 [20] and type 2 diabetes [21], can result from podocyte detachment [22] or apoptosis [23].

The molecular pathways leading to albuminuria and the pathologic glomerular alterations are far from completely understood. There is an evident need for animal models for studies of the pathogenesis and the potential treatment strategies of diabetic nephropathy. The existing mouse models include induction of diabetes by streptozotocin [24], naturally mutated mouse lines like db/db [25] and Akita mice [26], and more recent genetically engineered models, for example, Ove26 mice [27] and endothelial nitric oxide synthase deficient diabetic mice [28]. Many of these models recapitulate the features of early nephropathy, various degrees of albuminuria and mild-to-moderate mesangial expansion, but rarely more advanced glomerulopathy [29, 30].

The homozygous transgenic mice expressing kinase-negative epidermal growth factor receptor (EGF-R) under the pancreatic duodenal homeobox-1 (pdx-1) promoter (E1-DN mice) are diabetic due to impaired postnatal growth of  $\beta$ -cell mass and subsequent reduced production of insulin [31]. Even the heterozygous E1-DN mice have impaired glucose tolerance in intraperitoneal glucose tolerance test [31]. The E1-DN mice are viable without insulin and can live up to one year. Thus, they can serve as a model to study the effects of long-term hyperglycaemia. The aim of this study was to characterize the development of renal injury in the diabetic E1-DN mice.

## 2. Materials and Methods

**2.1. Animals.** E1-DN mice in FVB background were generated previously [31]. The transgene comprised of a human kinase-deficient EGF-R cDNA with a myc-tag and a growth hormone polyA tail under mouse Pdx-1 promoter [31]. Mice were genotyped by dot blot analysis as previously described, and the homozygotes were identified based on blood glucose levels [31, 32]. Animals were maintained according to the principles of laboratory animal care, and the experiments were approved by the National Animal Experiment Board. Male E1-DN mice were examined, and male wild-type littermates were used as controls. Kidney samples were also collected from male nonlittermate controls of the same mouse strain in the same animal facility. During the one-year study period, mortality was 37.5% for the homozygous E1-DN mice, 12.5% for the heterozygous E1-DN mice, and 10% for the wild-type mice.

**2.2. Blood Glucose and Urine Albumin Measurements.** Random-fed blood glucose values were measured from tail vein with OneTouch Ultra Glucometer (Lifescan, Milpitas, CA, USA). Urine was collected as 24-hour samples in individual metabolic cages. The volume of urine was measured, and albumin concentration determined with mouse albumin ELISA kit (CellTrend, Luckenwalde, Germany).

**2.3. Histology.** Kidney samples were fixed in 10% formalin, dehydrated, and embedded in paraffin. Sections (5  $\mu$ m) were deparaffinised, stained with haematoxylin-eosin or periodic acid-Schiff (PAS) using standard procedures, and examined with Nikon Eclipse 800 microscope (Nikon Instruments Inc., Melville, NY, USA). Image-Pro Analyzer 6.0 (Media Cybernetics, Bethesda, MD, USA) software was used to measure the percentage of PAS-positive area in the glomerular tuft.

**2.4. Immunohistochemistry.** Immunoperoxidase staining was performed as previously described [33] using anti-activated caspase-3 (cleaved caspase-3, Asp175; Cell Signaling, Danvers, MA, USA) and anti-Ki-67 IgGs (Bethyl Laboratories, Montgomery, TX, USA) as primary antibodies, and VectaStain Elite ABC Kit (Vector Laboratories, Burlingame, CA) and 3-amino-9-ethylcarbazole (AEC) reagent (Sigma-Aldrich, St. Louis, MO, USA) for detection. Proliferation index was defined as the percentage of Ki-67 positive tubular cells and calculated from 100 microscope fields (approximately 10 000 cells) per mouse.

**2.5. Immunofluorescence.** Kidney samples were snap frozen in Tissue-Tek OCT-compound (Sakura, Alphen aan den Rijn, The Netherlands). Sections (5  $\mu$ m) were fixed with ice-cold acetone for 10 minutes, washed, blocked with CAS-block (Zymed, South San Francisco, CA, USA), and incubated with anti-nephrin GP-N2 (Progen Biotechnik GmbH, Heidelberg, Germany) and anti-activated caspase-3 (Cell Signaling) IgGs diluted in ChemMate (Dako, Glostrup, Denmark) and labeled with Alexafluor 488- and 555-conjugated secondary antibodies (Invitrogen, Carlsbad, CA, USA). After mounting in Moviol or Vectashield Mounting Medium (Vector Laboratories), the slides were analyzed using Leica SP2 confocal microscope (Leica Microsystems, Wetzlar, Germany). The staining intensity of nephrin was measured from a stack of five consecutive images using FIJI image analysis software and divided by the glomerular area.

**2.6. Electron Microscopy.** Kidney cortical samples were fixed in 2.5% glutaraldehyde in 0.1 M phosphate buffer (pH 7.2–7.4) at room temperature for 2 h, followed by postfixation in 1% osmium tetroxide for 2 h, stained en-bloc in 1% uranyl acetate in 10% ethanol for 1 h, dehydrated in ethanol, and embedded in LX-112 (Ladd Research Industries, Williston, VT). Thin sections were stained with uranyl acetate and lead citrate and examined in a JEM-1400 Transmission Electron Microscope (Jeol, Tokyo, Japan) equipped with Olympus-Morada digital camera (Olympus Soft Imaging Solutions GmbH, Münster, Germany). The mesangial volume fraction, defined as mesangial cells, extracellular matrix, and the GBM, was calculated by morphometric analysis adapted from the

method in [34], using the Fiji Software. The thickness of the GBM was measured from random capillary loops. Capillary loops with obvious bulging were excluded from the analysis to avoid overestimating the thickness of the GBM. The foot process width was determined as described in [35]. Shortly, the number of foot processes per capillary loop was counted, divided by the length of the GBM, and multiplied by  $\pi/4$ . The mesangial volume fraction and the foot process width are expressed as averages of measurements of three capillary loops per glomerulus.

**2.7. Statistics.** The data are presented as means  $\pm$  standard error of mean (SEM), unless stated otherwise. Significance of the differences between the groups was evaluated by Student's unpaired *t*-test for normally distributed variables and by Mann-Whitney *U* test for nonnormally distributed variables or in case of a small sample size. For analyzing the correlation, Spearman's rho test was used.  $P < 0.05$  was used as the limit for statistical significance. Analyses were performed using Excel (Microsoft, Redmond, WA, USA) or SPSS PASW Statistics (version 18) (IBM, Armonk, NY, USA) software.

### 3. Results

**3.1. Diabetic E1-DN Mice Develop Albuminuria.** Monitoring of the blood glucose levels showed that the homozygous male E1-DN mice were overtly diabetic, as reported previously [31]. The blood glucose level was highest in young animals and stayed elevated during the whole follow-up (Figure 1(a)). The E1-DN heterozygous male mice were significantly hyperglycaemic at young age (Figure 1(a)), but at older age their blood glucose levels gradually decreased. Body weight did not differ significantly between the homozygous and wild-type mice at any time point (data not shown). Urinary albumin excretion and urine volumes were followed by 24-hour urine collections in metabolic cages. The E1-DN homozygous mice were polyuric when compared to the wild-type mice (Figure 1(b)). At young age also the heterozygous E1-DN mice had increased urine volumes (Figure 1(b)), consistent with the hyperglycaemia. An increase in albumin excretion rate (AER) in homozygous E1-DN mice was detected at the age of 10 weeks when compared to wild-type mice (Figure 1(c)). At 20 weeks some of the homozygous E1-DN mice developed massive albuminuria, in range of milligrams per 24 hours. Substantial variation was detected between individual mice in the homozygous E1-DN group; the mice with the highest blood glucose values developed the most severe albuminuria, and a strong correlation between the albumin excretion and blood glucose was evident at 20 weeks ( $r = 0.71$ ,  $P < 0.001$ ) (Figure 1(d)).

**3.2. E1-DN Mice Develop Mesangial Expansion and Glomerular Sclerosis.** Mesangial expansion is a characteristic finding of diabetic glomerulopathy. Mesangial area, visualized by PAS staining, was found to be increased by 25% in the homozygous E1-DN mice when compared to the wild-type mice (35% versus 28%,  $P < 0.01$ , Student's *t*-test,  $n = 30$ –70 glomeruli per group) (Figures 2(a)–2(e)). Electron microscopy confirmed an increase of 22% in the mesangial volume fraction

in the homozygous E1-DN mice (36% versus 29%,  $P < 0.05$ , Student's *t*-test,  $n = 14$ –38 glomeruli per group) (Figure 2(f)). In two homozygous E1-DN mice with the highest albumin excretion, the mesangial matrix accumulation was classified as focal, global nodular sclerosis by an expert pathologist who examined the samples blinded from the genotypes.

**3.3. Albuminuric E1-DN Mice Exhibit Tubular Changes.** Flattened tubular epithelial cells and dilated tubular lumens were observed in the kidneys of albuminuric homozygous E1-DN mice in which the albumin excretion exceeded 1000  $\mu\text{g}/24$  h at 20 weeks of age (Figures 3(a) and 3(b)). To study the tubular injury further, we stained proliferating cells with an antibody for Ki-67 (Figures 3(c) and 3(d)). Significantly increased tubular proliferation was observed in the albuminuric E1-DN mice (proliferation index 0.70%), compared to the control mice in which only sporadic proliferating cells were detected (proliferation index 0.18%) ( $P < 0.01$ , Student's *t*-test,  $n = 3$ –4 mice per group).

**3.4. Podocyte Apoptosis Is Increased in E1-DN Mice.** To study whether apoptosis plays a role in the glomerular injury in the E1-DN mice, apoptotic glomerular cells were stained with an antibody for activated caspase-3. Apoptotic cells were counted from 10 glomeruli from each mouse ( $n = 4$ –8 mice per group) by two researchers independently. Increased number of apoptotic cells was detected in the glomeruli of E1-DN homozygous mice when compared to wild-type and heterozygous E1-DN mice both at the age of 20 weeks (6.5 versus 1.0 apoptotic cells per 10 glomeruli,  $P < 0.02$ , Mann-Whitney *U* test), and in the oldest age group of 56–57 weeks (9.8 versus 4.4 apoptotic cells per 10 glomeruli,  $P < 0.02$ , Mann-Whitney *U* test) (Figures 4(a)–4(c)), although the amount of apoptotic glomerular cells was sparse in all mice. To characterize the nature of the apoptotic glomerular cells, we performed a double labelling for cleaved caspase-3 and nephrin revealing that the apoptotic cells were podocytes (Figure 4(d)).

**3.5. Nephrin Expression Is Reduced in Diabetic E1-DN Mice.** The expression of nephrin, the key molecule of the slit diaphragm structure connecting the podocyte foot processes, was studied by immunofluorescence staining and confocal microscopy (Figures 5(a) and 5(b)). Measurement of nephrin staining intensity indicated lower expression level in albuminuric homozygous E1-DN mice when compared to wild-type mice (Figure 5(c)). The expression patterns of other podocyte proteins examined, podocin and ZO-1, were not altered (data not shown).

**3.6. E1-DN Mice Develop Glomerular Basement Membrane Thickening and Podocyte Foot Process Widening.** Electron microscopic analysis of kidneys from two wild-type mice (age 50 weeks) and three homozygous E1-DN mice (age 40–50 weeks) revealed irregular thickening and bulging of the GBM and widening of the podocyte foot processes in the homozygous E1-DN mice (Figures 6(a)–6(c)). The width of the GBM was measured from random capillary loops in areas where the basement membrane was regularly shaped and

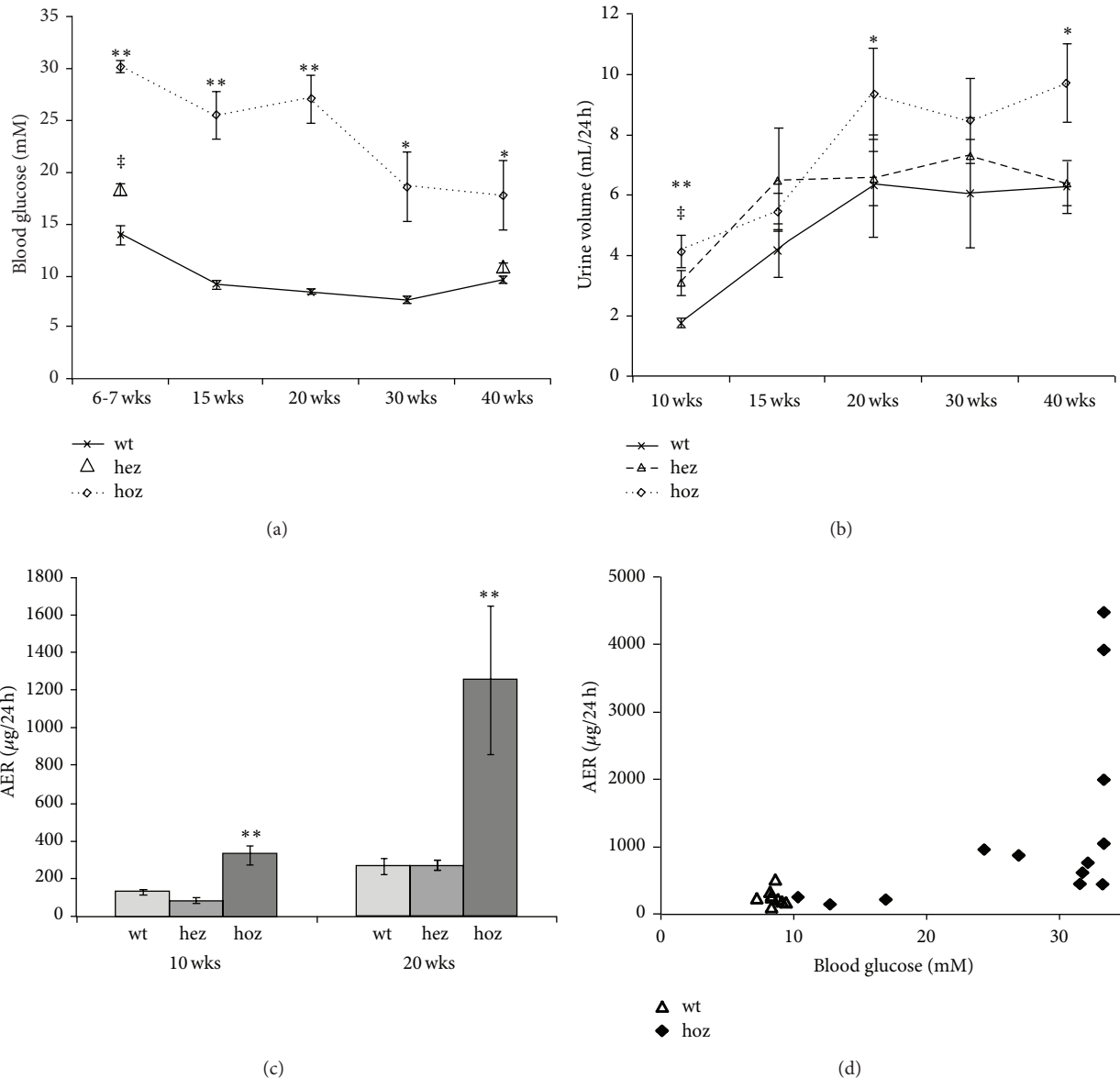


FIGURE 1: E1-DN mice develop hyperglycaemia and albuminuria. (a) Blood glucose is elevated in male E1-DN homozygous (hoz) mice ( $n = 8-16$ ) compared to the wild-type (wt) mice ( $n = 6-10$ ) at all the time points,  $**P < 0.01$ ,  $*P < 0.05$ . At 6-7 weeks of age also the male E1-DN heterozygous (hez) mice ( $n = 14-23$ ) are hyperglycaemic,  $^{\ddagger}P < 0.01$ , but at 40 weeks their blood glucose does not differ from the wt. (b) Urine volumes of the male E1-DN hoz ( $n = 9-16$ ), hez ( $n = 7-16$ ), and wt mice ( $n = 6-10$ ).  $**P < 0.01$  and  $*P < 0.05$  for hoz versus wt,  $^{\ddagger}P < 0.01$  for hez versus wt. (c) Increased albumin excretion rate (AER) is detected at both 10 and 20 weeks of age in the homozygous E1-DN male mice,  $**P < 0.01$ . Heterozygous mice do not develop albuminuria. In (a)–(c), data are shown as mean  $\pm$  SEM. Mann-Whitney  $U$  test was used to compare groups. (d) AER is correlated to blood glucose at 20 weeks of age,  $r = 0.71$ ,  $P < 0.001$  (Spearman's rho),  $n = 22$ . As the upper limit of the glucometer is 33.3 mM, the samples giving the “high” code were analysed as 33.3 mM.

foot processes appeared structurally normal and was found to be 43% higher in the E1-DN homozygous mice when compared to wild-type mice (258 nm versus 370 nm,  $P = 0.025$ , Mann-Whitney  $U$  test,  $n = 3-8$  glomeruli per group) (Figure 6(d)). Podocyte foot processes were also 45% wider in these hyperglycaemic and albuminuric E1-DN mice when compared to wild-type mice (423 nm versus 613 nm,  $P = 0.013$ , Mann-Whitney  $U$  test,  $n = 9-10$  glomeruli per group) (Figure 6(e)).

#### 4. Discussion

This study describes the development of albuminuria in relation to hyperglycaemia in the diabetic E1-DN mice, a transgenic mouse model expressing kinase-negative EGF-R in pancreatic islets [31], and characterizes the pathologic changes in glomeruli including mesangial expansion and glomerular sclerosis, thickening of the GBM and widening of foot processes in albuminuric mice. Increased apoptosis was

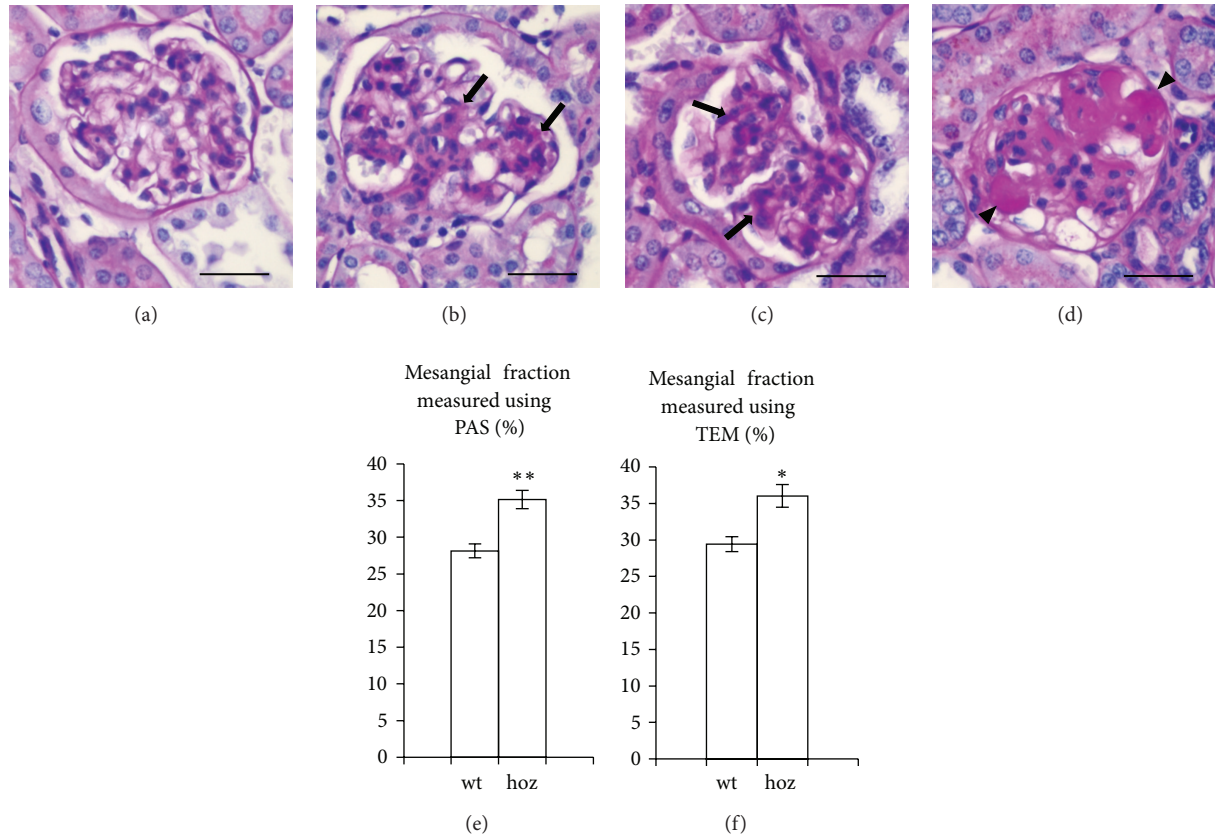


FIGURE 2: E1-DN mice present mesangial expansion and glomerular sclerosis. (a) Periodic acid-Schiff (PAS) staining of normal glomerulus of the wild-type mouse aged 50 weeks. ((b), (c)) Global mesangial expansion (arrows) is observed by PAS staining in the homozygous E1-DN mice aged 20 weeks (b) and 40 weeks (c). (d) Global nodular sclerosis (arrowheads) is seen in an E1-DN homozygous mouse aged 50 weeks. (e) The percentage of mesangial area in the glomerular tuft determined by morphometry of PAS-stained histological sections indicates an increase of 25% in the homozygous (hoz) E1-DN mice when compared to wild-type (wt) mice ( $n = 30$  glomeruli from three 50 weeks old wild-type mice and  $n = 70$  glomeruli from seven 20–50 weeks old homozygous mice). (f) Morphometric analysis performed on images obtained by transmission electron microscopy (TEM) confirms the increase of mesangial volume fraction by 22% in the glomeruli of E1-DN homozygous mice ( $n = 14$  glomeruli from two 50 weeks old wild-type mice and  $n = 38$  glomeruli from six 20–50 weeks old homozygous mice). In ((e), (f)), bars show mean  $\pm$  SEM. \*\* $P < 0.01$ , \* $P < 0.05$ , Student's  $t$ -test. Scale bar: 25  $\mu$ m.

identified as one mechanism contributing to glomerular injury. In addition to glomerular changes, the E1-DN mice showed flattened tubular epithelium with dilated lumens and increased proliferation of tubular cells.

The kinase-negative EGF-R is expressed in the  $\beta$ -cells of the pancreatic islets, and it functions in a dominant negative manner, reducing phosphorylation of the endogenous EGF-R in response to EGF family ligands, resulting in a significantly reduced  $\beta$ -cell mass, low insulin production and subsequently high blood glucose, and early-onset diabetes [31]. The renal phenotype we now report is purely secondary to the long-acting hyperglycaemia. As blood glucose levels were higher in male E1-DN mice when compared to females, and male mice are generally more prone to renal injury, only male mice were examined in this study.

The homozygous E1-DN mice developed substantial albuminuria. The mean AER was 2.5-fold higher in the homozygous E1-DN mice compared to the wild-type littermates already at the age of 10 weeks and nearly five-fold higher

at 20 weeks. The most severely affected mice had over 10-fold increase in AER. The individual variation in the levels of albuminuria can be explained by the variation in the blood glucose levels, as AER and blood glucose correlated at the age of 20 weeks. This reflects also the human diabetes, where hyperglycaemia is the main risk factor for diabetic nephropathy, as shown in several clinical studies [36, 37]. Intracellular excess of glucose is known to result in the formation of reactive oxygen species, which in turn cause inflammation and formation of advanced glycosylation end products [38].

Histological analyses revealed mesangial expansion and tubular changes in diabetic E1-DN mice. Mesangial expansion is an important factor in the progression of diabetic nephropathy [15], and mainly due to mesangial matrix accumulation, which can eventually lead to formation of nodular sclerosis, called Kimmelstiel-Wilson nodules [16]. The most severely affected E1-DN mice developed glomerular sclerosis resembling human diabetic glomerulopathy. Also tubular changes belong to the histological features of human diabetic

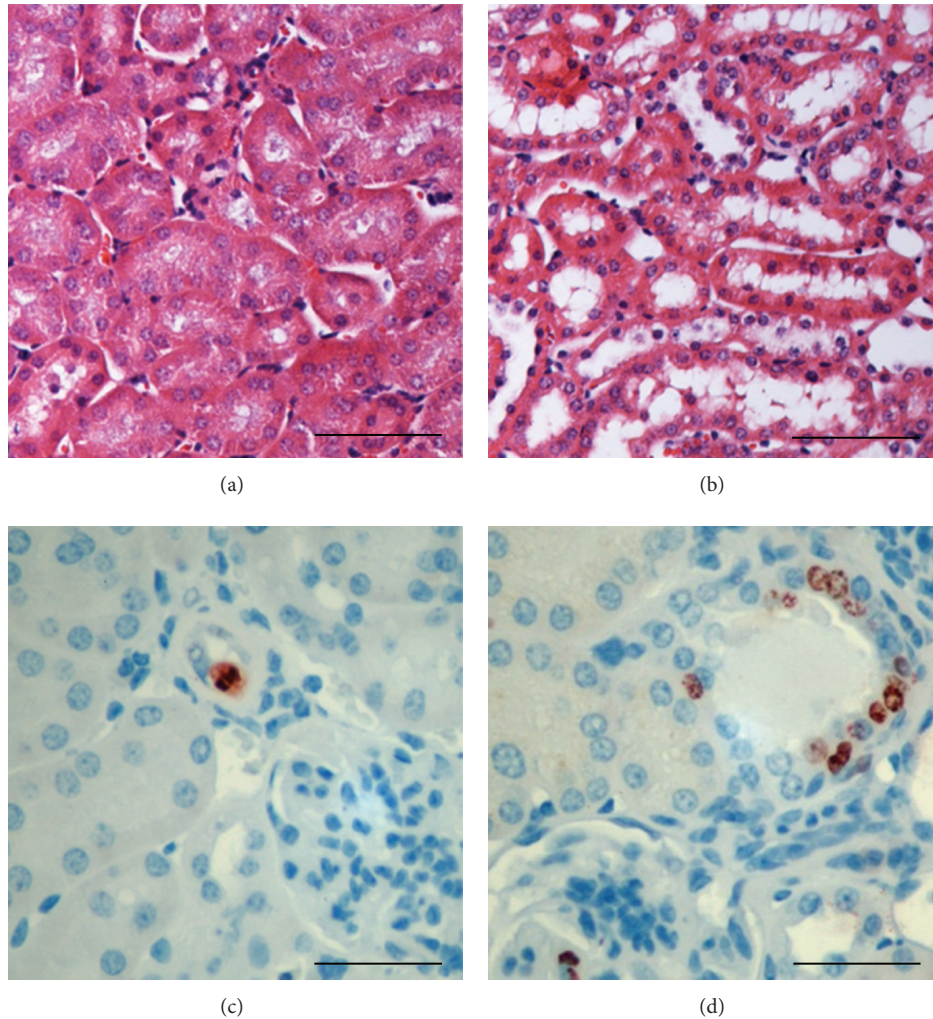


FIGURE 3: Renal tubules of E1-DN mice show morphological changes and increased proliferation. ((a), (b)) Hematoxylin and eosin staining shows flattened tubular epithelial cells in the albuminuric E1-DN homozygous mice (b) when compared to normal tall cuboidal epithelium in the wild-type mice (a). ((c), (d)) Immunostaining for Ki-67 reveals only occasional proliferating cells in the wild-type mice (c), whereas in the albuminuric E1-DN homozygous mice groups of proliferating cells are observed (d). Scale bar: 50  $\mu\text{m}$  ((a), (b)); 25  $\mu\text{m}$  ((c), (d)).

nephropathy [12] and have been shown to predict disease progression in patients with type 2 diabetes and overt proteinuria [39]. Increased proliferation of tubular cells, possibly representing an adaptive mechanism to injury, has previously been observed to contribute to the renal enlargement in streptozotocin-induced diabetes in rats [40] and has been detected also in db/db mice [41]. The data is in line with the results of this study, showing increased proliferation in the tubules of the albuminuric E1-DN mice.

Increased glomerular apoptosis has previously been observed in kidney samples of human patients with diabetes [23] and streptozotocin-treated diabetic rats [42]. Further, reactive oxygen species have been shown to mediate podocyte apoptosis in the db/db mouse model [43]. We observed an increased number of apoptotic cells in the glomeruli of homozygous E1-DN mice and found that the apoptotic cells were podocytes. Apoptosis was rare in both diabetic and control

mice, but as podocytes are terminally differentiated cells, even a small increase in the rate of apoptosis could affect the development of glomerular injury. Another mechanism for podocyte loss in diabetes is detachment. A recent study [22] described severe disruption and detachment of podocyte foot processes in patients with type 1 diabetes, leading to denuded areas of GBM, previously described in focal segmental glomerulosclerosis [44], and considered as part of the process leading to glomerular sclerosis [45]. In the E1-DN mice, no denuded areas of GBM were observed. However, podocyte foot process widening, a known feature of diabetic nephropathy [18, 19], was evident in the most albuminuric E1-DN mice. In addition, structural analysis by electron microscopy revealed thickening of the GBM, which is a well-documented and early finding in human diabetic nephropathy [13, 15]. The measurements of the thickness of the GBM were performed on areas where the GBM was of regular shape, but in

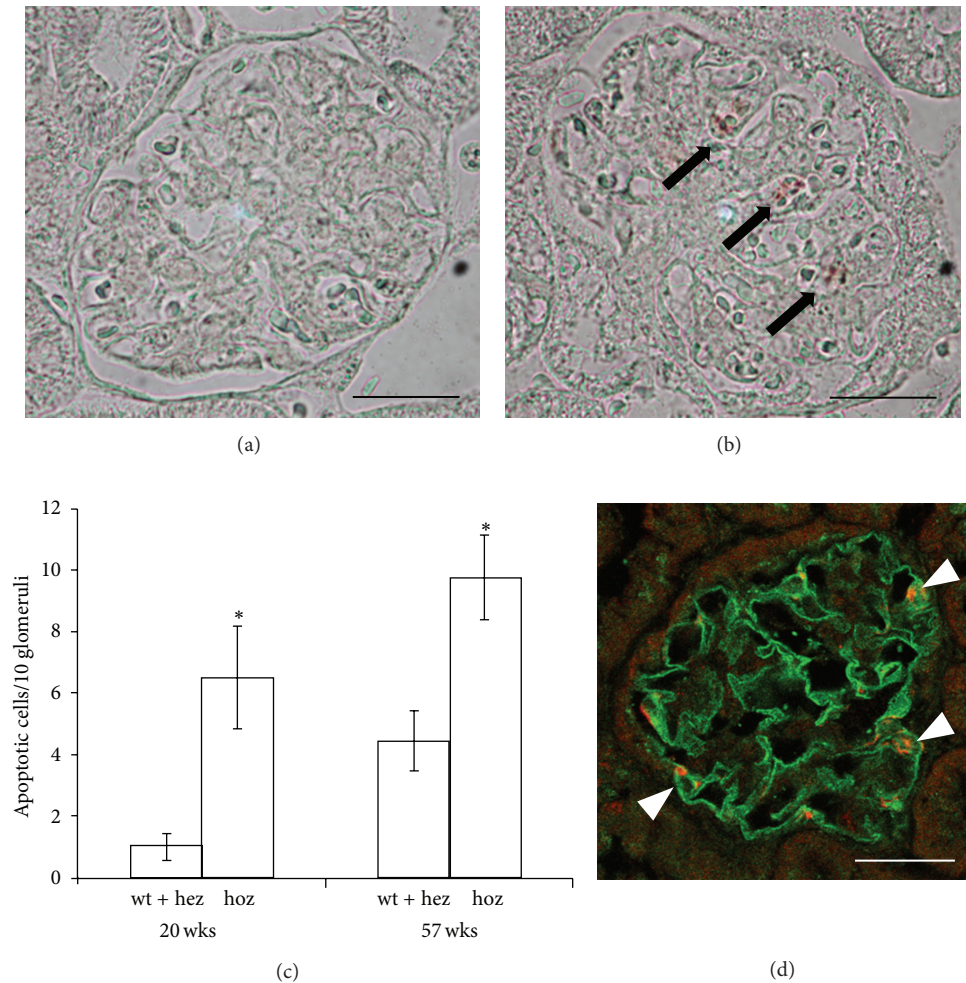


FIGURE 4: E1-DN mice show increased podocyte apoptosis. ((a), (b)) Staining for cleaved caspase-3 was used to identify apoptotic cells (arrows) in the glomeruli of wild-type (a) and homozygous E1-DN mice (b). (c) Apoptosis of glomerular cells is detected more often in the homozygous (hoz) E1-DN mice when compared to heterozygous (hez) and wild-type (wt) mice. Bars show the mean number of apoptotic cells per 10 glomeruli  $\pm$  SEM,  $n = 4-8$  mice/group. \* $P < 0.02$ , Mann-Whitney  $U$  test. (d) Confocal microscopy of kidney sections of 20 weeks old homozygous E1-DN mice stained for nephrin (green) and cleaved caspase-3 (red) indicates that the apoptotic cells in the glomeruli are podocytes. Scale bar: 25  $\mu$ m.

addition, areas of irregular bulging of the membrane were observed.

The expression of nephrin was found to be decreased in the glomeruli of the albuminuric E1-DN mice, consistent with previous results obtained with the streptozotocin mouse model [46]. Also in human diabetic nephropathy the expression of nephrin protein [47] and mRNA [48] have been reported to be reduced and inversely correlated with the degree of proteinuria [48]. Whether this is causative or secondary to the disease progression and podocyte injury remains to be investigated. However, it has been suggested that the downregulation of nephrin is a selective change, as the expression of podocin, another podocyte protein, has been reported to remain unchanged in diabetes in humans [49], as well as in a diabetic mouse model [46]. Consistent with that, the expression of podocin and ZO-1 were not

altered in immunofluorescence stainings of the E1-DN mouse glomeruli.

When compared to other mouse models of diabetes, E1-DN mice develop substantial albuminuria and glomerular pathology. It is notable that the renal changes are caused by hyperglycaemia instead of direct effects of the EGF-R transgene, and thus the E1-DN mouse model mimics human diabetes with poor glycaemic control. In addition, there is no need to consider the possible toxic effects on kidney, like in one of the most widely used murine models of diabetes, streptozotocin-induced destruction of pancreatic  $\beta$ -cells. The other widely used model, the db/db mouse, is insulin resistant and diabetic due to a mutation in the leptin receptor gene. Db/db mice serve as a good model for type 2 diabetes and albuminuria but do not develop severe glomerulopathy [25]. E1-DN mice are hypoinsulinemic [31] and show similarities

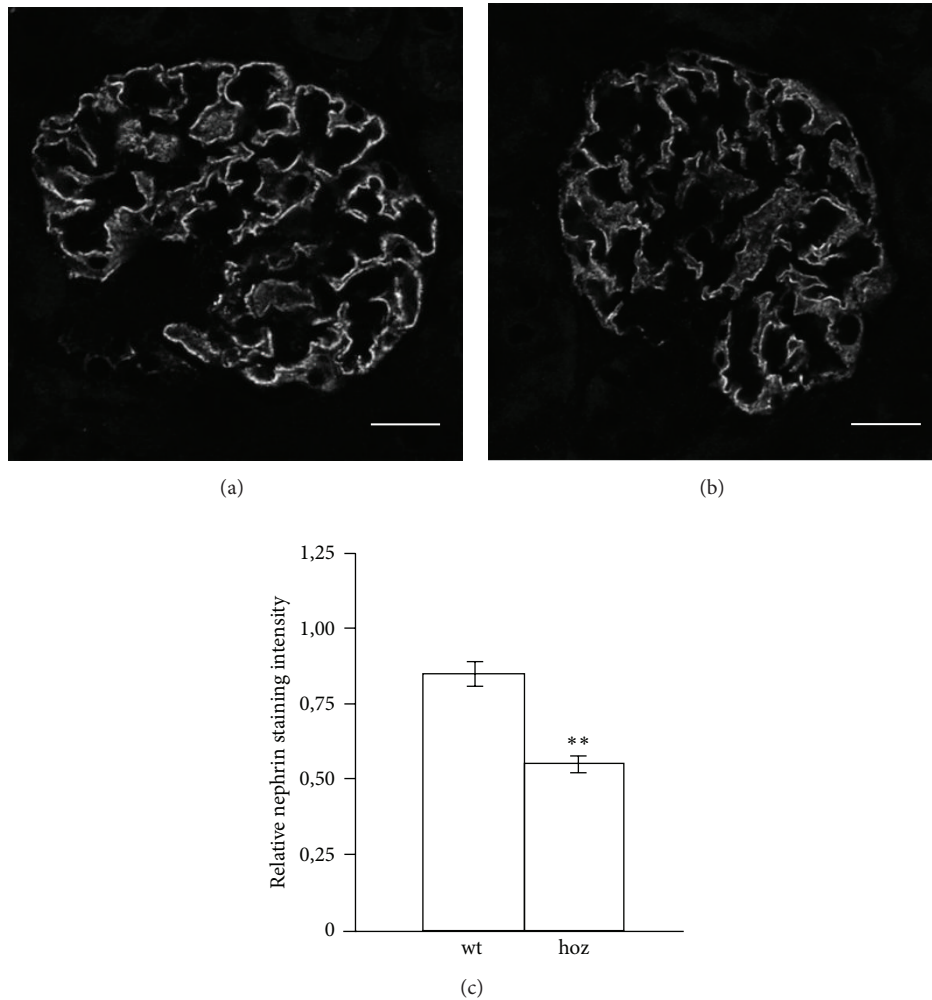


FIGURE 5: Expression of nephrin is reduced in the glomeruli of E1-DN mice. ((a), (b)) Confocal microscopy of wild-type (wt) (a) and homozygous (hoz) (b) E1-DN mouse kidney sections stained for nephrin. (c) Quantification of the expression level of nephrin in two wild-type mice and three albuminuric homozygous mice, five glomeruli per mice, reveals that the expression of nephrin is significantly lower in the E1-DN homozygous mice. Bars show mean  $\pm$  SEM. \*\* $P < 0.01$ , Student's  $t$ -test. Scale bar: 20  $\mu$ m.

with the OVE26 and Akita mice. The OVE26 is a promising mouse model of diabetic renal disease, overexpressing calmodulin in the pancreatic  $\beta$ -cells in mice in FVB background, and presenting high albuminuria, as well as severe glomerular pathology [27]. The Akita mice have a spontaneous mutation in insulin 2 gene and were originally described to have a modest renal phenotype in C57BL/6 strain [50]. When Akita mice were crossed to FVB/NJ background, they, however, developed high proteinuria and moderate mesangial expansion [26]. Recent studies thus indicate that the background strain of the mouse model is extremely important for the development of renal injury and that the FVB background is susceptible for renal disease. The FVB background may contribute to the relatively severe phenotype of the E1-DN mice.

One disadvantage of the E1-DN model is the large phenotypic variation between the individual mice, although the intensity of the renal phenotype is directly correlated

to the blood glucose levels. Thus, designing an intervention study with the E1-DN mouse model would require a large number of mice. Histological and structural changes develop relatively late; the most severe changes reported here were detected at the age of 50 weeks. This is common for many of the mouse models and not surprising, considering that overt human diabetic nephropathy usually develops after 15 to 20 years of diabetes duration.

## 5. Conclusions

The hyperglycaemic E1-DN mice develop substantial albuminuria and histological and structural changes including mesangial expansion, thickening of the GBM, podocyte foot process widening, and altered tubular epithelial cell morphology and proliferation. Reduced expression of nephrin and increased apoptosis of podocytes might contribute to the development of glomerular injury. Altogether, these changes

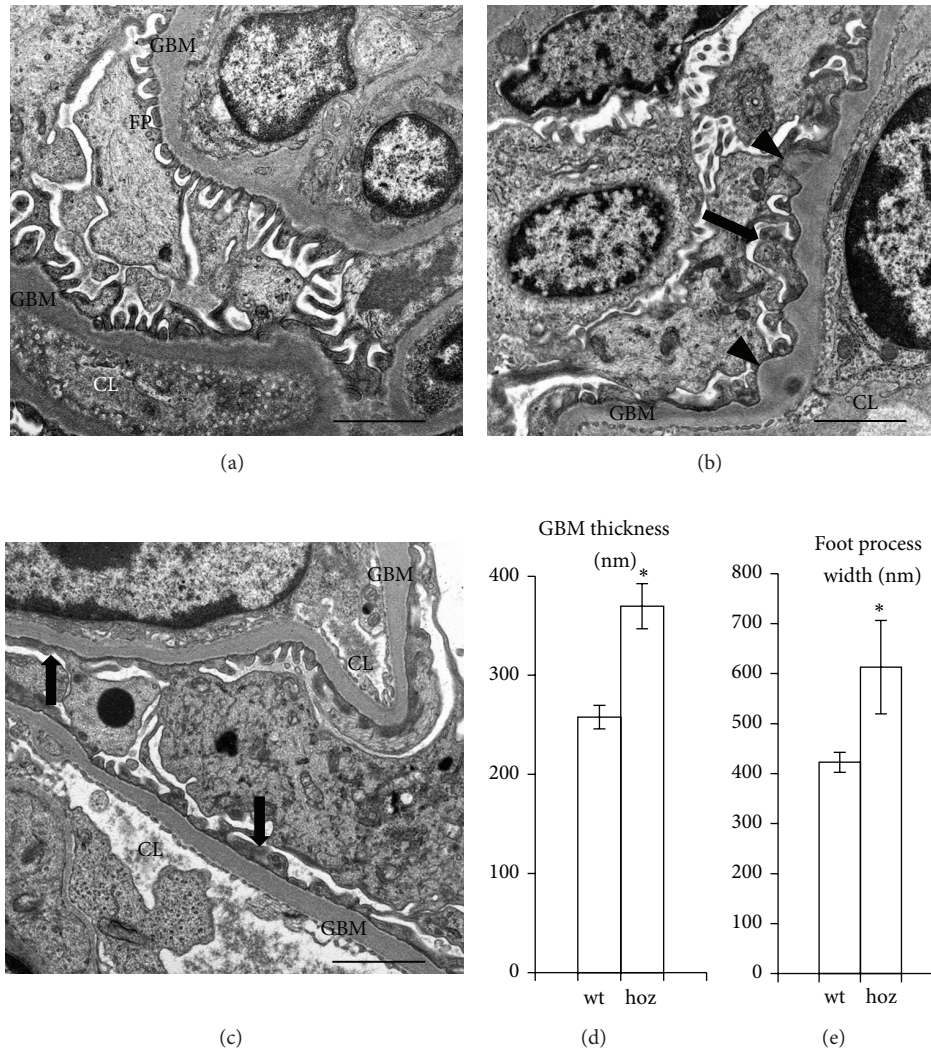


FIGURE 6: Electron microscopy indicates glomerular basement membrane thickening and podocyte foot process effacement in E1-DN mice. (a) In wild-type mouse (age 50 weeks) podocyte foot processes (FP) line regularly the glomerular basement membrane (GBM) around the capillary loops (CL). (b) In the E1-DN homozygous mouse (age 40 weeks) irregular thickening of the GBM (arrowheads) and podocyte foot process widening (arrow) are observed. (c) Foot process widening (arrows) is observed in 50 weeks old E1-DN homozygous mouse. (d) GBM is thicker in the E1-DN homozygous (hoz) mice (age 40–50 weeks) compared to the wild-type (wt) mice (age 50 weeks). The thickness of the GBM was calculated from three glomeruli in two wild-type and eight glomeruli in three homozygous E1-DN mice. (e) Podocyte foot processes are wider in the homozygous E1-DN mice (40–50 weeks of age) compared to the wild-type mice (50 weeks of age). Foot process width was calculated from 10 glomeruli in two wild-type and 9 glomeruli in three homozygous E1-DN mice. Bars show mean ± SEM. \* $P < 0.025$ , Mann-Whitney  $U$  test. Scale bar: 2  $\mu\text{m}$ .

are typical of human diabetic nephropathy, and the E1-DN mice can serve as a good model to study the pathogenesis of the diabetic renal disease.

**Conflict of Interests**

The authors declare that they have no conflict of interests.

**Acknowledgments**

The authors thank Marcel Messing, Niina Ruoho, Kirsi Lintula, Ulla Kiiski, and Tiiu Arümäe for skillful technical

assistance and the Paediatric Graduate School of the University of Helsinki for support. Biomedicum Imaging Unit is thanked for help with microscopy and Svetlana Zueva and Fang Zhao for help in electron microscopy. Dr. Kathryn White (Newcastle University, Newcastle upon Tyne, UK) and Dr. Panu Kovanen (University of Helsinki, Helsinki, Finland) are acknowledged for sharing their expertise in measuring the mesangial volume fraction and in analysing kidney histology, respectively. This study was financially supported by the European Research Council (242820; Sanna Lehtonen), the Academy of Finland (131255, 218021, 255551; Sanna Lehtonen), the Diabetes Research Foundation (Sanna Lehtonen),

the Helsinki University Central Hospital Research Grant (Jukka Tienari), the Foundation for Paediatric Research (Sanna Lehtonen), Kyllikki and Uolevi Lehtikoinen Foundation (Mervi E. Hyvönen), National Graduate School of Clinical Investigation (Mervi E. Hyvönen), the University of Helsinki Research Foundation (Vincent Dumont), and the Helsinki Biomedical Graduate Program (Vincent Dumont).

## References

- [1] G. Pambianco, T. Costacou, D. Ellis, D. J. Becker, R. Klein, and T. J. Orchard, "The 30-year natural history of type 1 diabetes complications: the Pittsburgh epidemiology of diabetes complications study experience," *Diabetes*, vol. 55, no. 5, pp. 1463–1469, 2006.
- [2] The Diabetes Control and Complications Trial Research Group, "The effect of intensive treatment of diabetes on the development and progression of long-term complications in insulin-dependent diabetes mellitus. The diabetes control and complications trial research group," *The New England Journal of Medicine*, vol. 329, pp. 977–986, 1993.
- [3] P. Hovind, L. Tarnow, K. Rossing et al., "Decreasing incidence of severe diabetic microangiopathy in type 1 diabetes," *Diabetes Care*, vol. 26, no. 4, pp. 1258–1264, 2003.
- [4] K. Borch-Johnsen and S. Kreiner, "Proteinuria: value as predictor of cardiovascular mortality in insulin dependent diabetes mellitus," *British Medical Journal*, vol. 294, no. 6588, pp. 1651–1654, 1987.
- [5] P.-H. Groop, M. C. Thomas, J. L. Moran et al., "The presence and severity of chronic kidney disease predicts all-cause mortality in type 1 diabetes," *Diabetes*, vol. 58, no. 7, pp. 1651–1658, 2009.
- [6] A. Kramer, V. Stel, C. Zoccali et al., "An update on renal replacement therapy in Europe: ERA-EDTA registry data from 1997 to 2006," *Nephrology Dialysis Transplantation*, vol. 24, no. 12, pp. 3557–3566, 2009.
- [7] E. Ritz, I. Rychlik, F. Locatelli, and S. Halimi, "End-stage renal failure in type 2 diabetes: a medical catastrophe of worldwide dimensions," *The American Journal of Kidney Diseases*, vol. 34, no. 5, pp. 795–808, 1999.
- [8] G. C. Viberti, R. J. Jarrett, R. D. Hill, A. Argyropoulos, U. Mahmud, and H. Keen, "Microalbuminuria as a predictor of clinical nephropathy in insulin-dependent diabetes mellitus," *The Lancet*, vol. 1, no. 8287, pp. 1430–1432, 1982.
- [9] M. L. Caramori, P. Fioretto, and M. Mauer, "The need for early predictors of diabetic nephropathy risk: is albumin excretion rate sufficient?" *Diabetes*, vol. 49, no. 9, pp. 1399–1408, 2000.
- [10] P. Hovind, P. Rossing, L. Tarnow, H. Toft, J. Parving, and H.-H. Parving, "Remission of nephrotic-range albuminuria in type 1 diabetic patients," *Diabetes Care*, vol. 24, no. 11, pp. 1972–1977, 2001.
- [11] M. E. Molitch, M. Steffes, W. Sun et al., "Development and progression of renal insufficiency with and without albuminuria in adults with type 1 diabetes in the diabetes control and complications trial and the epidemiology of diabetes interventions and complications study," *Diabetes Care*, vol. 33, no. 7, pp. 1536–1543, 2010.
- [12] P. Fioretto and M. Mauer, "Histopathology of diabetic nephropathy," *Seminars in Nephrology*, vol. 27, no. 2, pp. 195–207, 2007.
- [13] R. Østeeby, "Morphometric studies of the peripheral glomerular basement membrane in early juvenile diabetes. I. Development of initial basement membrane thickening," *Diabetologia*, vol. 8, no. 2, pp. 84–92, 1972.
- [14] S. M. Mauer, M. W. Steffes, E. N. Ellis, D. E. Sutherland, D. M. Brown, and F. C. Goetz, "Structural-functional relationships in diabetic nephropathy," *The Journal of Clinical Investigation*, vol. 74, no. 4, pp. 1143–1155, 1984.
- [15] P. Fioretto, M. W. Steffes, D. E. Sutherland, and M. Mauer, "Sequential renal biopsies in insulin-dependent diabetic patients: structural factors associated with clinical progression," *Kidney International*, vol. 48, no. 6, pp. 1929–1935, 1995.
- [16] P. Kimmelstiel and C. Wilson, "Inter-capillary lesions in the glomeruli of the kidney," *The American Journal of Pathology*, vol. 12, no. 1, pp. 83–98, 1936.
- [17] R. Bader, H. Bader, K. E. Grund, S. Mackensen-Haen, H. Christ, and A. Bohle, "Structure and function of the kidney in diabetic glomerulosclerosis. Correlations between morphological and functional parameters," *Pathology Research and Practice*, vol. 167, no. 2–4, pp. 204–216, 1980.
- [18] E. N. Ellis, M. W. Steffes, B. Chavers, and S. M. Mauer, "Observations of glomerular epithelial cell structure in patients with type I diabetes mellitus," *Kidney International*, vol. 32, no. 5, pp. 736–741, 1987.
- [19] U. B. Berg, T. B. Torbjörnsdotter, G. Jaremko, and B. Thalme, "Kidney morphological changes in relation to long-term renal function and metabolic control in adolescents with IDDM," *Diabetologia*, vol. 41, no. 9, pp. 1047–1056, 1998.
- [20] M. W. Steffes, D. Schmidt, R. McCrery et al., "Glomerular cell number in normal subjects and in type 1 diabetic patients," *Kidney International*, vol. 59, no. 6, pp. 2104–2113, 2001.
- [21] M. E. Pagtalunan, P. L. Miller, S. Jumping-Eagle et al., "Podocyte loss and progressive glomerular injury in type II diabetes," *The Journal of Clinical Investigation*, vol. 99, no. 2, pp. 342–348, 1997.
- [22] M. Toyoda, B. Najafian, Y. Kim, M. L. Caramori, and M. Mauer, "Podocyte detachment and reduced glomerular capillary endothelial fenestration in human type 1 diabetic nephropathy," *Diabetes*, vol. 56, no. 8, pp. 2155–2160, 2007.
- [23] D. Verzola, M. T. Gandolfo, F. Ferrario et al., "Apoptosis in the kidneys of patients with type II diabetic nephropathy," *Kidney International*, vol. 72, no. 10, pp. 1262–1272, 2007.
- [24] E. H. Leiter, "Multiple low-dose streptozotocin-induced hyperglycemia and insulinitis in C57BL mice: influence of inbred background, sex, and thymus," *Proceedings of the National Academy of Sciences of the United States of America*, vol. 79, no. 2, pp. 630–634, 1982.
- [25] K. Sharma, P. McCue, and S. R. Dunn, "Diabetic kidney disease in the db/db mouse," *American Journal of Physiology—Renal Physiology*, vol. 284, no. 6, pp. F1138–F1144, 2003.
- [26] J.-H. Chang, S.-Y. Paik, L. Mao et al., "Diabetic kidney disease in FVB/NJ akita mice: temporal pattern of kidney injury and urinary nephrin excretion," *PLoS ONE*, vol. 7, no. 4, Article ID e33942, 2012.
- [27] S. Zheng, W. T. Noonan, N. S. Metreveli et al., "Development of late-stage diabetic nephropathy in OVE26 diabetic mice," *Diabetes*, vol. 53, no. 12, pp. 3248–3257, 2004.
- [28] H. J. Zhao, S. Wang, H. Cheng et al., "Endothelial nitric oxide synthase deficiency produces accelerated nephropathy in diabetic mice," *Journal of the American Society of Nephrology*, vol. 17, no. 10, pp. 2664–2669, 2006.
- [29] M. D. Breyer, E. Böttinger, F. C. Brosius III et al., "Mouse models of diabetic nephropathy," *Journal of the American Society of Nephrology*, vol. 16, no. 1, pp. 27–45, 2005.
- [30] C. E. Alpers and K. L. Hudkins, "Mouse models of diabetic nephropathy," *Current Opinion in Nephrology and Hypertension*, vol. 20, no. 3, pp. 278–284, 2011.

- [31] P. J. Miettinen, J. Ustinov, P. Ormio et al., "Downregulation of EGF receptor signaling in pancreatic islets causes diabetes due to impaired postnatal  $\beta$ -cell growth," *Diabetes*, vol. 55, no. 12, pp. 3299–3308, 2006.
- [32] E. Hakonen, J. Ustinov, I. Mathijs et al., "Epidermal growth factor (EGF)-receptor signalling is needed for murine beta cell mass expansion in response to high-fat diet and pregnancy but not after pancreatic duct ligation," *Diabetologia*, vol. 54, no. 7, pp. 1735–1743, 2011.
- [33] M. E. Hyvönen, P. Saurus, A. Wasik et al., "Lipid phosphatase SHIP2 downregulates insulin signalling in podocytes," *Molecular and Cellular Endocrinology*, vol. 328, no. 1-2, pp. 70–79, 2010.
- [34] R. Østerby, H. J. G. Gundersen, G. Nyberg, and M. Aurell, "Advanced diabetic glomerulopathy: quantitative structural characterization of nonoccluded glomeruli," *Diabetes*, vol. 36, no. 5, pp. 612–619, 1987.
- [35] J. G. van den Berg, M. A. van den Bergh Weerman, K. J. M. Assmann, J. J. Weening, and S. Florquin, "Podocyte foot process effacement is not correlated with the level of proteinuria in human glomerulopathies," *Kidney International*, vol. 66, no. 5, pp. 1901–1906, 2004.
- [36] D. M. Nathan, B. Zinman, P. A. Cleary, and et al, "Modern-day clinical course of type 1 diabetes mellitus after 30 years' duration: the diabetes control and complications trial/epidemiology of diabetes interventions and complications and Pittsburgh epidemiology of diabetes complications experience (1983–2005)," *Archives of Internal Medicine*, vol. 169, no. 14, pp. 1307–1316, 2009.
- [37] P. Reichard, M. Pihl, U. Rosenqvist, and J. Sule, "Complications in IDDM are caused by elevated blood glucose level: the Stockholm Diabetes Intervention Study (SDIS) at 10-year follow up," *Diabetologia*, vol. 39, no. 12, pp. 1483–1488, 1996.
- [38] M. Brownlee, "Biochemistry and molecular cell biology of diabetic complications," *Nature*, vol. 414, no. 6865, pp. 813–820, 2001.
- [39] T. Okada, T. Nagao, H. Matsumoto, Y. Nagaoka, T. Wada, and T. Nakao, "Histological predictors for renal prognosis in diabetic nephropathy in diabetes mellitus type 2 patients with overt proteinuria," *Nephrology*, vol. 17, no. 1, pp. 68–75, 2012.
- [40] R. Rasch and J. O. R. Nørgaard, "Renal enlargement: comparative autoradiographic studies of <sup>3</sup>H-thymidine uptake in diabetic and uninephrectomized rats," *Diabetologia*, vol. 25, no. 3, pp. 280–287, 1983.
- [41] M. S. Mozaffari, R. Abdelsayed, J. Y. Liu, I. Zakhary, and B. Baban, "Renal distal tubule proliferation and increased aquaporin 2 level but decreased urine osmolality in db/db mouse: treatment with chromium picolinate," *Experimental and Molecular Pathology*, vol. 92, no. 1, pp. 54–58, 2012.
- [42] S. Menini, C. Iacobini, G. Oddi et al., "Increased glomerular cell (podocyte) apoptosis in rats with streptozotocin-induced diabetes mellitus: role in the development of diabetic glomerular disease," *Diabetologia*, vol. 50, no. 12, pp. 2591–2599, 2007.
- [43] K. Susztak, A. C. Raff, M. Schiffer, and E. P. Böttinger, "Glucose-induced reactive oxygen species cause apoptosis of podocytes and podocyte depletion at the onset of diabetic nephropathy," *Diabetes*, vol. 55, no. 1, pp. 225–233, 2006.
- [44] E. Grishman and J. Churg, "Focal glomerular sclerosis in nephrotic patients: an electron microscopic study of glomerular podocytes," *Kidney International*, vol. 7, no. 2, pp. 111–122, 1975.
- [45] W. Kriz, N. Gretz, and K. V. Lemley, "Progression of glomerular diseases: is the podocyte the culprit?" *Kidney International*, vol. 54, no. 3, pp. 687–697, 1998.
- [46] J. Menne, M. Meier, J.-K. Park et al., "Nephrin loss in experimental diabetic nephropathy is prevented by deletion of protein kinase C alpha signaling in-vivo," *Kidney International*, vol. 70, no. 8, pp. 1456–1462, 2006.
- [47] S. Doublier, G. Salvidio, E. Lupia et al., "Nephrin expression is reduced in human diabetic nephropathy: evidence for a distinct role for glycated albumin and angiotensin II," *Diabetes*, vol. 52, no. 4, pp. 1023–1030, 2003.
- [48] R. Langham, D. Kelly, A. Cox et al., "Proteinuria and the expression of the podocyte slit diaphragm protein, nephrin, in diabetic nephropathy: effects of angiotensin converting enzyme inhibition," *Diabetologia*, vol. 45, no. 11, pp. 1572–1576, 2002.
- [49] A. Benigni, E. Gagliardini, S. Tomasoni et al., "Selective impairment of gene expression and assembly of nephrin in human diabetic nephropathy," *Kidney International*, vol. 65, no. 6, pp. 2193–2200, 2004.
- [50] S. B. Gurley, C. L. Mach, J. Stegbauer et al., "Influence of genetic background on albuminuria and kidney injury in Ins2(+)/C96Y) (Akita) mice," *American Journal of Physiology: Renal Physiology*, vol. 298, no. 3, pp. F788–F795, 2010.

## Research Article

# Effect of Ovariectomy on Stimulating Intracortical Remodeling in Rats

Chun Lei Li,<sup>1</sup> Xi Ling Liu,<sup>1</sup> Wei Xin Cai,<sup>2</sup> Weijia William Lu,<sup>3</sup>  
Roger A. Zwahlen,<sup>2</sup> and Li Wu Zheng<sup>1</sup>

<sup>1</sup> Discipline of Oral Diagnosis & Polyclinics, Faculty of Dentistry, The University of Hong Kong, Prince Philip Dental Hospital, 34 Hospital Road, Hong Kong

<sup>2</sup> Discipline of Oral and Maxillofacial Surgery, Faculty of Dentistry, The University of Hong Kong, Hong Kong

<sup>3</sup> Department of Orthopedics & Traumatology, Li Ka Shing Faculty of Medicine, The University of Hong Kong, Hong Kong

Correspondence should be addressed to Li Wu Zheng; lwzheng@hku.hk

Received 2 July 2014; Revised 29 August 2014; Accepted 5 September 2014; Published 21 September 2014

Academic Editor: Monica Fedele

Copyright © 2014 Chun Lei Li et al. This is an open access article distributed under the Creative Commons Attribution License, which permits unrestricted use, distribution, and reproduction in any medium, provided the original work is properly cited.

**Objective.** Technically primates and dogs represent ideal models to investigate diseases characterized by abnormal intracortical remodeling. High expenses and ethical issues, however, restrict the use of those animals in research. Rodent models have been used as alternatives instead, but their value is limited, if none, because these animals lack intracortical bone remodeling. This study aimed at investigating the effect of ovariectomy onto the stimulation of intracortical remodeling in rat mandibles. **Materials and Methods.** Sixteen 12-week-old Sprague-Dawley (SD) female rats were randomly assigned into two groups, receiving either ovariectomy or sham operation. All the rats were sacrificed 18 weeks postoperatively. The entire mandibles were harvested for microcomputed tomography (micro-CT) and histomorphometric assessments. **Results.** Micro-CT examination showed significantly decreased bone mineral density ( $0.95 \pm 0.01$  versus  $1.01 \pm 0.02$  g/cm<sup>3</sup>,  $P < 0.001$ ) and bone volume ( $65.78 \pm 5.45$  versus  $87.41 \pm 4.12\%$ ,  $P < 0.001$ ) in ovariectomy group. Histomorphometric assessment detected a sixfold increased intracortical bone remodeling as well as an increased bone modeling in mandibles of ovariectomized rats. **Conclusion.** For the first time, to the authors' knowledge, it was detected that ovariectomy stimulates intracortical remodeling in rat mandibles. This animal model might be of use to study various bone diseases associated with an abnormal intracortical remodeling process.

## 1. Introduction

Bone remodeling plays a key role to maintain the skeletal functional integrity. It is a site and time-specific event combining bone resorption and formation. Higher mammals with the harversian system undergo both cancellous and intracortical bone remodeling, while lower mammals without harversian system, such as mice and rats, do not normally undergo intracortical remodeling [1–3].

Ovariectomized (OVX) rodents are a well-established animal model in osteoporosis studies [4, 5]. Apart from trabecular bone turnover changes [6, 7], recent studies reported that ovariectomy may induce intracortical remodeling in long bones [8, 9]. Whereas Kubek et al. found out that ovariectomy induced intracortical remodeling of jawbones in mice [10],

stimulation of intracortical remodeling in rats has not yet been investigated, so far.

The intracortical remodeling rate of human jawbones is around 20 times higher than that of iliac crest [11]. Some bone diseases associated with abnormal bone remodeling such as bisphosphonate related osteonecrosis of the jaws (BRONJ) always preferentially affect jawbones [12]. To study this disease *in vivo*, an adequate animal model therefore is of paramount interest. Even though primates and dogs represent ideal models, high expenses and ethical issues do restrict their use. Rodent models have been widely used to investigate bone diseases, but lack of intracortical bone remodeling [13] limited their value in investigating bone diseases with abnormal bone remodeling.

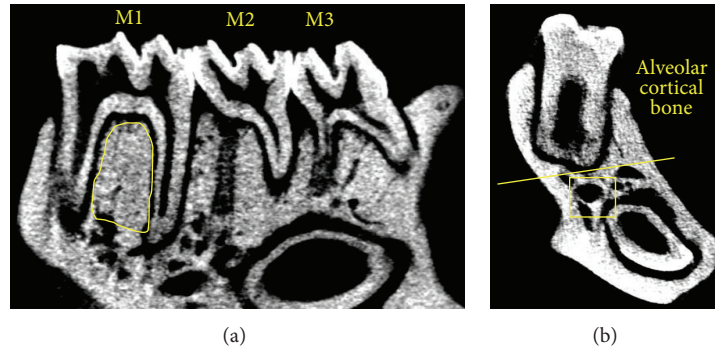


FIGURE 1: ROI selection in micro-CT and histomorphometry assessment. (a) Trabecular bone inside the circle is selected as the ROI in micro-CT assessment. (b) The bone area above the yellow line is defined as alveolar cortical bone; nonalveolar cortical bone is defined as the area below the yellow line except for trabecular bone (square).

This study investigated the stimulating effect of ovariectomy onto intracortical bone remodeling in rat mandibles.

## 2. Materials and Methods

**2.1. Animal Care.** The animal experiment was approved by the Committee on Use Live Animal for Teaching and Research, The University of Hong Kong. All rats were held in a 12:12 h light-dark cycle with each rat separated in a metal cage at 25 degree Celsius room temperature in the Laboratory Animal Unit of the University of Hong Kong. All animals were allowed free access to water and standard rodent diet. Their general well-being was monitored by a 24 h closed circuit television in the holding room during the entire experimental period.

**2.2. Ovariectomy (OVX) Surgery.** Sixteen 12-week-old, female Sprague-Dawley (SD) rats were randomly assigned into an OVX or a control group, with 8 in each. After a 7-day acclimatization period, the rats of the OVX group underwent a bilateral ovariectomy according to our standardized protocol already published elsewhere [14]. In brief, under general anesthesia, a 2 cm abdominal skin incision was performed. Using artery forceps, the ovarian fat pad was gently grasped and the ovaries were exposed. After removing the bilateral ovaries, the fat pad was repositioned into the abdomen. Wound closure was performed in two layers, adapting the muscle layer with single stitch sutures (Vicryl 5/0, Johnsons and Johnson, Hong Kong) and the skin layer with stainless steel wound clips. The control group animals underwent a similar procedure without removing the ovaries. All rats were given meloxicam (5 mg in 250 mL drinking water, Metacam, Boehringer Ingelheim, Germany) for 5 days postoperatively for pain relief [14].

**2.3. Fluorochrome Sequential Labeling.** Fluorochrome labeling using calcein green (15 mg/kg; C0875, Sigma-Aldrich, Saint Louis Mo, USA) and alizarin complexone (30 mg/kg; A3882, Sigma-Aldrich, Saint Louis, MO, USA) was performed 10 days and 1 day before the sacrifice, respectively. The

reagents were dissolved in sodium bicarbonate solution and administrated subcutaneously [15].

**2.4. Sample Preparation.** All rats were sacrificed 18 weeks postoperatively. Mandibles were harvested entirely and the attached soft tissue was carefully removed. All samples were fixed in 10% neutral buffered formalin solution for 2 days and then transferred to 70% ethanol for further use.

**2.5. Micro-CT Examination.** The changes of trabecular microarchitecture were assessed by micro-CT (SkyScan-1076 X-ray microtomography, SkyScan, Kontich, Belgium) according to the manufacturer's instructions. The X-ray source was supplied with 88 kV voltage and 100  $\mu$ A electrical current. Three-dimensional (3D) images were obtained at a resolution of 18  $\mu$ m/pixel. The raw images were reconstructed and analyzed using CTAn software (CTAn, version 1.12.0, SkyScan, Kontich, Belgium).

Trabecular bone in the interradicular septum of the first molar (M1) was selected as the region of interest (ROI) (Figure 1(a)). Its microstructure was assessed according to the following parameters: bone mineral density (BMD), bone volume/tissue volume (BV/TV), trabecular thickness (Tb.Th), trabecular number (Tb.N), and trabecular separation (Tb.Sp) [16].

**2.6. Histomorphometric Assessment.** Histomorphometric assessment was performed to evaluate the intracortical remodeling. Nondecalcified mandibles were dehydrated in graded ethanol (70%, 95%, and 100%) and embedded in methyl methacrylate (MMA, Technovit 7500, Kulzer, Hamburg, Germany). Mandibles were sectioned (~100  $\mu$ m thick) through the molar region in a mesial-distal direction using a diamond wire saw. The samples were mounted on slides and ground to a thickness of 80  $\mu$ m.

To ensure the measurement was performed at a similar region in all the animals, sections containing the deepest root of first molar in each animal were selected. The sections were examined under fluorescence microscope (Nikon, Tokyo, Japan).

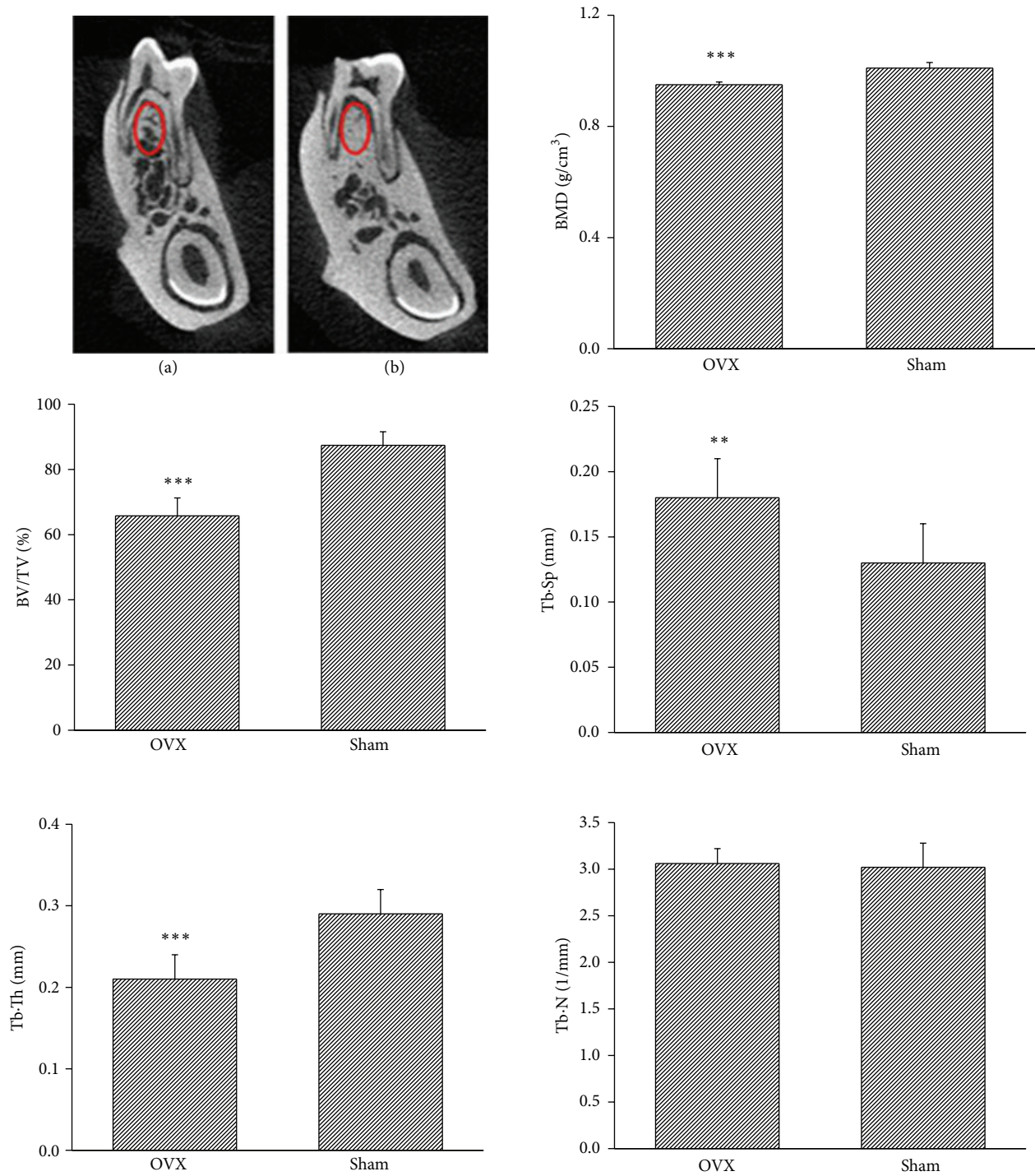


FIGURE 2: OVX changes the microarchitecture in rat mandibles. Micro-CT images show remarkable trabecular bone loss in OVX rats (a) compared with that in the control (b) group. BMD and BV/TV in OVX group are significantly decreased compared to those in control group. Tb·Th decreases and Tb·Sp increases significantly in OVX group. Tb·N shows no significant difference in both groups. BMD: bone mineral density; BV/TV: bone volume/tissue volume; Tb·Th: trabecular thickness; Tb·N: trabecular number; and Tb·Sp: trabecular separation. \*\*  $P < 0.01$  and \*\*\*  $P < 0.001$ .

2.6.1. *Intracortical Remodeling.* The alveolar cortical bone was defined as the area above the root at M1 region; nonalveolar cortical bone was defined as the area below the root except for trabecular bone (Figure 1(b)) [10].

To assess the intracortical remodeling, the total bone area (B.Ar), the bone surface (BS), the total length of the labeled bone surface (LS), the single labeled bone surface (sLS), the double labeled bone surface (dLS), and the mean

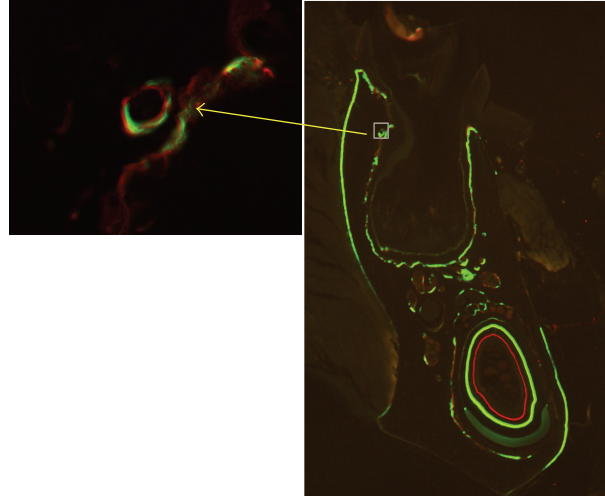


FIGURE 3: Photomicrograph of mandible in OVX rats viewed with fluorescent light. Labeled osteons (indicated by arrow) are found.

interlabel width (Ir.L.Wi) were measured. The mineralizing bone surface (MS) was calculated as  $0.5sLS + dLs$ . Mineral apposition rate (MAR,  $\mu\text{m}/\text{day}$ ) was calculated as  $\text{Ir.L.Wi}/10$  (10 was the interlabel time). For the osteons with only single label, MAR was set as 0.3 [17]. Surface-based bone formation rate (BFR) ( $\mu\text{m}^3/\mu\text{m}^2/\text{day}$ ) was calculated as  $\text{MAR} \times \text{MS}/\text{BS}$ . Intracortical BFR (%/year) was calculated as  $(\text{MAR} \times 0.5\text{BS}/\text{B.Ar}) \times 100 \times 365$ . All measurements were in accordance with a standard protocol [18].

**2.6.2. Bone Modeling.** Periodontal ligament attached bone surfaces were selected to determine whether bone modeling was affected by OVX. The parameters including MAR and BFR ( $\mu\text{m}^3/\mu\text{m}^2/\text{day}$ ) were calculated as described above.

**2.7. Statistical Analysis.** All data were presented as mean values  $\pm$  SD and analyzed by independent *t*-tests and non-parametric tests using IBM SPSS statistics software (version 19.0, IBM Corp, Armonk, NY, USA). The significance level was set as  $P < 0.05$ .

### 3. Results

**3.1. Clinical Examination.** General well-being was defined as normal daily food and water intake, unremarkable behavioral pattern, and normal daily activity of rats during entire experimental period.

**3.2. Micro-CT Examination.** In the control group, the trabecular bone presented as a well-connected network, while in the OVX group the trabecular bone withered and became separated. Quantitative analysis revealed that the BMD ( $P < 0.001$ ) and percentage of bone volume (BV/TV,  $P < 0.001$ ) were significantly decreased in OVX rats compared to those of the control group. The trabecular thickness decreased ( $P < 0.001$ ) whereas the trabecular separation increased ( $P < 0.01$ )

significantly in rats of OVX group. There was an increase in the number of trabeculae in OVX rats but the difference was not significant ( $P = 0.75$ ) (Figure 2).

### 3.3. Histomorphometric Assessment

**3.3.1. Intracortical Remodeling.** In the alveolar bone region, there was no significant difference related to the bone area between the OVX rats ( $3.19 \pm 0.73 \text{ mm}^2$ ) and the control group ( $2.81 \pm 0.48 \text{ mm}^2$ ). Labeled osteons were found in all OVX rats (Figure 3), indicating activated bone remodeling in the area. The average number of labeled osteons in OVX rats ( $2.48 \pm 1.03$  per  $\text{mm}^2$ ) was significantly higher ( $P < 0.01$ ) than the one in the control group ( $0.89 \pm 0.43$  per  $\text{mm}^2$ ). Histomorphometric assessment disclosed that intracortical MAR ( $P < 0.01$ ), surface-based BFR ( $P < 0.01$ ), and intracortical BFR ( $P < 0.01$ ) were all significantly stimulated in OVX rats (Figure 4(a)).

In nonalveolar regions, no significant difference in the bone area between OVX rats ( $4.28 \pm 0.38 \text{ mm}^2$ ) and the control group ( $4.33 \pm 0.22 \text{ mm}^2$ ) was detected. The number of labeled osteons in OVX rats ( $0.43 \pm 0.18$  per  $\text{mm}^2$ ) was significantly higher ( $P < 0.05$ ) than in the control group ( $0.19 \pm 0.17$  per  $\text{mm}^2$ ). Compared to the alveolar bone region, the number of labeled osteons was much less than in the nonalveolar bone region in both OVX rats ( $2.48 \pm 1.03$  versus  $0.43 \pm 0.18$  per  $\text{mm}^2$ ) and the control group ( $0.89 \pm 0.43$  versus  $0.19 \pm 0.17$  per  $\text{mm}^2$ ). In OVX rats, intracortical BFR was significantly increased compared to the control group. Regarding MAR and surface-based BFR, no significant difference between OVX rats and the control group was found (Figure 4(b)).

**3.3.2. Bone Modeling.** The MAR ( $1.47 \pm 0.47 \mu\text{m}/\text{day}$ ) and surface-based BFR ( $0.99 \pm 0.36 \mu\text{m}^3/\mu\text{m}^2/\text{day}$ ) in OVX rats were significantly higher ( $P < 0.01$ ) in the surface adjacent

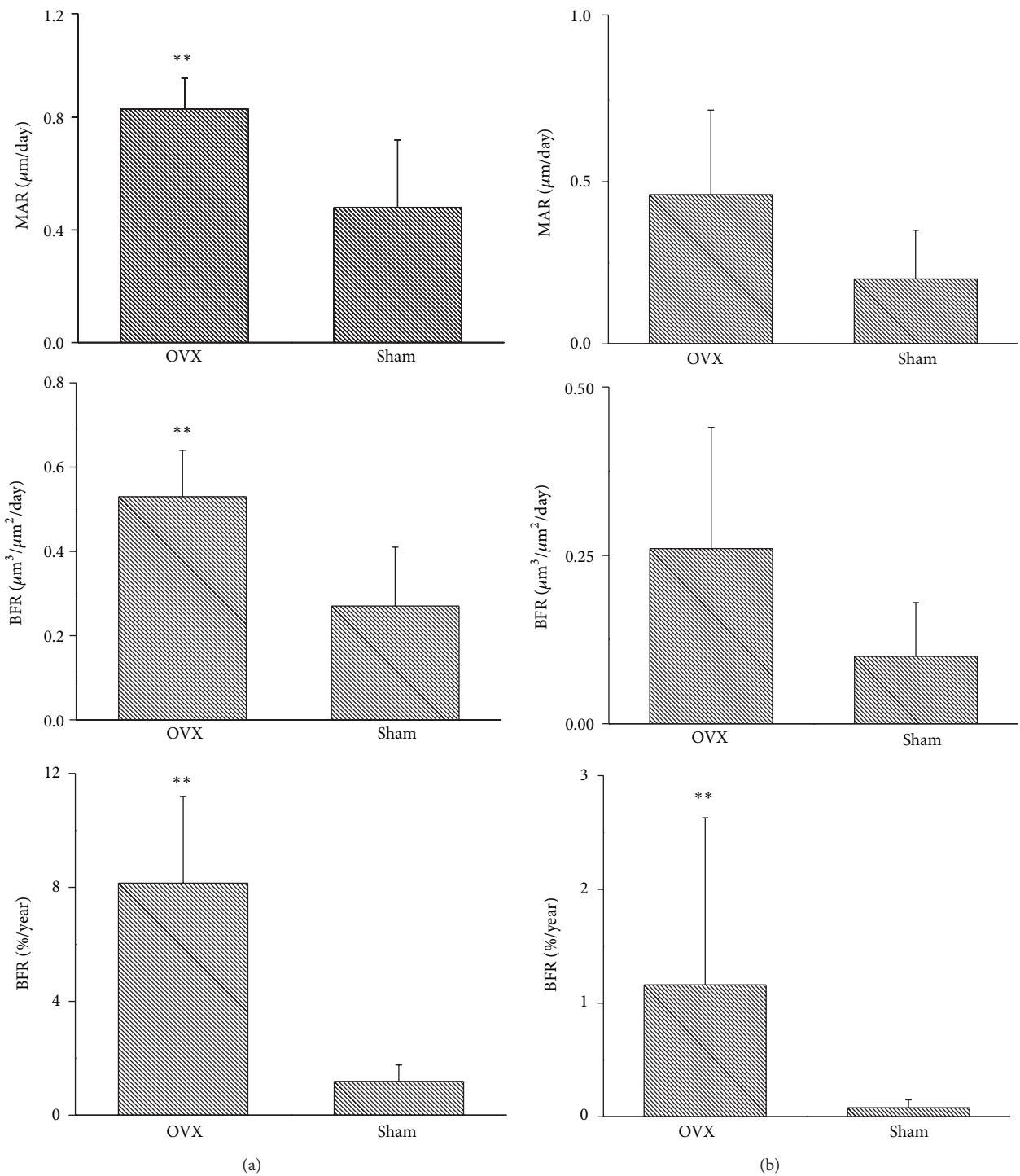


FIGURE 4: Ovariectomy stimulates remodeling activity in mandible of rat. In the alveolar cortical region (a), MAR, surface-based BFR ( $\mu\text{m}^3/\mu\text{m}^2/\text{day}$ ), and intracortical BFR (% year) are significantly higher in OVX rats than in the control group. In the nonalveolar region (b), intracortical BFR (% year) is significantly increased in OVX group, whereas MAR and surface-based BFR ( $\mu\text{m}^3/\mu\text{m}^2/\text{day}$ ) show no significant differences. MAR: mineral apposition rate and BFR: bone formation rate. \*\*  $P < 0.01$ .

to the periodontal ligament compared to those in the control group ( $0.53 \pm 0.11 \mu\text{m}/\text{day}$ ;  $0.16 \pm 0.05 \mu\text{m}^3/\mu\text{m}^2/\text{day}$ ).

#### 4. Discussion

Primates and dogs represent ideal animal models to investigate diseases characterized by abnormal intracortical remodeling. Both models show intracortical remodeling throughout the skeleton, just like humans [13, 19]. Ethical issues together with high expenses, however, do restrict their laboratory use. Rodents have been used instead to study these conditions, but their model value is limited because these animals usually do not display intracortical remodeling [13].

Some studies reported that intracortical remodeling in rodents could be stimulated under pathological conditions [8–10]. These findings raised the interest of using a “modified” rodent model mimicking human bone conditions to investigate various bone diseases. Some studies have demonstrated that ovariectomy remarkably stimulated intracortical remodeling in long bones of rats and mice [8]; however, the influence of ovariectomy on jawbones has not yet been fully understood.

Jawbones have a unique structure and undergo the highest intracortical remodeling rate throughout the skeleton [11, 20]. Many diseases associated with abnormal intracortical remodeling, such as BRONJ, affect the alveolar bone only [21]. Therefore it is of great interest to establish a rodent model which mimics the intracortical bone remodeling of the human skeleton.

This study investigated radiographic and histomorphometric changes in mandibular cancellous and cortical bones of OVX rats. Consistent with previous studies, both trabecular bone volume and bone mineral density decreased significantly after surgery [22, 23].

Histomorphometry is considered to be the gold standard in dynamic bone research. Better than other methods which estimate the remodeling status detecting humeral biomarkers, it may provide site-specific information directly by measuring MAR and BFR at different time points using the fluorochrome sequential labeling approach [15].

As mature mammals routinely undergo remodeling in cortical bones, the place where bone resorption and bone formation occur simultaneously, BFR evaluation might provide insight into the intracortical remodeling rate. In this study, active intracortical bone remodeling characterized by labeled osteons in the cortical bone region was found in both OVX rats and the control group. Rats after sham surgery manifested a very low-rate mandibular remodeling, whereas OVX rats disclosed significantly increased remodeling rates. In the alveolar region, ovariectomy stimulated a six-time higher intracortical BFR compared with that in control animals. These findings were similar to a previous report by Kubek et al. which so far is the only study addressing this issue in mandibles in a mouse model [10].

In the bone surface attached to the periodontal ligament, where bone modeling primarily takes place [24], a significantly increased bone formation rate was detected in OVX rats. On the contrary to this study, Kubek et al. [10] did

not find any significant increase in bone formation. This discrepancy may be attributed to the difference of animal species (C3H mice versus SD rat) and/or the length of the experiment, 8 weeks versus 18 weeks after surgery. Early after ovariectomy, the bone resorption surpasses the bone formation leading to bone loss; thereafter both processes reach a steady state. The time needed to reach this steady state varies in rats between 90 and 270 days [25]. To ensure that the analysis was performed during the steady state, a long experimental period of 18 weeks was selected in the here presented study.

The study of Kubek et al. [10] confirmed that OVX mice represented a useful tool to study BRONJ. Compared to mice, rats might represent a more versatile animal model in the research field of BRONJ as they also offer other investigations related to bone remodeling processes such as ligature induced-periodontal diseases or pulp-exposure induced periapical infections inducing BRONJ. Such conditions are technically difficult to be mimicked in mice because of the smaller size of teeth and jawbones.

#### 5. Conclusions

This study demonstrated that ovariectomy can stimulate intracortical remodeling in rat jawbones, to the authors' knowledge, for the first time. It might be taken into consideration that OVX rats are useful to study various bone diseases associated with abnormal intracortical bone remodeling processes, such as BRONJ.

#### Conflict of Interests

The authors declare that there is no conflict of interests regarding the publication of this paper.

#### Acknowledgments

This study was supported by the General Research Fund (HKU785412), Research Grant Council of Hong Kong. The authors appreciate the valuable technical assistance provided by Orthopedic Research Centre, Department of Orthopedics and Traumatology of the Li Ka Shing Faculty of Medicine, The University of Hong Kong.

#### References

- [1] L. Dalle Carbonare, M. T. Valenti, F. Bertoldo et al., “Bone microarchitecture evaluated by histomorphometry,” *Micron*, vol. 36, no. 7-8, pp. 609–616, 2005.
- [2] A. M. Parfitt, “The cellular basis of bone remodeling: the quantum concept reexamined in light of recent advances in the cell biology of bone,” *Calcified Tissue International*, vol. 36, no. 1, pp. S37–S45, 1984.
- [3] G. S. Beaupre, T. E. Orr, and D. R. Carter, “An approach for time-dependent bone modeling and remodeling—theoretical development,” *Journal of Orthopaedic Research*, vol. 8, no. 5, pp. 651–661, 1990.
- [4] D. N. Kalu, “The ovariectomized rat model of postmenopausal bone loss,” *Bone and Mineral*, vol. 15, no. 3, pp. 175–191, 1991.

- [5] G. Arcieri, E. Griffith, G. Gruenewaldt et al., "A survey of clinical experience with ciprofloxacin, a new quinolone antimicrobial," *Journal of Clinical Pharmacology*, vol. 28, no. 2, pp. 179–189, 1988.
- [6] R. T. Turner, G. L. Evans, and G. K. Wakley, "Mechanism of action of estrogen on cancellous bone balance in tibiae of ovariectomized growing rats: inhibition of indices of formation and resorption," *Journal of Bone and Mineral Research*, vol. 8, no. 3, pp. 359–366, 1993.
- [7] M. Tanaka, E. Toyooka, S. Kohno, H. Ozawa, and S. Ejiri, "Long-term changes in trabecular structure of aged rat alveolar bone after ovariectomy," *Oral Surgery, Oral Medicine, Oral Pathology, Oral Radiology, and Endodontics*, vol. 95, no. 4, pp. 495–502, 2003.
- [8] C. Y. Li, M. B. Schaffler, H. T. Wolde-Semait, C. J. Hernandez, and K. J. Jepsen, "Genetic background influences cortical bone response to ovariectomy," *Journal of Bone and Mineral Research*, vol. 20, no. 12, pp. 2150–2158, 2005.
- [9] W. S. S. Jee, S. Mori, X. J. Li, and S. Chan, "Prostaglandin E<sub>2</sub> enhances cortical bone mass and activates intracortical bone remodeling in intact and ovariectomized female rats," *Bone*, vol. 11, no. 4, pp. 253–266, 1990.
- [10] D. J. Kubek, D. B. Burr, and M. R. Allen, "Ovariectomy stimulates and bisphosphonates inhibit intracortical remodeling in the mouse mandible," *Orthodontics and Craniofacial Research*, vol. 13, no. 4, pp. 214–222, 2010.
- [11] L. P. Garetto, J. Chen, J. A. Parr, and W. E. Roberts, "Remodeling dynamics of bone supporting rigidly fixed titanium implants: a histomorphometric comparison in four species including humans," *Implant dentistry*, vol. 4, no. 4, pp. 235–243, 1995.
- [12] N. M. H. McLeod, V. Patel, A. Kusanale, S. N. Rogers, and P. A. Brennan, "Bisphosphonate osteonecrosis of the jaw: a literature review of UK policies versus international policies on the management of bisphosphonate osteonecrosis of the jaw," *The British Journal of Oral and Maxillofacial Surgery*, vol. 49, no. 5, pp. 335–342, 2011.
- [13] J. Jowsey, "Studies of Haversian systems in man and some animals," *Journal of Anatomy*, vol. 100, no. 4, pp. 857–864, 1966.
- [14] X. L. Liu, C. L. Li, W. W. Lu, W. X. Cai, and L. W. Zheng, "Skeletal site-specific response to ovariectomy in a rat model: change in bone density and microarchitecture," *Clinical Oral Implants Research*, 2014.
- [15] S. M. van Gaalen, M. C. Kruyt, R. E. Geuze, J. D. de Bruijn, J. Alblas, and W. J. A. Dhert, "Use of fluorochrome labels in in vivo bone tissue engineering research," *Tissue engineering Part B: Reviews*, vol. 16, no. 2, pp. 209–217, 2010.
- [16] A. M. Parfitt, M. K. Drezner, F. H. Glorieux et al., "Bone histomorphometry: standardization of nomenclature, symbols, and units: report of the ASBMR Histomorphometry Nomenclature Committee," *Journal of Bone and Mineral Research*, vol. 2, no. 6, pp. 595–610, 1987.
- [17] J. Foldes, M.-S. Shih, and A. M. Parfitt, "Frequency distributions of tetracycline-based measurements: implications for the interpretation of bone formation indices in the absence of double-labeled surfaces," *Journal of Bone and Mineral Research*, vol. 5, no. 10, pp. 1063–1067, 1990.
- [18] D. W. Dempster, J. E. Compston, M. K. Drezner et al., "Standardized nomenclature, symbols, and units for bone histomorphometry: a 2012 update of the report of the ASBMR Histomorphometry Nomenclature Committee," *Journal of Bone and Mineral Research*, vol. 28, no. 1, pp. 2–17, 2013.
- [19] M. L. Hillier and L. S. Bell, "Differentiating human bone from animal bone: a review of histological methods," *Journal of Forensic Sciences*, vol. 52, no. 2, pp. 249–263, 2007.
- [20] S. S. Huja, S. A. Fernandez, K. J. Hill, and Y. Li, "Remodeling dynamics in the alveolar process in skeletally mature dogs," *The Anatomical Record A: Discoveries in Molecular, Cellular, and Evolutionary Biology*, vol. 288, no. 12, pp. 1243–1249, 2006.
- [21] C. Walter, K. A. Grötz, M. Kunkel, and B. Al-Nawas, "Prevalence of bisphosphonate associated osteonecrosis of the jaw within the field of osteonecrosis," *Supportive Care in Cancer*, vol. 15, no. 2, pp. 197–202, 2007.
- [22] S. Kuroda, H. Mukohyama, H. Kondo et al., "Bone mineral density of the mandible in ovariectomized rats: analyses using dual energy X-ray absorptiometry and peripheral quantitative computed tomography," *Oral Diseases*, vol. 9, no. 1, pp. 24–28, 2003.
- [23] S. Kawamoto and E. Nagaoka, "The effect of oestrogen deficiency on the alveolar bone resorption caused by traumatic occlusion," *Journal of Oral Rehabilitation*, vol. 27, no. 7, pp. 587–594, 2000.
- [24] B. Melsen, "Tissue reaction to orthodontic tooth movement—a new paradigm," *European Journal of Orthodontics*, vol. 23, no. 6, pp. 671–681, 2001.
- [25] P. P. Lelovas, T. T. Xanthos, S. E. Thorma, G. P. Lyritis, and I. A. Dontas, "The laboratory rat as an animal model for osteoporosis research," *Comparative Medicine*, vol. 58, no. 5, pp. 424–430, 2008.